

ECCOMAS
European Community on
Computational Methods in
Applied Sciences



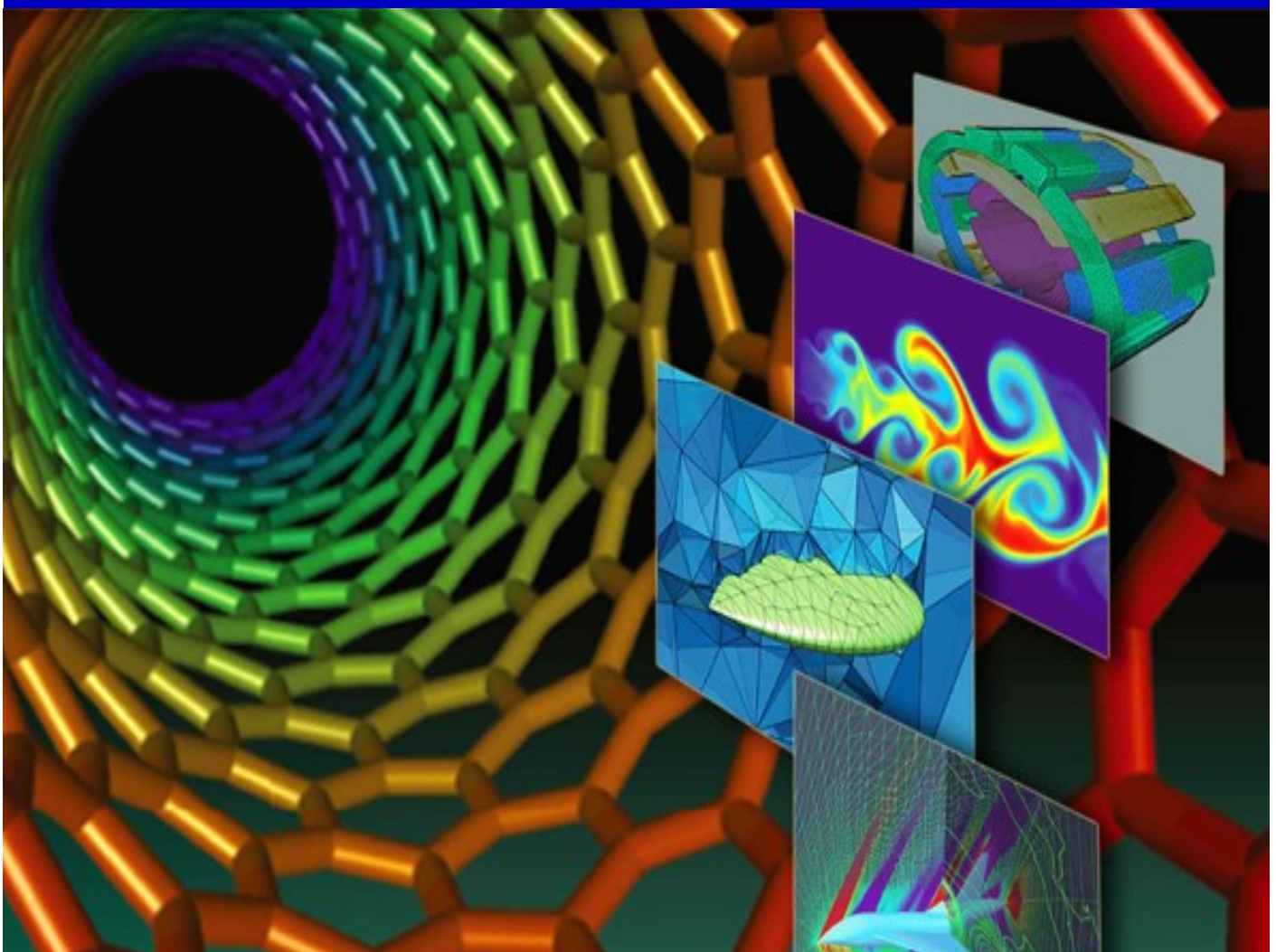
SEECCM III

3rd South-East European
Conference on Computational Mechanics

PROCEEDINGS

An IACM Special Interest Conference

M. Papadrakakis, M. Kojic, I. Tuncer (Eds)



SEECCM III

South-East European Conference on Computational Mechanics

Proceedings of the 3rd South-East European Conference
on Computational Mechanics
Held in Kos Island, Greece
12-14 June 2013

Edited by:

M. Papadrakakis

National Technical University of Athens, Greece

M. Kojic

Serbian Academy of Sciences and Arts, Serbia

I. Tuncer

Middle East Technical University, Turkey

A publication of:

Institute of Structural Analysis and Antiseismic Research
School of Civil Engineering
National Technical University of Athens (NTUA)
Greece

SEECCM III

South-East European Conference on Computational Mechanics

M. Papadrakakis, M. Kojic, I. Tuncer (Eds)

First Edition, February 2014

©The authors

ISBN : **978-960-99994-4-1**

PREFACE

This volume contains the full-length papers presented in the Proceedings of the 3rd South-East European Conference on Computational Mechanics (SEECCM III) that was held on June 12-14, 2013 on the Kos Island, Greece.

SEECCM III, is a special interest conference of ECCOMAS and IACM. Following the growing success of International and National Conferences on Computational Mechanics worldwide, the National Associations of Computational Mechanics of the South-East European countries decided to launch an initiative to promote achievements in Computational Mechanics in the South-East European Region. The first conference of this series was held at Kragujevac, Serbia in 2006 and the second on the island of Rhodes, Greece in 2009. The purpose of the Conference is to encourage research and development among young researchers, stimulate education in Universities and disseminate modern trends amongst scientists and engineers in the growing field of Simulation-Based Engineering Sciences. The SEECCM III Conference is supported by the National Technical University of Athens, Greece, the University of Kragujevac, Serbia, the Middle East Technical University, Turkey, the Greek Association for Computational Mechanics, the Serbian Association for Computational Mechanics, the Turkish National Committee on Theoretical and Applied Mechanics and the John Argyris Foundation.

The editors of this volume would like to thank all authors for their contributions. Special thanks go to the colleagues who contributed to the organization of the Minisymposia and to the reviewers who, with their work, contributed to the scientific quality of this e-book.

M. Papadrakakis

National Technical University of Athens, Greece

M. Kojic

Serbian Academy of Sciences and Arts, Serbia

I. Tuncer

Middle East Technical University, Turkey

ACKNOWLEDGEMENTS

The conference organizers acknowledge the support towards the organization of the “3rd South-East European Conference on Computational Mechanics” to the following organizations:

- Greek Association for Computational Mechanics (GRACM)
- Serbian Association for Computational Mechanics (SACM)
- Turkish National Committee on Theoretical and Applied Mechanics (TCNTAM)
- National Technical University of Athens, Greece
- Technical University of Crete, Greece
- John Argyris Foundation

Plenary Speakers and Invited Session Organizers

We would also like to thank the Plenary and Semi-Plenary Speakers and the Minisymposia Organizers for their help in the setting up of a high standard Scientific Programme.

Plenary Speakers: Jiun-Shyan Chen, Ekkehard Ramm, Paul Steinmann

Semi-Plenary Speakers: Sergio Idelsohn, Hermann Matthies, Nicolas Moës, Ernst Rank

MS Organizers: Guillaume Anciaux, Domenico Asprone, Ferdinando Auricchio, J-S Chen, Sheng-Wei Chi, Kent Danielson, George Deodatis, Themis Exarchos, Nenad Filipovic, Dimitris Fotiadis, Georgios Georgiou, Ulgen Gulcat, Kostas Housiadas, Spyros Karamanos, David Littlefield, Hermann Matthies, Nicolas Moës, Marco Paggi, Vissarion Papadopoulos, Manolis Papadrakakis, Alessandro Reali, Bojana Rosic, Jason Roth, Radovan Slavković, George Stefanou, Miroslav Živković

SUMMARY

Preface	iii
Acknowledgements	iv
Contents	vii
Minisymposia	
MS 1: Meshless Methods	1
<i>Organized by Ferdinando Auricchio and Domenico Asprone</i>	
MS 5: Meshfree and Particle Methods for Severe Loadings	13
<i>Organized by Kent Danielson, J-S Chen, Sheng-Wei Chi, David Littlefield and Jason Roth</i>	
MS 6: Computational Modeling of Cardiovascular Diseases	36
<i>Organized by Nenad Filipovic, Dimitris Fotiadis and Themis Exarchos</i>	
MS 8: Computational Non-Newtonian Fluid Mechanics	70
<i>Organized by Georgios Georgiou and Kostas Housiadas</i>	
MS 10: Some Interaction Problems in Computational Mechanics	94
<i>Organized by Ulgen Gulcat</i>	
MS 12: Numerical Implementation on Constitutive Models	181
<i>Organized by Spyros Karamanos</i>	
MS 15: Computational Contact Mechanics	205
<i>Organized by Nicolas Moës, Guillaume Anciaux and Marco Paggi</i>	
MS 17: Isogeometric Methods	260
<i>Organized by Alessandro Reali and Ferdinando Auricchio</i>	
MS 20: Computational Methods in the Study of Composite Materials	294
<i>Organized by Eustathios Theotokoglou and E. Sideridis</i>	
MS 21: Application of Finite Element Methods for the Analysis and Design of Steel and Composite Structures	312
<i>Organized by Euripidis Mistakidis</i>	
MS 22: The Multiscale Stochastic Finite Element Method	325
<i>Organized by George Stefanou, George Deodatis, Vissarion Papadopoulos and Manolis Papadrakakis</i>	
MS 24: Problems with Heterogeneous Materials	336
<i>Organized by Hermann Matthies, Radovan Slavković, Miroslav Živković and Bojana Rosic</i>	

Regular Sessions

RS 1: Biomechanics	358
RS 2: CAD, CAM and CAE	381
RS 3: Computational Environmental Science	394
RS 4: Computational Nanoscience and Nanotechnology	411
RS 5: Computational Solid and Structural Mechanics	455
RS 7: FEM: Modelling and Simulation	548
RS 8: Fluid Mechanics and Aerodynamics	599
RS 10: Geomechanics	621
RS 13: Optimization	639
RS 15: Uncertainty and Stochastic Analysis	682

CONTENTS

Minisymposia

MS 1: MESHLESS METHODS

STIFFNESS MATRIX COMPUTATION FOR ELEMENT FREE GALERKIN METHODS ON GPU	1
<i>Karatarakis Alexander, Metsis Panagiotis, Papadarakakis Manolis</i>	

MS 5: MESHFREE AND PARTICLE METHODS FOR SEVERE LOADINGS

SECOND ORDER GODUNOV SPH FOR HIGH VELOCITY IMPACT DYNAMICS	13
<i>Connolly Adam, Iannucci Lorenzo, Hillier R., Pope Dan</i>	

MS 6: COMPUTATIONAL MODELING OF CARDIOVASCULAR DISEASES

A COMPUTATIONAL STUDY OF THE INJECTION THERAPY FOR MYOCARDIAL INFARCTION DURING THE NECROTIC STAGE	36
<i>Skatulla Sebastian, Legner Dieter, Rama Ritesh, Mbewu James, Reddy B. D., Davis Neil, Franz Thomas</i>	

MODELING AND CORRELATION OF PLAQUE SIZE WITH HISTOLOGICAL AND BLOOD ANALYSIS DATA FOR ANIMAL RABBIT EXPERIMENTS	52
<i>Radovic Milos, Milosevic Zarko, Nikolic Dalibor, Saveljic Igor, Obradovic Milica, Petrovic Dejan, Zdravkovic Nebojsa, Teng Zhongzhao, Bird Joseph, Filipovic Nenad</i>	

MULTISCALE MODELING OF MOLECULAR DIFFUSION IN TISSUE	58
<i>Milosevic Miljan, Kojic Milos, Kojic Nikola, Ferrari Mauro, Ziemys Arturas</i>	

MS 8: COMPUTATIONAL NON-NEWTONIAN FLUID MECHANICS

SOLUTION OF VISCOPLASTIC FLOWS WITH THE FINITE VOLUME/MULTIGRID METHOD	70
<i>Syrakos Alexandros, Georgiou Georgios, Alexandrou Andreas</i>	

CESSATION FLOWS OF BINGHAM PLASTICS WITH SLIP AT THE WALL	82
<i>Damianou Yiolanda, Philippou Maria, Kaoullas George, Georgiou Georgios</i>	

MS 10: SOME INTERACTION PROBLEMS IN COMPUTATIONAL MECHANICS

A PARALLEL FULLY COUPLED APPROACH FOR LARGE-SCALE FLUID-STRUCTURE INTERACTION PROBLEMS	94
<i>Eken Ali, Sahin Mehmet</i>	

FLAPPING THIN AIRFOIL INTERACTING WITH THE GROUND	117
<i>Gülçat Ülgen</i>	

ATMOSPHERIC TURBULENT FLOW SOLUTIONS COUPLED WITH A MESOSCALE WEATHER PREDICTION MODEL	127
<i>Leblebici Engin, Ahmet Gökhan, Tuncer İsmail Hakkı</i>	
APPLICATION OF THE EFMM TO FLUID-STRUCTURE COUPLED ANALYSIS AND ITS PARALLELIZATION METHOD	137
<i>Nagaoka S., Nakabayashi Y., Yagawa G.</i>	
REDUCED ORDER MODELLING OF HIGH-FIDELITY COMPUTATIONAL FLUID-STRUCTURE INTERACTION ANALYSIS FOR AEROELASTIC SYSTEMS	149
<i>Acar Pinar, Nikbay Melike</i>	
DYNAMIC BEHAVIOUR OF LAMINATED PLATES SUBJECTED TO THERMOMECHANICAL LOADS	172
<i>Turkmen Halit, Susler Sedat, Kazanci Zafer</i>	
 MS 12: NUMERICAL IMPLEMENTATION ON CONSTITUTIVE MODELS	
A METRIC THEORY OF RATE INDEPENDENT AND RATE DEPENDENT PLASTICITY: THEORETICAL AND COMPUTATIONAL ASPECTS	181
<i>Panoskaltzis Vassilis, Soldatos Dimitris</i>	
 MS 15: COMPUTATIONAL CONTACT MECHANICS	
ABOUT THE IDENTIFICATION OF GENERIC TRIBOLOGICAL PARAMETERS, SOPHISTICATED COMPLETELY ANALYTICAL CONTACT MODELLING AND THE EFFECTIVE INDENTER CONCEPT APPLIED TO A COMPREHENSIVE 3D INCREMENTAL WEAR AND FRETTING MODEL FOR LAYERED SURFACES	205
<i>Schwarzer Norbert</i>	
QUALITATIVE FAILURE ANALYSIS ON LAMINATE STRUCTURES USING COMPREHENSIVE ANALYTICAL LINEAR ELASTIC CONTACT MODELLING	224
<i>Schwarzer Norbert, Heuer-Schwarzer Peggy</i>	
ROBUST DESIGN OPTIMIZATION IN PARALLEL COMPUTING ENVIRONMENT	245
<i>Lagaros Nikos, Papadrakakis Manolis</i>	
 MS 17: ISOGOMETRIC METHODS	
THE CHOICE OF QUADRATURE IN NURBS-BASED ISOGOMETRIC ANALYSIS	260
<i>Calabrò Francesco, Manni Carla</i>	
AN UNLOCKED IMPLICIT G1 CONTINUITY MULTI PATCH B-SPLINE INTERPOLATION FOR THE ANALYSIS OF 3D KIRCHHOFF LOVE ROD ELEMENTS	268
<i>Greco Leopoldo, Cuomo Massimo, Impollonia Nicola</i>	
COMPUTATION OF THE ISOGOMETRIC ANALYSIS STIFFNESS MATRIX ON GPU	278
<i>Karatarakis Alexander, Karakitsios Panagiotis, Papadrakakis Manolis</i>	

MS 20: COMPUTATIONAL METHODS IN THE STUDY OF COMPOSITE MATERIALS

- STUDY OF ASYMMETRIC GLASS REINFORCED PLASTIC BEAMS IN OFF-AXIS FOUR-POINT BENDING 294
Theotokoglou Efstathios, Sideridis Emilios

MS 21: APPLICATION OF FINITE ELEMENT METHODS FOR THE ANALYSIS AND DESIGN OF STEEL AND COMPOSITE STRUCTURES

- RESISTANCE OF DOOR OPENINGS IN TOWERS FOR WIND TURBINES 312
Tran Anh Tuan, Veljkovic Milan, Rebelo Carlos, Simões da Silva Luís

MS 22: THE MULTISCALE STOCHASTIC FINITE ELEMENT METHOD

- MODELING THE FAILURE OF STRUCTURES WITH STOCHASTIC PROPERTIES IN A SEQUENTIALLY LINEAR ANALYSIS FRAMEWORK 325
Georgioudakis Manolis, Stefanou George, Papadrakakis Manolis

MS 24: PROBLEMS WITH HETEROGENEOUS MATERIALS

- EMBANKMENT DAM STABILITY ANALYSIS USING FEM 336
Rakić Dragan, Živković Miroslav, Vulović Snežana, Divac Dejan, Slavković Radovan, Milivojević Nikola
- IMPLICIT INTEGRATION METHOD OF SHAPE MEMORY ALLOYS CONSTITUTIVE MODEL 348
Dunić Vladimir, Slavković Radovan, Busarac Nenad, Slavković Vukašin, Živković Miroslav

Regular Sessions

RS 1: BIOMECHANICS

- BLOOD FLOW SIMULATION IN THE AORTA PASSING THROUGH THE AORTIC ORIFICE BY VIRTUAL FLUX METHOD 358
Fukui Tomohiro, Morinishi Koji
- MATERIAL CHARACTERIZATION ISSUES IN FEA OF LONG BONES 370
Korunovic Nikola, Trajanovic Miroslav, Stevanovic Dalibor, Vitkovic Nikola, Stojkovic Milos, Milovanovic Jelena, Ilic Dragana

RS 2: CAD, CAM AND CAE

- DESIGN STUDY OF ANATOMICALLY SHAPED LATTICED SCAFFOLDS FOR THE BONE TISSUE RECOVERY 381
Stojkovic Milos, Korunovic Nikola, Trajanovic Miroslav, Milovanovic Jelena, Trifunovic Milan, Vitkovic Ni

RS 3: COMPUTATIONAL ENVIRONMENTAL SCIENCE

SIMULATING LANDFILL AERATION SYSTEMS USING COMPUTATIONAL FLUID DYNAMICS TECHNIQUES	394
<i>Fytanidis Dimitrios, Voudrias Evangelos</i>	

RS 4: COMPUTATIONAL NANOSCIENCE AND NANOTECHNOLOGY

VIBRATION AND ELASTIC BUCKLING ANALYSES OF SINGLE-WALLED CARBON NANOCONES	411
<i>Baykasoglu Cengiz, Celebi Alper Tunga, Icer Esra, Mugan Ata</i>	
NUMERICAL ANALYSIS ABOUT THE INFLUENCE OF INAPPROPRIATE SHAPE OF THE CROSS-SECTION OF MICROCHANNELS IN LAMINAR FLOW	425
<i>Hollweg Fabiano da Rosa, Oliveski Rejane de César, Dalla Corte Marcelo</i>	
NONLINEAR FRACTURE ANALYSIS OF CARBON NANOTUBES WITH STONE-WALES DEFECTS	446
<i>Baykasoglu Cengiz, Icer Esra, Celebi Alper Tunga, Mugan Ata</i>	

RS 5: COMPUTATIONAL SOLID AND STRUCTURAL MECHANICS

FAST DETECTION OF CHAOTIC OR REGULAR BEHAVIOR OF DOUBLE PENDULUM SYSTEM: APPLICATION OF THE FAST NORM VECTOR INDICATOR METHOD	455
<i>Dumitru Deleanu</i>	
WARPING TRANSMISSION IN 3-D BEAM ELEMENT INCLUDING SECONDARY TORSIONAL MOMENT DEFORMATION EFFECT	470
<i>Sapountzakis Evangelos, Tsipiras Vasileios, Gkesos Pavlos</i>	
A HYBRID DISPLACEMENT BOUNDARY ELEMENT FORMULATION FOR REISSNER PLATE WITH QUADRATIC ELEMENTS	481
<i>Naga Taha, Rashed Youssef</i>	
NUMERICAL INVESTIGATION OF A FULL-SCALE RC BRIDGE THROUGH 3D DETAILED NONLINEAR LIMIT-STATE SIMULATIONS	492
<i>Markou George</i>	
DESIGN OF RC SECTIONS IN THE ULTIMATE LIMIT STATE UNDER BENDING AND AXIAL FORCE ACCORDING TO EC2	520
<i>Plevris Vagelis, Papazafeiropoulos George, Papadrakakis Manolis</i>	

RS 7: FEM: MODELLING AND SIMULATION

COMPUTATIONAL SIMULATION OF CROSS ROLL STRAIGHTENING	548
<i>Petruska Jindrich, Navrat Tomas</i>	

GENERATING EMBEDDED REBAR ELEMENTS FOR LARGE-SCALE RC MODELS	556
<i>Markou George, Papadrakakis Manolis</i>	
NEURAL NETWORK APPROXIMATION OF THE MASONRY FAILURE UNDER BIAXIAL COMPRESSIVE STRESS	584
<i>Asteris Panagiotis, Plevris Vagelis</i>	
RS 8: FLUID MECHANICS AND AERODYNAMICS	
IMPROVING THE ACCURACY OF A FINITE-VOLUME METHOD FOR COMPUTING RADIATIVE HEAT TRANSFER IN THREE-DIMENSIONAL UNSTRUCTURED MESHES	599
<i>Lygidakis Georgios, Nikolos Ioannis</i>	
RS 10: GEOMECHANICS	
THE INFLUENCE OF PUMPING PARAMETERS IN FLUID-DRIVEN FRACTURES	621
<i>Sarris Ernestos, Papanastasiou Panos</i>	
RS 13: OPTIMIZATION	
STRUCTURAL AND MULTI-FUNCTIONAL OPTIMIZATION USING MULTIPLE PHASES AND A LEVEL-SET METHOD	639
<i>Allaire Grégoire, Jouve Francois, Michailidis Georgios</i>	
DISCRETE OPTIMIZATION APPROACH FOR STEEL FRAMES AND TRUSSES, BASED ON GENETIC ALGORITHM	650
<i>Balea Ioana, Hulea Radu, Stavroulakis Georgios</i>	
MULTI-OBJECTIVE SHAPE DESIGN OPTIMIZATION INTO AN EXTENDED FINITE ELEMENT METHOD (XFEM) FRAMEWORK	660
<i>Georgioudakis Manolis, Lagaros Nikos, Papadrakakis Manolis</i>	
EVALUATION OF WELDING RESIDUAL STRESS IN STAINLESS STEEL PIPES BY USING THE LCR ULTRASONIC WAVES	671
<i>Javadi Yashar, Plevris Vagelis</i>	
RS 15: UNCERTAINTY AND STOCHASTIC ANALYSIS	
ANALYSIS OF THE NONLINEAR STOCHASTIC DYNAMICS OF AN ELASTIC BAR WITH AN ATTACHED END MASS	682
<i>Cunha Jr Americo, Sampaio Rubens</i>	

STIFFNESS MATRIX COMPUTATION FOR ELEMENT FREE GALERKIN METHODS ON GPU

Alexander Karatarakis¹, Panagiotis Metsis² and Manolis Papadrakakis²

¹ Institute of Structural Analysis and Antiseismic Research National Technical University of Athens
Zografou Campus, Athens 15780
e-mail: alex@karatarakis.com

² Institute of Structural Analysis and Antiseismic Research National Technical University of Athens
Zografou Campus, Athens 15780
pmetsis@gmail.com, mpapadra@central.ntua.gr

Keywords: Meshless methods, Element Free Galerkin (EFG), preprocessing, stiffness matrix assembly, parallel computing, GPU acceleration

Abstract. *Meshless methods have a number of virtues in problems concerning crack growth and propagation, large displacements, strain localization and complex geometries, among other. Despite the fact that they do not rely on a mesh, meshless methods require a preliminary step for the identification of the correlation between nodes and Gauss points before building the stiffness matrix. This is implicitly performed with the mesh generation in FEM but must be explicitly done in EFG methods and can be time-consuming. Furthermore, the resulting matrices are more densely populated and the computational cost for the formulation and solution of the problem is much higher than the conventional FEM. This is mainly attributed to the vast increase in interactions between nodes and integration points due to their extended domains of influence. For these reasons, computing the stiffness matrix in EFG meshless methods is a very computationally demanding task which needs special attention in order to be affordable in real-world applications. In this paper, we address the pre-processing phase, dealing with the problem of defining the necessary correlations between nodes and Gauss points and between interacting nodes, as well as the computation of the stiffness matrix. A novel approach is proposed for the formulation of the stiffness matrix which exhibits several computational merits, one of which is its amenability to parallelization which allows the utilization of graphics processing units (GPUs) to accelerate computations.*

1. INTRODUCTION

In meshless methods (MMs) there is no need to construct a mesh, as in finite element method (FEM), which is often in conflict with the real physical compatibility condition that a continuum possesses [1]. Moreover, stresses obtained using FEM are discontinuous and less accurate while a considerable loss of accuracy is observed when dealing with large deformation problems because of element distortion. Furthermore, due to the underlying structure of the classical mesh-based methods, they are not well suited for treating problems with discontinuities that do not align with element edges. MMs were developed with the objective of eliminating part of the above mentioned difficulties [2]. With MMs, manpower time is limited to a minimum due to the absence of mesh and mesh related phenomena. Complex geometries are handled easily with the use of scattered nodes.

One of the first and most prominent meshless methods is the element free Galerkin (EFG) method introduced by Belytschko et al. [3]. EFG requires only nodal data, no element connectivity is needed to construct the shape functions. However a global background cell structure is necessary for the numerical integration. Moreover, since the number of interactions between nodes and/or integration points is heavily increased, due to large domains of influence, the resulting matrices are more densely populated and the computational cost for the formulation and solution of the problem is much higher than in the conventional FEM [3].

To improve the computational efficiency of MMs, parallel implementations like the MPI parallel paradigm has been used in large scale applications[4], [5] and several alternative methodologies have been proposed concerning the formulation of the problem. The smoothed FEM (SFEM) [6] couples FEM with meshless methods by incorporating a strain smoothing operation used in the mesh-free nodal integration method. The linear point interpolation method (PIM) [7] obtains the partial derivatives of shape functions effortlessly due to the local character of the radial basis functions. A coupled EFG/boundary element scheme [8], taking advantage of both the EFG and the boundary element method. Furthermore, solvers which perform an improved factorization of the stiffness matrix and use special algorithms for realizing the matrix-vector multiplication are proposed in [9], [10]. Divo and Kassab [11] presented a domain decomposition scheme on a meshless collocation method, where collocation expressions are used at each subdomain with artificial created interfaces. Wang et al. [7] presented a parallel reproducing kernel particle method (RKPM), using a particle overlapping scheme which significantly increases the number of shared particles and the time for communicating information between them. Recently, a novel approach for reducing the computational cost of EFG methods is proposed by employing domain decomposition techniques on the physical as well as on the algebraic domains [12]. In that work the solution of the resulting algebraic problems is performed with the dual domain decomposition FETI method with and without overlapping between the subdomains. The non-overlapping scheme has led to a significant decrease of the overall computational cost.

The present work aims at a drastic reduction of the computational effort required for the initialization phase and for assembling the stiffness matrix by implementing a novel node pair-wise procedure. It is believed that with the proposed computational handling of the pre-processing phase and the accelerated formulation of the stiffness matrix, together with recent improvements on the solution of the resulting algebraic equations [12], MMs are becoming computationally competitive and are expected to demonstrate their inherent advantages in solving real, large-scale engineering problems.

2. BASIC INGREDIENTS OF THE MESHLESS EFG METHOD

The approximation of a scalar function u in terms of Lagrangian coordinates in the meshless EFG method can be written as

$$u(\mathbf{x}, t) = \sum_{i \in S} \Phi_i(\mathbf{x}) u_i(t) \quad (1)$$

where Φ_i are the shape functions, u_i are the nodal values at particle i located at position \mathbf{x}_i , and S is the set of nodes i for which $\Phi_i(\mathbf{x}) \neq 0$. The shape functions in eq.(1) are only approximants and not interpolants, since $u_i \neq u(\mathbf{x}_i)$.

The shape functions Φ_i are obtained from the weight coefficients w_i , which are functions of a distant parameter $r = \|\mathbf{x}_i - \mathbf{x}\|/d_i$ where d_i defines the domain of influence (doi) of node i . The domain of influence is crucial to solution accuracy, stability and computational cost, as it defines the degree of continuity between the nodes and the bandwidth of the system matrices.

The approximation u^h is expressed as a polynomial of length m with non-constant coefficients. The local approximation around a point $\bar{\mathbf{x}}$, evaluated at a point \mathbf{x} is given by

$$u_L^h(\mathbf{x}, \bar{\mathbf{x}}) = \mathbf{p}^T(\mathbf{x}) \mathbf{a}(\bar{\mathbf{x}}) \quad (2)$$

where $\mathbf{p}(\mathbf{x})$ is a complete polynomial of length m and $\mathbf{a}(\bar{\mathbf{x}})$ contains non-constant coefficients that depend on \mathbf{x}

$$\mathbf{a}(\bar{\mathbf{x}}) = [a_0(\mathbf{x}) \quad a_1(\mathbf{x}) \quad a_2(\mathbf{x}) \quad \dots \quad a_m(\mathbf{x})]^T \quad (3)$$

In two dimensional problems, the linear basis $\mathbf{p}(\mathbf{x})$ is given by

$$\mathbf{p}^T(\mathbf{x}) = [1 \quad x \quad y], \quad m=3 \quad (4)$$

and the quadratic basis by

$$\mathbf{p}^T(\mathbf{x}) = [1 \quad x \quad y \quad x^2 \quad y^2 \quad xy], \quad m=6 \quad (5)$$

The unknown parameters $a_j(\mathbf{x})$ are determined at any point \mathbf{x} , by minimizing a functional $J(\mathbf{x})$ defined by a weighted average over all nodes $i \in 1, \dots, n$:

$$J(\mathbf{x}) = \sum_{i=1}^n w(\mathbf{x} - \mathbf{x}_i) [u_L^h(\mathbf{x}_i, \mathbf{x}) - u_i]^2 = \sum_{i=1}^n w(\mathbf{x} - \mathbf{x}_i) [\mathbf{p}^T(\mathbf{x}_i) \mathbf{a}(\mathbf{x}) - u_i]^2 \quad (6)$$

where the parameters u_i are specified by the difference between the local approximation $u_L^h(\mathbf{x}, \bar{\mathbf{x}})$ and the value u_i while the weight function satisfies the condition $w(\mathbf{x} - \mathbf{x}_i) \neq 0$. An extremum of $J(\mathbf{x})$ with respect to the coefficients $a_j(\mathbf{x})$ can be obtained by setting the derivative of J with respect to $\mathbf{a}(\mathbf{x})$ equal to zero. This condition gives the following relation

$$\mathbf{A}(\mathbf{x}) \mathbf{a}(\mathbf{x}) = \mathbf{W}(\mathbf{x}) \mathbf{u} \quad (7)$$

where

$$\mathbf{A}(\mathbf{x}) = \sum_{i=1}^n w(\mathbf{x} - \mathbf{x}_i) \mathbf{p}(\mathbf{x}_i) \mathbf{p}^T(\mathbf{x}_i) \quad (8)$$

$$\mathbf{W}(\mathbf{x}) = [w(\mathbf{x} - \mathbf{x}_1) \mathbf{p}(\mathbf{x}_1) \quad w(\mathbf{x} - \mathbf{x}_2) \mathbf{p}(\mathbf{x}_2) \quad \dots \quad w(\mathbf{x} - \mathbf{x}_n) \mathbf{p}(\mathbf{x}_n)] \quad (9)$$

Solving for $\mathbf{a}(\mathbf{x})$ in eq.(7) and substituting into eq.(2) the approximants u^h can be defined as follows:

$$u^h(\mathbf{x}) = \mathbf{p}^T(\mathbf{x}) [\mathbf{A}(\mathbf{x})]^{-1} \mathbf{W}(\mathbf{x}) \mathbf{u} \quad (10)$$

which together with eq.(1) leads to the derivation of the shape function Φ_i associated with node i at point \mathbf{x} :

$$\Phi_i(\mathbf{x}) = \mathbf{p}^T(\mathbf{x}) [\mathbf{A}(\mathbf{x})]^{-1} \mathbf{W}(\mathbf{x}_i) \quad (11)$$

A solution of a local problem $\mathbf{A}(\mathbf{x})\mathbf{z} = \mathbf{p}(\mathbf{x})$ of size $m \times m$ is performed whenever the shape functions are to be evaluated. This constitutes a drawback of moving least squares-based (MLS-based) MMs since the computational cost can be substantial and it is possible for the moment matrix $\mathbf{A}(\mathbf{x})$ to be ill conditioned [2].

The Galerkin weak form of the above formulation gives the discrete algebraic equation

$$\mathbf{K} \mathbf{u} = \mathbf{f} \quad (12)$$

with

$$\mathbf{K}_{ij} = \int_{\Omega} \mathbf{B}_i^T \mathbf{E} \mathbf{B}_j d\Omega \quad (13)$$

$$\mathbf{f}_i = \int_{\Gamma_i} \Phi_i \bar{\mathbf{t}} d\Gamma + \int_{\Omega} \Phi_i \mathbf{b} d\Omega \quad (14)$$

In 2D problems matrix \mathbf{B} is given by

$$\mathbf{B}_i = \begin{bmatrix} \Phi_{i,x} & 0 \\ 0 & \Phi_{i,y} \\ \Phi_{i,y} & \Phi_{i,x} \end{bmatrix} \quad (15)$$

and in 3D problems by

$$\mathbf{B}_i = \begin{bmatrix} \Phi_{j,x} & 0 & 0 \\ 0 & \Phi_{j,y} & 0 \\ 0 & 0 & \Phi_{j,z} \\ \Phi_{j,y} & \Phi_{j,x} & 0 \\ 0 & \Phi_{j,z} & \Phi_{j,y} \\ \Phi_{j,z} & 0 & \Phi_{j,x} \end{bmatrix} \quad (16)$$

Due to the lack of the Kronecker delta property of shape functions, the essential boundary conditions cannot be imposed the same way as in FEM. Several techniques are available such as Lagrange multipliers, penalty and EFG and FEM coupling.

For the integration of eq. (13), virtual background cells are considered by dividing the problem domain into integration cells over which a Gaussian quadrature is performed:

$$\int_{\Omega} \mathbf{f}(\mathbf{x}) d\Omega = \sum_J \mathbf{f}(\xi_J) \omega_{\Xi} \det J^{\xi}(\xi) \quad (17)$$

where ξ are the local coordinates and $\det J^{\xi}(\xi)$ is the determinant of the Jacobian.

3. GAUSS POINT-WISE FORMULATION OF THE STIFFNESS MATRIX

The stiffness matrix of eq. (13) is usually formed by adding the contributions of the products $\mathbf{B}_G^T \mathbf{E} \mathbf{B}_G$ of all Gauss points G to the stiffness matrix according to the formula:

$$\mathbf{K} = \sum_G \mathbf{B}_G^T \mathbf{E} \mathbf{B}_G = \sum_G \mathbf{Q}_G \quad (18)$$

where the deformation matrix \mathbf{B}_G is computed at the corresponding Gauss point. The

summation is performed for each Gauss point and affects all nodes within its domain of influence. Compared to FEM, the amount of calculations for performing this task is significantly higher since the domains of influence of Gauss points are much larger than the corresponding domains in FEM as is schematically shown in Fig. 1 for a domain discretized with EFG and FEM having equal number of nodes and Gauss points. Throughout this paper we do not address the issue of accuracy obtained by the two methods with the same number of nodes and Gauss points.

In FEM, each Gauss point is typically involved in element-level computations for the formation of the element stiffness matrix which is then added to the appropriate positions of the global stiffness matrix. Moreover, the shape functions and their derivatives are predefined for each element type and need to be evaluated on all combinations of nodes and Gauss points within each element. In EFG methods, however, the contribution of each Gauss point is directly added to the global stiffness matrix while the shape functions are not predefined and span across larger domains with a significantly higher amount of Gauss point-node interactions.

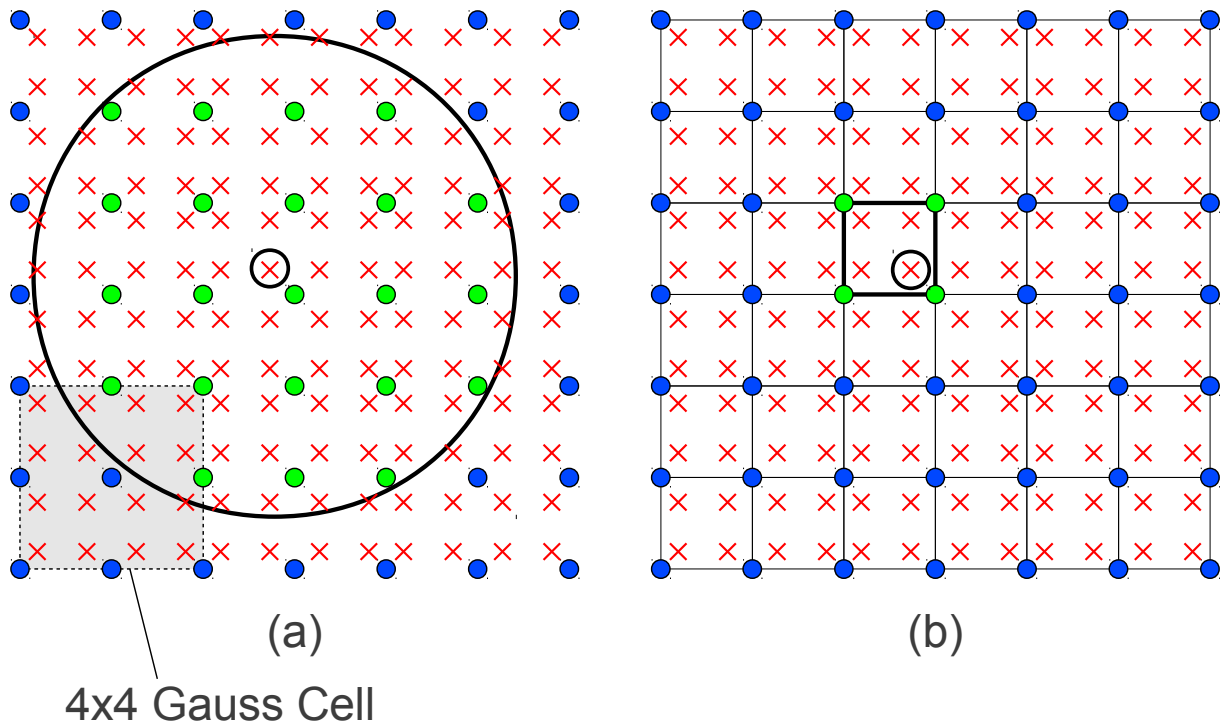


Fig. 1: Domain of influence of Gauss point \otimes in (a) EFG; (b) FEM, for the same number of nodes and Gauss points

Although, in EFG methods there is no need to construct a mesh, the correlation between nodes and Gauss points needs to be defined. This preliminary step before building the stiffness matrix is implicitly performed with the mesh creation in FEM but must be explicitly done in EFG methods and can be time-consuming if not appropriately handled. For the aforementioned reasons, computing the stiffness matrix in EFG meshless methods is a very computationally demanding task which needs special attention in order to be affordable in real-world applications.

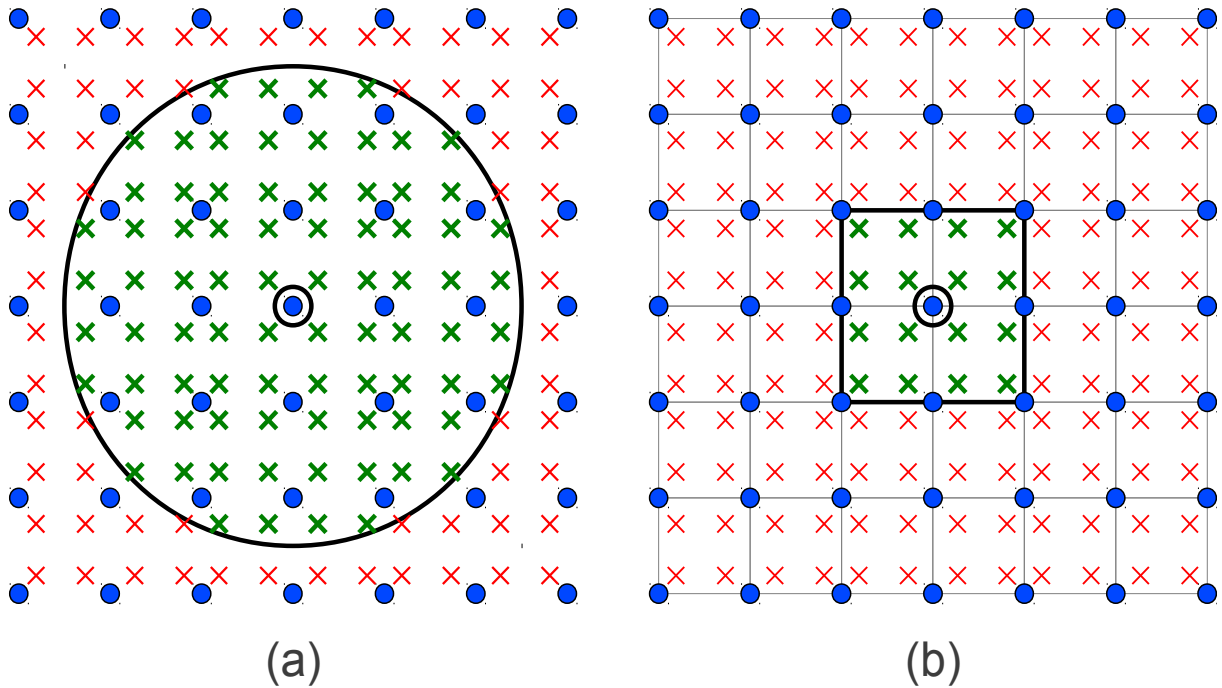


Fig. 2: Domain of influence of node  (a) EFG; (b) FEM, for the same number of nodes and Gauss points

3.1. Node-Gauss point correlation

In the initialization step, the basic entities are created, namely the nodes and the Gauss points together with their domains of influence. The domains of influence define the correlation between nodes and Gauss points. With the absence of an element mesh, the correlation of Gauss points and nodes must be established explicitly at the initialization phase.

A first approach is to search on the global physical domain for the Gauss points belonging to the domain of influence of each node. This approach performs a large amount of unnecessary calculations since the domains of influence are localized areas. In order to reduce the time spent for identifying the interaction between Gauss points and nodes, the search can be performed on Gauss regions.

A rectangular grid is created and we refer to each of the regions defined as a Gauss region. Each Gauss region contains a group of Gauss points. Given the coordinates of a particular node, it is immediately known in which region it is located. The search per node is conducted over the neighboring Gauss regions only instead of the global domain. Thus, regardless of the size of the problem, the search per node is restricted on a small number of Gauss regions.

The time required to define correlations in three 2D and three 3D elasticity problems with varying number of degrees of freedom (dof) are shown in Table 1. The 2D problems correspond to square domains and the 3D to cubic domains, with rectangular domains of influence (doi) with dimensionless parameter 2.5. These domains maximize the number of correlations and consequently the computational cost for the given number of nodes. In these examples, each Gauss region is equivalent to a single Gauss cell. Thus, in the 2D examples each Gauss cell contains 16 Gauss points (4×4 rule) and in the 3D examples 64 Gauss points ($4 \times 4 \times 4$ rule). The examples are run on a Core i7-980X which has 6 physical cores (12 logical cores) at 3.33GHz and 12MB cache. Each node can define its correlation independently of other nodes, which is amenable to parallel computations.

Example	Nodes	Gauss points	Search Time (seconds)		
			Global Serial	Regioned Serial	Regioned Parallel
2D-1	25.921	102.400	23	1,3	0,5
2D-2	75.625	300.304	300	3,4	1,0
2D-3	126.025	501.264	836	5,4	1,4
3D-1	9.221	64.000	7	3,7	0,9
3D-2	19.683	140.608	45	7,8	1,7
3D-3	35.937	262.144	157	15,7	3,3

Table 1: Computing time required for all node-Gauss point correlations

With the implementation of Gauss regions, the initialization phase of EFG methods in complex domains takes less time than FEM, since the generation of a finite element mesh can sometimes be laborious and time consuming [13]. At the end of the initialization step each node has a list of influencing Gauss points and each Gauss point has a list of influenced nodes.

3.2. Performance of the Gauss point-wise approach

The performance of the Gauss point-wise approach in the CPU is shown in Table 2. The proposed Gauss point-wise (GP) approach is compared with the “conventional” one which is a first approach that does not include several optimizations.

Example	dof	Gauss points	Time (seconds)		Ratio
			Conventional	Proposed GP	
2D-1	51.842	102.400	107	12	9
2D-2	152.250	300.304	313	34	9
2D-3	252.050	501.264	502	53	9
3D-1	27.783	64.000	2.374	241	10
3D-2	59.049	140.608	6.328	616	10
3D-3	107.811	262.144	13.302	1.165	11

Table 2: Computing time for the formulation of the stiffness matrix in the CPU implementations of the Gauss-point wise approach

4. NODE PAIR-WISE FORMULATION OF THE STIFFNESS MATRIX

An alternative way to perform the computation of the global stiffness matrix is the proposed node pair-wise approach. The computation of the global stiffness coefficient \mathbf{K}_{ij} is performed for all interacting $i-j$ nodes and is formed from contribution by the shared Gauss points of their domains of influence. Fig. 3 depicts two interacting nodes as a result of having common Gauss points in the intersection of their domains of influence and one node that is not interacting with the other two.

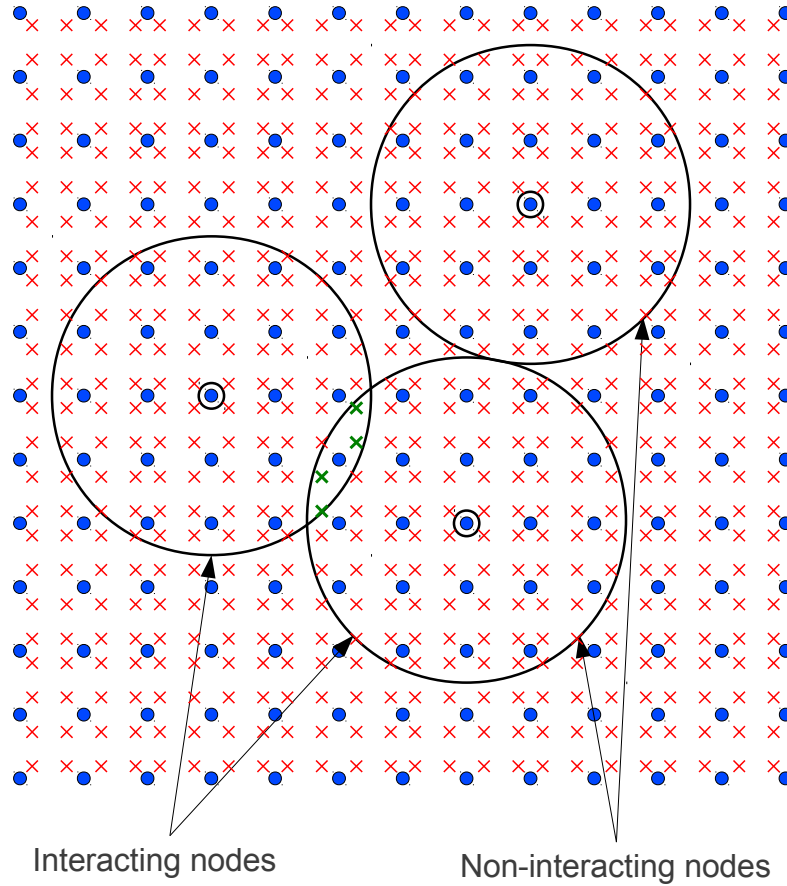


Fig. 3 Intersection of domains of influence

4.1. Computation of global stiffness coefficients for each interacting node pair

The computation of the stiffness elements for each interacting node pair is split in two phases. In the first phase, the shape function derivatives for each influenced node of every Gauss point are calculated as described in the Gauss point-wise method. Then, instead of continuing with the calculation of the stiffness matrix coefficients corresponding to a particular Gauss point, the shape function derivatives are stored for the calculation of \mathbf{Q}_{ij} matrices in the next phase. The required storage of all shape function derivatives is small so storing them temporarily is not an issue.

In the second phase, the stiffness matrix coefficients of each interacting node pair is computed. For each interacting node pair ij , the matrix \mathbf{Q}_{ij} is calculated over all shared Gauss points and summed to form the final values of the corresponding coefficients of the global matrix:

$$\mathbf{K}_{ij} = \sum_G \mathbf{Q}_{ij} = \sum_G \mathbf{B}_i^T \mathbf{E} \mathbf{B}_j \quad (19)$$

Both phases are amenable to parallelization, the first with respect to Gauss points and the second with respect to interacting node pairs, and involve no race conditions or the need for synchronization.

4.2. Parallelization features of the interacting node pairs approach

The interacting node pairs approach has certain advantages compared to the Gauss point-wise approach. The most important one is related to its amenability to parallelism, in contrast to the Gauss point-wise approach. Since in EFG methods each Gauss point affects a large number of nodes, each \mathbf{K}_{ij} submatrix is formed by a large number of stiffness contributions. Parallelizing the Gauss point-wise approach involves scatter parallelism, which is schematically shown in Fig. 4 for two Gauss points C and D . Each part of the sum can be calculated in parallel but there are conflicting updates to the same element of the stiffness matrix. These race conditions can be avoided with proper synchronization but in massively parallel systems like the GPU where thousands of threads may be working concurrently it is very detrimental to performance because all updates are serialized with atomic operations [14].

In the interacting node pairs approach, instead of constantly updating the matrix, the final values for the submatrix of each interacting node pair are calculated and then appended to the matrix. For the calculation of a submatrix, all contributions of the Gauss points belonging to the intersection of the the domains of influence of two interacting nodes should be summed together. Thus, the interacting node pairs approach utilizes gather parallelism as shown schematically in Fig. 5. In a parallel implementation, each working unit, or thread, prepares a submatrix \mathbf{K}_{ij} related to a specific interacting node pair ij . It gathers all contributions from the Gauss points and writes to a specific memory location accessed by no other thread. Thus, this method requires no synchronization or atomic operations. An important benefit of this approach is the indexing cost of the stiffness matrix elements. In the Gauss point-wise method each stiffness matrix element is updated a large number of times while in the proposed interacting node pair approach the final value is calculated and written only once.

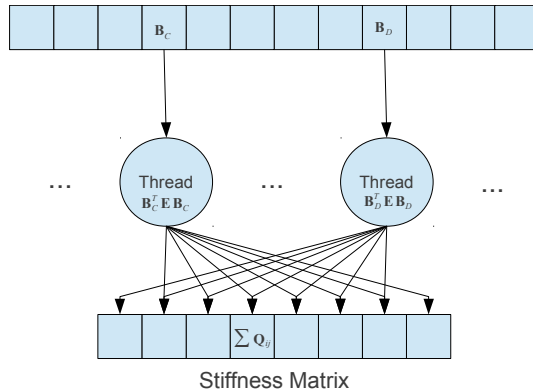


Fig. 4: Scatter parallelism required for the Gauss point-wise approach

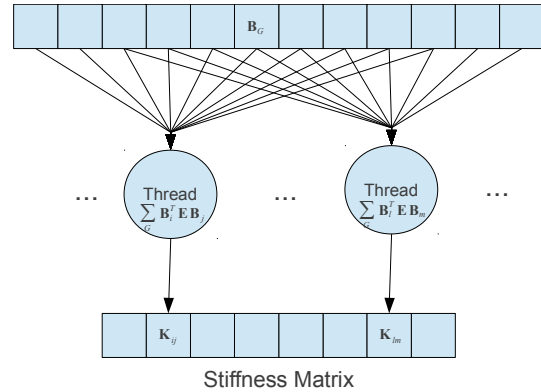


Fig. 5: Gather parallelism implemented in the interacting node pairs approach

5. NUMERICAL RESULTS IN 2D AND 3D ELASTICITY PROBLEMS

The two procedures elaborated in this work for the computation of the stiffness matrix in large-scale EFG meshless simulations are tested for the same 2D and 3D elasticity problems already used for testing throughout this paper. The geometric domains of these problems maximize the number of correlations and consequently the computational cost for the given number of nodes. The examples are run on the following hardware. CPU: Core i7-980X which has 6 physical cores (12 logical cores) at 3.33 GHz and 12MB cache. GPU: is a GeForce GTX680 with 1536 CUDA cores and 2GB GDDR5 memory.

The performance of the Gauss point-wise (GP) and node pair-wise (NP) approaches in the CPU are given in Table 3. The proposed Gauss point-wise approach is compared with the

Example	dof	Gauss points	CPU Time (seconds)		
			Conventional GP	Proposed GP	Proposed NP
2D-1	51.842	102.400	107	12	11
2D-2	152.250	300.304	313	34	28
2D-3	252.050	501.264	502	53	47
3D-1	27.783	64.000	2.374	241	134
3D-2	59.049	140.608	6.328	616	328
3D-3	107.811	262.144	13.302	1.165	645

Table 3: Computing time for the formulation of the stiffness matrix in the serial CPU implementations of the Gauss point-wise (GP) and node pair-wise (NP) approaches

“conventional” one without the previously described improvements.

The performance of the GPU implementation of the node pair-wise method is shown in Table 4. Speedup ratios of the GPU implementation compared to the CPU implementations is given in Table 5.

Example	dof	Gauss points	NP GPU Time (seconds)		
			Kernel 1	Kernel 2	Total
2D-1	51,842	102,400	0.05	0.19	0,2
2D-2	152,250	300,304	0.13	0.56	0,7
2D-3	252,050	501,264	0.21	0.89	1,1
3D-1	27,783	64,000	0.17	2.41	2,6
3D-2	59,049	140,608	0.32	6.17	6,5
3D-3	107,811	262,144	0.62	12.31	12,9

Table 4: Computing time for the formulation of the stiffness matrix in the GPU implementation of the interacting node-pair approach

Example	Speedup ratios of GPU implementation		
	Conventional GP	Proposed GP	Proposed NP
2D-1	450	50	46
2D-2	457	50	41
2D-3	456	48	43
3D-1	921	93	52
3D-2	975	95	50
3D-3	1.028	90	50

Table 5: Relative speedup ratios of GPU implementation compared to the CPU implementations

6. CONCLUDING REMARKS

The proposed improvements on the initialization phase through the utilization of Gauss regions significantly reduces the time required to create the necessary correlations between the entities of the meshless methods. With Gauss regions, the process scales very well, in contrast to globally searching, and the initialization takes only a small percentage of the problem formulation time.

The improvements in the Gauss point-wise approach for assembling the stiffness matrix offer an order of magnitude speedup compared to the conventional approach. This is

attributed to the reduced number of calculations in all parts of the process and the usage of an efficient sparse matrix format and an implementation specifically tailored for the formulation phase of the stiffness matrix. Indexing is a major factor affecting the computational cost. Therefore, the skyline format is faster due to its lower indexing cost, however the significantly higher memory requirement makes it problematic for larger problems where a sparse format is preferable or mandatory.

The proposed node pair-wise approach has several benefits over the Gauss point-wise approach. The most important being its amenability to parallelism especially in massively parallel systems like the GPUs. Each node pair can be processed separately by any available processor in order to compute the corresponding stiffness submatrix. The node pair approach is characterized as “embarrassingly parallel” since it requires no synchronization whatsoever between node pairs.

A GPU implementation is applied to the node pair-wise approach offering great speedups compared to CPU implementations. The node pairs keep the GPU constantly busy with calculations resulting in high hardware utilization which is evidenced by the high speedup ratios of approximately two orders of magnitude in the test examples presented. The node pair-wise approach can be applied as is to any available hardware achieving even lower computing times. This includes using many GPUs, hybrid CPU(s)/GPU(s) implementations and generally any available processing unit. The importance of the latter becomes apparent when considering contemporary and future developments like heterogeneous systems architecture (HSA).

In conclusion, the parametric tests performed in the framework of this study showed that with the proposed implementation along with the exploitation of currently available low cost hardware, the expensive formulation of the stiffness matrix in meshless EFG methods can be reduced by orders of magnitude. The presented node pair-approach enables the efficient utilization of any available hardware and in conjunction with fast initialization and its inherently parallelization features can accomplish high speedup ratios, which convincingly addresses the main shortcoming of meshless methods making them computationally competitive in solving large-scale engineering problems.

7. ACKNOWLEDGMENTS

This work has been supported by the European Research Council Advanced Grant “MASTER – Mastering the computational challenges in numerical modeling and optimum design of CNT reinforced composites” (ERC-2011-ADG_20110209).

8. REFERENCES

- [1] S. Li and W. K. Liu, “Meshfree and particle methods and their applications,” *Applied Mechanics Reviews*, vol. 55, no. 1, pp. 1–34, 2002.
- [2] V. P. Nguyen, T. Rabczuk, S. Bordas, and M. Dufloot, “Meshless methods: A review and computer implementation aspects,” *Mathematics and Computers in Simulation*, vol. 79, no. 3, pp. 763–813, 2008.
- [3] T. Belytschko, Y. Krongauz, D. Organ, M. Fleming, and P. Krysl, “Meshless methods: An overview and recent developments,” *Computer Methods in Applied Mechanics and Engineering*, vol. 139, no. 1–4, pp. 3–47, 1996.
- [4] K. T. Danielson, S. Hao, W. K. Liu, R. A. Uras, and S. Li, “Parallel computation of meshless methods for explicit dynamic analysis,” *International Journal for Numerical Methods in Engineering*, vol. 47, no. 7, pp. 1323–1341, 2000.

- [5] K. T. Danielson, R. A. Uras, M. D. Adley, and S. Li, "Large-scale application of some modern CSM methodologies by parallel computation," *Advances in engineering software*, vol. 31, no. 8, pp. 501–509, 2000.
- [6] G. R. Liu, K. Y. Dai, and T. T. Nguyen, "A smoothed finite element method for mechanics problems," *Computational Mechanics*, vol. 39, no. 6, pp. 859–877, 2007.
- [7] J. G. Wang and G. R. Liu, "A point interpolation meshless method based on radial basis functions," *International Journal for Numerical Methods in Engineering*, vol. 54, no. 11, pp. 1623–1648, 2002.
- [8] Y. T. Gu and G. R. Liu, "A coupled element free Galerkin/boundary element method for stress analysis of tow-dimensional solids," *Computer Methods in Applied Mechanics and Engineering*, vol. 190, no. 34, pp. 4405–4419, 2001.
- [9] W.-R. Yuan, P. Chen, and K.-X. Liu, "High performance sparse solver for unsymmetrical linear equations with out-of-core strategies and its application on meshless methods," *Applied Mathematics and Mechanics (English Edition)*, vol. 27, no. 10, pp. 1339–1348, 2006.
- [10] S. C. Wu, H. O. Zhang, C. Zheng, and J. H. Zhang, "A high performance large sparse symmetric solver for the meshfree Galerkin method," *International Journal of Computational Methods*, vol. 5, no. 4, pp. 533–550, 2008.
- [11] E. Divo and A. Kassab, "Iterative domain decomposition meshless method modeling of incompressible viscous flows and conjugate heat transfer," *Engineering Analysis with Boundary Elements*, vol. 30, no. 6, pp. 465–478, 2006.
- [12] P. Metsis and M. Papadrakakis, "Overlapping and non-overlapping domain decomposition methods for large-scale meshless EFG simulations," *Computer Methods in Applied Mechanics and Engineering*, vol. 229–232, pp. 128–141, 2012.
- [13] R. Trobec, M. Šterk, and B. Robič, "Computational complexity and parallelization of the meshless local Petrov-Galerkin method," *Computers and Structures*, vol. 87, no. 1–2, pp. 81–90, 2009.
- [14] W. W. Hwu and D. B. Kirk, "Parallelism Scalability," in *Programming and Tuning Massively Parallel Systems (PUMPS)*, Barcelona, 2011.

SECOND ORDER GODUNOV SPH FOR HIGH VELOCITY IMPACT DYNAMICS

A. Connolly¹, L. Iannucci¹, R. Hillier¹ and D. Pope²

¹Department of aeronautics
Imperial College London
South Kensington Campus
SW7 2AZ
e-mail: a.connolly08@imperial.ac.uk

² Defence Science and Technology Labs
Dstl Porton Down
Wiltshire
SP4 0JQ
e-mail: djpope@dstl.gov.uk

Keywords: SPH, Godunov, Riemann, MUSCL, high-velocity, impact

Abstract. *In this work the Godunov Smoothed Particle Hydrodynamics (SPH) method for material with strength is extended to second order in space. This is achieved by separating the continuum equations of motion into their constituent hydrodynamic and deviatoric parts and using a MUSCL-type reconstruction and limiting procedure for the left and right Riemann states. The split equations are then advanced in time sequentially using a first-order operator splitting procedure. The resulting equations require no user defined artificial damping parameters as sufficient numerical dissipation is introduced through the use of a Riemann solver. One and two dimensional elastic-plastic flows are chosen to demonstrate the efficacy of the proposed formulation and the results are compared with exact solutions, the original first order scheme and the standard artificial viscosity SPH scheme. The new method is then applied to the simulation of a representative ballistic impact on a ceramic armour material.*

1 INTRODUCTION

Traditionally in SPH the shock is smeared by applying an artificial viscosity [22] term to the momentum and energy equations. Several forms of artificial viscosity have been described in the literature [9, 22, 1] with the most common implementation (found in most SPH codes) being that of Monaghan *et al.* [22]. When using the artificial viscosity without special treatments [27, 4], care must be taken not to introduce excessive artificial smoothing into smooth regions away from the shock. This may be achieved by a time-consuming trial-and-error analysis [28] which may be very undesirable for the user.

The Godunov reformulation of the SPH equations have been developed [33, 12, 23] whereby the Riemann problem is solved between the two interacting particles. The solution of the Riemann problem in Lagrangian coordinates provides the post wave-breakup pressure and velocity at the interface between two interacting particles which introduces sufficient numerical dissipation for stable integration. The advantage of these Godunov reformulations is that no user-defined damping parameters or associated sensitivity analyses are required; sufficient damping is automatically introduced into the solution. The strictly conservative Godunov SPH method developed by Inutsuka (2002) [12] was developed for inviscid fluid simulations and maintains second-order spatial accuracy in smooth regions by a reconstruction procedure. The Godunov SPH method of Parshikov *et al.* (2002) [23] was developed for fluid and solid dynamics and is first-order accurate everywhere in the solution. This work presents an extension of the Parshikov *et al.* scheme for fluid and solid-dynamics to second-order in space, while ensuring exact conservation of energy. This is done by splitting the integration procedure into a hydrodynamic and a deviatoric step, thereby removing the complications caused by the material strength as described in [10] for a free-Lagrange Voronoi tessellation method. The Lie-Trotter splitting is used which is first-order in time.

The new method is derived in Section 3.3 and tests for one and two-dimensional solid-dynamics are presented in Section 4. Section 5 applies the new scheme to a representative ballistic impact simulation and Section 6 concludes the work.

1.1 Motivation

The effective viscosity of the Parshikov *et al.* scheme [23] is shown to be high, which is a direct consequence of the use of a first-order Godunov scheme [30]. A piecewise linear reconstruction of the (primitive variables in the inviscid-fluid case) field variables to the contact surface between particles i and j , before invoking the Riemann solution, extends the spatial order of accuracy to 2nd \mathcal{O} [32]. This is readily achieved using the SPH smoothed approximation of the gradient, as done in [33, 12]. Godunov's Theorem states that monotone linear schemes (having the property of not generating new extrema) for solving partial differential equations, can be at most first-order accurate [8]. Therefore, in order to achieve high-order spatial accuracy, without introducing new extrema which may lead to oscillations, a non-linear scheme must be used. This can be achieved using slope limiting procedures [30]. Such a scheme has high-order spatial accuracy in smooth regions of the solution but falls to low, or first order accuracy, in the vicinity of strong gradients or discontinuities. When considering the Cauchy stress tensor, its gradient results in a third-order tensor field (the implementation of which in three dimensions requires 18 elements per particle). This memory and computational requirement has meant that the Godunov SPH scheme for materials with strength has remained 1st \mathcal{O} accurate

in space. This work, then, is an attempt to remove the complication of the extension to 2nd \mathcal{O} of the Godunov SPH scheme caused by the inclusion of material strength.

2 SPH THEORY

The basis of the SPH method is in the approximation of a function of spatial coordinates $f(\mathbf{x})$ through the approximate kernel interpolation of the function at locations surrounding the point of interest. The usual derivation [21] is to start with the identity

$$f(\mathbf{x}) = \int f(\mathbf{x}')\delta(\mathbf{x} - \mathbf{x}') d\mathbf{x}'. \quad (1)$$

The delta function is replaced by some smoothing (or “kernel”) function $W(\mathbf{x} - \mathbf{x}', h)$ with the same property as the delta function as the smoothing length h tends to zero:

$$\lim_{h \rightarrow 0} W(\mathbf{x} - \mathbf{x}', h) = \delta(\mathbf{x} - \mathbf{x}'). \quad (2)$$

This gives the kernel approximation

$$f(\mathbf{x}) \approx \int f(\mathbf{x}')W(\mathbf{x} - \mathbf{x}', h) d\mathbf{x}'. \quad (3)$$

The kernel function should satisfy the unity condition

$$\int W(\mathbf{x} - \mathbf{x}', h) d\mathbf{x}' = 1 \quad (4)$$

and, in order to be computationally tractable, should be compact such that

$$W(\mathbf{x} - \mathbf{x}', h) = 0 \quad \text{if} \quad |\mathbf{x} - \mathbf{x}'| \geq \kappa h \quad (5)$$

where κ is some scaling factor. For each particle with a mass m_i and mass density ρ_i , noting that $d\mathbf{x}'$ denotes the integration volume (in three dimensions), equation (3) may be discretized as the Riemann summation

$$f(\mathbf{x}) \approx \sum_j \frac{m_j}{\rho_j} f(\mathbf{x}_j) W(\mathbf{x} - \mathbf{x}_j, h). \quad (6)$$

If the function is taken as the density field ρ , the SPH summation approximation of the density is obtained:

$$\rho(\mathbf{x}) \approx \sum_j m_j W(\mathbf{x} - \mathbf{x}_j, h). \quad (7)$$

It is clear from equation (7) that the kernel function should satisfy some physically intuitive properties, such as being non-negative, and monotonically decreasing as $h \rightarrow 0$. For this reason, a Gaussian, or Gaussian-like function is commonly chosen as the kernel. The derivative of a function may be obtained by using integration by parts and the divergence theorem to give

$$\nabla f(\mathbf{x}) \approx \int_S f(\mathbf{x}')W(\mathbf{x} - \mathbf{x}', h)\mathbf{n}dS - \int_\Omega f(\mathbf{x}')\nabla W(\mathbf{x} - \mathbf{x}', h)d\mathbf{x}'. \quad (8)$$

In general, the surface integral in equation (8) is neglected in the actual computation as it vanishes if the kernel support does not intersect the boundary of the material domain. For simulations involving free-surfaces, the neglect of the surface integral contributes to the boundary

deficiency in the SPH method. As the continuum equations of motion are first-order, equation (8) may be used to discretize the governing equations. Neglecting the surface integral, in one dimension, the errors in (8) may be estimated by taking the Taylor-series expansion around \mathbf{x}' to give

$$\begin{aligned}\nabla f(\mathbf{x}) &= - \int \left[f(\mathbf{x}) + (\mathbf{x} - \mathbf{x}')f'(\mathbf{x}) + \frac{(\mathbf{x} - \mathbf{x}')^2}{2!}f''(\mathbf{x}) + \right. \\ &\quad \left. \mathcal{O}((\mathbf{x} - \mathbf{x}')^3) + \dots \right] \nabla W(\mathbf{x} - \mathbf{x}', h) d\mathbf{x}' \\ &= \nabla f(\mathbf{x}) + \frac{f''(\mathbf{x})}{2} \int (\mathbf{x} - \mathbf{x}')^2 \nabla W(\mathbf{x} - \mathbf{x}', h) d\mathbf{x}' + \\ &\quad \mathcal{O}((\mathbf{x} - \mathbf{x}')^3).\end{aligned}\tag{9}$$

In (9) the second term in the Taylor expansion vanishes as, for even kernels $\int \nabla W d\mathbf{x}' = 0$. Therefore, the order of accuracy of the kernel approximation of the gradient is second-order, with errors of $\mathcal{O}(h^2)$. Similarly, the errors in the discrete approximation of (9) are of $\mathcal{O}(h^2)$ [25].

3 GOVERNING EQUATIONS

In the absence of body forces, the conservation equations for elastic flow are given as follows

$$\begin{aligned}\frac{D\rho}{Dt} &= -\rho \nabla \cdot \mathbf{v} \\ \frac{D\mathbf{v}}{Dt} &= \frac{1}{\rho} \nabla \cdot \boldsymbol{\sigma} \\ \frac{Du}{Dt} &= -\frac{\boldsymbol{\sigma}}{\rho} : \nabla \mathbf{v},\end{aligned}\tag{10}$$

where D/Dt is the substantial derivative and ρ , \mathbf{v} , u and $\boldsymbol{\sigma}$ are the material density, velocity, specific internal energy and Cauchy stress tensor respectively. The separation of the stress tensor into its dilatational and deviatoric components is assumed [35]

$$\boldsymbol{\sigma} = \boldsymbol{\tau} - P\mathbf{I},\tag{11}$$

where \mathbf{I} is the identity matrix.

3.1 Discretization

The variationally consistent discrete SPH equations [3] corresponding to (10) are given as [3]

$$\begin{aligned}\frac{D\rho_i}{Dt} &= \rho_i \sum_j \frac{m_j}{\rho_j} (\mathbf{v}_i - \mathbf{v}_j) \cdot \nabla_i W_{ij} \\ \frac{D\mathbf{v}_i}{Dt} &= \sum_j m_j \left(\frac{\boldsymbol{\sigma}_i + \boldsymbol{\sigma}_j}{\rho_i \rho_j} \right) \nabla_i W_{ij} \\ \frac{Du_i}{Dt} &= \frac{1}{2} \sum_j m_j \left(\frac{\boldsymbol{\sigma}_i + \boldsymbol{\sigma}_j}{\rho_i \rho_j} \right) (\mathbf{v}_i - \mathbf{v}_j) \cdot \nabla_i W_{ij},\end{aligned}\tag{12}$$

where the derivative of the kernel function $\nabla_i W_{ij}$ is defined as

$$\begin{aligned}\nabla_i W_{ij} &= \frac{\partial}{\partial \mathbf{x}_i} W(\mathbf{x}_i - \mathbf{x}_j, h) \\ &= \frac{\mathbf{x}_i - \mathbf{x}_j}{|\mathbf{x}_i - \mathbf{x}_j|} \frac{\partial W(|\mathbf{x}_i - \mathbf{x}_j|, h)}{\partial |\mathbf{x}_i - \mathbf{x}_j|} \\ &= -\nabla_j W_{ij}.\end{aligned}\tag{13}$$

3.2 Godunov reformulation of Parshikov *et al.*

In 2002 Parshikov *et al.* [23] directly introduced the Riemann solution to the SPH equations (12) by resolving the stresses and velocities along the vector of interaction and making the substitutions

$$\begin{aligned}P_{ij}^* &\leftarrow \frac{1}{2}(P_i + P_j) \\ v_{ij}^* &\leftarrow \frac{1}{2}(v_i^R + v_j^R) \\ \sigma_{ij}^* &\leftarrow \frac{1}{2}(\sigma_i^R + \sigma_j^R),\end{aligned}\tag{14}$$

where $v_{i,j}^R = \mathbf{v}_{i,j} \cdot \mathbf{e}_{ij}$, $\sigma_{i,j}^R = \boldsymbol{\sigma}_{i,j}^{x,y,z} \cdot \mathbf{e}_{ij}$ and the unit vector of interaction $\mathbf{e}_{ij} = \mathbf{x}_i - \mathbf{x}_j / |\mathbf{x}_i - \mathbf{x}_j|$. The substitution for the stresses requires the rotation of the stress tensor to the coordinate system $\mathbf{e}_{R,S,T}$ orthogonal to the vector of interaction \mathbf{e}_{ij} . The values with the star superscripts are not calculated using (14); instead the approximate acoustic wave primitive variable Riemann solver [30] is used to calculate the value of the stress and velocity in the star region in the three directions corresponding to $\mathbf{e}_{R,S,T}$ by

$$\begin{aligned}v_{ij}^{*R} &= \frac{v_j^R \rho_j c_j^l + v_i^R \rho_i c_i^l + \sigma_j^{RR} - \sigma_i^{RR}}{\rho_i c_i^l + \rho_j c_j^l} \\ \sigma_{ij}^{*R} &= \frac{\sigma_j^{RR} \rho_i c_i^l + \sigma_i^{RR} \rho_j c_j^l + \rho_i c_i^l \rho_j c_j^l (v_j^R - v_i^R)}{\rho_i c_i^l + \rho_j c_j^l} \\ v_{ij}^{*S} &= \frac{v_j^S \rho_j c_j^t + v_i^S \rho_i c_i^t + \sigma_j^{SR} - \sigma_i^{SR}}{\rho_i c_i^t + \rho_j c_j^t} \\ \sigma_{ij}^{*S} &= \frac{\sigma_j^{RS} \rho_i c_i^t + \sigma_i^{RS} \rho_j c_j^t + \rho_i c_i^t \rho_j c_j^t (v_j^S - v_i^S)}{\rho_i c_i^t + \rho_j c_j^t} \\ v_{ij}^{*T} &= \frac{v_j^T \rho_j c_j^t + v_i^T \rho_i c_i^t + \sigma_j^{TR} - \sigma_i^{TR}}{\rho_i c_i^t + \rho_j c_j^t} \\ \sigma_{ij}^{*T} &= \frac{\sigma_j^{RT} \rho_i c_i^t + \sigma_i^{RT} \rho_j c_j^t + \rho_i c_i^t \rho_j c_j^t (v_j^T - v_i^T)}{\rho_i c_i^t + \rho_j c_j^t}.\end{aligned}\tag{15}$$

In (15) c^l and c^t are the longitudinal and transverse wave speeds respectively. The resulting SPH equations are stated as

$$\begin{aligned}
\frac{D\rho_i}{Dt} &= 2\rho_i \sum_j \frac{m_j}{\rho_j} (v_{ij}^{*R} - v_i^R) \mathbf{e}_{ij} \cdot \nabla_i W_{ij} \\
\frac{D\mathbf{v}_i}{Dt} &= 2 \sum_j m_j \frac{\sigma_{ij}^{*R}}{\rho_i \rho_j} \mathbf{e}_{ij} \nabla_i W_{ij} \\
\frac{Du_i}{Dt} &= 2 \sum_j m_j \frac{\sigma_{ij}^{*R}}{\rho_i \rho_j} (v_{ij}^{*R} - v_i^R) \mathbf{e}_{ij} \cdot \nabla_i W_{ij}.
\end{aligned} \tag{16}$$

The algorithm presented in [23] corresponds to a spatially 1st \mathcal{O} Godunov method for solid mechanics and will form the basis of the work presented in forthcoming chapters. It is well known that the 1st \mathcal{O} Godunov method is highly diffusive, which is accentuated by the smoothing introduced by the SPH method. This is discussed in [23].

3.3 Second-order extension

In order to simplify the extension of the Godunov SPH method for materials with strength to second-order, it is proposed that the hydrodynamic and deviatoric parts of the stress tensor be used to sequentially and separately advance the density, velocity and specific internal energy in time. The SPH momentum and energy equations (12) are split into their constituent hydrodynamic and deviatoric parts as

$$\begin{aligned}
\frac{D\mathbf{v}_i}{Dt} &= \sum_j m_j \left(\frac{\boldsymbol{\tau}_i + \boldsymbol{\tau}_j}{\rho_i \rho_j} - \mathbf{I} \frac{P_i + P_j}{\rho_i \rho_j} \right) \nabla_i W_{ij} \\
\frac{Du_i}{Dt} &= \frac{1}{2} \sum_j m_j \left(\frac{\boldsymbol{\tau}_i + \boldsymbol{\tau}_j}{\rho_i \rho_j} - \mathbf{I} \frac{P_i + P_j}{\rho_i \rho_j} \right) (\mathbf{v}_j - \mathbf{v}_i) \cdot \nabla_i W_{ij},
\end{aligned} \tag{17}$$

where the first term in the brackets on the right hand side corresponds to the deviatoric part and the second term corresponds to the hydrodynamic part. The integration procedure is then split into the constituent hydrodynamic and deviatoric stages using Lie-Trotter splitting. The general form of splitting is

$$\frac{\partial f(t)}{\partial t} = Af(t) + Bf(t) \tag{18}$$

where $f(t)$ is some field-variable and A and B are linear differential operators corresponding to the deviatoric and hydrodynamic operations respectively. The sequential splitting algorithm is as follows

$$\begin{aligned}
\frac{\partial x(t)}{\partial t} &= Ax(t), \quad t \in [t^n, t^{n+1}] \quad \text{where} \quad x(t^n) = f(t^n) \\
\frac{\partial y(t)}{\partial t} &= By(t), \quad t \in [t^n, t^{n+1}] \quad \text{where} \quad y(t^n) = x(t^{n+1})
\end{aligned} \tag{19}$$

and the recombination of the split solution is given as $y(t^{n+1}) \approx f(t^{n+1})$. The splitting error is first-order in time and can be found by combining the Taylor series expansions of the two split functions $x(t)$ and $y(t)$ and taking the difference with the Taylor series expansion of the un-split

function around point $f(t^n) = f_n$. Applying this splitting algorithm to the SPH momentum and energy equations (17) gives

$$\begin{aligned}
\frac{D\tilde{\mathbf{v}}_i}{Dt} &= \sum_j m_j \left(\frac{\boldsymbol{\tau}_i + \boldsymbol{\tau}_j}{\rho_i \rho_j} \right) \cdot \nabla_i W_{ij}, \text{ where } \tilde{\mathbf{v}}_i(t^n) = \mathbf{v}_i(t^n) \\
\frac{D\check{\mathbf{v}}_i}{Dt} &= - \sum_j m_j \left(\frac{P_i + P_j}{\rho_i \rho_j} \right) \nabla_i W_{ij}, \text{ where } \check{\mathbf{v}}_i(t^n) = \tilde{\mathbf{v}}_i(t^{n+1}) \\
\frac{D\tilde{u}_i}{Dt} &= \frac{1}{2} \sum_j m_j \left(\frac{\boldsymbol{\tau}_i + \boldsymbol{\tau}_j}{\rho_i \rho_j} \right) (\mathbf{v}_j - \mathbf{v}_i) \cdot \nabla_i W_{ij}, \text{ where } \tilde{u}_i(t^n) = u_i(t^n) \\
\frac{D\check{u}_i}{Dt} &= -\frac{1}{2} \sum_j m_j \left(\frac{P_i + P_j}{\rho_i \rho_j} \right) (\tilde{\mathbf{v}}_j - \tilde{\mathbf{v}}_i) \cdot \nabla_i W_{ij}, \text{ where } \check{u}_i(t^n) = \tilde{u}_i(t^{n+1}),
\end{aligned} \tag{20}$$

where $\tilde{\mathbf{v}}_i = \mathbf{v}_i^n + \Delta\tilde{\mathbf{v}}_i$. In order to obtain sufficient numerical dissipation, the hydrodynamic terms are replaced with the Godunov SPH equations of Parshikov *et al.* [23] for an inviscid, non-radiating fluid to get

$$\begin{aligned}
\frac{D\tilde{\mathbf{v}}_i}{Dt} &= \sum_j m_j \left(\frac{\boldsymbol{\tau}_i + \boldsymbol{\tau}_j}{\rho_i \rho_j} \right) \cdot \nabla_i W_{ij}, \text{ where } \tilde{\mathbf{v}}_i(t^n) = \mathbf{v}_i(t^n) \\
\frac{D\check{\mathbf{v}}_i}{Dt} &= -2 \sum_j m_j \left(\frac{P_{ij}^*}{\rho_i \rho_j} \right) \nabla_i W_{ij}, \text{ where } \check{\mathbf{v}}_i(t^n) = \tilde{\mathbf{v}}_i(t^{n+1}) \\
\frac{D\tilde{u}_i}{Dt} &= \frac{1}{2} \sum_j m_j \left(\frac{\boldsymbol{\tau}_i + \boldsymbol{\tau}_j}{\rho_i \rho_j} \right) (\mathbf{v}_j - \mathbf{v}_i) \cdot \nabla_i W_{ij}, \text{ where } \tilde{u}_i(t^n) = u_i(t^n) \\
\frac{D\check{u}_i}{Dt} &= -2 \sum_j m_j \left(\frac{P_{ij}^*}{\rho_i \rho_j} \right) (\tilde{v}_{ij}^* \mathbf{e}_{ij} - \tilde{\mathbf{v}}_i) \cdot \nabla_i W_{ij}, \text{ where } \check{u}_i(t^n) = \tilde{u}_i(t^{n+1}),
\end{aligned} \tag{21}$$

where P_{ij}^* and \tilde{v}_{ij}^* are the pressure and velocity solutions of the Riemann-problem for the longitudinal wave-system. Note that, in contrast to the scheme of Parshikov *et al.* the Riemann problem needs only to be solved for the longitudinal wave system and no transformation of the stress-tensor is required. No dissipation is added to the deviatoric step of the split integration procedure and the spatial accuracy of the deviatoric momentum equation is second-order. By definition, the density is assumed to only change due to changes in volume, therefore the continuity equation is computed only in the hydrodynamic step. The continuity equation of Parshikov *et al.* [23] may be used

$$\frac{D\rho_i}{Dt} = 2\rho_i \sum_j \frac{m_j}{\rho_j} (\tilde{v}_{ij}^* \mathbf{e}_{ij} - \tilde{\mathbf{v}}_i) \cdot \nabla_i W_{ij}. \tag{22}$$

3.3.1 MUSCL-type reconstruction

To extend the hydrodynamic step in (21) to second-order, a linear reconstruction of the left and right states of the Riemann problem is used as first proposed for SPH in [11]. Using the SPH approximation of the gradient of a function, and taking into account the domain of influence,

the reconstruction of the left and right hand Riemann states is written as

$$\begin{aligned} f_R &= f(\mathbf{x}_i) - \frac{r_{ij}}{2} \nabla f(\mathbf{x}_i)_{mon} \cdot \mathbf{e}_{ij} [1 - c_i \Delta t] \\ f_L &= f(\mathbf{x}_j) + \frac{r_{ij}}{2} \nabla f(\mathbf{x}_j)_{mon} \cdot \mathbf{e}_{ij} [1 - c_j \Delta t], \end{aligned} \quad (23)$$

where $r_{ij} = |\mathbf{x}_i - \mathbf{x}_j|$, $c_{i,j}$ is the longitudinal sound speed at the particle's position and Δt is the current time-step. In order to satisfy the monotonicity constraint at the shock [8], the gradients of the primitive variables must be modified such that the first-order method is recovered. In [12] this is done by setting the gradients to zero when the interacting particles are approaching each other at a velocity close to the minimum wave speed of either interacting particles. A more advanced technique to automatically fulfill the monotonicity constraint by modifying the local gradient based on some sort of smoothness indicator, such as the ratio of successive gradients, as in [32]. This may be done by using one of a variety of different slope-limiter functions [30]. The resolved gradient

$$\Delta Q = \nabla Q \cdot \mathbf{e}_{ij} \quad (24)$$

is defined for particles i and j and the ratio of successive gradients r is defined as

$$\begin{aligned} r_i &= \frac{\Delta Q_j}{\Delta Q_i} \\ r_j &= \frac{\Delta Q_i}{\Delta Q_j} = \frac{1}{r_i}. \end{aligned} \quad (25)$$

The chosen slope-limiter function $\phi(r)$ can then be used to construct the monotonized slopes

$$\begin{aligned} \nabla f(\mathbf{x}_i)_{mon} &= \phi(r_i) \nabla f(\mathbf{x}_i) \\ \nabla f(\mathbf{x}_j)_{mon} &= \phi(r_j) \nabla f(\mathbf{x}_j), \end{aligned} \quad (26)$$

and using equation (23) the left and right Riemann states may be reconstructed. The following 2nd \mathcal{O} Total Variation Diminishing (TVD) slope limiters [30] were implemented due to their symmetry preserving features ($\phi(r) = 1/\phi(r)$)

$$\begin{aligned} \phi(r)_{mc} &= \max \left(0, \min \left(2r, \frac{1+r}{2}, 2 \right) \right) \\ \phi(r)_{sw} &= \max (0, \min (\beta r, 1), \min (r, \beta)), \quad 1 \leq \beta \leq 2 \\ \phi(r)_{vl} &= \frac{r + |r|}{1 + |r|}, \end{aligned} \quad (27)$$

where the subscripts *mc*, *sw* and *vl* stand for Monotonized Central, Sweby and van Leer limiters respectively. Setting the $\beta = 1$ and $\beta = 2$ in the Sweby limiter gives the *minmod* and *superbee* limiters of Roe [30], respectively. It was found that the *superbee* limiter performed well; it is used in all the 2nd \mathcal{O} simulations in this work.

3.4 Conservation

In order to conserve energy exactly in the split integration procedure, the energy equations (21) are modified. As in [12], the appropriate time-centering of the velocity field is used, along with the anti-symmetric nature of the kernel derivative (13), to obtain an expression which

vanishes for the sum over all pairs of interacting particles. The total energy at time $t = t^n$ is defined as (the sum of the kinetic and internal energies)

$$E^n = \sum_i m_i \left(\frac{1}{2}(\mathbf{v}_i^n)^2 + u_i^n \right). \quad (28)$$

For energy to be conserved, the total energy must remain constant over the time-step ($\Delta E = E^{n+1} - E^n = 0$)

$$\Delta E = \sum_i m_i \left(\frac{1}{2}(\mathbf{v}_i^{n+1})^2 + u_i^{n+1} - \frac{1}{2}(\mathbf{v}_i^n)^2 - u_i^n \right). \quad (29)$$

Equation (29) is modified to include the operator splitting by splitting it into two sequential sub-stages. The first step is

$$\begin{aligned} \Delta \tilde{E} &= \tilde{E} - E^n \\ &= \sum_i m_i \left(\frac{1}{2}(\tilde{\mathbf{v}}_i)^2 + \tilde{u}_i - \frac{1}{2}(\mathbf{v}_i^n)^2 - u_i^n \right) \\ &= \sum_i m_i \left(\Delta \tilde{\mathbf{v}}_i \left(\mathbf{v}_i^n + \frac{\Delta \tilde{\mathbf{v}}_i}{2} \right) + \Delta \tilde{u}_i \right) \\ &= 0, \end{aligned} \quad (30)$$

where $\Delta \tilde{\mathbf{v}}_i = \Delta t(d\tilde{\mathbf{v}}_i/dt)$, $\Delta \tilde{u}_i = \Delta t(d\tilde{u}_i/dt) = \tilde{u}_i - u_i^n$ and the fact that $\tilde{\mathbf{v}}_i = \mathbf{v}_i^n + \Delta \tilde{\mathbf{v}}_i$ has been used. The second step is

$$\begin{aligned} \Delta E &= E^{n+1} - \tilde{E} \\ &= \sum_i m_i \left(\frac{1}{2}(\mathbf{v}_i^{n+1})^2 + u_i^{n+1} - \frac{1}{2}(\tilde{\mathbf{v}}_i)^2 - \tilde{u}_i \right) \\ &= \sum_i m_i \left(\Delta \check{\mathbf{v}}_i \left(\tilde{\mathbf{v}}_i + \frac{\Delta \check{\mathbf{v}}_i}{2} \right) + \Delta \check{u}_i \right) \\ &= 0, \end{aligned} \quad (31)$$

where $\Delta \check{\mathbf{v}}_i = \Delta t(d\check{\mathbf{v}}_i/dt)$, $\Delta \check{u}_i = \Delta t(d\check{u}_i/dt) = u_i^{n+1} - \tilde{u}_i$ and similarly $\mathbf{v}_i^{n+1} = \tilde{\mathbf{v}}_i + \Delta \check{\mathbf{v}}_i$. The deviatoric part of the split energy equation is then modified to give

$$\frac{D\tilde{u}_i}{Dt} = \sum_j m_j \left(\frac{\boldsymbol{\tau}_i + \boldsymbol{\tau}_j}{\rho_i \rho_j} \right) (\bar{\mathbf{v}}_{ij} - \dot{\mathbf{x}}_i) \cdot \nabla_i W_{ij}, \quad (32)$$

where the substitution $\bar{\mathbf{v}}_{ij} = 0.5(\mathbf{v}_i + \mathbf{v}_j)$ is made and $\dot{\mathbf{x}}_i = \mathbf{v}_i + \Delta \tilde{\mathbf{v}}_i/2$ is the time-centered velocity. The use of this time-centering ensures that energy is conserved exactly in the first-step of the time-split integration procedure. This can be shown by substituting $\dot{\mathbf{x}}_i$ and (32) into (30) to give

$$\begin{aligned} \Delta \tilde{E} &= \sum_i m_i (\Delta \tilde{\mathbf{v}}_i \dot{\mathbf{x}}_i + \Delta \tilde{u}_i) \\ &= \Delta t \sum_i \sum_j \frac{\bar{\mathbf{v}}_{ij} m_i m_j}{\rho_i \rho_j} (\boldsymbol{\tau}_i + \boldsymbol{\tau}_j) \cdot \nabla_i W_{ij} \\ &= 0. \end{aligned} \quad (33)$$

For the hydrodynamic part of the split energy equation the method of Inutsuka [12] is followed;

$$\frac{D\tilde{u}_i}{Dt} = -2 \sum_j m_j \left(\frac{P_{ij}^*}{\rho_i \rho_j} \right) (\tilde{v}_{ij}^* \mathbf{e}_{ij} - \tilde{\mathbf{x}}_i) \cdot \nabla_i W_{ij}, \quad (34)$$

where $\tilde{\mathbf{x}}_i = \tilde{\mathbf{v}}_i + \Delta\tilde{\mathbf{v}}_i/2$ is the time-centered velocity in the second-step of the split integration procedure. Again, this use of the time-centering ensures that energy is conserved exactly in the second step of the split integration procedure, which can be shown by substituting $\tilde{\mathbf{x}}_i$ and (34) into (31) to give

$$\begin{aligned} \Delta E &= \sum_i m_i (\Delta\tilde{\mathbf{v}}_i \tilde{\mathbf{x}}_i + \Delta\tilde{u}_i) \\ &= -2\Delta t \sum_i \sum_j \frac{m_i m_j P_{ij}^* \tilde{v}_{ij}^* \mathbf{e}_{ij}}{\rho_i \rho_j} \cdot \nabla_i W_{ij} \\ &= 0. \end{aligned} \quad (35)$$

In the case of an inviscid fluid ($\boldsymbol{\tau} = \mathbf{0}$) the time centering of Inutsuka [12] is recovered as $\tilde{\mathbf{v}}_i = \mathbf{0}$. It is worth noting that, if the total energy is used as an indicator of the solution quality, for example, then the exactly conservative scheme presented above may not be advantageous. An appropriate system of units should be selected such that round-off error is minimized.

4 NUMERICAL TESTS

The chosen tests have exact solutions for comparison. From hereon in we refer to the first-order Godunov SPH scheme of Parshikov *et al.* [23] as *PM*, the new time-split Godunov SPH scheme as *TS* and the standard artificial viscosity scheme (with Monaghan-type artificial viscosity [22] and damping parameters $\alpha = \beta = 1$) as *AV*. In the *AV* scheme the second-order leap-frog integration scheme is used [19]. In this work the Godunov SPH scheme of Parshikov *et al.* [23] was implemented in one dimension only. In all cases the time-step was controlled by the *CFL* number of 0.5 and the initial smoothing length scaling factor was 1.2.

4.1 1D flyer-plate

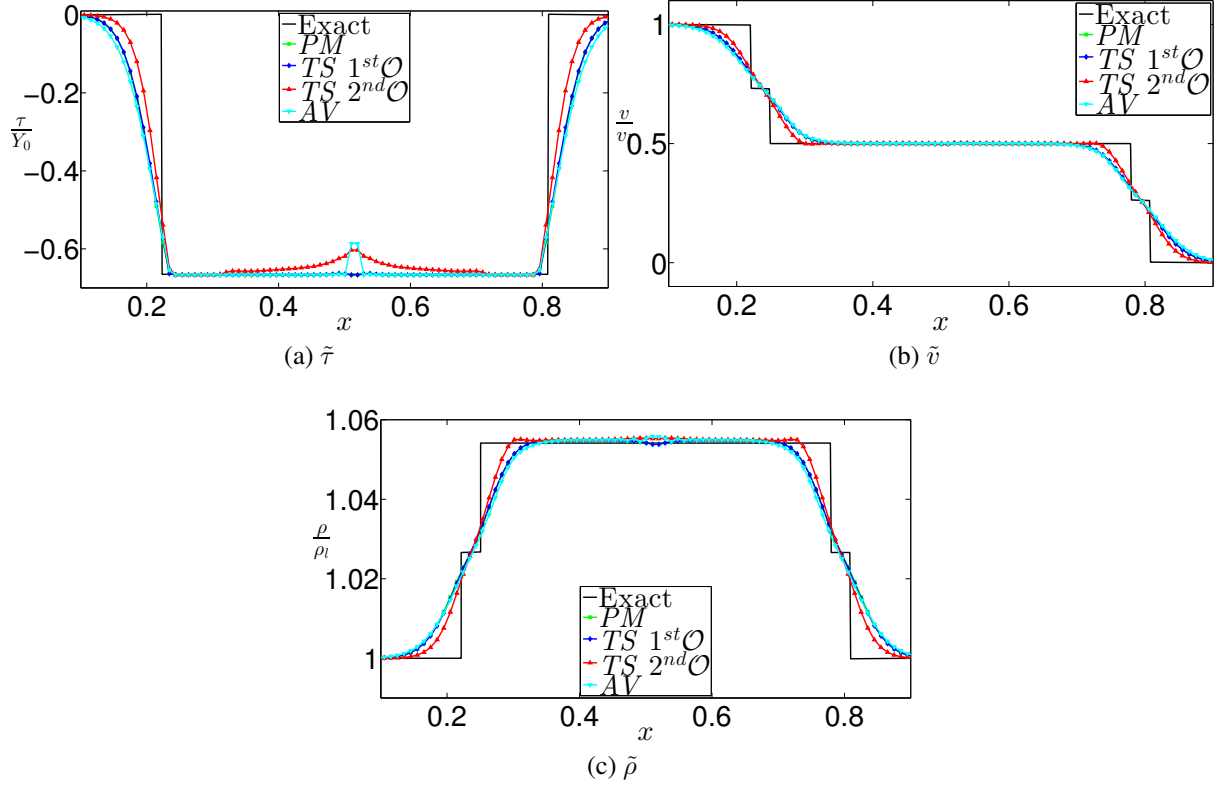
This example comes from [5] and consists of an impact of a high-velocity elastic-perfectly-plastic material with another identical material which is at rest. The impact produces an elastic precursor wave followed by a plastic shock-wave. An isothermal Mie-Grüneisen Equation of State (EOS) is used (as the Grüneisen coefficient is zero), defined as [5]

$$P(\rho) = \frac{\rho_0 c_0^2 \zeta}{1 - (S_1 - 1)\zeta}, \quad (36)$$

where $\zeta = \rho/\rho_0 - 1$. The material properties are given as $\rho_0 = 6.1 \text{ g/cm}^3$, $c_0 = 0.5077 \text{ cm}/\mu\text{s}$, $S_1 = 1.201$, $\mu = 0.481 \text{ MBar}$ and $Y_0 = 0.025 \text{ MBar}$ [5]. The initial conditions are given in Table 1. The solution is integrated until $t = 0.5\mu\text{s}$ and the domain is over $0 \leq x \leq 1$ with the left hand side defined as $x \leq 0.5$. Figure 1 shows the non-dimensional results using the different schemes 100 (equally spaced) particles in the domain against the exact solution [5].

$$\begin{array}{l|l}
\tau_l = 0 & \tau_r = 0 \\
\rho_l = \rho_0 & \rho_r = \rho_0 \\
v_l = 0.060281 \text{ cm}/\mu\text{s} & v_r = 0
\end{array}$$

Table 1: Initial conditions for the flyer-plate impact example (from [5]).


Figure 1: Results of the flyer-plate example using the different schemes for an initial inter-particle spacing of $\Delta x = 0.01$ cm. The exact solution [5] is given by the black line.

It can be seen from Figure 1 that the results from the *PM*, first order *TS* and *AV* schemes are similar, however the second-order *TS* scheme shows a more accurate description around the discontinuities in field variables. In the second-order *TS* scheme there is an error in the stress field around the contact discontinuity. The *AV* scheme shows a similar but more localised error. The difference in total energy for the different schemes is shown in Table 2.

Scheme	% ΔE_{tot}
<i>PM</i>	2.34
<i>TS</i> 1 st O	1.48×10^{-8}
<i>TS</i> 2 nd O	1.48×10^{-8}
<i>AV</i>	1.51

Table 2: Percentage errors in total energy for the flyer-plate impact example using the different schemes.

4.2 2D Collapsing ring

This problem involves the collapse of an axi-symmetrical beryllium ring which was first proposed by Howell and Ball [10]. The problem has an analytical solution [10] which derives from incompressible theory and the reduction to one-dimension. A detailed derivation of the analytical solution is presented in [10]. The analytical solution predicts a stopping radius at which all the initial kinetic energy is dissipated by irreversible plastic deformation into internal energy. Howell and Ball use the Osborne equation of state, but the analytical solution is independent of the pressure, therefore, as suggested in [24], the Mie-Grüneisen equation of state of the form

$$P(\rho, u) = \frac{\rho_0 c_0^2 (\eta - 1) (\eta - \frac{1}{2} \Gamma_0 (\eta - 1))}{(\eta - S_1 (\eta - 1))^2} + \rho_0 \Gamma_0 u, \quad (37)$$

where $\eta = \rho/\rho_0$ is used with parameters proposed in [24] of $\rho_0 = 1845.0 \text{ kg/m}^3$, $c_0 = 12870.0 \text{ m/s}$, $S_1 = 1.124$ and $\Gamma_0 = 2.0$. The elastic-perfectly-plastic constitutive model is used with $\mu = 15.1 \text{ GPa}$ and $Y_0 = 330.0 \text{ MPa}$. As mentioned in [10], for the test to be successful, the circumferential symmetry must be preserved and the stopping radii must converge towards the analytical solution. The initial velocity field is defined as

$$\mathbf{v}_i = -v_0 \frac{R_1}{r_i} \mathbf{e}_i, \quad (38)$$

where $v_0 = 417.1 \text{ m/s}$, $R_1 = 0.08 \text{ m}$ is the inner radius in the initial configuration, r_i is the distance of particle i from the origin and \mathbf{e}_i is the unit vector of the particle position. The analytical solution [10] predicts the inner and outer stopping radii to be 0.05 m and 0.0781 m respectively. As the *PM* scheme was implemented in one dimension only the results of the *TS* schemes are compared with the *AV* scheme using two different resolutions ($n_p = 8012$ and $n_p = 23,506$). In this example the two-shock approximate Riemann solver [7] is used in the *TS* scheme. The solution was integrated until $t = 130 \mu\text{s}$ which was just after the cessation of plastic deformation in each case. The final configurations for the lower resolution using the first and second order *TS* schemes and *AV* scheme, coloured by the effective plastic strain and τ_{xy} deviatoric stress, are shown in Figure 2. It can be seen that the stress field is noisy in the *AV* scheme suggesting that the dynamics of the deformation are not being properly predicted; a similar result is found for the other field variables.

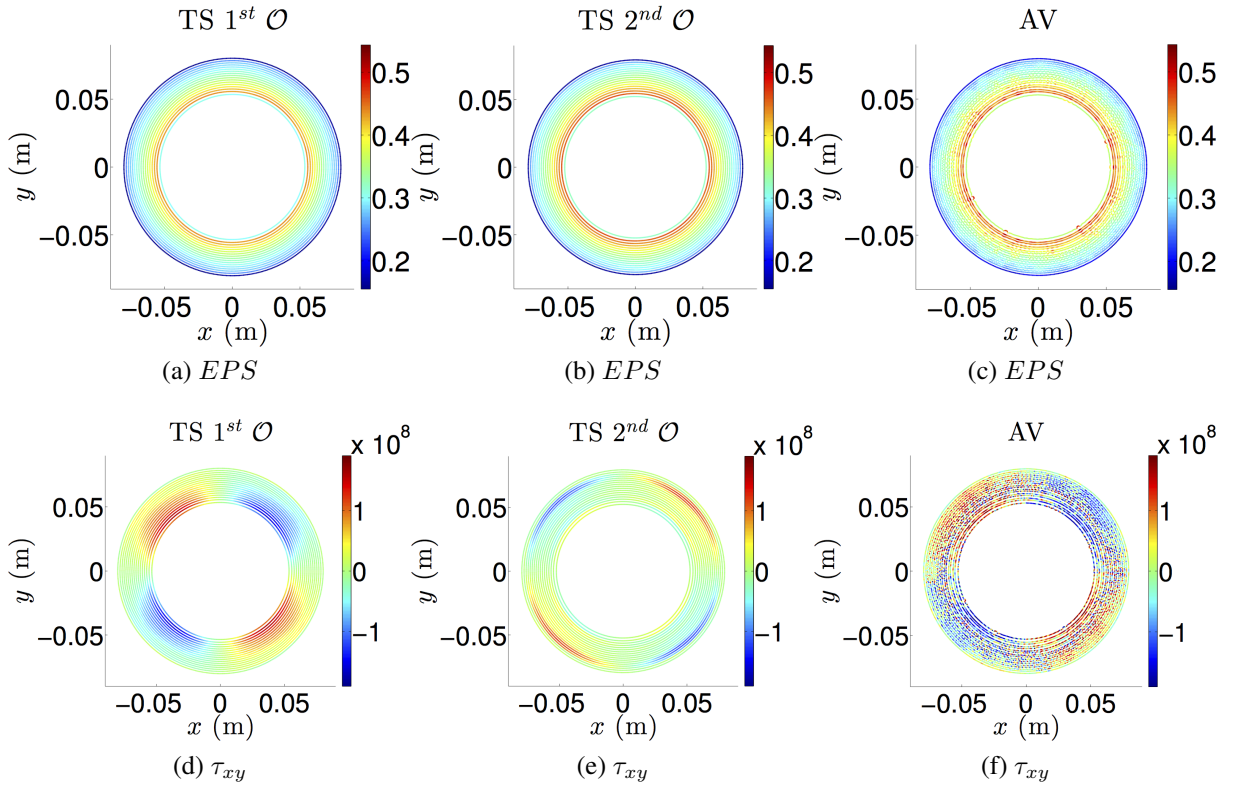


Figure 2: The final configurations (at $t = 130 \mu s$) for the lower resolution ($n_p = 8012$) ring collapse example using the different SPH schemes. The units of the colourmap for the τ_{xy} results are in Pa .

The difference in the colourmap for the τ_{xy} results between the 1st O and 2nd O TS schemes is due to the difference in phase of the elastic oscillation after the cessation of yielding. The results for the finest resolution are shown in Figure 3.

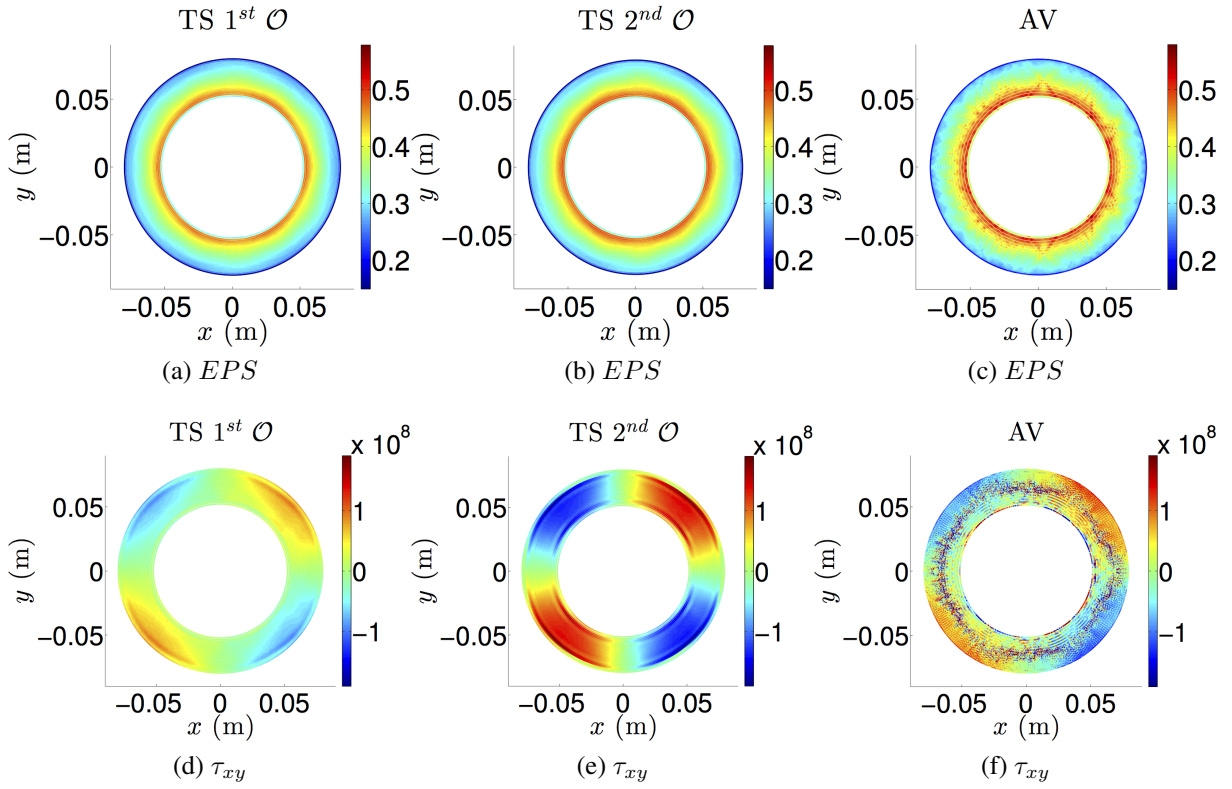


Figure 3: The final configurations (at $t = 130\mu\text{s}$) for the higher resolution ($n_p = 23,506$) ring collapse example using the different SPH schemes. The units of the colourmap for the τ_{xy} results are in Pa .

The particle configuration of the AV scheme shows a considerable amount of disorder and the inner ring of particles have lost their circumferential symmetry. Therefore, according to the criteria of [10], the AV scheme fails this test. For this reason only the inner and outer radii of the TS schemes are compared with the exact solution; this is shown as a function of time in Figure 4. The non-dimensional internal, kinetic and total energies for each of the schemes are shown in Figure 5. The percentage change in total energy (at $t = 130\mu\text{s}$) for each of the schemes is shown in Table 3. As the error in total energy in the TS scheme is due only to machine round-off, the error may be minimized by an appropriate choice of units.

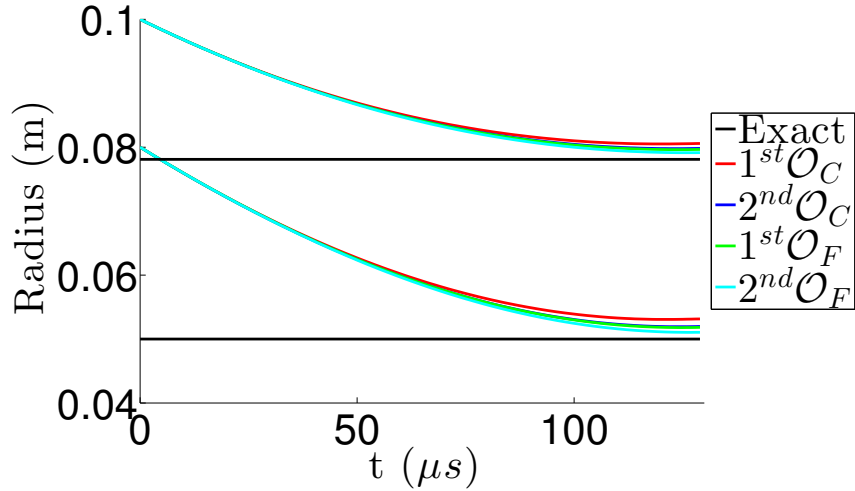


Figure 4: The inner and outer radii of the collapsing ring as a function of time using the *TS* scheme. The subscripts *C* and *F* in the legend mean the coarse and fine resolution respectively.

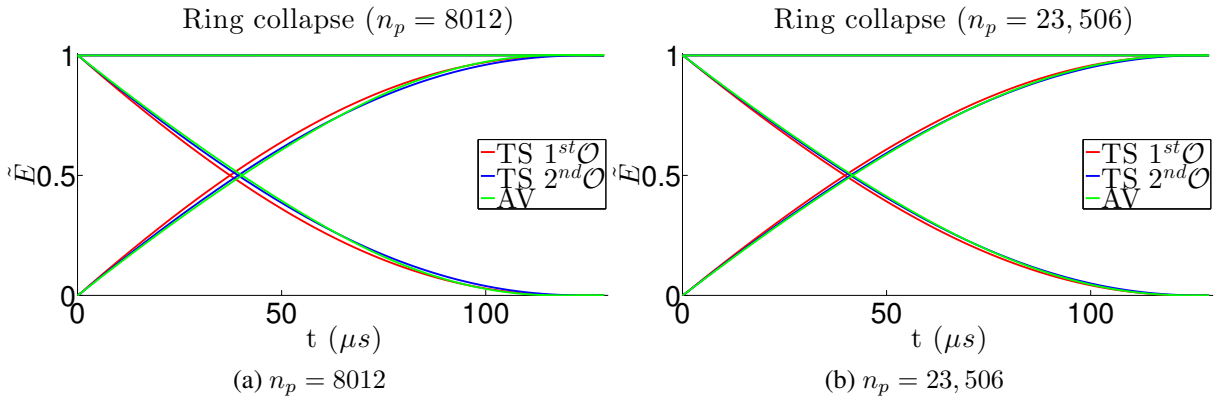


Figure 5: The non-dimensional internal (increasing), kinetic (decreasing) and total energies using the *TS* and *AV* schemes for the collapsing ring case.

Scheme	% ΔE_{tot} ($n_p = 8012$)	% ΔE_{tot} ($n_p = 23,506$)
<i>TS</i> 1 st \mathcal{O}	3.04×10^{-2}	2.75×10^{-11}
<i>TS</i> 2 nd \mathcal{O}	6.67×10^{-4}	2.09×10^{-7}
<i>AV</i>	1.12×10^{-1}	2.55×10^{-4}

Table 3: Percentage errors in total energy for the ring-collapse example using the different schemes. Note that the results using only the *AV* and *TS* schemes are shown as the *PM* scheme was implemented in one-dimension only.

5 APPLICATION

An impact of a steel projectile on a silicon carbide tile is simulated using the *AV* and first and second-order *TS* schemes in 2D plane strain. The steel is described using the Johnson-Cook [13] constitutive model and the Mie-Grüneisen EOS of the form in equation (37) and the

silicon carbide uses the piece-wise linear JH1 ceramic-damage model [14] with a polynomial EOS of the form (with bulking turned off)

$$P(\rho) = k_1\zeta + k_2\zeta^2 + k_3\zeta^3. \quad (39)$$

The Johnson-Cook flow-stress is purely phenomenological, includes terms to take account of the competition between thermal softening and strain hardening and takes the form

$$\sigma_y(\epsilon_p, \dot{\epsilon}_p, T) = (A + B(\epsilon_p^n)) \left[1 + C \ln \left(\frac{\dot{\epsilon}_p}{\dot{\epsilon}_0} \right) \right] \left[1 - \left(\frac{T - T_0}{T_m - T_0} \right)^m \right], \quad (40)$$

where A , B , C , m and n are user-defined parameters and ϵ_p is the plastic strain, $\dot{\epsilon}_p$ is the plastic strain rate, $\dot{\epsilon}_0$ is the reference strain rate, T is the current temperature, T_m is the melting temperature and T_0 is the reference temperature (in degrees Kelvin).

In the JH1 ceramic damage model the yield surface of the material is based upon two piece-wise linear curves; one represents the ‘‘intact’’ strength σ_i and one represents the ‘‘damaged’’ strength σ_d . The material damage is represented by a scalar variable D , where $0 \leq D \leq 1$. When $D < 1$ the strength is represented by the intact strength curve σ_i . A schematic of the JH1 constitutive model is shown in Figure 6. When $D = 1$ the material instantly fails and the

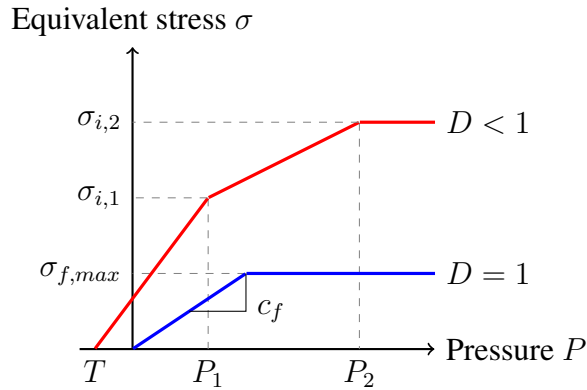


Figure 6: Schematic of JH1 constitutive model.

failed strength curve σ_d is followed. Note that when $D = 1$, the failure strength is only followed for compressive stresses. A gradual softening of the material is allowed in the JH2 constitutive equation [15], however it was found that some fundamental behaviours, such as interface dwell, were not captured accurately with a gradually softening material model [16]. The scalar damage variable D is allowed to increase monotonically as a function of the incremental plastic strain $\Delta\epsilon_p$ and failure strain ϵ_f through

$$D = \sum_t \frac{\Delta\epsilon_p}{\epsilon_f}. \quad (41)$$

The failure strain itself is a linear function of the hydrostatic pressure and is obtained by the interpolation of the line in Figure 7. In the case where $P = T$, the damage variable is set to unity. The material parameters for the silicon carbide target and steel projectile are given in Table 4.

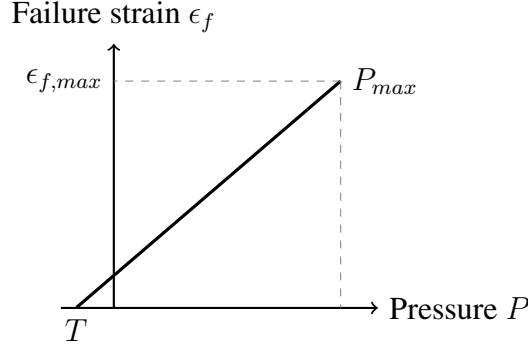


Figure 7: Schematic of JH1 failure strain curve.

<i>SiC EOS Parameter</i>	<i>Value</i>	<i>Steel EOS Parameter</i>	<i>Value</i>
ρ_0	3215 kg/m ³	ρ_0	7903 kg/m ³
k_1	2.2 MBar	S_1	1.4933
k_2	3.61 MBar	Γ_0	2.2
k_3	0	c_0	4.552 km/s
<i>SiC JH1 Parameter</i>	<i>Value</i>	<i>Steel JC Parameter</i>	<i>Value</i>
μ	1.93 MBar	μ	74.8 GPa
$\sigma_{i,1}$	7.1 GPa	A	300.0 MPa
P_1	2.5 GPa	B	1000.0 MPa
$\sigma_{i,2}$	12.2 GPa	C	0.07
P_2	10.0 GPa	M	1.0
$\sigma_{f,max}$	1.3 GPa	N	0.65
c_f	0.4	T_0	298°K
T	-750.0 MPa	T_m	1673°K
$\epsilon_{f,max}$	0.8	c_p	440 J/Kg K
P_{max}	99.75 GPa	χ	0.9
C	0.009	—	—

Table 4: Material parameters for the Johnson-Cook flow stress and Johnson-Holmquist ceramic damage models, from [26].

It is important to note that, in the time-split integration scheme, because the dilatational and deviatoric components are separate, a modification to the dilatational step must be made to reflect the failure model in the constitutive equation. In the case of either of the two interacting particles possessing a damage variable of unity the first-order Godunov scheme is recovered; no linear reconstruction or slope limiting is applied. The following algorithm is proposed for use between each interaction pair: Algorithm 1 ensures that hydrostatic tension is not sustained between damaged particles. It can be thought of as an extension to the limiting procedure in light of the constitutive equation used and the time-splitting procedure which separates the dilatational and deviatoric responses.

The projectile and target are rectangular and have dimensions of $l_p = 2$ cm, $w_p = 1$ cm and $l_t = 3$ cm, $w_t = 10$ cm respectively. In total there are 51,842 equally spaced particles in the domain. The projectile impacts the target with a velocity of 800 m/s. The results (using the

Algorithm 1 Modification to Riemann solution for instantaneous failure

```

if  $D_i = 1 \wedge D_j = 1$  then                                ▷ Both particles fully damaged
     $P_R \leftarrow P_i, P_L \leftarrow P_j$ 
     $v_R \leftarrow v_i^R, v_L \leftarrow v_j^R$ 
     $\rho_R \leftarrow \rho_i, \rho_L \leftarrow \rho_j$ 
    if  $P_i < 0$  then                                       ▷ Tension not allowed
         $P_i \leftarrow 0$ 
    end if
    if  $P_j < 0$  then                                       ▷ Tension not allowed
         $P_j \leftarrow 0$ 
    end if
    Calculate  $P_{ij}^*, v_{ij}^*$                                    ▷ Call Riemann solver
    if  $P_{ij}^* < 0$  then                                       ▷ No tension allowed
         $P_{ij}^* \leftarrow 0$ 
    end if
else if  $D_i = 1 \vee D_j = 1$  then                            ▷ One or more particle fully damaged
     $P_R \leftarrow P_i, P_L \leftarrow P_j$ 
     $v_R \leftarrow v_i^R, v_L \leftarrow v_j^R$ 
     $\rho_R \leftarrow \rho_i, \rho_L \leftarrow \rho_j$ 
    if  $D_i = 1$  then                                       ▷ If particle  $i$  damaged
        if  $P_i < 0$  then                                       ▷ Tension not allowed
             $P_i \leftarrow 0$ 
        end if
    end if
    if  $D_j = 1$  then                                       ▷ If particle  $j$  damaged
        if  $P_j < 0$  then                                       ▷ Tension not allowed
             $P_j \leftarrow 0$ 
        end if
    end if
    Calculate  $P_{ij}^*, v_{ij}^*$                                    ▷ Call Riemann solver
    if  $P_{ij}^* < 0$  then                                       ▷ No tension allowed
         $P_{ij}^* \leftarrow 0$ 
    end if
else                                                         ▷ Both particles undamaged
    Calculate  $P_{ij}^*, v_{ij}^*$                                    ▷ Call Riemann solver
end if

```

1st $\mathcal{O} TS$, 2nd $\mathcal{O} TS$ and AV schemes) of damage field after 5, 10 and 15 μ are shown in Figure 8. It can be seen from Figure 8 that the damage fields using the first order and second-order TS schemes are different to that using the AV scheme, however the second-order TS scheme shows the most similar damage field to the AV scheme. A region of spall is predicted near the back-face of the target in each case. Figure 9 shows the x component of the velocity for the three different schemes; it can be seen that the second-order TS scheme predicts the highest spall velocity.

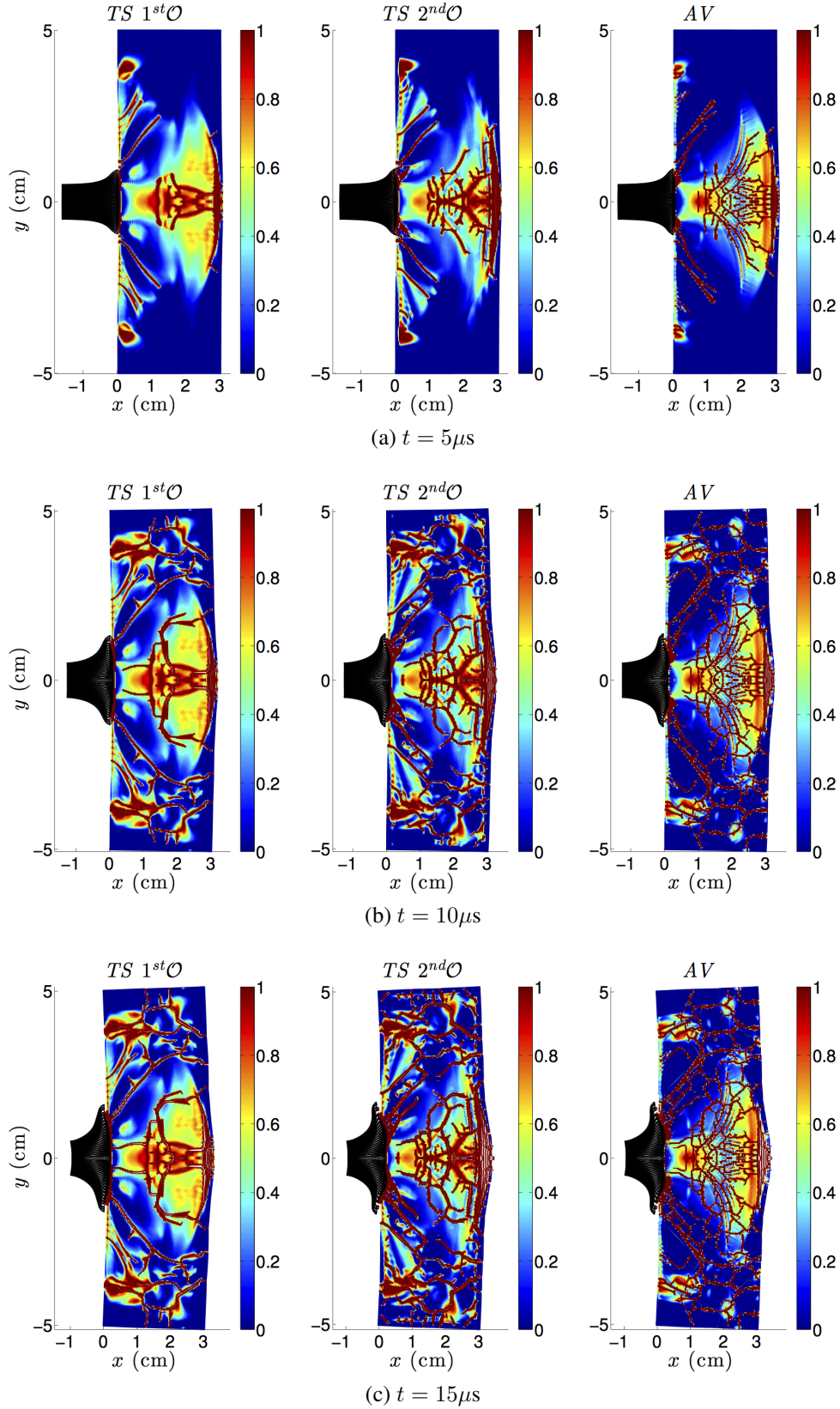


Figure 8: The results of the steel-SiC impact simulation showing scalar damage field for the three schemes at different instances. The steel projectile is shown in black.

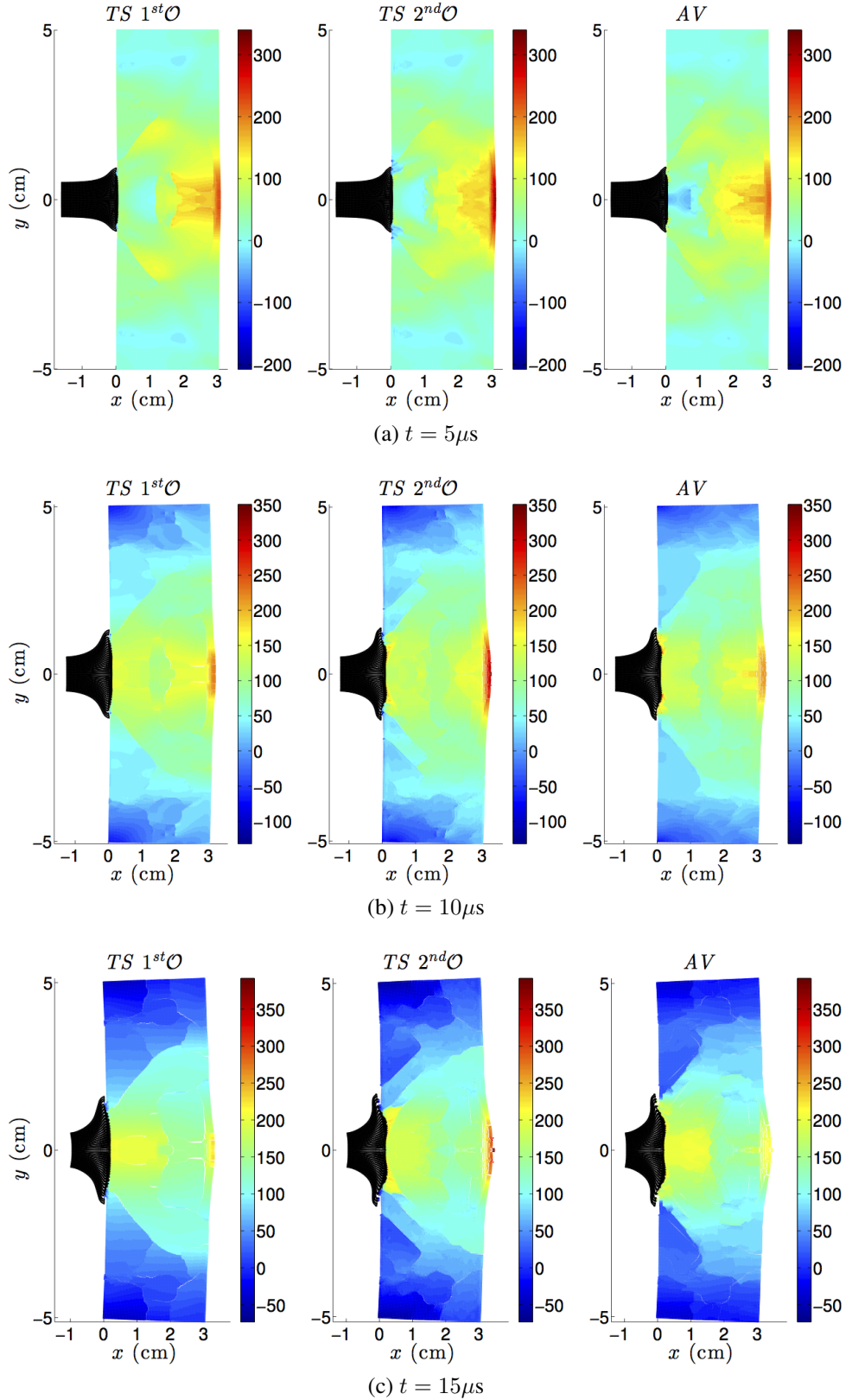


Figure 9: The results of the steel-SiC impact simulation showing x component of the velocity field for the three schemes at different instances. The steel projectile is shown in black.

6 CONCLUSIONS

An extension of the Godunov SPH method of Parshikov *et al.* [23] to second-order has been described for materials with strength. The method relies on the decomposition of the Cauchy stress tensor to its constituent hydrodynamic and deviatoric parts, which are then used within a Lie-Trotter splitting algorithm to integrate the continuum equations sequentially in time. The splitting procedure facilitates the second-order reconstruction of the left and right Riemann-states, as only the longitudinal wave system needs to be solved. In the two-dimensional ring collapse example, it is shown that, in contrast to the *AV* scheme, the *TS* schemes display less particle disorder. This may have the advantageous side effect of enhancing the relative accuracy of the particle approximation of the gradient. The *TS* scheme, however, inherits the kernel instability intrinsic to the SPH method [29] (when using an Eulerian kernel [2]), as the same particle approximation method is used to calculate the derivatives as in the standard *AV* scheme. Further accuracy may be added to the spatial integration procedure by adopting a mixed kernel and kernel gradient correction procedure [17, 18, 34]. An algorithm was proposed to incorporate, into the *TS* scheme, a constitutive model based on continuum damage mechanics such that the scheme could be used to simulate brittle materials. The *TS* scheme is more computationally expensive than both the *AV* and *PM* schemes (the 2nd \mathcal{O} scheme is approximately $2.5\times$ more expensive than the *AV* scheme), however advances in massively parallel GPU computing techniques may reduce this burden to the point where the *TS* scheme is practical [20, 36, 31, 6].

REFERENCES

- [1] D. S. Balsara. von-Neumann analysis of smoothed particle hydrodynamics - suggestions for optimal algorithms. *Journal of Computational Physics*, 121(1):357–372, 1995.
- [2] T. Belytschko, Y. Krongauz, D. Organ, M. Fleming, and P. Krysl. Meshless methods: An overview and recent developments. *Computer Methods in Applied Mechanics and Engineering*, 139(1-4):3 – 47, 1996.
- [3] J. Bonet, S. Kulasegaram, M. Rodriguez-Paz, and M. Profit. Variational formulation for the smooth particle hydrodynamics (SPH) simulation of fluid and solid problems. *Computer Methods in Applied Mechanics and Engineering*, 193(12-14):1245 – 1256, 2004.
- [4] L. Cullen and W. Dehnen. Inviscid smoothed particle hydrodynamics. *Monthly Notices of the Royal Astronomical Society*, 408(2):669–683, 2010.
- [5] V. A. Dobrev, T. E. Ellis, T. V. Kolev, and R. N. Rieben. High-order curvilinear finite elements for axisymmetric lagrangian dynamics. *Journal of Computational Physics*, (0):–, 2013.
- [6] J. M. Domanguez, A. J. Crespo, and M. Gomez-Gesteira. Optimization strategies for cpu and gpu implementations of a smoothed particle hydrodynamics method. *Computer Physics Communications*, 184(3):617 – 627, 2013.
- [7] J. K. Dukowicz. A general, non-iterative riemann solver for Godunov’s method. *Journal of Computational Physics*, 61(1):119 – 137, 1985.
- [8] S. K. Godunov. Difference methods for the numerical calculation of the equations of fluid dynamics. *Math Sbornik*, 47:221–306, 1959.

- [9] L. Hernquist and N. Katz. TREESPH - a unification of SPH with the hierarchical tree method. *Astrophysical Journal Supplement*, 70:419–446, 1989.
- [10] B. P. Howell and G. J. Ball. A free-lagrange augmented Godunov method for the simulation of elastic plastic solids. *Journal of Computational Physics*, 175(1):128–167, 2002.
- [11] S.-I. Inutsuka. Godunov-type SPH. *Memorie della Società Astronomia Italiana*, 65:1027–1031, 1994.
- [12] S.-I. Inutsuka. Reformulation of smoothed particle hydrodynamics with Riemann solver. *Journal of Computational Physics*, 179:238–267, 2002.
- [13] G. R. Johnson and W. H. Cook. A constitutive model and data for metals subjected to large strains, high strain rates and high temperatures. In *Proceedings of the 7th International Symposium on Ballistics*, 1983.
- [14] G. R. Johnson and T. J. Holmquist. *A computational constitutive model for brittle materials subjected to large strains, high strain rates and high pressures*. CRC Press, 1992. editors M. A. Meyers, L. E. Murr and K. P. Staudhammer and Marcel Dekker Inc.
- [15] G. R. Johnson and T. J. Holmquist. An improved computational constitutive model for brittle materials. *AIP Conference Proceedings*, 309(1):981–984, 1994.
- [16] G. R. Johnson, T. J. Holmquist, and S. R. Beissel. Response of aluminum nitride (including a phase change) to large strains, high strain rates, and high pressures. *Journal of Applied Physics*, 94(3):1639–1646, 2003.
- [17] N. Larson and J. P. Vila. Renormalized meshfree schemes I: consistency, stability, and hybrid methods for conservation laws. *SIAM Journal on Numerical Analysis*, 46(4):1912–1934, 2008.
- [18] N. Larson and J. P. Vila. Renormalized meshfree schemes II: convergence for scalar conservation laws. *SIAM Journal on Numerical Analysis*, 46(4):1935–1964, 2008.
- [19] G. R. Liu and M. B. Liu. *Smoothed Particle Hydrodynamics, a meshfree particle method*. World Scientific, 2003.
- [20] B. long Wang and H. Liu. Application of sph method on free surface flows on gpu. *Journal of Hydrodynamics, Ser. B*, 22(5, Supplement 1):912 – 914, 2010.
- [21] J. J. Monaghan. Smoothed particle hydrodynamics. *Reports on Progress in Physics*, 68:1703–1759, 2005.
- [22] J. J. Monaghan and R. A. Gingold. Shock simulation by the particle method SPH. *Journal of Computational Physics*, 52:374–389, 1983.
- [23] A. N. Parshikov and S. A. Medin. Smoothed particle hydrodynamics using interparticle contact algorithms. *Journal of Computational Physics*, 180(1):358–382, 2002.
- [24] M. Pierre-Henri, R. Abgrall, J. Breil, R. Loubère, and B. Rebourcet. A nominally second-order cell-centered Lagrangian scheme for simulating elastic-plastic flows on two-dimensional unstructured grids. Rapport de recherche RR-7975, INRIA, May 2012.

- [25] D. J. Price. Smoothed particle hydrodynamics and magnetohydrodynamics. *Journal of Computational Physics*, 231(3):759 – 794, 2012.
- [26] X. Quan, R. Clegg, M. Cowler, N. Birnbaum, and C. Hayhurst. Numerical simulation of long rods impacting silicon carbide targets using JH-1 model. *International Journal of Impact Engineering*, 33(1-12):634 – 644, 2006.
- [27] J. I. Read and T. Hayfield. SPHS: Smoothed Particle Hydrodynamics with a higher order dissipation switch. *Monthly Notices of the Royal Astronomical Society*, 2011. In press.
- [28] A. Shaw and S. R. Reid. Heuristic acceleration correction algorithm for use in SPH computations in impact mechanics. *Computational Methods in Applied Mechanics and Engineering*, 198(128):3962–3974, 2009.
- [29] J. Swegle, J. Hicks, and S. Attaway. Smoothed particle hydrodynamics stability analysis. *Journal of Computational Physics*, 116:123–134, 1995.
- [30] E. F. Toro. *Riemann Solvers and Numerical Methods for Fluid Dynamics: A Practical Introduction*. Springer, 1999.
- [31] D. Valdez-Balderas, J. M. Domanguez, B. D. Rogers, and A. J. Crespo. Towards accelerating smoothed particle hydrodynamics simulations for free-surface flows on multi-gpu clusters. *Journal of Parallel and Distributed Computing*, (0):–, 2012.
- [32] B. van Leer. Towards the ultimate conservative difference scheme - a second-order sequel to Godunov’s method. *Journal of Computational Physics*, 32(1):101–136, 1979.
- [33] J. Vila. On particle weighted methods and smooth particle hydrodynamics. *Mathematical Models and Methods in Applied Sciences*, 09(02):1935–1964, 1999.
- [34] J. P. Vila. SPH renormalized hybrid methods for conservation laws: Applications to free surface flows. In M. Griebel, M. A. Schweitzer, T. J. Barth, M. Griebel, D. E. Keyes, R. M. Nieminen, D. Roose, and T. Schlick, editors, *Meshfree Methods for Partial Differential Equations II*, volume 43 of *Lecture Notes in Computational Science and Engineering*, pages 207–229. 2005.
- [35] M. L. Wilkins. *Computer Simulation of Dynamic Phenomena*. Springer, 1998.
- [36] Q. Xiong, B. Li, and J. Xu. Gpu-accelerated adaptive particle splitting and merging in sph. *Computer Physics Communications*, (0):–, 2013.

A COMPUTATIONAL STUDY OF THE INJECTION THERAPY FOR MYOCARDIAL INFARCTION DURING THE NECROTIC STAGE

S. Skatulla¹, D. Legner¹, R.R. Rama¹, J. Mbewu², B. D. Reddy², N. Davies³ and T. Franz⁴

¹CERECAM, Department of Civil Engineering, University of Cape Town
7701 Rondebosch, Private Bag X3, South Africa
e-mail: {sebastian.skatulla,dieter.legner,riteshrao.rama}@uct.ac.za

²CERECAM, Department of Mathematics and Applied Mathematics
7701 Rondebosch, Private Bag X3, South Africa
e-mail: {daya.reddy,james.mbewu}@uct.ac.za

³CRVU, Chris Barnard Division of Cardiothoracic Surgery
7700 Mowbray, South Africa
e-mail: neil.davis@uct.ac.za

⁴CRVU, Chris Barnard Division of Cardiothoracic Surgery, University of Cape Town
PERC, Research Office, University of Cape Town
7701 Rondebosch, South Africa
Centre for High Performance Computing
7700 Rosebank, South Africa
e-mail: thomas.franz@uct.ac.za

Keywords: Myocardial Infarction, Injection Therapy, Computational Cardiology, Meshless Method.

Abstract. *Myocardial infarction is an increasing health problem worldwide. Due to an under-supply of blood, the cardiomyocytes in the affected region permanently lose their ability to contract. This in turn gradually weakens the overall heart function. A new therapeutic approach based on the injection of a gel into the infarcted area aims to support the healing and to inhibit adverse re-modelling that can lead to heart failure. A computational model is the basis for obtaining a better understanding of the heart mechanics, in particular, how myocardial infarction and gel injections affect its pumping performance. A strain invariant based stored energy function is proposed to account for the passive mechanical behaviour. The active contraction is represented by the Guccione model [1]. To incorporate injections an additive homogenization approach is introduced. The injectate has been characterized mechanically by indentation tests. As a numerical framework we are using the in-house code SESKA which is based on the Element-Free Galerkin method. The main focus of this contribution is to principally investigate how gel injections influence the mechanics and performance of the left ventricle during a full heart beat, i.e. in the diastolic filling and the systolic contraction phase. This investigation shows, that gel injections are able to reduce maximal fibre stresses caused by an infarct. This*

effect is dependent on the gel stiffness, whereas the higher the gel stiffness the more the diastolic filling is hampered, which is expected to influence pumping function as a side effect. A reduction of maximal fibre stresses is of importance with respect to prevent fatal rupture, which typically occurs during the necrotic phase. This might happen with preference in the highly stressed area, which based on the presented results can be found at the interface between infarct and healthy remote. The presence of stress peaks in that area is explained by the change of stiffness and contraction behaviour (contracting, non-contracting).

1 INTRODUCTION

Myocardial infarction, which constitutes a serious health problem, is a consequence of blockage of a coronary artery. Due to the resulting under-supply of oxygen, myocytes in the nearby region die. This in turn reduces the amount of contractile tissue and gradually weakens the overall heart function. Computational methods can be used to obtain a better understanding of how myocardial infarction affects cardiac function, and are therefore potentially useful in the design of suitable therapeutic treatments. A new therapeutic approach, which involves the injection of a gel into the infarcted heart, is the subject of this study.

Computational studies of the influence of injections into an infarcted heart were first carried out fairly recently. The usual approach to these problems has been the finite element method. WALL et al. [16] considered an infarcted ovine left ventricle (LV) and represented injections by modifying the material stiffness with regard to the healthy tissue. WENK et al. [18] primarily investigated the influence of polymeric injection patterns in a dog LV. In WENK et al. [17] an infarcted LV of a sheep and calcium hydroxiapatite-based injections were considered. KORTSMIT et al. [9] investigated the influence of polyethylene glycol-based hydrogel injections into an infarcted canine heart.

To reduce the complexity of the computational model most of the studies mentioned considered the left ventricle only. In WENK et al. [18] and NIEDERER et al. [11] the LV was idealized using an ellipsoidal geometry. Compared to the healthy remote, the infarcted tissue has to be described with different material properties. These change throughout the healing process (see for example GUPTA et al. [5], HOLMES et al. [7]). Research aimed at developing and optimizing injectable gels suitable to improve cardiac function has been initiated only recently (see NELSON et al. [10] for a good overview). A great variety of gels have been investigated: these range from biological to synthetic gels.

The present work focuses on the question of the potential of injection therapy and its effects in broad terms. Thus, instead of considering a realistic geometry of the left ventricle, a simplified ellipsoidal geometry which allows the fibre directions to be described in terms of prolated ellipsoidal coordinates is used (see also WENK et al. [18], NIEDERER et al. [11]).

The structure of the present contribution is as follows: In section 2 the constitutive models relevant to cardiac mechanics in this work are discussed. In section 3 the numerical model is described, benchmarked, and subsequently used to investigate healthy, infarcted and injected left ventricles. The results are presented in section 4 for diastolic filling and systolic isovolumetric contraction. Finally, section 5 concludes the work by briefly evaluating the applicability of the present model, the innovative aspects, and the findings. The section closes with comments on potential future investigations.

2 Constitutive modelling

2.1 Passive stress model

Passive behaviour in the left ventricle wall is modelled as a nonlinear, orthotropic and nearly incompressible hyperelastic material, with strain energy function

$$W = A(e^Q - 1)/2 + A_{\text{compr}} \{ \det[\mathbf{U}] \ln(\det[\mathbf{U}] - \det[\mathbf{U}] + 1) \} \quad . \quad (1)$$

Here, Q given by

$$Q = b_{11} \hat{E}_{11}^2 + b_{22} \hat{E}_{22}^2 + b_{33} \hat{E}_{33}^2 + b_{12} (\hat{E}_{12}^2 + \hat{E}_{21}^2) + b_{13} (\hat{E}_{13}^2 + \hat{E}_{31}^2) + b_{23} (\hat{E}_{23}^2 + \hat{E}_{32}^2) \quad (2)$$

(see USYK et al. [15]). The components \hat{E}_{ij} of the *Green* strain \mathbf{E} are relative to a local orthonormal basis \mathbf{V}_i with fibre axis \mathbf{V}_1 , sheet axis \mathbf{V}_2 , and sheet-normal axis \mathbf{V}_3 :

$$\begin{aligned} \mathbf{E} = & \hat{E}_{11}\mathbf{V}_1 \otimes \mathbf{V}_1 + \hat{E}_{22}\mathbf{V}_2 \otimes \mathbf{V}_2 + \hat{E}_{33}\mathbf{V}_3 \otimes \mathbf{V}_3 + \hat{E}_{12}(\mathbf{V}_1 \otimes \mathbf{V}_2 + \mathbf{V}_2 \otimes \mathbf{V}_1) \\ & + \hat{E}_{13}(\mathbf{V}_1 \otimes \mathbf{V}_3 + \mathbf{V}_3 \otimes \mathbf{V}_1) + \hat{E}_{23}(\mathbf{V}_2 \otimes \mathbf{V}_3 + \mathbf{V}_3 \otimes \mathbf{V}_2) \quad . \end{aligned} \quad (3)$$

The right stretch tensor is denoted by \mathbf{U} . Then Q may be expressed in the form

$$\begin{aligned} Q := & a_1(\text{tr}(\mathbf{M}^1\mathbf{E}))^2 + a_2(\text{tr}(\mathbf{M}^2\mathbf{E}))^2 + a_3(\text{tr}(\mathbf{M}^3\mathbf{E}))^2 \\ & + a_4\text{tr}(\mathbf{M}^1\mathbf{E}^2) + a_5\text{tr}(\mathbf{M}^2\mathbf{E}^2) + a_6\text{tr}(\mathbf{M}^3\mathbf{E}^2) \quad , \end{aligned} \quad (4)$$

with the structural tensors \mathbf{M}^i defined by

$$\mathbf{M}^1 = \mathbf{V}_1 \otimes \mathbf{V}_1 \quad , \quad \mathbf{M}^2 = \mathbf{V}_2 \otimes \mathbf{V}_2 \quad , \quad \mathbf{M}^3 = \mathbf{V}_3 \otimes \mathbf{V}_3 \quad . \quad (5)$$

Now the orthotropic constitutive model is used to represent transversely isotropic behaviour of the heart wall. Following OMENS et al. [12] and NIEDERER et al. [11] for the rat LV we use the set of material coefficients given in Tab. 1. A comparison of eq. 2 and eq. 4 yields

b_{11}	b_{22}	b_{33}	b_{12}	b_{13}	b_{23}
9.2	2.0	2.0	3.7	3.7	1.0

Table 1: Material coefficients used in the strain energy function eq. 1, eq. 2

the parameters for the strain invariant formulation in Tab. 2. The coefficients A and A_{compr}

a_1	a_2	a_3	a_4	a_5	a_6
2.8	1.0	1.0	6.4	1.0	1.0

Table 2: Material coefficients used in the strain invariant representation eq. 1, eq. 4

are determined by calibrating the numerical model of the left ventricle of the rat, as will be described later.

2.2 Active stress model

In the active stress formulation the sum of a passive stress \mathbf{S}_P representing the passive mechanical response of tissue to loads and an active contractile stress \mathbf{S}_A defines the total stress

$$\mathbf{S} = \mathbf{S}_P + \mathbf{S}_A \quad . \quad (6)$$

The passive stress is obtained from the passive mechanical constitutive law, so that when there is no active stress ($\mathbf{S}_A = \mathbf{0}$), the myocardium simply behaves passively. The active stress acts in the direction of the fibre \mathbf{V}_1 ; that is,

$$\mathbf{S}_A = T_A \mathbf{V}_1 \otimes \mathbf{V}_1 \quad . \quad (7)$$

The variable T_A represents the active tension developed in the myocyte and is derived from a cellular model of tension development in myocytes. For the purpose of studying the tissue-level mechanics of the heart the model of GUCCIONE et al. [4] is adopted. This model was

derived from biophysical considerations of calcium dynamics and crossbridge formation. The parameters used in the model were calibrated to fit experimental tension test data of a dog, while the magnitude of the active tension was modified to represent that of a rat. The Guccione model predicts the tension according to

$$T_A = T_{\max} \frac{Ca_0^2}{Ca_0^2 + ECa_{50}^2(l)} C_t(l, t) \quad (8)$$

where C_t represents the time transient, a function of time and sarcomere length, ECa_{50}^2 represents the calcium concentration at 50% tension, Ca_0 is the peak intracellular calcium concentration, l is the sarcomere length, and T_{\max} is the maximum tension developed. The functions C_t and ECa_{50} are given by

$$C_t = \frac{1}{2} (1 - \cos \omega(l, t)) \quad , \quad (9)$$

$$ECa_{50}(l) = \begin{cases} \frac{Ca_0^{\max}}{\sqrt{\exp[B(l-l_0)]-1}} & \text{for } l > l_0 \quad , \\ 0 & \text{for } l \leq l_0 \quad , \end{cases} \quad (10)$$

where t_0 is the time at maximum tension, B is a constant and l_0 is the sarcomere length below which there is no active tension developed. The sarcomere length is a function of the stretch with respect to the reference configuration in the fibre direction so that

$$l = l_R \sqrt{2\text{tr}((\mathbf{V}_1 \otimes \mathbf{V}_1)\mathbf{E}) + 1} = l_R \sqrt{2E_{\text{ff}} + 1} \quad (11)$$

where l_R is the sarcomere rest length in the undeformed reference configuration and E_{ff} the direct component of *Green* strain in the fibre direction. The time-dependence of the active tension is described by

$$\omega(l, t) = \begin{cases} \pi \frac{t}{t_0} & \text{for } 0 \leq t < t_0 \quad , \\ \pi \left[\frac{t-t_0}{t_r(l)} + 1 \right] & \text{for } t_0 \leq t < t_0 + t_r \quad , \\ 0 & \text{for } t \geq t_0 + t_r \quad , \end{cases} \quad (12)$$

which also takes into account the influence of the current sarcomere length on the duration of active contraction, that is, the length-dependence of the calcium sensitivity of proteins that cause tension development. The constant t_0 is the time to peak tension and t_r is the duration of the relaxation period described as a function of the sarcomere length

$$t_r = m \cdot l + b \quad (13)$$

with constants m and b . The parameters used in the Guccione model are given in Tab. 3.

T_{\max} [kPa]	Ca_0 [μM]	Ca_0^{\max} [μM]	B [$\frac{1}{\mu\text{m}}$]	l_0 [μm]	t_0 [ms]	m [$\frac{\text{s}}{\mu\text{m}}$]	b [ms]
56.7	4.35	4.35	4.75	1.58	250	1.0489	-1429

Table 3: Parameters used in Guccione model.

2.3 Homogenization approach

The infarcted and injected myocardial tissue is modelled as an homogenized, that is, averaged, material response. Similar approaches can be found for the case of elasticity in REESE et al. [13] or for elasto-plasticity in KLINKEL et al. [8]. Considering hyperelastic material behaviour, we introduce a stored energy function of the form

$$\psi = \sum_{I=1}^m n_I \psi_I(\mathbf{E}) \quad (14)$$

where m denotes the number of superimposed material phases and n_I , $I = 1, m$ the corresponding volume fractions associated with the stored energy functions ψ_I , each representing the material behaviour of a specific constituent. The weighted nature of the overall response is achieved by imposing the constraint $\sum_{I=1}^m n_I = 1$. The different material phases are linked by the kinematic constraint that the deformation gradient applies to all of them. Consequently, the averaged second *Piola-Kirchhoff* stress tensor is given by

$$\mathbf{S} = \frac{\partial \psi}{\partial \mathbf{E}} = \sum_{I=1}^m n_I \frac{\partial \psi_I}{\partial \mathbf{E}} \quad (15)$$

In particular, the healthy myocardium consists of one single active anisotropic phase, and the injected infarct region consists of two passive phases, an anisotropic and an isotropic one, the latter for the injected biogel. In this sense, at each point the stress response of the mixture as well as of each individual component can be obtained. The latter is useful, as the influence of the biogel, in terms of amount of injectate and stiffness, on the fibre stress experienced in the infarct area is of special interest.

3 Numerical model

In this section the numerical model for the healthy LV is first described and benchmarked by comparison with data from the literature. Secondly, the model is used to study the effect of the new therapeutic method on the idealized infarcted ventricle. More specifically, an infarcted left ventricle of a rat during diastolic filling and systolic isovolumetric contraction is considered. Fatal wall rupture commonly occurs in the necrotic phase, as stresses are elevated due to a increase in stiffness of the infarct tissue as well as wall thinning due to removal of dead tissue at that stage. Earlier infarct stages are commonly reserved for medicamentous or surgical treatment to dissolve or bypass the blockade. Later healing stages and remodelling are strongly influenced by boundary conditions which are set in the necrotic healing stage, e.g. see HOLMES et al. [7]. Thus, this contribution focuses on the impact of gel injections into the infarcted area during the necrotic healing phase.

An overlapping of the injectate into the border zone between infarct and healthy remote is considered. For the infarct stage it is assumed that the remaining healthy tissue within the border zone maintains its contractile properties. It is assumed further that the removed volume of dead tissue for both the infarct area and the border zone is in balance with the injectate volume. As the constitutive behaviour of the border zone for the different healing stages is still under scientific discussion, such an assumption does not represent reality. Nevertheless, it allows the phenomenology of the border zone and the essential aspects of injections to be captured in a general sense, in line with the purpose of this investigation. The area between the healthy remote and infarct (injection) region is referred to as the overlap zone.

	healthy zone	infarct zone	overlap zone
healthy (a)	100 %	0 %	0 %
infarcted (b)	84.2 %	15.8 %	0 %
injected (c)	71.0 %	15.8 %	13.2 %

Table 4: Volume fractions with respect to the total wall volume for (a) healthy, (b) infarcted, (c) injected case

3.1 Truncated ellipsoidal model of the rat left ventricle

The geometry of the left ventricle is assumed to be described by a truncated ellipsoid. This may conveniently be described in terms of prolate spheroidal coordinates (ξ, η, θ) which are related to the Cartesian ones (x, y, z) by

$$\begin{aligned}
 x &= C \cdot \sinh(\xi) \cdot \sin(\eta) \cdot \cos(\theta) \\
 y &= C \cdot \sinh(\xi) \cdot \sin(\eta) \cdot \sin(\theta) \\
 z &= C \cdot \cosh(\xi) \cdot \cos(\eta)
 \end{aligned} \tag{16}$$

In accordance with NIEDERER et al. [11] the endocardial and epicardial radii at the widest point are 2.4 mm and 5.1 mm, respectively. The distance from the apex to the base is 11.5 mm for the endocardium (endo) and 13.2 mm for the epicardium (epi). This corresponds to $\xi_{endo} = 0.31$, $\xi_{epi} = 0.60$ and the focal lengths $C_{endo} = 7.61$ mm, $C_{epi} = 8.01$ mm. It follows that $V_{cav}^{init} = 155.57 \mu\text{l}$ and $V_{myo}^{init} = 641.96 \mu\text{l}$ for the initial cavity volume and the initial myocardial wall volume, respectively. The varying fibre directions throughout the wall are adopted from RIJCKEN et al. [14]. With respect to the geometric boundary conditions the natural deformation of the LV during a heartbeat shows that almost the whole LV undergoes vertical, horizontal and transversal movements simultaneously. Only the movement of the base is restricted. Hence, the endocardial ring is fixed at the base and the surface displacement of the base is restrained in the vertical direction.

3.2 Model calibration

The numerical model of the healthy left ventricle is calibrated by using pressure-volume relations given in the literature. In combination with the parameters given in Tab. 2 the coefficients $A = 1.00$ kPa and $A_{compr} = 300.00$ kPa are chosen (see eq. 1), to adjust the passive stress model as discussed in section 2.1. With this choice the relation between cavity volume and increasing cavity pressure applied to the endocardial wall of the present numerical model agrees well with results reported in the recent literature: see Fig. 1. Furthermore, for the cavity pressure $p_{cav} = 30.0$ mmHg the calculated myocardial wall volume $V_{myo} = 639.98 \mu\text{l}$ is still very close to the initial one $V_{myo}^{init} = 641.96 \mu\text{l}$, hence the myocardial wall behaves nearly isochorically.

3.3 Case study

We distinguish three cases: (a) a healthy LV; (b) an infarcted LV; and (c) infarcted and injected LV (see Fig. 2). The relevant volume fractions for these three cases can be found in Tab. 4, where with respect to the grading given in WENK et al. [19] an infarct of grade 1 ($< 20\%$) is considered here. A fatal rupture of the infarct tissue generally occurs during the necrotic phase. This motivates the consideration of an infarct at that healing stage, and the investigation of the influence of a hydrogel injection directly into the infarct zone (red). To represent the fact that the hydrogel injection stops abruptly at the infarct border, we consider a so-called overlap zone

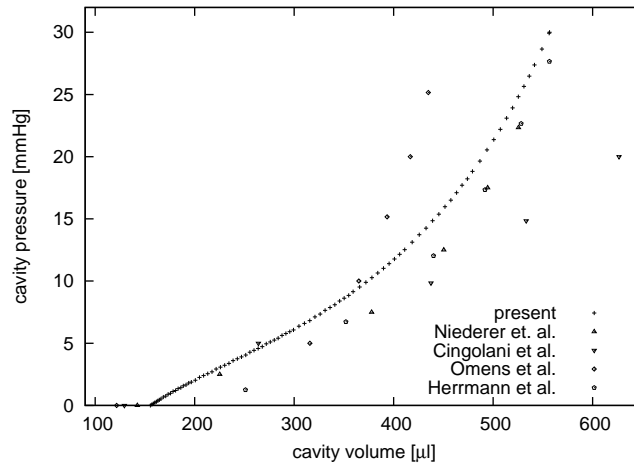


Figure 1: Pressure-volume relation for the left ventricle using the present model compared with data from NIEDERER et al. [11], CINGOLANI et al. [3], OMENS et al. [12], HERRMANN et al. [6]

(grey) into the healthy remote (blue). In order to model a smooth transition the overlap zone has a reduced gel volume fraction compared to the gel volume fraction of the infarct area. The infarct zone and overlap zone are incorporated by intersecting the truncated ellipsoid with two spheres of different radii. To represent the stiffening of the infarct tissue during the necrotic

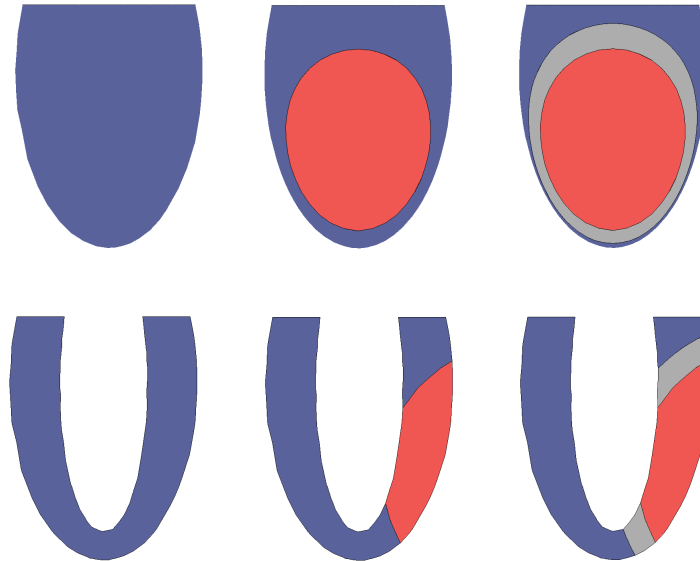


Figure 2: Front view (top row) and vertical cut (bottom row) of the (a) healthy, (b) infarcted, (c) injected LV with healthy remote (blue), infarct (red) and overlap zone (grey)

stage of healing considered here (see for example GUPTA et al. [5], HOLMES et al. [7]), the infarct stiffness is set at twice that of the healthy remote. That is, the weighting factor in the passive stress model is $A = 2.00 \text{ kPa}$, see eq. 1. Based on unpublished experiments and characterization procedures, the hydrogel compound is approximated by a Neo-Hookean material model with the material parameters $\mu = 24.6 \text{ Pa}$ and $\lambda = 983.6 \text{ Pa}$, which are from now on referred to collectively using the notation kgel . We subdivide the injection case (c) into four cases (c1), (c2), (c3), (c4), referring respectively to 0.25 kgel , 0.50 kgel , 0.75 kgel , 1.0 kgel . Hereby, (c4) represents the actual hydrogel, whereas (c1) - (c3) are hypothetical injectates with

reduced stiffness. That is μ and λ of (c4) given above are multiplied by the factor 0.25, 0.50 and 0.75, respectively. To account for the wall-thinning effect, in case (b) the infarct volume contains 90% infarct material and 10% of a dummy material with negligible stiffness, representing the dead material transported away at the micro-structural level. The hydrogel-treated infarct region, case (c), is made up of a homogenized mixture of infarct and hydrogel material. Basically, the volume of the injectate in that case replaces the dummy material of case (b). The overlap zone is modelled with 95% healthy tissue and 5% hydrogel. This mixture ratio reflects the assumption that the injectate enters the healthy tissue surrounding the infarct within a limited radius, referred to as the overlap zone. The mixing of materials is achieved by employing the homogenization approach discussed in section 2.3.

4 Numerical results

The results for the healthy (a), infarcted (b) and injected (c1) - (c4) cases are now shown separately for diastolic filling and systolic isochoric contraction. During diastolic filling the cavity pressure p_{cav} is increased up to $p_{cav}^{EDF} = 7.5$ mmHg, marking the end of the diastolic filling phase. At the outset of the systolic isovolumetric contraction phase the active stress model of section 2.2 is initiated and the cavity pressure is increased up to a value $p_{cav}^{ESIC} = 37.5$ mmHg while the cavity volume is enforced to be constant. The pressure values p_{cav}^{EDF} and p_{cav}^{ESIC} for the rat left ventricle are adopted from NIEDERER et al. [11]. The computational model is developed using the element-free Galerkin method (see for example BELYTSCHKO et al. [1]), implemented in the in-house code *SESKA*. The numerical model of the left ventricle consists of 1700 particles. It was found that further refinements did not lead to any significant change in the results.

4.1 Diastolic filling

Comparing the healthy case (a) with the infarct case (b) in Fig. 3, an overall reduction in cavity volume is observed during diastolic filling, which indicates that the overall infarct stiffness is increased in the necrotic healing stage. This is reasonable and is also reported in the literature, for example by BOGEN et al. [2], HOLMES et al. [7], as the resulting infarct stiffness takes into account two kinds of effects: (i) a slight reduction in stiffness as a portion of dead myocytes has been transported away leading to a lower material density on micro-structural level and thus, a reduced effective wall thickness; (ii) a significant increase of stiffness of the remaining infarcted myocardium GUPTA et al. [5]. The homogenized, i.e. averaged, stiffness in the infarct zone is consequently higher than in the healthy remote, explaining the reduction in LV compliance. For all injectates (c1) - (c4), the end-diastolic cavity volume is predicted to be smaller than in case (a) and (b), see Fig. 3, which indicates that the injectate (c4) is fairly stiff. Even the hypothetically considered injectates (c1) - (c3) with reduced stiffness hamper diastolic filling considerably.

This finding is confirmed by the deformation results obtained at the end of diastolic filling p_{cav}^{EDF} , shown in terms of a representative vertical cut in Fig. 4 for all cases considered. A qualitative comparison with the undeformed configuration, see Fig. 2, reveals that the infarct and injectate stiffnesses are inversely related to the wall thickness reduction in the respective regions for cases (b) - (c). The deformation behaviour in the healthy remote is similar for all the cases (a) - (c). We consider next the myocardial fibre stress and effective strain, and compare qualitatively the mechanical response for the cases considered.

Fig. 5 shows no significant increase in end-diastolic tissue fibre stress for the infarcted case (b).

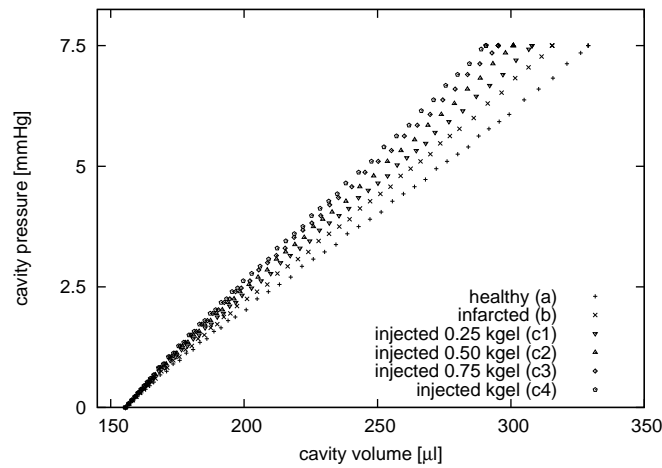


Figure 3: Pressure-volume relations during diastolic filling of healthy (a), infarcted (b), injected (c1) - (c4) left ventricle

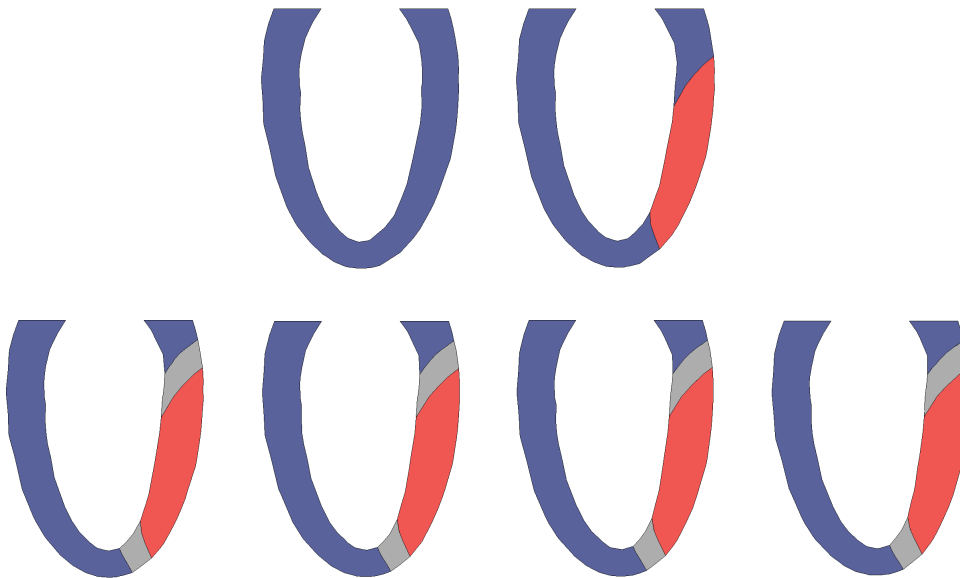


Figure 4: Deformation of the left ventricle at the end of diastolic filling - top row: (a) healthy (left), (b) infarcted (right); bottom row: injected (c1), (c2), (c3), (c4) from left to right

However, it can be seen that the stiffer the injectate in cases (c1) - (c4), the greater the reduction in the tissue fibre stresses compared to healthy case (a) and infarcted case (b), respectively. This is explained by the fact that a stiffer injectate has a reinforcing effect and thus reduces the myocardial fibre stress.

Fig. 6 shows that the effective strains are clearly reduced due to the higher stiffness of the infarct case (b), and are even further reduced when hydrogel is injected, as in cases (c1) - (c4). This observation is confirmed by studying the pressure-volume relation Fig. 3 and the deformed cross-sections Fig. 4, which indicates a decrease in filling compliance.

4.2 Systolic isovolumetric contraction

In contrast to the diastolic filling phase, the left ventricle during the systolic isovolumetric phase is subjected to active contraction at constant cavity volume, causing an increase in cavity

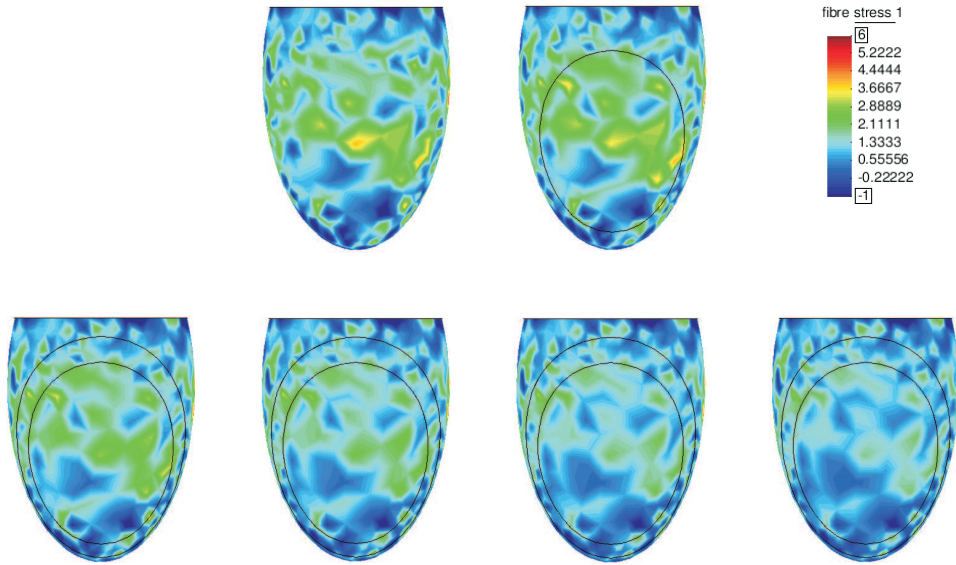


Figure 5: Fibre stress distribution at the end of diastolic filling - top row: (a) healthy (left), (b) infarcted (right); bottom row: injected (c1), (c2), (c3), (c4) from left to right

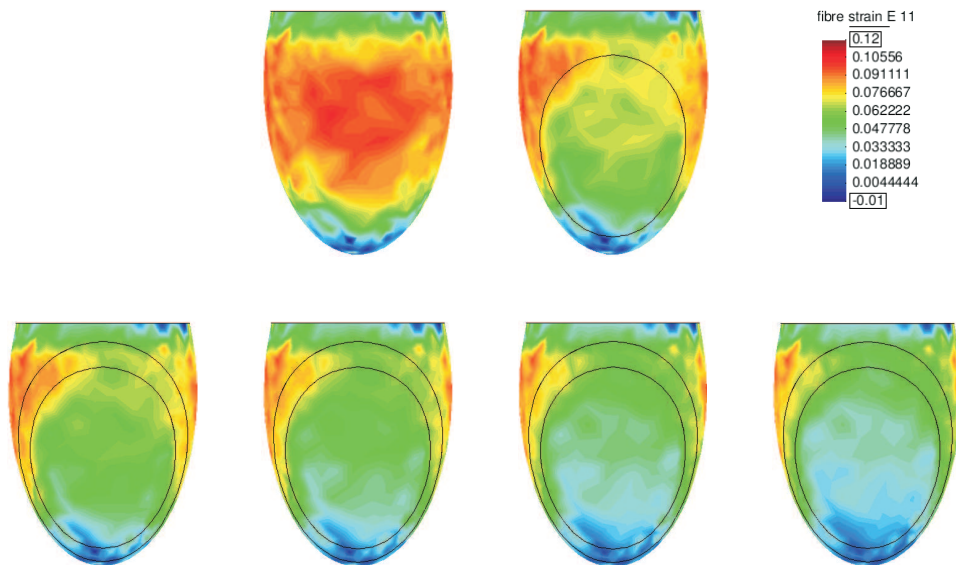


Figure 6: Distribution of strain in fibre direction at the end of diastolic filling - top row: (a) healthy (left), (b) infarcted (right); bottom row: injected (c1), (c2), (c3), (c4) from left to right

pressure. Qualitatively, the resulting deformation at the end of systolic isovolumetric contraction depicted in Fig. 7 shows a slight vertical elongation accompanied by a wall-thickness reduction as compared with the configuration at end-diastolic filling in Fig. 4. This feature of the deformation correlates with the constant cavity volume during isovolumetric contraction and the almost incompressible constitutive modeling of the LV wall. In accordance with NIEDERER et al. [11] longitudinal shortening and an increase in wall thickness is only to be expected for systolic ejection, which is not considered in the framework of this contribution. Compared to the diastolic phase the deformation in cases (b) and (c) occurs in a less symmetric way than for the diastolic phase. Fig. 8 illustrates on the one hand drastically reduced fibre stresses within the infarcted region for the untreated infarct case (b) and the injected infarct cases (c1) - (c4) compared to the healthy case (a). On the other hand it can be observed that at the interface

between the healthy and infarcted area in case (b) the maximal fibre stresses are greater than for the healthy case (a). Studying the injected cases (c1) - (c4), it can be seen that the injection relieves this highly stressed zone of case (b) even below healthy levels, whereas the stiffness of the injectate is without major influence. Due to the loss of active contraction the infarcted region is almost completely subjected to stretch, see Fig. 9. This feature can also be observed for all injection cases.

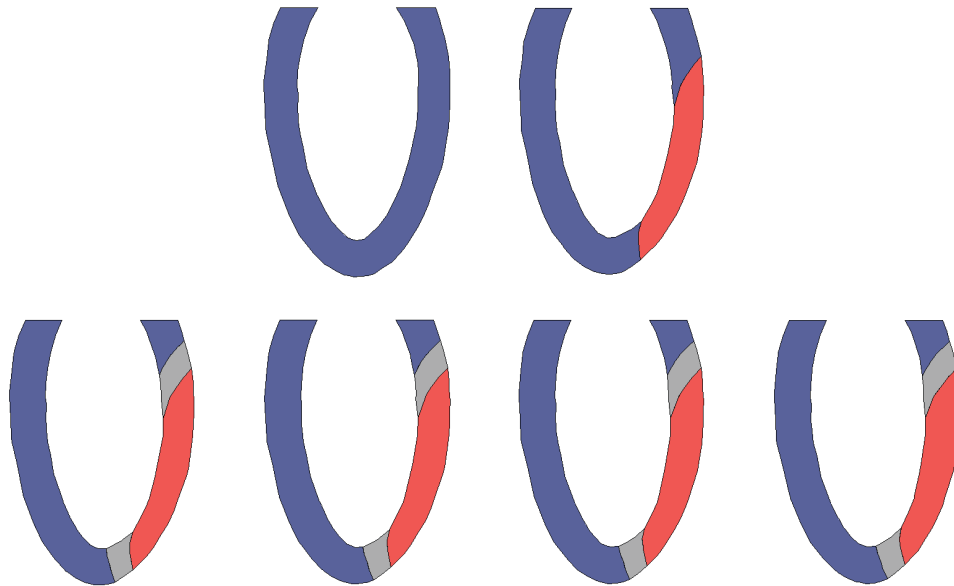


Figure 7: Deformation of the left ventricle at the end of isovolumetric systolic contraction - top row: (a) healthy (left), (b) infarcted (right); bottom row: injected (c1), (c2), (c3), (c4) from left to right

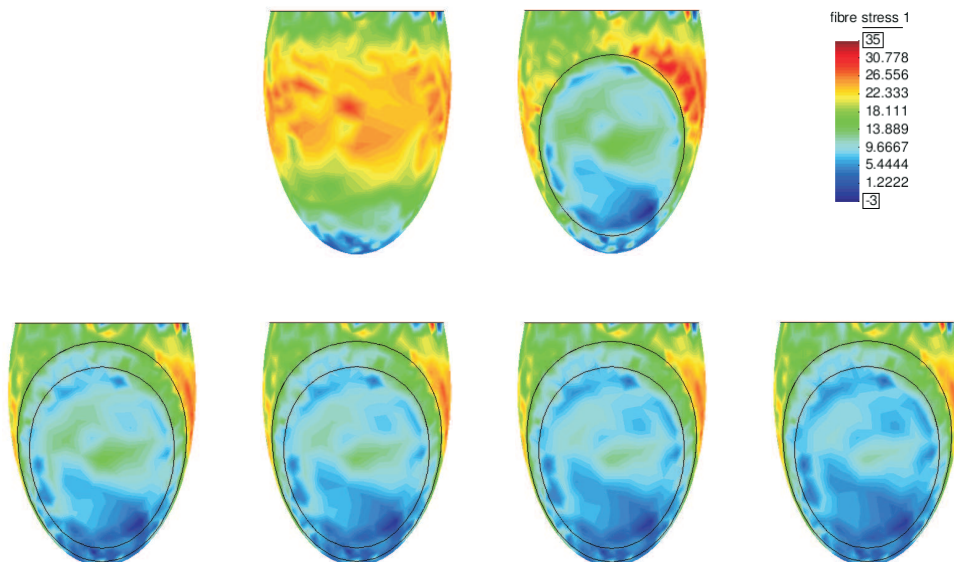


Figure 8: Fibre stress distribution at the end of isovolumetric systolic contraction - top row: (a) healthy (left), (b) infarcted (right); bottom row: injected (c1), (c2), (c3), (c4) from left to right

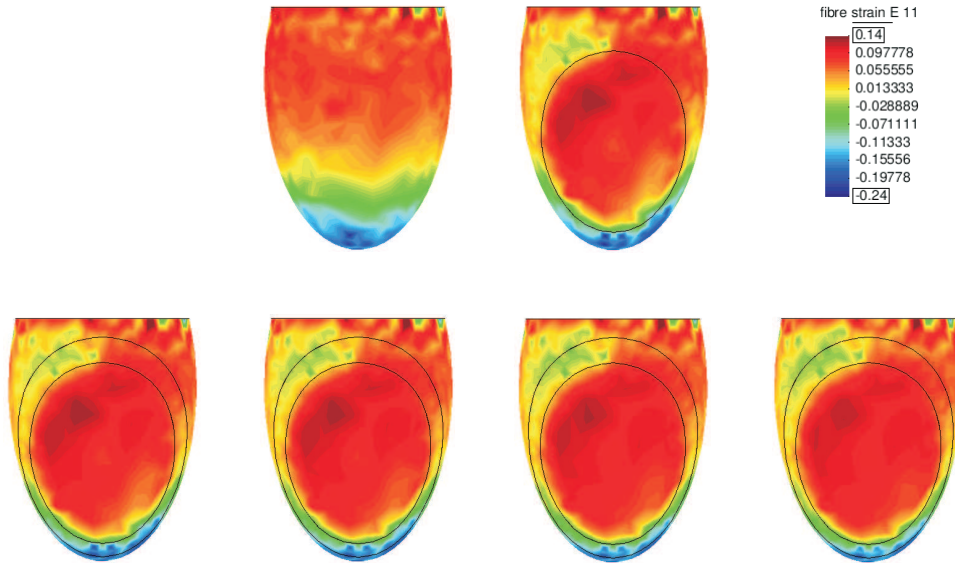


Figure 9: Distribution of strain in fibre direction at the end of isovolumetric systolic contraction - top row: (a) healthy (left), (b) infarcted (right); bottom row: injected (c1), (c2), (c3), (c4) from left to right

5 Conclusion

5.1 The applicability of the model

The objective of the present investigation is not to provide definitive, quantitative results for a realistic LV. Instead, the focus of the contribution has been to study qualitatively the influence of hydrogel injections into an infarcted left ventricle, modelled by a geometry that is simple yet able to capture key features. Of particular interest are representative values for the pressure, volume, deformation, and stress and strain quantities. In this regard, for the sake of simplicity a rotational symmetric geometry is used and an overlap zone representing a more realistic gel distribution is considered. Further, the active contraction is simultaneously initiated throughout the LV. Attention is restricted to the necrotic healing phase by considering a grade 1 infarct, with the assumption that the amount of injectate is equal to the amount of removed tissue for both the infarct and the overlap zone.

5.2 Novel aspects of this contribution

A meshless method is used as the basis for the numerical model and simulations. A strain invariant-based stored energy function is introduced, allowing frame-invariant and more compact expressions for the stress tensors and material tensors. A homogenization approach is introduced to account for representative material behaviour of an arbitrary mix of different materials and volume fractions. Four different injection types are investigated and compared with the healthy and infarcted case, where one of them is a realistic gel which is being used in current experiments.

5.3 Findings

This investigation shows that gel injections are able to reduce maximal fibre stresses caused by an infarct. The higher the gel stiffness the more the diastolic filling is hampered, which is expected to influence pumping function as a side effect. A reduction of maximal fibre stresses is of importance with respect to the prevention of fatal rupture, which typically occurs during

the necrotic phase. This could be more likely in the highly stressed area, which on the basis of the results presented can be found at the interface between the infarct and healthy remote. The presence of stress peaks in that area is explained by the discontinuity of stiffness and contraction behaviour (contracting, non-contracting).

5.4 Recommendations / Outlook

It would be of interest to investigate the effects of injections only at the interface zone, thus providing a smoother transition of mechanical properties. As such a strategy would also reduce the amount of injectate, and the net reduction of overall pumping function might be less pronounced, which could be confirmed, for example, in terms of monitoring typical cardiac parameters like stroke volume, ejection fraction, etc. Nevertheless, with respect to later healing stages the injection modalities that account, for example, for weaker infarct stiffness causing thinning of the infarct zone itself, followed by negative remodeling of the LV might be different. Thus, the timing of the injections and the chosen injectate degradabilities are other important aspects for future investigations, within a dynamic context, to contribute to a more complete understanding and assessment of the therapeutic suitability of the gel.

5.5 Acknowledgement

The research leading to this work has been supported by the Centre for High Performance Computing of South Africa. The financial support of the Claude Leon Foundation through a postdoctoral fellowship for D.L. is gratefully acknowledged. B.D.R. acknowledges the support of the National Research Foundation through the South African Research Chair in Computational Mechanics.

References

- [1] T. Belytschko, Y. Krongauz, D. Organ, M. Fleming, and P. Krysl. Meshless methods: An overview and recent developments. *Comput. Methods Appl. Mech. Engrg.*, 139:3–47, 1996.
- [2] D.K. Bogen, S.A. Rabinowitz, A. Needleman, T.A. McMahan, and W. H. Abelmann. An analysis of the mechanical disadvantage of myocardial infarction in the canine left ventricle. *Circulation Research*, 47:728–41, 1980.
- [3] O.H. Cingolani, X.P. Yang, M.A. Cavaasin, and O. A. Carretero. Increased systolic performance with diastolic dysfunction in adult spontaneously hypertensive rats. *Hypertension*, 43:249–254, 2003.
- [4] J. M. Guccione, L. K. Waldman, A. D. McCulloch, et al. Mechanics of active contraction in cardiac muscle: Part ii—cylindrical models of the systolic left ventricle. *Journal of biomechanical engineering*, 115(1):82, 1993.
- [5] K. B. Gupta, M. B. Ratcliffe, M. A. Fallert, L. H. Edmunds, and D. K. Bogen. Changes in passive mechanical stiffness of myocardial tissue with aneurysm formation. *Circulation*, 89:2315–2326, 1994.

- [6] K. L. Herrmann, A. D. McCulloch, and J. H. Omens. Glycated collagen cross-linking alters cardiac mechanics in volume-overload hypertrophy. *Am J Physiol Heart Circ Physiol*, 284:1277–1284, 2003.
- [7] J. W. Holmes, T. K. Borg, and J. W. Covell. Structure and mechanics of healing myocardial infarcts. *Annual Review of Biomedical Engineering*, 7:223–253, 2005.
- [8] S. Klinkel, C. Sansour, and W. Wagner. An anisotropic fibre-matrix material model at finite elastic-plastic strains. *Computational Mechanics*, 35:409–417, 2005.
- [9] J. Kortsmits, N.H. Davies, R. Miller, J.R. Macadangdang, P. Zilla, and T. Franz. The effect of hydrogel injection on cardiac function and myocardial mechanics in a computational post-infarction model. *Computer Methods in Biomechanics and Biomedical Engineering*, 2012.
- [10] D M Nelson, Z Ma, K L Fujimoto, R Hashizume, and W R Wagner. Intra-myocardial biomaterial injection therapy in the treatment of heart failure: Materials, outcomes and challenges. *Acta Biomaterialia*, 7:1–15, 2011.
- [11] S.A. Niederer and N.P. Smith. The role of the Frank-Starling law in the transduction of cellular work to whole organ pump function: A computational modeling analysis. *PLoS Comput Biol*, 5:1–5, 2009.
- [12] Jeffrey H. Omens, Deidre A. MacKenna, and Andrew D. McCulloch. Measurement of strain and analysis of stress in resting rat left ventricular myocardium. *Journal of Biomechanics*, 26:665–676, 1993.
- [13] S. Reese, T. Raible, and P. Wriggers. Finite element modelling of orthotropic material behaviour in pneumatic membranes. *International Journal of Solids and Structures*, 52: 9525–9544, 2001.
- [14] J. Rijcken, P. H. Bovendeerd, A. J. Schoofs, D. H. van Campen, and T. Arts. Optimization of cardiac fiber orientation for homogeneous fiber strain during ejection. *Ann Biomed Eng*, 27(3):289–97, 1999.
- [15] T.P. Usyk, R. Mazhari, and A.D. McCulloch. Effect of laminar orthotropic myofiber architecture on regional stress and strain in the canine left ventricle. *Journal of Elasticity*, 61:143–164, 2000.
- [16] Samuel T Wall, Joseph C Walker, Kevin E Healy, Mark B Ratcliffe, and Julius M Guccione. Theoretical impact of the injection of material into the myocardium. *Circulation*, 114:2627–2635, 2006.
- [17] J. F. Wenk, P. Eslami, Z. Zhang, C. Xu, E. Kuhl, J.H. Gorman III, J.D. Robb, Ratcliffe M.B., R.C. Gorman, and J.M. Guccione. A novel method for quantifying the in-vivo mechanical effect of material injected into a myocardial infarction. *Ann Thorac Surg*, 92: 935–941, 2011.
- [18] J.F. Wenk, S.T. Wall, R.C. Peterson, S.L. Helgerson, H.N. Sabbah, M. Burger, N. Stander, M.B. Ratcliffe, and J.M. Guccione. A method for automatically optimizing medical devices for treating heart failure: designing polymeric injection patterns. *Journal of biomechanical engineering*, 131:121011, 2009.

- [19] J.F. Wenk, Z. Zhang, G. Cheng, D. Malhotra, G. Acevedo-Bolton, M. Burger, T. Suzuki, D. A. Saloner, W. Wallace, J. Guccione, and M.B. Ratcliffe. First finite element model of the left ventricle with mitral valve: Insights into ischemic mitral regurgitation. *Ann Thorac Surg*, 89:1546–1554, 2010.

MODELING AND CORRELATION OF PLAQUE SIZE WITH HISTOLOGICAL AND BLOOD ANALYSIS DATA FOR ANIMAL RABBIT EXPERIMENTS

Milos Radovic^{1,2}, Zarko Milosevic^{1,2}, Dalibor Nikolic^{1,2}, Igor Saveljic^{1,2}, Milica Obradovic^{1,2}, Dejan Petrovic^{1,2}, Nebojsa Zdravkovic², Zhongzhao Teng³, Joseph Bird³, and Nenad Filipovic^{1,2}

¹ Bioengineering Research and Development Center- BioIRC
Prvoslava Stojanovica 6, 34000 Kragujevac, Serbia
e-mail: mradovic@kg.ac.rs

² University of Kragujevac, Faculty of Engineering, Faculty of Medicine
Sestre Janjic 6, 34000 Kragujevac, Serbia
e-mail: fica@kg.ac.rs

³ University of Cambridge
Cambridge, Great Britain
e-mail: jleb2@medschl.cam.ac.uk

Keywords: Finite Element Model (FEM), Computer Fluid Dynamic (CFD), Atherosclerosis, Wall Shear Stress, Plaque, Regression.

Abstract. *Atherosclerosis is becoming the number one cause of death worldwide. Animal experiments are very important to better understand physiological conditions for atherosclerosis development. We here examined influence of wall shear stress (WSS), histological and blood analysis data on the atherosclerosis lesion development for animal model. The histological cross-sections and blood analysis (cholesterol, HDL, LDL and triglycerides) data are provided from study of 19 rabbits fed by atherogenic diet at Cambridge University, within the ARTreat project research (www.artreat.kg.ac.rs). The Navier-Stokes and continuity equations were the governing equations for modeling fluid dynamics in the lumen. Convection diffusion equations were used for modeling LDL transport. For coupling fluid dynamics and solute dynamics Kedem-Katchalsky equations were used. Four regression models: multiple regression, polynomial regression, factorial regression and response surface regression are used for fitting experimental data for the plaque size. These models showed strong correlation between plaque size and input experimental data. The results represent a progress in the assessment of stroke risk for a given patient's geometry and blood analysis data.*

1 INTRODUCTION

Atherosclerosis is a disease of the large arteries characterized by the blood vessel endothelial dysfunction and lipid, cholesterol, calcium and cell elements accumulations inside blood vessel wall. It is commonly referred as plaque formation, vascular remodeling, acute and chronic obstruction of blood vessel lumen, blood flow disorder and lower oxygenation of relevant tissues. Many studies confirmed different risk factor which contributes development and spreading of the atherosclerosis, the most common are hyperlipidemia, higher blood pressure and sugar values, cigarette consumption, age and sex. Great contribution to atherosclerosis development gives mechanical quantities such as low shear stress areas which causes endothelium dysfunctions and atherogenesis [1]-[3].

In order to simulate stenosis, collars have been placed around the carotid arteries for each of 19 rabbits. After that, rabbits have been fed by atherogenic diet at Cambridge University. In order to measure plaque size proximal to collar, these rabbits were sacrificed after 8, 12 and 16 weeks of atherogenic diet. In this way, we obtained data about plaque progression in three different time steps. We also did 3D reconstruction of these arteries and calculated WSS distribution by using CFD simulations. We modeled relationship between WSS and blood analysis data (cholesterol, HDL, LDL and triglycerides) on one hand and plaque size, determined from histology, on the other hand. Four different regression models have been tested for modeling this relationship: multiple regression, factorial regression, second order polynomial regression and response surface regression [4,5]. The goal of this paper is to optimize regression models according to experimental data and wall shear stress distribution, calculated from CFD simulations.

2 MATHEMATICAL MODEL

In order to simulate blood flow through rabbit's carotids we generated 3D finite element models by using IVUS medical images [6]. Wall free model were used for simulating blood flow in the lumen. This model treats wall as rigid. All nodes that represent the wall and inlet of the artery are totally constrained. Also initial velocities are prescribed at inlet nodes. Fluid is assumed to be steady, incompressible and laminar. For modeling fluid dynamics in the lumen Navier-Stokes equations were used (1), (2):

$$-\mu\nabla^2 u_i + \rho(u_j \cdot \nabla)u_i + \nabla p_i = 0 \quad (1)$$

$$\nabla u_i = 0 \quad (2)$$

where u_i is blood velocity, p_i is pressure, μ is blood dynamic viscosity and ρ is blood density.

By using 3D simulations we calculated wall shear stress distribution for all 19 rabbits. Figure 1 shows wall shear stress distribution for rabbits 5, 6, 7 and 8. It can be observed that all rabbit geometries have at the collar position narrow zone where shear stress is high. Also the zone between start and end collar points is more narrow than zones before and after collar position. That directly has influence on the shear stress distribution where mostly low shear stress zones are before and after the collar. These zones are highly risk for plaque formation and development. We have chosen to observe the zone proximal to collar, and tried to find correlation between plaque size (in this zone) on one hand and wall shear stress and blood analysis data on the other hand. In order to find this correlation we used different general regression models: multiple regression, factorial regression, polynomial regression and response surface regression.

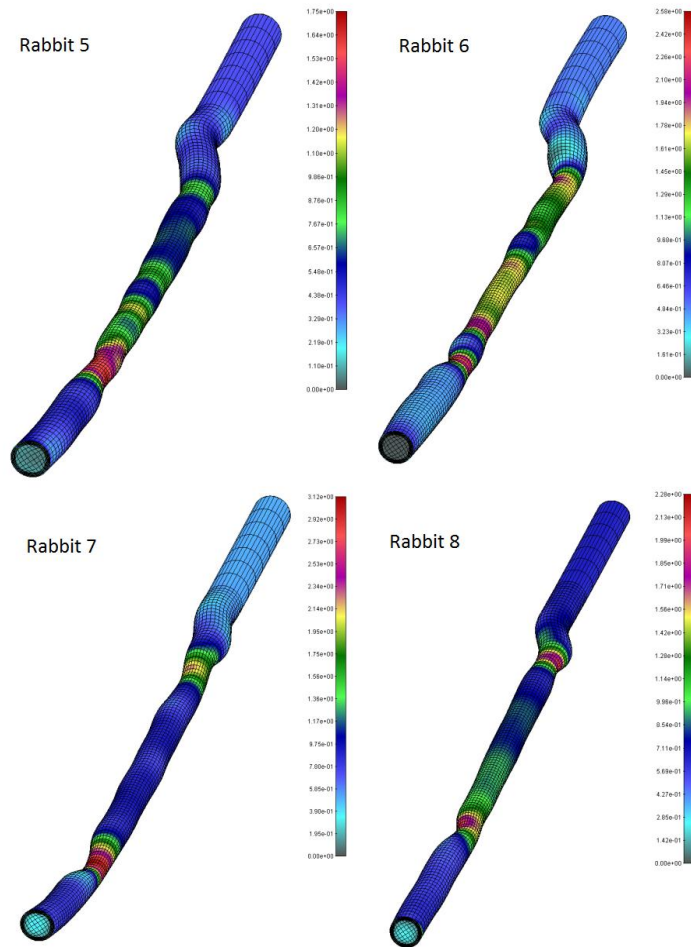


Figure 1: Wall shear stress distribution for rabbits 5, 6, 7 and 8.

3 FITTING DATA

In this section we try to model relationship between blood analysis data (cholesterol, HDL, LDL and triglycerides) and WSS on one hand and plaque progression on the other hand. In order to model this relationship we used multiple regression, factorial regression, polynomial regression and response surface regression. Table 1 contains data we used to model this relationship.

Rabbit ID	INPUTS						OUTPUT
	Time [weeks]	WSS [Pa]	Cholesterol [mmol/L]	HDL [mmol/L]	LDL [mmol/L]	Triglycerides [mmol/L]	$\frac{A_{\text{endothelial}}}{A_{\text{intima}} + A_{\text{media}}}$ [%]
Rabbit 3	16	1.39	8.1	0.98	6.6	1.1	8.635
.
.
Rabbit 16	12	5	34.6	0.7	32.4	3.2	14.195
.
.
Rabbit 19	8	2.47	7.5	0.87	6.4	0.5	7.62

Table 1: Data Used to Fit Regression Models.

As can be seen from table 1, as a measures of plaque size we used $\frac{A_{\text{endothelial}}}{A_{\text{intima}} + A_{\text{media}}}$, where $A_{\text{endothelial}}$ is plaque area inside endothelium, A_{intima} is intima area and A_{media} is media area.

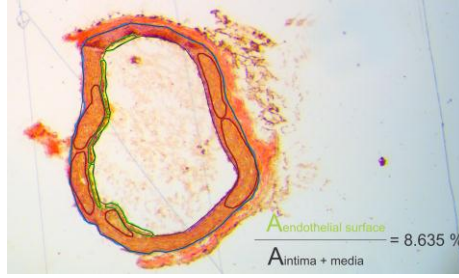


Figure 2: Carotid artery cross section for rabbit 3.

The following regression models have been tested:

- Multiple regression:

$$OUTPUT = a_0 + \sum_{i=1}^6 (a_i \cdot INPUT_i) \quad (3)$$

- Second order polynomial regression:

$$OUTPUT = a_0 + \sum_{i=1}^6 (a_i \cdot INPUT_i + b_i \cdot INPUT_i^2) \quad (4)$$

- Factorial regression:

$$OUTPUT = a_0 + \sum_{i=1}^6 (a_i \cdot INPUT_i) + \sum_{i=1}^6 \sum_{j=1}^6 (c_{i,j} \cdot INPUT_i \cdot INPUT_j); \forall i \leq j: c_{i,j} = 0 \quad (5)$$

- Quadratic response surface regression:

$$OUTPUT = a_0 + \sum_{i=1}^6 (a_i \cdot INPUT_i) + \sum_{i=1}^6 (b_i \cdot INPUT_i^2) + \sum_{i=1}^6 \sum_{j=1}^6 (c_{i,j} \cdot INPUT_i \cdot INPUT_j); \forall i \leq j: c_{i,j} = 0 \quad (6)$$

where

$$INPUT = \begin{bmatrix} Time \\ WSS \\ Cholesterol \\ HDL \\ LDL \\ Triglycerides \end{bmatrix},$$

and $OUTPUT$ is $\frac{A_{\text{endothelial}}}{A_{\text{intima}} + A_{\text{media}}}$.

Coefficients a , b and c from equations (3)-(6) are determined by using INPUT-OUTPUT data (table 1). We used a simplex optimization method developed by John Nelder and Roger Mead [7] to reach the best fit. This method involves only function evaluations (no derivatives).

Regression models have been tested by using leave-one-out cross validation procedure. As a measure of accuracy we calculated relative mean squared error:

$$RMSE = \frac{(p_1 - t_1)^2 + \dots + (p_n - t_n)^2}{(t_1 - \bar{t})^2 + \dots + (t_n - \bar{t})^2} \quad (7)$$

where p_i is i -th predicted value of the output, t_i is i -th target value of the output and \bar{t} is average value of the output

$$\bar{t} = \frac{1}{n} \sum_{i=1}^n t_i$$

The RMSE represents the ratio between total squared error of our model and total squared error of default predictor (i.e. a model which always predicts an average output value). The value of RMSE less than 1.0 indicates that the model is useful [8]. The lower the RMSE, the more accurate is the model. Table 2 shows relative squared error and correlation coefficient values for all four tested regression models. We can conclude that all four regression models are useful (RMSE<1). Also, we can conclude that polynomial regression model gave the best result among tested (RMSE=0.408).

Regression model	RMSE	Correlation coefficient
Multiple regression	0.801	0.573
Polynomial regression	0.408	0.792
Factorial regression	0.480	0.772
Response surface regression	0.562	0.711

Table 2: Relative Squared Errors for Tested Regression Models.

Results of polynomial regression model compared with experimental results are depicted on figure 3.

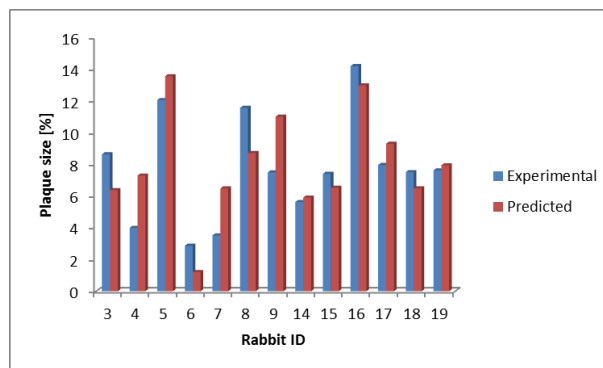


Figure 3: Comparison of experimental and predicted values (polynomial regression model).

4 CONCLUSION

In this paper we tried to model relationship between WSS, blood analysis data (cholesterol, HDL, LDL and triglycerides) on one hand and plaque size (determined from histology) on the

other hand. Among four tested regression models, second order polynomial regression gave the best result. Obtained results show that there is a strong connection between plaque size and input data. The achieved results represent progress in the assessment of stroke risk for a given patient's geometry and blood analysis data.

REFERENCES

- [1] A.M. Malek, S.L. Alper, S. Izumo, Hemodynamic shear stress and its role in atherosclerosis, *Journal of the American Medical Association – JAMA*, **282(21)**, 2035-2042, 1999.
- [2] K.C. Koskinas, Y.S. Chatzizisis, A.B. Baker, E.R. Edelman, P.H. Stone, C.L. Feldman, The role of low endothelial shear stress in the conversion of atherosclerotic lesions from stable to unstable plaque, *Current Opinion in Cardiology*, **24(6)**, 580-590, 2009.
- [3] M.S. Akram, J.D. André, Wall Shear Stress and Early Atherosclerosis, *American Journal of Roentgenology – AJR*, **174(6)**, 1657-1665, 2000.
- [4] T. Hill, P. Lewicki, *Statistics: Methods and applications, a comprehensive reference for science, industry, and data mining*, StatSoft inc., Tilsa, Oklahoma, 2006.
- [5] Z. Hamed, *Data mining to examine the treatment of osteomyelitis*, ProQuest, UMI Dissertation Publishing, Ann Arbor, USA, 2011.
- [6] N. Filipovic, M. Kojic, M. Ivanovic, B. Stojanovic, L. Otasevic, V. Rankovic, *MedCFD, Specialized CFD software for simulation of blood flow through arteries*, Kragujevac, Serbia, University of Kragujevac, 2006.
- [7] J. Nelder, R. Mead, A simplex method for function minimization, *Computer Journal*, **7(4)**, 308-313, 1965.
- [8] I. Kononenko, M. Kukar, *Machine learning and data mining*, Horwood Publishing Chichester, UK, 2007.

MULTISCALE MODELING OF MOLECULAR DIFFUSION IN TISSUE

Miljan Milosevic¹, Milos Kojic^{1, 2}, Nikola Kojic³, Mauro Ferrari² and Arturas Ziemys²

¹ Belgrade Metropolitan University - Bioengineering Research and Development Center BioIRC
Prvoslava Stojanovica 6, 3400 Kragujevac, Serbia
e-mail: miljan.m@kg.ac.rs

² The Methodist Hospital Research Institute, The Department of Nanomedicine
6670 Bertner Ave., R7-116, Houston, TX 77030
e-mail: mkojic@hsph.harvard.edu, mferrari@tmhs.org, aziemys@tmhs.org

³ Center for Engineering in Medicine and Surgical Services, Massachusetts General Hospital
Harvard Medical School, Boston, MA 02114
e-mail: kojic@mit.edu

Keywords: diffusion, hierarchical modeling, complex media, microstructural model, equivalent continuum model, numerical homogenization.

Abstract. *Tissue can be considered as a composite medium through which occurs transport of molecules. Transport of matter by diffusion within this medium is affected not only by internal microstructural geometry, but also by physico-chemical interactions between solid phase (proteins, fibers) and transported molecules or particles. We implement a new hierarchical multiscale microstructural model [1], [2] for simulation of transport of molecules through tissue. Our model is based on a novel numerical homogenization procedure. The equivalent diffusion parameters of the continuum model consist of equivalent bulk commonly used diffusion coefficients and new equivalent distances from the solid surface. Numerical examples include, among others, a model of diffusion within tissue in the vicinity of a capillary through which molecules are transported by convection. A study of the effects of collagen mesh density within tissue on transported molecule concentration profiles is presented.*

1 INTRODUCTION

Classical continuum theories of diffusion through homogenous media are based on Fick's law:

$$\mathbf{J} = -D\nabla c \quad (1)$$

where \mathbf{J} is the mass flux along concentration gradient ∇c with diffusion coefficient (diffusivity) D . However, in complex media, phase interface may occupy a substantial portion of diffusion domain so that diffusion transport is affected by molecular interactions with the surface, and predictions following equation (1) may become inaccurate. MD (molecular dynamics) modeling and experiments have shown that diffusive transport of molecules and particles in nanochannels is affected by their proximity to a solid surface [3], [4]. Using MD analysis, it is shown in [3] that molecular diffusivity depends on both concentration and confinement effects. Therefore, modeling of these transport regimes needs novel approaches that could bring molecular scale information into complex macroscale models of nanofluidic devices. An ideal scenario is to properly transfer MD information to macroscopic models. Hierarchical (multiscale) modeling approach, introduced in [1] and which couples MD and Finite Element Method (FEM), offer this possibility.

Here, we will introduce a multiscale hierarchical model for diffusion at the microstructural level (further termed as 'microstructural model'), within a small reference volume (RV), Figure 3b. The implemented method is effective, robust and generalizable to a variety of problems where diffusion governs transport. Further, we formulate a 'continuum' model which employs the results obtained by the microstructural model for diffusion within the RV. Our method relies on the fundamental condition of the equivalency of mass-release kinetics between the continuum and microstructural models for a given region of space and over a prescribed concentration range. The continuum model is based on constitutive parameters, which include equivalent 'bulk' diffusion coefficients (characterizing free, or Fickian, diffusion within the solvent) and equivalent distances from an imaginary surface (describing surface effects within the microstructure, [1]). Constitutive parameters, depending only on the structural geometry and the material properties of the diffusing constituents, are evaluated for three orthogonal coordinate directions – enabling modeling of general 3D diffusion conditions.

2 METHODS

2.1 MD simulations and scaling function for diffusion coefficient

Molecular Dynamics (MD) has been used for several decades [5]. It is based on statistical mechanics, where motion of particles is described according to the Newtonian mechanics:

$$m_i \dot{\mathbf{v}}_i = \mathbf{F}_i \quad (2)$$

where m_i , $\dot{\mathbf{v}}_i$ and \mathbf{F}_i are mass, acceleration and resulting force (including interaction forces from the neighboring particles and external forces), respectively. The interaction forces include bonded (repulsive-attractive, bending and torsion) and non-bonded (electrostatic, van der Waals) terms. The Force Field (FF) represents a functional form of behavior of chemical structures and is evaluated from potential energy function, $E = E_{intra} + E_{inter}$, of CHARMM FF [6] which is used in our MD models. MD simulations for calculating diffusion coefficients in nanochannels were carried out [1],[7] using NAMD 2.6 [8] with a TIP3P water model [9] and NVT (fixed number of particles N, pressure P, volume V) ensembles. CHARMM compatible amorphous silica force field [10] was employed to model the silica nanochannel, which is

modeled by charged hydrophilic amorphous silica phase to match the silica properties after the fabrication process. Glucose diffusion coefficients were calculated from 30 ns trajectories by using the mean square displacement $\langle r^2 \rangle$:

$$\langle r^2 \rangle = 2dDt \quad (3)$$

where the factor $d = 1, 2, 3$ depends on the dimensionality of the space, and t is time. The diffusivity along the surface normal (z -direction) was evaluated, from the surface up to the middle of the nanochannel. The diffusivity results include dependence on distance from the wall and glucose concentrations (Figure 1A).

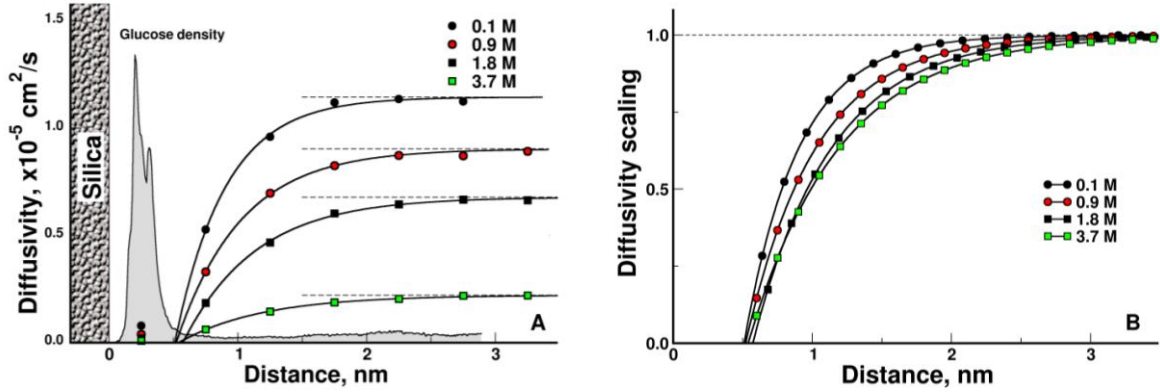


Figure 1: a) Calculated glucose diffusivity and b) scaling functions of the proximity to the silica surface for several concentrations; according to [1].

The MD calculated diffusivity is normalized with respect to the “bulk” value D_{bulk} corresponding to diffusivity far from the surface, where influence of the surface is negligible. Hence, we have:

$$D = S D_{bulk} \quad (4)$$

where:

$$S = S(h, c), \quad 0 \leq S \leq 1 \quad (5)$$

is the scaling function which depends on the distance from the wall surface h and concentration c . Calculated scaling function is shown in Figure 1B.

Experimental investigations showed that $D(\equiv D_{bulk})$ for glucose depends on concentration, although data are quite different (see [1] and references given therein). For examples shown here we have chosen the glucose D according to the largest data set of [11] that spans over a wide range of concentrations, from 0 to 3.36 M, with linear dependence $D(c)$.

2.2 Finite element model

We here consider unsteady diffusion where the diffusion coefficient depends on both concentration and spatial position of a point within the model. FE solution procedures for nonlinear diffusion problems have been well established and successfully used in various applications (e.g. [12],[13],[14],[15]). The basic mass balance equation, which also includes Fick’s law in equation (1), is transformed into the incremental-iterative system of linear balance equations for a finite element [15]:

$$\left(\frac{1}{\Delta t} \mathbf{M} + {}^{n+1} \mathbf{K}^{(i-1)} \right) \Delta \mathbf{C}^{(i)} = {}^{n+1} \mathbf{Q}^{S(i-1)} + {}^{n+1} \mathbf{Q}^{V(i)} - {}^{n+1} \mathbf{K}^{(i-1)} {}^{n+1} \mathbf{C}^{(i-1)} - \frac{1}{\Delta t} \mathbf{M} {}^{n+1} \mathbf{C}^{(i-1)} - {}^n \mathbf{C} \quad (6)$$

where \mathbf{C} is the vector of nodal concentrations; the left upper indices n and $n+1$ denote values at the start and end of the time step n of size Δt ; the indices i and $i-1$ correspond to the current and previous equilibrium iteration; \mathbf{Q}^S and \mathbf{Q}^V are surface and volumetric nodal fluxes for the element; and components of the matrices \mathbf{M} and \mathbf{K} are:

$$M_{IJ} = \int_V N_I N_J dV \quad (7)$$

$${}^{n+1} K_{IJ}^{(i-1)} = \int_V {}^{n+1} D^{(i-1)} N_{I,i} N_{J,i} dV \quad (8)$$

Here N_I and N_J are the interpolation functions, and ${}^{n+1} D^{(i-1)}$ is the diffusion coefficient corresponding to the last known concentration ${}^{n+1} c^{(i-1)}$ at a point within the finite element. Assembly of equations (6) and solution procedures are performed in a usual manner that is well described in the computational mechanics literature (e.g. [12]).

In our models we have incorporated concentration and interface effects, according to equation (4) into the FEM model. Implementation of the expression (4) is illustrated in Figure 2. Note that linear interpolation between scaling curves is used.

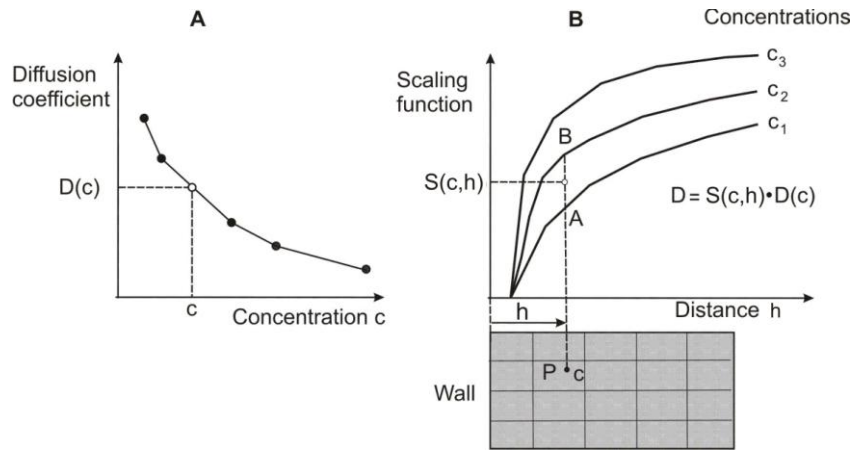


Figure 2: Determination of diffusion coefficient at a spatial point P using dependence on concentration and surface effects. The “bulk” value is first determined from the curve $D(c)$, A; then the scaling function is evaluated from family of curves shown in B. Linear interpolation curves $S(c,h)$ is adopted (between points A and B in the figure); according to [16].

2.3 Generalization of the hierarchical model to porous media

Here we outline a generalization of the hierarchical model to diffusion in complex porous media, consisting of distributed solid constituents within fluid. For simplicity of presentation of this generalization, we assume a medium with solid fibers, as sketched in Figure 3.

The main idea here is to determine equivalent diffusion parameters of a homogenous porous medium which capture the internal structure of a composite medium in a way that diffusion properties are preserved. To achieve this, we first take a reference volume around a

material point (in a form of a cube) around that point, Figure 3a, and discretize it into finite elements (Figure 3b).

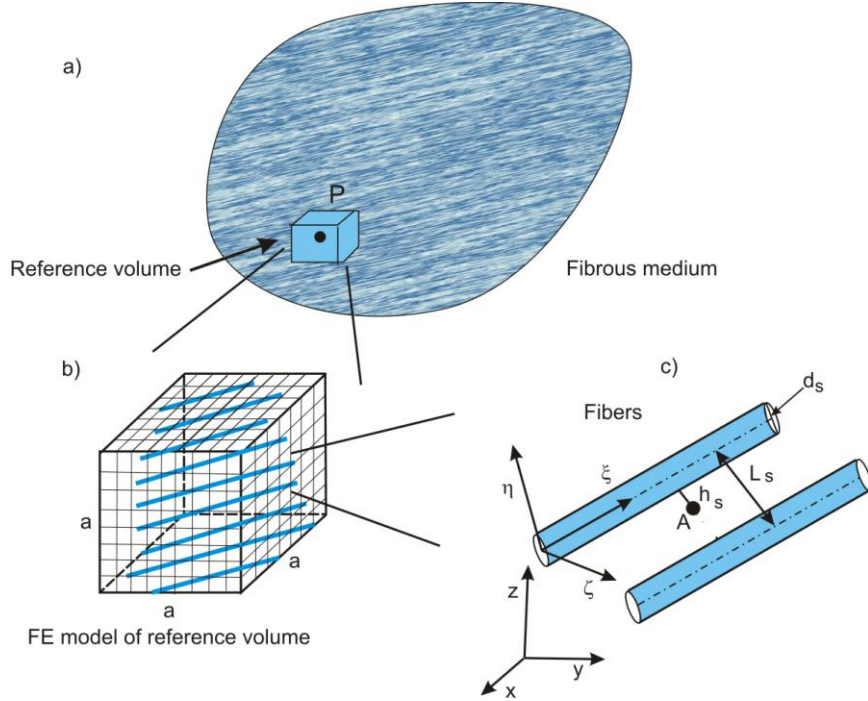


Figure 3. Concept of extension of hierarchical model to porous medium with fibers. a) Fibrous medium with reference volume at a material point P; b) Reference volume discretized into finite elements; c) Geometry of the internal structure – fibers of a s-group, with diameter d_s and with mutual distance L_s , and point A at distance h_s from the fiber surface.

Here we take the real internal microstructure and calculate diffusion in three orthogonal directions. In this FE model it is possible to properly take into account the surface effects, as sketched in Figure 3c. Namely, for a point A in the medium we calculate distance from the closest fiber surface of an s-group, and evaluate scaling function S_s as described above for diffusion within a nanochannel. We assume that scaling functions are different for the normal and tangential directions, hence we have three scaling functions $S_\xi^s, S_\eta^s, S_\zeta^s$ in the local fiber directions ξ, η, ζ , so that the diagonal diffusion matrix (tensor) $D_{\xi\xi}^s, D_{\eta\eta}^s, D_{\zeta\zeta}^s$ in the local coordinate system is:

$$\begin{aligned} D_{\xi\xi}^s &= S_\xi^s D_{bulk} \\ D_{\eta\eta}^s &= S_\eta^s D_{bulk} \\ D_{\zeta\zeta}^s &= S_\zeta^s D_{bulk} \end{aligned} \quad (9)$$

where D_{bulk} is the bulk modulus. The diffusion tensor in the global coordinate system x, y, z can be obtained by tensorial transformation of the second-order tensor:

$$\mathbf{D}_{xyz}^s = \mathbf{T}^s \mathbf{D}_{\xi\eta\zeta}^s \mathbf{T}^{sT} \quad (10)$$

where the components of the transformation matrix contains cosines of angles between local and global axes:

$$T_{ij}^s = \cos(x_i, \xi_j) \quad i,j=1,2,3 \quad (11)$$

Here x_i and ξ_j stand for global (x,y,z) and local coordinate (ξ, η, ζ) systems.

2.4 Numerical homogenization procedure and continuum model

We introduce a novel numerical homogenization procedure to determine the appropriate diffusion properties of a continuum model with a given microstructure. The basic condition governing this procedure is the equivalence of mass fluxes (through any surface in the diffusion domain) for the microstructural and continuum model, at any time during diffusion process. Considering mass release curves for diffusion through an RV around a spatial point, we have that the mass flux J_i in direction x_i is given as:

$$J_i = \left(\frac{dm}{dt} \right)_i \quad (12)$$

This derivative is geometrically represented as the tangent to the mass release curve $m(t)_i$ for the direction x_i , therefore the fluxes are equal for both models if their mass release curves are the same. This interpretation of flux equality through an RV is analogous to the mass balance condition in a differential volume used in continuum mechanics.

Next, we calculate diffusion through the reference volume using equivalent quantities of a porous homogenous medium within the RV. The porosity n is evaluated from the internal structure of the RV. For each diffusion direction i (i.e. x,y,z), the steps are as follows:

1. Calculate mass release using initial diffusion using given $D_{bulk} \cdot c$.
2. Perform changes on the value D_0 until the mass release curve is close enough to the true curve, when the value is \bar{D}_0 .
3. Using \bar{D}_0 calculate initial mass release curve taking into account equivalent values of the transformation matrix $\bar{\mathbf{T}}$ and equivalent distance from the solid surface \bar{h}_0 .
4. Search for the distance \bar{h}_i when difference between the calculated and true mass release curves is within a selected error tolerance.

In the above calculations of the equivalent transformation matrix and initial equivalent distance \bar{h}_0 , a weighted procedure, which takes into account volumes belonging to FE nodes, is implemented (details not given here).

The presented concept of evaluation of parameters related to equivalent homogenous porous medium represents a numerical homogenization procedure. It can be extended to non-homogenous media, by varying equivalent parameters, or to stochastic characteristics. Application of introduced numerical homogenization method (NHM) is illustrated in the Results section.

3 RESULTS

3.1 Diffusion within agarose polymer solution

Here, we first present detailed analysis of the microstructural model and provide prediction of equivalent continuum model. We use the internal structure of the gel obtained by imag-

ing[17], shown in Fig. 4a with discretized agarose fibers, with a porosity of 97%. Fiber are discretized using “Agarose Fibers” interface software developed in BioIRC research and development center (Fig. 4b).

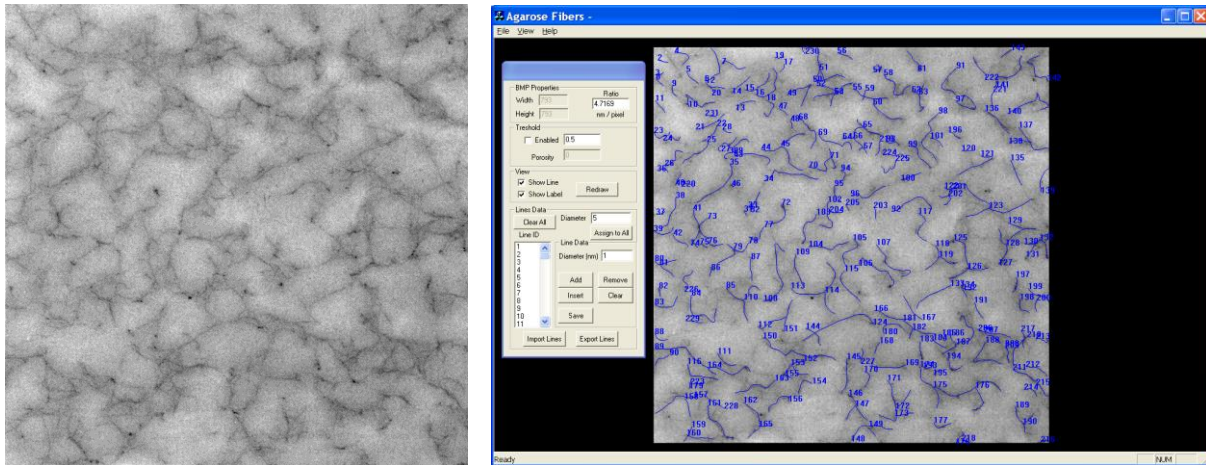


Figure 4. a) Internal microstructure obtained by imaging [17]; b) Fibers recognition software developed in BioIRC research and development center.

As expected, the calculated diffusion in the x and y directions are roughly equivalent, since the size of the RV ($1,868 \times 1,868 \mu\text{m}$) is large enough so that the overall characteristics are the same in the two directions. Both microstructural and continuum models are used, giving the same total mass release.

In order to gain further insight into the diffusion within this polymer gel, we examine the mass flux and concentration distributions (Fig. 5a). Here, we consider the diffusion of molecules whose radius is 5 nm. The upper left panel shows the distribution of mass fluxes in the direction of diffusion at the end of the first time step, time $t = 0.5$ s. The field displays the variation of the flux due to the distribution of agarose fibers, with zero-values within the fibers and at the fiber surfaces. Diagrams of concentration and mass flux along the coordinate axes are shown in the lower-left and upper-right panels. Based on continuum solutions, the concentration decreases approximately linearly along horizontal line, and remains constant along vertical cross-section; flux- x is roughly constant along horizontal cross-section, and flux- y is equal to zero along vertical cross-section. On the other hand, microstructural solutions have variations, with zero-values at the points corresponding to fibers. Finally, the right lower panel shows both cumulative mass release and flux- x change in time during FEM simulation. Taken together, the continuum model incorporates the microstructural flux fluctuations in order to achieve an equivalence of mass fluxes between the microstructural and continuum models through a given RV.

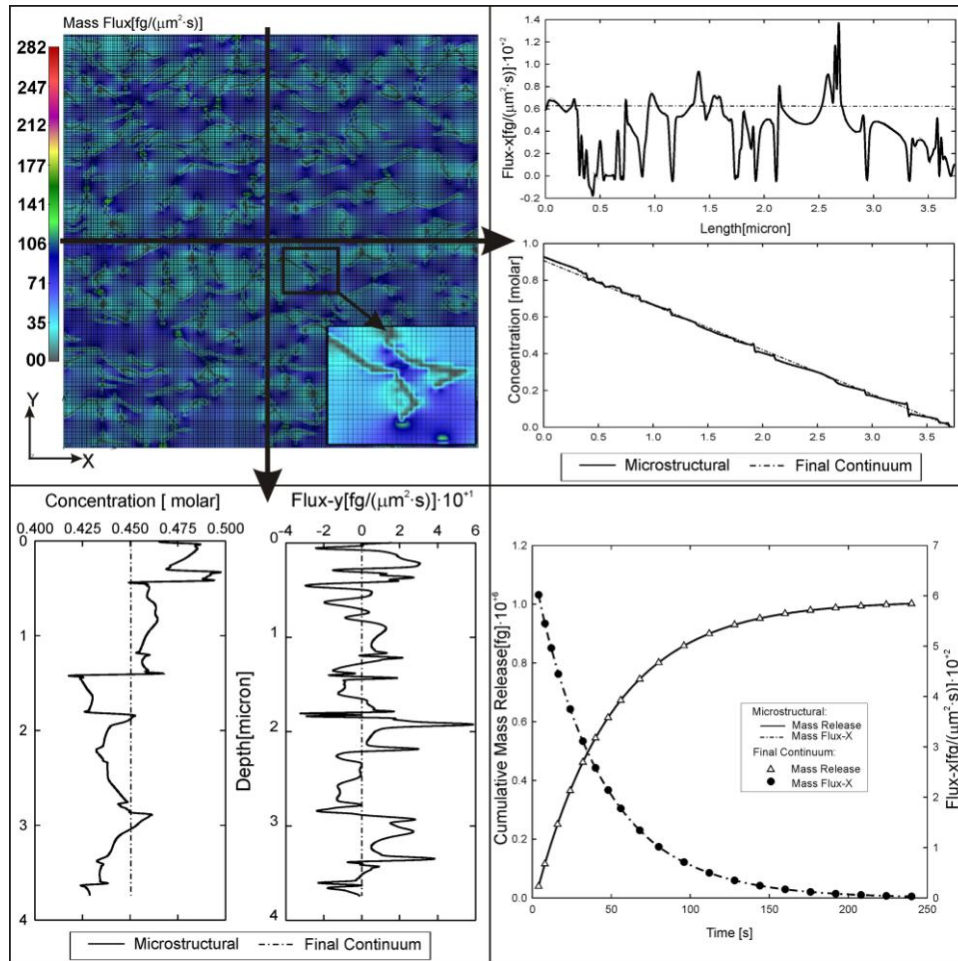


Figure 5. Diffusion within an agarose polymer gel. **Upper left panel:** Mass flux-x distribution at time $t=0.5s$; gray contours within the field shows zero-flux at fibers points. **Upper right panel:** Distribution of mass flux and concentration in the x-direction, microstructural (full line) and continuum (dashed line) along horizontal cross-section. **Lower left panel:** Distribution of mass flux and concentration in the y-direction, microstructural (solid line) and continuum (dashed line) along vertical cross-section. **Lower right panel:** Change of both cumulative mass release and flux-x in time for microstructural and continuum model.

3.2 Therapeutic particle transport across capillary wall

The space around a capillary is discretized as schematically shown in Figure 6. Due to axial symmetry, we use a part of the cylindrical domain defined by an angle (here it is 1/8 of full circle), as shown in Figure 6b. The diffusion space consists of two regions: a) sink domain corresponding to homogenous tissue medium, and b) sleeve domain which contains collagen fibers. The unsteady and nonlinear diffusion problem is solved in a standard manner, by employing incremental-iterative solution scheme [15]. Boundary conditions for the computational model are as follows: It is assumed that at the capillary surface concentration of molecules is constant over time, while far in the tissue (at the model external cylindrical surface) concentration is equal to zero.

Here we are exploring how structure of collagen, which is natural biological polymer constituting to structure of capillary walls, affects the diffusion of 80 nm liposome (PLD) and 1 nm size chemotherapeutic molecule doxorubicin (DOX).

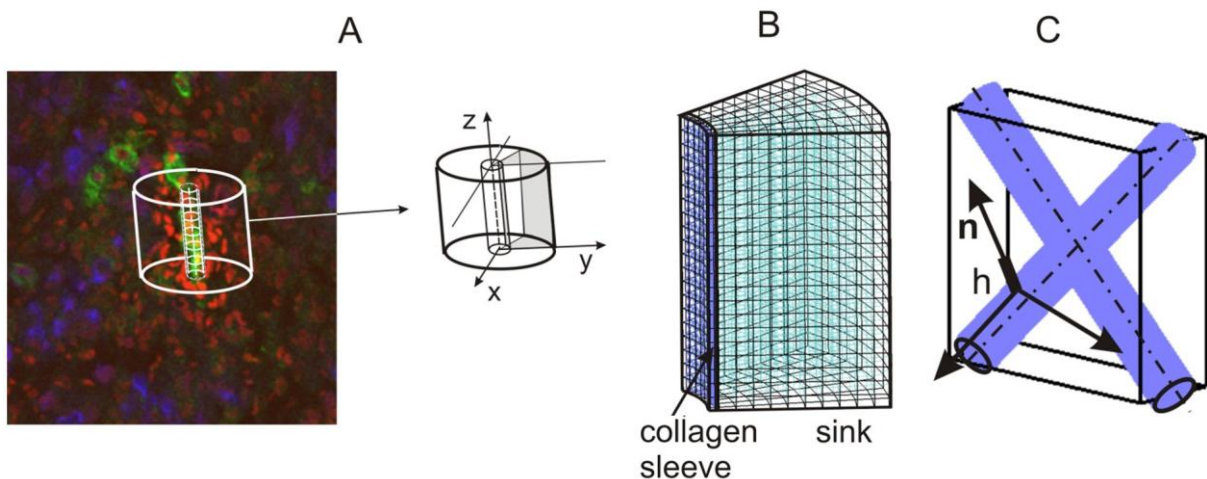


Figure 6. Finite element model: a) Schematics of the cylindrical diffusion domain around capillary and segment of the domain used in calculation. b) Finite element mesh for the collagen sleeve and sink regions. c) Finite elements with fibers; local coordinate system is used for evaluation of the diffusion coefficient, with h representing distance from the fiber surface along the normal \mathbf{n} to the surface.

We have first formulated a microstructural hierarchical diffusion model, In order to investigate how collagen sleeve may control mass transport through capillary wall, we have created the collagen sleeve model that mimics a collagen surrounding capillaries [18-21]. For simplicity, particle concentrations inside and outside of a vessel were kept constant, and other structural elements of capillary wall were omitted to focus on collagen structural effects only. The later has real implication to drug penetration when endothelium cells are absent because of damage. We study the diffusion transport of liposomes and doxygen, different by size and physico-chemical properties, in response to different structures of collagen fiber mesh.

First, we investigate how surface effects affect mass diffusion by evaluating DOX and PLD mass release through collagen sleeve made of 3 mesh layers (each layer of thickness 10 nm) and adopting the following three assumptions: no fibers, fibers without surface effects, and fibers with surface effects on diffusion. It is taken that the concentration on the vessel surface is 0.02 M, while concentration at the outer surface of the sleeve is equal to zero, and both concentrations are kept constant over time.

Figure 7a compares diffusion mass transfer for all three cases and demonstrates the method. The differences of mass release between DOX and PLD in bulk (no fibers) are due to differences in diffusivity coefficients of particles. DOX mass release does not reveal substantial differences through 200 nm mesh in case with or without surface effects. That may be explained by small size of DOX molecule comparing to the openings in mesh (the ratio of the particle area projection to the tangential plane through which diffusion occurs, with respect to the pore area in the same plane, is $2.07 \cdot 10^{-5}$). PLD diffusion through collagen with 200 and 400 nm meshes not accounting for interactions with surface shows almost no differences, where the ratios of the particle area with respect to the pore area in the tangential plane are 0.0132 and 0.00323 respectively. However, the inclusion of surface effects makes a dramatic difference in PLD diffusion showing that smaller mesh openings will impede diffusion more and difference between 200 and 400 nm becomes substantial (Figure 7a). The inclusion of surface effects into the model also shows that diffusion mass transfer is strongly reduced when compared to mass release through the medium without fibers and using the classical Fickian diffusion law.

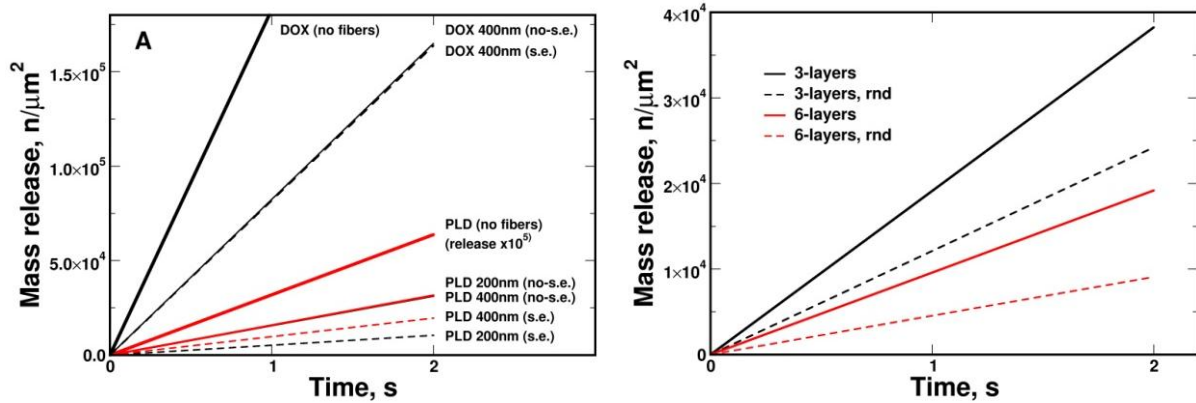


Figure 7. Fiber surface effects on diffusion. **a)** The effects of fibers and interface on DOX and PLD mass release through 3 collagen sheets of 200 and 400 nm mesh-size (*no-s.e.* – no surface effect; *s.e.* – with surface effects). **b)** Collagen mesh randomness significantly reduces the PLD mass release rate; random mesh solutions are displaced by dashed line.

Because the actual collagen mesh is not ordered structure and it is random, the effect of randomness was investigated. Figure 7b depicts mass release of PLD through 400 nm mesh having 3 and 6 mesh layers in a collagen sleeve, in case of ordered and randomized fiber composition. Randomized meshes showed significantly reduced mass release comparing to ordered meshes. For randomized mesh fluxes are approximately reduced by 30% in a 3-layers sleeve, and 50% in a 6-layer sleeve. Because DOX size is small comparing to mesh openings, there was no similar effect observed with DOX. Results show that randomized meshes may create larger obstruction for diffusion.

4 SUMMARY AND CONCLUSIONS

In summary, we have first formulated a microstructural hierarchical diffusion model, which includes surface interaction effects, for a general microstructural geometry. In this model, the interaction effects are incorporated through scaling functions (evaluated using MD), which represent the ratios between the real and bulk diffusion coefficients. The scaling functions, expressed in terms of distance from the solid surfaces and concentration, are calculated in the local coordinate system of the solid surface. Therefore, two domains of diffusion are distinguished: the bulk diffusion domain (with Fickian diffusion) and the domain near surfaces, with non-Fickian hindered diffusion. In both domains, diffusion is calculated by using the FE method. The surface effects become apparent when comparing the slower mass release kinetics (with surface interactions) with purely Fickian mass release (without surface effects).

This microstructural model is then employed within a novel numerical homogenization procedure to establish the equivalent continuum diffusion model. The procedure is general since it is applicable to an internal, structural geometry of any complexity, and can include different solid material sets with different material properties. The procedure relies on the condition that mass release curves of the two models must be equal. Constitutive diffusion parameters of the continuum model are determined for the three coordinate directions and include the traditional bulk diffusion coefficients, and also equivalent distances from the solid surfaces to account for surface interaction effects on diffusion. Furthermore, these constitutive parameters can depend on the local concentration. Our approach, consisting of a microstructural model and numerical homogenization procedure is general and robust, and offers new possibilities in modeling diffusion through complex materials, including molecular transport in biological systems (e.g. intercellular spaces and tissues). The presented methodology can

serve as a tunable platform for constructing intricate multiscale hierarchical diffusion models with additional complexity and effects, such as multiple molecule types (e.g. different proteins/ligands), multiple surfaces (e.g. various cell types with different receptors), and various media (e.g. different solvents). These multiscale models provide a basis for a deeper, more accurate representation of fundamental transport processes occurring throughout nature.

Numerical homogenization procedure presented in this work is analogous to homogenization procedures previously presented in linear and nonlinear solid mechanics, heat transfer and diffusion, where different types of RV were used (e.g. [22],[23],[24]). Previous homogenization procedures have limitations due to the special assumptions made regarding microstructure (e.g. periodicity) as well as relying on various asymptotic expansions of analytic forms. Our method is not only general, but also includes concentration-dependent parameters within a wide range of concentrations over which diffusion occurs.

By incorporating surface effects of polymer fibers into our recently developed multiscale diffusion model, it was found that DMX was free to diffuse through collagen sleeve containing 1 to 6 fiber meshes with mesh size 50 to 800 nm. However, LPS showed substantial decrease of flux through collagen sleeves of 3 mesh layers and smaller than 200 nm mesh sizes. This finding explains higher efficacy of particle-based drug carriers.

5 ACKNOWLEDGMENTS

This project has been supported with federal funds from NASA under the contracts NNJ06HE06A and NNX08AW91G, Department of Defense under the contract DODW81XWH-09-1-0212, as well as funds from State of Texas Emerging Technology Fund, Nano Medical Systems (NMS), Alliance of NanoHealth (ANH), and University of Texas at Houston. The authors acknowledge the Texas Advanced Computing Center (TACC) at The University of Texas at Austin for providing HPC resources that have contributed to the research results reported within this paper.

The authors acknowledge support from Ministry of Education and Science of Serbia, grants OI 174028 and III 41007, City of Kragujevac, and from FP7-ICT-2007 project (grant agreement 224297, ARTreat).

REFERENCES

- [1] Ziemys A., Kojic M., Milosevic M., Kojic N., Hussain F., Ferrari M., Grattoni A. (2011). *Hierarchical modeling of diffusive transport through nanochannels by coupling molecular dynamics with finite element method*, Journal of Computational Physics, 230, 5722–5731.
- [2] Kojic M., Milosevic M., Kojic N., Ferrari M., Ziemys A., Numeric modeling of diffusion in complex media with surface interface effects, Contemporary Materials, III-2, 153-166, 2012.
- [3] Ziemys A., Grattoni A., Fine D., Hussain F., Ferrari M., *Confinement effects on monosaccharide transport in nanochannels*, The Journal of Physical Chemistry B (2010) 132–137.
- [4] Aggarwal N., Sood J., Tankeshwar K., *Anisotropic diffusion of a fluid confined to different geometries at the nanoscale*. Nanotechnology, 2007. 18(33): p. 5.

- [5] Rappaport D.C., *The Art of Molecular Dynamics Simulation*, Cambridge University Press, (2004).
- [6] MacKerell Jr A., et al., *CHARMM: The Energy Function and Its Parameterization with an Overview of the Program*, J. Phys. Chem. B, 102(18), 3586-3616 (1998).
- [7] Ziemys A., Ferrari M., Cavasotto C. N. *Molecular Modeling of Glucose Diffusivity in Silica Nanochannels*. J. Nanosci. Nanotechnol. 2009, 9, 6349–6359.
- [8] Phillips J. C., Braun R., Wang W., Gumbart J., Tajkhorshid E., Villa, E., Chipot, C., Skeel, R. D., Kale´ L., Schulten K., *Scalable molecular dynamics with NAMD*. J. Comput. Chem. 2005, 26, 1781–1802.
- [9] Jorgensen W. L., Chandrasekhar J., Madura J. D., Impey R. W., Klein, M. L., *Comparison of simple potential functions for simulating liquid water*. J. Chem. Phys. 1983, 79, 926–935.
- [10] Cruz-Chu E. R., Aksimentiev A., Schulten K., *Water-silica force field for simulating nanodevices*. J. Phys. Chem. B 2006, 110, 21497–21508.
- [11] Gladden J.K., Dole M., *Diffusion in supersaturated solution-II: glucose solutions*. J. Am. Chem. Soc., 1953. 75: p. 3900-3904.
- [12] Bathe K.J., *Finite Element Procedures*. Prentice-Hall, Inc., Englewood Cliffs, N.J., (1996).
- [13] T. Hughes, *The finite element method: linear static and dynamic finite element analysis*. 2000, New York: Dover Publications.
- [14] Kojic, N., A. Kojic, and M. Kojic, *Numerical determination of the solvent diffusion coefficient in a concentrated polymer solution*. Communications in Numerical Methods in Engineering, 2006. 22(9): p. 1003-1013.
- [15] Kojic M., Filipovic, N., Stojanovic, B. and Kojic N. (2008), *Computer Modeling in Bioengineering*, Theoretical Background, Examples and Software, J Wiley and Sons, Chichester.
- [16] Kojic M., Milosevic M., Kojic N., Ferrari M., Ziemys A., *On diffusion in nanospace*, JSSCM, Vol. 5 / No. 1, 2011 / pp. 84-109.
- [17] Griess, G. A., Guiseley, K. B. & Serwer, P. The relationship of agarose gel structure to the sieving of spheres during agarose gel electrophoresis. *Biophysical Journal* **65**, 138-148 (1993).
- [18] P.D. Yurchenco and G.C. Ruben, *The Journal of cell biology*, 1987, **105**, 2559-2568.
- [19] R. Timpl, H. Wiedemann, V. Delden, H. Furthmayr, and K. Kuhn, *European Journal of Biochemistry*, 1981, **120**, 203-211.
- [20] M. Van der Rest and R. Garrone, *The FASEB journal*, 1991, **5**, 2814-2823.
- [21] G. Laurie, C. Leblond, and G. Martin, *The Journal of cell biology*, 1982, **95**, 340-344.
- [22] Nicolas M. O., Oden J. T., Vemagantia K. and Remacle, *Simplified methods and a posteriori estimation for the homogenization of representative volume elements*, J. F., Comput. Methods Appl. Mech. Engrg. 176, 265-278 (1999).
- [23] Chapman S. J., Shipley R. J., Jawad R., *Multiscale modelling of fluid flow in tumours*, Bull. Math. Biology 70, 2334–2357 (2008).
- [24] Yu W., Tnag T., *Variational asymptotic method for unit cell homogenization of periodically heterogeneous materials*, Int. J. Solids Struct. 44 (22-23), 7510–7525 (2007).

SOLUTION OF VISCOPLASTIC FLOWS WITH THE FINITE VOLUME / MULTIGRID METHOD

Alexandros Syrakos¹, Georgios C. Georgiou², and Andreas N. Alexandrou³

¹ Oceanography Centre, University of Cyprus
PO Box 20537, 1678 Nicosia, Cyprus
e-mail: syrakos.alexandros@ucy.ac.cy

² Department of Mathematics and Statistics, University of Cyprus
PO Box 20537, 1678 Nicosia, Cyprus
e-mail: georgios@ucy.ac.cy

³ Department of Mechanical and Manufacturing Engineering, University of Cyprus
PO Box 20537, 1678 Nicosia, Cyprus
e-mail: andalex@ucy.ac.cy

Keywords: Finite Volume Method, Viscoplastic Flows, Papanastasiou Regularisation, Multigrid, Lid-driven Cavity

Abstract. *We investigate the performance of the finite volume method in solving viscoplastic flows. The square lid-driven cavity flow of a Bingham plastic is chosen as the test case and the constitutive equation is regularised as proposed by Papanastasiou [J. Rheol. 31 (1987) 385-404]. The numerical results obtained for Bingham numbers up to 10 and Reynolds numbers up to 5000 compare favourably with reported results obtained through other methods. The effects of the Reynolds and Bingham numbers are also investigated. It is shown that the convergence rate of the standard SIMPLE pressure-correction algorithm, which is used to solve the algebraic equation system that is produced by the finite volume discretisation, severely deteriorates as the Bingham number increases, with a corresponding increase in the non-linearity of the equations. Using the SIMPLE algorithm in a multigrid context [Syrakos & Goulas, Int. J. Numer. Methods Fluids 52 (2006) 1215-1245] dramatically improves convergence, although the multigrid convergence rates are not as high as those for Newtonian flows.*

1 INTRODUCTION

Viscoplastic materials behave as solids at low stress levels, but flow when the stress exceeds a critical value, the *yield stress*, τ_y . Materials which are suspensions of particles or macromolecules, such as pastes, gels, foams, drilling fluids, food products, and nanocomposites, can be considered to fall into this category. Bingham plastics are the simplest viscoplastic materials, which exhibit a linear stress to rate-of-strain relationship once the material yields. The constant of proportionality of this linear relationship is called the *plastic viscosity*, μ . Thus, the Bingham constitutive equation is the following:

$$\begin{cases} \dot{\boldsymbol{\gamma}} = \mathbf{0}, & \tau \leq \tau_y \\ \boldsymbol{\tau} = \left(\frac{\tau_y}{\dot{\gamma}} + \mu \right) \dot{\boldsymbol{\gamma}}, & \tau > \tau_y \end{cases} \quad (1)$$

where $\boldsymbol{\tau}$ is the stress tensor and $\dot{\boldsymbol{\gamma}}$ is the rate of strain tensor, $\dot{\boldsymbol{\gamma}} \equiv \nabla \mathbf{u} + (\nabla \mathbf{u})^T$, \mathbf{u} being the velocity vector. The magnitudes of these two tensors are $\tau = [\boldsymbol{\tau} : \boldsymbol{\tau}/2]^{1/2}$ and $\dot{\gamma} = [\dot{\boldsymbol{\gamma}} : \dot{\boldsymbol{\gamma}}/2]^{1/2}$.

The discontinuity of the Bingham constitutive equation poses significant difficulties to numerical solution methods. A way to overcome this difficulty is to approximate the Bingham constitutive equation by a regularised constitutive equation which treats the whole material as a fluid and is valid throughout the domain, approximating the solid regions by locally assigning a very high value to the viscosity. Such methods can be implemented with minimal modification to Newtonian flow solvers. One of the most successful regularisation approaches is that by Papanastasiou [1], which has been adopted in the present work. The regularisation is achieved through the introduction of an exponential term, so that the constitutive equation (1) is replaced by the single equation, applicable throughout the material,

$$\boldsymbol{\tau} = \left[\frac{\tau_y}{\dot{\gamma}} \{1 - \exp(-m\dot{\gamma})\} + \mu \right] \dot{\boldsymbol{\gamma}} \quad (2)$$

where m denotes the stress growth parameter, which needs to be ‘‘sufficiently’’ large. Using this approximation, we adapted the finite volume method described in [2] to enable it to simulate flows of Bingham plastics. The method was applied successfully in the case of creeping flows in [3]. In the present work, the method is applied also to non-zero Reynolds number flows, with the Reynolds number reaching values as high as 5000.

The finite volume method (FVM) is a popular method for solving fluid flows, employed by many general-purpose CFD solvers. However, there are a limited number of published results on the use of the finite-volume method to solve Bingham flow problems. Neofytou [4] used a FVM in conjunction with the SIMPLE algebraic solver [5] to simulate the lid-driven cavity flow of various non-Newtonian fluids, including a Papanastasiou-regularised Bingham plastic at relatively low yield stress values. Turan and co-workers [6] also used a commercial FVM/SIMPLE code employing the bi-viscosity model in order to simulate natural convection of a Bingham plastic in a square cavity. The FVM was also used to solve flows of a Casson fluid through a stenosis [7] and through a sudden expansion [8], at rather low yield-stress values. Also, de Souza Mendes et al. [9] and Naccache and Barbosa [10] used the FVM in order to simulate viscoplastic flow through an expansion followed by a contraction.

The present method is tested on the popular lid-driven cavity problem: A square cavity of side L is filled with a fluid which is set to motion by the lid of the cavity which moves with a tangential velocity U . Two are the relevant dimensionless numbers for this flow: the Reynolds

number, which, in the case of Bingham fluids, is defined in terms of the plastic viscosity,

$$Re \equiv \frac{\rho UL}{\mu} \quad (3)$$

and the Bingham number Bn , defined as

$$Bn \equiv \frac{\tau_y L}{\mu U} \quad (4)$$

The lid-driven cavity problem has also been used to test methods for solving viscoplastic flows. The aforementioned work of Neofytou [4] is, to the authors knowledge, the only one which employed the finite volume method. However, since it is restricted to very low Bingham numbers, it was not used in the present study for purposes of validation. To validate the present results, the works of Vola et al [13] and Prashant and Derksen [14] were used. Vola et al [13] used an augmented Lagrangian method [15], which obviates the need for regularisation, combined with finite elements. Prashant and Derksen [14] used the lattice-Boltzmann method and a bi-viscosity model (O'Donovan and Tanner [16]) where solid regions are approximated by fluids of a constant high viscosity.

The governing equations are summarised in Section 2, the finite volume method and the algebraic solver are described in Section 3, and the results of the lid-driven cavity simulations are given in Section 4. The paper ends with some conclusions in Section 5.

2 GOVERNING EQUATIONS

The flow is assumed to be steady-state, two-dimensional, incompressible, and isothermal. By scaling the fluid velocity by U , and the pressure and stress by $\mu U/L$, the continuity and momentum equations can be written in the following dimensionless forms:

$$\nabla \cdot \mathbf{u} = 0 \quad (5)$$

$$Re \cdot \mathbf{u} \cdot \nabla \mathbf{u} = -\nabla p + \nabla \cdot \boldsymbol{\tau} \quad (6)$$

where \mathbf{u} is the dimensionless velocity of the fluid, p is the dimensionless pressure, and $\boldsymbol{\tau}$ is the dimensionless stress tensor, which is calculated according to the dimensionless form of the Papanastasiou constitutive equation,

$$\boldsymbol{\tau} = \left[\frac{Bn}{\dot{\gamma}} \{1 - \exp(-M\dot{\gamma})\} + 1 \right] \dot{\gamma} \quad (7)$$

where M is the dimensionless stress growth parameter, defined as:

$$M \equiv \frac{mU}{L} \quad (8)$$

Equations (5), (6) and (7) together with the no-slip wall boundary conditions fully determine the flow problem which is solved numerically.

The Papanastasiou regularisation (7) corresponds to a dimensionless apparent viscosity of

$$\eta = \frac{Bn}{\dot{\gamma}} \{1 - \exp(-M\dot{\gamma})\} + 1 \quad (9)$$

The higher the value of M , the better (7) approximates the actual Bingham constitutive equation, $\tau = [Bn/\dot{\gamma} + 1]\dot{\gamma}$, in the yielded regions of the flow field ($\tau < Bn$), and the higher the apparent viscosity is in the unyielded regions, making them behave approximately as solid bodies. For practical reasons though, M must not be so high as to cause problems to the numerical methods used to solve the above equations.

3 NUMERICAL METHOD

The finite volume method employed here is based on that described in [2]. The domain is discretised into 512×512 square control volumes of equal size. Coarser grids are constructed by removing every second grid line from the immediately finer grid. The velocity components, pressure, and viscosity are stored at control volume centres. The convective and viscous fluxes are discretised using 2nd-order central differences. The mass fluxes are discretised using momentum interpolation as described in [11], to suppress pressure oscillations. The resulting algebraic system is solved using the SIMPLE algorithm, with the only modification being that at the start of every SIMPLE iteration the viscosity is updated according to (9), using the current estimate of the velocity field. To accelerate convergence, SIMPLE is used in a multigrid framework. Due to the high degree of nonlinearity of the problem, the standard multigrid algorithm fails to converge except at small Bingham numbers, $Bn < 0.5$. To overcome this problem, we applied the modification suggested by Ferziger and Peric [12]; on coarse grids the viscosity is not updated according to (9), but it is interpolated (restricted) from the immediately finer grid and held constant within the multigrid cycle. Therefore the viscosity is updated only on the finest grid, which means that the procedure is not purely multigrid, but it has single-grid features. This technique was observed to slow down the multigrid convergence by a small amount, but it makes the algorithm more robust and capable of achieving convergence up to high Bingham numbers (depending also on the value of M). Other measures that were found necessary in order to achieve convergence are the following: a large number of pre- and post-smoothing steps should be used (4 or more, depending on the Bn number); a number of additional SIMPLE iterations (e.g. 5 – 10) may have to be performed on the finest grid between multigrid cycles; very small values of the underrelaxation factor a_p for pressure should be used in the SIMPLE smoother (e.g. 0.01); also, relatively small values should be assigned to the velocity underrelaxation factor, $a_u \approx 0.3$, for $Re \geq 2000$; and the coarse grid corrections may have to be underrelaxed by a constant $\alpha_{MG} \approx 0.9$ prior to prolongation to the fine grid.

4 NUMERICAL RESULTS

The lid-driven cavity problem has been solved for Reynolds numbers up to 5000, and for Bingham numbers up to 10. Unless otherwise stated, the results were obtained on the 512×512 grid, using $M = 400$.

Figures 1 – 3 describe the evolution of the flow field as the Reynolds number increases, for $Bn = 0, 1$, and 10, respectively. The main characteristics of the flow field are a main vortex near the centre of the cavity, and (usually) two unyielded zones, one at the bottom of the cavity and one near the vortex centre, the latter not being in contact with the cavity walls. The unyielded zones, which are of course absent for $Bn = 0$, grow in size as the Bingham number increases. At the bottom of the cavity, for $Bn = 1$, there appear two unyielded zones, one at each of the lower corners, which merge into a single zone as Bn increases. The unyielded zones at the bottom of the cavity are motionless, as they touch the motionless sides of the cavity and have to obey the no-slip condition. The figures however reveal extremely weak vortices at the lower

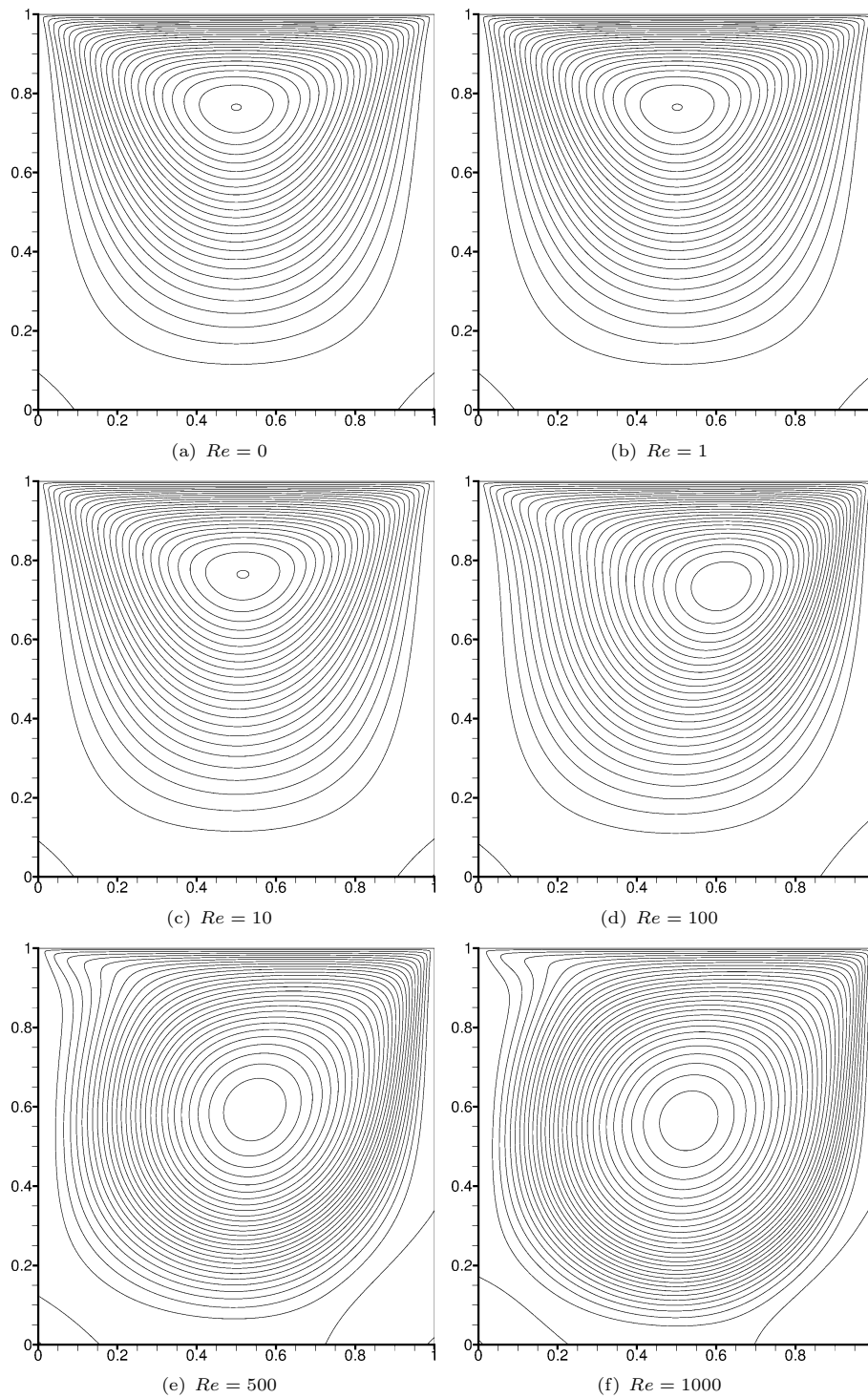


Figure 1: Streamlines in Newtonian flow ($Bn = 0$), plotted at intervals of 0.004 starting from zero.

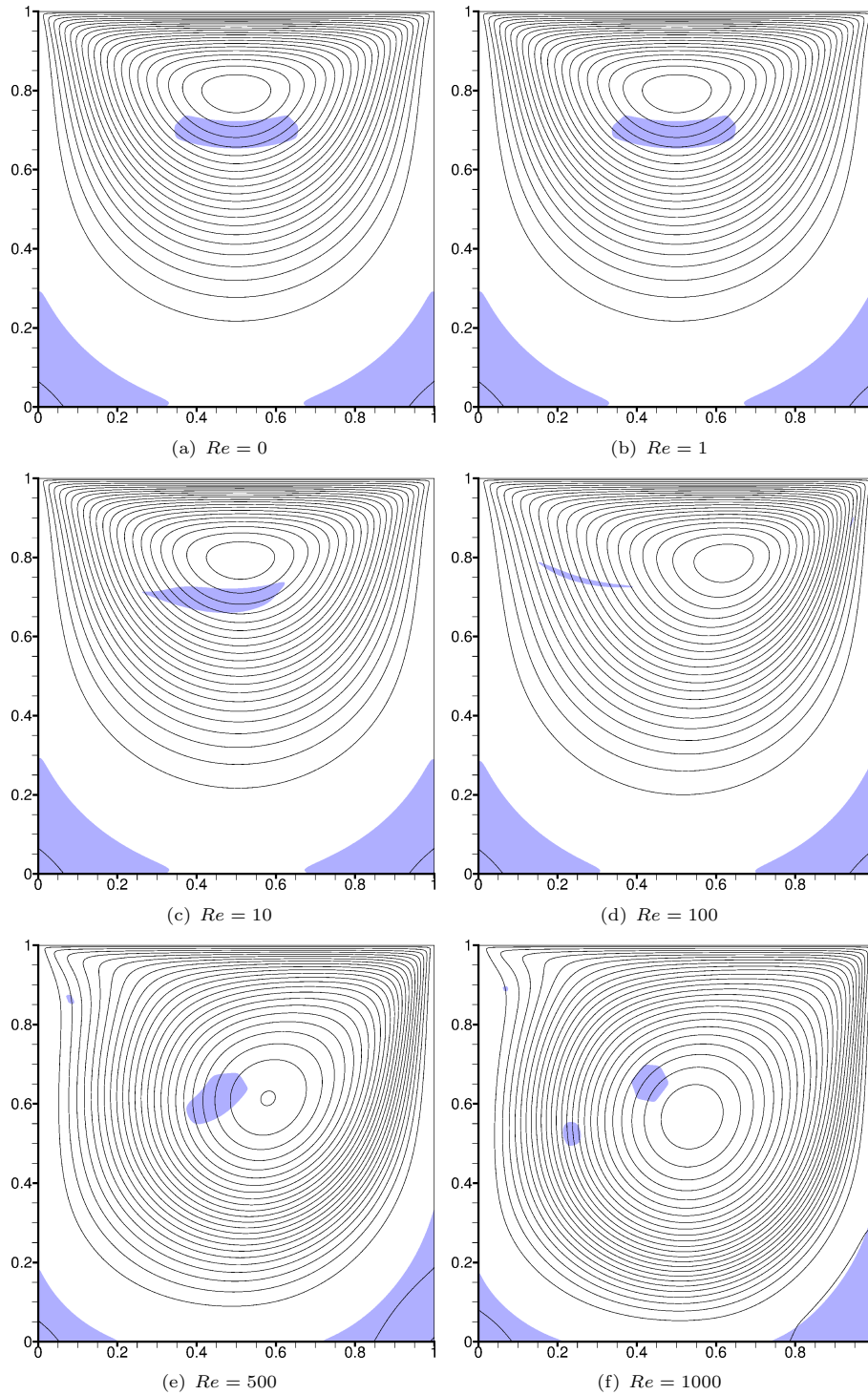


Figure 2: Streamlines in Bingham flow for $Bn = 1$, plotted at intervals of 0.004 starting from zero. Unyielded areas ($\tau < Bn$) are shown shaded.

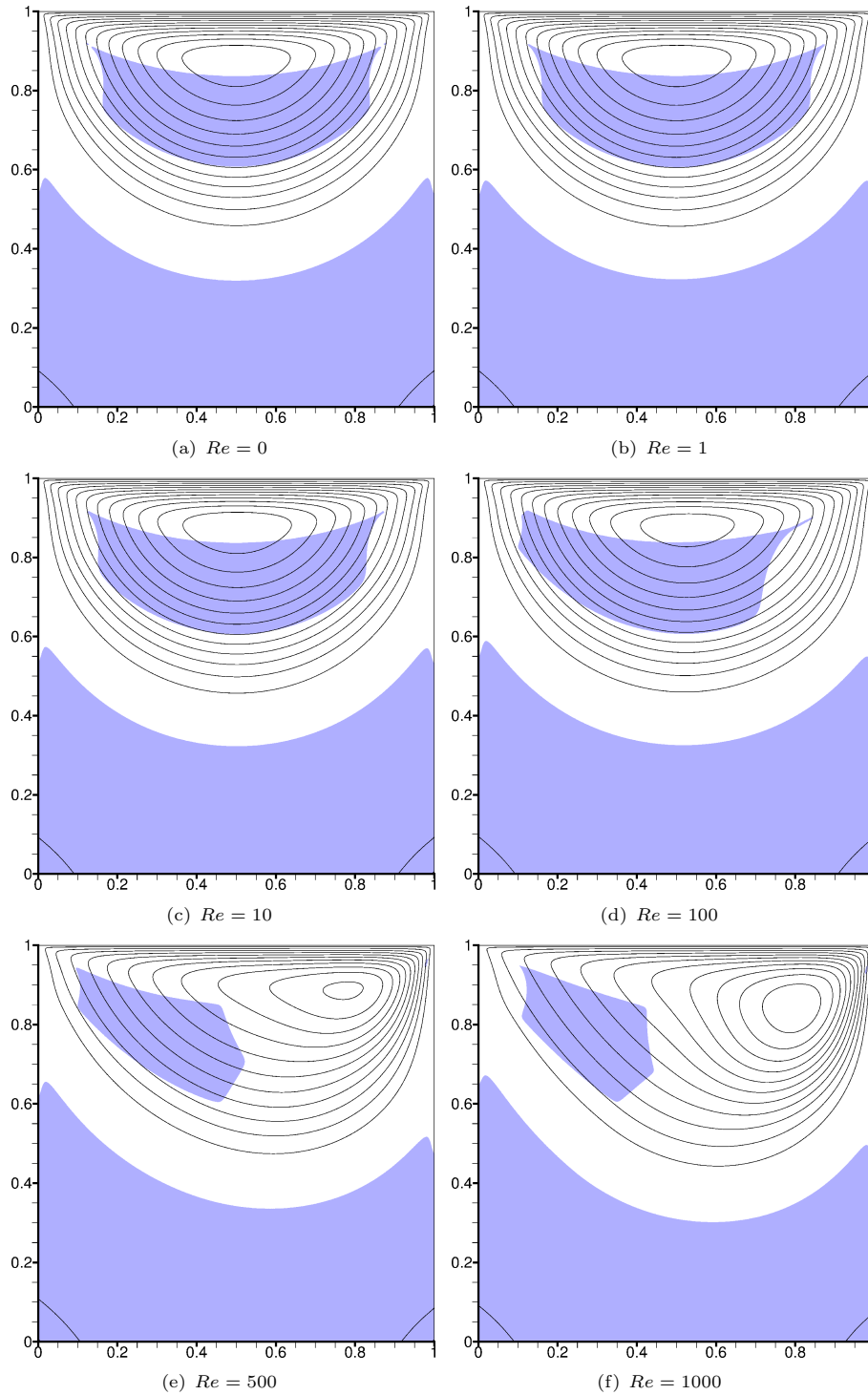


Figure 3: Streamlines in Bingham flow for $Bn = 10$, plotted at intervals of 0.004 starting from zero. Unyielded areas ($\tau < Bn$) are shown shaded.

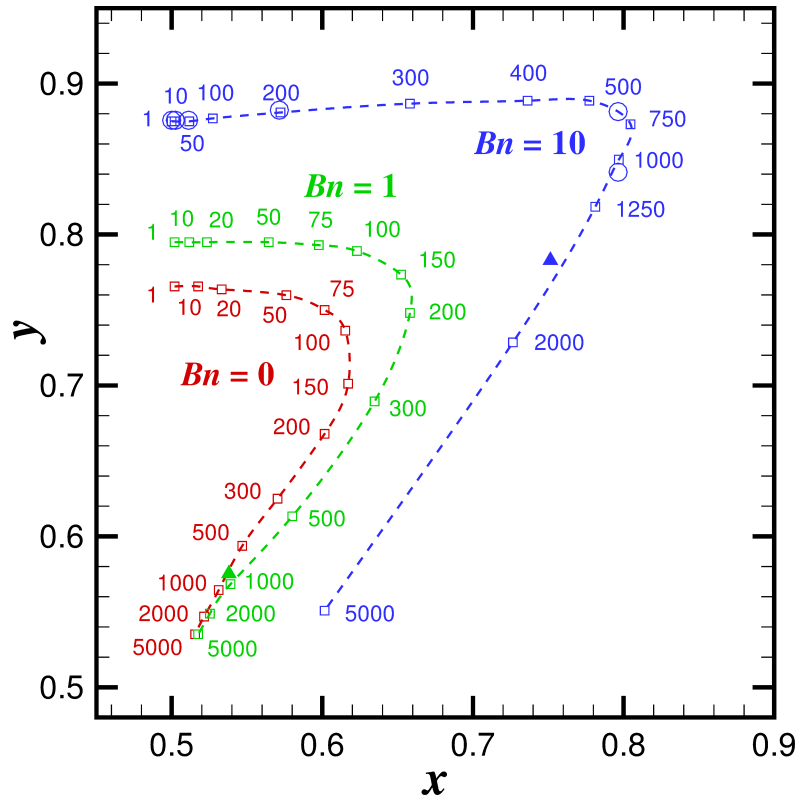


Figure 4: The position of the vortex centre, for various values of Re and Bn . The results of the present study are shown as empty squares (\square), with the Reynolds number written next to each square. The results of Vola et al [13] ($Re = 1000$: $Bn = 1, 10$) and of Prashant and Derksen [14] ($Re = 0.5, 10, 50, 200, 600, 1000$: $Bn = 10$), are indicated by filled triangles (\blacktriangle) and empty circles (\circ), respectively.

corners; these are in fact an artifact of the Papanastasiou regularisation which treats all of the material as a fluid. On the other hand, the unyielded region that is close to the vortex centre and does not touch the cavity walls is clearly not motionless. This can be seen from the streamlines' spacing inside these regions, which shows that the velocity is non-zero. These regions move as solid bodies. The fact that the flow is steady-state means that these "solid bodies" lose mass on their downstream boundary at a rate equal to that at which they gain mass on their upstream boundary, so that their location and size remains fixed in time. In other words, a fluid particle "solidifies" on entry to this region, and following the streamline path it later exits the region, at which point it becomes "fluid" again.

The position of the vortex centre for various Re and Bn numbers is shown in Figure 4. The present results are close to those of Vola et al [13] and Prashant and Derksen [14], except for the ($Re=1000$, $Bn=10$) case, where there is some discrepancy between the present results and those of Vola et al. However, the agreement is very good with the results of Prashant and Derksen [14]. Figure 4 shows that there is a trend in which, as the Reynolds number increases, the main vortex initially moves towards the downstream side wall, and then, beyond a certain Reynolds number, it moves towards the cavity centre. As Bn increases, these phenomena are postponed to higher Reynolds numbers and, in addition, the vortex moves higher towards the lid, as the bottom of the cavity becomes filled with "solid" material and the flow region is restricted.

Tables 1 – 2 contain results on the x -component of velocity along the vertical centreline, for

Table 1: Values of the x -component of velocity along the vertical centreline for $Re = 1000$, $Bn = 1$. The order of grid convergence, q , is defined by Eq. (10).

grid	128×128	256×256	512×512	512×512	512×512	q
y	$M = 400$	$M = 400$	$M = 400$	$M = 200$	$M = 100$	
1.000	1.00000	1.00000	1.00000	1.00000	1.00000	-
0.990	0.83434	0.83687	0.83734	0.83734	0.83733	2.41
0.980	0.68125	0.68471	0.68593	0.68592	0.68591	1.51
0.960	0.46586	0.47143	0.47274	0.47273	0.47271	2.09
0.930	0.34382	0.34918	0.35050	0.35048	0.35046	2.02
0.900	0.30799	0.31269	0.31389	0.31387	0.31383	1.97
0.850	0.26486	0.26900	0.27007	0.27005	0.27000	1.95
0.800	0.21625	0.21965	0.22054	0.22053	0.22052	1.93
0.700	0.11957	0.12136	0.12184	0.12186	0.12190	1.90
0.600	0.03123	0.03185	0.03203	0.03205	0.03207	1.78
0.500	-0.05486	-0.05520	-0.05526	-0.05523	-0.05517	2.55
0.400	-0.14093	-0.14186	-0.14206	-0.14204	-0.14201	2.21
0.300	-0.23422	-0.23608	-0.23652	-0.23650	-0.23647	2.08
0.220	-0.30655	-0.30973	-0.31051	-0.31049	-0.31046	2.02
0.180	-0.32376	-0.32847	-0.32969	-0.32969	-0.32968	1.95
0.140	-0.29831	-0.30398	-0.30552	-0.30555	-0.30559	1.88
0.100	-0.23360	-0.23851	-0.23989	-0.23994	-0.24002	1.82
0.050	-0.13004	-0.13274	-0.13354	-0.13359	-0.13367	1.76
0.000	0.00000	0.00000	0.00000	0.00000	0.00000	-

 Table 2: Values of the x -component of velocity along the vertical centreline for $Re = 1000$, $Bn = 10$. The order of grid convergence, q , is defined by Eq. (10).

grid	128×128	256×256	512×512	512×512	512×512	q
y	$M = 400$	$M = 400$	$M = 400$	$M = 200$	$M = 100$	
1.000	1.00000	1.00000	1.00000	1.00000	1.00000	-
0.990	0.78014	0.78237	0.78283	0.78295	0.78318	2.28
0.980	0.58320	0.58552	0.58662	0.58683	0.58719	1.07
0.960	0.28798	0.29236	0.29359	0.29400	0.29476	1.83
0.920	0.03885	0.04330	0.04480	0.04544	0.04665	1.57
0.880	-0.02432	-0.02168	-0.02059	-0.02003	-0.01896	1.29
0.850	-0.03940	-0.03904	-0.03892	-0.03850	-0.03769	1.59
0.750	-0.05502	-0.05520	-0.05520	-0.05493	-0.05439	8.26
0.650	-0.06670	-0.06763	-0.06802	-0.06771	-0.06715	1.25
0.580	-0.07537	-0.07575	-0.07589	-0.07576	-0.07549	1.52
0.540	-0.07895	-0.07926	-0.07934	-0.07908	-0.07857	1.89
0.500	-0.07775	-0.07911	-0.07949	-0.07911	-0.07838	1.81
0.460	-0.06274	-0.06498	-0.06561	-0.06550	-0.06529	1.84
0.420	-0.03891	-0.04167	-0.04257	-0.04274	-0.04303	1.61
0.380	-0.01636	-0.01878	-0.01977	-0.02021	-0.02102	1.27
0.340	-0.00363	-0.00390	-0.00429	-0.00505	-0.00648	-0.52
0.300	-0.00096	-0.00087	-0.00084	-0.00164	-0.00318	1.60
0.200	-0.00043	-0.00043	-0.00042	-0.00084	-0.00165	0.92
0.100	-0.00021	-0.00020	-0.00020	-0.00040	-0.00080	0.68
0.000	0.00000	0.00000	0.00000	0.00000	0.00000	-

$Re = 1000$ and $Bn = 1$ and 10, respectively. These were obtained on various grids and with various values of M , estimated at the selected points using linear interpolation. The points selected differ for the various Bn numbers, and they were chosen so as to provide good descriptions of the profiles. The results listed can be used to check grid convergence and “ M -convergence”, i.e. whether an M -independent solution has been reached. The exponent q in Tables 1 and 2 is the order of grid convergence, defined as (see [12])

$$q \equiv \frac{\log\left(\frac{u_{256}-u_{128}}{u_{512}-u_{256}}\right)}{\log(2)} \quad (10)$$

where the subscripts denote the grid where u was calculated. Since the equations were discretised using 2nd order accurate central differences, q should equal 2.

Table 1 shows that, for $Bn = 1$, the method indeed exhibits a 2nd order rate of convergence with grid refinement, with the exponent q being very close to 2. From the difference between the solutions of the two finest grids and the $q = 2$ order of convergence, a discretisation error of the order of 0.02 is estimated. The difference between using $M = 200$ and $M = 400$ is very small, meaning that grid coarseness appears to be a larger source of error than the magnitude of M in this particular case.

From Table 2, it is deduced that for $Bn = 10$, the order of grid convergence is now clearly below 2, and in particular the mean value of the exponent q is just over 1.5 (excluding extreme values). This is a sign that the grid is not fine enough. The discretisation error on grid 512×512 appears to be about 0.5%, assuming 2nd order convergence. The difference between using different M indices is also larger. These observations lead to the conclusion that finer grids and larger values of M should be used with larger Bingham numbers.

Finally, Figure 5 shows the reduction of the algebraic residuals as a function of the computational effort for $Re = 1000$ and $Bn = 1$ and 10, as typical examples. The ordinate is the the L^∞ -norm of the residual vector of the x -momentum equations,

$$\|r\|_\infty = \max_{P=1,\dots,N} \{|r_P|\} , \quad (11)$$

where r_P is the residual, expressed per unit volume, of the x -momentum equation of control volume P and N is the total number of control volumes in the grid. The computational effort is measured in equivalent fine-grid SIMPLE iterations. For the multigrid cases, the number of equivalent fine-grid SIMPLE iterations is obtained by multiplying the number of cycles by the number of fine-grid SIMPLE iterations that cost computationally the same as a single cycle. In particular, n_C cycles of type $W(\nu_1, \nu_2) - \nu_3$ cost approximately the same as $n_S = n_C \cdot [2(\nu_1 + \nu_2) + \nu_3]$ SIMPLE iterations on the finest grid. For example, one $W(6,6)$ -10 cycle costs the same as 34 fine-grid SIMPLE iterations. It should be noted that the cost of restriction and prolongation is omitted in this calculation, since it is very small compared to the cost of the SIMPLE iterations, especially if one considers that the numbers of pre- and post-smoothing iterations are large, and fine-grid iterations are also carried out between cycles. Therefore, multigrid and single-grid convergence rates are directly comparable in Figure 5. The SIMPLE underrelaxation factors were chosen differently in the multigrid and single-grid cases, in order to make the solvers more efficient in each case.

Figure 5 also shows that the multigrid procedure greatly accelerates the convergence of SIMPLE. One can notice that as the grid becomes finer, the multigrid convergence slows down in general - this is not typical multigrid behaviour, and is explained by the fact that the present multigrid method contains single-grid features, as described in Section 3. For $Bn = 10$, on the 256×256 and 512×512 grids the procedure converges fast at the initial stages, due to a good initial guess, but slows down at later stages of iteration. The convergence rates decrease as Bn increases, and are significantly worse than those typically exhibited in Newtonian flows.

5 CONCLUSIONS

The present work has shown that the finite volume method, coupled with the SIMPLE algebraic solver in a multigrid framework, can be easily adapted to use the Papanastasiou regularisation for the simulation of Bingham flows for a wide range of Reynolds and Bingham numbers. The method has been tested on the lid-driven cavity problem, yielding results that agree with

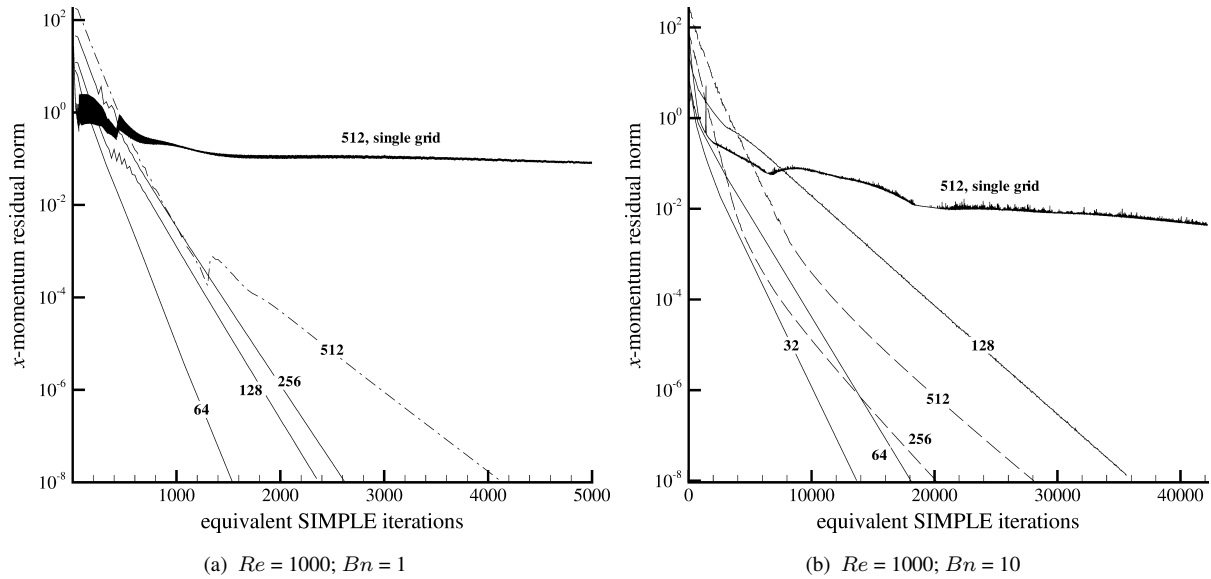


Figure 5: Maximum x -momentum residual per unit volume (11) versus computational effort, for $Re = 1000$ and $Bn = 1$ and 10 . The results refer to the SIMPLE/multigrid algebraic solver, using the 8×8 as the coarsest grid, except for a single-grid case which is indicated on each figure. The number on each curve indicates the finest grid (n means that the finest grid has $n \times n$ control volumes). The algebraic solver parameters are the following (see Section 3 for definitions): For $Bn = 1$, W(5,5)-5 cycles, $\alpha_{MG} = 1.0$, $a_u = 0.7$, and $a_p = 0.02$ (multigrid) or 0.2 (single grid). For $Bn = 10$, W(6,6)-10 cycles, $\alpha_{MG} = 0.9$, and $\{a_u, a_p\} = \{0.5, 0.02\}$ (multigrid) or $\{0.7, 0.2\}$ (single grid). On each grid, the solution of the immediately coarser grid was used as the initial guess.

those of previously published works, which employed different solution methods. It is observed that as the Bingham number increases, it becomes more difficult for the SIMPLE/multigrid method to solve the algebraic system that results from the finite volume discretisation. Also, to maintain a certain level of accuracy, the Papanastasiou exponent M and the grid density should increase as the Bingham number increases. This causes additional difficulties to the algebraic solver. The multigrid framework is necessary for the solver to be efficient, as the convergence of SIMPLE alone is too slow. The method is currently being tested on yet higher Bn numbers.

ACKNOWLEDGEMENTS

This work was supported by the Cyprus Research Promotion Foundations Framework Programme for Research, Technological Development and Innovation 2009-2010 (DESMI 2009-2010), co-funded by the Republic of Cyprus and the European Regional Development Fund, and specially under Grant ΑΕΙΦΟΡΙΑ/ΦΥΣΗ/0609(BIE)/15.

REFERENCES

- [1] T.C. Papanastasiou, Flows of materials with yield. *Journal of Rheology*, **31**, 385–404, 1987.
- [2] A. Syrakos, A. Goulas, Finite volume adaptive solutions using SIMPLE as smoother. *International Journal for Numerical Methods in Fluids*, **52**, 1215–1245, 2006.

- [3] A. Syrakos, G.C. Georgiou, A.N. Alexandrou, Solution of the square lid-driven cavity flow of a Bingham plastic using the finite volume method. *Journal of Non-Newtonian Fluid Mechanics*, **195**, 19–31, 2013.
- [4] P. Neofytou, A 3rd order upwind finite volume method for generalised Newtonian fluid flows. *Advances in Engineering Software*, **36**, 664–680, 2005.
- [5] S.V. Patankar, D.B. Spalding, A calculation procedure for heat, mass and momentum transfer in three-dimensional parabolic flows. *International Journal of Heat and Mass Transfer*, **15**, 1787–1806, 1972.
- [6] O. Turan, N. Chakraborty, R.J. Poole, Laminar natural convection of Bingham fluids in a square enclosure with differentially heated side walls. *Journal of Non-Newtonian Fluid Mechanics*, **165**, 901–913, 2010.
- [7] P. Neofytou, D. Drikakis, Effects of blood models on flows through a stenosis. *International Journal for Numerical Methods in Fluids* **43**, 597–635, 2003.
- [8] P. Neofytou, D. Drikakis, Non-Newtonian flow instability in a channel with a sudden expansion. *Journal of Non-Newtonian Fluid Mechanics*, **111**, 127–150, 2003.
- [9] P.R. de Souza Mendes, M.F. Naccache, P.R. Varges, F.H. Marchesini, Flow of viscoplastic liquids through axisymmetric expansions-contractions. *Journal of Non-Newtonian Fluid Mechanics*, **142**, 207–217, 2007.
- [10] M.F. Naccache, R.S. Barbosa, Creeping flow of viscoplastic materials through a planar expansion followed by a contraction. *Mechanics Research Communications*, **34**, 423–431, 2007.
- [11] A. Syrakos, A. Goulas, Estimate of the truncation error of finite volume discretization of the NavierStokes equations on colocated grids. *International Journal for Numerical Methods in Fluids*, **50**, 103–130, 2006.
- [12] J.H. Ferziger, M. Perić, *Computational methods for fluid dynamics, 3rd Edition*. Springer, 2002.
- [13] D. Vola, L. Boscardin, J.C. Latché, Laminar unsteady flows of Bingham fluids: a numerical strategy and some benchmark results. *Journal of Computational Physics*, **187**, 441–456, 2003.
- [14] Prashant, J.J. Derksen, Direct simulations of spherical particle motion in Bingham liquids. *Computers and Chemical Engineering*, **35**, 1200–1214, 2011.
- [15] M. Fortin, R. Glowinski, *Augmented Lagrangian Methods: applications to the numerical solution of boundary-value problems*. North-Holland, 1983.
- [16] E.J. O’Donovan, R.I. Tanner, Numerical study of the Bingham squeeze film problem. *Journal of Non-Newtonian Fluid Mechanics*, **15**, 75–83, 1984.

CESSATION FLOWS OF BINGHAM PLASTICS WITH SLIP AT THE WALL

Yiolanda Damianou¹, Maria Philippou², George Kaoullas³, and Georgios C. Georgiou⁴

¹ Dept. of Mathematics and Statistics, University of Cyprus, PO Box 20537, 1678 Nicosia, Cyprus
e-mail: damianou.yiolanda@ucy.ac.cy

² Dept. of Mathematics and Statistics, University of Cyprus, PO Box 20537, 1678 Nicosia, Cyprus
e-mail: mariaf@ucy.ac.cy

³ Dept. of Mathematics and Statistics, University of Cyprus, PO Box 20537, 1678 Nicosia, Cyprus
e-mail: gkaoullas@gmail.com

⁴ Dept. of Mathematics and Statistics, University of Cyprus, PO Box 20537, 1678 Nicosia, Cyprus
e-mail: georgios@ucy.ac.cy

Keywords: Herschel-Bulkley Fluid, Bingham Plastic, Slip Yield Stress, Poiseuille Flow, Cessation Flow, Stopping Time.

Abstract. *We use finite elements in space and a fully implicit scheme in time in order to solve the cessation of axisymmetric Poiseuille flow of a Bingham plastic under the assumption that slip occurs along the wall. The Papanastasiou regularization of the constitutive equation is employed and a power-law expression is used to relate the wall shear stress to the slip velocity. The numerical results show that the velocity becomes and remains uniform before complete cessation and that the stopping time is finite only when the exponent $s < 1$. In the case of Navier slip ($s=1$), the stopping time is infinite for any non-zero Bingham number and the volumetric flow rate decays exponentially. When $s > 1$, the decay is much slower, i.e. polynomial. The asymptotic expressions for the volumetric flow rate in the case of full-slip are also derived.*

1 INTRODUCTION

If the pressure-gradient applied in fully-developed Poiseuille flow of a Newtonian fluid is suddenly set to zero, the velocity decays to zero exponentially, i.e. the theoretical stopping time is infinite [1]. This is not the case for materials exhibiting yield stress, e.g. Bingham plastics. In fact, theoretical upper bounds on the stopping time have been derived [2, 3]. These bounds depend on the density, the viscosity, the yield stress, a new geometric constant, and the leading eigenvalue of the second-order linear differential operator for the interval under consideration. The above asymptotic bounds have been verified by means of numerical simulations. Chatzimina et al. [4] carried out finite element calculations with the regularized Papanastasiou model for Couette and Poiseuille flows of Bingham plastics. The numerical simulations showed in particular that the decay of the volumetric flow rate, which is exponential in the Newtonian case, is accelerated and eventually becomes linear as the yield stress is increased. More recently, the Poiseuille flows of ideal Bingham plastics have been solved numerically using the Augmented Lagrangian method [5].

The objective of the present work is to compute numerically the stopping times in the case of the cessation of the axisymmetric Poiseuille flow of a Bingham fluid allowing slip of the material along the wall (Fig. 1). However, in the discussion of the steady-state solutions we consider the more general Herschel-Bulkley model in which the stress tensor $\underline{\underline{\tau}}$ is given by

$$\begin{cases} \underline{\underline{\dot{\gamma}}} = \underline{\underline{0}}, & \tau \leq \tau_0 \\ \underline{\underline{\tau}} = \left(\frac{\tau_0}{\dot{\gamma}} + \dot{\gamma}^{n-1} \right) \underline{\underline{\dot{\gamma}}}, & \tau \geq \tau_0 \end{cases} \quad (1)$$

where τ_0 is the yield stress, k is the consistency index, n is the power-law exponent, and

$$\underline{\underline{\dot{\gamma}}} \equiv \nabla \underline{\underline{u}} + (\nabla \underline{\underline{u}})^T \quad (2)$$

is the rate of strain tensor, where $\underline{\underline{u}}$ is the velocity vector and the superscript T denotes the transpose. The magnitudes of $\underline{\underline{\dot{\gamma}}}$ and $\underline{\underline{\tau}}$, denoted respectively by $\dot{\gamma}$ and τ , are defined by

$$\dot{\gamma} \equiv \sqrt{\frac{1}{2} \Pi_{\dot{\gamma}}} = \sqrt{\frac{1}{2} \dot{\gamma} : \dot{\gamma}} \quad \text{and} \quad \tau \equiv \sqrt{\frac{1}{2} II_{\tau}} = \sqrt{\frac{1}{2} \tau : \tau} \quad (3)$$

where the symbol II stands for the second invariant of a tensor. The power-law fluid and the Bingham plastic are special cases of the Herschel-Bulkley fluid, recovered by setting $\tau_0=0$ and $n=1$, respectively.

In the present work, a generalized slip model is employed of the form

$$\begin{cases} u_w = 0, & \tau_w \leq \tau_c \\ \tau_w = \tau_c + \beta u_w^s, & \tau_w > \tau_c \end{cases} \quad (4)$$

where τ_w is the wall shear stress, u_w is the slip or sliding velocity (i.e. the relative velocity of the fluid with respect to that of the wall), τ_c is the slip yield stress, β is the slip coefficient and s is the exponent. When $\tau_c=0$ and $s=1$ the classical Navier slip is recovered. When $\tau_c=0$, the no-slip and full-slip limiting cases are recovered when $\beta \rightarrow \infty$ and 0, respectively.

The slip yield stress τ_c may be smaller or greater than the yield stress τ_0 depending on the material. For example, Seth et al. [6] reported that the slip yield stress is much lower in the case of concentrated suspensions of soft deformable particles.

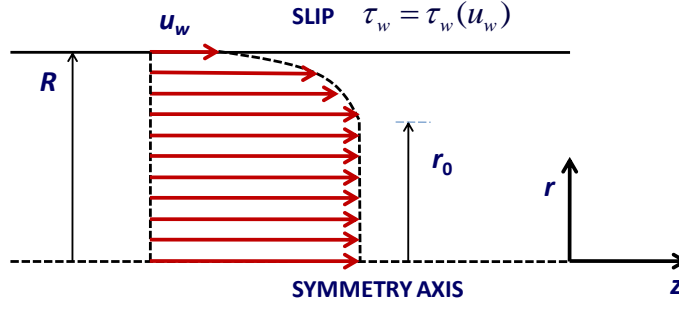


Figure 1: Axisymmetric Poiseuille flow of a Herschel-Bulkley fluid

2 GOVERNING EQUATIONS

We consider the laminar flow of a Herschel-Bulkley fluid in a tube of radius R , as shown in Fig. 1. The constitutive equation of the material is simplified as follows:

$$\begin{cases} \frac{\partial u_z}{\partial r} = 0, & |\tau_{rz}| \leq \tau_0 \\ \tau_{rz} = -\tau_0 - k \left(-\frac{\partial u_z}{\partial r} \right)^n, & |\tau_{rz}| \geq \tau_0 \end{cases} \quad (5)$$

where τ_{rz} is the shear stress and u_z is the axial velocity.

Under the assumptions of unidirectionality and zero gravity, the z -momentum equation for any fluid becomes

$$\rho \frac{\partial u_z}{\partial t} = -\frac{\partial p}{\partial z} + \frac{1}{r} \frac{\partial}{\partial r} (r \tau_{rz}) \quad (6)$$

where ρ is the density.

To dedimensionalize the governing equations we scale lengths by the tube radius, R , the velocity by the mean steady-state velocity, V , in the capillary, the pressure and the stress components by kV^n/R^n , and time by $\rho R^{n+1}/(kV^{n-1})$, where ρ is the constant density of the fluid. With these scalings the dimensionless forms of Eqs. (5) and (6) are as follows:

$$\begin{cases} \frac{\partial u_z}{\partial r} = 0, & |\tau_{rz}| \leq Bn \\ \tau_{rz} = -Bn - \left(-\frac{\partial u_z}{\partial r} \right)^n, & |\tau_{rz}| \geq Bn \end{cases} \quad (7)$$

and

$$\frac{\partial u_z}{\partial t} = G + \frac{1}{r} \frac{\partial}{\partial r} (r \tau_{rz}) \quad (8)$$

where all variables are now dimensionless (for simplicity, the same symbols are used),

$$Bn \equiv \frac{\tau_0 R^n}{kV^n} \quad (9)$$

is the Bingham number, and G is the dimensionless pressure gradient.

The dimensionless form of the slip equation is

$$\begin{cases} u_w = 0, & \tau_w \leq B_c \\ \tau_w = B_c + Bu_w^s, & \tau_w > B_c \end{cases} \quad (10)$$

where

$$B_c \equiv \frac{\tau_c R^n}{kV^n} \quad (11)$$

is the slip yield stress number and

$$B \equiv \frac{\beta R^n}{kV^{n-s}} \quad (12)$$

is the usual slip number. (The no-slip and full-slip limiting cases are recovered when $B \rightarrow \infty$ and 0, respectively.) In the special case $\tau_c = \tau_0$, the slip yield stress number, B_c , coincides with the Bingham number, Bn .

3 STATE –STATE HERSCHEL-BULKLEY FLOWS WITH SLIP

The solution of the steady, incompressible Poiseuille flow of a Herschel-Bulkley fluid in the special case of Navier slip ($B_c=0$, $s=1$) has been provided under different forms by Kalyon et al. [7]. Taking into account the slip yield stress, leads to some interesting flow regimes, which are discussed below.

In steady-state, the dimensionless wall shear stress for any generalized Newtonian fluid is $\tau_w = G/2$. Depending on the value of the applied pressure gradient, G , and the relative values of B_c and Bn , there are four different possibilities:

- (i) If $G \leq \min\{2B_c, 2Bn\}$, then no flow occurs.
- (ii) If $G \geq \max\{2B_c, 2Bn\}$, then we have non-uniform flow with wall slip and yielded/unyielded regions in the flow domain. The dimensionless velocity profile is given by

$$u_z(r) = u_w + \frac{n}{2^{1/n}(n+1)} G^{1/n} \begin{cases} (1-r_0)^{1/n+1}, & 0 \leq r \leq r_0 \\ [(1-r_0)^{1/n+1} - (r-r_0)^{1/n+1}], & r_0 \leq r \leq 1 \end{cases} \quad (13)$$

where

$$u_w = \left(\frac{G - 2B_c}{2B} \right)^{1/s} \quad (14)$$

and

$$r_0 = \frac{2Bn}{G} \leq 1 \quad (15)$$

is the yield point. The dimensionless pressure-gradient is a solution of the following equation:

$$2^{1/n} \frac{3n+1}{n} (1-u_w) G^3 = (G - 2Bn)^{1/n+1} \left[G^2 + \frac{4nBn}{2n+1} G + \frac{8n^2 Bn^2}{(n+1)(2n+1)} \right] \quad (16)$$

- (iii) If $2Bn < G < 2B_c$, then the fluid flows without slip ($u_w=0$) with distinct yielded and unyielded regions. Equations (10) and (13) still apply.

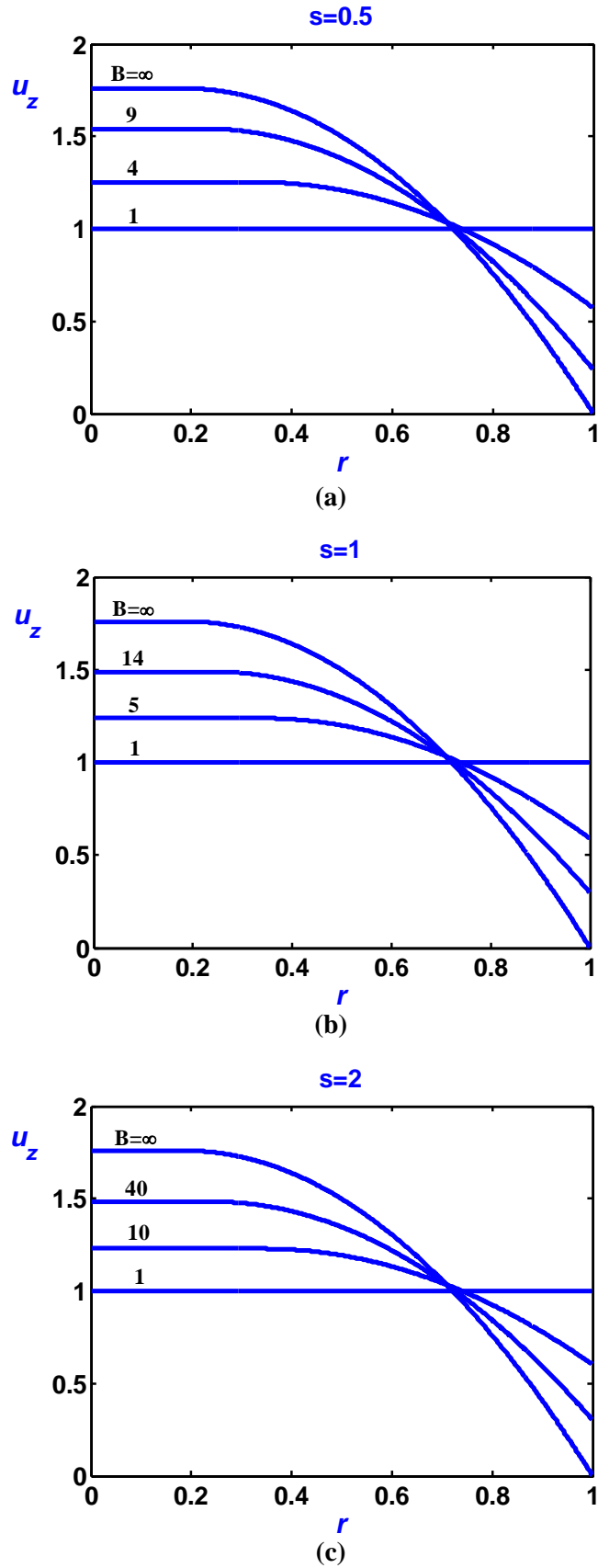


Figure 2: Velocity profiles in axisymmetric Poiseuille flow of a Bingham plastic ($Bn=1$) with zero slip yield stress ($B_c=0$) and different values of the slip number: (a) $s=0.5$, (b) $s=1$, and (c) $s=2$.

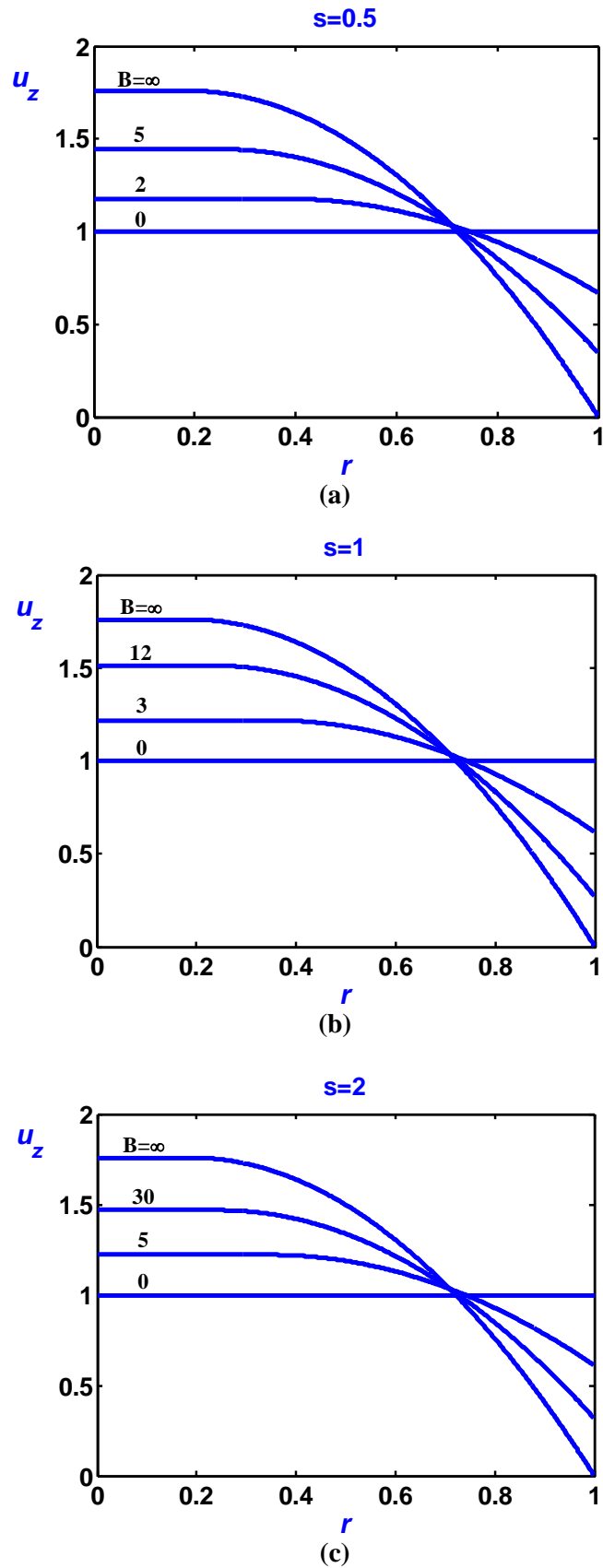


Figure 3: Velocity profiles in axisymmetric Poiseuille flow of a Bingham plastic with $Bn = B_c = 1$ and different values of the slip number: (a) $s = 0.5$, (b) $s = 1$, and (c) $s = 2$.

(iv) Finally, if $2B_c < G < 2Bn$, the fluid is unyielded everywhere in the flow domain, sliding with unit velocity.

When no-slip is applied, r_0 tends to unity asymptotically as Bn goes to infinity. Otherwise, it is deduced from Eq. (16) that a flat velocity profile ($u_x=u_w=1$) is attained when $G=2Bn>2B_c$. In the Newtonian case ($Bn=0$), the velocity tends to a plug profile ($u_x=u_w=1$) in the limit of zero B (full slip). Interestingly, with viscoplastic fluids, the plug velocity profile is attained at a finite non-zero value of B at which the yield distance r_0 becomes 1. The critical slip number for this extreme case is obtained from Eq. (14):

$$B_{crit} = Bn - B_c \quad (17)$$

Hence, for given Bn and B_c , solutions for slip numbers below B_{crit} are not admissible. Similarly, when B and B_c are given, there exists a critical upper bound for the Bingham number, $Bn_{crit}=B+B_c$, which cannot be exceeded. At Bn_{crit} both the yield distance and the slip velocity become 1. This implies that the flow becomes plug at a critical wall shear stress, which is consistent with experimental observations on highly filled suspensions [8].

The case of Herschel-Bulkley flow with Navier slip ($B_c=0$ and $s=1$) has been discussed in detail by Damianou et al. [9], who, however, employed a different definition of the slip number (A_1 in their paper corresponds to $1/(2B)$). Here we consider first Bingham flow ($n=1$) with zero slip yield stress ($B_c=0$).

The effect of the exponent s when B_c is still zero is illustrated in Fig. 2, where we plot velocity profiles for Bingham flow ($n=1$) with $Bn=1$ and various slip numbers. The velocity becomes flat at the critical slip number $B_{crit}=Bn$.

Let us now focus on the special case when $Bn=B_c$, in which only the flow regimes (i) and (ii) are possible. In other words, slip occurs as soon as flow occurs and there are no bounds for the slip and Bingham numbers. For simplicity, we once again restrict ourselves to the Bingham-plastic case ($n=1$).

The effect of the exponent s for $Bn=B_c=1$ is illustrated in Fig. 3. The critical value of the slip number for the velocity to become flat is $B_{crit}=0$. As expected, slip effects are delayed, i.e., compared to the $B_c=0$ case, similar changes in the velocity profile are observed at lower values of B .

4 TIME-DEPENDENT BINGHAM FLOWS WITH SLIP

The time-dependent Bingham plastic flow is solved numerically, since it is not amenable to analytical solution. Instead of the ideal Bingham model (5), in our numerical simulations we use the regularized constitutive equation proposed by Papanastasiou [10], which in dimensionless form is given by

$$\tau_{rz} = \left\{ \frac{Bn[1 - \exp(-M \dot{\gamma})]}{\dot{\gamma}} + 1 \right\} \frac{\partial u_z}{\partial r} \quad (18)$$

where $\dot{\gamma} = |\partial u_z / \partial r|$, while the stress growth exponent M is given by

$$M \equiv \frac{mV}{H} \quad (19)$$

where m is a stress growth exponent.

To solve the problem we used 100 quadratic elements in space and finite differences in time. For the time discretization, we used the standard fully implicit Euler backward-

difference scheme with a dimensionless time step $dt \leq 10^{-4}$. The criteria for convergence of the system of equations were that the norm of the error for the velocities and the norm of the residuals were both less than 10^{-4} .

The general stopping criterion for the “numerical cessation” of the flow was that the norm of the dimensionless deceleration was less than a small number ε . Here $\varepsilon = (\rho H^2/\mu V)10^{-3}$, where $\mu V/\rho H^2$ is the *characteristic deceleration*. The total dimensionless time, T_f , found with the above criterion and with constant $dt = 10^{-4}$, is given in all figures where transient solutions are shown.

As discussed in Section 3, in the case of Bingham flow, steady-state plug velocity profiles are admissible when Navier slip is allowed [9]. The critical slip number for attaining a uniform steady-state velocity profile in axisymmetric Poiseuille flow is $B_{\text{crit}}=Bn-B_c$.

4.1 Results for zero slip yield stress

The numerical simulations of the cessation flow show that the velocity becomes and remains uniform before complete cessation. The evolution of the velocity when $Bn=1$, $B=5$ and $s=1$ is illustrated in Fig. 4. Obviously, as the slip number is increased, the initial velocity profile becomes more flat and a uniform profile is attained earlier during cessation.

Figure 5 shows the evolution of the volumetric flow rate Q for $Bn=1$ and different slip numbers for three representative values of the exponent s : 0.5, 1, and 2. One observes that the stopping time is finite only in the case of no slip ($B \rightarrow \infty$) when $s < 1$. When s is fixed, the stopping time increases with the slip coefficient. In the case of Navier slip ($s=1$), the stopping time is infinite for any non-zero Bingham number and the volumetric flow rate decays exponentially. When $s > 1$, the decay is much slower.

Let t_c denote the critical time at which the velocity becomes uniform, i.e. $u_z = u_w(t_c) = u_{wc}$. Integrating the momentum equation (8) over the tube cross-section leads to the following ODE:

$$\frac{du_w}{dt} = -2\tau_w = -2Bu_w^s \quad (20)$$

Therefore, when $s=1$, the velocity decays exponentially:

$$u_z = u_{wc} \exp[-2B(t-t_c)], \quad t > t_c \quad (21)$$

where $u_{wc} = u_w(t_c)$. Otherwise,

$$u_z = u_{wc} [1 - 2(1-s)B(t-t_c)]^{1/(1-s)}, \quad t > t_c \quad (22)$$

It is clear that the stopping time is finite only if $s < 1$. The asymptotic estimate of the stopping time is then

$$t_s = t_c + \frac{1}{2(1-s)B} \quad (23)$$

In Figure 6, we compare the slip velocities predicted using Eqs. (21) and (22) with the numerical solutions taking $Bn=1$ and $B=1$, considering three different values for s (0.1, 1, and 2), and assuming that $u_{wc}=1$ and $t_c=0$. Given that B is close to Bn , the numerical results practically coincide with the theoretical estimates.

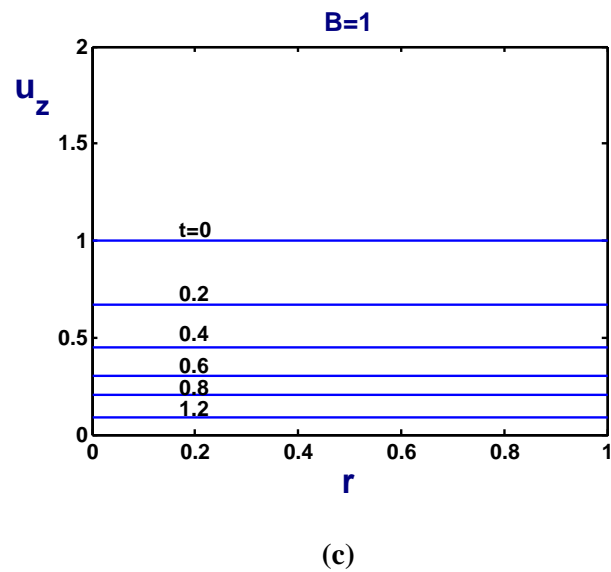
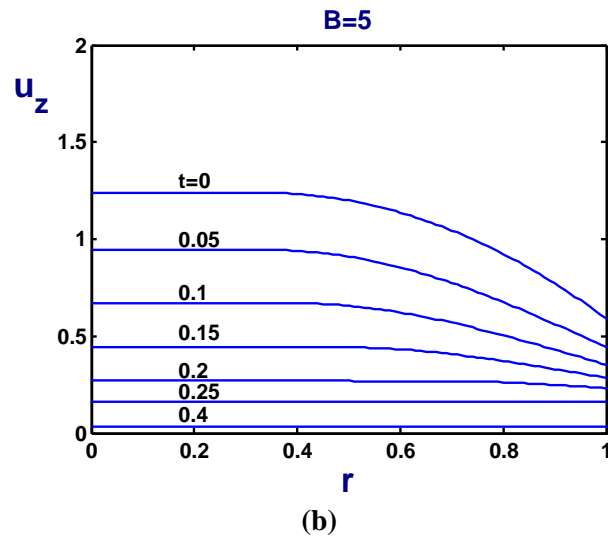
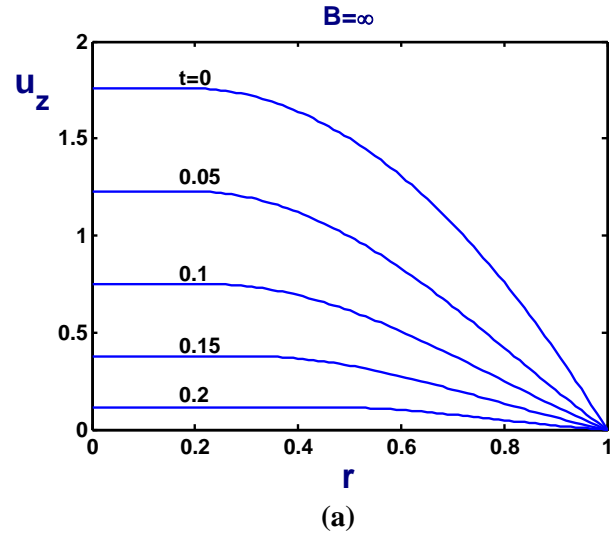


Figure 4: Evolution of the velocity in cessation flow of a Bingham plastic with $Bn=1$, $s=1$ and zero slip yield stress ($B_c=0$): (a) $B=\infty$ (no slip); (b) $B=5$; and (c) $B=1$ (plug flow).

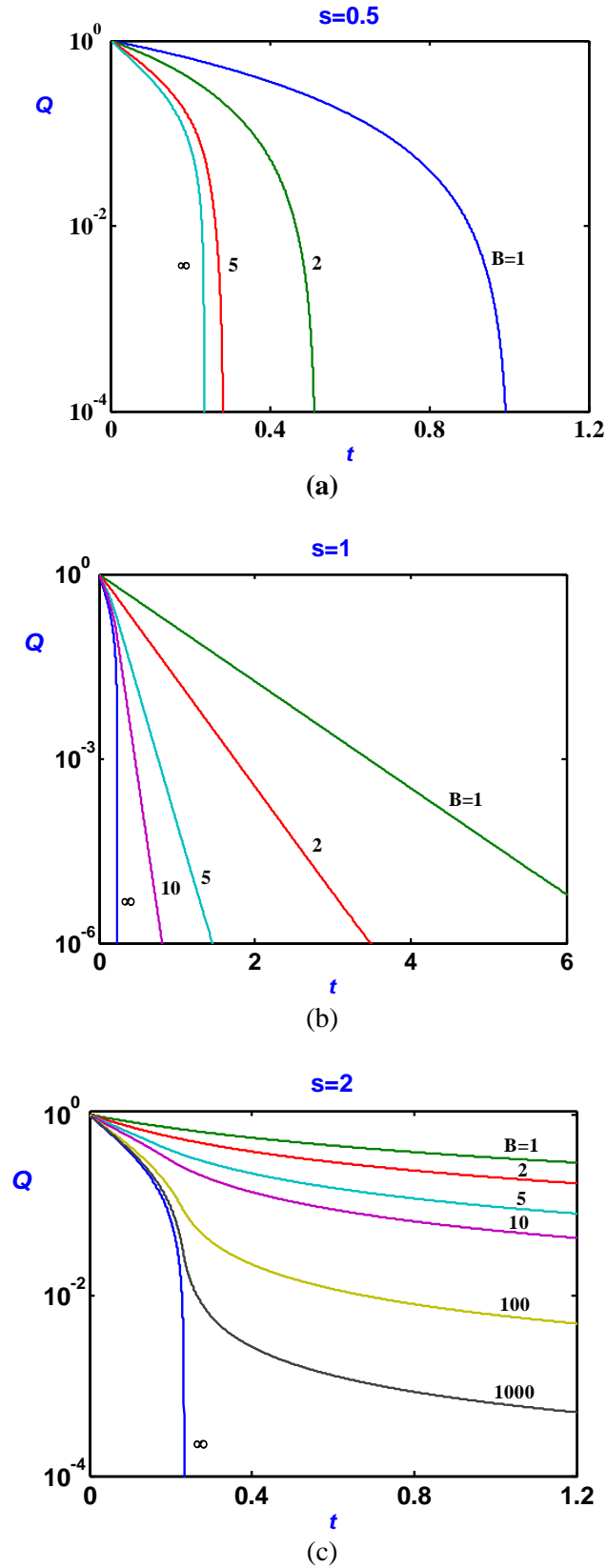


Figure 5: Evolution of the volumetric flow rate in cessation flow of a Bingham plastic with $Bn=1$, zero slip yield stress ($Bc=0$) and various slip numbers: (a) $s=0.5$; (b) $s=1$; and (c) $s=2$.

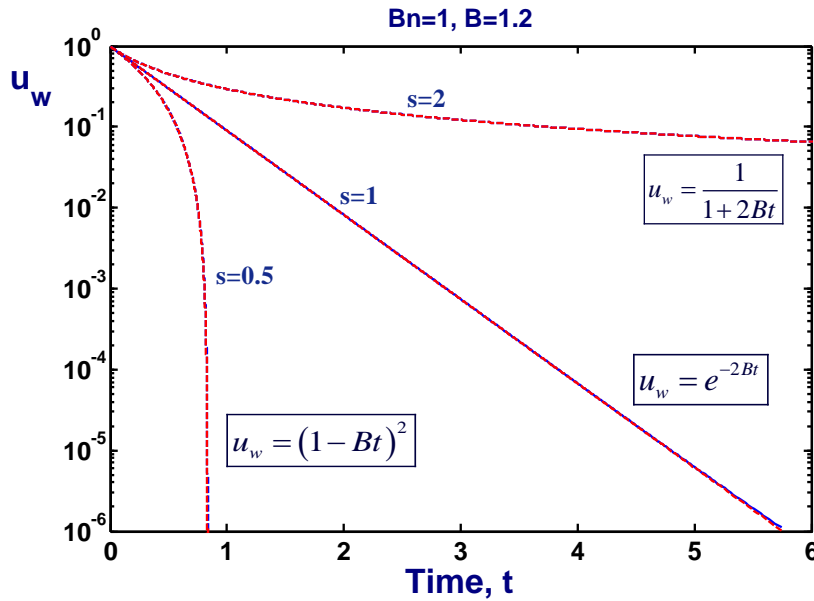


Figure 6: Evolution of the slip velocity in cessation flow of a Bingham plastic with $Bn=1$, $B=1$, and zero slip yield stress ($B_c=0$): (a) $s=0.5$; (b) $s=1$; and (c) $s=2$. The predictions of Eq. (36) taking $u_{wc}=1$ and $t_c=0$ essentially coincide with the numerical solution.

5 CONCLUSIONS

We have solved the cessation of axisymmetric Poiseuille flow of a Bingham plastic with wall slip employing a power law slip equation and the Papanastasiou regularization for the constitutive equation. The numerical results for zero slip yield stress show that in this case the velocity becomes and remains uniform before complete cessation. Moreover, the stopping time is finite only when the slip equation exponent $s < 1$. The decay of the volumetric flow rate is exponential when $s=1$, and much slower when $s > 1$. As for the future plans, we are currently exploring the effect of a non-zero slip yield stress.

REFERENCES

- [1] T. Papanastasiou, G. Georgiou, A. Alexandrou, *Viscous Fluid Flow*, CRC Press, Boca Raton, 2000.
- [2] R. Glowinski, *Numerical Methods for Nonlinear Variational Problems*, Springer-Verlag, New York, 1984.
- [3] R.R. Huilgol, B. Mena, J.-M. Piau, Finite stopping time problems and rheometry of Bingham fluids, *Journal of Non-Newtonian Fluid Mechanics*, **102**, 97-107, 2002.
- [4] M. Chatzimina, G. Georgiou, I. Argyropaidas, E. Mitsoulis, R.R. Huilgol, Cessation of Couette and Poiseuille flows of a Bingham plastic and finite stopping times, *Journal of Non-Newtonian Fluid Mechanics*, **129**, 117-127, 2005.
- [5] L. Muravleva, E. Muravleva, G.C. Georgiou, E. Mitsoulis, Numerical simulations of cessation flows of a Bingham plastic with the Augmented Lagrangian Method, *Journal of Non-Newtonian Fluid Mechanics*, **165**, 544-550, 2010.

- [6] J.R. Seth, M. Cloitre, R.T. Bonnecaze, Influence of short-range forces on wall-slip in microgel pastes, *Journal of Rheology*, **52**, 1241-1268, 2008.
- [7] D.M. Kalyon, P. Yaras, B. Aral, U. Yilmazer, Rheological behavior of a concentrated suspension: A solid rocket fuel stimulant, *Journal of Rheology*, **37**, 35-53, 1993
- [8] U. Yilmazer, D.M. Kalyon, Slip effects in capillary and parallel disk torsional flows of highly filled suspensions, *Journal of Rheology*, **33**, 1197-1212, 1989.
- [9] Y. Damianou, G.C. Georgiou, I. Moulitsas, Combined effects of compressibility and slip in flows of a Herschel-Bulkley fluid, *Journal of Non-Newtonian Fluid Mechanics*, **193**, 89-102 (2013).
- [10] T.C. Papanastasiou, Flows of materials with yield, *Journal of Rheology*, **31**, 385-404, 1987.

A PARALLEL FULLY COUPLED APPROACH FOR LARGE-SCALE FLUID-STRUCTURE INTERACTION PROBLEMS

Ali Eken¹ and Mehmet Sahin²

Faculty of Aeronautics and Astronautics
Astronautical Engineering Department
Istanbul Technical University, Maslak
Istanbul, 34469, TURKEY

¹ e-mail: ekena@itu.edu.tr

² e-mail: msahin@itu.edu.tr

Keywords: Fluid-Structure Interactions, Unstructured Finite Volume Method, Finite Element Method, Large Displacements, Large-Scale Computations; Monolithic Approaches.

Abstract. *A fully coupled numerical algorithm has been developed for the numerical simulation of large-scale fluid structure interaction problems. The incompressible Navier-Stokes equations are discretized using an Arbitrary Lagrangian-Eulerian (ALE) formulation based on the side-centered unstructured finite volume method. The side-centered arrangement of the primitive variables leads to a stable numerical scheme and it does not require any ad-hoc modifications in order to enhance the pressure-velocity coupling. The continuity equation is satisfied within each element exactly and the summation of the continuity equations can be exactly reduced to the domain boundary, which is important for the global mass conservation. A special attention is also given to satisfy the discrete geometric conservation law (DGCL). The nonlinear elasticity equations are discretized within the structure domain using the Galerkin finite element method. The structural behaviour of solid domain is governed by the constitutive laws for the nonlinear Saint Venant-Kirchhoff material. The resulting algebraic nonlinear equations are solved in a fully coupled form using the restricted additive Schwarz method with the flexible GMRES(m) algorithm. The implementation of the fully coupled preconditioned iterative solvers is based on the PETSc library for improving the efficiency of the parallel code. The present numerical algorithm is validated for a Newtonian fluid interacting with an elastic rectangular bar behind a circular cylinder, a three-dimensional elastic solid confined in a rectangular channel and a pulsatile flow in a flexible tube, which mimics the case of pulsatile blood flow through elastic arteries.*

1 INTRODUCTION

The fluid-structure interaction (FSI) problem is probably one of the most addressed multi-physics problems in the literature, not only for its numerous applications in engineering and biomechanics, but also for the computational challenges involved in its numerical modeling and simulation. The FSI problem is mainly characterized by the mutual interaction between a movable or deformable structure with an internal or surrounding fluid flow. Typical examples in engineering applications involve aeroelastic phenomena like flutter of aircraft wings [1, 2] or turbine blades [3] and tail buffeting [4], inflation of parachutes [5] or airbags [6], design of sails [7] or tent structures [8], structural effect of strong wind on bridges [9] and tall buildings [10], and many others. On the other hand, much of the work in biomedical applications include blood flow in the veins and arteries [11], dynamics of heart valves [12, 13], deformations and aggregations of blood cells [14, 15]. Accurate prediction of fluid-structure interactions is crucial for many engineering structures in order to avoid potential aeroelastic/hydroelastic instabilities, which may cause catastrophic failures of the structure. A typical example for such a case is wing flutter, which occurs as a result of exchange of energy between different modes of the structure because of fluid-structure interactions leading to large amplitudes and stresses, which can tear an airframe apart.

There are mainly two approaches for the modeling of fluid-structure interaction problems: partitioned (segregated) [16, 17, 18] or fully coupled (monolithic) [19, 20, 21] methods. In the partitioned approach, separate solvers are used for the fluid and structure subproblems. The main advantage of the partitioned approach is the ability to reuse existing solvers, which allows the application of different, possibly more efficient computational methods specifically developed for either the fluid or the structure subproblems. Both explicit or implicit methods can be used in order to couple the fluid and structure solvers in partitioned procedures. In explicit partitioned methods, which are also known as loosely or weakly coupled methods, typically a fixed point (Picard) iteration is employed to obtain a coupled solution. Although the implementation of this method is relatively easy, it does, however, suffer some serious drawbacks. The fixed point iterations tend to converge slowly if at all, and the iterations may diverge in the presence of strong fluid-solid interactions due to a comparable fluid-to-solid density ratio, which is encountered frequently in FSI problems in biomechanics [22, 23]. In addition, weakly coupled partitioned methods can not satisfy the incompressibility constraint of the fluid [24] during standard alternating FSI iterations when the fluid domain is entirely enclosed by Dirichlet boundary conditions. For strong coupling in partitioned procedures, on the contrary, several fluid and structure computations are performed in a single time-step until a satisfactory convergence tolerance is reached. This approach, however requires costly sub-iterations, and the sub-iteration convergence may not be guaranteed. In a fully coupled approach, the fluid and structure equations are discretised and solved simultaneously as a single equation system for the entire problem. However, this requires an efficient numerical technique for the solution of a large system of coupled nonlinear algebraic equations, which poses the major challenge of monolithic FSI approaches, especially in large scale problems. Although monolithic solver are believed to be too expensive for use in large-scale problems, more recent studies [25, 26] demonstrate that monolithic solvers are competitive even in test cases with very weak FSI, where their segregated counterparts do not suffer from any convergence problems. In this context, Muddle et al. [21] presented a block preconditioner for the efficient solution of the linear systems by Krylov subspace solvers. Behr and Tezduyar [27] presented solution strategies for large scale flow simulations and Johnson and Tezduyar [28] proposed mesh update strategies

in parallel computations. Gee et al. [20] applied an algebraic multigrid technique to the entire fluidstructure interaction system of equations. Barker and Cai [29] developed a scalable parallel finite element solver for the simulation of blood flow in compliant arteries using scalable Newton-Krylov algorithms with an overlapping restricted additive Schwarz method.

One of the most well-known methods used to capture the interaction between structure and fluid is the Arbitrary Lagrangian Eulerian (ALE) method as described in Hirt et al. [30]. In the ALE method, the mesh follows the interface between the fluid and solid boundary and the governing equations are discretized on a moving mesh. This differs from the standard Eulerian formulation in a way that the mesh movement has to fulfill special conditions in order to maintain the accuracy and the stability of the time integration scheme. This condition is satisfied by the enforcement of the so-called geometric conservation law (GCL) as coined by Thomas and Lombard [31]. The ALE approach was subsequently adopted within the finite element context to solve free surface problems of incompressible viscous fluid flow [32]. In the case of an FSI problem, the deformable fluid-structure interface is taken into account and the fluid points at the fluid-solid interface are moved in a Lagrangian way [33]. This article presents a new numerical algorithm based on the ALE formulation for a fully coupled solution of the large-scale FSI problems where the fluid is modelled by the incompressible Navier-Stokes equations and the structure is modeled by the St. Venant-Kirchhoff model. The governing equations of the fluid domain are discretized using an Arbitrary Lagrangian-Eulerian (ALE) formulation based on the side-centered unstructured finite volume method where the velocity vector components are defined at the mid-point of each cell face while the pressure is defined at the element centroid. The present arrangement of the primitive variables leads to a stable numerical scheme and it does not require any *ad-hoc* modifications in order to enhance the pressure-velocity coupling. This approach was initially used by Hwang [34] and Rida *et al.* [35] for the solution of the incompressible Navier-Stokes equations on unstructured triangular meshes. The most appealing feature of the present finite volume approach is that it leads to the classical five-point Laplace operator for the pressure Poisson equation as in the classical MAC scheme [36] which is very important for the efficient solution of the large-scale FSI problems. Because, numerical simulations of FSI problems in general require large computational resources, and it is typically the fluid subproblem that requires the most computational resources in the coupled system [37]. In the present work, a special attention will be given to satisfy the continuity equation exactly within each element and the summation of the continuity equations can be exactly reduced to the domain boundary, which is important for the global mass conservation. The mesh deformation within the fluid domain is achieved by using an algebraic approach based on the minimum distance function at each time level while avoiding re-meshing in order to enhance numerical robustness. The deformation of the solid domain is governed by the constitutive laws for the nonlinear Saint Venant-Kirchhoff material and the classical Galerkin finite element is used to discretise the governing equations in a Lagrangian frame. Newmark [38] type generalized- α method [39] is employed to integrate in time the solid dynamic equilibrium equation.

The remainder of this paper is organized as follows: Section 2 provides some details on the present FSI method. The mathematical and numerical formulations of the ALE based unstructured finite volume method for the fluid and the finite element method for the structure are given in detail. In Section 3, the proposed method is validated for three reference FSI benchmark problems: A steady Newtonian fluid interacting with an elastic bar behind a cylinder, a three-dimensional elastic solid in a steady channel flow and a pulsatile flow in a flexible tube, which mimics the case of pulsatile blood flow through elastic arteries. Concluding remarks are provided in Section 4.

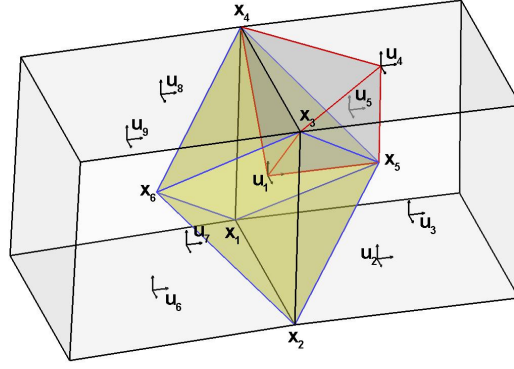


Figure 1: Three-dimensional unstructured mesh with a dual control volume for the velocity components.

2 MATHEMATICAL and NUMERICAL FORMULATION

2.1 Fluid model

The integral form of the incompressible NavierStokes equations that govern the motion of an arbitrary moving control volume $\Omega(t)$ with boundary $\partial\Omega(t)$ can be written in the Cartesian coordinate system in dimensionless form as follows: the momentum equations

$$Re \int_{\Omega_d} \frac{\partial \mathbf{u}}{\partial t} dV + Re \oint_{\partial\Omega_d} [\mathbf{n} \cdot (\mathbf{u} - \dot{\mathbf{x}})] \mathbf{u} dS + \oint_{\partial\Omega_d} \mathbf{n} p dS = \oint_{\partial\Omega_d} \mathbf{n} \cdot \nabla \mathbf{u} dS \quad (1)$$

the continuity equation

$$- \oint_{\partial\Omega_e} \mathbf{n} \cdot \mathbf{u} dS = 0 \quad (2)$$

In these equations, V is the control volume, S is the control volume surface area, \mathbf{n} represents the outward normal vector, \mathbf{u} represents the local fluid velocity vector, $\dot{\mathbf{x}}$ represents the grid velocity (the velocity vector of the control volume surface), p is the pressure and Re is the dimensionless Reynolds number. Figure 1 illustrates typical two neighboring hexahedral elements with a dual finite volume constructed by connecting the element centroids to the common vertices shared by the both hexahedral elements. The local fluid velocity vector components are defined at the mid-point of each face.

2.2 Solid model

The structural behaviour of solid domain is governed by the following conservation of momentum in the Lagrangian framework where the material derivative becomes a partial derivative with respect to time

$$\rho \frac{\partial^2 \mathbf{d}}{\partial t^2} = \nabla \cdot \boldsymbol{\sigma}_s + \rho \mathbf{b} \quad (3)$$

where ρ is the solid material density, \mathbf{d} is the displacement vector, $\boldsymbol{\sigma}_s$ is the Cauchy stress tensor and \mathbf{b} is the body forces. The material is defined by the Cauchy stress tensor using the following

constitutive law for the St. Venant-Kirchhoff material:

$$\mathbf{S} = J\mathbf{F}^{-1}\sigma_s\mathbf{F}^{-\top} \quad (4)$$

$$\mathbf{F} = (\mathbf{I} + \nabla\mathbf{d}) \quad (5)$$

$$\mathbf{E} = \frac{1}{2}(\mathbf{F}^\top\mathbf{F} - \mathbf{I}) \quad (6)$$

$$\mathbf{S} = \lambda\text{trace}(\mathbf{E})\mathbf{I} + 2\mu\mathbf{E} \quad (7)$$

$$\mathbf{\Pi} = \mathbf{F}\mathbf{S} \quad (8)$$

where \mathbf{S} is the second Piola-Kirchhoff stress tensor, \mathbf{F} is the deformation gradient tensor, $J = \det(\mathbf{F})$ is the deformation gradients determinant, \mathbf{E} is the Green-Lagrange strain tensor, $\mathbf{\Pi}$ is the non-symmetric first Piola-Kirchhoff stress tensor and λ and μ are the material Lamé's constants. Then the equation of motion with respect to the initial configuration is given by

$$\rho_0 \frac{\partial^2 \mathbf{d}}{\partial t^2} = \nabla \cdot \mathbf{\Pi} + \rho_0 \mathbf{b} \quad (9)$$

where ρ_0 is the solid material density per unit undeformed volume.

2.3 Interface conditions

A main requirement for the coupling schemes is to fulfill two coupling conditions: the kinematic and the dynamic continuity across the fluid-solid interface at all times. The kinematic boundary conditions on the fluid-structure interface is driven by requiring continuity of the velocity

$$\mathbf{u} = \dot{\mathbf{d}} \quad (10)$$

while the dynamic condition means that the following equilibrium equation holds for the surface traction at the common fluid-structure interaction boundary

$$\sigma_s \mathbf{n}_s = -\sigma_f \mathbf{n}_f \quad (11)$$

where \mathbf{n}_s and \mathbf{n}_f denote the outward-pointing unit normal on the fluid-structure boundary, viewed from the structure and fluid domains, respectively. Here, σ_s represents the Cauchy stress tensor of the structural field and σ_f is the stress tensors in the case of an incompressible Newtonian fluid. The constitutive relation for the fluid stress tensor is given by

$$\sigma_f = -p\mathbf{I} + \mu(\nabla\mathbf{u} + \nabla\mathbf{u}^\top) \quad (12)$$

where μ is the fluid dynamic viscosity.

2.4 Numerical discretization of ALE formulation for fluid domain

The momentum equations along the x -, y - and z -directions are discretized over the dual finite volume shown in Figure 1 and the dual volume involves only the right and left elements that share the common face where the components of the velocity vector are discretized. The discrete contribution from the right cell shown in Figure 1 is given below for each term of the momentum equation along the x -direction. The time derivative

$$Re \left[\frac{3u_1^{n+1}}{4\Delta t} + \frac{\sum_i u_i^{n+1}}{6 \cdot 4\Delta t} \right] V_{12345} - Re \left[\frac{3u_1^n}{4\Delta t} + \frac{\sum_i u_i^n}{6 \cdot 4\Delta t} \right] V_{12345} \quad \text{with } i = 1, 2, 3, 4, 5, 10 \quad (13)$$

The convective term due to fluid motion

$$\begin{aligned}
 & \frac{1}{2} Re [\mathbf{u}_{125}^n \cdot \mathbf{A}_{125}^{n+1}] u_{125}^{n+1} + \frac{1}{2} Re [\mathbf{u}_{125}^n \cdot \mathbf{A}_{125}^n] u_{125}^{n+1} \\
 & + \frac{1}{2} Re [\mathbf{u}_{235}^n \cdot \mathbf{A}_{235}^{n+1}] u_{235}^{n+1} + \frac{1}{2} Re [\mathbf{u}_{235}^n \cdot \mathbf{A}_{235}^n] u_{235}^{n+1} \\
 & + \frac{1}{2} Re [\mathbf{u}_{345}^n \cdot \mathbf{A}_{345}^{n+1}] u_{345}^{n+1} + \frac{1}{2} Re [\mathbf{u}_{345}^n \cdot \mathbf{A}_{345}^n] u_{345}^{n+1} \\
 & + \frac{1}{2} Re [\mathbf{u}_{415}^n \cdot \mathbf{A}_{415}^{n+1}] u_{415}^{n+1} + \frac{1}{2} Re [\mathbf{u}_{415}^n \cdot \mathbf{A}_{415}^n] u_{415}^{n+1}
 \end{aligned} \tag{14}$$

The convective term due to mesh motion

$$\begin{aligned}
 & -\frac{1}{2} Re [\dot{\mathbf{x}}_{125}^{n+1} \cdot \mathbf{A}_{125}^{n+1}] u_{125}^n - \frac{1}{2} Re [\dot{\mathbf{x}}_{125}^{n+1} \cdot \mathbf{A}_{125}^n] u_{125}^n \\
 & -\frac{1}{2} Re [\dot{\mathbf{x}}_{235}^{n+1} \cdot \mathbf{A}_{235}^{n+1}] u_{235}^n - \frac{1}{2} Re [\dot{\mathbf{x}}_{235}^{n+1} \cdot \mathbf{A}_{235}^n] u_{235}^n \\
 & -\frac{1}{2} Re [\dot{\mathbf{x}}_{345}^{n+1} \cdot \mathbf{A}_{345}^{n+1}] u_{345}^n - \frac{1}{2} Re [\dot{\mathbf{x}}_{345}^{n+1} \cdot \mathbf{A}_{345}^n] u_{345}^n \\
 & -\frac{1}{2} Re [\dot{\mathbf{x}}_{415}^{n+1} \cdot \mathbf{A}_{415}^{n+1}] u_{415}^n - \frac{1}{2} Re [\dot{\mathbf{x}}_{415}^{n+1} \cdot \mathbf{A}_{415}^n] u_{415}^n
 \end{aligned} \tag{15}$$

The pressure term

$$\begin{aligned}
 & \left[\frac{p_1 + p_2 + p_5}{3} \right]^{n+1} \mathbf{A}_{125}^{n+1} \cdot \mathbf{i} + \left[\frac{p_2 + p_3 + p_5}{3} \right]^{n+1} \mathbf{A}_{235}^{n+1} \cdot \mathbf{i} \\
 & + \left[\frac{p_3 + p_4 + p_5}{3} \right]^{n+1} \mathbf{A}_{345}^{n+1} \cdot \mathbf{i} + \left[\frac{p_4 + p_1 + p_5}{3} \right]^{n+1} \mathbf{A}_{415}^{n+1} \cdot \mathbf{i}
 \end{aligned} \tag{16}$$

The viscous term

$$\begin{aligned}
 & - \left[\left(\frac{\partial u}{\partial x} \right)_{125}^{n+1} \mathbf{A}_{125}^{n+1} \cdot \mathbf{i} + \left(\frac{\partial u}{\partial y} \right)_{125}^{n+1} \mathbf{A}_{125}^{n+1} \cdot \mathbf{j} + \left(\frac{\partial u}{\partial z} \right)_{125}^{n+1} \mathbf{A}_{125}^{n+1} \cdot \mathbf{k} \right] \\
 & - \left[\left(\frac{\partial u}{\partial x} \right)_{235}^{n+1} \mathbf{A}_{235}^{n+1} \cdot \mathbf{i} + \left(\frac{\partial u}{\partial y} \right)_{235}^{n+1} \mathbf{A}_{235}^{n+1} \cdot \mathbf{j} + \left(\frac{\partial u}{\partial z} \right)_{235}^{n+1} \mathbf{A}_{235}^{n+1} \cdot \mathbf{k} \right] \\
 & - \left[\left(\frac{\partial u}{\partial x} \right)_{345}^{n+1} \mathbf{A}_{345}^{n+1} \cdot \mathbf{i} + \left(\frac{\partial u}{\partial y} \right)_{345}^{n+1} \mathbf{A}_{345}^{n+1} \cdot \mathbf{j} + \left(\frac{\partial u}{\partial z} \right)_{345}^{n+1} \mathbf{A}_{345}^{n+1} \cdot \mathbf{k} \right] \\
 & - \left[\left(\frac{\partial u}{\partial x} \right)_{415}^{n+1} \mathbf{A}_{415}^{n+1} \cdot \mathbf{i} + \left(\frac{\partial u}{\partial y} \right)_{415}^{n+1} \mathbf{A}_{415}^{n+1} \cdot \mathbf{j} + \left(\frac{\partial u}{\partial z} \right)_{415}^{n+1} \mathbf{A}_{415}^{n+1} \cdot \mathbf{k} \right]
 \end{aligned} \tag{17}$$

where V_{12345} is the volume of the pyramid between the points \mathbf{x}_1 , \mathbf{x}_2 , \mathbf{x}_3 , \mathbf{x}_4 and \mathbf{x}_5 shown in Figure 1, \mathbf{A}_{125} , \mathbf{A}_{235} , \mathbf{A}_{345} and \mathbf{A}_{415} are the area vectors of the dual volume triangular surfaces, Δt is the time step, the values \mathbf{u}_{125} , \mathbf{u}_{235} , \mathbf{u}_{345} and \mathbf{u}_{415} are the velocity vectors defined at the mid-point of each dual volume area and p_1 , p_2 , p_3 , p_4 and p_5 are the pressure values at the points

$\mathbf{x}_1, \mathbf{x}_2, \mathbf{x}_3, \mathbf{x}_4$ and \mathbf{x}_5 , respectively. However, the pressure values at $\mathbf{x}_1, \mathbf{x}_2, \mathbf{x}_3$ and \mathbf{x}_4 are not known. To compute the pressure at \mathbf{x}_1 , as an example, a second-order Taylor series expansion can be written as

$$p_i = p_1 + \frac{\partial p}{\partial x} \Big|_{\mathbf{x}=\mathbf{x}_1} (x_i - x_1) + \frac{\partial p}{\partial y} \Big|_{\mathbf{x}=\mathbf{x}_1} (y_i - y_1) + \frac{\partial p}{\partial z} \Big|_{\mathbf{x}=\mathbf{x}_1} (z_i - z_1) \quad (18)$$

where i represents the neighboring hexahedral elements connected to the \mathbf{x}_1 point. This overdetermined system of linear equations may be solved in a least square sense using the normal equation approach, in which both sides are multiplied by the transpose. The modified system is solved using the singular value decomposition provided by the Intel Math Kernel Library in order to avoid the numerical difficulties associated with solving linear systems with near rank deficiency. The velocity components are also computed at the points $\mathbf{x}_1, \mathbf{x}_2, \mathbf{x}_3$ and \mathbf{x}_4 in a similar manner. The velocity vector gradient components defined at the mid-point of each dual volume faces are computed by the use of the Green-Gauss theorem:

$$\nabla u = \frac{\partial u}{\partial x} \mathbf{i} + \frac{\partial u}{\partial y} \mathbf{j} + \frac{\partial u}{\partial z} \mathbf{k} = \frac{1}{V_C} \oint_{\partial\Omega_c} u d\mathbf{A} \quad (19)$$

where V_C covolume consists two tetrahedral elements that share the same dual volume surface area and have their fourth vertices at the upwind and downwind velocity locations of the same dual volume surface area (for \mathbf{A}_{125} , the locations where \mathbf{u}_1 and \mathbf{u}_2 are defined). The right-hand side of the equations (19) is evaluated using the mid-point rule on each of the covolume faces. It should be noted that for the present finite-volume surface integrals involve only triangular planar surfaces for the momentum equations. The convective velocity vector components $u_{125}, u_{235}, u_{345}$ and u_{415} are computed using the least square interpolations [40, 41]. As an example,

$$u_{125} = \beta [u_1 + \nabla u_1 \mathbf{r}_1] + (1 - \beta) [u_2 + \nabla u_2 \mathbf{r}_2] \quad (20)$$

where β is a weight factor determining the type of convection scheme used, ∇u_1 and ∇u_2 are the gradients of velocity components where the u_1 and u_2 velocity components are defined and \mathbf{r}_1 and \mathbf{r}_2 are the distance vectors from the mid-point of the dual volume surface to the locations where the gradients of velocity components are computed. For evaluating the gradient terms, ∇u_1 and ∇u_2 , a least square procedure is used in which the velocity data is assumed to behave linearly. In order to satisfy the geometric conservation law (GCL) at the discrete level, the grid velocity components are computed through the use of the first-order backward differences.

$$\dot{\mathbf{x}}^{n+1} = \frac{\mathbf{x}^{n+1} - \mathbf{x}^n}{\Delta t} \quad (21)$$

This will ensure that the numerical scheme preserve a uniform flow solution exactly independent of the mesh motion. In comparison to the staggered methods, the use of the both velocity components significantly simplifies the discretization of the governing equations as well as the implementation of physical boundary conditions. The discretization of the momentum equation along the y - and z -direction follows very closely the ideas presented here. The continuity equation (2) is integrated within each hexahedral elements and evaluated using the mid-point rule on each of the element faces

$$-\sum_{i=1}^6 [u^{n+1} A_x]_i + [v^{n+1} A_y]_i + [w^{n+1} A_z]_i = 0 \quad (22)$$

where $\mathbf{A} = A_x \mathbf{i} + A_y \mathbf{j} + A_z \mathbf{k}$ is the hexahedral element surface area vector and u, v and w are the velocity vector components defined at the mid-point of each hexahedral element face. The discretization of above equations leads to a saddle point problem of the form:

$$\begin{bmatrix} A_{11} & 0 & 0 & A_{14} \\ 0 & A_{22} & 0 & A_{24} \\ 0 & 0 & A_{33} & A_{34} \\ A_{41} & A_{42} & A_{43} & 0 \end{bmatrix} \begin{bmatrix} u \\ v \\ w \\ p \end{bmatrix} = \begin{bmatrix} b_1 \\ b_2 \\ b_3 \\ 0 \end{bmatrix} \quad (23)$$

where, A_{11}, A_{22} and A_{33} are the convection diffusion operators, $(A_{14}, A_{24}, A_{34})^\top$ is the pressure gradient operator and (A_{41}, A_{42}, A_{43}) is the divergence operator. It should also be noted that on an uniform Cartesian mesh the multiplication of the matrices $B_{41}B_{14} + B_{42}B_{24} + B_{43}B_{34}$ gives the classical five-point Laplace operator as in the MAC scheme [36] which is extremely important for the efficient implementation of the present preconditioned iterative solvers.

2.5 Galerkin finite element discretization for solid domain

The weak form of the equations can be obtained by multiplying the equation (9) by the test functions, and integrating over the volume of the element as follows

$$\int_{\Omega_s} N_i \rho \frac{\partial^2 \mathbf{d}}{\partial t^2} dV_0 = \int_{\Omega_s} N_i (\nabla \cdot \mathbf{\Pi} + \rho \mathbf{b}) dV_0 \quad (24)$$

Integrating by parts one has

$$\int_{\Omega_s} N_i \rho \frac{\partial^2 \mathbf{d}}{\partial t^2} dV_0 = \int_{\Omega_s} \nabla \cdot (N_i \mathbf{\Pi}) dV_0 - \int_{\Omega_s} \mathbf{\Pi} \nabla N_i dV_0 + \int_{\Omega_s} N_i \rho \mathbf{b} dV_0 \quad (25)$$

The first term can be related to a surface integral by the divergence theorem over the closed surface of the element, and the weak form in tensor notation can be obtained as

$$\int_{\Omega_s} N_i \rho \frac{\partial^2 \mathbf{d}}{\partial t^2} dV_0 = \oint_{\partial \Omega_s} (N_i \mathbf{\Pi}) \mathbf{n} dS_0 - \int_{\Omega_s} \mathbf{\Pi} \nabla N_i dV_0 + \int_{\Omega_s} N_i \rho \mathbf{b} dV_0 \quad (26)$$

The displacements at any point in the isoparametric hexahedral element are approximated by a linear combination of the displacements at the nodal points of the element

$$\begin{Bmatrix} d_x \\ d_y \\ d_z \end{Bmatrix} = \begin{bmatrix} N_1 & 0 & 0 & N_2 & 0 & 0 & N_3 & 0 & 0 & \cdots & N_8 & 0 & 0 \\ 0 & N_1 & 0 & 0 & N_2 & 0 & 0 & N_3 & 0 & \cdots & 0 & N_8 & 0 \\ 0 & 0 & N_1 & 0 & 0 & N_2 & 0 & 0 & N_3 & \cdots & 0 & 0 & N_8 \end{bmatrix} \begin{Bmatrix} d_{x1} \\ d_{y1} \\ d_{z1} \\ \vdots \\ d_{x8} \\ d_{y8} \\ d_{z8} \end{Bmatrix} = \mathbf{N} \mathbf{d} \quad (27)$$

The stiffness matrix for the hexahedral element is obtained from the discretization of the third integral term of the weak form of the equations (26).

$$\int_{\Omega_s} \mathbf{\Pi} \nabla N_i dV_0 = \int_{\Omega_s} \mathbf{F} \mathbf{S} \nabla N_i dV_0 = \int_{\Omega_s} (\mathbf{I} + \nabla \mathbf{d}) \mathbf{S} \nabla N_i dV_0 \quad (28)$$

The operation of the second Piola-Kirchhoff stress tensor on ∇N_i can explicitly given in matrix notation as

$$\mathbf{S} \nabla N_i = [B_i]^\top \{S\} \quad (29)$$

The integral can be obtained, at this stage, as

$$\int_{\Omega_s} \mathbf{\Pi} \nabla N_i dV_0 = \int_{\Omega_s} (\mathbf{I} + \nabla \mathbf{d}) [B_i]^\top \{S\} dV_0 \quad (30)$$

where

$$(\mathbf{I} + \nabla \mathbf{d}) [B_i]^\top = [B_i]^\top + \nabla \mathbf{d} [B_i]^\top = [B_i]^\top + [B_i]_{NL}^\top \quad (31)$$

The second Piola-Kirchhoff stress tensor can be written as

$$\begin{Bmatrix} S_{xx} \\ S_{yy} \\ S_{zz} \\ S_{xy} \\ S_{xz} \\ S_{yz} \end{Bmatrix} = \underbrace{\begin{bmatrix} \lambda + 2\mu & \lambda & \lambda & 0 & 0 & 0 \\ \lambda & \lambda + 2\mu & \lambda & 0 & 0 & 0 \\ \lambda & \lambda & \lambda + 2\mu & 0 & 0 & 0 \\ 0 & 0 & 0 & \mu & 0 & 0 \\ 0 & 0 & 0 & 0 & \mu & 0 \\ 0 & 0 & 0 & 0 & 0 & \mu \end{bmatrix}}_{\mathbf{C}} \begin{Bmatrix} E_{xx} \\ E_{yy} \\ E_{zz} \\ 2E_{xy} \\ 2E_{xz} \\ 2E_{yz} \end{Bmatrix} \quad (32)$$

where the Green-St. Venant strain tensor can be obtained in vector form using the definition given in (5) and (6). Defining the displacement field in terms of the nodal displacements using (27), the the Green-St. Venant strain tensor in vector form can be obtained as

$$\{E\} = [\mathbf{B} + \frac{1}{2} \mathbf{B}_{NL}] \{\mathbf{d}\} \quad (33)$$

Hence, the element stiffness matrix can be calculated as

$$\mathbf{K}_{(e)} = \int_{\Omega_s} (\mathbf{B} + \mathbf{B}_{NL})^\top \mathbf{C} (\mathbf{B} + \frac{1}{2} \mathbf{B}_{NL}) dV_0 \quad (34)$$

It should be noted that we do not use the Newton's method here. The element mass matrix can be obtained from the inertial term in the equation (26) by substituting the displacements equation (27) one has

$$\mathbf{M}_{(e)} = \int_{\Omega_s} \rho \mathbf{N}^T \mathbf{N} dV_0 \quad (35)$$

Finally, the boundary loads are imposed on the face of the surface elements by the surface integral term given in the equation (26)

$$\oint_{\partial\Omega_s} N_i \begin{bmatrix} \Pi_{xx} & \Pi_{xy} & \Pi_{xz} \\ \Pi_{yx} & \Pi_{yy} & \Pi_{yz} \\ \Pi_{zx} & \Pi_{zy} & \Pi_{zz} \end{bmatrix} \begin{Bmatrix} n_x \\ n_y \\ n_z \end{Bmatrix} dS_0 = \oint_{\partial\Omega_s} N_i \begin{bmatrix} \sigma_{xx} & \sigma_{xy} & \sigma_{xz} \\ \sigma_{yx} & \sigma_{yy} & \sigma_{yz} \\ \sigma_{zx} & \sigma_{zy} & \sigma_{zz} \end{bmatrix}_s \begin{Bmatrix} \hat{n}_x \\ \hat{n}_y \\ \hat{n}_z \end{Bmatrix} dS \quad (36)$$

where $\hat{\mathbf{n}}$ is the surface normal vector given in the deformed solid domain

$$\hat{\mathbf{n}} = \hat{n}_x \mathbf{i} + \hat{n}_y \mathbf{j} + \hat{n}_z \mathbf{k} \quad (37)$$

Then the following equilibrium equation is applied at the common fluid-structure interaction boundary

$$\sigma_s \hat{\mathbf{n}}_s = -\sigma_f \hat{\mathbf{n}}_f \quad (38)$$

Upon assembly of the element matrices the following dynamic system of equations can be obtained for the structure.

$$\mathbf{M}\ddot{\mathbf{d}} + \mathbf{R}(\mathbf{d}) = \mathbf{F} \quad (39)$$

where \mathbf{M} , $\mathbf{R}(\mathbf{d})$ and \mathbf{F} are the global mass matrix, nonlinear residual due to material stiffness and load vector respectively, and \mathbf{d} is the vector of global displacements. In the present approach the system given in (40) is solved using the generalized- α method of Chung and Hulbert [39].

2.6 Generalized- α method

Upon assembly of the element matrices the following dynamic system of equations can be obtained for the structure.

$$\mathbf{M}\ddot{\mathbf{d}} + \mathbf{R}(\mathbf{d}) = \mathbf{F} \quad (40)$$

where \mathbf{M} , $\mathbf{R}(\mathbf{d})$ and \mathbf{F} are the global mass matrix, nonlinear residual due to material stiffness and load vector respectively, and \mathbf{d} is the vector of global displacements. In the present approach the system given in (40) is solved using the generalized- α method of Chung and Hulbert [39]. The generalized- α method is an implicit, onestep time integration scheme based on Newmark like approximations [38] in the time domain and the modified form of the equation of motion becomes

$$\mathbf{M}\ddot{\mathbf{d}}_\alpha + \mathbf{R}(\mathbf{d}_\alpha) = \mathbf{F}_\alpha \quad (41)$$

The method relies on the following interpolations that relate positions, velocities, and accelerations:

$$\mathbf{d}_{n+1} = \mathbf{d}_n + \Delta t \dot{\mathbf{d}}_n + \frac{\Delta t^2}{2} \left[(1 - 2\beta) \ddot{\mathbf{d}}_n + 2\beta \ddot{\mathbf{d}}_{n+1} \right] \quad (42)$$

$$\dot{\mathbf{d}}_{n+1} = \dot{\mathbf{d}}_n + (1 - \gamma) \Delta t \ddot{\mathbf{d}}_n + \gamma \Delta t \ddot{\mathbf{d}}_{n+1} \quad (43)$$

The acceleration term is solved from equations (42) and then inserted into the equation (43). The modified equations can be written as

$$\ddot{\mathbf{d}}_{n+1} = \frac{1}{\beta \Delta t^2} (\mathbf{d}_{n+1} - \mathbf{d}_n) - \frac{1}{\beta \Delta t} \dot{\mathbf{d}}_n - \left(\frac{1}{2\beta} - 1 \right) \ddot{\mathbf{d}}_n \quad (44)$$

$$\dot{\mathbf{d}}_{n+1} = \frac{\gamma}{\beta \Delta t} (\mathbf{d}_{n+1} - \mathbf{d}_n) - \left(\frac{\gamma}{\beta} - 1 \right) \dot{\mathbf{d}}_n - \left(\frac{\gamma}{2\beta} - 1 \right) \Delta t \ddot{\mathbf{d}}_n \quad (45)$$

where β and γ are the Newmark parameters. Subscripts α denote evaluation of the respective quantities within the time interval

$$\ddot{\mathbf{d}}_\alpha = (1 - \alpha_M) \ddot{\mathbf{d}}_n + \alpha_M \ddot{\mathbf{d}}_{n+1} \quad (46)$$

$$\mathbf{R}_\alpha = (1 - \alpha_F) \mathbf{R}(\mathbf{d}_n) + \alpha_F \mathbf{R}(\mathbf{d}_{n+1}) \quad (47)$$

$$\mathbf{F}_\alpha = (1 - \alpha_F) \mathbf{F}(\mathbf{d}_n) + \alpha_F \mathbf{F}(\mathbf{d}_{n+1}) \quad (48)$$

Substituting for the displacement and acceleration at time level $n + 1$, the following system of equations is obtained

$$\begin{aligned} \alpha_M \frac{1}{\beta \Delta t^2} \mathbf{M} \mathbf{d}_{n+1} + \alpha_F \mathbf{R}(\mathbf{d}_{n+1}) - \alpha_F \mathbf{F}(\mathbf{d}_{n+1}) &= (1 - \alpha_F) \mathbf{F}(\mathbf{d}_n) - (1 - \alpha_F) \mathbf{R}(\mathbf{d}_n) \\ &- (1 - \alpha_M) \mathbf{M} \ddot{\mathbf{d}}_n + \alpha_M \mathbf{M} \left[\frac{1}{\beta \Delta t^2} \mathbf{d}_n + \frac{1}{\beta \Delta t} \dot{\mathbf{d}}_n + \left(\frac{1}{2\beta} - 1 \right) \ddot{\mathbf{d}}_n \right] \end{aligned} \quad (49)$$

The resulting scheme is second order accurate and an appropriate selection of the involved time integration parameters allow for unconditional stable solutions of nonlinear dynamics. The classical Newmark method can be derived for $\alpha_M = \alpha_F = 1$.

2.7 Mesh deformation algorithm

A FSI algorithm requires a scheme for moving mesh vertices as the fluid-structure interfaces deform, rotate and translate. Several mesh deforming algorithms have been presented in the literature including the spring analogy [42], the elastic medium analogy [28], the edge swapping algorithm [43] and the remeshing algorithm [44]. These methods generally require solving discrete equations using iterative methods and the computational effort for these methods in three-dimension is not negligible. Therefore, we employ an alternative algebraic method [45] which assumes an exponential decay of the mesh displacement away from the fluid-structure interaction based on the minimum distance function. In addition, the equations of linear elasticity can be solved within the fluid domain and the robustness of the method can be further improved by modifying the Youngs module based on the distance function in order to increase the stiffness of small elements close to the fluid-structure interaction [46].

2.8 Coupled System of Equations

When the fluid and structure solvers are coupled with the interface conditions given in the section 2.3 and the mesh deformation algorithm described in the section 2.7, the following linear algebraic system of equations are obtained.

$$\begin{bmatrix} A_{uu} & A_{uu\Gamma} & A_{up} & 0 & 0 & A_{uq} \\ 0 & A_{u\Gamma u\Gamma} & 0 & 0 & A_{ud\Gamma} & 0 \\ A_{pu} & A_{pu\Gamma} & 0 & 0 & 0 & 0 \\ 0 & 0 & 0 & A_{dd} & A_{dd\Gamma} & 0 \\ A_{d\Gamma u} & A_{d\Gamma u\Gamma} & A_{d\Gamma p} & A_{d\Gamma d} & A_{d\Gamma d\Gamma} & 0 \\ 0 & 0 & 0 & 0 & A_{qd\Gamma} & A_{qq} \end{bmatrix} \begin{bmatrix} \mathbf{u} \\ \mathbf{u}_\Gamma \\ p \\ \mathbf{d} \\ \mathbf{d}_\Gamma \\ \mathbf{q} \end{bmatrix} = \begin{bmatrix} b_1 \\ 0 \\ 0 \\ b_4 \\ b_5 \\ 0 \end{bmatrix} \quad (50)$$

where Γ represents the variables at the common fluid-structure interface, \mathbf{q} is the amount of mesh deformation within the fluid domain. These equations can be written as:

$$\begin{bmatrix} A_{uu} & A_{up} & A_{ud} & A_{uq} \\ A_{pu} & 0 & 0 & 0 \\ A_{du} & A_{dp} & A_{dd} & 0 \\ 0 & 0 & A_{qd} & A_{qq} \end{bmatrix} \begin{bmatrix} \mathbf{u} \\ p \\ \mathbf{d} \\ \mathbf{q} \end{bmatrix} = \begin{bmatrix} d_1 \\ 0 \\ d_3 \\ 0 \end{bmatrix} \quad (51)$$

In practice, the solution of equation (51) does not converge very quickly and it is rather difficult to construct robust preconditioners for the whole coupled system because of the zero-block diagonal resulting from the divergence-free constraint. In the present paper, we use an upper triangular right preconditioner which results in a scaled discrete Laplacian instead of a zero block in the original system. Then the modified system becomes

$$\begin{bmatrix} A_{uu} & A_{up} & A_{ud} & A_{uq} \\ A_{pu} & 0 & 0 & 0 \\ A_{du} & A_{dp} & A_{dd} & 0 \\ 0 & 0 & A_{qd} & A_{qq} \end{bmatrix} \begin{bmatrix} I & \hat{A}_{up} & 0 & 0 \\ 0 & I & 0 & 0 \\ 0 & 0 & I & 0 \\ 0 & 0 & 0 & I \end{bmatrix} = \begin{bmatrix} A_{uu} & A_{uu}\hat{A}_{up} + A_{up} & A_{ud} & A_{uq} \\ A_{pu} & A_{pu}\hat{A}_{up} & 0 & 0 \\ A_{du} & A_{du}\hat{A}_{up} + A_{dp} & A_{dd} & 0 \\ 0 & 0 & A_{qd} & A_{qq} \end{bmatrix} \quad (52)$$

and the zero block is replaced with $-A_{pu}A_{up}$, which is a scaled discrete Laplacian. Unfortunately, this leads to a significant increase in the number of non-zero elements due to the matrix-matrix multiplication. However, it is possible to replace the $-A_{up}$ block matrix in the upper triangular right preconditioner with a computationally less expensive matrix, $-\hat{A}_{up}$. The

calculations indicate that the largest contribution for the pressure gradients in the momentum equations comes from the right and left elements that share the common edge/face where the components of the velocity vector are discretized. Therefore, we will use the contribution from these two elements for the $-\hat{A}_{up}$ matrix which leads maximum three non-zero entries per row. Although, this approximation does not change the convergence rate of an iterative solver significantly, it leads to a significant reduction in the computing time and memory requirement. The present one-level iterative solver is based on the restricted additive Schwarz method with the flexible GMRES(m) algorithm. Since the zero block is removed, a block-incomplete factorization coupled with the reverse Cuthill-McKee ordering [47] can be used within each partitioned sub-domains. The implementation of the preconditioned Krylov subspace algorithm and matrix-matrix multiplication were carried out using the PETSc [48] software package developed at the Argonne National Laboratories. METIS library [49] is used to decompose the flow domain into a set of sub-domains.

3 NUMERICAL EXPERIMENTS

In this section, the proposed FSI algorithm described in Section 2 is validated for an unsteady Newtonian fluid interacting with an elastic rectangular bar behind a circular cylinder, a three-dimensional elastic solid confined in a rectangular channel and a pulsatile flow in a flexible tube, which mimics the case of pulsatile blood flow through elastic arteries.

3.1 Test Case I: Fluid–structure interaction of an elastic bar behind a rigid cylinder

The first case corresponds to the FSI benchmark problem proposed by Hron and Turek [50]. The problem consists of an elastic bar behind a rigid circular cylinder which is placed asymmetrically between parallel lateral walls as shown in Figure 2.

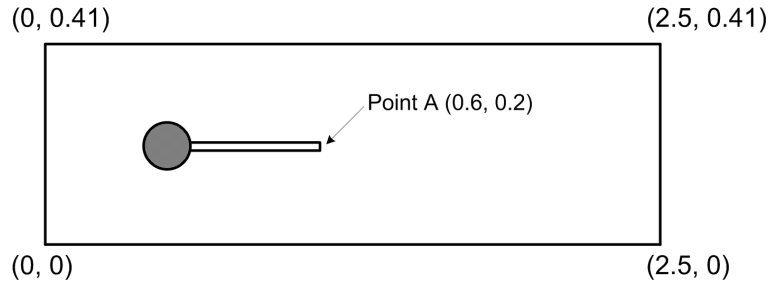


Figure 2: The geometric description of the first validation case.

The parameters $H = 0.41$ is the 2D channel height, $L = 2.5$ is the channel length, $D = 0.1$ is the cylinder diameter, $l = 0.35$ is the bar length and $h = 0.02$ is the bar height. The cylinder is positioned at $(0.2, 0.2)$ from the left bottom corner of the channel. The control point A is attached to the structure and moving in time starting from $(0.6, 0.2)$. The inflow velocity is set to

$$u(y) = 1.5\langle U \rangle \frac{y(H-y)^2}{(H/2)^2} = 1.5\langle U \rangle \frac{4.0}{0.1681} y(0.41-y) \quad (53)$$

where $\langle U \rangle$ is the mean inflow velocity. The outlet boundary conditions are set to natural (traction-free) boundary conditions:

$$\frac{\partial u}{\partial x} = p, \quad \frac{\partial v}{\partial x} = 0 \quad (54)$$

Table 1: Fluid and structure properties for Test Case I

		FSI1	FSI2
Fluid	Density ρ_f	1000	1000
	Dynamic viscosity μ_f	1×10^{-3}	1×10^{-3}
	Mean Inflow velocity $\langle U \rangle$	0.2	2
Solid	Density ρ_s	1000	1000
	Poisson ratio ν_s	0.4	0.4
	Shear modulus μ_s	0.5×10^6	2×10^6

Table 2: Displacements at point A for FSI1 of Test Case I. $Re = 20$.

	DOF	$d_x [\times 10^{-3}]$	$d_y [\times 10^{-3}]$
Present FSI solver	375,216	0.022387	0.81408
Hron and Turek [50]	304,128	0.022732	0.82071
Degroote et al. [52]	320,372	0.022651	0.83478
Richter and Wick [53]	351,720	0.022695	0.81556

We consider two cases with two different inflow speeds and shear moduli for this test problem with the physical parameters indicated in Table 1. FSI1, where the Reynolds number $Re = 20$, results in a steady state solution, while FSI2, which corresponds to FSI3 of Hron and Turek [50], results in an unsteady flow solution with the Reynolds number $Re = 200$. For the present test case, we use an unstructured mesh with 78,921 quadrilateral elements and 79,806 nodes, which result in a total of 375,216 DOF for the whole domain. The mesh is highly refined close to the solid surfaces using local mesh refinement algorithms within the CUBIT [51] library. The computed u -velocity vector components for FSI2 are shown in Figure 3 with the streamlines at different time levels. The streamlines indicate an alternating large recirculation zone just behind the cylinder. The time variation of vertical displacement for FSI2 at point $A(0.6, 0.2)$ on the tip of the bar is given in Figure 4. The computed deformations at point A for the steady and the unsteady flow solutions are tabulated in Table 2 and 3 with comparisons to the computations from different authors. The present results are in relative good agreement with the results in the literature and the present calculations can correctly predict the amplitude of the oscillations for the unsteady flow solution (FSI2). The period of oscillations for the elastic structure is about 0.1805 s. The motion of the structure and the corresponding displacements of the reference point are illustrated in Figure 5 for one complete cycle.

3.2 Test Case II: 3D FSI problem of an elastic beam in a cross flow

In the second example, the present FSI solver is validated for a 3-dimensional stationary problem, where an elastic beam is immersed in a rectangular channel as illustrated in Figure 6. The dimensions of the channel is $[0, 1.5] \times [0, 0.4] \times [-0.4, 0.4]$ while the dimensions of solid domain is $[0.4, 0.5] \times [0, 0.2] \times [-0.2, 0.2]$. The problem is considered to be symmetric in the xy -plane. The present problem is solved by Richter [56] using a variational monolithic Ar-

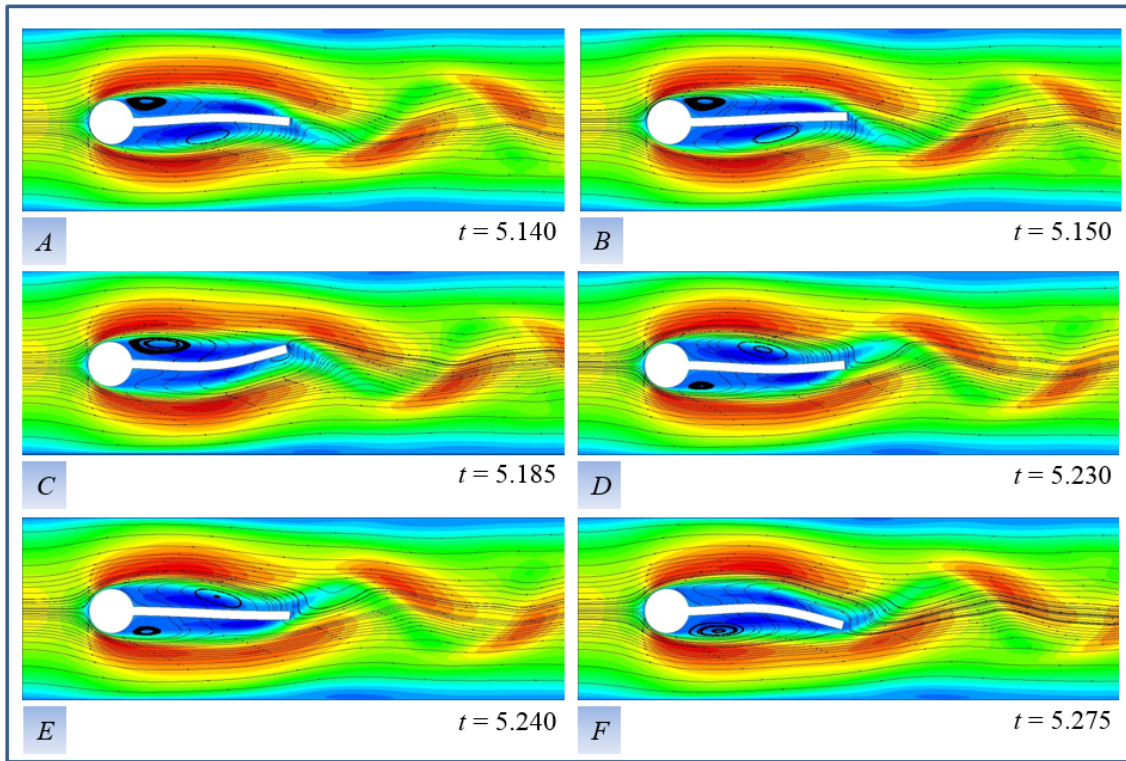


Figure 3: The computed u -velocity vector component contours with the streamlines for an elastic bar behind a rigid cylinder at $Re = 200$.

Table 3: Displacements at point A for FSI2 of Test Case I. $Re = 200$.

	DOF	$d_x [\times 10^{-3}]$	$d_y [\times 10^{-3}]$
Present FSI solver	375, 216	-2.521 ± 2.655	$+1.327 \pm 33.659$
Hron and Turek [50]	304, 128	-2.69 ± 2.53	$+1.48 \pm 34.38$
Wick [54]	72, 696	-2.84 ± 2.67	$+1.28 \pm 34.61$
Chabannes et al. [55]	86, 256	-2.90 ± 2.77	$+1.33 \pm 34.90$

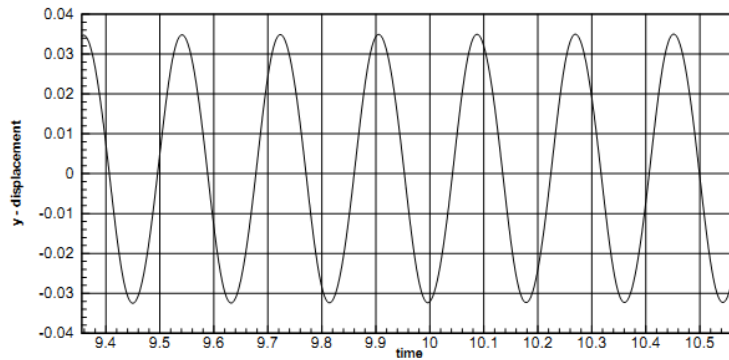


Figure 4: The time variation of vertical displacement for an elastic bar behind a rigid cylinder at $Re = 200$.

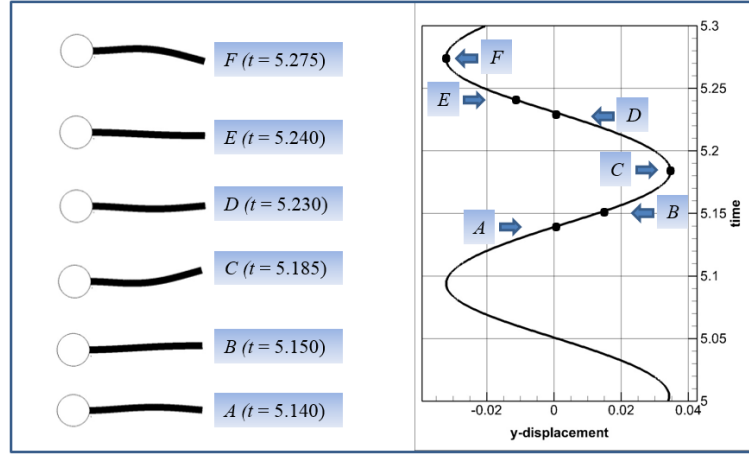


Figure 5: The motion of the elastic bar at $Re = 200$ for one complete cycle.

bitrary Lagrangian Eulerian formulation with local mesh refinement, resulting upto 7,600,775 DOF. The author provides the structure displacement values in x - and y -direction at the point $A(0.45, 0.15, 0.15)$ and the drag forces on the solid body. The inlet velocity has a parabolic

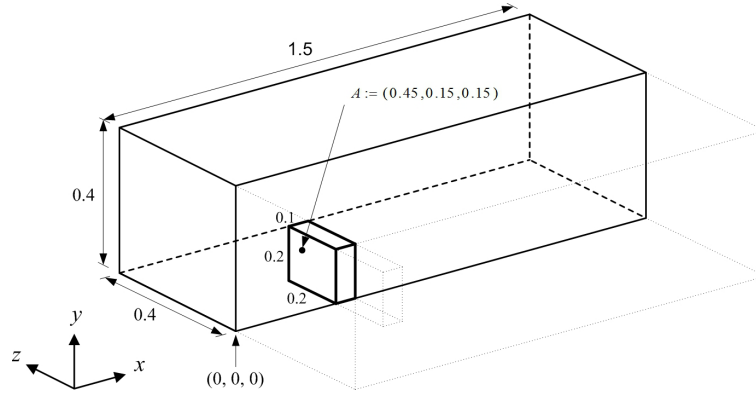


Figure 6: The geometry for 3D FSI problem.

distribution given

$$u(y, z) = \frac{0.3}{0.2^2 \times 0.4^2} y (0.4 - y) (0.4^2 - z^2) \quad (55)$$

with the maximum value of $u_{max} = 0.3$. The outlet boundary conditions are set to natural (traction-free) boundary conditions.

The Reynolds number is based on an average inflow velocity ($\langle U \rangle = 0.2$) and an obstacle of height $h = 0.2$ and its value is $Re = 40$. The properties for the fluid and the solid are tabulated in Table 4. The computational mesh consists of 362,224 hexahedral elements and 374,523 vertices leading to 4,096,6514 DOF. The mesh is initially constructed from a Cartesian mesh and then two levels of refinement are performed near the solid walls. The computed u -velocity vector component isosurfaces with the streamtraces are shown in Figure 7 at $Re = 40$. In addition, the streamtraces computed on the solid walls are shown in Figure 8 on the front and on the back side of the solid body. The computed deformation vector components at the point $A(0.45, 0.15, 0.15)$ are given in Table 5 for more precise comparison and the values are compared with the results of Richter [56]. The results are relatively in good agreement.

Table 4: Fluid and structure properties for test case II

Fluid		Structure	
Density	$\rho_f = 1000$	Density	$\rho_s = 1000$
Kinematic viscosity	$\nu_f = 10^{-3}$	Poisson ratio	$\nu_s = 0.4$
Average Inflow velocity	$\langle U \rangle = 0.2$	Shear Modulus	$\mu_s = 5 \times 10^5$

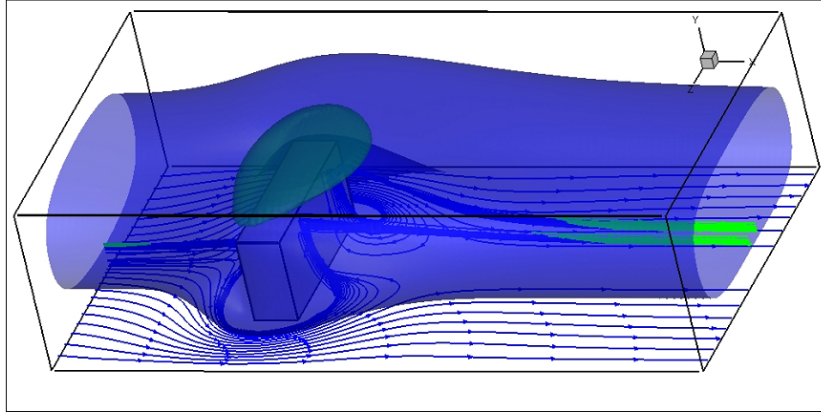


Figure 7: The computed u -velocity vector component isosurfaces with the streamtraces for an elastic bar confined in a rectangular channel at $Re = 40$.

Table 5: Displacement at point A for Test Case II

	Present FSI solver	Richter [56]
DOF	4,096,651	7,600,775
Δx	5.753204×10^{-5}	5.9280×10^{-5}
Δy	8.735848×10^{-7}	-
Δz	8.533534×10^{-7}	-

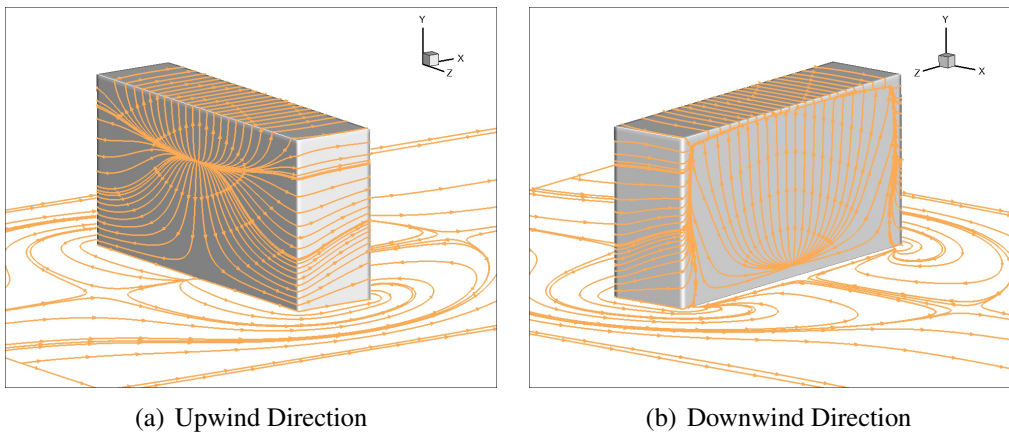


Figure 8: The computed streamtraces on the solid walls for an elastic bar confined in a rectangular channel at $Re = 40$.

3.3 Test Case III: Pressure-pulse in a flexible tube

In the last example we consider a three-dimensional dynamic FSI benchmark problem proposed by [57], which has been considered by many authors [58, 59, 20]. The problem is related to the blood flow through elastic arteries and the test configuration consists of an incompressible viscous flow through a flexible circular tube with an inner radius of 0.5 cm and a wall thickness of 0.1 cm . The tube wall is clamped at both ends and a pressure boundary condition is imposed on the fluid at the inflow and outflow boundaries. The fluid is initially at rest and a pressure of $1.3332 \times 10^{-4} \text{ dyn/cm}^2$ is imposed on the inflow boundary for $t < 0.003 \text{ s}$, while at the outflow boundary, the pressure is set to zero throughout the analysis. The physical properties for the Saint Venant-Kirchhoff material and the Newtonian fluid used for the third test case are listed in Table 6. The mesh for this test case consists of 148,480 hexahedral elements and 154,305 vertices for the whole computational domain. Throughout the computations, the time step is set to 1×10^{-4} . In Figure 9, the time variations of the radial components of displacement and velocity of the inner tube wall at half the length of the pipe are presented for the first 0.02 s of motion. The snapshot of the computed deformation contours at 0.0069 s is given in Figure 10, which is comparable with the structural deformation result presented in [20]. It should be noted that the wall deformation presented in Figure 10 are exaggerated by a factor of 10 for clarity. In the future, we will repeat the same problem with the second-order backward difference in the fluid domain.

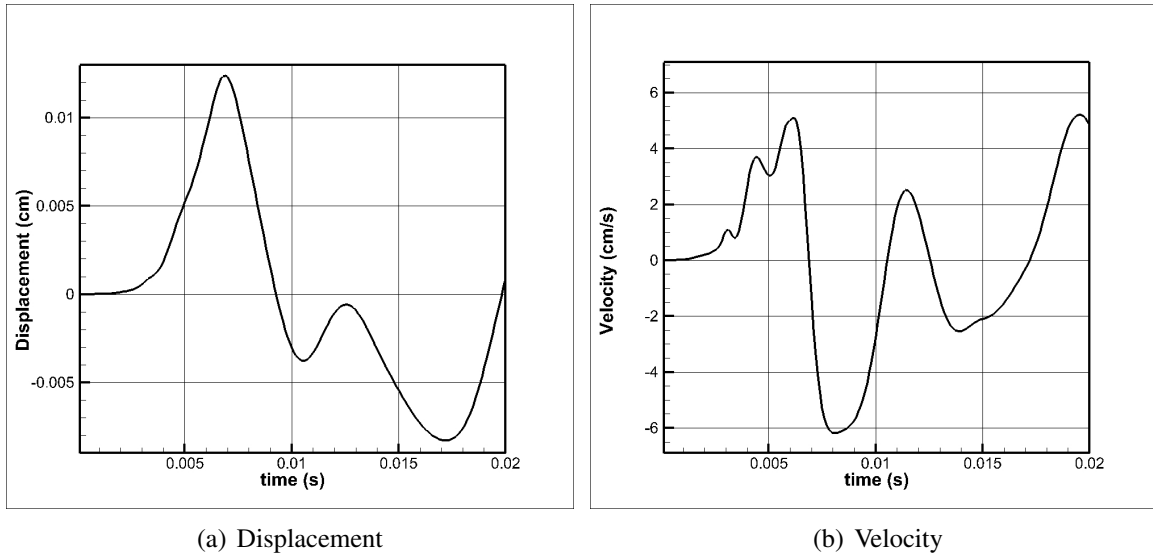


Figure 9: Radial components of displacement and velocity of the inner tube wall at half the length of the pipe.

Table 6: Fluid and structure properties for test case III

Fluid		Structure	
Density	$\rho_f = 1 \text{ g/cm}^3$	Density	$\rho_s = 1.2 \text{ g/cm}^3$
Dynamic viscosity	$\mu_f = 3 \times 10^{-2} \text{ g/cm} \cdot \text{s}$	Poisson ratio	$\nu_s = 0.3$
		Young modulus	$E_s = 3 \times 10^6$

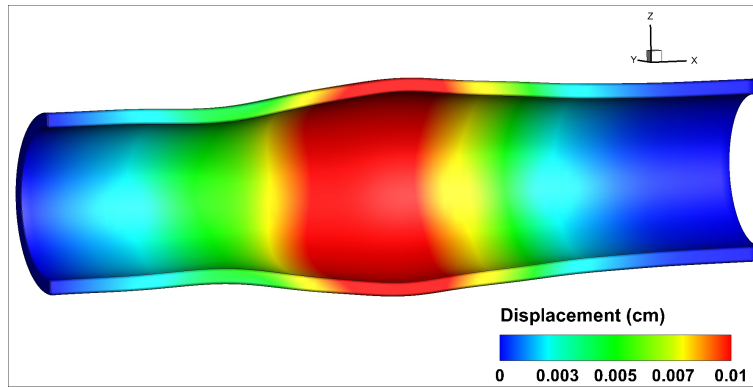


Figure 10: The computed radial displacement contours at $t = 0.0069s$. The wall deformation are exaggerated by a factor of 10 for clarity.

4 CONCLUSIONS

A new algorithm based on the ALE formulation is presented for a fully coupled solution of the large-scale FSI problems where the fluid is modeled by the incompressible Navier-Stokes equations and the structure is modeled by the St. Venant-Kirchhoff model. The present ALE formulation does not require any *ad-hoc* modifications in order to enhance the pressure-velocity coupling. The continuity equation is satisfied within each element exactly and the summation of the continuity equations can be exactly reduced to the domain boundary, which is important for the global mass conservation. A special attention is also given to satisfy the Geometric Conservation Law (GCL) on moving meshes at discrete level. The deformation of the solid domain is governed by the constitutive laws for the nonlinear Saint Venant-Kirchhoff material and the classical Galerkin finite element is used to discretize the governing equations in a Lagrangian frame. The implementation of the preconditioned coupled iterative solvers is based on the PETSc library for improving the efficiency of the parallel code. The present numerical algorithm is validated for a Newtonian fluid interacting with an elastic rectangular bar behind a circular cylinder, a three-dimensional elastic solid confined in a rectangular channel and a pulsatile flow in a flexible tube, which mimics the case of pulsatile blood flow through elastic arteries.

5 ACKNOWLEDGMENTS

The authors acknowledge financial support from Turkish National Scientific and Technical Research Council (TUBITAK) through project number 112M107. The authors also gratefully acknowledge the use of the Chimera machine at the Faculty of Aeronautics and Astronautics at ITU, the computing resources provided by the National Center for High Performance Computing of Turkey (UYBHM) under grant number 10752009 and the computing facilities at TUBITAK ULAKBIM, High Performance and Grid Computing Center.

REFERENCES

- [1] X. Zhao, Y. Zhu, and S. Zhang, “Transonic wing flutter predictions by a loosely-coupled method,” *Computers & Fluids*, vol. 58, no. 0, pp. 45 – 62, 2012.
- [2] X. Chen, G.-C. Zha, and M.-T. Yang, “Numerical simulation of 3-d wing flutter with fully coupled fluidstructural interaction,” *Computers & Fluids*, vol. 36, no. 5, pp. 856 – 867,

2007.

- [3] Y.-J. Lee, Y.-T. Jhan, and C.-H. Chung, “Fluidstructure interaction of frp wind turbine blades under aerodynamic effect,” *Composites Part B: Engineering*, vol. 43, no. 5, pp. 2180 – 2191, 2012.
- [4] E. Sheta and L. Huttshell, “Characteristics of f/a-18 vertical tail buffeting,” *Journal of Fluids and Structures*, vol. 17, no. 3, pp. 461 – 477, 2003.
- [5] S. Sathe, R. Benney, R. Charles, E. Doucette, J. Miletti, M. Senga, K. Stein, and T. Tezduyar, “Fluidstructure interaction modeling of complex parachute designs with the spacetime finite element techniques,” *Computers & Fluids*, vol. 36, no. 1, pp. 127 – 135, 2007.
- [6] W. Sinz and S. Hermann, “The development of a 3d-navierstokes code for the simulation of an airbag inflation,” *Simulation Modelling Practice and Theory*, vol. 16, no. 8, pp. 885 – 899, 2008.
- [7] B. Augier, P. Bot, F. Hauville, and M. Durand, “Experimental validation of unsteady models for fluid structure interaction: Application to yacht sails and rigs,” *Journal of Wind Engineering and Industrial Aerodynamics*, vol. 101, no. 0, pp. 53 – 66, 2012.
- [8] M. Glück and M. Breuer and F. Durst and A. Halfmann and E. Rank, “Computation of fluidstructure interaction on lightweight structures,” *Journal of Wind Engineering and Industrial Aerodynamics*, vol. 89, no. 1415, pp. 1351 – 1368, 2001.
- [9] H. Zhang, L. Liu, M. Dong, and H. Sun, “Analysis of wind-induced vibration of fluid-structure interaction system for isolated aqueduct bridge,” *Engineering Structures*, vol. 46, no. 0, pp. 28 – 37, 2013.
- [10] A. L. Braun and A. M. Awruch, “Aerodynamic and aeroelastic analyses on the caarc standard tall building model using numerical simulation,” *Computers & Structures*, vol. 87, no. 910, pp. 564 – 581, 2009.
- [11] X. Yang, Y. Liu, and J. Yang, “Fluid-structure interaction in a pulmonary arterial bifurcation,” *Journal of Biomechanics*, vol. 40, no. 12, pp. 2694 – 2699, 2007.
- [12] J. D. Hart, F. Baaijens, G. Peters, and P. Schreurs, “A computational fluid-structure interaction analysis of a fiber-reinforced stentless aortic valve,” *Journal of Biomechanics*, vol. 36, no. 5, pp. 699 – 712, 2003.
- [13] T. B. Le and F. Sotiropoulos, “Fluidstructure interaction of an aortic heart valve prosthesis driven by an animated anatomic left ventricle,” *Journal of Computational Physics*, no. 0, pp. –, 2012.
- [14] D. Alizadehrad, Y. Imai, K. Nakaaki, T. Ishikawa, and T. Yamaguchi, “Quantification of red blood cell deformation at high-hematocrit blood flow in microvessels,” *Journal of Biomechanics*, vol. 45, no. 15, pp. 2684 – 2689, 2012.
- [15] Y. Liu and W. K. Liu, “Rheology of red blood cell aggregation by computer simulation,” *Journal of Computational Physics*, vol. 220, no. 1, pp. 139 – 154, 2006.

- [16] K. C. Park, C. A. Felippa, and J. A. Deruntz, “Stabilization of staggered solution procedures for fluid-structure interaction analysis,” in *Computational Methods for Fluid-Structure Interaction Problems* (T. Belytschko and T. L. Geers, eds.), pp. 94–124, ASME, 1977.
- [17] H. G. Matthies and J. Steindorf, “Partitioned strong coupling algorithms for fluidstructure interaction,” *Computers & Structures*, vol. 81, no. 811, pp. 805 – 812, 2003.
- [18] J. Degroote and J. Vierendeels, “Multi-solver algorithms for the partitioned simulation of fluidstructure interaction,” *Computer Methods in Applied Mechanics and Engineering*, vol. 200, no. 2528, pp. 2195 – 2210, 2011.
- [19] F. J. Blom, “A monolithical fluid-structure interaction algorithm applied to the piston problem,” *Computer Methods in Applied Mechanics and Engineering*, vol. 167, no. 34, pp. 369 – 391, 1998.
- [20] M. W. Gee, U. Kttler, and W. A. Wall, “Truly monolithic algebraic multigrid for fluidstructure interaction,” *International Journal for Numerical Methods in Engineering*, vol. 85, no. 8, pp. 987–1016, 2011.
- [21] R. L. Muddle, M. Mihajlovic, and M. Heil, “An efficient preconditioner for monolithically-coupled large-displacement fluid-structure interaction problems with pseudo-solid mesh updates,” *Journal of Computational Physics*, vol. 231, no. 21, pp. 7315 – 7334, 2012.
- [22] J. Janela, A. Moura, and A. Sequeira, “A 3d non-newtonian fluidstructure interaction model for blood flow in arteries,” *Journal of Computational and Applied Mathematics*, vol. 234, no. 9, pp. 2783 – 2791, 2010.
- [23] F. Nobile, “Coupling strategies for the numerical simulation of blood flow in deformable arteries by 3d and 1d models,” *Mathematical and Computer Modelling*, vol. 49, no. 1112, pp. 2152 – 2160, 2009.
- [24] C. Förster, W. A. Wall, and E. Ramm, “Artificial added mass instabilities in sequential staggered coupling of nonlinear structures and incompressible viscous flows,” *Computer Methods in Applied Mechanics and Engineering*, vol. 196, no. 7, pp. 1278 – 1293, 2007.
- [25] M. Heil, A. L. Hazel, and J. Boyle, “Solvers for large-displacement fluid structure interaction problems: segregated versus monolithic approaches,” *Computational Mechanics*, vol. 43, pp. 91–101, Dec. 2008.
- [26] U. Küttler, M. Gee, C. Förster, A. Comerford, and W. A. Wall, “Coupling strategies for biomedical fluidstructure interaction problems,” *International Journal for Numerical Methods in Biomedical Engineering*, vol. 26, no. 3-4, pp. 305–321, 2010.
- [27] M. Behr and T. E. Tezduyar, “Finite element solution strategies for large-scale flow simulations,” *Computer Methods in Applied Mechanics and Engineering*, vol. 112, no. 14, pp. 3–24, 1994.
- [28] A. Johnson and T. Tezduyar, “Mesh update strategies in parallel finite element computations of flow problems with moving boundaries and interfaces,” *Computer Methods in Applied Mechanics and Engineering*, vol. 119, no. 12, pp. 73 – 94, 1994.

- [29] A. T. Barker and X.-C. Cai, “Scalable parallel methods for monolithic coupling in fluid-structure interaction with application to blood flow modeling,” *Journal of Computational Physics*, vol. 229, pp. 642–659, Feb. 2010.
- [30] C. Hirt, A. Amsden, and J. Cook, “An arbitrary lagrangian-eulerian computing method for all flow speeds,” *Journal of Computational Physics*, vol. 14, no. 3, pp. 227 – 253, 1974.
- [31] P. D. Thomas and C. K. Lombard, “Geometric Conservation Law and Its Application to Flow Computations on Moving Grids,” *AIAA Journal*, vol. 17, pp. 1030–1037, Oct. 1979.
- [32] T. J. Hughes, W. K. Liu, and T. K. Zimmermann, “Lagrangian-eulerian finite element formulation for incompressible viscous flows,” *Computer Methods in Applied Mechanics and Engineering*, vol. 29, no. 3, pp. 329 – 349, 1981.
- [33] J. Donea, S. Giuliani, and J. Halleux, “An arbitrary lagrangian-eulerian finite element method for transient dynamic fluid-structure interactions,” *Computer Methods in Applied Mechanics and Engineering*, vol. 33, no. 13, pp. 689 – 723, 1982.
- [34] Y.-H. Hwang, “Calculations of Incompressible Flow on a Staggered Triangular Grid, Part I: Mathematical Formulation,” *Numerical Heat Transfer Part B - Fundamentals*, vol. 27, pp. 323–336, Apr. 1995.
- [35] S. Rida, F. McKenty, F. L. Meng, and M. Reggio, “A staggered control volume scheme for unstructured triangular grids,” *International Journal for Numerical Methods in Fluids*, vol. 25, pp. 697–717, Sept. 1997.
- [36] F. H. Harlow and J. E. Welch, “Numerical Calculation of Time-Dependent Viscous Incompressible Flow of Fluid with Free Surface,” *Physics of Fluids*, vol. 8, pp. 2182–2189, Dec. 1965.
- [37] C. Farhat, *CFD-Based Nonlinear Computational Aeroelasticity*. John Wiley & Sons, Ltd, 2004.
- [38] N. M. Newmark, “A method of computation for structural dynamics,” *Journal of the Engineering Mechanics Division*, vol. 85, no. 3, pp. 67–94, 1959.
- [39] J. Chung and G. M. Hulbert, “A Time Integration Algorithm for Structural Dynamics With Improved Numerical Dissipation: The Generalized- α Method,” *Journal of Applied Mechanics*, vol. 60, p. 371, 1993.
- [40] W. K. Anderson and D. L. Bonhaus, “An implicit upwind algorithm for computing turbulent flows on unstructured grids,” *Computers & Fluids*, vol. 23, no. 1, pp. 1–21, 1994.
- [41] B. Timothy, *A 3-D upwind Euler solver for unstructured meshes*. Meeting Paper Archive, American Institute of Aeronautics and Astronautics, 1963. doi:10.2514/6.1991-1548.
- [42] J. T. Batina, “Unsteady euler airfoil solutions using unstructured dynamic meshes,” *AIAA Journal*, vol. 28, no. 8, pp. 1381–1388, 1990.
- [43] M. Dai and D. P. Schmidt, “Adaptive tetrahedral meshing in free-surface flow,” *Journal of Computational Physics*, vol. 208, no. 1, pp. 228 – 252, 2005.

- [44] A. A. Johnson and T. E. Tezduyar, “Advanced mesh generation and update methods for 3d flow simulations,” *Computational Mechanics*, vol. 23, pp. 130–143, 1999.
- [45] T. Gerhold and J. Neumann, *The Parallel Mesh Deformation of the DLR TAU-Code*, vol. 96 of *Notes on Numerical Fluid Mechanics and Multidisciplinary Design (NNFM)*, ch. 20, pp. 162–169. Springer Berlin Heidelberg, 2008.
- [46] M. Sahin and K. Mohseni, “An arbitrary lagrangianeulerian formulation for the numerical simulation of flow patterns generated by the hydromedusa aequorea victoria,” *Journal of Computational Physics*, vol. 228, no. 12, pp. 4588 – 4605, 2009.
- [47] E. Cuthill and J. McKee, “Reducing the bandwidth of sparse symmetric matrices,” in *Proceedings of the 1969 24th national conference*, ACM '69, (New York, NY, USA), pp. 157 – 172, ACM, 1969.
- [48] S. Balay, J. Brown, , K. Buschelman, V. Eijkhout, W. D. Gropp, D. Kaushik, M. G. Knepley, L. C. McInnes, B. F. Smith, and H. Zhang, “PETSc users manual,” Tech. Rep. ANL-95/11 - Revision 3.3, Argonne National Laboratory, 2012.
- [49] G. Karypis and V. Kumar, “A fast and high quality multilevel scheme for partitioning irregular graphs,” *SIAM Journal on Scientific Computing*, vol. 20, no. 1, pp. 359–392, 1999.
- [50] S. Turek and J. Hron, “Proposal for numerical benchmarking of fluid-structure interaction between an elastic object and laminar incompressible flow,” in *Fluid-Structure Interaction* (H.-J. Bungartz and M. Schfer, eds.), vol. 53 of *Lecture Notes in Computational Science and Engineering*, pp. 371–385, Springer Berlin Heidelberg, 2006.
- [51] T. D. Blacker, S. Benzley, S. Jankovich, R. Kerr, J. Kraftcheck, R. Kerr, P. Knupp, R. Leland, D. Melander, R. Meyers, S. Mitchell, J. Shepard, T. Tautges, and D. White, “Cubit mesh generation environment users manual volume 1,” tech. rep., Albuquerque, NM.
- [52] J. Degroote, R. Haelterman, S. Annerel, P. Bruggeman, and J. Vierendeels, “Performance of partitioned procedures in fluidstructure interaction,” *Computers & Structures*, vol. 88, no. 78, pp. 446 – 457, 2010.
- [53] T. Richter and T. Wick, “Finite elements for fluidstructure interaction in ale and fully eulerian coordinates,” *Computer Methods in Applied Mechanics and Engineering*, vol. 199, no. 4144, pp. 2633 – 2642, 2010.
- [54] T. Wick, “Solving monolithic fluid-structure interaction problems in arbitrary lagrangian eulerian coordinates with the deal.ii library,” tech. rep., University of Heidelberg, 2011.
- [55] V. Chabannes, G. Pena, and C. Prud’Homme, “High order fluid structure interaction in 2D and 3D. Application to blood flow in arteries.” Submitted to Elsevier Journal of Computational and Applied Mathematics (JCAM), Feb. 2012.
- [56] T. Richter, “Goal-oriented error estimation for fluidstructure interaction problems,” *Computer Methods in Applied Mechanics and Engineering*, vol. 223-224, no. 0, pp. 28 – 42, 2012.

- [57] J.-F. Gerbeau and M. Vidrascu, “A quasi-newton algorithm based on a reduced model for fluid-structure interaction problems in blood flows,” *ESAIM: Mathematical Modelling and Numerical Analysis*, vol. 37, pp. 631–647, 6 2003.
- [58] U. Küttler and W. A. Wall, “Fixed-point fluidstructure interaction solvers with dynamic relaxation,” *Computational Mechanics*, vol. 43, pp. 61–72, 2008.
- [59] A. Malan and O. Oxtoby, “An accelerated, fully-coupled, parallel 3d hybrid finite-volume fluidstructure interaction scheme,” *Computer Methods in Applied Mechanics and Engineering*, vol. 253, no. 0, pp. 426 – 438, 2013.

FLAPPING THIN AIRFOIL INTERACTING WITH THE GROUND

Ülgen Gülçat

Istanbul Technical University, Faculty of Aeronautics and Astronautics, Istanbul 34469, Turkey
gulcat@itu.edu.tr

Keywords: Ground Effect, Steady, Unsteady

Abstract: *The rotary wing and the flapping wing technology for the MAVs (Micro Air Vehicle) demand the studies of unsteady aerodynamic effects on the vehicles performing near the ground. In this study, a fast and robust numerical method based on the general formulae for the lift and propulsive forces, acting on a heaving-plunging airfoil, induced by a vortex sheet and its ground image, is developed and implemented. The Keldish-Lavrentiev series expansion of the Kernel function is employed to find the effect of the image vortex sheet on the airfoil. Coupled with the unsteady aerodynamics, the unsteady boundary layer equations cast in the velocity-vorticity formulation are solved numerically to predict the viscous drag on the airfoil performance under the: i) restrained condition where the mean distance to the ground remains the same, and ii) unrestrained condition for which the airfoil ascends or descends freely during its interaction with the ground. Applications of these two different performances with Reynolds number of 3040 and 10 000, which are examples from the current literature, yield satisfactory results.*

In the presence of ground, the distance between the ground and the wing is going to change because of plunge motion as

$$h'_g(t) = h'_o - h' \cos(\alpha t) \quad (2)$$

The relation between the downwash w_a and the equation of the motion of the body reads as

$$w_a(x, t) = \frac{\partial z_a}{\partial x'} + U \frac{\partial z_a}{\partial x'} \quad (3)$$

where, $z_a(x, t) = -h(t) - \alpha(t)x'$ for a pitching-plunging thin airfoil which is pitching about its mid chord. For simple harmonic motion, the amplitude of the vortex sheet strength $\bar{\gamma}_a$, with the effect of the image of the bound and the wake vortices according to the Biot-Savart law [4] induces the following downwash amplitude

$$\bar{w}_a(x) - \frac{ik\bar{\Omega}}{2\pi} \int_1^\infty e^{-ik\xi} \left(\frac{1}{x-\xi} - \frac{x-\xi}{(x-\xi)^2 + 4h_g^2} \right) d\xi = -\frac{1}{2\pi} \int_{-1}^1 \bar{\gamma}_a(\xi, t) \left(\frac{1}{x-\xi} - \frac{x-\xi}{(x-\xi)^2 + 4h_g^2} \right) d\xi \quad (4)$$

where, $\bar{\Omega} = \bar{\Gamma}_a e^{ik} / b = e^{ik} \int_{-1}^1 \bar{\gamma}_a(x) dx$, is the amplitude of the reduced circulation which contributes to the second term of the integral as the ground effect and b is the half-chord. The integral equation above is inverted with the approach of Keldysh and Lavrentiev, as described in [2], as follows. The kernel of the integral at the right hand is expanded into the Taylor series given below

$$K(x-\xi) = \frac{1}{x-\xi} - \frac{x-\xi}{(x-\xi)^2 + 4h^2} = \frac{1}{x-\xi} + h^{-1} \sum_{n=0}^\infty K_n \left(\frac{x-\xi}{h} \right)^n, \quad K_n = (-1)^{(n+1)/2} 2^{-(n+1)}, \quad n = 1, 3, 5, \dots \quad (5)$$

Note that, the same function also acts as the coefficient of the exponent in the second term of left hand side of (4), which will be expanded into power series as given in (5).

Then the bound vortex sheet strength with two terms becomes

$$\bar{\gamma}_a(x) = \sum_{n=1}^\infty h_g^{-n} \bar{\gamma}_n \cong \bar{\gamma}_o + \bar{\gamma}_2 / h_g^2 \quad (5)$$

For $\bar{\gamma}_2$, in terms of $\bar{\gamma}_o$ which is the out of ground effect, we have for the first term in the series as described in [5]. After the inversion of the integral (4) for pitching and plunging motion the full expression for the reduced circulation amplitude becomes

$$\frac{\bar{\Omega}}{U} = \frac{-2\pi[\bar{\alpha} + ik(\bar{h} + \bar{\alpha}/2)] - \frac{\pi}{2} \left[ik\bar{h} + \left(1 - \frac{3ik}{4}\right)\bar{\alpha} \right] / h_g^2}{ik[C_1(k)] + ik \left\{ \frac{3}{16} \left(\frac{1}{2k^2} - \frac{1}{4ik} \right) e^{-ik} + \frac{1}{4} \left[\left(-\frac{1}{k^2} + \frac{3}{2ik} \right) e^{-ik} + \frac{3}{2} C_1(k) - C_2(k) \right] \right\} / h_g^2} \quad (6)$$

First terms of the numerator and the denominator of (6) gives the reduced circulation without the presence of ground as h_g goes to infinity.

2.1 Lift and propulsive forces

The integration of unsteady lifting pressure coefficient gives the total of circulatory and the non-circulatory lift as follows [5]

$$\begin{aligned}
 \bar{C}_l = & 2\pi C(k) [\bar{\alpha} + ik(\bar{h} + \bar{\alpha}/2)] - \pi k^2 (\bar{h} + \bar{\alpha}) + \frac{\pi}{2} \left[ik\bar{h} + \left(1 - \frac{3ik}{4}\right)\bar{\alpha} \right] / h_g^2 \\
 & + ik \frac{\bar{\Omega}}{U} \left\{ \frac{3}{16} \left(\frac{1}{2k^2} - \frac{1}{4ik} \right) e^{-ik} + \frac{1}{4} \left[\left(-\frac{1}{k^2} + \frac{3}{2ik} \right) e^{-ik} + \frac{3}{2} C_1(k) - C_2(k) \right] \right\} / h_g^2 \\
 & - k^2 \frac{\bar{\Omega}}{U} \left\{ \frac{5}{16} \left(\frac{1}{k^2} - \frac{1}{2ik} \right) e^{-ik} + \frac{5}{4} \left(\frac{e^{-ik}}{ik} + C_1(k) \right) - 2 \left(\frac{e^{-ik}}{k^2} + C_2(k) \right) \right\} / h_g^2
 \end{aligned} \tag{7}$$

In (7), the second and the last terms represent the contributions of the apparent mass to the lift. The steady state value of the lift coefficient, for $k=0$, becomes $C_l = 2\pi\bar{\alpha}(1+0.25/h_g^2)$ as expected [1].

The propulsive force due to flapping is generated by the leading edge suction, which is given in terms of the vortex sheet strength evaluated at the leading edge, as follows [6]

$$S = -(\pi \rho \bar{P}^2 + \alpha L), \quad \bar{P} = \lim_{x' \rightarrow -b} \left[\bar{\gamma}_a(x') \frac{\sqrt{b+x'}}{2} \right] \tag{8-a,b}$$

In order to calculate P in (8-b), sum of all vortex sheet strengths at the leading edge is obtained as $(\bar{\gamma}_a = U/2 \bar{C}_{pa})_{LE}$, hence from (8-b) we have

$$\bar{P} = \sqrt{2b} \left\{ U \left[C(k)\bar{\alpha} + ikC(k)(\bar{h} + \bar{\alpha}/2) - ik\bar{\alpha}/2 \right] + \frac{U}{4h_g^2} \left[\bar{\alpha} + ik(\bar{h} + \bar{\alpha}) \right] + \frac{ik\bar{\Omega}}{4\pi h_g^2} \left[\left(-\frac{3}{4k^2} + \frac{7}{8ik} \right) e^{-ik} + C_1(k) - C_2(k) \right] \right\} \tag{9}$$

We have to note here that the apparent mass term makes no contribution to the leading edge suction force because of the limiting process described in (8-b).

2.2 Drag

The drag force, here, is evaluated from the unsteady boundary layer equations in velocity (u,v) and vorticity, ω , formulation expressed in body attached coordinates x-y [3]

$$\frac{\partial u}{\partial x} + \frac{\partial v}{\partial y} = 0 \tag{10}$$

and

$$\frac{\partial \omega}{\partial t} + u \frac{\partial \omega}{\partial x} + v \frac{\partial \omega}{\partial y} = \frac{1}{\text{Re}} \frac{\partial^2 \omega}{\partial y^2} \tag{11}$$

wherein, (10-11) are the continuity and the vorticity transport equations, respectively. In addition, the definition of vorticity in the boundary layer reads as

$$\omega = -\frac{\partial u}{\partial y} \tag{12}$$

The skin friction is obtained from the surface vorticity value as follows

$$c_f = -\frac{2}{\text{Re}} \omega_o \tag{13}$$

2.3 Numerical formulation

The boundary layer equations given above are discretized with finite differencing. Accordingly, (11) is discretized on a Cartesian grid with finite steps of Δt in time, Δx and Δy in space. Equation (12) is integrated with the trapezoidal rule to give the edge velocity as follows

$$U_e|_i = -\int_0^{\delta} \omega dy|_i = -\left[\omega_{i,0} / 2 + \sum_{j=1}^{J-1} \omega_{i,j} \right] \Delta y \quad (14)$$

Discretizing (11) in time and x direction with forward differencing and y direction with central differencing, and combining with (14), we obtain the following matrix equation at each time level in the following manner

$$\begin{bmatrix} 1/2 & 1 & 1 & \dots & 1 \\ a_2 & d_2 & c_2 & \dots & \\ \cdot & a_3 & d_3 & c_3 & \cdot \\ \cdot & \cdot & \cdot & \cdot & \cdot \\ \cdot & \cdot & \cdot & a_J & d_J \end{bmatrix}_i \begin{pmatrix} \omega_{i,0} \\ \omega_{i,1} \\ \omega_{i,2} \\ \cdot \\ \omega_{i,J-1} \end{pmatrix} = \begin{pmatrix} -U_e / \Delta y \\ b_2 \\ b_3 \\ \cdot \\ b_J \end{pmatrix}_i \quad (15)$$

here, the coefficient matrix is given in terms of the known quantities of velocity and the vorticity. The velocity field at the discrete locations are calculated from the vorticity definition for u and the continuity equation for v as follows:

$$u_{i,j} = -\int_0^{y_j} \omega dy|_i = -\left[\sum_{m=1}^{j-1} (\omega_{i,m-1} + \omega_{i,m}) / 2 \right] \Delta y, \quad j=2,\dots,J \quad (16)$$

and

$$v_{i,j}^n = v_{i,j-1}^n - \frac{\Delta y}{2\Delta x} (u_{i,j} + u_{i,j-1} - u_{i-1,j} - u_{i-1,j-1})^n, \quad j=2,J \quad (17)$$

3 APPLICATIONS, RESULTS AND DISCUSSIONS

The effect of the ground on a thin airfoil, here, is going to be demonstrated with several applications. First, the steady state case is studied. Afterwards, two different unsteady cases are going to be demonstrated as to determining the ground effect on an airfoil where the mean distance to the ground kept constant with i) only plunging, and with ii) pitching and plunging. Finally, the unrestrained plunging airfoil is free to translate horizontally and vertically with the propulsive and lift force change due to the presence of the ground.

3.1 Steady case

The lift change near the ground under the angle of attack α is given with three terms involving h as [1]

$$C_l = 2\pi\alpha \left(1 + \frac{1}{4h^2} - \frac{3}{32h^4} - \frac{1}{512h^6} \right) \quad (18)$$

The second term in (18) has a positive effect on the lift, whereas the last two terms reduces the lift for values of h less than a critical value which makes all three terms to add to zero. This critical value $h_{cr} \approx 0.62$. Hence, two different steady cases are considered. The distance to the ground $h < 0.62$ and $h > 0.62$. Figure 2 shows the first steady case where the airfoil descends because h being less than h_{cr} . Here, y is the vertical distance and v is the vertical velocity with respect to reduced time $s = Ut/b$.

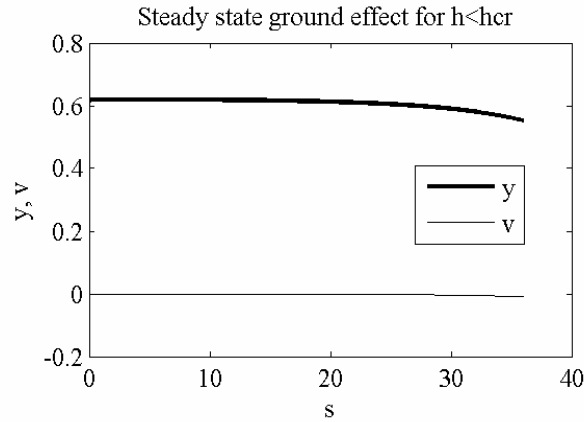


Fig2. Descending airfoil due the ground effect

Shown in Fig.3 is the second case where the ground effect is positive on the lift.

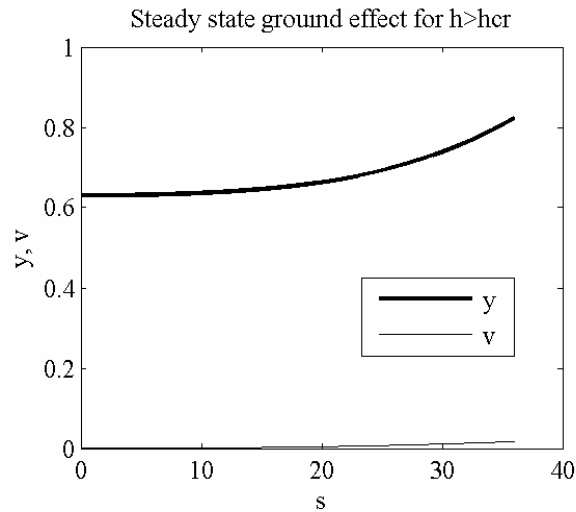


Fig3. Ascending airfoil due the ground effect

3.2 Unsteady restrained case

The mean distance to the ground for this case is kept constant. The solution procedure, here, is as follows:

- i) at a given time level n , the lift and the propulsive force are evaluated with (7) and (8-a),
- ii) the drag is found with integrating (13) over the top and bottom surfaces,
- iii) the net propulsive force is obtained as the difference between the propulsive force and the drag.

Shown in Fig.4 are the variations of the force coefficients for the heaving-plunging airfoil. Here, the reduced frequency value $k=\omega b/U=0.5$ is taken for the airfoil plunging near the ground with $h'_g(t) = 1.1 - 0.4 \cos(ks)$ being the variable distance to the ground. The averaged net propulsive force coefficients, obtained with integration of $C_s=(S+D)/(\rho U^2 b)$ over a period of time from Fig.4, are $C_T=-0.0431$ with the ground effect and $C_T=-0.0206$ without the ground effect which yields more than 100% increase in thrust.

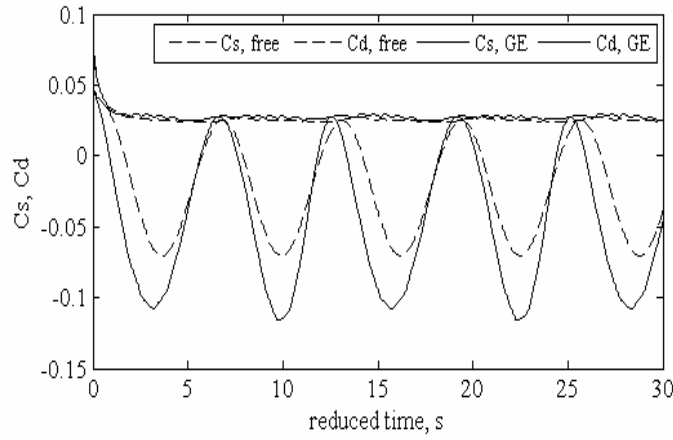


Fig4. Propulsive force coefficient variation with time for $k=0.5$ and $Re=10\ 000$

For the pitching plunging airfoil the following motion is imposed similar to that given in [7]

$$h_g = 1.1 - 0.3 \cos(ks)$$

$$\alpha = -10.4^\circ \cos(ks + 79.9^\circ)$$

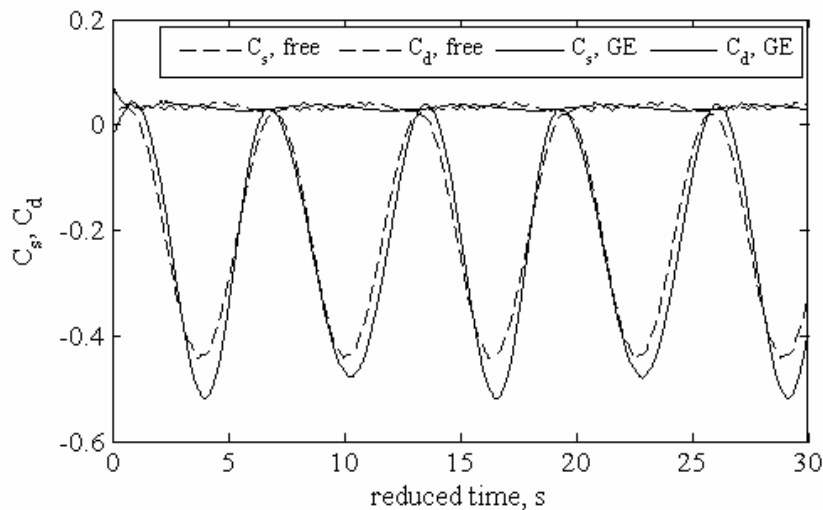


Fig5. Propulsive force coefficient variation for pitch and plunge with time for $k=0.5$ and $Re=10\ 000$

It has been already demonstrated that adding pitch to the plunge with a phase difference increases the propulsive force coefficients [7]. The averaged net propulsive force coefficients for this case are found to be -0.244 with the ground effect and -0.166 without the presence of the ground which causes almost 50% increase.

3.3 Unsteady unrestrained case

Unsteady effect is studied with the parameters of an ornithopter study given in [8] for a plunging airfoil with $h=y(s)+0.61\cos(ks)$, $y(0)=1.1$. Here, $k=0.5$ and the $Re=3040$ so $kh=0.3>0.2$ criteria is satisfied. Shown in Fig.6 are the vertical y , and the horizontal x , displacement of the airfoil versus the reduced frequency s where at each time step the position of the airfoil is determined using the Runge-Kutta method for the following system of ODE written in non-dimensional coordinates

$$\begin{aligned} \frac{d^2 x}{ds^2} &= C_s(s) \frac{b}{U^2} g, \quad x(0) = 0 \\ \frac{d^2 y}{ds^2} &= \Delta C_l(s) \frac{b}{U^2} g, \quad y(0) = 1.1 \end{aligned} \tag{19-a,b}$$

During calculation of horizontal displacement, only the contribution coming from the acceleration caused by the thrust is considered. Here, g is the acceleration due to gravity.

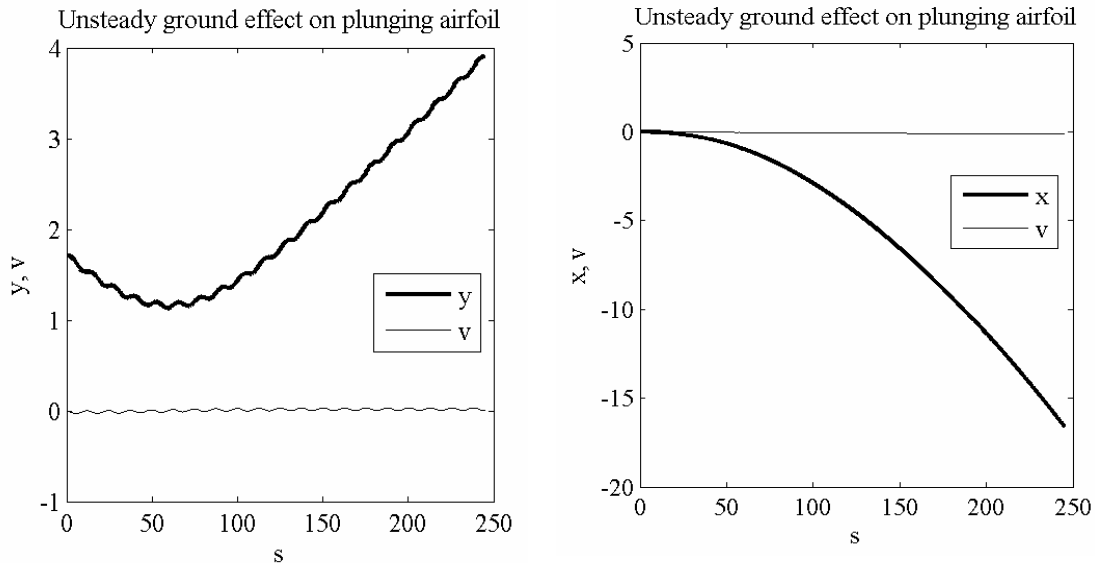


Fig6. Left, vertical y , and right horizontal displacement x and their rates v under the unsteady ground effect

Figure 7 shows the unrestrained actual path of the airfoil under the influence of the ground which is obtained by solving (19-a,b) with variable force coefficients determined simultaneously using the solution procedure described in **section 3.2**. Here, the horizontal distance covered includes the contribution of the free stream together with the acceleration due to thrust.

The computational time does not exceed a few seconds for more than a 12 000 time steps for the boundary layer solutions coupled with the path determination through solution of system of ODEs all performed with a MATLAB [9] code.

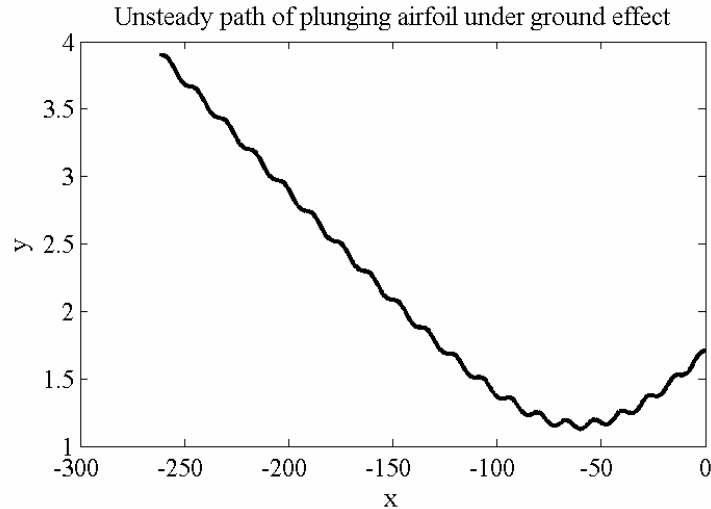


Fig.7 Trajectory of motion under the unsteady ground effect

4 CONCLUSIONS

The effect of the presence of ground on the airfoils, with emphasis on flapping, is analyzed with vortex sheets and their images coupled with unsteady boundary layer for predicting the viscous drag.

For the steady case, there is a critical value of the distance to the ground below that value the airfoil undergoes a descending motion rather than an ascending one.

The flapping airfoil, for the motion where the mean distance to the ground kept constant, produces considerably more thrust when pitch added to the plunge with a phase difference, as given in literature.

The unrestrained airfoil with plunging only, gains small altitude because of flapping under the influence of ground.

Acknowledgment: The help from Dr. Seher Durmaz for producing the graphs and the format of the text is greatly appreciated.

REFERENCES

- [1] A. Plotkin, C.G. Kennel, Thickness-Induced Lift on a Thin Airfoil in Ground Effect, *AIAA JOURNAL*, **19-11**, 1484-1486, 1981
- [2] J. Katz, A. Plotkin, *Low-Speed Aerodynamics*, McGraw-Hill, New York, 1991.

- [3] U. Gulcat, Propulsive Force of a Flexible Flapping Thin Airfoil, *Journal of Aircraft*, 46-2, 465-473, 2009
- [4] R.L. Bisplinghoff, H. Ashley, R.L. Halfman, *Aeroelasticity*, Dover Publications Inc., New York, 1996.
- [5] U.Gulcat, Ground Effect on the Performance of a Thin Airfoil, *Journal of Aircraft*, (Submitted), October 2012.
- [6] I.E. Garrick, Propulsion of a Flapping and the Oscillating Airfoils,” NACA TR-567, 1936.
- [7] M. Kaya, I.H. Tuncer, K.D. Jones, M.F. Platzer, Optimization of Flapping Motion Parameters for Two Airfoils in a Biplane Configuration, *Journal of Aircraft*, 46-2, 583-592, 2009
- [8] T.J. Mueller, J.D. Laurier, Aerodynamics of Small Vehicles, *Ann. Rev. Fluid. Mech.*, 35, 89-111, 2003.
- [9] MATLAB, Ver. 7.11.0.584. The MathWorks, Inc., August 16, 2010.

ATMOSPHERIC TURBULENT FLOW SOLUTIONS COUPLED WITH A MESOSCALE WEATHER PREDICTION MODEL

Engin LEBLEBİCİ¹, Gökhan AHMET², and İsmail H. TUNCER³

¹²³Department of Aerospace Engineering
Middle East Technical University (METU),
METU Centre of Wind Energy (METUWind)
06800 Ankara, TURKEY
e-mail: enginl@ae.metu.edu.tr
gahmet@ae.metu.edu.tr
tuncer@ae.metu.edu.tr

Keywords: Unsteady Navier-stokes solutions, Weather prediction software, Unstructured grids, Unsteady boundary condition coupling

Abstract. *Atmospheric turbulent flow solutions coupled with a mesoscale meteorological weather prediction software are obtained on terrain fitted high resolution computational grids using FLUENT as a CFD tool. The terrain topology of interest, which may be obtained in various resolution levels, is accurately modeled using unstructured grids. The widely used meteorological weather prediction software WRF is used to provide unsteady boundary conditions for the CFD solution domain. Due to difference of mesh structure and resolution, the coupling procedure is challenging. As an addition to previous works, improvements over the coupling procedure are done by using modified boundary conditions to match the ground surfaces of both low resolution WRF data and FLUENT flowfield. Unsteady boundary conditions are implemented through the User Defined Functions developed for FLUENT. The main objectives of this study are to overcome the challenges of the coupling of the solvers and to obtain unsteady, turbulent atmospheric flow solutions accurately using low resolution atmospheric weather prediction models for spatially and time varying boundary conditions and high resolution Navier-Stokes solutions over topographical terrains.*

1 INTRODUCTION

Accurate predictions of unsteady rural and urban atmospheric flow fields have a wide range of usage such as micro-site selection for wind farms and pollution tracking, each of which are of current research topics with several examples in literature[1, 2, 3].

As wind farms consisting of a large number of wind turbines have a high initial investment cost, wind farm siting must be given a significant importance[4, 5]. Low resolution wind energy potential atlases have the necessary statistical information for macro-siting of wind farms but lack the precision for the micro-siting. Therefore; high resolution, more accurate wind field information may be needed for micro-siting in order to improve the power output of a wind-farm.

Bowen(2004)[6] in a Risø-R Report states that Botta et al (1992)[7], Bowen and Saba (1995)[8], Reid (1995)[9] and Sempreviva et al (1986)[10]'s experience in the operation of commercial wind farms (Lindley et al., 1993[11]) has confirmed that effects from the local complex terrain on the site characteristics of each turbine have a significant influence on the output (and perhaps even the viability) of a wind energy project.

F.J.Zajackowski et.al.[12] compares Numerical Weather Prediction Models (NWP) and Computational Fluid Dynamics (CFD) simulations. They conclude that NWP can take radiation, moist convection physics, land surface parametrization, atmospheric boundary layer physics closures, and other physics into account, but wind flow features finer than 1 km are not captured by the turbulence physics of such models. CFD simulations, however, have proven to be useful at capturing the details of smaller scales due to a finer scale topography, and details around urban features such as high-rise buildings.

In the previous work done by Leblebici et. al.[13], FLUENT is coupled with WRF using the unsteady weather prediction data from WRF as unsteady boundary conditions. As the resolution of the WRF solutions' and FLUENT solutions' are not the same, the ground level of both solution domains does not coincide. To overcome this problem, the regions where the ground level of FLUENT is below the WRF ground level velocity is taken as zero. But this approach may yield in inaccuracies in the atmospheric boundary layer profile.

The objective of this study is to develop a methodology to obtain accurate and turbulent atmospheric flow solutions on high resolution terrain fitted grids to accurately model the boundary layer flow near the ground for a given region coupled with unsteady WRF weather prediction solutions. The main development over the previous study[13] is improved boundary conditions which will be explained in the Method section.

2 METHOD

In this study, a coupled flow solution methodology with an atmospheric weather forecast software, WRF, and a commercial flow solver, FLUENT, is developed. WRF produces a low resolution, unsteady atmospheric weather forecast data, which provides the unsteady boundary conditions for turbulent flow solutions obtained with FLUENT on terrain fitted, high resolution unstructured grids. Also, the accuracy of the boundary conditions are assessed and improved.

The coupling procedure and basic flowchart representing the solution methodology is also given in Figure 1 and Figure 2.

WRF is a fully compressible, Eulerian, η -coordinate based, nest-able, non-hydrostatic, numerical weather prediction model with a large suite of options for numerical schemes and parametrization of physical processes [14]. WRF uses an η based coordinate system instead of an orthogonal Cartesian coordinate system. The vertical coordinate, η , is defined as:

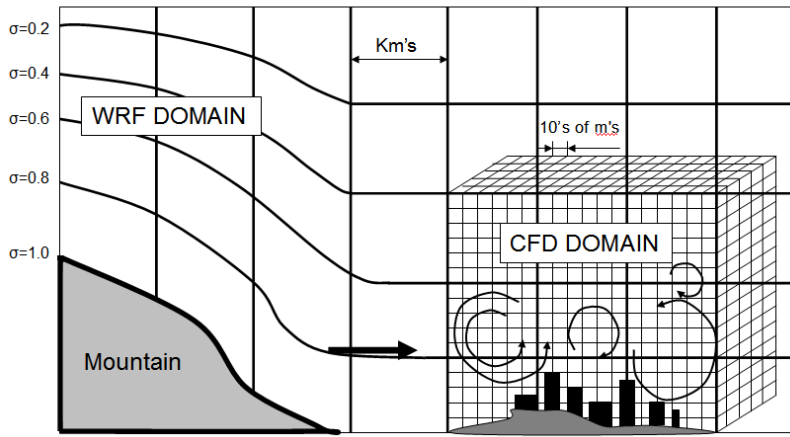


Figure 1: Coupling WRF with FLUENT

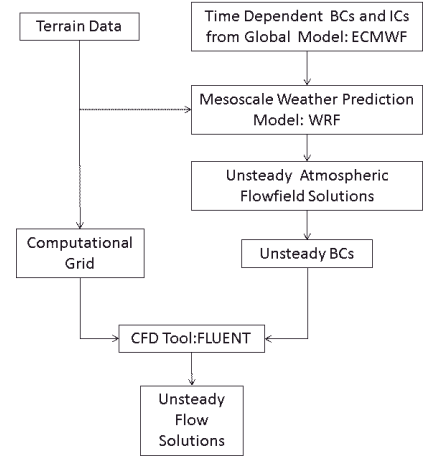


Figure 2: Flowchart

$$\eta = \frac{p - p_{ht}}{p^*} \quad (1)$$

and pressure perturbation p^* is simply

$$p^* = p_{hs} - p_{ht} \quad (2)$$

where p is pressure, p_{hs} is surface pressure, and p_{ht} is the pressure at the top of the model. As seen in Figure3, the η coordinate system causes a poor representation of the surface topography.

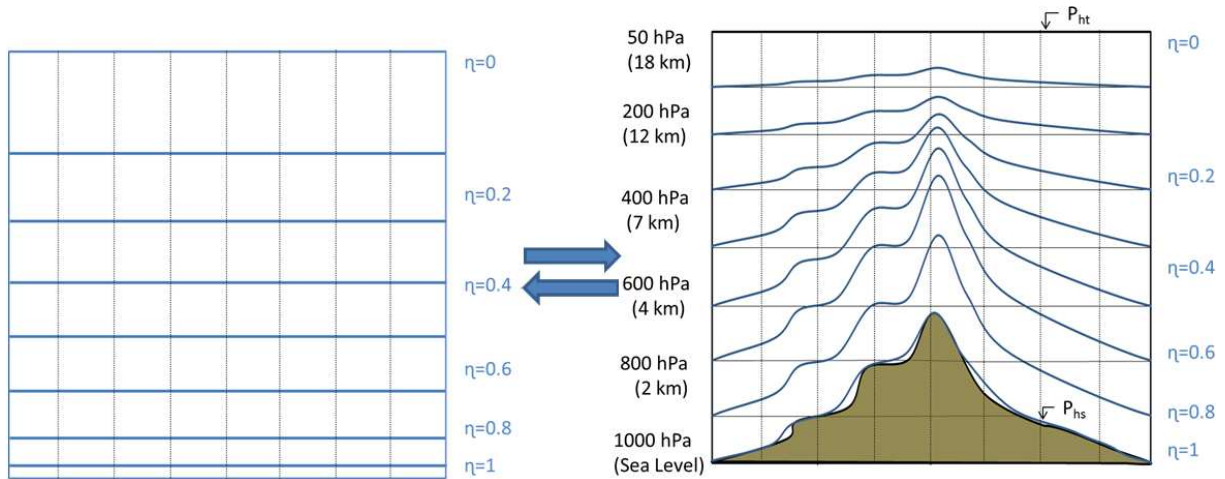


Figure 3: η Coordinate system

Some of the major difficulties in computing turbulent flow solutions using computational fluid dynamics tools are obtaining and utilizing the unsteady boundary conditions and obtaining the regional high resolution topographical data.

In this study, unsteady WRF solutions are first obtained over the geographical domain of interest. The local terrain data is downloaded automatically from UCAR (University Corporation of Atmospheric Research) server via WRF. The time dependent initial and boundary conditions for the WRF solution is obtained from ECMWF (European Centre of Medium Range Weather Forecast). The unsteady boundary conditions needed for the FLUENT solution at its domain

boundaries, which fall into the larger scale WRF domain, are then extracted from the WRF solution at 5 minute time intervals.

In computational grids for FLUENT solutions, the high resolution terrain topography is generated using the data obtained from ASTER GDEM Worldwide Elevation at 1.5 arc-sec resolution (≈ 30 meter). The vertical and horizontal grid resolution on the ground for the terrain fitted unstructured grids is about 20 meters. These grids also resolve the atmospheric boundary layers and stretch up to about 2000 meter altitude.

It should be noted that WRF has a horizontal resolution of 1km and a vertical resolution of about 50m on the ground which stretches rapidly. In addition, as shown in Figure4 the surface boundaries in the WRF and FLUENT domains differ significantly mainly due to the high resolution topographic data used in the generation of the FLUENT domain, and due to the η coordinate system employed in WRF.

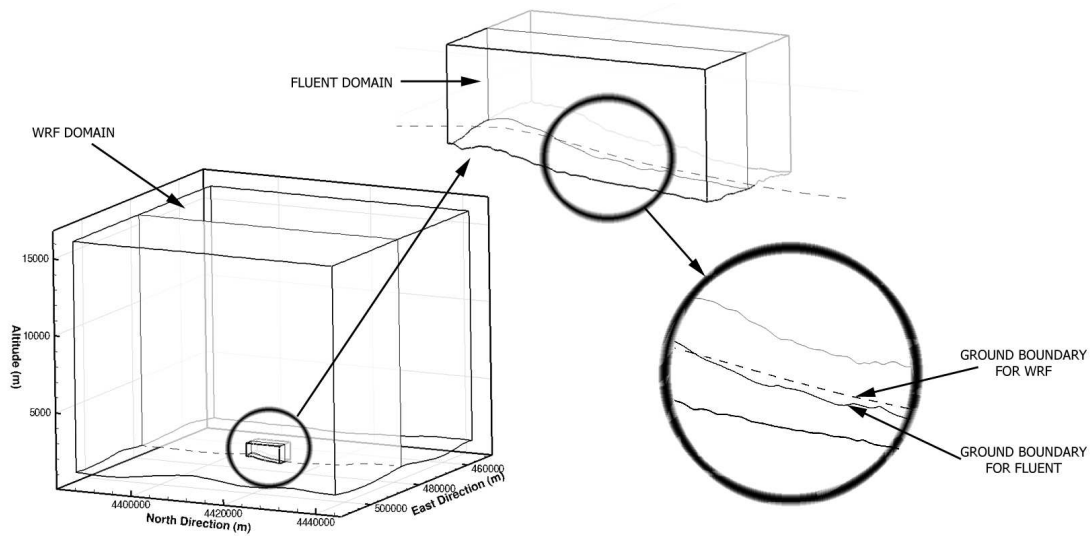


Figure 4: WRF and FLUENT solution domains and close-up views

Due to the difference in resolution boundary condition data from WRF should be interpolated accordingly to the FLUENT flowfield's boundaries. In the previous work [13], the values from WRF are interpolated using a fictitious surface at least below the ground level of fluent is generated for the interpolation of boundary conditions at the FLUENT's boundaries. But this method results in zero velocity boundary conditions near the ground level of FLUENT where WRF's ground level is higher. To overcome this problem, vertical distances from the ground are calculated for each of the faces in the boundaries in FLUENT domain and x-velocity, y-velocity and z-velocity at these distances above the ground level of WRF domain are taken as boundary conditions.

The unsteady boundary conditions for the FLUENT solutions are interpolated for the outer boundary cells from the WRF solution at every 5 minute, and then linearly interpolated for the time steps between 5 minute intervals by means of User Defined Functions (UDF) within FLUENT. Three UDFs are developed for determining the boundary cells and boundary faces, for reading the appropriate unsteady boundary information data obtained from the WRF solution, and for interpolating the flow variables at the boundary faces.

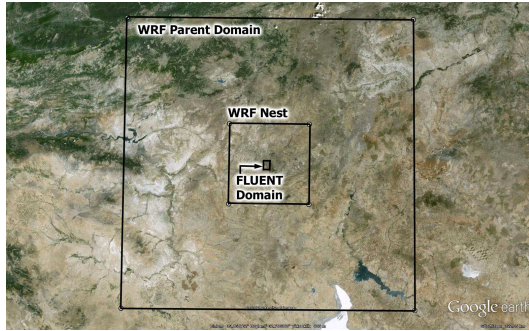


Figure 5: Borders of WRF nests and FLUENT solution domain

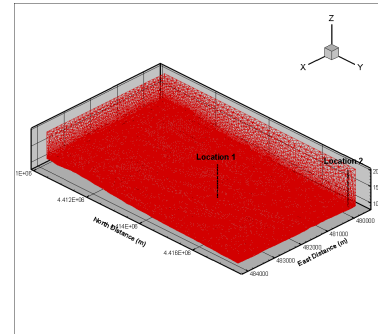


Figure 6: Location of the points on which BL profiles are taken

3 RESULTS AND DISCUSSION

In this study, turbulent atmospheric flow solutions coupled with WRF and the commercial flow solver FLUENT are carried out around METU campus in Ankara/TURKEY on high resolution unstructured grids.

Nested WRF solutions are first obtained for a 12 hour period, within a parent domain of 3 km horizontal resolution and a nest of 1km resolution around METU campus in Ankara. The parent and the nested solution domains, which are of 70x58(horizontal) x 50(vertical) size, are given in Figure 5. Unsteady solutions in the nested domain is saved in 5 minute time intervals, which are used to extract the unsteady boundary conditions for the FLUENT solution.

Gambit is employed to generate computational grids for FLUENT solutions. The high resolution topographic data for the domain of interest is taken from the ASTER-GDEM data set which has a horizontal resolution of about 30 meter. Terrain fitted unstructured grids with vertical and horizontal grid resolution on the ground about 20 meters are generated.

η coordinate system may result in the disturbances due to complex terrain not to be captured. Both the usage of high resolution terrain data and unstructured grids defined in Cartesian coordinate system instead of η coordinate system makes it possible to analyze the flowfield in the vicinity of the ground better especially in complex terrains.

The atmospheric flow solutions over the domain of interest are successfully obtained for a 12 hour period first with WRF, and then with FLUENT on terrain fitted unstructured grids in a coupled fashion with the WRF solution.

As previously mentioned in Method section, ground levels of WRF and FLUENT domains does not match exactly due to the difference in resolution. To overcome the problems this phenomenon may yield for the accuracy of the boundary conditions, distance from the ground is calculated at each face at the boundaries of the FLUENT domain and using this information FLUENT domains ground level and WRF's are matched.

The unsteady flowfields obtained with the previous boundary conditions and improved boundary conditions are shown along with the WRF results in Figure 7 in terms of the velocity magnitude contours and streamlines taken on a horizontal surface at 940m altitude, which is about 30m above the ground. It is observed that in general all the solutions are in agreement in the large scale but FLUENT solutions have a higher resolution of the flowfield as well as the surface topography than the WRF solution as expected. The turbulent flow solutions with FLUENT capture detailed flow features especially at the 3rd and 6th hours of the solution when the wind velocity is relatively low. At the 12th hour, when the wind velocity increases, the computed flowfields are in more agreement. Nevertheless, the velocity magnitudes computed by WRF and FLUENT may still differ at various locations by as much as 50%.

As for the comparison between two FLUENT solutions, it is seen that usage of the improved boundary conditions resulted in capturing a swirl at the 3rd hour whereas in the previous study there was not such a feature and also the flow pattern at 6th hour is somewhat different and seems more realistic. Overall, both FLUENT solutions agrees with each other.

Figure 8 presents the 3-D streamlines over the FLUENT solution domain and the WRF solution domain. Similar to the sectional views in Figure 7, the 3-D views reveals the differences in the resolution of the topography and the flow features. In contrast to the smoother wind fields in WRF solutions, the the FLUENT solutions predict a more complex and a detailed wind field.

For understanding the effects of the change in boundary conditions, boundary layer profiles in the vicinity of the ground (up to 250 meters above the ground level) are plotted in Figure 9 at two different locations. Location 1 (Zone 36 482020E-4414690N in UTM coordinate system) is located about the center of the domain and used to analyze the effects far from the boundaries whereas Location 2 (Zone 36 479800E-4417370N in UTM coordinate system) used to observe the effects near the boundaries as seen in Figure 6.

As seen in Figure 9, at location 2 which is near the boundaries of the FLUENT domain, improvement in boundary conditions resulted in a more realistic boundary layer profiles and also the difference between WRF solution and new FLUENT solutions are smaller compared to the old FLUENT solution. Looking at the boundary layer profiles at location 1, it can be said that the difference in the flowfield solution due to improved boundary conditions is not negligible.

Although the FLUENT solutions are high-fidelity and have higher resolutions in the surface topology and in the solution domain in comparison to the WRF solutions, their accuracy should first be validated with the observation data. It is hard to draw a conclusion about whether improved boundary conditions are better. Nevertheless, increased accuracy near the boundaries may imply that it is so. In addition, the accuracy of the FLUENT solutions may also be established through grid resolution studies. In this preliminary study, higher grid resolutions are avoided due to the fact that FLUENT can not be run in the parallel mode in the presence of UDFs, and serial computations with the total number of cells exceeding 10^7 become prohibitively resource demanding.

4 CONCLUSIONS

In this preliminary study, the unsteady atmospheric flowfields are successfully computed with a commercial viscous flow solver, FLUENT, coupled with a meteorological weather prediction software, WRF. The unsteady boundary conditions for the FLUENT solution are extracted from the unsteady WRF solution. It is shown that the FLUENT solutions on terrain fitted unstructured grids provide high resolution atmospheric flowfields, and are in agreement with the WRF solution globally. As for improving the boundary conditions, it can be seen that it increases accuracy with respect to WRF. However, the accuracy of the FLUENT solutions should be assessed first in a grid convergence study, which is the next stage in our research. In addition, all the solutions should ultimately be validated against the atmospheric observation data. The methodology developed is highly promising in micro-siting of wind farms and in accurate prediction of power production of operational wind farms.

5 ACKNOWLEDGEMENT

This project is partially supported by "The Scientific and Technological Research Council of Turkey" (TUBITAK) under the project no: 112M104 and this support is greatly acknowledged.

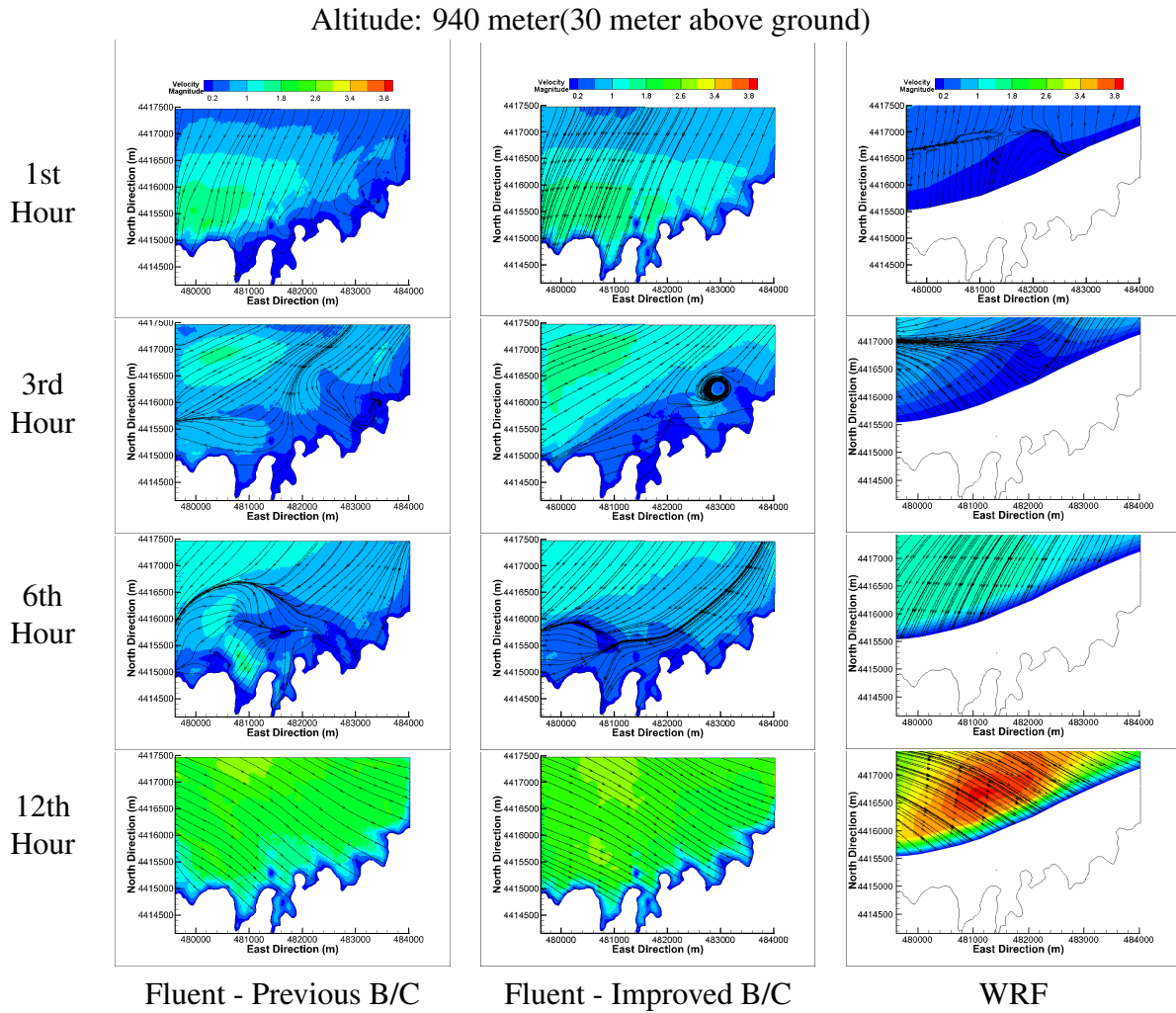
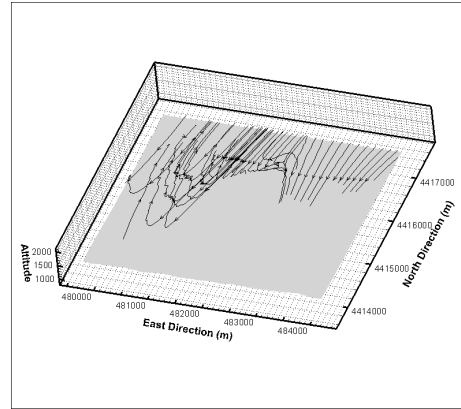
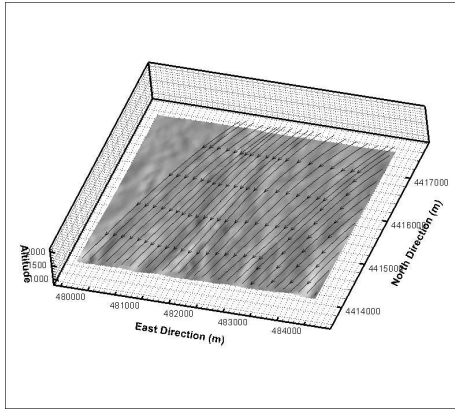
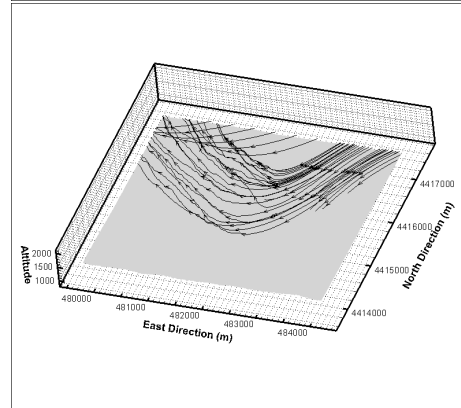
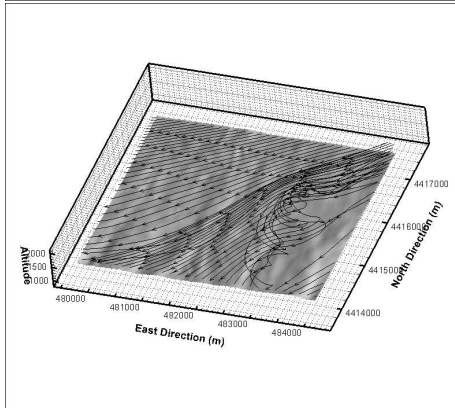


Figure 7: Velocity contours and streamlines at 940m altitude at the 1st, 3rd, 6th, 12th hours of the solutions

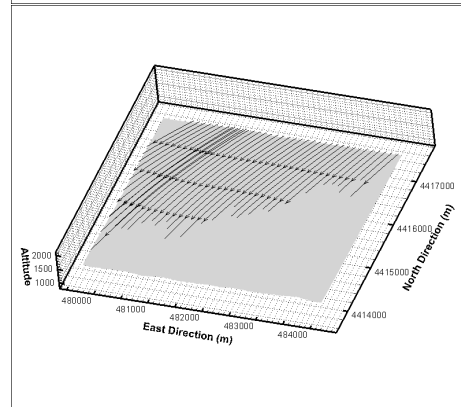
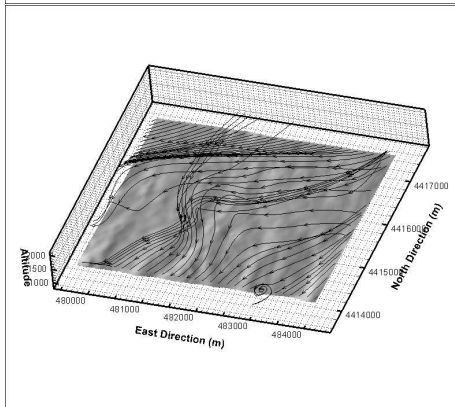
1st
Hour



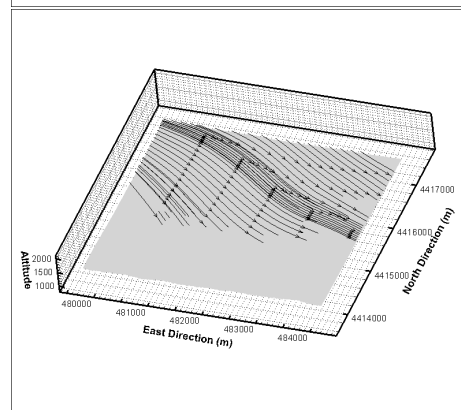
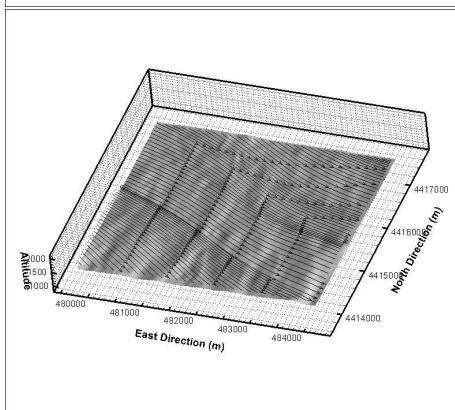
3rd
Hour



6th
Hour



12th
Hour

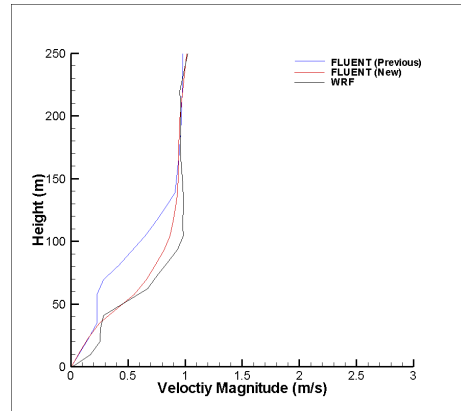
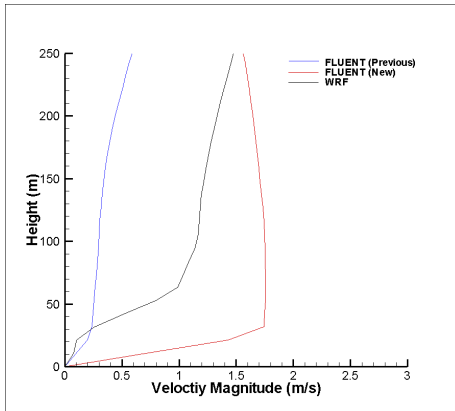


FLUENT solutions

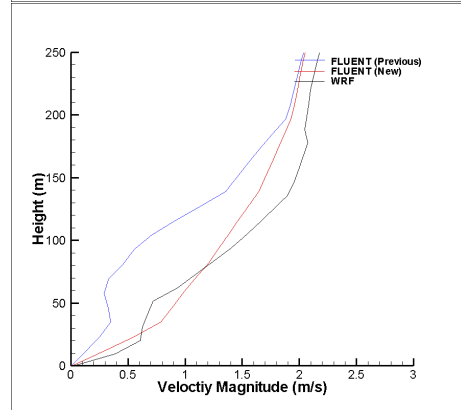
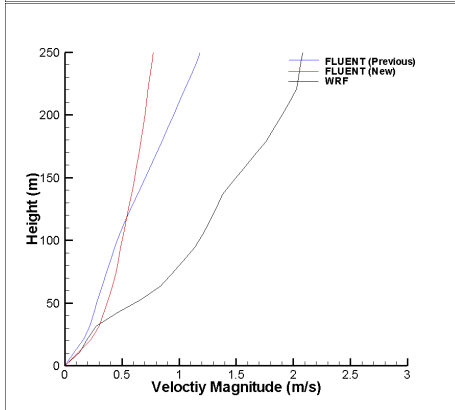
WRF solutions

Figure 8: 3D representation of streamlines about 940 m altitude at the 1st, 3rd, 6th, 12th hours of the solution

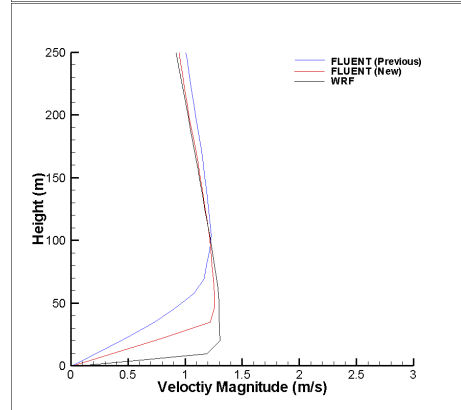
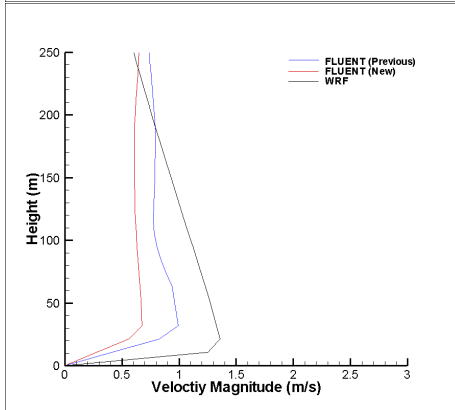
1st
Hour



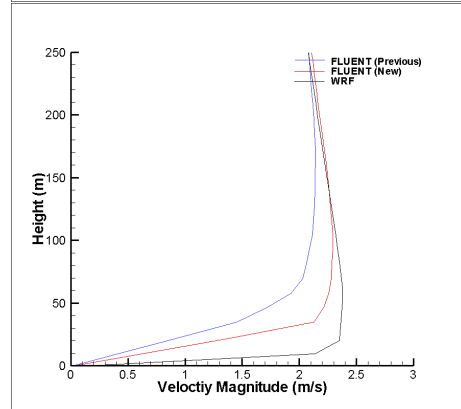
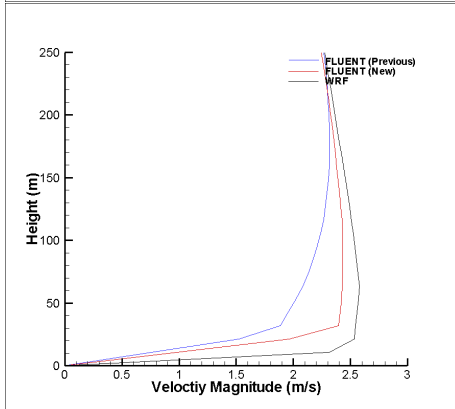
3rd
Hour



6th
Hour



12th
Hour



Location 1

Location 2

Figure 9: Boundary Layer Profiles at Location 1(right) and Location 2(left) at 1st, 3rd, 6th and 12th hours

REFERENCES

- [1] Yilmaz, E., 2009, Purdue School of Engineering and Technology, *Extreme Wind and Air Quality Modeling/Simulation for a Metropolitan Area*, (IUPUI, Indianapolis, IN) Presentation.
- [2] Cochran, B.C., Damiani, R.R., 2008, WindPower 2008, *Harvesting Wind Power from Tall Buildings*, (Houston, Texas).
- [3] Politis, E.S., Chaviaropoulos, P.K., 2008, European Wind Energy Conference and Exhibition Brussels, *Micrositing and classification of wind turbines in complex terrain*, (Belgium).
- [4] Damiani, R., Cochran, B., Orwig, K., Peterka, J., 2008, American Wind Energy Association, *Complex Terrain: A Valid Wind Option?*.
- [5] Derickson R.G., Peterka J.A., 2004, American Institute of Aeronautics and Astronautics *Development of a Powerful Hybrid Tool for Evaluating Wind Power in Complex Terrain: Atmospheric Numerical Models and Wind Tunnels*.
- [6] Anthony J. Bowen nad Niels G. Mortensen, 2004, Risø National Laboratory, *WAsP prediction errors due to site orography*, (Denmark, Roskilde).
- [7] Botta, G., Castagna, R., Borghetti, M. and Mantegna, D., 1992, Jour. Wind Eng. Ind. Aerodyn. **39** *Wind analysis on complex terrain - The case of Acqua Spruzza*, pp 357-66.
- [8] Bowen, A.J. and Saba, T., 1995, 9th International Conference on Wind Engineering, *The evaluation of software for wind turbine siting in hilly terrain*, (India)
- [9] Reid, S.J., 1995, BWEA Conference, *Modelling of channelled winds.*, (Warwick, UK), pp 391-6
- [10] Sempreviva, A.M., Troen, I. and Lavagnini, A., 1986, European Wind Energy Association Conference and Exhibition, *Modelling of wind power potential in Sardinia*. (Rome Italy).
- [11] Lindley, D., Musgrove, P., Warren, J. and Hoskin, R., 1993, 15th BWEA Annual Wind Energy Conference, *Operating experience from four UK wind farms*. (York, UK), p 41-45.
- [12] Frank J.Zajaczkowski, SueEllenHaupt, KerrieJ.Schmehl, 2011 Journal of Wind Engineering and Industrial Aerodynamics **99** *A preliminary study of assimilating numerical weather prediction data into computational fluid dynamics models for wind prediction*, pp 320-329.
- [13] Leblebici E., Ahmet G., Tuncer I.H., 2012, *The Science of Making Torque, it Atmospheric Turbulent Flow Solutions Coupled with a Mesoscale Weather Prediction Model, For Wind - Center for Wind Energy Research, Oldenburg, GERMANY*
- [14] William C. Skamarock, Joseph B. Klemp, Jimy Dudhia, David O. Gill, Dale M. Barker, Michael G. Duda, Xiang-Yu Huang, Wei Wang, Jordan G. Powers, 2008, National Center for Atmospheric Research, *A Description of the Advanced Research WRF Version 3*, (Boulder, Colorado, USA)

APPLICATION OF THE EFMM TO FLUID-STRUCTURE COUPLED ANALYSIS AND ITS PARALLELIZATION METHOD

Shinsuke NAGAOKA¹, Yasushi NAKABAYASHI², and Genki YAGAWA³

¹ Toyo University, Center for Computational Mechanics Research
e-mail: nagaoka.ccmr@gmail.com

² Faculty of Information Sciences and Arts, Toyo University
nakabayashi@toyo.jp

³ Toyo University, Center for Computational Mechanics Research
yagawag@gmail.com

Keywords: Enriched Free Mesh Method, SUPG/PSPG Stabilized FEM, Parallel Computing, Fluid-Structure Coupled Problem

Abstract. *There is a new fluid-structure coupled analysis method that combines a structure analysis method using Enriched Free Mesh Method (EFMM); a type of meshless analysis methods and a fluid analysis method using SUPG/PSPG stabilized FEM. In this study, solutions for problems during the parallelization of the abovementioned method are described. In EFMM, it is relatively easy to parallelize problems which do not require remeshing such as static analyses. Application of EFMM, on the other hand, becomes challenging on the problems needs remeshing due to issues in analysis algorithm of EFMM. Nevertheless, parallelization is essential in the fluid-structure coupled analysis. There fore, we propose a method for parallelization of EFMM in this study.*

1 INTRODUCTION

Recently, as the popularity of numerical analysis is rising along advancement in computer performance. Especially, Finite Element Method (FEM)[1] that is the most famous numerical analysis method is applying into a lot of fields.

Variety of different phenomena affecting each other is called coupled phenomenon in the numerical analysis field[2]. Majority of phenomena occurring in our bodies are coupled phenomena. However, only a few number s of coupled analysis have been performed, compared with single phenomenon cases.

In the management of coupled phenomena, various unsolved problems are left, compared to the cases of single phenomena comparison. The reason for this is that these problems are not able to be solved solely by improvement in calculators, but rather they have close relationships with their analysis algorithm.

The phenomenon that fluid and structure are affecting each other is called fluid-structure coupled phenomenon. Recently, fluid-structure coupled phenomenon is becoming a very important issue in a lot of field.

2 PURPOSES

The new fluid-structure coupled analysis method that is already proposed by us is using Enriched Free Mesh Method (EFMM)[3] and SUPG/PSPG stabilized FEM[4-7]. These methods are used linear elements. In short, nodes on boundary of fluid analysis field and structure analysis field can be consistent completely.

As a result, we were able to find solutions for the problems during considering coupling effects at the fluid-structure interface that is important in facing fluid-structure problems.

Moreover, when conducting numeric computations using a finite element method, generally highly accurate elements with intermediate nodes are used, but in our proposed method, only linear elements are used at the fields of fluid analysis and structure analysis to conduct mesh generation as described previously. Although highly accurate elements were not used, accuracy of the analyses of this method improved relative to the conventional analysis using only linear elements. This result indicates a possibility of reduction in the calculation resources and computation volume that are disadvantages during management of large-scale problems.

Thus, our proposed method is a very effective method. Because, the new fluid-structure coupled analysis method that is combining EFMM and FEM can resolve a lot of problems of coupled analysis.

However, we found a major problem in this proposed method when conducting parallelization that is essential for large-scale analysis in recent years. This is caused by analysis algorithm of EFMM. Additionally, in numerical analysis using EFMM, application of the conventional domain decomposition method based on elements is challenging. Moreover, due to the abovementioned problems, increase of communication volume between each processor that is a critical problem in parallelization occurs, resulting in reduction of analysis efficiency and parallelization efficiency.

Therefore, in the present study, to apply the fluid-structure coupled analysis method combining previously proposed EFMM and SUPG/PSPG stabilized FEM to parallelization analysis, procedures that solve problems during parallelization of the structural analysis method are proposed.

3 FLUID-STRUCTURE COUPLED ANALYSIS METHOD

In this chapter, we discuss a new fluid-structure coupled analysis method combining previously proposed EFMM and SUPG/PSPG stabilized FEM.

When conducting analysis considering fluid-structure interaction effects, it is desirable that node locations are consistent on the interface between fluid and structure domain as shown in Fig. 1. As a reason, if fluid-structure interface is inconsistent when considering the coupling effects of two different fields, it is necessary to interpolate the analysis results between the nodes. Algorithm of fluid-structure coupled analysis becomes complicated by interpolation process. Moreover, analysis accuracy will be decreased.

Since linear tetrahedral elements are used in both EFMM and SUPG/PSPG stabilized FEM for their analysis, integrity at fields of fluid analysis and structure analysis can be obtained. In addition, these analysis methods have features that the accuracy of the analysis will be improved relative to the conventional analysis solely using linear elements.

As an example of application of this method on the biological field, we present the simulation results of capillary blood flow-derived erythrocyte deformation and changes in flow at the fluid field that accompanies the deformation. Fig 3 is an analysis model that is used in this numerical example.

In this analysis, membrane of red blood cell is using as a structure analysis model. On the other hand, capillary is using as a fluid analysis model. Fig. 4 and Fig. 5 are analysis result of this numerical example. Fig. 4 shows a changing in the blood flow in the capillary by change shape of membrane of red blood cell. Fig. 5 shows a changing shape of membrane of red blood cell by blood flow.

In blood vessels with smaller diameter than that of erythrocytes such as capillaries, erythrocytes deform themselves with taking forms of parachutes as they travel[8][9]. In this numerical analysis, this phenomenon is well computed.

Especially in the results of the structure analysis, the highest pressure was observed at the center of erythrocytes on the upstream side. The pressure makes large depression at the center of the erythrocyte membrane on the upstream side, taking forms of parachutes as with erythrocytes observed in our body.

From these analysis result, we can obtain fine analysis result computed by our proposed method that is combining EFMM and SUPG/PSPG stabilized FEM compared with phenomenon that is observed in our body.

4 PARALLEL EFMM

Our new fluid-structure coupled analysis method can be possible to obtain fine analysis result.

Although the coupled analysis using combination of EFMM and SUPG/PSPG stabilized FEM showed excellent performance when conduction single process without parallelization, several problems are found once parallelization is attempted.

The greatest source of the problems during parallelization is found in the analysis algorithm of EFMM. The analysis algorithm of EFMM is described in the next section.

4.1 Fundamental concept of EFMM

EFMM is based on FMM (Free Mesh Method)[10][11], which is one of mesh-less method. The most important feature of FMM is that it requires only the coordinate data of each node in analysis domains as the input information. Based on the given coordinate data of nodes, a lo-

cal elements cluster is created at each node. To produce such a local elements cluster, there are a variety of methods including the diagonal comparison method, the packaging method, and the method for developing a Delaunay triangle[12][13] for each central node based on the planar relative relation between a Voronoi polygon and a Delaunay triangle.

Here, the node located at the center of a local elements cluster is called the central node, while nodes located at the edge of the elements cluster are called the satellite nodes(see Fig. 6).

In EFMM analysis, stiffness matrix is calculated by different way with conventional FEM and FMM using this local elements cluster.

In the next section, formulation of EFMM will be described.

4.2 Formulation of EFMM

In EFMM, the displacement and the strain fields are respectively, assumed in independent locations, and these two fields are linked with the Hellinger-Reissner principle[14](see Fig. 7). The principle, in which displacement u and strain ε are assumed to be independent variables, is given by

$$\Pi(\varepsilon, u) = \int_{\Omega} \{\varepsilon\}^T [D] \{\partial u\} d\Omega - \frac{1}{2} \int_{\Omega} \{\varepsilon\}^T [D] \{\varepsilon\} d\Omega - \int_{\Omega} \{u\}^T \{b\} d\Omega - \int_{S_{\sigma}} \{u\}^T \{\tilde{t}\} dS \quad (1)$$

with

$$\{\partial u\} = [B] \{\bar{u}\}, \{u\} = [N^u] \{\bar{u}\}, \{\varepsilon\} = [N^{\varepsilon}] \{\bar{\varepsilon}\} \quad (2)$$

Where $\{\bar{u}\}$ represents the nodal displacement, $\{\bar{\varepsilon}\}$ the unknown parameter of strain, $\{b\}$ the body force, $\{\tilde{t}\}$ the surface force on the boundary S_{σ} , and Ω the analysis domain. $[N^{\varepsilon}]$ is an arbitrary function that determines the strain of a local region, which can be assumed as

$$[N^{\varepsilon}] = \begin{bmatrix} p^T & 0 & 0 & 0 & 0 & 0 \\ 0 & p^T & 0 & 0 & 0 & 0 \\ 0 & 0 & p^T & 0 & 0 & 0 \\ 0 & 0 & 0 & p^T & 0 & 0 \\ 0 & 0 & 0 & 0 & p^T & 0 \\ 0 & 0 & 0 & 0 & 0 & p^T \end{bmatrix} \quad (3)$$

where

$$p^T = [1 \quad x \quad y \quad z] \quad (4)$$

The stationary condition of Eq.(1) is expressed by

$$\int_{\Omega} \delta \{\varepsilon\}^T [D] ([B] \{\bar{u}\} - [N^{\varepsilon}] \{\bar{\varepsilon}\}) d\Omega = 0 \quad (5)$$

and

$$\int_{\Omega} \delta\{u\}^T [B]^T [D] [N^{\varepsilon}] \{\bar{\varepsilon}\} d\Omega - \int_{\Omega} \delta\{u\}^T \{b\} d\Omega - \int_{S_{\sigma}} \delta\{u\}^T \{\tilde{t}\} dS = 0 \quad (6)$$

These equations are written as follows,

$$\begin{bmatrix} -A & C \\ C^T & 0 \end{bmatrix} \begin{Bmatrix} \bar{\varepsilon} \\ \bar{u} \end{Bmatrix} = \begin{Bmatrix} f_1 \\ f_2 \end{Bmatrix} \quad (7)$$

where

$$\begin{cases} A = \int_{\Omega} [N^{\varepsilon}]^T [D] [N^{\varepsilon}] d\Omega \\ C = \int_{\Omega} [N^{\varepsilon}]^T [D] [B] d\Omega \\ f_1 = 0 \\ f_2 = \int_{\Omega} [N^u]^T \{b\} d\Omega + \int_{\Gamma} [N^u]^T \{\tilde{t}\} d\Gamma \end{cases} \quad (8)$$

Next, Eq. (7) is condensed to the following equation:

$$C^T (A^{-1} C \bar{u}) = f_2 \quad (9)$$

Finally, the local enriched stiffness matrix is derived as

$$[k_{HR}] = C^T A^{-1} C \quad (10)$$

Above enriched stiffness matrix is expected to give more accurate solutions than the usual FEM or FMM with the linear displacement base.

This is a formulation of EFMM.

4.3 Treatment for Parallel EFMM

Not every single case using EFMM faces difficulty in parallelization. Specifically, it is possible to conduct parallelization process without a major problem in the cases of static analyses that do not require mesh regeneration in general. In that case, the parallelization CG method was solved in high speed by conducting the local element cluster-by-local element cluster method based on the conventional element-by-element method for EFMM that carries on the process by each local element.

On the other hand, in the cases of adaptive problems that require mesh regeneration, parallelization process becomes difficult due to the feature of analysis algorithm in EFMM.

The intended problems are fluid-structure coupled problems. In a majority of the fluid-structure coupled problems, the mesh form changes over time because of the interaction between fluid and structure. In addition, due to increase in the number of analysis fields, the number of mesh for the analysis also rises substantially. Thus, implementation of parallelization is absolutely essential.

The reason for difficulty in application of parallel EFMM on adaptive analysis is that all nodes in the entire analysis field create a local elements cluster around the nodes (see Fig.6). Generating stiffness matrices by each local element cluster and adding the stiffness matrices generated by each node and the entire stiffness matrix, it is possible to obtain the stiffness matrix of the entire analysis field.

Since stiffness matrices are generated by each node, about 100% of the parallelization efficiency can be achieved in generation of the local stiffness matrix. Fig. 8 indicates changes in the parallelization efficiency when parallelization process was added to generation process of the stiffness matrix by EFMM for certain analysis model.

As can be seen, since this is the analysis model based on nodes, it is possible to obtain high levels of parallelization efficiency in the cases of application of EFMM on parallelization analysis.

Nevertheless, since EFMM is a special analysis method based on nodes, the coordinate data of nodes outside of the analysis field depending on the local stiffness matrix generated by nodes in the analysis field are required in addition to coordinate data of nodes in its assigned field when conducting element based field separation. As a result, when coordinate values of nodes changes with analysis such as adaptive analysis, coordinate values of the moved nodes should be transmitted between each field along with the changes. This causes a large amount of the communication cost since this communication was required in each analysis step.

Therefore, in this study, domain decomposition based on elements is conducted on EFMM (see Fig. 9) and using nodes solely in the field, the local elements cluster is generated to develop a stiffness matrix.

This method eliminates data communication of coordinate values at each node even after remeshing. On the other hand, although this is an analysis method based on nodes, local elements clusters are generated in that identical nodes serve as central nodes in multiple fields. The local elements clusters having an identical node as a central node in multiple fields can cover the domain integration, but static condensing that is essential for stiffness matrix process is not performed precisely. Resultantly, an inaccurate stiffness matrix is generated, causing the reduction of analysis accuracy.

Therefore, we performed evaluation regarding the relationship between analysis accuracy of EFMM with the field process based on elements and the number of the parallelization processor. Cantilever model like a Fig. 10 is used in this numerical example. And, example of domain decomposition is shown in Fig. 11. Since the entire stiffness matrix obtained by this method becomes an asymmetric matrix rather than a symmetric matrix that is obtained in original EFMM analysis, a solver that can manage asymmetric matrices such as GPBi-CG method will be needed.

In Fig. 12, x-axis means number of processors, y-axis means normalized displacement. As can be seen in Fig.11, analysis accuracy decreases in inverse proportion to the number of parallelization processors. When field separation is performed, inaccurate local elements clusters are generated near the boundary. The number of the inaccurate local elements clusters increases as the number of analysis separation rises because of the increase of boundaries between each field. Resultantly, inaccurate element stiffness matrices were largely computed, lowering the analysis accuracy.

Nevertheless, based on the tendency of the analysis results, it is suggested that the difference can be miniscule if the number of nodes in the entire analysis field are high. Relative to the enormous increase of the communication cost at the time of accurate parallelization of EFMM based on nodes, this method showed a great benefit.

5 CONCLUSIONS

- In this study, solutions for various problems during the parallelization of fluid-structure coupled analysis using EFMM are proposed.
- The proposed method in this study showed decreasing tendency in the analysis results since this method obtains a different type of a stiffness matrix from the one supposed to be obtained originally. Especially as the number of domain decomposition increases, the abovementioned tendency became prominent from the examples of the numerical analysis. However, it was also revealed that by preparing a large enough number of nodes for analysis, the numerical errors can be minute scales. This method is considered to have a great benefit in terms of the communication cost from accurate parallelization of EFMM.
- When conducting domain decomposition, generation of inaccurate local elements clusters should be minimized as much as possible. To parallelize EFMM, a new domain decomposition method based on nodes should be developed since it is an analysis method based on nodes originally. On the other hand, since a conventional domain decomposition method based on elements can be applied in this method, the communication volume at the analysis as well as inaccurate local elements clusters can be minimized.
- Here are research topics for future studies.
 - Detailed evaluation of parallelization efficiency.
 - Evaluation of analysis accuracy when using a large number of processors.
 - Implementation of the large-scale parallelization fluid-structure coupled analysis combining EFMM applying this method and SUPG/PSPG stabilized FEM.

6 FIGURES

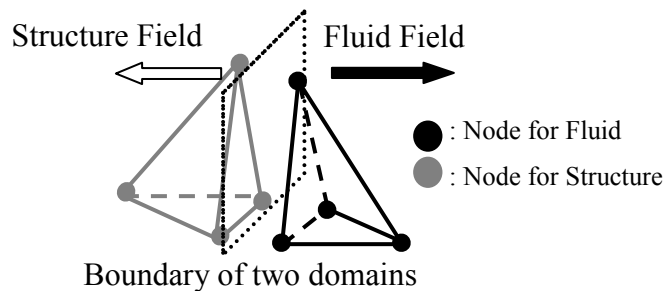


Fig. 1 Boundary of two types of analysis field retaining element formation consistent to each other

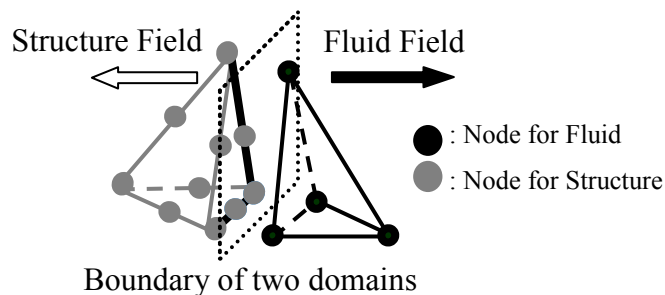


Fig. 2 Boundary of two types of analysis field retaining elements formation inconsistent to each other incompatible boundary

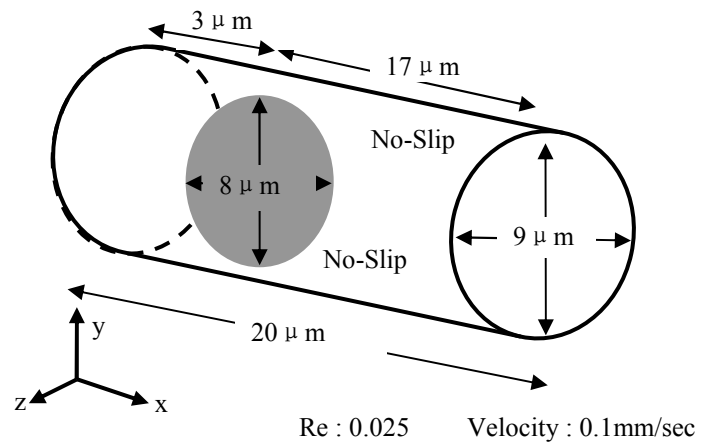


Fig. 3 Analysis model

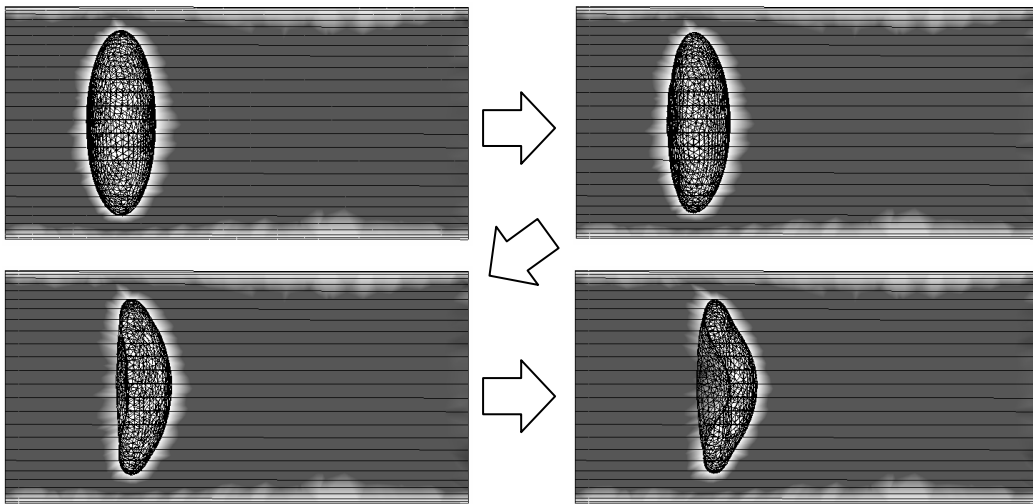


Fig. 4 Fluid analysis result

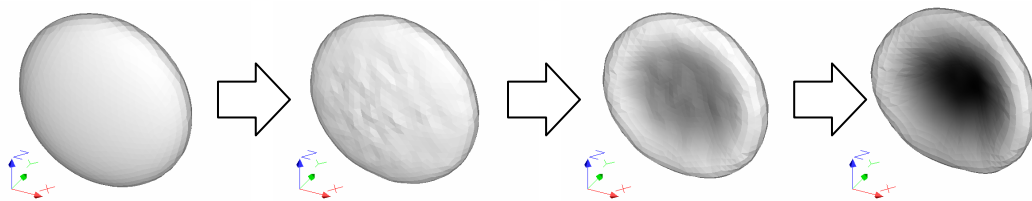


Fig. 5 Structure analysis result

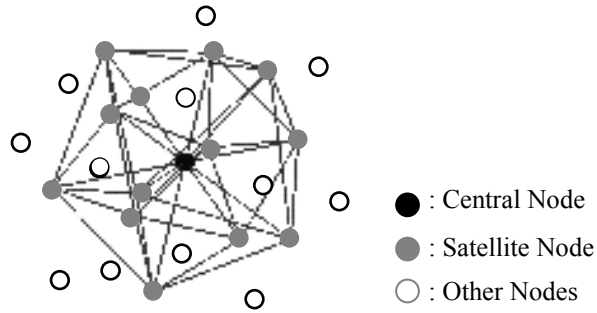


Fig. 6 Fundamental concept of local elements cluster

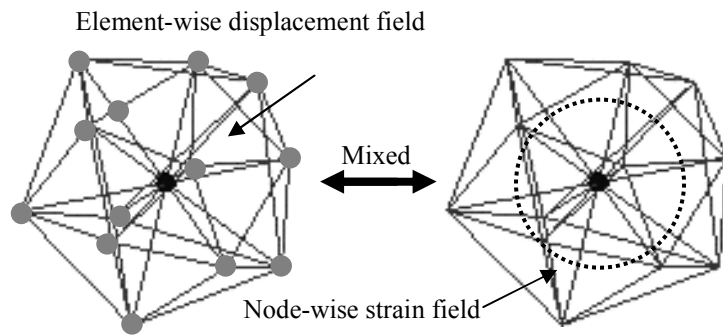


Fig. 7 Two types of field postulated in local elements cluster

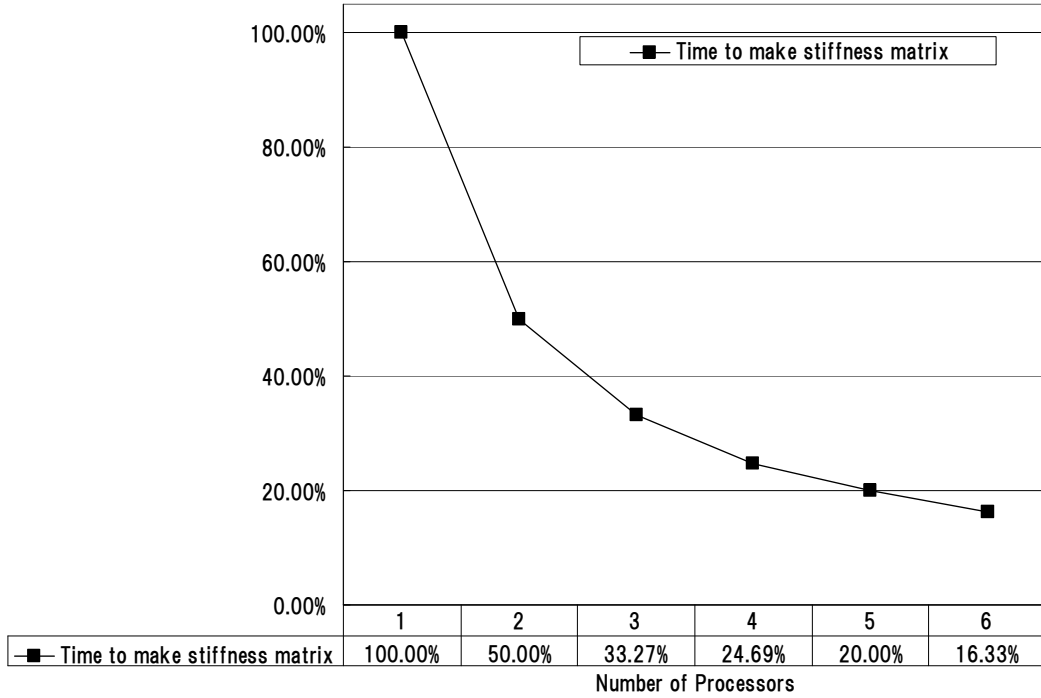


Fig. 8 Relationship between number of processors and time to make stiffness matrix

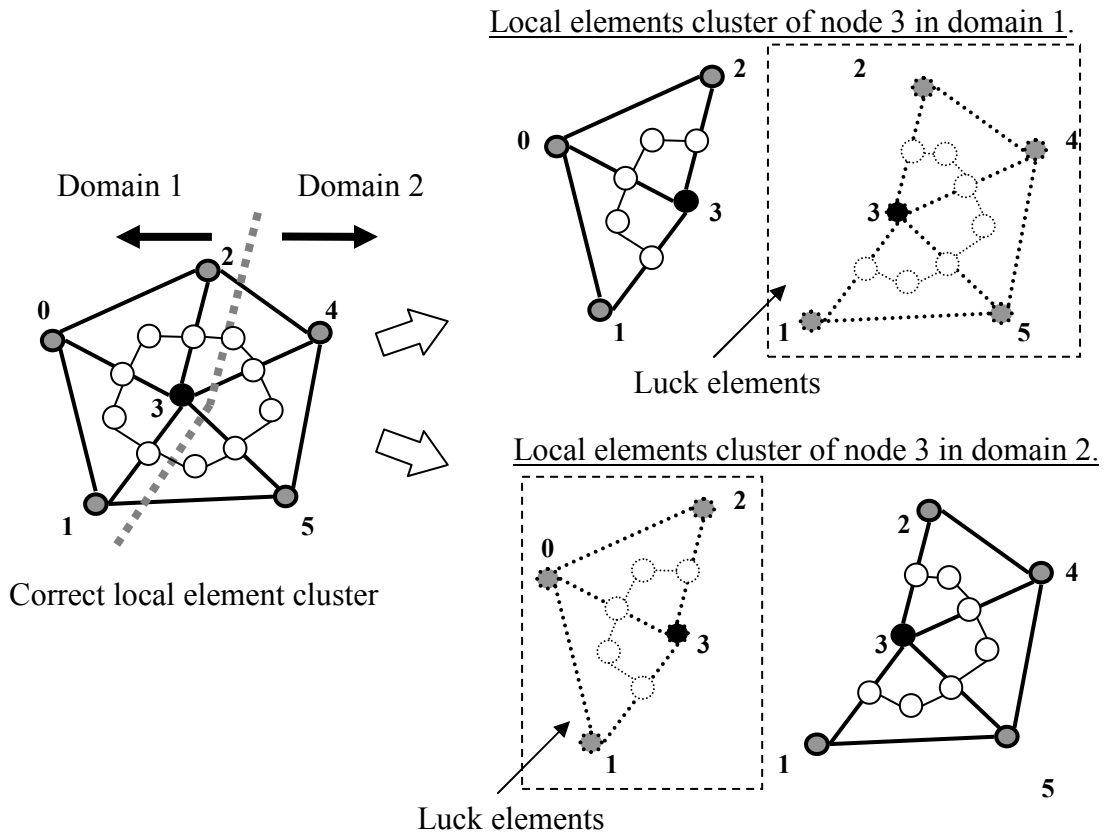


Fig. 9 Example of domain decomposition

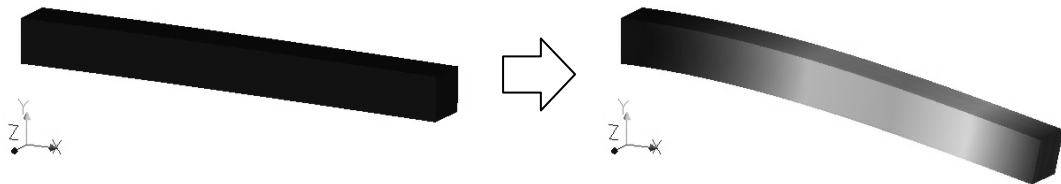


Fig. 10 Cantilever model

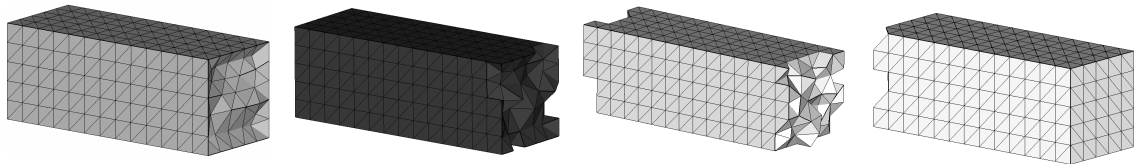


Fig. 11 Example of domain decomposition

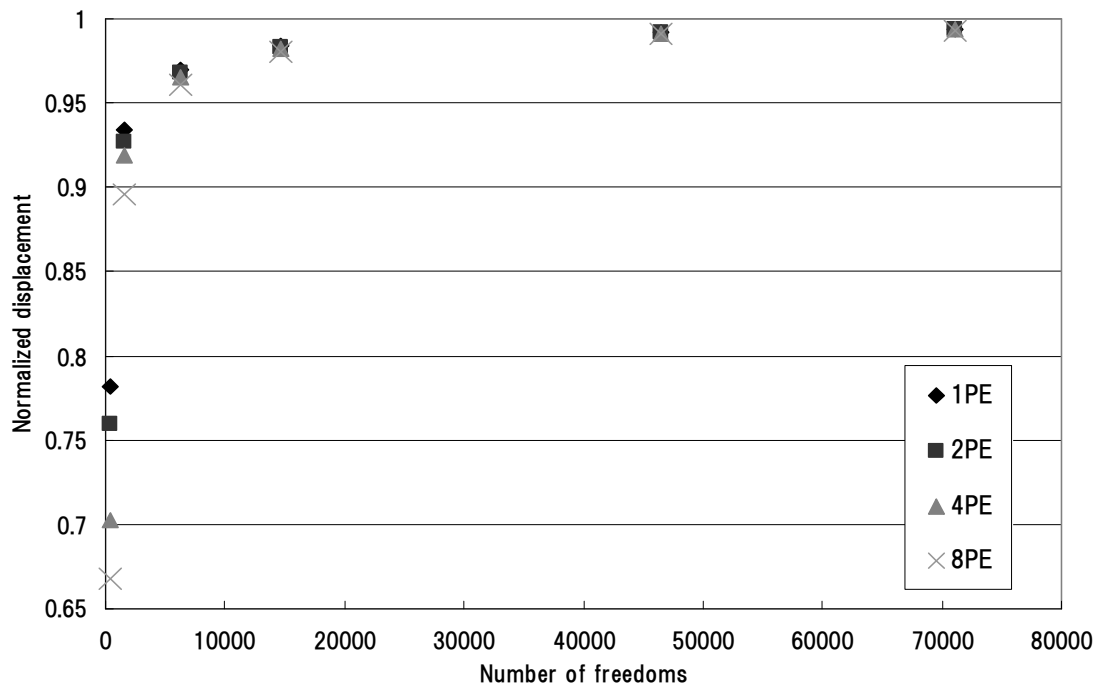


Fig. 12 Relationship between analysis accuracy and number of processors

REFERENCES

- [1] Zienkiewicz OC, Taylor RL, *The finite element method, 5th edn.* Elsevier, Amsterdam, 2000
- [2] Yagawa G, Miyazaki, N, *Handbook for Computational Mechanics*, Asakura Publishing Co., Ltd, 2007
- [3] Yagawa G, Matsubara H, *Enriched free mesh method: an accuracy improvement for node-based fem, computational plasticity.* Comput Methods Appl Sci 7:207-219, 2007
- [4] Brooks AN, Hughes TJR, *Streamline upwind/Petrov Galerkin formulations for convection dominated flows with particular emphasis on the incompressible Navier-Stokes equations*, Comput Methods Appl Mech Eng 32:199-259, 1982
- [5] Tezduyar TE, *Stabilized finite element formulations for incompressible flow computations*, Adv Appl Mech 28:1-44, 1992
- [6] Tezduyar TE, Mittal S, Ray SE, Shih R, *Incompressible flow computations with stabilized bilinear and linear equal-order-interpolation velocity-pressure elements*, Comput Methods Appl Mech Eng 95:221-242, 1992
- [7] Tezduyar TE, *Computation of Moving Boundaries and Interfaces and Stabilization Parameters*, Int J Numer Methods Fluid 43:555-575, 2003
- [8] Tanaka M, Sakamoto T, Sugawara S, Nakajima H, Katahira Y, Ohtsuki S, Kanai H, *Blood flow structure and dynamics, and ejection mechanism in the left ventricle*, J Cardiol 52:86-101, 2008

- [9] Kanno H, Morimoto M, Fujii H, Tsujimura T, Aai H, Noguchi T, Kitamura Y, Miwa S, *Primary structure of marine red blood cell-type Pyruvate Kinase (PK) and molecular characterization of PK deficiency identified in the CBA strain*, Blood 86:3205-3210, 1995
- [10] Yagawa G, Yamada T, *Free mesh method a new meshless finite element method*, Comput Mech 18:383-386, 1996
- [11] Yagawa G, Yamada T, *Performance of Parallel computing of free mesh method*, In: Proceedings of the 45th National Congress of Theoretical & Applied Mechanics, 1996
- [12] Berg M, Cheong , Kreveld M, Overmars M, *Computational geometry : algorithms and applications*, 3rd edn. Springer, New York, 2008
- [13] Inaba M, Fujisawa T, Okuda Y, Yagawa G, *Local mesh generation algorithm for free mesh method*, The Japan Society of Mechanical Engineers [No.02-9] Dynamic and Design Conference, 2002
- [14] Zienkiewicz OC, Taylor RL, *Matrix finite element method I (Revision new publication)*, Kagaku Gijutsu Shuppan, Inc, 1996

REDUCED ORDER MODELLING OF HIGH-FIDELITY COMPUTATIONAL FLUID-STRUCTURE INTERACTION ANALYSIS FOR AEROELASTIC SYSTEMS

Pınar Acar¹ and Melike Nikbay²

^{1, 2} Istanbul Technical University, Maslak, Istanbul, 34469, Turkey
e-mail: acarpin@itu.edu.tr, nikbay@itu.edu.tr

Keywords: Aeroelasticity, Fluid-Structure Interaction, Reduced Order Modelling, Polynomial Chaos Expansion, Proper Orthogonal Decomposition, HIRENASD, S⁴T.

Abstract. *We investigate model reduction techniques through computational aeroelastic analyses of the HIRENASD and S⁴T wings. The aim of the present work is to construct accurate and computationally efficient reduced order models for high-fidelity aeroelastic computations. Firstly, the aeroelastic analyses of the specified wings are performed by high-fidelity structural and aerodynamic models to substantiate the fluid-structure interaction. Concerning high amount of computational time required to perform such high-fidelity fluid-structure interaction analyses, the model orders are reduced by introducing relevant reduction techniques such as Polynomial Chaos Expansion and Proper Orthogonal Decomposition. The final aeroelastic analyses performed on these reduced models agree well with the initial high-fidelity computational analyses.*

1 INTRODUCTION

Model reduction is a powerful numerical approach and has been applied to many disciplines such as fluid dynamics, aeroelasticity, structural dynamics and control. In general, the complex high-fidelity numerical models accurately represent the problem. However, in many cases, a burden of computational time is required to achieve the solution. When this is the case, it is nearly impossible to perform some applications requiring great amount of computational efforts such as uncertainty quantification and multidisciplinary optimization. The reduced models can successfully represent the full model with an optimal basis. Thus, they can save great amount of computational time and effort while modelling the problem and finding its solutions. In the present work, the reduced modelling strategy is used to represent the high-fidelity computational models of the HIRENASD and S⁴T wings to perform static aeroelastic and flutter analyses. The major anticipation from the constructed reduced models is to present accurate solutions while providing a considerable reduction in the computational time. The fundamental steps of the reduced order modelling (ROM) strategy of this work starts with the construction of the high-fidelity computational models. These computational models are developed to perform static aeroelastic analyses of the HIRENASD and S⁴T wings, and flutter analysis of the S⁴T wing in ZEUS software. ZEUS is an Euler Unsteady Aerodynamic Solver developed for aeroelastic solutions of complex geometries [1]. It involves automated mesh generation scheme and overset grid capability for complex configurations while using Cartesian grid and employing boundary layer coupling. It also uses modal data importer and ZAERO 3D spline module, and constructs structural grids. ZEUS uses central difference with JST (Jameson-Schmidt-Turkel) Artificial Dissipation Scheme for flux construction and Green's Integral Boundary Layer Method for turbulence model [1]. Aeroelastic analyses in ZEUS require the own input file and modal solution from the finite element solver. In the present work, Nastran is used as the structural solver for the modal analysis. Aerodynamic mesh is generated and Fluid Structure Interaction (FSI) is provided in ZEUS to perform the required aeroelastic analyses after importing the modal solution. Once the aeroelastic analyses are accomplished for the reference cases, they should be repeated based on the design samples generated to construct the reduced models. After generating an adequate number of sampling, the model reduction is performed by using non-intrusive Polynomial Chaos Expansion (PCE) and Proper Orthogonal Decomposition (POD) methods. Both the PCE and POD methods aim to ameliorate the computational efficiency.

The origin of the PCE is based on homogenous chaos theory of Wiener [2]. The PCE represents the high-fidelity model in terms of generalized orthogonal functions [3]. It estimates coefficients of these orthogonal polynomials based on a set of response function evaluations and makes use of sampling and linear regression. In literature, the PCE method is generally used to quantify uncertainties in a computational problem. For example, Eldred and Burkardt [4] investigated the non-intrusive PCE method to quantify the uncertainties in different example problems and compared its results with Stochastic Collocation Method. Witteveen and Bijl [5] applied PCE to the problems with nonlinear input variables and compared their results with Monte Carlo Simulation (MCS) method. Reduced models are useful for examining responses near the mean values. However, they are not capable of predicting responses with large variations in the input [6]. With an exception, the PCE method allows large variations in the input parameters and is far more efficient than MCS [7]. In the present work, the PCE method is used to construct reduced models in order to investigate its accuracy when small variations are considered. The results of the PCE are then compared to the results of the POD based reduced models and the high-fidelity computational models.

The POD method, which is also known as Karhunen-Loeve decomposition [8, 9] or principal component analysis [10], is an efficient method that has been widely utilized for model reduction of large-scale systems [11]. It defines the given higher-order system as a linear combination of independent and orthogonal basis functions. The POD method has numerous application areas such as fluid dynamics [12, 13], aeroelasticity [14, 15] and design optimization [16, 17]. This method is an extension of the numerical technique known as Singular Value Decomposition (SVD). For example, Chatterjee [18] discussed POD and SVD with their applications to two example problems: low-rank approximations of a surface and a posteriori analysis of data from a simulated vibroimpact system respectively. The first example problem of his study is also used as a benchmark problem in the present work for validation purpose. Pinnau [19] applied POD method to a heat transfer problem specified by a nonlinear parabolic partial differential equation. Zhang et. al [20] applied POD method to the study of the aerodynamics of a membrane wing under the MAV flight condition. The choice of the data set plays a crucial role to construct reduced models based on POD method. There are different techniques to apply the POD method such as balanced POD [11] and constrained POD scheme [21]. However, the most prominent is the method of snapshots introduced by Sirovich [22], which is also the main approach of the POD method in the present work. In this method, the data set is chosen as snapshots that include the spatial distribution of a numerical simulation and should reflect the system characteristics.

In the final step of the present work, the static aeroelastic and flutter analyses of the HIRENASD and S⁴T wings are performed for the reference cases by using the PCE and POD based reduced models. Then, the accuracies of the reduced models are compared to the high-fidelity computational models. Both the PCE and POD methods give satisfactory results while their accuracies will be investigated in a more detailed manner throughout the present work. But first, the theoretical background of the FSI will be discussed and then the computational aeroelastic models for the HIRENASD and S⁴T wings will be introduced. After completing the aeroelastic analyses based on the reference data, the main focus of the present study will be on model reduction strategy and applications.

2 THEORETICAL BACKGROUND

The present work firstly concentrates on the static aeroelastic analyses of the HIRENASD and S⁴T wings, and flutter analysis of the S⁴T wing. All the aeroelastic analyses require structural and aerodynamic modelling, and FSI to determine the output parameters. Here, the aerodynamic modelling and FSI are constructed by using ZEUS software.

ZEUS is ZONA's Euler Unsteady Aerodynamic Solver that integrates the essential disciplines required for aeroelastic design and analysis [23]. It uses an Euler equation solver with/without viscous effects as the underlying aerodynamic force generator coupled with the structural finite element modal solution to solve various aeroelastic problems such as flutter, maneuver loads, store ejection loads, gust loads, and static aeroelastic/trim analysis. In the present work, the modal solutions for the HIRENASD and S⁴T wings are based on NASA's structural models developed in Nastran software.

The Euler equation solver of ZEUS employs the Euler equations on a Cartesian grid system using a cell-centered finite volume method with dual-time stepping algorithm for unsteady solutions. The viscous effects are included by coupling the Euler solution with a steady boundary-layer equation. For turbulence closure, the Green's lag entrainment is employed. Because of solving the Euler equations with boundary layer coupling, the requirement of large computing resources by a Navier-Stokes code can be avoided by ZEUS. Therefore, ZEUS provides a good

balance between the complete modelling of the flow physics and the computational efficiency [23].

2.1 Unsteady Euler Solver on Stationary Cartesian Grid

ZEUS is an unsteady aerodynamics generator based on a stationary Cartesian grid. It solves the time-accurate Euler equations using a cell-centered central-differencing finite-volume method with JST artificial dissipation scheme [24] implemented for stability of the flow solver [23].

2.1.1 Time-Accurate Euler Method

The three-dimensional unsteady Euler equations in conservative differential form and in curvilinear coordinates can be defined as follows:

$$\frac{\partial Q}{\partial t} + \frac{\partial H_1}{\partial \xi} + \frac{\partial H_2}{\partial \eta} + \frac{\partial H_3}{\partial \zeta} = 0 \quad (1)$$

where Q is the product of conservative flow variables vector, q , and the inverse of the transformation Jacobian, J . H_1 , H_2 and H_3 are convective fluxes in three curvilinear coordinate directions where:

$$Q = Jq = J \begin{bmatrix} \rho \\ \rho u \\ \rho v \\ \rho w \\ e \end{bmatrix}; \quad H_1 = J \begin{bmatrix} \rho U \\ \rho u U + p \xi_x \\ \rho v U + p \xi_y \\ \rho w U + p \xi_z \\ (e + p) U - p \xi_t \end{bmatrix}$$

$$H_2 = J \begin{bmatrix} \rho V \\ \rho u V + p \eta_x \\ \rho v V + p \eta_y \\ \rho w V + p \eta_z \\ (e + p) V - p \eta_t \end{bmatrix}; \quad H_3 = J \begin{bmatrix} \rho W \\ \rho u W + p \zeta_x \\ \rho v W + p \zeta_y \\ \rho w W + p \zeta_z \\ (e + p) W - p \zeta_t \end{bmatrix}$$

U, V, W and u, v, w are the three components of the flow velocity in curvilinear and Cartesian coordinates, respectively.

2.2 Computational Aeroelastic Analysis

The computational aeroelastic analysis requires the interaction between the structural modal solution of Nastran and the aerodynamic model constructed in ZEUS. The FSI is also provided in ZEUS software to perform both static aeroelastic and flutter analyses. For a general aeroelastic system, the time-dependent equations of motion can be defined as shown below:

$$[M] \{\ddot{u}\} + [C] \{\dot{u}\} + [K] \{u\} = \{F_a\} + \{F_e\} \quad (2)$$

where $[M]$, $[C]$ and $[K]$ are generalized mass, damping and stiffness matrices while $[F_a]$ shows steady forces matrix, $[F_e]$ denotes time-dependent external forces matrix and $\{u\}$ is the displacement vector. The above equation must be considered for the flutter analyses. However, the time dependent terms and external forces should be omitted for static aeroelastic analyses:

$$[K] \{u\} = \{F_a\} \quad (3)$$

3 COMPUTATIONAL AEROELASTIC ANALYSES OF THE HIRENASD AND S⁴T WINGS

The static aeroelastic and flutter analyses of the HIRENASD and S⁴T wings are accomplished in ZEUS. The aeroelastic analyses concentrate on the calculation of steady aerodynamic coefficients for both the HIRENASD and S⁴T wings, and also determination of the flutter boundaries of the S⁴T wing. In the following two sections, these analyses and outcomes will be evaluated in more details.

3.1 Static Aeroelastic Analysis of the HIRENASD Wing

The first application of this section is the static aeroelastic analysis of the HIRENASD (HIGH REynolds Number Aero-Structural Dynamics) wing to determine steady aerodynamic coefficients. The HIRENASD project was initiated at RWTH Aachen University in 2004. The main purpose of this project is to analyze steady and unsteady aeroelastic experiments in transonic flight regime with a supercritical elastic wing model [25]. The HIRENASD wind-tunnel model was tested in the European Transonic Windtunnel (ETW) in 2006 by Aachen University's Department of Mechanics with funding from the German Research Foundation [26]. The test medium of ETW is nitrogen gas under cryogenic conditions [25]. The wing has a 34° degree of backward sweep angle and a supercritical wing profile BAC 3-11. The aerodynamic reference area is 0.3926 m² while the mean chord length is 0.3445 m [25]. The HIRENASD wing model planform and assembly are illustrated in Fig. 1. Further explanations and elaborations for the wing properties, computational models used to perform the aeroelastic analyses, and static response data can be found in the former study of Nikbay et. al [27].

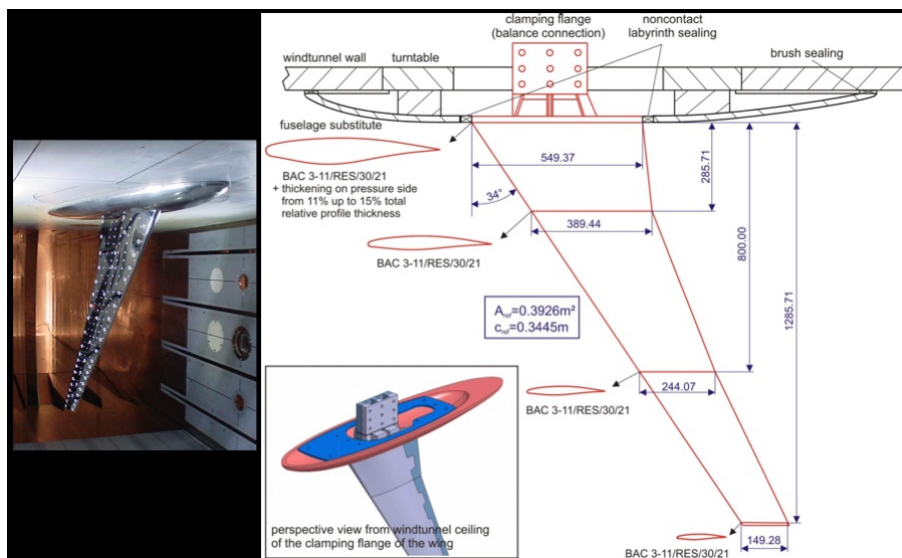


Figure 1: Model planform and assembly of the HIRENASD wing [26].

The steady aeroelastic analysis of the HIRENASD wing is accomplished for the "Low Reynolds Case" [27]. The free vibration analysis is performed in Nastran, and then this modal solution is used as the structural model in the aeroelastic solution by ZEUS. The modal analysis is based on the latest HIRENASD FEM model of NASA, HIRENASD Modeshapes Nov 2011 Model [28]. The aerodynamic mesh is generated in ZEUS by using 164 x 62 x 55 block elements. The convergence of the calculated aerodynamic coefficients is shown in Fig. 2.

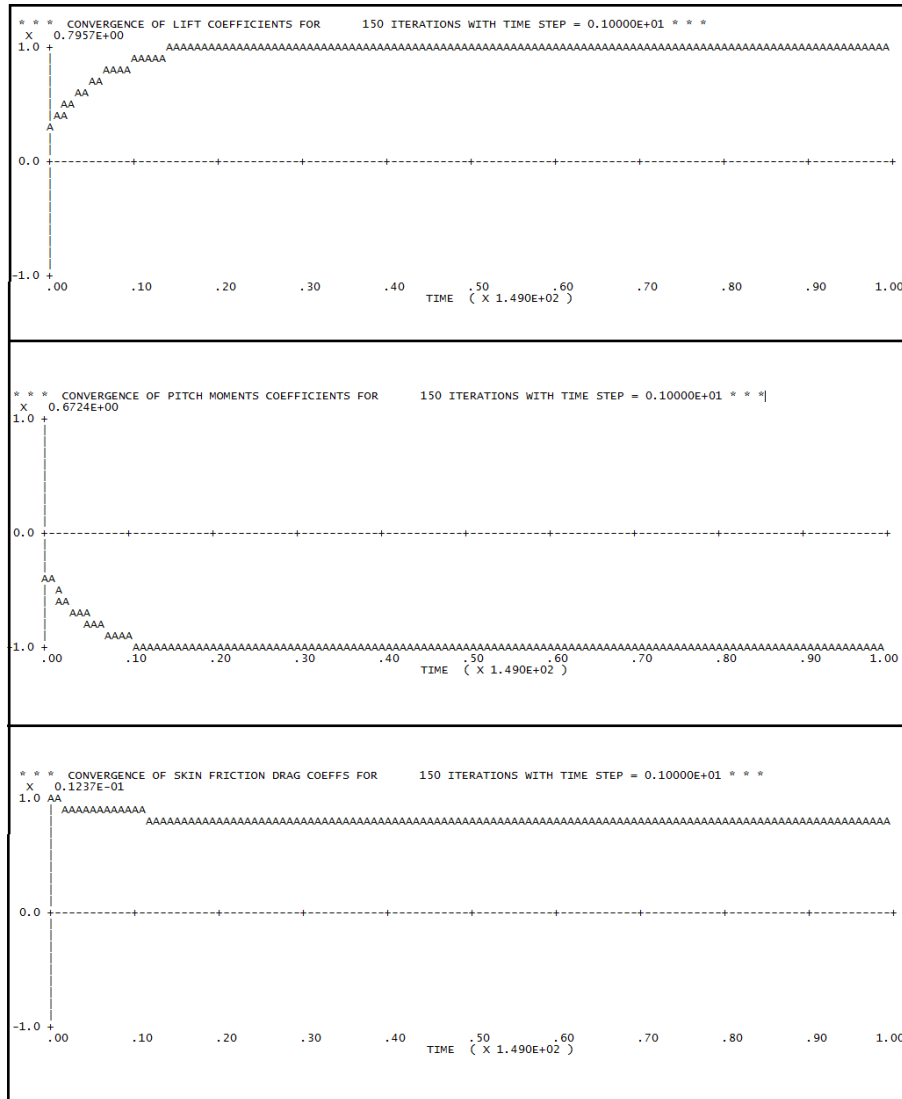


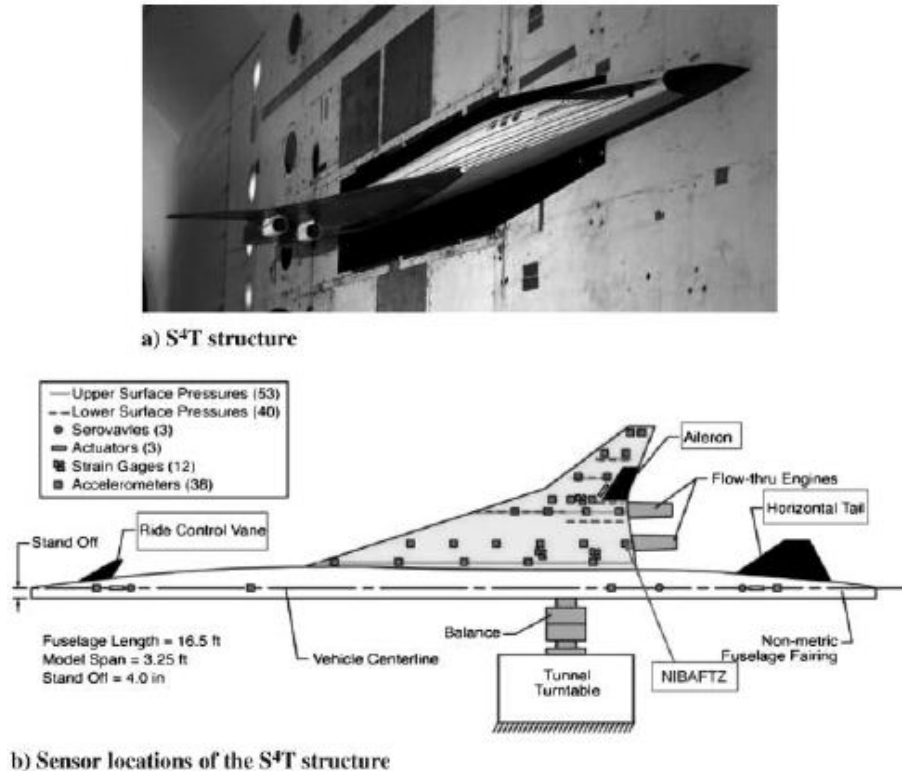
Figure 2: Convergence of aerodynamic coefficients for the HIRENASD wing.

3.2 Static Aeroelastic and Flutter Analyses of the S⁴T Wing

The second application for the present work relates to the static aeroelastic and flutter analyses of the S⁴T wing. The S⁴T wing is a complex aeroelastic semi-span wind-tunnel model, which is designed for aeroelastic/aeroservoelastic analysis [29]. The wind-tunnel model is 16.5 ft in length with a model span of 3.25 ft. The fuselage of the wing consists of a graphite-epoxy flexible beam attached to an aluminum C-channel rigid beam. Fig. 3 shows the wing configuration.

Since a series of wind tunnel tests of the S⁴T model for the Mach numbers ranging from 0.6 to 1.2 have been performed at NASA Langley Research Center to measure the steady and unsteady characteristics, the output parameters are specified as steady lift, moment and drag coefficients, flutter speed and flutter dynamic pressure to provide comparable computational data for all cases. First, the structural model of NASA is used to perform the modal analysis and then the aerodynamic mesh is constructed in ZEUS (Fig. 4). The size of aerodynamic block mesh (Fig. 5) is 143 x 82 x 78.

The static aeroelastic analysis employs the first 25 structural modes. However, 10 structural

Figure 3: S⁴T wing configuration [30].

modes are used in the flutter analysis to reduce the computational time since the flutter analysis takes about 8 hours. The flutter analysis results for the S⁴T wing cases are summarized in Table 1 while the steady coefficients will be given with the results of the reduced models in Table 3. The variation of flutter dynamic pressure with respect to Mach number is illustrated in Fig. 6.

4 GENERAL CONCEPTS OF ROM METHODS

The reduced modelling strategy is fundamentally based on a disparate approach compared to high-fidelity computational models. In terms of accuracy, the main focus of model reduction is to form an almost equivalent surrogate for computationally expensive models. Acquisition of the reduced models requires few high-fidelity computational analyses depending on the number of specified input parameters, complexity of the high-fidelity models and expected accuracy level. Once the representative model is constructed, further analyses with various values of the input variables can be accomplished via this reduced model. Since an in-house computational code is developed for each model reduction technique introduced by the present work, the computational time significantly decreases compared to the time requirement of the high-fidelity computational models. The model reduction techniques are utilized throughout the present study considering two different applications. The first application focuses on static aeroelastic responses of the HIRENASD wing while the second case relates to both static and flutter analyses of the S⁴T wing.

In this section, the numerical techniques used to generate a reduced model basis are introduced at first. Then, these methods are verified by using a benchmark problem from literature. Detailed comparison for the accuracy of the PCE and POD based reduced models with the high-fidelity computational analyses clarifies the importance of considered sample number, ap-

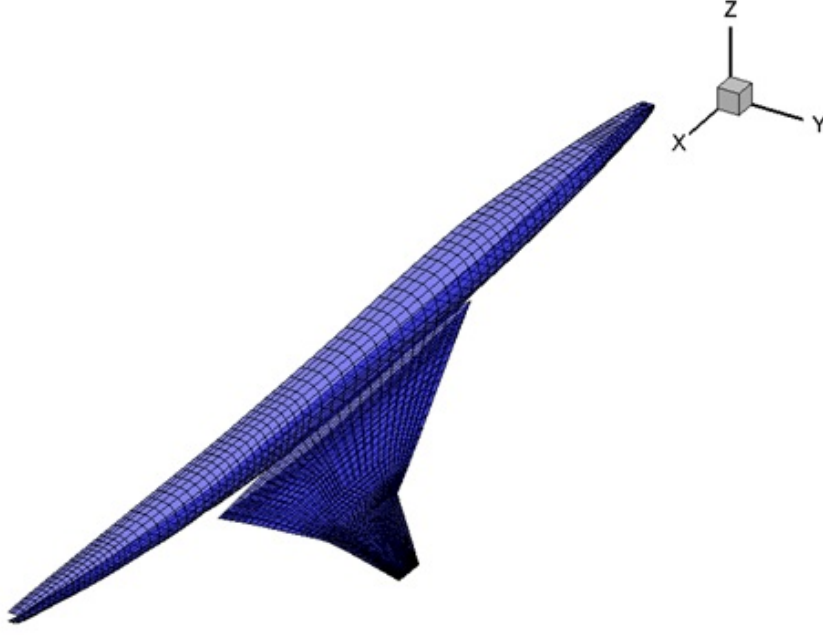


Figure 4: Aerodynamic surface mesh of the S⁴T wing.

proximation order and computational complexity.

4.1 Polynomial Chaos Expansion (PCE)

Non-intrusive PCE defines a reduced model basis in terms of orthogonal polynomials. In the present study, the Hermite polynomials are used as the orthogonal polynomials. The definition of the first few Hermite polynomials are given below in terms of the standard variable, ξ :

$$H_0(\xi) = 1 \quad (4)$$

$$H_1(\xi) = \xi \quad (5)$$

$$H_2(\xi) = \xi^2 - 1 \quad (6)$$

$$H_3(\xi) = \xi^3 - 3\xi \quad (7)$$

$$H_4(\xi) = \xi^4 - 6\xi^2 + 3 \quad (8)$$

$$H_5(\xi) = \xi^5 - 10\xi^3 + 15\xi \quad (9)$$

$$H_6(\xi) = \xi^6 - 15\xi^4 + 45\xi^2 - 15 \quad (10)$$

The chaos coefficients can be calculated by using the following relation for a two-dimensional system:

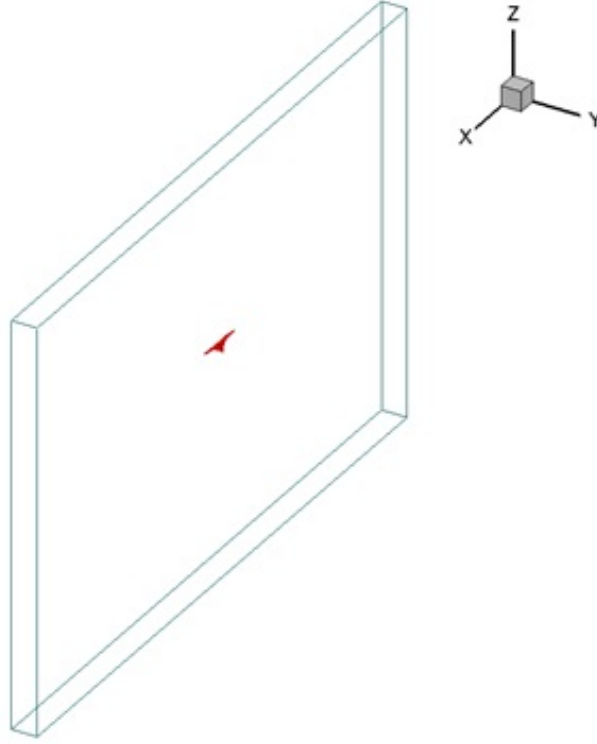


Figure 5: Aerodynamic block element of the S⁴T wing.

$$\begin{pmatrix} u_1 \\ u_2 \\ \cdot \\ \cdot \\ u_n \end{pmatrix} = \begin{bmatrix} H_{01} & H_{11} & \cdot & \cdot & H_{p1} \\ H_{02} & H_{12} & \cdot & \cdot & H_{p2} \\ \cdot & \cdot & \cdot & \cdot & \cdot \\ \cdot & \cdot & \cdot & \cdot & \cdot \\ H_{0n} & H_{1n} & \cdot & \cdot & H_{pn} \end{bmatrix} \begin{pmatrix} a_1 \\ a_2 \\ \cdot \\ \cdot \\ a_p \end{pmatrix} \quad (11)$$

where u_i ($i = 1$ to n) is output response which is known from the analyses and a_j ($j = 1$ to p) shows chaos coefficients to be determined. The order of the approximation is denoted by p and n shows the dimension. In this matrix system, the parameters H_{ji} indicate the multiplication of H_j and H_i functions defined in Eq. (4) to (10). However, in two-dimensional case, H_j is the function of the first standard random variable, ξ , while H_i is the function of the second standard random variable, η . The reduced model can be constructed by using the chaos coefficients. In order to calculate the chaos coefficients, linear regression can be applied. Considering the standard normal variables ξ and η , a general linear regression model can be defined in closed form as below:

$$U = H\hat{a} + \varepsilon \quad (12)$$

The regression coefficients, \hat{a} , can be computed by using Eq. (13):

$$\hat{a} = (H^T H)^{-1} H^T U \quad (13)$$

M	ρ (slin/in ³)	ω_f (Hz)	Q_f (psf)	U_f (ft/s)	Flutter Mode
0.60	6.958E-8	7.836	79.992	333	2
0.65	5.929E-8	7.809	79.292	360.75	2
0.70	5.112E-8	7.781	78.788	388.50	2
0.75	4.453E-8	7.746	78.420	416.25	2
0.80	3.914E-8	7.709	78.153	444	2
0.85	3.467E-8	7.663	77.960	471.25	2
0.90	3.093E-8	7.592	77.818	499.50	1
0.95	2.603E-8	7.587	75.002	527.25	1
1.05	2.840E-8	7.821	89.986	582.75	2
1.10	2.588E-8	7.832	99.994	610.50	2
1.15	2.723E-8	7.825	114.977	638.25	2
1.20	2.827E-8	7.828	130.003	666	2

Table 1: Flutter results for the S⁴T wing.

After determining the regression coefficients, the reduced model for the reference initial design can be constructed by using the below relation:

$$U_j(\xi^*, \eta^*) = a_1 H_{0j}(\xi^*, \eta^*) + a_2 H_{1j}(\xi^*, \eta^*) + \dots + a_p H_{pj}(\xi^*, \eta^*) \quad (14)$$

where ξ^* and η^* are the values of the standard random variables in the initial design.

4.1.1 Validation of PCE

The PCE method is firstly validated by an example problem [2] which is defined as:

$$z(x, t) = e^{-|(x-0.5)(t-1)|} + \sin(xt), \quad 0 \leq x \leq 1, \quad 0 \leq t \leq 2 \quad (15)$$

The solution to this function is computed for the uniformly distributed 25 x points and 50 t points. Table 2 shows the relative error values with respect to the order of approximations and the number of samples while the analytical model and the PCE approximations are also plotted together (Fig. 7). The figures correspond to the 100000 samples.

The results conclude that a higher order approximation gives more accurate results. Moreover, the number of samples used to calculate the chaos coefficients significantly affects the accuracy level. Since randomly distributed samples are used in this example, it is quite difficult to determine an optimum sample number for the non-intrusive calculation.

4.2 Proper Orthogonal Decomposition (POD)

POD method is explored to construct reduced models for the static aeroelastic and flutter analyses of the HIRENASD and S⁴T wings. The present section introduces the general mathematical concepts for the POD method.

The data obtained from any physical model has regularities. The POD is generally used in the presence of regularities in order to reduce the model. In the POD method, the effect of the first mode is the highest and the second mode is less effective than it and so on. The system is defined as a linear combination of independent and orthogonal basis functions. The functions

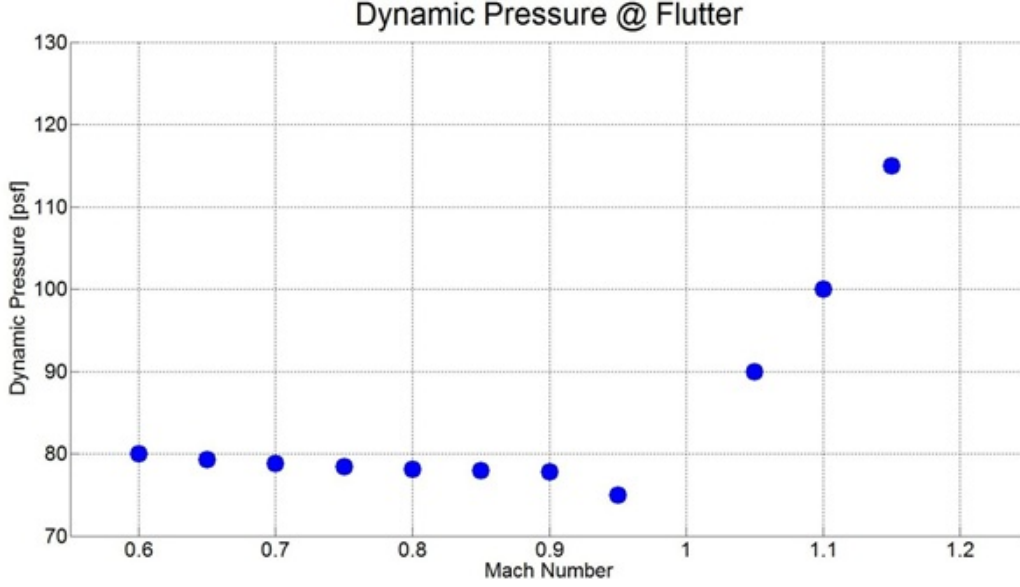


Figure 6: Dynamic pressure - Mach number relation for the S⁴T wing.

are known as "POD basis functions" and required to represent the reduced model. An n th order physical model can be expressed as a linear combination given as below:

$$M = a_1\varphi_1 + a_2\varphi_2 + \dots + a_k\varphi_k \quad (16)$$

where M is an output response for a snapshot of the variables, a_i are POD coefficients, φ_i are POD basis functions and k is the order of reduced model ($k < n$). In this study, the "method of snapshots" is used for ROM. This method represents any given physical system with a snapshot matrix with responses representing the basic features of the model. The correlation matrix is defined in terms of the snapshot matrix and the number of POD basis vectors:

$$C = \frac{1}{n}T.T^T \quad (17)$$

where the snapshot matrix, T , is an $n \times m$ matrix (m is number of snapshots) and can be constructed by using the output parameters. The POD basis vectors and coefficients are calculated through the eigenvalues and eigenvectors of the correlation matrix. The number of required POD basis vectors (POD modes) is computed by considering the captured energy from the original model. The total captured energy is defined in Eq. (18).

$$E_{total} = \sum_{i=1}^n \lambda_i \quad (18)$$

where λ is normalized eigenvalues of the correlation matrix, C , and n is the required number of POD modes to reach the specified captured energy level. In the present work, the captured energy level is taken 99.9 % in all applications.

The construction of the POD based reduced models requires the use of SVD technique. In this method, the factorization of a real matrix, T is given below:

$$[T]_{k \times p} = [P]_{k \times k}[\Gamma]_{k \times p}[V]_{p \times p}^T \quad (19)$$

Approximation Method	Sample Number	Error
2 nd Order PCE	10	13.93%
2 nd Order PCE	100	8.00%
2 nd Order PCE	1000	7.42%
2 nd Order PCE	100000	7.41%
4 th Order PCE	10	172.78%
4 th Order PCE	100	3.74%
4 th Order PCE	1000	3.21%
4 th Order PCE	100000	3.18%
6 th Order PCE	10	399.71%
6 th Order PCE	100	1.61%
6 th Order PCE	1000	1.18%
6 th Order PCE	100000	1.18%

Table 2: Error values for different order PCE approximations and sample numbers.

where P , the columns of which consist of the eigenvectors of $[T][T]^T$ is left singular vector of T while V , the columns of which consist of the eigenvectors of $[T]^T[T]$ is right singular vector of T . $[\Gamma]$ is a diagonal matrix representing the square roots of POD eigenvalues, λ_i . The POD coefficients can be computed by using the relation below:

$$a_i = T^T \cdot \varphi \quad (20)$$

4.2.1 Validation of POD

For validation, the same example problem given in Eq. (16) is considered. Fig. 8 shows the analytical solution and POD solutions for different mode numbers while Table 3 shows the relative error values with respect to the analytical solution for the POD method with different mode numbers and PCE with different orders. The total number of samples is 1250 for all cases in order to compare the POD and PCE methods.

Method	Relative Error
POD (1 mode)	7.94%
POD (2 modes)	5.56%
POD (3 modes)	0.12%
POD (4 modes)	0.029%
POD (5 modes)	0.0005%
PCE (2 nd Order)	7.46%
PCE (4 th Order)	3.16%
PCE (6 th Order)	1.27%

Table 3: Comparison of different ROM techniques for the example problem.

The above table basically indicates that the POD gives quite accurate results beginning from 3 modes. The accuracy level of the PCE is much lower than POD even a higher order approximation is used. The accuracy of the PCE can still be enhanced, however, in this case the

computational procedure will certainly become more complex. On the hand, the accuracy level of the POD can easily be increased if needed since using additional POD modes is just a simple computational step in programming.

5 PCE AND POD BASED ROM FOR STATIC AEROELASTIC ANALYSIS OF THE HIRENASD WING

In the present work, the model reduction techniques are firstly applied to the high-fidelity computational model of the HIRENASD wing. The reduced model depends on the aerodynamic input parameters selected as Mach number and angle of attack while steady lift, drag and moment coefficients are investigated as output static responses. The ROM strategy is based on the 6th order PCE and POD. The PCE and POD calculations are again 2-dimensional since two input variables (angle of attack and Mach number) are specified. 40 generated random design samples are found to provide satisfactory results with respect to the high fidelity static analysis with ZEUS software. These samples are used to construct the PCE and POD based reduced models for static aeroelastic response of the HIRENASD wing for Low Reynolds test conditions. For the PCE based reduced model, Fig. 9-11 illustrate the step-by-step values of the output parameters with respect to the number of design samples while Fig. 12 shows the error values of the output parameters with respect to the sample number. The results of the PCE and POD based reduced models are given by Table 4.

Parameter	Computational	PCE-ROM	PCE Error	POD-ROM	POD Error
c_L	0.3966	0.3982	0.4098%	0.3986	0.5039%
c_D	0.1188	0.1198	0.8027%	0.1190	0.1561%
c_M	-0.6665	-0.6753	1.3144%	-0.6603	0.9345%

Table 4: Results and relative errors for reduced models.

The calculated error values for 40 design samples seem to be sufficient, however, it can be enhanced by the use of more design samples or other sampling methods. The PCE and POD based reduced models give similar results in this application.

6 PCE AND POD BASED ROM FOR STATIC AEROELASTIC AND FLUTTER ANALYSES OF THE S⁴T WING

The ROM strategy is secondly applied to the high-fidelity computational aeroelastic model of the S⁴T wing. The 6th order PCE and POD methods are used to represent the static aeroelastic and flutter analyses of the S⁴T wing. In these studies, the input parameters are defined as Mach number and angle of attack while steady lift, moment and drag coefficients, flutter dynamic pressure and flutter speed are designated as output variables. The random sampling set is generated by considering $M = 0.6$ case where angle of attack varies between -0.3 and 1.0 degrees. 24 design samples are generated to construct the reduced models. Fig. 13-17 show the convergence of the PCE and POD based reduced models to the reference analysis, which was performed for $M = 0.6$ and $\alpha=0^\circ$ case. The results of the PCE and POD based reduced models and the reference analysis are depicted by Table 5 while the relative error values for the constructed reduced models can be investigated via Table 6. Table 6 clearly shows that the PCE and POD techniques provide sufficient accuracy levels. However, the POD method gives more accurate results as in the static aeroelastic model of the HIRENASD wing.

Method	c_L	c_D	c_M	V_f (ft/s)	Q_f (psf)
Reference	-0.0708834	0.00329277	-0.00392818	332.9993107	79.99559666
PCE-ROM	-0.0737	0.0032	-0.0039	332.9653	79.9801
POD-ROM	-0.0695	0.0034	-0.0039	332.9957	79.9928

Table 5: Results of reference analysis, and PCE and POD based ROMs for the S⁴T wing.

Method	Error of c_L	Error of c_D	Error of c_M	Error of V_f	Error of Q_f
PCE	3.974 %	2.817 %	0.717%	0.010%	0.019%
POD	1.952%	3.257%	0.717%	0.001%	0.003%

Table 6: Relative error values of the PCE and POD methods for the S⁴T wing.

7 CONCLUSIONS AND FUTURE WORK

The present work introduces reduced modelling strategy based on PCE and POD techniques. The model reduction is performed to represent the high-fidelity computational aeroelastic analyses of the HIRENASD and S⁴T wings. First, the initial high-fidelity aeroelastic analyses are accomplished by using Nastran and ZEUS software. After the construction of the PCE and POD based reduced models, the reference aeroelastic analyses are also performed via these models. Both the PCE and POD methods give satisfactory results. However, the POD method is just a step ahead in terms of accuracy.

For future work, the computational efficiency of the reduced models can be exploited more. For instance, instead of using high-fidelity computational models, the structural and aerodynamic uncertainties may be quantified through the reduced models to save computational time.

REFERENCES

- [1] P. C. Chen, Z. Zhang, A. Sengupta and D. Liu, Overset Euler/Boundary Layer Solver with Panel Based Aerodynamic Modeling for Aeroelastic Applications. *Journal of Aircraft*, Vol. 46, No. 6, pp. 2054-2068, 2009.
- [2] N. Wiener, The homogenous chaos. *American Journal of Mathematics*, Vol. 60, pp: 897-936, 1938.
- [3] M. S. Eldred, Recent Advances in Non-Intrusive Polynomial Chaos and Stochastic Collocation Methods for Uncertainty Analysis and Designs. *50th AIAA/ASME/ASCE/AHS/ASC Structures, Structural Dynamics, and Materials Conference*, AIAA 2009-2274, Palm Springs, California, USA, 2009.
- [4] M. S. Eldred and J. Burkardt, Comparison of Non-Intusive Polynomial Chaos and Stochastic Collocation Methods for Uncertainty Quantification. *47th AIAA Aerospace Sciences Meeting and Exhibit*, AIAA 2009-0976, Orlando, FL, USA, 2009.
- [5] J. A. S. Witteveen and H. Bijl, Using Polynomial Chaos for Uncertainty Quantification in Problems with Nonlinearities. *47th AIAA/ASME/ASCE/AHS/ASC Structures, Structural Dynamics, and Materials Conference*, AIAA 2006-2066, Newport, Rhode Island, USA, 2006.

- [6] P. Beran and W. Silva, Reduced Order Modeling: New Approaches to Computational Physics. *39th AIAA Aerospace Sciences Meeting and Exhibit*, AIAA 2001-0853, Reno, NV, USA, 2001.
- [7] R. G. Ghanem and P. D. Spanos, Stochastic Finite Element Methods: A spectral Approach. Springer-Verlag, 1991.
- [8] K. Karhunen, Zur Spektraltheorie stochastischer Prozesse. *Ann. Acad. Sci. Fennicae. Ser. A. I. Math.-Phys.*, 1946 (34): 7, 1946.
- [9] M. Loeve, Fonctions aleatoire de second ordre. *Revue*, 48: 195-206, 1946.
- [10] H. Hoetelling, Simplified calculation of principal component analysis. *Psychometrika*, 1: 27-35, 1935.
- [11] T. Bui-Thanh and K. Willcox, Model Reduction for Large Scale CFD Applications Using the Balanced Proper Orthogonal Decomposition. *17th AIAA Computational Fluid Dynamics Conference*, AIAA 2005-4617, Toronto, Canada, 2005.
- [12] P. A. LeGresley and J. Alonso, Investigation of Non-Linear Projection for POD Based Reduced Order Models for Aerodynamics. *39th AIAA Sciences Meeting and Exhibit*, AIAA 2001-0926, Reno, NV, USA, 2001.
- [13] K. C. Hall, J. P. Thomas and E. H. Dowell, Investigation of Non-Linear Proper Orthogonal Decomposition Technique for Transonic Unsteady Aerodynamic Flows. *AIAA Journal*, Vol. 38, No. 10, pp: 1853-1862, 2000.
- [14] J. P. Thomas, E. H. Dowell and K. C. Hall, Three-Dimensional Transonic Aeroelasticity Using Proper Orthogonal Decomposition-Based Reduced-Order Models. *Journal of Aircraft*, Vol. 40, No. 3, pp: 544-551, 2003.
- [15] T. Lieu and M. Lesoinne, Parameter Adaptation of Reduced Order Models for Three-Dimensional Flutter Analysis. *42nd AIAA Aerospace Sciences Meeting and Exhibit*, AIAA 2004-888, Reno, Nevada, USA, 2004.
- [16] M. Allen, G. Weickum and K. Maute Application of Reduced Order Models for the Stochastic Design Optimization of Dynamic Systems. *10th AIAA/ISSMO Multidisciplinary Analysis and Optimization Conference*, AIAA 2004-4614, Albany, NY, USA, 2004.
- [17] R. F. Coelho, P. Breitkopf and C. Knopf-Lenoir, Model reduction for multidisciplinary optimization - application to a 2D wing. *Structural and Multidisciplinary Optimization*, Vol. 37, No. 1, pp: 29-48, 2008.
- [18] A. Chatterjee, An Introduction to the Proper Orthogonal Decomposition. *Current Science-Bangalore*, Vol. 78, No. 7, pp: 808-817, 2000.
- [19] R. Pinnau, Model Reduction via Proper Orthogonal Decomposition. *Model Order Reduction: Theory, Research Aspects and Applications*, Springer, 2008.

- [20] B. Zhang, Y. Lian and W. Shyy, Proper Orthogonal Decomposition for Three-Dimensional Membrane Wing Aerodynamics. *33rd AIAA Fluid Dynamics Conference and Exhibit*, AIAA 2003-3917, Orlando, FL, 2003.
- [21] M. Xiao, P. Breilkopf and R. F. Coelho, Model Reduction by CPOD and Kriging Application to the Shape Optimization of an Intake Port. *Structural and Multidisciplinary Optimization*, 41 (4), 555-574, 2010.
- [22] L. Sirovich, Turbulence and the dynamics of coherent structures. III. *Quart. Appl. Math.*, Vol. 45, No. 3, pp: 561-590, 1987.
- [23] ZEUS: A CFD Code for Aeroelasticians User Manual, Version 3.2, Zona Technology, February 2012.
- [24] A. Jameson, W. Schmidt, E. Turkel, Numerical Solution of the Euler Equations by Finite Volume Methods Using Runge Kutta Time Stepping Schemes, AIAA 81-1259, 1981.
- [25] J. Ballmann, A. Boucke, B. H. Chen, L. Reimer, A. Dafnis, S. Bsing and C. Buxel, Aero-Structural Wind Tunnel Experiments with Elastic Wing Models at High Reynolds Number (HIRENASD - ASDMAD). *International Forum on Aeroelasticity and Structural Dynamics (IFASD)*, IFASD 2011-105, Paris, France, 2011.
- [26] P. Chwalowski, J. P. Florance, J. Heeg, C. D. Wieseman, B. Perry, Preliminary Computational Analysis of the HIRENASD Configuration in Preparation for the Aeroelastic Prediction Workshop. *International Forum of Aeroelasticity and Structural Dynamics (IFASD)*, IFASD 2011-108, Paris, France, 2011.
- [27] M. Nikbay, P. Acar, C. Kilic and Z. Zhang, Steady and Unsteady Aeroelastic Computations of HIRENASD Wing for Low and High Reynolds Numbers. *Presented in 1st Aeroelastic Prediction Workshop (AePW-1)*, Honolulu, HI, USA, 2012.
- [28] "<https://c3.nasa.gov/dashlink/resources/489/>", March 2013.
- [29] B. Perry, W. A. Silva, J. R. Florance, C. D. Wieseman, A. S. Pototzky, M. D. Sanetrik, et al., Plans and Status of Wind-Tunnel Testing Employing an Aeroservoelastic Semispan Model. *48th AIAA/ASME/ASCE/AHS/ASC Structures, Structural Dynamics, and Materials Conference*, AIAA 2007-1770, Honolulu, HI, USA, 2007.
- [30] J. Zeng, S. L. Kukreja and B. Moulin Experimental Model-Based Aeroelastic Control for Flutter Suppression and Gust-Load Alleviation. *Journal of Guidance, Control, and Dynamics*, Vol. 35, No. 5, pp. 1377-1390, 2012.

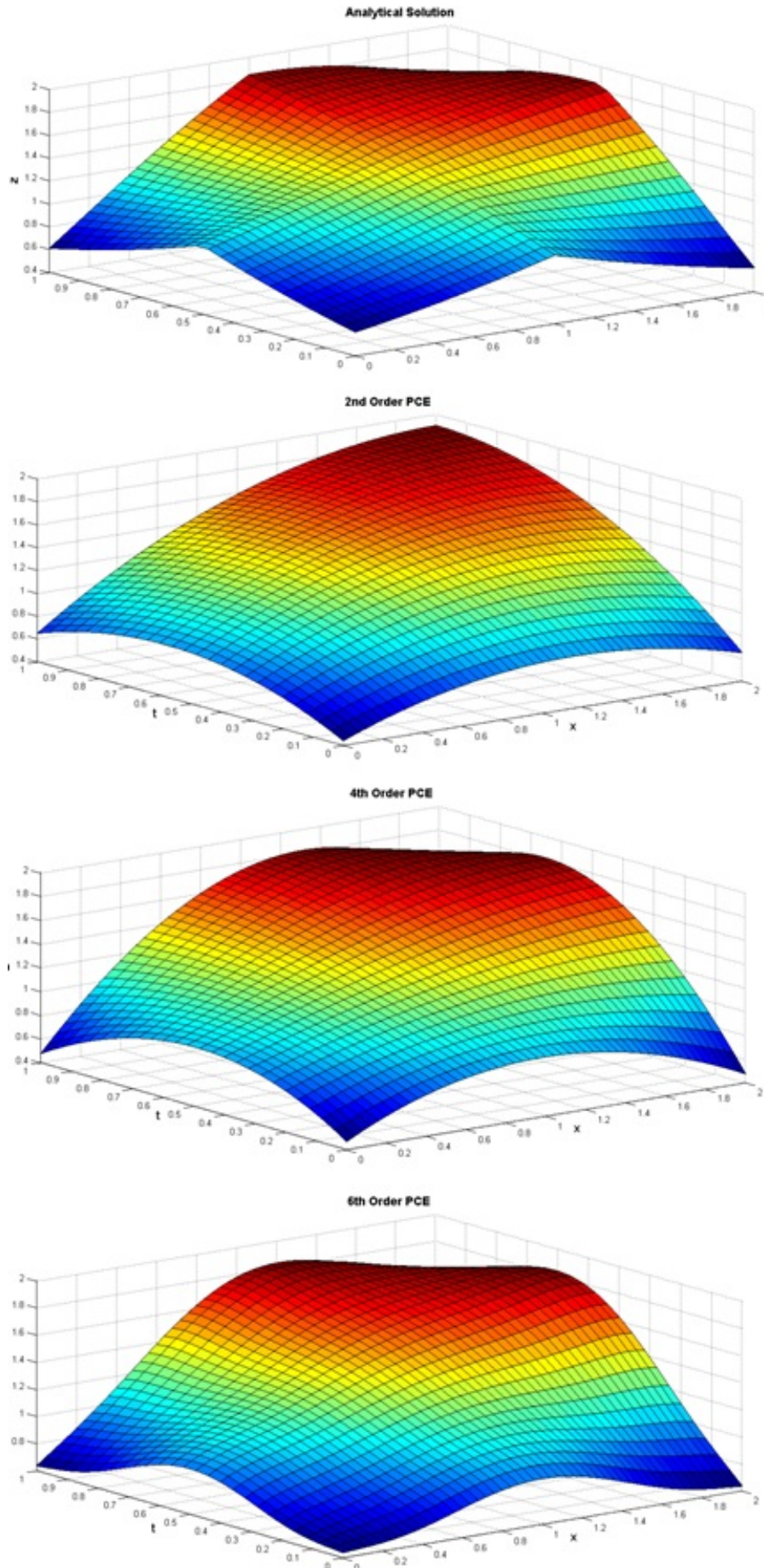


Figure 7: Comparison of analytical solution and PCE results.

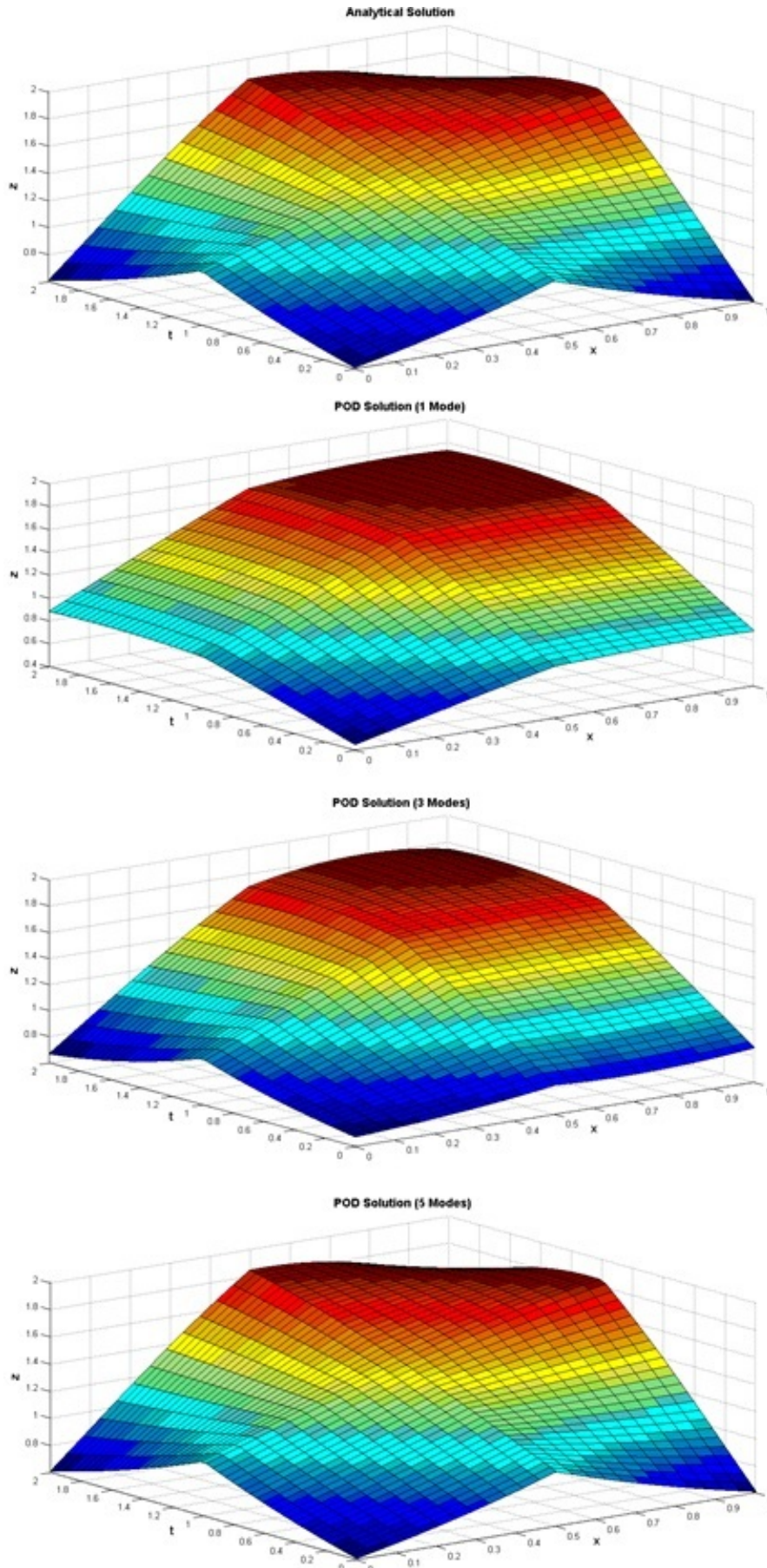


Figure 8: Comparison of analytical solution and POD results.

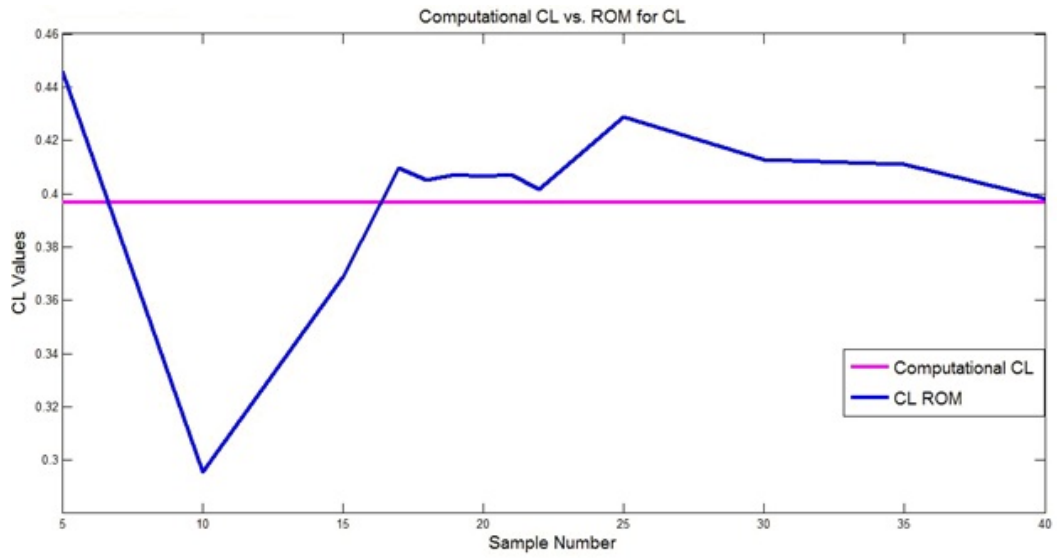


Figure 9: c_L variation of the HIRENASD PCE-ROM with respect to sample number.

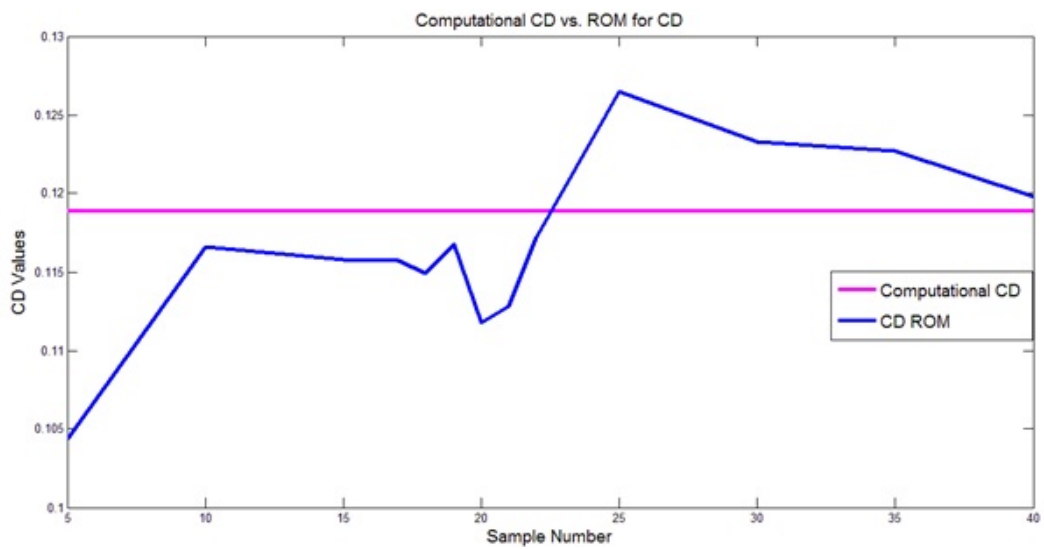


Figure 10: c_D variation of the HIRENASD PCE-ROM with respect to sample number.

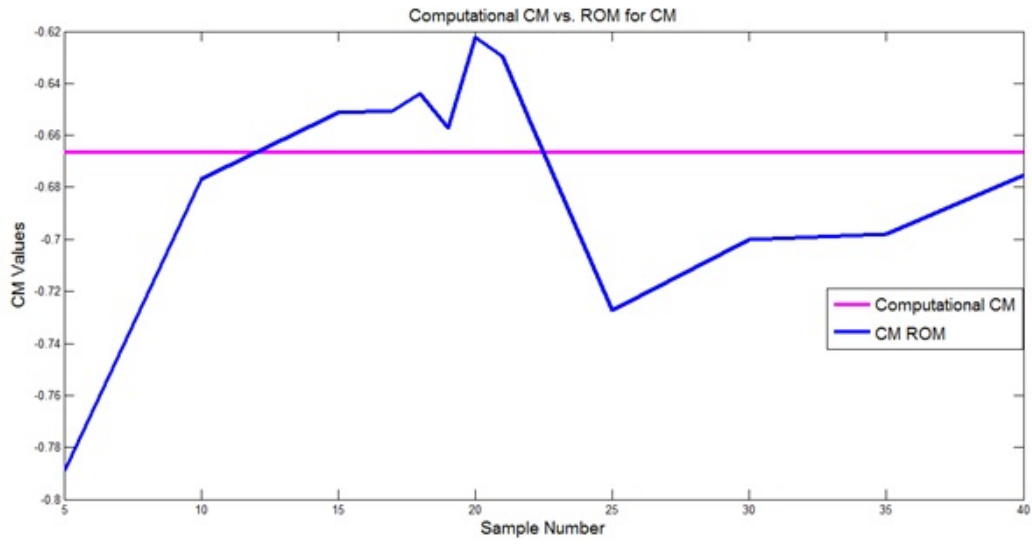


Figure 11: c_M variation of the HIRENASD PCE-ROM with respect to sample number.

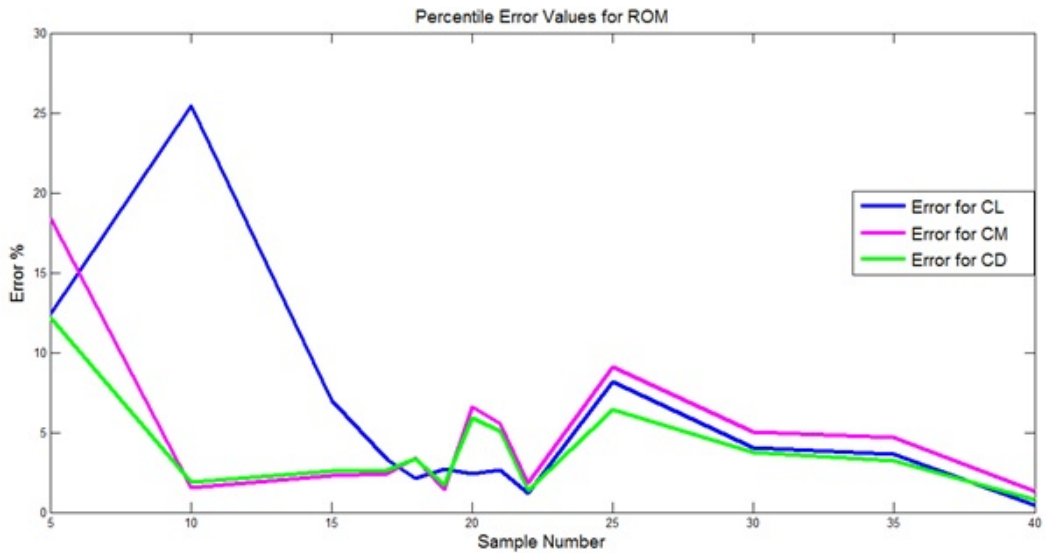


Figure 12: Relative error values for the HIRENASD PCE-ROM with respect to sample number.

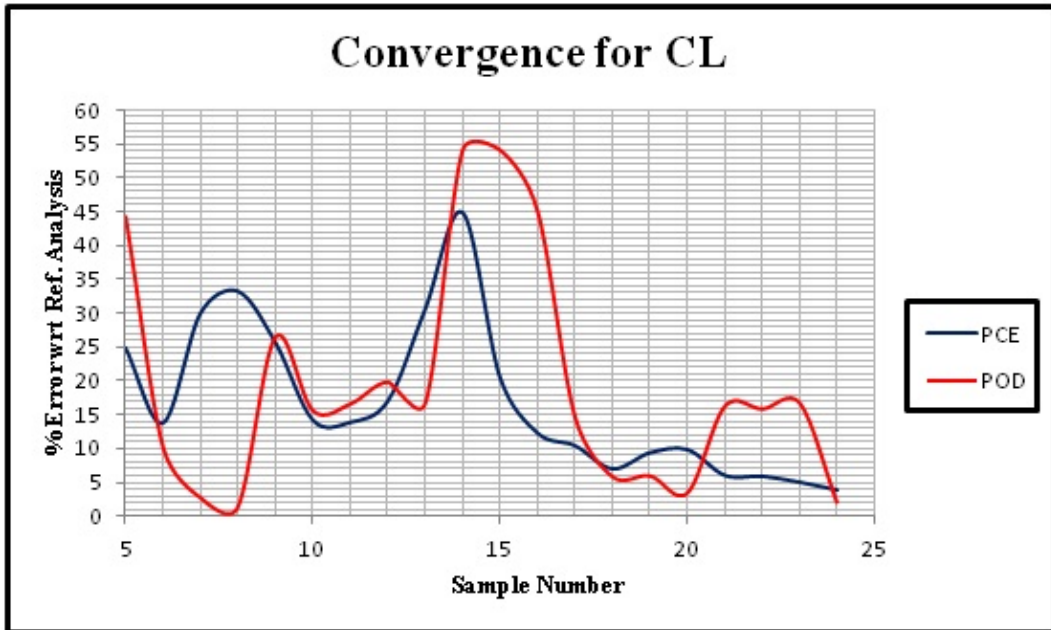


Figure 13: Convergence of the S^4T PCE and POD methods for c_L parameter with respect to sample number.

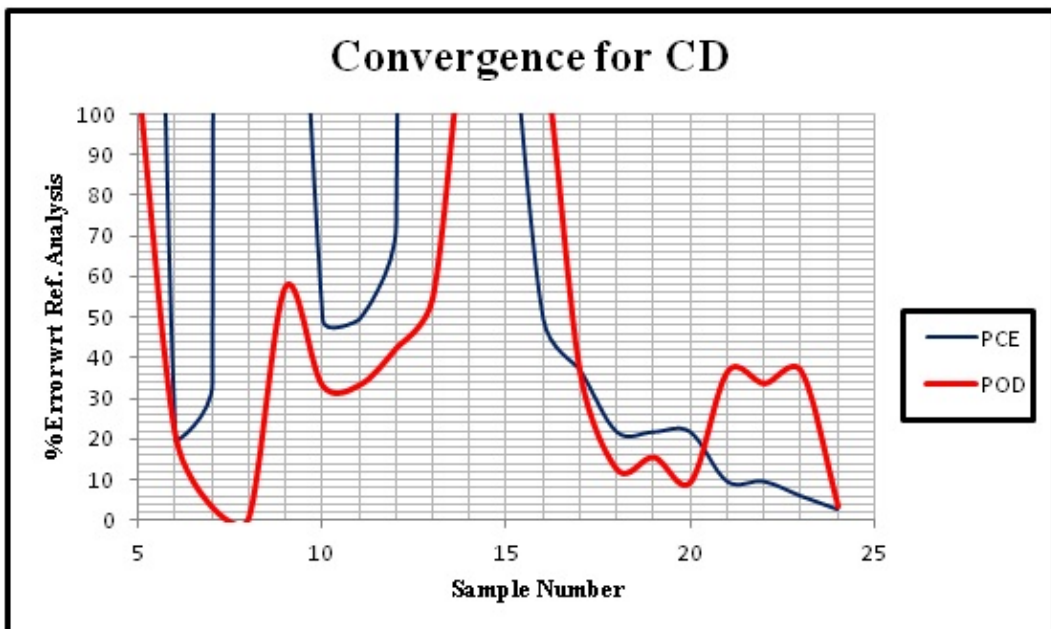


Figure 14: Convergence of the S^4T PCE and POD methods for c_D parameter with respect to sample number.

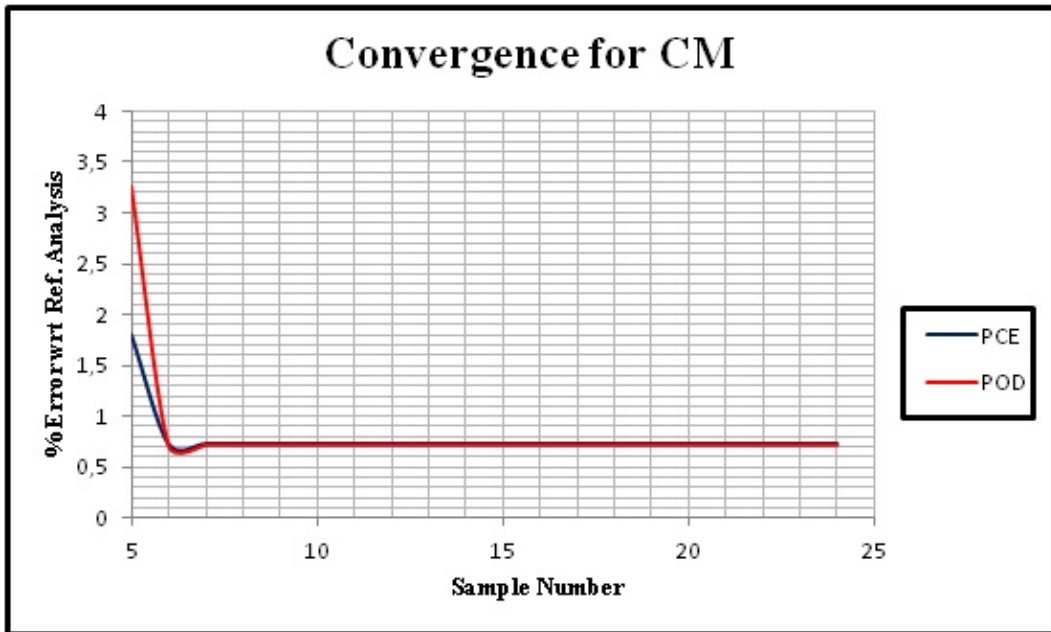


Figure 15: Convergence of the S⁴T PCE and POD methods for c_M parameter with respect to sample number.

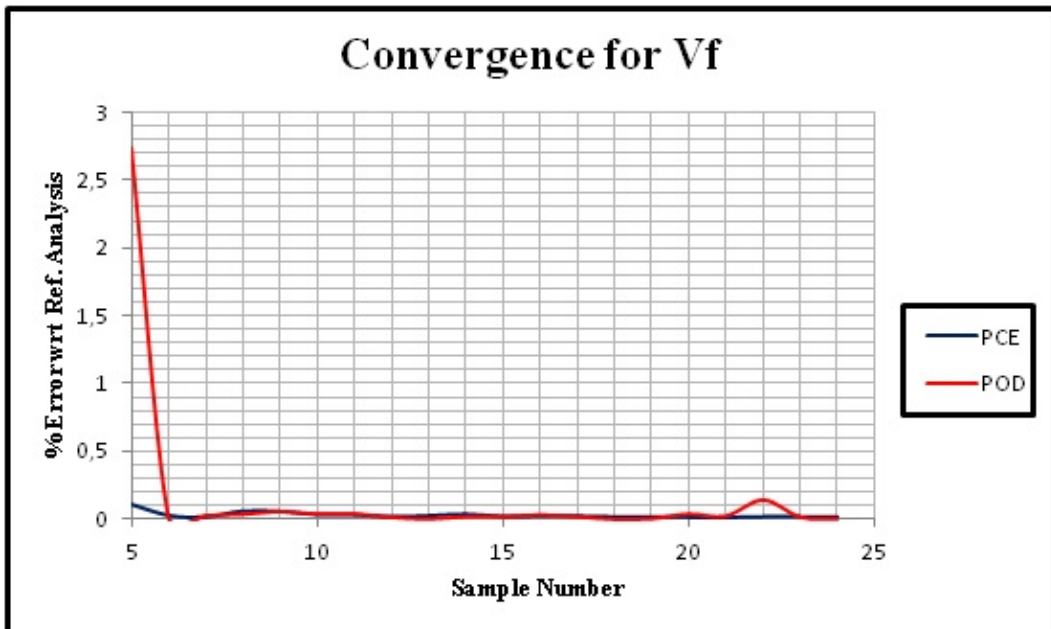


Figure 16: Convergence of the S⁴T PCE and POD methods for V_f parameter with respect to sample number.

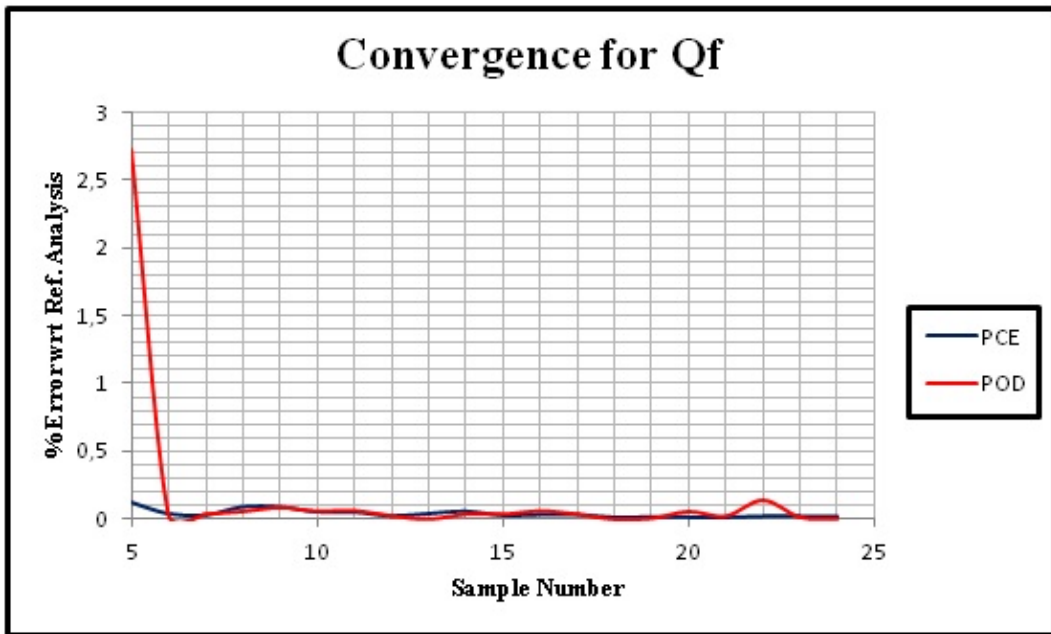


Figure 17: Convergence of the S⁴T PCE and POD methods for Q_f parameter with respect to sample number.

DYNAMIC BEHAVIOUR OF LAMINATED PLATES SUBJECTED TO THERMOMECHANICAL LOADS

Halit S. Turkmen¹, Sedat Susler¹, and Zafer Kazanci²

¹ Faculty of Aeronautics and Astronautics
Istanbul Technical University, Istanbul, Turkey
e-mail: halit@itu.edu.tr

¹ Faculty of Aeronautics and Astronautics
Istanbul Technical University, Istanbul, Turkey
suslers@itu.edu.tr

² Aerospace Engineering Department
Turkish Air Force Academy, Istanbul, Turkey
z.kazanci@hho.edu.tr

Keywords: Blast, Thermomechanical Loading, Large Deflection, Dynamic Response, Non-linear, Laminated Plate.

Abstract. *The engineering structures may be subjected to the dynamic loads such as blast. Therefore, in the design of such structures, the effect of the blast loading should be taken into account. There are two possible effects of the blast: sudden pressure and the temperature rise. In this study, a closed form solution is presented for the thermomechanical transient analysis of the simply supported laminated composite plates subjected to blast loading. In-plane stiffness and inertia effects are considered in the formulation of the problem and transverse shear stresses are ignored. The geometric nonlinearity effects are taken into account by using the von Karman large deflection theory of thin plates. Approximate solution functions are assumed for the space domain and substituted into the equations of motion. The Galerkin method is used to obtain the nonlinear differential equations in the time domain. The finite difference method is applied to solve the system of coupled nonlinear equations. The displacement-time and strain-time histories are obtained for critical cases and compared the isothermal condition. The method presented here can be used for the dynamic response analysis of laminated plates in preliminary design.*

1 INTRODUCTION

The composite plate structures are used in many engineering applications such as aircraft structures, automobiles, space vehicles, wind turbines and a wide range of defense industry to build the lightweight components and vehicles. Moreover, predicting the dynamic response of plates subjected to time dependent loads is very important for the more reliable design process. For instance, the engineering structures may be subjected to the blast load. Therefore, in the design of such structures, the effect of the blast loading should be taken into account. There are two possible effects of the blast: sudden pressure and the temperature rise. In wind turbines, the blades may be subjected to the wind and thermal effects at the same time.

There are several studies found on both linear and nonlinear analysis of isotropic and laminated composite flat plates subjected to air blast loading [1-7]. Susler et al. investigated nonlinear dynamic response of tapered laminated composite plate [8] and tapered sandwich plate [9] along the thickness subjected to blast load. All these previous studies were considered in the absence of temperature effects. There are also previous studies about transient analysis of laminated composite plates subjected to thermomechanical loads [10-12].

In this study, a closed form solution is presented for the thermomechanical transient analysis of the simply supported laminated composite plates subjected to blast loading. In-plane stiffness and inertia effects are considered in the formulation of the problem and transverse shear stresses are ignored. The geometric nonlinearity effects are taken into account by using the von Karman large deflection theory of thin plates. Approximate solution functions are assumed for the space domain and substituted into the equations of motion. The Galerkin method is used to obtain the nonlinear differential equations in the time domain. The finite difference method is applied to solve the system of coupled nonlinear equations. The displacement-time and strain-time histories are obtained for some critical cases and compared with the results of isothermal blast loaded conditions. The method presented here can be used for the dynamic response analysis of laminated plates subjected to thermomechanical loads in preliminary design.

2 FORMULATION OF THE PROBLEM

In this section, a mathematical model is presented for the simply supported laminated composite plate subjected to combined loading of the air blast and temperature rise. The rectangular plate with the length a and the width b is depicted in Figure 1.

The strain-displacement relations for the von Kármán plate theory is defined for the isothermal case in Equation (1). If there is a temperature increment from a reference state ($\Delta T = T - T_{ref}$) which will affect the plate, thermal strains will be occurred and this leads to a different form of stress-strain relations shown in Equation (2).

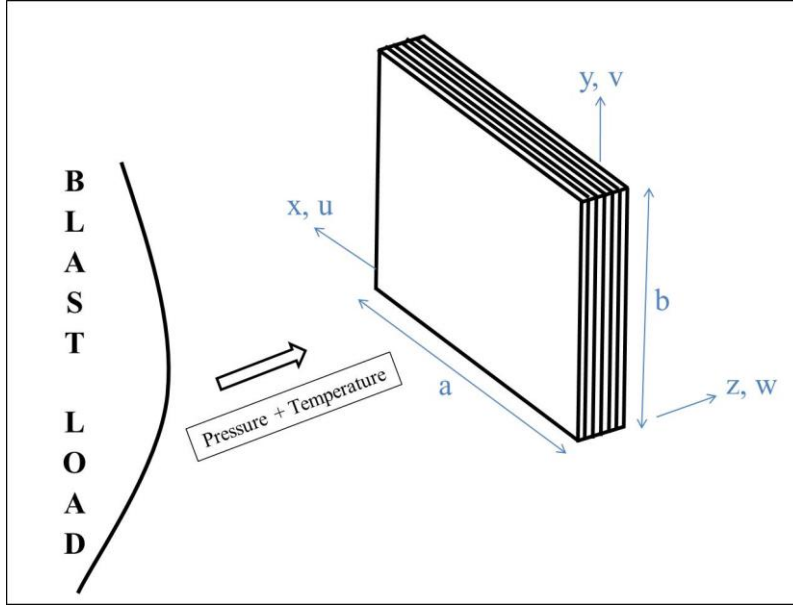


Figure 1: The schematic view of the plate subjected to the blast load.

$$\begin{aligned}\varepsilon_x &= \varepsilon_x^0 + z\kappa_x = \frac{\partial u^0}{\partial x} + \frac{1}{2}\left(\frac{\partial w^0}{\partial x}\right)^2 - z\frac{\partial^2 w^0}{\partial x^2} \\ \varepsilon_y &= \varepsilon_y^0 + z\kappa_y = \frac{\partial v^0}{\partial y} + \frac{1}{2}\left(\frac{\partial w^0}{\partial y}\right)^2 - z\frac{\partial^2 w^0}{\partial y^2} \\ \varepsilon_{xy} &= \varepsilon_{xy}^0 + z\kappa_{xy} = \frac{\partial u^0}{\partial y} + \frac{\partial v^0}{\partial x} + \frac{\partial w^0}{\partial x}\frac{\partial w^0}{\partial y} - 2z\frac{\partial^2 w^0}{\partial x\partial y}\end{aligned}\quad (1)$$

$$\begin{Bmatrix} \sigma_x \\ \sigma_y \\ \sigma_{xy} \end{Bmatrix}^{(k)} = \begin{bmatrix} \bar{Q}_{11} & \bar{Q}_{12} & \bar{Q}_{16} \\ \bar{Q}_{12} & \bar{Q}_{22} & \bar{Q}_{26} \\ \bar{Q}_{16} & \bar{Q}_{26} & \bar{Q}_{66} \end{bmatrix}^{(k)} \begin{Bmatrix} \varepsilon_x - \alpha_x \Delta T \\ \varepsilon_y - \alpha_y \Delta T \\ \varepsilon_{xy} - 2\alpha_{xy} \Delta T \end{Bmatrix}\quad (2)$$

In the constitutive equations, α_x , α_y and α_{xy} are transformed thermal coefficients of expansion and are expressed in Equation (3) by using longitudinal (α_1) and transverse (α_2) thermal coefficients of expansion of a lamina. α_1 and α_2 are defined as engineering constants of required material.

$$\begin{aligned}\alpha_x &= \alpha_1 \cos^2 \theta + \alpha_2 \sin^2 \theta \\ \alpha_y &= \alpha_1 \sin^2 \theta + \alpha_2 \cos^2 \theta \\ 2\alpha_{xy} &= 2(\alpha_1 - \alpha_2) \sin \theta \cos \theta\end{aligned}\quad (3)$$

The stresses have linear variation through the thickness of each layer. If it is assumed that the temperature increment varies linearly consistently with the mechanical strains, ΔT will be expressed as [13]:

$$\Delta T = T_0(x, y, t) + zT_1(x, y, t)\quad (4)$$

The membrane strains and curvatures for a nonisothermal problem will be transformed into Equation (5). According to the constitutive relations of a laminated composite plate and using

Equations (4) and (5), the force and moment resultants in a compact form for the nonisothermal case are written in Equation (6).

$$\{\varepsilon^0\} = \begin{Bmatrix} \varepsilon_x^0 - \alpha_x T_0(x, y, t) \\ \varepsilon_y^0 - \alpha_y T_0(x, y, t) \\ \varepsilon_{xy}^0 - 2\alpha_{xy} T_0(x, y, t) \end{Bmatrix}, \quad \{\kappa\} = \begin{Bmatrix} \kappa_x - \alpha_x T_1(x, y, t) \\ \kappa_y - \alpha_y T_1(x, y, t) \\ \kappa_{xy} - 2\alpha_{xy} T_1(x, y, t) \end{Bmatrix} \quad (5)$$

$$\begin{Bmatrix} N \\ M \end{Bmatrix} = \begin{bmatrix} A & B \\ B & D \end{bmatrix} \begin{Bmatrix} \varepsilon_0 \\ \kappa \end{Bmatrix} - \begin{Bmatrix} N^T \\ M^T \end{Bmatrix} \quad (6)$$

where the thermal force and moment resultants are given in Equation (7) [13]. A_{ij} , B_{ij} and D_{ij} are the extensional, coupling and bending stiffness matrices.

$$\{N^T\} = \sum_{k=1}^N \int_{z_k}^{z_{k+1}} [\bar{Q}]^{(k)} \{\bar{\alpha}\}^{(k)} \Delta T dz, \quad \{M^T\} = \sum_{k=1}^N \int_{z_k}^{z_{k+1}} [\bar{Q}]^{(k)} \{\bar{\alpha}\}^{(k)} \Delta T z dz \quad (7)$$

If an assumption is made that all layers have the same engineering constants and the same orientation, the thermal force and moment resultants have the same stiffness matrices as the mechanical resultants. Equation (8) will have the following open form and thermal force and moment resultants will be described as Equation (9). The superscript $()^T$ indicates thermal expressions.

$$\begin{Bmatrix} N_x \\ N_y \\ N_{xy} \\ M_x \\ M_y \\ M_{xy} \end{Bmatrix} = \begin{bmatrix} A_{11} & A_{12} & A_{16} & B_{11} & B_{12} & B_{16} \\ A_{12} & A_{22} & A_{26} & B_{12} & B_{22} & B_{26} \\ A_{16} & A_{26} & A_{66} & B_{16} & B_{26} & B_{66} \\ B_{11} & B_{12} & B_{16} & D_{11} & D_{12} & D_{16} \\ B_{12} & B_{22} & B_{26} & D_{12} & D_{22} & D_{26} \\ B_{16} & B_{26} & B_{66} & D_{16} & D_{26} & D_{66} \end{bmatrix} \begin{Bmatrix} \varepsilon_x^0 - \alpha_x T_0(x, y, t) \\ \varepsilon_y^0 - \alpha_y T_0(x, y, t) \\ \varepsilon_{xy}^0 - 2\alpha_{xy} T_0(x, y, t) \\ \kappa_x - \alpha_x T_1(x, y, t) \\ \kappa_y - \alpha_y T_1(x, y, t) \\ \kappa_{xy} - 2\alpha_{xy} T_1(x, y, t) \end{Bmatrix} \quad (8)$$

$$\begin{Bmatrix} N_x^T \\ N_y^T \\ N_{xy}^T \\ M_x^T \\ M_y^T \\ M_{xy}^T \end{Bmatrix} = \begin{bmatrix} A_{11} & A_{12} & A_{16} & B_{11} & B_{12} & B_{16} \\ A_{12} & A_{22} & A_{26} & B_{12} & B_{22} & B_{26} \\ A_{16} & A_{26} & A_{66} & B_{16} & B_{26} & B_{66} \\ B_{11} & B_{12} & B_{16} & D_{11} & D_{12} & D_{16} \\ B_{12} & B_{22} & B_{26} & D_{12} & D_{22} & D_{26} \\ B_{16} & B_{26} & B_{66} & D_{16} & D_{26} & D_{66} \end{bmatrix} \begin{Bmatrix} \alpha_x T_0(x, y, t) \\ \alpha_y T_0(x, y, t) \\ 2\alpha_{xy} T_0(x, y, t) \\ \alpha_x T_1(x, y, t) \\ \alpha_y T_1(x, y, t) \\ 2\alpha_{xy} T_1(x, y, t) \end{Bmatrix} \quad (9)$$

Using the force and moment resultants with the strain-displacement relations in the virtual work and applying the variational principles, the nonlinear and nonisothermal dynamic equations of a laminated composite plate in a compact form can be obtained in terms of mid-plane displacements in Equations (10). L_{ij} and N_i denote linear and nonlinear operators.

$$\begin{aligned}
L_{11}u^0 + L_{12}v^0 + L_{13}w^0 + N_1(w^0) + \bar{m}\ddot{u}^0 - (q_x + q_x^T) &= 0 \\
L_{21}u^0 + L_{22}v^0 + L_{23}w^0 + N_2(w^0) + \bar{m}\ddot{v}^0 - (q_y + q_y^T) &= 0 \\
L_{31}u^0 + L_{32}v^0 + (L_{33} + L_{33}^T)w^0 + N_3(u^0, v^0, w^0) + \bar{m}\ddot{w}^0 - (q_z + q_z^T) &= 0
\end{aligned} \tag{10}$$

The boundary conditions for the simply supported plates are given in Equation (11) and Equation (12). Besides, initial conditions are shown in Equation (13).

$$\begin{aligned}
u^0(0, y, t) = u^0(a, y, t) = u^0(x, 0, t) = u^0(x, b, t) &= 0 \\
v^0(0, y, t) = v^0(a, y, t) = v^0(x, 0, t) = v^0(x, b, t) &= 0 \\
w^0(0, y, t) = w^0(a, y, t) = w^0(x, 0, t) = w^0(x, b, t) &= 0
\end{aligned} \tag{11}$$

$$\begin{aligned}
M_x &= 0 \text{ at } x = 0, a \\
M_y &= 0 \text{ at } y = 0, b
\end{aligned} \tag{12}$$

$$\begin{aligned}
u^0(x, y, 0) = 0 \quad , \quad v^0(x, y, 0) = 0 \quad , \quad w^0(x, y, 0) = 0 \\
\dot{u}^0(x, y, 0) = 0 \quad , \quad \dot{v}^0(x, y, 0) = 0 \quad , \quad \dot{w}^0(x, y, 0) = 0
\end{aligned} \tag{13}$$

The blast load is expanded in Fourier series and only the first term is chosen. It is assumed to be varying exponentially in time and Friedlander decay function is used to express the air blast load as shown in Equation (14). p_m is the peak pressure, t_p is positive phase duration, and φ is a waveform parameter.

$$p(x, y, t) = p_m \left(1 - \frac{t}{t_p} \right) e^{-\frac{\varphi t}{t_p}} \tag{14}$$

$T_0(x, y, t)$ and $T_1(x, y, t)$ in Equation (4) are defined in Equation (15) as variables along the length a and the width b . Equation (4) and Equation (15) are also time dependent functions with the assumption of Friedlander function as the blast load.

$$\begin{aligned}
T_0(x, y, t) &= T^0 \sin \frac{\pi x}{a} \sin \frac{\pi y}{b} \left\{ \left(1 - \frac{t}{t_p} \right) e^{-\frac{\varphi t}{t_p}} \right\} \\
T_1(x, y, t) &= T^1 \sin \frac{\pi x}{a} \sin \frac{\pi y}{b} \left\{ \left(1 - \frac{t}{t_p} \right) e^{-\frac{\varphi t}{t_p}} \right\}
\end{aligned} \tag{15}$$

Approximate solution functions are chosen crucially by considering the results of static large deformation analysis of laminated composite and shown in Equation (16). Only the first term of the series for in-plane displacements and out-of-plane displacements for the simply supported plate is accounted.

$$\begin{aligned}
u^0 &= U_{II}(t) y^2 (y - b)^2 \sin \frac{2\pi x}{a} \\
v^0 &= V_{II}(t) x^2 (x - a)^2 \sin \frac{2\pi y}{b} \\
w^0 &= W_{II}(t) \sin \frac{\pi x}{a} \sin \frac{\pi y}{b}
\end{aligned} \tag{16}$$

The time dependent nonlinear differential equations are obtained by applying the Galerkin method to the equations of motion given in Equation (10). The nonlinear-coupled equations of motion are then solved by using the finite difference method. Finally, the equations of motion are reduced into a form that can be easily solved by one of the methods for solution of linear equation systems such as Gauss elimination method or LU decomposition.

3 NUMERICAL RESULTS

The dynamic behaviour of thermomechanically affected simply supported composite plate is obtained using a closed form solution by writing a FORTRAN program. The pressure distribution because of the blast loading is assumed to be uniform on the plate, and the parameters shown in Equation (14) are $p_m=29$ kN/m², $t_p=0.0018$ s, $\alpha=0.35$. The constants of temperature increment (T^0 and T^1) in Equation (15) are selected as 40 °C, 80 °C and 120 °C to understand the effect of temperature variation on the dynamic response. Only square shaped plates are considered in this paper and the dimensions are taken as $a=b=220$ mm. The plates are made of six layers of laminae, which are assumed to be behaving linearly and elastically. The layers are perfectly bonded. The composite material type is AS/3501 and the fiber orientation angle is chosen as 0° for all layers. The material properties of AS/3501 unidirectional carbon epoxy are given in Table 1.

AS/3501 Carbon Epoxy	
E_1 (GPa)	137.895
E_2 (GPa)	8.963
ν_{12}	0.3
G_{12} (GPa)	7.102
ρ (kg/m ³)	1590
α_1 (1/°C)	1.8×10^{-6}
α_2 (1/°C)	54×10^{-6}
Thickness (mm)	0.12954

Table 1: Material properties [13].

The displacement-time histories of the selected points obtained by using closed form solution are shown in Figure 2 and compared with the isothermal blast loaded plate. The thermal load increases the displacement amplitude as expected. The comparative strain-time histories at the middle, top and bottom surfaces for the center of the plate are shown in Figure 3a-c, respectively. Figure 4 shows the displacement-time and strain-time histories at the middle surface for the center of the plate subjected to only time dependent thermal forces. The effect of temperature increment is also shown in Figure 4 by using three different cases.

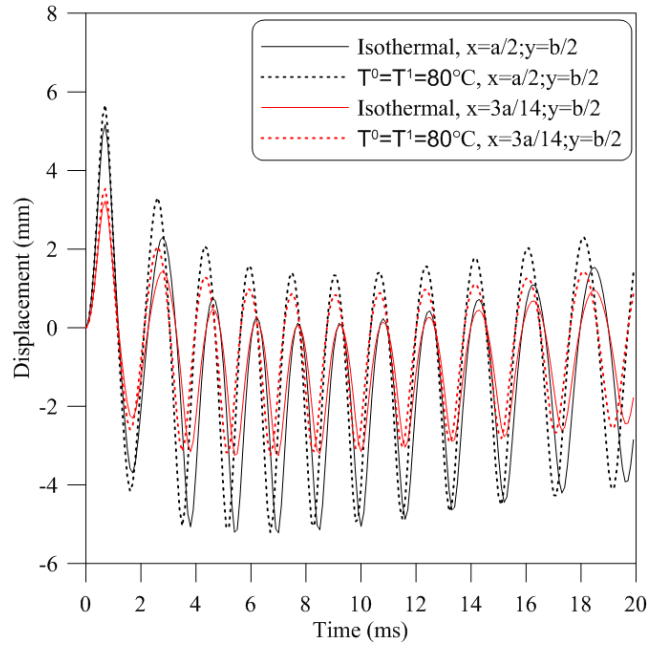


Figure 2: The displacement-time histories of the selected points for nonisothermal and isothermal blast loaded case.

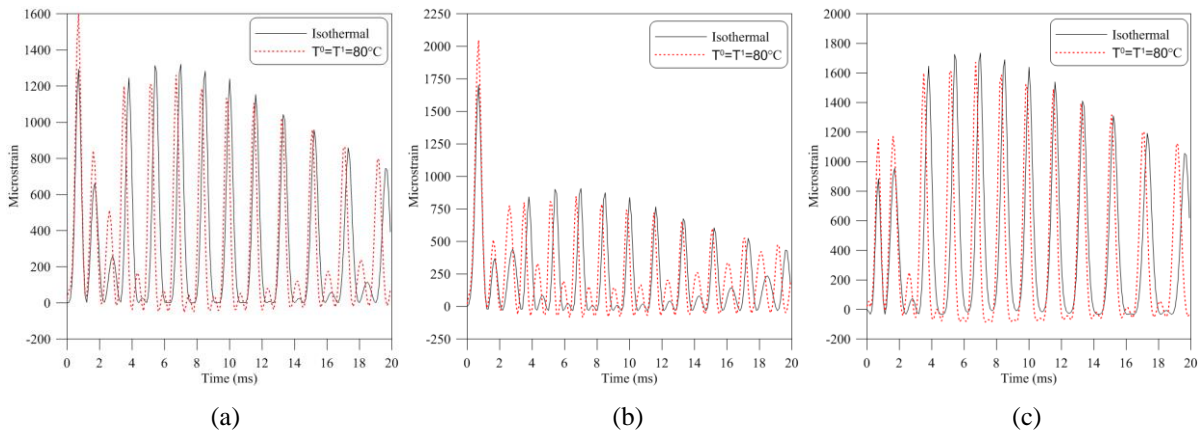


Figure 3: The strain-time histories for the center of the plate for nonisothermal and isothermal blast loaded case.

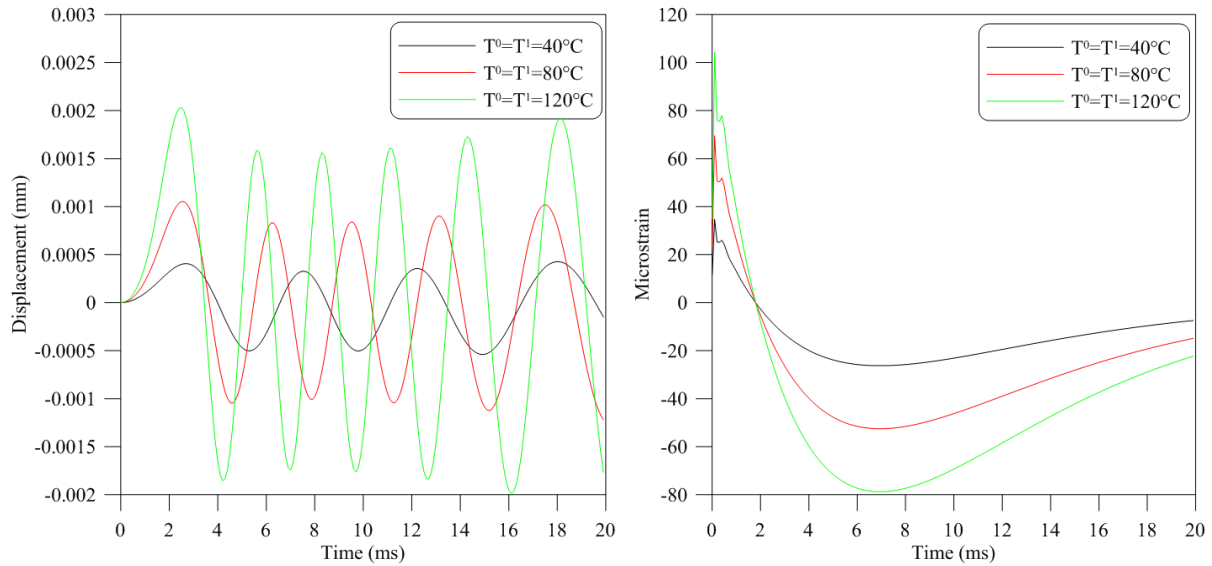


Figure 4: The displacement-time and strain-time histories for the center of the plate subjected to only time dependent thermal effects.

4 CONCLUSION

In this study, the dynamic response of thermomechanically loaded laminated composite plate is investigated theoretically. The displacement-time and strain-time histories are obtained for selected points. The strain-time histories are obtained at the mentioned points on the top, middle and bottom surfaces of the plate. The temperature rise during the blast or shock loading increases the displacement amplitude and strain. Therefore it is important to consider the temperature changes during the blast or shock loading in the design of structures which are subjected to thermal effects.

REFERENCES

- [1] G. Chandrasekharappa, H.R. Srirangarajan, Nonlinear response of elastic plates to pulse excitations. *Computers&Structures*, **27**, 373-378, 1987.
- [2] L.A. Louca, Y.G. Pan, Response of stiffened and unstiffened plates subjected to blast loading. *Engineering Structures*, **20**, 1079-1086, 1998.
- [3] H.S. Turkmen, Z. Mecitoğlu, Nonlinear structural response of laminated composite plates subjected to blast loading. *AIAA Journal*, **37**, 1639-1647, 1999.
- [4] H.S. Turkmen, Z. Mecitoğlu, Dynamic response of a stiffened laminated composite plate subjected to blast load. *Journal of Sound and Vibration*, **221**, 371-389, 1999.
- [5] L. Librescu, S.Y. Oh, J. Hohe, Linear and non-linear dynamic response of sandwich panels to blast loading. *Composites: Part B*, **35**, 673-683, 2004.
- [6] Z. Kazancı, Z. Mecitoğlu, Nonlinear damped vibrations of a laminated composite plate subjected to blast load. *AIAA Journal*, **44**, 2002-2008, 2006.
- [7] Z. Kazancı, Z. Mecitoğlu, Nonlinear dynamic behavior of simply supported laminated composite plates subjected to blast load. *Journal of Sound and Vibration*, **317**, 883-897, 2008.

- [8] S. Susler, H.S. Turkmen, Z. Kazancı, The nonlinear dynamic behaviour of tapered laminated plates subjected to blast loading. *Shock and Vibration*, **19**, 1235-1255, 2012.
- [9] S. Susler, Z. Kazancı, H.S. Turkmen, Nonlinear dynamic behaviour of tapered sandwich plates subjected to blast loading. *15th European Conference On Composite Materials (ECCM15)*, Venice, Italy, June 24-28, 2012.
- [10] R. Rolfes, K. Rohwer, Integrated thermal and mechanical analysis of composite plates and shells. *Composite Science and Technology*, **60**, 2097-2106, 2000.
- [11] H.S. Shen, J.J. Zheng, X.L. Huang, Dynamic response of shear deformable laminated plates under thermomechanical loading and resting on elastic foundations. *Composite Structures*, **60**, 57-66, 2003.
- [12] K.K. Shukla, Y. Nath, E. Kreuzer, Buckling and transient behaviour of layered composite plates under thermomechanical loading. *ZAMM Zeitschrift fur Angewandte Mathematik und Mechanik*, **85**, 163-175, 2005.
- [13] J.N. Reddy, *Mechanics of laminated composite plates and shells theory and analysis, 2nd Edition*. CRC Press, 2004.

A METRIC THEORY OF RATE INDEPENDENT AND RATE DEPENDENT PLASTICITY: THEORETICAL AND COMPUTATIONAL ASPECTS

Vassilis P. Panoskaltsis¹ and Dimitris Soldatos¹

¹Department of Civil Engineering, Demokritos University of Thrace,
12 Vassilissis Sofias Street, Xanthi 67100, GREECE
email: vpanoska@civil.duth.gr

Keywords: Internal Variables, Finite Deformations, Characteristic Times, Generalized Plasticity, Viscoplasticity, Covariance, Material Metric, Lie Derivative, Loading Unloading Conditions, Time Discretization, Backward Euler, Predictor Corrector Algorithm.

Abstract. *A new internal variable theory for the description of solid materials having mechanisms with different characteristic times, is developed within a finite deformation framework. The theory relies crucially on the consistent combination of a general viscoplastic theory and a new version of rate – independent generalized plasticity theory. In this new version of rate – independent generalized plasticity the concepts of viscous range and viscous process have been introduced, while, as in classical generalized plasticity, the notion of yield surface, as a basic ingredient, is not involved. The formulation is developed initially in a material setting and then is extended to a covariant one by applying some basic elements and results from the tensor analysis on manifolds. By introducing the material (intrinsic) metric as a primary internal variable, accounting for both rate dependent and rate independent phenomena within the body, a constitutive model is proposed. The ability of the model in simulating several patterns of the complex response of metals under quasi – static and dynamic loadings is assessed by representative numerical examples, after appropriate approximations of the Lie derivatives of tensorial quantities have been derived.*

1 INTRODUCTION

The first author of this publication has gotten interested earlier (in the nineties) in the important subject of modeling materials with different characteristic times, namely with characteristic times very short and of the same order compared to a loading process. The first type of mechanisms gives rise to instantaneous plastic strains and the second type to creep strains, which are developed slowly. He and his co-workers have developed models for the description of the behavior of concrete materials by combining in series internal variable theories of viscoelasticity and plasticity, Panoskaltzis et al. [1, 2, 3, 4, 5]. In the first four publications a plasticity model is combined with a viscoelasticity one, while in the fifth generalized plasticity formulations are combined with viscoplasticity ones. All these models were developed within the realm of small strains.

It should be mentioned that it came as a surprise to this author that very few works had been published on this subject, earlier than his. These are works that have been published in the early sixties (Landau et al. [6], Ivlev [7] and Naghdi and Murch [8]). In those publications, several combinations of a rate – dependent theory with a rate – independent one have been proposed, again within the context of infinitesimal deformation.

Nevertheless, the mechanisms responsible for instantaneous plastic strains as well as viscoelastic strains are usually introducing large deformations and can be found in different classes of materials such as metals (e.g., metal forming processes, high – velocity impact, penetration mechanics), shape memory alloys (e.g., finite deformations occurring during phase transformations) and soils (e.g., liquefaction and cyclic mobility in sands). Therefore, a more general development within the context of a large deformation theory, is definitely needed. This is the reason for revisiting this subject. Our new development includes the following basic characteristics:

(a) *A local internal variable theory presented in a covariant setting.* The internal variable vector is assumed to consist of two components. The first of them, which is related to the *rate – dependent* properties of the material, is described by a general viscoplastic formulation which leaves the kinematics of the problem and the number and the nature of the internal variables entirely unspecified. In this sense, the formulation includes both, a number of models which have been developed in order to describe time dependent phenomena in metals and in particular highly nonlinear viscoelastic behavior (e.g., Bodner and Partom [9], Rubin [10, 11, 12]), as well as, the classical overstress models (e.g., Malvern [13], Perzyna, [14, 15], Phillips and Wu [16], Chaboche [17]). The second component, which is related to the *rate – independent* material properties is described by the framework of generalized plasticity (Lubliner [18, 19, 20]) which includes *classical plasticity as a special case* (e.g., see Lubliner [20], Panoskaltzis et al. [21, 22]). The crucial advantage of this approach resides in the compatibility of the two theories, in the sense that neither viscoplasticity nor generalized plasticity employs the concept of the yield surface as a basic ingredient. Unlike the classical formulations of viscoplasticity and rate – independent plasticity, which usually are developed in the stress space, the proposed formulation is developed in the strain (deformation) space. Such formulation, besides inheriting the advantages of the strain space over the stress space (Naghdi [23]), seems more essential for a *covariant formulation* since it employs as a control variable the right Cauchy – Green deformation tensor, which is defined as the pull – back of the spatial metric by the deformation. As in our previous approaches (see Panoskaltzis et al. [22, 24, 25]) within the context of the rate – independent theory, the covariant formulation is achieved naturally by introducing manifold spaces (see, for instance, Bishop and Goldberg [26], Lovelock

and Rund [27]), not only for the body of interest and the ambient space, but also for the state space, that is the set of all realizable states over a material point. Accordingly, the motion of the body which is considered as a time dependent mapping within the ambient space, is extended to a local dynamical process by considering the state space as a fiber over the body particles (e.g., see Panoskaltsis et al. [22, 24, 25]). In turn, the involvement of the standard pull – back/push – forward operations of the tensor analysis on manifolds (e.g., Marsden and Hughes [28, p.67], Stumpf and Hoppe [29]) leads to the introduction of the convected Lie derivative (e.g., see Marsden and Hughes [28, p. 95], Stumpf and Hoppe [29]), which eventually leads to a covariant formulation of the theory.

(b) *A constitutive model which is based on the concept of the “physical” metric.* This is a rather new and powerful concept that has been introduced in the phenomenological description of solid materials by Valanis [30] and was extended by Valanis and Panoskaltsis [31] (see also Panoskaltsis et al. [22, 25]). According to this theory, the intrinsic material (“physical”) metric, namely the (body) metric in the material configuration, can be considered as a *basic internal variable*, modeling non – affine deformation. In his original work Valanis [30], by considering the physical metric’s time derivative with respect to either the Newtonian time or the intrinsic time, derived hereditary constitutive equations for viscoelastic and plastic solids, respectively. Within the present study the concept is revisited and it is used for the construction of a material model. This model is based on a hyperelastic extension of a J_2 flow theory to the finite deformation regime. In particular, it is shown how the “physical” metric can be used as a measure of viscoplastic deformation which is due to mechanisms with different characteristic times within the material substructure. The proposed model belongs to the class of *multi – mechanism models*, which constitutes at the present time a very active area of research (e.g., see Taleb and Cailletaud [32], Sai [33]). This model is based on the following basic ingredients:

- i. A hyperelastic constitutive equation for the characterization of the stress response.
- ii. A von – Mises type of expression, with isotropic hardening, for the (suitably defined) yield surface.
- iii. A normality flow rule in terms of the material metric.

The ability of the proposed model in simulating several patterns of the extremely complex response of metals under quasi – static and dynamic loadings is assessed by representative numerical examples.

2 DEVELOPMENT OF CONSTITUTIVE THEORY

We follow the geometrical approach of Marsden and Hughes [28], proposed within the context of non – linear elasticity (see also Stumpf and Hoppe [29]). Approaches of this type have been also considered within the context of isothermal formulations of classical plasticity by Simo [34], Miehe [35], Panoskaltsis et al. [22, 24, 25], and within a non – isothermal framework by Duszek and Perzyna [36] and Le and Stumpf [37]. Accordingly, we consider both the body of interest and the ambient space S , as three dimensional Riemannian manifolds and we denote by B the reference configuration of the body with points labeled by $\mathbf{X}(X^1, X^2, X^3)$. A motion of B within the ambient space is defined as a time dependent mapping $\mathbf{x}: B \rightarrow S$ given as

$$\mathbf{x} = \mathbf{x}(\mathbf{X}, t), \quad (1)$$

which maps the points of the reference configuration B onto the points $\mathbf{x}(x^1, x^2, x^3)$ of the ambient space S . The deformation gradient is defined to be the tangent map of the motion, i.e.,

$$\mathbf{F}(\mathbf{X}, t) = \frac{\partial \mathbf{x}}{\partial \mathbf{X}}, \quad (2)$$

with determinant $J = \det \mathbf{F}(\mathbf{X}, t) > 0$.

In the absence of thermal effects, the material state at the referential point \mathbf{X} may be determined by the right Cauchy – Green deformation tensor defined as the pull – back of the spatial metric \mathbf{g} , by the motion (1), that is

$$\mathbf{C} = \mathbf{F}^T \mathbf{g} \mathbf{F}, \quad (3)$$

which is assumed to lie on a manifold C , and the internal variable vector \mathbf{Q} , which in turn is assumed to lie on another manifold Q . The *state space*, that is the product manifold $D = C \times Q$ is assumed to be attached at the point \mathbf{X} so that the set $\{\mathbf{X}\} \times D$ is a fiber of \mathbf{X} . Furthermore, we note that the set $\{\mathbf{X}\} \times D$ is an open subset of $B \times D$ and so it is a local manifold. Since we study materials *with both rate – dependent and rate – independent characteristics* we assume that the internal variable vector be composed of two internal variable vectors \mathbf{V} and \mathbf{P} , which belong to the manifolds V and P respectively; the former of them is associated with the material rate – dependent properties while the latter is associated with the material rate – independent ones.

A *local process* Ψ in the state space D is defined as a curve in D , i.e., as a mapping from the time interval of interest I to the state space D , i.e.,

$$\Psi: I \in R \rightarrow D,$$

defined as

$$\Psi(t) = \begin{bmatrix} \mathbf{C}(t) \\ \mathbf{V}(t) \\ \mathbf{P}(t) \end{bmatrix}.$$

The direction and the speed of such a process are determined by the tangent vector

$$\dot{\Psi}(t) = \begin{bmatrix} \dot{\mathbf{C}}(t) \\ \dot{\mathbf{V}}(t) \\ \dot{\mathbf{P}}(t) \end{bmatrix}, \text{ where the superimposed dot stands for the time derivative.}$$

Since, the component $\dot{\mathbf{C}}$ of $\dot{\Psi}$, is always known under deformation control, the components $\dot{\mathbf{V}}$ and $\dot{\mathbf{P}}$ have to be determined. By considering just a first order differential equation, that is by imposing some limitations concerning the memory of the material, the rate – dependent component of the internal variable vector may be assumed to be given as

$$\dot{\mathbf{V}} = \mathbf{A}(\mathbf{C}, \mathbf{V}), \quad (4)$$

where $\mathbf{A} : C \times V \rightarrow TD$ is a vector field to be interpreted as a tensorial function of the denoted arguments, associated with the rate – dependent material properties. A local process may be defined as *elastic* if it lies entirely in a six dimensional submanifold of D (actually the deformation space C) defined by $\mathbf{V}=\text{const.}$, otherwise is defined as *inelastic*. Accordingly, an *elastic domain* (at $\mathbf{V}=\text{const.}$) may be defined as a submanifold of the deformation space C comprising the deformation points which can be reached by an elastic process from the current deformation point. If the elastic domain has a non empty interior, its boundary is a five dimensional manifold, the points of which have a coordinate neighborhood on it, which is attached to the interior in much the same way as the surface of a solid is attached to its interior. The latter manifold may be defined as a *yield surface*. We are now stating the following important remarks, that underscore our theory which is developed here.

REMARK 2.1. The *existence of a yield surface* classifies the viscoplastic models frequently met in the literature (e.g., see the review paper by Naghdi [23]) into two major categories as follows: In view of Equation (4) one can conclude that an elastic domain can be defined at any material state in $C \times V$, by the equation

$$\mathbf{A}(\mathbf{C}, \mathbf{V}) = \mathbf{0}.$$

The case in which the function \mathbf{A} is a non – vanishing function of its arguments corresponds to a viscoplastic model, where an elastic domain does not exist and every process results in inelastic behavior at any deformation level, no matter how small it is. A viscoplastic model of this type is termed as a “unified” constitutive model (e.g., Bodner and Partom [9], Rubin [10, 11, 12]). On the other hand, if it is assumed that a yield (hyper) surface exists and is given by an expression of the form

$$G(\mathbf{C}, \mathbf{V}) = 0,$$

where $G : C \times V \rightarrow R$ is a scalar function, then by considering for the function \mathbf{A} an expression of the form

$$\mathbf{A} = \frac{1}{\eta} \langle \Gamma(G) \rangle \mathbf{B}(\mathbf{C}, \mathbf{V}),$$

where the function $\langle \Gamma(G) \rangle$ is defined as

$$\langle \Gamma(G) \rangle = \begin{cases} 0 & \text{for } G \leq 0 \\ \Gamma(G) & \text{for } G > 0, \end{cases}$$

where η is a (temperature dependent) viscosity, and \mathbf{B} a vector field in TD , the proposed viscoplastic formulation is reduced to the classical overstress concept due to Perzyna [14, 15]. Models of this kind have been also proposed among others, by Malvern [13], Phillips and Wu [16] and Chaboche [17].

REMARK 2.2. Within the present formulation it is implied that if an elastic domain exists, then the values of the plastic internal variables \mathbf{P} are constant within this domain, since the

rate – independent material mechanisms are always activated after the rate – dependent ones have done so.

The *characterization of the rate – independent response* of the material, *in conjunction to the rate – dependent one*, will be described by appropriately *extending* the generalized plasticity framework (for the rate – independent generalized plasticity framework see Lubliner [18, 19, 20] and Panoskaltsis et al. [21, 22, 24]) as follows. The *viscous* (quasistatic) *range* will be introduced and it will be defined as the submanifold of $C \times V$ which *encompasses the states that can be reached by a process which does not activate the rate – independent mechanisms within the material*, that is one with $\mathbf{P} = \text{constant}$. This process may be either an elastic process –belonging to C – or an inelastic process belonging to $C \times V$, that is one with a tangent

vector of the form $\dot{\Psi}(t) = \begin{bmatrix} \dot{\mathbf{C}}(t) \\ \dot{\mathbf{V}}(t) \\ \mathbf{0} \end{bmatrix}$.

Such an *inelastic process* will be defined as *viscous*. The boundary of the viscous range will be defined as a *loading surface* (e.g., Eisenberg and Phillips [38], Lubliner [39, 20]). On the loading surface we may construct a coordinate system similar to a coordinate system on the yield surface. A state lying on a loading surface may be defined as a *viscoplastic state*, while an *inelastic process*, which results in a change of the plastic internal variable vector \mathbf{P} will be defined as *viscoplastic process*. The rate equation for the evolution of \mathbf{P} is closely related to the notion of the viscoplastic process, which in turn may be systematically studied on the basis of the *loading rate concept* (see Lubliner [40, 18, 20]). This is defined as the inner product of the outward normal to the loading surface (a one – form on the cotangent space $T^*C \times V$), with the projection of the tangent to the process vector onto the space $C \times V$, that is

$$L(\mathbf{C}, \mathbf{V}, \dot{\mathbf{C}}, \dot{\mathbf{V}}) = \frac{\partial F}{\partial \mathbf{C}} : \dot{\mathbf{C}} + \frac{\partial F}{\partial \mathbf{V}} \dot{\mathbf{V}}, \quad (5)$$

where $F : D \rightarrow R$ is the mathematical expression for the loading surface in D . The loading rate determines the speed and the direction of a process from a *viscoplastic state relatively to its viscous range*. If $L \leq 0$, then the viscous range is *invariant* under the flow of $(\dot{\mathbf{C}}, \dot{\mathbf{V}})$ (e.g., see Abraham et al. [41, pp. 256 – 258]) and the process is *viscous*. If $L > 0$, then the viscous range *is not invariant* anymore and a new viscoplastic state at a new value of \mathbf{P} is initiated. Accordingly, the rate equation for the evolution of the plastic internal variable vector \mathbf{P} (see also Lubliner [18, 19] for the rate – independent case), may be stated as

$$\dot{\mathbf{P}} = H(\mathbf{C}, \mathbf{V}, \mathbf{P}) \mathbf{D}(\mathbf{C}, \mathbf{P}) \langle L \rangle, \quad (6)$$

in which H is a scalar function of the state variables, which enforces the defining property of a viscoplastic state, i.e., the value of H must be positive at any viscoplastic state and zero in any other one. Finally, \mathbf{D} is another vector field in TD , enforcing the rate – independent properties of the material and $\langle \cdot \rangle$ stands from now on for the McCauley bracket defined as

$$\langle x \rangle = \begin{cases} x, & \text{if } x \geq 0 \\ 0, & \text{if } x < 0. \end{cases}$$

The formulation is supplemented by the general loading – unloading conditions of the new theory, which follow by using the basic Equations (4) and (6), as:

$$\left\{ \begin{array}{l} \text{If } \mathbf{A}(\mathbf{C}, \mathbf{V}) = \mathbf{0}: \text{ Elastic domain.} \\ \text{If } \mathbf{A}(\mathbf{C}, \mathbf{V}) \neq \mathbf{0} \text{ and } H(\mathbf{C}, \mathbf{V}, \mathbf{P}) = 0: \text{ Viscous process.} \\ \text{If } \mathbf{A}(\mathbf{C}, \mathbf{V}) \neq \mathbf{0} \text{ and } H(\mathbf{C}, \mathbf{V}, \mathbf{P}) \neq 0: \text{ If } L \leq 0: \text{ Viscous process,} \\ \hspace{10em} \text{If } L > 0: \text{ Viscoplastic process.} \end{array} \right. \quad (7)$$

A particular case of interest appears when a yield surface exists and coincides with the initial loading surface (see the concise discussion of Eisenberg and Phillips [38]). This case corresponds to a material which exhibits both rate – dependent and rate – independent characteristics, with the *yield criterion of the instantaneous rate – independent behavior governing both*. Another particular case of interest arises when both functions \mathbf{A} and H in Equations (4) and (6) are non – vanishing. In this case every state is a viscoplastic one, every process results in viscous response and the material possesses a rate – dependent quasi – yield surface (see Lubliner [39], Panoskaltis et al. [24]).

An equivalent description in the spatial configuration can be derived by extending the motion (1) to a dynamical process $\underline{\mathbf{P}}$ by considering the local vector bundle mapping (e.g., Abraham et al. [41, p. 67])

$$\underline{\mathbf{P}}: B \times D \rightarrow S \times D',$$

where D' is the state space “as seen” in the current configuration. This mapping is defined as

$$\underline{\mathbf{P}}(\mathbf{X}, \mathbf{C}, \mathbf{Q}, t) = ((\mathbf{x}), \mathbf{x}_*(\mathbf{C}), \mathbf{x}_*(\mathbf{Q})) = ((\mathbf{x}), \mathbf{g}, \mathbf{q}), \quad (8)$$

where $\mathbf{x}_*(\cdot)$ stands for the push – forward operator and \mathbf{q} denotes the push – forward of the internal variable vector \mathbf{Q} and is defined on the basis of the general transformation law (e.g., Lovelock and Rund [27, p. 66]) in component form as

$$q^{j_1 \dots j_r}_{i_1 \dots i_s} = \frac{\partial x^{j_1}}{\partial X^{I_1}} \dots \frac{\partial x^{j_r}}{\partial X^{I_r}} \frac{\partial X^{K_1}}{\partial x^{i_1}} \dots \frac{\partial X^{K_s}}{\partial x^{i_s}} Q^{I_1 \dots I_r}_{K_1 \dots K_s}. \quad (9)$$

As a result, by applying a push – forward operation to Equations (4) and (6) the equivalent assessment of the basic equations in the spatial description is obtained as

$$\mathbf{L}_v \mathbf{v} = \mathbf{a}(\mathbf{g}, \mathbf{v}, \mathbf{F}), \quad (10)$$

$$\mathbf{L}_v \mathbf{p} = h(\mathbf{g}, \mathbf{v}, \mathbf{p}, \mathbf{F}) \mathbf{d}(\mathbf{g}, \mathbf{p}, \mathbf{F}) \langle l \rangle, \quad (11)$$

where \mathbf{v} , \mathbf{p} , \mathbf{a} , \mathbf{d} are the push – forwards onto the spatial configuration of the material tensorial quantities \mathbf{V} , \mathbf{P} , \mathbf{A} , \mathbf{D} ; h is the equivalent expression for the (scalar invariant) state function H and l stands for the *loading rate* in the spatial configuration defined as

$$l = \frac{\partial f}{\partial \mathbf{g}} : \mathbf{L}_v \mathbf{g} + \frac{\partial f}{\partial \mathbf{v}} \mathbf{L}_v \mathbf{v}. \quad (12)$$

In this equation, f is the expression for the loading surfaces in the spatial configuration, i.e., $f : D' \rightarrow R$ with $f(\mathbf{g}, \mathbf{v}, \mathbf{p}, \mathbf{F}) = 0$, while $\mathbf{L}_v(\cdot)$ denotes the Lie derivative, defined as the convected derivative relative to the current configuration (e.g., Stumpf and Hoppe, [29]). We note the dependence of the state functions on the deformation gradient \mathbf{F} , which is due to the forward operation by which Equations (10) and (11) are derived from basic Equations (4) and (6). The loading – unloading conditions (7) in the current configuration in view of Equations (10), (11) and (12) can be stated as:

$$\left\{ \begin{array}{l} \text{If } \mathbf{a}(\mathbf{g}, \mathbf{v}, \mathbf{F}) = \mathbf{0}: \text{ Elastic domain.} \\ \text{If } \mathbf{a}(\mathbf{g}, \mathbf{v}, \mathbf{F}) \neq \mathbf{0} \text{ and } h(\mathbf{g}, \mathbf{v}, \mathbf{p}, \mathbf{F}) = \mathbf{0}: \text{ Viscous process.} \\ \text{If } \mathbf{a}(\mathbf{g}, \mathbf{v}, \mathbf{F}) \neq \mathbf{0} \text{ and } h(\mathbf{g}, \mathbf{v}, \mathbf{p}, \mathbf{F}) \neq \mathbf{0}: \text{ If } l \leq 0: \text{ Viscous process,} \\ \text{If } l > 0: \text{ Viscoplastic process.} \end{array} \right. \quad (13)$$

REMARK 2.3. Unlike our approaches to the rate – independent theory (see Panoskaltsis et al. [21, 22, 24]) we refrain from characterizing conditions (7) (or (13)) as *loading – unloading criteria*, since the loading rate L (or equivalently l) is dependent on the viscous internal variable and its rate, which are in general *non – controllable* quantities.

REMARK 2.4. As it has been already mentioned the case of combined rate – dependent and rate – independent behavior has been studied by Naghdi and Murch [8]. In their approach Naghdi and Murch, propose a general formulation on the basis of a combination of a theory of linear viscoelasticity, expressed in terms of convolution integrals, in series with a theory of classical plasticity. As a result, unlike the present approach where the non – necessity of the existence of a yield surface has led to the absence of the plastic consistency parameter, in their approach the consistency parameter is determined from the consistency condition of the instantaneous plasticity. For the earlier works of Panoskaltsis and co-workers we note that in Panoskaltsis et al. [1] a viscoelastic model has been introduced in series with a rate – independent internal variable plastic model, while in Panoskaltsis et al. [2, 3, 4] a viscoelastic model has been introduced in series with an internal variable *rate – dependent plastic* model (i.e., one with the *initial* yield depending on the rate), for modeling of concrete materials.

REMARK 2.5. We note the dependence of the loading surface on the internal variable vector \mathbf{V} , which in turn means that the loading surface even though is related to the rate – independent properties of the material, *is itself rate – dependent*. This consideration is based on the experimentally observed behavior according to which, the activation of the rate – independent mechanisms within the material (yielding) is a rate – dependent phenomenon.

REMARK 2.6. The case in which a rate – independent loading surface is involved corresponds to a combination of a viscoplastic theory with rate – independent generalized plasticity in an uncoupled setting. Then the rate – independent formulation reduces to that of standard generalized plasticity (see Lubliner [20]; see also Panoskaltsis et al. [21, 22, 24]) with the term *elastic* replaced throughout by the term *viscous*. Such a formulation has its origins in the work of Landau et al. [6], where a combination of a viscoelastic theory with a perfectly plastic solid

obeying a von Mises yield criterion has been proposed within the context of infinitesimal deformation.

3 THE PHYSICAL METRIC

The basic objective of this section is the introduction of a tangible strain space constitutive model. The proposed model is based on a consistent implementation of a rather new and powerful concept, namely the “physical” metric concept (see Valanis [30] and Valanis and Panoskaltzis [31]). The basic idea relies on the fact that the *intrinsic material* (“physical”) *metric, namely the (body) metric in the material configuration*, can be considered as a basic internal variable associated with the non – affine deformation. Unlike the original theory of Valanis [30], where the concept was introduced within the context of hereditary constitutive relations, in the present proposal the *metric* concept is introduced within the framework of materials with internal variables; in this sense, the proposed model resembles a model by Panoskaltzis et al. [22] within the context of rate – independent generalized plasticity. Moreover, in contrast to the theoretical presentation given in section 2, where in general it has been assumed that different mechanisms within the material substructure are responsible for rate – dependent (viscous) and rate – independent (plastic) phenomena, within the specific model formulation it is assumed that the same mechanisms are responsible for the combined (viscoplastic) material response, which in turn is described in terms of the physical metric. Since we deal with large scale viscoplastic flow, the kinematics of the problem together with the principle of spatial covariance suggest that a formulation of the model in terms of the *spatial metrics* and *their convected (Lie) derivatives* is more natural. Further, in the current configuration, the spatial metric usually has a diagonal form, which makes the computations simpler than those in the reference configuration where the metric \mathbf{C} is fully populated (e.g., see Miehe [35], Panoskaltzis et al. [24]).

Accordingly, the stress response is assumed to be governed by an isotropic strain energy function which is given in terms of the invariants of the tensor $\mathbf{g}\mathbf{b}$, where \mathbf{b} is the left Cauchy – Green tensor, defined as the push – forward of the reciprocal (contravariant) metric \mathbf{G}^{-1} , i.e., $((\mathbf{b} = \mathbf{x}_* (\mathbf{G}^{-1}) = \mathbf{F}\mathbf{G}^{-1} \mathbf{F}^T)$, as

$$\hat{\psi}(I_1, I_3) = \gamma \ln \sqrt{I_3} + \mu I_3^{-\frac{1}{3}} [-\ln \sqrt{I_3} + \frac{1}{2}(I_1 - 3)], \quad (14)$$

where $I_1 = tr(\mathbf{b}\mathbf{g})$ and $I_3 = det(\mathbf{b}\mathbf{g})$, are the first and third invariants of $\mathbf{b}\mathbf{g}$, ρ_0 is the referential density ($\rho_0 = \rho J$) and γ and μ are Lamé’ type elastic constants. Then, the Kirchhoff stress tensor $\boldsymbol{\tau}$ ($\boldsymbol{\tau} = \mathbf{J}\boldsymbol{\sigma}$), is given as (see, e.g., Marsden and Hughes [28, p. 204])

$$\boldsymbol{\tau} = 2\rho_0 \frac{\partial \hat{\psi}}{\partial \mathbf{g}} = \gamma \ln \sqrt{I_3} \mathbf{g}^{-1} + \mu I_3 [\mathbf{b} - \mathbf{g}^{-1}]. \quad (15)$$

The loading surfaces are assumed to be given by a von – Mises expression of the form (e.g., Simo [34])

$$f(\boldsymbol{\tau}, \mathbf{g}, \alpha) = \sqrt{\tau^{ij} \tau^{kl} g_{ik} g_{jl} - \frac{1}{3} (\tau^{kl} g_{kl})^2} - \sqrt{\frac{2}{3}} (\sigma_y + K\alpha), \quad (16)$$

where α is a scalar internal variable which controls the isotropic hardening of the von – Mises loading surface, σ_y is a model parameter to be interpreted as the uniaxial yield stress in the absence rate dependent phenomena and K is the isotropic hardening modulus. The yield surface is assumed to be similar to the loading surfaces and it is defined by an expression of the form

$$g(\boldsymbol{\tau}, \mathbf{g}, \alpha) = \sqrt{\tau^{ij} \tau^{kl} g_{ik} g_{jl} - \frac{1}{3} (\tau^{kl} g_{kl})^2} - \sqrt{\frac{2}{3}} k (\sigma_y + K\alpha), \quad (17)$$

where k is the similarity ratio ($0 \leq k \leq 1$).

The evolution of the (contravariant) metric \mathbf{b} is assumed to be given by a normality flow rule on both the yield and the loading surfaces, which resembles the one derived on the basis of the maximum plastic dissipation by Simo [34], as

$$\mu I_3^{-\frac{1}{3}} \text{dev}(\mathbf{L}_v \mathbf{b}) = -2\bar{\mu} \frac{\langle \mathbf{g} \rangle^x}{\eta} \mathbf{v} - 2\bar{\mu} \frac{\langle f \rangle}{|f| \beta} \mathbf{n} \langle \mathbf{v} : \mathbf{L}_v \mathbf{g} \rangle, \quad (18)$$

where $\text{dev}(\cdot)$ stands for the deviatoric operator in the spatial configuration that is $\text{dev}(\cdot) = (\cdot) - \frac{1}{3} [\mathbf{g} : (\cdot)] \mathbf{g}^{-1}$, $\bar{\mu} = \mu I_3^{-\frac{1}{3}} I_1$, $\mathbf{n} = \frac{\text{dev} \boldsymbol{\tau}}{\|\text{dev} \boldsymbol{\tau}\|}$, $\mathbf{v} = \frac{\partial f}{\partial \mathbf{g}}$, is the normal vector to the loading surfaces in the deformation space, η is a viscosity type of parameter, x is a model parameter related to the rheological characteristics of the material and β is an additional parameter that is related to the rate independent part of the model (see Panoskaltzis et al. [21, 22, 24]).

The evolution equation for the isotropic hardening variable, in accordance with the infinitesimal theory of plasticity (e.g., see Simo and Hughes [42, p. 90]), is assumed to be given as

$$\dot{\alpha} = \sqrt{\frac{2}{3}} \left(\frac{\langle \mathbf{g} \rangle^y}{\eta} + \frac{\langle f \rangle}{|f| \beta} \langle \mathbf{v} : \mathbf{L}_v \mathbf{g} \rangle \right), \quad (19)$$

where y is an additional model parameter.

As in the general theory the loading – unloading conditions of the model together with the corresponding rate – equations for the evolution of the internal variables, can be derived directly from Equations (18) and (19) by dropping the McCauley brackets as:

$$\left\{ \begin{array}{l}
\text{If } g \leq 0: \text{ Elastic domain,} \\
\quad \text{dev}(\mathbf{L}_v \mathbf{b}) = \mathbf{0}, \quad \dot{\alpha} = 0. \\
\text{If } g > 0 \text{ and } (f \leq 0 \text{ or } \mathbf{v} : \mathbf{L}_v \mathbf{g} \leq 0): \text{ Viscous process,} \\
\quad \mu I_3^{-\frac{1}{3}} \text{dev}(\mathbf{L}_v \mathbf{b}) = -2\bar{\mu} \frac{g^x}{\eta} \mathbf{v}, \\
\quad \dot{\alpha} = \sqrt{\frac{2}{3}} \frac{g^y}{\eta}. \\
\text{If } f > 0 \text{ and } \mathbf{v} : \mathbf{L}_v \mathbf{g} > 0: \text{ Viscoplastic process,} \\
\quad \mu I_3^{-\frac{1}{3}} \text{dev}(\mathbf{L}_v \mathbf{b}) = -2\bar{\mu} \frac{g^x}{\eta} \mathbf{v} - 2\bar{\mu} \frac{1}{\beta} \mathbf{n}(\mathbf{v} : \mathbf{L}_v \mathbf{g}), \\
\quad \dot{\alpha} = \sqrt{\frac{2}{3}} \left(\frac{g^y}{\eta} + \frac{1}{\beta} (\mathbf{v} : \mathbf{L}_v \mathbf{g}) \right).
\end{array} \right. \tag{20}$$

Finally, the normal vector $\mathbf{v} = \frac{\partial g}{\partial \mathbf{g}}$ to the yield (and the loading surfaces), after lengthy computations (e.g., see Simo [34]), can be found to be

$$\mathbf{v} = \frac{\partial g}{\partial \mathbf{g}} = \frac{\partial f}{\partial \mathbf{g}} = \bar{\mu} \left(\mathbf{n} + \frac{\|\text{dev} \boldsymbol{\tau}\|}{\bar{\mu}} \text{dev}[\mathbf{n}^2] \right). \tag{21}$$

To this end it is instructive to make the following remarks:

REMARK 4.11. The particular case where $k = 1$ corresponds to the material which exhibits both rate – dependent and rate – independent response, with the same yield criterion governing both. Such a case is of extreme importance in the study of large scale viscoplastic flow where the elastic strains are negligible and the material response is governed entirely by that appearing in the post yielding regime.

REMARK 4.12. The particular case $k = 0$ corresponds to a material with response being identical to that described by a Maxwell fluid in series with the generalized plasticity model. The limiting case where $k = 0$ and $\sigma_y = 0$ corresponds to a model with a *rate – dependent quasi – yield surface*, which is defined by Equation (16). This surface, besides being a rate – dependent loading surface, serves and as a loading potential for the rate – dependent part of the model.

4 COMPUTATIONAL ASPECTS AND NUMERICAL SIMULATIONS

4.1 Time integration algorithm

In the last section, we examine the ability of the proposed model in simulating several patterns of the behavior of metals under quasi – static and dynamic loading conditions. The mod-

el can be implemented numerically by employing a predictor – corrector scheme, which is based on the ideas developed, within the context of a classical elastic – plastic formulation, by Simo and Hughes [42, pp. 311 – 321]. Nevertheless, in sharp contrast with the classical elastic – plastic case, *the internal variables are no longer constrained to lie within the closure of an elastic domain*, since neither viscoplasticity nor generalized plasticity employ the concept of the yield surface as a basic ingredient (see Lubliner [20], Panoskaltsis et al. [21, 24]). Accordingly, unlike the classical elastoplastic case where the evolution equations define a unilaterally constrained problem of evolution governed by the Kuhn – Tucker conditions (e.g., see Simo and Hughes [42, p. 84]), in the present case the evolution equations form a differential system, which must obey the loading – unloading conditions of the model.

The corresponding algorithmic problem is stated as follows: Let $I = [0, T]$, be the time interval of interest. It is assumed that at time $t_n \in I$, the configuration of the body of interest $b_n \in S$, defined as

$$b_n = \{\mathbf{x}_n = \mathbf{x}_n(\mathbf{X}) \mid \mathbf{X} \in B\},$$

along with the state variables are known, i.e.,

$$\{\mathbf{x}_n, \boldsymbol{\tau}_n, \mathbf{b}_n, \alpha_n\},$$

are the known data at time t_n . Assume a time increment Δt_n , which drives the time to $t_{n+1} = t_n + \Delta t$ and the body configuration to

$$b_{n+1} = \{\mathbf{x}_{n+1} = \mathbf{x}_{n+1}(\mathbf{X}) \mid \mathbf{X} \in B\},$$

where

$$\mathbf{x}_{n+1}(\mathbf{X}) = \mathbf{x}_n(\mathbf{X}) + \mathbf{U}(\mathbf{X}) = \mathbf{x}_n(\mathbf{X}) + \mathbf{u}(\mathbf{x}_n(\mathbf{X})),$$

and \mathbf{u} is the incremental displacement field, which is assumed to be given.

Then the algorithmic problem in hand is to update the stress tensor and the internal variables to the time step t_{n+1} in a manner consistent with the continuous Equations (15) and (20).

The solution of the problem can be performed by means of a time – discretization of the governing equations of the model on the basis of the backward Euler scheme, which is first – order accurate and unconditionally stable. Because *of the presence of Lie derivatives within the continuous equations adequate approximations for these objects can be derived on the basis of the defining identity of the (convected) Lie derivative and the general tensorial transformation law* (see Panoskaltsis et al. [21, 24]). In particular, the defining identity for the Lie derivative of a tensor \mathbf{q} of type $\begin{pmatrix} r \\ s \end{pmatrix}$ in the b_{n+1} configuration is

$$L_{\mathbf{v}} \mathbf{q}_{n+1} = \mathbf{x}_{n+1*} \left(\frac{\partial}{\partial t} \mathbf{x}_{n+1}^* (\mathbf{q}) \right). \quad (22)$$

By performing a pull – back operation Equation (22) can be stated as

$$\mathbf{x}_{n+1}^* (\mathbf{L}_v \mathbf{q}_{n+1}) = \frac{\partial}{\partial t} (\mathbf{x}_{n+1}^* (\mathbf{q}_{n+1})) = \dot{\mathbf{Q}}_{n+1} \approx \frac{1}{\Delta t} (\mathbf{Q}_{n+1} - \mathbf{Q}_n), \quad (23)$$

which in turn may be written in component form on the basis of the general tensorial transformation law (see Equation (9)) as

$$\begin{aligned} & \left[\frac{\partial X^{I_1}}{\partial x_{n+1}^{i_1}} \dots \frac{\partial X^{I_r}}{\partial x_{n+1}^{i_r}} \frac{\partial x_{n+1}^{j_1}}{\partial X^{J_1}} \dots \frac{\partial x_{n+1}^{j_s}}{\partial X^{J_s}} \right] \mathbf{L}_v \left(q^{i_1 \dots i_r}_{j_1 \dots j_s} \right)_{n+1} = \frac{1}{\Delta t} \left[\left(Q^{I_1 \dots I_r}_{J_1 \dots J_s} \right)_{n+1} - \left(Q^{I_1 \dots I_r}_{J_1 \dots J_s} \right)_n \right] = \\ & = \frac{1}{\Delta t} \left[\frac{\partial X^{I_1}}{\partial x_{n+1}^{k_1}} \dots \frac{\partial X^{I_r}}{\partial x_{n+1}^{k_r}} \frac{\partial x_{n+1}^{l_1}}{\partial X^{J_1}} \dots \frac{\partial x_{n+1}^{l_s}}{\partial X^{J_s}} \left(q^{k_1 \dots k_r}_{l_1 \dots l_s} \right)_{n+1} - \frac{\partial X^{I_1}}{\partial x_n^{k_1}} \dots \frac{\partial X^{I_r}}{\partial x_n^{k_r}} \frac{\partial x_{n+1}^{l_1}}{\partial X^{J_1}} \dots \frac{\partial x_{n+1}^{l_s}}{\partial X^{J_s}} \left(q^{k_1 \dots k_r}_{l_1 \dots l_s} \right)_n \right], \end{aligned} \quad (24)$$

from which $\mathbf{L}_v \left(q^{i_1 \dots i_r}_{j_1 \dots j_s} \right)_{n+1}$ can be determined as

$$\mathbf{L}_v \left(q^{i_1 \dots i_r}_{j_1 \dots j_s} \right)_{n+1} = \frac{1}{\Delta t} \left[\left(q^{i_1 \dots i_r}_{j_1 \dots j_s} \right)_{n+1} - \frac{\partial x_{n+1}^{i_1}}{\partial x_n^{k_1}} \dots \frac{\partial x_{n+1}^{i_r}}{\partial x_n^{k_r}} \frac{\partial x_n^{l_1}}{\partial x_{n+1}^{j_1}} \dots \frac{\partial x_n^{l_s}}{\partial x_{n+1}^{j_s}} \left(q^{k_1 \dots k_r}_{l_1 \dots l_s} \right)_n \right], \quad (25)$$

where the tensor with components

$$\left(f^i_j \right)_{n+1} = \frac{\partial x_{n+1}^i}{\partial x_n^j} = \frac{\partial x_{n+1}^i}{\partial X^I} \frac{\partial X^I}{\partial x_n^j} = \left(F^i_I \right)_{n+1} \left((F^{-1})^I_j \right)_n, \quad (26)$$

is defined as *the relative deformation gradient* with respect to the configuration b_{n+1} (e.g., Simo and Hughes, [42, p. 279]). By means of Equation (25) an approximation for the covariant $\binom{0}{2}$ metric \mathbf{g} may be derived as

$$\mathbf{L}_v \left(g_{ij} \right)_{n+1} = \frac{1}{\Delta t} \left[\left(g_{ij} \right)_{n+1} - \frac{\partial x_n^i}{\partial x_{n+1}^k} \frac{\partial x_n^j}{\partial x_{n+1}^l} \left(g_{kl} \right)_n \right], \quad (27)$$

or equivalently

$$\mathbf{L}_v \mathbf{g}_{n+1} = \frac{1}{\Delta t} \left(\mathbf{g}_{n+1} - \mathbf{f}_{n+1}^{T-1} \mathbf{g}_n \mathbf{f}_{n+1}^{-1} \right). \quad (28)$$

In a similar manner the approximation for the contravariant $\binom{2}{0}$ (body) metric \mathbf{b} can be found to be

$$\mathbf{L}_v(\mathbf{b}^{ij})_{n+1} = \frac{1}{\Delta t} [(\mathbf{b}^{ij})_{n+1} - \frac{\partial x_{n+1}^i}{\partial x_n^k} \frac{\partial x_{n+1}^j}{\partial x_n^l} (\mathbf{b}^{kl})_n], \quad (29)$$

or equivalently

$$\mathbf{L}_v \mathbf{b}_{n+1} = \frac{1}{\Delta t} (\mathbf{b}_{n+1} - \mathbf{f}_{n+1} \mathbf{b}_n \mathbf{f}_{n+1}^T). \quad (30)$$

Accordingly, the time discrete counterparts of Equations (15) and (20) may be determined as

$$\boldsymbol{\tau}_{n+1} = \gamma \ln \sqrt{I_{3,n+1}} \mathbf{g}_{n+1}^{-1} + \mu I_{3,n+1}^{\frac{1}{3}} [\mathbf{b}_{n+1} - \mathbf{g}_{n+1}^{-1}], \quad (31)$$

and

$$\left\{ \begin{array}{l} \text{If } \mathbf{g}_{n+1} \leq 0: \text{ Elastic domain,} \\ \quad \text{dev} \left[\frac{1}{\Delta t} (\mathbf{b}_{n+1} - \mathbf{f}_{n+1} \mathbf{b}_n \mathbf{f}_{n+1}^T) \right] = \mathbf{0}, \quad \alpha_{n+1} = \alpha_n \\ \text{If } \mathbf{g}_{n+1} > 0 \text{ and } (f_{n+1} \leq 0 \text{ or } \mathbf{v}_{n+1} : \frac{1}{\Delta t} (\mathbf{g}_{n+1} - \mathbf{f}_{n+1}^{T-1} \mathbf{g}_n \mathbf{f}_{n+1}^{-1}) \leq 0): \text{ Viscous process,} \\ \quad \mu J_{n+1}^{\frac{2}{3}} \text{dev} \left[\frac{1}{\Delta t} (\mathbf{b}_{n+1} - \mathbf{f}_{n+1} \mathbf{b}_n \mathbf{f}_{n+1}^T) \right] = -2 \bar{\mu}_{n+1} \frac{g_{n+1}^x}{\eta} \mathbf{n}_{n+1}, \\ \quad \frac{\alpha_{n+1} - \alpha_n}{\Delta t} = \sqrt{\frac{2}{3}} \frac{g_{n+1}^y}{\eta} \\ \text{If } f_{n+1} > 0 \text{ and } \mathbf{v}_{n+1} : \frac{1}{\Delta t} (\mathbf{g}_{n+1} - \mathbf{f}_{n+1}^{T-1} \mathbf{g}_n \mathbf{f}_{n+1}^{-1}) > 0: \text{ Viscoplastic process,} \\ \quad \mu I_{3,n+1}^{\frac{1}{3}} \text{dev} \left[\frac{1}{\Delta t} (\mathbf{b}_{n+1} - \mathbf{f}_{n+1} \mathbf{b}_n \mathbf{f}_{n+1}^T) \right] = -2 \bar{\mu}_{n+1} \frac{g_{n+1}^x}{\eta} \mathbf{n}_{n+1} - \\ \quad - 2 \bar{\mu}_{n+1} \frac{1}{\beta} \mathbf{n}_{n+1} [\mathbf{v}_{n+1} : \frac{1}{\Delta t} (\mathbf{g}_{n+1} - \mathbf{f}_{n+1}^{T-1} \mathbf{g}_n \mathbf{f}_{n+1}^{-1})], \\ \quad \frac{\alpha_{n+1} - \alpha_n}{\Delta t} = \sqrt{\frac{2}{3}} \left(\frac{g^y}{\eta} + \frac{1}{\beta} [\mathbf{v}_{n+1} : \frac{1}{\Delta t} (\mathbf{g}_{n+1} - \mathbf{f}_{n+1}^{T-1} \mathbf{g}_n \mathbf{f}_{n+1}^{-1})] \right) \end{array} \right. \quad (32)$$

where $\mathbf{g}_{n+1} = \mathbf{g}(\mathbf{x}_{n+1})$, g_{n+1} , f_{n+1} , \mathbf{n}_{n+1} , $\bar{\mu}_{n+1}$ are quantities which are expressible in terms of the basic variables. It is observed that Equation (31) and the rather complicated Equations (32) form a system of three independent equations in three unknowns (\mathbf{b}_{n+1} , α_{n+1} , $\boldsymbol{\tau}_{n+1}$). The solution of this system can be performed by a *three step predictor – corrector algorithm*, the steps of which are dictated by *the time discrete loading – unloading conditions* which are included in Equation (32) as well. Algorithmic details regarding the enforcement of the time discrete loading – unloading conditions and the solution of the system within the framework of a large

deformation rate – independent constitutive theory can be found in Panoskaltsis et al. [21, 24]).

REMARK 4.13. We note the absence of the consistency condition and accordingly of the consistency parameter from the time discrete equations. Due to this absence the resulting system is simpler than the classical elastic – plastic case and more computer power is preserved.

REMARK 4.14. By noting that *any objective derivative of a tensorial quantity \mathbf{q} differs from its convected Lie derivative by terms depending on \mathbf{q} and the Lie derivative of the spatial metric \mathbf{g}* (e.g., Marsden and Hughes [28, p.100], Stumpf and Hoppe [29]), Equation (25) can be used as a basis for an objective approximation of other objective derivatives which may be used in place of the convected derivative, used herein.

The predictions of the model introduced will be illustrated by considering two problems of large scale viscoplastic flow, namely the extension of a material block and the combined extension and inflation of a thick – walled cylinder.

4.2 Extension of a material block (plane strain)

The extension problem, in order to avoid necking phenomena within the specimen, is assumed to be that of a (laterally) constrained one, which is defined as

$$x^1 = (1 + \lambda)X^1, \quad x^2 = X^2, \quad x^3 = X^3.$$

The basic material parameters are those considered in Simo and Hughes [42, p. 326] where the elastic – plastic upsetting of an axisymmetric billet is examined,

$$\gamma = 384.62, \quad \mu = 833.33, \quad \sigma_y = 1.00, \quad K = 3.00.$$

The additional model parameters are set equal to

$$k = x = y = 1, \quad \eta = 10,000, \quad \beta = 1,000.$$

The predictions of the model for straining of the block up to 100%, for six different *displacement* rates ($\frac{d\lambda}{dt} = 10^{-5}, 10^{-2}, 10^{-1}, 3 \times 10^{-1}, 1, 10^6$) are shown in Figure 1. By referring to the results of this figure, we note that the predicted response is independent of the displacement rate, over a large dynamic range (from 1 to 10^6). For those rates the response is *entirely governed by the rate – independent part* of the model. On the other hand there is a *strong rate – effect for lower rates* ($10^{-5} \leq \frac{d\lambda}{dt} \leq 10^{-1} \text{ sec}^{-1}$). In this sense the predicted response is identical to that described by Bodner [43] for a fully annealed FCC metal.

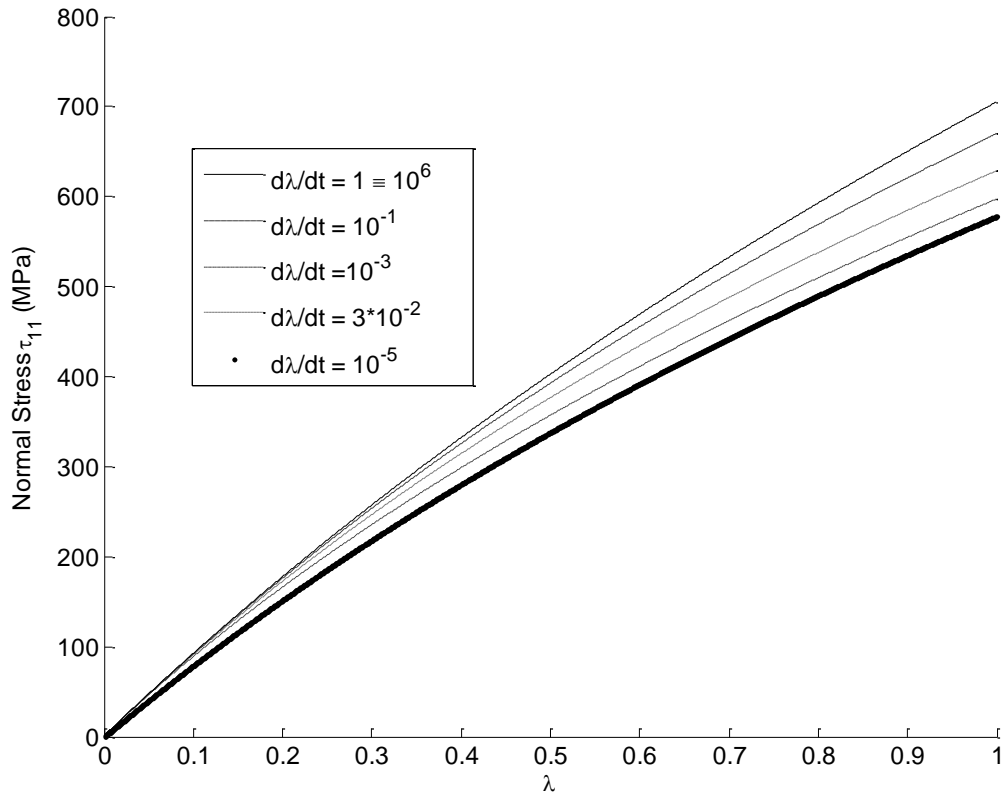


Figure 1: Restrained tension of a material block. Normal stress versus λ for different loading rates.

In order to check the model predictions in the case of an instantaneous change of rate in the course of deformation, we consider two additional straining histories. The first one involves an increasing change of rate and is given by

$$\frac{d\lambda}{dt} = \begin{cases} 10^{-3} & \text{for } 0 \leq \lambda \leq 0.1, \\ 3 \times 10^{-2} & \text{for } 0.1 \leq \lambda \leq 0.5, \\ 10^{-1} & \text{for } 0.5 \leq \lambda \leq 1. \end{cases}$$

The corresponding stress – deformation curve is shown in Figure 2, together with the original stress – deformation curves in the cases where the displacement rate remains constant throughout the test. By referring to the results of Figure 2, we conclude that after the first rate increase (from $\frac{d\lambda}{dt} = 10^{-3}$ to $\frac{d\lambda}{dt} = 3 \times 10^{-2}$), the material point “leaves” the original stress – deformation curve (for $\frac{d\lambda}{dt} = 10^{-3}$) and reaches asymptotically the original stress – defor-

mation which corresponds to the higher rate $\frac{d\lambda}{dt} = 3 \times 10^{-2}$. Upon a further rate increase (from $\frac{d\lambda}{dt} = 3 \times 10^{-2}$ to $\frac{d\lambda}{dt} = 10^{-1}$), the material point “crosses” the original stress – deformation curve corresponding to the lower rate ($\frac{d\lambda}{dt} = 10^{-1}$) and reaches asymptotically the corresponding original stress – deformation curve which corresponds to the new higher rate ($\frac{d\lambda}{dt} = 10^{-1}$).

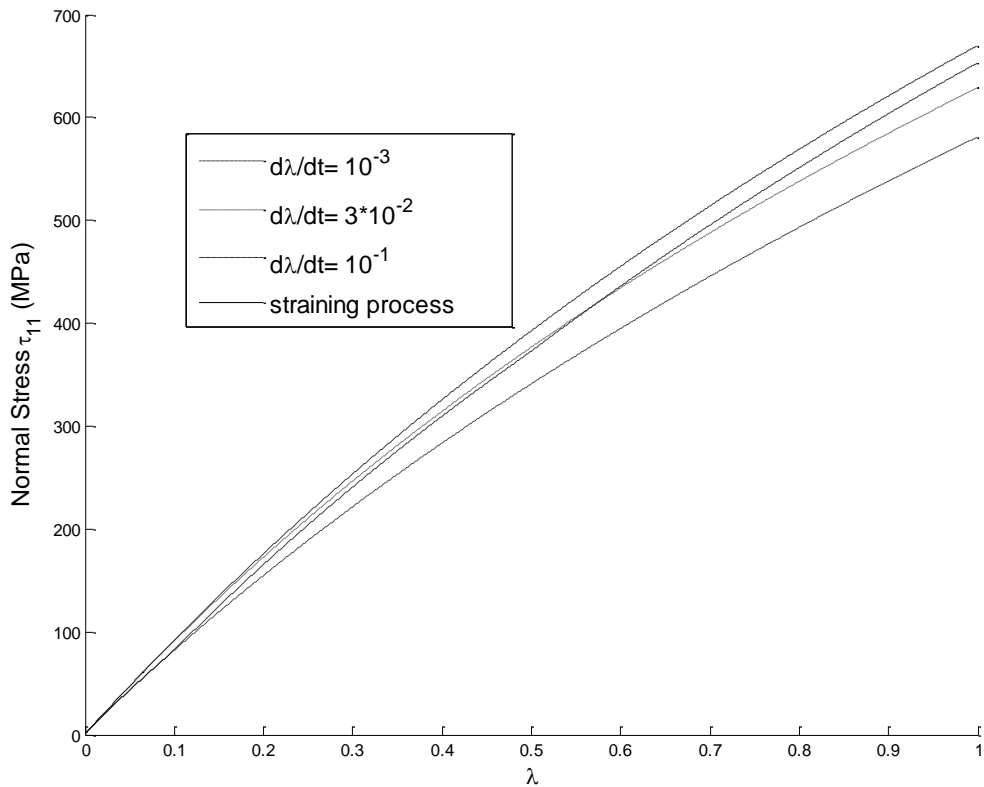


Figure 2: Restrained tension of a material block. Normal stress versus λ for increasing changes in displacement rate.

The second loading history comprises a decreasing change of loading rate and is given by

$$\frac{d\lambda}{dt} = \begin{cases} 10^{-1} & \text{for } 0 \leq \lambda \leq 0.3, \\ 3 \times 10^{-2} & \text{for } 0.3 \leq \lambda \leq 0.7, \\ 10^{-3} & \text{for } 0.7 \leq \lambda \leq 1. \end{cases}$$

The results of this test are shown in Figure 3. By referring to these results, we conclude that after the first decrease of the displacement rate (from $\frac{d\lambda}{dt} = 10^{-1}$ to $\frac{d\lambda}{dt} = 3 \times 10^{-2}$), the material point “leaves” the original stress – deformation curve (for $\frac{d\lambda}{dt} = 10^{-1}$) and after a while follows the original stress – deformation curve which corresponds to the lower rate ($\frac{d\lambda}{dt} = 3 \times 10^{-2}$). A similar response appears upon a further decrease of the rate (from $\frac{d\lambda}{dt} = 3 \times 10^{-2}$ to $\frac{d\lambda}{dt} = 10^{-3}$) with the material point eventually following the original stress – deformation curve corresponding to the lowest displacement rate. In both cases the predicted response is identical with the experimentally observed behavior in metallic materials (see Metals Handbook [44]).

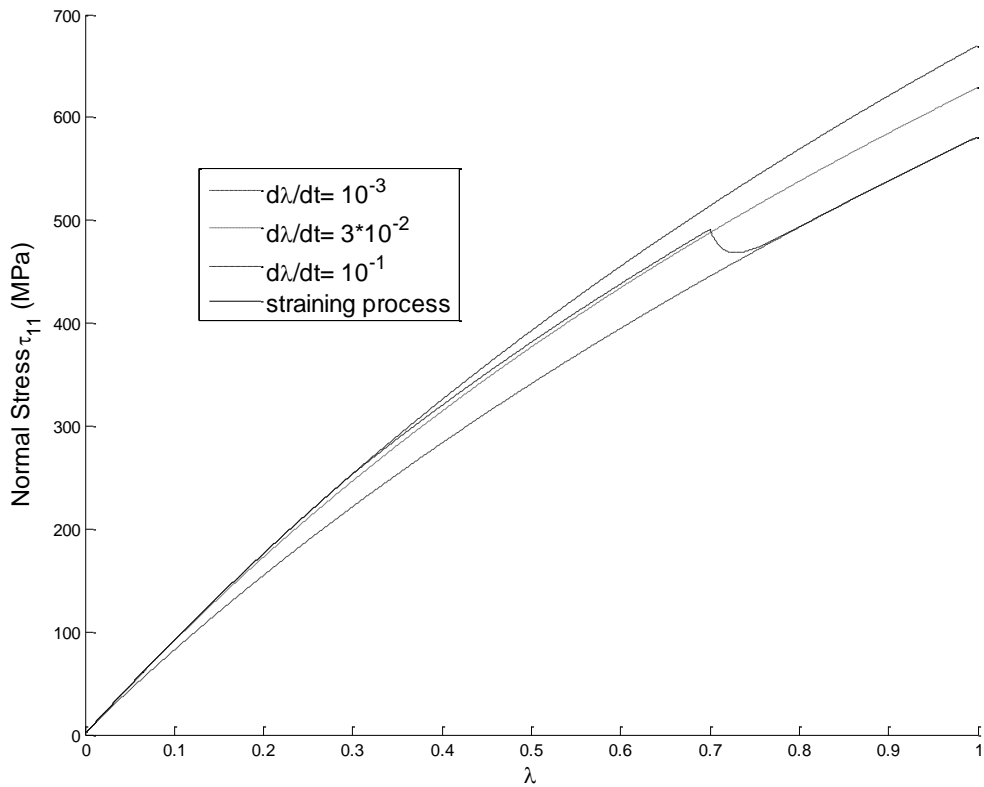


Figure 3: Restrained tension of a material block. Normal stress versus λ for decreasing changes in displacement rate.

4.3 Combined extension and inflation of a thick – walled cylinder

The combined extension and inflation of a thick - walled cylinder problem to be studied, is defined in a cylindrical polar coordinate system (see Ogden [45]) as

$$r^2 - a^2 = \frac{1}{\varpi} (R^2 - A^2), \quad \theta = \Theta, \quad z = (1 + \varpi)Z,$$

where a and A are the inner and the outer radii of the cylinder and ϖ is the axial displacement. The same problem has been also discussed within the context of the rate – independent theory by Panoskaltzis et al. [22]. The model parameters are those considered by Simo and Hughes [42, p. 324], where a similar plane strain problem is examined:

$$\gamma = 40,000, \quad \mu = 3,800, \quad \sigma_y = 0.5, \quad K = 0.00 \quad \text{and} \quad k=x=y=1, \quad \eta=\beta=10,000.$$

The cylinder is loaded under displacement control by controlling the displacement rates in both the azimuthal and the axial directions, simultaneously. Without loss of generality both rates are assumed equal. The specimen is loaded for three different rates ($\frac{d\varpi}{dt} = 5 \times 10^{-2}$, 10^{-1} and 1) until the corresponding displacement reaches a prescribed constant value ($\varpi = 18\%$), and then the displacement is kept constant leading to stress relaxation. The corresponding *time history of stress* in both radial and axial directions is depicted in Figures 4 and 5.

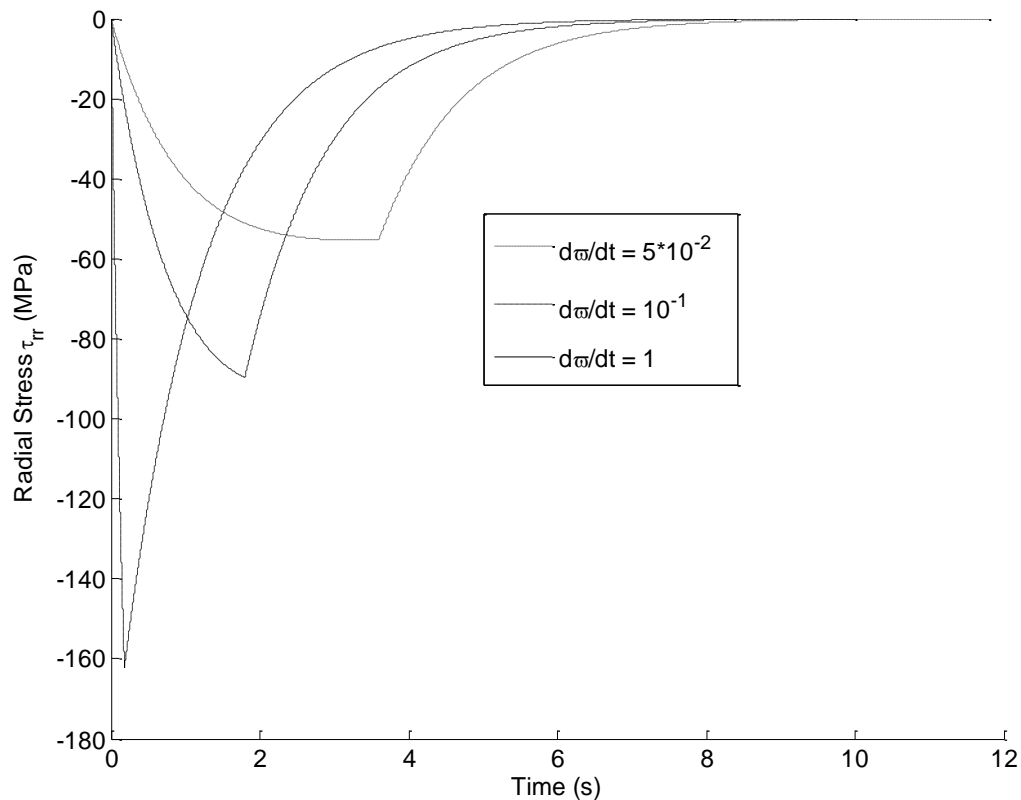


Figure 4: Combined Extension and inflation of a thick – walled cylinder. Radial stress versus time for different loading rates.

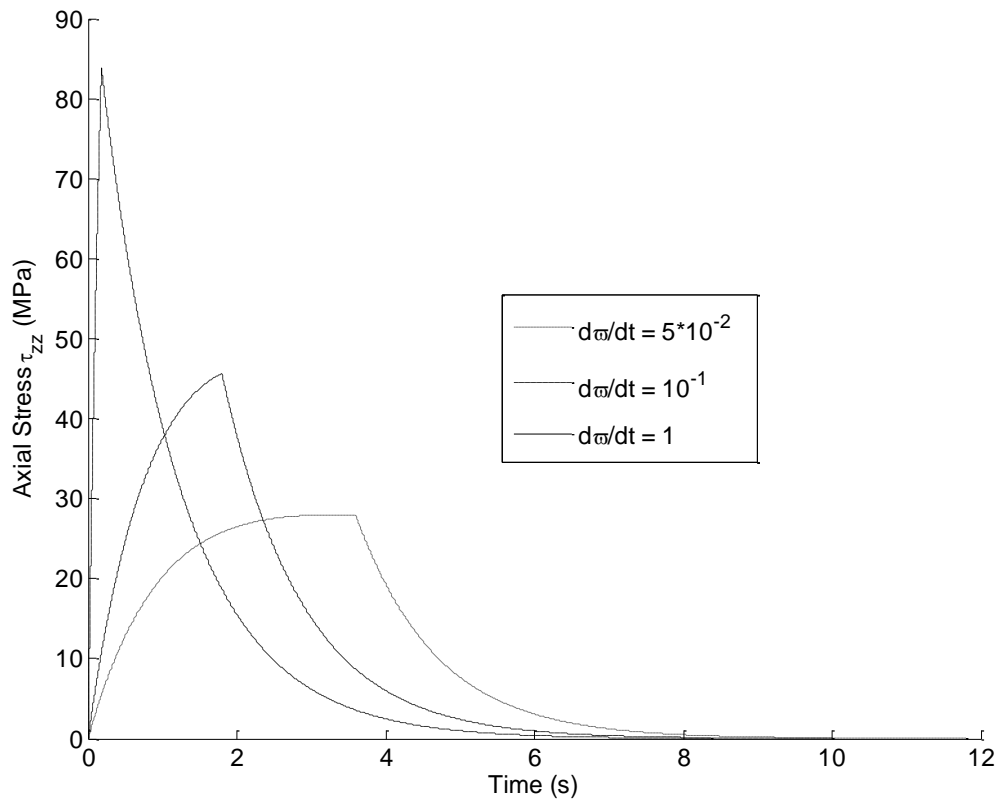


Figure 5: Combined extension and inflation of a thick – walled cylinder. Axial stress versus time for different loading rates.

5 CONCLUSIONS

The important problem of modeling solid materials with different characteristic times has been revisited. A new internal variable theory has been developed within finite deformations. The proposed theory relies crucially on the consistent combination of a general viscoplastic formulation and *a new version* of rate – independent generalized plasticity. In this new version of rate – independent generalized plasticity the concepts of viscous range and viscous process have been defined. The proposed formulation is presented in a covariant setting and in particular includes the following basic ingredients:

1. A manifold structure of the theory, which accounts not only for the body of interest and the ambient space, but for the state space as well. Accordingly, the state space is considered as a fiber over the material point, a procedure leading to a local vector bundle mapping, which is used for the identification of the dynamical process under examination.
2. Loading-unloading conditions, which have been derived in the material and in the spatial configurations.

Also, in the course of our development, important observations regarding the theories of plasticity and viscoplasticity, leading to a better understanding of those field theories, are made.

Furthermore, the concept of *physical metric* introduced by Valanis [30] and elaborated further by Valanis and Panoskaltzis [31] has been revisited within the context of a material model. The model is based on an extension of a J_2 flow theory to the finite deformation regime and considers the material metric as a basic internal variable describing both rate – dependent and rate – independent mechanisms within the body. For the numerical implementation of the model suitable approximations for the Lie derivatives of tensorial quantities are obtained. In addition, the loading-unloading conditions, which have been derived, are used. It is noted that the suitability of the model for large scale computations has been proved by:

- (a) The derivation of a novel first order – accurate time integration algorithm.
- (b) A series of numerical simulations, which show the ability of the model in predicting several patterns of the extremely complex response of metals under quasi – static and dynamic conditions.

REFERENCES

- [1] Panoskaltzis, V.P., Lubliner, J., Monteiro, P.J.M. A viscoelastic-plastic-damage model for concrete. In: C.S. Desai et al. (eds.) *Constitutive Laws for Engineering Materials*, pp. 317-320. ASME Press, N.Y., N.Y., (1991).
- [2] Panoskaltzis, V.P., Lubliner, J., Monteiro, P.J.M. Rate dependent plasticity and damage for concrete. In: P. W. Brown (ed.) *Cement Manufacture and Use*, pp. 27-40. *ASCE Special Publication*, ASCE, N.Y., (1994).
- [3] Panoskaltzis, V.P. and Bahuguna, S. Micro and macromechanical aspects of the behavior of concrete materials with special emphasis on energy dissipation and on cyclic creep. *Journal of the Mechanical Behavior of Materials*, V. 6, No. 2, pp. 119-134, (1996).
- [4] Panoskaltzis, V.P., Papoulia, K.D. and Bahuguna, S. Effect of rate on strength and energy dissipation of concrete materials. In: G.D. Manolis, D.E. Beskos, and C.A. Brebbia (eds.) *Earthquake Resistant Engineering Structures*, pp. 419-429, Computational Mechanics Publications, London, (1996).
- [5] Panoskaltzis, V.P., Bahuguna, S. and Soldatos, D. On the description of mechanisms with different characteristic times in solid materials: A non-conventional approach. *Mechanics Research Communications*, V. 25, No. 2, pp. 155-164, (1998).
- [6] Landau, H.G., Weiner, J.H., Zwicky, Jr, E. E. Thermal stress in a viscoelastic-plastic plate with temperature dependent yield stress. *J. Appl. Mech. ASME* **27**, 297 – 302 (1960).
- [7] Ivlev, D. D. On the theory of transient creep. In: *Problems of continuum mechanics* (English Edition), Society for industrial and applied mathematics, Philadelphia, 198 – 201 (1961).
- [8] Naghdi, P.M., Murch, S.A. On the mechanical behavior of viscoelastic/plastic solids. *J. Appl. Mech. ASME* **30**, 321-328 (1963).
- [9] Bodner, S.R., Partom, Y. Constitutive equations for elastic – viscoplastic strain – hardening materials. *J. Appl. Mech. ASME* **42**, 385-389 (1975).
- [10] Rubin, M.B. An elastic – viscoplastic model for large deformation. *Int. J. Eng. Sci.* **24**, 1083-1095 (1986).
- [11] Rubin, M.B. An elastic – viscoplastic model for metals subjected to high compression. *J. Appl. Mech. ASME* **54**, 532-538 (1987).
- [12] Rubin, M.B. An elastic-viscoplastic model exhibiting continuity of solid and fluid states. *Int. J. Eng. Sci.* **25**, 1175-1191 (1987).

- [13] Malvern, L.E. The propagation of longitudinal waves of plastic deformation in a bar exhibiting a strain rate effect. *J. Appl. Mech. ASME* **18**, 203 – 208 (1951).
- [14] Perzyna, P. The constitutive equations for rate sensitive plastic materials. *Quart. Appl. Math.* **20**, 321-332 (1963).
- [15] Perzyna, P. On the thermomechanical foundations of viscoplasticity. In: Lindholm, U.S. (ed.) *Mechanical Behavior of Materials under Dynamic Loads*, pp. 61-76. Springer - Verlag, New York, (1968).
- [16] Phillips, A., Wu, H.C. A theory of viscoplasticity. *Int. J. Solids Struct.* **9**, 15 – 30 (1973).
- [17] Chaboche, J. L. Viscoplastic constitutive equations for the description of cyclic and anisotropic behaviour of metals. *Bull. Acad. Polonaise Sci.* **25**, 33 – 42 (1977).
- [18] Lubliner, J. A simple theory of plasticity. *Int. J. Solids Struct.* **10**, 313-319 (1974).
- [19] Lubliner, J. A maximum – dissipation principle in generalized plasticity. *Acta Mech.* **52**, 225 – 237 (1984).
- [20] Lubliner, J. Non-isothermal generalized plasticity. In: H. D. Bui and Q. S. Nyugen (eds.), *Thermomechanical couplings in solids*, pp. 121-133, (1987).
- [21] Panoskaltzis, V.P., Polymenakos, L.C., Soldatos D. Eulerian structure of generalized plasticity: Theoretical and computational aspects. *J. Engrg. Mech. ASCE*, **134**, 354-361 (2008).
- [22] Panoskaltzis, V. P., Soldatos, D., Triantafyllou, S. P. The concept of physical metric in rate – independent generalized plasticity. *Acta Mech.* **221**, 49 -64 (2011).
- [23] Naghdi, P.M. A critical review of the state of finite plasticity. *Zeit. Angew. Math. Phys.* **41**, 315-387 (1990).
- [24] Panoskaltzis, V.P., Polymenakos, L.C., Soldatos D. On large deformation generalized plasticity. *Journal of Mechanics of Materials and Structures* **3**, 441-457 (2008).
- [25] Panoskaltzis, V.P., Soldatos, D., Triantafyllou, S.P. A geometric theory of plasticity. In: IVth International Conference on Computational Methods for Coupled Problems in Science and Engineering, COUPLED PROBLEMS 2011, M. Papadrakakis, E. Oñate and B. Schrefler (Eds.), *e-Book Full Papers*, pp. 506-520. Kos, Greece, 20-22 June, (2011).
- [26] Bishop, R. L., Goldberg, I. *Tensor analysis on manifolds*, Dover Publications, New York, (1980).
- [27] Lovelock, D. and Rund, H. *Tensors, differential forms and variational principles*. Dover Publications, New York (1989).
- [28] Marsden, J. E. and Hughes, T. J. R. *Mathematical foundations of elasticity*. Dover Publications, New York (1994).
- [29] Stumpf, H., Hoppe, U. The application of tensor algebra on manifolds to nonlinear continuum mechanics - Invited survey article. *Z. Angew. Math. Mech.* **77**, 327 - 339 (1997).
- [30] Valanis, K.C. The concept of physical metric in thermodynamics. *Acta Mech.* **113**, 169 - 184 (1995).
- [31] Valanis K.C., Panoskaltzis V.P. Material metric, connectivity and dislocations in continua. *Acta Mech.* **175**, 77 - 103 (2005).
- [32] Taleb, L., Cailletaud, G. An updated version of the multimechanism model for cyclic plasticity. *Int. J. Plast.* **26**, 859 – 874 (2010).
- [33] Sai, K.: Multi-mechanism models: Present state and future trends. *Int. J. Plast.* **27**, 250 – 281 (2011).
- [34] Simo, J. C. A Framework for finite strain elastoplasticity based on maximum plastic dissipation and multiplicative decomposition Part I: Continuum formulation. *Computer Methods Appl. Mech. Engrg.* **66**, 199 - 219 (1988).

- [35] Miehe, C. A constitutive frame of elastoplasticity at large strains based on the notion of a plastic metric. *Int. J. Solids Struct.* **35**, 3859 - 3897 (1998).
- [36] Duszek, M. K., Perzyna, P. The localization of plastic deformation in thermoplastic solids. *Int. J. Solids Struct.* **27**, 1419- 1443 (1991).
- [37] Le, K.H., Stumpf, H. Constitutive equations for elastoplastic bodies at finite strain: thermodynamic implementation. *Acta Mech.* **100**, 155 - 170, (1993).
- [38] Eisenberg, M.A., Phillips, A. A theory of plasticity with non-coincident yield and loading surfaces. *Acta Mech.* **11**, 247 - 260 (1971).
- [39] Lubliner, J. On loading, yield and quasi-yield hypersurfaces in plasticity theory. *Int. J. Solids Structures* **11**, 1011-1016 (1975).
- [40] Lubliner, J. On the structure of the rate equations of materials with internal variables. *Acta Mech.* **17**, 109 - 119 (1973).
- [41] Abraham, R., Marsden, J.E., Ratiu, T. *Manifolds, tensor analysis and applications*, 2nd ed., Springer - Verlag, New Work (1988).
- [42] Simo, J.C. and Hughes, T.J.R. *Computational inelasticity*. Springer – Verlag, New York. (1997).
- [43] Bodner, S.R. Constitutive equations for dynamic material behavior. In: Lindolm, U.S. (Ed.), *Mechanical behavior of materials under dynamic loads*, pp. 176-190. Springer - Verlag, New York, (1968).
- [44] American Society for Metals: *Metals Handbook*, 9th Edition, (1989).
- [45] Ogden, R.W. *Non - Linear elastic deformations*. Dover Publications, New York (1997).

ENDLESSLY TOUCHABLE – THE NEXT GENERATION OF SURFACE AND COATING OPTIMIZATION

ABOUT THE IDENTIFICATION OF GENERIC TRIBOLOGICAL PARAMETERS, SOPHISTICATED COMPLETELY ANALYTICAL CONTACT MODELING AND THE EFFECTIVE INDENTER CONCEPT APPLIED TO A COMPREHENSIVE 3D INCREMENTAL WEAR AND FRETTING MODEL FOR LAYERED SURFACES

Norbert Schwarzer¹

¹ Saxonian Institute of Surface Mechanics SIO
Tankow 2, 18569 Ummanz / Rügen,
Germany, www.siomec.de

e-mail: n.schwarzer@siomec.de

Keywords: Tribology, contact problems, nanoindentation, scratch, wear, extended Hertzian

Abstract. *To obtain tribological parameters like Archard's wear depth parameter kd usually requires some severe effort in performing and analyzing complex tribological experiments. The paper features an approach where such parameters are extracted from effective interaction potentials [1], which themselves are built up and fed from more physical-oriented measurements like Nanoindentation and PHYSICAL scratch. By using such effective material potentials one can derive critical loading situations leading to failure (decomposition strength) for any contact situation. A subsequent connection of these decomposition or failure states with the corresponding stress or strain distributions allows the development of rather comprehensive tribological parameter models applicable in wear and fatigue simulations as demonstrated in this work.*

From this a new sophisticated wear model has been developed on the basis of the effective indenter concept [1, 2] by using the extended Hertzian approach [3, 4]. The models do not only allow to analyze certain tribological experiments like the well known pin-on disk test or the more recently developed nano-fretting tests, but also to forward simulate such tests and even give hints for better component life-time predictions. The work will show how the procedure in principle is to be applied and a few examples will be presented in the corresponding talk.

Introduction

In order to achieve the goal set in the headline, namely, the extraction of generic tribological or wear parameters it is necessary to combine quite a few fields and/or concepts of material science. Therefore this introduction needs to cover the following issues:

- first principle based interatomic potential description of mechanical material behavior
- the effective indenter concept
- the extension of the Oliver and Pharr method to analyze nanoindentation data to layered materials and time dependent mechanical behavior
- the physical scratch and/or tribological test and its analysis

Simple first principle based interatomic potential description of mechanical material behavior

It was shown in [5] that on the basis of an effective potential function like the Morse potential given as

$$V_{\text{Morse}} = \varepsilon \left[e^{-2p(r-r_0)} - 2e^{-p(r-r_0)} \right] \quad (1)$$

a contact problem can be evaluated using the mechanical parameters derived from such a potential. Here p , ε , σ are material parameters and r_0 usually denotes the equilibrium bond length. In such a case the potential would define the pair interaction. Here however, as in [1, 5], we will apply the potential as an effective one with r_0 denoting the lattice constant (see also [6]). With respect to molecular dynamic simulation such an effective potential could be the basis for the extraction of the necessary pair and higher order interactions as demonstrated in [6]. For our study however, we will not need this, because we are only interested in the mechanical constants, especially the Young's modulus and the decomposition strength. Having this, one can apply the method described in [5] to simulate a mechanical contact problem, thereby even taking nonlinear effects like the pressure dependency of the Young's modulus into account.

Brief story about the "effective indenter concept" and its extension to layered materials

Surface usually is not bulk and so, subsequently the behavior of surfaces, especially their mechanical behavior can be dramatically different from what one might expect by just applying bulk concepts to surface problems like contact situations with very surface-located, surface-dominated stress and strain fields. In tribo and wear problems this very often compromises our ability to simulate and understand the physical processes taking place in certain tests (e.g. [7 - 11]). In order to improve this situation we therefore resort to a stringent application of a layered material model considering and modeling the mechanical surface always as - at least potentially - having a property profile starting from the mechanical bulk values in depth usually well known for a certain material to rather often completely different properties on the top-most surface layer. In the case of coated materials this model extension, of course, can easily be justified by the explicit coating structure. However, we should stress the point of also carefully and critically considering apparent "homogenous surfaces" as - rather often - being of gradient or somehow layered character.

The "effective indenter concept" itself can mathematically be described or understood as some kind of quasi conform coordinate transformation transforming the difficult problem of a curved surface contacted by a well defined indenter (like a cone) into a flat surface loaded with a complexly formed indenter. Already in 1995 Bolshakov, Oiver and Pharr [12] introduced this "Concept of the Effective Indenter" and refined it in a series of wonderful publica-

tions until in 2002 the paper about “Understanding of nanoindentation unloading curves” [13] was published by Pharr and Bolshakov.

The extension of this concept is simply performed by substituting the homogenous half space model describing the loaded sample body by a layered half space model [14].

Brief description of the extension of the Oliver and Pharr method to analyze nanoindentation data to layered materials and time dependent mechanical behavior

As it is a well established fact, that the classical Oliver and Pharr method [15], as an approach based upon the homogenous half space model, cannot directly be applied to layered materials and small structures, the author here refers to the literature [e.g. 16]. Soon after the publication of the Oliver and Pharr method it became clear that there is a physical concept this method can be based on which was called the “Concept of the Effective Indenter” [13, 14]. During a small conference in Italy in 1999, the author learned of that concept and decided to work out a theory solving not only the problem for the mechanical contact of an indenter with general shape of symmetry of revolution, but also to extend this solution to layered structures. He published its solution in 2004 [17]. Later on he also presented a variety of applications together with Pharr, Chudoba, Richter and others [18 - 23]. As a rather stubborn theoretician however, the author needed some motivation from most of the authors mentioned above, especially Pharr, before he realized that the “effective indenter theory”, even though powerful, was not something one could easily give to the engineer or an indenter experimentalist and expect him to use it as a tool for the analysis of indentation data. The reason for this is the complexity of the formulae building up the solution. Thus, the whole approach was brought into a software package named FilmDoctor® [24].

Making the classical Oliver and Pharr method fit for time dependent mechanical behavior

In an indentation test we always find complex 3-dimensional stress states with usually all stress components being non-zero. Thus, as Fischer-Cripps put it "the nature of the loading is a complex mixture of hydrostatic compression, tension, and shear" [25]. In the case of viscous behavior we also have to understand that we even have complex mixtures of stress and strain rates. These however, usually influence the time dependent mechanical parameters [26]. This automatically means that at different positions we find different stress and strain states and rates leading to different mechanical parameters (time dependent) at different positions within the material. This automatically makes the system of linear partial differential equations of linear Elasticity non-linear in the moment viscosity (even elastic viscosity) comes into play. In order to keep things simple however, we will not go here for a non-linear basic solution, but try to find effective, phenomenological descriptions for visco-elastic, visco-plastic contact problems based on the concept of a time dependent effective indenter.

Introduction into the physical scratch and/or tribological test and its analysis

The standard scratch test is a widely used method to test the mechanical stability of coatings on different types of substrates and has become a sensitive technique to control the reliability of the manufacturing process. It is based on various standards [27, 28].

Since the part above covered the calculation of true mechanical layered surface properties by nanoindentation, all mechanical values are known which are not only required to properly dimension (fine-tune) a scratch or tribology test for specific surface structures, but also is of need for a physical analysis of these tests. The following flow chart might give an illustrative understanding into such a test procedure.

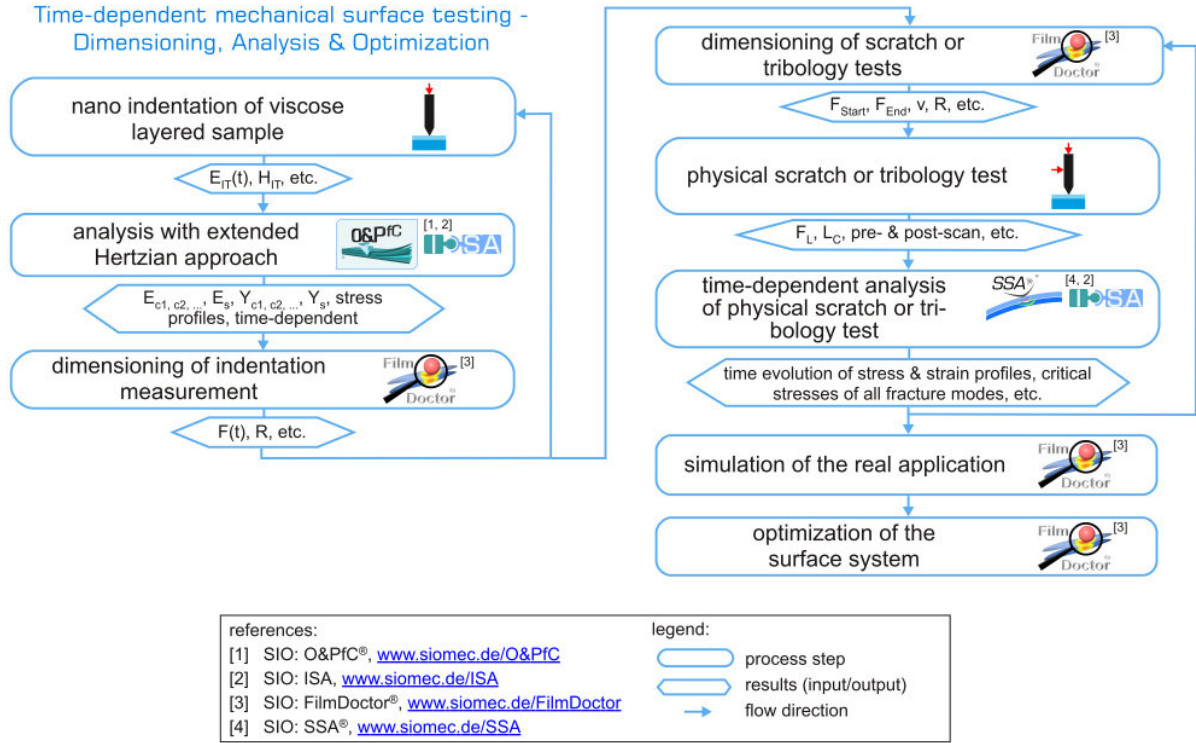


Fig. 1: A flow chart of the procedure of mechanical characterization and optimization of arbitrary structured surfaces with possibly time dependent mechanical properties

The reader will find illustrative examples and a much more comprehensive elaboration of the method in [29] and [30].

Theory

First principle based interatomic potential description of mechanical material behavior

As shown in [1] the pressure P and bulk modulus B can be derived from an effective potential. Thereby it is convenient to express P and B in units of B_0 (B at $P=0$) and by substituting the lattice distance r by $r=c \cdot r_0$ result in the relations:

$$P/B_0 = \frac{e^{r_0 p(1-c)}}{r_0 p c^2} \left[1 - e^{r_0 p(1-c)} \right]; \quad B/B_0 = \frac{e^{r_0 p(1-c)}}{r_0 p c^2} \left[2(1+r_0 p c) e^{r_0 p(1-c)} - 2 - r_0 p c \right] \quad (2)$$

We also take as estimates for the critical r leading to decomposition (c.f. [1]) the following expressions which have to be solved numerically ($r_{00} = p \cdot r_0$):

$$6(1+c_m r_{00}) - 3e^{r_{00}(c_m-1)} (2+c_m r_{00}) = 0 \quad (3)$$

to extract the critical c -value c_m for maximum $P(c)$.

As a purely mathematically based measure for the critical bond length or in our case of an effective potential the lattice distance, the inflexion point for $c_{ifp} > c_m$ could be used. This can be numerically obtained for the Morse potential via:

$$6+c_{ifp} r_{00} (4+c_{ifp} r_{00}) - 2e^{r_{00}(1-c_{ifp})} (3+2c_{ifp} r_{00} (2+c_{ifp} r_{00})) = 0 \quad (4)$$

The effective indenter concept

In order to have a sufficiently great variability for the definition of differently shaped “effective indenters”, we apply the extended Hertzian approach as shown for example in [31]. With this approach normal and even tangential load distributions of the form [17]

$$\sigma_{zz0}(r, \varphi) = \sum_{n=0}^N c_{\sigma n} r^n \sqrt{a^2 - r^2} \quad (5)$$

$$\tau_{rz0}(r, \varphi) = \sum_{n=0}^N c_{\tau rn} r^n \sqrt{a^2 - r^2}$$

$$\tau_{xz0}(r, \varphi) = \sum_{n=0}^N c_{\tau xn} r^n \sqrt{a^2 - r^2} \quad (6)$$

$$\tau_{yz0}(r, \varphi) = \sum_{n=0}^N c_{\tau yn} r^n \sqrt{a^2 - r^2}$$

with $n=0,2,4,6$ and arbitrary constants c (and by following the instructions of the mathematical procedures for obtaining the complete potential functions as given in [17] even arbitrary high but only even N) can be solved completely.

Together with lateral loads (occurring in all scratch- and tribotesters or the next generation of nanoindenters and their applications, see e.g. [31, 33, 34]) one often faces tilting moments leading to a normal surface stress distribution of the form

$$\sigma_{zz0}(r, \varphi) = \sum_{n=0}^N c_{\sigma n} r^{n+1} \cos(\varphi) \sqrt{a^2 - r^2}. \quad (7)$$

These stresses can for example occur when the indenter shaft is dragged over the surface. Because the shaft itself is elastic and thus would be bent during the lateral loading, an unavoidable tilting moment results and acts on the contacted surface. Also curved surfaces (e.g. due to roughness) can lead to such tilting moments.

A defect model: Tool for the construction of relatively general intrinsic stress distributions caused by internal inhomogeneities

In order to simulate the internal complex material structure of porous or composite materials, certain defect fields must be developed and combined with the external loads. Circular disc-like inclusions could for example be simulated by the use of plane defects within the layered half space. So, introducing circular defects of radii a_i of the loading type:

$$\begin{aligned} \tau_{rz0}(r_i = \sqrt{(x-x_i)^2 + (y-y_i)^2}, z_i + 0) &= \sum_{n=0}^N c_{\tau i,n} r_i^n \sqrt{a_i^2 - r_i^2} \\ \tau_{rz0}(r_i = \sqrt{(x-x_i)^2 + (y-y_i)^2}, z_i - 0) &= -\sum_{n=0}^N c_{\tau i,n} r_i^n \sqrt{a_i^2 - r_i^2} \end{aligned} \quad (8)$$

$$\begin{aligned} \sigma_{zz0}(r_i = \sqrt{(x-x_i)^2 + (y-y_i)^2}, z_i + 0) &= \sum_{n=0}^N c_{\sigma i,n} r_i^n \sqrt{a_i^2 - r_i^2} \\ \sigma_{zz0}(r_i = \sqrt{(x-x_i)^2 + (y-y_i)^2}, z_i - 0) &= -\sum_{n=0}^N c_{\sigma i,n} r_i^n \sqrt{a_i^2 - r_i^2}. \end{aligned} \quad (9)$$

(with x_i, y_i, z_i denoting the centre of the defect and $n=0,2,4,6$) directly allows us the application of the extended Hertzian approach [17] that provides a complete solution of the elastic field of the defect loading given above. By superposing a multitude of such “defect dots”, one could model (simulate) a very great variety of material inhomogeneities and intrinsic stress distributions. The evaluation of the complete elastic field is straight forward. It only requires the evaluation of certain derivatives of the potential functions given in [17].

Finally, we need to take into account the curvature of the surfaces in order to its effect on the resulting contact pressure distribution [32]. As the theoretical approach would not find enough space in this short note, the author will publish the necessary details elsewhere. However, the interested reader may derive the results presented here by comparing the solutions of the Laplace equation in Cartesian and Paraboloidal coordinates.

The extension of the Oliver and Pharr method to analyze nanoindentation data to layered materials and time dependent mechanical behavior

Oliver and Pharr [15] have shown that the force removal curve from elasto-plastic deformations with a Berkovich indenter can be described by a power function:

$$F = C \cdot (h - h_0)^m \quad (10)$$

Applying now the concept of the effective indenter as shown in fig. 2 one can easily deduce that such an unloading curve can be connected with an Indenter of the shape.

$$Z(r) = B \cdot r^n, \quad (11)$$

with:

$$\begin{aligned} m &= 1 + \frac{1}{n} \\ C &= 2 \cdot E_r \cdot \left[\frac{n}{n+1} \right] \cdot \left(\frac{1}{B} \cdot \left[1 - \varepsilon \cdot \frac{n}{n+1} \right] \right)^{\frac{1}{n}} \\ \frac{1}{E_r} &= \frac{1 - \nu_i^2}{E_i} + \frac{1 - \nu_s^2}{E_s} \\ \varepsilon &= m \cdot \left[1 - \frac{1}{\sqrt{\pi}} \frac{\Gamma\left(\frac{m}{2 \cdot m - 2}\right)}{\Gamma\left(\frac{2 \cdot m - 1}{2 \cdot m - 2}\right)} \right] \end{aligned} \quad (12)$$

The indices i and s are standing for the indenter and sample, respectively.

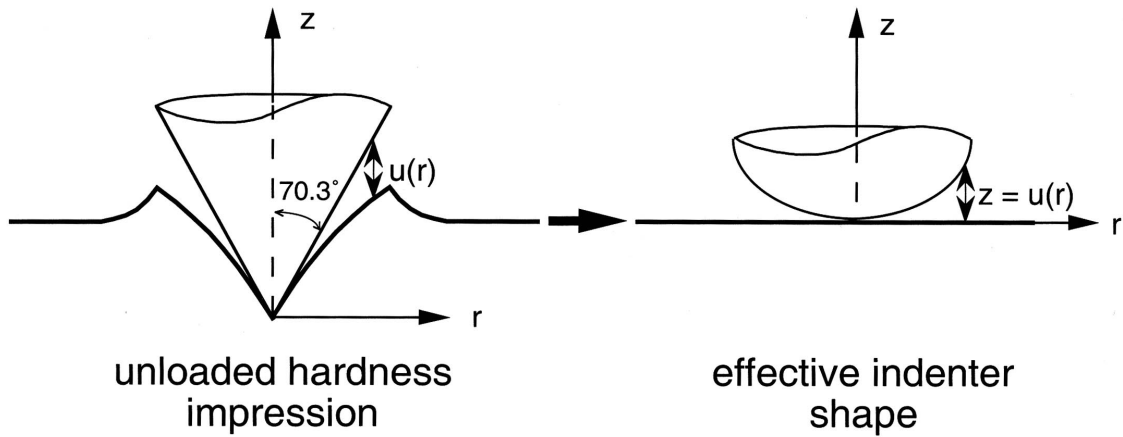


Fig. 2: The effective indenter concept (see: G. M. Pharr, A. Bolshakov: J. Mater. Res., Vol. 17, No. 10, Oct 2002) transferring the theoretical difficult problem of a well defined sharp indenter on a elasto-plastically deformed surface with complex shape (left hand side) by an effective indenter on a flat surface.

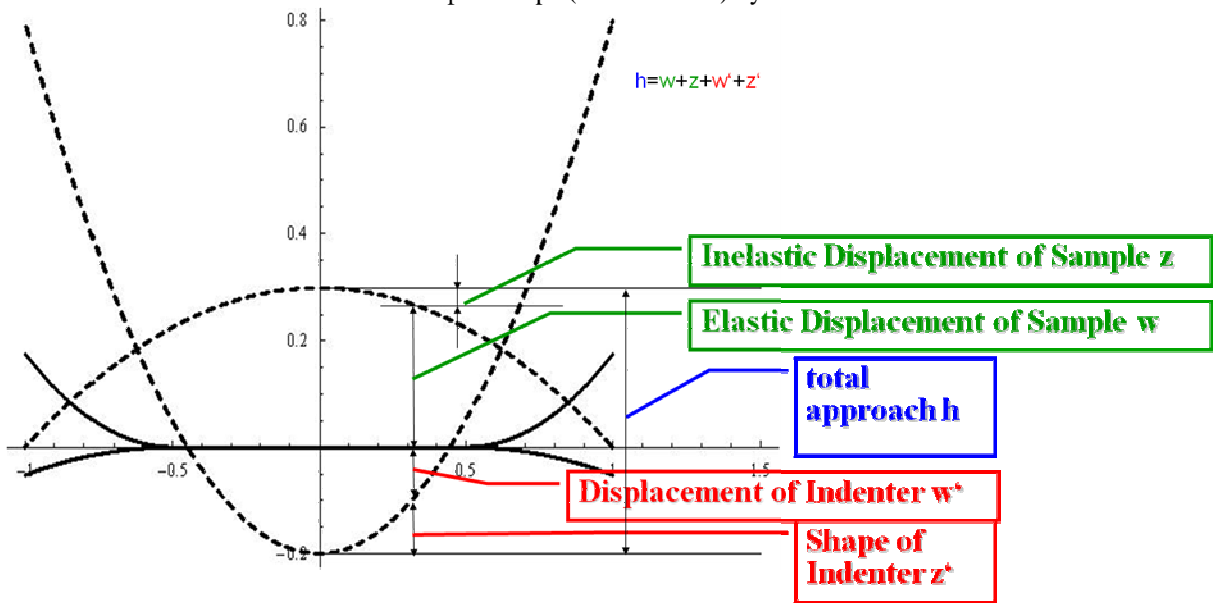


Fig. 3: Formulating the contact equation $h=w+z+w'+z'$ with respect to partial plastic deformation z of the sample surface

For this one needs to reformulate the basic contact equation incorporating the plastically deformed surface of the sample with the locally defined shape function (fig. 3)

$$z(r) = B_S \cdot r^n, \tag{13}$$

Together with the following approach for the indenter part being in contact with the sample surface of the kind

$$z'(r) = B_I \cdot r^n, \tag{14}$$

we obtain

$$w(r) + w'(r) = h - (B_I + B_S) \cdot r^n, \tag{15}$$

as the new governing contact equation with the parameters $B=B_I+B_S$ and n defining the effective indenter shape $Z(r)$, as given above.

Similarly also more general effective indenter concepts can be derived, like this one

$$\begin{aligned}
 w_s(r) + w_I(r) &= h - \frac{r^2}{d_0} - \frac{r^4}{d_2} - \frac{r^6}{d_4} - \frac{r^8}{d_6} \\
 &= h - r^2 \left(\frac{1}{d_0^{Indenter}} - \frac{1}{d_0^{plastic\ shape}} \right) - r^4 \left(\frac{1}{d_2^{Indenter}} - \frac{1}{d_2^{plastic\ shape}} \right), \\
 &\quad - r^6 \left(\frac{1}{d_4^{Indenter}} - \frac{1}{d_4^{plastic\ shape}} \right) - r^8 \left(\frac{1}{d_6^{Indenter}} - \frac{1}{d_6^{plastic\ shape}} \right) \\
 &= h - r^2 (c'_0 - c_0) - r^4 (c'_2 - c_2) - r^6 (c'_4 - c_4) - r^8 (c'_6 - c_6)
 \end{aligned} \tag{16}$$

based on a locally paraboloid surface with r-terms r^0 , r^2 , r^4 , r^6 and r^8 . The reader might easily recognize the extended Hertzian character [22] of the basic contact equation given above as the more simpler Hertzian contact would read:

$$\begin{aligned}
 w_s(r) + w_I(r) &= h - \frac{r^2}{d_0} \\
 &= h - r^2 \left(\frac{1}{d_0^{Indenter}} - \frac{1}{d_0^{plastic\ shape}} \right), \\
 &= h - r^2 (c'_0 - c_0)
 \end{aligned} \tag{17}$$

Some of the following examples and discussions will be based on these more general approaches. However, due to the wide use of the power law fit given above we will explicitly concentrate on the practical examples being performed using the power law approach. In [17] and [22] it is shown how these general contact approaches can be applied and how the complete elastic fields have to be evaluated while the extension to the case of layered materials is been elaborated in [14]. Extension to tilting and lateral loads is given in [22] and [24]. The next thing of need now is a time dependent analysis method for ordinary quasi-static nanoindentation tests (e.g. [35] with application [36]). Our approach will be of the following kind [25]:

$$F = C * (h - h_0)^m \quad \rightarrow \quad F = C(t) * (h - h_0(t))^{m(t)} \tag{18}$$

with t denoting the time.

The next step is the introduction of a time dependent material model. Here we resort to the well known three parameter approach given by a Young's modulus of the following kind $E(t) = E_0 + E_1 \text{Exp}[-t/\tau_R]$ ($\tau_R \equiv \tau \dots$ relaxation time).

Now we substitute the time dependent Young's modulus into the function C(t) of equation (18) and obtain

$$F = 2 \cdot \left(\frac{1 - \nu_i^2}{E_i} + \frac{1 - \nu_s^2}{E_{s0} + E_{s1} \cdot e^{-\frac{t}{\tau}}} \right)^{-1} \cdot \left[\frac{n}{n+1} \right] \cdot \left(\frac{1}{B} \cdot \left[1 - \varepsilon(n) \cdot \frac{n}{n+1} \right] \right)^{\frac{1}{n}} * (h - h_0)^{\left(1 + \frac{1}{n}\right)} \tag{19}$$

This makes the classical fit of the three constants h_0 , m and C a time dependent 6-parameter fit of h_0 , n , B and the material constants E_0 , E_1 and τ_R . It is clear that so many parameters in just one curve will automatically lead to numerical difficulties and instabilities. Thus, even in the pure visco-plastic case it is strongly suggested to use a variety of curves (3 might be good number) obtained with different unloading speeds or at different maximum loads with similar unloading times.

In cases of time dependent inelastic behavior (like visco-plasticity) or more complex constitutive laws also n , B and h_0 have to be taken as $n(t)$, $B(t)$, $h_0(t)$ making the fit even more complex. The same holds in the visco-elastic case for just h_0 when there are great differences between unloading time and τ_R (comparable strain rates). The parameters n and B on the other hand are then only geometrical parameters and do not explicitly depend on time. A more detailed derivation and discussion of this extension is to be found in [37].

Theory for the physical scratch and/or tribological test

The governing contact equation and stress distributions for more general loading condition as occurring during tests like scratch and pin on disc have already been given in the section "the effective indenter concept". The evaluation of the complex stress and strain fields for these tests is elaborated in the references given there. However, as these evaluations are rather cumbersome and lengthy, the reader is also referred to a software package performing such calculations in an automated and quick manner [24].

It should explicitly pointed out here, that knowledge of the complete stress and strain field is essential for a proper failure characterization (scratch) or wear mechanism analysis (tribo). An example is presented in the figures below.

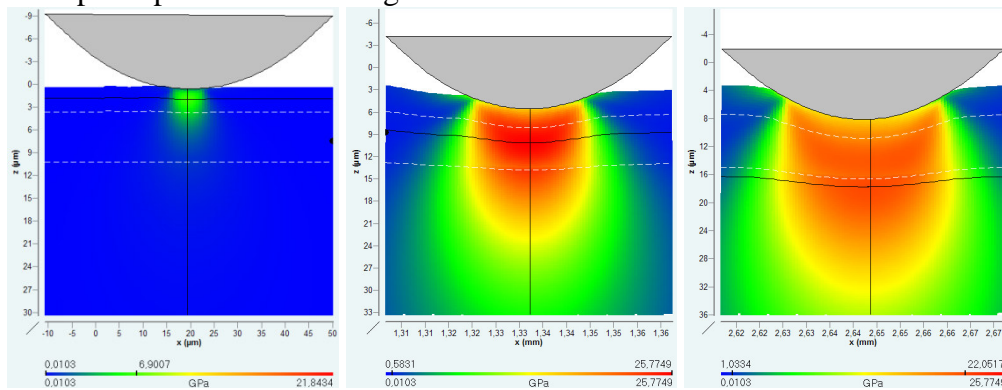


Fig. 4: The evolution of von-Mises stress during the scratch test shown at three measurement points: (a) at the beginning of the scratch test, (c) in the moment of LC failure, and (b) in between. The black cross hairs indicate the location of the maximum.

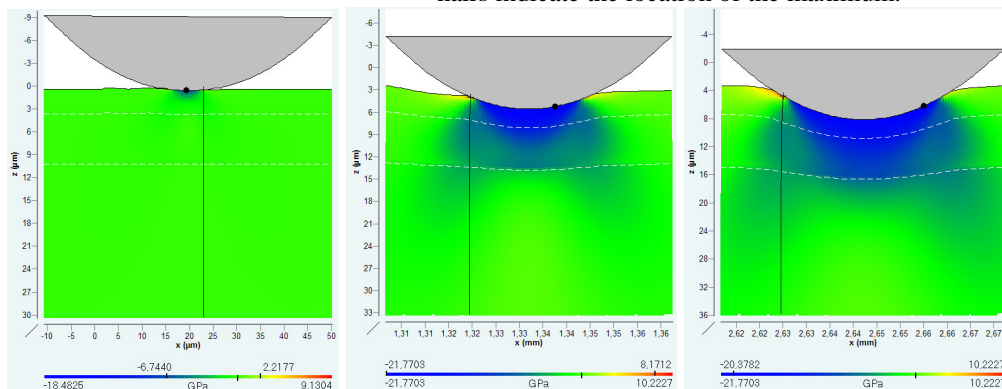


Fig. 5: The evolution of normal stress in scratch direction illustrated at three measurement points: (a) at the beginning of the scratch test, (c) in the moment of LC failure, and (b) in between. The black cross hairs indicate the location of maximum tensile stress.

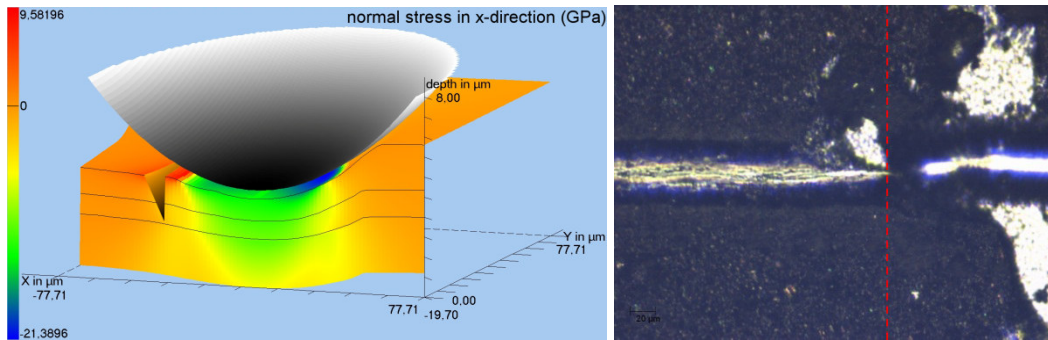


Fig. 6: Illustrative scheme of the failure mechanism (a) and an optical graph of the post-scratch surface (b) in which the corresponding LC position is marked by the red dashed line.

Hence, only such a physical analysis of mechanical contact measurements like instrumented indentations, scratch and tribo-tests enables one to find out why a surface structure fails under certain loading conditions. These results provide indications on how the investigated coating structure can be improved.

From quasi-static experiments and parameters to dynamic wear, fretting and tribological tests

Now we need to establish the relationship between quasi-static characteristics, like hardness, yield strength, Young's modulus etc. etc. and highly dynamic characteristics like wear, fretting and other tribological processes and effects.

First of all, it must be understood that within the concept of this approach the process of wear, fretting or general tribological process is a to be considered as a multi-physical multi body (asperity) ensemble of contact situation (called load dots, c.f. [40]) with each having its own geometry, load conditions (including tilting, normal, lateral, twisting loads plus frictional caused temperature fields) and – in complex cases with debris – also multiple time scales, meaning various parts of the global tribological contact are running in their own speed. Of course, we will then have to take temperature effects often coupling back into the mechanical properties and time dependent material behavior (c.f. section “The extension of the Oliver and Pharr method to analyze nanoindentation data to layered materials and time dependent mechanical behavior”) into account. However, the mathematics of partial differential equations does provide an interesting short cut here. It is due to the similarity of the governing differential equations that having found the solution for the contact problem immediately gives us the solution for the temperature field or any other “diffusion-like” problem. So, the layered solution for any diffusion problem can be extracted from the elastic solution by letting the Poisson's ratio go to infinity leading to perfectly non-singular field solution for the diffusion problem in question.

Beside that: The connection between non-physical parameters (like hardness) towards wear is not the intention of the paper. In fact, there is no such connection – strictly speaking. Something not generic like hardness simply cannot – not generally – be extended or applied to a dynamic process like wear. To put it metaphorically: Somebody who intends to model the gravity and curvature of space around a very dense star will probably not try to start with Galilei's fall experiments and concepts but uses the Einstein field equations instead.

Where is the role of debris particles?

They are just adding up to the complex jumble of contact situations mentioned above.

How are strain rate effects taken into account?

By applying either piecewise 3-parameter models or solving the nonlinear governing system of equations with time-stress- and strain-dependent material parameters (c.f. section “The extension of the Oliver and Pharr method to analyze nanoindentation data to layered materials and time dependent mechanical behavior”).

How are intrinsic stress been taken into account?

Intrinsic stresses are just adding to the external stresses (and strain) fields and lead to a subsequent shift of onset of inelastic behavior, be it fracture, plastic flow or phase transition. Therefore it is very important to know and consider intrinsic stresses as accurately as possible. Here "accurately" explicitly means that intrinsic stresses are usually not homogeneously distributed but also present a complex field adding up to the deformation field coming from external loading situations.

How is the wear of the system (both the softer and harder of the materials) accounted for?

By decomposition limits extracted from the first principle approaches as described in the procedure-plan below. The concepts of "softer" or "harder" have nothing to do with this general approach.

How can this be achieved in a rather general manner?

The most general way would be to extract decomposition limits from the first principle approaches as described in [2]. These limits have then to be compared with the deformation fields obtained in the multiple complex contact model describing our tribo, fretting or wear experiments. Thereby, we explicitly point out, that wear cannot be connected by a simple k_d -value (simple Archard's law) to the deformation or stress field. Instead, in the most simple and linear case, the tribo-effect is a tensor, coupling with wear-moduli to every deformation field component in a fully covariant manner. More correctly any tribo-process could be linearly generalized like:

$$tribo - effect_{ij} = k_{ijkl}^{\sigma} \sigma^{kl} + k_{ijkl}^{\epsilon} \epsilon^{kl} + k_{ijkl}^u u^k u^l + \sum_{n=1}^N k^{S_n} \delta_{ij} S_n \quad (20)$$

Here we used the following denotations: k_{ijkl}^{xx} -tensors are tensors coupling to the various field values or tensors like the stress σ^{kl} , strain ϵ^{kl} , displacement-vector u^i or scalar values S_n , like free or distortion energy strain work etc.. The symbol δ_{ij} is the Kroenecker symbol. In most cases, wear for instance, it should be sufficient to consider only the stresses:

$$tribo - effect_{ij} \equiv w_{ij} = k_{ijkl} \sigma^{kl} \quad (21)$$

Wherefrom the scalar wear-depth h_w has to be evaluated via:

$$h_w = w_{ij} n^i n^j \quad (22)$$

With n^i denoting the surface normal unit vector.

As we can see, the Archard's law given with a scalar wear coefficient k_d by the simple relation $h_w = k_d * \sigma^{33}$ is nothing but a rather dramatic simplification of equation (21) being possible wherever either the stress is dominated by its normal component in the surface normal direction (here we named it σ^{33}) or where the coefficient tensor k_{ijkl} is zero except for those components coupling to the normal surface stress σ^{33} , which would then read:

$$h_w = w_{ij} n^i n^j = k_{ijkl} \sigma^{kl} n^i n^j = k_{33kl} \sigma^{kl} \simeq k_{3333} \sigma^{33} \equiv k_d \sigma^{33} \quad (23)$$

We can deduce now that for complex contact conditions, where the stress tensor is fully set and no component is dominant against all the others one should be rather careful with the assumption of having the wear-tensor being of the most simple, Archard's-law-like kind

$k_{33kl} = \begin{pmatrix} 0 & 0 & 0 \\ 0 & 0 & 0 \\ 0 & 0 & k_{3333} \end{pmatrix}$. One better also takes the other stresses into account and investigates

their possible influence regarding the resulting global wear, which, in this case, has to be taken as the sum over all stress-components in connection with the wear-tensor

$$h_w = k_{33kl} \sigma^{kl} = k_{3311} \sigma^{11} + k_{3322} \sigma^{22} + k_{3333} \sigma^{33} + 2(k_{3312} \sigma^{12} + k_{3313} \sigma^{13} + k_{3323} \sigma^{23}) \quad (24)$$

Here we have made use of the symmetry of the stress tensor, also requiring a symmetric wear-tensor.

Even though, in principle, we have now said what is of need, we explicitly point out again, that wear cannot be connected by a simple k_d -value (simple Archard's law) to the deformation or stress field. Instead, in the most simple cases, the wear is a tensor, coupling with wear-moduli or wear-components to every stress component in a fully covariant manner:

$$w_{ij} = k_{ijkl} \sigma^{kl} \quad (25)$$

We also point out, that in the general law as given above the hydrostatic (sphere) and deviatoric stress parts are distinguishable. Such a simplified law might read:

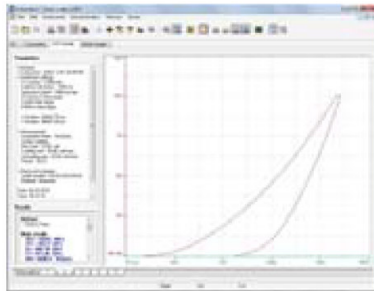
$$w_{ij} = \delta_{ij} (k_{dM} \sigma_M + k_{dH} \sigma_H + k_{dI} \sigma^I) \quad (26)$$

With σ_M, σ_H denoting the von Mises and the hydrostatic stress, respectively.

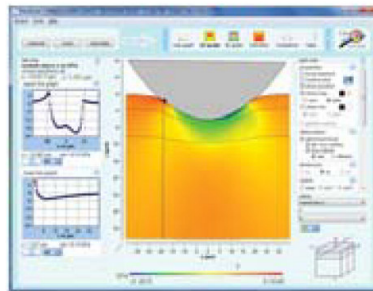
The Procedure and Results

Now we need to connect the various models and concepts introduced and elaborated above in order to construct a compact optimization circle including wear test and simulation.

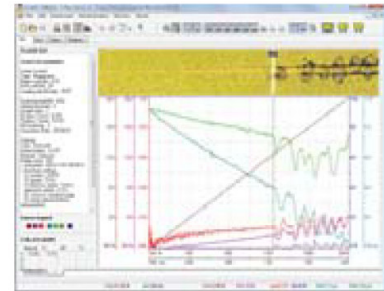
This shall be illustrated by the means of a practical example for cutting tools as follows:



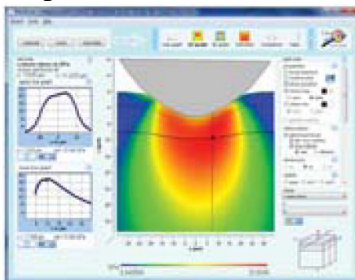
Step 1



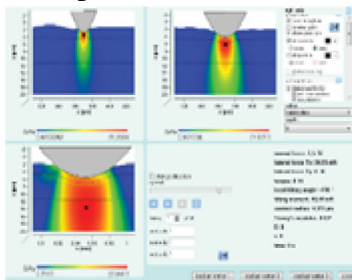
Step 2



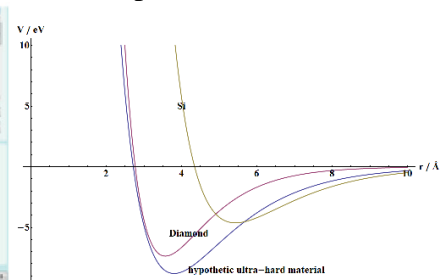
Step 3



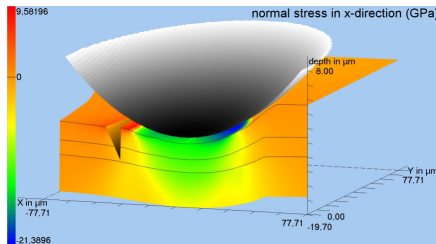
Step 4



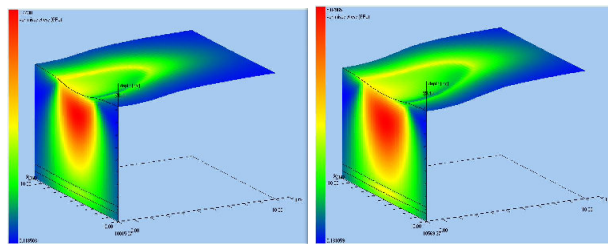
Step 5



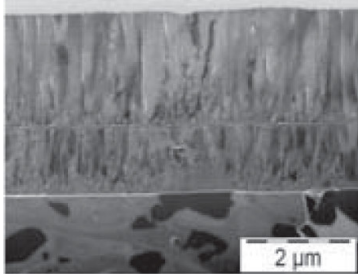
Step 6



Step 7



Step 8 (from middle of wear test to its end)



Step 9 (reproduced from [46], with permission of the authors)

Step 1:

Nanoindentation tests are performed to accurately measure the materials properties of the substrate and coatings, taking into account possible property profiles [38, 39].

Step 2:

With the mechanical properties previously measured by nanoindentation, a calculation of the stress-strain fields of a simulated scratch allows a perfect dimensioning of the scratch test [29, 30].

Step 3:

Scratch testing with the defined conditions is performed.

Step 4:

An advanced analysis with integration of the residual penetration depth, pre-scan surface profile, and friction coefficient is made with the simulation software in order to perfectly know the stress-strain field [24].

Step 5:

For better understanding, an animation of the scratch is created (examples under: www.siomec.de/en/096/Examples).

Step 6:

From the results of the previous steps effective interatomic potentials are evaluated and decomposition parameters are derived as shown in [5]. These parameters are used to design a tribo-test optimum for the later application in question.

Step 7:

Performance of tribo-test as designed in step 6 and analysis by inversed global increment wear model [9] improved with layered half space model and extended Hertzian approach.

Step 8:

For better understanding, an animation of the tribo- resp. wear-test is created (c.f. figures 7 - 15 below).

Step 9:

Optimization of coating-substrate system. Going to next circle.

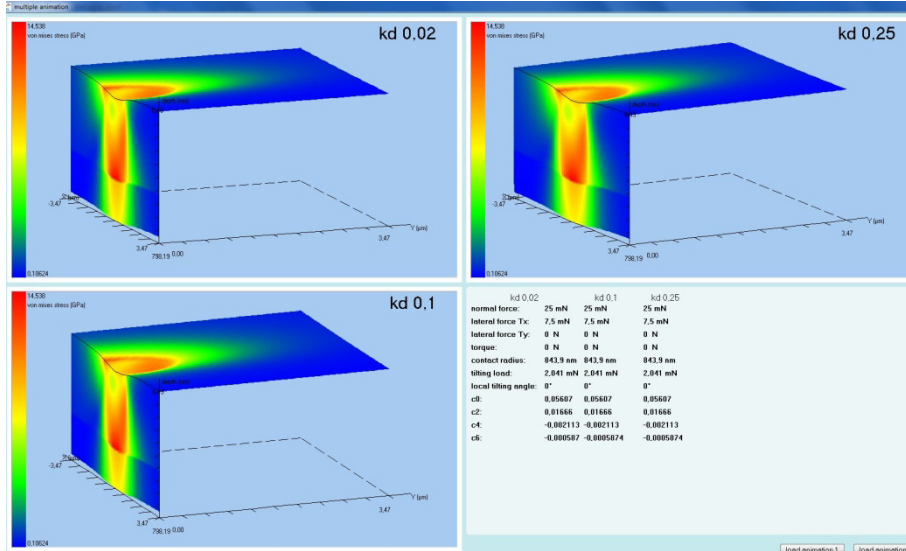


Fig. 7: Wear track evaluation of an oscillating pin (linear wear track) on three different coating materials. Beginning of the Wear test. Von Mises stress.

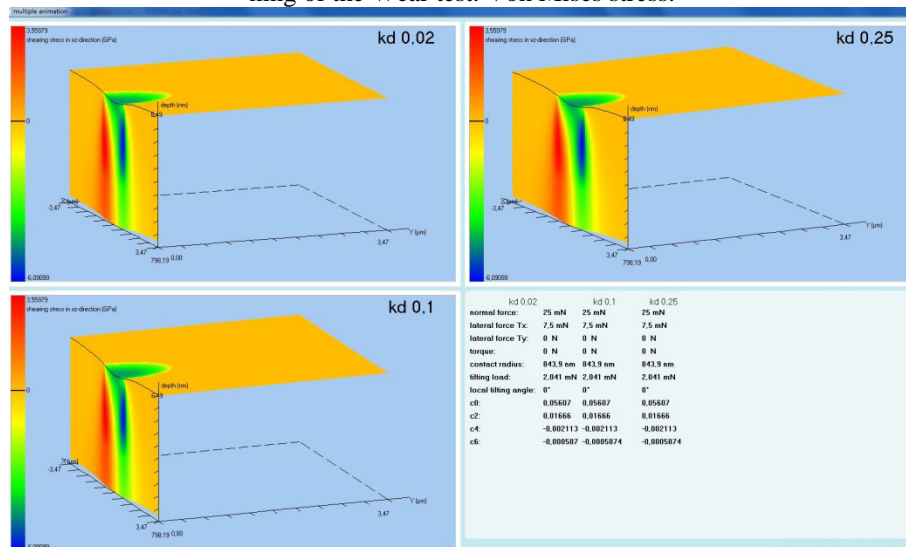


Fig. 8: Wear track evaluation of an oscillating pin (linear wear track) on three different coating materials. Beginning of the Wear test. Shear stress in normal-lateral direction.

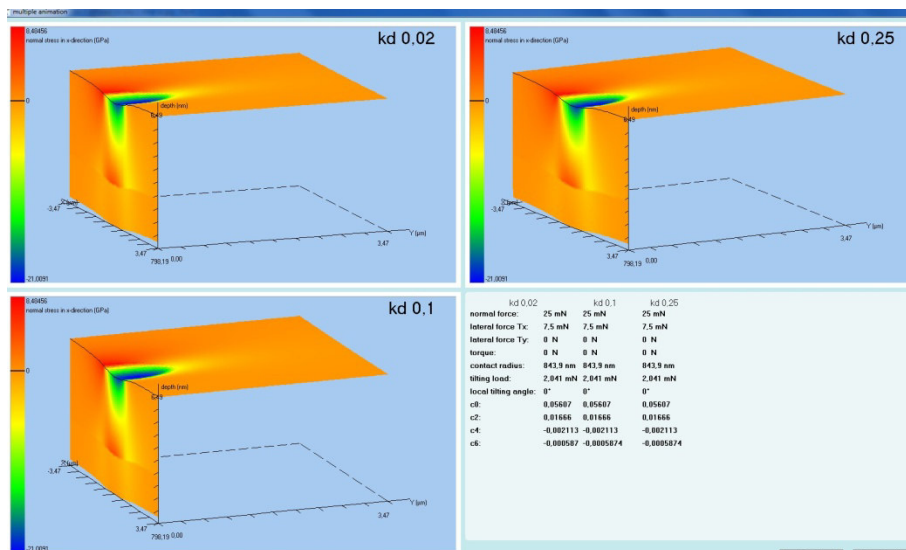


Fig. 9: Wear track evaluation of an oscillating pin (linear wear track) on three different coating materials. Beginning of the Wear test. Normal lateral stress in direction of the moving pin.

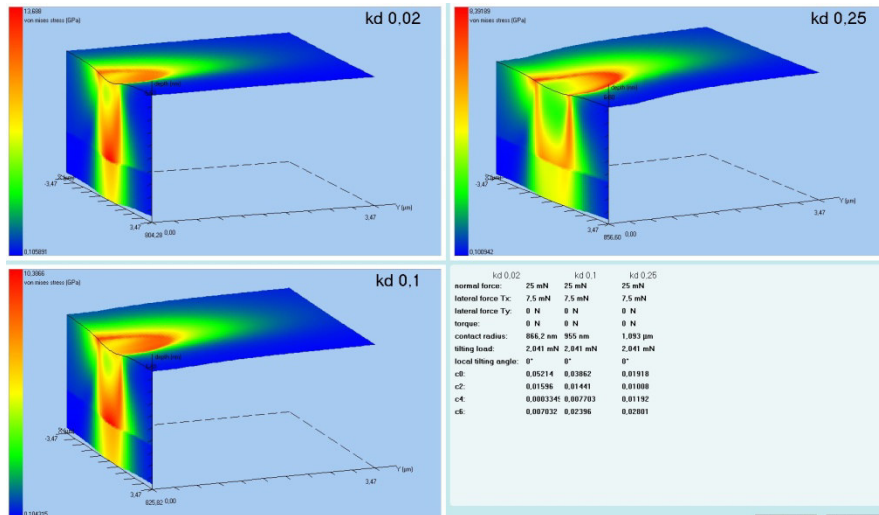


Fig. 10: Wear track evaluation of an oscillating pin (linear wear track) on three different coating materials. Middle of the Wear test. Von Mises stress.

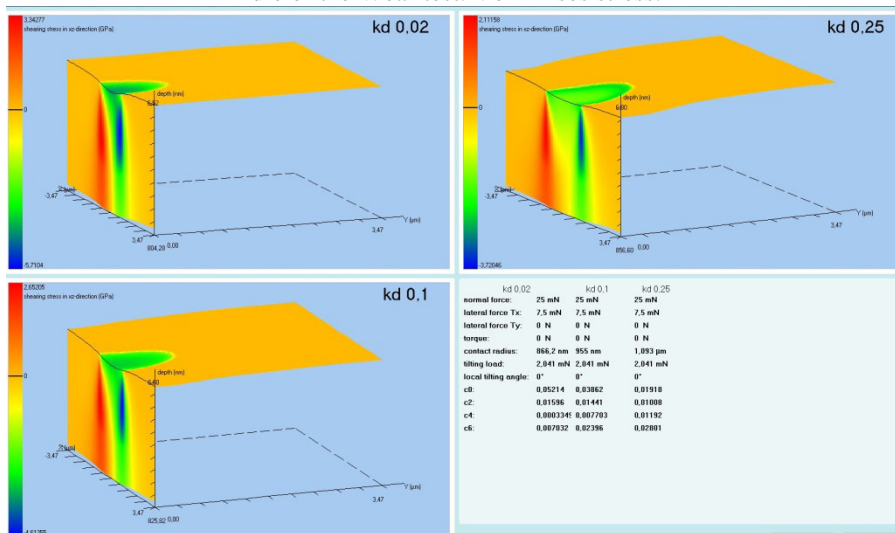


Fig. 11: Wear track evaluation of an oscillating pin (linear wear track) on three different coating materials. Middle of the Wear test. Shear stress in normal-lateral direction.

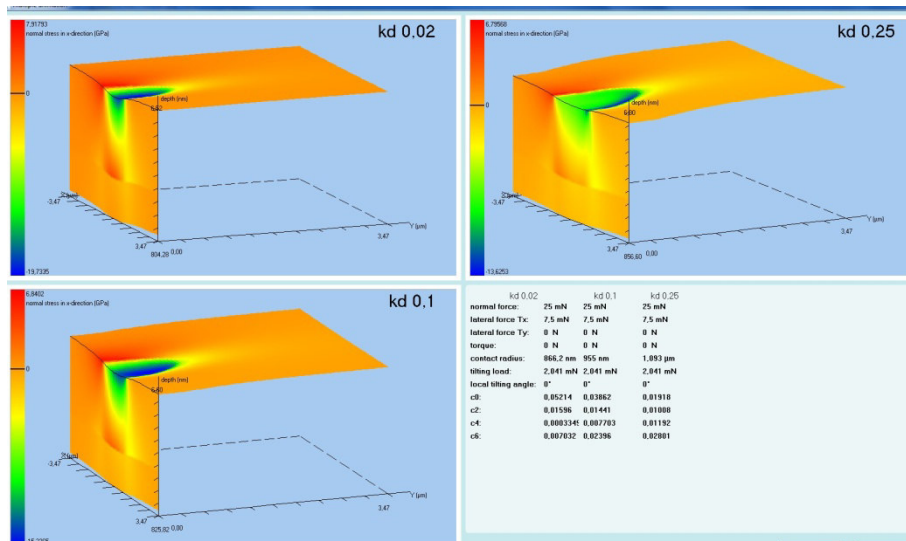


Fig. 12: Wear track evaluation of an oscillating pin (linear wear track) on three different coating materials. Middle Beginning of the Wear test. Normal lateral stress in direction of the moving pin.

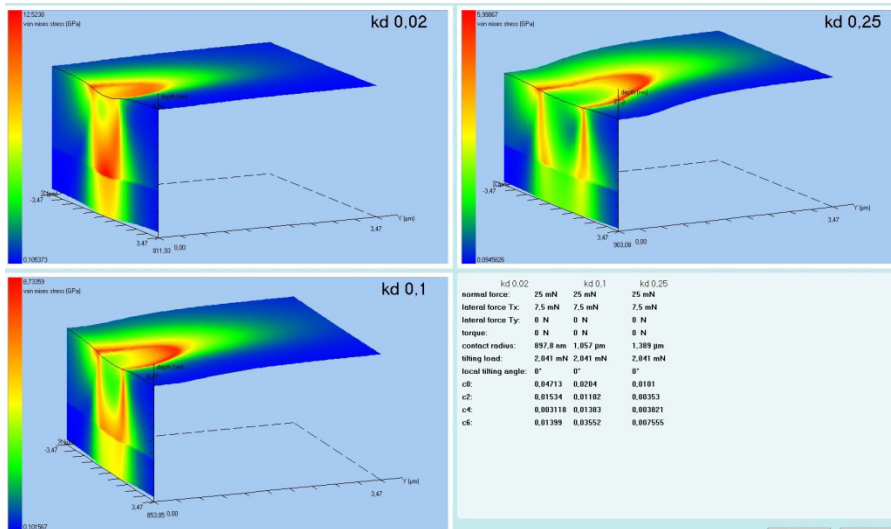


Fig. 13: Wear track evaluation of an oscillating pin (linear wear track) on three different coating materials. End of the Wear test. Von Mises stress.

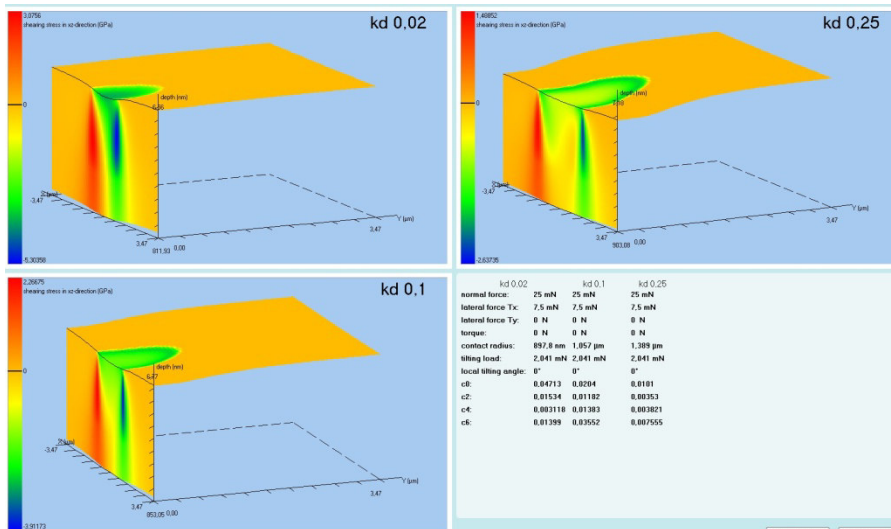


Fig. 14: Wear track evaluation of an oscillating pin (linear wear track) on three different coating materials. End of the Wear test. Shear stress in normal-lateral direction.

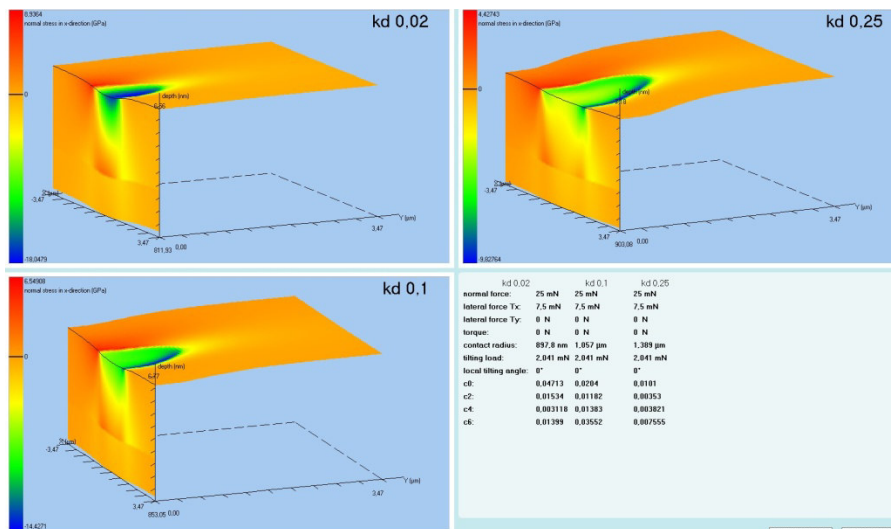


Fig. 15: Wear track evaluation of an oscillating pin (linear wear track) on three different coating materials. End of the Wear test. Normal lateral stress in direction of the moving pin.

Examples

The method was applied, sometimes in parts sometimes completely, to a variety of examples which are published elsewhere (e.g. [29, 30] and [41 – 45]).

Conclusions

By combining the global increment wear model with the concept of the effective indenter, the extended Hertzian approach and a layered half space solution for contact problems with rather arbitrary combinations of normal, lateral and tilting loads a general, quick and powerful wear model has been created.

Inversion of the model makes it fit for parameter identification problems.

Further adding first principle models, like effective interatomic interaction potentials allows a deeper understanding of those failure mechanisms being responsible for wear results observable in practical tests.

Acknowledgements

This work was partially funded through the European Metrology Research Programme (EMRP) Project IND05 MeProVisc. The EMRP is jointly funded by the EMRP participating countries within EURAMET and the European Union.

References

- [1] N. Schwarzer, Short note on the effect of pressure induced increase of Young's modulus, Philosophical Magazine, accepted January 2012, vol. 92, issue 13, pp. 1631-1648
- [2] N. Schwarzer, G. M. Pharr: „On the evaluation of stresses during nanoindentation with sharp indenters”, Thin Solid Films, Vol. 469-470C pp. 194-200
- [3] N. Schwarzer, T. Chudoba, G. M. Pharr: „On the evaluation of stresses for coated materials during nanoindentation with sharp indenters”, Surf. Coat. Technol, Vol 200/14-15 pp 4220-4226
- [4] N. Schwarzer: "The extended Hertzian theory and its uses in analysing indentation experiments", Phil. Mag. 86(33-35) 21 Nov - 11 Dec 2006 5153 – 5767, Special Issue: “Instrumented Indentation Testing in Materials Research and Development”
- [5] N. Schwarzer, "Is ultra-hardness possible - a brief feasibility study", www.siomec.de/ultra-hard-coatings, also invited for publication in Phil. Mag.
- [6] M. Lie, N. X. Chen, Möbius inversion transform for diamond-type materials and phonon dispersions, Physical Review B, 52, No. 2 (1995), 997 - 1003
- [7] T. Dick, G. Cailletaud, (2006) Computational Materials Science, 38, 113-125
- [8] J. M. Guilemany, S. Dosta, J. R. Miguel, (2006) Surface and Coatings Technology 201, 1180-1190
- [9] V. Hegadekatte, N. Huber, O. Kraft, (2006) Tribology Letters 24, 51-60
- [10] R. Holm, (1946) Electric contacts , Almqvist and Wiksells Boktryckeri AB, Uppsala
- [11] K. Holmberg, A. Matthews, (2009) Coatings Tribology. 2nd edition, Springer, Amsterdam, The Netherlands
- [12] A. Bolshakov, W.C. Oliver, and G.M. Pharr, MRS Symp. Proc 356, p 675 (1995)
- [13] Pharr GM, Bolshakov B (2002) Understanding nanoindentation unloading curves, J. Mater. Res., Vol. 17, No. 10, Oct 2002
- [14] N. Schwarzer: ”Arbitrary load distribution on a layered half space”, ASME Journal of Tribology, Vol. 122, No. 4, October 2000, 672 - 681
- [15] W. C. Oliver, G. M. Pharr, An improved technique for determining hardness and elastic modulus using load and displacement sensing indentation experiments, J. Mat. Res. 7 (1992) 1564-1583.

- [16] T. Chudoba, K. Herrmann, Härtereitechnische Mitteilungen, HTM 56 (2001) 258
- [17] N. Schwarzer, J. Phys. D: Appl. Phys., 37 (2004) 2761-2772
- [18] N. Schwarzer, G. M. Pharr, Thin Solid Films, Vol. 469-470C pp. 194-200
- [19] N. Schwarzer, T. Chudoba, G. M. Pharr, Surf. Coat. Technol, Vol. 200/14-15 pp 4220-4226
- [20] N. Schwarzer, T. Chudoba, F. Richter, Surf. Coat. Technol., Vol 200/18-19 pp 5566-5580
- [21] N. Schwarzer, Thin Solid Films 494 (2006) 168 – 172
- [22] N. Schwarzer, Phil. Mag. 86(33-35) 21 Nov - 11 Dec 2006 5153 – 5767
- [23] R. Puschmann, N. Schwarzer, F. Richter, S. Frühauf, S. E. Schulz: “An applicable concept for the indentation of thin porous films”, proceedings of the NanoMech 5, 7-9 September 2004 in Hückelhoven, Germany, also in Z. Metallkd. 96 (2005) 11, 1-6
- [24] FilmDoctor: Software demonstration package, www.siomec.de/FilmDoctor
- [25] A.C. Fischer-Cripps, A simple phenomenological approach to nanoindentation creep, Materials Science and Engineering A 385 (2004) 74–82
- [26] D. François, A. Pineau, A. Zaoui, Mechanical Behaviour of Materials, Kluwer Academic Publishers, The Netherlands, 1998
- [27] ISO 20502 Fine ceramics (advanced ceramics -advanced technical ceramics) - Determination of adhesion of ceramic coatings by scratch testing
- [28] ASTM C1624 Standard Test Method for Adhesion Strength and Mechanical Failure Modes of Ceramic Coatings by Quantitative Single Point SCRATCH Testing
- [29] M. Fuchs, G. Favaro, " Physical characterization of coated surfaces, Part II: Scratch Test", Application Bulletin No. 38 of CSM instruments, free download at: www.csm-instruments.com/en/Physical-characterization-of-coated-surfaces-Part-II-%3A-Scratch-Test
- [30] N. Schwarzer, Q.-H. Duong, N. Bierwisch, G. Favaro, M. Fuchs, P. Kempe, B. Widrig, J. Ramm, Optimization of the Scratch Test for Specific Coating Designs, Surface and Coatings Technology, volume 206, issue 6, year 2011, pp. 1327 - 1335
- [31] N. Schwarzer, (2007) “Intrinsic stresses – Their influence on the yield strength and their measurement via nanoindentation”, online archives of the Saxonian Institute of Surface Mechanics www.siomec.de/pub/2007/001
- [32] N. Schwarzer, "Modelling of Contact Problems of Rough Surfaces", online archives of the Saxonian Institute of Surface Mechanics www.siomec.de/pub/2007/007
- [33] N. Schwarzer, Some Basic Equations for the Next Generation of Surface Testers Solving the Problem of Pile-up, Sink-in and Making Area-Function-Calibration obsolete, JMR Special Focus Issue on “Indentation Methods in Advanced Materials Research”, J. Mater. Res., Vol. 24, No. 3, March 2009, 1032 - 1036
- [34] N. Schwarzer, Basic Equations for the Next Generation of Surface Testers for the Case of an Elastic Indenter and a Layered Samples, online archive of the Saxonian Institute of Surface Mechanics, www.siomec.de/pub/2008/001
- [35] N. Schwarzer: Analyse und Simulation der mechanischen Eigenschaften beschichteter Polymere unter Berücksichtigung der meist zeitabhängigen Materialparameter, 19. NDVaK, 19. u. 20.10. 2011 Dresden, Germany, ISBN 978-3-9812550-3-4, pp. 96 - 101
- [36] J.G. Kohl, N.X. Randall, N. Schwarzer, T.T. Ngo, J.M. Shockley, and R.P. Nair, "An Investigation of Scratch Testing of Silicone Elastomer Coatings with a Thickness Gradient", Journal of Applied Polymer Science, Vol. 124, 2978–2986 (2012), pp. 2978-2986
- [37] N. Schwarzer, "Determination of storage and loss modulus from quasi-static nanoindentation experiments", submitted to Phil. Mag. September 2012

- [38] V. Linss, N. Schwarzer, T. Chudoba, M. Karniychuk, F. Richter: “Mechanical Properties of a Graded BCN Sputtered Coating with Varying Young's Modulus: Deposition, Theoretical Modelling and Nanoindentation”, *Surf. Coat. Technol.*, 195 (2005) pp 287 - 297
- [39] T. Chudoba, N. Schwarzer, V. Linss, F. Richter: „Determination of Mechanical Properties of Graded Coatings using Nanoindentation”, proceedings of the ICMCTF 2004 in San Diego, California, USA, also in *Thin Solid Films* (2004): 469-470C pp. 239-247
- [40] N. Schwarzer: „Modelling of the mechanics of thin films using analytical linear elastic approaches“, *Habilitationsschrift der TU-Chemnitz 2004, FB Physik Fester Körper*, www.siomec.de/pub/2007/001
- [41] T. Chudoba, N. Schwarzer, A. Gies: „3D micro scratch tests in combination with a comprehensive stress analysis – a new tool for the understanding of surface failures“ submitted as oral presentation for ICMCTF 2013, will also be submitted for the ICMCTF-proceedings
- [42] A. Gies, T. Chudoba, N. Schwarzer, J. Becker: „Influence of the coating structure of a-C:H-W coatings on their wear-performance: a theoretical approach and its practical confirmation“, submitted as oral presentation for ICMCTF 2013, will also be submitted for the ICMCTF-proceedings
- [43] N. Bierwisch, N. Schwarzer, El Seweifi, M. Griepentrog, P. Reinstädt: „Examples for the time dependent effective indenter concept“, submitted as poster presentation for ICMCTF 2013, will also be submitted for the ICMCTF-proceedings
- [44] N. Schwarzer: “How to Make Tribological Tests Physical?”, submitted as oral presentation, for ICMCTF 2013, will also be submitted for the ICMCTF-proceedings
- [45] Florian Seibert, Max Döbeli, Doris M. Fopp-Spori, Kerstin Glaentz, Helmut Rudigier, Norbert Schwarzer, Beno Widrig, Jürgen Ramm, Comparison of arc evaporated Mo-based coatings versus Cr1N1 and ta-C coatings by reciprocating wear test, wear, submitted February 2012, accepted October 2012
- [46] E. Bemporad, M. Sebastiani, M.H. Staia, E. Puchi Cabrera, Tribological studies on PVD/HVOF duplex coatings on Ti6Al4V substrate, *Surface & Coatings Technology* 203 (2008) 566–571

QUALITATIVE FAILURE ANALYSIS ON LAMINATE STRUCTURES USING COMPREHENSIVE ANALYTICAL LINEAR ELASTIC CONTACT MODELLING

Norbert Schwarzer¹ and Peggy Heuer-Schwarzer²

¹ Saxonian Institute of Surface Mechanics SIO
Tankow 2, 18569 Ummanz / Rügen,
Germany, www.siomec.de

e-mail: n.schwarzer@siomec.de

² ESAE & ZumKranich
Tankow 2, 18569 Ummanz / Rügen,
Germany

e-mail: p.heuer@esae.de

Keywords: Impact, contact mechanics, Young's modulus, Yield strength, transverse isotropy, laminates, windsurfing, light weight construction, fracture toughness, fibers, foams, layered structures, anisotropy, fracture, mechanical properties, analytical modeling.

Abstract. *Recently developed completely analytical tools for the modelling of contact problems on thin film structures are adapted to allow the investigation of arbitrarily mixed purely isotropic and transversally isotropic laminate structures under impact loads. The new tool is applied to model a variety of load problems resulting in the failure of windsurfing boards consisting of a relatively thin laminate shell and a soft polymer foam core. It is shown that local impact and distributed bending loads due to "bad landing" after high jumps or contact with parts of the sailing gear (the so called rig) especially the front part of the boom are leading to the most critical stress distributions resulting in failure. So, most of the investigated boards were damaged because the rider (windsurfer) landed flat and thus produced a sudden impact force under his feet (impact defect). Other overloading occurred due to overturning of so called loop movements or the landing of the board exactly on respectively between two waves and this way producing high bending moments. Some of those typical loads are analysed in detail and the stresses occurring in the complex structure of the windsurfing boards are evaluated.*

Introduction

Laminate structures are playing an important role everywhere it comes to combine lightness and flexibility with high stability and reliability. So numerous publications are available treating laminate composites with respect to the latter quality characteristics. Especially of interest has been the effect of impact and bending loads. So we find a lot of recently published papers treating the problem of contact and impact loading experimentally [1 - 6].

Especially interesting concerning the topic of this paper however is the work of Miyano et al [7] where laminate structures have been tested explicitly for the purpose of marine use. A crucial point is the determination of the mechanical properties of laminate structures. Here, indentation experiments have been proven of being of great use (see e.g. [8, 9]).

The determination of the mechanical properties by computational methods has been treated for example in [10 - 15]. While the latter papers have at least additionally applied analytical methods, there are many publications using only FE-Modelling in order to extract mechanical properties of laminate structures (e.g. [16 - 18]). The practically important problem of optimising laminate structures has been performed using failure signatures and safety criteria by Harik [19] and applying a so called Tabu search in [20].

In order to optimise windsurfing board laminate structures against impact and bending loads sufficiently fast evaluating approaches are required allowing to model contact problems on multi-layer structures for staked orthotropic, isotropic and transverse isotropic layers with a high number of relatively thin layers. Here, as we wanted to do “practical field studies directly on the spot” of application of laminated windsurfing boards, we needed a very fast evaluating relatively easy to use model. So, despite the fact that there are completely analytical models for the correct three dimensional description of mechanical contact problems on layered orthotropic materials available [21, 22], we needed to down scale these approaches in order to make them applicable for this project. Neglecting most of the unisotropic properties of the windsurfing board laminate structures we found, that in fact we obtained sufficiently good agreement with the observed failure mechanism by using a transversely isotropic approach (see part “Theory II” of this paper). The evaluation time was at least 100times faster than that of the approach presented in [21, 22]. The additional demand to make the model also usable and understandable for mathematically less trained team members (professional windsurfers for example) required a properly programmed surface [23].

A short survey especially considering the accuracy and the calculation time shall present the development of the approach used here. Applying the model of the layered half space and using the method of image loads or image contacts, Schwarzer has been able to model up to 4 layers including the substrate [24]. The approach brought very good agreement with experimental results in the case of single layer and bi-layer structures, but unfortunately it is not applicable on real multilayers with more than 5 layers. The main reason for this is due to the high calculation time increasing exponentially with the number of layers. The same holds for some other methods like the perturbation [25] or the boundary and the finite element method [26]. There is a variety of publications about multilayered and graded coatings available [27 - 30], but non of them provides a sufficiently convenient and fast method allowing to treat contact problems on mixed pure and transversely isotropic or orthotropic laminate structures under contact loading as we want to consider here. It has been shown by Stone [31] (see also [32] and [33]), that in the case of a layered half space a sufficiently high number of layers can be modelled due to the method of integral transformation. He even modelled mixed pure and transversely isotropic layer structures under normal stress distribution. However in those cases, where the laminate structure is thin or in about the same scale as the area of the load applied on the laminated body in question, this method is not applicable due to numerical instabilities. So, if one for example wants to model impact and bending loads on hulls of boats,

fuselages or other rather thin walled constructions the so called “model of the thick plate” is required. Thus, based on the approach of Lurie [34] Schwarzer [35] has developed a model allowing the investigation of thick layered plates under any arbitrary contact or bending load. The model has been included into a computer program evaluating mixed pure isotropic and transversely isotropic laminate structures with up to 100 different layers on an ordinary personal computer in an acceptable calculation time.

Theory I. – layered half space

Apart from finite element or boundary element methods the integral transform method seems to be the only one allowing real multilayer modelling with more than 10 layers. As we are here only interested in contact areas of symmetry of revolution, we seek for a solution of the Navier equation for equilibrium in linear elasticity (see e.g. [31]) containing Bessel functions. Thus, the method is based upon the following approach for circular contact areas where, in the case of pure isotropy, the displacements within the i -th layer are given by:

$$\mathbf{r} \mathbf{u}_i = \begin{pmatrix} u_i \\ v_i \\ w_i \end{pmatrix} = c \int_0^{\infty} \begin{pmatrix} f(u) \left((A+B+Bu z) e^{uz} - (D-F+Fu z) e^{-uz} \right) J_1[ur] \frac{x}{r} \\ f(u) \left((A+B+Bu z) e^{uz} - (D-F+Fu z) e^{-uz} \right) J_1[ur] \frac{y}{r} \\ f(u) \left((-A+(2-4\nu-uz)B) e^{uz} - (D+(2-4\nu+uz)F) e^{-uz} \right) J_0[ur] \end{pmatrix} du \quad (1)$$

$J_n(z)$ denotes the Bessel function of the first kind of order n , x, y, z are the Cartesian coordinates with z being the axis of indentation and $r^2 = x^2 + y^2$. The function $f(u)$ needs to be determined in accordance with the normal load distribution applied. So would for example a constant pressure distribution within a contact circle of radius a lead to (see e.g. [36]):

$$f(u) = \frac{a}{u} J_1[au]. \quad (2)$$

The constant c must satisfy the condition, that the acting overall force F on the surface is opposite equal to the integral over the normal stress $\sigma_{zz}(r, \varphi, z)$ at this position (we set it $z=0$). Thus we have:

$$c = - \frac{F}{\int_0^{\infty} \int_0^{2\pi} \sigma_{zz}(r, \varphi, z=0) d\varphi dr}. \quad (3)$$

For transverse isotropic layers the approach must read:

$$\mathbf{r} \mathbf{u}_i = \begin{pmatrix} u_i \\ v_i \\ w_i \end{pmatrix} = c \int_0^{\infty} \begin{pmatrix} f(u) \left(A e^{uz/\gamma_1} + B e^{uz/\gamma_2} - (D e^{-uz/\gamma_1} + F e^{-uz/\gamma_2}) \right) J_1[ur] \frac{x}{r} \\ f(u) \left(A e^{uz/\gamma_1} + B e^{uz/\gamma_2} - (D e^{-uz/\gamma_1} + F e^{-uz/\gamma_2}) \right) J_1[ur] \frac{y}{r} \\ f(u) \left(m_1 \left(\frac{A}{\gamma_1} e^{uz/\gamma_1} + \frac{D}{\gamma_1} e^{-uz/\gamma_1} \right) + m_2 \left(\frac{B}{\gamma_2} e^{uz/\gamma_2} + \frac{F}{\gamma_2} e^{-uz/\gamma_2} \right) \right) J_0[ur] \end{pmatrix} du \quad (4)$$

The γ_k ($k=1, 2$) have to be obtained from $\gamma_k^2 = n_k$, whereas n_k denote the two (real or conjugate complex) roots of the equation

$$A_{11}A_{44}n^2 + [A_{13}(A_{13} + 2A_{44}) - A_{11}A_{33}]n + A_{33}A_{44} = 0. \quad (5)$$

The constants m_k ($k=1, 2$) are related to γ_k as

$$\frac{A_{11}\gamma_k^2 - A_{44}}{A_{13} + A_{44}} = \frac{(A_{13} + A_{44})\gamma_k^2}{A_{33} - \gamma_k^2 A_{44}} = m_k \quad (6)$$

Rearranging all terms of (4) containing γ_1 and denoting the resulting function F_1 and doing the same with all term containing γ_2 obtaining a function F_2 the elastic field can be evaluated due to:

$$u + iv \equiv u^c = \Lambda(F_1 + F_2 + iF_3); \quad \Lambda = \frac{\partial}{\partial x} + i \frac{\partial}{\partial y} \quad ; \quad w = m_1 \frac{\partial F_1}{\partial z} + m_2 \frac{\partial F_2}{\partial z}. \quad (7)$$

$$\sigma_1 = 2A_{66} \frac{\partial^2}{\partial z^2} \left([\gamma_1^2 - (1+m_1)\gamma_3^2] F_1 + [\gamma_2^2 - (1+m_2)\gamma_3^2] F_2 \right), \quad (8)$$

$$\sigma_2 = 2A_{66}\Lambda^2 (F_1 + F_2), \quad (9)$$

$$\sigma_{zz} = A_{44} \frac{\partial^2}{\partial z^2} \left(\gamma_1^2 (1+m_1) F_1 + \gamma_2^2 (1+m_2) F_2 \right), \quad (10)$$

$$\tau_z = A_{44}\Lambda \frac{\partial}{\partial z} \left((1+m_1) F_1 + (1+m_2) F_2 \right), \quad (11)$$

($\gamma_3^2 = A_{44}/A_{66}$). To simplify the stress field the following combinations were used (Fabrikant [37])

$$\sigma_1 = \sigma_{xx} + \sigma_{yy} = \sigma_{rr} + \sigma_{\varphi\varphi}, \quad \sigma_2 = \sigma_{xx} - \sigma_{yy} + 2i\tau_{xy} = e^{2i\varphi} (\sigma_{rr} - \sigma_{\varphi\varphi} + 2i\tau_{r\varphi}), \quad \tau_z = \tau_{xz} + i\tau_{yz} = e^{i\varphi} (\tau_{rz} + i\tau_{\varphi z}).$$

The yet unknown constants A, B, D and F have to be determined for each layer due to the boundary conditions at the interfaces of the multilayer structure. From equations (1) and (4) the complete elastic field at any point within the loaded laminate structure can be evaluated applying the formulae (8) to (11). For more information the reader is referred to the original works of Schwarzer [35], Fabrikant [37] and Stone [31]. A special software package has been developed in order to automate the calculations becoming immensely complex and cumbersome in the case of high numbers of layers [23, 38].

Theory II. – layered thick plate

In order to obtain numerically stable approaches in the case of laminate structures being thin compared to the size of the contact zone (or in about the same scale), the integral transformation method must be substituted by a suitable series procedure. For our purpose here the following approaches will suffice:

Isotropic case i-th layer:

$$\vec{u}_i = \begin{pmatrix} u_i \\ v_i \\ w_i \end{pmatrix} = \sum_{n=1}^{\infty} c_n \begin{pmatrix} u^2 \left((A + B + Buz) e^{uz} - (D - F + Fuz) e^{-uz} \right) J_1[ur] \frac{x}{r} \\ u^2 \left((A + B + Buz) e^{uz} - (D - F + Fuz) e^{-uz} \right) J_1[ur] \frac{y}{r} \\ u^2 \left((-A + (2 - 4\nu - uz) B) e^{uz} - (D + (2 - 4\nu + uz) F) e^{-uz} \right) J_0[ur] \end{pmatrix} \quad (12)$$

transverse isotropic case i-th layer:

$$\vec{u}_i = \begin{pmatrix} u_i \\ v_i \\ w_i \end{pmatrix} = \sum_{n=1}^{\infty} c_n \begin{pmatrix} u^2 \left(A e^{uz/\gamma_1} + B e^{uz/\gamma_2} - (D e^{-uz/\gamma_1} + F e^{-uz/\gamma_2}) \right) J_1[ur] \frac{x}{r} \\ u^2 \left(A e^{uz/\gamma_1} + B e^{uz/\gamma_2} - (D e^{-uz/\gamma_1} + F e^{-uz/\gamma_2}) \right) J_1[ur] \frac{y}{r} \\ u^2 \left(m_1 \left(\frac{A}{\gamma_1} e^{uz/\gamma_1} + \frac{D}{\gamma_1} e^{-uz/\gamma_1} \right) + m_2 \left(\frac{B}{\gamma_2} e^{uz/\gamma_2} + \frac{F}{\gamma_2} e^{-uz/\gamma_2} \right) \right) J_0[ur] \end{pmatrix} \quad (13)$$

The parameter u must now be set $u = \frac{\lambda_n}{r_0}$, with λ_n denoting the n -th root of the equation

$J_0(r)=0$. The parameter r_0 must be chosen such, that it is big compared to the lateral dimensions of the investigated laminate part and sufficiently small in order to reduce the number of terms of the series approach necessary to generate a proper surface load distribution. In the calculations presented here, up to 1000 terms were used.

Application to a variety of board failure problems in windsurfing

Windsurfing – some basics and the equipment

First sailing attempts with a prototype of a sailboard dates back to the late 1950's, when the founding father of windsurfing, Newman Darby, wanted to combine sailing and wave surfing. The first windsurf board was about 3.5m long and weighted 27kg and Darby was considered rather a weirdo than the man with a great vision he obviously was. Since then, many things have changed: as the material and shapes of the equipment developed constantly, heavy and unwieldy polyethylene boards were substituted by laminated board structures, the jumps and moves become more and more radical and windsurfing is nowadays one of the most popular water sports all over the world.

Windsurf equipment consists of two major parts: the complete rig with a mast making the rig stand upright, a sail to catch the wind, turn it into sail force and drive the craft, and a boom which spreads the sail and on which the windsurfer holds on, gives direction and controls the wind pressure and thus the speed.

The second part of the vehicle is the board (figures 1 and 2). The bow is very often called the board's nose and is bent slightly upwards. On the stern, also called tail, are three foot straps located, two front, and one hind strap (on some board, usually those for race or speed performances there could be also more straps), in which the rider (windsurfer) finds a foothold when sailing fast over rough (choppy) water and jumping. A certain area under those foot straps is covered with rubber foot pads, making it more comfortable for the surfer, preventing him from slipping and finally protecting both rider and board against hard impact. A tail fin, or skag, is the main lateral pressure centre under water (lateral plane) when the board is planing (see below) and thus, sets up resistance against drifting off course.

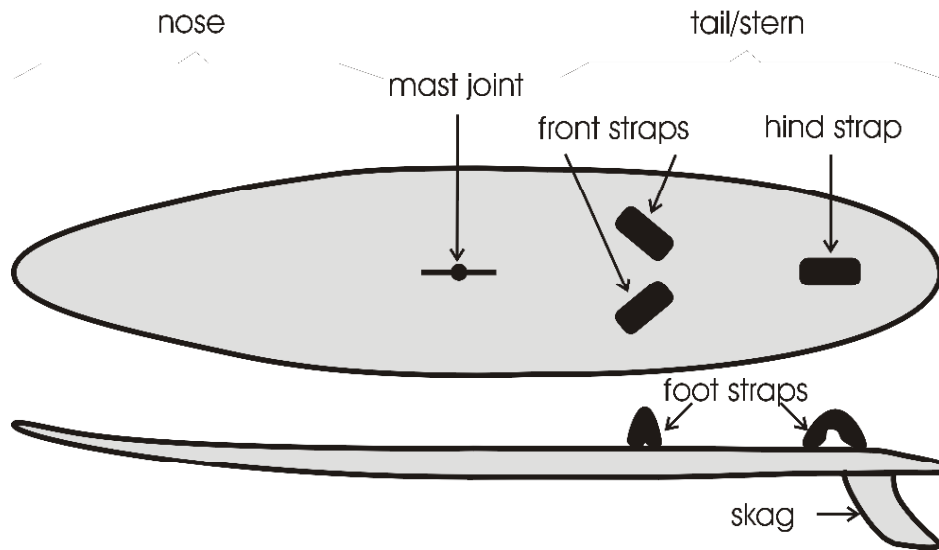


Fig. 1 Main parts of a windsurfing board

Depending on the purpose and shape, a modern typical wave board weights about 8 kg and has a length of 2.5m to 2.8m.

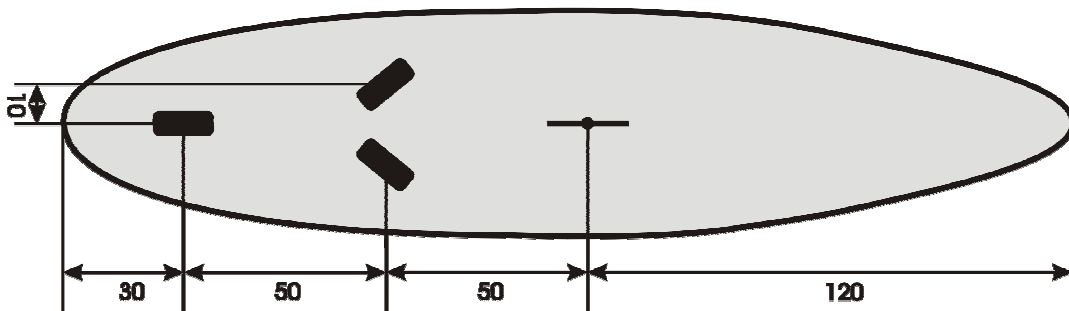


Fig. 2 Co-ordinate system and measures of a typical wave board

Both parts, rig and board, are connected by a flexible mast joint that allows the rig to be tilted in any direction. By tilting the rig and with that, changing the incidence angle toward the wind, the sail force is moved whereas the lateral pressure centre (skag and all parts under water) stays the same and thus the board can be steered easily and without a rudder.

With a harness, which connects the rider's waist to the sail, the advanced windsurfer can transfer the power from the wind pressure caught in his sail to his body and with that, the required muscle power in hands and arms reduce to a bearable minimum so that even light and delicately built female windsurfers, even if very rare, could in principle practice this interesting sport without the need of special muscle training.

When the windsurfer gets faster, he is able to climb his own bow wave produced by his board when moving and thus, edging out water, and he will ride down this bow wave and becomes even faster. This state is called "planing" and now the rider can crawl into the foot straps and perform a great variety of so called speed moves and jumps (figures 3 and 4).



Fig. 3 Number one reason for board failure: jumps

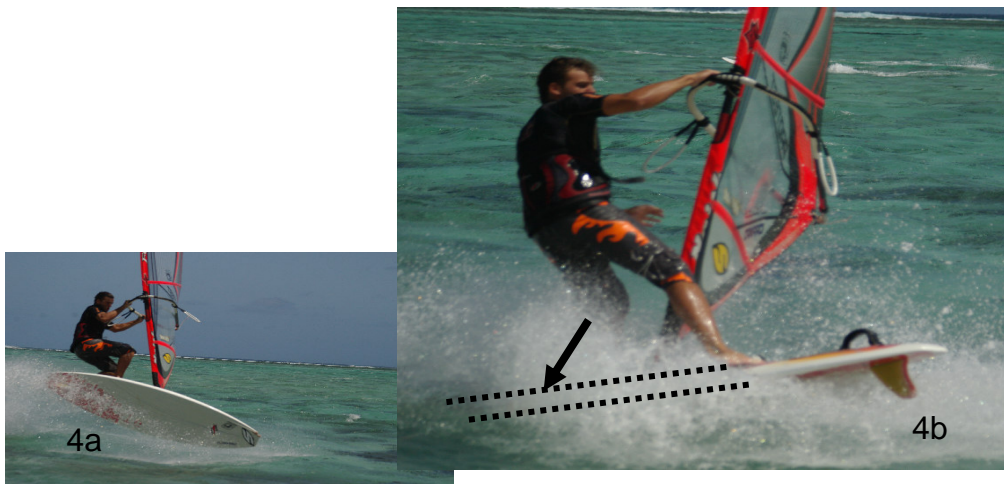


Fig. 4 "Willy Skipper": impact load on the nose part

Some of the most popular and spectacular movements are so called loop jumps. Therefore, the rider jumps high into the air and turns his rig, his board and himself either forward or backward so that he lands -if all goes well- after one or even two full rotations in riding direction. But those moves together with almost all other forms of jumps are not only spectacular and create a stir, they are also dangerous for both: the windsurfer and the equipment.

Board failure problems

A thorough analysis of the failure problems observable on windsurfing boards shows that there are two major mechanisms leading to damage. First, there are impact loads. They are mainly induced due to so called flat landing after high jumps (the rider lands his board flat on the water surface and thus produces a momentarily high impulse under his feet and the board's mast joint). In other cases we have catapult like plunges due to strong gusts pulling the rig and sometimes also the rider, who is fixed to the rig with the harness, forward onto the nose part of the board. This can lead to hits with the front of the boom or body parts of the rider into the surface of the nose part of the board. There are also some spectacular moves (e.g. the so called "Willy Skipper") requiring that the rider lands feet first on the nose this way producing relatively high impact forces. The second class of main failure mechanism are bending loads

coming from overturning of so called loop jumps, landing between waves or so called nose or tail dives after high jumps.

Within those two classes of failure mechanisms we here concentrate on the following critical situations:

1. impact load on the board's nose surface due to hard contact with either body parts of the rider or the rig (see fig. 4)
2. impact load in the foot pad area (under the foot straps) due to flat landing
3. bending load due to landing on or between two waves, where nose and tail are supported by the peaks of the waves while the rest of the board hangs unsupported over the trough
4. bending load caused by hard tail first landing
5. skag hits reef
6. bending load caused by hard nose dive landing or due to over rotation after loop jumps

During our investigation we had to realise that in almost all cases of board destruction it was rather impossible to reconstruct the force and momentum situation in the moment of failure in detail. This was mainly due to the fact that the riders could only give vague information about their speed, height of the jump (fig. 3), buffer effect of the sail during lading, momentum of rotation etc. or in some cases even their own weight. Further, the investigated boards, though in principle of similar shape and structure, differed widely in details concerning the number of used laminate reinforcements, thicknesses of distinct parts of the boards, used materials within the layered structure and their order (glass fibre, carbon fibre, honeycomb reinforcements...) etc.. Under these circumstances it doesn't seem reasonable to assume concrete load conditions and board constructions. One rather should apply typical load distributions simulating the critical situations and see whether or not the resulting stress distributions coincide with the observed board failure. Thus, we have constructed a relatively simple "model windsurfing board" out of either a layered half space or a layered thick plate model in accordance with the load problem in question. In order to describe board reinforcements in lateral direction, a stability weight function has been introduced in some cases. This weight function is directly related to the lateral change of thickness of the laminate structure.

The first two problems 1 and 2 can be tackled by applying the half space model. We use the material parameters given in table 1 and 2. The water was assumed as to act as some kind of substrate supporting the board structure during the impact such that it could be modelled as being elastic. Here it was of absolutely no importance which concrete elastic parameters for the "substrate" were chosen. As a series of trial evaluations showed the "water-parameters" could be anywhere between rigid and extremely soft without significantly changing the stress distribution within the surface part of the board we are interested in here. Further, as explained above we are just interested in the resulting stress distribution and not any absolute values. Thus, the coefficients of the Young's modulus tensor are given as a function of a parameter E , where a concrete number can be assigned to as soon as concrete board structures are chosen and absolute forces are known. For the resulting qualitative stress distribution however, only the geometrical conditions and the relative material properties of the layers are of importance. Because we are using the half space and the thick plate model we have to treat the results in the vicinity of the board edges with great caution. But it had been shown experimentally and theoretically [39] that even in the case of a sharp rectangular edge (quarter space) the elastic field near the contact does not differ more than about 15 % from the half space model as long as the distance from the edge does not fall below one contact radius. But

as we here only have blunt “edges” and all contacts and failures considered are placed respectively found close to the board’s middle, the maximum error might be about 10%, which will suffice for our qualitative failure discussion.

At first we investigate the effect of the impact load on the foam core of the board (fig. 5):

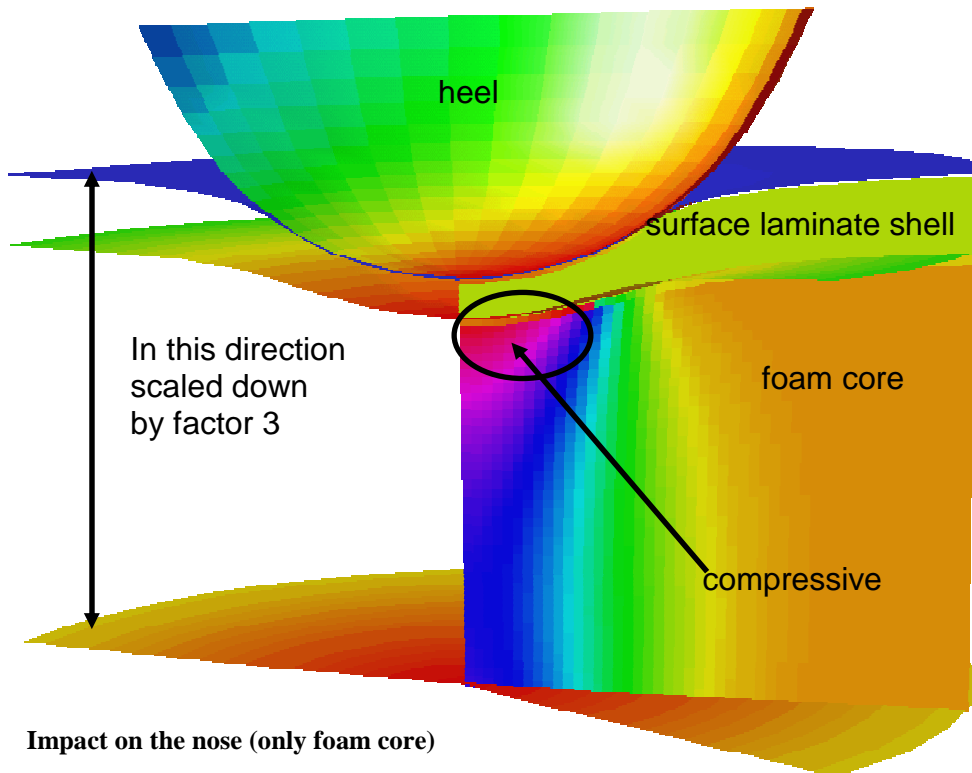


Fig. 5 Impact on the nose (only foam core)

As we know from investigating damaged boards, the foam is compressed under the contact zone. It often delaminates from the laminate surface shell (monochrome drawn layer in fig. 5) thus, building a vacancy and leaving the laminate shell unsupported. The figure shows the hydrostatic stress having a strong compressive maximum directly under the indenter (e.g. heel of the rider or front part of the boom...) leading to the material compression. In figure 6 the radial stress within the laminate shell is presented.

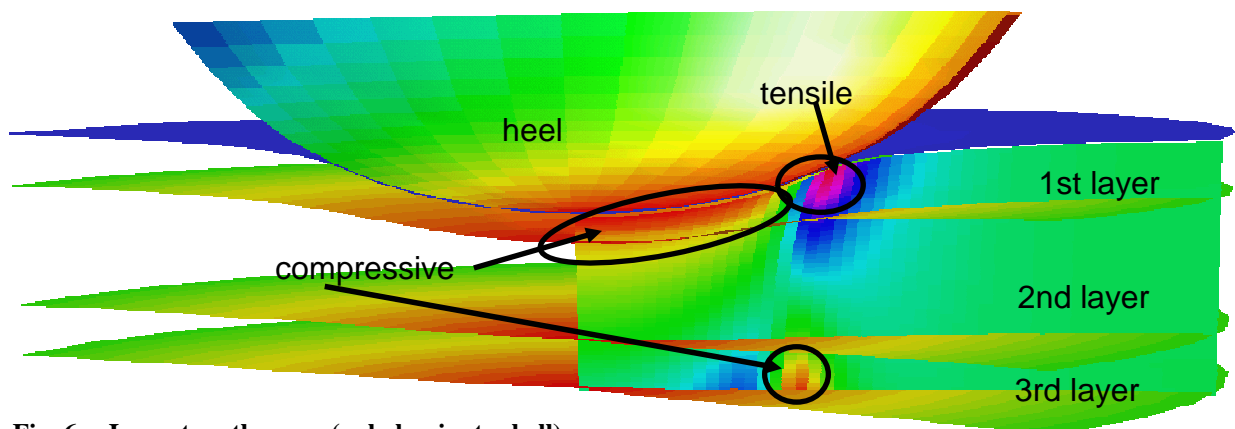


Fig. 6 Impact on the nose (only laminate shell)

It shows a pronounced tensile stress maximum at the contact rim which might lead to mode I fracture (Hertzian cone crack). And in fact this type of failure could be observed rather often on the front surface part of windsurfing boards (figure 7: due to its anisotropy the Hertzian here runs along main fibre direction of the laminate tissue structure).



Fig. 7 Surface fracture damage due to impact load

Under extreme conditions (Fig. 8: Damaged nose part of a windsurfing board after huge impact: the rider (about 75kg) fell foot first from a height of about 3 meters directly onto the nose of his board) the impact might be even so strong that the board breaks through completely.



Fig. 8 Complete nose damage due to impact load

The picture changes completely when the impact load is applied onto the foot pad area (problem 2). Here elongated or star like cracks coming from the contact centre are observed rather than circular cracks (see small photograph in figure 10). This becomes clear when we investigate the radial stresses within the laminate under the rider's heel (fig. 9):

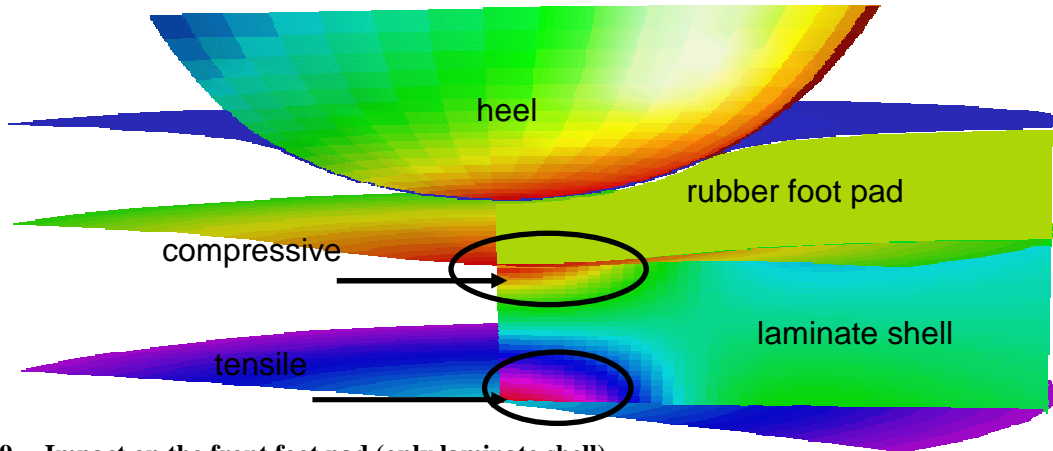


Fig. 9 Impact on the front foot pad (only laminate shell)

While, due to the buffer effect of the rubber food pad, there are rather no tensile stresses at the surface of the laminate layer we see, that this time the tensile stress maximum is to be found at the contact centre on the bottom of the laminate shell. But as already seen in problem 1 for the nose part of the board, the foam core is also compressed under the foot pad area due to a maximum of compressive hydrostatic stresses (fig. 10). This effect is widely known by wind-surfers, so that second hand boards are always tested here by simply pressing the thumb hard on the area where usually the heel would be in order to see whether impact damage had already occurred.

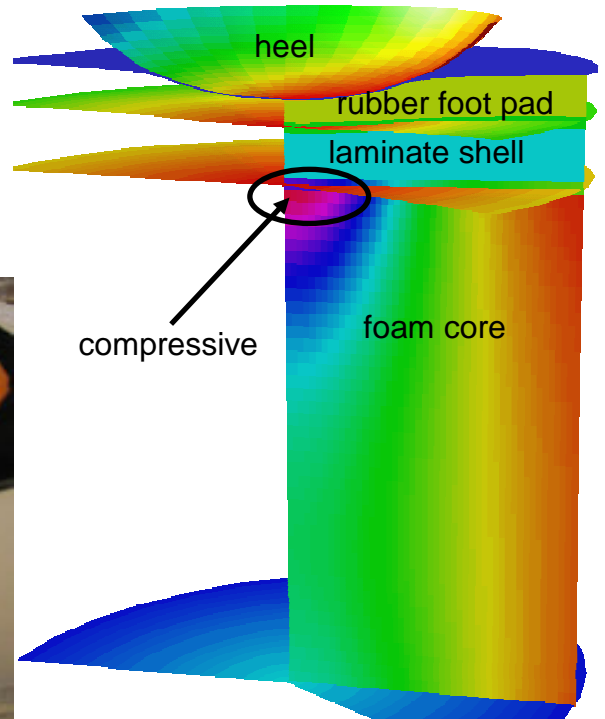


Fig. 10 Impact on the front foot pad (only foam core)

The third problem is demonstrated in figure 11 (lower picture):

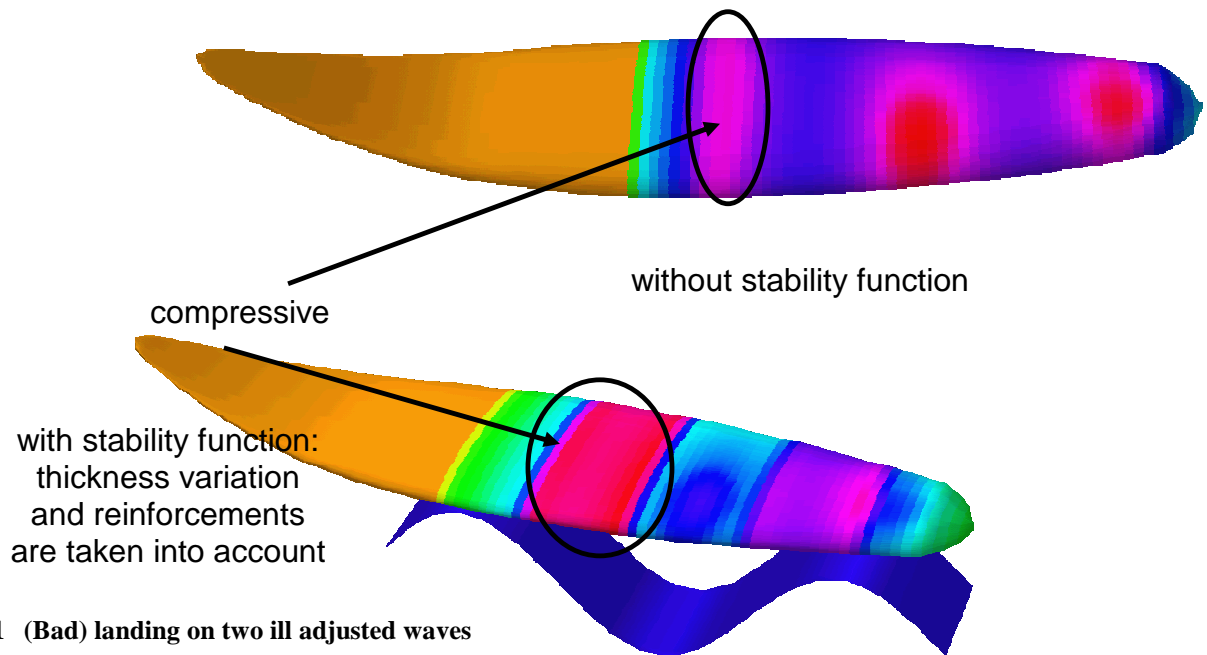


Fig. 11 (Bad) landing on two ill adjusted waves

The material parameters used for the evaluation are given in table 3. Analysing the typical load distribution between front and hind leg by using ten different professional windsurfers put on a so called windsurf simulator equipped with three scales (one for each foot and an additional one for the mast) we obtained a sufficiently consistent load picture. Applying the “model of the thick layered plate” we evaluated the normal stress distribution shown in figure 11 (upper picture). Taking into account that the laminate thickness is not homogenous over the whole surface by introducing a simple “stability function” a refined stress distribution can be obtained (fig. 11, lower picture). Here the stresses shown in figure 11 (upper picture) were simply multiplied with the inverse of the laminate shell thickness. The result, namely a maximum of compressive stresses between mast and front foot pads, is in good agreement with the observed failure (fig. 12).

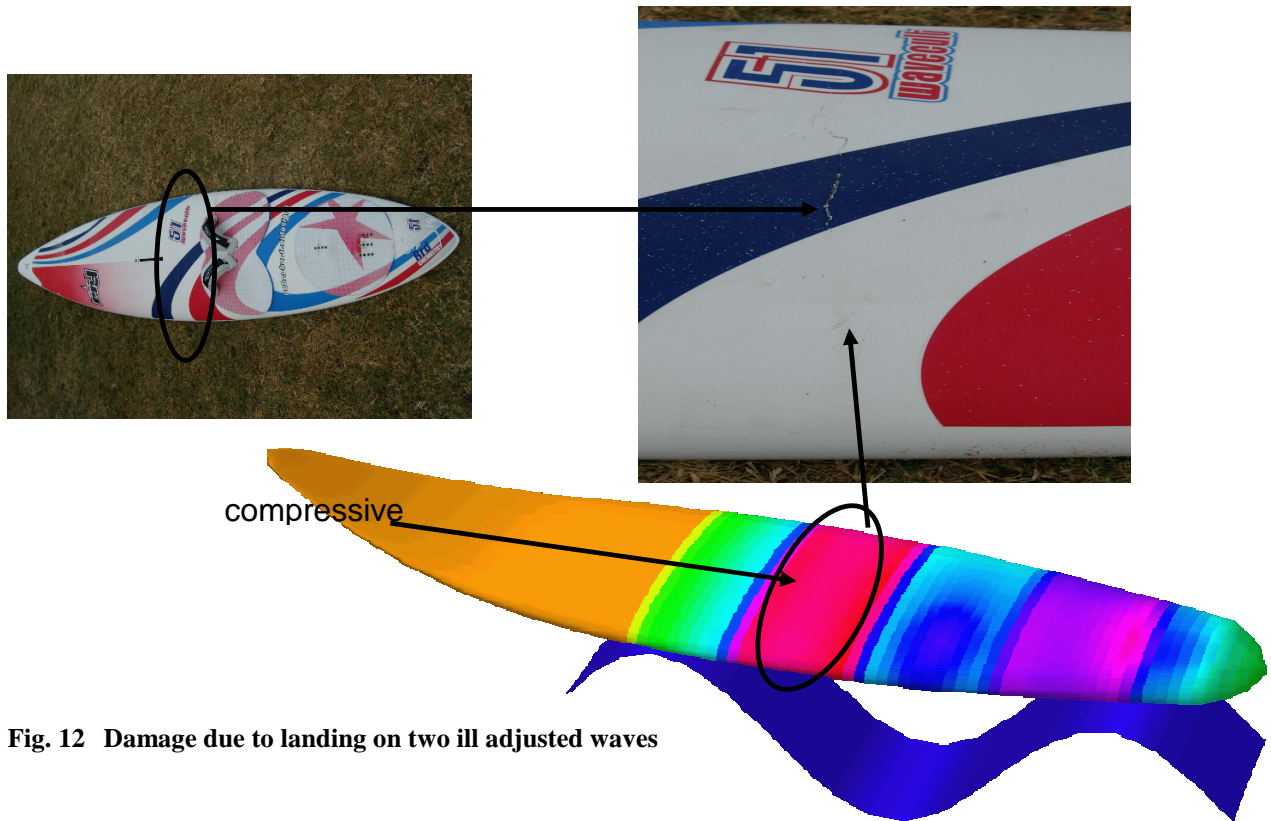


Fig. 12 Damage due to landing on two ill adjusted waves

In the case of a hard tail landing (problem 4, demonstrated in the figures 13 and 14) the damage (fracture between the front and hind foot straps as shown in the small photograph of figure 14) is caused by high tensile stresses within the board's surface (see arrow and red area in fig. 14).



Fig. 13 Tail landing

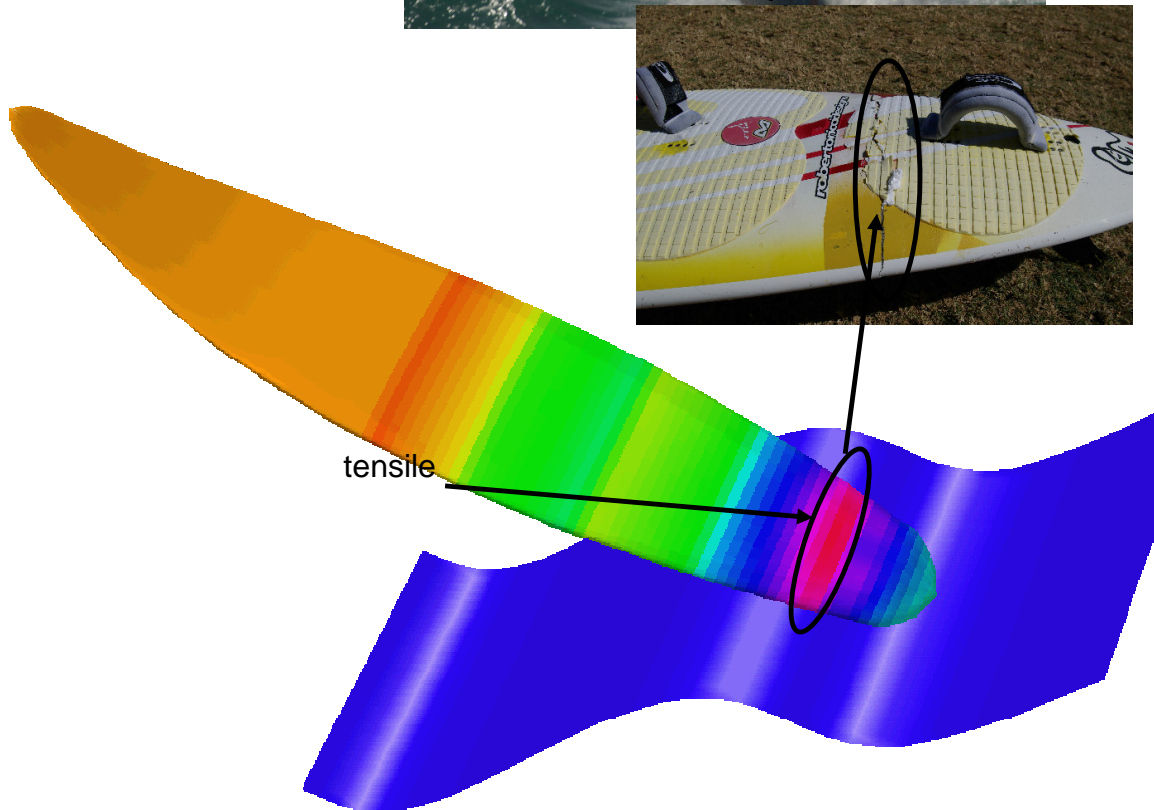


Fig. 14 Stresses and damage due to hard tail landing

Similar damage can be observed in the case 5, where the rider hits an under water obstacle (e.g. protruding parts of the reef) with the skag of his windsurfing board. Depending on the speed of the windsurfer, the impact momentum can be big enough to produce huge tensile stresses in the surface laminate (figure 15) right in front of the hind foot strap immediately leading to rapture between the two foot pads (small photograph in figure 15):

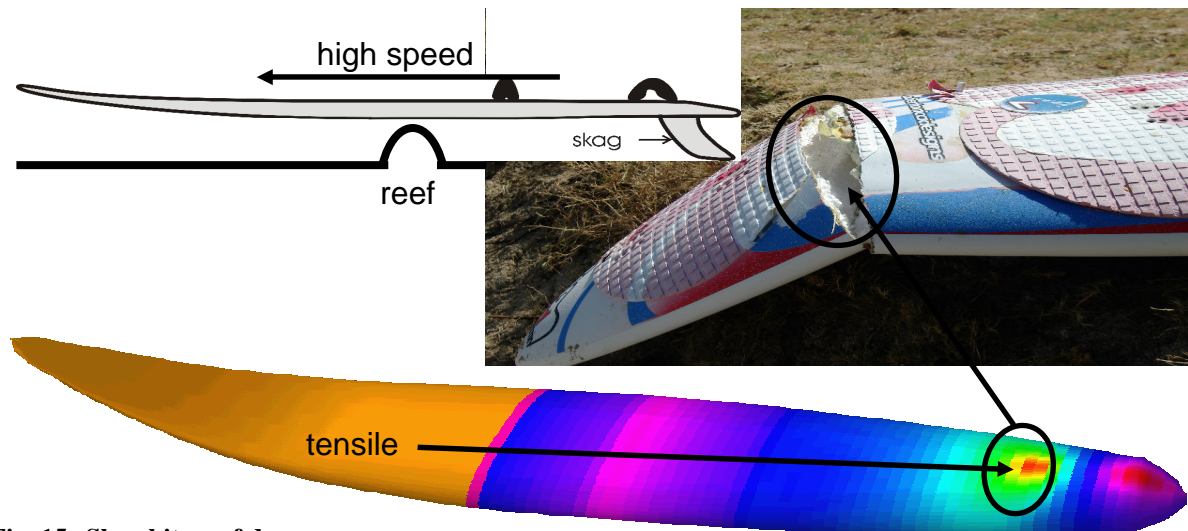


Fig. 15 Skag hits reef damage

As one can see the result of this type of impact loading can be quite disastrous. However in the special case of the photograph in figure 15 the “skag hits reef”-impact only initialised the fracture. The rest was done when the rider tried to come back to the shore, planning over a fairly choppy (which means rough) surfing spot, thereby successively bending the board’s tail up and down and so gradually opening the crack more and more until it got almost severed from the rest of the board.

Finally we consider the nose dive landing after an ordinary jump or an overturned front or back loop (problem 6, see figure 16).



Fig. 16 Example for loop jump

It can result in high compressive stresses on the surface (figure 17) and tensile stresses on the board's bottom (figure 18) around the mast joint. Here fracture before or behind the mast can occur (figure 19: Here, too, the rider – one of the authors, this time – lost parts of the bottom laminate on the way back to the beach through a very rough shore break zone with relatively high waves.).

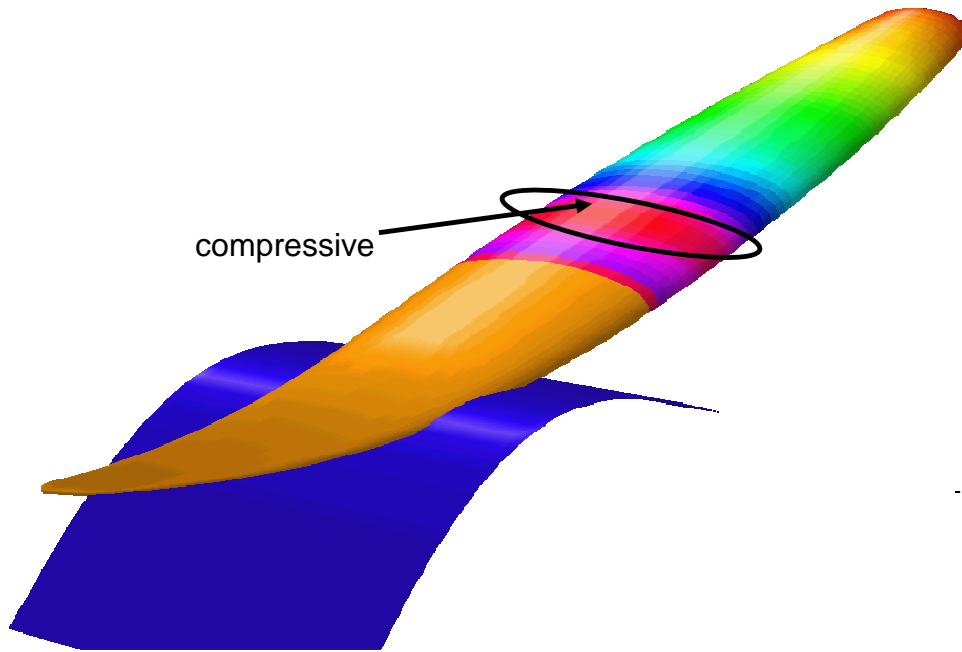


Fig. 17 Stresses due to hard nose dive (surface)

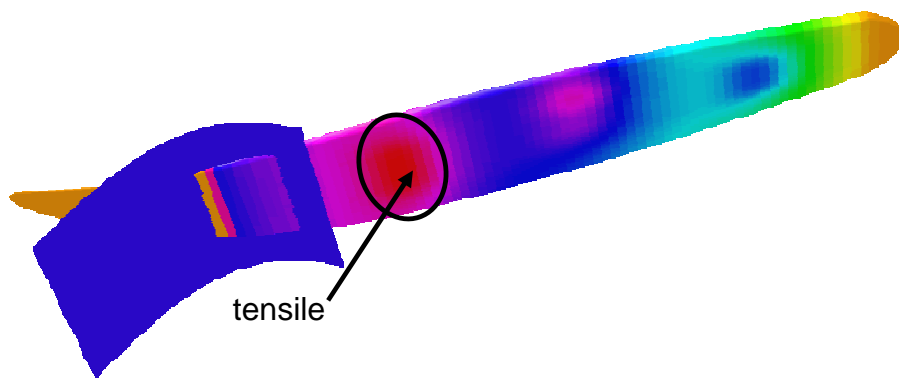


Fig. 18 Stresses due to hard nose dive (bottom)



Fig. 19 Complete bottom fracture due to hard nose dive

Conclusions

It had been shown, that the typical damage of quite a variety of failure mechanisms occurring on the laminate structures of windsurfing boards can qualitatively described using the layered half space and the layered thick plate model. Laminate thickness variations and reinforcements had been included via a so called stability function. Very good agreement between the observed failures and the location and type of the stress maxima evaluated from the theoretical model was obtained for all considered damages. It was found, that apart from accidents like hitting the reef with the skag or falling on the board's nose, mainly jumps are responsible for most of the observed board failures. Thus, the model might be used as a tool to find out weak spots within the structure of a windsurfing board during shape design and development. The method could also be applied to other laminate structures such as those used in the boat and aircraft or even car industry in order to support the design and construction of impact resistant structures.

Acknowledgements

The authors are thankful to Rocky Legoy from the RRD-Windsurfing centre on Mauritius, Kevin Berichon from Holly Mackerel Productions, Australia, Stefan Gabler and Holger Schneider, Germany for a variety of helpful discussions and demonstrations. We also want to thank all those riders who damaged their boards, allowed us to interview them in the moment of grieve and even granted us to photograph and thoroughly analyse the board failure.

References

- [1] B. Okutan, Composites Part B: Engineering, Vol. 33, No 8, Dec. 2002, 567-578
- [2] J. Lopez-Puente, R Zaera, C. Navarro, Composites Part B: Engineering, Vol. 33, No 8, Dec. 2002, 559-566
- [3] T. A. Anderson, Composites Part B: Engineering, Vol. 36 (2005), 135-142

- [4] T. Gomez-del Rio, E. Barbero, C. Navarro, *Composites Part B: Engineering*, Vol. 36 (2005), 41-50
- [5] N.K. Naik, R. Ramasimha, H. Arya, S.V. Prabhu, N. ShamaRao, *Composites Part B: Engineering*, Vol. 32 (2001), 565-574
- [6] M. De Freitas, A. Silva, L. Reis, *Composites Part B: Engineering*, Vol. 31 (2000), 199-207
- [7] Y. Miyano, M. Nakada, N. Semine, *Composites Part B: Engineering*, Vol. 35 (2004), 497-502
- [8] S. K. Khanna, P. Ranganathan, S.B. Yedla, R.M. Winter, K. Paruchuri, *J. Eng. Mat. Technol.*125 (2003) 90-96
- [9] G. Caprino, A. Langella, V. Lopresto, *Composites Part B: Engineering*, Vol. 34 (2003), 319-325
- [10] I.M. Daniel, E.E. Gdoutos, K.-A. Wang, J.L. Abot, *Int. J. Damage Mech.*, 11 (2002) 309-334
- [11] M. Zako, Y. Uetsuji, *Int. J. Damage Mech.*, 11 (2002) 187-202
- [12] D. Luo, S. Takezono, K. Tao, H. Minamoto, *Int. J. Damage Mech.*, 12 (2003) 141-162
- [13] H. Altenbach, *Z. angew. Math. Phys.* 51 (2000) 629-649
- [14] R. Akkerman, *Composites Part B: Engineering*, Vol. 33 (2002), 133-140
- [15] H.-L. Yeh, H.-Y. Yeh, *Composites Part B: Engineering*, Vol. 31 (2000), 57-64
- [16] P. Thamburaj, M. H. Santare, *J. Eng. Mat. Technol.*125 (2003) 412-417
- [17] B. Shan, A. A. Pelegri, *J. Eng. Mat. Technol.*125 (2003) 353-360
- [18] J.W. Park, Y.H. Kim, *Computational Mechanics*, Vol. 29, No. 3, 226-242
- [19] V. M. Harik, *J. Eng. Mat. Technol.*125 (2003) 385-393
- [20] N. Pai, A. Kaw, M. Weng, *Composites Part B: Engineering*, Vol. 34 (2003), 405-413
- [21] C.C. Chao, C.Y. Tu, *Composites Part B: Engineering*, Vol. 30 (1999), 9-22
- [22] C.Y. Tu, C.C. Chao, *Composites Part B: Engineering*, Vol. 30 (1999), 23-41
- [23] FilmDoctor: Software package for the evaluation of the elastic fields of arbitrary combinations of normal, tilting, twisting and tangential loads of the type

$$\text{“load} \sim \sum_{n=1}^6 c_n * r^n \sqrt{a^2 - r^2} \text{”}$$
 (with n=0,2,4,6), available from the internet at:
<http://www.siomec.de/filmdoctor>
- [24] N. Schwarzer, *Arbitrary load distribution on a layered half space*, *ASME Journal of Tribology*, 122 (2000) 672 – 681
- [25] H. Gao, C.-H. Chiu, J. Lee, *Elastic contact versus indentation modelling of multi-layered materials*, *Int. J. Solids Structures* 29 (1992) 2471-2492
- [26] C. Saizonou, R. Kouitat-Njiwa, J. von Stebut, *Surface engineering with functionally graded coatings: a numerical study based on the boundary element method*, *Surf. Coat. Technol.* 153 (2002) 290-297
- [27] A. E. Giannakopoulos, P. Pallot, *J. Mech. Phys. Solids* 48 (2000) 1597
- [28] A. E. Giannakopoulos, *Thin Solid Films* 332 (1998) 172
- [29] A. E. Giannakopoulos, S. Suresh, *Int. J. Solids Structures* 34 (1997) 2393
- [30] S. M. Aizikovich, V. M. Alexandrov, J. J. Kalker, L. I. Krenev, I. S. Trubchik, *Int. J. Solids Structures* 39 (2002) 2745
- [31] D. S. Stone, *J. Mater. Res.* 13 (1998) 3207
- [32] V. Linss, N. Schwarzer, T. Chudoba, M. Karniychuk, F. Richter: “Mechanical Properties of a Graded BCN Sputtered Coating with Varying Young's Modulus: Deposition, Theoretical Modelling and Nanoindentation”, *Surf. Coat. Technol.*, 195 (2005) pp 287 - 297
- [33] T. Chudoba, N. Schwarzer, V. Linss, F. Richter: „Determination of Mechanical Properties of Graded Coatings using Nanoindentation”, *proceedings of the ICMCTF 2004 in San Diego, California, USA*, also in *Thin Solid Films* (2004): 469-470C pp. 239-247

- [34] A. I. Lurje: „Three Dimensional Problems of the Theory of Elasticity”, Interscience Publishers, 1964
- [35] N. Schwarzer: „Modelling of the mechanics of thin films using analytical linear elastic approaches“, Habilitationsschrift der TU-Chemnitz 2004, FB Physik Fester Körper, <http://archiv.tu-chemnitz.de/pub/2004/0077>
- [36] A. J. Jerri: "Integral and discrete transforms with applications and error analysis", Marcel Dekker, Inc., New York, 1992
- [37] V. I. Fabrikant: "Application of potential theory in mechanics: A Selection of New Results", Kluwer Academic Publishers, The Netherlands, 1989
- [38] OPfC, SSA and FilmDoctor-ISA, mechanical test analysing software and software for the calculation of stresses and deformations in coated systems, available in the internet at: <http://www.siomec.de/shop>.
- [39] N. Schwarzer, I. Hermann, T. Chudoba, F. Richter: "Contact Modelling in the Vicinity of an Edge", Surface and Coatings Technology 146-147 (2001) 371-377

Tables

Table 1: Material Parameters for the board's nose part

Layer	A_{11}	A_{12}	A_{13}	A_{33}	A_{44}	Thickness
Transversally isotropic	$75 \cdot E_1$	$15 \cdot E_1$	$1.2 \cdot E_1$	$1.8 \cdot E_1$	$1.6 \cdot E_1$	0.5mm
Isotropic	$1.2 \cdot E_2$	$0.4 \cdot E_2$	$0.4 \cdot E_2$	$1.2 \cdot E_2$	$0.4 \cdot E_2$	2mm
Transversally isotropic	$75 \cdot E_1$	$15 \cdot E_1$	$1.2 \cdot E_1$	$1.8 \cdot E_1$	$1.6 \cdot E_1$	0.5mm
Foam core Isotropic	$1.2 \cdot E_3$	$0.4 \cdot E_3$	$0.4 \cdot E_3$	$1.2 \cdot E_3$	$0.4 \cdot E_3$	82mm
Transversally isotropic	$75 \cdot E_1$	$15 \cdot E_1$	$1.2 \cdot E_1$	$1.8 \cdot E_1$	$1.6 \cdot E_1$	0.5mm
Isotropic	$1.2 \cdot E_2$	$0.4 \cdot E_2$	$0.4 \cdot E_2$	$1.2 \cdot E_2$	$0.4 \cdot E_2$	4mm
Transversally isotropic	$75 \cdot E_1$	$15 \cdot E_1$	$1.2 \cdot E_1$	$1.8 \cdot E_1$	$1.6 \cdot E_1$	0.5mm

$$E_2=6 E_1=100 E_3=E$$

Table 2: Material Parameters for the board's foot pad area

Layer	A_{11}	A_{12}	A_{13}	A_{33}	A_{44}	Thickness
Rubber pad Isotropic	$1.2 \cdot E_0$	$0.4 \cdot E_0$	$0.4 \cdot E_0$	$1.2 \cdot E_0$	$0.4 \cdot E_0$	6mm
Transversally isotropic	$75 \cdot E_1$	$15 \cdot E_1$	$1.2 \cdot E_1$	$1.8 \cdot E_1$	$1.6 \cdot E_1$	0.5mm
Isotropic	$1.2 \cdot E_2$	$0.4 \cdot E_2$	$0.4 \cdot E_2$	$1.2 \cdot E_2$	$0.4 \cdot E_2$	3mm
Transversally isotropic	$75 \cdot E_1$	$15 \cdot E_1$	$1.2 \cdot E_1$	$1.8 \cdot E_1$	$1.6 \cdot E_1$	0.5mm
Transversally isotropic	$75 \cdot E_1$	$15 \cdot E_1$	$1.2 \cdot E_1$	$1.8 \cdot E_1$	$1.6 \cdot E_1$	0.5mm
Isotropic	$1.2 \cdot E_2$	$0.4 \cdot E_2$	$0.4 \cdot E_2$	$1.2 \cdot E_2$	$0.4 \cdot E_2$	4mm
Transversally isotropic	$75 \cdot E_1$	$15 \cdot E_1$	$1.2 \cdot E_1$	$1.8 \cdot E_1$	$1.6 \cdot E_1$	0.5mm
Foam core Isotropic	$1.2 \cdot E_3$	$0.4 \cdot E_3$	$0.4 \cdot E_3$	$1.2 \cdot E_3$	$0.4 \cdot E_3$	70mm
Transversally isotropic	$75 \cdot E_1$	$15 \cdot E_1$	$1.2 \cdot E_1$	$1.8 \cdot E_1$	$1.6 \cdot E_1$	0.5mm
Isotropic	$1.2 \cdot E_2$	$0.4 \cdot E_2$	$0.4 \cdot E_2$	$1.2 \cdot E_2$	$0.4 \cdot E_2$	4mm
Transversally isotropic	$75 \cdot E_1$	$15 \cdot E_1$	$1.2 \cdot E_1$	$1.8 \cdot E_1$	$1.6 \cdot E_1$	0.5mm

$$E_2=10 E_0=6 E_1=100 E_3=E$$

Table 3: Material Parameters used for the bending load calculations

Layer	A_{11}	A_{12}	A_{13}	A_{33}	A_{44}	Thickness
Transversally isotropic	$75 \cdot E_1$	$15 \cdot E_1$	$1.2 \cdot E_1$	$1.8 \cdot E_1$	$1.6 \cdot E_1$	0.5mm
Isotropic	$1.2 \cdot E_2$	$0.4 \cdot E_2$	$0.4 \cdot E_2$	$1.2 \cdot E_2$	$0.4 \cdot E_2$	4mm
Transversally isotropic	$75 \cdot E_1$	$15 \cdot E_1$	$1.2 \cdot E_1$	$1.8 \cdot E_1$	$1.6 \cdot E_1$	0.5mm
Foam core Isotropic	$1.2 \cdot E_3$	$0.4 \cdot E_3$	$0.4 \cdot E_3$	$1.2 \cdot E_3$	$0.4 \cdot E_3$	80mm

Transversaly isotropic	$75 * E_1$	$15 * E_1$	$1.2 * E_1$	$1.8 * E_1$	$1.6 * E_1$	0.5mm
Isotropic	$1.2 * E_2$	$0.4 * E_2$	$0.4 * E_2$	$1.2 * E_2$	$0.4 * E_2$	4mm
Transversaly isotropic	$75 * E_1$	$15 * E_1$	$1.2 * E_1$	$1.8 * E_1$	$1.6 * E_1$	0.5mm

$E_2=6 E_1=100 E_3=E$

ROBUST DESIGN OPTIMIZATION IN PARALLEL COMPUTING ENVIRONMENT

Nikos D. Lagaros and Manolis Papadrakakis

Institute of Structural Analysis & Antiseismic Research
School of Civil Engineering
National Technical University of Athens
Zografou Campus, Athens 157 80, Greece
e-mail: {nlagaros,mpapadra}@central.ntua.gr

Keywords: Parallel computing, dynamic load balancing algorithm, exploitation of the computing strategies, structural robust design optimization, multi-objective optimization, metaheuristics.

Abstract. *In engineering problems, randomness and uncertainties are inherent. Robust design procedures, formulated in the framework of multi-objective optimization, have been proposed in order to take into account the various sources of randomness and uncertainty. These design procedures require orders of magnitude more computational effort than the conventional analysis or the optimum design processes since a very large number of finite element analyses is required to be dealt. It is therefore an imperative need to exploit the capabilities of the computing resources in order to deal with this kind of problems. In particular, parallel computing is implemented at the level of the metaheuristic optimization, by exploiting the physical parallelization feature of the nondominated sorting evolution strategies method, as well as at the level of the repeated structural analyses required for assessing the behavioural constraints and for calculating the objective functions. In this study an efficient dynamic load balancing algorithm (DLBA) for the optimum exploitation of the available computing resources is proposed and, without loss of generality, DLBA is applied to the task of computing the desired feasible Pareto front. In such problems the computation of the complete Pareto front with feasible designs only, constitutes a very challenging task. The proposed algorithm achieves linear speedup factors and almost 100% speedup factor values with reference to the sequential procedure.*

1 INTRODUCTION

Real world engineering systems always have imperfections or deviations from the nominal state which affect their response. These uncertainties are reflected in any optimized design obtained via an optimization methodology and thus it can never be materialized in an absolute way. A deterministic formulation of a structural optimization problem ignores the unavoidable scatter of the structural parameters; hence, the performance of the optimum designs obtained through deterministic formulations may be much different than expected. In recent years, design optimization studies have become increasingly concerned with the treatment of uncertainty and randomness and various stochastic formulations for the optimum design of structures have been proposed [1]. The methodological context for defining such designs is referred either as robust design optimization (RDO) or as reliability-based optimization (RBO). The aim of RDO formulations [2-5] is to improve product quality or stabilize performances by minimizing the effects of variations. The main goal of RBO formulations is to design for safety with respect to extreme events by determining optimum designs satisfying both deterministic and probabilistic constraints. In the combined reliability-robust design optimization (RRDO) formulation proposed in [6], which is an extension of the other two formulations, the probability of failure of the structure and/or the probability of violation of the constraints are taken into account as a set of probabilistic constraints together with the deterministic constraints considered by the RDO formulations, both RDO and RRDO are formulated as two-objective optimization problems. This type of problems is extremely computationally intensive since a vast number of finite element (FE) analyses should be performed.

In the present work, the nondominated sorting evolution strategies II (NSES-II) [7] method is used for the solution of the two-objective RDO sizing optimization problems of large-scale three-dimensional skeletal structures, while the required random characteristics of the structural response are computed with the Monte Carlo simulation method using the Latin hypercube sampling technique. It is therefore appropriate to perform the required computations in a parallel or distributed computing environment in order to be able to conduct RDO studies efficiently. In particular, the computations required by the NSES-II method are implemented in a two level parallelization scheme: (i) at the level of the optimization procedure exploiting the physical parallelization feature of the NSES-II method and (ii) at the level of the solution of every finite element analysis required for calculating the constraint and objective functions in order to assess each candidate design vector. The solution of the structural analysis problems encountered is performed with the finite element tearing and interconnecting (FETI) domain decomposition method [8-10]. The two objective functions considered in the RDO formulation are the material volume of the structure and the variance of a structural response parameter, while uncertainty on loads, material properties and member cross-sections is taken into consideration. Furthermore, each candidate design is checked whether it satisfies the corresponding code requirements for the design of structures [11]. In such problems it is desirable covering the Pareto front with feasible designs only, this task constitutes a very challenging task. In an effort to achieve the desired feasible Pareto front it is proposed an efficient dynamic load balancing algorithm for the optimum exploitation of the available computing resources. The proposed algorithm achieves linear speedup factors and almost 100% speedup factor values with reference to the sequential procedure. In order to prove the efficiency of the proposed dynamic load balancing algorithm synchronous and asynchronous variants of NSES-II method are implemented; while three constraint handling techniques are also considered.

It should be stated that the implementation of the proposed dynamic load balancing algorithm is not limited to the solution of RRDO problems only. It is applicable in any problem where an extremely large number of FE analyses are to be dealt. For example: (i) Structural reliability analysis problems implementing simulation based procedures into a heterogeneous computing environment (i.e. heterogeneous cloud computing platform). (ii) Metaheuristic structural design optimization carried out into a heterogeneous computing environment. (iii) Stochastic structural design optimization where the number of simulations required for assessing a design is not fixed; it depends on how small probabilities are sought. It should be stated also that the proposed method is applicable both in the case of the physical parallelization and in the case of a two level parallelization scheme where domain decomposition FE

solution methods are implemented in conjunction with the physical parallelization characteristic of the problem at hand.

2 ROBUST DESIGN OPTIMIZATION

A robust structural design optimization problem is formulated as a two-objective optimization problem where in addition to the objective function representing the initial construction cost or the structural weight, the influence of the random nature of structural parameters and loading conditions on the structural performance is also considered as an objective function [12].

2.1 Formulation of the optimization problem

The mathematical description of the generic RDO problem implemented in this study is formulated as follows:

$$\begin{aligned} \min_{s \in \mathcal{F}} \quad & [W(s), \sigma_u(s, \mathbf{r})]^T \\ \text{subject to} \quad & \bar{g}_j(s, \mathbf{r}) \leq 0, \quad j = 1, \dots, k \\ \text{where} \quad & \mathbf{r} \sim N(\boldsymbol{\mu}_r, \boldsymbol{\sigma}_r^2) \end{aligned} \quad (1)$$

where $W(s)$ and $\sigma_u(s, \mathbf{r})$ are the two objectives to be minimized, corresponding to the weight of the structure and the standard deviation of the structural response, respectively; s and \mathbf{r} are the vectors of the design and random variables; $\bar{g}_j(s, \mathbf{r})$ are the mean values of the k constraint functions ($j=1, 2, \dots, k$); \mathcal{F} is the feasible region, defined as the region of the design space for which the constraints of Eq. (1) are satisfied:

$$\mathcal{F} = \{s \in R^d \mid \bar{g}_j(s, \mathbf{r}) \leq 0 \quad j = 1, \dots, k\} \quad (2)$$

while R^d is a discrete set from which the design variables s take values.

2.2 Solving the multi-objective optimization problem

Several methods have been proposed for treating structural multi-objective optimization problems [13-15]. For the present study an improved version of the genetic algorithm based NSGA-II method [16] is implemented where the genetic algorithms are replaced by the mixed evolution strategies (ES) algorithm. The ES algorithm has been proven very efficient for solving single objective structural optimization problems [17]. The resulting algorithm, proposed in [7], is denoted as NSES-II($\mu+\lambda$) or NSES-II(μ, λ) depending on the selection scheme.

In a mixed optimization problem, with discrete and continuous design variables, solved with the ES algorithm, each individual is equipped with a set of parameters:

$$\begin{aligned} \mathbf{a} &= [(s_d, \boldsymbol{\gamma}), (s_c, \boldsymbol{\sigma}, \boldsymbol{\alpha})] \in (I_d, I_c) \\ I_d &= D^{n_d} \times R_+^{n_\gamma} \\ I_c &= R^{n_c} \times R_+^{n_\sigma} \times [-\pi, \pi]^{n_\alpha} \end{aligned} \quad (3)$$

where s_d and s_c are the vectors of discrete and continuous design variables, respectively. Vectors $\boldsymbol{\gamma}$, $\boldsymbol{\sigma}$ and $\boldsymbol{\alpha}$ are the distribution parameter vectors. Vector $\boldsymbol{\gamma}$ corresponds to the variances of the Poisson distribution, vector $\boldsymbol{\sigma} \in R_+^{n_\sigma}$ corresponds to the standard deviations ($1 \leq n_\sigma \leq n_c$) of the normal distribution while vector $\boldsymbol{\alpha} \in [-\pi, \pi]^{n_\alpha}$ corresponds to the inclination angles ($n_\alpha = (n_c - n_\sigma / 2)(n_\sigma - 1)$) that define a linear correlation of mutations of the continuous design variables s_c .

Let $\mathbf{B}_p^{(g)} = \{\mathbf{a}_1, \dots, \mathbf{a}_\mu\}$ denotes a parent population of individuals at the g^{th} generation. The genetic operators used in the mixed discrete ES method are denoted by the following mappings:

$$\begin{aligned}
 \text{rec} &: (\mathbf{I}_c)_{(g)}^\mu \rightarrow (\mathbf{I}_c)^\lambda \text{ recombination} \\
 \text{mut} &: (\mathbf{I}_c)^\lambda \rightarrow (\mathbf{I}_c)^\lambda \text{ mutation} \\
 \text{sel}_\mu^k &: (\mathbf{I}_c)^k \rightarrow (\mathbf{I}_c)_{(g+1)}^\mu \text{ selection, } k \in \{\lambda, \mu+\lambda\}
 \end{aligned} \tag{4}$$

A single iteration of the mixed ES, which is a step from the parent population \mathbf{B}_p^g to the next generation, \mathbf{B}_p^{g+1} is modelled by the mapping:

$$\text{opt}_{\text{ES}} : (\mathbf{I}_c)_{(g)}^\mu \rightarrow (\mathbf{I}_c)_{(g+1)}^\mu \tag{5}$$

NSES-II($\mu+\lambda$) is a generational algorithm, where a parent population is used in order to create the offspring population; then, both populations are combined to define the new parent population. An alternative to the generational metaheuristic (evolution strategies in the present study) is the steady-state (SS) evolution strategies, where there is only a single population (not a parent and an offspring one). The new individuals are incorporated directly in the evolution process; thus, parents and offspring coexist in the same population. The steady-state evolution strategies algorithm is characterized by incrementing the intensification capability of the search process. A steady-state variant of NSES-II($\mu+\lambda$) can easily be implemented by using an offspring population of size one. This means that the ranking and crowding procedures are applied each time a new individual is created, thus the computational complexity of the algorithm increases. In the rest of this work the steady-state variant is referred as NSES-II_{ss} while the original algorithm is referred as NSES-II_{gen}.

2.3 Parallel metaheuristic multi-objective optimization

Multi-objective optimization problems require searching for a whole set of optimum solutions (Pareto front) instead of a single optimum solution and therefore the need for parallel computing in metaheuristic multi-objective (MMO) optimization is even greater. A direct application of a MMO method (without loss of the generality the NSES-II($\mu+\lambda$) algorithm considered in the current study) in parallel computing environment is to exploit the physical parallelization feature of the MMO method into a master-slave scheme. In this approach, the master processor performs the steps of the NSES-II($\mu+\lambda$) algorithm while both master and workers processors evaluate the objective functions of the new individuals assigned. This parallel variant is referred as synchronous generational NSES-II($\mu+\lambda$) and it is denoted as NSES - II_{gen}^{syn}. According to this scheme, λ individuals are created and sent to the master and workers processors for assessment; when all of them have been assessed and returned to the master processor the new generation is completed. The performance of NSES - II_{gen}^{syn} algorithm depends on the number of available processors while it does not take advantage of the number of processors if it is higher than the population size λ . The asynchronous variant takes advantage of the number of the processors that are higher than λ . The idea in the asynchronous approach is to use all the available processors, which use to be larger than the population size of the algorithm. The asynchronous generational NSES-II($\mu+\lambda$), denoted as NSES - II_{gen}^{asy}, is based on the synchronous variant but N_{proc}^{gen} individuals are created instead of λ , where N_{proc}^{gen} is the available number of processors. Furthermore, when an assessed individual is received by the master, a new one is generated and sent for assessment to an idle processor. The NSES - II_{gen}^{asy} algorithm is still generational, because when the offspring population is filled, a new generation is completed. In NSES - II_{gen}^{asy} the master does not have to wait until all the individuals of a generation have been assessed. As a consequence, the search capabilities of this algorithm are different compared to NSES - II_{gen}^{syn}, since it is possible that individuals generated later to be inserted into the evolution process before than individuals generated earlier. As it was mentioned before, the steady-state scheme in metaheuristics allows improving the exploitation of the search, so the purposes of the asynchronous steady-state NSES-II denoted as NSES - II_{SS}^{asy} is twofold: to achieve this behaviour in a master-slave NSES-II and to reduce the time needed to solve MOPs using as many processors as possible. In NSES - II_{SS}^{asy}, the master processor also generates as many individuals as available processors. Once each evaluated solution is received, it is inserted in the population applying ranking and crowding. As in NSES - II_{gen}^{asy},

when idle workers are detected, new individuals are created and sent for evaluation to an idle processor.

Lee and Hajela [18] described an adaptation of genetic algorithms for multidisciplinary optimization problems in parallel computing environment. Coello Coello *et al.* [19] discussed different paradigms for parallel implementation of MMO methods, while new concepts on migration, replacement and niching schemes were discussed by VanVeldhuizen *et al.* [20]. de Toro Negro *et al.* [21] proposed a parallel genetic algorithm with a structured population in the form of a set of islands, while Wilson and Moore [22] proposed a parallel algorithm using multiple optimization criteria, independent populations of individuals which consist of multiple chromosomes. Durillo *et al.* [23] studied three parallel approaches (a synchronous and two asynchronous) for the nondominated sorting genetic algorithms II (NSGA-II) method based on the master-worker paradigm. Kipouros *et al.* [24] presented a multi-objective variant of the tabu search optimization algorithm implemented in parallel computers for the aerodynamic design optimization of turbo machinery blades. Bharti *et al.* [25] focused on the optimal design of morphing aircraft wings employing a wing structure composed of an internal layout of cables and struts using a parallelized variant of the NSGA-II method. Fan and Chanh [26] tested the efficiency of a parallel particle swarm multi-objective evolutionary algorithm in a variety of test functions taken from the literature. Nebro and Durillo [27] proposed a thread-based parallel version of a multi-objective evolutionary algorithm, while Zhou and Tan [28] applied a parallel version of multi-objective particle swarm optimization on graphics processing units. Mezmaz *et al.* [29] investigated the problem of scheduling precedence-constrained parallel applications on heterogeneous computing systems such as cloud computing infrastructures and proposed a parallel bi-objective hybrid genetic algorithm.

The above mentioned implementations are limited to the exploitation of the physical parallelization feature of the MMO methods. Furthermore, the feasibility of the designs comprising the Pareto front curve was satisfied with the use of constraint handling procedures that does not guaranty 100% feasibility. In this study the parallel implementation is performed both at the level of MMO method as well as at the level of the repeated FE analyses required for calculating the objective and constraint functions. This was performed implementing both the synchronous and asynchronous schemes with the generational or the steady-state implementation while a domain decomposition FE solution method was also considered. In particular, both NSES - Π^{syn}_{gen} and NSES - Π^{syn}_{SS} algorithms are implemented in this study. Furthermore, the feasibility of the designs is satisfied by implementing three constraint handling techniques either by rejecting any infeasible design in order to produce reliable Pareto front curves or a superiority of feasible points technique.

2.4 Constraint Handling Techniques

Metaheuristics are initially developed to solve unconstrained optimization problems; however, during the last decades several methods have been proposed for handling constrained optimization problems as well. A detailed survey can be found in the works by Coello Coello [30,31]. Indicatively three methods have been selected in this study in order to prove that the efficiency of the proposed dynamic load balancing algorithm is not dependant on the constraint handling technique. In particular in this study methods belonging to the methods of superiority of feasible points and rejection of infeasible points have been implemented.

3 OPTIMUM EXPLOITATION OF PARALLEL COMPUTING STRATEGIES

The use of metaheuristics in RDO problems requires a large number of FE analyses for the calculation of the objective and constraint functions at each optimization step. This is due to the characteristic of metaheuristic multi-objective optimization algorithms that they work simultaneously with a population of design points in the space of the design variables. This allows for a straightforward implementation of the optimization procedure in parallel computing environments (physical parallelization). Therefore, in the case of the NSES-II($\mu+\lambda$) algorithm adopted for solving the RDO problem, $N_{anal} = \lambda \cdot N_{sim}$ FE analyses can be performed independently and concurrently in every generation, where λ is the size of the population and N_{sim} is the number of the LHS samples considered. Thus, a complete finite element analysis

can be allocated to a processor, without the need for inter-processor communication during the solution phase, and the analyses can be performed simultaneously on the available processors.

3.1 Parallel computing strategies

In multi-objective optimization there exists no unique design which represents the optimum for all criteria. Thus, the common optimality condition used in single-objective optimization is replaced by the so called Pareto optimum. A design vector $\underline{s} \in \mathcal{F}$ is called Pareto optimum for a multi-objective optimization problem with m objective functions (all to be minimised) if there is no other design vector $\underline{s} \in \mathcal{F}$ such that:

$$f_i(\underline{s}) \leq f_i(\underline{s}) \text{ for } i = 1, \dots, m \quad (6)$$

with $f_i(\underline{s}) < f_i(\underline{s})$ for at least one objective i

The geometric locus of the Pareto optimum solutions is called Pareto front and represents the solution of the optimization problem with multiple objectives. A typical Pareto front curve is depicted in Figure 1 for two objective functions $f_1(x)$ and $f_2(x)$ both to be minimized. It can be seen that the definition of Eq. (6) is satisfied for designs a and c , since there exists no feasible design that is better than the two designs with reference to both objective functions. On the other hand the feasible designs of the hatched region are better compared to the design b with reference to both objective functions. Consequently, designs a and c belong to the Pareto front while design b does not constitute a Pareto optimum. The checks described in Eq. (6) can be performed only if the designs \underline{s} and \underline{s} are feasible. Therefore in MMO only feasible solutions are accepted, hence the following three cases can occur at each generation of a MMO procedure: (i) All members of the population are feasible; (ii) all members of the population are infeasible and (iii) some of the members are feasible and some are not feasible.

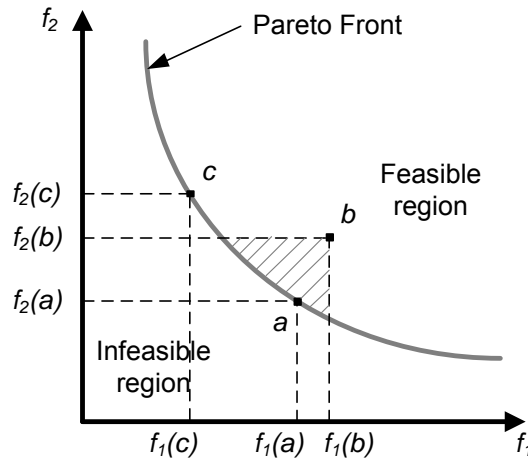


Figure 1: Typical Pareto front curve

According to the NSES-II($\mu+\lambda$) optimization procedure a population of λ vectors is produced in every generation. In order to check their feasibility in the framework of a robust design optimization, $N_{\text{anal}} = \lambda \cdot N_{\text{sim}}$ FE analyses are performed. There are two different schemes to perform these analyses in parallel within a generation step:

- i) Perform the optimization steps in serial mode and the corresponding FE analysis in parallel mode on the N_{proc} processors with the FETI solver.
- ii) Perform in parallel mode both the optimization steps and the corresponding FE analyses. In this case the $N_{\text{anal}} = \lambda \cdot N_{\text{sim}}$ FE analyses, required in every generation of the optimization procedure, can be performed concurrently and each solution of the finite element equations can also be performed in parallel mode with the FETI solver. These analyses correspond to the offspring vectors which are generated during the evolution process and according to the constraints check they are feasible or infeasible. In the case of an infeasible

ble offspring vector a new one is being generated until a feasible one is found. The feasibility check requires new N_{sim} FE analyses for each new offspring vector. Therefore, if λ_i out of λ designs were found infeasible, then $N_{anal} = \lambda_i \cdot N_{sim}$ new FE analyses must be carried out at this phase of the generation step. The optimal load balancing of this task is not a straightforward procedure. It is clear that, during the evolution procedure for reaching the optimum, different number of FE analyses that can be performed independently and concurrently are required while it is not obvious how many processors will be involved for the solution of each finite element problem to perform the constraints check. For this reason it is necessary to propose a dynamic load balancing algorithm (DLBA) for the fully exploitation of the available computing resources at any phase of the offspring generation of the optimization procedure.

3.2 Dynamic load balancing algorithm

In this section an optimization problem is formulated in order to achieve the optimum dynamic load balancing at each phase during the generation step of the optimization procedure. This problem is stated as follows: define the optimum way to accommodate N_{anal} FE analyses, which can be performed independently and/or concurrently, into a parallel computing environment composed by N_{proc} processors with the least required computing time. In the case of a cluster composed by a multi-core node environment, $N_{proc} = \text{number of nodes} \times \text{number of cores}$. According to the proposed DLBA every FE analysis can be alternatively performed on N_{sub} different domain decompositions varying on the number of subdomains. It is assumed, without this being restricting, that each subdomain is handled by one processor. Therefore, the dynamic load balancing optimization procedure is formulated as to define the optimum number of FE analyses performed implementing the i^{th} ($i=1, \dots, N_{sub}$) decomposition, that requires the least computing time to carry out N_{anal} FE analyses.

The full exploitation of the available resources can be stated as an optimization problem as follows:

$$\begin{aligned}
 \min_{\mathbf{n}_{anal}} \quad & Time(N_{anal}) \\
 \mathbf{n}_{anal} = & [n_{anal}(1), n_{anal}(2), \dots, n_{anal}(N_{sub})]^T \\
 n_{anal}(i) \in & [0, N_{anal}], i=1, \dots, N_{sub} \\
 \text{and} \quad & \sum_{i=1}^{N_{sub}} n_{anal}(i) = N_{anal}
 \end{aligned} \tag{7}$$

where $n_{anal}(i)$ ($i=1, 2, \dots, N_{sub}$) are the design variables of the dynamic load balancing optimization problem and corresponds to the number of FE analyses performed implementing the i^{th} decomposition. The total computing time ($Time$) is calculated according to a two-step procedure as follows:

Step 1

In the first step the time required for performing the FE analyses for every possible decomposition that can be accommodated by the entire cluster of processors (N_{proc}) without any remaining idle processors, is calculated. This time ($Time_1$) is obtained as follows:

$$n_{cluster}(i) = \text{int} \left[\frac{n_{anal}(i) \cdot n_{sub}(i)}{N_{proc}} \right] \tag{8a}$$

$$Time_1 = \sum_{i=1}^{N_{sub}} n_{cluster}(i) \cdot t_{sub}(i) \tag{8b}$$

where $n_{cluster}(i)$ denotes the number of times the cluster of processors will be used to perform FE analyses implementing $n_{sub}(i)$ decomposition, $n_{sub}(i)$ is the number of subdomains that the structure is subdivided (each subdomain is handled by one processors) according to the i^{th} de-

composition, $t_{sub}(i)$ is the time required for performing a single analysis implementing FETI with $n_{sub}(i)$ decomposition, while $Res_{anal}(i)$:

$$Res_{anal}(i) = n_{anal}(i) - n_{cluster}(i) \cdot \frac{N_{proc}}{n_{sub}(i)} \quad (9)$$

denotes the residual FE analyses that remain to be performed implementing the $n_{sub}(i)$ decomposition.

Step 2-Synchronous Implementation

In the second step, $Time_2$ defined the time required to perform the residual FE analyses that have not been performed in *Step 1*, in pursue of feasible solutions by the design vectors. This step is described in Figure 2, where in every use of the entire cluster of processors, groups of the residual FE analyses implementing different model partitioning types are accommodated by a part of the cluster. With the unused part of the cluster additional FE analyses are performed implementing other partitioning types ordered from the type with the least number of subdomains to that with the greater one.

```

1 Begin
2 Repeat
3   For i = 1 To Nsub-1 Do Begin
4     ncluster(i) = int ⌊  $\frac{Res_{anal}(i) \cdot n_{sub}(i) + Res_{anal}(i+1) \cdot n_{sub}(i+1)}{N_{proc}}$  ⌋
5     Time2 = Time2 + ncluster(i) · tsub(i)
6     Resanal(i+1) = Resanal(i+1) -  $\frac{[n_{cluster}(i) \cdot N_{proc} - Res_{anal}(i) \cdot n_{sub}(i)]}{n_{sub}(i+1)}$ 
7   End
8   Until all analyses are performed
9 End
(a)

1 Begin
2 Repeat
3   For i = 1 To Nsub-1 Do Begin
4     ncluster(i) = int ⌊  $\frac{Res_{anal}(i) \cdot n_{sub}(i) + Res_{anal}(i+1) \cdot n_{sub}(i+1)}{N_{proc}}$  ⌋
5     Time2 = Time2 + ncluster(i) · tsub(i)
6     Resanal(i+1) = Resanal(i+1) -  $\frac{[n_{cluster}(i) \cdot N_{proc} - Res_{anal}(i) \cdot n_{sub}(i)]}{n_{sub}(i+1)}$ 
7   End
8   Until all analyses are performed
9 End
(b)
    
```

Figure 2: The second step for the calculation of the required computing time for the case of (a) Synchronous and (b) Asynchronous Implementation

Step 2-Asynchronous Implementation

In the second step, $Time_2$ defined the time required to perform the residual FE analyses that have not been performed in *Step 1*, in pursue of feasible solutions by the design vectors. This step is described in Figure 2, where in every use of the entire cluster of processors, groups of the residual FE analyses implementing different model partitioning types are accommodated by a part of the cluster. With the unused part of the cluster additional FE analyses are performed implementing other partitioning types ordered from the type with the least number of subdomains to the that with the greater one.

4 NUMERICAL RESULTS

For the purposes of this study, the robust design of a double-layered space truss aircraft hangar is considered.

4.1 Description of the test example

The hangar is intended to service three planes at a time requiring a total clear width of 194 m and a clear depth of 89 m, therefore an area of $100 \times 200 \text{ m}^2$ is designed to be covered. The

space truss that consists of 51448 elements, 13031 nodes and 38961 degrees of freedom. Due to engineering practice demands, the members are divided into groups having the same structural properties. This grouping of elements results in a trade-off between the use of more material and the need of symmetry and uniformity of the structure for practical reasons. Furthermore, it has to be taken into account that due to manufacturing limitations the design variables are not continuous but discrete, since cross-sections belong to a certain predefined set provided by the manufacturers. Thus the design variables considered are the cross-sectional dimensions of the members of the structure, taken from the circular hollow section (CHS) table. The total number of design variables is eight, since the hangar's elements follow the pattern of the member groups schematically depicted in the truss of Figure 3. The mean value of the modulus of elasticity is 200 GPa and the nominal yield stress is $\sigma_y=235$ MPa (S 235). Equivalent to the vertical uniform load of 0.10 kN, are considered as uniform vertical forces applied at all joints. In addition, a maximum load of 50 kN corresponding to crane is equally distributed at the central sixteen nodes of the roof. The structure is hinged at the boundaries along the transverse direction. Loading conditions are grouped in two categories: (i) dead loads (G) and (ii) live loads (Q). Thus each truss member is checked for actions that correspond to the load combination $1.35G+1.50Q$.

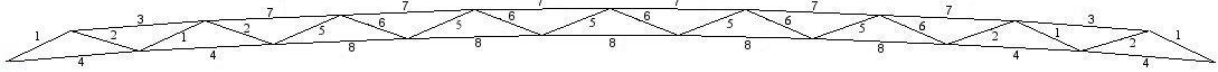


Figure 3: Description of the design variables for the aircraft hangar

In this study three types of behavioural constraints are imposed for the steel type of structures considered: (i) stress, (ii) compression force (for buckling) and (iii) displacement constraints. The stress constraint can be written as follows:

$$\begin{aligned}\sigma_{\max} &\leq \sigma_a \\ \sigma_a &= \frac{\sigma_y}{1.10}\end{aligned}\quad (10)$$

where σ_{\max} is the maximum axial stress of each element group for all load cases, σ_a is the allowable axial stress according to Eurocode 3 [11] and σ_y is the yield stress. For members under compression an additional constraint is used for buckling:

$$\begin{aligned}|P_{c,\max}| &\leq P_{cc} \\ P_{cc} &= \frac{P_e}{1.05} \\ P_e &= \frac{\pi^2 EI}{L^2}\end{aligned}\quad (11)$$

where $P_{c,\max}$ is the maximum axial compression force for all load cases, P_e is the critical Euler buckling force taken as the first buckling mode of a pin-connected member, L is the length of each member, while E and I are the material modulus of elasticity and the cross section moment of inertia, respectively. Similarly, the displacement constraints can be written as:

$$|d| \leq d_a \quad (12)$$

where d is the displacement at a certain node or the maximum nodal displacement for all load cases and d_a is the allowable value of the displacement at a certain node or the maximum allowable nodal displacement.

4.2 Solution of the multi-objective problem

For the test example considered, two objective functions have been taken into account, the

weight of the structure and the standard deviation of the maximum vertical nodal displacement, subject to constraints on stresses, element buckling and displacements imposed by the European design code [11]. A constraint of 500 mm on the maximum deflection is imposed in addition to the stress constraints described in Eqs. (13) and (14). The random variables that have been considered are two per design variable: the external diameter D and the thickness t of the circular hollow section. Apart from the cross-sectional dimensions of the structural members, the material properties (modulus of elasticity E and yield stress σ_y) and the loads have been considered as random variables, in total 19 random variables are used. The characteristics of the random variables are based on the work by Ellingwood *et al.* [32], where the mean value of the yield stress for the structural steel is 17% higher than its nominal value.

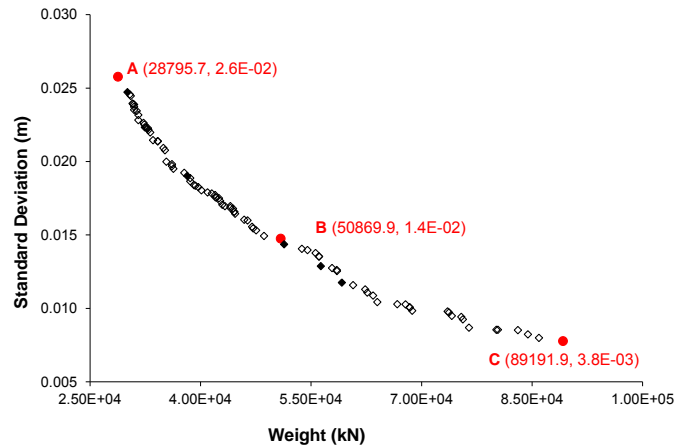


Figure 4: Pareto front curve for the RDO problem

For the solution of the multi-objective optimization problem, with any loss of the generality, the NSES-II($\mu+\lambda$) method is employed based on previous experience of the author [33] where $\mu = \lambda = 100$, while a sample size $N_{sim} = 20$ is used. These Monte Carlo simulations are considered adequate when generated with LHS for estimating the mean values and standard deviations in the framework of RDO problems, while the population size is the one employed in the original NSGA-II algorithm [16]. Furthermore, 200 generations are implemented since they were found sufficient to obtain a good quality Pareto front curve in a previous work by the authors [7]. The resultant Pareto front curve for the RDO formulation of Eq. (1) is depicted in Figure 4, with the structural weight on the horizontal axis and the standard deviation of the maximum vertical nodal displacement on the vertical axis. The three designs (A, B and C) are selected from the Pareto front curve for comparative reasons. They represent two extreme designs, corresponding to the two ends of the Pareto front curve, and one compromise design. In particular, design A indicates the Pareto optimum when the weight of the structure is the dominant criterion, design C is the Pareto optimum when the standard deviation of the maximum response is the dominant criterion, while design B indicates a compromise optimum design when both criteria are significant. Comparing design C with the other two designs, it can be seen that design C requires three times more material compared to design A and 40% more compared to design B. On the other hand, the variance of the response for the design C is almost one order of magnitude less compared to that of the other two designs.

4.3 Computational efficiency of the DLBA - Death Penalty case

For the purposes of this work a cluster for parallel computing, consisting of 25-nodes is used. Each cluster node consists of the Intel Core 2 Quad Q6600 2.4 GHz with 4 physical cores. For the test example considered both sequential and parallel test runs are carried out. The FETI solution requires partitioning of the FE model in a number of subdomains. For this purpose, a preprocessing step is performed for the domain decomposition of the finite element model upon its creation. Thus, before running the optimization procedure, the geometric configuration of the space truss is decomposed into 2, 5, 10, 25 and 50 subdomains with optimal aspect

ratios obtained with TOP/DOMDEC [34]. The number of subdomains depends on the structure, while those selected for the problem at hand were found adequate in a previous work by the author [35]. Upon the creation of each decomposition, every structural element member is assigned to a subdomain on the basis of its distance from the geometrical centre of the subdomain. The minimum distance of each element from the geometric centre of the subdomain designates the subdomain in which the element belongs. The implementation of the proposed dynamic load balancing algorithm requires the computational demands for the FE analysis performed with 1, 2, 5, 10, 25 and 50 subdomains, where each subdomain is allocated to one processor. The computing time required for a single analysis is not affected by any candidate design under consideration, because the truss configuration remains the same during the RDO procedure.

Before assessing the various parallelization schemes implemented in this study, a parametric study is performed with reference to the DE method that is used for the solution of the optimization problem of Eq. (7). The solution of this problem can be performed with any single objective optimization algorithm. The selection of the DE method is based on previous experience of the author [36,37] where it was found very robust. In order to identify the best combination of the parameters for DE algorithm, 30 combinations of the parameters are generated by means of LHS, while for each combination 100 optimization runs are performed in order to calculate the mean and the coefficient of variation with reference to the objective function value. All runs are performed with a cluster of processors comprising $N_{proc} = 100$ cores. The population size NP of the optimization algorithm is defined in the range of [50, 200], while the probability CR and constant F are defined in the range of [0, 1]. Worth noticing is that for all combinations of the characteristic parameters the best objective function value is finally reached, while COV is below 1%. The characteristic parameters adopted for the implementation of DE method are as follows: population size NP = 195, probability CR = 0.58 and constant F = 0.32.

Number of processors	Case 1	Case 2	Case 3		DLBA	
			NSES - Π_{gen}^{syn}	NSES - Π_{SS}^{asy}	NSES - Π_{gen}^{syn}	NSES - Π_{SS}^{asy}
50	9.69×10^5	2.74×10^5	1.97×10^5	1.97×10^5	7.42×10^4	7.35×10^4
75	6.55×10^5	1.85×10^5	1.31×10^5	1.31×10^5	5.04×10^4	5.00×10^4
100	4.88×10^5	1.38×10^5	9.85×10^4	9.85×10^4	3.79×10^4	3.76×10^4
250	2.07×10^5	5.81×10^4	3.94×10^4	3.94×10^4	1.63×10^4	1.59×10^4
500	1.11×10^5	3.11×10^4	1.97×10^4	1.97×10^4	8.65×10^3	8.56×10^3

Table 1: Computational performance of NSES-II($\mu+\lambda$) for the case of the death penalty constraint handling technique (computing time in secs)

The performance of the NSES-II(100+100) optimization method in serial and parallel computing environments is presented in Table 1. The parallel implementations are performed in five different clusters with 50, 75, 100, 250 and 500 cores. The first three clusters are based on the existing cluster with 100 cores, while the other two are simulated clusters having 250 and 500 cores. In addition to the proposed dynamic load balancing algorithm three other parallelization patterns are examined. *Case 1*: The optimizer is performed in parallel and the solver in serial mode with a skyline solver. The set of the λ_i designs that are found to be infeasible define a subgeneration where each design is dealt by one processor. *Case 2*: The optimizer is performed in parallel and the solver is implemented in serial mode with FETI solver, where the infeasible designs are dealt with in a similar fashion as in *Case 1*. *Case 3*: The optimizer and the solver are implemented in parallel mode, where the infeasible designs are dealt independently while the solution part is performed with parallel FETI in more than one processor. In *Case 3* the implementation of FETI in all five different clusters was performed with 50 subdomains (i.e. in 50 processors). The sequential time required for solving the problem at hand is 1.29×10^7 seconds with a skyline serial solver and 3.65×10^6 seconds with the FETI solver, where almost one order of magnitude reduction of the computing time is achieved with the sequential FETI solver compared to the skyline solver.

From Table 1 it can be concluded that the proposed procedure managed to reduce the computing time by more than one order of magnitude compared to Case 1, by 4 times compared to Case 2 and by 3 times compared to Case 3. Furthermore, Figure 5 depicts the speedup factors achieved with the implementation of Cases 2 and 3 compared to that of the proposed dynamic load balancing procedure. In this Figure it can be seen that an almost 100% efficiency is achieved with the DLBA, which is much greater compared to that achieved with Cases 2 and 3. Worth mentioning is that the proposed procedure is independent of the population size and the number of Monte Carlo simulations used for the calculation of the statistical properties of the response.

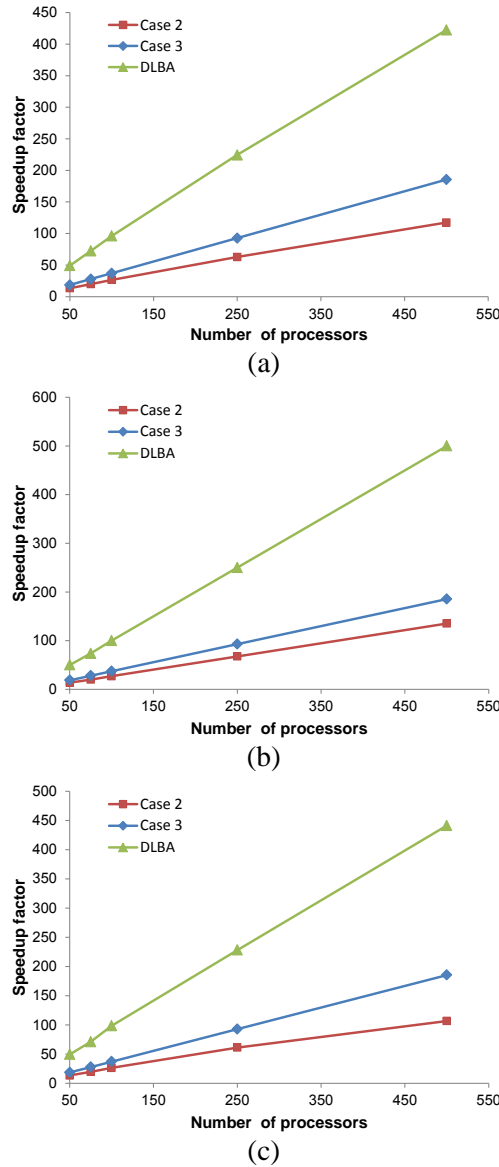


Figure 5: Speedup factors achieved with various parallelization patterns for the NSES - Π_{gen}^{sym} scheme for the case of (a) the death penalty, (b) the superiority of feasible points and (c) the death penalty step size control constraint handling technique

5 CONCLUSIONS

- In most cases the design of structures is based on deterministic parameters and is focused on the satisfaction of the deterministically defined design code provisions. A deterministic optimized design is not always a safe design, since such formulations ignore the random properties that affect the structural performance, hence formulations considering

uncertainties should be considered. In this work the highly computationally intensive problem of robust structural design optimization is considered, taking into account randomness on both structural capacity and demand. The problem is formulated as a two-objective optimization problem subjected to stress and displacement constraints. A modified nondominated sorting genetic algorithm optimization method is proposed where genetic algorithms are replaced by evolution strategies for the solution of the multi-objective optimization problems. The optimization algorithm is more reliable since it guarantees the feasibility of the Pareto front.

- An important characteristic of the nondominated sorting evolution strategies is that this method works simultaneously with a population of feasible designs only in the search space. This feasibility requirement does not allow for a straightforward implementation of the optimization procedure in parallel computing environments. In this case, a large and variable number of finite element structural analyses can be performed independently and concurrently at each subgeneration step of the optimization procedure. The computational efficiency of the metaheuristic multi-objective optimization algorithms is enhanced with the implementation of parallel domain decomposition algorithms for the solution of the repeated finite element problems and the dynamic exploitation of the available parallel computing resources.
- In this study an efficient dynamic load balancing algorithm is proposed achieving optimum exploitation of the computing resources. The dynamic load balancing problem is dealt with the differential evolution algorithm and the computational efficiency is almost 100%. The reduction of the computational effort achieved is ranging from three times to more than one order of magnitude compared to parallel implementations without the dynamic load balancing. The proposed procedure is independent of the population size and the Monte Carlo simulations used for the calculation of the statistical properties of the response and it is independent on the available computing resources.

REFERENCES

- [1] Tsompanakis, Y., Lagaros, N.D., Papadrakakis (Eds.), M. *Structural Optimization Considering Uncertainties*, Taylor & Francis, 2007.
- [2] Park, G.J., Lee, T.H., Lee, K.H., Hwang, K.H. Robust design: An overview, *AIAA Journal* 2006; 44(1): 181-191.
- [3] Beyer, H.-G., Sendhoff, B. Robust optimization - A comprehensive survey, *Computer Methods in Applied Mechanics and Engineering* 2007; 196(33-34): 3190-3218.
- [4] Lagaros, N.D., Fragiadakis, M. Robust performance based design optimization of steel moment resisting frames, *Journal Earthquake Engineering* 2007; 11(5): 752-772.
- [5] Schevenels, M., Lazarov, B.S., Sigmund, O. Robust topology optimization accounting for spatially varying manufacturing errors, *Computer Methods in Applied Mechanics and Engineering* 2011, 200(49-52): 3613-3627.
- [6] Youn, B.D., Choi, K.K., Du, L., Gorsich, D. Integration of possibility-based optimization and robust design for epistemic uncertainty, *Journal of Mechanical Design Transactions of the ASME* 2007; 129(8): 876-882.
- [7] Lagaros, N.D., Papadrakakis, M. Seismic design of RC structures: a critical assessment in the framework of multi-objective optimization, *Earthquake Engineering and Structural Dynamics* 2007; 36(12): 1623-1639.

-
- [8] Farhat, C., Roux, F.-X. A method of finite element and interconnecting and its parallel solution algorithm, *International Journal for Numerical Methods in Engineering* 1991; 32: 1205-1227.
- [9] Farhat, C., Roux, F.-X. Implicit parallel processing in structural mechanics, *Computational Mechanics Advances* 1994; 2: 1-124.
- [10] Bitzarakis, S., Papadrakakis, M., Kotsopoulos, A., Parallel solution techniques in computational structural mechanics, *Computer Methods in Applied Mechanics and Engineering* 1997; 148: 75-104.
- [11] EC3. *Eurocode 3: Design of steel structures, Part 1.1: General Rules and Rules for Buildings*. European Committee for Standardisation: Brussels, Belgium, The European Standard EN 1993-1-1: 2005.
- [12] Lagaros, N.D., Plevris, V., Papadrakakis, M. Multi-objective design optimization using cascade evolutionary computations, *Computer Methods in Applied Mechanics and Engineering* 2005; 194(30-33): 3496-3515.
- [13] Coello Coello, C.A. An updated survey of GA-based multi-objective optimization techniques, *ACM Computing Surveys* 2000; 32(2): 109-143.
- [14] Zitzler, E., Deb, K., Thiele, L. Comparison of multiobjective evolutionary algorithms: empirical results. *Evolutionary Computation* 2000; 8(2): 173-195.
- [15] Marler, R.T., Arora, J.S. Survey of multi-objective optimization methods for engineering, *Structural and Multidisciplinary Optimization* 2004; 26(6): 369-395.
- [16] Deb, K., Pratap, A., Agarwal, S., Meyarivan, T. A fast and elitist multi-objective genetic algorithm: NSGA-II. *IEEE Transactions on Evolutionary Computation* 2002; 6(2): 182-197.
- [17] Lagaros, N.D., Fragiadakis, M., Papadrakakis, M. Optimum design of shell structures with stiffening beams, *AIAA Journal* 2004; 42(1): 175-184.
- [18] Lee, J., Hajela, P. Parallel genetic algorithm implementation in multidisciplinary rotor blade design, *Journal of Aircraft* 1996; 33(5): 962-969.
- [19] Coello Coello, C.A., Van Veldhuizen, D.A., Lamont, G.B. *Evolutionary Algorithms for Solving Multi-objective Problems*, Kluwer Academic Publishers, 2002.
- [20] VanVeldhuizen, D.A., Zydallis, J.B., Lamont, G.B., Considerations in engineering parallel multiobjective evolutionary algorithms, *IEEE Transactions on Evolutionary Computation* 2003; 7(2): 144-173.
- [21] de Toro Negro, F., Ortega, J., Ros, E., Mota, S., Paechter, B., Martín, J.M. PSFGA: Parallel processing and evolutionary computation for multiobjective optimisation, *Parallel Computing* 2004; 30(5-6): 721-739.
- [22] Wilson, L.A., Moore, M.D. Cross-pollinating parallel genetic algorithms for multiobjective search and optimization, *International Journal of Foundations of Computer Science* 2005; 16(2): 261-280.
- [23] Durillo, J.J., Nebro, A.J., Luna, F., Alba, E. A study of master-slave approaches to parallelize NSGA-II, IPDPS Miami 2008 - Proceedings of the 22nd IEEE International Parallel and Distributed Processing Symposium, 2008.

- [24] Kipouros, T., Jaeggi, D.M., Dawes, W.N., Parks, G.T., Savill, A.M., Clarkson, P.J., Insight into high-quality aerodynamic design spaces through multi-objective optimization, *Computer Modeling in Engineering and Sciences* 2008; 37(1): 1-44.
- [25] Bharti, S., Frecker, M., Lesieutre, G. Optimal morphing-wing design using parallel nondominated sorting genetic algorithm II, *AIAA Journal* 2009; 47(7): 1627-1634.
- [26] Fan, S.-K.S., Chang, J.-M. A parallel particle swarm optimization algorithm for multi-objective optimization problems, *Engineering Optimization* 2009, 41(7): 673-697.
- [27] Nebro, A.J., Durillo, J.J. A study of the parallelization of the multi-objective metaheuristic MOEA/D. *Lecture Notes in Computer Science* 2010; Volume 6073 LNCS: 303-317
- [28] Zhou, Y., Tan, Y. GPU-based parallel multi-objective particle swarm optimization, *International Journal of Artificial Intelligence* 2011; 7(11): 125-141.
- [29] Mezmaiz, M., Melab, N., Kessaci, Y., Lee, Y.C., Talbi, E.-G., Zomaya, A.Y., Tuytens, D. A parallel bi-objective hybrid metaheuristic for energy-aware scheduling for cloud computing systems, *Journal of Parallel and Distributed Computing* 2011; 71(11): 1497-1508.
- [30] Mezura-Montesa, E., Coello Coello, C.A., Constraint-handling in nature-inspired numerical optimization: Past, present and future, *Swarm and Evolutionary Computation* 2011; 1: 173-194.
- [31] Arias-Montano, A., Coello Coello, C.A., Mezura-Montesa, E., Multiobjective evolutionary algorithms in aeronautical and aerospace engineering, *IEEE Transaction on Evolutionary Computation* 2012; 16(50): 662-694.
- [32] Ellingwood, B.R., Galambos, T.V., MacGregor, J.G., Cornell, C.A. *Development of a Probability-Based Load Criterion for American National Standard A58*, National Bureau of Standards, Washington, DC, 1980.
- [33] Mitropoulou, Ch.Ch., Fourkiotis, Y., Lagaros, N.D., Karlaftis, M.G. Metaheuristics in structural design optimization, in *Metaheuristic Applications in Structures and Infrastructures*, Amir Hossein Gandomi, Xin-She Yang, Siamak Talatahari and Amir Hossein Alavi (Eds.), Elsevier, 2013.
- [34] Sharp, M., Farhat, C. TOPDOMDEC – *A totally object oriented program for visualization, domain decomposition and parallel processing*. User's manual, PGSoft and University of Colorado, Boulder, USA, 1994.
- [35] Papadrakakis, M., Lagaros, N.D., Fragakis, Y. Parallel computational strategies for structural optimization, *International Journal for Numerical Methods in Engineering* 2003; 58(9): 1347-1380.
- [36] Lagaros, N.D., Karlaftis, M.G. A critical assessment of metaheuristics for scheduling emergency infrastructure inspections, *Swarm and Evolutionary Computation* 2011; 1(3): 147-163.
- [37] Lagaros, N.D., Papadrakakis, M. Applied soft computing for optimum design of structures, *Structural and Multidisciplinary Optimization* 2012; 45: 787-799.

THE CHOICE OF QUADRATURE IN NURBS-BASED ISOGEOMETRIC ANALYSIS

Francesco Calabrò¹ and Carla Manni²

¹Dipartimento DIEI
Università di Cassino e del Lazio Meridionale, Italy
e-mail: calabro@unicas.it

² Dipartimento di Matematica
Università di Roma Tor Vergata, Italy
e-mail: manni@mat.uniroma2.it

Keywords: Quadrature, Isogeometric Analysis, Refinable functions

Abstract. *The construction of ad-hoc quadrature rules for Isogeometric Analysis is an issue that has been considered as the greater inter-element regularity can give considerable savings in terms of computational effort. In NURBS-based Isogeometric Analysis the request for the quadrature is to give exact result for piece-wise polynomials (on the elements) of degree p with r continuous derivatives. A choice for the basis for this space are the B-splines, that are considered because of their properties related to support, refinability and regularity. In this work we intend to present some preliminary results on the use of global quadrature rules capable of exact results with respect to these basis functions, focusing on differences and potentiality.*

1 Introduction

The construction of ad-hoc quadrature rules for Isogeometric Analysis (IgA) is an issue that has been considered as the greater inter-element regularity can give considerable savings in terms of computational effort [1, 6].

In NURBS-based IgA the request for the quadrature is to give exact result for piece-wise polynomials of degree p with r continuous derivatives. A choice for the basis for this space are the B-splines, that are considered because of their properties related to support, refinability and regularity. In this work we intend to review the possible choices of quadrature rules when one intends to calculate integrals involving B-splines on the whole support of these functions for uniform knots sequences. This changes the usual prospective because actual software constructs the discrete problem element-by-element. In the authors' opinion what presented in [1, 6] gives a good way to treat cases of interest, while in this new prospective there are many roads to be explored, especially in the uniform case, where many properties can be used.

The results presented are preliminary, and consider only the calculation of integrals of the type

$$\int_0^{p+1} \mathcal{N}_p(x) f(x) dx \quad (1)$$

where $\mathcal{N}_p(x)$ is the cardinal B-spline of degree p . These integrals arise when the right hand side (the forcing term) is considered in IgA with maximal regularity ($r = p - 1$). All the others that have to be computed¹ are made with the translated copies of function \mathcal{N}_p thus are of the same type.

Obviously, (1) are not the only integrals that have to be considered for the construction of the discrete counterpart of the differential problems, and the question related to the other cases such as Mass and Stiffness matrices will be considered in a forthcoming work.

Since now, the most common technique to calculate these integrals with a quadrature rule is to consider a proper composite Gauss formula: using the piece-wise polynomial expression of B-splines one can consider the Gauss quadrature that integrates exactly polynomials of degree p on each subinterval in order to gain exactness. This choice is not optimal from a computational point of view, but is in line with what is done in finite element software.

What we want to focus on is that many properties of the B-splines can be considered in order to construct quadrature formulae that achieve some exactness requirement. The intent of this paper is to report and compare some of these quadrature rules.

We begin with an introduction on B-splines and some of their properties. The construction of the different quadrature rules is outlined in Section 3. At last, we collect some conclusions.

2 Preliminars on B-splines

We will denote by $\mathcal{N}_p(x)$ the cardinal B-spline of degree p over the uniform knots sequence $\{0, 1, \dots, p + 1\}$ which is defined recursively as follows:

$$\mathcal{N}_0(x) := \begin{cases} 1 & \text{if } 0 \leq x < 1 \\ 0 & \text{otherwise} \end{cases}$$

and:

$$\mathcal{N}_p(x) := \frac{x}{p} \mathcal{N}_{p-1}(x) + \frac{p+1-x}{p} \mathcal{N}_{p-1}(x-1), \quad \forall p \geq 1.$$

¹We will consider here the case of periodic uniform knot vector.

Translated copies of cardinal B-splines are a basis for 0-periodic splines of degree p and regularity $p - 1$. Among all the properties, we recall the following [3]:

$$\begin{aligned} \text{Positivity: } & \mathcal{N}_p(x) \geq 0 \quad \forall x \in \mathbb{R}, \\ \text{Minimal support: } & \mathcal{N}_p(x) = 0 \quad \forall x \notin [0, p + 1], \\ \text{Symmetry: } & \mathcal{N}_p\left(\frac{p+1}{2} + x\right) = \mathcal{N}_p\left(\frac{p+1}{2} - x\right). \end{aligned}$$

An other relevant property that we will use is the fact that B-splines solve a refinement equation. Define the vector \mathbf{a} (called mask) as:

$$\mathbf{a} := \{a_j, j = 0, \dots, p + 1\}, \quad a_j := \frac{1}{2^p} \binom{p+1}{j}.$$

Then the cardinal B-spline is the only² function solution of the refinement equation:

$$\mathcal{N}_p(x) = \sum_j a_j \mathcal{N}_p(2x - j). \quad (2)$$

In the next section we will use the following result on the product of B-splines (see Lemma 4 in [4]):

$$\int_{\mathbb{R}} \mathcal{N}_p(x) \mathcal{N}_q(x + k) dx = \mathcal{N}_{p+q+1}(p + 1 + k) = \mathcal{N}_{p+q+1}(q + 1 - k). \quad (3)$$

3 Quadrature formulae

Given a generic function $\phi(x)$, an n -point quadrature rule is a choice of n ordered points and relative weights $(\xi_i, \omega_i)_{i=1, \dots, n}$ such that

$$\int_a^b \phi(x) dx \simeq \sum_{i=1}^n \omega_i \phi(\xi_i).$$

The number of quadrature points n fixes the number of function evaluations needed in order to compute the value of the integral, thus is the parameter to be considered for the computational cost. A quadrature rule is said to be *exact* on the family of functions $\{\phi_j\}_{j=1, \dots, M}$ if

$$\int_a^b \phi_j(x) dx = \sum_{i=1}^n \omega_i \phi_j(\xi_i) \quad \forall j = 1, \dots, M. \quad (4)$$

Conditions (4) represent M non-linear equations in the $2n$ unknowns (ξ_i, ω_i) . In most cases the resolution of this system is ill-conditioned [8]. Classically, exactness is required on polynomials up to a fixed degree; in particular, the n -point Gauss rule is the (only) n -point rule that is exact for polynomials up to degree $2n - 1$.

A notable case is when the exactness is required with test functions being of product type: $\phi_j(x) = \tilde{\phi}_j(x)\Phi(x)$. Then the required quadrature is made to be exact on test functions $\tilde{\phi}_j(x)$ with respect to a weighted measure $\Phi(x)dx$. In this case the theory on Gauss quadrature with

²All functions that solve a refinement equation are equal apart from a multiplicative constant: B-splines are obtained renormalizing the L^1 norm to be 1.

respect to a general measure can be applied. An example can be found in [5].

Recently, exactness on general families of functions has been also explored. In [8] conditions are given such that a quadrature rule that integrates exactly M independent test functions using $\lceil \frac{M}{2} \rceil$ points exists and a procedure in order to calculate it is presented. This formulae are named *Generalized Gaussian* with respect to the test functions, and are used in [1, 6] for the construction of rules exact on spline functions.

Varying the exactness requirements or fixing some properties on the distribution of nodes different quadrature rules can be derived. The aim of this section is to present some of these that seem well-fitted for the calculation of (1).

We emphasize that the requirement on the use of an optimal number of points has to be related to the possibility to reuse the function evaluations $\{f(\xi_i)\}$. This because the integrals of type (1) have to be calculated for each basis function that, as seen, are translated copies of the one in $[0, p + 1]$. For this reason, if the quadrature points are translant-invariant on the unitary elements $[l, l + 1]$ (or on multiples of these) then the function evaluations can be reused.

3.1 Composite Gauss rule

Call $(\xi_i^G, \omega_i^G)_{i=1, \dots, N_G}$ the quadrature rule that exactly integrates polynomials of degree p in $[0, 1]$ using the fewest number of nodes. Then one can consider the following quadrature:

$$\begin{aligned} \int_0^{p+1} \mathcal{N}_p(x) f(x) dx &= \sum_{l=0}^p \int_l^{l+1} \mathcal{N}_p(x) f(x) dx \approx \\ &\approx \sum_{l=0}^p \sum_{i=1}^{N_G} \omega_i^G \mathcal{N}_p(\xi_i^G + l) f(\xi_i^G + l). \end{aligned}$$

This formula is exact only for constant $f(x)$ and uses $p \times N_G$ quadrature points; as seen in the previous section, $N_G = \lceil \frac{p+1}{2} \rceil$.

3.2 Half-point rule

In [6] it is proposed to use the rule $(\xi_i^{HP}, \omega_i^{HP})_{i=1, \dots, N_{OPT}}$ where $\omega_i^{HP} = 2$ and $\xi_i^{HP} = 2i$ if p is even, $\xi_i^{HP} = 1/2 + 2i$ if p is odd; $N_{OPT} = \lceil \frac{p+1}{2} \rceil$. The nodes are equispaced, not symmetric in $[0, p + 1]$ and the weights are equal. This formula is exact for constant integrand functions f . In Table 1 we report some of the calculated rules. Last line is added for rapid comparison with what we will present in next sections.

	$p = 2$	$p = 3$	$p = 4$
Nodes $\{\xi_i^{HP}\}$	$\{2\}$	$\{0.5, 2.5\}$	$\{2, 4\}$
Weights $\{\omega_i^{HP}\}$	$\{2\}$	$\{2, 2\}$	$\{2, 2\}$
B-spline values on nodes $\{\mathcal{N}_p(\xi_i^{HP})\}$	$\{1/2\}$	$\{1/48, 23/48\}$	$\{11/24, 1/24\}$

Table 1: Half-point rules.

When searching for quadrature with the requirement that it is exact only for constant functions one can also consider other simple rules. This choice was introduced in [6] because it turns to be optimal in terms of function evaluations when integration is made in an element-wise fashion.

	$p = 3$	$p = 4$
Nodes $\{\xi_i\}$	$\{1.05131670195, 2, 2.94868329805\}$	$\{1.427619470524, 2.5, 3.572380529476\}$
Weights $\{\omega_i\}$	$\{5/27, 17/27, 5/27\}$	$\{25/138, 44/69, 25/138\}$

Table 2: Weighed Gauss rule, $n = 3$.

3.3 Weighed Gauss rule

Following the approach in [5] one can search for a quadrature rule that is optimal with respect to the weighted measure $\mathcal{N}_p(x)dx$, solving exactness requirements (4) on monomials. This leads to a nonlinear problem that in general is difficult to solve. In the case of interest we can use the refinability property (2) so that the computation becomes stable. We refer to [5, 9] for the details on the construction of such rules. In Table 2 we report the calculated rules in the case $n = 3$, $p = 3, 4$. The nodes and the weights are symmetric in $[0, p + 1]$ and all weights are positive. The formula, moreover, is exact for all f polynomial up to degree $2n - 1$.

3.4 Fixed points rule

If preassigned samples of the integrand function f have to be used in order to calculate the integral (or some distribution of nodes has to be considered) the quadrature that attains the maximum polynomial degree of exactness is well known to be the interpolation-based one. In the case of integrals of the type (1) one can consider to use samples of function f and construct a quadrature to be used for integration with respect to the weighted measure $\mathcal{N}_p(x)dx$. The use of the refinement properties of the B-splines leads to a stable procedure for the calculation of these quadrature rules. We refer to [2] for the algorithmic details.

This procedure is very powerful in order to obtain exactness on polynomials maintaining the evaluations of the integrand function in points with requested properties, such as translate invariance and symmetry. In Table 3 we have reported the calculated quadrature in some cases for rapid comparison. In particular, the first two lines report the quadrature that give exactness on linear polynomials constructed on the same nodes considered by the Half-point rule seen before. The next two lines take in account all the points to be used by the formula when used on the translated intervals. The relation with the Half-point rule is evident comparing the calculated weights.

	$p = 3$	$p = 4$
Fixed Nodes $\{\xi_i\}$	$\{0.5, 2.5\}$	$\{2, 4\}$
Weights $\{\omega_i\}$	$\{1/4, 3/4\}$	$\{3/4, 1/4\}$
	$p = 3$	$p = 4$
Fixed Nodes $\{\xi_i\}$	$\{0.5, 1.5, 2.5, 3.5\}$	$\{1, 2, 3, 4\}$
Weights $\{\omega_i\}$	$\{1/48, 23/48, 23/48, 1/48\}$	$\{1/24, 11/24, 11/24, 1/24\}$

Table 3: Fixed points rules of optimal polynomial degree.

3.5 Quasi-Interpolant-based rules

A recent paper [10] has highlighted that in order to calculate the integrals arising in Iso-geometric analysis, one can try to substitute the integrand function with a proper combination

of function with the property that the integral of these new functions are known. This general approach is similar to the one that uses modified moments in order to calculate the quadrature rules. In the cited reference quasi-interpolation with B-splines is used and the approach is named *quadrature-free*: in this case we can use equation (3) seen in the previous section (see [4, Lemma 4]). The resulting formulae are very versatile and can gain exactness also in spline spaces [7, 11]. In general one can write:

$$\begin{aligned} \int_0^{p+1} \mathcal{N}_p(x)f(x) dx &= \int_{-\infty}^{+\infty} \mathcal{N}_p(x)f(x) dx \approx \\ \int_{-\infty}^{+\infty} Q(f(x))\mathcal{N}_p(x) dx &= \int_{-\infty}^{+\infty} \sum_j \eta_j(f)\mathcal{N}_q(x+j)\mathcal{N}_p(x) dx = \\ \sum_j \eta_j(f) \int_{-\infty}^{+\infty} \mathcal{N}_q(x+j)\mathcal{N}_p(x) dx &= \sum_j \eta_j(f)\mathcal{N}_{p+q+1}(p+1+j), \end{aligned} \quad (5)$$

where we have denoted by $Q(f)$ a generic quasi-interpolation operator of f and then considered the particular choice of a projection on B-splines of degree q constructed from a local projector [7]:

$$Q(f(x)) := \sum_j \eta_j(f)\mathcal{N}_q(x+j).$$

In this section we will fix the quadratic case $q = 2$. Then we can construct a projection using only points of the type $l/2$, $l = 0, \dots, 2(p+1)$ obtaining a quadrature rule exact for f polynomial up to degree 2 and for B-splines of degree 2.

Fixed $q = 2$, $p \geq 2$, we have $j = -2, \dots, p$ and the projection that gains the best properties of exactness and uses only values of the integrand function in points of the kind $l/2$ is (compare with [7]):

$$\begin{aligned} \eta_{-2}(f) &= (5/2)f(0) - 2f(1/2) + (1/2)f(1); \\ \eta_j(f) &= 1/2[-f(j+1) + 4f(j+1/2+1) - f(j+2)], \quad j = -1, 0, p-1; \\ \eta_p(f) &= (5/2)f(p+1) - 2f(p+1/2) + (1/2)f(p) \end{aligned} \quad (6)$$

With this choice of the projector, we can rearrange (5) in order to write the following the quadrature:

$$\begin{aligned} \int_0^{p+1} \mathcal{N}_p(x)f(x) dx &\approx \left[\left(\frac{5}{2}\right) f(0) - 2f(1/2) + \left(\frac{1}{2}\right) f(1) \right] \mathcal{N}_{\tilde{p}}(p-1) + \\ &\quad \left[\left(\frac{1}{2}\right) f(p) - 2f(p+1/2) + \left(\frac{5}{2}\right) f(p+1) \right] \mathcal{N}_{\tilde{p}}(2p+1) + \\ &\quad \sum_{j=-1}^{p-1} \frac{1}{2} [-f(j+1) + 4f(j+1/2+1) - f(j+2)] \mathcal{N}_{\tilde{p}}(p+1+j) \end{aligned} \quad (7)$$

where $\tilde{p} = p + 3$. In the case $p = q = 2$ the quadrature is reported in Table 3.5.

4 Conclusions

In this work we have considered some available choices for the computation of integrals arising in Isogeometric methods when considering the integrals on the support of the B-splines. From this preliminary work we can conclude the following.

Nodes $\{\xi_i\}$	$\{0, 0.5, 1, 1.5, 2, 2.5, 3\}$
Weights $\{\omega_i\}$	$\{-7/80, 5/12, -91/240, 11/10, -91/240, 5/12, -7/80\}$

Table 4: Quadrature rule based on the quasi-interpolant of equation (6) in the case $q = p = 2$.

- The use of quadrature on fixed nodes can give good properties both on the exactness and on the computational requirements. This is also empathized by the connection with the Half point rule, that is the optimal one introduced in the element-wise computations.
- The use of quasi-interpolant projector on B-splines can be very useful in order to get exactness on spline spaces. Moreover, the resulting quadrature rules are simple to compute, due to equation (3). From the point of view of the resulting quadrature rule, more analysis is needed in order to study -ad ex.- the quantity $\sum |\omega_i|$ that is crucial when convergence properties are considered.

REFERENCES

- [1] F. Auricchio, F. Calabrò T.J.R. Hughes, A. Reali, G. Sangalli, A simple algorithm for obtaining nearly optimal quadrature rules for NURBS-based isogeometric analysis. *Computer Methods in Applied Mechanics and Engineering*, **249-252**, 15-27, 2012.
- [2] F. Calabrò, C. Manni, F. Pitolli, Computation of quadrature rules for integration with respect to refinable functions on fixed nodes. Submitted 2012.
- [3] C.de Boor, *A practical guide to splines, Revised edition*. Springer-Verlag, New-York 2001.
- [4] C. Garoni, C. Manni, F. Pelosi, S. Serra-Capizzano, H. Speleers, On the spectrum of stiffness matrices arising from isogeometric analysis. Submitted 2012.
- [5] W. Gautschi, L. Gori, F. Pitolli, Gauss quadrature for refinable weight functions. *Appl. Comput. Harmon. Anal.* **8** no. 3, 249-257, 2000.
- [6] T.J.R. Hughes, A. Reali, G. Sangalli, Efficient Quadrature for NURBS-based isogeometric analysis. *Computer Methods in Applied Mechanics and Engineering*, **199(58)**, 301–313, 2010.
- [7] B.G. Lee, T. Lyche, K. Morken, Some examples of quasi-interpolants constructed from local spline projectors. In: *Lyche, T., Schumaker, L.L. (Eds.), Mathematical Methods for Curves and Surfaces. Oslo, 2000*. Vanderbilt University Press, pp. 243-252, 2001.
- [8] J. Ma, V. Rokhlin, S. Wandzura, Generalized Gaussian quadrature rules for systems of arbitrary functions. *SIAM J. Numer. Anal.*, **33(3)**, 971-996, 1996.
- [9] G. Mantica, A stable Stieltjes technique for computing orthogonal polynomials and Jacobi matrices associated with a class of singular measures. *Constr. Approx.* **12** n.4, 509-530, 1996.
- [10] A. Mantzaflaris, B. Juttler, Exploring Matrix Generation Strategies in Isogeometric Analysis. Submitted 2013

- [11] P. Sablonniere, Univariate spline quasi-interpolants and applications to numerical analysis. *Rendiconti del Seminario Matematico di Torino* **63** (3) 211-222, 2005.

AN UNLOCKED IMPLICIT G^1 CONTINUITY MULTI PATCH B-SPLINE INTERPOLATION FOR THE ANALYSIS OF 3D KIRCHHOFF-LOVE ROD ELEMENTS

L. Greco¹, M. Cuomo¹, N. Impollonia¹

¹Dipartimento di Ingegneria Civile ed Ambientale (DICA)
Viale A. Doria 6, 95100 Catania, Italy
e-mail: mcuomo@dica.unict.it, leopoldo.greco@virgilio.it

Keywords: Isogeometric analysis, Kirchhoff-Love rod, G^1 multi patch analysis, geometric continuity, locking, assumed strain formulation

Abstract. *We present a multi patch assumed strain formulation (with implicit G^1 -continuity at the ends of the element) for 3D space Kirchhoff-Love rod; rotations are introduced at the ends of the element as degree of freedom similarly to the Hermitian interpolation for Euler Bernoulli beam problem. In this way the G^1 continuity is ensured. Due to the general curved geometry a strong coupling appears in the membrane-flexural-torsion (m-f-t) problem, so that a pure displacement formulation leads in general to a locked element (membrane, flexural and torsion locking phenomena can occur). The multi patch approach presented, based on G^1 continuity (low degree of continuity), does not present locking in contrast to the B-Spline (high degree of continuity) element, in a pure displacement approach. However, both the approaches present spurious mode in the deformations, i.e. in the stress resultants. In order to avoid this pathology we adopt a standard assumed strain formulation (or B-bar) approach, projecting the tangent strain measures onto lower degree spaces, (by means of standard L^2 projections). In particular, considering a polynomial degree interpolation (p) for the displacements, the membrane and torsional strain measures are projected on a $(p-1)$ space, while the two flexural strain measures are projected on a $(p-2)$ space. In this way a very easy definition of the B-bar operators is attained, since the integrations are performed numerically. The strategy is very appealing for the design of free-locking general curve rod elements, and it provides very accurate results for different polynomial degrees as it is shown by means of presented example.*

1 INTRODUCTION

Displacement based formulations for structural model are known to suffer for locking phenomenon. In the case of general space curved K.L. rods a strong coupling appears in the membrane-flexural-torsion (m-f-t) problem, so that many source of locking affect the solution. In recent works [6, 7] Armero et al. have developed a new C^1 finite element for 3D Kirchhoff-Love rod adopting an assumed strain formulation, based on mixed (Hermitian and Lagrangian) interpolation, for overcoming the spurious strain modes. In [9] Elguedj et al., on the basis of [8], present a comparison between discrete strain gap (DSG) approach, as proposed in [5] by means of a collocation of the strain gaps, and the classical B-bar formulation for overcoming the locking in isogeometric analysis. They show that for both membrane and shear locking, the ASM approach is more accurate with respect to DSG. Locking in flexural an torsional dominated problems for curve elements is investigated in [10]. In [4] Beirao et al. present a collocation isogeometric approach to avoid the shear locking in beam. In this paper a multi-patch isogeometric formulation for K.L. rods is investigated, with respect to its ability to avoid locking.

In [3] a multi-patch isogeometric analysis of space rod by means of Lagrange's multipliers was presented. Multi-patch approaches with implicit G^1 continuity have been introduced in [2], in which it's proposed an element that consists in a generalization of standard cubic Hermite interpolation. It has been obtained performing a transformation on the displacement coordinate space, as illustrated in figure 1 for open Bspline generated by means of a knot vector with and without internal knots. The torsional angle ϕ is interpolated by means of a standard C^0 Bspline functions. In order to avoid locking an L^2 projection of the strains is considered, particularly, considering a p -degree interpolation for the degree of freedom (\mathbf{u}, ϕ) the function spaces for the axial, flexural and torsional strain measures are scaled, respectively, to $p-1$, $p-2$ and $p-1$ degree interpolations. In general, an isogeometric L^2 B-bar approach generates a full stiffness matrix, since the assumed strain interpolating bases are not-null everywhere. Contrarily to the high-continuity isogeometric B-bar formulation presented in [9], the multi patch G^1 continuous formulation presented in this paper allows to strongly reduces the band-width in the stiffness matrix.

2 THE INTERPOLATION

The multi patch isogeometric interpolation of non polar rods used in this paper has been introduced in [2]. It consists in a generalization of the Hermite interpolation to general open Bspline interpolations. The displacement degree of freedom of the the second and second last control points are re-parametrized introducing the end rotations as degree of freedom. Since the torsion angle ϕ is C^0 continuous, a G^1 constraints is ensured. The stiffness matrix is, then, easily assembled.

2.1 The G^1 interpolation of the centroid curve

At the ends of an open B-spline the tangent vector has the same direction defined by the two couple of end points. Let $\mathbf{P}_0(\lambda)$, with $\lambda \in [0, 1]$, be the Lagrangian centroid curve. We adopt for the representation of this curve an open B-Spline description given by

$$\mathbf{P}_0(\lambda) = \sum_{i=1}^n b_i^p(\lambda) \mathbf{P}_{0,i} \quad (1)$$

where p is the degree and $n = p + 1$ is the number of control points, $b_i^p(\lambda)$ is the i -th function and $\mathbf{P}_{0,i}$ is the generic control point. Let $\mathbf{p}(\lambda)$, with $\lambda \in [0, 1]$, be the generic current centroid

curve,

$$\mathbf{p}(\lambda) = \sum_{i=1}^n b_i^p(\lambda) \mathbf{P}_i \quad (2)$$

A coordinate transformation is performed mapping the second, \mathbf{P}_2 , and the second-last, \mathbf{P}_{n-1} , control points by means of the spatial rotations and the deformation of the end control segments directors $\tilde{\mathbf{t}}_{0,1}$ and $\tilde{\mathbf{t}}_{0,2}$ as follows

$$\mathbf{P}_2 = \mathbf{P}_1 + \rho_1 \tilde{\mathbf{R}}_1 \tilde{\mathbf{t}}_{0,1}, \quad \mathbf{P}_{n-1} = \mathbf{P}_n + \rho_2 \tilde{\mathbf{R}}_2 \tilde{\mathbf{t}}_{0,2}, \quad (3)$$

where the initial non unit directors are defined by the difference of the control points

$$\tilde{\mathbf{t}}_{0,1} = \mathbf{P}_{0,2} - \mathbf{P}_{0,1}, \quad \tilde{\mathbf{t}}_{0,2} = \mathbf{P}_{0,n-1} - \mathbf{P}_{0,n}, \quad (4)$$

in this way, from equation 3 the current non unit directors become

$$\tilde{\mathbf{t}}_1 = \mathbf{P}_2 - \mathbf{P}_1 = \rho_1 \tilde{\mathbf{R}}_1 \tilde{\mathbf{t}}_{0,1}, \quad \tilde{\mathbf{t}}_2 = \mathbf{P}_{n-1} - \mathbf{P}_n = \rho_2 \tilde{\mathbf{R}}_2 \tilde{\mathbf{t}}_{0,2}, \quad (5)$$

where $\tilde{\mathbf{R}}_1$ and $\tilde{\mathbf{R}}_2$ are the spatial rotations operators, and the scalars ρ_1 and ρ_2 are the relative change in the lengths of these vectors, given by

$$\rho_1 = \frac{\|\mathbf{P}_2 - \mathbf{P}_1\|}{\|\mathbf{P}_{0,2} - \mathbf{P}_{0,1}\|} = \frac{\|\tilde{\mathbf{t}}_1\|}{\|\tilde{\mathbf{t}}_{0,1}\|}, \quad \rho_2 = \frac{\|\mathbf{P}_{n-1} - \mathbf{P}_n\|}{\|\mathbf{P}_{0,n-1} - \mathbf{P}_{0,n}\|} = \frac{\|\tilde{\mathbf{t}}_2\|}{\|\tilde{\mathbf{t}}_{0,2}\|}. \quad (6)$$

The generic configuration of the centroid curve is given by

$$\begin{aligned} \mathbf{p}(\lambda) = & b_1^p(\lambda) \mathbf{P}_1 + \\ & + b_2^p(\lambda) \left(\mathbf{P}_1 + \rho_1 \tilde{\mathbf{R}}_1 \tilde{\mathbf{t}}_{0,1} \right) + \\ & + b_3^p(\lambda) \mathbf{P}_3 + \dots + b_{n-2}^p(\lambda) \mathbf{P}_{n-2} + \\ & + b_{n-1}^p(\lambda) \left(\mathbf{P}_n + \rho_2 \tilde{\mathbf{R}}_2 \tilde{\mathbf{t}}_{0,2} \right) + \\ & + b_n^p(\lambda) \mathbf{P}_n. \end{aligned} \quad (7)$$

Observing that $\tilde{\mathbf{R}}_1^T \tilde{\mathbf{t}}_1 = \tilde{\mathbf{t}}_{0,1}$ and $\tilde{\mathbf{R}}_2^T \tilde{\mathbf{t}}_2 = \tilde{\mathbf{t}}_{0,2}$ and that $\dot{\tilde{\mathbf{R}}}_1 \tilde{\mathbf{R}}_1^T = \tilde{\omega}_1 \times (\bullet)$ and $\dot{\tilde{\mathbf{R}}}_2 \tilde{\mathbf{R}}_2^T = \tilde{\omega}_2 \times (\bullet)$ the velocity of the centroid curve mapped as in equation 7 is given by

$$\begin{aligned} \dot{\mathbf{p}}(\lambda) = & (b_1^p(\lambda) + b_2^p(\lambda)) \dot{\mathbf{P}}_1 + \\ & + b_2^p(\lambda) \left(-\rho_1 \tilde{\mathbf{t}}_1 \times \tilde{\omega}_1 + \dot{\rho}_1 \tilde{\mathbf{t}}_1 \right) \\ & + b_3^p(\lambda) \dot{\mathbf{P}}_3 + \dots + b_{n-2}^p(\lambda) \dot{\mathbf{P}}_{n-2} + \\ & + b_{n-1}^p(\lambda) \left(-\rho_2 \tilde{\mathbf{t}}_2 \times \tilde{\omega}_2 + \dot{\rho}_2 \tilde{\mathbf{t}}_2 \right) \\ & + (b_n^p(\lambda) + b_{n-1}^p(\lambda)) \dot{\mathbf{P}}_n. \end{aligned} \quad (8)$$

2.2 The C^0 interpolation of the torsional angle

The tangent increment of the torsional angle is given by

$$\dot{\phi}(\lambda) = \sum_{i=1}^n b_i^p(\lambda) \dot{\phi}_i \quad (9)$$

but the first and the last term must be represented in terms of the end rotations, observing that $\hat{\mathbf{t}}|_0 = \hat{\mathbf{t}}_1$ and $\hat{\mathbf{t}}|_1 = -\hat{\mathbf{t}}_2$ and that $\dot{\phi} = \tilde{\boldsymbol{\omega}} \cdot \hat{\mathbf{t}}$ the interpolation of the velocity of rotation around the centroid curve, is

$$\begin{aligned} \dot{\phi}(\lambda) = & b_1^p(\lambda) \tilde{\boldsymbol{\omega}}_1 \cdot \hat{\mathbf{t}}_1 + \\ & + b_1^p(\lambda) \dot{\phi}_2 \dots + b_{n-1}^p(\lambda) \dot{\phi}_{n-1} \\ & + b_n^p(\lambda) \tilde{\boldsymbol{\omega}}_2 \cdot (-\hat{\mathbf{t}}_2). \end{aligned} \quad (10)$$

Considering, for each control point, the vector of the increments of the degrees of the freedom $\dot{\mathbf{q}}$ defined as

$$\dot{\mathbf{q}}^T = \{\dot{\mathbf{P}}_1, \tilde{\boldsymbol{\omega}}_1, \dot{\rho}_1, \dot{\phi}_2; \dot{\mathbf{P}}_3, \dot{\phi}_3, \dots, \dot{\mathbf{P}}_{n-2}, \dot{\phi}_{n-2}; \dot{\phi}_{n-1}, \dot{\rho}_2, \dot{\mathbf{P}}_n, \tilde{\boldsymbol{\omega}}_2\} \quad (11)$$

the velocity of the centroid curve, $\dot{\mathbf{p}}$, and of the torsional angle, $\dot{\phi}$, are given respectively by

$$\dot{\mathbf{p}}(\lambda)^{3,1} = \mathbb{B}_c^p(\lambda)^{3,4n} \dot{\mathbf{q}}^{4n,1} \quad (12)$$

and

$$\dot{\phi}(\lambda) = \mathbb{B}_\phi^p(\lambda)^{1,4n} \dot{\mathbf{q}}^{4n,1}, \quad (13)$$

where the operators $\mathbb{B}_c^p(\lambda)$ and $\mathbb{B}_\phi^p(\lambda)$ are defined as

$$\begin{aligned} \mathbb{B}_c^p(\lambda) = & \{(b_1^p + b_2^p) \mathbf{I}^{3,3}, -b_2^p (\tilde{\mathbf{t}}_1 \times (\bullet))^{3,3}, b_2^p (\tilde{\mathbf{t}}_1)^{3,1}, \mathbf{0}^{3,1}, \\ & b_3^p \mathbf{I}^{3,3}, \mathbf{0}^{3,1}, \dots, b_{n-2}^p \mathbf{I}^{3,3}, \mathbf{0}^{3,1}, \\ & \mathbf{0}^{3,1}, b_{n-1}^p (\tilde{\mathbf{t}}_2)^{3,1}, (b_{n-1}^p + b_n^p) \mathbf{I}^{3,3}, -b_{n-1}^p (\tilde{\mathbf{t}}_2 \times (\bullet))^{3,3}\}, \end{aligned} \quad (14)$$

and

$$\begin{aligned} \mathbb{B}_\phi^p(\lambda) = & \{(\mathbf{0}^T)^{1,3}, b_1^p (\tilde{\mathbf{t}}_1^T)^{1,3}, 0, b_2^p, \\ & (\mathbf{0}^T)^{1,3}, b_3^p, \dots, (\mathbf{0}^T)^{1,3}, b_{n-2}^p, \\ & b_{n-1}^p, 0, (\mathbf{0}^T)^{1,3}, b_n^p (\tilde{\mathbf{t}}_2^T)^{1,3}\}. \end{aligned} \quad (15)$$

where \mathbf{I} is the identity operator, $\mathbf{0}^T = \{0, 0, 0\}$ and

$$-\tilde{\mathbf{t}}_j \times (\bullet) = \begin{pmatrix} 0 & +\tilde{\mathbf{t}}_j \cdot \mathbf{E}_z & -\tilde{\mathbf{t}}_j \cdot \mathbf{E}_y \\ -\tilde{\mathbf{t}}_j \cdot \mathbf{E}_z & 0 & +\tilde{\mathbf{t}}_j \cdot \mathbf{E}_x \\ +\tilde{\mathbf{t}}_j \cdot \mathbf{E}_y & -\tilde{\mathbf{t}}_j \cdot \mathbf{E}_x & 0 \end{pmatrix}, \quad \tilde{\mathbf{t}}_j = \begin{pmatrix} \tilde{\mathbf{t}}_j \cdot \mathbf{E}_x \\ \tilde{\mathbf{t}}_j \cdot \mathbf{E}_y \\ \tilde{\mathbf{t}}_j \cdot \mathbf{E}_z \end{pmatrix}, \quad j = 1, 2. \quad (16)$$

Figures 1(a) and 1(b) are related to Bernstein's polynomials of degree 3 and it is clear that the transformation proposed yields to the Hermite shape functions. Figures 1(c) and 1(d) are related to Bernstein's polynomials of degree 4 and corresponding transformed G^1 -functions; Figures 1(e) and 1(f) are related to a B-Spline of degree 3 with internal knots and corresponding transformed G^1 -B-Spline.

2.3 Strain measures

The velocity of the deformations have been evaluated [1, 2] and are represented by means of the compatibility operators, $\mathbf{B}_{(\bullet)}$, as follows:

$$\begin{aligned} \varepsilon(\mathbf{q}_0, \dot{\mathbf{q}}) = & \mathbf{B}_\varepsilon^T(\mathbf{q}_0) \dot{\mathbf{q}}, & \chi_n(\mathbf{q}_0, \dot{\mathbf{q}}) = & \mathbf{B}_{\chi_n}^T(\mathbf{q}_0) \dot{\mathbf{q}} \\ \chi_\nu(\mathbf{q}_0, \dot{\mathbf{q}}) = & \mathbf{B}_{\chi_\nu}^T(\mathbf{q}_0) \dot{\mathbf{q}}, & \gamma(\mathbf{q}_0, \dot{\mathbf{q}}) = & \mathbf{B}_\gamma^T(\mathbf{q}_0) \dot{\mathbf{q}}. \end{aligned} \quad (17)$$

3 THE ASSUMED STRAIN FORMULATION

The assumed strain method (ASM), proposed in [6, 8, 9] consists in a L^2 -projection of the strain measures, by means of the weak definition of the compatibility equation. Let b_i^p be the generic i -th function of degree p , that interpolates the displacement field $\mathbf{q} = (\mathbf{u}, \phi)$. The axial, bending and twisting deformations are projected onto the spaces, respectively, b_ε^{p-1} , b_χ^{p-2} and b_γ^{p-1} , with lower polynomial and continuity degrees. A B-bar formulation for G^1 multi-patch interpolations with *BSpline* without internal knots is presented next. We remark that, the displacements functional space adopted is G^1 continuous as defined in the previous section, while the strain measures are projected onto standard open BSpline space with lower polynomial degree and lower parametric continuity.

3.1 The B-bar operators

For the Kirchhoff-Love rod the strain measures consistent with a (weak) compatibility conditions are given by modified $\bar{\mathbf{B}}$ -operators

$$\bar{\varepsilon}(\dot{\mathbf{d}}) = \bar{\mathbf{B}}_\varepsilon^T \dot{\mathbf{d}}, \quad \bar{\chi}_n(\dot{\mathbf{d}}) = \bar{\mathbf{B}}_{\chi_n}^T \dot{\mathbf{d}}, \quad \bar{\chi}_\nu(\dot{\mathbf{d}}) = \bar{\mathbf{B}}_{\chi_\nu}^T \dot{\mathbf{d}}, \quad \bar{\gamma}(\dot{\mathbf{d}}) = \bar{\mathbf{B}}_\gamma^T \dot{\mathbf{d}}, \quad (18)$$

where these modified $\bar{\mathbf{B}}$ -operators are given by

$$\bar{\mathbf{B}}_\varepsilon^T = (\mathbf{b}^{p-1})^T \bar{\mathbf{G}}^{-1} \int_L (\mathbf{b}^{p-1} \mathbf{B}_\varepsilon^T) dL, \quad \bar{\mathbf{B}}_\gamma^T = (\mathbf{b}^{p-1})^T \bar{\mathbf{G}}^{-1} \int_L (\mathbf{b}^{p-1} \mathbf{B}_\gamma^T) dL, \quad (19)$$

and

$$\bar{\mathbf{B}}_{\chi_n}^T = (\mathbf{b}^{p-2})^T \bar{\bar{\mathbf{G}}}^{-1} \int_L (\mathbf{b}^{p-2} \mathbf{B}_{\chi_n}^T) dL, \quad \bar{\mathbf{B}}_{\chi_\nu}^T = (\mathbf{b}^{p-2})^T \bar{\bar{\mathbf{G}}}^{-1} \int_L (\mathbf{b}^{p-2} \mathbf{B}_{\chi_\nu}^T) dL, \quad (20)$$

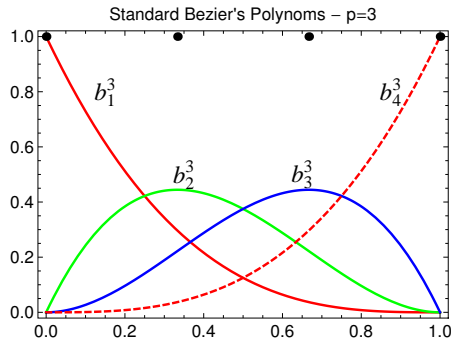
in which the $\bar{\mathbf{G}}$ and $\bar{\bar{\mathbf{G}}}$ are the corresponding *mass* matrices

$$\bar{\mathbf{G}} = \int_L (\mathbf{b}^{p-1} \otimes \mathbf{b}^{p-1}) dL, \quad \bar{\bar{\mathbf{G}}} = \int_L (\mathbf{b}^{p-2} \otimes \mathbf{b}^{p-2}) dL. \quad (21)$$

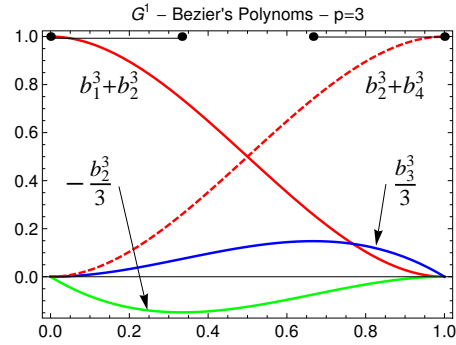
The stiffness operator is defined analogously to a pure displacement formulation. Numeric integration is performed at level of the element considering $p + 1$ Gauss-Lobatto points.

4 NUMERICAL EXAMPLES

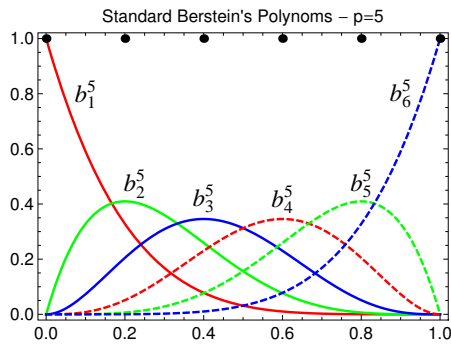
In this section three simple cases of curved rods are considered in which the case of membrane, flexural and both locking pathologies. The material parameters are $E = 2 * 10^8 [kN/m^2]$, $\nu = 0.25$. The radius of the centroid is $R = 1 [m]$ and the force at the end has intensity $\|f\| = 1 [kN]$. In the first two numerical example $\hat{\mathbf{n}}(S) = \hat{\mathbf{e}}_z = \{0, 0, 1\}$ and $\hat{\mathbf{v}}(S) = \hat{\mathbf{t}} \times \hat{\mathbf{n}}(S)$ are considered while in the last example an initial torsion angle $\phi(S) = \frac{\pi S}{2}$ it is considered.



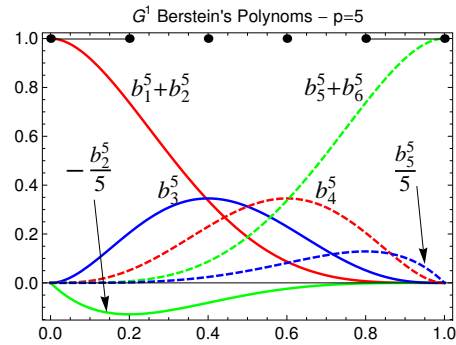
(a) C^0 Bernstein interpolation functions (polynomial degree p=3).



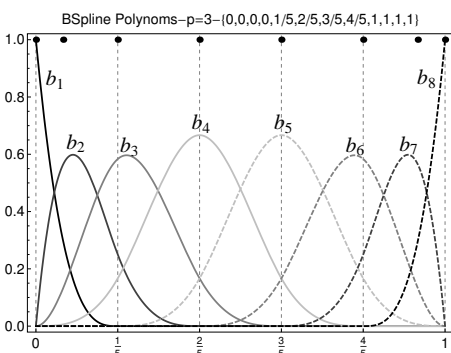
(b) G^1 Bernstein interpolation functions (Hermitian f. p=3).



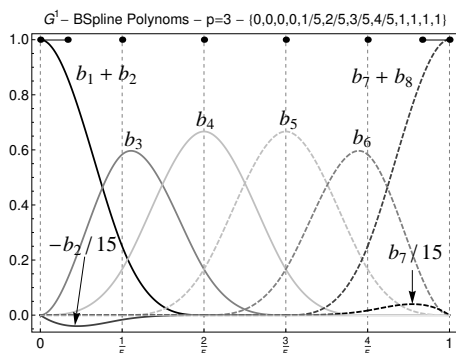
(c) C^0 Bernstein interpolation functions (polynomial degree p=5).



(d) G^1 Bernstein interpolation functions (polynomial degree p=5).



(e) Standard C^0 open BSpline interpolation (polynomial degree p=3).



(f) G^1 open BSpline interpolation (polynomial degree p=3).

Figure 1: Transformation of shape function from standard C^0 open BSpline to G^1 open BSpline shape functions, (with or without internal knots).

4.1 Example 1: 2D Arch with a point force at the end

In this section it is considered a circular 2D arch with a point force at the end, see figure 2(a). Figures 2(b) and 2(c) show the comparison in the error in L^2 norm for the u_y displacement's component, (for two polynomials degrees $p = 3, 4$), between a pure displacement and B-bar approach, in the case of multi patch interpolation. The rate of the convergence is highlighted. Figures 2(d) and 2(e) show the L^2 error with the ratio R/h_v for different discretizations, either

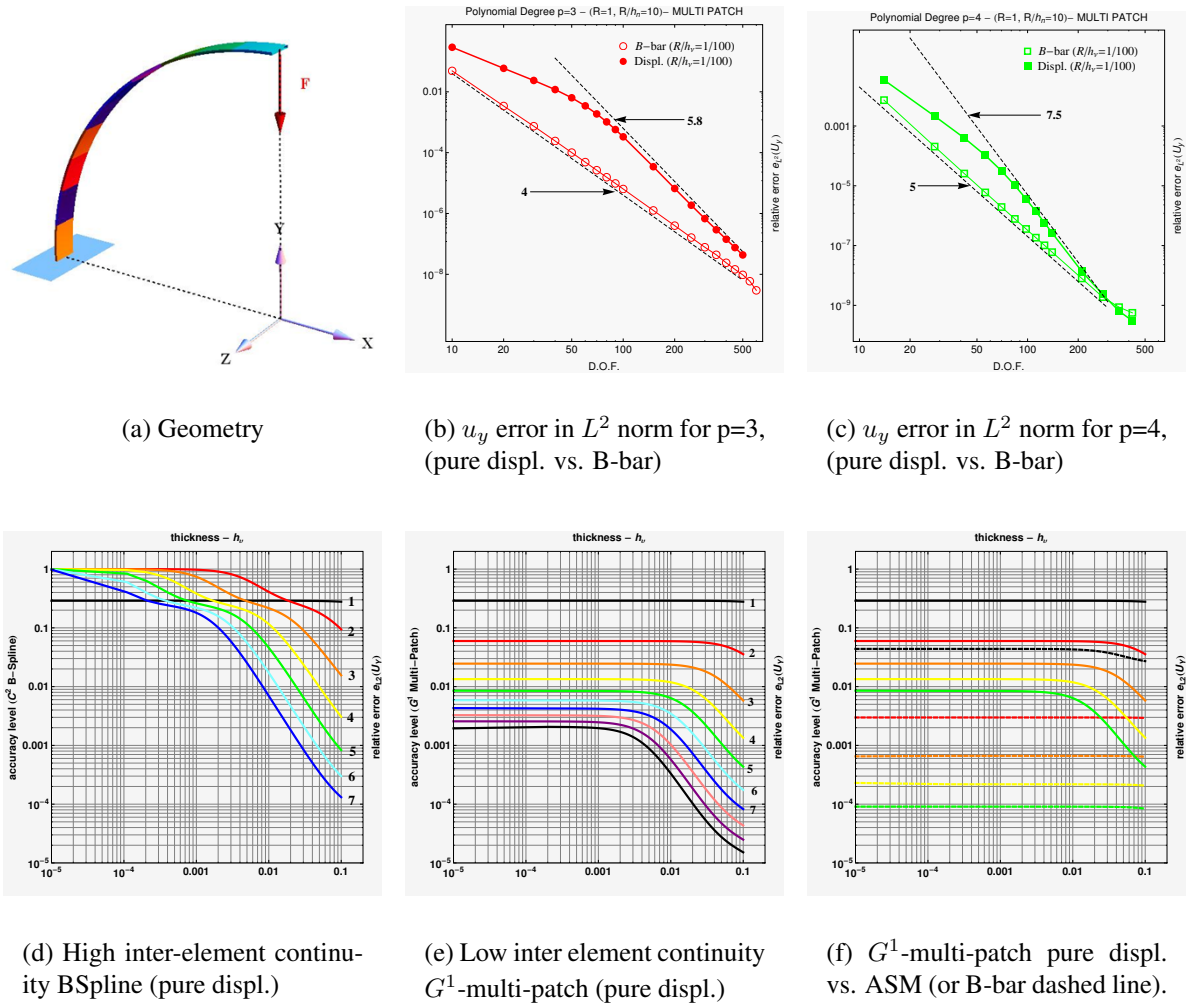


Figure 2: Cantilever 2D arch with a shear at the end, (membrane locking).

for a BSpline and a multi patch approach; drastic membrane locking appears in the case of BSpline interpolation that disappears in the case of the multi patch approach. However spurious modes occurs on the axial stress that is reflected in a reduction of the accuracy in the solution, see Figure 2(e). Therefore a B-bar approach is necessary for an accurate definition of the strains in a multi patch approach. Figure 2(f) show the comparison between the accuracy level obtained with a pure displacement and a \bar{B} formulation in the case of the multi-patch approach.

4.2 Example 2: 3D Arch with a point force at the end

In this section it is considered a circular 3D arch with a point force at the end, see figure 3(a). Figure 3(b) shows the comparison for the convergence's rate of the relative L^2 error norm for

the u_z solution, (for the polynomials degree $p = 3$ and ratio $R/h_\nu = 100$), between the pure displacement and the \bar{B} formulation both the case of the G^1 -multi-patch approach. Figure 4(d)

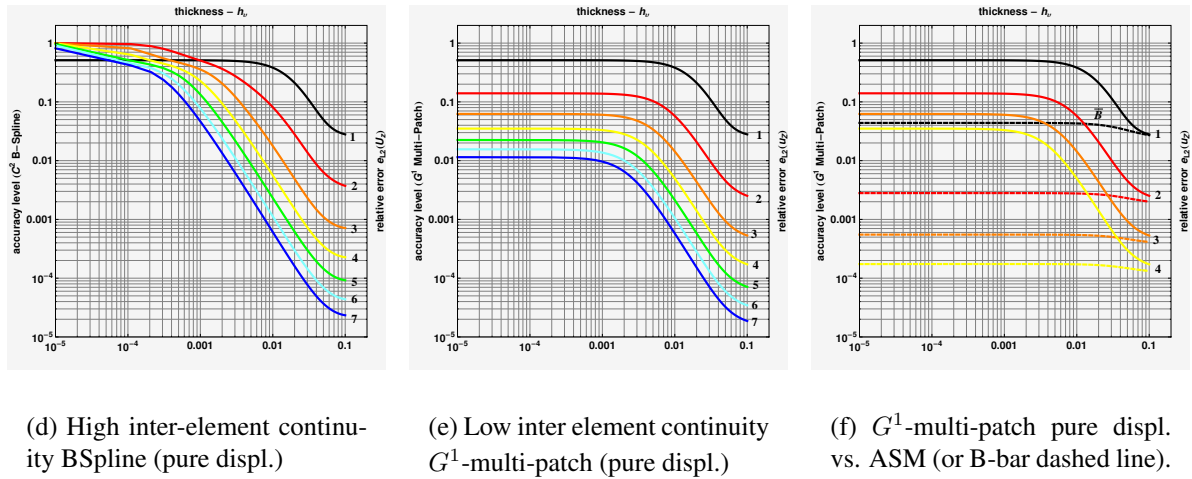
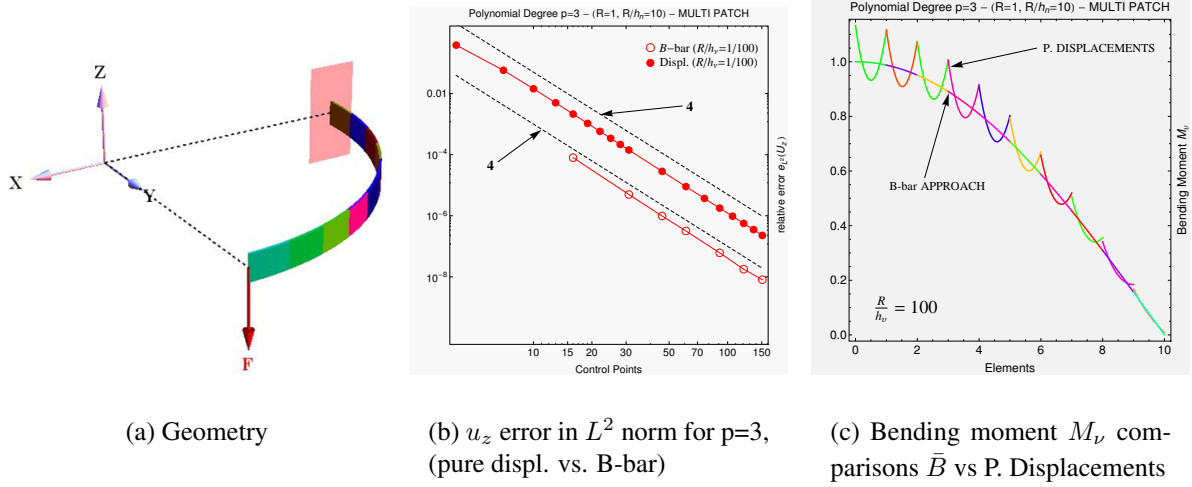


Figure 3: Cantilever 3D arch with a shear at the end, (flexural locking).

and 4(e) show the error in L^2 norm as function of the ratio R/h_ν for different discretizations in the case of BSpline (high inter element continuity) and in the case of the G^1 multi-patch approach (low inter element continuity), for a pure displacement formulation. In the case of the BSpline interpolation flexural locking appears while in the case of the multi patch approach no locking appears. As previously observed oscillations can occur in the bending moment M_ν for a pure displacement approach so that a \bar{B} formulation is necessary. For the multi patch approach only, figure 3(f) shows the comparison in the accuracy level obtained with a pure displacement and a \bar{B} (dashed lines) formulation respectively.

4.3 Example 3: 3D pre-twisted arch with a point force at the end

In this section is considered a pre-twisted circular 3D arch with a shear at the end, see figure 4(a). Figure 4(b) shows the comparison for the convergence rate of the error in L^2 norm of the u_z displacement component, (for polynomial degrees $p = 3, 4$), for the G^1 multi-patch approach using the pure displacement and the \bar{B} formulation. Figure 4(c) shows a real example of a pre-

twisted curve rod, i.e. a *Glulam* pre-twisted curve wood beam. Figure 4(d) and 4(e) show the

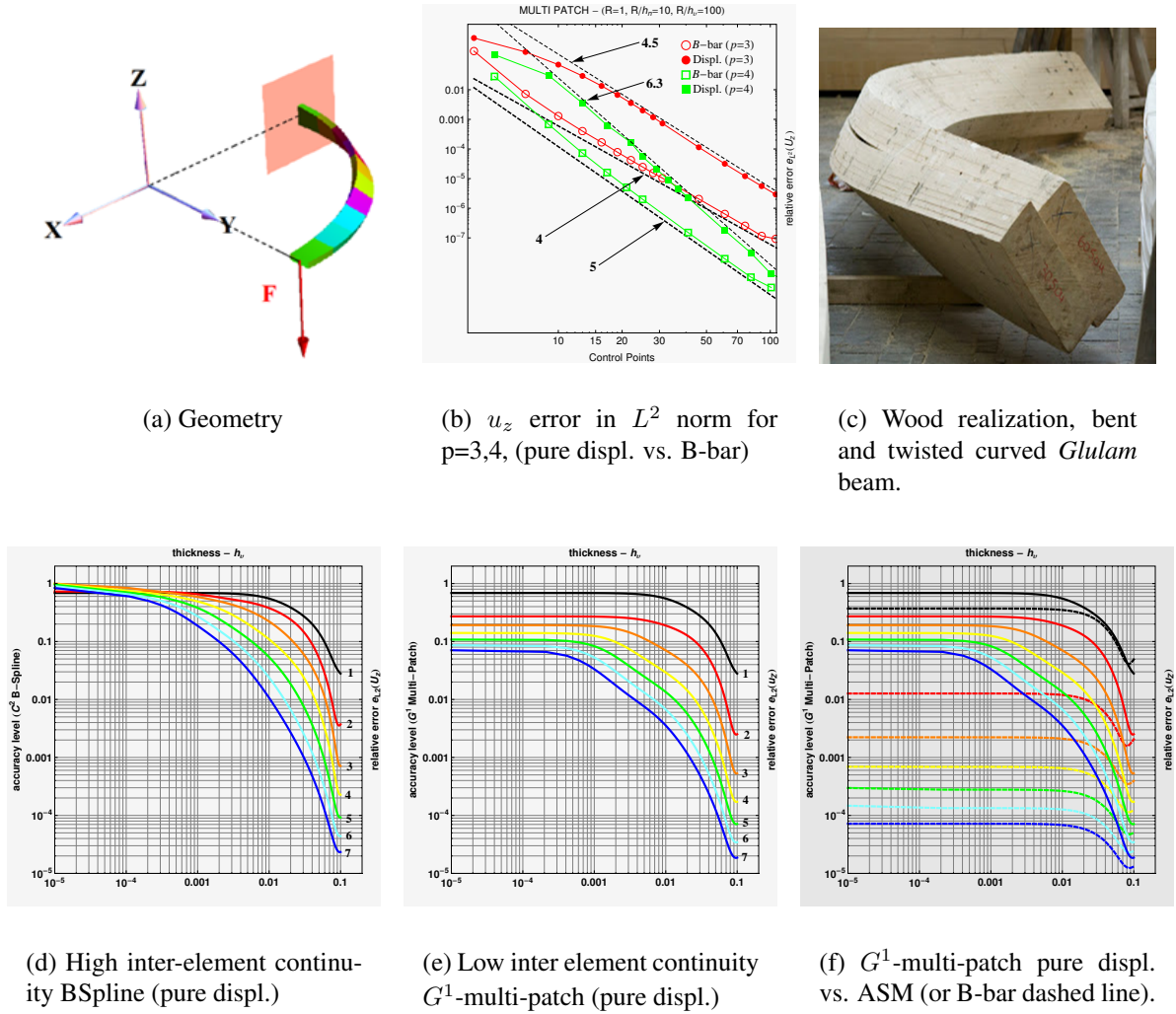


Figure 4: Pre-twisted cantilever 3D arch with a shear at the end, (flexural locking).

trend of the L^2 error norm with respect to the ratio R/h_v for different discretizations, in the case of BSpline (high-continuity) and G^1 multi-patch approaches; As opposite to the displacement formulations, no flexural locking appears in the multi patch approach but significant oscillations can occur in the bending deformations. A \bar{B} approach solve this problem as shown figure 4(f) when a comparison in the accuracy level between pure displacement and \bar{B} (dashed lines) for multi-patch approach are presented.

5 CONCLUSIONS

- The paper has presented a isogeometric generalization of the G^1 -Hermitian interpolation for 3D space Kirchhoff-Love rods.
- The influence of the inter element continuity level on the locking phenomena for 3D Kirchhoff-Love space rods has been show, comparing the case of Bspline and G^1 -multi patch approaches. The multi patch approach strongly reduce locking.

- A G^1 -multi patch assumed strain formulation has been presented, (in which is obtained a banded stiffness matrix contrary to the case of BSpline interpolation); It reduces the oscillations in the stress resultants.

REFERENCES

- [1] L. Greco, M. Cuomo, B-Spline interpolation of Kirchhoff-Love space rods. *Computer Methods in Applied Mechanics and Engineering*, <http://dx.doi.org/10.1016/j.cma.2012.11.017>, available online 5 December 2012.
- [2] L. Greco, M. Cuomo, An implicit G^1 continuity B-Spline interpolation for the analysis of 3D-Space assembly of Kirchhoff-Love rods. *submitted to CMAME, 2013*,
- [3] L. Greco, Multi-patch isogeometric analysis of space rods. *YIC2012*, 24-27 April, Aveiro, Portugal.
- [4] L. Beirao, C. Lovadina, A. Reali Avoiding shear locking for the Timoshenko beam problem via isogeometric collocation methods. *Computer Methods in Applied Mechanics and Engineering*, **241-244**, 38–51, 2012.
- [5] R. Echter, M. Bischoff Numerical efficiency, locking and unlocking of NURBS finite elements. *Computer Methods in Applied Mechanics and Engineering*, **199**, 374–382, 2010.
- [6] F. Armero, J. Valverde, Invariant Hermitian Finite Elements for Thin Kirchhoff Love Rods. I: The linear Plane Case. *Computer Methods in Applied Mechanics and Engineering*, **213-216**, 458–485, 2012.
- [7] F. Armero, J. Valverde, Invariant Hermitian Finite Elements for Thin Kirchhoff Love Rods. II: The Linear Three-Dimensional Case. *Computer Methods in Applied Mechanics and Engineering*, **213-216**, 427–457, 2012.
- [8] T. Elguedj, Y. Bazilevs, V.M. Calo, T.J.R. Hughes, B-bar and F-bar Projection Methods for Nearly Incompressible Linear and Nonlinear Elasticity and Plasticity using Higher-order NURBS Elements. *Computer Methods in Applied Mechanics and Engineering*, **197**, 5257–5296, 2007.
- [9] R. Bouclier, T. Elguedj, A. Comberscure, Locking free isogeometric formulation of curved thick beams. *Computer Methods in Applied Mechanics and Engineering*, **245-246**, 144–162, 2012.
- [10] Md. Ishaquddin, P. Raveendranath, J.N. Reddy, Flexure and torsion locking phenomena in out-of-plane deformation of Timoshenko curved beam element. *Finite Elements in Analysis and Design*, **51**, 22–30, 2012.

COMPUTATION OF THE ISOGEOMETRIC ANALYSIS STIFFNESS MATRIX ON GPU

Alexander Karatarakis¹, Panagiotis Karakitsios² and Manolis Papadrakakis²

¹ Institute of Structural Analysis and Antiseismic Research National Technical University of Athens
Zografou Campus, Athens 15780
e-mail: alex@karatarakis.com

² Institute of Structural Analysis and Antiseismic Research National Technical University of Athens
Zografou Campus, Athens 15780
pkarak@hotmail.com, mpapadra@central.ntua.gr

Keywords: Isogeometric analysis, Gauss quadrature, NURBS, Stiffness matrix assembly, Parallel computing, GPU acceleration

Abstract. *Due to high regularity across mesh elements of isogeometric analysis, this new method achieves higher accuracy per degree of freedom and improved spectrum properties, among others, compared to finite element analysis. However, this inherent feature of isogeometric analysis reduces the sparsity pattern of stiffness matrix and requires more elaborate numerical integration schemes for its computation. For these reasons, the assembly of the stiffness matrix in isogeometric analysis is a computationally demanding task, which needs special attention in order to be affordable in real-world implementations. In this paper we address the computational efficiency of assembling the stiffness matrix using the standard element-wise Gaussian quadrature. A novel approach is proposed for the formulation of the stiffness matrix which exhibits several computational merits, among them its amenability to parallelization and the efficient utilization of the graphic possessing units to drastically accelerate computations.*

1 INTRODUCTION

Isogeometric analysis (IGA) was recently introduced by Hughes et al. [1] and since then it has attracted a lot of attention for solving boundary value problems as a result of using the same basis functions adopted from CAD community for describing the domain geometry and for building the numerical approximation of the solution.

Despite IGA's promising methodology and superior features [1]–[4] compared with finite element analysis (FEA) the computation of mass, stiffness and advection matrices is more laborious, which increase the cost of IGA in real-world applications. For a certain number of degrees of freedom, IGA, due to its higher inter-element continuity, produces quite more elements than FEA. This leads to an increase of the number of Gauss points and consequently of the computational cost for assembling the characteristic matrices. This drawback increases dramatically the computational cost in the multivariate domains, especially for 3D cases.

It was shown [2], [3] that standard element-wise Gauss rules are inefficient, because they do not take precise account of the preserved smoothness at the element boundaries in the case of higher-order NURBS and polynomial B-SPLines, and that the higher the inter-element regularity is the fewer the required number of Gauss points per element. However, recently proposed integration rules, although they are optimal or nearly optimal in terms of the number of function evaluations, they are either cumbersome to implement [2] or need special consideration to be given to the boundary elements [3]. In an effort to deal with the overhead in the computation of IGA characteristic matrices, collocation methods have been introduced for obtaining higher order accurate methods with a minimum number of quadrature points [5].

Applications of graphics processing units (GPUs) to scientific computations are attracting a lot of attention due to their low cost in conjunction with their inherently remarkable performance features. Driven by the demands of the gaming industry, graphics hardware has substantially evolved over the years with remarkable floating point arithmetic performance. Unlike CPUs, GPUs have an inherent parallel throughput architecture that focuses on executing many concurrent threads slowly, rather than executing a single thread very fast.

A number of studies in engineering applications have been recently reported on a variety of GPU platforms using implicit computational algorithms [6]–[16]. Linear algebra applications have also been a topic of scientific interest for GPU implementations [17]–[20]. A hybrid CPU-GPU implementation of domain decomposition methods is presented in [21] where speedups of the order of 40x have been achieved with just one GPU.

The present work achieves a drastic reduction of the computational effort required for assembling the stiffness matrix of IGA by implementing a novel control point pair-wise procedure recently proposed for the computation of the stiffness matrix in element-free Galerkin formulations [22]. This approach is amenable to parallel computations since it does not have race conditions or need synchronization and it is particularly suitable for massively parallel systems with GPUs. The numerical results indicate that the proposed methodology succeeds in overcoming the drawback of the quadrature cost associated with IGA by performing the assembly of the stiffness matrix in orders of magnitude less computation time than that of the standard element-wise Gauss quadrature scheme.

2 BASIC INGREDIENTS OF THE ISOGOMETRIC ANALYSIS METHOD

2.1 Non-Uniform Rational B-SPLines (NURBS)

In IGA there is no approximate mesh since, even in the case of very coarse meshes, the exact geometry is always represented. For the implementation of IGA three spaces should be defined: the physical space, the parameter space and the index space. For NURBS shape functions, the parameter space is very important as all calculations refer there, while the index space plays an auxiliary role. The input data is drawn from the physical space, which contains the Cartesian coordinates of the control points and their corresponding weights. The number of basis functions is equal to the number of degrees of freedom. The unknowns of the resulting algebraic equations correspond to the displacements of the control points, while the knots are the boundaries of the corresponding isogeometric elements. In the case of uniform knot vector, knot spans have the same size in the parameter space while in the physical space they can have any size depending on the corresponding control points and shape functions. The discretized NURBS-model is subdivided into patches which are subdomains with the same material and geometry type and consist of a full tensor product grid of elements. In this respect, they are analogous to elements in FEA as the basis functions are interpolatory at its boundaries.

A knot vector is a non-decreasing set of coordinates in the parameter space, written as $\Xi = \{\xi_1, \xi_2, \dots, \xi_{n+p+1}\}$, where $\xi_i \in \mathbb{R}$ is the i^{th} knot, i is the knot index, $i=1,2,\dots,n+p+1$, p is the polynomial order and n is the number of basis functions used to construct the B-Spline curve. The knots partition the parameter space into elements. Element boundaries in the physical space are simply the images of knot lines under the B-Spline mapping. Figure 1 illustrates the quadratic C^1 continuous B-Spline basis functions, which are produced by the open uniform knot vector $\Xi = \{0,0,0,1,2,3,4,5,6,7,8,9,9,9\}$. Control points are shown as circles, while knots as rectangles. The interval $[0,9]$ is a single patch and consists of 9 elements and 11 control points, which correspond to 11 B-Spline basis functions.

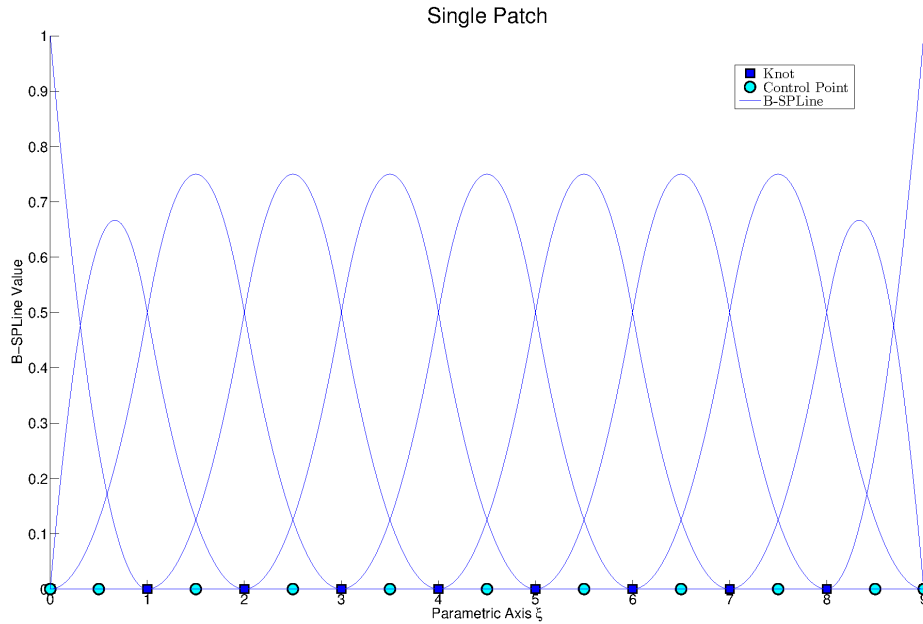


Fig. 1. C^1 continuous quadratic basis derived from open uniform knot vector
 $\Xi = \{0, 0, 0, 1, 2, 3, 4, 5, 6, 7, 8, 9, 9, 9\}$

Given an open uniform knot vector $\Xi = \{\xi_1, \xi_2, \dots, \xi_{n+p+1}\}$, the B-SPLine basis functions $N_i^p(\xi)$ are defined by the Cox-de Boor recursion formula:

$$N_i^0(\xi) = \begin{cases} 1, & \text{if } \xi_i \leq \xi < \xi_{i+1} \\ 0, & \text{otherwise} \end{cases} \quad (1)$$

$$N_i^p(\xi) = \frac{\xi - \xi_i}{\xi_{i+p} - \xi_i} N_i^{p-1}(\xi) + \frac{\xi_{i+p+1} - \xi}{\xi_{i+p+1} - \xi_{i+1}} N_{i+1}^{p-1}(\xi) \quad (2)$$

Due to their higher regularity between inter-element boundaries, they exhibit greater overlapping in comparison with the shape functions of FEA. Their basic feature is their tensor product nature. In the case of polynomial B-SPLines, basis functions are used as shape functions, while in the case of NUBRS, shape functions are produced from the following formula in 1D case:

$$R_i^p(\xi) = \frac{N_i^p W_i}{\sum_{i=1}^n \{N_i^p(\xi) W_i\}} \quad (3)$$

in the 2D case:

$$R_{i,j}^{p,q}(\xi, \eta) = \frac{N_i^p(\xi) M_j^q(\eta) W_{i,j}}{\sum_{i=1}^n \sum_{j=1}^m N_i^p(\xi) M_j^q(\eta) W_{i,j}} \quad (4)$$

in the 3D case:

$$R_{i,j,k}^{p,q,r}(\xi, \eta, \zeta) = \frac{N_i^p(\xi) M_j^q(\eta) L_k^r(\zeta) W_{i,j,k}}{\sum_{i=1}^n \sum_{j=1}^m \sum_{k=1}^l N_i^p(\xi) M_j^q(\eta) L_k^r(\zeta) W_{i,j,k}} \quad (5)$$

where W_i are weight factors with a full tensor product nature:

$$W_{i,j} = W_i W_j \quad (6)$$

$$W_{i,j,k} = W_i W_j W_k \quad (7)$$

The approximation of 1D displacement field in terms of control point variables can be written as

$$u(\xi) = \sum_{i=1}^n \left[R_i^p(\xi) u_{CPi} \right] \quad (8)$$

where $R_i^p(\xi)$ are the shape functions, n is the number of basis functions or control points, p is the polynomial order and u_{CPi} is the displacement of control point i . The exact geometry is described by

$$X(\xi) = \sum_{i=1}^n \left[R_i^p(\xi) X_{CPi} \right] \quad (9)$$

where X_{CPi} are the Cartesian coordinate of the control point i .

There is a connection between polynomial basis order p , knot multiplicity m and continuity/regularity k , given by

$$k = p - m, \quad 1 \leq m \leq p + 1 \quad (10)$$

Regularity -1 means discontinuity and it appears for the extreme knots of a single patch. In this case, basis functions are interpolatory at these extreme knots. Regularity 0 resembles to the case of finite elements and is the minimum continuity for interior knots with basis functions interpolatory at that knots. The case of maximum continuity is $p-1$ and occurs when every interior knot is repeated only once.

Assuming an one-dimensional case, polynomial order p , multiplicity m and number of elements n^{el} , the corresponding number of control points n , which are directly linked to the number of degrees of freedom, is equal to

$$n = (p+1)n^{el} - (k-1)(n^{el}-1) \quad (11)$$

The corresponding knot vector has $n+p+1$ knot values. The external knots are repeated $p+1$ times and the interior m times.

2.2 Stiffness matrix formulation

A given domain is represented with several NURBS-based isogeometric models, depending on its geometry features. Every NURBS-based models decomposed into subdomains, the so-called patches, according to the variance of its geometry and material. The more abrupt the geometry is, the more subdomains are considered. They can be assumed as macro-elements consisting of a tensor product mesh of elements and they are assembled in the same way as in finite elements. The arrays for the patches are constructed and assembled in element-by-element fashion by numerically integrating contributions over each element. In the parameter space, elements are rectangular.

The equilibrium equations applied to control points of the whole domain are expressed as

$$\mathbf{K} \mathbf{u} = \mathbf{f} \quad (12)$$

In order to formulate the total stiffness matrix, the stiffness matrix of every patch $i=1, \dots, N_p$ has to be calculated:

$$\mathbf{K}^i = \int_V (\mathbf{B}^i)^T \mathbf{E}^i \mathbf{B}^i dV = \iiint_{\xi, \eta, \zeta} (\mathbf{B}^i)^T \mathbf{E}^i \mathbf{B}^i \det \mathbf{J}^i d\xi d\eta d\zeta \quad (13)$$

where \mathbf{E}^i , \mathbf{B}^i are the elasticity and deformation matrix of the patch i respectively.

We will present below the stiffness matrix formulation in 2D elasticity cases. For the 3D case, the formulation is analogous. Assuming n , m control points per parametric axis ξ , η respectively, the 2D control points are $N=nm$ (full tensor product) and the deformation matrix \mathbf{B} is given by:

$$\mathbf{B} = \mathbf{B}_1 \mathbf{B}_2 \quad (14)$$

$(3 \times N) \quad (3 \times 4)(4 \times N)$

with

$$\mathbf{B}_1 = \frac{1}{\det \mathbf{J}(\xi)} \begin{bmatrix} J_{22} & -J_{12} & 0 & 0 \\ 0 & 0 & -J_{21} & J_{11} \\ -J_{21} & J_{11} & J_{22} & -J_{12} \end{bmatrix} \quad (15)$$

and

$$\mathbf{B}_2 = \begin{bmatrix} R_{1,\xi} & 0 & R_{2,\xi} & 0 & \dots & R_{N,\xi} & 0 \\ R_{1,\eta} & 0 & R_{2,\eta} & 0 & \dots & R_{N,\eta} & 0 \\ 0 & R_{1,\xi} & 0 & R_{2,\xi} & 0 & \dots & R_{N,\xi} \\ 0 & R_{1,\eta} & 0 & R_{2,\eta} & 0 & \dots & R_{N,\eta} \end{bmatrix} \quad (16)$$

$(4 \times N)$

The Jacobian matrix is local to patches rather than to elements and is given by

$$\mathbf{J}(\xi, \eta) = \underbrace{\begin{bmatrix} R_{1,\xi}(\xi, \eta) & R_{2,\xi}(\xi, \eta) & \dots & R_{N,\xi}(\xi, \eta) \\ R_{1,\eta}(\xi, \eta) & R_{2,\eta}(\xi, \eta) & \dots & R_{N,\eta}(\xi, \eta) \end{bmatrix}}_{(2 \times N)} \underbrace{\begin{bmatrix} X_{CP1} & Y_{CP1} \\ X_{CP2} & Y_{CP2} \\ \vdots & \vdots \\ X_{CPN} & Y_{CPN} \end{bmatrix}}_{(N \times 2)} = \underbrace{\begin{bmatrix} J_{11} & J_{12} \\ J_{21} & J_{22} \end{bmatrix}}_{(2 \times 2)} \quad (17)$$

where $R_l(\xi, \eta)$ is the shape function that corresponds to the control point l , with Cartesian coordinates X_{CPl} , Y_{CPl} , and

$$R_{l,\xi}(\xi, \eta) = \frac{dR_l(\xi, \eta)}{d\xi}, \quad R_{l,\eta}(\xi, \eta) = \frac{dR_l(\xi, \eta)}{d\eta} \quad (18)$$

The derivatives in eq. (18) are obtained by applying the quotient rule to eq. (4).

2.3 Quadrature rule

The Gauss quadrature rule is applied to the non-zero knot spans as in FEA. However, the standard element-wise Gauss rule requires extensive function evaluations due to increased support of the shape functions. According to [3], for the case of an one-dimensional function of order p the optimal (minimum exact) number of Gauss points per element is equal to $(p+1)/2$ or $(p+2)/2$, for odd and even p respectively. For the computation of the stiffness matrix in 1D elasticity case, the integrand's order is equal to $q=2p-2$ and the optimal number of Gauss points per element is equal to $(q+2)/2=p$. For 2D and 3D elasticity cases, the integrand's order is equal to $q=2p$ and the optimal number of Gauss

points per element is equal to $(q+2)/2 = p+1$. The above rules are optimal for the case of minimum continuity. For higher continuity, new macro-element rules have been proposed [2], [3], which are more efficient, but also more involved and difficult to implement.

3 ELEMENT-WISE FORMULATION OF THE STIFFNESS MATRIX

In order to build the stiffness matrix of a domain (or patch), the contributions of all Gauss points need to be added. The contributions are expressed by the products $\mathbf{B}_G^T \mathbf{E} \mathbf{B}_G$

$$\mathbf{K} = \sum_G \mathbf{B}_G^T \mathbf{E} \mathbf{B}_G = \sum_G \mathbf{Q}_G \tag{19}$$

where the deformation matrix \mathbf{B}_G is computed at the corresponding Gauss point.

However, instead of adding each Gauss contribution to the global stiffness matrix, the standard procedure is to first build the stiffness matrix of each element by adding the contributions of all Gauss points G of the element to its local stiffness matrix:

$$\mathbf{K}_E = \sum_{E_G} \mathbf{B}_G^T \mathbf{E} \mathbf{B}_G = \sum_{E_G} \mathbf{Q}_G \tag{20}$$

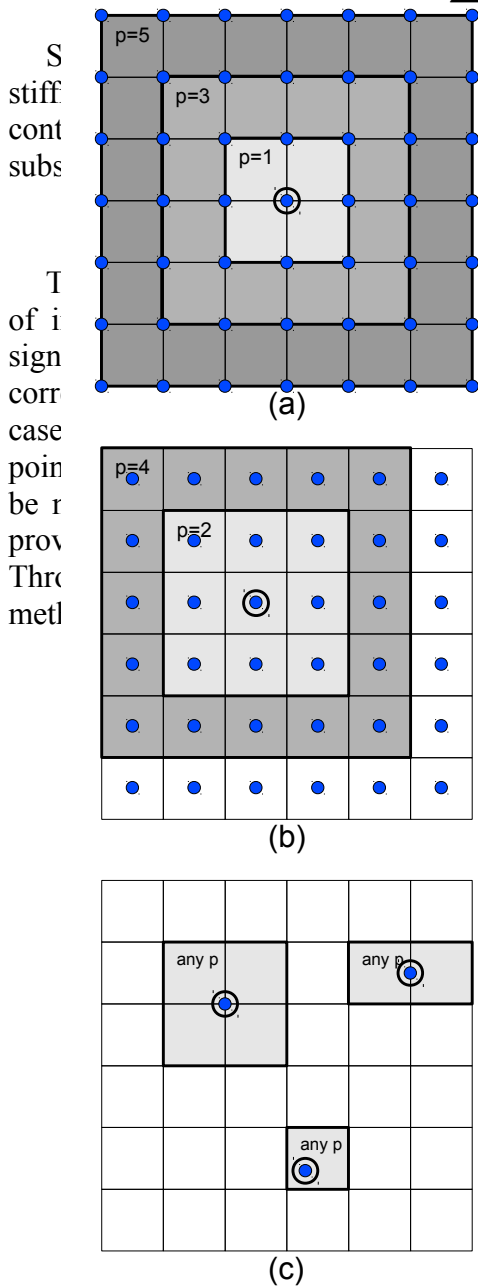


Fig. 2. Areas influencing a control point in (a) IGA (p odd); (b) IGA (p even); (c) FEA. The influencing entities are the Gauss points in the shaded areas.

element modify conditions locally is beneficial for the stiffness matrix. Each Gauss point has a certain amount of influence. In comparison between the two cases shown in Fig. 2, the first case is more "rigid" so the control points or elements

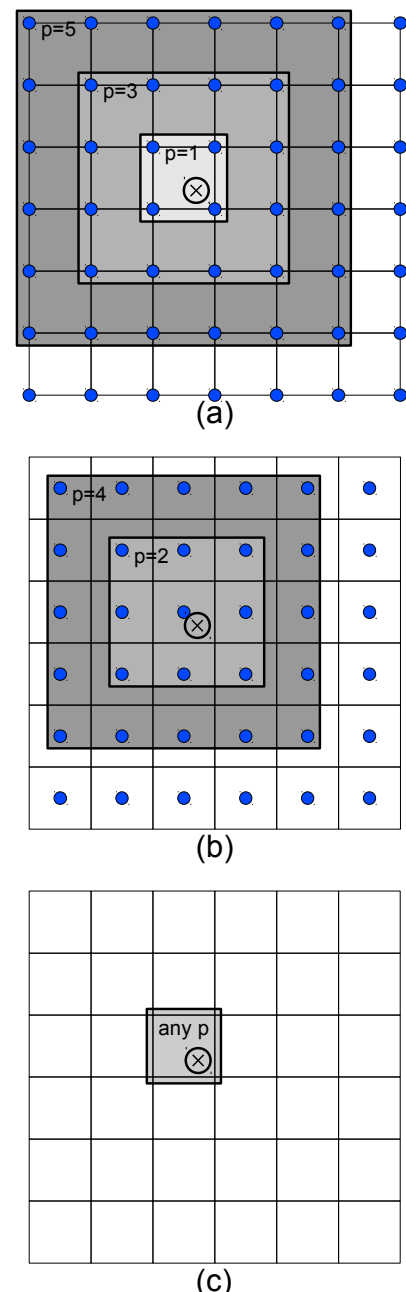


Fig. 3. Control points/nodes influenced by Gauss point in (a) IGA (p odd); (b) IGA (p even); (c) FEA.

In FEA, each Gauss point is involved in computations with nodes within its own element. The shape functions and their derivatives are predefined for each element type and need to be evaluated on all combinations of nodes and Gauss points within the element. In IGA, however, each Gauss point is involved in computations with control points of surrounding areas as well (Fig. 3), while the shape functions are not predefined and span across larger domains with a significantly higher amount of Gauss-control point interactions.

The domain stiffness matrix is large and therefore needs to be stored with appropriate efficient storage methods. Depending on the method used for the solution of the resulting equations and constraints imposed by the hardware (e.g. memory limit), it may be in sparse format, skyline format, multi-diagonal format (since the grid is structured), etc. Throughout this work a sparse matrix format specifically tailored for the assembly phase is used.

For equivalent meshes, the bandwidth is the same between the two methods but IGA has a larger amount of interactions and, consequently, denser stiffness matrices. Furthermore, the computation of each non-zero coefficient is more laborious because the control point pairs have a lot more shared elements (on average) and consequently significantly more Gauss point contributions.

3.1 Performance of the element-wise approach

The examples that will be presented through this work are detailed in Table 1, while the performance of the element-wise (EW) approach in the CPU is shown in Table 2. The proposed EW approach is compared with the “conventional” one without several improvements and code optimizations. The examples are run on a Core i7-980X which has 6 physical cores (12 logical cores) at 3.33GHz and 12MB cache. The examples have no trivial knot spans in order to maximize the number of calculations.

Example	p	n	Control points	dof	Elements	Gauss points	
P2-1	2	225	50,625	101,250	49,729	447,561	
P2-2	2	500	250,000	500,000	248,004	2,232,036	
P2-3	2	633	400,689	801,378	398,161	3,583,449	
2D	P3-1	3	225	50,625	101,250	49,284	788,544
	P3-2	3	320	102,400	204,800	100,489	1,607,824
	P3-3	3	388	150,544	301,088	148,225	2,371,600
2D	P4-1	4	160	25,600	51,200	24,336	608,400
	P4-2	4	225	50,625	101,250	48,841	1,221,025
	P4-3	4	275	75,625	151,250	73,441	1,836,025
3D	P2-1	2	19	6,859	20,577	4,913	132,651
	P2-2	2	26	17,576	52,728	13,824	373,248
	P2-3	2	33	35,937	107,811	29,791	804,357
	P3-1	3	19	6,859	20,577	4,096	262,144
	P3-2	3	21	9,261	27,783	5,832	373,248
	P3-3	3	26	17,576	52,728	12,167	778,688
	P4-1	4	15	3,375	10,125	1,331	166,375
	P4-2	4	17	4,913	14,739	2,197	274,625
	P4-3	4	19	6,859	20,577	3,375	421,875

Table 1. Example details of 2D square ($n \times n$) and 3D cubic ($n \times n \times n$) domains.

As shown in Table 2, by optimizing the element-wise method, we were able to achieve about 3X and 5X speedup in 2D and 3D cases, respectively.

Example	dof	CPU Time (seconds)		Speedup Ratio	
		Conventional element wise	Proposed element wise		
2D	P2-1	101,250	14	5	2.7
	P2-2	500,000	60	20	2.9
	P2-3	801,378	96	32	3.0
	P3-1	101,250	41	14	2.9
	P3-2	204,800	83	27	3.1
	P3-3	301,088	124	39	3.1
	P4-1	51,200	56	19	3.0
	P4-2	101,250	113	36	3.1
	P4-3	151,250	171	57	3.0
3D	P2-1	20,577	37	8	4.8
	P2-2	52,728	98	21	4.8
	P2-3	107,811	212	43	5.0
	P3-1	20,577	305	59	5.2
	P3-2	27,783	430	83	5.2
	P3-3	52,728	900	168	5.3
	P4-1	10,125	635	131	4.9
	P4-2	14,739	1,055	218	4.9
	P4-3	20,577	1,599	333	4.8

Table 2. Computing time for the formulation of the stiffness matrix in the CPU implementations of the element-wise approach.

4 CONTROL POINT PAIR-WISE FORMULATION OF THE STIFFNESS MATRIX

An alternative way to perform the computation of the global stiffness matrix is the proposed control point pair-wise approach. The computation of the global stiffness coefficient \mathbf{K}_{ij} is performed for all interacting $i-j$ control points and is formed from contributions by the shared Gauss points of their domains of influence. Two control points are interacting if there is at least one Gauss point that influences both control points. In IGA, it is more convenient to define two control points as being interacting if there is at least one element shared by both control points, but care must be taken in cases where there are trivial knot spans which have no Gauss points.

4.1 Interacting control point pairs and their shared elements

The interacting control point pairs approach initially identifies a) the interacting control point pairs and b) the shared elements of the interacting control point pairs. The interacting control points associated with a specific control point are those located within a fixed range dictated by the order p of each axis.

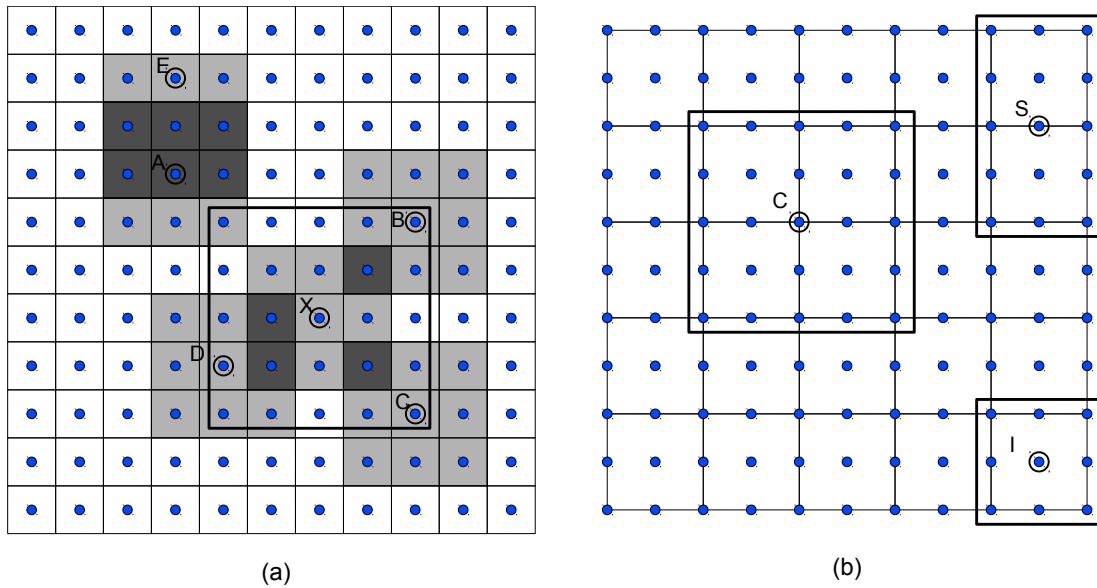


Fig. 4. Interacting control points/nodes for $p = 2$: (a) IGA; (b) FEA.

In FEA the nodes interact through neighboring elements only and thus the interacting node pairs can be easily defined from the element-node connectivity (Fig. 4b). In IGA, however, a control point pair contributes non-zero entries to the stiffness matrix, and therefore is active, if there is at least one (non-empty) element shared between the two control points (Fig. 4a). Thus, control point X interacts with B,C,D, but not with A or E. If the basis order is p , then the interacting control points extend up to p elements in all directions. This can be observed for $p=2$ in Fig. 4a. The gray shaded regions are the influence domains of each control point. The thick-lined rectangles in Fig. 4 include all control points/nodes that are interacting with the corresponding control point/node.

4.2 Computation of global stiffness coefficients for each interacting control point pair

The computation of the stiffness elements for each interacting control point pair is split in two phases. In the first phase, the shape function derivatives for each influenced control point of every Gauss point are calculated as in the element-wise method. In the second phase, instead of continuing with the calculation of the stiffness matrix coefficients corresponding to a particular element, the stiffness matrix coefficients of each interacting control point pair is computed. Both phases are amenable to parallelization.

4.3 Performance of the control point pair-wise approach

Table 3 shows the time required for the two phases with the control point pair-wise (CPPW) approach as well as the total computing time for the formulation of the stiffness matrix. Comparing the serial CPU times with the corresponding values of the element-wise (EW) approach (Table 2), it can be observed that the CPPW approach performs better than the EW approach. Furthermore, contrary to the EW approach, the CPPW approach is amenable to parallelization, even in massively parallel processors, as will be subsequently discussed.

Example	dof	CPU Time (seconds)			
		Shape Functions	Assembly	Total	
2D	P2-1	101,250	2	2	4
	P2-2	500,000	10	6	17
	P2-3	801,378	17	10	27
	P3-1	101,250	7	5	12
	P3-2	204,800	13	10	23
	P3-3	301,088	18	16	34
	P4-1	51,200	8	8	16
	P4-2	101,250	15	17	31
	P4-3	151,250	21	26	47
3D	P2-1	20,577	2	4	7
	P2-2	52,728	6	10	17
	P2-3	107,811	12	23	36
	P3-1	20,577	9	33	42
	P3-2	27,783	12	46	58
	P3-3	52,728	24	95	119
	P4-1	10,125	11	73	84
	P4-2	14,739	18	123	141
	P4-3	20,577	27	184	211

Table 3. Computing time for the formulation of the stiffness matrix in the serial CPU implementation of the control point pair-wise (CPPW) approach.

4.4 Parallelization features of the interacting control point pair-wise approach

The CPPW approach has certain advantages compared to the EW approach, the most important one being its amenability to parallelism. In the element-wise approach, each element contributes to different stiffness coefficients and the coefficients are continuously updated with the contributions of each element. The final value of a particular coefficient is formed once all contributions have been considered. Therefore, parallelizing the element-wise approach involves scatter parallelism, which is schematically shown in Fig. 5 for two elements C and D . Each part of the sum can be calculated in parallel but there are conflicting updates to the same coefficients of the stiffness matrix. These race conditions can be avoided with proper synchronization but in massively parallel systems like the GPU where thousands of threads may be working concurrently it is very detrimental to performance because all updates are serialized with atomic operations [23].

In the CPPW approach, the final values for the submatrix of each interacting control point pair are calculated and appended to the matrix, instead of constantly updating the matrix. For the calculation of a submatrix, all contributions of the Gauss points belonging to the intersection of the the domains of influence of two interacting control points should be summed together. Thus, the interacting control point pairs approach utilizes gather parallelism as shown schematically in Fig. 6.

In a parallel implementation, each working unit, i.e. a thread or group of threads, prepares a submatrix \mathbf{K}_{ij} related to a specific interacting control point pair ij . It gathers all contributions from the Gauss points and writes to a specific memory location accessed by no other thread. Thus, this method requires no synchronization or atomic operations.

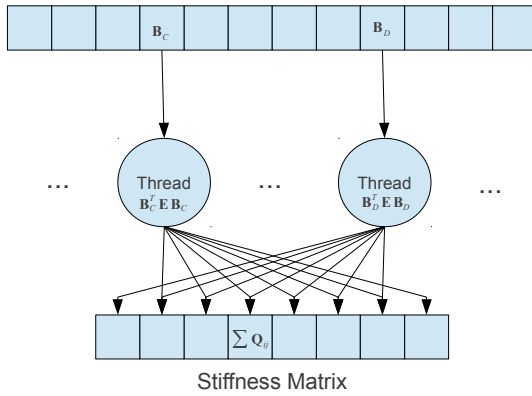


Fig. 5. Scatter parallelism required for the element-wise approach.

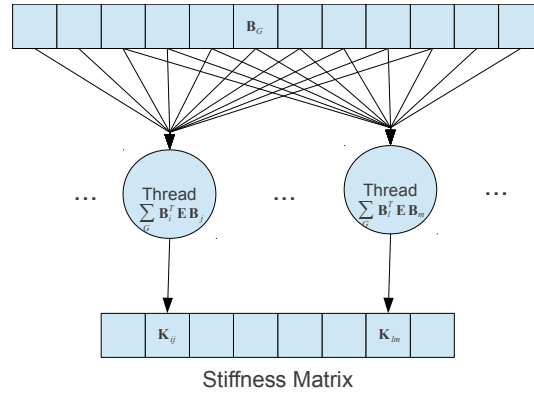


Fig. 6. Gather parallelism implemented in the interacting control point pairs approach.

4.5 Performance of the GPU implementations of the control point pair-wise approach

Table 4 shows the time needed for the GPU implementation. The results utilize one GPU, a GeForce GTX680 with 1536 CUDA cores and 2GB GDDR5 memory.

Example	dof	CPPW GPU Time (seconds)			
		Kernel 1	Kernel 2	Total	
2D	P2-1	101,250	0.05	0.08	0.1
	P2-2	500,000	0.23	0.34	0.6
	P2-3	801,378	0.35	0.53	0.9
	P3-1	101,250	0.13	0.18	0.3
	P3-2	204,800	0.23	0.35	0.6
	P3-3	301,088	0.36	0.51	0.9
	P4-1	51,200	0.21	0.20	0.4
	P4-2	101,250	0.38	0.38	0.8
	P4-3	151,250	0.60	0.54	1.1
3D	P2-1	20,577	0.07	0.10	0.2
	P2-2	52,728	0.18	0.25	0.4
	P2-3	107,811	0.38	0.51	0.9
	P3-1	20,577	0.37	0.56	0.9
	P3-2	27,783	0.51	0.78	1.3
	P3-3	52,728	1.03	1.61	2.6
	P4-1	10,125	0.49	1.07	1.6
	P4-2	14,739	0.80	1.79	2.6
	P4-3	20,577	1.19	2.68	3.9

Table 4. Computing time for the formulation of the stiffness matrix in the coalesced GPU implementation of the interacting control point-pair approach with a GTX 680.

5 NUMERICAL RESULTS FOR 2D AND 3D ELASTICITY PROBLEMS

Throughout this work, the two approaches for the computation of the stiffness matrix are tested in 2D and 3D elasticity problems. The geometric domains and parameters of these problems maximize the number of correlations and consequently the computational cost for the given number of control points. The examples are run on the following hardware. CPU: Core i7-980X which has 6 physical cores (12 logical cores) at 3.33 GHz and 12MB cache. GPU: GeForce GTX680 with 1536 CUDA cores and 2GB GDDR5 memory.

The performance of the serial element-wise (EW) and control point pair-wise (CPPW) approaches in the CPU is given in Table 5. These implementations have been explored in Sections 3.1 and 4.3 for the two approaches, respectively.

Example	dof	CPU Time (seconds)			
		Conventional EW	Proposed EW	Proposed CPPW	
2D	P2-1	101,250	14	5	4
	P2-2	500,000	60	20	17
	P2-3	801,378	96	32	27
	P3-1	101,250	41	14	12
	P3-2	204,800	83	27	23
	P3-3	301,088	124	39	34
	P4-1	51,200	56	19	16
	P4-2	101,250	113	36	31
	P4-3	151,250	171	57	47
3D	P2-1	20,577	37	8	7
	P2-2	52,728	98	21	17
	P2-3	107,811	212	43	36
	P3-1	20,577	305	59	42
	P3-2	27,783	430	83	58
	P3-3	52,728	900	168	119
	P4-1	10,125	635	131	84
	P4-2	14,739	1,055	218	141
	P4-3	20,577	1,599	333	211

Table 5. Computing time for the formulation of the stiffness matrix in the serial CPU implementations of the element-wise (EW) and node pair-wise (CPPW) approaches

The performance of the GPU implementations of the control point pair-wise method is shown in Table 4. Speedup ratios of the GPU implementation compared to the CPU implementations is given in Table 6.

Example	dof	Speedup ratios of GPU implementation			
		Conventional EW	Proposed EW	Proposed CPPW	
2D	P2-1	101,250	107	39	33
	P2-2	500,000	106	36	30
	P2-3	801,378	109	36	30
	P3-1	101,250	134	46	39
	P3-2	204,800	143	46	40
	P3-3	301,088	143	46	39
	P4-1	51,200	141	47	40
	P4-2	101,250	150	49	42
	P4-3	151,250	151	50	42
3D	P2-1	20,577	222	46	41
	P2-2	52,728	234	49	40
	P2-3	107,811	241	49	41
	P3-1	20,577	329	63	45
	P3-2	27,783	334	64	45
	P3-3	52,728	340	64	45
	P4-1	10,125	407	84	54
	P4-2	14,739	409	84	54
	P4-3	20,577	413	86	54

Table 6. Relative speedup ratios of GPU (GTX 680) implementation compared to the CPU (Core i7-980X) implementations.

6 CONCLUDING REMARKS

The proposed control point pair-wise approach has several benefits over the element-wise approach. The most important one is its amenability to parallelism especially in massively parallel systems like the GPUs. Each control point pair can be processed separately by any available processor in order to compute the corresponding stiffness submatrix. The control point pair approach can be characterized as “embarrassingly parallel” since it requires no synchronization whatsoever between node pairs.

A GPU implementation is applied to the control point pair-wise approach offering significant speedups compared to CPU implementations. The granularity of the control point pair-wise approach offers ample parallelism and results in high hardware utilization which is evidenced by speedup ratios achieved with just one GPU in the test examples presented. The control point pair-wise approach can be applied as is to any available hardware achieving even lower computing times. This includes using many GPUs, hybrid CPU(s)/GPU(s) implementations and generally any available processing unit. The importance of this portability becomes apparent when considering contemporary and future developments like heterogeneous systems architecture (HSA).

In conclusion, the parametric tests performed in the framework of this study showed that with the proposed implementation along with the exploitation of currently available low cost hardware, the expensive formulation of the stiffness matrix in IGA methods can be reduced by orders of magnitude. The presented control point pair-approach enables the efficient utilization of any available hardware and can accomplish high speedup ratios, which convincingly addresses a shortcoming of isogeometric analysis, making it computationally competitive in solving large-scale problems in computational mechanics.

7 ACKNOWLEDGMENTS

This work has been supported by the European Research Council Advanced Grant “MASTER – Mastering the computational challenges in numerical modeling and optimum design of CNT reinforced composites” (ERC-2011-ADG_20110209). The first author has also been supported by the John Argyris Foundation and the second author by the Alexander S. Onassis Foundation.

8 REFERENCES

- [1] T. J. R. Hughes, J. A. Cottrell, and Y. Bazilevs, “Isogeometric analysis: CAD, finite elements, NURBS, exact geometry and mesh refinement,” *Computer Methods in Applied Mechanics and Engineering*, vol. 194, no. 39–41, pp. 4135–4195, 2005.
- [2] F. Auricchio, F. Calabrò, T. J. R. Hughes, A. Reali, and G. Sangalli, “A simple algorithm for obtaining nearly optimal quadrature rules for NURBS-based isogeometric analysis,” *Computer Methods in Applied Mechanics and Engineering*, vol. 249–252, pp. 15–27, 2012.
- [3] T. J. R. Hughes, A. Reali, and G. Sangalli, “Efficient quadrature for NURBS-based isogeometric analysis,” *Computer Methods in Applied Mechanics and Engineering*, vol. 199, no. 5–8, pp. 301–313, 2010.
- [4] J. A. Cottrell, T. J. R. Hughes, and Y. Bazilevs, *Isogeometric Analysis: Toward Integration of CAD and FEA*, 1st ed. Wiley, 2009.
- [5] F. Auricchio, L. Beirão da Veiga, T. J. R. Hughes, A. Reali, and G. Sangalli, “Isogeometric collocation for elastostatics and explicit dynamics,” *Computer Methods in Applied Mechanics and Engineering*, vol. 249–252, pp. 2–14, 2012.
- [6] I. C. Karpolis, X. S. Trompoukis, V. G. Asouti, and K. C. Giannakoglou, “CFD-based analysis and two-level aerodynamic optimization on graphics processing units,” *Computer Methods in Applied Mechanics and Engineering*, vol. 199, no. 9–12, pp. 712–722, 2010.
- [7] E. Elsen, P. LeGresley, and E. Darve, “Large calculation of the flow over a hypersonic vehicle using a GPU,” *Journal of Computational Physics*, vol. 227, no. 24, pp. 10148–10161, 2008.
- [8] J. C. Thibault and I. Senocak, “Accelerating incompressible flow computations with a Pthreads-CUDA implementation on small-footprint multi-GPU platforms,” 2010.
- [9] M. de la Asunción, J. M. Mantas, and M. J. Castro, “Simulation of one-layer shallow water systems on multicore and CUDA architectures,” 2010.
- [10] H. Zhou, G. Mo, F. Wu, J. Zhao, M. Rui, and K. Cen, “GPU implementation of lattice Boltzmann method for flows with curved boundaries,” *Computer Methods in Applied Mechanics and Engineering*, vol. 225–228, pp. 65–73, 2012.
- [11] A. Sunarso, T. Tsuji, and S. Chono, “GPU-accelerated molecular dynamics simulation for study of liquid crystalline flows,” *Journal of Computational Physics*, vol. 229, no. 15, pp. 5486–5497, 2010.
- [12] J. A. Anderson, C. D. Lorenz, and A. Travesset, “General purpose molecular dynamics simulations fully implemented on graphics processing units,” *Journal of Computational Physics*, vol. 227, no. 10, pp. 5342–5359, 2008.
- [13] E. Wadbro and M. Berggren, “Megapixel topology optimization on a graphics processing unit,” *SIAM Review*, vol. 51, no. 4, pp. 707–721, 2009.
- [14] D. Komatitsch, G. Erlebacher, D. Göddeke, and D. Michéa, “High-order finite-element seismic wave propagation modeling with MPI on a large GPU cluster,” *Journal of*

- Computational Physics*, vol. 229, no. 20, pp. 7692–7714, 2010.
- [15] T. Takahashi and T. Hamada, “GPU-accelerated boundary element method for Helmholtz’ equation in three dimensions,” *International Journal for Numerical Methods in Engineering*, vol. 80, no. 10, pp. 1295–1321, 2009.
- [16] G. R. Joldes, A. Wittek, and K. Miller, “Real-time nonlinear finite element computations on GPU - Application to neurosurgical simulation,” *Computer Methods in Applied Mechanics and Engineering*, vol. 199, no. 49–52, pp. 3305–3314, 2010.
- [17] S. Tomov, J. Dongarra, and M. Baboulin, “Towards dense linear algebra for hybrid GPU accelerated manycore systems,” *Parallel Computing*, vol. 36, no. 5–6, pp. 232–240, 2010.
- [18] O. Schenk, M. Christen, and H. Burkhart, “Algorithmic performance studies on graphics processing units,” *Journal of Parallel and Distributed Computing*, vol. 68, no. 10, pp. 1360–1369, 2008.
- [19] J. M. Elble, N. V. Sahinidis, and P. Vouzis, “GPU computing with Kaczmarz’s and other iterative algorithms for linear systems,” *Parallel Computing*, vol. 36, no. 5–6, pp. 215–231, 2010.
- [20] A. Cevahir, A. Nukada, and S. Matsuoka, “High performance conjugate gradient solver on multi-GPU clusters using hypergraph partitioning,” *Computer Science - Research and Development*, vol. 25, no. 1–2, pp. 83–91, 2010.
- [21] M. Papadrakakis, G. Stavroulakis, and A. Karatarakis, “A new era in scientific computing: Domain decomposition methods in hybrid CPU-GPU architectures,” *Computer Methods in Applied Mechanics and Engineering*, vol. 200, no. 13–16, pp. 1490–1508, 2011.
- [22] A. Karatarakis, P. Metsis, and M. Papadrakakis, “GPU-Acceleration of stiffness matrix calculation and efficient initialization of EFG meshless methods,” *Computer Methods in Applied Mechanics and Engineering*, vol. 258, pp. 63–80, 2013.
- [23] W. W. Hwu and D. B. Kirk, “Parallelism Scalability,” in *Programming and Tuning Massively Parallel Systems (PUMPS)*, Barcelona, 2011.

Study of Asymmetric Glass Reinforced Plastic Beams in Off-Axis Four-Point Bending

Efstathios E. Theotokoglou¹ and Emilio P. Sideridis¹

¹ School of Applied Mathematical and Physical Sciences,
Department of Mechanics Laboratory of Testing and Materials,
The National Technical University of Athens, Zographou Campus,
Theocaris Bld., GR-0157 73, Athens, Greece
stathis@central.ntua.gr

Keywords: Asymmetric Glass Reinforced Plastic Beams, Off-Axis Four Point Bending, Computational Analysis, Stress Analysis, Composite Materials, Interlaminar Shear Strength.

Abstract. *The present paper deals with the computational study of asymmetric glass reinforced plastic beams in off-axis four point bending and the comparison of the induced results with experimental and analytical results. The measurement of the interlaminar shear strength of composite beams, an important design variable in many applications, may be successfully performed by the asymmetric bending test. A three dimensional finite element analysis is adopted throughout the composite beams in order to, on the one hand, correlate with the experimental results and, on the other hand to obtain the stress distributions at the supports and at the loading points where usually there is an abrupt variation due to the indentation existing because of the noses. From the Finite Element Analysis and the experimental investigation possible crack initiation positions are determined.*

1 INTRODUCTION

The glass reinforced plastic (GRP), pipes and components are widely used in the process plant and chemical industries in applications requiring corrosion resistance. Also the need to reduce vehicle weight and consideration for mass production techniques, among other things, has led the automotive industry to consider randomly-oriented chopped-fibre reinforced plastics as near-term substitutes for steel in structural panels.

In order to perform stress and stiffness analyses of chopped-fibre/resin composites, it is essential that the properties be known since in general these materials appear as anisotropic and heterogeneous. But if the fibres are randomly distributed with respect to orientation and position then samples of material which contain statistically significant numbers of fibres will appear to be isotropic. If several such samples are compared, the composite will appear to be homogeneous. If the fibres have a preferred orientation, then the composite will appear to be anisotropic.

Since, the composite panel properties depend on the elastic properties and volume fractions of the constituent materials and are affected by the fabrication techniques and most of them are stiffness or strength designed it is useful to investigate this subject.

An important property which affects the application of glass-reinforced plastics (GRP) is the interlaminar shear strength, which characterizes the interface between fibre and matrix [1]. As a result of low interlaminar shear strength, failure of the composite often occurs in the interlaminar region. Possible interlaminar shear failures have been observed due to high transverse shear forces arising as a result of large changes in bending moment along or around a beam or a shell under combined loading. Such conditions can occur in a pipe where the thickness changes, are abrupt and excessive, and can be produced with internal pressure [2] (or other types of loading [3]), or in smooth pipe bends under flexure [4, 5]. Consequently the interlaminar shear strength is an important design parameter in many applications. Since there is a need for reliable data, a testing procedure for determining interlaminar shear properties has already been developed [6]. The interlaminar fracture toughness in end notched flexure specimens [7] and the interlaminar shear fracture of interleaved graphite/epoxy composites [8] have been examined. The fracture of sandwich beams in three point bending has also been considered [9, 10].

Material	E_x (GPa)	E_y (GPa)	E_z (GPa)	ν_{xy}	ν_{xz}	ν_{yz}	G_{xy} (GPa)	G_{xz} (GPa)	G_{yz} (GPa)
R.R.L.	4.52	4.52	4.52	0.354	0.354	0.354	1.669	1.669	1.669
C.S.M.	9.14	9.14	5.484	0.328	0.197	0.328	3.44	1.371	1.371

Table 1: Material properties of the constituent materials.

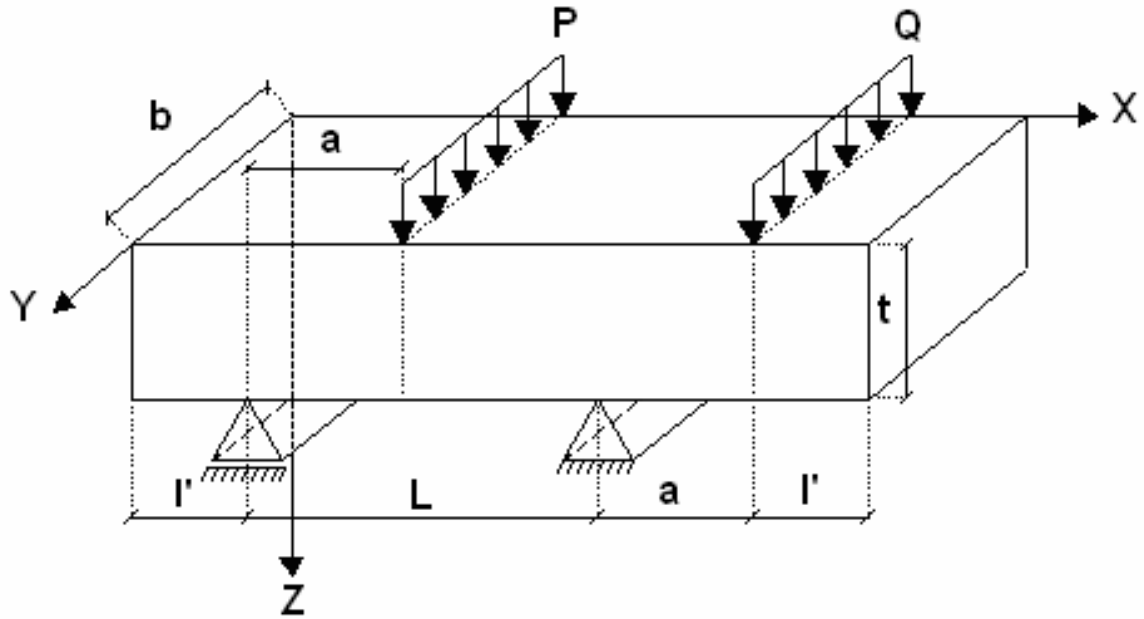


Figure 1(a): A composite beam in asymmetric four point bending

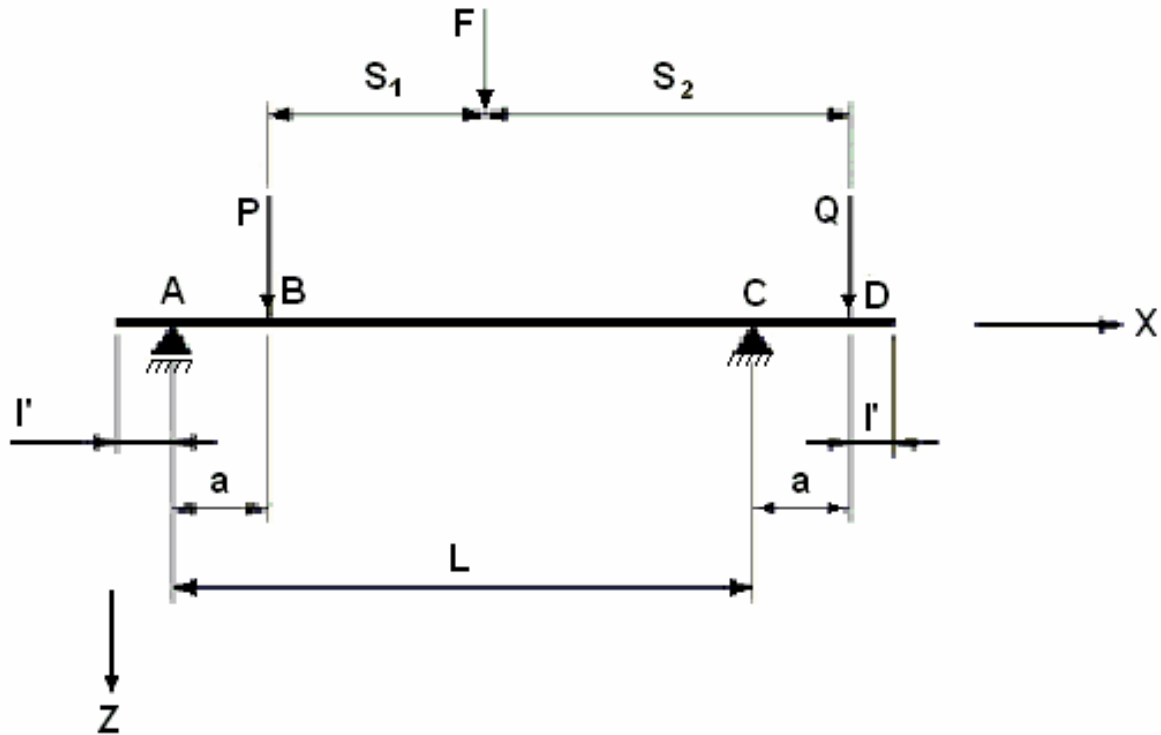


Figure 1(b): The laminates in asymmetric four point bending

In the recent literature several research works which confront the bending behavior of off-axis composites can be found. In [11] the longitudinal off-axis bending compliances of composites using four-point bending tests was examined whereas in [12, 13] analytical, numerical and experimental results have been developed in order to study the displacements field for any fiber orientation. On the other hand the nonlinear analysis of off-axis pultruded composite beams has been performed in [14] and the behavior of woven fabric composites in off-axis end-loaded bending using the theory of plastica in [15].

The main aim of this paper is to continue to shed some more light into the performances of thick composite beams under asymmetric off-axis four-point bending and to study the interlaminar shear failure by investigating the asymmetric GRP laminates. For this reason composite specimens having Resin Rich Layers (RRL) thus forming asymmetric constructions have been considered (Laminate T3) as a continuation of a previous work carried out previously on symmetric laminates [16] made only from Chopped Strand Mat material (Laminate T1) (Fig. 2). The materials properties used in the analysis are given in Table 1.

According to a series of experiments in asymmetric four-point bending which had been performed on these laminates shear failure or flexural failure depending on the parameters introduced has been observed.

In the sequel, a three dimensional linear Finite Element Analysis (FEA) is carried out in the undamaged composite beams in order to, on the one hand, correlate with experimental results and, on the other hand, to obtain the stress distribution versus the vertical axis of the beam at the supports and at the loading points where usually there is an abrupt variation due

to the indentation existing because of the noses. Finally from the FEA, possible crack initiation positions have been identified and compared with those from the experimental work.

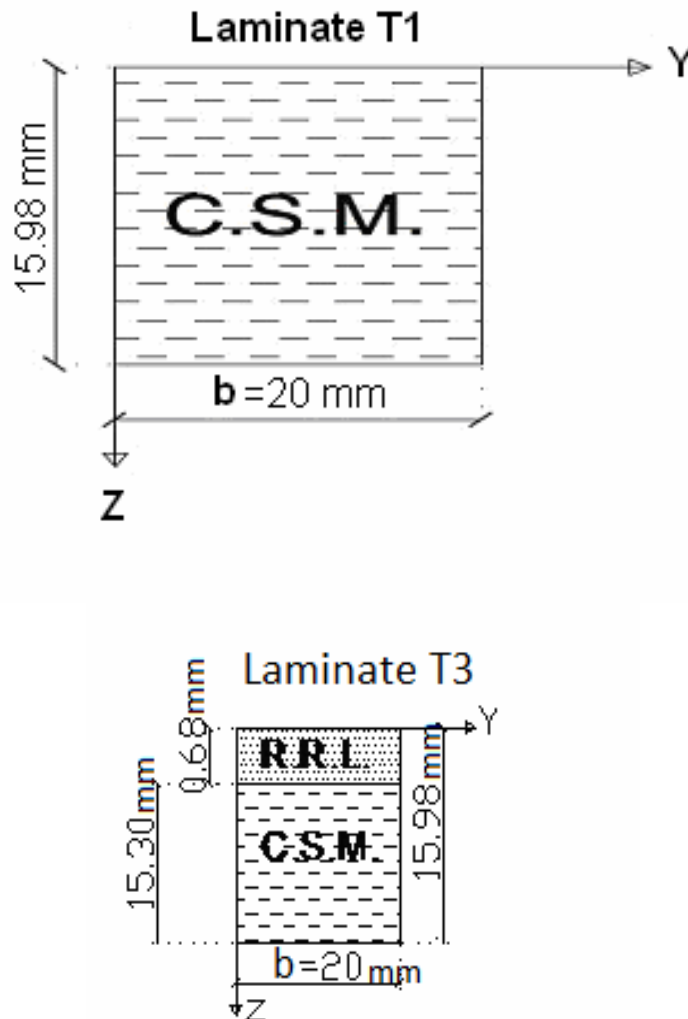


Figure 2: The laminates T_1 and T_3 used in asymmetric four point bending

2 ANALYSIS OF THE OFF-AXIS BENDING PROBLEM

Let us consider the asymmetric four point loading shown in Figures 1(a) and 1(b) where the applied load F is divided into unequal parts P and Q , which are equal to the supports forces at points A and C respectively.

From equilibrium and geometrical considerations, it is easily obtained

$$P = \frac{FS_2}{1+\lambda}, \quad Q = \frac{FS_1}{L}, \quad (1)$$

$$\frac{P}{Q} = \frac{S_2}{S_1} = \lambda, \quad Q = \frac{F}{1+\lambda}, \quad a = \frac{\lambda-1}{\lambda+1}L \quad (2)$$

In the above relationships L is the distance between supports (span length), a is the distance between the support A (or C) and the loading point at B (or D) (Fig. 1(b)) and λ is the loading factor.

The stresses at any point in the beam can be calculated to a first approximation by using the mechanics of materials theory [6]. Thus the normal stress σ_{xx} has its maximum value at points B and C (Fig. 1(b)) as:

$$\sigma_{xx} = \frac{6F(\lambda-1)L}{(1+\lambda)^2 bt^2}, \quad (3)$$

where b and t designate the width and thickness of the beam respectively as it can be seen in Fig.1(a).

Similarly the maximum shear stress at the part (BC) of the beam is:

$$\sigma_{xz} = \frac{3(1-\lambda)F}{2(1+\lambda)bt} \quad (4)$$

Dividing the last two equations, it is obtained:

$$\frac{\sigma_{xx}}{\sigma_{xz}} = \frac{4L}{(1+\lambda)t} = C, \quad (5)$$

where C denotes the ratio of maximum normal stress to maximum shear stress at failure.

Thus it can be observed that in the off – axis four point test method in addition to span length / thickness (L/t) ratio which is the main parameter in the three point bending and symmetric four point bending tests, the loading factor λ ($= P/Q$) defining the ratio of the forces at the supports becomes an important parameter which characterizes the type of failure i.e. shear failure at the neutral axis near the middle plane or tensile (or compressive) flexural failure at the upper or lower part of the laminate beam.

According to the Bernoulli-Euler theory, the elastic deflection arising from a flexural-stress at point B (Fig. 1) in a rectangular beam is [6]:

$$\delta_F = \frac{8\lambda(\lambda-1)^2 FL^3}{E(\lambda+1)^5 bt^3} \quad (6)$$

The elastic shear deflection at the same point is:

$$\delta_s = \frac{12\lambda(\lambda-1)FL}{5G(\lambda+1)^3 bt} \quad (7)$$

The ratio of shear modulus to elastic modulus $\left(\frac{G}{E}\right)$ is much lower for composites than for the metals and hence shear deformation is more significant in composites.

The total deflection δ_t is the sum of the bending and shear components, that is

$$\delta_t = \delta_F + \delta_s = \frac{4\lambda(\lambda-1)FL}{(\lambda-1)^3 bt} \left\{ \frac{2(\lambda-1)}{E(\lambda+1)^2} \left(\frac{L}{t}\right)^2 + \frac{3}{5G} \right\} \quad (8)$$

and the ratio of the two deflections is

$$\frac{\delta_S}{\delta_F} = \frac{3}{10} \left(\frac{E}{G} \right) \left(\frac{t}{L} \right)^2 \frac{(\lambda+1)^2}{\lambda-1} \quad (9)$$

It can be seen that $\frac{\delta_S}{\delta_F}$ depends not only on the ratio of the two modules and the span length-thickness ratio, which characterize symmetric three-point and four-point bending tests, but also on the loading factor λ

The apparent flexural modulus E_α can be found by assuming that the total deflection δ_t is due to flexure only, and is given by:

$$E_\alpha = \frac{8\lambda(\lambda-1)^2 FL^3}{(\lambda+1)^5 bt^3 \delta_F \left(1 + \frac{\delta_S}{\delta_F} \right)} \quad (10)$$

For the apparent flexural modulus to be as nearly equal to the true flexural modulus as possible, the shear deflection must be compared to the flexural deflection that is

$$\frac{\delta_S}{\delta_F} \ll 1$$

3 EFFECTS OF SURFACE RESIN-RICH LAYER.

The existence of non-uniformity in a laminate generally influences the stresses and the moduli. In particular, a resin-rich layer on either or both of the surfaces can significantly affect the flexural modulus.

Since the tensile modulus of the fibre is much larger than that of the resin, the direct contribution of the latter to the ability of a fibre-reinforced laminate to resist flexural deformation is usually small, and can be neglected as a first approximation. Therefore, resin layers on the outer surface of a laminate have little influence on the deflection of a laterally loaded beam. However, surface resin-rich layers contribute to the laminate thickness which is used in computing moduli, and can therefore; have a significant effect on the computed flexural modulus.

If a laminate composite of total thickness t has resin-rich layers (RRL) on either or both surfaces of combined thickness, t_{RRL} , then the thickness of the part of the composite containing reinforcing fibres is

$$t_0 = t - t_{RRL} \quad (11)$$

At first, it is easily observed that the existence of surface RRL can affect determination of the fibre content, ν_f , of a composite as it is obtained from burn-off tests. Allowance can be made for this using the following expression (See Appendix)

$$\nu_{fc} = \frac{1}{1 - \frac{t_{RRL}}{t}} \nu_f \quad (12)$$

From Eq. (3) by taking into account the RRL it can be obtained that:

$$\sigma_{xx} = \frac{6F(\lambda-1)L}{(\lambda+1)^2 bt_0^2}, \quad \sigma'_{xx} = \frac{6F(\lambda-1)L}{(\lambda+1)^2 bt^2},$$

where the bending normal stress of the laminate of thickness t be σ'_{xx} and for the laminate without resin rich-layer be σ_{xx} .

Thus, by dividing

$$\frac{\sigma'_{xx}}{\sigma_{xx}} = \frac{t_0^2}{t^2} = \left(\frac{t - t_{RRL}}{t} \right)^2 = \left(1 - \frac{t_{RRL}}{t} \right)^2 \approx 1 - 2 \frac{t_{RRL}}{t} \quad (13)$$

Similarly for the shear stress from Eq. (4) by taking into account the RRL can be obtained that :

$$\sigma_{xz} = \frac{3(1-\lambda)F}{2(1+\lambda)bt_0}, \quad \sigma'_{xz} = \frac{3(1-\lambda)F}{2(1+\lambda)bt}$$

where σ'_{xz} and σ_{xz} denote the shear stress of the laminate of thickness t and the laminate without RRL respectively. Again by dividing

$$\frac{\sigma'_{xz}}{\sigma_{xz}} = \frac{t_0}{t} = \frac{t - t_{RRL}}{t} = 1 - \frac{t_{RRL}}{t} \quad (14)$$

Eqs. (13) and (14) show that laminate stresses are sensitive to t_{RRL} which is highly variable in a hand lay-up composite and suggests that caution should be exercised in interpreting test results.

Let the apparent flexural modulus of the laminate of thickness t be E'_α and for the laminate without resin-rich layers be E_α . From Eq. (10) if the laminate deflections under load F are equated,

$$E'_\alpha = E_\alpha \left(\frac{t_0}{t} \right)^3 \quad (15)$$

Using Eq. (11) this can be written in terms of total thickness and resin-rich layer thickness :

$$E'_\alpha = E_\alpha \left(1 - \frac{t_{RRL}}{t} \right)^3 \approx E_\alpha \left(1 - \frac{3t_{RRL}}{t} \right) \quad (16)$$

It can be observed that the resin-rich layer has a more significant effect on the apparent flexural modulus than on the stresses when Eq. (16) is compared with Eqs. (13), (14). This effect is double and triple with respect to the other two cases for the stresses.

4 EXPERIMENTAL WORK AND RESULTS

The materials used during the off-axis bending experiments were flat GRP laminates produced by Resinform Ltd using Atlac 382-OSA polyester resin modified by Bisphenol and reinforced with powder bound glass fiber-Chopped Strand Mat (CSM).

The lamination procedure gives usually rise to Resin – Rich surface Layers (RRL) which in practice is provided for corrosion resistance. In order to study the effect of a RRL and also to create an asymmetric laminate, the uneven (rough) side of the laminate was machined, thus avoiding the variations in the thickness of the specimens, factor which plays important role during bending.

The fibre content fraction M_f was determined from burn – off tests according to British Standards (BS) 2782. The result was $M_f = 0.33 \pm 0.01$. For each panel specimens were cut from each of the two perpendicular directions using a band-saw. The edges of the specimens were machined in a milling machine to the shape of a prismatic specimen having total nominal length of 10mm and nominal width of 11mm according to the above BS.

Before testing, the width and thickness of each specimen were measured with a micrometer at three points inside the specimen length. From these measurements, mean values of thickness and width were calculated for each specimen.

The experimental test apparatus consisted of an adjustable anvil which was mounted on a circular base that fits onto a compressive load cell on a Instron Universal testing machine of 100kN capacity. The radius of a loading nose and support nose is 5mm according to BS 2782. Before the tests the load cell should be calibrated. By employing strain-gauges and Linear Variable Displacement Transducers (LVDT), the stress strain and load-deflection curves can be plotted to determine material properties. A Peckel automatic data logger with an Anadix printer was used to record the strain and deflections. The cross-head was 0.5mm/min. The specimen shape and dimensions (Fig. 2) are as follows: $L = 56\text{mm}$, $a = 18.7\text{mm}$, $l' = 10\text{mm}$ and a loading factor $\lambda (= P/Q = 2)$. The CSM layers had a thickness of 15.30mm whereas the RRL had a thickness of 0.68mm, thus obtaining a total thickness of $t = 15.98\text{mm}$.

Four rectangular specimens were used for each laminate with a nominal thickness of 16mm and a width of 20mm after machining. During the tests, photos of some specimens had been taken of to record the crack formation process and the type of failure (flexural, shear or mix). From the experimental investigation the beams usually fail in shear at the (BC) region of the beam (Fig. 1a, 1b), namely between the load P and the right support C where cracking appeared at the middle plane depending on L and λ values.

Consequently by varying L and λ (with constant laminate thickness) one can obtain the two types of failure. For shear failures the ratios of $\max \sigma_{xx}$ to $\max \sigma_{xz}$ at failure should be grouped below C (Eq. 5) and for flexural failures the ratios of $\max \sigma_{xx}$ at failure to $\max \sigma_{xz}$ should be grouped above C . However, in some cases, there is a transitional (mix) case where the mode of failure changes from specimen to specimen.

The following observations had been made from the experiments [6]. An increase in normal stress σ_{xx} with increasing L/t or decreasing λ is apparent. In addition, it had been observed that the shear strength depends upon L/t and λ even for shear failures. This effect, which can be related to the discrepancies observed during the calculations, could be due to local stress concentrations, especially at the loading noses or the supports which are ignored in the simple beam theory. Alternatively, it could be a combined stress effect. If the shear strength is enhanced by the presence of a transverse compressive stress, then an increase in shear strength at smaller L/t would be expected.

Also, the effects of indentation near the supports or loading noses where the stresses change in an abrupt manner can be the reason of the shift and the different variation mainly in the shear stress obtained also by the FEA near and far off the supports, as it is exposed later.

Finally as to the influence of the existence of a RRL in the material, the fibre weight fraction M_f was determined from burn-off tests according to BS 2782 as $M_f = 0.330 \pm 0.01$. The corresponding volume fraction from Eq. (A1) is $\nu_f = 0.190 \pm 0.01$. From Equation (12) by excluding the RRL this value becomes $\nu_{fc} = 0.197$, whereas the experimental value from burn-off tests for the same materials without RRL is $\nu_{fc} = 0.200 \pm 0.01$.

Also from Equations (13)-(15) excluding the RRL of thickness $t_{RRL} = 0.68mm$ we obtain for the laminate of thickness $t \cong 16mm$

$$\sigma'_{xx} = 0.915\sigma_{xx}, \sigma'_{xz} = 0.958\sigma_{xz} \text{ and } E'_a = 0.875E_a \text{ respectively.}$$

The results show the influence of RRL on these properties of the laminate.

5 THREE DIMENSIONAL FINITE ELEMENT ANALYSES

A main goal of this paper is to investigate through the Finite Elements Analysis (FEA) some points which are difficult to clarify by experiments and/or analytical solutions and also if it is possible to make a correlation among them. Indeed, it is not easy to find out what occurs near the loading points and near the supports during a bending test where there is an abrupt change in some magnitudes such as bending moments which influence the stresses.

The fact that the test method used is an asymmetric off-axis bending, in our opinion, makes the investigation more difficult when compared to a symmetric four points or three point bending test. Therefore, a precious numerical method such as FE can contribute for understanding many issues and points and thus can act as a complementary useful tool to detect possible irregularities. Consequently, we consider that both methods experiments and FE constitute a totality and complete each other.

The uncracked laminates T3 are studied numerically in asymmetric off-axis four point bending by using the general purpose finite element program ANSYS [17]. In the three-dimensional analysis, the entire beam is modeled and the domain is filled with 8-node solid brick elements (SOLID 45). In order to verify our numerical results three finite elements meshes have been used with different mesh refinement with 18, 36 and 54 elements in the thickness direction at the part (BC) (Fig.1) of the beam where the maximum shear stresses are appeared. The results for the 36 and 40 elements in the thickness direction are almost similar.

5.1 Analysis of the T3 Specimen

In the three dimensional finite element mesh considered, the width of the beam is discretized with 20 elements, the thickness of the beam with 37 elements, and the length of the beam at the parts (AB) and (CD) (Fig. 1) with 30 elements. In the thickness direction 6 elements are considered in the upper RRL and 31 elements in the lower CSM. The loads at failure are taken $P=14800N$, and $Q=7400N$ from the experimental investigation [6].

The deflection obtained by the finite element method at point B (Fig. 1(b)), are taken at the same surface points where the deflection are measured in the experiments and an average value of them $\delta \left[= (\delta L_1 + \delta L_2) / 2 \right]$ is given in Table 2. The maximum deflection appeared in the middle section at the end of the beam ($x= 94.7mm$, $y= 10mm$, $z= 15.98mm$)

From the stress analysis of the simple supported composite beam of laminate T3 in asymmetric bending, the maximum normal stresses appeared (Fig. 3) at the point B where the load P is applied and at the support C (Fig.1(b)), where the moments and the shear forces take their maximum values. The maximum shear stresses appeared at the parts (BC), (AB) and (CD) of the beam where the shear forces take their maximum values.

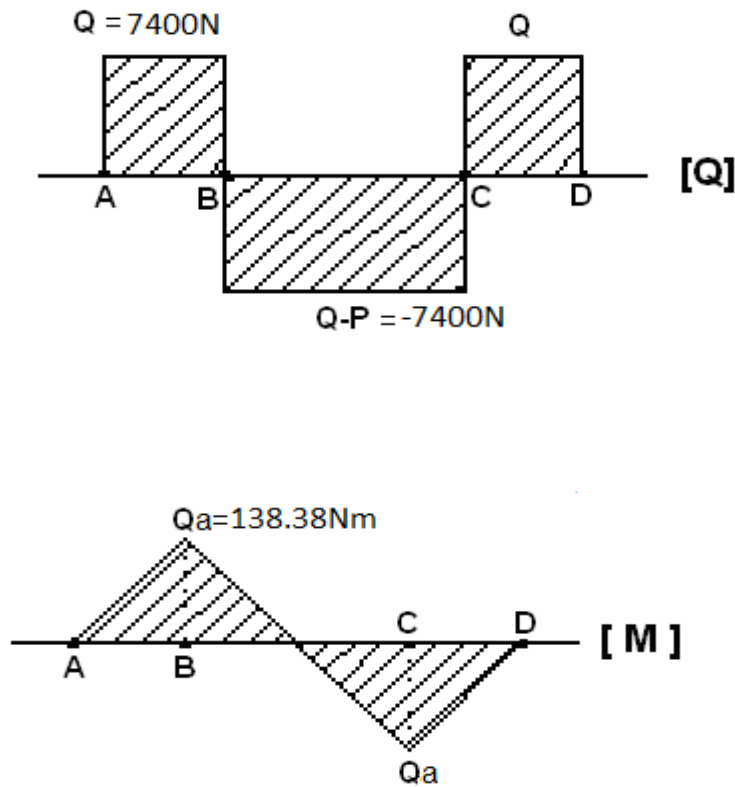


Figure 3: The diagrams of shear forces Q and bending moments M of the laminate T3 in asymmetric bending

From the three dimensional finite element analyses the maximum reasonable normal and shear stresses are also given (Table 3). The maximum σ_{xx} and σ_{xz} stresses are determined at a middle longitudinal cross section of the beam. The max σ_{xx} and σ_{xz} are found at a distance about 2.5 mm to the left of the point B (Fig. 1) where the load P is applied inside the CSM material and close to the interface ($z \approx 1.1$ mm) between the CSM and RRL materials of the T3 specimen. High σ_{xx} and σ_{xz} stresses are also observed near the right support C, and high σ_{xz} near the middle of the part (BC) of the beam.

Deflection	Max(x= 94.7mm)	B(x=28.7mm)
δ	1.545mm	1.179mm

Table 2: Deflections from the finite element analysis for laminate T3.

Maximum Stresses	Close to B ($x \approx 26.12$ mm)	Close to C ($x \approx 76$ mm)	Between B and C ($x \approx 47.4$ mm)
$\max \sigma_{xx}$	175.51MPa	140.695MPa	2.087
$\max \sigma_{xz}$	43.475MPa	36.358MPa	33.301

Table 3: The $\max \sigma_{xx}$ and $\max \sigma_{xz}$ stresses from the finite element analysis for laminate T3.

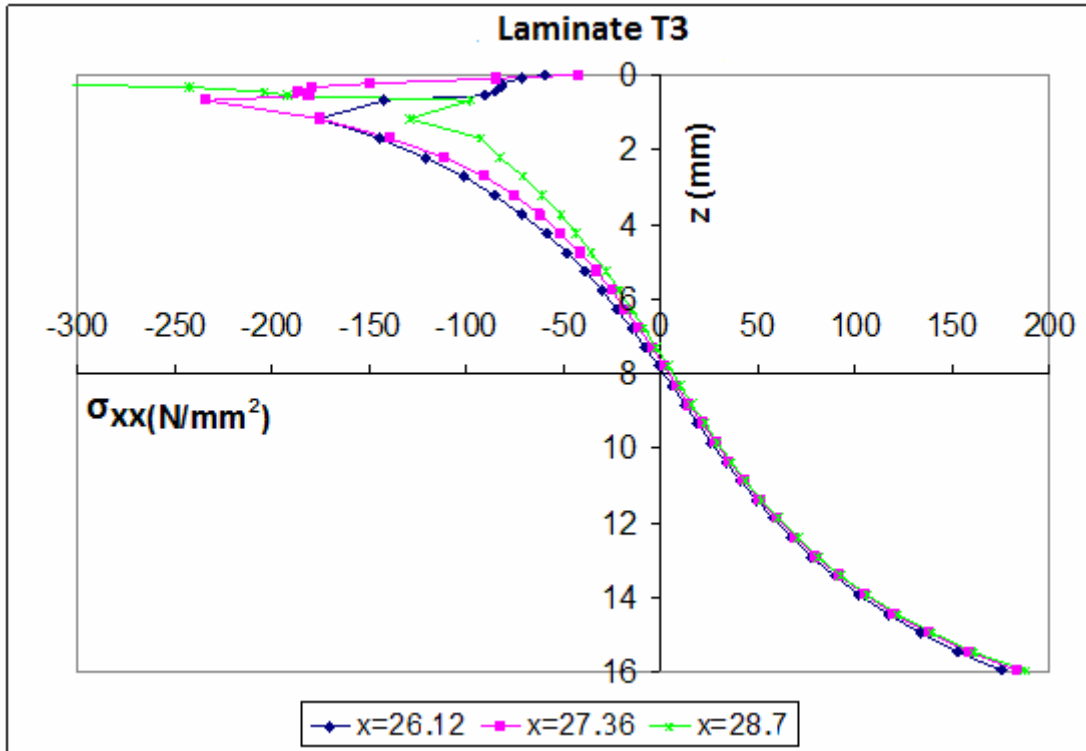


Figure 4: σ_{xx} -stress distributions through the beam thickness of laminate T3 close to point B where the load is applied.

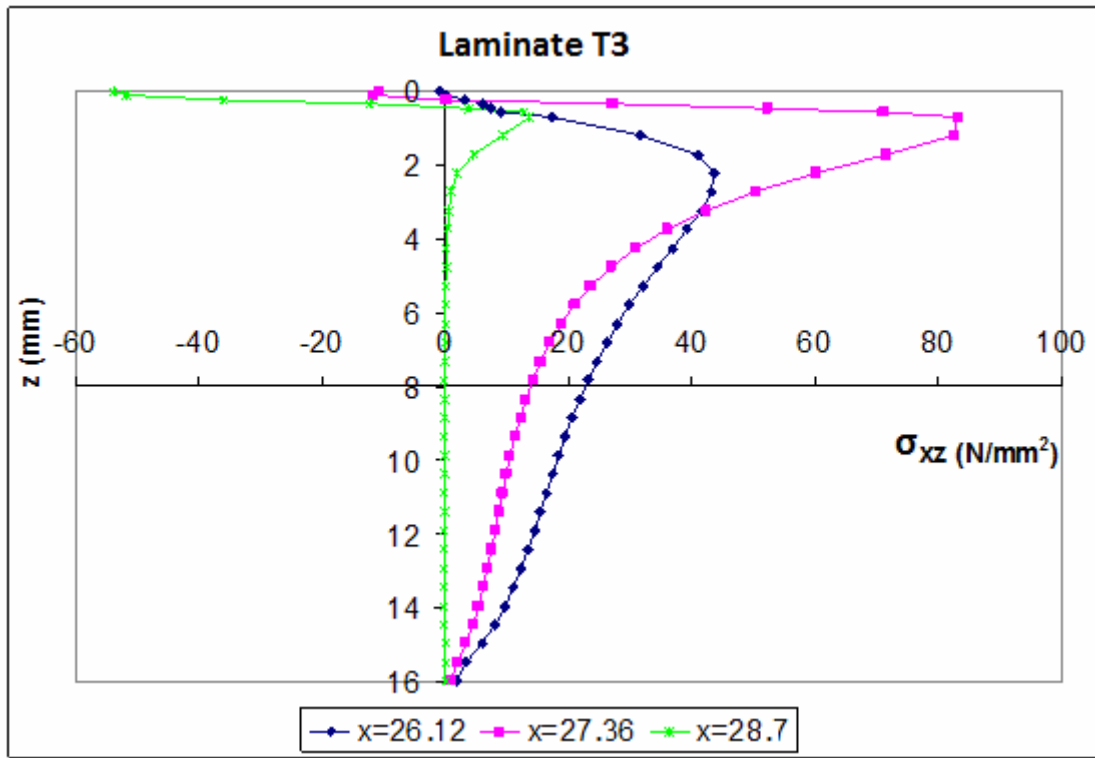


Figure 5: σ_{xz} -stress distributions through the beam thickness of laminate T3 close to the point B where force P is applied.

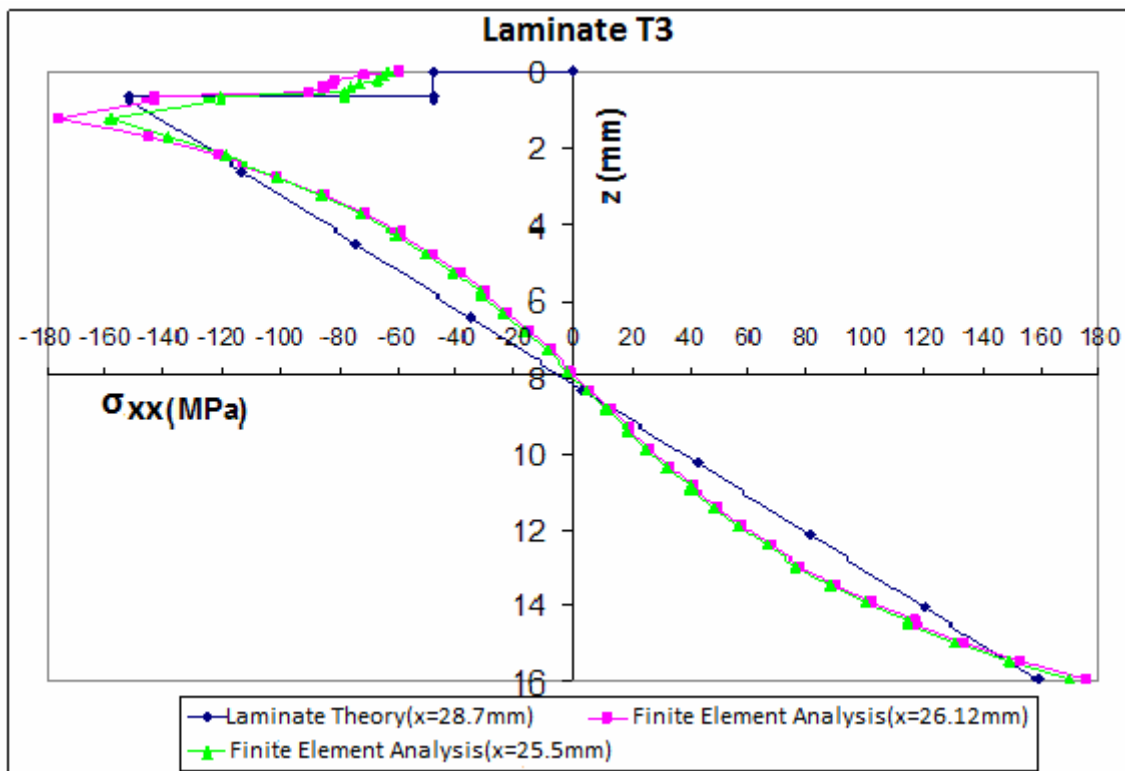


Figure 6: σ_{xx} -stress distributions through the beam thickness of laminate T3.

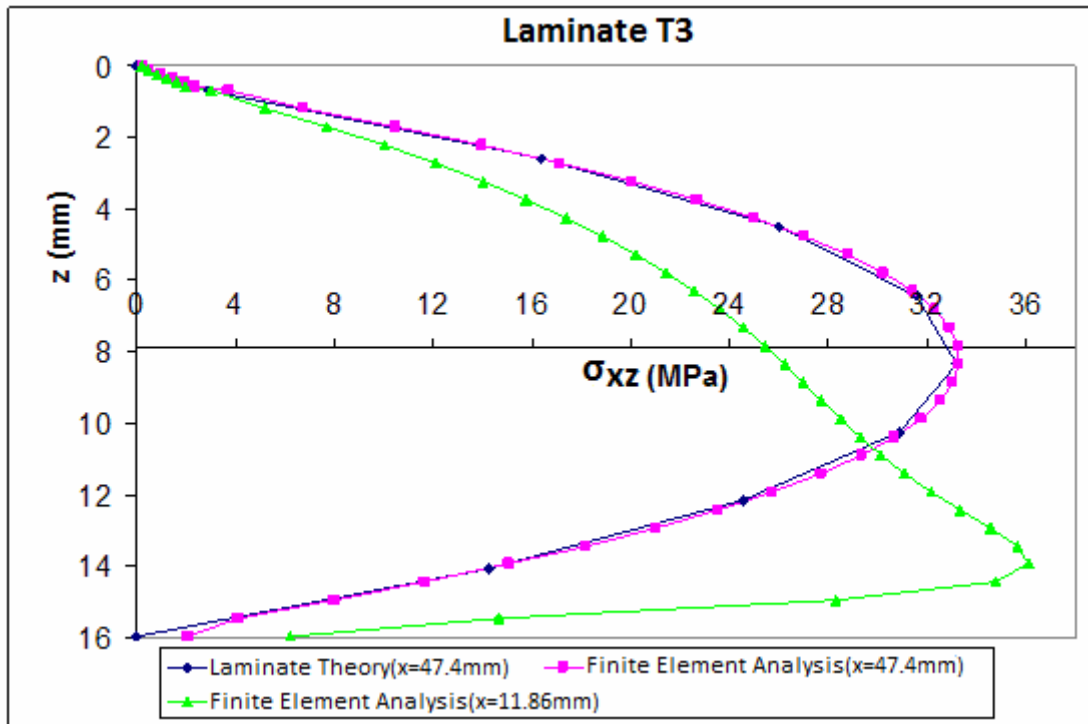


Figure 7: σ_{xz} -stress distributions through the beam thickness of laminate T3.

T3	(i) Lami- nate the- ory	(ii) FEA x= 26.12mm	Percent- age Dif- ference (ii)- (i) (%)	(iii) FEA x= 25.5mm	Percent- age Dif- ference (iii)- (i) (%)	
Point B						
max σ_{xx} (MPa)	151.95	175.51	13.4	158.07	3.9	Inter- face(z=0.68)
max σ_{xx} (MPa)	158.94	175.54	9.45	169.88	6.4	Lower tensile fiber (z=15.98)

Table 4: Percentage differences between the laminate theory and FE results for $\max \sigma_{xx}$ of laminate T3 close to the point B where the force P is applied.

T3	(i) Laminate theory	(ii) FEA x= 47.4mm	Percent- age Dif- ference (ii)- (i) (%)	(iii) FEA x= 11.86mm	Percent- age Dif- ference (iii)- (i) (%)
Point C					
max σ_{xz} (MPa)	33.224	33.301	0.23	36.110	8.7

Table 5: Percentage differences between the laminate theory and FE results for $\max \sigma_{xz}$ stresses of laminate T3.

In Figure 4 the variation of normal σ_{xx} stress distributions obtained from FEM calculations are given near the point B ($x=28.7\text{mm}$) and at different distances from it, where the maximum

reasonable σ_{xx} is obtained. It is observed that at the point B the σ_{xx} -distribution tend to very high values as it was expected from linear theory of elasticity. The σ_{xx} -distributions as we move away from the support approach the linear variation. In addition the σ_{xz} -distributions close to the point B and at different distances from it are given in Figure 5. It is observed that the σ_{xz} -distributions as we move away from the singular point B tend to become parabolic as it was expected from laminate theory. However by taking into consideration Equation (5), the ratios of the maximum normal to the maximum shear stresses from the FEA (Table 3) at the parts of the beam where the maximum stresses appeared, were always lower than the values of C (=4.673) for laminate T3. Hence it is also verified from the finite element analysis that the laminate T3 fails in shear. Furthermore from the finite element analyses and the maximum σ_{xx} , σ_{xz} stresses (Table 3) developed in the beam it is verified that the RRL material has already failed in flexure. This happens because the max σ_{xx} stresses overpass the stress failure in flexure of the RRL material about 47.5 MPa determined experimentally [6].

In Figure 6 the distribution of maximum normal stress, σ_{xx} vs the laminate thickness as obtained from laminate theory in Equation (3) and also from finite elements method (FEM) is illustrated. It can be observed that the stress variation according to laminate theory shows a linear variation, as expected, similar to that of a simple beam considering that the RRL layer has already failed. Nearly the same variation is also obtained from FEM calculations far off the supports ($x=26.12\text{mm}$, 25.5mm). The stress distribution is not completely linear. It is like a small curve. It reminds the normal stress distribution in curved beams where σ_{xx} has a hyperbolic distribution. In addition the percentage differences between the laminate theory and the FEA close to the point B where the maximum σ_{xx} stresses appear, at the interface between the RRL and CSM materials and at the lower part of the laminate beam are presented in Table 4. On the other hand in Figure 7 the distribution of maximum shear stress, σ_{xz} vs the laminate thickness as obtained from laminate theory in Equation (4), and from FEA is illustrated. It can be observed that the stress variation according to laminate theory shows a parabolic variation as expected, similar to that of a simple beam. Nearly the same variation is also obtained from FEM calculations far off the supports ($x = 47.4\text{mm}$). However, the variation of shear stress obtained from FEA is very different near the support A (Fig. 1(b)) i.e. at $x = 11.86\text{mm}$. The parabolic variation with a maximum at the neutral axis becomes a curve with a different shape the maximum of which shifts to the lower part of the laminate beam as in the case of failures due to normal stress (tensile or compressive) where the specimen fails either at its lower part or at the upper part, which it does not occur in our case where from the experiments a shear failure at the neutral axis was observed. In addition the percentage differences between the laminate theory and the FEA results for the maximum σ_{xz} stresses in the middle of the part (BC) (Fig. 1(b)) and close to the support A, are presented in Table 5.

6. CONCLUSIONS

The study of asymmetric glass reinforced plastic beams in asymmetric off-axis four point bending was examined experimentally and numerically.

At first an experimental investigation was carried out where specimens were tested to failure. From the experimental verification and from a wide range of tested specimens it was shown that the main observation is that they fail in shear at the part of the beam between the area where the load was applied and the right support of the beam (Fig. 1(b)). From the experiments was also observed that it was difficult to find out what occurs near the loading

points and near the supports during a bending test where there is an abrupt change in bending moment which influences the stresses fact that, in our opinion, can be thoroughly investigated by FE Method.

A linear three dimensional finite element analysis was performed. It was used a linear FE analysis because the behavior of the corresponding composite beams for laminates T1 (Fig.2) [16] from the experiments, was up to the failure linear. Considering the stress picture for the failure loads obtained from the experiments, the main problem from the numerical investigation was also in shear into the same part of the beam where shear failure was observed from the experiments, between the right support of the beam and the point B where the load P was applied. This was also verified from Equation (5), because the ratios of the resulted maximum stresses from the finite element analysis were always lower than $C(= 4L/(1+\lambda)t)$. Thus, initial crack formation may occur in the middle plane of the T3 material and inside the CSM material.

From the proposed analysis results that the classical laminate theory in the case of asymmetric glass reinforced plastic beams in asymmetric off-axis four points bending could not accurately predict the failure of composite beams. In addition the introduction of the external RRL material (T3 specimen) although influences in some extent the fibre content, the stresses and the elastic modulus as evaluated, does not affect substantially the interlaminar shear strength of GRP specimens because of the lower flexural strength of it comparing with the CSM material.

REFERENCES

- [1] R. Kitching, J. N. Ashton, E. Sideridis, An interlaminar shear test for fibre reinforced plastics. *COMP 88 Symposium on Phase Interaction in Composite Materials*, The University of Patras, Greece, 1988.
- [2] A. S. Clarke, A study of differences of strength properties and geometric variations of commercially produced straight GRP piping from three manufacturers. *MSc Dissertation*, University of Manchester, 1980.
- [3] C. J. Kirk, Effect of geometric design parameters on the flexural behaviour of glass reinforced plastic pipe intersections. *PhD thesis*, University of Manchester, 1980.
- [4] A. L. Tan, Strength and flexibility of glass reinforced plastic pipes and pipe bends. *PhD thesis*, University of Manchester, 1983.
- [5] P. Myler, Glass reinforced plastic pipe bends under a variety of loads. *PhD thesis*, University of Manchester, 1985.
- [6] E. Sideridis, J.N. Ashton, R. Kitching, Measurement of the interlaminar shear stress of glass-reinforced plastics of different construction using the off-axis four point bending test. *Composite Structures*, **18**, 139-161, 1991.
- [7] L.A. Carlsson, J.W. Gillespie Jr, R.B. Pipes, On the analysis and design of the End Notched Flexure (ENF) specimen for mode II testing. *Journal of Composite Materials*, **20**, 594-604, 1986.
- [8] L.A. Carlsson, J.W. Gillespie, Interlaminar shear fracture of interleaved graphite/epoxy composites. *Composites Science and Technology*, **43**, 55-69, 1992
- [9] E.E. Theotokoglou, D. Hortis, L.A. Carlsson, H. Mahfuz, Numerical study of fractured sandwich composites under flexural loading. *Journal of Sandwich Structures and Materials*, **10**, 75-94, 2008.

- [10] E. E. Theotokoglou, I. I. Toulmoussis, Crack kinking in sandwich structures under three point bending. *Theoretical and Applied Fracture Mechanics*, **53**, 158- 164, 2010.
- [11] M. Grediac, Four–point bending tests on off-axis composites. *Composite Structures*, **24**, 89-98, 1993.
- [12] F. Mujika, I. Mondragon, On the displacement field for unidirectional off-axis composites in 3-point flexure – Part 1: Analytical approach. *Journal of Composite Materials*, **37**, 1041-1066, 2003.
- [13] F. Mujika, A. De Benito, I. Mondragon, On the displacement field for unidirectional off-axis composites in 3-point flexure – Part II: Numerical and experimental results. *Journal of Composite Materials*, **37**, 1191-1217, 2003.
- [14] H. Killic, H.-A. Rami, Elastic-degrading analysis of pultruded composite structures. *Composite Structures*, **60**, 43-55, 2003.
- [15] P. K. Majumdar, P. Fazzino, K. L. Reifsnider, Behavior of woven fabric composites in off-axis end-loaded bending. *International SAMPE Symposium and Exhibition (Proceedings)*. Baltimore, MD, USA, Code 79037, Volume 54, May 18-21, 2009.
- [16] E.E. Theotokoglou, E. Sideridis, Study of composite beams in asymmetric four-point bending. *Journal of Reinforced Plastics and Composites*, **30**, 1125-1137, 2011.
- [17] ANSYS Engineering Analysis System, *User’s Manual*, Swanson Analysis Systems, Inc., 2007.

APPENDIX

Determination of the volume fraction ν_f of fibres, given the weight fraction of the fibres.

The British Standards (BS), method of determining ν_f of fibres is to burn off the resin from a measured portion of the specimen. This gives the percentage weight of the glass fibres:

$$\nu_f = \frac{\frac{M_f}{\rho_f}}{\frac{M_f}{\rho_f} + \frac{M_m}{\rho_m}} = \frac{1}{1 + \left(\frac{M_m}{M_f}\right)\left(\frac{\rho_f}{\rho_m}\right)} = \frac{1}{1 + \left(\frac{\rho_f}{\rho_m}\right)\left(\frac{1}{M_f} - 1\right)}, \quad (A_1)$$

where

ν_f, ν_m = volume fraction of fibres and matrix.

M_f, M_m = weight fraction of fibres and matrix

ρ_f, ρ_m = specific density of fibres and matrix.

However, to obtain the volume fraction of a composite excluding the Resin-Rich Layer (RRL):

$$\begin{aligned}
 v_{fc} &= \frac{v_f}{v_f + (v_m - v_{RRL})} = \frac{v_f}{v_f + v_m - \left(\frac{t_{RRL}}{t}\right)(v_f + v_m)} = \frac{1}{\left\{1 + \frac{M_m}{M_f} \left(\frac{\rho_f}{\rho_m}\right)\right\} \left(1 - \frac{t_{RRL}}{t}\right)} = \\
 &= \frac{1}{1 + \left(\frac{\rho_f}{\rho_m}\right) \left(\frac{1}{M_f} - 1\right) \left(1 - \frac{t_{RRL}}{t}\right)} = v_f \frac{1}{\left(1 - \frac{t_{RRL}}{t}\right)},
 \end{aligned} \tag{A2}$$

where

t_{RRL} = thickness of the RRL, t = total thickness.

RESISTANCE OF DOOR OPENINGS IN TOWERS FOR WIND TURBINES

Anh Tuan Tran¹, Milan Veljkovic², Carlos Rebelo³ and Luis Simoes da Silva⁴

¹, ² Luleå University of Technology
University Campus, Porsön, S-97 187 Luleå, Sweden
e-mail: anhtuan.tran@ltu.se and milan.veljkovic@ltu.se

³, ⁴ University of Coimbra
Polo II da Universidade, 3030-788 Coimbra, Portugal
e-mail: crebelo@dec.uc.pt and luiss@dec.uc.pt

Keywords: Wind tower, Strength of door openings, Geometry imperfection, Buckling, Nonlinear.

Abstract. *In this paper, a study of resistance of a lower part of a wind tower including a door opening is presented. Nonlinear 3-D shell element models with real geometry of lower tower segment have been used to simulate the thin walled shell structure in order to study the influence of door opening on the strength of the tower. Two possible alternatives for strengthening the door openings were considered: (i) increasing thicknesses of plate around the opening and (ii) stiffening the opening by a stiffener. Buckling analysis and nonlinear analysis were performed to obtain critical buckling modes and strength of the tower segment. Nominal material properties of different steel grades were considered to investigate possibility of using higher strength steels. A parametric study considering possible local shell imperfections according to EN1993-1-6 has been considered. Additionally, comparative studies have been performed based on the FE model without door opening.*

1 INTRODUCTION

The basic components of a horizontal axis wind turbines (HAWT) are composed of a generator, a tower and foundation. Steel towers are manufactured and assembled from segments by welding or bolting. One important and indispensable part of tower is a door opening. It is used for operation and maintenance of wind turbines. However, this part affects significantly the strength of towers. In numerical simulation, steel tower of wind turbines have been considered as thin walled shell structure. Many deep researches of thin walled structures have been carried out [1, 2, 3]. Principles of design of thin walled structures can be found in EN1993-1-6 [4, 5]. Several researches have been performed to study behaviour of tower for wind turbines. Numerical analysis was carried out by D.L.Karabalis with real geometry of a wind turbine [6]. Stresses at door opening and buckling analysis were reported. Another experimental and numerical investigation of wind turbine tower under bending has been performed by Dimopoulos [7]. In this research, six specimens of down scaled models: two models without opening, two opening models without stiffening and two models with stiffener were tested. Comparisons of results from numerical and experimental study were presented. However, influences of varying thickness and stiffener of door opening on strength of the tower were not taken into account in any of these studies.

The principal purpose of this paper is to study in more detail the effect on the strength of steel tower of door opening and respective stiffening countermeasure like thickness increase or stiffeners. The parameters taken into account in this study correspond to real designs situation of steel wind turbine towers. Concerning the analysis methodologies, firstly, linear perturbation analysis of models have been performed in order to get elastic buckling modes and eigenvalues in 'perfect' geometry. Secondly, nonlinear analysis of models with imperfection geometry from buckling mode has been considered. Comparative studies based on varying parameters and steel grade were also carried out and included in this paper.

2 FINITE ELEMENT MODEL

The lower segment of steel tower of real wind turbine structure was modelled using Abaqus. Three types of FE models of the cylindrical shell were considered: model without opening, models with door opening surrounded by thicker steel shell (models with varying thickness) and models with door opening surrounded by welded stiffener (models with stiffener). Geometries of the tower segment are as follows: 6666 mm of height and diameters of 4150 mm on the bottom and 3919 mm on the top. Thickness of wall of models is 37 mm. Thickness of door opening and stiffener range from 37 mm to 60 mm. Details of geometries are showed in Fig 1. Boundary conditions were determined according to EN1993-1-6 [5] and referred to case of open tank with anchors: BC3 (radially - W, meridionally - U and rotation - R_ϕ are free) and BC1f (radially - W and meridionally - U are restrained and rotation - R_ϕ is free) on the top and bottom of the structure respectively, (see Fig 2). External load was applied on the model through a reference point [8] coupled with the cross section on the top of model.

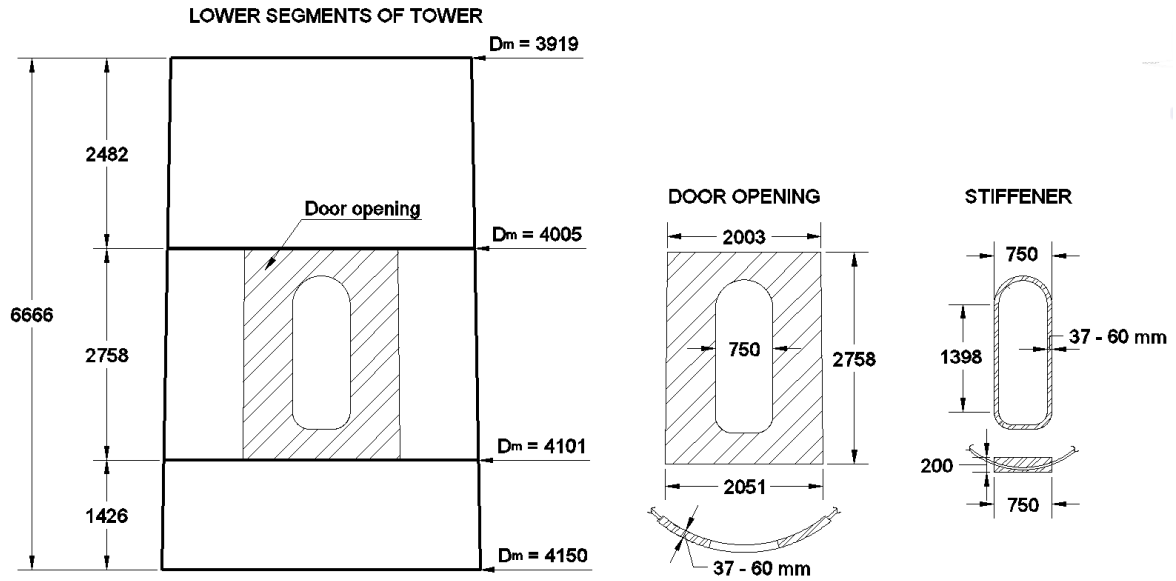


Figure 1: Geometry of Models.

The commercial finite element analysis program Abaqus [8] was used in the analyses of the models. In Abaqus, different types of shell elements are available for use: S3 (shell element with 3 nodes and full numerical integration), S4 (shell element with 4 nodes and full numerical integration), S4R (shell element with 4 nodes and reduced numerical integration), S8R (shell element with 8 nodes and reduced numerical integration). Shell element S4R is appropriate for large strain of buckling and riks analyses. Therefore, this type of shell element was used in this study. The quality and symmetry of mesh was especially considered in order to get more accurate results. The FE mesh was divided in two parts: the wall part and the door opening part including varying thickness or stiffener, (see Fig 2).

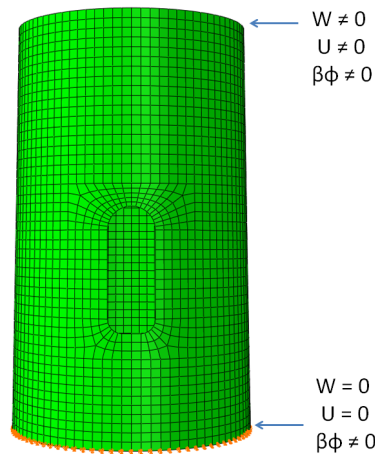


Figure 2: Boundary conditions.

3 MATERIAL CHARACTERISTICS

Steel S355 has been widely used to manufacture segments of steel towers for wind turbines. However, higher strength steels have been also studied and applied on manufacturing towers of wind turbines. In this study, S500 and S650 were also considered in order to investigate the possibility of using higher strength steel. In elastic domain, the Young's modulus of $E=210$ GPa and the Poissons ratio $\nu=0.3$ were used. In plastic domain, the engineering stress - strains relationship was converted into true stress - true plastic strains relationship using following equations:

$$\sigma_{true} = \sigma_{nom}(1 + \epsilon_{nom}) \quad (1)$$

$$\epsilon_{true} = \ln(1 + \epsilon_{nom}) - \frac{\sigma_{true}}{E_0} \quad (2)$$

Fig 3 shows the curve of true stress and true plastic strain of Steels S355, S500 and S650 as input parameters to Abaqus.

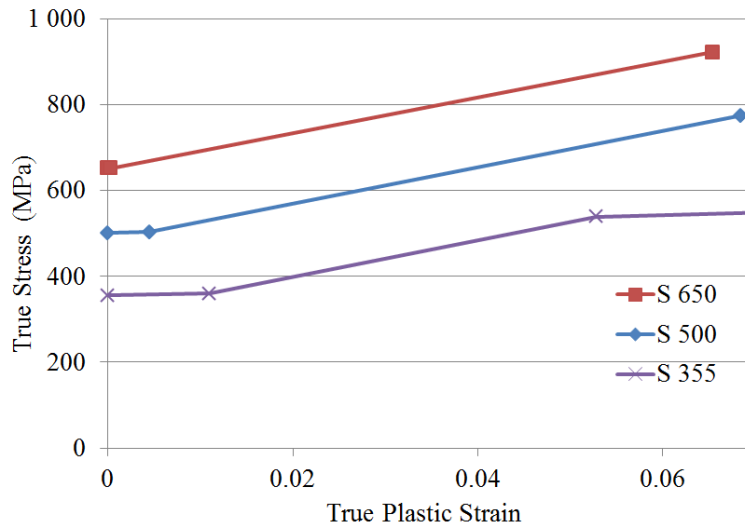


Figure 3: True stress and True strain curve of Steels.

4 NUMERICAL INVESTIGATION

4.1 Geometrical imperfection

Geometrical imperfection was used as input parameter to nonlinear analysis. This value influences the ultimate strength and deformation of the models. Equations to calculate the geometrical imperfection are recommended by EN1993-1-6[4] as follows:

$$\Delta w_k = \frac{1}{Q} \sqrt{\frac{r}{t}} \quad (3)$$

where: t is thickness, r is radius and Q is the meridional compression fabrication quality parameter. This value depends on fabrication tolerance quality class and is given in Tab 1.

Fabrication quality parameter	Description	Q
Class A	Excellent	40
Class B	High	25
Class C	Normal	16

Table 1: Values of fabrication quality parameter Q.

4.2 Parametric study

A total of 35 FE models of lower segments of steel tower were analysed and compared in the parametric studies. Models with thickness of door openings or stiffener ranging from 37 mm to 60 mm were analysed. Thickness of tower wall was kept constant equal to 37 mm and the total height was kept at 6666 mm. In order to compare results, the model without door opening has the same height and 37 mm of wall thickness. All the models had the same diameters. In addition, characteristics of Steel S500 and S650 were considered for comparative analyses.

4.3 Geometrically and materially nonlinear imperfection analysis (GMNIA)

The sequence of buckling analyses consist of Linear analysis (LA), Geometrically nonlinear analysis (GNA), Geometrically and Materially nonlinear analysis (GMNA) and Geometrically and Materially nonlinear analyses with imperfection modes (GMNIA). These analyses depend on calculation level and slenderness parameters. The relations between these analyses are presented in Fig 4.

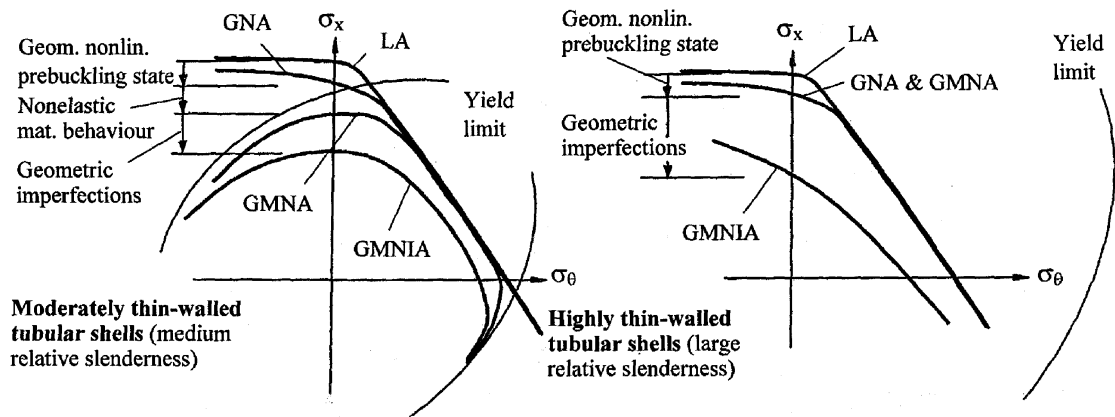


Figure 4: Sequence of analyses of buckling [9].

In the GMNIA analyses, buckling analysis is initially performed in order to get buckling modes. It should be noted that buckling analysis is carried out in linear elastic domain. Secondly, imperfection model of first buckling mode is considered. The basis of GMNIA analysis is the Risk method. This method was developed by Wempner (1971)[10], Riks (1972, 1979)[11, 12] and later supplemented by other several authors. In the Riks method, nonlinear static equilibrium solution is to produced for unstable phenomena. Load magnitude is treated as unknown value and modified until convergence reaches equilibrium path. The method is suitable for the analyses of thin walled structures. [13, 14].

5 RESULTS AND DISCUSSION

5.1 Buckling analysis

The most important in buckling analysis is the calculation of the eigenvalues and respective mode shapes of the structure. In Abaqus, the essential equation in buckling analysis is presented [8] as follows:

$$K^{MN}v^M = 0 \quad (4)$$

where: K^{MN} is the tangential stiffness matrix when loads are applied, v^M is nontrivial displacement solution. The critical buckling loads are defined as follows:

$$P^N + \lambda_i Q^N. \quad (5)$$

where: P^N is preload pattern, Q^N is perturbation load pattern, λ_i is eigenvalue.

Fig 5 presents the results of the first buckling mode of the models. Buckling mode shape of the model without door opening is characterized by local buckling waves. The magnitude of deformations decrease gradually from top to bottom of the model. In model with varying thickness and model with stiffener, buckling occurs at door opening with different deformations.

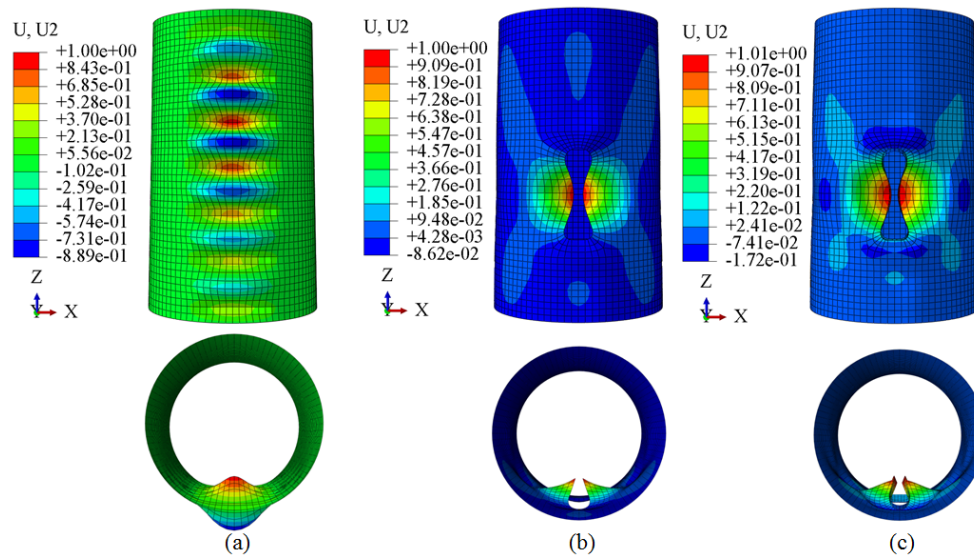


Figure 5: First buckling mode of the models: (a) Model without door opening, (b) Model of a door opening with varying thickness, (c) Model of a door opening with stiffener.

The eigenvalues presented in Table 2 increase gradually among modes of each model. It is interesting to emphasize that the first eigenvalue of model with varying thickness and of the model with stiffener decrease to 47.6 % and 69.8 % respectively in comparison with the model without door opening. Eigenvalues of model with varying thickness are smaller than model with stiffener (68.2 % of first mode and 74.2 % of third mode).

5.2 Nonlinear analysis

After performing the buckling analysis, geometrically and materially nonlinear analyses with imperfection modes (GMNIA) were carried out in order to predict ultimate strength of the structure. In Abaqus, the Riks analysis uses load multiplier as unknown value. The multiplier

	Model without door opening	Model of a door opening with varying thickness	Model of a door opening with stiffener
Mode 1	-1.000	0.476	0.698
Mode 2	1.000	0.487	0.712
Mode 3	1.002	0.580	0.782

Table 2: Comparison of eigenvalues between models.

is increased during the analysis until collapse of the structure. Magnitude of the proportional load is defined [8] as follows:

$$P_{total} = P_0 + \lambda(P_{ref} - P_0) \quad (6)$$

where: P_0 is the dead load, P_{ref} is reference load vector and λ is load proportionality factor.

Fig 6 shows moment-rotation curves of models with the same primary input parameters, in which, the half of tower with door opening is under compression. Thickness of both door opening and stiffener is 60 mm. These values are close to real for design of wind towers. The curves consist of two parts: the linear behaviour before buckling point and nonlinear behaviour in post-buckling. In first part, three curves are linear and almost coincident. In second part, the curves behave nonlinear up to ultimate strengths of 175.7 MNm, 193 MNm and 189.7 MNm corresponding respectively to model without door opening, model with varying thickness and model with stiffener respectively. In conclusion, values of ultimate strength show that both stiffening solutions are sufficient to strengthen the structure. However the big differences in the ultimate strengths justify further studies to optimize stiffening solutions.

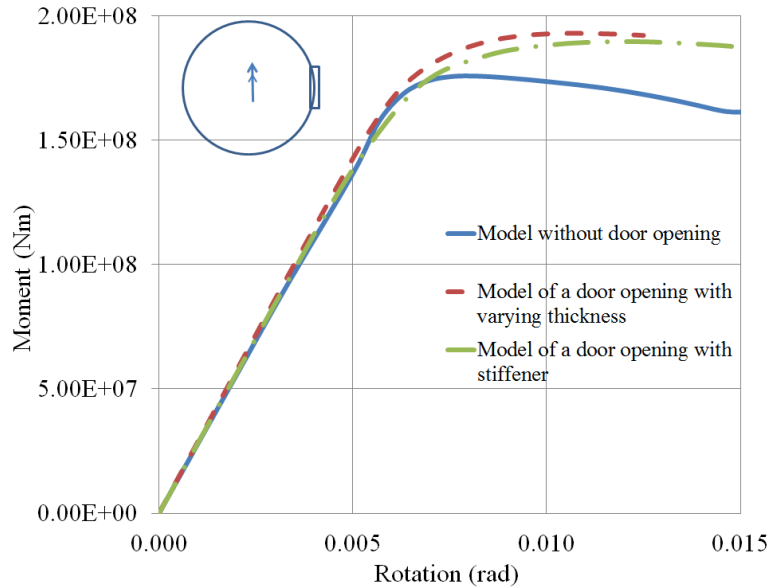


Figure 6: Relation between moment and rotation of models - door opening under compression.

Fig 7 presents moment-rotation relationship of models which have the half of tower with door opening under tension. Ultimate strength of model with varying thickness and model with stiffener are 194.9 MNm and 192.0 MNm, respectively. In comparison with models that have a half of tower with door opening under compression, the difference is just 1%. It may lead to

conclusion that the position of a door opening (under compression or tension) does not affect the ultimate strength of towers with the same conditions.

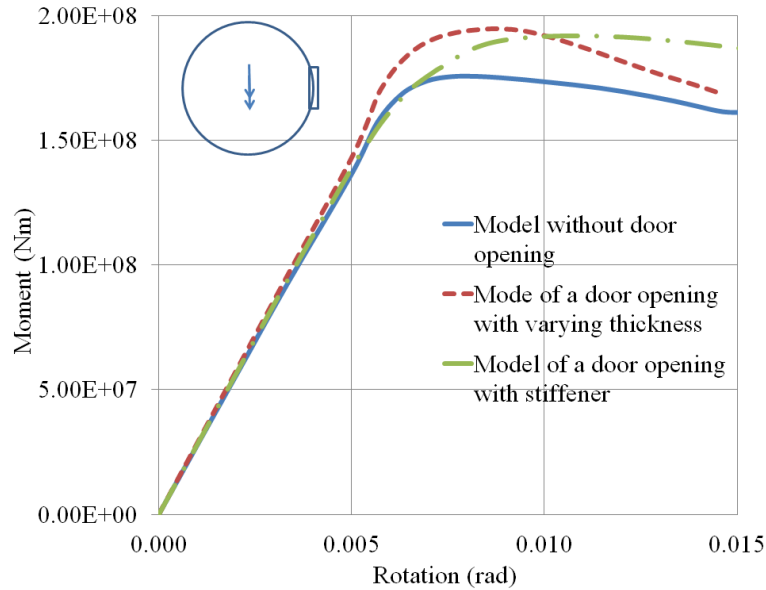


Figure 7: Relation between moment and rotation of models - door opening under tension.

Fig 8 presents the distribution of normal stresses at ultimate load in all models. Distribution of normal stresses in the model with varying thickness shows big difference between wall area and door opening area. Stress concentration occurs around door opening. Normal stresses in tension and compression in the model with varying thickness are 382.4 MPa and -457.0 MPa respectively. As mentioned above, the ultimate load of model without door opening is lowest (175.7 MNm). However, its normal stress in tension is the highest (412.6 MPa). Besides, that normal stress in compression of model with stiffener is minimum (-495.8 MPa). It should be noted that Steel S355 was used in analyses of these models. It proves that yield phenomenon appeared in parts of the models.

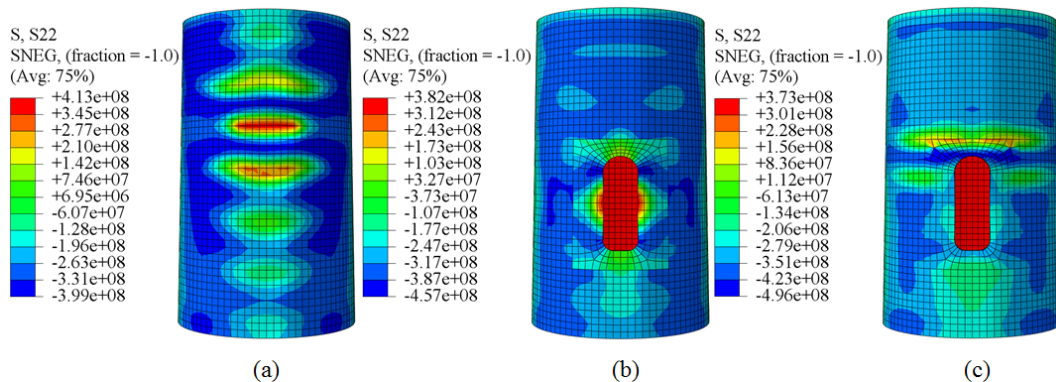


Figure 8: Distribution of normal stress at ultimate load: (a) Model without door opening, (b) Model of a door opening with varying thickness, (c) Model of a door opening with stiffener.

Fig 9 shows distribution of reaction forces of the models for 0.0002 rad rotation applied on the top of the top of the models. The three curves almost coincide. They are typical shapes

of distribution of reaction forces in linear part. It is interesting to emphasize effects of door opening on distribution of reaction forces. Outside the area of door opening, the curves of reaction forces are smooth. The results also show that distribution of reaction forces of models are approximate in pre-buckling part.

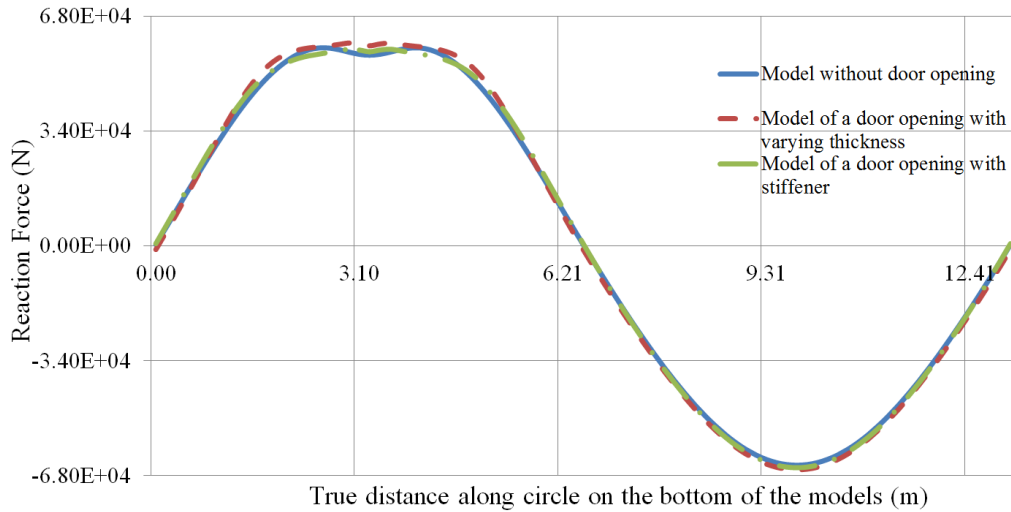


Figure 9: Distribution of reaction forces of the models at 0.0002 rad of rotation.

Fig 10 shows distribution of reaction forces of the models corresponding to 0.013 rad rotation applied on the top of the models. It should be noted that the figure presents distribution of reaction forces in nonlinear part. The curves of model with varying thickness and model with stiffener are almost coincident. Influence of buckling on distribution of reaction forces are significant. Minimum reaction forces at door opening area of the model with varying thickness and the model with stiffener are 921.6 kN and 895.1 kN respectively. However, at the same position, reaction force of model without opening is only 242.2 kN.

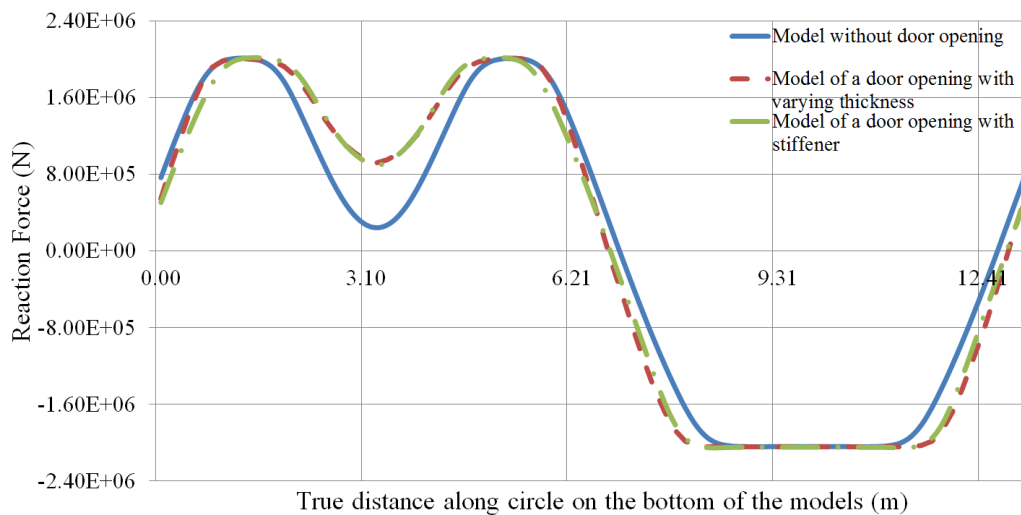


Figure 10: Distribution of reaction forces of the models at 0.013 rad of rotation.

5.3 Optimal designs of door opening and stiffener

In this study, varying thickness around door opening and of stiffener were considered. These results were analysed and compared with the results of model without opening in order to optimize the thickness of door opening and stiffener as well. The thickness range from 37 mm to 60 mm. These values are appropriate to design the stiffening of door opening. Table 3 presents results of relations between thickness, moment and rotation at ultimate load of the models. As mentioned above, the ultimate moment of model without opening is 175.7 MNm. In comparative studies of the door opening with varying thickness and of the door opening with stiffener, 51 mm of thickness of door opening and 37 mm of stiffener are sufficient to strengthen the structures.

Thickness (mm)	Door opening		Stiffener	
	Moment (MNm)	Rotation (rad)	Moment (MNm)	Rotation (rad)
37	163.910	0.01464	182.203	0.01357
39	163.092	0.01869	182.920	0.01357
41	163.531	0.01186	183.772	0.01088
43	165.130	0.01186	184.107	0.01357
45	167.618	0.01015	184.668	0.01357
47	170.473	0.01015	185.252	0.01357
49	173.347	0.01015	185.864	0.01357
51	176.392	0.01015	186.631	0.01186
53	179.654	0.01015	187.703	0.01186
55	183.084	0.01015	188.555	0.01186
57	187.160	0.01037	189.078	0.01186
59	190.870	0.01079	189.520	0.01186
60	192.976	0.01058	189.719	0.01186

Table 3: Relation between thickness, moment and rotation at ultimate load of the models.

5.4 Use of higher strength steels

In practice, design of wind towers is based on Steel S355. In this research, higher strength steels S500 and S650 were used for door opening and stiffener in order to study decrease of thickness without affecting the strength of towers.

Fig 11 presents moment-rotation curves of the tower when steel S355, S500 and S650 were used for the stiffener. The curves are similar in shape. Ultimate load is approximately 182 MNm. However, the thickness of stiffener significantly decreased as higher strength steels were used. It should be noted that in case of steel S355, the thickness of stiffener is 37 mm. When S500 and S650 are used, the thickness of stiffener decreases to 29 mm and 23 mm respectively. These correspond to approximate to 78% and 62% of the thickness of stiffener when steel S355 is used.

Fig 12 shows curves of moment versus rotation of the tower as Steel S355, S500 and S650 were used for the door opening. The shape of curves changed significantly as higher strength steels were used. Ultimate load is approximately 177 MNm. However, difference between pre-buckling and post-buckling is detected. The thickness of door opening significantly decreased

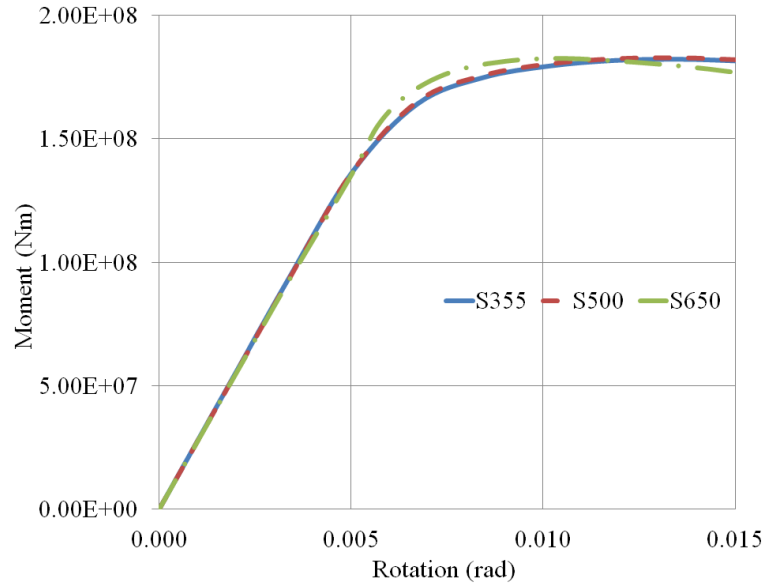


Figure 11: Comparison of using higher grade steels for stiffener.

as higher strength steels were used. It decreased to 41 mm and 35 mm for steel grades S500 and S650 respectively. It decreased approximately 20% and 33% in comparison to the thickness of door opening (51 mm) when steel S355 was used.

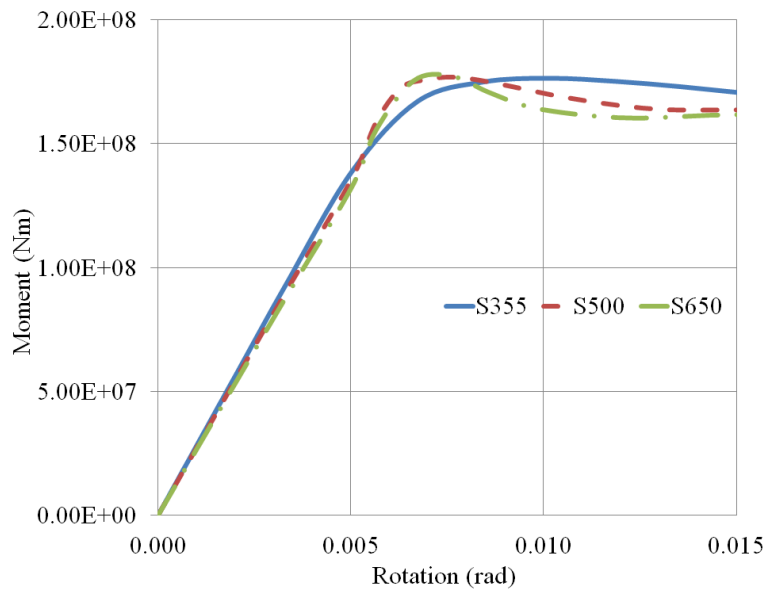


Figure 12: Comparison of using higher grade steels for door opening.

6 CONCLUSION

In this paper, the influence of door opening and respective stiffening were investigated. Comparative studies between model without opening, models with door opening surrounded by thicker steel shell and models with door opening surrounded by welded stiffener were presented. Linear and nonlinear moment-rotation behaviours of the thin walled structures were analysed. Results from comparative studies in cases of door opening under compression and tension showed that the position of door opening did not affect significantly the ultimate strength of tower (1% of difference) in the same conditions. Parametric study aiming at optimal designs of door opening and stiffener showed that 37 mm of stiffener and 51 mm of thickness around door opening are sufficient to obtain the same resistance in comparison with the model without door opening and 37 mm of wall thickness. In addition, results from studies when higher strength steels are used, have shown that thickness of door opening and stiffener decreased significantly when higher strength steels are used. Thickness of door opening just equalled approximately 80% and 67% of its value as steel S355 was used. Thickness of stiffener decreased by 22% and 38% as steel S500 and S650 were used for stiffener respectively.

REFERENCES

- [1] A.K. Karamanos, Bending instabilities of elastic tubes. *International Journal of Solid and Structures*, **39**, 2059–2085, 2002.
- [2] M. Pircher, R.Q. Bridge, Buckling of thin-walled silos and tanks under axial load - Some new aspects. *Journal of Structural Engineering*, **127**, 1129–1136, 2001.
- [3] R. Sliz, M.Y. Chang, Reliable and accurate prediction of the experimental buckling of thin-walled cylindrical shell under an axial load. *Thin-walled Structures*, **49**, 409–421, 2011.
- [4] EN-1993-1-6. Design of steel structures, Part 1-6: *Strength and Stability of Shell Structures*, Brussels, Belgium: European Committee for Standardization, 2007.
- [5] J.M. Rotter, H. Schmidt, *Buckling of steel shells European design recommendations*. ECCS, 2008.
- [6] N. Bazeos, G.D. Hatzigeorgiou, I.D. Hondros, H. Karamaneas, D.L. Karabalis, D.E. Beskos, Static, seismic and stability analyses of a prototype wind turbine steel tower. *Engineering Structures*, **24**, 1015–1025, 2002.
- [7] C.A. Dimopoulos, C.J. Gantes, Experimental investigation of buckling of wind turbine tower cylindrical shells with opening and stiffening under bending. *Thin-walled Structures*, **54**, 140–155, 2012.
- [8] Abaqus, *Abaqus documentation v6.12*. Simulia Dassault Systmes, 2012.
- [9] Th.A. Winterstetter, H. Schmidt, Stability of circular cylindrical steel shells under combined loading. *Thin-walled Structures*, **40**, 893–909, 2002.
- [10] G.A. Wempner, Discrete approximation related to nonlinear theories of solids. *International Journal of Solid and Structures*, **7**, 1581–1599, 1971.

- [11] E. Riks, The application of Newton's method to problem of elastic stability. *Journal of Applied Mechanics*, **39**, 1060–1065, 1972.
- [12] E. Riks, An incremental approach to the solution of snapping and buckling problems. *International Journal of Solid and Structures*, **15**, 529–551, 1979.
- [13] J.G. Teng, C.Y. Song, Numerical models for nonlinear analysis of elastic shell with Eigenmode-Affine imperfections. *International Journal of Solid and Structures*, **38**, 3263–3280, 2001.
- [14] T. Kobayashi, Y. Mihara, F. Fujii Path-tracing analysis for post-buckling process of elastic cylindrical shells under axial compression. *Thin-walled Structures*, **61**, 180–187, 2012.

MODELING THE FAILURE OF STRUCTURES WITH STOCHASTIC PROPERTIES IN A SEQUENTIALLY LINEAR ANALYSIS FRAMEWORK

Manolis Georgioudakis^{1*}, George Stefanou^{1,2} and Manolis Papadrakakis¹

¹Institute of Structural Analysis & Antiseismic Research
School of Civil Engineering
National Technical University of Athens
Zografou Campus, 15780 Athens, Greece

² Institute of Structural Analysis & Dynamics of Structures
Department of Civil Engineering
Aristotle University of Thessaloniki
54124 Thessaloniki, Greece

e-mail: {geoem,stegeasa}@mail.ntua.gr, mpapadra@central.ntua.gr

Keywords: sequentially linear analysis, saw-tooth softening, stochastic finite element, Monte Carlo simulation

Abstract. *This paper investigates the influence of uncertain spatially varying material properties on the fracture behavior of structures made of softening materials. To model the structural failure, the sequentially linear solution procedure proposed by Rots (2001) is used, which replaces the incremental (nonlinear) finite element analysis by a series of scaled linear analyses and the nonlinear stress-strain law by a saw-tooth curve. The effect of uncertain material properties (Young's modulus, tensile strength, fracture energy) on the variability of the load-displacement curves and crack paths is examined. The uncertain properties are described by homogeneous stochastic fields using the spectral representation method in conjunction with translation field theory. The response variability is computed by means of direct Monte Carlo simulation. The influence of the variation of each random parameter as well as of the probability distribution, coefficient of variation and correlation length of the stochastic fields is quantified. It is shown that the response statistics are affected by the spectral characteristics of the stochastic fields.*

1 INTRODUCTION

In recent years, several numerical techniques have been developed to model the failure of structures in the framework of the finite element method (FEM). There are two essential proposed approaches which are dealing with physical discontinuities (e.g. cracks, slip lines) by enriching the (continuous) displacement field of standard finite elements either on nodal level [5] (Extended Finite Element Method - XFEM) or on elemental level [6] (Embedded Finite Element Method - EFEM). Unlike with standard finite elements, mesh refinement is not necessary in these methods to capture the discontinuities and the simulation can be performed with relatively coarse meshes. A comparative study of the two approaches can be found in [7] but the detailed assessment of relative errors, rates of convergence and computational cost is still an open area of research.

It is well-known in failure mechanics that material softening is often responsible for unstable structural behavior [1]. Even if the boundary value problem is mathematically well posed, instabilities may arise in the incremental (nonlinear) solution schemes used in the aforementioned FE methods due to negative tangent stiffness. These instabilities can lead to more than one solution of the system of equations and thus to alternative equilibrium states or bifurcations of the equilibrium path. As a consequence, the robustness of the numerical procedure used for solving the nonlinear problem is strongly affected. In order to overcome these problems, an alternative method, called Sequentially Linear Analysis (SLA), has been introduced by Rots [9]. This method replaces the incremental (nonlinear) FE analysis by a series of scaled linear analyses and the nonlinear stress-strain law by a saw-tooth curve.

In this paper, SLA is implemented in a stochastic setting to investigate the influence of uncertain spatially varying material properties on the fracture behavior of structures made of softening materials. A benchmark structure (notched beam) is analyzed and comparisons with nonlinear analysis results are provided. The effect of uncertain Young's modulus, tensile strength and fracture energy on the variability of the load-displacement curves and crack paths is examined. The uncertain properties are described by homogeneous stochastic fields using the spectral representation method in conjunction with translation field theory [13], [4]. The response variability is computed by means of direct Monte Carlo simulation. The influence of the variation of each random parameter as well as of the probability distribution, coefficient of variation and correlation length of the stochastic fields is quantified. It is shown that the response statistics are affected by the spectral characteristics of the stochastic fields.

2 BRIEF REVIEW OF SEQUENTIALLY LINEAR ANALYSIS (SLA)

Modeling fracture through an *event-by-event* cracking procedure by imposing an increment of damage, is an attractive alternative to typical nonlinear FE analysis, where modeling proceeds by imposing increment of displacement or force. In this way, it is unnecessary to make large jumps in damage during a single load or displacement step, which is usually the source of convergence problems. To capture brittle events directly with SLA there is no need to iterate around these critical points.

To this purpose, a tensile softening curve of negative slope is replaced by a series of saw-teeth which maintain a positive tangent stiffness (see Fig. 1). The incremental/iterative Newton-Raphson method is replaced by a series of linear analyses, each with a reduced positive stiffness, until the global analysis is complete. It has been shown that this *event-by-event* strategy is robust and reliable [10], and circumvents bifurcation problems, in contrast to regular nonlinear FE analysis.

A brief review of SLA is provided below. More details about this method can be found in [2] and [3].

2.1 General procedure

The structure is discretized in the framework of standard FEM, using elastic continuum elements and all material properties (Young's modulus, Poisson's ratio and initial strength) are initially assigned to them. Subsequently, the following steps are carried out sequentially without need of changing the initial mesh:

- Perform a linear-elastic FE analysis with a unit external load and calculate the principal stresses;
- Loop over all integration points for all elements and find the *critical element* for which the stress level divided by its current strength is the highest in the whole structure;
- Calculate the critical load multiplier, belonging to the critical integration point, i.e. the current strength divided by the stress level;
- Scale the reference load proportionally by the critical load multiplier;
- Increase the damage in the critical integration point by reducing the stiffness E and strength f_t according to the saw-tooth tensile-based constitutive relation (see Section 2.2);
- Repeat the previous cycle of steps continuously, until the damage has spread sufficiently into the structure.

In this way, the nonlinear response is extracted by linking consecutively the results of each cycle. The smoothness of $P - \delta$ curves depends of course on the smoothness (number N of teeth) of the saw-tooth model (see Section 2.2). The SLA procedure allows only one integration point to change its status from elastic to softening at each time, while in nonlinear FE analysis, the use of load increments implies that multiple integration points may crack simultaneously and the local stiffnesses at these points switch from positive to negative, following the softening constitutive laws for quasi-brittle materials.

2.2 Saw-tooth model

In this work, the generalized tooth size approach (Model C) [11] with no requirement of special techniques to handle mesh-size objectivity is adopted, in order to obtain objective results with respect to the mesh as well as to overcome the lack of consistency. The way in which the stiffness and strength of the critical elements are progressively reduced at each "event", is shown schematically in Fig. 1 where the softening curve of negative slope in the constitutive stress-strain relation is replaced by a discretized saw-tooth diagram of positive slopes which provides the correct energy dissipation. The linear softening stress-strain curve is defined by the Young's modulus E , the tensile strength f_t and the area under the saw-tooth diagram. This area, (see Fig. 1) is always equal to the fracture energy G_f (which is considered here as a material property) divided by the crack bandwidth h , which is associated with the size, orientation and integration rule of the finite element. In case of linear softening, the ultimate strain ϵ_u is given by:

$$\epsilon_u = \frac{2G_f}{f_t h} \quad (1)$$

Both Young's modulus E and strength f_t can be reduced at the same time in the sequentially linear strategy by a factor a , according to:

$$E_i = \frac{E_{i-1}}{a}, \quad \text{for } i = 1, 2, \dots, N \quad (2)$$

where i and $i - 1$ denote the current and previous step, respectively, in the saw-tooth diagram. To find the rule of reducing Young's modulus E as well as strength f_t by ratio a_i in step i according to Fig. 1, we have:

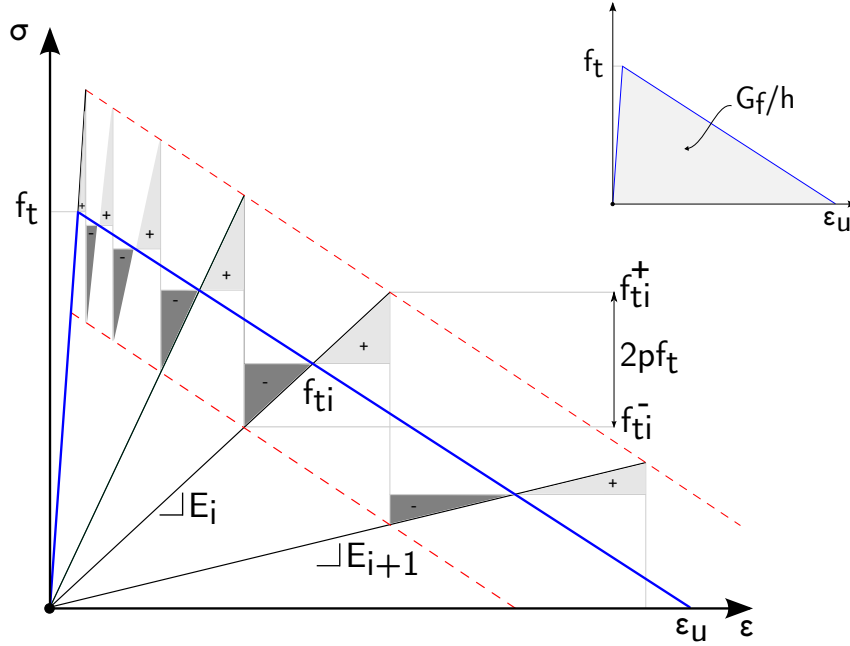


Figure 1: Saw-tooth model and definition of G_f

$$f_{ti}^- = f_{ti}^+ - 2pf_t \quad (3)$$

$$E_{i+1} = \frac{f_{ti}^-}{\epsilon_i} \quad (4)$$

$$a_{i+1} = \frac{E_i}{f_{ti}^-} \epsilon_i = \frac{f_{ti}^+}{f_{ti}^-} = \frac{f_{ti}^+}{f_{ti}^+ - 2pf_t} \quad (5)$$

Thus, for the case of linear softening (Fig. 1) the value of f_{ti}^+ can be easily defined as:

$$f_{ti}^+ = \epsilon_u^+ E_i \frac{D}{E_i + D} \quad (6)$$

where,

$$\epsilon_u^+ = \epsilon_u + p \frac{f_t}{D} \quad (7)$$

The number N of teeth is automatically evaluated, depending on the arbitrary parameter p defined by the user. For smaller values of p , a higher number N of teeth is needed to cover the softening branch, leading to more exact results. In the overall procedure, the difference between the sum of *positive* triangles above the real curve and the sum of *negative* triangles below it must vanish, as shown in Fig. 1.

3 REPRESENTATION OF UNCERTAIN MATERIAL PROPERTIES

3.1 Non-Gaussian translation fields

Both Gaussian and non-Gaussian stochastic fields are used in this paper for the representation of uncertain material properties. However, the Gaussian assumption for variables bounded by physical constraints (e.g. material properties that should be strictly positive) is questionable because it leads to a non-zero probability of violation of these constraints. This is why the simulation of non-Gaussian stochastic processes and fields has received considerable attention in the field of computational stochastic mechanics.

Since all the joint multi-dimensional density functions are needed to fully characterize a non-Gaussian stochastic field, a number of studies have been focused on producing a more realistic (approximate) definition of a non-Gaussian sample function from a simple transformation of some underlying Gaussian field with known second-order statistics. Thus, if $g(\mathbf{x})$ is a homogeneous zero-mean Gaussian field with unit variance and spectral density function (SDF) $S_{gg}(\boldsymbol{\kappa})$ (or equivalently autocorrelation function $R_{gg}(\xi)$), a homogeneous non-Gaussian stochastic field $f(\mathbf{x})$ with power spectrum $S_{ff}^T(\boldsymbol{\kappa})$ can be defined as:

$$f(\mathbf{x}) = F^{-1} \cdot \Phi[g(\mathbf{x})] \quad (8)$$

where Φ is the standard Gaussian cumulative distribution function and F is the non-Gaussian marginal cumulative distribution function of $f(\mathbf{x})$. The transform $F^{-1} \cdot \Phi$ is a memory-less translation since the value of $f(\mathbf{x})$ at an arbitrary point \mathbf{x} depends on the value of $g(\mathbf{x})$ at the same point only and the resulting non-Gaussian field is called a translation field [4]. Translation fields can be used to represent various non-Gaussian phenomena and have a number of useful properties such as the analytical calculation of crossing rates and extreme value distributions.

3.2 The spectral representation method

In the present work, Eq. 8 is used for the generation of non-Gaussian translation sample functions representing the uncertain material properties of the problem. Sample functions of the underlying homogeneous Gaussian field $g(\mathbf{x})$ are generated using the spectral representation method. This method is well suited in the context of Monte Carlo simulation (MCS) technique used for calculating the response variability of stochastic structural systems (e.g. [14]). For a two-dimensional stochastic field, the i -th sample function is given by [13]:

$$g^{(i)}(x, y) = \sqrt{2} \sum_{n_1=0}^{N_1-1} \sum_{n_2=0}^{N_2-1} [A_{n_1 n_2}^{(1)} \cos(\kappa_{1n_1} x + \kappa_{2n_2} y + \phi_{n_1 n_2}^{(1)(i)}) + A_{n_1 n_2}^{(2)} \cos(\kappa_{1n_1} x + \kappa_{2n_2} y + \phi_{n_1 n_2}^{(2)(i)})] \quad (9)$$

where $\phi_{n_1 n_2}^{(j)(i)}$, $j = 1, 2$ represent the realization for the i -th simulation of the independent random phase angles uniformly distributed in the range $[0, 2\pi]$. $A_{n_1 n_2}^{(1)}$, $A_{n_1 n_2}^{(2)}$ have the following expressions

$$A_{n_1 n_2}^{(1)} = \sqrt{2S_{gg}(\kappa_{1n_1}, \kappa_{2n_2})\Delta\kappa_1\Delta\kappa_2} \quad (10a)$$

$$A_{n_1 n_2}^{(2)} = \sqrt{2S_{gg}(\kappa_{1n_1}, -\kappa_{2n_2})\Delta\kappa_1\Delta\kappa_2} \quad (10b)$$

where

$$\kappa_{1n_1} = n_1 \Delta \kappa_1 \quad \kappa_{2n_2} = n_2 \Delta \kappa_2 \quad (11)$$

$$\Delta \kappa_1 = \frac{\kappa_{1u}}{N_1} \quad \Delta \kappa_2 = \frac{\kappa_{2u}}{N_2} \quad (12)$$

$$n_1 = 0, 1, \dots, N_1 - 1 \quad \text{and} \quad n_2 = 0, 1, \dots, N_2 - 1 \quad (13)$$

$N_j, j = 1, 2$, represent the number of intervals in which the wave number axes are subdivided and $\kappa_{ju}, j = 1, 2$, are the upper cut-off wave numbers which define the active region of the power spectrum $S_{gg}(\kappa_1, \kappa_2)$ of the stochastic field. The last means that S_{gg} is assumed to be zero outside the region defined by

$$-\kappa_{1u} \leq \kappa_1 \leq \kappa_{1u} \quad \text{and} \quad -\kappa_{2u} \leq \kappa_2 \leq \kappa_{2u} \quad (14)$$

The SDF used in the numerical example (see Section 5) is of square exponential type:

$$S_{gg}(\kappa_1, \kappa_2) = \sigma_g^2 \frac{b_1 b_2}{4\pi} \exp \left[-\frac{1}{4} (b_1^2 \kappa_1^2 + b_2^2 \kappa_2^2) \right] \quad (15)$$

where σ_g denotes the standard deviation of the stochastic field and b_1, b_2 denote the parameters that influence the shape of the spectrum, which are proportional to the correlation lengths of the stochastic field along the x, y axes, respectively. The SDF of the translation field will be different from S_{gg} due to the spectral distortion caused by the transform of Eq. 8.

4 STOCHASTIC FINITE ELEMENT ANALYSIS

4.1 Stochastic stiffness matrix

It is assumed that the Young's modulus E , tensile strength f_t and fracture energy G_f of the material are represented by two dimensional uni-variate (2D-1V) homogeneous stochastic fields. The variation of E is described as follows:

$$E(x, y) = E_0 [1 + f(x, y)] \quad (16)$$

where E_0 is the mean value of the elastic modulus and $f(x, y)$ is a zero-mean homogeneous stochastic field. The two other properties are varying in a similar way. The stochastic stiffness matrix is derived using the midpoint method i.e. one integration point at the centroid of each finite element is used for the computation of the stiffness matrix. This approach gives accurate results for relatively fine meshes as that used in the numerical example keeping the computational cost at reasonable levels [15].

Using the procedure described in the previous section, a large number N_{SAMP} of sample functions are produced, leading to the generation of a set of stochastic stiffness matrices. The associated structural problem is solved N_{SAMP} times and the response variability can finally be calculated by obtaining the response statistics of the N_{SAMP} simulations.

4.2 Variability response function approach

The concept of variability response function (VRF) has been introduced in [12] as an alternative way to MCS for computing the response variability of stochastic systems. The VRF has been established for a variety of structural systems including trusses, frames, plane stress/plane

strain systems and plates with a single or with multiple correlated random properties. It is possible to express the vector of displacement variances as a function of the VRF of the system:

$$Var(\mathbf{u}) = \int_{-\infty}^{\infty} \mathbf{VRF}(\boldsymbol{\kappa}) S_{ff}(\boldsymbol{\kappa}) d\boldsymbol{\kappa} \quad (17)$$

A closed-form expression of $\mathbf{VRF}(\boldsymbol{\kappa})$ for plane stress/strain systems can be found in [17] where it is shown that it is a function of the deterministic parameters describing the geometry, material properties and loading of the structure. VRFs are useful mainly for two reasons: (i) they provide insight into the mechanisms controlling the response of stochastic systems and, (ii) they allow the establishment of spectral-distribution-free upper bounds on the response variability:

$$\int_{-\infty}^{\infty} \mathbf{VRF}(\boldsymbol{\kappa}) S_{ff}(\boldsymbol{\kappa}) d\boldsymbol{\kappa} \leq \mathbf{VRF}(\hat{\boldsymbol{\kappa}}) \int_{-\infty}^{\infty} S_{ff}(\boldsymbol{\kappa}) d\boldsymbol{\kappa} = \mathbf{VRF}(\hat{\boldsymbol{\kappa}}) \sigma_f^2 \quad (18)$$

where $\hat{\boldsymbol{\kappa}}$ is the wave number at which the VRF takes its maximum value. This upper bound is physically realizable and corresponds to the case in which the random field $f(x, y)$ becomes a sinusoid with random phase angle:

$$f(x, y) = \sqrt{2} \sigma_f \cos(\hat{\kappa}_1 x + \hat{\kappa}_2 y + \phi) \quad (19)$$

where ϕ is a random phase angle uniformly distributed between 0 and 2π and σ_f is the standard deviation of the random sinusoid.

In addition to providing a means for computing spectral-distribution-free upper bounds on the response variability, the VRF can qualitatively reveal which types of spectral density function will cause significant response variances (see Eq. 17). That is, VRFs provide insight into the importance of the shape of the spectral density functions of the random properties on the response variance.

A VRF can be alternatively estimated numerically using a fast MCS procedure based on Eq. 17. The numerical estimation of the VRF through fast MCS is very important as the closed-form analytic expressions existing in the literature involve modulating functions that are very difficult to establish even in the simplest cases of statically indeterminate linear beams [8] or statically determinate beams with nonlinear (power) constitutive laws [16]. The fast MCS procedure can be implemented into the framework of a deterministic FE code making this approach very general. In addition, this approach is usually very efficient as convergence is achieved with a number of samples as low as 10 for each wave number.

5 NUMERICAL EXAMPLE

A symmetric notched beam [10] is analyzed in this section to illustrate the capabilities of the proposed methodology. The geometry, boundary conditions, loading and FE mesh of the beam are shown in Fig. 2. The thickness of the beam is 50 mm and the notch depth is 10 mm. Four-node linear quadrilateral elements are used with an element size of $h=10\text{mm}$ in the vicinity of the notch and a 2x2 Gaussian integration rule in plane stress conditions. The uncertain parameters of the problem are the Young's modulus E , tensile strength f_t and fracture energy G_f of the material with mean values equal to 38 kN/mm^2 , 3 N/mm^2 and 0.06 N/mm , respectively. The spatial fluctuation of the uncertain parameters is described by 2D-1V homogeneous Gaussian as well as lognormal translation stochastic fields, sample functions of which are generated using

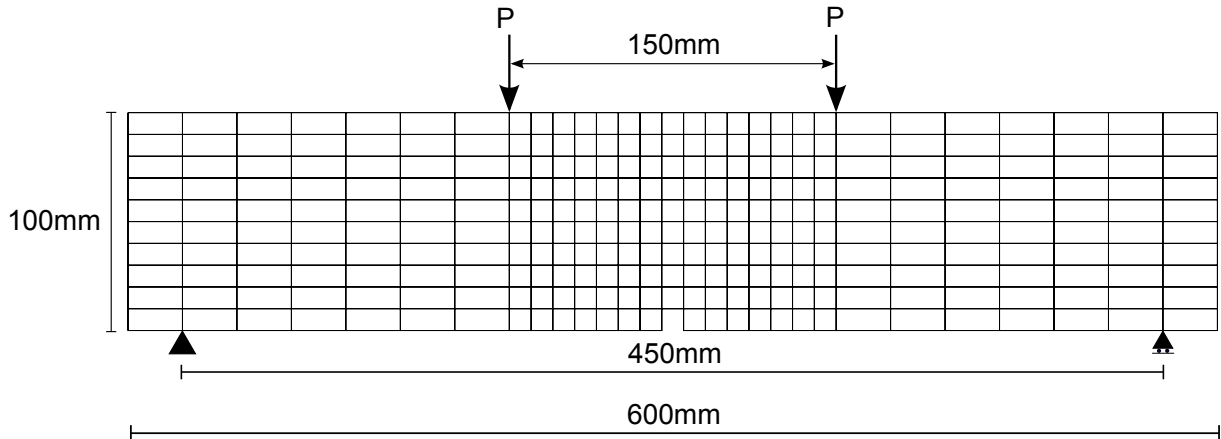


Figure 2: Notched beam (Geometry and FE mesh)

Eqs. 8, 9. Three different values ($b = 1, 10, 100$) of the correlation length parameter b ($= b_1 = b_2$) are used, corresponding to stochastic fields of low, moderate and strong correlation. The response variability is computed using MCS with a sample size equal to 100. Note that the displacement is monitored at the point where the load is applied.

Load-displacement curves corresponding to a 10% variation of E , G_f with $b = 1$ are depicted in Fig. 3. Moreover, load-displacement curves corresponding to a 20% variation of E ,

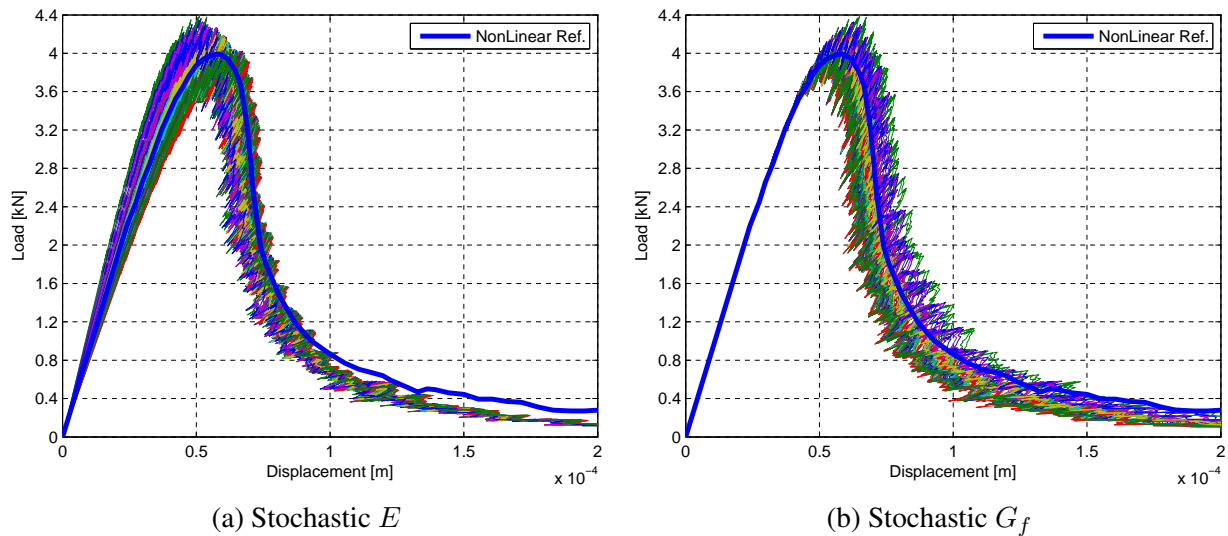


Figure 3: Load-displacement curves for stochastic parameters E and G_f with $\sigma = 10\%$ and $b = 1$ (Lognormal case).

G_f with $b = 100$ are presented in Fig. 4. As shown in Figs. 3a, 4a, the variation of E affects the stiffness of the structure. Larger values of the coefficient of variation and of the correlation length of the stochastic fields lead to more significant variability of the load-displacement curves, as expected (Fig. 4). The response variability can also be computed using the VRF, which is shown in Fig. 5 for stochastic Young's modulus. Due to its quadrant symmetry, only a quarter of this function is shown in this figure. It is worth noting the irregular shape of the VRF, which can be attributed to the saw-tooth approach used in SLA. In addition, its computation

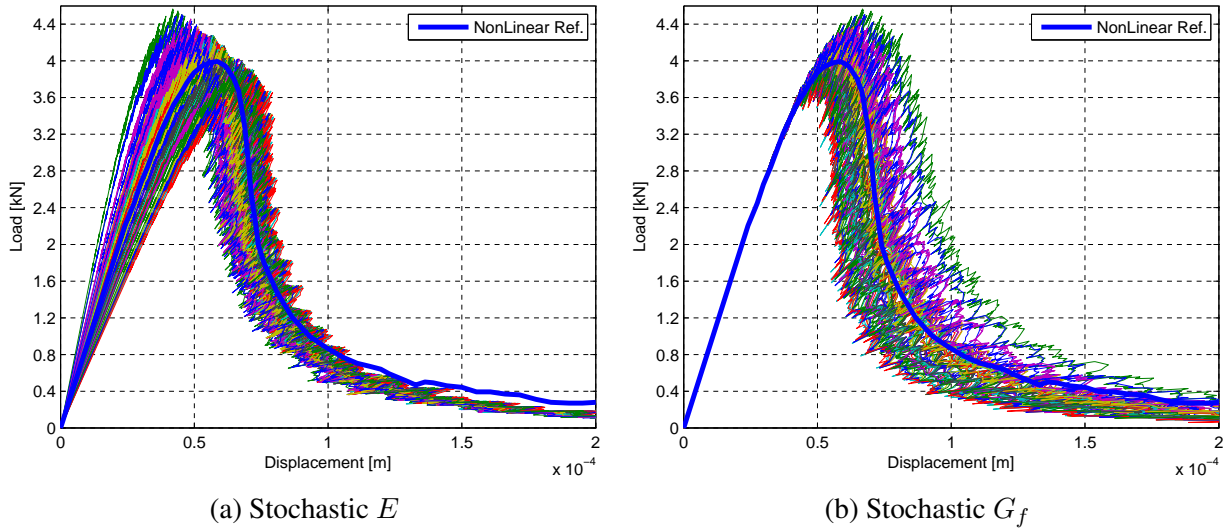


Figure 4: Load-displacement curves for stochastic parameters E and G_f with $\sigma = 20\%$ and $b = 100$ (Lognormal case).

through fast MCS can be more expensive than direct MCS in this case (especially for a small number of samples). This is due to the fact that the whole load-displacement curve is computed for each wave number pair in the fast MCS procedure.

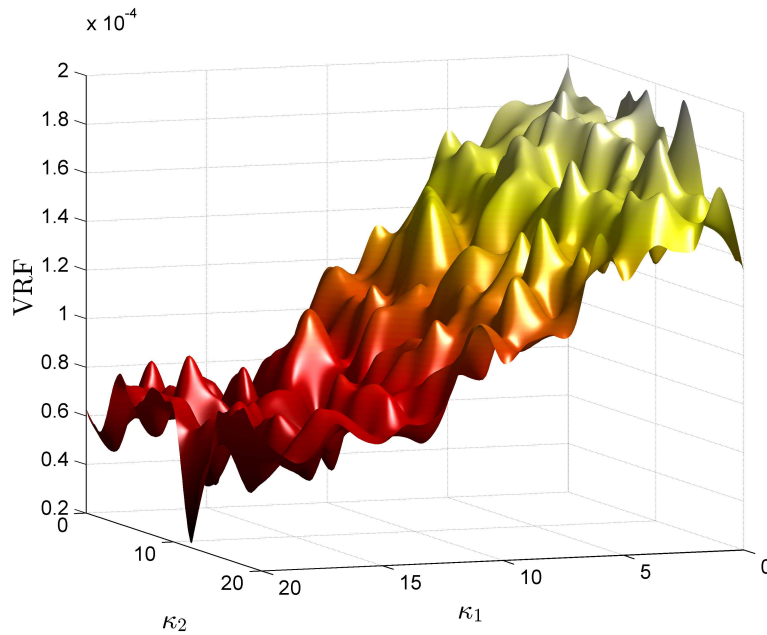


Figure 5: Variability Response Function (VRF) of peak load

6 CONCLUSIONS

In this paper, the sequentially linear analysis approach was implemented in a stochastic setting to investigate the influence of uncertain spatially varying material properties on the fracture behavior of structures made of softening materials. The uncertain properties were described by homogeneous stochastic fields using the spectral representation method in conjunction with translation field theory. The response variability was computed by means of direct Monte Carlo simulation. The influence of the variation of each random parameter as well as of the probability distribution, coefficient of variation and correlation length of the stochastic fields has been quantified. The analysis of a benchmark structure (notched beam) has shown that the load-displacement curves are affected by the spectral characteristics of the stochastic fields. The extension of SLA to the stochastic framework offers an efficient means to perform parametric investigations of the fracture behavior of structures in the case of variable material properties. The comparison of the results with existing experimental data can help to validate the assumptions made for the statistical characteristics of the stochastic fields.

ACKNOWLEDGEMENTS

This work is implemented within the framework of the research project "MICROLINK: Linking micromechanics-based properties with the stochastic finite element method: a challenge for multiscale modeling of heterogeneous materials and structures" - Action "Supporting Postdoctoral Researchers" of the Operational Program "Education and Lifelong Learning" (Action's Beneficiary: General Secretariat for Research and Technology), and is co-financed by the European Social Fund (ESF) and the Greek State. The provided financial support is gratefully acknowledged by the second author.

REFERENCES

- [1] Z.P. Bažant & L. Cedolin, *Stability of Structures: Elastic, Inelastic, Fracture and Damage Theories*. World Scientific Publishing Company, 2010.
- [2] M. DeJong, M. A.N. Hendriks & J.G. Rots, Sequentially linear analysis of fracture under non-proportional loading. *Engineering Fracture Mechanics*, **75**, 5042–5056, 2008.
- [3] M.J. DeJong, B. Belletti, M. A.N. Hendriks & J.G. Rots, Shell elements for sequentially linear analysis: Lateral failure of masonry structures. *Engineering Structures*, **31**, 1382–1392, 2009.
- [4] M. Grigoriu, Simulation of Stationary Non-Gaussian Translation Processes. *Journal of Engineering Mechanics*, **124**, 121–126, 1998.
- [5] N. Moes, J. Dolbow & T. Belytschko, A finite element method for crack growth without remeshing. *International Journal for Numerical Methods in Engineering*, **46**, 131–150, 1999.
- [6] J. Oliver, Modelling Strong Discontinuities in Solid Mechanics via Strain Softening Constitutive Equations. Part 1: Fundamentals. *International Journal for Numerical Methods in Engineering*, **39**, 35753600, 1996.

- [7] J. Oliver, A.E. Huespe & P.J. Sanchez, A comparative study on finite elements for capturing strong discontinuities: E-FEM vs X-FEM. *Computer Methods in Applied Mechanics and Engineering*, **195**, 4732–4752, 2006.
- [8] V. Papadopoulos, G. Deodatis, & M. Papadrakakis, Flexibility-based upper bounds on the response variability of simple beams. *Computer Methods in Applied Mechanics and Engineering*, **194**, 1385–1404, 2005.
- [9] J. Rots, Sequentially linear continuum model for concrete fracture. *Fracture Mechanics of Concrete Structures*, in de Borst R., Mazars, J., Pijaudier-Cabot, G. & van Mier, J. (Eds.). Lisse: Balkema, 831–839, 2001.
- [10] Jan G. Rots, S. Invernizzi, Regularized sequential linear saw-tooth softening model. *Int. J. Numer. Anal. Meth. Geomech.*, **28**, 821–856, 2004.
- [11] Jan G. Rots, B. Belletti & S. Invernizzi, Robust modeling of RC structures with an event-by-event strategy. *Engineering Fracture Mechanics*, **75**, 590–614, 2008.
- [12] M. Shinozuka, Structural Response Variability, *Journal of Engineering Mechanics*, **113**, 825–842, 1987.
- [13] M. Shinozuka & G. Deodatis, Simulation of multi-dimensional Gaussian stochastic fields by spectral representation, *Applied Mechanics Reviews (ASME)*, **49**, 29–53, 1996.
- [14] G. Stefanou & M. Papadrakakis, Stochastic finite element analysis of shells with combined random material and geometric properties. *Computer Methods in Applied Mechanics and Engineering*, **193**, 139–160, 2004.
- [15] G. Stefanou, The stochastic finite element method: Past, present and future. *Computer Methods in Applied Mechanics and Engineering*, **198**, 1031–1051, 2009.
- [16] K. Teferra & G. Deodatis, Variability response functions for beams with nonlinear constitutive laws. *Probabilistic Engineering Mechanics*, **29**, 139–148, 2012.
- [17] F.J. Wall & G. Deodatis, Variability Response Functions of Stochastic Plane Stress/Strain Problems. *Journal of Engineering Mechanics*, **120**, 1963–1982, 1994.

EMBANKMENT DAM STABILITY ANALYSIS USING FEM

Dragan Rakić¹, Miroslav Živković¹, Snežana Vulović¹, Dejan Divac², Radovan Slavković¹, Nikola Milivojević²

¹ University of Kragujevac, Faculty of Engineering
Kragujevac, Serbia
e-mail: drakic@kg.ac.rs

² Jaroslav Cerni Institute for the Development of Water Resources
Belgrade, Serbia
e-mail: divac.dejan@gmail.com

Keywords: Embankment dam, Finite element method, Dam stability.

Abstract. *This paper presents stability analysis of embankment dam with the surrounding heterogeneous rock mass using finite element method. In order to perform stability analysis of the dam and surrounding rock mass, several elastic-plastic material models for soil are customized and implemented in program package PAK. A 3D FE model of the embankment dam and the surrounding rock mass containing various material distributions according to their real distribution was made. The model includes a wider area around the dam in order to minimize the influence of the boundary conditions. The initial material parameters were determined using the identification of material parameters on the basis of the material from the dam body. Analysed dam is equipped with dam crest displacement transducers, as well as with transducers for the total and pore pressure in the clay core. Certain deviations have been noticed while comparing the measured values of these quantities with the results of the simulation. Since the analysed dam has been in operation for a long time, these deviations from the initial values of the parameters are caused due to the changes of the mechanical properties of materials during the dam operation. These changes are caused by several factors: the settlement of the dam and foundation, flushing of the material in the body of the dam and foundation, load changes, etc. In order to take into account the change of mechanical properties in materials and achieve the results of numerical simulation to describe the behaviour of the dam as close to the real behaviour, the calibration of the material parameters is carried out. Calibration of material parameters was performed using the measured displacements of the dam crest, as well as pore and total pressures in the clay core. Using the calibration we obtain new material parameters which give results of the numerical simulation that are closer to the behaviour of the real dam. In this manner we manage the dam safety and we can predict its future behaviour.*

1 INTRODUCTION

Rock-fill dams belong to the group of embankment dams, which due to their providence, adaptability and fewer demands concerning the fundament strength, represent the most frequently used type of barrier constructions. Comprehension of mechanical behaviour of dam material is essential for the design and analysis of its stability. Nowadays, finite element method is commonly used for dam stability analysis. In order to accurately reproduce mechanical behaviour of the dam using this method in stability analysis, key factor is selection of an appropriate constitutive model. Adopted constitutive model is to efficiently reproduce material behaviour of the dam being influenced by different load types. After adopting the appropriate constitutive model, it is necessary to determine its parameters. These data are often obtained by analysing sample material in the laboratory according to which material characteristics necessary for stability analysis are calculated. This is valid both for stability calculation in the construction phase and for stability calculation during dam exploitation.

As the dam, which is the subject of the paper, has been used for a long time, mechanical characteristics of dam material changed as the consequence of material consolidation and stress redistribution in the dam body. Additionally, small material particles are flushed due to the fluid flow through the dam body resulting in inhomogeneity in the dam material. Due to these reasons, adopted material parameters determined in the laboratory represent only initial parameters for strength calculations. Thus, it is necessary to conduct calibration of the dam model to assimilate numerical simulation results to the measured values.

In order to follow the changes in the dam body, transducers of stress and pore pressure are installed during the dam construction. The dam is also equipped by benchmarks for measuring crest dam displacement being conducted periodically.

After calibration of the dam model by using measured values on the real dam, calculations of object safety factors are conducted using the method of shear strength reduction. Shear strength of all materials in the dam body is gradually reduced until the failure or until the stability loss in numerical calculations.

2 CONSTITUTIVE LAWS FOR SOIL

Two constitutive models are used in the analysis of Prvonek dam stability. Generalized Hoek-Brown constitutive model [1] is used for mechanical behaviour simulation of upstream and downstream slope of the rockfill dam and surrounding rock mass whereas Mohr-Coulomb constitutive model [2] is used for mechanical behaviour simulation of clay core and sand filters. These constitutive models are adopted according to laboratory tests of materials the dam is consisted of. Both constitutive models are implemented in the program PAK [3]. Theoretical bases of the used constitutive models are presented further in the paper.

2.1 Mohr-Coulomb constitutive model

Mohr-Coulomb represents elastic-plastic constitutive model whose failure surface is in the space of principal stresses defined by hexagonal pyramid whose height coincides with the hydrostatic axis (Figure 1). This surface divides the principal stress space into the domain of purely elastic and purely plastic strains.

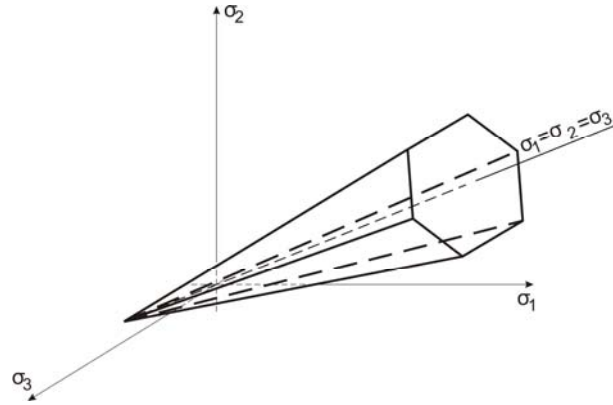


Figure 1 Mohr-Coulomb failure surface

Failure surface equation of this constitutive model is the function of the stress level and is defined by the following form:

$$f = \frac{I_1}{3} \sin \phi + \sqrt{{}^t J_{2D}} \left(\cos \theta - \frac{1}{\sqrt{3}} \sin \theta \sin \phi \right) - c \cos \phi \quad (1)$$

whereas the surface of plastic potential is defined as:

$$g = \frac{I_1}{3} \sin \psi + \sqrt{{}^t J_{2D}} \left(\cos \theta - \frac{1}{\sqrt{3}} \sin \theta \sin \psi \right) \quad (2)$$

In the equations (1) and (2), values I_1 and J_{2D} represent first stress invariant and second deviatoric stress invariant, respectively. Values ϕ , ψ and c represent material constants whereas value θ represents Lode's angle. This angle can be calculated using second and third deviatoric stress invariants in the following form:

$$\theta = \frac{1}{3} \arcsin \left(-\frac{3\sqrt{3}}{2} \frac{J_{3D}}{J_{2D}^{3/2}} \right) \quad -\frac{\pi}{6} \leq \theta \leq \frac{\pi}{6} \quad (3)$$

2.2 Generalized Hoek-Brown constitutive model

Generalized Hoek-Brown constitutive model [1] represents the elastic-plastic model whose failure surface, in the space of principal stresses, is defined by hexagonal pyramid of hyperbolic form, whose height coincides with the hydrostatic axis (Figure 2). This surface also divides the principal stress space into the domain of purely elastic and purely plastic strains.

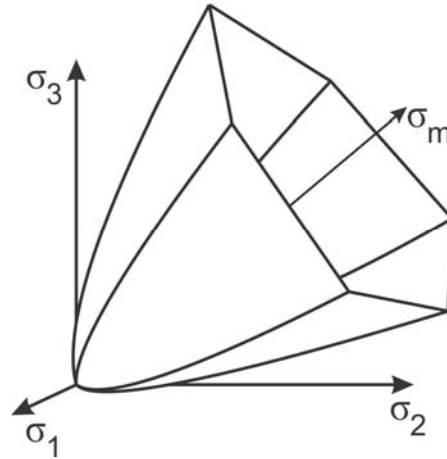


Figure 2 Failure surface of generalized Hoek-Brown constitutive model

Failure surface equation of generalized Hoek-Brown constitutive model is the function of stress level and is presented as:

$$f = \frac{I_1}{3} m_b \sigma_c^{\left(\frac{1-a}{a}\right)} - s \sigma_c^{\frac{1}{a}} + 2^{\frac{1}{a}} \left(\sqrt{J_{2D}} \cos \theta \right)^{\frac{1}{a}} + m_b \sqrt{J_{2D}} \sigma_c^{\left(\frac{1-a}{a}\right)} \left(\cos \theta - \frac{1}{\sqrt{3}} \sin \theta \right) \quad (4)$$

whereas the surface of plastic potential is formulated as:

$$g = \frac{I_1}{3} m_{bdil} \sigma_c^{\left(\frac{1-a}{a}\right)} - s \sigma_c^{\frac{1}{a}} + 2^{\frac{1}{a}} \left(\sqrt{J_{2D}} \cos \theta \right)^{\frac{1}{a}} + m_{bdil} \sqrt{J_{2D}} \sigma_c^{\left(\frac{1-a}{a}\right)} \left(\cos \theta - \frac{1}{\sqrt{3}} \sin \theta \right) \quad (5)$$

Values I_1 and J_{2D} represent first stress invariant and second deviatoric stress invariant, whereas m , σ_c , s and a are material constants. Lode's angle θ is calculated using the equation(3).

3 METHOD OF SAFETY EVALUATION

3.1 Overview of shear strength reduction method

In the stability analysis of the Prvonek dam, shear strength reduction (SSR) method [4] was used. Shear strength reduction method represents the use of finite element method for calculation of construction safety factor with a gradual decrease of shear material strength until reached the state of boundary equilibrium. In other words, material shear strength is reduced until there is a convergence of numerical solutions. The maximum value of the strength reduction factor, which the stability condition is satisfied for, represents the safety factor S of the structure [5]. The procedure of the shear strength reduction method for both constitutive models is described in this paper.

3.2 SSR using Mohr-Coulomb material model

In the case of using Mohr-Coulomb model, shear stress during failure is described by equation:

$$\tau = c + \sigma \tan \phi \quad (6)$$

Reduced shear strength for Mohr-Coulomb material model can be presented in the equation:

$$\frac{\tau}{F} = \frac{c}{F} + \sigma \frac{\tan \phi}{F} \quad (7)$$

where τ is shear stress during failure, σ is corresponding normal stress, c and ϕ are material constants (cohesion and internal friction angle), whereas F represents shear strength reduction factor. Shear strength reduction of this model can be schematically presented as in (Figure 3).

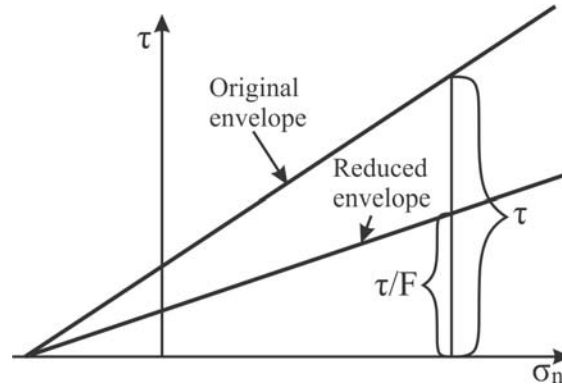


Figure 3 Shear strength reduction for Mohr-Coulomb model

In order to determine safety factor using SSR method, it is necessary to determine maximum value of shear strength reduction factor F with satisfied stability condition. Numerically, this indicates the increase of shear strength reduction factor until there is a convergence of numerical calculation within the given tolerance. In the case of exceeded stability, shear strength of material is exceeded as well which is manifested through divergence in numerical calculation.

Equation (7) indicates that it is necessary to determine maximum value of shear strength reduction F with satisfied stability condition or to calculate the following:

$$c_r = \frac{c}{F} \quad \phi_r = \arctan\left(\frac{\tan \phi}{F}\right) \quad (8)$$

According to the equation (8), it is concluded that shear strength reduction in Mohr-Coulomb model is based on reduction of material constants c and ϕ . Described procedure is implemented in the program PAK and is used in stability analysis of Prvonek dam.

3.3 SSR using generalized Hoek-Brown material model

As it was previously mentioned, shear strength defined using generalized Hoek-Brown failure surface has nonlinear character [6], so reduced shear strength cannot be calculated using simple reduction of material parameters as in the previous case.

Shear strength reduction of constitutive model with nonlinear failure surface consists of the following steps:

- Reduction of failure envelope by shear strength factor F ,
- Determination of material parameters corresponding to the reduced envelope using method for error minimization,
- Use of calculated parameters describing reduced failure curve in the repeated FEM analysis.

Relations for shear stress are defined using the principal stresses in the following form [1]:

$$\tau = (\sigma_1 - \sigma_3) \frac{\sqrt{1 + am_b \left(m_b \frac{\sigma_3}{\sigma_{ci}} + s \right)^{a-1}}}{2 + am_b \left(m_b \frac{\sigma_3}{\sigma_{ci}} + s \right)^{a-1}} \quad (9)$$

Reducing the shear stress equation (9) using shear strength reduction factor F , reduced failure envelope is obtained as (Figure 4):

$$\tau^{red} = \frac{\tau_f}{F} = (\sigma_1 - \sigma_3) \frac{\sqrt{1 + a^{red} m_b^{red} \left(m_b^{red} \frac{\sigma_3}{\sigma_{ci}^{red}} + s^{red} \right)^{a^{red}-1}}}{2 + a^{red} m_b^{red} \left(m_b^{red} \frac{\sigma_3}{\sigma_{ci}^{red}} + s^{red} \right)^{a^{red}-1}} \quad (10)$$

where σ_{ci}^{red} , m_b^{red} , s^{red} and a^{red} represent material parameters of reduced failure envelope and they are to be determined.

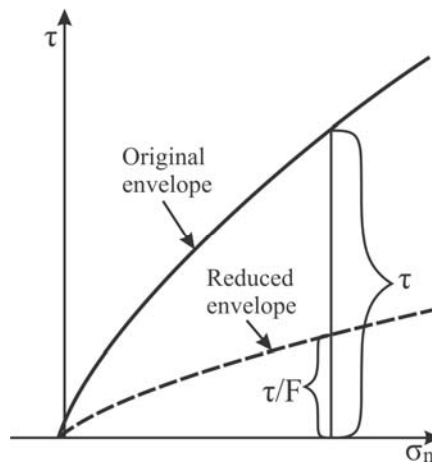


Figure 4 Shear strength reduction for Hoek-Brown model

New material parameters in the equation (10) are not possible to be determined directly, as in the previous case, so it is necessary to use some error minimization methods (fitting):

$$\varepsilon(\sigma_n)^2 = (\tau^{apr} - \tau^{red})^2 \quad (11)$$

Values τ^{apr} and τ^{red} represent approximated and reduced values of shear stress, respectively. Parameters calculated in this manner are used in the repeated calculation of object stability.

4 CALIBRATION OF CONSTITUTIVE LAW PARAMETERS

As it is previously mentioned, parameter determining of adopted constitutive models is essential for accuracy of numerical simulation in embankment dams. Samples of all geotechnical environments of the dam body are analysed in the laboratory. These analyses obtained the data necessary to define failure surface of the corresponding constitutive models [7].

Result of shear test with estimated failure surface for one geotechnical environment is presented in Figure 5. Failure surface of adopted constitutive model is obtained by fitting the experimental results and failure surface with applying the following condition:

$$\varepsilon = (\tau^* - \tau_f)^2 \rightarrow \varepsilon_{\min} \quad (12)$$

In the equation (12) value τ^* represents shear stress during failure obtained through analysis, whereas τ_f is calculated shear stress for the same value of the normal stress. Value ε represents estimation error which is necessary to be minimized.

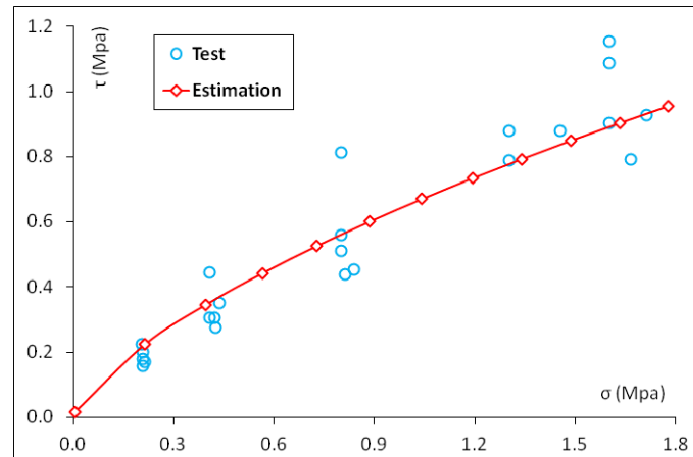


Figure 5 Results of material parameter identification

Determining of material constants represents the input for dam stability calculation. However, besides determining of material constants there is a certain deviation in numerical simulation results from the results of measuring on the real dam. This deviation is caused by dam material inhomogeneity as the consequence of different settlements as well as of dam material degradation throughout time. This leads to redistribution of the stress state in the dam body so the initial parameters are to be modified and the dam model calibration is to be conducted [8]. Stresses and/or displacements can be used as model calibration values (multicriteria optimization).

5 STABILITY ANALYSIS OF THE DAM

5.1 Main features of the dam

Construction of analysed Prvonek dam is a rock fill embankment with a inclined central clay core and filter zones (Figure 6). On the spot of the dam, valley is of asymmetrical ravine type with the slope on the left riverside of 45°, and on the right of about 35°. Upstream the dam, the valley is widened which morphologically makes the barrier spot more suitable for accumulation formation.

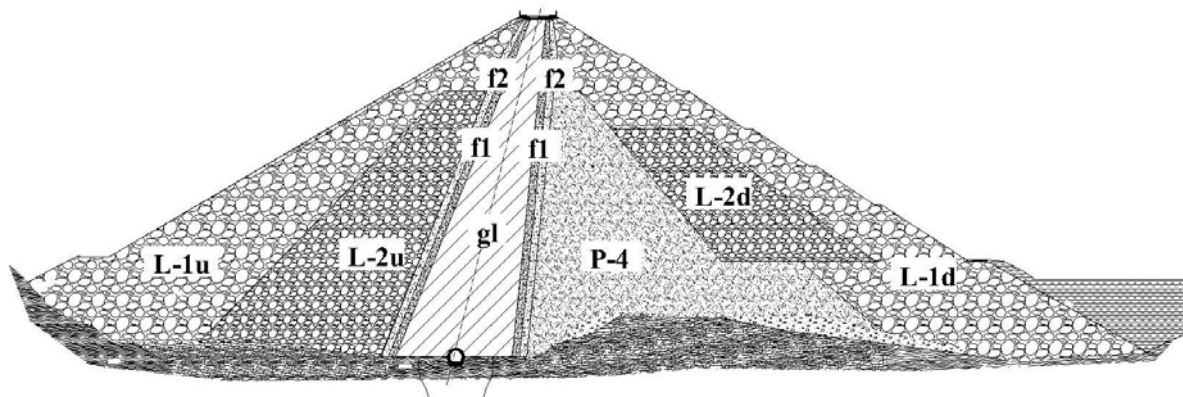


Figure 6 Cross-section of the dam

Terrain of barrier spot in the surrounding of barrier construction is modelled with the dimensions in the base, 498 x 1000 meters, from elevation of 370 to 630 metres. Model boundaries include a wider area around the object with the aim of setting the real boundary conditions as well as all proper quasi-homogenous zones. 3D 8-node finite elements with incompatible modes are used for modelling. A 3D mesh of finite elements is also developed with the total of 94986 nodes and 87128 elements. For dam stability analysis program PAK [3] is used. Finite element mesh of the dam model with surrounding rock mass is presented in Figure 7.

Natural boundary conditions are used in the analysis: horizontal node displacement is restricted on the model side boundaries, vertically on the boundary plane whereas displacements are restricted in all the directions on the lower model boundary.

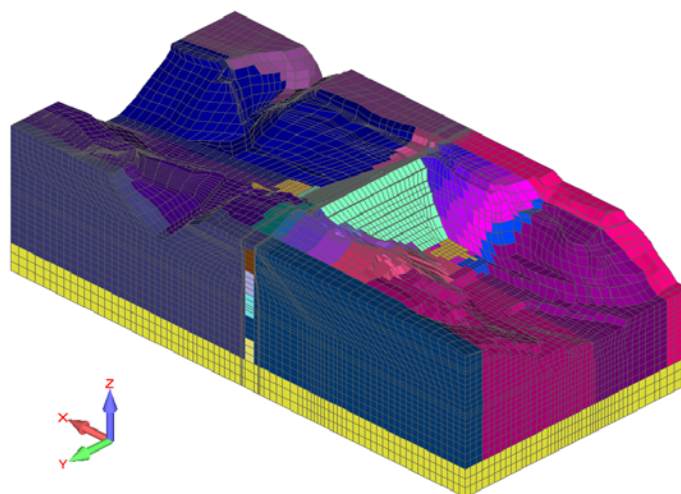


Figure 7 FE model of the dam and environment

Criteria for dam stability analysis are considered from the aspect of upstream and downstream slope stability. Minimal safety factors [9] are presented in Table 1.

Analysis condition	Required minimum safety factor	Slope
End-of-Construction	1.3	Upstream and Downstream
Steady seepage	1.5	Downstream
Maximum surcharge poo	1.4	Downstream
Rapid drawdown	1.1-1.3	Upstream

Table 1 Required factors of safety

5.2 Model calibration

In order to consider water flow through the dam, filtration analysis was previously conducted. According to these calculations, filtration forces and pore pressures in the model are obtained. In order to determine the accurate distribution of these loads, it is also necessary to conduct the calibration of filtration model parameters (Figure 8). Thus, effective instead of total stresses are used in the strength calculation:

$$\sigma_{ij}' = \sigma_{ij} + \delta_{ij} p \quad (13)$$

where: σ_{ij}' - effective stresses, σ_{ij} - total stresses, p - pore pressures.

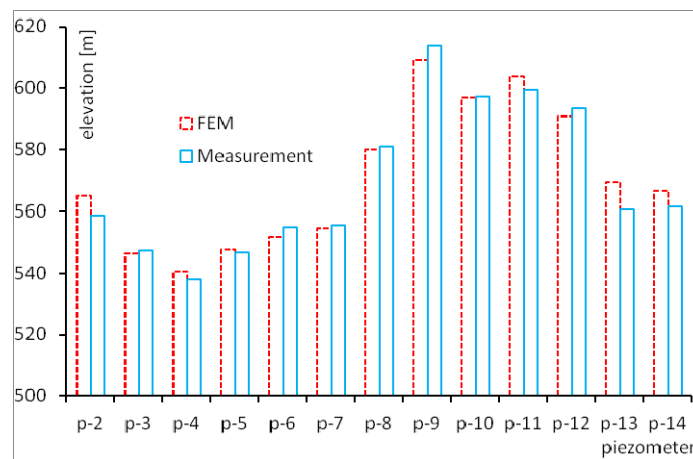


Figure 8 Pore pressures

After the use of such obtained material parameters, calculations are repeated and dam crest displacements of measured values are compared to the values obtained in numerical calculation (Figure 9 and Figure 10).

According to the analysis of measured displacement values, it is concluded that a year after instalment of measuring devices there were no significant dam crest displacements whereas all the measuring was conducted with slight changes of water level in accumulation. Measuring conducted two years from instalment of measuring devices show a significant displacement increase in horizontal direction (downstream), with a slight change of water level in accumulation, which is caused by dam material creep.

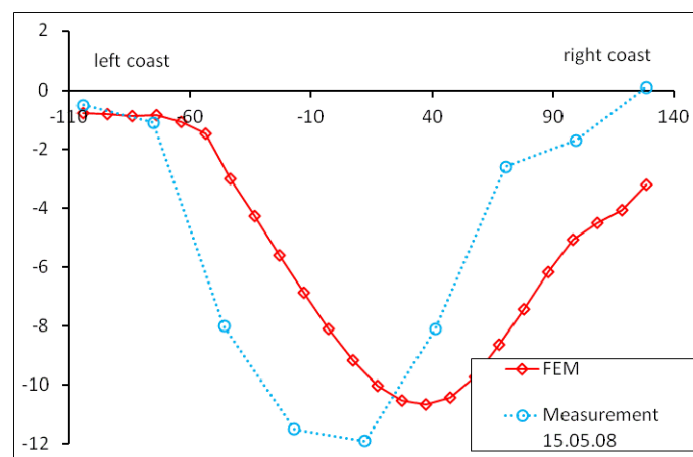


Figure 9 Horizontal displacement of the dam crest – downstream

Since used material models do not consider the creep effect, calibration of material constants is conducted according to the measured values of displacement in the first year after instalment of measuring devices.

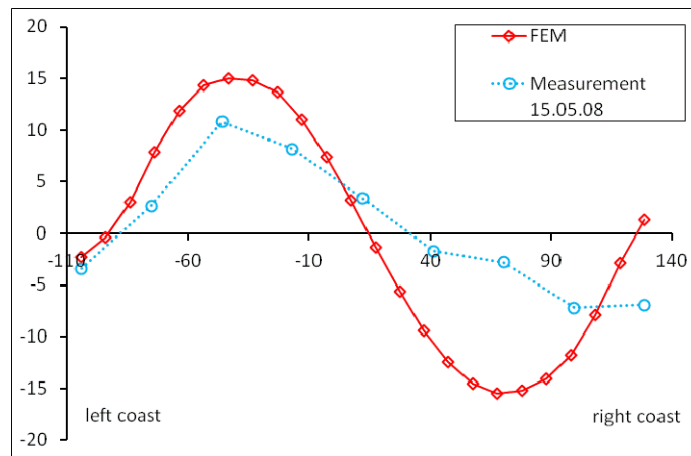


Figure 10 Horizontal displacement of the dam crest - transverse

Analysis of obtained displacements indicates that the displacement character obtained in FEM simulation corresponds to the character of measured displacements.

5.3 Analysis results

Stress-strain analyses were conducted using material parameters adopted after the calibration. Following stress-strain analyses were conducted [9]:

- Stability calculation during steady-state flow on normal water level.
- Stability calculation during steady-state flow on maximum water level.
- Analysis of rapid drawdown. Simulation of rapid drawdown was conducted from the elevation level of 614.7 meters to the level of 580.00 meters in 4.5-day period.
- Analysis of earthquake effect. After setting of initial conditions, quasi-static analysis was done with given horizontal acceleration. The influence of accumulation on the dam was considered by giving hydrodynamic pressure according to Zangar distribution [10].

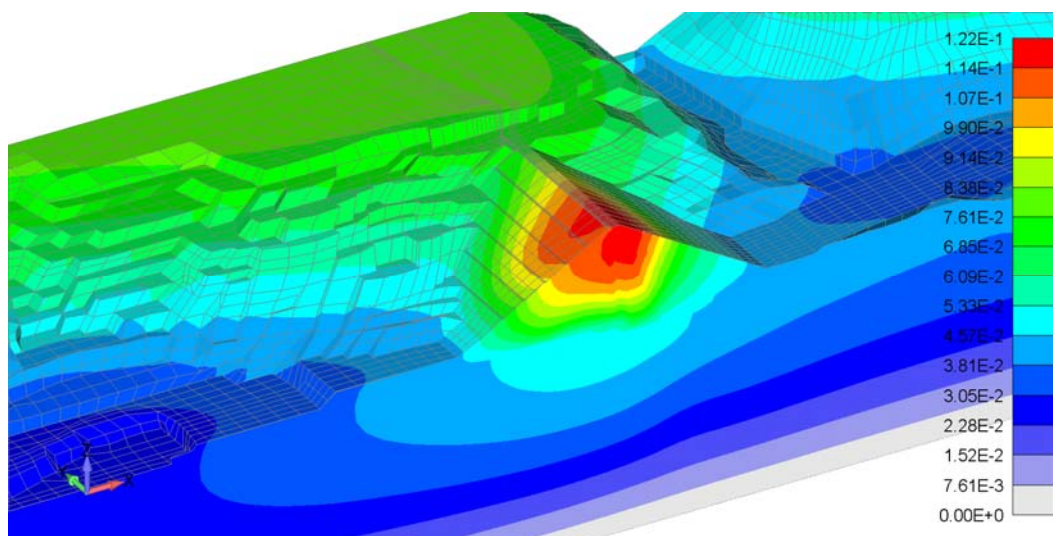


Figure 11 Total displacement distribution (y= 0.0 m)

Total displacement distribution for the case of stationary flow on the normal water level is shown in Figure 11. Maximum displacement (78.5mm) was observed in the core zone of the dam.

Plastic strain distribution for the case of stationary flow on the normal water level (613.56m) is shown in Figure 12. Maximum value of plastic strain appears in the core and filter zone closer to upstream dam slope.

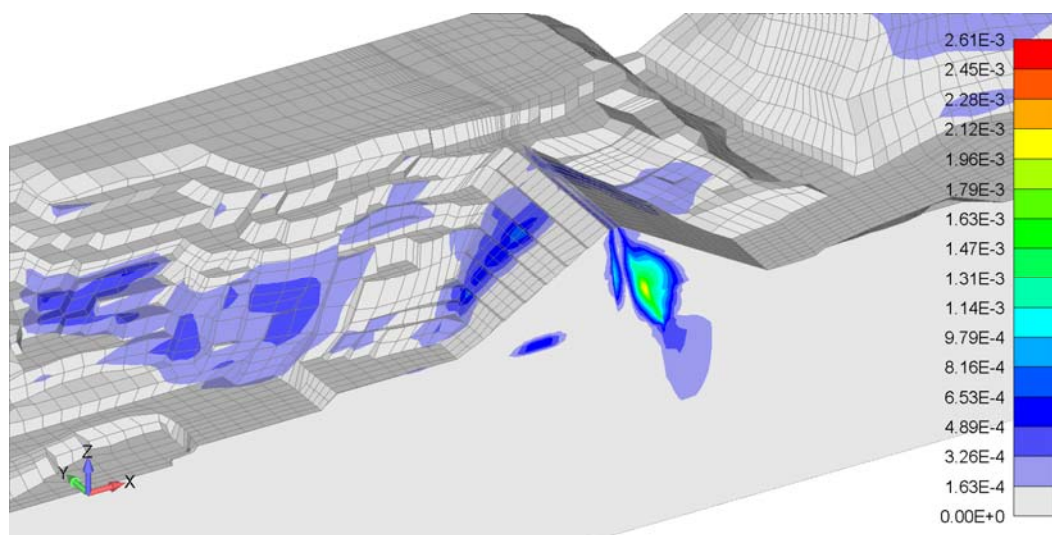


Figure 12 Equivalent plastic strain distribution ($y=0.0$ m)

After the analysis, calculations of dam safety factor were conducted using the shear strength reduction method of all the materials in the dam body according to the previously described procedure. Obtained safety factors for all analysed cases are greater than demanded values of safety factors presented in Table 1.

6 CONCLUSIONS

Stress-strain analysis of the Prvonek dam, which represents the central object of water supply system in city of Vranje, was conducted. A 3D model, based on finite element method was formed for stress-strain analysis. During numerical model forming, the analysis of results of geophysical and geomechanical researches related to engineering features of rock mass was done. Parameterization of abstracted quasi-homogenous zones in terms of parameters for stress-strain analysis was conducted.

Stress-strain processes were analysed using elastic-plastic model in order to obtain distribution of pore pressures in numerical model. After the obtained loads, construction stability was calculated.

In numerical analysis of dam stability generalized Hoek-Brown and Mohr-Coulomb constitutive models were used. All material samples embedded in the dam body were analysed to obtain the initial material parameters of adopted constitutive models. However, besides this material constant determining, there are certain discordances between FEM simulation and the results of measuring on the dam. Deviations are caused by material inhomogeneity of the real object (consolidation, flushing) during the time. In order to increase accuracy of stress-strain calculations, after determining material parameters, dam model calibration was done using multicriteria optimization.

Measuring markers were set on the real dam in order to implement model calibration on displacements. Two years of measuring after instalment of measuring devices proved signifi-

cant increase of displacement in horizontal direction with a slight change of water level in accumulation. This was caused by creep dam material. As available constitutive models do not consider the creep effect, calibration of material constants was conducted according to the measured displacement values in the first year after the instalment of measuring devices.

After the stress-strain analysis for all defined cases of loads, global dam safety factor was obtained. This was conducted using the method of shear strength reduction factor. Obtained safety factors for all analysed cases were higher than minimum approved values for this type of dam so it is concluded that the analysed Prvonek dam is stable.

Acknowledgements

The authors gratefully acknowledge partial support by Ministry of Science and Technology of the Republic of Serbia, grants TR37013 and TR32036.

REFERENCES

- [1] E. Hoek, C. Carranza-Torres / B. Corkum, „Hoek-Brown failure criterion - 2002 edition,“ u *Proceedings of the 5th North American Rock Mechanics Symposium and the 17th Tunnelling Association of Canada: NARMS-TAC 2002*, Toronto, Canada, 2002.
- [2] Balmer, „A general analytical solution for Mohr's envelope,“ *American Society for Testing and Materials*, vol. 52, pp. 1260-1271, 1952.
- [3] M. Kojić, R. Slavković, M. Živković / N. Grujović, „PAK-finite element program for linear and nonlinear structural analysis and heat transfer,“ University of Kragujevac, Faculty of Engineering, Kragujevac.
- [4] W. Fu / Y. Liao, „Non-linear shear strength reduction technique in slope stability calculation,“ *Computers and Geotechnics*, t. 37, pp. 288-298, 2010.
- [5] A. Nakamura, F. Cai / K. Ugai, „Embankment basal stability analysis using shear strength reduction finite element method,“ 2008.
- [6] R. E. Hammah, T. E. Yacoub, B. C. Corkum / J. H. Curran, „The Shear Strength Reduction Method for the Generalized Hoek-Brown Criterion,“ u *Proceedings of the 40th U.S. Symposium on Rock Mechanics Alaska Rocks 2005 Conference (ARMA)*, held in Anchorage, Alaska, USA, June 2005.
- [7] P. Pramthawee, P. Jongpradist / W. Kongkitkul, „Evaluation of hardening soil model on numerical simulation of behaviors of high rockfill dams,“ *Songklanakarinn Journal of Science and Technology*, t. 33, br. 3, pp. 325-334, 2011.
- [8] P. J. & P. K. P. Pramthawee, „3D numerical analysis of high rockfill dam construction with consideration of shear dilatancy,“ u *Rock Mechanics, Fuenkajorn & Phien-wej*, 2011.
- [9] U.S. Army Corps of Engineers, „Engineering and Design - Slope Stability - EM 1110-2-1902,“ U.S. Army Corps of Engineers, Washington DC, 2003.
- [10] V. Saouma, „MERLIN - Theory Manual,“ University of Colorado, Boulder, Boulder, 2006.

IMPLICIT INTEGRATION METHOD OF SHAPE MEMORY ALLOYS CONSTITUTIVE MODEL

Vladimir Lj. Dunić¹, Radovan B. Slavković², Nenad M. Busarac¹, Vukašin R. Slavković¹
and Miroslav M. Živković²

¹Faculty of Engineering, University of Kragujevac
address
e-mail: {vladimirdunic,nbusarac,vukasinsl}@gmail.com

² Faculty of Engineering, University of Kragujevac
address
e-mail: {radovan,zile}@kg.ac.rs

Keywords: shape memory alloys, implicit stress integration, trial stress direction, large strain theory, governing parameter method

Abstract. *Shape memory alloys (SMA) material is widely used in many applications of interest where it is necessary to recover permanent strains. There are many constitutive models which describe that phenomenon. The SMA model described by Lagoudas in [1] and [2] is modified and implemented into the PAK software package [3]. Development of this model is motivated by previous papers of Lagoudas and Auricchio groups and it considers governing parameter method applied on phenomenological behavior of SMA materials. All variables are derived to depend on effective values of stress and strain and now we have only one scalar equation to solve in the integration point. Critical thermodynamic force is also modified to match new integration method. Integration is done for the deviatoric and mean stress using trial stress direction for each time step. Difference between the return mapping algorithm and the integration in the trial deviatoric stress direction can be neglected for nearly proportional loading [2]. The second case provide possibility to solve large strain problems in the similar manner, using the same constitutive model relations. One dimensional loaded examples of super-elasticity, shape memory and thermally induced phase transformation effect proposed by Lagoudas group are verified by modified governing parameter method using the PAK software. Several large strain examples are examined under uniaxial and non-proportional loading and the results are compared with the experimental results proposed in referenced papers.*

1 INTRODUCTION

Shape memory alloys are smart materials which have possibility to recover permanent deformations. Those deformations occur due to phase transformation between austenite and martensite. Austenite transforms to martensite by lattice shearing mechanism [4]. The phase transformation can produce two effects: superelasticity $T > A_f$ and the shape memory effect $T < A_s$, where T is given temperature and A_s and A_f are austenite start and finish temperature. Super- or pseudo- elasticity produces inelastic strains recoverable during the unloading process. The shape memory effect produces a permanent strain which can be recovered by heating [4]. The SMAs are widely used materials in the aerospace, medical and petroleum industries [5]. There are two groups of such models: micromechanics-based models and phenomenological models [1]. In the first group the information about the microstructure of the SMA are necessary for prediction, while the phenomenological models need energy potentials over the volume. In this work, we propose a model inspired by the Lagoudas theory [6]. The Lagoudas model, implemented by UMAT subroutine into Abaqus, was modified and adopted using the governing parameter method proposed by Kojic [7]. All variables are derived to depend on effective values of stress, strain and martensitic volume fraction. The critical thermodynamic force is modified to match new integration method. Integration is done for the deviatoric and mean stress using trial stress direction. Constitutive model verification is difficult due to the lack of experimental data, but some experimental results [8] are of great importance. The obtained results of numerical simulations are in close agreement with the results from literature [9] in one dimensional loaded examples of super-elasticity and shape memory. The large strain example is examined under non-proportional loading and the results are similar with the experimental results proposed in referenced papers.

2 CONSTITUTIVE MODEL FORMULATION

2.1 GIBBS FREE ENERGY FUNCTION

The constitutive model for any material can be derived from a free energy function and internal and external state variables. The phase transformation model for SMA materials formulated by Boyd and Lagoudas [10] and Lagoudas [6] is basic framework for this work. The external state variables are total stress $\boldsymbol{\sigma}$ and temperature T . Internal state variables are the martensitic volume fraction ξ and the transformation strain \mathbf{e}_{tr} . We have transformed thermodynamic potential given by Gibbs free energy function G into the two different form for the forward and reverse transformation. We are starting from the basic form of Gibbs free energy given by Qidwai and Lagoudas [11]

$$G(\boldsymbol{\sigma}, T, \xi, \mathbf{e}_{tr}) = -\frac{1}{2\rho} \boldsymbol{\sigma} : \mathbf{C}^{-1} : \boldsymbol{\sigma} - \frac{1}{\rho} \boldsymbol{\sigma} : [\boldsymbol{\alpha}(T - T_0) + \mathbf{e}_{tr}] + c \left[(T - T_0) - T \ln\left(\frac{T}{T_0}\right) \right] - s_0 T + u_0 + \frac{1}{\rho} f(\xi) \quad (1)$$

where T_0 is a reference temperature. The function $f(\xi)$ is a transformation hardening function. The material parameters c , u_0 , s_0 , \mathbf{C}^{-1} , $\boldsymbol{\alpha}$, c and u_0 are the effective specific heat, the effective specific internal energy, the effective specific entropy, the effective compliance tensor and the effective thermal expansion tensor, respectively. These effective material parameters can be determined using pure phases parameters and the martensitic volume fraction ξ by the rule of mixture.

Using the Legendre transformation between Gibbs free energy, the internal energy u and the first and second law of thermodynamics substituted into the Clausius-Planck inequality, we obtain [6]:

$$D_{int} = \boldsymbol{\sigma} : \dot{\mathbf{e}}_{tr} + \left(-\rho \frac{\partial G}{\partial \xi} \right) \dot{\xi} \geq 0 \quad (2)$$

which states that in irreversible processes the internal dissipation of energy is greater or equal zero.

2.2 EVOLUTION EQUATIONS OF STATE VARIABLES

The main assumption for the evolution of internal state variables is: any change in the current microstructural state of the material is strictly a result of a change in the martensitic volume fraction [1, 6, 10, 11]. In that case, it is assumed that transformation strain rate is:

$$\dot{\mathbf{e}}_{tr} = \boldsymbol{\Lambda}_{tr} \dot{\xi}; \quad \boldsymbol{\Lambda}_{tr} = \begin{cases} \frac{3}{2} H \frac{\mathbf{S}}{\bar{S}}; & \dot{\xi} > 0 \\ H \frac{\mathbf{e}_{tr}}{\bar{e}_{tr}}; & \dot{\xi} < 0 \end{cases} \quad (3)$$

where $\boldsymbol{\Lambda}_{tr}$ is the transformation tensor and H is a maximum uniaxial transformation strain. The transformation tensor will be in the direction of the deviatoric stress \mathbf{S} during the forward phase, while, during the reverse phase, it will be in the direction of transformation total strain tensor \mathbf{e}_{tr} [6]. The deviatoric stress tensor \mathbf{S} , the effective (von Mises equivalent) stress \bar{S} and the effective transformation strain \bar{e}_{tr} are defined by:

$$\mathbf{S} = \boldsymbol{\sigma} - (\sigma_m) \mathbf{1}; \quad \bar{S} = \sqrt{\frac{3}{2} \mathbf{S} : \mathbf{S}}; \quad \bar{e}_{tr} = \sqrt{\frac{2}{3} \mathbf{e}_{tr} : \mathbf{e}_{tr}} \quad (4)$$

where σ_m is mean stress and $\boldsymbol{\sigma}$ is total stress tensor.

Substituting the equation (3) into the Clausius-Planck inequality (2), we obtain:

$$\left(\boldsymbol{\sigma} : \boldsymbol{\Lambda} - \rho \frac{\partial G}{\partial \xi} \right) \dot{\xi} = \pi \dot{\xi} \geq 0 \quad (5)$$

where π is the general thermodynamic force. For the given Gibbs free energy (1), the explicit evaluation of π is:

$$\begin{aligned} \pi(\boldsymbol{\sigma}, T, \xi) = & \boldsymbol{\sigma} : \boldsymbol{\Lambda} + \frac{1}{2} \boldsymbol{\sigma} : \Delta \mathbf{C}^{-1} : \boldsymbol{\sigma} + \boldsymbol{\sigma} : \Delta \boldsymbol{\alpha} (T - T_0) - \\ & \rho \Delta c \left[(T - T_0) - T \ln \left(\frac{T}{T_0} \right) \right] + \rho \Delta s_0 T - \rho \Delta u_0 - \frac{\partial f}{\partial \xi} \end{aligned} \quad (6)$$

The transformation function Φ is introduced by Lagoudas as [6, 11]:

$$\Phi = \begin{cases} \pi - Y; & \dot{\xi} > 0 \\ -\pi - Y & \dot{\xi} < 0 \end{cases} \quad (7)$$

where Y is threshold value. The transformation function Φ should satisfy the condition $\Phi = 0$ during phase transformation. It represents transformation surfaces for $0 < \xi < 1$ and the two boundary surfaces for $\xi = 0$ and $\xi = 1$ of each transformation surface family.

Different hardening functions $f(\xi)$ can be used to describe interaction between the austenit and the martensit. Cosine model proposed by Liang and Rogers is given as[6, 12]:

$$f(\xi) = \begin{cases} \int_0^\xi -\frac{\rho\Delta s_0}{a_c^M} [\pi - \arccos(2\xi - 1)] d\xi + (\mu_1^c + \mu_2^c)\xi; & \dot{\xi} > 0 \\ \int_0^\xi -\frac{\rho\Delta s_0}{a_c^A} [\pi - \arccos(2\xi - 1)] d\xi + (\mu_1^c + \mu_2^c)\xi; & \dot{\xi} < 0 \end{cases} \quad (8)$$

In above equations $a_c^M, a_c^A, \mu_1^c, \mu_2^c$ are transformation strain hardening parameters. Introducing equation (8) into the (6) and using the parameters for the cosine model given by Liang and Rogers [12] using the previous equations in (7), the final form of the transformation function is obtained as:

$$\Phi = \begin{cases} H\bar{S} + \frac{1}{2} \left(\frac{1}{3}\bar{S}^2 \left(\frac{1}{G^M} - \frac{1}{G^A} \right) + 3\sigma_m^2 \left(\frac{1}{c_m^M} - \frac{1}{c_m^A} \right) \right) + 3\sigma_m (\alpha^M - \alpha^A) \Delta T + \\ \rho\Delta s_0 (T - M_s) - \rho\Delta s_0 \frac{M_s - M_f}{\pi} [\arccos(2\xi - 1) - \pi]; & \dot{\xi} > 0 \\ -\mathbf{S}^* : {}^t \mathbf{e}_{tr} \frac{H}{t_{etr}} + 3G\Delta\xi H^2 - \frac{1}{2} \left(\frac{1}{3}\bar{S}^2 \left(\frac{1}{G^M} - \frac{1}{G^A} \right) + 3\sigma_m^2 \left(\frac{1}{c_m^M} - \frac{1}{c_m^A} \right) \right) - \\ 3\sigma_m (\alpha^M - \alpha^A) \Delta T - \rho\Delta s_0 (T - A_f) + \\ \rho\Delta s_0 \frac{A_f - A_s}{\pi} [\arccos(2\xi - 1) - \pi]; & \dot{\xi} < 0 \end{cases} \quad (9)$$

3 NUMERICAL IMPLEMENTATION OF STRESS INTEGRATION PROCEDURE

3.1 STRESS INTEGRATION

The most common strategy for implicit stress integration procedure for the rate independent models is the return mapping [7]. It consists of two steps: (a) prediction of the trial elastic state (elastic predictor), and (b) stress correction due to the phase transformation (inelastic corrector). The trial elastic deviatoric stress ${}^{t+\Delta t} \mathbf{S}_*^E$ and the mean stress ${}^{t+\Delta t} \sigma_m^E$ are calculated with the assumption that there is no phase transformation in the time step:

$${}^{t+\Delta t} \mathbf{S}_*^E = 2{}^{t+\Delta t} G {}^{t+\Delta t} \mathbf{e}_*^{E'}; \quad {}^{t+\Delta t} \sigma_m^E = {}^{t+\Delta t} c_m ({}^{t+\Delta t} e_{*m}^E - {}^{t+\Delta t} e^{th}) \quad (10)$$

In the case of the small strains, the trial elastic deviatoric strain ${}^{t+\Delta t} \mathbf{e}_*^{E'}$, the trial elastic mean strain ${}^{t+\Delta t} e_{*m}^E$ and thermal strain ${}^{t+\Delta t} e^{th}$ are:

$${}^{t+\Delta t} \mathbf{e}_*^{E'} = {}^{t+\Delta t} \mathbf{e} - e_m \mathbf{I} - {}^t \mathbf{e}^{tr}; \quad {}^{t+\Delta t} e_{*m}^E = \frac{1}{3} \sum_{k=1}^3 {}^{t+\Delta t} e_{kk}; \quad {}^{t+\Delta t} e^{th} = {}^{t+\Delta t} \alpha \Delta T \quad (11)$$

where ${}^{t+\Delta t} G$ is shear modulus, ${}^{t+\Delta t} c_m$ is 1/3 of bulk modulus K and ${}^{t+\Delta t} \alpha$ is coefficient of thermal expansion, which depend on ξ . The total strain at the end of time step and the transformation at the start of the time step are ${}^{t+\Delta t} \mathbf{e}$ and ${}^t \mathbf{e}^{tr}$, respectively.

3.2 ITERATIVE SOLUTION OF TRANSFORMATION FUNCTION EQUATION

This work is based on developments from the literature and it is inspired by Kojic and Bathe [7], Simo and Hughes [13] and Qidwai and Lagoudas [1, 11]. The total strain \mathbf{e} and temperature T are given variables and the SMA constitutive model outputs total stress $\boldsymbol{\sigma}$ and updates internal variables. The problem is defined by total strain relation given by Lagoudas in [6], the flow rule (3) and the transformation function (9). First, a thermoelastic prediction assumes that the transformation strain increment $\Delta {}^{t+\Delta t} \mathbf{e}_{tr}$ is zero (11). The governing parameter method has

been used instead the convex cutting plane algorithm. The difference between them is in the direction of the transformation correction. In the convex cutting plane algorithm, direction of the transformation correction is changed during the iteration, while, the governing parameter method assumes trial deviatoric stress direction (10) from the beginning of the time step.

Increment of transformation strain in time step is:

$$\Delta^{t+\Delta t} \mathbf{e}_{tr} = \Delta^{t+\Delta t} \xi^{(k)} \mathbf{\Lambda} \left({}^{t+\Delta t} \mathbf{S}_*^E \right) \quad (12)$$

The algorithm begins at iteration $k = 0$ with the thermoelastic prediction (10) with assumption that there is no evolution in the internal variables ${}^{t+\Delta t} \mathbf{e}_{tr}^{(0)} = {}^t \mathbf{e}_{tr}$ and ${}^{t+\Delta t} \xi^{(0)} = {}^t \xi$ [6].

The transformation function is calculated with trial stress and the condition ${}^{t+\Delta t} \Phi^{(0)} \leq 0$ is checked for violation [1]. If there is no violation, the elastic solution is accepted as final. If ${}^{t+\Delta t} \Phi^{(0)} \leq 0$ is violated, correction of the solution should satisfy $\Phi = 0$. For that purpose it is possible to find solution of the non-linear equation (9) by various methods like Newton-Raphson method or bisections.

By application of chain rule to the transformation function (9) for the next iteration is:

$${}^{t+\Delta t} \Phi^{(k)} + d^{t+\Delta t} \Phi^{(k)} = {}^{t+\Delta t} \Phi^{(k+1)} = {}^{t+\Delta t} \Phi^{(k)} + \frac{\partial {}^{t+\Delta t} \Phi^{(k)}}{\partial \xi} d^{t+\Delta t} \xi^{(k)} \simeq 0 \quad (13)$$

Since, the transformation function does not depend on change of stress direction, using the Newton-Raphson iterative scheme we can calculate increment of martensitic volume fraction ξ as:

$$d^{t+\Delta t} \xi^{(k)} = - \frac{{}^{t+\Delta t} \Phi^{(k)}}{\frac{\partial {}^{t+\Delta t} \Phi^{(k)}}{\partial \xi}} \quad (14)$$

During the iteration process, the step increment of martensitic volume fraction and the martensitic volume fraction are updated as:

$$\Delta^{t+\Delta t} \xi^{(k+1)} = \Delta^{t+\Delta t} \xi^{(k)} + d^{t+\Delta t} \xi^{(k)}; \quad {}^{t+\Delta t} \xi = {}^t \xi + \Delta^{t+\Delta t} \xi^{(k+1)} \quad (15)$$

The iterative scheme continues until ${}^{t+\Delta t} \Phi^{(k+1)}$ is smaller than some tolerance or ${}^{t+\Delta t} \xi^{(0)}$ reaches a boundary values of 0 or 1. Finally, with known value of martensitic volume fraction ${}^{t+\Delta t} \xi$, we calculate deviatoric stress at the end of time step as:

$${}^{t+\Delta t} \mathbf{S}^E = \begin{cases} \frac{{}^{t+\Delta t} \bar{S}^E}{{}^{t+\Delta t} \bar{S}_*^E} {}^{t+\Delta t} \mathbf{S}_*^E; & \dot{\xi} > 0 \\ {}^{t+\Delta t} \mathbf{S}_*^E - 2 {}^{t+\Delta t} G H \Delta^{t+\Delta t} \xi \frac{{}^t \mathbf{e}_{tr}}{t \bar{e}_{tr}}; & \dot{\xi} < 0 \end{cases} \quad (16)$$

where effective Von Mises deviatoric stress is calculated as:

$${}^{t+\Delta t} \bar{S} = \begin{cases} {}^{t+\Delta t} \bar{S}_*^E - 3 {}^{t+\Delta t} G H \Delta^{t+\Delta t} \xi; & \dot{\xi} > 0 \\ \sqrt{{}^{t+\Delta t} \bar{S}_*^E{}^2 - 6 {}^{t+\Delta t} G H \Delta^{t+\Delta t} \xi \frac{{}^{t+\Delta t} \mathbf{S}_*^E \cdot {}^t \mathbf{e}_{tr}}{t \bar{e}_{tr}} + 9 {}^{t+\Delta t} G H \Delta^{t+\Delta t} \xi t \bar{e}_{tr}}; & \dot{\xi} < 0 \end{cases} \quad (17)$$

The total stress and the transformation strain (using the equation (12)), at the end of time step now can be calculated as:

$${}^{t+\Delta t} \boldsymbol{\sigma} = {}^{t+\Delta t} \mathbf{S} + {}^{t+\Delta t} \sigma_m \mathbf{I}; \quad {}^{t+\Delta t} \mathbf{e}_{tr} = {}^t \mathbf{e}_{tr} + \begin{cases} \frac{3 H \Delta^{t+\Delta t} \xi^{(k+1)}}{2 {}^{t+\Delta t} \bar{S}} {}^{t+\Delta t} \mathbf{S}; & \dot{\xi} > 0 \\ \frac{H \Delta^{t+\Delta t} \xi^{(k+1)}}{t \bar{e}_{tr}} {}^t \mathbf{e}_{tr}; & \dot{\xi} < 0 \end{cases} \quad (18)$$

3.3 APPLICATION TO LARGE STRAIN THEORY

For the large strain theory, we are using basic assumption of multiplicative decomposition of total deformation gradient on elastic and inelastic part ${}^t\mathbf{F} = {}^t\mathbf{F}^E {}^t\mathbf{F}^{tr}$, where ${}^t\mathbf{F}^{tr}$ corresponding to deformation from reference to local stress free configuration and ${}^t\mathbf{F}^E$ from local stress free to current configuration.

The trial elastic left Cauchy-Green deformation tensor ${}^{t+\Delta t}\mathbf{B}_*^E$ can be calculated using saved data for ${}^t\mathbf{B}^E$ or ${}^t\mathbf{C}_{tr}^{-1}$ from previous time step as [14]:

$${}^{t+\Delta t}\mathbf{B}_*^E = {}^{t+\Delta t}\overline{\mathbf{F}} {}^t\mathbf{B}^E {}^{t+\Delta t}\overline{\mathbf{F}}^T \quad \text{or} \quad {}^{t+\Delta t}\mathbf{B}_*^E = {}^{t+\Delta t}\overline{\mathbf{F}} {}^t\mathbf{C}_{tr}^{-1} {}^{t+\Delta t}\overline{\mathbf{F}}^T \quad (19)$$

where the left Cauchy-Green elastic strain tensor is ${}^t\mathbf{B}^E = {}^t\mathbf{F}^E {}^t\mathbf{F}^{E^T}$ and the right Cauchy-Green inelastic strain tensor is ${}^t\mathbf{C}^{tr} = {}^t\mathbf{F}^{tr^T} {}^t\mathbf{F}^{tr}$. The modified relative and total deformation gradient are ${}^{t+\Delta t}\overline{\mathbf{F}}$ and ${}^{t+\Delta t}\overline{\mathbf{F}}$ [7, 13].

In the case of logarithmic strains, the trial elastic deviatoric strain ${}^{t+\Delta t}\mathbf{e}_*^{E'}$ is:

$${}^{t+\Delta t}\mathbf{e}_*^{E'} = \sum_{k=1}^3 \ln \left({}^{t+\Delta t}\lambda_{*k}^{E'} \right) {}^{t+\Delta t}\mathbf{p}_k^E {}^{t+\Delta t}\mathbf{p}_k^E \quad (20)$$

where ${}^{t+\Delta t}\lambda_{*k}^{E'}$ are the trial principal stretches and ${}^{t+\Delta t}\mathbf{p}_k^E$ are the corresponding principal directions of the tensor ${}^{t+\Delta t}\mathbf{B}_*^E$. In the case of Green-Lagrange strain tensor, the trial elastic deviatoric strain ${}^{t+\Delta t}\mathbf{e}_*^{E'}$ is:

$${}^{t+\Delta t}\mathbf{e}_*^{E'} = \frac{1}{2} \left({}^{t+\Delta t}\mathbf{B}_*^E - \mathbf{I} \right) \quad (21)$$

The trial elastic mean strain ${}^{t+\Delta t}\mathbf{e}_{*m}^E$ is:

$${}^{t+\Delta t}\mathbf{e}_{*m}^E = \frac{1}{3} \ln \left[\det \left({}^{t+\Delta t}\mathbf{F} \right) \right] \quad (22)$$

For known trial elastic state, the same integration procedure described for small strain case is applied for large strains.

Update of the left Cauchy-Green tensor ${}^{t+\Delta t}\mathbf{B}^E$ for the logarithmic strains is done as [7, 14]

$${}^{t+\Delta t}\mathbf{B}^E = \sum_{k=1}^3 \exp \left(2 {}^{t+\Delta t}\mathbf{e}_k^{E'} \right) {}^{t+\Delta t}\mathbf{p}_k^E {}^{t+\Delta t}\mathbf{p}_k^E \quad (23)$$

where ${}^{t+\Delta t}\mathbf{e}_k^{E'}$ are elastic deviatoric strains in the principal directions calculated as:

$${}^{t+\Delta t}\mathbf{e}_k^{E'} = \frac{{}^{t+\Delta t}S_k}{2 {}^{t+\Delta t}G} \quad (24)$$

Here, ${}^{t+\Delta t}S_k$ are deviatoric stresses components in the principal directions ${}^{t+\Delta t}\mathbf{p}_k^E$ [7, 14]. For the case of Green-Lagrange strain tensor, the left Cauchy-Green tensor ${}^{t+\Delta t}\mathbf{B}^E$ is:

$${}^{t+\Delta t}\mathbf{B}^E = 2 \left({}^{t+\Delta t}\mathbf{e}^E + \mathbf{I} \right) \quad (25)$$

where ${}^{t+\Delta t}e^E$ total elastic strain tensor is:

$${}^{t+\Delta t}e^E = \frac{{}^{t+\Delta t}\mathbf{S}}{2{}^{t+\Delta t}G} + e_m \mathbf{I} \quad (26)$$

The transformation strain is calculated using the right Cauchy-Green transformation strain tensor:

$${}^{t+\Delta t}\mathbf{C}_{tr}^{-1} = {}^{t+\Delta t}\overline{\mathbf{F}}^{-1} {}^{t+\Delta t}\mathbf{B}^E {}^{t+\Delta t}\overline{\mathbf{F}}^{-T} \quad (27)$$

The transformation strain ${}^{t+\Delta t}e_{tr}$, in logarithmic strain case and for the Green-Lagrange strain tensor, at the end of time step is:

$${}^{t+\Delta t}e_{tr} = \sum_{k=1}^3 \ln({}^{t+\Delta t}\lambda_l^{tr}) {}^{t+\Delta t}\mathbf{q}_l^{tr} {}^{t+\Delta t}\mathbf{q}_l^{tr}; \quad {}^{t+\Delta t}e_{tr} = \frac{1}{2} ({}^{t+\Delta t}\mathbf{C}_{tr} - \mathbf{I}) \quad (28)$$

where ${}^{t+\Delta t}\lambda_l^{tr}$ are the principal stretches and ${}^{t+\Delta t}\mathbf{q}_l^{tr}$ are the principal directions of the tensor ${}^{t+\Delta t}\mathbf{C}_{tr}$.

4 NUMERICAL EXAMPLES

Comparison with the numerical and experimental examples from literature is used to demonstrate accuracy of proposed model. Two uniaxial and one multiaxial non-proportional loading example are presented in this work. Material parameters are adopted according to data given in literature [1, 9]. The material parameters required for calculation are the Youngs moduli for austenite and martensite E_A and E_M , thermal expansion coefficients α_A and α_M , martensite start and finish and austenite start and finish temperatures at zero stress M_0^s, M_0^f, A_0^s and A_0^f , maximum transformation strain H and austenite and martensite stress influence coefficients $\rho\Delta s_A$ and $\rho\Delta s_M$.

4.1 Uniaxial tests

Two uniaxial tests are done at different temperatures to show pseudo-elasticity effect and shape memory effect. Results are compared with the literature [1, 9] and the good agreement was obtained. Both tests were done using the same model of 3D unit cube made of "NiTiInol" alloy. The boundary and loading conditions and the material parameters are taken according to literature [9]. The model consists of two equal finite elements. The material parameters from [9], used in those examples, are given in Table 1.

Table 1: Material parameters of Nickel-Titanium alloys used in uniaxial examples [9]

E_A	E_M	α_A	α_M
70.000 MPa	30.000 MPa	$22.0 \cdot 10^{-6} K^{-1}$	$22.0 \cdot 10^{-6} K^{-1}$
M_{0s}	M_{0f}	A_{0s}	A_{0f}
291K	271K	295K	315K
H	ν	$\rho\Delta s_A$	$\rho\Delta s_M$
0.05	0.33	$-0.35 \text{ MPa } K^{-1}$	$-0.35 \text{ MPa } K^{-1}$

4.1.1 Pseudo-elasticity example

The first example describes the superelastic effect of the SMAs. The material is on constant temperature $325K$, which is higher than the austenitic finish temperature $A_{0f} = 315K$. The cube is loaded in uniaxial tension stress $\sigma = 600MPa$ in 100 steps until full martensitic phase is achieved. The material is then unloaded in 100 equal steps to stress free configuration. As it can be seen in Figure 1, all transformation strains were fully recovered.

4.1.2 Shape memory effect example

The second example demonstrates the shape memory effect. A temperature was $295K$ which is between the austenitic A_{0s} and martensitic M_{0s} start temperature. The uniaxial tension $\sigma = 600MPa$ was applied in 100 steps until the full transformation strain is achieved and than the cube was relaxed in another 100 steps to zero stress. After the relaxation, there were residual strains and the material was in the martensitic phase. Than, the cube was heated above the austenitic finish temperature to $350K$ in 100 steps and the transformation strains are completely recovered as it is given in Figure 2.

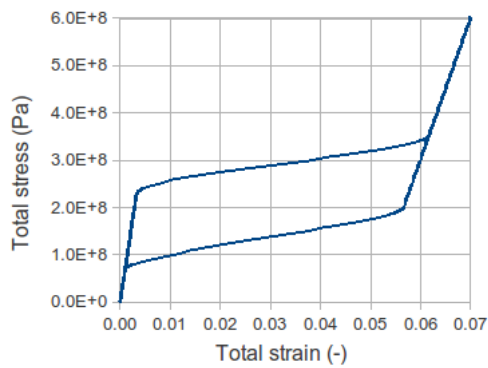


Figure 1: Stress-strain diagram for super-elasticity example

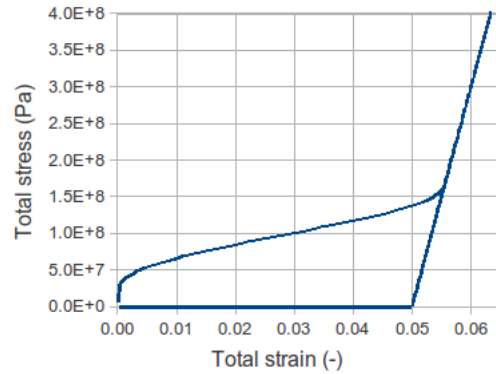


Figure 2: Stress-strain diagram for shape memory effect example

4.2 Large strain non-proportional example

This examples describes the model prediction for non-proportional loading with superelasticity effect. The test temperature is set to $308K$ which is $25K$ more than austenitic finish temperature $A_{0s} = 283K$, so superelastic behaviour is expected. This example is experimentally examined and the obtained data are available in literature [1, 2]. Tension-torsion experiment of thin wall specimen [8] made of CuAlZnMn alloy is used for this purpose. Axial stress of $240MPa$ and then the shear stress of $200MPa$ were applied combined at the same side of cube, while the opposite side is fully constrained. After that, first tension was unloaded and than shear strain were recovered. Material parameters that were used for this simulation are used from the literature [1].

Table 2: Material parameters of CuAlZnMn [8] alloy used in non-proportional example [1]

E_A	E_M	α_A	α_M
30.000 MPa	10.000 MPa	$10.0 \cdot 10^{-6} K^{-1}$	$10.0 \cdot 10^{-6} K^{-1}$
M_{0s}	M_{0f}	A_{0s}	A_{0f}
278K	183K	188K	283K
H	ν	$\rho\Delta s_A$	$\rho\Delta s_M$
0.035	0.30	$-0.28 \text{ MPa } K^{-1}$	$-0.28 \text{ MPa } K^{-1}$

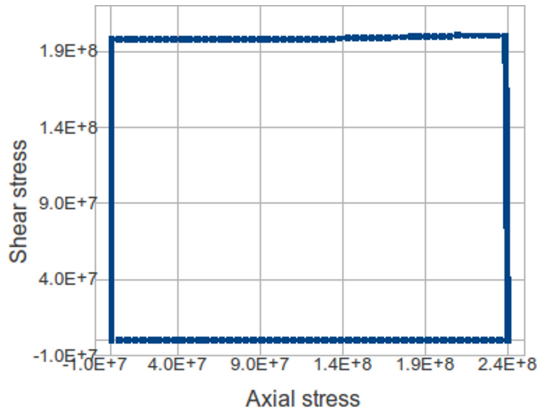


Figure 3: Axial–shear stress diagram for non proportional example

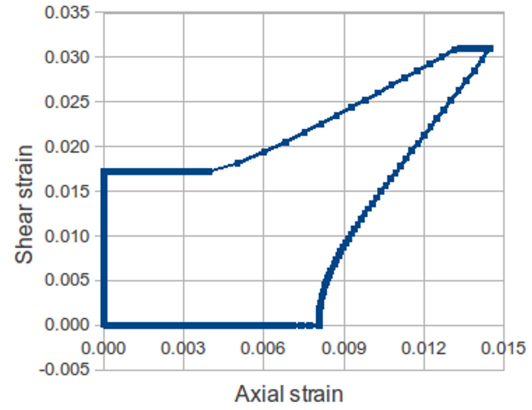


Figure 4: Axial–shear strain diagram for non proportional example

Multiaxial tension-torsion non-proportional loading path is compared with the experimental results [8] and numerical results from the literature [1, 2, 4].

5 CONCLUSIONS

The theory presented by Lagoudas has been modified. The total stress is decomposed on deviatoric and mean part and the stress integration is done in direction of the trial deviatoric stress. The solutions are similar to one obtained by return mapping algorithm. Instead of solving transformation function with several dependent variables, we have to solve only one scalar non-linear equation by Newton-Raphson method or using bisections. In the non-proportional example results are qualitatively similar to experimental results obtained by Šittner [8]. That change gave possibility to extend small strain theory and solve examples with large strains. Introducing multiplicative decomposition of deformation gradient and Green-Lagrange or logarithmic strain tensor, the same solution procedure can be used to find solution.

REFERENCES

- [1] D.Lagoudas, D.Hartl, Y.Chemisky, L.Machado, P.Popov, Constitutive model for the numerical analysis of phase transformation in polycrystalline shape memory alloys, *International Journal of Plasticity*, **32–33**, 155–183, 2012.
- [2] J.Arghavani, F.Auricchio, R.Naghdabadi, A.Reali, S.Sohrabpour, A 3-D phenomenological constitutive model for shape memory alloys under multiaxial loadings, *International Journal of Plasticity*, **26**, 7, 976–991, 2010.

- [3] M.Kojić, R.Slavković, M.Živković, N.Grujović, *PAK-S Program for FE Structural Analysis, User Manual*, Faculty of Mechanical Engineering, University of Kragujevac, Kragujevac, 2013.
- [4] M.Panico, L.C.Brinson, A three-dimensional phenomenological model for martensite re-orientation in shape memory alloys, *Journal of the Mechanics and Physics of Solids*, **55**, 11, 2491–2511, 2007.
- [5] D.J.Hartl, G.Chatzigeorgiou, D.C.Lagoudas, Three-dimensional modeling and numerical analysis of rate-dependent irrecoverable deformation in shape memory alloys, *International Journal of Plasticity*, **26**, 10, 1485–1507, 2010.
- [6] D.C. Lagoudas, *Shape Memory Alloys: Modeling and Engineering Applications*, Springer, 2010.
- [7] M.Kojić, K.J.Bathe, *Inelastic Analysis of Solids and Structures, 1st edition. Computational Fluid and Solid Mechanics*, Springer-Verlag Berlin and Heidelberg GmbH KG, Berlin, 2005.
- [8] P.Šittner, Y.Hara, M.Tokuda, Experimental study on the thermoelastic martensitic transformation in shape memory alloy polycrystal induced by combined external forces, *Metallurgical and Materials Transactions A*, **26**, 10, 1073–5623, 1995.
- [9] D.Lagoudas, Z.Bo, M.Qidwai, P.Entchev, SMA UM: User Material Subroutine for Thermomechanical Constitutive Model of Shape Memory Alloys, *Texas A&M University*, College Station, TX, March 2003.
- [10] J.G. Boyd, D.C. Lagoudas, A thermodynamical constitutive model for shape memory materials. Part I. The monolithic shape memory alloy, *International Journal of Plasticity*, **12**, 6, 805–842, 1996.
- [11] M.A.Qidwai, D.C.Lagoudas, Numerical implementation of a shape memory alloy thermomechanical constitutive model using return mapping algorithms, *International Journal for Numerical Methods in Engineering*, **47**, 6, 1097–0207, 2000.
- [12] D.Lagoudas, Z.Bo, M.Qidwai, A unified thermodynamic constitutive model for SMA and finite element analysis of active metal matrix composites, *Mechanics of Composite Materials and Structures*, **3**, 2, 1075–9417, 1996.
- [13] J.C.Simo, T.J.R.Hughes, *Computational Inelasticity, Interdisciplinary applied mathematics: Mechanics and materials*, Springer, 1998.
- [14] M.Kojić, I.Vlastelica, M.Živković, Implicit stress integration procedure for small and large strains of the Gurson material model, *International Journal for Numerical Methods in Engineering*, **53**, 12, 1097–0207, 2002.

BLOOD FLOW SIMULATION IN THE AORTA PASSING THROUGH THE AORTIC ORIFICE BY VIRTUAL FLUX METHOD

T. Fukui¹ and K. Morinishi²

¹ Department of Mechanical and System Engineering, Kyoto Institute of Technology
Gosyokaido-cho, Matsugasaki, Sakyo-ku, Kyoto 606-8585, Japan
e-mail: fukui@kit.ac.jp

² Department of Mechanical and System Engineering, Kyoto Institute of Technology
Gosyokaido-cho, Matsugasaki, Sakyo-ku, Kyoto 606-8585, Japan
e-mail: morinisi@kit.ac.jp

Keywords: Aortic Valves, Sinus of Valsalva, Vorticity, Wall Shear Stress, Virtual Flux Method, Regularized Lattice Boltzmann Method, Multi-block Method.

Abstract. *Transposition of the great arteries (TGA) is one of the most severe congenital heart disease. The arterial switch operation (ASO) is the procedure of preference for treatment of TGA. After ASO, some patients suffer from circulatory system problems such as neo-aortic root dilatation and neo-aortic valve regurgitation, and supraaortic pulmonary stenosis. The neo-aortic root dilatation is often explained by the structural vascular difference between normal great arteries and the neo-aorta after ASO. Since the aortic and pulmonary roots generally remain in situ after ASO, i.e., the original pulmonary artery is connected to the left ventricle (LV), whereas the original aorta is connected to the right ventricle, the neo-aorta has no sinus of Valsalva after ASO. The influence of these morphological changes on the blood flow field at the aortic root should be investigated in detail as well as the structural vascular difference to consider the circulatory system problems. In this study, we apply the virtual flux method (VFM), which is a tool to describe stationary or moving body shapes in a Cartesian grid, to the 2D aortic valves with a multi-block method for high resolution near the valves, and reproduce the blood flow fields around the aortic valves and the sinus of Valsalva by RLBM, and consider the influence of longitudinal length of sinus of Valsalva on blood flow fields around the aortic valves. As a result, we found that the longitudinal length of the sinus affects development of vortices around the aortic valves strongly. We also found that the WSS increases toward the distal edge of the sinus, indicating the WSS value at the distal edge of the sinus is dependent on the longitudinal length of the sinus of Valsalva.*

1 INTRODUCTION

Transposition of the great arteries (TGA) is one of the most severe congenital heart disease. Since the aorta arises from the right ventricle in TGA, blood in the systemic circulation is always rich in carbon dioxide and poor in oxygen. On the other hand, the pulmonary circulation in TGA is always full of blood with oxygen. The systemic and pulmonary circulations are completely separated in TGA. The arterial switch operation (ASO) is the procedure of preference for treatment of TGA. Although many reports have shown good results after ASO [1,2,3], some patients suffer from circulatory system problems such as neo-aortic root dilatation and neo-aortic valve regurgitation [4,5], and supraaortic pulmonary stenosis [6] after ASO. Diameters of aortic annulus and sinus of Valsalva 20 years after ASO are significantly wider in comparison to a normal population of young adults, whereas ascending aorta diameters are well preserved in our population and are not significantly different to the values in a normal population, demonstrating that dilatation of the aortic root is due to a localized problem [7]. This localized dilatation of the aortic root is often explained by the structural vascular difference between normal great arteries and the neo-aorta after ASO [8].

Fluid dynamic forces against the arterial wall should be considered as well as the structural difference. The morphology of the aorta and aortic valves movement strongly affect the blood flow fields in the aorta, especially at the root of the aorta. In addition, the sinus of Valsalva, which lies at the aortic root, plays an important role for aortic valves behavior [9]. Since the aortic and pulmonary roots generally remain in situ after ASO, i.e., the original pulmonary artery is connected to the left ventricle (LV), whereas the original aorta is connected to the right ventricle, the neo-aorta has no sinus of Valsalva after ASO. Moreover, there are some cases that the curvature of the neo-aortic root is extremely larger than that in a normal population due to ASO. The influence of these morphological changes on the blood flow field at the aortic root should be investigated in detail.

In the past study, we performed numerical simulation of blood flows around aortic valves by lattice Boltzmann method [10,11]. The method of lattice Boltzmann equation (LBM) is a simple kinetic-based approach for fluid flow computation. The LBM has advantages its simple coding and its locality, which makes it intrinsically parallelizable [12], and has been applied to many problems relevant to blood flow simulation [13,14,15]. However, stability of the simulation by LBM is strictly dependent on its relaxation time, which leads to restriction of the Reynolds number. Since blood flow simulation in the aorta is accompanied by high Reynolds number, it is necessary to improve stability of LBE. Izham et al. [16] proposed regularized lattice Boltzmann method (RLBM), which is based on the observation of symmetric condition in Chapman-Enskog expansion by Latt & Chopard [17], and it has successfully achieved higher stability in numerical simulation at high Reynolds number. In this study, we apply the virtual flux method (VFM) [18], which is a tool to describe stationary or moving body shapes in a Cartesian grid, to the 2D aortic valves with a multi-block method [19,20] for high resolution near the valves, and reproduce the blood flow fields around the aortic valves and the sinus of Valsalva by RLBM, and consider the influence of longitudinal length of sinus of Valsalva on blood flow fields around the aortic valves.

2 METHODS

2.1 Computational models

Numerical simulation of blood flow in aorta with valves and sinus of Valsalva is performed. Figure 1 shows the schematic view of the 2-dimensional axisymmetric simulation model used in this study. The longitudinal length L and diameter D are set to 200 mm and 20 mm. The valve leaflets are modeled as arcs of a circle with a radius of $D/\sqrt{2}$, and placed at 80 mm ($= 4D$) from the inlet. The shape of the sinus of Valsalva is approximated as a semi-ellipse. The longitudinal length a and depth b of the sinus of Valsalva are set to $a = 30$ mm and $b = 15$ mm for case 1, and $a = 40$ mm and $b = 15$ mm for case 2, respectively. The arterial wall and valves are described by virtual flux method on Cartesian coordinate as described below.

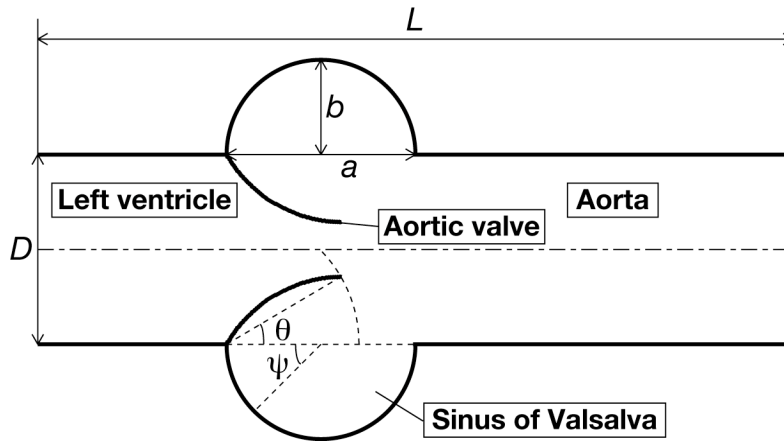


Figure 1: Schematic view of the computational model.

2.2 Governing equations

The discrete velocity Boltzmann equation (DVBE) is as follows,

$$\frac{\partial f_\alpha}{\partial t} + \mathbf{e}_\alpha \cdot \nabla f_\alpha = \mathbf{\Omega}_\alpha, \quad (1)$$

where \mathbf{e}_α is the discrete particle velocity, f_α is the distribution function associated with \mathbf{e}_α , and $\mathbf{\Omega}_\alpha$ is the collision operator. The collision operator, which is very complicated, is usually approximated by the simple single-relaxation-time Bhatnagar-Gross-Krook (BGK) model [21]:

$$\mathbf{\Omega}_\alpha = -\frac{1}{\tau} (f_\alpha - f_\alpha^{(eq)}), \quad (2)$$

where $f_\alpha^{(eq)}$ is the equilibrium distribution function, and τ is the relaxation time. The evolution of the distribution function f_α for the lattice Boltzmann equation (LBE) can be written as

$$f_\alpha(\mathbf{x} + \mathbf{e}_\alpha \Delta t, t + \Delta t) - f_\alpha(\mathbf{x}, t) = -\frac{1}{\tau} \{f_\alpha(\mathbf{x}, t) - f_\alpha^{(eq)}(\mathbf{x}, t)\}. \quad (3)$$

In this study, we use a 2D square lattice model with 9 velocities, which is referred to as the D2Q9 model. It is shown that the Navier-Stokes equations can be derived from the LBE through a Chapman-Enskog expansion procedure in the incompressible limit [22] with a relaxation time τ as

$$\tau = \frac{3\nu}{c\delta x} + \frac{\delta t}{2}. \quad (4)$$

The most common choice for the equilibrium distribution function $f_\alpha^{(eq)}$ is the truncated form of the Maxwell distribution, which is a very good approximation for small Mach numbers [23].

$$f_\alpha^{(eq)} = \omega_\alpha \rho \left[1 + \frac{3(\mathbf{e}_\alpha \cdot \mathbf{u})}{c^2} + \frac{9(\mathbf{e}_\alpha \cdot \mathbf{u})^2}{2c^4} - \frac{3\mathbf{u}^2}{2c^2} \right], \quad (5)$$

where ω_α is the weight coefficients.

The single-relaxation-time (SRT) LBM has been widely used for its simplicity, efficiency and ease of parallel programming implementation, however, it requires relatively large number of grids to simulate flows at even moderately high Reynolds number. In Chapman-Enskog expansion procedure, the non-equilibrium part of first-order is symmetrical with respect to spatial reflection. Latt et al. [17] observed that this symmetric condition is not necessarily satisfied and appear to take a non-negligible value in numerical simulations using SRT-LBM. Based on this observation, they considered a regularization step that enforces symmetrical property and proposed regularized lattice Boltzmann method (RLBM).

The relationships between stress tensor and distribution function in RLBM [16] is defined as

$$\Pi_{ij} = \sum_\alpha e_{\alpha i} e_{\alpha j} f_\alpha, \quad (6)$$

where Π_{ij} is the stress tensor. The non-equilibrium part of the distribution and stress tensor were given as

$$f_\alpha^{(neq)} = f_\alpha - f_\alpha^{(eq)}, \quad (7)$$

$$\Pi_{ij}^{(neq)} = \Pi_{ij} - \Pi_{ij}^{(eq)}. \quad (8)$$

From the Chapman-Enskog expansion, the non-equilibrium part of ε -order can be explicitly derived as below,

$$f_\alpha^{(neq)} \approx f_\alpha^1 = -\frac{\delta t}{c_s^2} \tau \omega_\alpha \mathbf{Q}_{\alpha ij} \partial_i \rho u_j, \quad (9)$$

$$\Pi_{ij}^{(neq)} \approx \sum_\alpha e_{\alpha i} e_{\alpha j} f_\alpha^1 = -\delta t c_s^2 \tau (\partial_i \rho u_j + \partial_j \rho u_i), \quad (10)$$

where $\mathbf{Q}_{\alpha ij}$ is defined as

$$\mathbf{Q}_{\alpha ij} = e_{\alpha i} e_{\alpha j} - c_s^2 \delta_{ij}, \quad (11)$$

where c_s is the sound speed, and f_α^1 is then written as

$$f_\alpha^1 = \frac{\omega_\alpha}{2c_s^4} \mathbf{Q}_{\alpha ij} \Pi_{ij}^{(neq)}. \quad (12)$$

By enforcing $f_\alpha^{(neq)} = f_\alpha^1$, the final form of the relaxation process can be written as

$$f_\alpha = f_\alpha^{(eq)} + \left(1 - \frac{1}{\tau} \right) f_\alpha^1. \quad (13)$$

The viscous stress tensor τ_{ij} can be evaluated using the non-equilibrium part of the distribution function [24] as

$$\tau_{ij} = \left(1 - \frac{1}{2\tau}\right) \sum_{\alpha} f_{\alpha}^{(neq)}(\mathbf{x}, t) \left(e_{\alpha i} e_{\alpha j} - \frac{1}{D} \mathbf{e}_{\alpha} \cdot \mathbf{e}_{\alpha} \delta_{ij} \right). \quad (14)$$

The aortic valves are assumed to be rigid, and their motion obeys following rigid-body rotation

$$\mathbf{T} = I \frac{d\boldsymbol{\omega}}{dt}, \quad (15)$$

where \mathbf{T} is the torque, I is the inertia moment, and $\boldsymbol{\omega}$ is the angular velocity of the valve. The torque \mathbf{T} is evaluated by force differences between LV-facing and aortic-facing surfaces of the valve,

$$\mathbf{T} = \sum (\mathbf{f}^{\text{Ao}} - \mathbf{f}^{\text{LV}}) \cdot \mathbf{r}, \quad (16)$$

where r is the radius of rotation. The forces acting on the valve are obtained by pressure p and viscous stress τ_{ii} as follows,

$$\mathbf{f} = (p + \tau_{ii}) \cdot d\mathbf{r}. \quad (17)$$

The inertia moment of the valve I is estimated by assuming the density of the valve is equal to that of the blood. The angular velocity $\boldsymbol{\omega}$ is obtained by first-order Euler method.

$$\boldsymbol{\omega}(t + \Delta t) = \boldsymbol{\omega}(t) + \Delta t \frac{\mathbf{T}(t)}{I}. \quad (18)$$

2.3 Boundary conditions

The virtual flux method (VFM) enables us to estimate flow field around arbitrary body shapes properly in a Cartesian grid [18]. In this study, we apply the VFM to express arbitrary body shapes appropriately in case that boundary points are not located on the cell vertex. Figure 2 shows an example of virtual flux boundary, where the virtual boundary point b is placed between cell vertexes 1 and 3. When the distribution function at vertex 1 is obtained, the distribution function at vertex 3, which includes the effect of the virtual boundary, is necessary, and vice versa. The macroscopic quantities on the virtual boundary point b are then determined to satisfy the boundary conditions. No-slip condition on the boundary, for example, is attained to assume zero pressure gradient and zero velocity on the boundary.

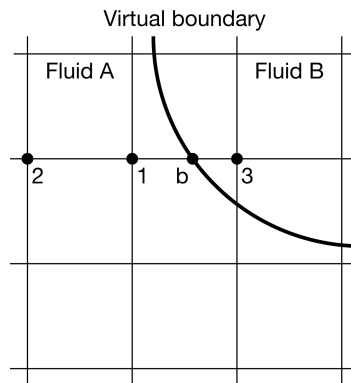


Figure 2: Schematic view of the virtual boundary in a Cartesian grid. The virtual boundary separates Fluid A from Fluid B completely.

Next, the equilibrium distribution function $p_\alpha^{(eq)}$ and distribution function p_α at the virtual boundary point b are obtained from the macroscopic quantities there. The distribution function p_α at the vertex 3 is then estimated to extrapolate that at the virtual boundary point b.

$$p_{\alpha,3} = \frac{p_{\alpha,b} - (1-s)p_{\alpha,1}}{s}. \quad (19)$$

Axial velocity u at the inlet and pressure p at the outlet are given as shown in Fig. 3. Other parameters are linearly extrapolated. No-slip conditions are assumed on the wall and valve leaflets. The Reynolds number Re at the peak velocity in Fig. 3 corresponds to 2,000.

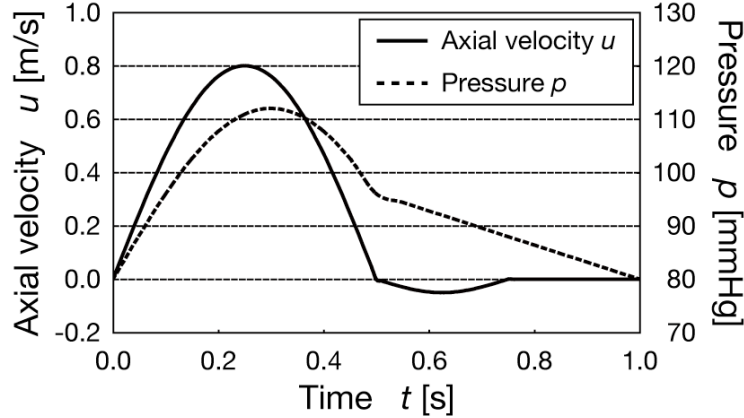


Figure 3: Axial velocity at the inlet and pressure at the outlet. The Reynolds number Re at the peak velocity corresponds to 2,000. The period of the cardiac cycle is set to 1.0 s

2.4 Multi-block method

A multi-block method [19,20] was used for high resolution near the aortic valves. Figure 4 illustrates the interface structure between two blocks of different lattice spacing. The ratio of the lattice space between the coarse and fine blocks is

$$m = \frac{\delta x_c}{\delta x_f}, \quad (20)$$

where δx_c and δx_f are the coarse and fine lattice sizes, respectively. In order to keep a consistent viscosity in the entire flow field involving different lattice sized, the relation between relaxation times τ_f on the fine grid and τ_c on the coarse grid must obey the following rule:

$$\tau_f = \frac{1}{2} + m \left(\tau_c - \frac{1}{2} \right). \quad (21)$$

Since the velocity and density are continuous across the interface between the two blocks, the equilibrium part across the interface follows:

$$f_{\alpha,c}^{(eq)}(\mathbf{x}, t) = f_{\alpha,f}^{(eq)}(\mathbf{x}, t). \quad (22)$$

To maintain the continuity for the stress across the interface, the non-equilibrium part across the interface follows:

$$\left(1 - \frac{1}{2\tau_c} \right) f_{\alpha,c}^{(neq)}(\mathbf{x}, t) = \left(1 - \frac{1}{2\tau_f} \right) f_{\alpha,f}^{(neq)}(\mathbf{x}, t). \quad (23)$$

For the lattice Boltzmann method, in order to make sure that the interface uses information at the correct time level, three-point Lagrangian formulation is also used for the temporal interpolation at the interface.

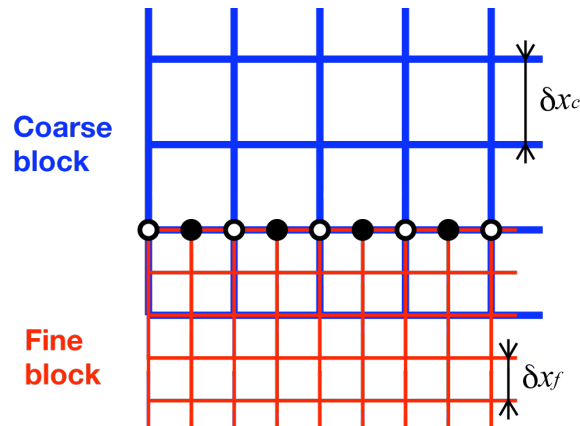
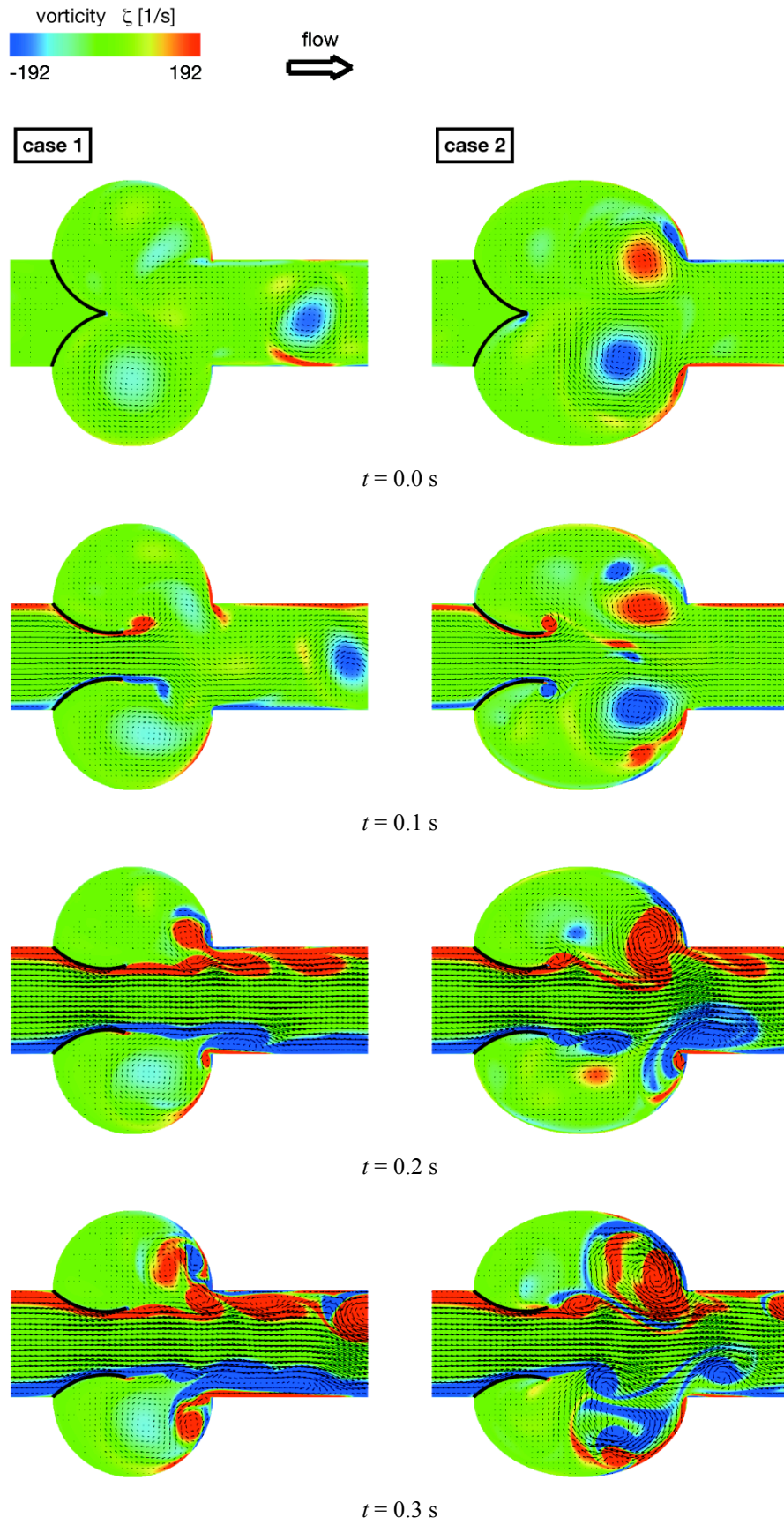


Figure 4: Interface structure between two blocks of different lattice spacing.

3 RESULTS AND DISCUSSION

Figure 5 shows the vorticity distribution and velocity vectors on the left for case 1 and right for case 2 in the eighth cardiac cycle at the time interval of 0.1 s. When the pressure at the left ventricle (LV) exceeds that on the aorta, the valves start to open and blood flows toward the aorta passing through the aortic orifice. Vortices evolved from the tip of the valve spread and strike on the distal edge of the sinus of Valsalva, then they are divided into multiple ($t = 0.3 \sim 0.4$ s). This vortical motion has the advantage of preventing the valve leaflet from bulging outward to contact the walls of the sinuses. The vortices for case 2 are more dominant near the distal edge of the sinus, indicating that there needs an appropriate longitudinal length of the sinus for vortex development. These vortical motions then lead blood flow fields in the aorta to be more complicated. The open sinus chamber thus can be supplied with fluid to fill the increasing volume behind the valve leaflets as they move toward closure ($t = 0.5 \sim 0.6$ s). After the valves close the aortic orifice, multiple vortices do not completely dissipate in the aorta as well as in the sinus of Valsalva in diastole, so that they persist until the next systole. The aortic valve movements in systole have minor differences from cycle to cycle due to these vortices.

Figure 6 shows the time averaged wall shear stress (WSS) ratio τ_2 / τ_1 distribution on the LV-facing surface and aortic-facing surface of the aortic valves. The averaged WSS data in five cardiac cycles of case 2 τ_2 is divided by that of case 1 τ_1 . The WSS ratio τ_2 / τ_1 on the LV-facing surface is relatively flat. On the other hand, the WSS ratio on the aortic-facing surface increases toward the tip of the valve. Figure 7 shows the time averaged WSS ratio distribution on the sinus wall in five cardiac cycles. The sinus position $\psi = 0$ and π rad correspond to proximal and distal edges of the sinus of Valsalva, respectively as shown in Fig. 1. The WSS ratio increases toward the distal edge of the sinus, indicating the WSS value at the distal edge of the sinus is dependent on the longitudinal length of the sinus of Valsalva.



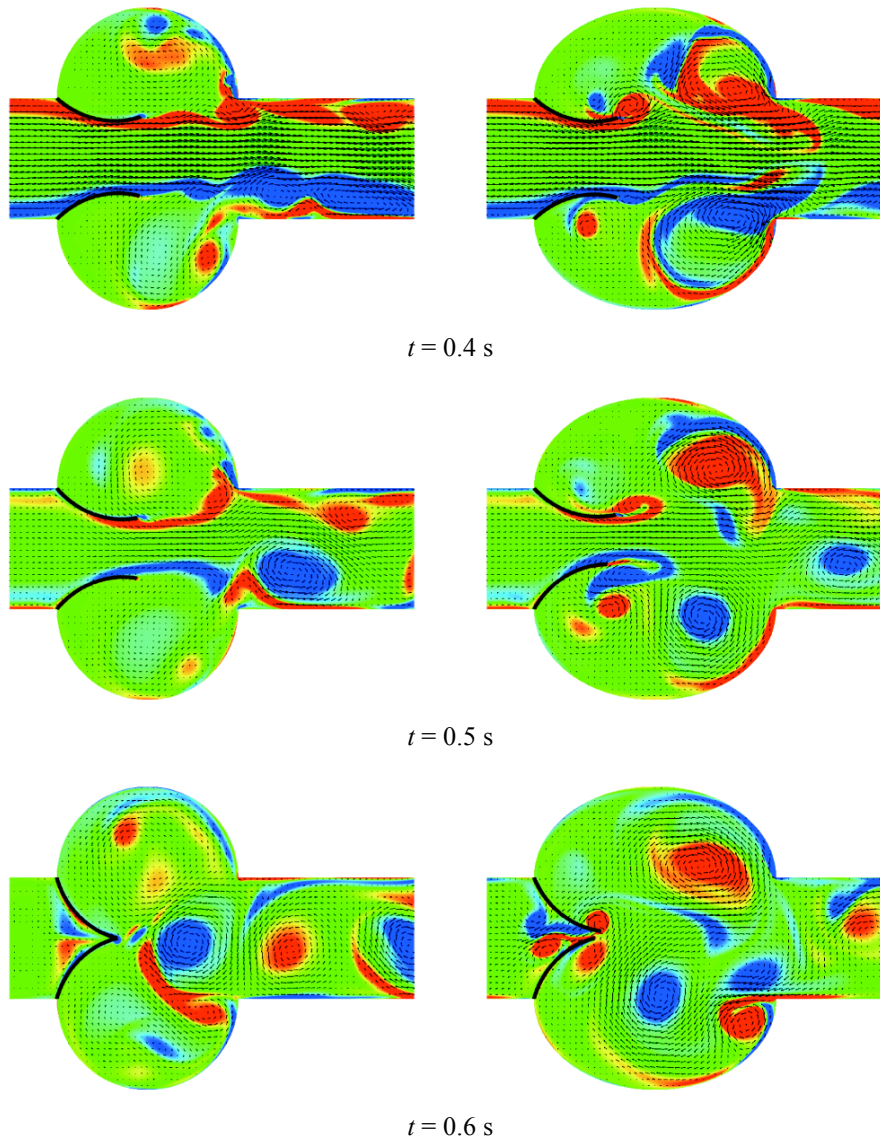


Figure 5: Vorticity distribution and velocity vectors on the left for case 1 and right for case 2 in the eighth cardiac cycle at the time interval of 0.1 s.

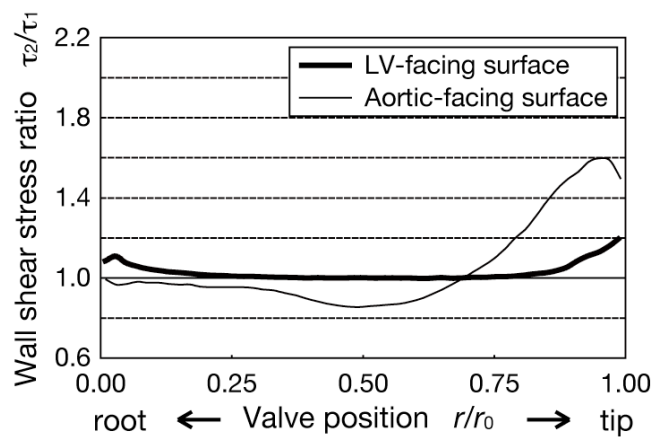


Figure 6: Time averaged WSS ratio distribution on the LV-facing and aortic-facing surfaces.

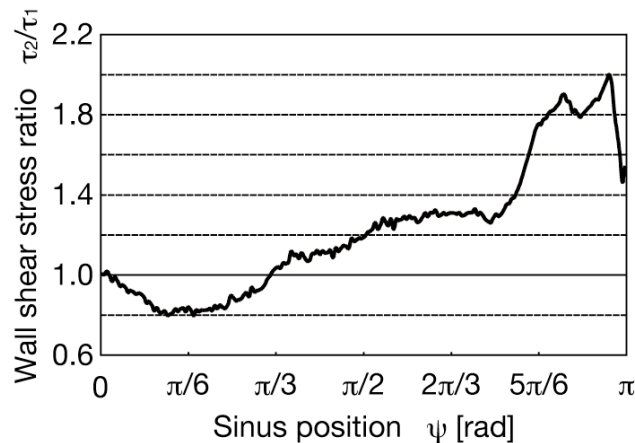


Figure 7: Time averaged WSS ratio distribution on the sinus wall. The sinus position $\psi = 0$ and π rad correspond to proximal and distal edges of the sinus of Valsalva, respectively.

The vortices evolved from the tip of the valve strike on the distal edge of the sinus and spread within the sinus of Valsalva. These vortices affect the WSS distribution of the valves on the tip of the aortic-facing surface and sinus wall near the distal edge. It is well known that the WSS plays a dominant role in determining the physiological mechanics of the endothelial cell in all generations of arteries, and developing vascular pathology such as atherosclerosis [25,26,27]. According to Malek et al. [28], the value of the low shear stress that causes atherosclerosis initiation is 0.4 Pa. Statistically significant inverse relationships between intima-media thickness and local WSS have also been reported [29,30]. It is, therefore, important to investigate the WSS distribution in time and space in order to predict the precise region where cardiovascular disease occurs. Our computational scheme is suitable and promising to reproduce heart valves behavior with neither re-mesh nor re-construction of the model. Incorporating effect of deflection or bending of the heart valves behavior to our computational model will enable us to consider more accurate WSS distribution on the aortic valves in the future work.

REFERENCES

- [1] C. Planche, J. Bruniaux, F. Lacour-Gayet, J. Kachaner, J.P. Binet, D. Sidi, E. Villain, Switch operation for transposition of the great arteries in neonates. A study of 120 patients, *Journal of Thoracic Cardiovascular Surgery*, **96**, 354-363, 1988.
- [2] R. Pretre, D. Tamisier, P. Bonhoeffer, P. Mauriat, P. Pouard, D. Sidi, P. Vouhe, Results of the arterial switch operation in neonates with transposed great arteries, *Lancet*, **357**, 1826-1830, 2001.
- [3] W.G. Williams, B.W. McCrindle, D.A. Ashburn, R.A. Jonas, C. Mavroudis, E.H. Blackstone, Outcomes of 829 neonates with complete transposition of the great arteries 12-17 years after repair, *European Journal of Cardio-thoracic Surgery*, **24**, 1-10, 2003.
- [4] C.J. McMahon, W.J. Ravekes, E.O. Smith, S.W. Denfield, R.H. Pignatelli, C.A. Altman, N.A. Ayres, Risk factors for neo-aortic root enlargement and aortic regurgitation following arterial switch operation, *Pediatric Cardiology*, **25**, 329-335, 2004.
- [5] J. Losay, A. Touchot, A. Capderou, J.D. Piot, E. Belli, C. Planche, A. Serraf, Aortic valve regurgitation after arterial switch operation for transposition of the great arteries:

- Incidence, Risk factors, and Outcome, *Journal of the American College of Cardiology*, **47**, 2057-2062, 2006.
- [6] M.F. Swartz, A. Sena, N. Atallah-Yunes, C. Meagher, J.M. Cholette, F. Gensini, G.M. Alfieri, Decreased incidence of supra-valvar pulmonary stenosis after arterial switch operation, *Circulation*, **126**, S118-S122, 2012.
- [7] K.D.H.M. Vandekerckhove, N.A. Blom, S. Lalezari, D.R. Koolbergen, M.E.B. Rijlaarsdam, M.G. Hazekamp, Long-term follow-up of arterial switch operation with an emphasis on function and dimensions of left ventricle and aorta, *European Journal of Cardio-thoracic Surgery*, **35**, 582-588, 2009.
- [8] S. Lalezari, M.G. Hazekamp, M.M. Bartelings, P.H. Schoof, A.C. Gittenberger-De Groot, Pulmonary artery remodeling in transposition of the great arteries: relevance for neo-aortic root dilatation, *Journal of Thoracic Cardiovascular Surgery*, **126**, 1053-1060, 2003.
- [9] Y.C. Fung, *Biomechanics Circulation*, 2nd edition, New York Berlin Heidelberg: Springer-Verlag, 42-48, 1997.
- [10] T. Fukui, K. Morinishi, Aortic valve oscillation due to vortices in the sinus of Valsalva by virtual flux method, in *Proceedings of the 8th KSME-JSME Thermal and Fluids Engineering Conference*, 2012, 1-4.
- [11] T. Fukui, K. Morinishi, Numerical simulation of blood flows in the aorta with aortic valves by virtual flux method, in *Proceedings of the European Congress on Computational Methods in Applied Sciences and Engineering*, 2012, 1-10.
- [12] T. Kruger, F. Varnik, D. Raabe, Shear stress in lattice Boltzmann simulations, *Physical Review E*, **79**(046704), 1-14, 2009.
- [13] J. Boyd, J. Buick, J.A. Cosgrove, P. Stansell, Application of the lattice Boltzmann model to simulated stenosis growth in a two-dimensional carotid artery, *Physics in Medicine and Biology*, **50**, 4783-4796, 2005.
- [14] M. Tamagawa, H. Kaneda, M. Hiramoto, S. Nagahama, Simulation of thrombus formation in shear flows using lattice Boltzmann method, *Artificial Organs*, **33**(8), 604-610, 2009.
- [15] L. Axner, A.G. Hoekstra, A. Jeays, P. Lawford, R. Hose, P.M.A. Sloot, Simulations of time harmonic blood flow in the Mesenteric artery: comparing finite element and lattice Boltzmann methods, *Biomedical Engineering Online*, **8**(23), 1-8, 2009.
- [16] M. Izham, T. Fukui, K. Morinishi, Application of regularized lattice Boltzmann method for incompressible flow simulation at high Reynolds number and flow with curved boundary, *Journal of Fluid Science and Technology*, **6**(6), 812-821, 2011.
- [17] J. Latt, B. Chopard, Lattice Boltzmann method with regularized precollision distribution functions, *Mathematics and Computers in Simulation*, **72**, 165-168, 2006.
- [18] I. Tanno, K. Morinishi, K. Matsuno, H. Nishida, Validation of virtual flux method for forced convection flow, *JSME International Journal*, **B49**(4), 1141-1148, 2006.
- [19] D. Yu, R. Mei, W. Shyy, A multi-block lattice Boltzmann method for viscous fluid flows, *International Journal for Numerical Method in Fluids*, **39**, 99-120, 2002.

-
- [20] Y. Peng, C. Shu, Y.T. Chew, X.D. Niu, X.Y. Lu, Application of multi-block approach in the immersed boundary-lattice Boltzmann method for viscous fluid flows, *Journal of Computational Physics*, **218**, 460-478, 2006.
- [21] P.L. Bhatnagar, E.P. Gross, M. Krook, A model for collision processes in gases: I. Small amplitude processes in charged and neutral one-component system, *Physical Review*, **94**, 511-525, 1954.
- [22] J.D. Sterling, S. Chen, Stability analysis of lattice Boltzmann methods, *Journal of Computational Physics*, **123**, 196-206, 1996.
- [23] Y.H. Quian, D. d'Humieres, P. Lallemand, Lattice BGK models for Navier-Stokes equation, *Europhysics Letters*, **17**, 479-484, 1992.
- [24] R. Mei, D. Yu, W. Shyy, Force evaluation in the lattice Boltzmann method involving curved geometry, *Physical Review E*, **65**(041203), 1-14, 2002.
- [25] C.G. Caro, J.M. Fitzgerald, R.C. Schroter, Atheroma and arterial wall shear: observation, correlation and proposal of a shear dependent mass transfer mechanism for atherogenesis, *Proceedings of the Royal Society*, **177**, 109-159, 1971.
- [26] D.L. Fry, Certain histological and chemical responses of the vascular interface to acutely induced mechanical stress in the aorta of the dog, *Circulation Research*, **24**, 93-108, 1969.
- [27] D.P. Giddens, C.K. Zarins, S. Glagov, The role of fluid mechanics in the localization and detection of atherosclerosis, *Journal of Biomechanical Engineering*, **115**, 588-594, 1993.
- [28] A.M. Malek, A.L. Alper, S. Izumo, Hemodynamic shear stress and its role in atherosclerosis, *Journal of the American Medical Association*, **282**, 2035-2042, 1999.
- [29] A. Gnasso, C. Carallo, C. Irace, V. Spagnuolo, G. De Novara, P.L. Mattioli, A. Pujia, Association between intima-media thickness and wall shear stress in common carotid arteries in healthy male subjects, *Circulation*, **94**, 3257-3262, 1996.
- [30] C. Irac, C. Cortese, E. Fiaschi, C. Carallo, E. Farinaro, A. Gnasso, Wall shear stress is associated with intima-media thickness and carotid atherosclerosis in subjects at low coronary heart disease risk, *Stroke*, **35**, 464-468, 2004.

MATERIAL CHARACTERIZATION ISSUES IN FEA OF LONG BONES

Nikola D. Korunovic^{1*}, Miroslav D. Trajanovic¹, Dalibor M. Stevanovic¹,
Nikola M. Vitkovic¹, Milos S. Stojkovic¹, Jelena R. Milovanovic¹ and Dragana S. Ilic²

¹ Faculty of Mechanical Engineering, University of Nis
Aleksandra Medvedeva 14, 18000 Nis, Serbia
nikola.korunovic@masfak.ni.ac.rs
miroslav.trajanovic@masfak.ni.ac.rs
dalibor.stevanovic85@gmail.com
vitko@masfak.ni.ac.rs
miloss@masfak.ni.ac.rs
jeki@masfak.ni.ac.rs

² Clinical Center Nis
Bulevar Zorana Djindjica 48, 18000 Nis
e-mail: gagus@ninet.rs
gagus@ninet.rs

Keywords: Subject specific FEA, material mapping, CT, femur.

Abstract. *One of the main issues that arise during preparation of models for subject specific finite element analysis (FEA) of long bones is the accuracy of material characterization. This paper tends to identify the most common sources of material characterization errors, which are sometimes also interconnected with bone geometry reconstruction errors, in order to help in creation of more accurate finite element models of long bones. Reconstruction of patient's bone geometry is usually based on medical images obtained by means of computational tomography (CT). Material characterization is performed either by segmentation of the model to characteristic zones that are assigned typical averaged material properties, or by local material mapping, based on bone density values estimated from CT numbers. Some of the main factors that influence material characterization accuracy are the choice of material model, the approach to material properties averaging, x-ray tube parameters, scanner calibration, relations between CT image gray values and bone density and relations between bone density and elastic properties of the bone. The paper brings a comparison of numerical results obtained from a number of subject-specific analyses of human femur, in which the approaches to material modeling were varied. Material modeling was performed using either geometry segmentation with material properties averaging or local material mapping. The results of the analyses were examined and mutually compared, and the influence of material characterization errors to analyses results was identified and explained.*

1 INTRODUCTION

Finite element analysis (FEA) is widely accepted as a technique for subject-specific evaluation of stress state in human bones, bone fixators and implants, with the purpose of surgery planning or bone tissue strength evaluation [1, 2]. It is especially useful in non-standard cases of bone fractures or tissue degradation. Such are the cases when it is not easy to choose an appropriate fixator from a number of standard ones, or when it is necessary to design a custom implant and predict its mechanical properties. The use of FEA in surgery planning is most valuable for less experienced orthopedists, as it may help them choose an adequate fixator and place it correctly on the bone.

Surgery planning often requires that the analyses are conducted in a very short time, i.e. in a few hours, thus a compromise approach to preprocessing and processing phases of FEA must be taken. In such conditions, one of the main issues that arise during finite element (FE) model preparation is the accuracy of material characterization.

This paper tends to identify the common sources of material characterization errors in FEA of long bones. It also brings the comparison of numerical results obtained from a number of subject-specific analyses of human femur, in which the approaches to material modeling were varied. Material modeling was performed either by geometry segmentation with material properties averaging or by local material mapping. The results of the analyses indicate that material characterization strategies have a significant influence on results accuracy in subject specific FEA of long bones.

2 BONE MATERIAL CHARACTERIZATION

The differences in intensity and direction of the stresses in various bone segments cause the differences in bone remodeling process, so the structure and density of remodeled bone tissue vary inside the bone. As a consequence, elastic properties of the bone also vary from point to point. Bone material characterization for use in FEA is performed either by segmentation of the model to characteristic zones that are assigned typical (averaged) material properties, or by local material mapping, based on bone density values estimated from radiological density (i.e. gray values or HUs). The second approach gained popularity in subject-specific FEA of bones, as it can be used to quickly model the inhomogeneous material properties.

Some of the main factors that influence material characterization accuracy are the choice of material model, the approach to material properties averaging, x-ray tube parameters, scanner calibration, relations between CT image gray values and bone density and relations between bone density and elastic properties of the bone.

Material properties are usually modeled as linear isotropic or anisotropic. While a number of studies have shown that anisotropic properties yield more accurate results [3, 4], they are much more tedious to determine and apply. It is also claimed that the difference in results is not worth the extra time and effort necessary for orthotropic material modeling [5]. This is even more relevant in the case of subject-specific bone analysis.

One of the earliest approaches used for bone material characterization in FEA is the assignment of averaged material properties to different bone segments. According to it, the bone is divided at least to cortical and spongy volume segments, but those may be further subdivided into zones that are expected to have notably different material properties [6, 7]. The idea behind the process is relatively simple, but it has a number of drawbacks. The major one is the use of average elastic properties that are assigned to different bone segments, as elastic properties of bone tissue may vary significantly throughout the bone volume. This is especially true for long bones like femur or tibia. Recognition and creation of zones inside the bone also requires significant time and effort, which does not speak in favor of this option, espe-

cially concerning subject-specific FEA. The mentioned drawbacks will be illustrated in an example presented in the next chapter.

On the other hand, local material mapping strategies imply the assignment of unique elastic properties to each finite element of the bone model, based on the density of bone tissue at the corresponding location, which is estimated from CT images. Elastic properties may be constant over the whole finite element, or they may vary spatially within elements volume. Empirical equations are used to establish relations between reported CT image gray values and tissue density, as well as between tissue density and elastic properties [8, 9]. As commercial FEA codes often accept only a limited number of material definitions (material cards), the whole range of possible values of an elastic property, like Young's modulus, is usually subdivided into a number of intervals, and each finite element is assigned a mid value of the interval to which it's calculated value belongs. While this approach enables a fast assignment of material properties to FE model, it must be performed carefully, as there are many issues that may influence the accuracy of results obtained by subsequent analyses. Some of those are:

- *Correlation between results accuracy and number of material intervals.* It is known that analysis results tend to converge to exact solution with a rising number of elements in a mesh [1, 10]. The same tendency is also present in the case of a rising number of material intervals [11]. Prior to an analysis, an optimal number of material definitions should be chosen through a convergence analysis, or an empirically estimated value for a certain bone type and mesh size should be used.
- *Calibration of CT dataset.* Depending on CT scanner type, CT tube parameters and even of oscillations in supply voltage, the reported CT numbers (gray values or HUs), in different scans of the same bone, may vary. Thus the calibration of CT dataset using a phantom is recommended, to establish a correct relation between reported CT numbers and radiological density of bone tissue ρ_{QCT} [8].
- *The relation between radiological density ρ_{QCT} and ash density ρ_{ash} .* It should ideally be equal to 1, but there are deviations present, which depend on bone tissue type and specific bone specimen. If possible, they should be taken into account [8].
- *The relation between ash density ρ_{ash} and apparent density ρ_{app} .* The ratio ρ_{ash}/ρ_{app} is close to 0.6 in human cortical bone, while for spongy bone it ranges from 0.34 to 0.62 [8]. There are also possible difficulties in experimental determination of the densities, as explained in [8]. For practical use, empirical relations that directly connect HU values and apparent density are often used, which either take into account or ignore all mentioned issues.
- *The relation between ash density ρ_{ash} or apparent density ρ_{app} and elasticity modulus E .* The relations presented in literature are numerous [9, 12, 13], and they yield surprisingly different results, as shown in [9].
- *Material mapping algorithm.* As already mentioned, two approaches are used to assign material properties to finite elements of subject-specific models, and those imply the assignment of either spatially variable or constant material properties. Material properties that vary spatially inside each finite element cannot be simply defined in FEA codes. Thus they have not been used very much, although they are reported to yield more accurate strain results [14]. The constant values assignment approach has many variations, depending on how the average value of a material property is calculated from CT numbers. The main difference between those variations is reflected in the av-

eraging technique used. According to the simplest one, density values are assigned to every finite element node, based on the nearest value on CT sampling grid, and then a weighted average of nodal values is assigned to the element [14]. According to another technique, average element density is calculated from eight points surrounding element centroid [14]. The aforementioned techniques are found to produce inaccurate results when elements are significantly larger than the spacing of CT sampling grid. One of the more advanced techniques starts with averaging of densities from CT grid points that belong to a finite element [11]. A consecutive improvement of this technique implies that an average HU value for a finite element is calculated by numerical integration of HU field [15]. According to a further improved technique, Young's modulus field is first calculated from HU field and then averaged by numerical integration [16], to compensate for the fact that the averaging procedure is not commutative, as modulus-density relations are usually nonlinear. Other approaches are also present in literature, like the one based on the intermediate step of material blocks creation [17]. This approach is said to be more accurate than the others, when finite element size is larger than the volume occupied by voxels chosen for property averaging, or when element size is comparable to or smaller than voxel size. Material mapping algorithms may also assign inaccurate (lower than real) values of material properties to boundary layers of finite elements, as some of the voxels used for averaging do not or only partially belong to bone tissue. Material mapping algorithm is certainly one of the most important factors affecting bone material characterization accuracy, and an universal one is still not recognized.

- *The dependence of material mapping results on mesh size.* This issue is partially connected to the choice of material mapping algorithm, as already explained. If finite elements are too large, a number of factors that influence FEA results accuracy may be present. At some locations within FE model, element size may be large comparing to the thickness of cortical bone, so it may also cover a large portion of spongy bone. As a result of material properties averaging, a too small value of Young's modulus or other elastic property may be assigned to it. Averaging of material properties may be the cause of inaccuracies even if a finite element covers only a single tissue type, in cases when the tissue is highly porous, as spongy bone for example. The mentioned problem is also interconnected with CT image voxel size.
- *Connection between material mapping results and accuracy of geometry reconstruction.* If cortical bone is much thinner than CT image voxel size, gray values of voxels that contain a thin layer of cortical bone may be much lower than the usual equivalent of cortical bone, as averaging algorithms also take into account large portions of adjacent soft tissue or spongy bone. Thus, threshold based methods used for bone surface reconstruction may omit some voxels, and the surface of the cortical bone in corresponding areas may not be detected at all. The simplest way to avoid this situation is to reduce the lower threshold value, so a greater portion of the surface is recognized. Unfortunately, in this case some of the tissue surrounding cortical bone (periosteum) is also recognized as a cortical bone, and so are the denser segments of spongy bone. Thus, the reconstructed bone surfaces may be inaccurate, e.g. the reconstructed outside surface may be larger than the real one. This approach represents a trade-off that enables bone surface reconstruction to be performed more quickly. However, in this case the averaging of material properties assigned to finite elements situated on the bone surface may produce too low values of elastic properties, as density of connective tissue that surrounds the bone gets included in the calculation.

3 MATERIAL CHARACTERIZATION STUDY

In order to explore the influence of material characterization approaches to the results of FEA of long bones, a study was performed on a number of subject-specific models of human femur that were assigned material properties using a number of different approaches.

3.1 Finite element models and material characterization

A CT scan of lower extremities, characterized by pixel size of 0.782mm, was used as a basis for creation of 5 different FE femur models, with the following features:

- **Model 1** (Figure 1). Only the external femur surface was reconstructed from CT images. Femur volume was meshed with quadratic tetrahedron elements, using average edge size of 3mm at the bone surface and fast element growth towards the inside of the bone. Material mapping was performed in order to assign material properties to all elements, using the empirically obtained relation between HU values and bone density (Eq. 1) and relation between bone density and Young's modulus taken from [12] (Eq. 2). Three variations of the model were created, (**model 1a**, **model 1b** and **model 1c**), using 20, 100 and 300 material definitions, covering the range of Young's modulus values from 0 to 19GPa.

$$\rho_{app} [g / cm^3] = 0.1957 + 0.001053 HU \quad (1)$$

$$E [N / mm^2] = 6950 \cdot \rho_{app}^{1.49} \quad (2)$$

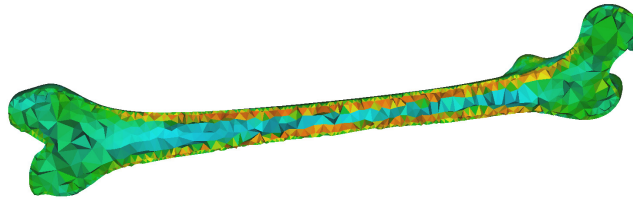


Figure 1: Cross section of femur FE model, with mapped material properties (model 1)

- **Model 2** (Figure 2). The same external surface that was used to create model 1, was used as external surface of model 2. In this case the inner surface of the cortical bone was also constructed. It was done by merging the surface of medullary cavity, reconstructed from CT images, and two surfaces that were offset from external femur surface in epiphyses areas, using offset value of 1 mm. The offset surfaces were created in order to approximate the thin part of cortical bone that could not be properly reconstructed from CT images. Two zones inside femur model were created, one inside the inner cortical bone surface, and one between the inner and outer cortical surfaces. The zoned model was meshed using the same mesh parameters as in the case of model 1. Material mapping was performed using the same relations that were used for model 1.

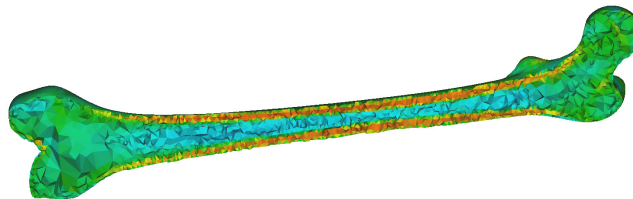


Figure 2: Cross section of zoned femur FE model, with mapped material properties (model 2)

- **Model 3** (Figure 3). Separate zones inside the model were created for cortical bone and medullary cavity. The volume of spongy bone was divided into a number of zones, according to usual distribution of trabecular density, as described in [6]. Material characterization was performed by assignment of constant Young's modules to the elements belonging to cortical bone zone and to the elements belonging to spongy bone zones (Table 1). A very small value of Young's modulus (1MPa) was also assigned to elements inside medullary cavity, where bone marrow is situated. Material properties were defined using trial and error approach, in order for model 1 to have the same value of maximum displacement as model 2.

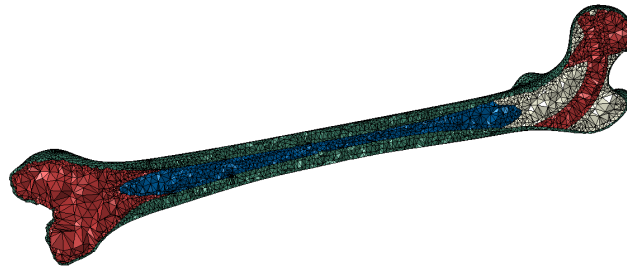


Figure 3: Cross section of zoned femur FE model, with constant averaged material properties (model 3)

Compared to model 2, model 1 contains larger elements near the surface, each of them partially covering the cortical bone and partially the spongy bone. Model 2 contains considerable smaller elements near the external surface, most of them covering only the cortical bone and some of them also covering only the small portions of spongy bone.

Boundary conditions and loads were chosen such as to simulate one legged stance, according to [18] (Figure 4).

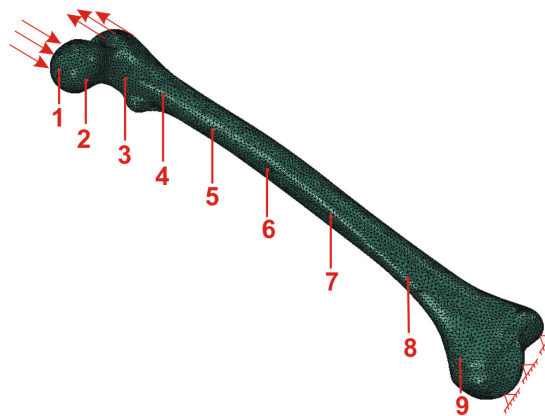


Figure 4: One of FE femur models with symbolically presented boundary conditions and loads. The points that were used to monitor analysis results are also shown.

The main goals of the study were defined as follows:

- To compare the results of the analyses obtained using FE models to which material properties were assigned using either material mapping approach or combined zoning-mapping approach (model 1 vs. model 2).
- To compare the results of the analyses performed on FE models which were assigned material properties in two different ways, by combined zoning - material mapping procedure or by zoning and constant average material properties assignment (model 2 vs. model 3).

- To identify some of the ways in which material characterization strategy affects the results of subject specific FEA of long bones.

3.2 Results

Nodal displacements and equivalent Von Misses stress field were monitored over whole models and especially at selected nodes, shown in Figure 4. Before the study was performed, the influence of the number of different material definitions to analysis results was investigated using model 1 (Figure 5). Because the results obtained using three different numbers of material definitions were very similar, the study was continued using only model 1b (containing 100 material definitions), which will in further text be referred to as model 1. In order to properly compare the results, model 2 was also mapped using 100 material definitions.

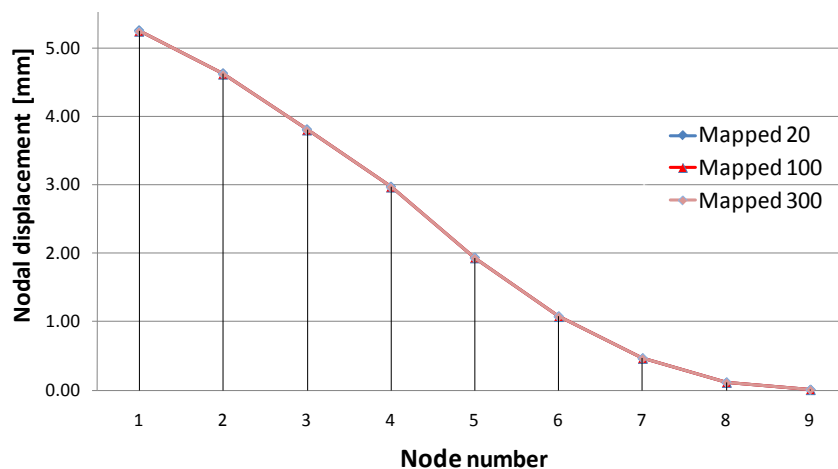


Figure 5: Magnitude of displacement at selected nodes, obtained by analysis of femur models in which material properties were defined using 20, 100 or 300 material cards (1a, 1b and 1c).

Although the same material mapping equations were used for models 1 and 2, the difference between nodal displacements obtained using the two models is notable, and it ranges from 4.7 to some 11.3%, for nodes 1 - 8 (Figure 6). As quadratic elements were used, it was not expected that mesh size variation alone should produce such a difference. Thus, it is speculated that the observed difference is the consequence of material mapping approach. It is probable that the larger portion of model 2 was assigned higher values of Young's coefficient than in the case of model 1. As it contains smaller elements near the surface, material properties averaging process may not have taken into account as large portions of spongy bone as it did in the case of model 1, where the elements near the surface are larger.

As already mentioned, material properties of model 3 were adjusted, in order to achieve the same maximal displacement as in the case of model 2, under the same loading conditions (Figure 7). As it may be seen from the graphic, displacement value at node 1 obtained by FEA of the two models is the same, but at nodes 2-5 it is noticeably different. That means that the deformed shape of model 3 is different from deformed shape of model 2. As it may be seen from Table 1, equivalent Young's modulus of cortical bone ($E_{\text{cortical}}=12.7$ GPa), that is defined in order to achieve the same maximal displacement over the model, is quite low considering the range of values reported for human cortical bone (10.9 - 20.6 GPa) [19]. On the other hand, the range of Young's modulus values for model 2, which results from material mapping process, is approximately 0 - 19 GPa. It is hard to determine this range for cortical bone only, as some elements at epiphyses have gotten smaller modulus values, because tissue density is averaged based on pixels that partially cover the spongy bone.

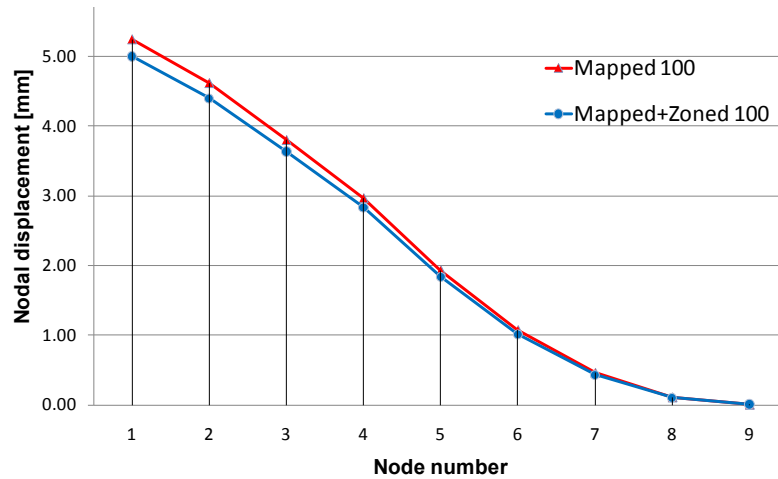


Figure 6: Displacement magnitude at selected nodes, obtained by analysis of models 1 and 2 (mapped material properties and zoned + mapped material properties)

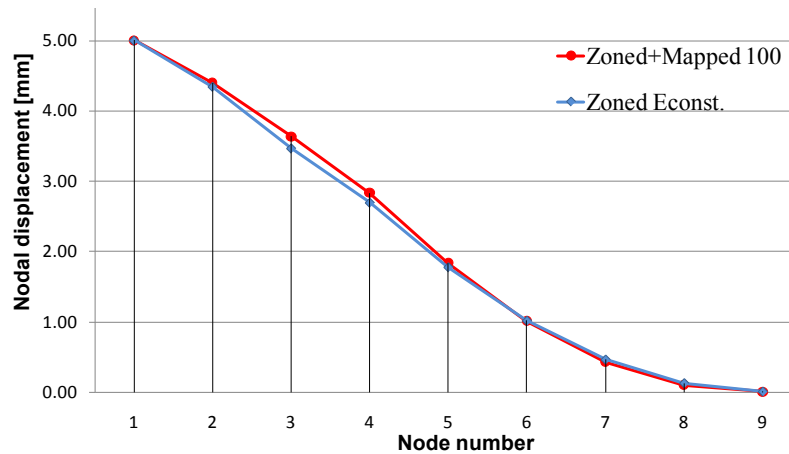


Figure 7: Total displacement at selected nodes, for models 2 and 3 (zoned + mapped material properties and zoned with constant material properties)

The conclusions that may be drawn from comparison of analysis results obtained using models 2 and 3, are:

- It is hard to determine the average material properties that will be assigned to different bone segments when zoning approach is used.
- Even if results obtained using local material mapping and zoning / average material properties assignment approaches are similar in one part of FE model, they may be different in the other part.
- There will always be some error present when zoning / average material properties assignment approach is used, as in reality elastic properties of cortical bone vary from point to point.

Equivalent stress field obtained by FEA of models 1 - 3 is shown in Figure 8. It is obvious that numerically obtained stresses at the surface of models 1 and 2 are very similar, while the stresses at the surface of model 3 are quite different. This difference is the consequence of difference in Young's modulus distribution, which is variable in first two cases, and constant in the third. On one side, it is more realistic to have variable Young's modulus over the model, but as the consequence of the nature of material mapping, and especially of averaging techniques used, it happens that for models 1 and 2 the maximal value of stress is located rather unrealistically, deep under the bone surface.

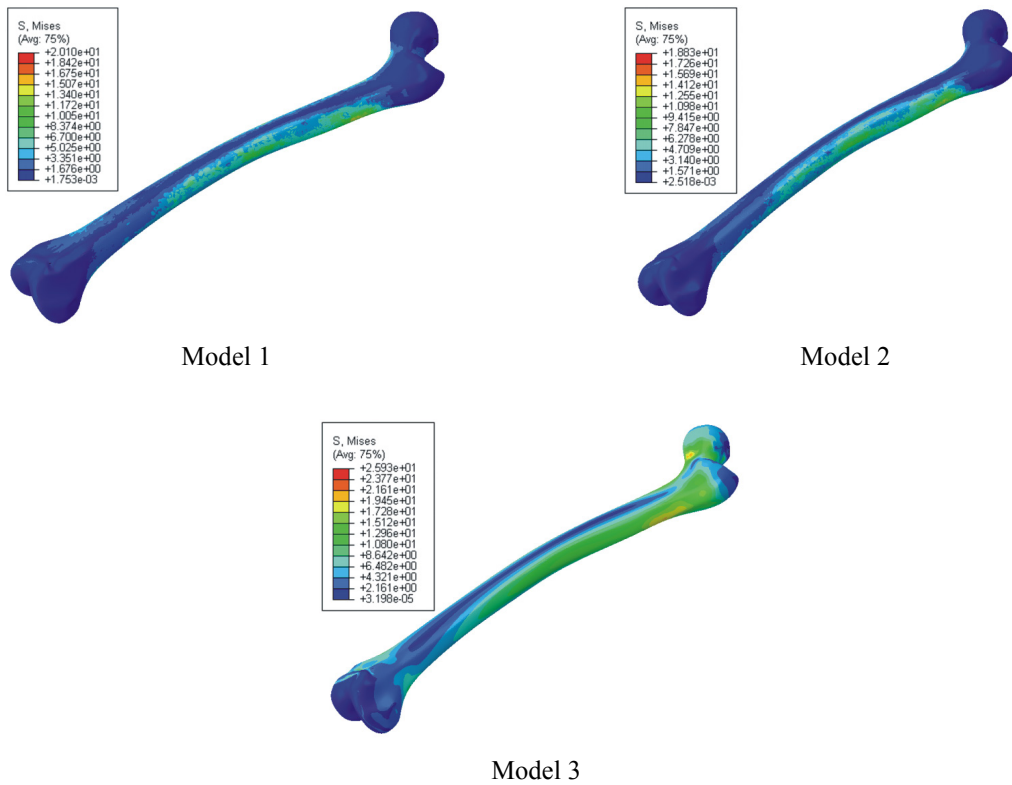


Figure 8: Equivalent stress field obtained by FEA of models 1-3

The maximal values of displacement, stress and strain obtained by FEA of all three femur models are given in Table 1. It may be noticed that the analysis of the zoned model, where constant averaged material properties were used, yields considerably smaller value of maximal strain.

Femur model	Material characterization	Number of elements	Number of nodes	Max. displacement u[mm]	Max. Eq. Stress [MPa]	Max. strain
1a	Mapped, 20 material definitions	59 926	98 298	5.50	20.26	0.00192
1b	Mapped, 100 material definitions	59 926	98 298	5.49	20.10	0.00202
1c	Mapped, 300 material definitions	59 926	98 298	5.49	20.26	0.00201
2	Zoned + Mapped, 100 material definitions	149 712	217 762	5.24	18.33	0.00200
3	Zoned, $E_{cortical}=12.7\text{GPa}$, $E_{trabecular}=0.07\text{-}0.3\text{GPa}$	149 712	217 726	5.25	25.93	0.00839

Table 1: Material characterization, model sizes and maximal values of displacement, stress and strain field variables for various femur models used in the study.

4 CONCLUSIONS

Common sources of geometry material characterization errors in subject specific FEA of long bones, according to literature and experience of the authors, were identified and discussed in the paper. The study was performed in order to investigate this topic in more depth,

in which various approaches were used to create a number of subject specific models of human femur. The same boundary conditions were applied to all finite element models used in the study. Comparison of the obtained results led to the conclusions that follow.

In the presented study, local material mapping approach was compared with zoning / constant material properties approach, as well as with combination of those two. The difference of up to 11.3% in nodal displacements between mapped and zoned / mapped models was noticed. It is considered to be the consequence of combined influence of material properties averaging technique used during material mapping and size of finite elements located near the bone surface. The difference in deformed shapes between mapped and zoned models was also significant, which is the consequence of material characterization approach, as the same mesh was created on the two compared models. It is concluded that zoning / constant material properties assignment method will always produce a significant error in stress / strain prediction and that it is hard to estimate an averaged value of Young's modulus which will represent the elasticity of bone tissue over a whole long bone. A tendency of mapped FEA models to report the maximal stress values deep beneath the bone surface is also identified as a consequence of material characterization approach.

ACKNOWLEDGMENT

The paper is a result of multidisciplinary research in the domain of bioengineering in real medical practice (Virtual Human Osteoarticular System and its Application in Preclinical and Clinical Practice¹) which is sponsored by the Ministry of Science and Technology of the Republic of Serbia - project id III 41017 for the period of 2011-2014. We are grateful to prof. dr sci. med. Milorad Mitkovic and prof. dr sci. med. Stojanka Arsic from University Clinical Center of Nis, Serbia.

REFERENCES

- [1] M. Viceconti, M. Davinelli, F. Taddei, A. Cappello, Automatic generation of accurate subject-specific bone finite element models to be used in clinical studies. *Journal of Biomechanics*, **37**, 1597-1605, 2004.
- [2] E. Schileo, F. Taddei, A. Malandrino, L. Cristofolini, M. Viceconti, Subject-specific finite element models can accurately predict strain levels in long bones. *Journal of Biomechanics*, **40**, 2982-2989, 2007.
- [3] V. Baca, Z. Horak, P. Mikulenska, V. Dzupa, Comparison of an inhomogeneous orthotropic and isotropic material models used for FE analyses. *Medical Engineering & Physics*, **30**, 924-930, 2008.
- [4] H. Yang, X. Ma, T. Guo, Some factors that affect the comparison between isotropic and orthotropic inhomogeneous finite element material models of femur. *Medical Engineering & Physics*, **32**, 553-560, 2010.
- [5] L. Peng, J. Bai, X. Zeng, Y. Zhou, Comparison of isotropic and orthotropic material property assignments on femoral finite element models under two loading conditions. *Medical Engineering & Physics*, **28**, 227-233, 2006.

¹ <http://vihos.masfak.ni.ac.rs>

- [6] M. Trajanović, N. Korunović, J. Milovanović, N. Vitković, M. Mitković, Application of computer models of Mitković selfdynamizable internal fixator in rehabilitation of femur traumas. *Facta Universitatis*, **8**, 27-38, 2010.
- [7] K.E. Rudman, R.M. Aspden, J.R. Meakinj, Compression or tension? The stress distribution in the proximal femur. *BioMedical Engineering OnLine*, 5:12 doi:10.1186/1475-925X-5-12., 2006.
- [8] E. Schileo, E. Dall'Ara, F. Taddei, A. Malandrino, T. Schotkamp, M. Baleani, M. Viceconti, An accurate estimation of bone density improves the accuracy of subject-specific finite element models. *Journal of Biomechanics*, **41**, 2483-2491, 2008.
- [9] B. Helgason, E. Perilli, E. Schileo, F. Taddei, S. Brynjólfsson, M. Viceconti, Mathematical relationships between bone density and mechanical properties: a literature review. *Clinical Biomechanics*, **23**, 135-146, 2008.
- [10] D. Stevanović, N. Korunović, M. Trajanović, M. Trifunović, J. Milovanović, M. Stojković, Finite element model of human tibia and preliminary analysis, I. Cosic eds. *11th International scientific conference MMA 2012 - Advanced production technologies*, Novi Sad, Serbia, September 20-21, 2012.
- [11] C. Zannoni, R. Mantovani, M. Viceconti, Material properties assignment to finite element models of bone structures: a new method. *Medical Engineering & Physics*, **20**, 735-740, 1998.
- [12] E.F. Morgan, H.H. Bayraktar, T.M. Keaveny, Trabecular bone modulus-density relationships depend on anatomic site. *Journal of Biomechanics*, **36**, 897-904, 2003.
- [13] T.S. Kaneko, J.S. Bell, M.R. Pejcic J. Tehranzadeh, J.H. Keyak, Mechanical properties, density and quantitative CT scan data of trabecular bone with and without metastases. *Journal of Biomechanics*, **37**, 523-530, 2004.
- [14] B. Helgason, F. Taddei, H. Palsson, E. Schileo, L. Cristofolini, M. Viceconti, S. Brynjólfsson, A modified method for assigning material properties to FE models of bones. *Medical Engineering & Physics*, **30**, 444-453, 2008.
- [15] F. Taddei, A. Pancanti, M. Viceconti, An improved method for the automatic mapping of computed tomography numbers onto finite element models. *Medical Engineering & Physics*, **26**, 61-69, 2004.
- [16] F. Taddei, E. Schileo, B. Helgason, L. Cristofolini, M. Viceconti, The material mapping strategy influences the accuracy of CT-based finite element models of bones: An evaluation against experimental measurements. *Medical Engineering & Physics*, **29**, 973-979, 2007.
- [17] G.U. Unnikrishnan, E.F. Morgan, A New material mapping procedure for quantitative computed tomography-based, continuum finite element analyses of the vertebra. *J Biomech Eng.*, **133**, doi:10.1115/1.4004190., 2011.
- [18] S. Sowmianarayanan, A. Chandrasekaran, R. Krishnakumar, Finite Element Analysis of Proximal Femur Nail for Subtrochanteric Fractured Femur. Taylor & Francis Group eds. *International ANSYS Conference: A World of Simulation*, Pittsburgh, May 2-4, 2006.
- [19] Y. H. An, R. A. Draughn, *Mechanical Testing of Bone and the Bone-Implant Interface*, ISBN 1420073567, 9781420073560. Taylor & Francis, 2010.

DESIGN STUDY OF ANATOMICALLY SHAPED LATTICE SCAFFOLDS FOR THE BONE TISSUE RECOVERY

Milos S. Stojkovic¹, Nikola D. Korunovic¹, Miroslav D. Trajanovic¹,
Jelena R. Milovanovic¹, Milan B. Trifunovic¹ and Nikola M. Vitkovic¹

¹ Faculty of Mechanical Engineering, University of Nis
Aleksandra Medvedeva 14, 18000, Nis, Serbia
e-mail: miloss@masfak.ni.ac.rs
nikola.korunovic@masfak.ni.ac.rs
miroslav.trajanovic@masfak.ni.ac.rs
jeki@masfak.ni.ac.rs
milant@masfak.ni.ac.rs
vitko@masfak.ni.ac.rs

Keywords: lattice scaffold, elastic properties, FEA, structural modulus, tissue engineering.

Abstract. *The current major scaffold design concepts for bone tissue recovery are characterized by labyrinthine design. Their main shortcomings are low level of permeability for new growing tissue, poor design adaptability in regard to particular anatomy and required bio-mechanical conditions during recovery, as well as very demanding post processing after free form fabrication. In contrast to the most of the existing solutions, latticed scaffold design does not try to imitate the trabecular structure and rejects the labyrinthine concept. It is characterized by simple 3D latticed support structure, which provides a high level of permeability for the new growing tissue cells, and in the same time a proper level of bio-adhesiveness. In addition, its design is easy to manage in order to make it follow the particular anatomical shape and at the same time provide the required elastic properties and structural strength. The paper presents a part of design concept proving process, which is related to stress analysis of the anatomically shaped lattice scaffold design. The aim of the analysis was to identify functional relation between design parameters and elastic properties of the scaffold. The established relations are crucial for getting optimal values of elastic properties of scaffold that are required in a specific trauma-fixation case. The design study shown in the paper was done for the case of lattice scaffold anatomically shaped to the upper part of proximal diaphyseal trauma of rabbit tibia. Design parameters which were altered within the design study were lattice's struts cross-sectional area, density of the struts and angle of the struts intersection. The analysis showed that structural flexibility of latticelike scaffold may easily be changed through modification of three selected design parameters. In this way, it is confirmed that the proposed type of scaffold has an important capability to adapt its elastic properties to the required values, while being able to keep its great permeability and geometrical consistency to the particular anatomy of trauma region.*

1 INTRODUCTION

For more than 15 years of research, numerous design concepts [1-7] of scaffolds that are aimed for the bone tissue recovery have been developed. However, there are still challenges to overcome in an effort to optimize design of the bone tissue scaffolds. Those challenges arise from the two opposite groups of requirements. The demands of the first group are:

- to provide maximal permeability of the scaffold volume for the new growing tissue cells,
- to ensure biocompatibility with native tissue,
- to control biodegradability of the scaffold and
- to maximize simplicity of the scaffold fixation and implantation.

The demands of the second group are:

- to achieve the high level of bio-adhesiveness of the scaffold structure elements,
- to provide high level of geometrical, i.e. anatomical consistency (*congruency*),
- to manage the mechanical properties of the scaffold (e.g. structural strength and stiffness) to ensure required deformations and
- to ensure high level of design manufacturability.

One of the very important demands is to find the design which is capable of being changed easily, in order to ensure the required deformations of the scaffold and bone graft. This deformation is crucial for stimulation of the ossification process inside the bone graft but also between the native tissue and graft. In the cases of large traumas, where it is necessary to temporarily or permanently substitute the missing piece of the bone, the scaffold has to hold the bone graft, but also to enable load transfer through its struts. In accordance to that function, it is very important to be able to manage the mechanical properties of the scaffold by changing its design. Depending on type of trauma and fixation frame that is selected, surgeon should choose and implant a proper scaffold. Besides the fact that scaffold design should coincide to anatomy of traumatized or missing piece of the bone, it should also provide proper biomechanical features, e.g. structural stiffness.

A number of studies are reported in literature that are related to investigation or optimization of elastic properties and structural strength of scaffolds, fabricated using various additive technologies. Most of them are performed on idealized or unit cell scaffold structures, subjected to axial loading, with or without comparison with experimental results. Just a moderate number of studies are taking into account realistic, physiological loading conditions and the whole bone-scaffold-fixation frame assembly. In [8] three titanium scaffolds of different porosity were subjected to finite element analysis (FEA), and the results were compared mutually and with experimental ones. While FEA proved to be a good technique for prediction of elastic properties of the scaffold, the results were notable different from experimental ones. The reason for this lays in the fact that the real geometry of the scaffold, which was produced using a rapid prototyping technique, was quite different than idealized scaffold geometry used in FEA. Similar results were obtained in [9], where polyamide and polycaprolactone scaffolds, fabricated using selective laser sintering were subjected to tensile and compression tests as well as to FEA. In [10] both representative volume elements of scaffold and both representative volume elements of bones were subjected to FEA. A good overview of the studies present in literature so far is given in [11]. In this paper, the suitability of open-porous titanium scaffolds to act as bone scaffolds is tested. A number of scaffold designs with variable porosity were subjected to axial compression up to the occurrence of structural failure, and the results were compared to numerically obtained ones. Moreover, in aforementioned study the scaffolds were custom designed to fit a large missing part of femoral bone, and FEA was performed to predict the behavior of all designs variations under physiological loading conditions.

In all the papers the tendency was present to establish correlations between scaffold design parameters and its elastic properties. Effective porosity was often used as an universal scaffold design feature, while structural modulus was most often used to characterize resulting elastic properties of the scaffolds.

The main goal of the studies described in this paper was to prove that elastic properties of the lattice scaffold may easily be changed to achieve the required mechanical properties, while keeping its permeability and other favorable features of lattice design described in the next chapter.

2 LATTICE SCAFFOLD DESIGN CONCEPT

Anatomically shaped latticed scaffold (in further text abbreviation ASLS will be used) is a new design concept of scaffold aimed to hold implanted bone graft. It is designed in a way to provide high level of permeability, maximal geometrical congruency to particular anatomy, manageable design, simple and efficient fixation and high level of manufacturability. One of the most important objectives of this kind of scaffold is to enable orthopaedic treatment of large scale trauma and to ensure thorough bone tissue recovery. Striving to that goal, the imperative was to create design which is easy to change and consequently easy to tune its elastic properties and structural strength. Having this feature the ASLS design could be tailored for required fixation case i.e. for required load distribution between fixation and traumatized bone region.

Briefly, ASLS consists of two groups of simple struts (Figure 1). The struts in the first group follow the geometry of outer wrapping surface of the bone but they also follow the geometry of inner wrapping surface (near the medullary cavity). These *wrapping struts* form outer and inner surrounding support of the latticelike structure, which is characterized by densely interlaced lattice. Yet, this wrapping lattice is still sparse enough to enable easy penetration of vascular and nerve tissue/structures/ to the interior of the bone graft, ensuring the preconditions for bone tissue growth. The struts of the second group are located in the space of (future) spongy bone and they connect wrapping lattice structures providing required strength of the scaffold as a whole.

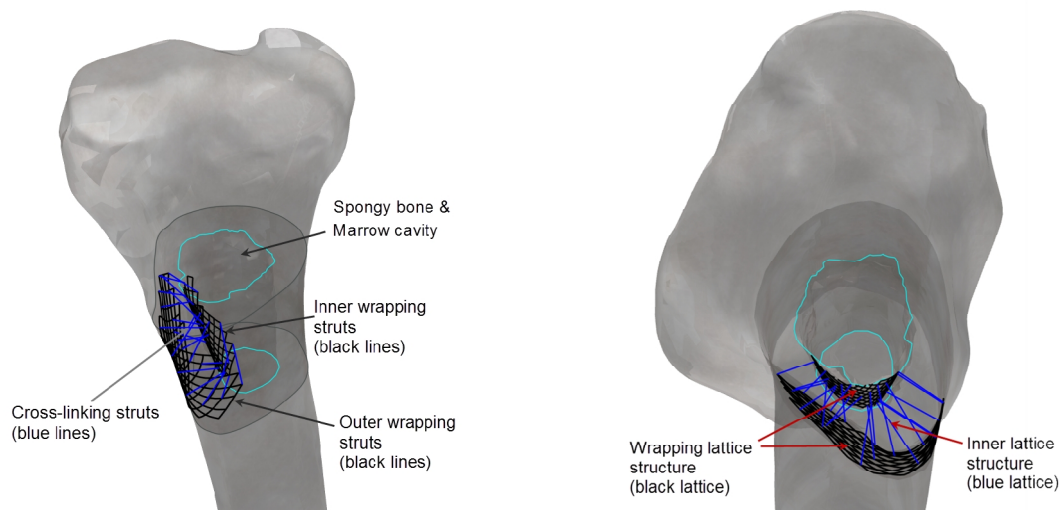


Figure 1: Design concept of ASLS (Anatomically Shaped Lattice Scaffold)

The second group of the struts is called *inner structure of cross-linking struts* and it is characterized by sparsely interlaced lattice than wrapping ones. Low density of the inner

structure is designed to assure easier and deeper vascularization and innervation of the bone graft (Figure 2-a). In addition, low density of the ASLS inner structure enables free transformation of the bone graft into the bone tissue as well as its interconnection to the neighboring healthy bone tissue and muscles. Furthermore, due to the bioadhesive process the cross-linking struts become the carriers and highways for cells colonization (*ossification centerlines*).

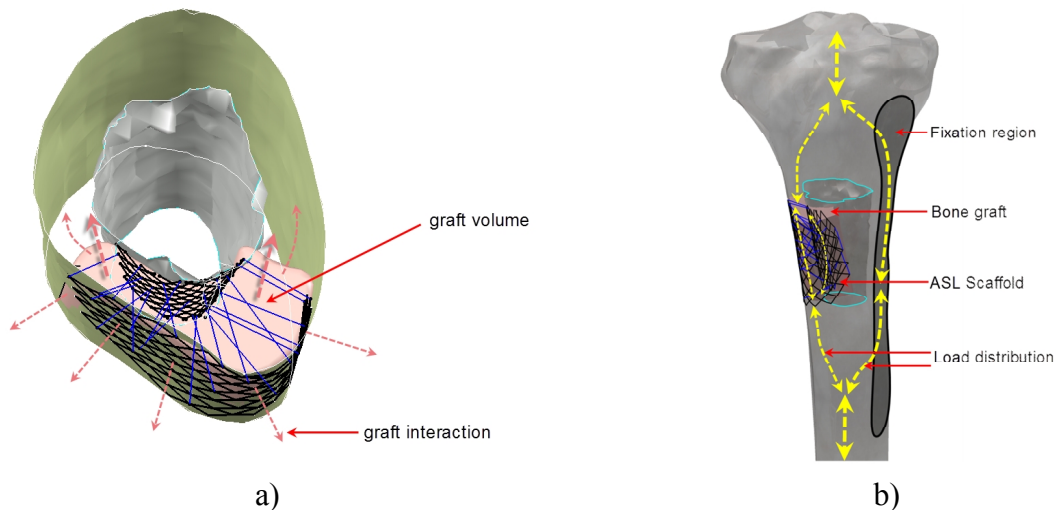


Figure 2: Bone graft insertion (a) and load distribution schema (b)

Another, very important feature of the ASLS design is its ability to withstand a component of the mechanical load, which is required to convey by the traumatized bone in order to keep ossification process within the bone graft active (Figure 2-b). Main component of the mechanical load will be transferred via fixation structure. This requirement imposes optimization of the ASLS design according to the trauma and fixation case and consequently in regard to the load that ASLS has to withstand (Figure 2-b). In the following chapter a short study is described, which was performed in order to prove that elastic properties of the proposed lattice scaffold design may easily be adjusted to the required structural stiffness, which will enable expected range of displacement. Design flexibility is achieved by modification of principal design parameters, such as lattice's struts cross-sectional area, density of the struts and angle of struts intersection.

3 DESIGN STUDIES

For the purpose of present and future design studies, two models of ASLS were created. Both ASLS samples were designed to match anatomical shape of the upper part of proximal diaphyseal trauma of rabbit tibia (Figure 3).

The first model was designed to wrap the whole bone's tube in the defect region (Figure 4). The main purpose of this model (in further referred to as *fully wrapped scaffold*), was to study the sensitivity of elastic properties of lattice design to change of principal design parameters. Compared to usual scale of the defect found in orthopaedic practice, this scaffold model may be considered too large and unfeasible.

The second model, showed in Figure 5, is congruent to the realistic shape of bone defect (Figure 3), and is based on CT images of rabbit tibia. This model was subjected to a load case that approximately represents physiological loading after the surgery. Then the sensitivity study similar to first one was performed, in which the struts angle was changed and the response of bone-scaffold assembly obtained.



Figure 3: ASLS for proximal diaphyseal trauma of rabbit tibia

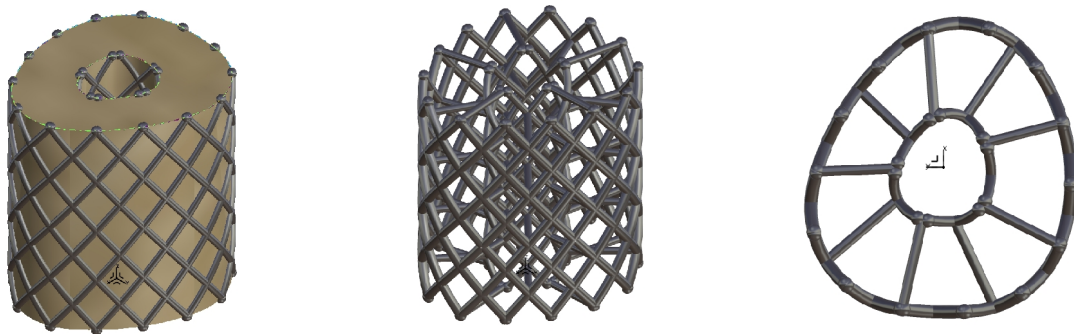


Figure 4: ASLS for complete envelopment of the bone – fully wrapped ASLS

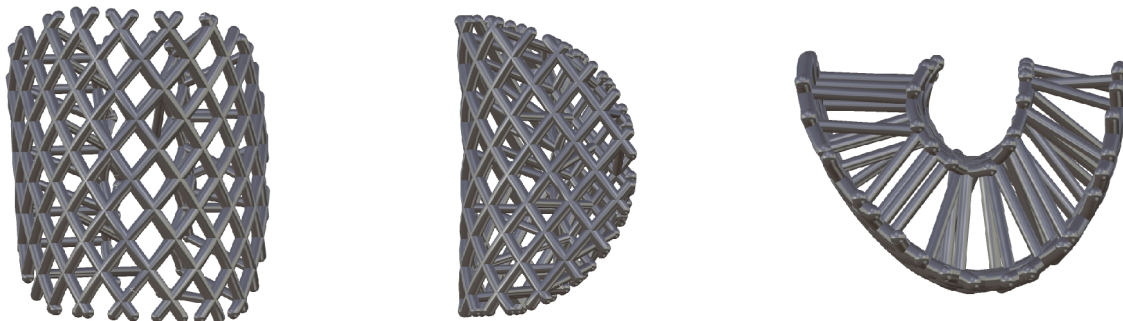


Figure 5: ASLS for realistic bone defect ($D = 8m$)

3.1 Sensitivity study of fully wrapped ASLS design elastic properties to principal parameters changes

In order to study the sensitivity of elastic properties of *fully wrapped* ASLS design (Figure 4) to variations of major design parameters, finite element model was built and positioned between two very stiff cylindrical bodies with parallel inner surfaces. It was then subjected to axial compression, with the force acting on one of the surfaces, the other one being fixed. Frictionless contact was defined between the scaffold and two other bodies, using multipoint constraint approach. Such boundary conditions have been chosen in order to minimize their effect on scaffold deformation, so that the changes in stress-strain field may be correlated only to changes in principal design parameters. The values of three different design parameters (density of the struts, lattice's struts cross-sectional area and angle of struts intersection) were

changed during the study. In this way, a total of seven scaffold instances, driven by parameters values given in Table 1, were created (Figure 6).

Scaffold porosity, defined according to Eq. (1), was also used, as derived parameter describing scaffold geometry.

$$\text{Scaffold porosity} = \left(1 - \frac{V_{\text{str}}}{V_{\text{circumscribed}}} \right) \times 100\% \quad (1)$$

where V_{str} is the effective volume of scaffold struts and $V_{\text{circumscribed}}$ is the volume of approximately cylindrical body circumscribing the scaffold (490.8mm^3).

Instance No.	Struts density [mm^{-1}]	Struts diameter [mm]	Struts cross-sectional area [mm^2]	Struts angle [$^\circ$]	Struts effective volume [mm^3]	Porosity
1	0.67	0.4	0.16	52	56.31	0.885
2	0.53	0.4	0.16	52	46.1236	0.906
3	0.43	0.4	0.16	52	36.7678	0.925
4	0.67	0.32	0.1024	52	38.94	0.921
5	0.67	0.48	0.23	52	80.42	0.836
6	0.67	0.4	0.16	32	53.2	0.892
7	0.67	0.4	0.16	72	55.82	0.886

Table 1: Fully wrapped ASLS instances used in the study, and corresponding parameter values.

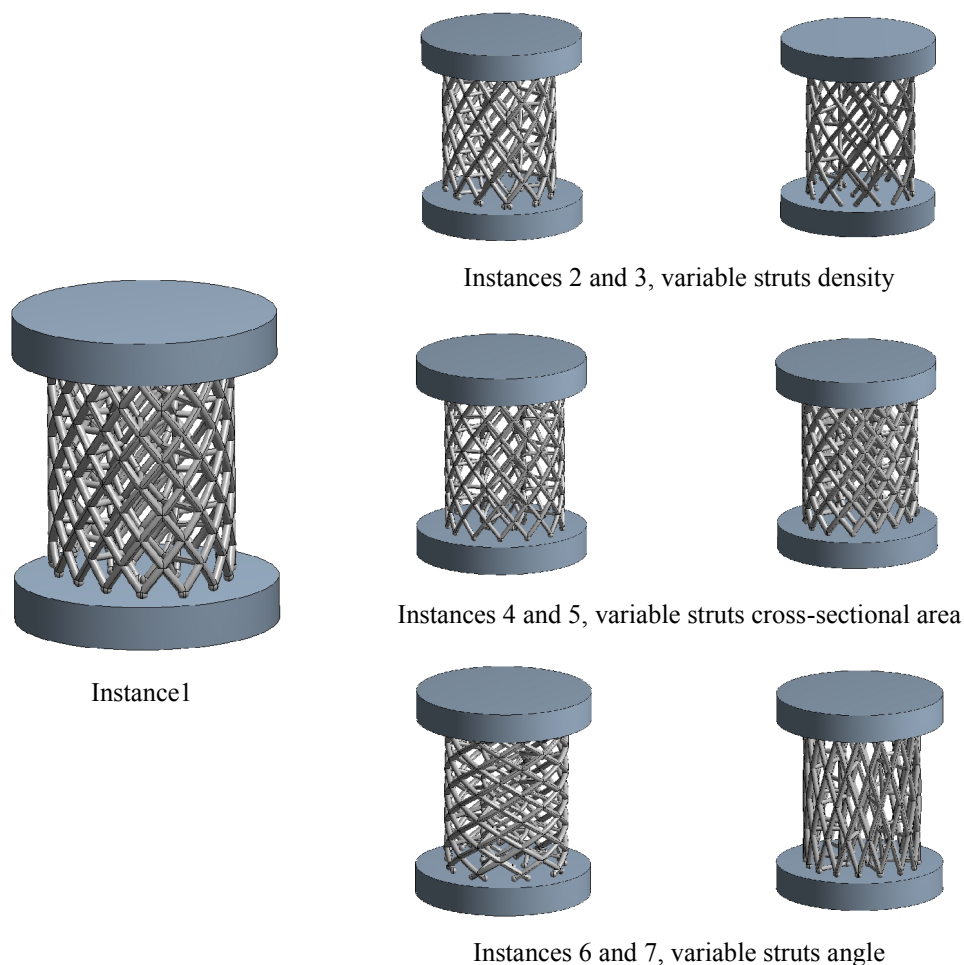


Figure 6: Instances of fully wrapped ASLS, obtained by change of principal design parameters.

Maximal axial displacement \mathbf{u}_x and maximal equivalent Von-Misses stress σ_{VM} were monitored as output quantities, as well as structural stiffness \mathbf{K}_S (Eq. 2) and structural modulus E_S (Eq. 3):

$$K_S = \frac{F}{\Delta l} \quad (2)$$

where F is the axial load and Δl is the change of initial scaffold length,

$$E_S = \frac{F \cdot l_0}{A \cdot \Delta l} \quad (3)$$

where l_0 is the initial scaffold length (10mm) and A is the area of the front surface of approximately cylindrical body circumscribing the scaffold (49.08mm).

Linear elastic material model was used to represent elastic behavior of the scaffold. Scaffold was supposed to be built from Arcam Ti6Al4V titanium alloy, characterized by typical values of Young's modulus (120GPa), Poisson's ratio (0.36), yield strength (950MPa) and ultimate tensile strength (1020MPa). Hypothetic, extremely stiff, material was used to model the bodies between which the scaffold is pressed, with Young's modulus set to 1×10^6 GPa. Each of FE model instances was meshed with 10 node quadratic tetrahedron elements, using average global edge length of 0.2mm. Depending on instance, mesh size varied from 47000 to 105000 elements. Finite element model of the fifth instance is shown in Figure 7.

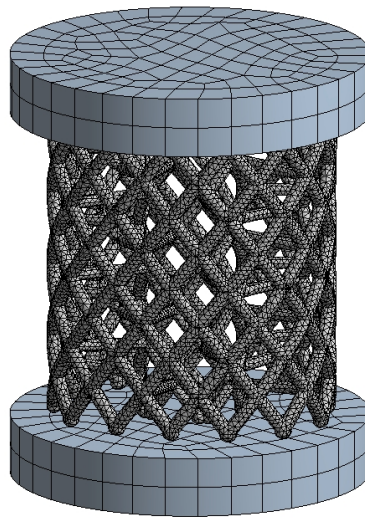


Figure 7: Finite element model of fully wrapped ASLS.

In order to check if nonlinear behavior is present in scaffold compression, large deflection effects were initially considered in the analyses and five different load intensities were applied: 20, 40, 60, 80 and 100N. As it may be seen from Figure 8, resulting structural stiffness of the scaffold, was found to be nearly independent of load intensity, so the study was continued using load intensity of 60N, which was chosen as a representative one in case of long bones of the rabbit.

Typical results of the analyses conducted within the study, are shown in Figure 9. Complete set of maximal values of axial displacement and equivalent Von-Misses stress, as well as values of structural stiffness and structural elasticity, obtained numerically for all instances, is given in Table 2. Maximal values of stress in the scaffold are in all cases well below yield strength of titanium alloy (950MPa).

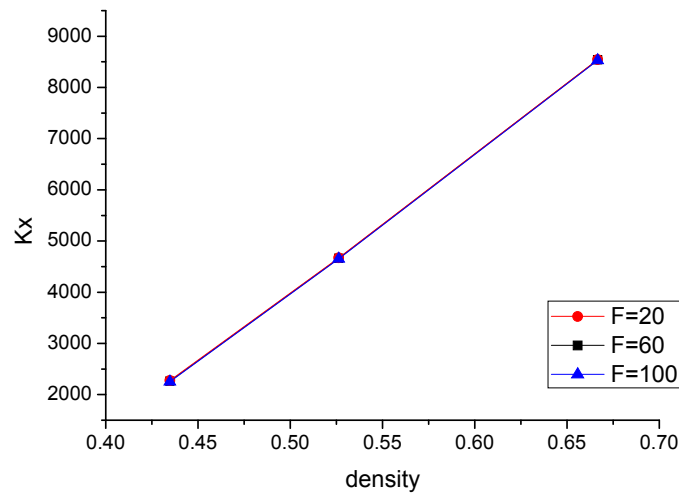


Figure 8: Structural stiffness of fully wrapped ASLS, calculated at three different load intensities. The independence of stiffness from load intensity confirms nearly linear behavior of the structure.

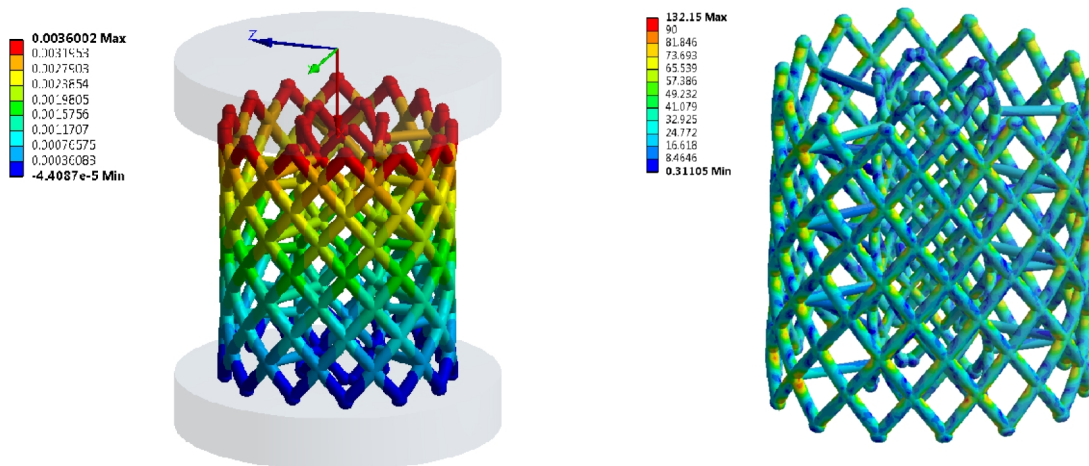


Figure 9: Resulting fields of axial displacement u_x and equivalent Von-Mises stress σ_{VM} , for instances 5 and 1 respectively.

Instance No.	$u_x \text{ max}$ [mm]	K_S [N/mm]	E_S [N/mm ²]	$\sigma_{VM \text{ max}}$ [N/mm ²]
1	0.00703	8537.0	1739.4	132.15
2	0.01287	4662.8	950.0	217.25
3	0.02652	2262.1	460.9	350.46
4	0.01447	4145.5	844.6	230.16
5	0.00360	16665.9	3395.7	212.42
6	0.03614	1659.8	338.2	278.81
7	0.00282	21282.0	4336.2	63.42

Table 2: Output values resulting from design study of fully wrapped ASLS design and calculated quantities.

Based on the complete set of results, sensitivity of structural stiffness and modulus to principal design parameters was estimated. Figure 10 shows that a nearly linear correlation exists between struts density and structural modulus. Correlation between struts cross-section area and structural modulus is a bit further from linear one (Figure 11), while the one between structural modulus and struts angle is noticeably nonlinear (Figure 12).

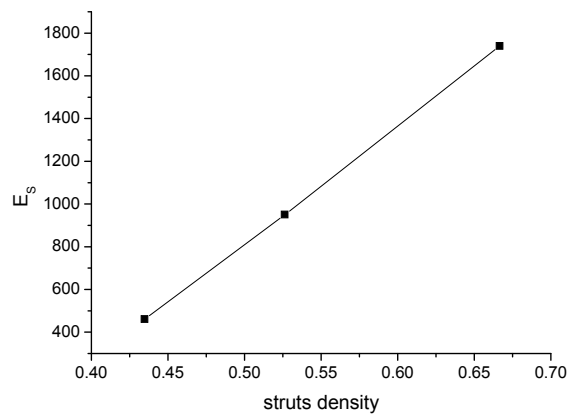


Figure 10: Sensitivity of structural modulus E_s to change of struts density.

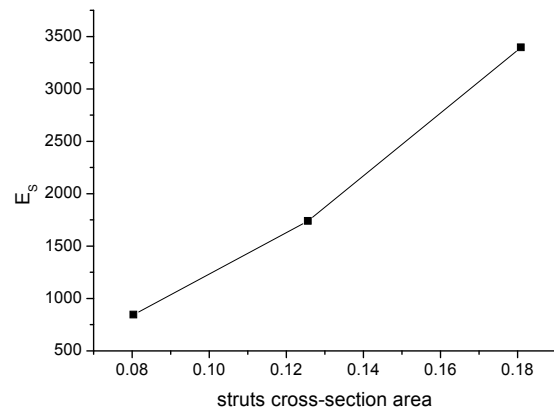


Figure 11: Sensitivity of structural modulus E_s to change of struts density.

In an attempt to find an universal design parameter that could be used to predict the value of structural modulus of lattice design scaffold, correlation between structural modulus and porosity was also observed. When all the instances were considered, a meaningful correlation could hardly be established, as dispersion of modulus values was very large. But, when the instances 6 and 7, which were obtained by change of struts angle, were not considered in regression analysis, a very close linear fit with a large value of R^2 was obtained (Figure 13). This fact, together with correlation shown in Figure 10, proves that the value of struts angle has very large effect on structural modulus of lattice scaffold and that the correlation between those two is highly nonlinear.

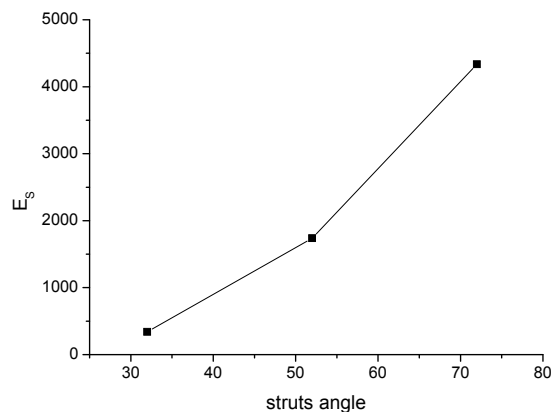


Figure 12: Sensitivity of structural modulus E_s to change of struts angle.

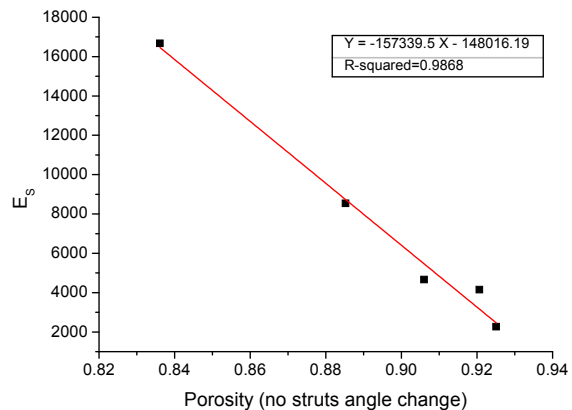


Figure 13: Sensitivity of structural modulus E_s to change of porosity (instances with changed struts angle are not considered).

3.2 Sensitivity study of realistic shape lattice scaffold elastic properties to change of struts angle

Scaffold shape and loads are never as ideal as shown in previous study, in which they were deliberately simplified to explore the mechanical behavior of fully wrapped ASLS design. To get a step closer to reality, a more realistic scaffold was modeled and assembled with a model of rabbit tibia segment, based on CT images. Three assembly instances were created, with variable struts angle (Figure 14).

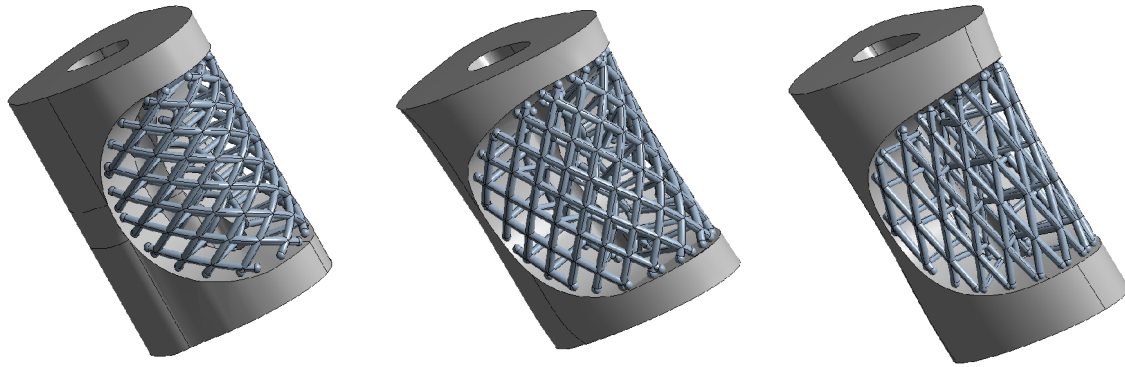


Figure 14: Three instances of bone segment-scaffold assembly, in which struts angle was modified to take representative values of 32°, 52° and 72° respectively.

Scaffold material was defined in the same way as in the previous study, and bone material was set to be linear elastic, characterized by mid value of Young's modulus reported in literature [12] for rabbit tibia (22GPa), typical reported Poisson's ratio (0.33) and ultimate tensile strength (195MPa). Fixation of the scaffold to the bone was approximated by bonded contact between neighboring surfaces of the two components. To approximate the axial load acting on the bone, one of the frontal surfaces of the bone was fixed, while equally distributed load of 60N was applied to the other (Figure 15).

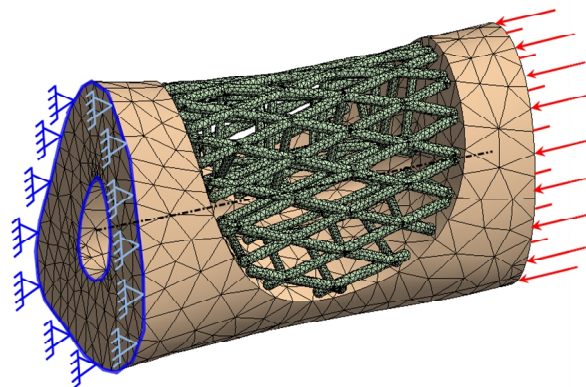


Figure 15: Finite element model of bone segment-scaffold assembly. Boundary condition and load shown in the picture are defined on front surfaces of the bone segment.

Typical results of the analyses conducted within the study, are shown in Figure 16 and Figure 17.

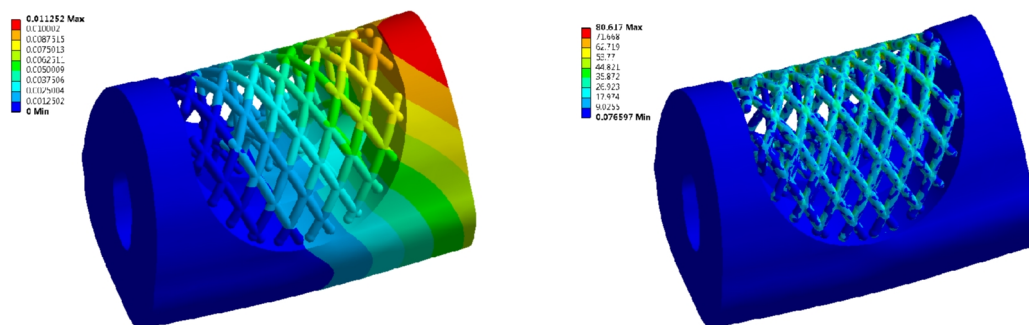


Figure 16: Total deformation and equivalent stress field on bone segment - scaffold assembly. Struts angle is set to 32°.

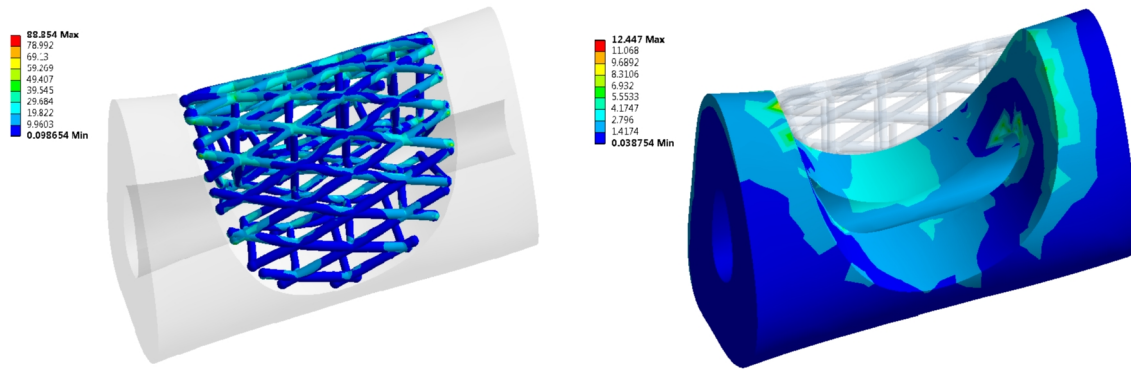


Figure 17: Equivalent stress field on bone and scaffold shown separately. Struts angle is set to 72°.

From previous images it may be seen that maximum value of equivalent stress in the scaffold (88.8MPa at struts angle of 72°) is much lower than Yield strength of titanium alloy (950MPa). The same is true for maximal stress in the bone (12.5MPa at struts angle of 72°), which is well below ultimate bone strength (195MPa). Correlation between struts angle and defect length dilatation obtained during the study is shown in Figure 18.

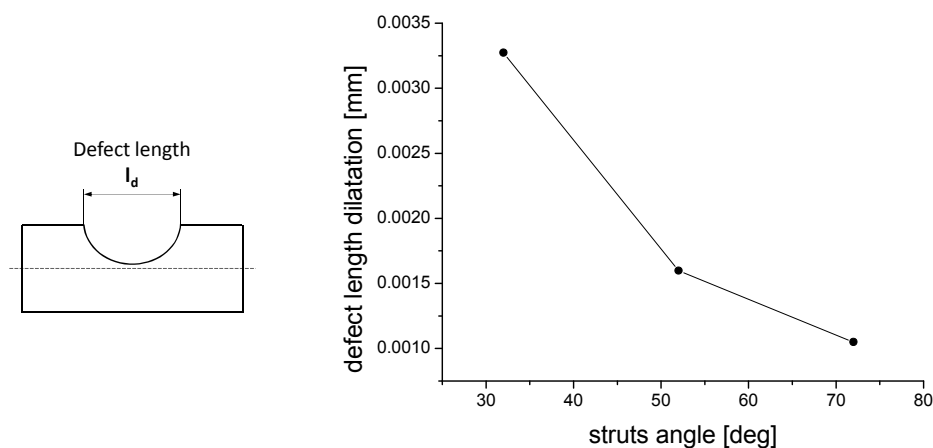


Figure 18: Bone defect length dilatation vs. struts angle.

As in the previous study, conducted on the fully wrapped ASLS design, it is obvious that struts angle is the design parameter which has a major influence on elastic properties of lattice scaffold. Moreover, the correlation between struts angle and structural stiffness of the scaffold is noticeably nonlinear, which is probably due to the fact that axial compression of the struts starts to dominate over other deformation modes as struts direction gets closer to load axis (in this case at struts angle of 90°).

4 CONCLUSIONS

Design studies described in the paper showed that the design concept of *anatomically shaped lattice scaffold* enables the easy control of scaffold's stiffness by changing the three main design parameters: density and cross-sectional area of the struts and angle of struts intersection. In current research a scaffold design was studied that was anatomically shaped according to the upper part of proximal diaphyseal trauma of rabbit tibia. Furthermore, the design study helped to determine functional relationships between these three design parameters and mechanical properties of the scaffold structure. Knowing these dependencies, it is

much easier to properly customize the design of ASLS and to pair it with a fixation frame, in order to ensure a proper load distribution between fixation and scaffold as well as to keep the ossification process active inside the bone graft. Thus, it may be concluded that customization of ASLS design to the particular anatomy of a traumatized piece of the bone as well as to the requested load distribution, improves tissue recovery.

Finally, the results of these design studies call for the research of new materials, which will have to be equivalently strong as titanium, but will be characterized by controllable biodegradability.

ACKNOWLEDGMENT

The paper arose as a result of multidisciplinary research in the domain of bioengineering in real medical practice (Virtual Human Osteoarticular System and its Application in Preclinical and Clinical Practice¹) which is sponsored by the Ministry of Science and Technology of the Republic of Serbia - project id III 41017 for the period of 2011-2014. We are grateful to Dr. sci. med. Dragana S. Ilic, prof. dr sci. med. Milorad Mitkovic and prof. dr sci. med. Stojanka Arsic from University Clinical Center of Nis, Serbia.

REFERENCES

- [1] S.J. Hollister, R.D. Maddox, J.M. Taboas, Optimal design and fabrication of scaffolds to mimic tissue properties and satisfy biological constraints. *Biomaterials*, 23, 4095-4103, 2002.
- [2] C.K. Chua, K.F. Leong, C.M. Cheah, S.W. Chua, Development of a tissue engineering scaffold structure library for rapid prototyping. Part 1: Investigation and classification. *The International Journal of Advanced Manufacturing Technology*, 21, 291-301, 2003.
- [3] D.W. Hutmacher, M. Sittinger, M.V. Risbud, Scaffold-based tissue engineering: rationale for computer-aided design and solid free-form fabrication systems. *Trends in Biotechnology*, 22, 354-362, 2004.
- [4] J. Nam, B. Starly, A. Darling, W. Sun, Computer aided tissue engineering for modeling and design of novel tissue scaffolds. *Computer-Aided Design and Applications*, 1, 633-640, 2004.
- [5] M.A. Wettergreen, B.S. Bucklen, B. Starly, E. Yuksel, W. Sun, M.A.K. Liebschner, Creation of a unit block library of architectures for use in assembled scaffold engineering. *Computer-Aided Design*, 37, 1141-1149, 2005.
- [6] S.J. Hollister, C.Y. Lin, Computational design of tissue engineering scaffolds. *Computer Methods in Applied Mechanics and Engineering*, 196, 2991-2998, 2007.
- [7] C. Gomez, A. Shokoufandeh, W. Sun, Unit-cell based design and modeling in tissue engineering applications, *Computer-Aided Design and Applications*, 4, 649-659, 2007.
- [8] G. Ryan, P. McGarry, A. Pandit, D. Apatsidis, Analysis of the Mechanical Behavior of a Titanium Scaffold With a Repeating Unit-Cell Substructure. *Journal of biomedical materials research. Part B, Applied biomaterial*, 90, 894-906, 2009.

¹ <http://vihos.masfak.ni.ac.rs>

- [9] S. Cahill, S. Lohfeld, P. E. McHugh, Finite element predictions compared to experimental results for the effective modulus of bone tissue engineering scaffolds fabricated by selective laser sintering. *Journal of materials science. Materials in medicine*, 20, 1255-1262, 2009.
- [10] L. McIntosh, J.M. Cordell, A.J. Wagoner Johnson, Impact of bone geometry on effective properties of bone scaffolds. *Acta Biomaterialia*, 5, 680-692, 2009.
- [11] J. Wieding, R. Souffran, W. Mittelmeie, R.Bader, Finite element analysis on the biomechanical stability of open porous titanium scaffolds for large segmental bone defects under physiological load conditions. *Medical engineering & physics*, (Article in Press DOI: 10.1016/j.medengphy.2012.06.006), 2012.
- [12] Y. H. An, R. A. Draughn, *Mechanical Testing of Bone and the Bone–Implant Interface*, . CRC Press, 2010.

SIMULATING LANDFILL AERATION SYSTEMS USING COMPUTATIONAL FLUID DYNAMICS TECHNIQUES

Dimitrios K. Fytanidis¹ and Evangelos A. Voudrias²

¹ Department of Civil Engineering, Democritus University of Thrace
GR-67100, Xanthi, Greece
dfytanid@civil.duth.gr

² Department of Environmental Engineering, Democritus University of Thrace
GR-67100, Xanthi, Greece
voudrias@env.duth.gr

Keywords: Landfill aeration, Aerobic degradation, Aeration well, Zone of influence.

Abstract. *The present study is an application of Computational Fluid Dynamics (CFD) on the numerical modeling of aeration systems of uncontrolled landfills. More specifically, the CFD algorithms provided by the commercial solver ANSYS Fluent 14.5, combined with an in-house source code developed to complement the main solver was used. Coupling the multiphase flow with a biochemical algorithm, the complex biochemical process of organic solid waste stabilization using aeration was simulated. Air was considered to enter the solid waste region which was partially saturated, using aeration wells. Multiphase flow both for the air and liquid phase was simulated taking into consideration the oxygen (O₂) transfer across phases. Unsaturated flow effects, such as capillary pressure and unsaturated hydraulic conductivity, were taken into consideration during the simulation using proper functions that were included in the main solver. After the initial model set up, a sensitivity analysis for basic biochemical parameters was implemented, examining the effect of various kinetic parameters variation. Moreover, pilot scale simulations were performed. The results obtained were in good agreement with corresponding previous experimental and computational results of the literature. Finally, a case study was simulated for a hypothetical landfill aeration well.*

1 INTRODUCTION

Landfill aeration is the process in which air is inserted in the mass of solid waste, usually via passive or forced aeration wells, in order to reduce its biodegradable organic load. During last decades, aeration systems have been globally used as a quick, effective and low-emission technology for the aerobic biological stabilization of landfills [1]. Although many studies have reported the successful use of this method presenting the results of its application in the field [1-7], knowledge gaps for the effective design of these systems still remain due to the fact that its design is still based on preliminary pilot-scale field experiments and former practical experience [8]. Cossu et al. [7] tried to use flow modeling, combined with corresponding pilot experimental data, in order to define the radius of influence of aeration wells in the field.

Numerous models are available in the literature concerning the modeling of aerobic biodegradation processes of organic solid waste, however only few of them are time and space integrated by means of being able to capture the space and time variation of the examined quantities. Moreover, most of these studies do not refer to landfill aeration, investigating other aerobic processes, such as composting, which is a similar process for organic solid waste treatment and stabilization. Thus, previous experience can be used for the assessment of the method of landfill aeration. This is very important due to the lack of an extensive research on biodegradation process kinetics of landfill aeration in the literature.

Biochemical kinetics of aerobic biodegradation processes, such as composting and landfill aeration are affected by various environmental parameters as [9, 10]: (1) temperature, (2) moisture, (2) oxygen concentration, (3) free air space and (4) pH. Extensive reviews are available in the literature [9-11] concerning the used of different kinetics for the description of aerobic biodegradation of organic solid waste as well as for the correction factors used in order to take into consideration the effect of the aforementioned environmental parameters.

Only a few simulation models in the literature describe temporal and spatial variations of aerobic degradation of organic solid waste as well as the flow field properties. However, Bari and Koenig [12, 13], using a multi-layer (1-D) model and experimental investigations for a forced aeration composting process, proved that this kind of spatial variations for the temperature and biodegradable volatile solid fields really exist. El-Fadel et al. [14-16], in their work, presented one of the first temporally and spatially dynamic model for the simulation of the generation and transport of gas during the anaerobic biodegradation of organic solid waste in a landfill. The “Landfill Degradation And Transport” of the Waste Management Research Group of the University of Southampton (UK) [17] is one of the first models that have been used in order to simulate the biodegradation of organic solid waste for both anaerobic [18, 19] and aerobic [20, 21] conditions. The LDAT model combines a multi-component biodegradation model with a fluid mechanics solver for the flow field calculations.

The present study is an application of Computational Fluid Dynamics (CFD) on the simulation of organic solid waste stabilization using aeration systems. A multiphase model is used in order to simulate the flow of gaseous and liquid phases. Unsaturated flow effects, such as capillary suction and hydraulic conductivity variation due to moisture degree saturation, were also taken into consideration. Moreover, oxygen (O_2) transport in both liquid and gaseous phases was simulated using proper advection-dispersion-reaction equations whilst the oxygen mass transfer across the phases due to its concentration gradient was also simulated. Energy equations were solved in order to calculate the temperature field as well as the heat generation due to the organic solid waste biodegradation and the other biochemical processes, which were included as source/sink terms in the energy conservation equations. Finally, the concentrations of the biodegradable organic solid waste and biomass were calculated solving proper biochemical kinetics, which were coupled with the main fluid flow solver. For the solution of the aforementioned equations, the commercial

solver ANSYS Fluent 14.5 [22] was used combined with an in-house source code which includes the biochemical model to simulate the organic solid waste stabilization and biomass production, as well as some additional terms of the flow equations that alter the main commercial CFD solver.

2 MATHEMATICAL MODEL

For the simulation of multiphase flow during landfill aeration, the Control or Finite Volume approach was used which is included in the commercial solver ANSYS Fluent 14.5, combined with an in-house code which was developed in ANSI C programming language and the "User Defined Functions" (UDFs) macros, which are included in the main CFD solver. The developed model aims to: (1) simulate the air-water flow in the unsaturated porous media of solid waste, (2) simulate the oxygen transport in both the phases (air and water) modeling the oxygen mass transfer across the interphase of the phases, (3) simulate the temperature variations due to the heat production and consumption due to the biochemical processes of the model and (4) simulate concentration of the organic solid waste and of the biomass using proper biochemical kinetics combined with some correction factors which include the effect of the environmental parameters, such as the temperature and the oxygen concentration on the biochemical reaction rates.

More specifically, our in-house subroutines define the capillary pressure effect for the water momentum equation, calculate the hydraulic conductivity of each phase as a function of moisture saturation, define the transport mechanism for the oxygen mass transfer across phases as well as the sink/source term due to the biochemical reaction of the organic solid biodegradation, calculate the temporal and spatial variations of the biodegradable organic solid waste and biomass including the effect of environmental factors and define proper source/sink terms in the energy equations, in order to estimate the temperature field and variation for each phase.

2.1 Flow equations

Both phases (air and water) were assumed to follow the Navier-Stokes-Brinkman equations for the momentum conservation in each CV which is an extended Darcy's model for an "Euler-Euler" multiphase approach [22] used for unsaturated flow:

$$\frac{\partial \varepsilon a_q \rho_q \bar{V}_q}{\partial t} + \nabla \varepsilon a_q \rho_q \bar{V}_q \bar{V}_q = -\varepsilon a_q \nabla P + \nabla \varepsilon \bar{\tau} + \varepsilon a_q \rho_q \bar{g} - a_q^2 \frac{\mu_q}{kk_r} \bar{V}_q - \varepsilon a_q \nabla P_c \quad (1)$$

where ε is the total porosity of the medium [dimensionless], a_q is the volume fraction of q phase [m^3/m^3], ρ_q is the density of q phase [kg/m^3], \bar{V}_q is the Darcy velocity of q phase [m/sec], P is the pressure [Pa], τ shear stress [Pa], g is the acceleration of the gravity [m/sec^2], μ_q is the dynamic viscosity of q phase, k is the intrinsic or saturated permeability of q phase [m^2], k_r is the relative permeability [dimensionless] and P_c [Pa] is the capillary pressure. Relative permeability was calculated using the van Genuchten formulation [23]:

$$k_r = S_e^{0.5} (1 - (1 - S_e^{1/\gamma})^\gamma)^2 \quad (2)$$

for the aquatic phase and:

$$k_r = (1 - S_e)^{0.5} (1 - S_e^{1/\gamma})^{2\gamma} \quad (3)$$

for the gaseous phase, where S_e is the saturation calculated as:

$$S_e = \frac{a_w - a_{wr}}{a_{ws} - a_{wr}} \quad (4)$$

where a_w is the volume fraction of water, a_{wr} is the residual saturation, a_{ws} is the maximum saturation, and α [l/m], β and γ are the van Genuchten constants, where $\gamma = 1 - \frac{1}{\beta}$. The term

$\gamma a_q \nabla P_c$ for the capillary pressure effect was included only in the wetting phase and was calculated using the van Genuchten [23] – Mualem [24] formula:

$$P_c = -\frac{\rho_w g}{\alpha} \left(\left(\frac{1}{S_e} \right)^{1/\gamma} - 1 \right)^{1/\beta} \quad (5)$$

where ρ_w is the liquid phase density [kg/m^3].

A continuity equation was solved for the air phase:

$$\frac{\partial \varepsilon a_q \rho_q}{\partial t} + \nabla \varepsilon a_q \rho_q \bar{V}_q = \varepsilon S_q \quad (6)$$

where S_q is the mass source/sink term, whilst water volume fraction was calculated using the equation for the sum of volume fraction of all phases (that equals unit):

$$\sum_{i=gas,liquid} a_i = 1 \quad (7)$$

Oxygen mass transfer was simulated using a standard advection-dispersion-reaction equation for each phase [22]:

$$\frac{\partial \varepsilon a_q \rho_q C_p^q}{\partial t} + \nabla \varepsilon a_q \rho_q C_p^q \bar{V}_q = -\varepsilon a_q \rho_q \nabla \bar{J} + S_p \quad (8)$$

where C_p^q is the oxygen concentration in q phase [kg_c/kg_q], S_p is the sink/source term of oxygen mass due to its consumption due to organic solid waste biodegradation as well as due to its mass transfer across the phases' interface and \bar{J} the dispersion term calculated as:

$$\bar{J} = -D \times \nabla C_p^q \quad (9)$$

where D is the dispersion coefficient [m^2/sec].

The reason of the oxygen mass transfer across air and water is its concentration gradient across them, namely the difference between the real and the equilibrium oxygen concentration which was calculated, using Henry's Law:

$$H_c(T) = \frac{C_p^{eql}}{C_p^{eqg}} \quad (10)$$

where $H_c(T)$ is the dimensionless form of Henry's constant, C_p^{eql} is the equilibrium concentration of p species in water (*liquid* phase), C_p^{eqg} is the equilibrium concentration of p species in air (*gaseous* phase). Henry's constant can be calculated according to the following equation [25]:

$$H_H(T) = H_H^{T_o} \cdot \exp\left(-\alpha_H \left(\frac{1}{T_o} - \frac{1}{T} \right)\right) \quad (11)$$

where $H_H^{T_o}$ is the dimensioned Henry's constant [M/atm] at T_o [$^{\circ}K$] temperature, α_H is the constant of exponential decrease [$^{\circ}K$] and T is the Temperature [$^{\circ}K$]. In the present study, α_H equals 1800 $^{\circ}K$ [25] while $H_H^{T_o}$ for O_2 equals 1.30×10^{-3} M/atm at 25 $^{\circ}C$ [25].

Thus, oxygen mass transfer rate between the phases' interphase was calculated as [26, 27]:

$$R_{pq_p} = a_p \rho_p K_{pq_p} \left(C_p^{eqp} - C_p^p \right) \quad (12)$$

where R_{pq} is the mass flux of p species from phase q to phase p (with $R_{pq} = -R_{qp}$), a_p is the volume fraction of phase p [m^3/m^3], ρ_p is the density of p phase [kg/m^3], K_{pq} is the mass transfer rate of p species from phase q to phase p [1/sec], C_p^{eq} is the equilibrium concentration of p species in phase p [kg_c/kg_p] and C_p^c is the concentration of p species in the phase p [kg_c/kg_p].

Finally, for each phase an energy equation was solved:

$$\frac{\partial \varepsilon a_q \rho_q h_q}{\partial t} + \nabla \varepsilon a_q \rho_q h_q \bar{V}_q = -\varepsilon a_q \rho_q \frac{\partial P}{\partial t} + \varepsilon \bar{\tau}_q : \nabla \bar{V}_q - \nabla \varepsilon q_q + S_q \quad (13)$$

where h_q is the specific enthalpy of q phase [J/kg_q] and S_q is the sink/source term of energy which includes the energy production/consumption due to biochemical processes, calculated based on the enthalpies of Table 1 and the reaction rates of the biochemical reaction (see paragraph 2.2) and the heat transfer across phases which is using the Ranz and Marshal's model [28, 29] for the estimation of the volumetric heat transfer coefficient [W/m^2] between the phases.

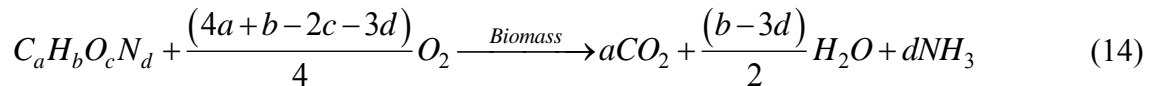
a/α	Species	Symbol	Molecular Weight	Enthalpy of formation ¹	Reference
1	Solid Waste	$C_6H_9O_{3.56}N_{0.32}$	142.44	-15073.4	[17]
2	Oxygen	O_2	32	-365.94	[30]
3	Carbon dioxide	CO_2	44	-9528.64	[31]
4	Water	H_2O	18	-15879.40	[30]
5	Ammonia	NH_3	17	-4722.94	[30]
6	Ammonium ion	NH_4^+	18	-7361.11	[30]
7	Hydrogen ion	H^+	1	0.0	[30]
8	Biomass	$C_5H_7NO_2$	99	-13790.9	[17]
9	Glucose	$C_6H_{12}O_6$	180	-7061.11	[31]

¹ in kJ/kg

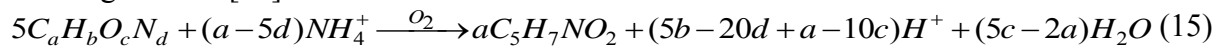
Table 1: Molecular Weight and enthalpy of formation for the used species.

2.2 Biodegradation kinetics

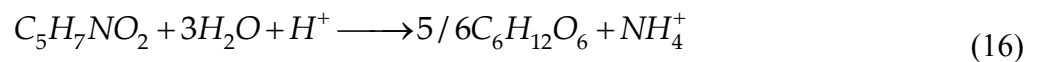
The system of biochemical equations taken into consideration in the model is presented below, starting with the chemical equation for the biodegradable solid waste [32]:



where a , b , c and d are constants referred to waste chemical composition. The chemical equation for bacteria growth is [20]:



The chemical equation for the biomass death is [20, 33]:



For the purpose of the present study, the chosen values for these constants were 6, 9, 3.56 and 0.32 [34].

Two kinds of biochemical kinetics were used in the present study in order to estimate the biochemical reaction rate of equation (14): (1) Monod kinetics and (2) first-order kinetics. The Monod equation is [10, 14-16, 20]:

$$S_S = \frac{dC_S}{dt} = -k_m \frac{C_S}{K_S + C_S} C_B \quad (17)$$

where S_S is the solid waste biodegradation rate [$kg/m^3 \cdot sec$], C_S is the concentration of the biodegradable solid waste [kg/m^3], t is the time [sec], k_m is the maximum biodegradation constant [sec^{-1}], K_S is the half saturation constant for the solid waste [kg/m^3] and C_B is the biomass concentration in the waste matrix [kg/m^3]. The first order kinetics is expressed as [9, 10]:

$$S_S = \frac{dC_S}{dt} = -k' C_S \quad (18)$$

where k' is the effective/corrected biodegradation rate [sec^{-1}].

The biochemical reaction rates of equations (14) and (15) were coupled using the concept of the yield coefficient according to which:

$$S_S = \frac{dC_S}{dt} = \frac{S_B}{Y_s} = \frac{1}{Y_s} \frac{dC_B}{dt} \quad (19)$$

where S_B is the biomass production rate [$kg/m^3 \cdot sec$] and Y_s is the yield coefficient which connects kinetics of biodegradable solid waste and biomass [$kg_B m^3 \cdot sec / kg_S m^3 \cdot sec$].

As it was mentioned in the introduction, temperature, moisture, oxygen concentration, free air space and pH are the main environmental parameters that alter the biochemical reaction rate of organic solid waste biodegradation. Thus, correction factors for temperature and oxygen were used for both the Monod and the first-order kinetics. Although correction factors for the free air space and the moisture were not applied, the volume fraction of the examined fluids (water and air) change during the simulation as the fluids move and thus alter the concentration of oxygen and the temperature field including that effect in the model. Finally, pH correction factor is not considered in the present study.

In order to simulate the effect of temperature on biochemical kinetics of the organic solid waste biodegradation, the cardinal temperatures correction factor of Rosso et al. [35] was used:

$$k_{temp} = \frac{(T - T_{max}) \times (T - T_{min})^2}{(T_{opt} - T_{min}) \times [(T_{opt} - T_{min}) \times (T - T_{opt}) - (T_{opt} - T_{max}) \times (T_{opt} + T_{min} - 2T)]} \quad (20)$$

where T_{min} , T_{max} and T_{opt} are the cardinal temperatures, namely the minimum, maximum and optimal temperatures for the aerobic biodegradation [$^{\circ}C$ or $^{\circ}K$] and T is the temperature [$^{\circ}C$ or $^{\circ}K$].

The corresponding correction factor for the oxygen concentration was assumed to be [10, 36]:

$$k_{O_2} = \frac{C_{O_2}}{K_{O_2} + C_{O_2}} \quad (21)$$

where C_{O_2} is the concentration of oxygen [kg/m^3] and K_{O_2} is the half saturation constant for oxygen [kg/m^3].

Finally, the following equation was used for the estimation of biomass decay rate, S_D , of equation (16):

$$S_D = k_d k_{temp2} C_B \quad (22)$$

where k_d is the bacterial decay rate in [sec^{-1}] and k_{temp2} is the correction factor of temperature for the decay rate, calculated according to the following equation [37]:

$$k_{temp2} = 2.142 \times 10^{-4} T^2 - 2.356 \times 10^{-2} T + 1.348 \quad (5^\circ C < T < 75^\circ C) \quad (23)$$

2.3 Model assumptions and solution methods

All the above equations were solved with the assumptions that flow and mass transfer in the landfill can be described as a porous media flow, according to equations of paragraph 2.2. Solid waste porous media was considered to be rigid (not-deformable), flow was considered to be incompressible, fluids and porous media were assumed to be in thermal equilibrium, biomass and biodegradable solid waste was considered to be in fixed position and biodegradation was considered to take place in the liquid phase.

For the solution of the aforementioned equations, the commercial solver ANSYS Fluent 14.5 was used. More specifically, the used solver was "pressure based" with first-order numerical schemes for the spatial and temporal discretization while velocity-pressure coupling was achieved using the "phase coupled SIMPLE" algorithm [22]. All the equations for the biochemical process were solved implicitly, while the coupling with the flow equation was achieved using sink/source terms. The convergence criterion for the calculations was set at 10^{-12} .

3 RESULTS

The research group of the University of Southampton examined the solid waste aeration in a rectangular container (24 m long, 8 m wide and 3 m deep) [17, 20, 21]. This geometry is reproduced in two dimensions (Figure 1). Air was assumed to enter the container through a 2 m inlet at the bottom of the geometry (red line of Figure 1), which was simulated as a "pressure inlet" boundary condition whilst the top of the geometry was considered open ("pressure outlet", blue line of Figure 1). Finally walls of the container were considered impermeable ("non-slip wall" boundary condition, black line of Figure 1).

The chemical formula of the examined organic solid waste was assumed to be $C_6H_9O_{3.56}N_{0.32}$ [34]. Concerning the hydraulic properties of solid waste, the intrinsic permeability and porosity of solid waste were assumed to be $10.23 \times 10^{-11} m^2$ and 0.50, van Genuchten's constants α , β , and γ were assumed to be 0.5, 2 and 0.8 respectively [17] and the relative saturation of the waste was assumed to be 0.20 [38]. Moreover, the used values for the biochemical modeling are available at Table 2.

The relative pressure at the bottom of geometry (inlet) was gradually increased from 40 Pa at the beginning of the simulation to 500 Pa at $t = 0.4$ days. The simulation period was set at 1.5 days. Pressure field variation over time is presented in Figure 2 for $t = 1, 3, 6, 9$ and 12 h, while directions of velocity vectors at steady state (after $t = 0.4$ days) are shown in Figure 3. The ability of the present model to capture time-dependent boundary conditions can be useful during hybrid aeration process simulation, in which wells alter their operation during their use acting as positive/negative pressure wells.

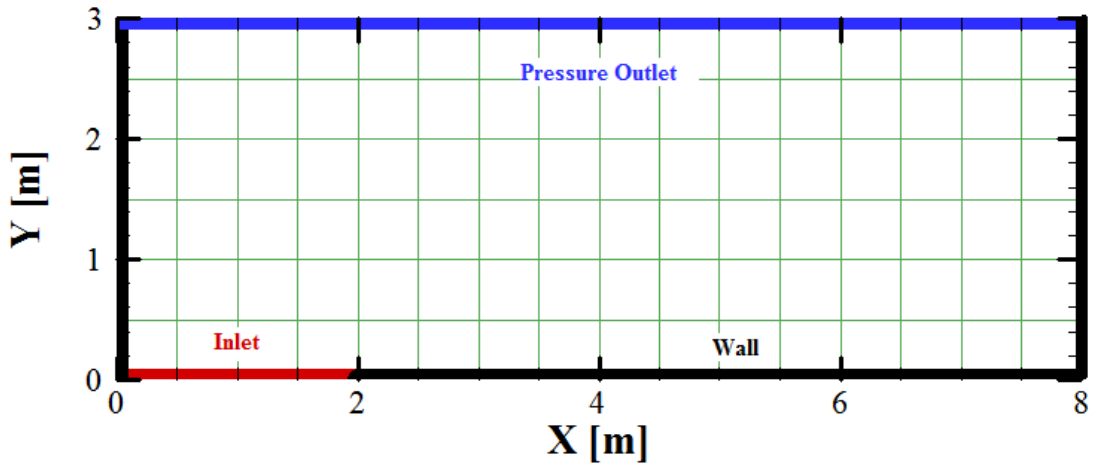


Figure 1. Examined two-dimensional geometry from [17, 20, 21]

Parameter	Value	Reference
Maximum biodegradation rate for Monod kinetics	1 day^{-1}	[39]
Maximum biodegradation rate for 1st order kinetics	0.05 day^{-1}	Estimated from data of [20]
Minimum temperature for biodegradation	$5 \text{ }^{\circ}\text{C}$	[9]
Optimum temperature for biodegradation	$58.6 \text{ }^{\circ}\text{C}$	[9]
Maximum temperature for biodegradation	$71.6 \text{ }^{\circ}\text{C}$	[9]
Biodegradable solid waste half saturation constant	1 kg/m^3	[20]
Oxygen half saturation constant	$0.007 \times 10^{-3} \text{ kg/m}^3$	[36]
Biomass decay rate	0.05 day^{-1}	[39]
Yield Coefficient	0.1	[21]
	$\text{kg}_B \text{ m}^3\text{-sec/}$	
	$\text{kg}_S \text{ m}^3\text{-sec}$	

Table 2: Values of biochemical parameters of the used kinetics in the present study.

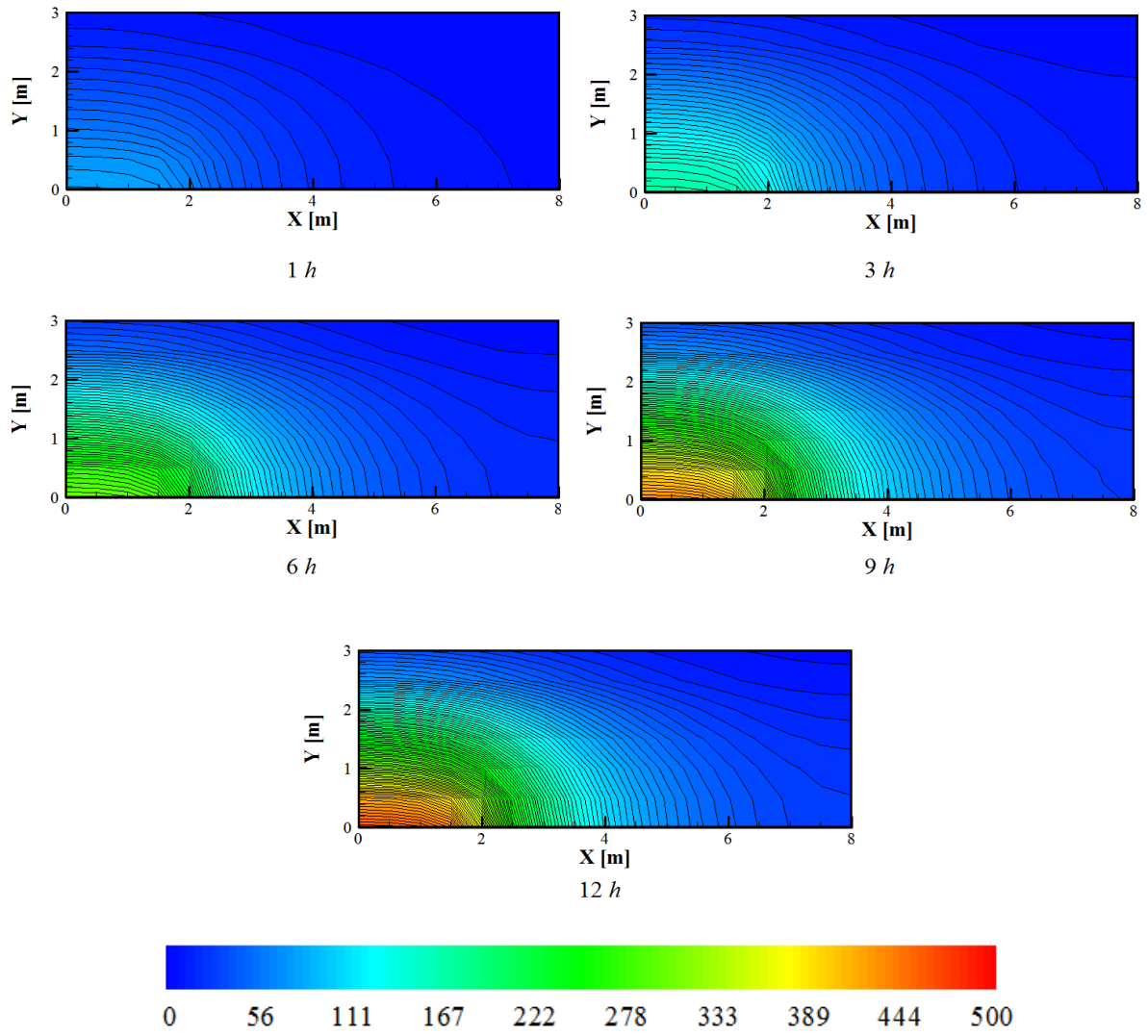


Figure 2. Relative pressure distribution [*Pa*]

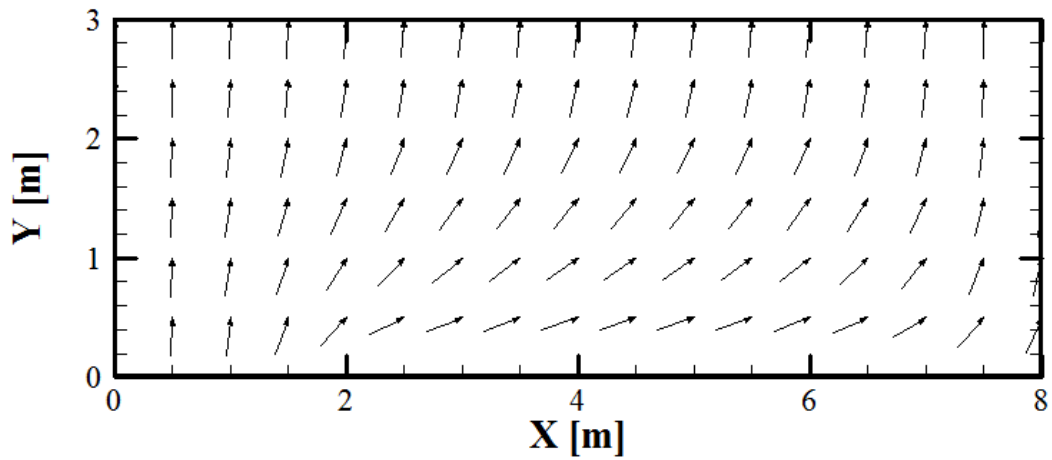


Figure 3. Directional velocity vectors

Rees-White et al. [20] used the "LDAT" model in order to simulate solid waste aeration in a 3m stack, presenting corresponding experimental investigations of the temperature field. In Figure 4, computational results of the present model for temperature versus time, using both Monod and first-order kinetics are shown and compared against reported data of previous investigations [20]. Hydraulic parameters were assumed to be the same as in the previous box aeration simulation and biochemical parameters were assumed to be those of Table 2. Initial biodegradable solid waste concentration was considered to be 200 kg/m^3 , while initial aerobic biomass concentration was set at 1 kg/m^3 , oxygen concentration in air was 0.177 kg/m^3 and temperature was $21.3 \text{ }^\circ\text{C}$. Simulation period was 2.5 days. It is shown that the present model's results are close to the previous experimental and computational results from Rees-White et al. [20].

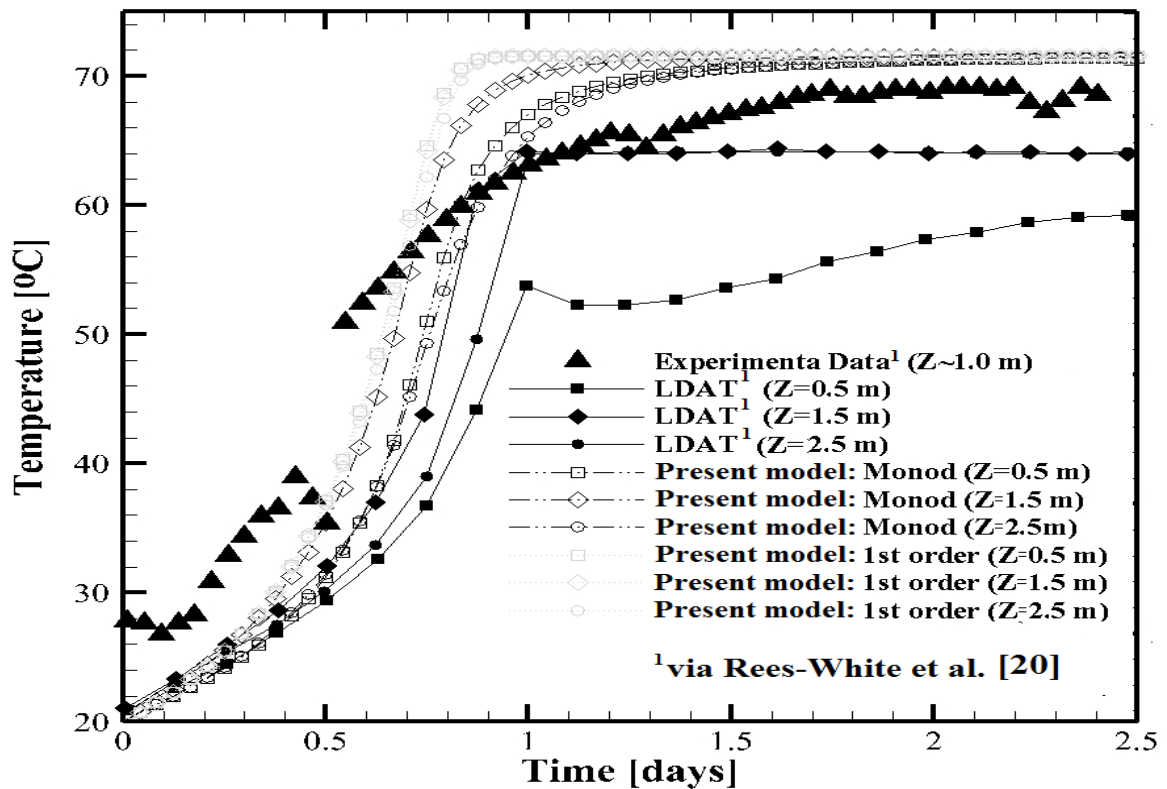


Figure 4. Temperature results of the present model versus experimental and computational results of Rees-White et al. [20]

Using the geometry of Figure 3, a sensitivity analysis for basic biochemical parameters was conducted using the same initial values. In order to compare the results a monitoring point at the center of the geometry was considered ($X = 4 \text{ m}$ and $Y = 1.5 \text{ m}$), while boundary conditions are again the same.

As it is mentioned in paragraph 2.2, the biodegradation rate of organic solid waste is affected by temperature according to equation (20). In Figure 5, the results of biodegradable solid waste concentration and temperature versus time are presented for various values of maximum biodegradation rate constant. Maximum biodegradation rate seems to affect the time instant, when the maximum temperature is reached. After the maximum temperature is reached, relatively slow biodegradation rates occur for all the k_m values. A 25% increase of k_m value results in a decrease of 0.20 days for the time needed to reach the maximum temperature, while a 50% decrease of its

value results in a 0.30-day earlier reach of the maximum temperature. On the other hand, when k_m decreases by 25 and 50% a delay of 0.5 and 1 day respectively is observed.

In Figure 6, results of biodegradable solid waste concentration and temperature are shown for various values of oxygen half saturation constant. The model is more sensitive to maximum biodegradation rate than to oxygen half saturation, thus, a 50% increase of K_{O_2} results in a 0.1 days delay to reach the maximum temperature, while a 50% decrease of K_{O_2} results in a relatively insignificant effect on the results.

In Figure 7, the effect of the value of biodegradable solid waste half saturation constant on biodegradable solid waste concentration and the temperature is shown. An 100% increase of the solid waste half saturation constant has almost no-effect on the results compared to the results of the default values. An 1000% increase ($10 \times K_S$) of solid waste half saturation constant has again small effect on the results presenting probably the need of more accurate experimental investigation of K_S , as small K_S values compared to biodegradable solid waste concentration C_S result in zero order kinetics.

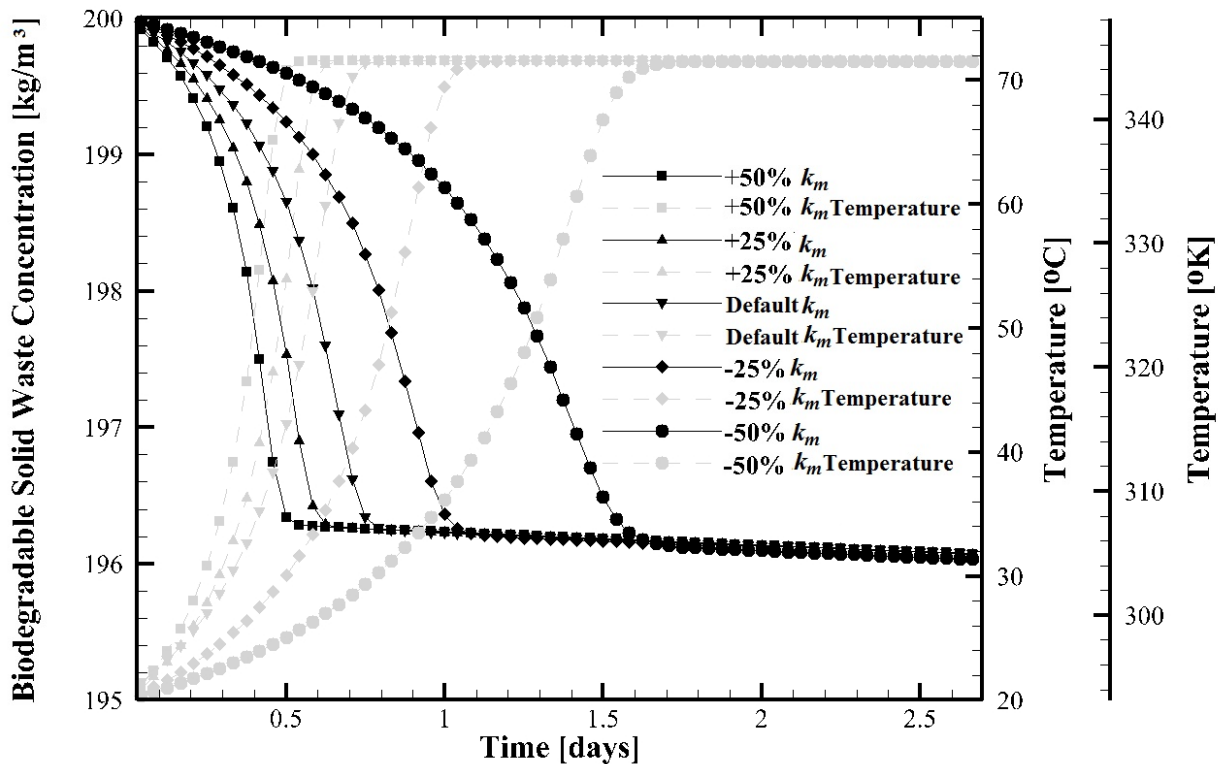


Figure 5. Biodegradable solid waste concentration (black lines) and temperature (gray lines) results for various maximum biodegradation rates

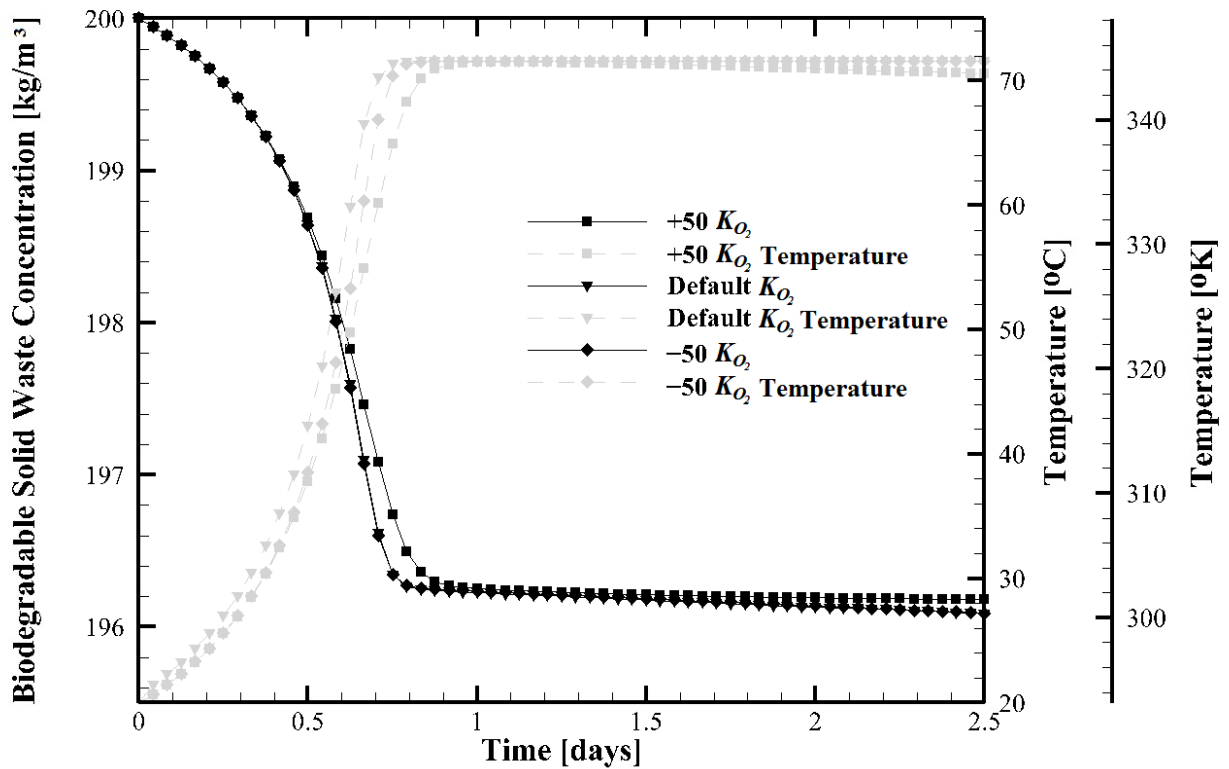


Figure 6. Biodegradable solid waste concentration (black lines) and temperature (gray lines) results for various oxygen half saturation constants

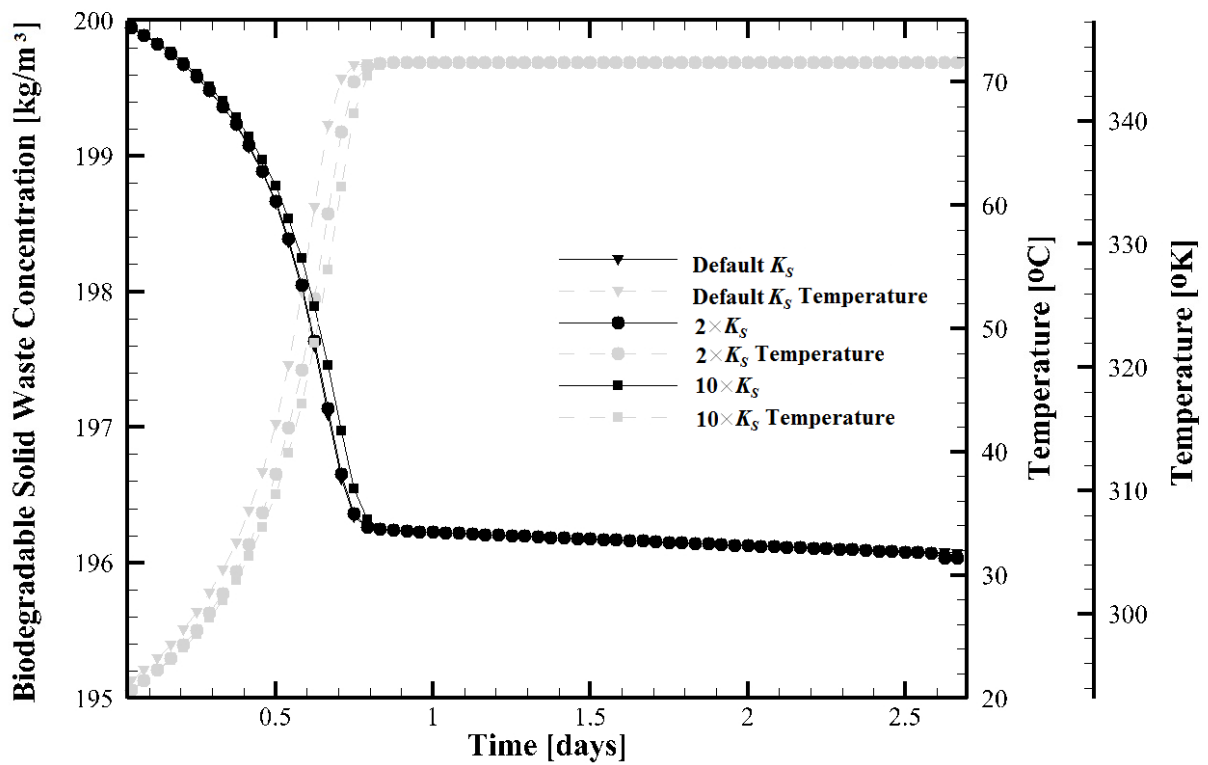


Figure 7. Biodegradable solid waste concentration (black lines) and temperature (gray lines) results for various biodegradable solid waste half saturation constants

Finally, a hypothetical case of an aeration well was examined in order to define its radius of influence. The aeration well with an internal diameter of 15 cm was assumed in the middle of a 20.0 m×20.0 m domain. The intrinsic permeability of the solid waste was assumed to be $10 \times 10^{-11} \text{ m}^2$, porosity 0.33 whilst van Genuchten's constants α , β , and γ were assumed to be 0.5, 2 and 0.8 [17] respectively. Initial free pore moisture was assumed to be 23%. The applied relative pressure difference at the inlet was 5000 Pa.

Cossu and Cestaro [40] defined the radius of influence of an aeration well, assuming a low limit of 2 cmH₂O pressure. Applying the present model with the same down radius pressure limit, a radius of influence of 7.5 m was determined (Figure 8). In addition to the pressure-based zone of influence, Cossu and Cestaro [40] defined "an alternative" well radius of influence based on a limit of 13-14% for oxygen concentration. In our case, an oxygen-based radius of influence of 11.2 m was determined, using the same limit of 13-14% ($\sim 0.186 \text{ kg/m}^3$) for oxygen concentration (Figure 9). This is a value in the range of 10-14 m that was investigated from previous researchers [40].

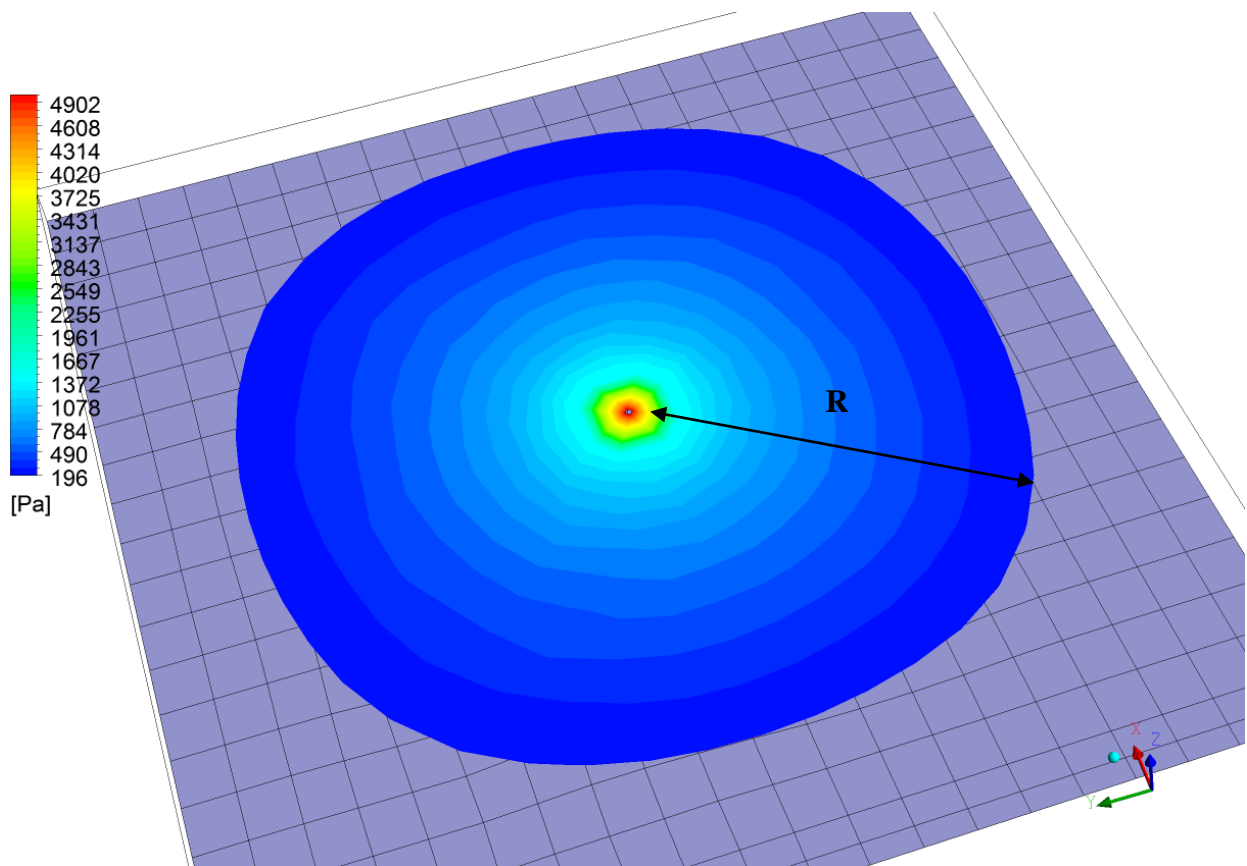


Figure 8. Relative pressure difference in a single well [Pa]

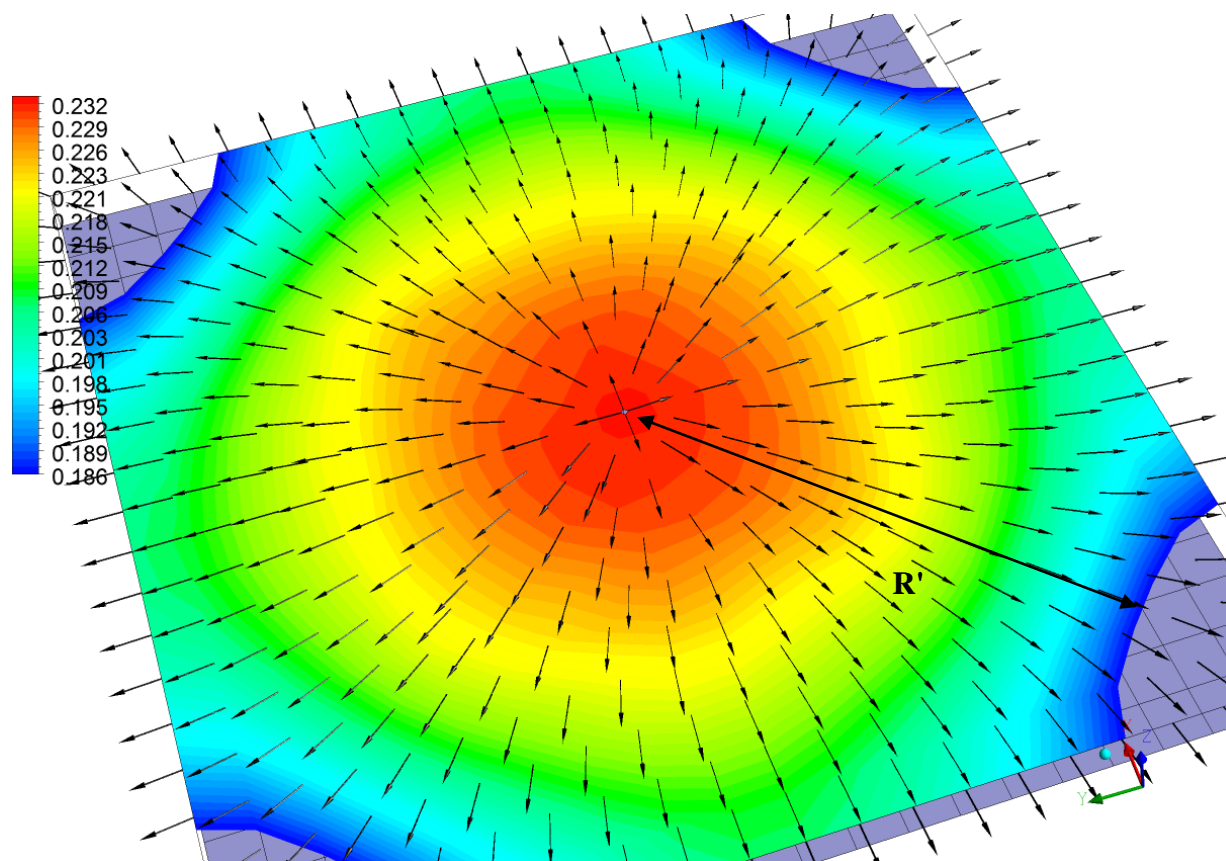


Figure 9. Oxygen concentration [kg/m^3] results and directional velocity vectors

4 CONCLUSIONS

In the present work, a computational model for the simulation of the aeration process of solid waste was developed. Computational Fluid Dynamics techniques and the algorithms included in the commercial solver ANSYS Fluent 14.5 were used. An in-house code was developed to alter the main solver and simulate the complex biochemical processes of landfill aeration. The computational investigation of some applications was conducted and the following conclusions were drawn:

- The present model uses a highly adaptable approach, which allows the use of multiple hydraulic properties for the porous media (including the capillary effect) and multiple biochemical kinetics (1st-order and Monod) and correction factor for the estimation of the effect of the environmental parameters (temperature, oxygen concentration etc).
- After a quantitative comparison, the model seems to predict accurately the temperature measured in previous works.
- The sensitivity analysis showed the high dependence of the biodegradation rate on temperature. The model is more sensitive to maximum biodegradation rate than to oxygen half saturation constant. Finally, the need for a more accurate experimental determination of the organic solid waste half saturation constant was emphasized.
- The model proved to be a useful tool for the estimation of the radius of influence for an aeration well using both pressure and oxygen concentration for its definition.

Concluding, it has to be noted that simulation of solid waste aeration is a relatively new research area, having most of the current modeling approaches to be "batch" or "point" models. Thus, the present study tried to focus on the development and application of a computational model that would combine a fluid flow model for the complex multiphase flow of water and air with a biochemical model for the biodegradation of the organic solid waste, aiming to bring the simulation of aeration systems from the area of research to engineering practice.

5 ACKNOWLEDGEMENTS

The authors wish to thank Professor Mutashem El-Fadel from American University of Beirut for the information from his previous work he provided. Moreover, the authors would like to thank the members of Waste Management Research Group of University of Southampton for making freely available their reports and model and especially Dr Richard Beaven, Dr Tristant Rees-White and Dr Kiki Zardava for the information and data they provided. Finally, we would like to thank the anonymous reviewers for their valuable and helpful comments.

REFERENCES

- [1] M. Ritzkowski, R. Stegmann, Landfill aeration worldwide: Concepts, indications and findings, *Waste Management*, 32 (7), 1411-1419, 2012.
- [2] H.-K. Heyer, K. Hupe, J. Heerenklage, M. Ritzkowski, R. Stegmann, Aeration of old landfills as an innovative method of process enhancement and remediation, in *Sardinia 1999, Seventh International Waste Management and Landfill Symposium*, S. Margherita di Pula, Cagliari, Italy, 4-8 October, 1999.
- [3] H.-K. Heyer, K. Hupe, A. Koop, M. Ritzkowski, R. Stegmann, The low pressure aeration of landfills. Experience, operation and costs, in *Sardinia 2003, Ninth International Waste Management and Landfill Symposium*, S. Margherita di Pula, Cagliari, Italy, 6-10 October, 2003.
- [4] H.-K. Heyer, K. Hupe, A. Koop, R. Stegmann, Aerobic in situ stabilization of landfills in the closure and aftercare period, in *Sardinia 2005, Tenth International Waste Management and Landfill Symposium*, S. Margherita di Pula, Cagliari, Italy, 3-7 October, 2005.
- [5] H.-K. Heyer, K. Hupe, A. Koop, R. Stegmann, Aerobic in situ stabilization of landfills. Long-term experience and new developments, in *Sardinia 2007, Eleventh International Waste Management and Landfill Symposium*, S. Margherita di Pula, Cagliari, Italy, 1-5 October, 2007.
- [6] H.-K. Heyer, M. Ritzkowski, K. Hupe, R. Stegmann, Long term landfill aeration by means of a wind driven air venting and aeration system, in *Sardinia 2009, Twelfth International Waste Management and Landfill Symposium*, S. Margherita di Pula, Cagliari, Italy, 5-9 October, 2009.
- [7] R. Cossu, R. Raga, D. Rossetti, S. Cestaro, M. Zane, Preliminary tests and full scale applications of in situ aeration, in *Sardinia 2007, Eleventh International Waste Management and Landfill Symposium*, S. Margherita di Pula, Cagliari, Italy, 1-5 October, 2007.
- [8] S. Cestaro, R. Cossu, D. Rossetti, Full-scale application of Aerobic in situ stabilization of an old landfill in north Italy, in *Forth Intercontinental Landfill Research Symposium*, Gällivare, Sweden, 14-16 June, 2006.

- [9] M. Baptista, Modelling of the kinetics of municipal solid waste composting in full-scale mechanical-biological treatment plants, New University of Lisbon, Lisbon, 2009.
- [10] R.T. Haug, *The practical handbook of compost engineering*. Florida, USA: Lewis Publishers, 1993.
- [11] I. G. Mason, Mathematical modelling of the composting process: A review, *Waste Management*, 26, 3-21, 2006.
- [12] Q. H. Bari, A. Koenig, Kinetic analysis of forced aeration composting- II. Application of multilayer analysis for the prediction of biological degradation, *Waste Management & Research*, 18, 313-319, 2000.
- [13] Q. H. Bari, A. Koenig, Application of a simplified mathematical model to estimate the effect of forced aeration on composting in a closed system, *Waste Management*, 32, 2037-2045, 2012.
- [14] M. El-Fadel, A. N. Findikakis, J. O. Leckie, Numerical Modelling of Generation and Transport of Gas and Heat in Landfills I. Model Formulation, *Waste Management & Research*, 14, 483-504, 1996.
- [15] M. El-Fadel, A. N. Findikakis, J. O. Leckie, Numerical Modelling of Generation and Transport of Gas and Heat in Sanitary Landfills II. Model Application," *Waste Management & Research*, 14, 537-551, 1996.
- [16] M. El-Fadel, A. N. Findikakis, J. O. Leckie, Numerical Modelling of Generation and Transport of Gas and Heat in Sanitary Landfills III. Sensitivity Analysis, *Waste Management & Research*, 15, 87-102, 1997.
- [17] University of Southampton, Waste Management Research Group, Available: www.civil.soton.ac.uk/research/airflow, 2011.
- [18] J. White, J. Robinson, Q. Ren, Modelling the biochemical degradation of solid waste in landfills, *Waste Management*, 24, 227-240, 2004.
- [19] J. White, D. Nayagum, HPM4 landfill modeling challenge-Application of the university of Southampton Landfill process model LDAT, in *Forth International Conference of "Hydro-Physico-Mechanics of Landfills*, Santander, Spain, 27-28 April, 2011.
- [20] T. Rees-White, R. Beaven, J. White, D. Nayagum, P. Braithwaite, B. Purcell, Monitoring and modeling air flow and distribution at a forced-air aerobic waste treatment plant, in *Waste 2008: Waste and Resource Management - a Shared Responsibility*, Stratford-upon-Avon, Warwickshire, England, 16-17 September, 2008.
- [21] R. P. Beaven, J. K. White, P. Braithwaite, Application of the University of Southampton landfill degradation and transport model (LDAT) to an aerobic treatment field experiment, in *Global Waste Management Symposium*, Colorado, USA, 8-10 September, 2008.
- [22] ANSYS Inc., Fluent Theory Guide, Available: <http://www.ansys.com>, 2012.
- [23] M. T. van Genuchten, A Closed-form Equation for Predicting the Hydraulic Conductivity of Unsaturated Soils, *Soil Sci. Soc. Am. J.*, 44, 892-898, 1980.
- [24] Y. Mualem, A new model for predicting the hydraulic conductivity of unsaturated porous media, *Water Resources Research*, 12, 513-522, 1976.
- [25] R. Sander, Compilation of Henry's Law constants for inorganic and organic species of potential importance in environmental chemistry. Available: <http://www.henrys-law.org>, 1999.
- [26] ANSYS Inc., Fluent Theory Guide, Available: <http://www.ansys.com>, 2012.
- [27] W. J. Weber, F. A. DiGiano, *Process dynamics in environmental systems: Environmental science and Technology service*. New York, USA: John Wiley and Sons, 1996.
- [28] W. E. Ranz, W. R. Marshall, Evaporation from Drops. Part I, *Chem. Eng. Prog.*, 48, 141-146, 1952.

- [29] W. E. Ranz, W. R. Marshall, Evaporation from Drops. Part II, *Chem. Eng. Prog.*, 48, 173–180, 1952.
- [30] M.M. Benjamin, *Water Chemistry International Edition*, Boston, USA: McGraw-Hill Higher Education 2002.
- [31] Wikipedia, Standard enthalpy change of formation (data table), Available: [http://en.wikipedia.org/wiki/Standard_enthalpy_change_of_formation_\(data_table\)](http://en.wikipedia.org/wiki/Standard_enthalpy_change_of_formation_(data_table)), 2012.
- [32] G. Tchobanoglous, H. Theisen, S.A. Vigil, *Integrated solid waste management. Engineering Principles and Management Issues*, McGraw-Hill International Editions, New York, USA, 1993.
- [33] T. Reichel, A Haarsrick, D. C. Hempel, Modeling long-term landfill emission - a segregated landfill model, in *Sardinia 2005, Tenth International Waste Management and Landfill Symposium*, S. Margherita di Pula, Cagliari, Italy, 3-7 October, 2005.
- [34] R. Iannelli, D. Giraldi, M. Pollini, F. Russomanno, Effect of pure oxygen injection as an alternative to air and oxygen-enriched air in the composting processes, in *Sardinia 2005, Tenth International Waste Management and Landfill Symposium*, S. Margherita di Pula, Cagliari, Italy, 3-7 October, 2005.
- [35] L. Rosso, J. R. Lobry, J. P. Flandrois, An Unexpected Correlation between Cardinal Temperatures of Microbial Growth Highlighted by a New Model, *Journal of Theoretical Biology*, 162, 447-463, 1993.
- [36] F. Sole-Mauri, J Illa, A. Margí, F. X. P Prenafeta-Boldú, X. Flotats, An integrated biochemical and physical model for the composting process, *Bioresource Technology*, 98, 3278-3293, 2007.
- [37] Y. P. Lin, G. H. Huang, H. W. Lu, L. He, Modeling of substrate degradation and oxygen consumption in waste composting processes, *Waste Management*, 28, 1375-1385, 2008.
- [38] G. Stoltz, A. Tinet, M. Staub, L. Oxarango, J. Gourc, Moisture Retention Properties of Municipal Solid Waste in Relation to Compression, *Journal of Geotechnical and Geoenvironmental Engineering*, 138 (4), 535-543, 2012.
- [39] S. Y. Kim, Y. Tojo, T. Matsuto, Compartment model of aerobic and anaerobic biodegradation in a municipal solid waste landfill, *Waste Management & Research*, 25 (6), 524-537, 2007.
- [40] R. Cossu, S. Cestaro, Modeling in situ aeration process, in *Sardinia 2005, Tenth International Waste Management and Landfill Symposium*, S. Margherita di Pula, Cagliari, Italy, 3-7 October, 2005.

VIBRATION AND ELASTIC BUCKLING ANALYSES OF SINGLE-WALLED CARBON NANOCONES

Cengiz Baykasoglu¹, Alper T. Celebi¹, Esra Icer¹ and Ata Mugan¹

¹: Istanbul Technical University, Faculty of Mechanical Engineering, 34437, Istanbul, Turkey
e-mails: baykasoglu@itu.edu.tr, *celebial@itu.edu.tr, icere@itu.edu.tr, mugan@itu.edu.tr

Keywords: Single-Walled Carbon Nanocones, Vibration Analysis, Buckling Analysis, Molecular Mechanics, Finite Element Method.

Abstract. *This paper reports the result on elastic buckling and vibration behaviors of single-walled carbon nanocones (SWCNCs) having the potential usage in atomic force microscope and scanning tunneling microscope tips. The modeling work employs the molecular mechanics based finite element approach in which Euler-Bernoulli beam element formulations are used with consistent mass matrix. Free-free, free-clamped and clamped-clamped boundary conditions are considered in vibration analysis of SWCNCs; on the other hand, axial compression and bending loading conditions are taken into account in elastic buckling behavior of SWCNCs. The effects of cone height and disclination or apex angles on the buckling force and natural frequencies of SWCNCs are investigated. Vibration analysis results indicate that the natural frequency decreases with increasing cone height in all types of SWCNCs, whereas it increases as the disclination angle increases. Buckling analysis results indicate that as the disclination angle increases, the critical buckling load increases in axial compression loading and decreases in bending loading. In addition, it is observed that bending loading is more critical than axial compression loading for buckling behavior of SWCNCs if the disclination angle increases.*

1 INTRODUCTION

Since the experimental detection of carbon nanotubes (CNTs) in 1991 [1], extensive studies have been conducted on its extraordinary properties and researchers have been interested in other carbon based nanostructures such as graphene sheets (GSs), fullerenes and carbon nanocones (CNCs). CNCs are conical graphitic structures and have very promising mechanical, electrical and thermal properties [2-7]. Ge and Sattler [8] first proposed that five apex angles such as 19.2° , 38.9° , 60° , 86.6° and 123.6° can be used to distinguish CNCs. Krishnan et al. [9] verified the existence of the five types of CNCs experimentally. CNCs are suited for high resolution and/or high intensity applications due to its small size, high stiffness and conical geometry; thus, it can be used as scanning probe tips (i.e., atomic force microscope (AFM) and scanning tunneling microscope (STM) probes), electron field emitters and in nanoindentation applications [9-13].

Understanding the mechanical behavior of CNCs is important and very useful in designing the components having nanocone structures. Experimental measurements for prediction of the mechanical properties of CNCs are very difficult and costly. Thus, computational tools are widely used to characterize mechanical properties of CNCs [6, 7, 14-17, 28]. Kumar et al. [6] investigated the Young's and shear modulus of CNCs employing second-generation reactive empirical bond-order potential. Wei et al. [7] examined the elastic and plastic properties of SWCNTs by using molecular dynamics (MD) simulations. Tsai and Fang [14] and Liew et al. [15] analyzed the buckling behavior of CNCs by using MD simulations. Liao et al. [16] investigated tensile and compressive behaviors of open-tip CNCs employing MD simulations. Abadi et al. [17] studied free vibrational properties of CNCs based on a nonlocal continuum shell model. Atomistic based finite element (FE) modeling approaches have been used to analyze CNCs and other carbon based structures in many recent works in literature due to its computational time and cost advantages. Odegard et al. [18] developed a model that links the molecular mechanics and solid mechanics, which is established by equating the molecular potential energy terms with the mechanical strain energy of a representative volume element of a continuum model. Li and Chou in the works [19-22] developed a similar approach to model CNTs and GSs similar to space-frame structures and investigated the elastic, vibrational and buckling characteristics of CNTs and/or GSs. Cantilevered and bridged single walled carbon nanotubes (SWCNTs) are taken into account to predict fundamental frequencies of SWCNTs [21] that are found to be in the range of 10 GHz – 1.5 THz. Both axial compression and bending loading conditions are considered in the elastic buckling behavior of the CNTs in [22] where buckling forces are reported to be in the range of ~0.1– 39 nN. Li and Chou [22] reported that the buckling load in axial compression is higher than bending load. Tserpes and Papanikos [23] introduced an atomistic FE method based on the approach of Li and Chou [19] to model CNTs by using commercial FE codes; they identified the C-C bond thickness d , Young's modulus E and shear modulus G by using the AMBER force model [19]. By using the methods developed by Li and Chou [19] and Tserpes and Papanikos [23]; Hashemnia et al. [24] and Sakhaee-Pour et al. [25] examined natural frequencies and mode shapes of single-layered graphene sheets (SLGSs) and Sakhaee-Pour et al. [25] predicted fundamental frequencies of SLGSs with equivalent lengths that are found to be in the range of 2.4 GHz – 3.5 THz; Sakhaee-Pour et al. [26] studied natural frequencies and mode shapes SWCNTs; Sakhaee-Pour [27] analyzed elastic buckling of SLGSs; Lee and Lee [28] studied vibrational behaviors of SWCNTs and SWCNCs, and predicted fundamental frequencies of SWCNCs below 20 GHz with a cone having the height of 20 Å; Mir et al. [29] studied natural frequencies and mode shapes of SWCNTs; Cheng et al. [30] and Fan et al. [31] examined mechanical properties of CNTs such as Young's modulus, shear modulus, natural frequency and buckling load;

Avila et al. [32] analyzed elastic and vibrational properties of GSs and CNTs; we studied two- and three-dimensional modal and transient analyses of SLGSs in [33]. In the works [19 -27, 29, 30-33], Euler-Bernoulli beam elements are used to represent bond interactions between C-C atoms in GSs, CNTs and CNCs. In addition, in the works [20, 21, 24-26, 28, 31,32] studying the vibrations of GSs, CNTs and CNCs, the global mass matrix is derived based on the assumption that the carbon nuclei masses are concentrated at the joints of the frame structure in GSs, CNTs and CNCs, and lumped mass matrix for the beam elements is used. On the other hand, consistent mass matrices for Euler-Bernoulli beam elements are used in the studies [29, 33]. In Mir et al. [29], density of beam elements is selected to be the density of continuum model of GSs (i.e., 2300 kg/m³) in the MM models (i.e., see Table 1). However, due to this assumption, the total mass of the MM model is different from the mass of the original structure which also affects the associated natural frequencies. In the work [33], equivalent density parameter for the beam elements is derived by using the equivalency of natural frequencies of the MM model and continuum plane-stress FE model of SLGSs that is found to be 5500 kg/m³. It is noteworthy that transient dynamics analyses can be performed by using Newmark method due to the advantages of consistent mass matrix which does not yield singularity in numerical integrations. On the other hand, Scarpa and Adhikari [34,35] proposed a beam model considering the shear deformation effects and they found the C-C bond thickness d , Poisson's ratio ν , Young's modulus E and shear modulus G by using the AMBER force model constants [19]. Both of the models in Li and Chou [19] and Scarpa and Adhikari [34] yield the same deformation results as the structural mechanics stiffness constants in the AMBER force model are equal [33] if the corresponding element properties are used given in Table 1. Lee and Lee [28] used Timoshenko beam element formulations which include shear deformation effects but they employed Euler-Bernoulli beam element constants (i.e., see Table 1) [23]; this assumption affects the natural frequencies of SWCNC that are found to be lower than those of Euler-Bernoulli beam elements. If shear deformation effects are considered, parameters of shear beam formulations given in Scarpa and Adhikari [34, 35] should be used.

Even though there are some studies on nanocones, no study exists on buckling behavior of SWCNCs by using atomic based FE approach. In addition, Lee and Lee [28] studied of vibrations of SWCNCs; however, they did not examine the effects of cone height and used Timoshenko beam formulations with Euler-Bernoulli beam parameters which may lead to lower modal frequencies than actual values. Motivated by these facts, vibration and elastic buckling analysis of SWCNCs are completed by using the MM based FE approach [19, 23] where Euler-Bernoulli beam elements with consistent mass matrix are used. In vibration analysis of SWCNCs, free-free, free-clamped and clamped-clamped boundary conditions are considered. Axial compression and bending loading conditions are taken into account in the elastic buckling behavior of the SWCNCs. In all analyses, the disclination angles of 120°, 180° and 240° are used while the cone height is varying.

2 FE MODEL OF SWCNCs

2.1 Structures of SWCNCs

The GSs are the basic structural elements of CNTs, CNCs and fullerenes, and their geometry is uniquely determined. However, a lot of possibility exists for CNTs (i.e., armchair, zigzag and chiral types CNTs) and CNCs having five possible closed cone structures that can be constructed by using GSs [36, 37]. By rotating a fragment of GSs in multiples of 60°, we obtain the original structure due to the hexagonal symmetry of GSs that is the only way to generate smoothly joined CNC by folding over a GS and the overlaps are called the disclinations.

Folding over a GS in this manner, creates five possible closed distinct CNC structures and the apex angles of a cone can be calculated as follows [38]

$$\alpha = 2 \arcsin\left(1 - \frac{\theta}{360}\right) \quad (1)$$

where θ is the disclination angle in degrees. Taking θ as 60° , 120° , 180° , 240° and 300° , the apex angles of CNCs are calculated 112.9° , 83.6° , 60° , 38.9° and 19.2° , respectively. The CNTs can be seen as a special case of the CNCs with a zero apex angle.

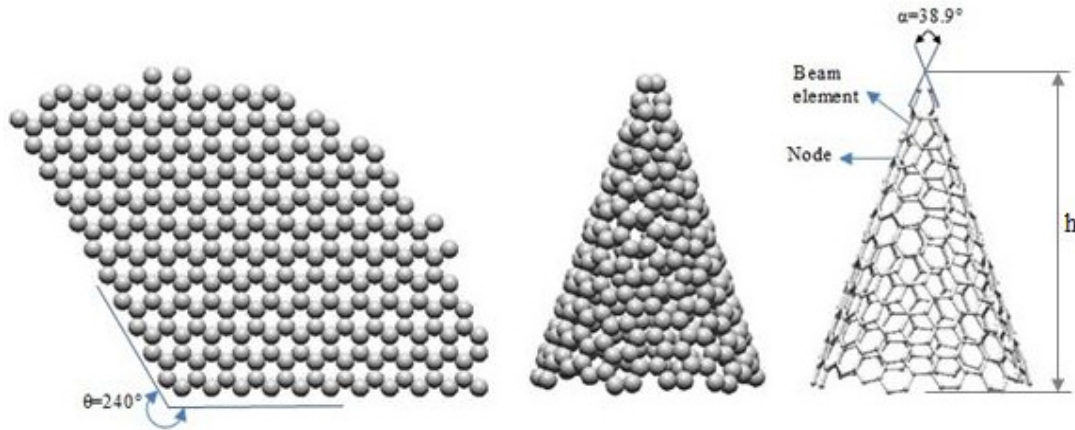


Figure 1: The cone sheet with the dislocation angle of 240° corresponding to the cone with apex angle of 38.9° SWCNC and its equivalent FE model.

Figure 1 shows the cone sheet with the dislocation angle of 240° corresponding to the cone with apex angle of 38.9° SWCNC and its equivalent FE model. Other types of SWCNCs and FE models can be produced in a similar way as shown in Figure 1. The larger the apex angle of a SWCNC, the larger the bottom radii and number of atoms.

2.2 Application of atomistic FE modeling approach to SWCNCs

For the simulation of vibration and elastic buckling behaviors of SWCNCs, an atomistic FE modeling approach is used. When carbon based nanostructures such as GSs, CNTs and CNCs are subjected to external forces, the positions of the atomic nuclei are controlled by the covalent bonds between C-C atoms. Hence, the deformation pattern of these nanostructures is very similar to deformation of the frame structures. To this end, SWCNCs are modeled as 3-D space frame-like structures in simulations and a covalent bond between two carbon atoms is represented by an Euler-Bernoulli beam element having consistent mass matrices (i.e., see Figure 1). The element stiffness matrix and consistent mass matrix for a 3-D Euler-Bernoulli beam element are given by Equations (2) and (3), respectively.

$$\mathbf{K} = \begin{bmatrix} K_{ii} & K_{ij} \\ K_{ij} & K_{jj} \end{bmatrix} \quad \mathbf{M} = \begin{bmatrix} M_{ii} & M_{ij} \\ M_{ij} & M_{jj} \end{bmatrix} \quad (2)$$

where the sub-matrices, K_{ii} , K_{ij} , K_{jj} , M_{ii} , M_{ij} and M_{jj} are given by

$$\begin{aligned}
 K_{ii} &= \begin{bmatrix} \frac{EA}{L} & 0 & 0 & 0 & 0 & 0 \\ 0 & \frac{12EI_x}{L^3} & 0 & 0 & 0 & \frac{6EI_x}{L^2} \\ 0 & 0 & \frac{12EI_y}{L^3} & 0 & -\frac{6EI_y}{L^2} & 0 \\ 0 & 0 & 0 & \frac{GJ}{L} & 0 & 0 \\ 0 & 0 & -\frac{6EI_y}{L^2} & 0 & \frac{4EI_y}{L} & 0 \\ 0 & \frac{6EI_x}{L^2} & 0 & 0 & 0 & \frac{4EI_x}{L} \end{bmatrix}, & K_{ij} &= \begin{bmatrix} -\frac{EA}{L} & 0 & 0 & 0 & 0 & 0 \\ 0 & -\frac{12EI_x}{L^3} & 0 & 0 & 0 & \frac{6EI_x}{L^2} \\ 0 & 0 & -\frac{12EI_y}{L^3} & 0 & -\frac{6EI_y}{L^2} & 0 \\ 0 & 0 & 0 & -\frac{GJ}{L} & 0 & 0 \\ 0 & 0 & \frac{6EI_y}{L^2} & 0 & \frac{2EI_y}{L} & 0 \\ 0 & -\frac{6EI_x}{L^2} & 0 & 0 & 0 & \frac{2EI_x}{L} \end{bmatrix} \\
 K_{jj} &= \begin{bmatrix} \frac{EA}{L} & 0 & 0 & 0 & 0 & 0 \\ 0 & \frac{12EI_x}{L^3} & 0 & 0 & 0 & -\frac{6EI_x}{L^2} \\ 0 & 0 & \frac{12EI_y}{L^3} & 0 & \frac{6EI_y}{L^2} & 0 \\ 0 & 0 & 0 & \frac{GJ}{L} & 0 & 0 \\ 0 & 0 & \frac{6EI_y}{L^2} & 0 & \frac{4EI_y}{L} & 0 \\ 0 & -\frac{6EI_x}{L^2} & 0 & 0 & 0 & \frac{4EI_x}{L} \end{bmatrix}, & M_{ii} &= \rho AL \begin{bmatrix} \frac{1}{3} & 0 & 0 & 0 & 0 & 0 \\ 0 & \frac{13}{35} & 0 & 0 & 0 & \frac{11L}{210} \\ 0 & 0 & \frac{13}{35} & 0 & -\frac{11L}{210} & 0 \\ 0 & 0 & 0 & \frac{J}{3A} & 0 & 0 \\ 0 & 0 & -\frac{11L}{210} & 0 & \frac{L^2}{105} & 0 \\ 0 & \frac{11L}{210} & 0 & 0 & 0 & \frac{L^2}{105} \end{bmatrix} \\
 M_{ij} &= \rho AL \begin{bmatrix} \frac{1}{6} & 0 & 0 & 0 & 0 & 0 \\ 0 & \frac{9}{70} & 0 & 0 & 0 & \frac{13L}{420} \\ 0 & 0 & \frac{9}{70} & 0 & -\frac{13L}{420} & 0 \\ 0 & 0 & 0 & \frac{J}{6A} & 0 & 0 \\ 0 & 0 & \frac{13L}{420} & 0 & -\frac{L^2}{140} & 0 \\ 0 & -\frac{13L}{420} & 0 & 0 & 0 & -\frac{L^2}{140} \end{bmatrix}, & M_{jj} &= \rho AL \begin{bmatrix} \frac{1}{3} & 0 & 0 & 0 & 0 & 0 \\ 0 & \frac{13}{35} & 0 & 0 & 0 & -\frac{11L}{210} \\ 0 & 0 & \frac{13}{35} & 0 & \frac{11L}{210} & 0 \\ 0 & 0 & 0 & \frac{J}{3A} & 0 & 0 \\ 0 & 0 & \frac{11L}{210} & 0 & \frac{L^2}{105} & 0 \\ 0 & -\frac{11L}{210} & 0 & 0 & 0 & \frac{L^2}{105} \end{bmatrix} \tag{3}
 \end{aligned}$$

where L denotes the initial length of a C-C bond and equals to 0.1421 nm. In addition, for the computational model, numerical values of the following stiffness parameters should be given a priori: A is the cross-sectional area, E and G are respectively the Young's and shear moduli, I and J are respectively the moment of inertia and polar moment of inertia of the cross section and ρ is the beam element density. To obtain E , G , A , I and J , energy equivalence concept is employed. In this analogy, stretching, bending and twisting potential energy terms based on the MM and structural mechanics models are assumed to be independent of each other and then corresponding terms are set equal to each other in these two models. Under the small deformation assumption and by using harmonic expressions of potential energy in the MM model, Li and Chou [19] obtained the following relations by using energy equivalence concept

$$\frac{EA}{L} = k_r, \quad \frac{EI}{L} = k_\theta, \quad \frac{GJ}{L} = k_\tau \tag{4}$$

where k_r , k_θ and k_τ respectively denote the bond stretching, angle bending and torsional force constants, respectively. Assuming that the cross section of beam elements is uniform and circular, then the Young's modulus E , the shear modulus G and diameter of the cross sec-

tion d are obtained by plugging in the cross sectional area $A = \pi d^2 / 4$, moment of inertia $I_x = I_y = \pi d^4 / 64$ and polar moment of inertia $J = \pi d^4 / 32$ as follows [23]

$$E = \frac{k_r^2 L}{4\pi k_\theta}, \quad G = \frac{k_r^2 k_\tau L}{8\pi k_\theta^2} \quad d = 4 \sqrt{\frac{k_\theta}{k_r}} \quad (5)$$

In this study, the AMBER force model is chosen [19, 23]. The AMBER force model constants k_r , k_θ and k_τ are taken as $6.52 \times 10^{-7} \text{ N nm}^{-1}$, $8.76 \times 10^{-10} \text{ N nm rad}^{-2}$ and $2.78 \times 10^{-10} \text{ N nm rad}^{-2}$, respectively. Table (1) summarizes the properties of the Euler-Bernoulli beam element which are the inputs of the FE models.

2.3 Vibrational and buckling analyses of SWCNCs

In this study, SWCNCs with disclination angles of 120° , 180° and 240° are taken into account which satisfied the continuity condition at the folding of the cone sheet. The tip of the SWCNCs is not explicitly modeled in vibrational and buckling analysis due to geometric limitations (e.g., see Figure 1). The smallest model has 180 atoms and 258 bonds, while the largest model has 3592 atoms and 5312 bonds. Free-free, free-clamped and clamped-clamped boundary conditions are taken into account in vibrational analysis, and axial compression and bending loading conditions are considered in elastic buckling analysis.

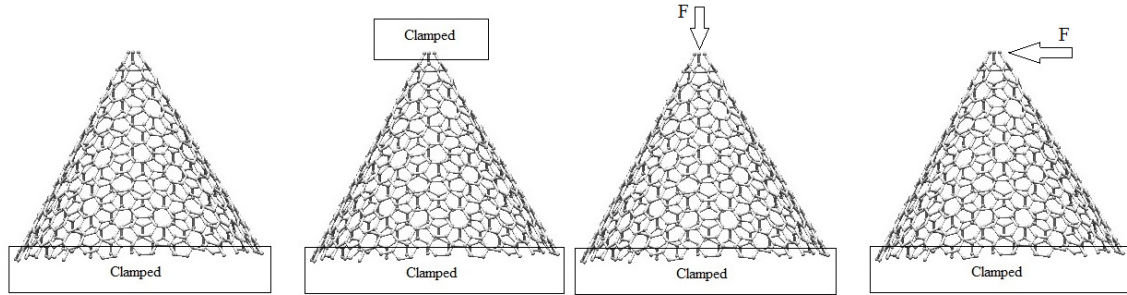


Figure 2: Free-clamped and clamped-clamped boundary conditions in vibrational analysis and axial compression and bending loading conditions in buckling analysis.

Figure 2 shows the boundary and loading conditions for vibrational and buckling analyses of the SWCNCs. All computations of the MM model are completed by using a computer code developed in MATLAB environment, no damping is considered in computational models and the results are verified by using Ansys[®] software. After assembling the element stiffness and consistent mass matrices, the natural frequencies and corresponding mode-shapes are obtained by solving the following eigenproblem

$$(\mathbf{K} - \omega_i^2 \mathbf{M})\mathbf{d} = \mathbf{0} \quad (6)$$

where \mathbf{K} , \mathbf{M} , \mathbf{d} and ω_i are the global stiffness matrix, global mass matrix, displacement vector and the natural frequencies, respectively. In addition, the natural frequency is equal to $\omega = 2\pi f$, where f has the unit of Hertz. Similarly, critical buckling load and corresponding mode shapes are calculated by solving the following eigenproblem

$$(\mathbf{K}_0 - \lambda \bar{\mathbf{K}}_1)\boldsymbol{\psi} = \mathbf{0} \quad (7)$$

where \mathbf{K}_θ is the global stiffness matrix, $\bar{\mathbf{K}}_1$ is the geometric stiffness matrix and $\boldsymbol{\psi}$ is the buckling-mode shape. The factor λ at which buckling occurs is designated as λ_{cr} , and $P_{cr} = \lambda_{cr}P$ [39].

	Present work	Lee and Lee[28]	Mir et al. [29]	Scarpa et al. [34]
Mass matrix type	Consistent	Lumped	Consistent	-
Beam type	Euler-Bernoulli	Shear Beam	Euler-Bernoulli	Shear Beam
Cross-sectional area, A	1.687 \AA^2	1.687 \AA^2	1.687 \AA^2	0.554 \AA^2
Density [22]	$5.5 \times 10^{-27} \text{ kg/ \AA}^3$	$2.3 \times 10^{-27} \text{ kg/ \AA}^3$	$2.3 \times 10^{-27} \text{ kg/ \AA}^3$	-
Elastic modulus, E	$5.488 \times 10^{-8} \text{ N/\AA}^2$	$5.488 \times 10^{-8} \text{ N/\AA}^2$	$5.488 \times 10^{-8} \text{ N/\AA}^2$	$16.71 \times 10^{-8} \text{ N/\AA}^2$
Shear modulus, G	$8.711 \times 10^{-9} \text{ N/\AA}^2$	$8.711 \times 10^{-9} \text{ N/\AA}^2$	$8.711 \times 10^{-9} \text{ N/\AA}^2$	$80.8 \times 10^{-9} \text{ N/\AA}^2$
Poisson's ratio, ν	Not needed	0.3	Not needed	0.034
Bond thickness, d	1.47 \AA	1.47 \AA	1.47 \AA	0.84 \AA

Table 1: Properties of the beam elements in literature.

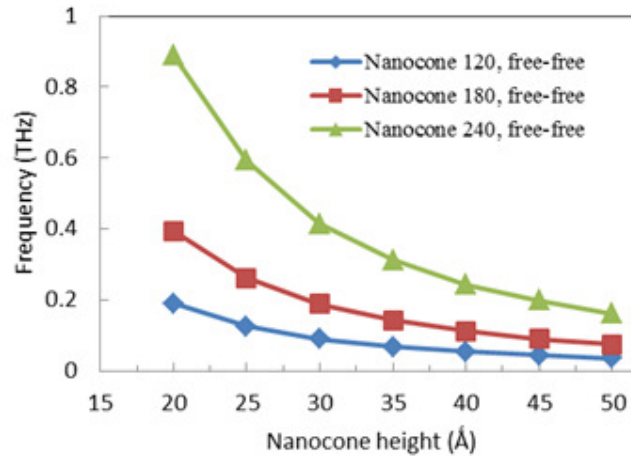


Figure 3: Variation of the first natural frequency of SWCNCs having the disclination angles of 120°, 180° and 240° as the cone height changes for the free-free boundary condition.

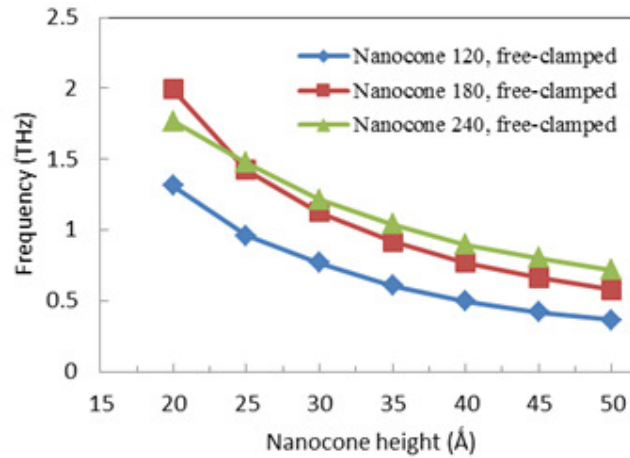


Figure 4: Variation of the first natural frequency of SWCNCs having the disclination angles of 120°, 180° and 240° as the cone height changes for the free-clamped boundary condition.

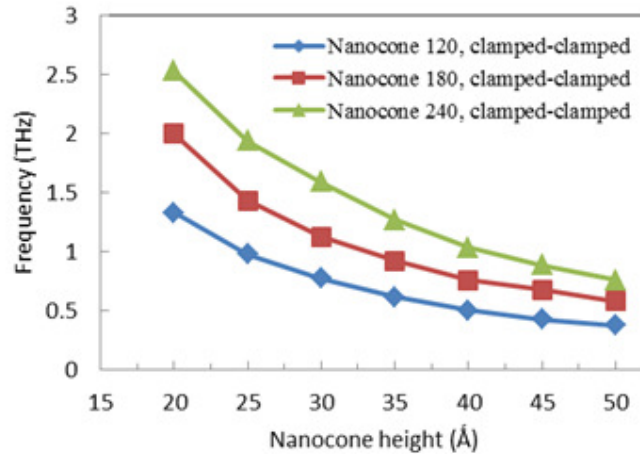


Figure 5: Variation of the first natural frequency of SWCNCs having the disclination angles of 120° , 180° and 240° as the cone height changes for the clamped-clamped boundary condition.

The effects of cone height and disclination angles on the natural frequencies of SWCNCs are examined in vibration analysis where natural frequencies and corresponding mode shapes are obtained. Figures 3, 4 and 5 show the variations of the first fundamental frequencies of SWCNCs versus cone height for free-free, free-clamped and clamped-clamped boundary conditions, respectively. As can be seen in these figures, the first natural frequency decreases with increasing cone height in all types of SWCNCs, whereas it increases as the disclination angle increases except for the SWCNCs having the disclination angle of 240° and height of 20 \AA . In addition, the SWCNCs with disclination angles of 240° are more sensitive to variations in height and boundary conditions than the other SWCNCs in vibrational analysis due its small apex angle. When free-clamped and clamped-clamped boundary conditions are considered, the first fundamental frequencies of SWCNCs, are found to be in the range of $0.36 - 2.52 \text{ THz}$. Lee and Lee [28] used Timoshenko beam element formulations which include shear deformation effects but they employed Euler-Bernoulli beam element constants (i.e., see Table 1) [23]; this assumption affects the natural frequencies of SWCNC that are found to be lower than those of Euler-Bernoulli beam elements. In addition, density of beam elements is selected to be the density of GSs (i.e. 2300 kg/m^3) in the MM model. Hence, natural frequencies of SWCNCs are found to be less than 100 GHz in all calculations for the same type of SWCNCs having the height of 20 \AA and with free-clamped and clamped-clamped boundary conditions. These frequency ranges are comparable with those of CNTs and SLGSs (i.e., $10 \text{ GHz} - 1.5 \text{ THz}$ for SWCNTs and $2.4 \text{ GHz} - 3.5 \text{ THz}$ for SLGSs) which are reported in literature [21, 25].

Figures 6 and 7 show respectively the variations in the first ten natural frequencies for the free-free and clamped-clamped SWCNCs having the height of 50 \AA and disclination angles of 120° , 180° and 240° . It is noteworthy that variations in the first ten natural frequencies for the free-clamped SWCNCs which are not presented here for limited space are very close to those of clamped-clamped boundary conditions since relatively small radius of the cone tips has little effect on the vibrational behavior of the SWCNCs for these two boundary conditions.

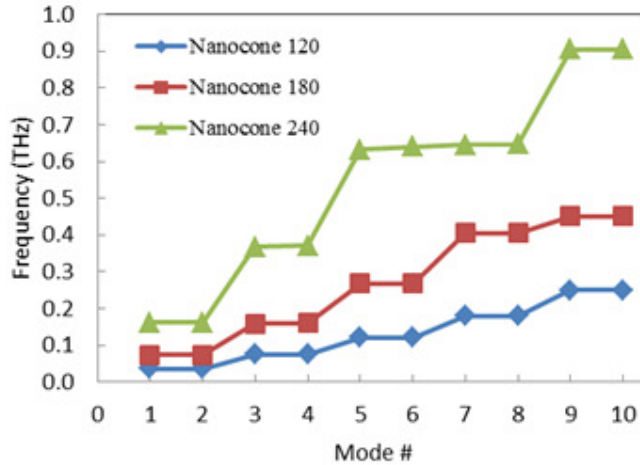


Figure 6: First ten natural frequencies of SWCNCs having the height of 50 Å and disclination angles of 120°, 180° and 240° for free-free boundary condition.

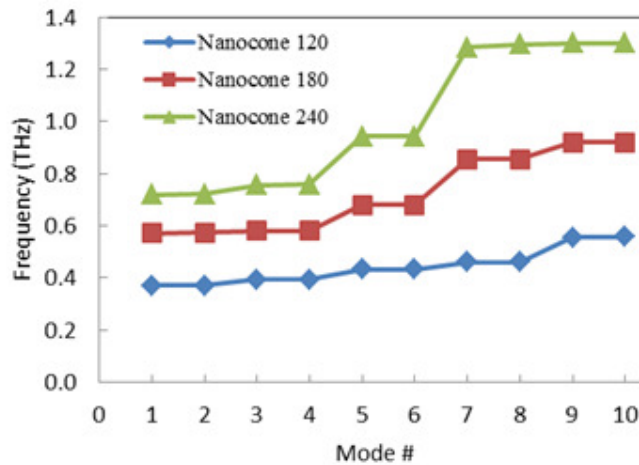


Figure 7: First ten natural frequencies of SWCNCs having the height of 50 Å and disclination angles of 120°, 180° and 240° for clamped-clamped boundary condition.

Figures 8 and 9 show respectively the first five vibration modes of SWCNCs having the disclination angle of 120° and height of 30 Å for the free-free and free-clamped boundary conditions. The mode shapes of clamped-clamped SWCNCs are also similar to those of free-clamped SWCNCs, that are not presented here for limited space. In addition, the second mode shape is very similar to the first mode shape in both figures, that are not presented for limited space as well.

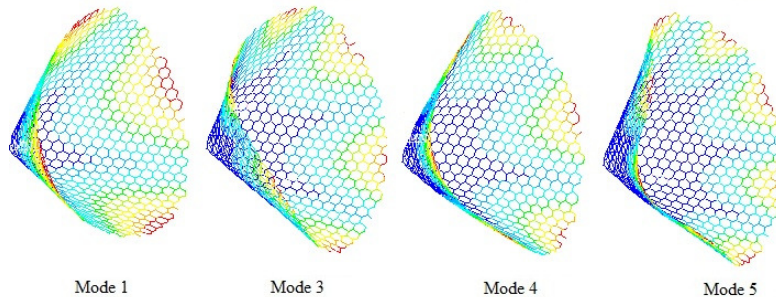


Figure 8: Vibrational modes of SWCNC having the disclination angle of 120°, height of 30 Å for free-free boundary condition.

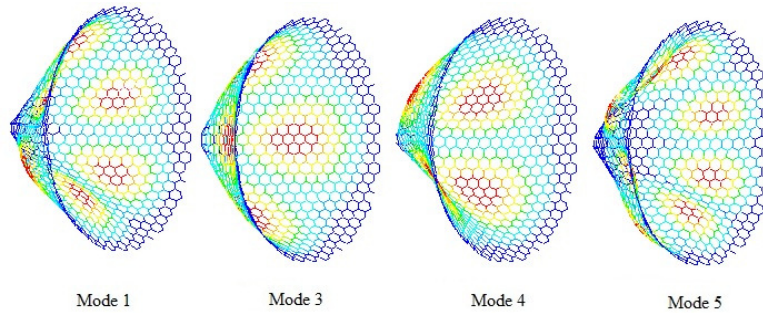


Figure 9: Vibrational modes of SWCNC having the disclination angle of 120° , height of 30 \AA for free-clamped boundary condition.

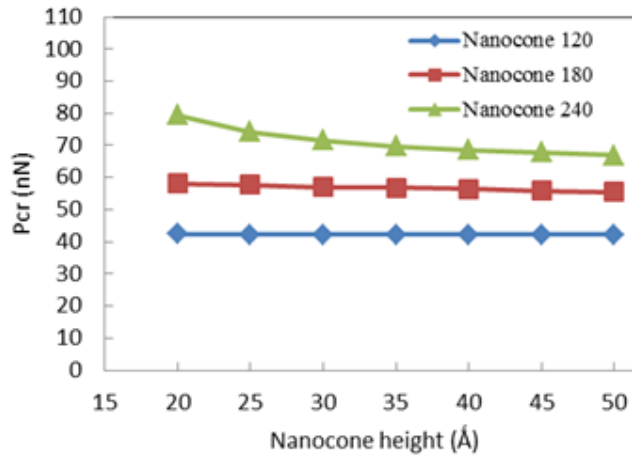


Figure 10: Variation of the first critical buckling load for the SWCNCs having the disclination angles of 120° , 180° and 240° as the cone height changes under axial compression loading condition.

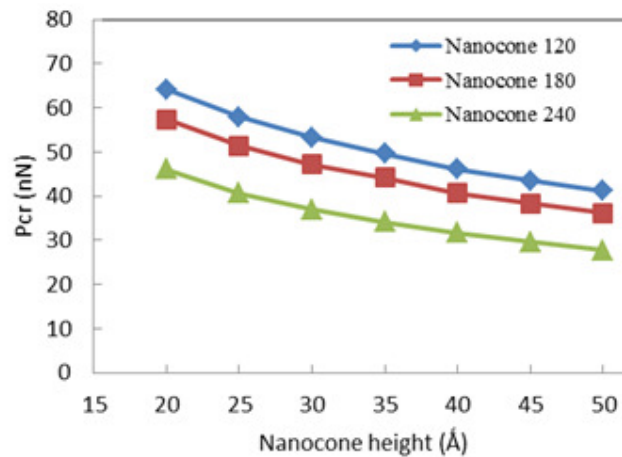


Figure 11: Variation of the first critical buckling load for the SWCNCs having the disclination angles of 120° , 180° and 240° as the cone height changes under bending loading condition.

Similar to vibration analysis, the effects of cone height and disclination angles on the critical buckling load and associated buckling modes of SWCNCs are studied by completing elastic buckling analysis. Figures 10 and 11 show respectively the variations of the first critical

buckling load of SWCNCs as the cone height changes for the axial and bending loading conditions. Buckling analysis results indicate that as the disclination angle increases, the critical buckling load increases in axial compression loading and decreases in bending loading. The buckling load in axial compression is larger than bending load for SWCNCs having the disclination angles of 180° and 240° , and it is smaller than that of bending load for SWCNCs having the disclination angle of 120° . Hence, it is concluded that bending loading is more critical than axial compression loading for buckling behavior of SWCNCs as the disclination angle increases. In addition, the cone height affects the bending buckling forces more than the axial compression buckling forces. The axial and bending buckling forces are found to be in the range of 42 – 79 nN and 27 – 64 nN, respectively. These ranges are comparable with those of CNTs (i.e., ~ 0.1 – 39 nN) which are reported in literature [22].

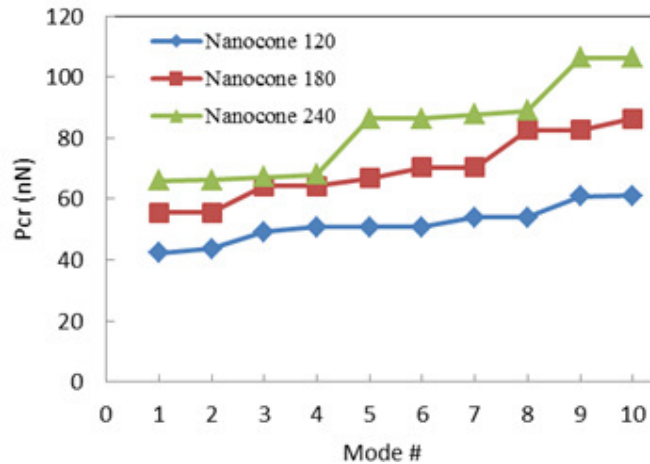


Figure 12: First ten buckling mode of SWCNCs having the disclination angles of 120° , 180° and 240° , and height of 50 \AA for the axial loading

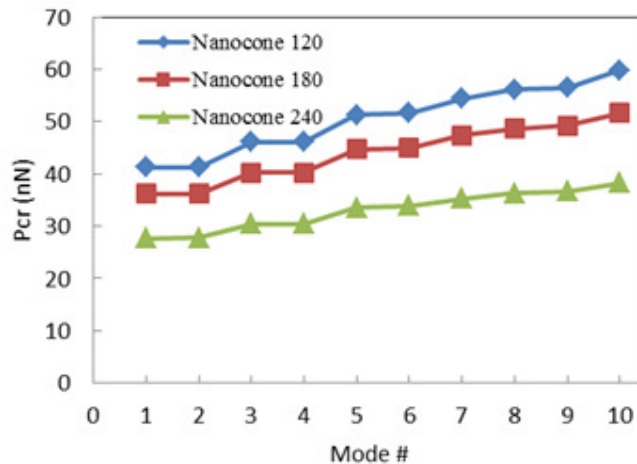


Figure 13: First ten buckling mode of SWCNCs having the disclination angles of 120° , 180° and 240° , and height of 50 \AA for the bending loading.

Figures 12 and 13 show the first ten buckling loads for the SWCNCs having the height of 50 \AA . As can be seen the figures, the elastic buckling modes of the SWCNCs have similar pattern except for the SWCNC with the disclination angle of 240° under axial compression loading.

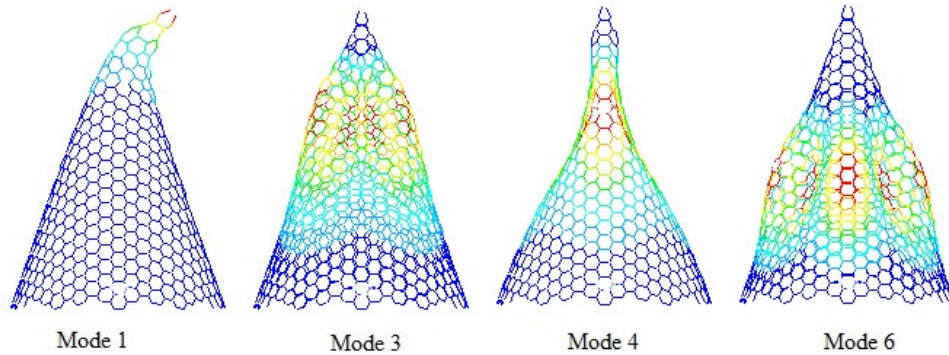


Figure 14: The first six buckling modes of the SWCNC having the disclination angle of 240° under the axial compression loading.

Figure 14 shows the first six buckling modes of the SWCNCs with the disclination angle of 240° and height of 50 \AA under the axial compression. Since the second and fifth buckling modes are respectively very similar to the first and sixth buckling modes, they are not presented here for limited space.

3 CONCLUSIONS

In this paper, the elastic buckling and vibration behaviors of SWCNCs are investigated. The MM based FE approach is used to achieve this goal. The axial compression and bending loading conditions are considered in elastic buckling behavior of SWCNCs while free-free, free-clamped and clamped-clamped boundary conditions are considered in vibration analysis of SWCNCs. The effects of cone height and apex angles on the buckling force and natural frequencies of SWCNCs are also studied. Vibration analysis results indicate that the natural frequency decreases with increasing cone height in all types of SWCNCs, whereas it increases as the disclination angle increases. Buckling analysis results indicate that as the disclination angle increases, the critical buckling load increases in axial compression loading and decreases in bending loading. In addition, it is observed that bending loading is more critical than axial compression loading for buckling behavior of SWCNCs if the disclination angle increases. When free-clamped and clamped-clamped boundary conditions are considered, fundamental frequencies of the SWCNCs are found to be in the range of $0.36 - 2.52 \text{ THz}$. The axial and bending buckling forces are found to be in the range of $42 - 79 \text{ nN}$ and $27 - 64 \text{ nN}$, respectively. These results are comparable with the results for CNTs and SLGSs in literature in most cases and it can be used in designing atomic force microscope (AFM) and scanning tunneling microscope (STM) tips. In the future, fracture and transient dynamics analyses can be performed in order to evaluate the damage and dynamic behavior of SWCNCs. Moreover, Morse potential can be employed in the MM model for large deformation problems.

REFERENCES

- [1] S. Iijima, Helical microtubules of graphitic carbon. *Nature*, **354**, 56-58, 1991.
- [2] S.P. Jordan, V.H. Crespi, Theory of carbon nanocones: mechanical chiral inversion of a micron-scale three-dimensional object. *Physical Review Letters*, **93**, 255504, 2004.

- [3] P.E. Lammert, V.H. Crespi, Graphene cones: Classification by fictitious flux and electronic properties. *Physical Review B*, **69**, 035406, 2004.
- [4] S. Berber, Y.K. Kwon, D. Tomanek, Electronic and structural properties of carbon nanocones. *Physical Review B*, **62**, 2291-2294, 2000.
- [5] N. Yang, G. Zhang, B. Li, Carbon nanocone: A promising thermal rectifier. *Applied Physics Letters*, **93**, 243111, 2008.
- [6] D. Kumar, V. Verma, H.S. Bhatti, K., 2011 Elastic moduli of carbon nanohorns. *Journal of Nanomaterials*, **2011**, 127952, 2011.
- [7] J.X. Wei, K.M. Liew, X.Q. He, Mechanical properties of carbon nanocones. *Applied Physics Letters*, **91**, 261906, 2007.
- [8] M. Ge, K. Sattler, Observation of fullerene cones. *Chemical Physics Letters*, **220**, 192-196, 1994.
- [9] A. Krishnan, E. Dujardin, M.M.J. Treacy, J. Hugdahl, S. Lynum, T. W. Ebbesen, Graphitic cones and the nucleation of curved carbon surface. *Nature*, **388**, 451-454, 1997.
- [10] J. Sripirom, S. Noor, U. Köhler, A. Schulte, Easy made and handled carbon nanocones for scanning tunneling microscopy and electroanalysis. *Carbon*, **49**, 2402-2412, 2011.
- [11] C. Chen, L.H. Chen, X.R. Ye, C. Daraio, S. Jin, C.A. Orme, A. Quist, R. Lal, Extreme sharp carbon nanocone probe for atomic force microscopy imaging. *Applied Physics Letters*, **88**, 153102, 2006.
- [12] J.Y. Hsieh, C. Chen, J.L. Chen, C.I. Chen, C.C. Hwang, The nanoindentation of a copper substrate by single-walled carbon nanocone tips: A molecular dynamics study. *Nanotechnology*, **20** 095709, 2009.
- [13] S.S. Yu, W. T. Zheng, Effect of N/B doping on the electronic and field emission properties for carbon nanotubes, carbon nanocones, and graphene nanoribbons. *Nanoscale*, **2** 1069, 2010.
- [14] P.C. Tsai, T.H. Fang, A molecular dynamics study of the nucleation, thermal stability and nanomechanics of carbon nanocones. *Nanotechnology*, **18**, 105702, 2007.
- [15] K.M. Liew, J.X. Wei, X.Q. He, Carbon nanocones under compression: Buckling and post-buckling behaviors. *Physical Review B*, **75**, 195435, 2007.
- [16] M.L. Liao, C.H. Cheng, Y.P. Lin, Tensile and compressive behaviors of open-tip carbon nanocones under axial strains. *Journal of Materials Research*, **26**, 1577-1584, 2011.
- [17] R.D.F. Abadi, M.M. Fotouhi, H. Haddadpour, Free vibration analysis of nanocones using nonlocal continuum model. *Physics Letters A*, **375**, 3593-3598, 2011.
- [18] G.M. Odegard, T.S. Gates, L.M. Nicholson, K.E. Wise, Equivalent-continuum modeling of nano-structured materials. *Composite Science and Technology*, **62**, 1869-1880, 2002.
- [19] C. Li, T.W. Chou, A structural mechanics approach for the analysis of carbon nanotubes International. *Journal Solids Structures*, **40**, 2487-2499, 2003.
- [20] C. Li, T.W. Chou, Vibrational behaviors of multiwalled-carbon-nanotube-based nanomechanical resonators. *Applied Physics Letters*, **84**, 12, 2004.

- [21] C. Li, T.W. Chou, Single-walled carbon nanotubes as ultrahigh frequency nanomechanical resonators. *Physical Review B*, **68**, 073405, 2003.
- [22] C. Li, T.W. Chou, Modeling of elastic buckling of carbon nanotubes by molecular structural mechanics approach. *Mechanics of Materials*, **36**, 1047-1055, 2004.
- [23] K.I. Tserpes, P. Papanikos, Finite element modeling of single-walled carbon nanotubes. *Composites Part B*, **36**, 468-477, 2005.
- [24] K. Hashemnia, M. Farid, R. Vatankhah, Vibrational analysis of carbon nanotubes and single-layered graphene sheets using molecular structural mechanics approach. *Computational Materials Science*, **47**, 79-85, 2009.
- [25] A. Sakhaee-Pour, M.T. Ahmadian, R. Naghdabadi, Vibrational analysis of single-layered graphene sheets. *Nanotechnology*, **19**, 085702, 2008.
- [26] A. Sakhaee-Pour, M.T. Ahmadian, A. Vafai, Vibrational analysis of single-walled carbon nanotubes using beam element. *Thin-Walled Structures*, **47**, 646-652, 2009.
- [27] A. Sakhaee-Pour, Elastic buckling of single-layered graphene sheet. *Computational Material Science*, **45**, 266-270, 2009.
- [28] J.H. Lee, B.S. Lee, Modal analysis of carbon nanotubes and nanocones using FEM. *Computational Materials Sciences*, **51**, 30-42, 2012.
- [29] M. Mir, A. Hosseini, G. Majzoobi, A numerical study of vibrational properties of single-walled carbon nanotubes. *Computational Materials Science*, **43**, 540-548, 2008.
- [30] H.C. Cheng, Y.L. Liu, Y.C. Hsu, W.H. Chen, Atomistic-continuum modeling for mechanical properties of single-walled carbon nanotubes. *International Journal of Solids and Structures*, **46**, 1695-1704, 2009.
- [31] C.W. Fan, Y.Y. Liu, C. Hwu, Finite element simulation for estimating the mechanical properties of multi-walled carbon nanotubes. *Applied Physics A*, **95**, 819-831, 2009.
- [32] A.F. Avila, A.C. Eduardo, A.S. Neto, Vibrational analysis of graphene based nanostructures. *Computer and Structures*, **89**, 878-892, 2011.
- [33] C. Baykasoglu, A. Mugan, Dynamic analysis of single-layer graphene sheets. *Computational Material Science*, **55**, 228-236, 2012.
- [34] F. Scarpa, S. Adhikari, A mechanical equivalence for Poisson's ratio and thickness of C-C bonds in single wall carbon nanotubes. *Journal of Physics D: Applied Physics*, **41**, 085306, 2008.
- [35] F. Scarpa, S. Adhikari, A.S. Phani, Effective elastic mechanical properties of single layer graphene sheets. *Nanotechnology*, **20**, 065709, 2009.
- [36] G. Brinkmann, N.V. Cleemput, Classification and generation of nanocones. *Discrete Applied Mathematics*, **159**, 1528-1539, 2011.
- [37] B. Ekşioğlu, A. Nadarajah, Structural analysis of conical carbon nanofibers. *Carbon*, **44**, 360-373, 2006.
- [38] P.J.F. Harris, *Carbon nanotubes and related structures*. Cambridge University Press Cambridge UK, 1999.
- [39] T.J.R. Hughes, *The finite element method, linear static and dynamic finite element analysis*. Prentice-Hall, 2000.

NUMERICAL ANALYSIS ABOUT THE INFLUENCE OF INAPPROPRIATE SHAPE OF THE CROSS-SECTION OF MICROCHANNELS IN LAMINAR FLOW

Fabiano Da Rosa Hollweg¹, Rejane De Césaró Oliveski², Marcelo Dalla Corte²

¹ Universidade do Vale do Rio dos Sinos
Av. Unisinos, 950, São Leopoldo, RS 93022-000, Brazil
e-mail: fabiano.hollweg@gmail.com

² Universidade do Vale do Rio dos Sinos
Av. Unisinos, 950, São Leopoldo, RS 93022-000, Brazil
decesaroo@gmail.com, marcelodallacorte@gmail.com

Keywords: microchannels, Poiseuille, Nusselt, CFD.

Abstract. *In the past decades, several experimental investigations performed to the hydrodynamics and heat transfer in microscale laminar flow have showed divergences to the Darcy friction factor and the Poiseuille and Nusselt numbers, when the results obtained for the same ones were compared to those provided by classical theory. There are reports of deviations to the Darcy friction factor and the Poiseuille and Nusselt numbers attributed to geometric imperfections at the cross-section of the microchannels. The aim of this numerical study is to analyze how the hydrodynamic and heat transfer characteristics in single-phase laminar flow, of a fluid with constant thermophysical properties, can be affected by imperfections at the cross-section of the microchannels. The results obtained for single-phase laminar flow of water in microchannels with imperfections at the cross-section are compared to those obtained for a geometrically perfect microchannel through Poiseuille and Nusselt numbers. Deviations at Poiseuille and Nusselt numbers due to imperfections at the cross-section of the microchannels were verified. The results showed that Nusselt number is more sensitive to shape of the cross-section of the microchannels than Poiseuille number. This study showed that knowledge about the geometrical shape of the cross-section of the microchannels is important to determine properly the hydrodynamic parameters of the flow, such as Poiseuille number. This study was carried out through computational fluid dynamics (CFD) and the numerical model made up by mass conservation, Navier-Stokes and energy equations.*

1 INTRODUCTION

In recent years, the reduction of electronic devices in several application fields, such as biomedicine, chemistry and electronics has been providing high efficiency related to the space in equipments. At the same time, this reduction in physical space is counterweighted by the high performance required at the refrigeration systems in such equipment. Therefore, thermal control is one of the most critical areas for the development of modern microelectronic devices [1-5].

A lot of experimental studies [1, 2, 5-21], besides theoretical [22-24] and numerical studies [5, 25-28], have been carried out, in the past decades, seeking to investigate the hydrodynamics and heat transfer characteristics in microscale. The results obtained in several of these studies show diversions among themselves and, also, with the conventional theory. In general, the reported divergences can be viewed through analysis of the Darcy friction factor or the Poiseuille and Nusselt numbers, when the results obtained for them are compared to those provided by conventional theory [1, 2, 19, 21].

There are reports of friction factors and Poiseuille numbers either above [2, 6, 12, 23, 26] or below [7-10, 16] of what is predicted by the classical theory, as well as in good agreement with it [2, 11-14, 16, 18]. Some researchers attribute the deviations found for the friction factor or Poiseuille number to variations of the cross-section of microchannels due to the surface roughness [6, 12, 14, 17]. Other researchers attribute these deviations to deformations existing in the cross-section of the microchannels [2, 21], to aspect ratio of channels [2, 5, 8, 17] and, also, to scaling effects, such as viscous dissipation [19, 26] and electrokinetic effect [22, 23], for example. Uncertainty analysis carried out in several experimental studies attribute to the inaccuracy in the measurement of hydraulic diameter of the microchannels as one of the main reasons of errors in determining the friction factor and Poiseuille number in microscale flow [1, 16, 19-21]. Additionally, there are reports [8, 18] of deviations to the friction factor that showed dependence on the Reynolds number.

In relation to microscale heat transfer, some researchers have reported results obtained for the Nusselt number in good agreement with the classical theory [25, 30-33]. However, other researchers have indicated that differences in rates and coefficients of heat transfer, as well as in Nusselt number, can be related to the flow velocity and fluid temperature [16, 34-36], the Reynolds number [9], the heat transfer conjugated [2, 37-39], the viscous dissipation [16, 20, 26, 40, 41], the surface roughness [42], the aspect ratio of microchannels [5, 43] and the conductivity of the material that compose them [2, 37-39], besides experimental uncertainties [4, 30-33, 44]. Some numerical studies [45, 46] showed that the Nusselt number is more sensitive to the shape of the cross-section of the microchannels in comparison to other parameters, such as surface roughness, for example. Furthermore, there are numerical and theoretical studies that consider simplifications which differ a lot from what actually should occur experimentally as, for example, the negligence of viscous dissipation in numerical model [28, 47], the true boundary condition at the limits [44] and the consideration of the fluid with constant thermo-physical properties, in general.

Thereby, geometrical parameters of the microchannels, experimental uncertainties and the presence of several possible scaling effects, at once, complicate the identification of probable error sources in experimental studies in this application area. Therefore, the use of numerical techniques can be advantageous in the study of flow in microscale, since significant effects in this field, such as surface roughness, viscous dissipation and geometric imperfections of the microchannels, for example, can be considered separately in numerical model.

The aim of this numerical study is to analyze how the hydrodynamic and heat transfer characteristics can be affected by imperfections at the cross-section of the microchannels, in

single-phase laminar flow of a fluid with constant thermophysical properties. Other scaling effects, such as viscous dissipation and electrokinetic effect, for example, are not considered in the numerical model. The results obtained for single-phase laminar flow of water in microchannels with imperfections at the cross-section are compared to the ones obtained for a geometrically perfect microchannel through Poiseuille and Nusselt numbers. The results of this study were determined through mass conservation, Navier-Stokes and energy equations, by computational fluid dynamics (CFD).

2 COMPUTATIONAL MODEL

Computational models for the imperfect microchannels and the corresponding perfect microchannel of this study are based on the work by Steinke and Kandlikar [21] to a heatsink made up of an array of microchannels in a silicon substrate, which was used by Steinke et al. [48]. The perfect (ideal) microchannel of this study, called Microchannel 1, has a rectangular cross-section. Two imperfect microchannels were considered. One of these has rectangular cross-section whereas the other has a kind of a trapezoidal cross-section, these being the Microchannels 2 and 3, respectively. The outline cross-section geometry of these microchannels is shown in Figure 1.

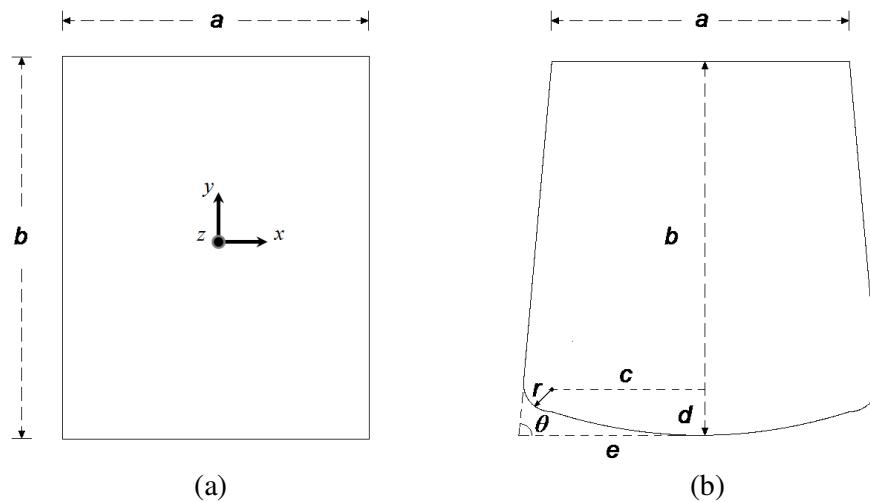


Figure 1: Scheme adopted for the computational model of the Microchannels (a) 1, 2 and (b) 3.

The Microchannel 1 consists of a tube with rectangular cross-section of width $a = 200 \mu\text{m}$ and height $b = 250 \mu\text{m}$. The Microchannel 2 considers an inaccuracy in the measurements of the width and height of the cross-section of Microchannel 1, so that $a = 201 \mu\text{m}$ and $b = 247 \mu\text{m}$. The Microchannel 3 consists of an tube with a kind of trapezoidal cross-section of $a = 194 \mu\text{m}$ and $b = 244 \mu\text{m}$. At the bottom of the cross-section of it, the base is almost curved and with rounded corners. The channel walls form angle of $\theta = 85^\circ$ with the horizontal. Other measurements indicated for Microchannel 3, in Figure 1(b), are $c = 97 \mu\text{m}$, $d = 33.9 \mu\text{m}$, $e = 118.5 \mu\text{m}$ and $r = 18.51 \mu\text{m}$. The length L chosen for all microchannels was 0.223 m to ensure conditions of hydrodynamically and thermally developed flow near the outlet of the tubes ($L/D_h \cong 1,000$).

Table 1 shows the geometric details concerning the microchannels of this study.

Data	Microchannels		
	1	2	3
a [μm]	200	201	194
b [μm]	250	247	244
AR [-]	0.80	0.81	0.80
L [m]	0.223	0.223	0.223
Per [μm]	900.00	896.00	870.95
A_c [$\times 10^3 \mu\text{m}^2$]	50.00	49.65	50.76
A_s [$\times 10^6 \mu\text{m}^2$]	200.70	199.81	194.22
D_h [μm]	222.22	221.64	233.14
η [%]	0	-0.26	+4.91

Table 1: Geometric parameters of the microchannels studied.

According to Table 1, the perimeter (Per) and surface area (A_s) of the Microchannel 3 are smaller than Microchannels 1 and 2. The cross-section area (A_c) of Microchannel 3 is higher than Microchannels 1 and 2. The same occurs for the relative deviation (η) on hydraulic diameter (D_h) of them. The aspect ratio (AR) of Microchannel 2 varied a little in relation to the Microchannels 1 and 3.

The values of a and b used for the Microchannel 2 were based on non-destructive measures of the cross-section of the heatsink studied by Steinke and Kandlikar [21]. According to the researchers, these measures refer to the values of the width and height of the cross-section of the microchannels obtained by optical measurement techniques. The values of a and b used for the Microchannel 3 are based on destructive measures of the heatsink, which was cleaved, according Steinke and Kandlikar [21]. After that, by the analysis of the images of its cross-section, obtained by a scanning electron microscope (SEM), the researchers found that the cross-section of the microchannels showed a kind of trapezoidal aspect, as shown in Figure 2.

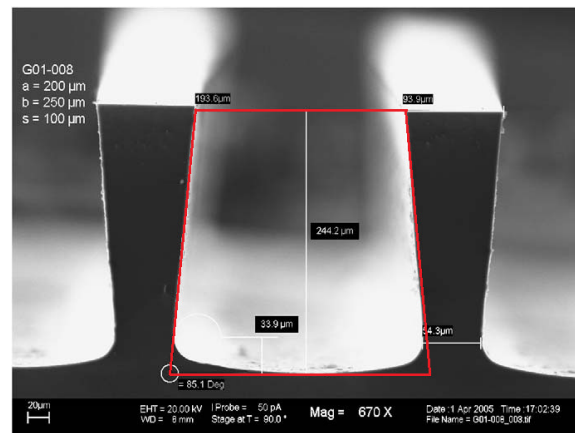


Figure 2: Image of the deformed cross-section of the microchannels of the heatsink studied by Steinke and Kandlikar [21].

In the original work by Steinke et al. [48], the microchannels were covered, on top of the cross-section, by a transparent cover of pyrex, which is not shown in Figure 2. An ideal trapezoid is indicated by red lines, for comparison with the deformed shape of the cross-section of the channel.

In all simulations, the working fluid chosen was water and the Reynolds numbers (Re) considered were 200, 400, 600 and 800, according to the work by Steinke and Kandlikar [21].

To transfer heat to fluid, it was considered a constant heat flux (q_s'') of 2 kW/m² applied on the surface of microchannels¹. The entrance region of the microchannels was considered with simultaneous development of hydrodynamic and thermal boundary layers.

3 MATHEMATICAL MODEL

The fluid used is incompressible and with constant properties. The flow regime is laminar and permanent. Neither the viscous dissipation is considered, nor the gravitational effects. Based on these considerations, the equations of mass conservation, Eq. (1), Navier-Stokes, Eqs. (2-4), and energy, Eq. (5), in rectangular coordinates, are presented in the following:

$$\frac{\partial u}{\partial x} + \frac{\partial v}{\partial y} + \frac{\partial w}{\partial z} = 0, \quad (1)$$

$$u \frac{\partial u}{\partial x} + v \frac{\partial u}{\partial y} + w \frac{\partial u}{\partial z} = -\frac{1}{\rho} \frac{\partial p}{\partial x} + \nu \left(\frac{\partial^2 u}{\partial x^2} + \frac{\partial^2 u}{\partial y^2} + \frac{\partial^2 u}{\partial z^2} \right), \quad (2)$$

$$u \frac{\partial v}{\partial x} + v \frac{\partial v}{\partial y} + w \frac{\partial v}{\partial z} = -\frac{1}{\rho} \frac{\partial p}{\partial y} + \nu \left(\frac{\partial^2 v}{\partial x^2} + \frac{\partial^2 v}{\partial y^2} + \frac{\partial^2 v}{\partial z^2} \right), \quad (3)$$

$$u \frac{\partial w}{\partial x} + v \frac{\partial w}{\partial y} + w \frac{\partial w}{\partial z} = -\frac{1}{\rho} \frac{\partial p}{\partial z} + \nu \left(\frac{\partial^2 w}{\partial x^2} + \frac{\partial^2 w}{\partial y^2} + \frac{\partial^2 w}{\partial z^2} \right), \quad (4)$$

$$u \frac{\partial T}{\partial x} + v \frac{\partial T}{\partial y} + w \frac{\partial T}{\partial z} = \alpha \left(\frac{\partial^2 T}{\partial x^2} + \frac{\partial^2 T}{\partial y^2} + \frac{\partial^2 T}{\partial z^2} \right), \quad (5)$$

where u , v and w are the velocity components of the fluid in the x , y and z directions, respectively, ρ , ν , α , p and T are the specific mass, the kinematic viscosity, the thermal diffusivity, the pressure and the temperature of the fluid, respectively.

The hydraulic diameter D_h is defined by

$$D_h = \frac{4A_c}{Per}. \quad (6)$$

For tubes with rectangular cross-section of width a and height b , the aspect ratio AR of its cross-section² is defined by

$$AR = \frac{a}{b}. \quad (7)$$

The Darcy friction factor f , the hydrodynamic resistance R_{hyd} and the hydrodynamic power P_{hyd} of the flow are defined, respectively, by

¹ In the study of Steinke and Kandlikar [21], the researchers studied only the hydrodynamic behavior of the flow, which was considered adiabatic. In the present study, looking forward to evaluate the impact of imperfections at the cross-section of the microchannels considered on the thermal behavior of the flow, it was decided to do an idealization. Therefore, it was considered a constant heat flux applied on the entire surface of the microchannels considered. Thus, it is possible to compare the results obtained to the local Nusselt number of this study with the theoretically predicted value [49] for this thermal condition.

² For tubes with trapezoidal cross-section, a in the Eq. (7) will be the smallest width of the cross-section [49].

$$f = \frac{2\rho D_h A_c^2 \Delta p}{\dot{m}^2 L}, \quad (8)$$

$$\Delta p = R_{hyd} Q, \quad (9)$$

and

$$P_{hyd} = \Delta p Q, \quad (10)$$

where Δp is the drop pressure and \dot{m} is the mass flow rate, which is related to the volumetric flow rate Q by

$$\dot{m} = \rho Q = \rho w_m A_c, \quad (11)$$

where w_m is the mean velocity of flow.

The Poiseuille number Po and the Reynolds number Re are defined, respectively, as:

$$Po = f Re, \quad (12)$$

$$Re = \frac{\rho w_m D_h}{\mu}, \quad (13)$$

where μ is the dynamic viscosity of the fluid.

The shear stress τ on the walls of channels, in the region of hydrodynamically developed laminar flow, is related to the pressure gradient dp/dz and the hydraulic diameter D_h of channels by

$$\tau = \frac{1}{4} D_h \left(\frac{dp}{dz} \right). \quad (14)$$

The hydrodynamic entrance length L_{he} is defined by

$$L_{he} = 0.1 Re D_h. \quad (15)$$

The local Nusselt number Nu is defined by

$$Nu = \frac{h D_h}{k}, \quad (16)$$

where k is the thermal conductivity of fluid and h is the local heat transfer coefficient, which is determined by

$$h = \frac{q_s''}{T_s - T_m} = \frac{1}{R_{ct}}, \quad (17)$$

where R_{ct} is the convection thermal resistance, T_s is the surface temperature of tubes and T_m is the mean temperature of fluid in cross-section, which is defined by

$$T_m = \frac{\int_{A_c} \rho w c_v T dA_c}{\dot{m} c_v}, \quad (18)$$

where c_v is the specific heat of fluid at constant volume.

The mean temperature gradient dT_m/dz for tubes with constant cross-section is defined by

$$\frac{dT_m}{dz} = \frac{q_s'' Per}{\dot{m}c_p}, \quad (19)$$

where c_p is the specific heat of fluid at constant pressure.

The total convection heat transfer rate q_{conv} for the tubes is defined by

$$q_{conv} = q_s'' A_s. \quad (20)$$

The thermal entrance length L_{te} is defined by

$$L_{te} = L_{he} Pr, \quad (21)$$

where Pr is the Prandtl number.

The magnitude of deviation ε of a generic variable Φ , in relation to the theoretical value expected for it, Φ_t , is determined by

$$\varepsilon_\Phi = \frac{|\Phi - \Phi_t|}{\Phi_t} \times 100\%, \quad (22)$$

whereas the deviation on the hydraulic diameter of the imperfect microchannels, related to the hydraulic diameter of the Microchannel 1, is particularly indicated by η (so that $\eta = \pm \varepsilon_{D_h}$).

The dimensionless height y^* of the cross-section of tubes is defined by

$$y^* = \frac{y}{b}, \quad (23)$$

whereas the dimensionless axial position z^* is given by

$$z^* = \frac{z}{L}. \quad (24)$$

The dimensionless local velocity in the flow direction w^* is defined by

$$w^* = \frac{w}{w_m}. \quad (25)$$

The dimensionless local temperature T^* is defined by

$$T^* = \frac{T - T_{m,i}}{\Delta T_m}, \quad (26)$$

where ΔT_m is the difference between the mean temperatures at outlet ($T_{m,o}$) and at inlet ($T_{m,i}$) of tubes.

4 NUMERICAL SOLUTION AND MESH INDEPENDENCE TEST

In the commercial software Ansys CFX-12, which was used to analyze the problem, the differential equations, Eqs. (1-5), were discretized and numerically solved for each point at the computational domain.

As a boundary condition to hydrodynamic problem, at the exits of all tubes a static pressure of 0 Pa was taken. At the entry of tubes a temperature of 293.15 K was taken and the velocity was computed according to the value of Reynolds number used in simulation. The temperature and the entry velocity were used as their initial field. The boundary condition on

the walls is with no slip and with a constant heat flux. The mesh used was hexahedral, with refinement next to the walls and also in the inlet and outlet sections of tubes. The error stability criterion used, for which the solution is taken as convergent, was 1×10^{-6} .

The determination of the number of elements for the meshes was made by analysis of Po and Nu . This analysis was performed for the case of flow with $Re = 800$, which provides the greatest thermal entrance length.

Table 2 shows the results of analysis for Po and Nu , and their respective numerical errors ε , for different meshes, for the Microchannel 1.

Mesh	Number of Elements	Po [-]	ε_{Po} [%]	Nu [-]	ε_{Nu} [%]
1	8,932	57.882491	0.612708	3.247690	5.069233
2	82,128	57.617176	0.151531	3.122779	1.028114
3	341,138	57.572184	0.073326	3.093280	0.073763
4	514,598	57.536471	0.011248	3.093279	0.073730
5	1,062,708	57.526555	0.005988	3.088316	0.086833
6	1,707,198	57.521075	0.015514	3.087702	0.106697
7	2,721,708	57.517642	0.021482	3.086934	0.131543

Table 2: Number of elements, Po , Nu and their respective numerical errors ε , for the Microchannel 1.

According with Table 2, the error analysis for Poiseuille number ε_{Po} shows that the result obtained by mesh 5 presented good agreement related to the theoretically provided value, $Po_t = 57.53$ [49], for tubes of rectangular cross-section with $AR = 0.8$. The error analysis for the local Nusselt number ε_{Nu} shows that the results obtained by meshes 3 and 4 presented the best accordance with the theoretical provided value, $Nu_t = 3.091$ [49], for tubes with rectangular cross-section with $AR = 0.8$. However, the analysis of ε_{Nu} for mesh 5 shows that the Nu of this mesh presented good agreement also with $Nu_t = 3.091$, when compared to the results obtained by other meshes. Thus, the refinement applied to mesh 5 was considered appropriate for this study (with $Po = 57.53$ and $Nu = 3.09$). The same was also applied to the Microchannel 2.

Table 3 shows the results of analysis for Po and Nu , and their respective numerical errors ε , for different meshes, for the Microchannel 3.

Mesh	Number of Elements	Po [-]	ε_{Po} [%]	Nu [-]	ε_{Nu} [%]
1	3,528	57.048818	0.836401	3.538608	14.481009
2	26,448	55.658113	3.253758	3.538455	14.476060
3	225,498	55.206327	4.039063	3.303791	6.884212
4	1,133,808	55.128093	4.175051	3.291820	6.496927
5	2,008,908	55.132183	4.167942	3.288696	6.395859
6	2,784,078	55.103206	4.218310	3.288623	6.393497
7	3,431,538	55.102080	4.220267	3.288478	6.388806

Table 3: Number of elements, Po , Nu and their respective numerical errors ε , for the Microchannel 3.

According with Table 3, the analysis of ε_{Po} shows that the results obtained by meshes from 4 to 7 didn't show very significant change related to the ones obtained by meshes from 1 to 3. The analysis of ε_{Nu} shows that the results obtained by meshes from 5 to 7 are almost independent of the refinement applied to them. Thus, the refinement applied to mesh 5 was considered appropriate for this study (with $Po = 55.13$ and $Nu = 3.29$).

As the analysis of ε_{Po} and ε_{Nu} for the Microchannel 3 was performed based on the theoretical values of Po_t e Nu_t concerning to the Microchannel 1, ε_{Po} is low for the mesh 1. It occurs because the Po of this mesh, which presents the lowest number of elements, is nearer Po_t concerning to the Microchannel 1. From mesh 2, Po is reduced as the refinement applied is increased until it reaches a value according to the imperfection at geometry of the cross-section of this tube.

Figure 3 shows an aspect of cross-section of the meshes selected to represent the microchannels of this study.

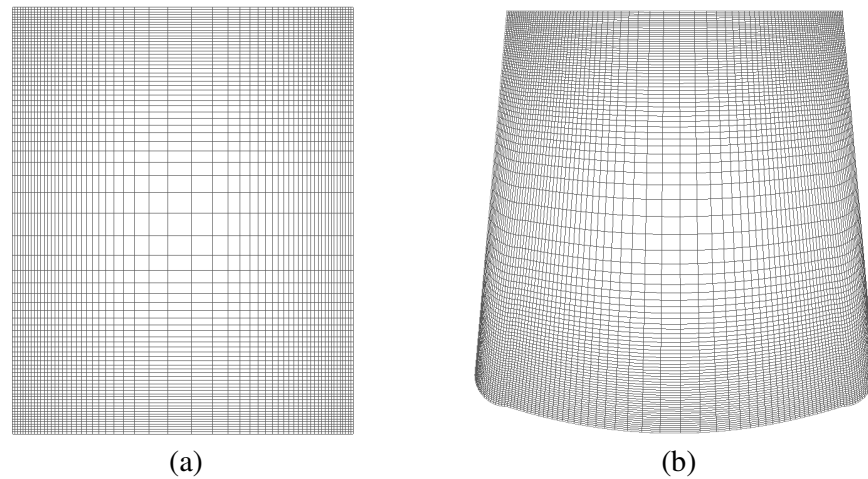


Figure 3: Cross-section of the meshes selected to represent the Microchannels (a) 1, 2 and (b) 3.

Figure 3(a) shows the cross-section of meshes selected to represent the Microchannels 1 and 2, whereas the Figure 3(b) shows the cross-section of the mesh selected to represent the Microchannel 3. In both meshes, it can be noticed the high level of refinement applied on the wall of Microchannels to ensure the correct development of hydrodynamic and thermal boundary layers.

5 PROCEDURE ADOPTED

First, the thermophysical properties of water (ρ , μ , k , c_p and Pr) were based on the mean temperature of entrance of water ($T_{m,i}$) defined in numerical model, for the Reynolds number Re considered. Afterwards, the mean temperature of water in the outlet ($T_{m,o}$) of Microchannel 1 was determined by mean temperature difference ΔT_m between the mean temperatures in the ends of this tube, which was obtained by integration of mean temperature gradient, Eq. (19), along the full length L of the tube. Thereby, all thermophysical properties of water were evaluated based on the mean temperature of reference \bar{T} given by arithmetic average between the mean temperatures of water at inlet ($T_{m,i}$) and at outlet ($T_{m,o}$) of the tube. This procedure was performed iteratively until \bar{T} didn't vary more significantly, assuming a convergence criterion of 0.1%. Then, the thermophysical properties of the fluid were considered constant and configured in the simulations, for both the Microchannel 1 and for the Microchannels 2 and 3.

The determination of Darcy friction factor f in region of hydrodynamically developed laminar flow, for the Microchannels, considered the drop pressure in this region, the length of this region ($L - L_{he}$) and the mass flow rate obtained from the simulations. The hydraulic diameter D_h and the cross-section area A_c used were the correspondents to the Microchannel 1.

Thus, according to Eq. (8), for the Microchannels 2 and 3 (imperfects), the deviations to Darcy friction factor f are due to changes in the drop pressure and mass flow rate, because of the imperfections in the cross-section area of the same ones. Therefore, the Poiseuille number Po is determined by Eq. (12) based on Darcy friction factor f obtained by Eq. (8).

The determination of local Nusselt number Nu in the region of thermally developed laminar flow ($L - L_{te}$), for all Microchannels, considered their local heat transfer coefficient h and the hydraulic diameter D_h of Microchannel 1. In the case of h , which is provided by Eq. (17), the surface temperature of microchannels T_s corresponds to average of the surface temperatures along the perimeter of the cross-section of the channels, at the axial position z considered. Therefore, the deviations for Nu at the imperfect microchannels are due to changes in h through the mean temperature T_m of the fluid in the cross-section and in the surface temperature T_s of these tubes, due to imperfections at the cross-section of these tubes.

6 RESULTS AND DISCUSSIONS

This section shows the results for Poiseuille Po and local Nusselt Nu numbers for the microchannels considered.

First, it is presented an analysis of the velocity and temperature profiles, in dimensionless form, for some dimensionless axial positions taken in the central plane of the channels (with $x = y = 0$), in the hydrodynamically and thermally developed flow, with $Re = 200$. The results related to the geometric, hydrodynamic and thermal quantities of flow in the tubes analysed are shown in table³.

Subsequently, the results to Poiseuille Po and local Nusselt Nu numbers are shown, as well as deviations ε for the same ones, through graphics.

6.1 Velocity and Temperature Profiles

Figure 4 shows the velocity and temperature profiles for the Microchannels considered in the flow with $Re = 200$. For $z^* \cong 0.36, 0.63, 0.90$, Figure 4(a) shows the velocity profile, whereas Figures 4(b-d) show the temperature profile.

³ The quantities determined in the region of hydrodynamically and thermally developed flow are indicated respectively by hd and td subscripts. However, some of these quantities were determined for the full length of tubes, including the hydrodynamic and thermal entrance effects. In this case, these quantities are indicated by their apparent value (subscript *app*), as occurs in some studies [21].

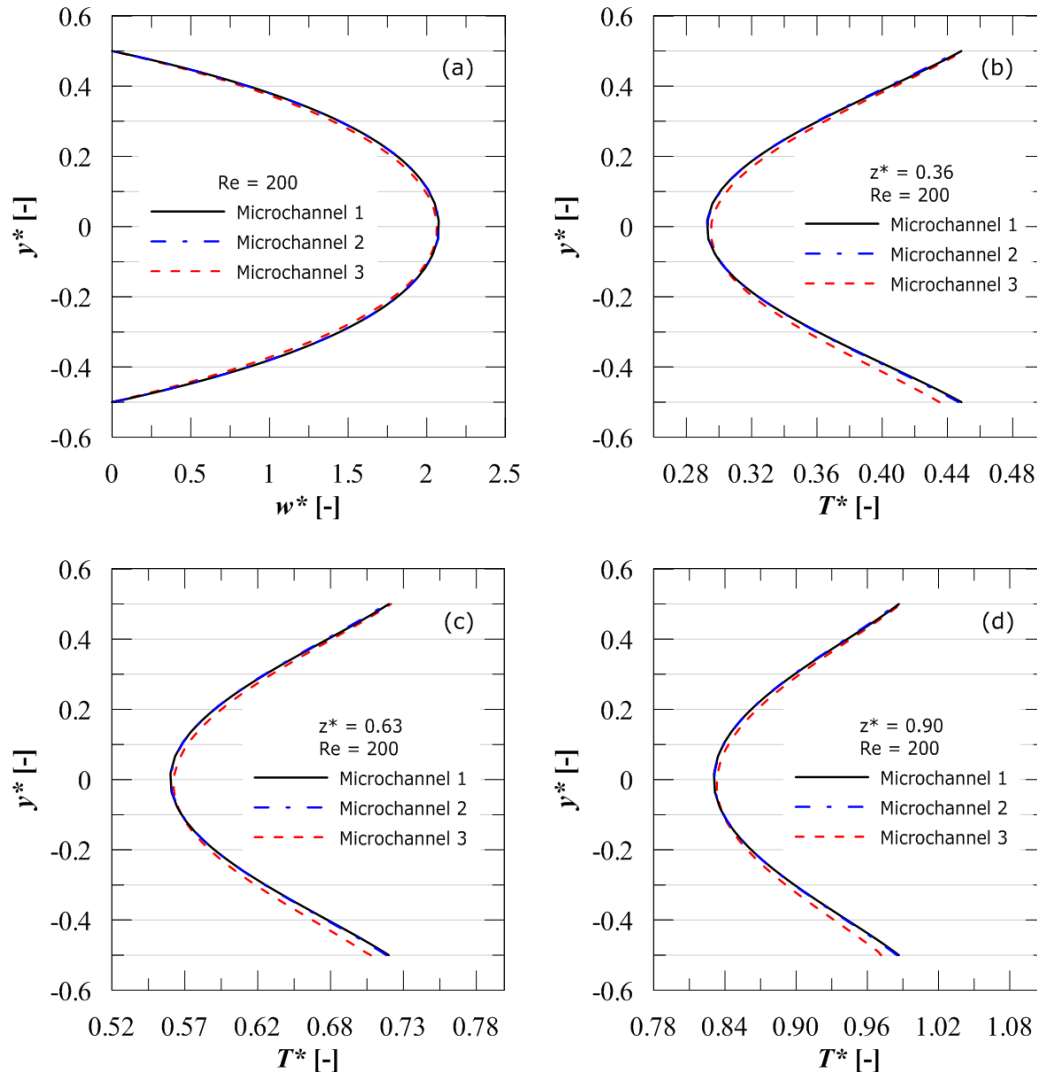


Figure 4: Microchannels with $Re = 200$ and $q_s'' = 2 \text{ kW/m}^2$: Profiles of (a) velocity and (b-d) temperature in the central plane of the channels (with $x = y = 0$).

Figure 4(a) shows that the velocity profile for the Microchannel 2 is equal to the Microchannel 1, since its η was only -0.26% , according to Table 1. The velocity profile of Microchannel 3 is slightly closed, since its η was of $+4.91\%$. It indicates that the mean velocity w_m in Microchannel 3 is lower than in Microchannels 1 and 2.

According to the temperature profiles in Figures 4(b-d), it is clear that they are perfectly symmetrical and basically identical for the Microchannels 1 and 2, and for similar reasons to those mentioned for the velocity profile in these tubes. However, it is observed that the temperature profiles of the Microchannel 3 are slightly distorted. They show that temperatures in the upper half of the cross-section of this tube are higher compared to ones in the lower half of its cross-section.

As shown in Figure 1(b) and in Figure 2, the irregularity of the perimeter of the cross-section of the Microchannel 3 shows a larger distribution of area in the lower half of the cross-section of this tube and reduced at the top of the channel. Thus, there is a greater amount of fluid flowing on the lower half of the cross-section of this tube. Hence, the fluid

heating should be lower in this region than in the upper half of the cross-section of this tube. Therefore, the fluid temperature in the lower half of the cross-section of this tube tends to be lower than in its upper half, as shown in temperature profiles of Figures 4(b-d).

Particularly, Figure 5 shows the velocity and temperature contours in the cross-section of the Microchannels 1 and 3⁴ for $z^* \cong 0.36$, in the flow with $Re = 200$. Figures 5(a-b) show the velocity contours for the Microchannels 1 and 3, respectively, whereas Figures 5(c-d) show the temperature contours for the Microchannels 1 and 3, respectively.

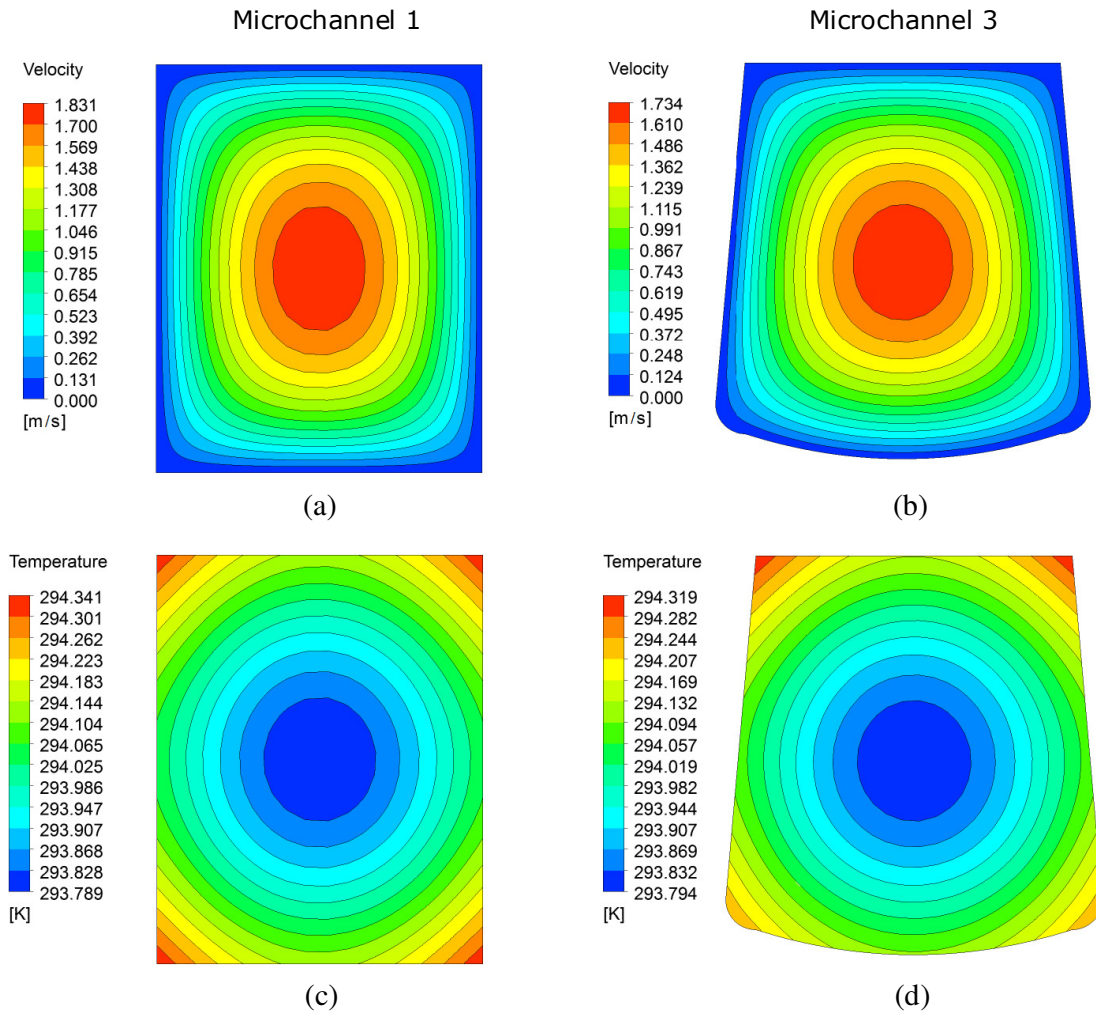


Figure 5: Contours of (a-b) velocity and (c-d) temperature in the cross-section of the Microchannels 1 and 3, respectively, in $z^* = 0.36$ with $Re = 200$.

As shown by velocity columns in Figures 5(a-b), the maximum velocity in Microchannel 3 is lower than in the Microchannel 1, as analyzed in the velocity profiles of Figure 4(a). Also, it can be seen clearly, as shown in Figure 5(d), that the temperatures at the upper half of the cross-section of the Microchannel 3 are higher compared to those in the lower half of its cross-section, as indicated in the analysis of temperature profiles of the Figures 4(b-d). As

⁴ As the temperature and velocity profiles for Microchannel 1 and 2 are similar, as shown in Figure 4, it was decided to show only the velocity and temperature contours for the Microchannels 1 and 3 in order to make it easy to compare.

shown in Figure 5(d), the temperatures at the upper corners of the cross-section of the Microchannel 3 are higher compared to those in the lower corners of the cross-section of this channel. In the case of the Microchannel 1, the temperatures at its four corners of the cross-section are equal, as expected, according to Figure 5(c).

Table 4 shows the results concerning to the geometric, hydrodynamic and thermal quantities for the tubes considered in the flow with $Re = 200$.

Data	Microchannels		
	1	2	3
η [%]	0	-0.26	+4.91
w_m [m/s]	0.8802	0.8825	0.8391
D_h [μm]	222.22	221.64	233.14
Per [μm]	900.00	896.00	870.95
A_s [$\times 10^6 \mu\text{m}^2$]	200.70	199.81	194.22
A_c [$\times 10^3 \mu\text{m}^2$]	50.00	49.65	50.76
$(dp/dz)_{(hd)}$ [kPa/m]	500.37	503.56	448.95
$P_{hyd(app)}$ [mW]	4.93	4.94	4.28
$\Delta p_{(app)}$ [kPa]	112.05	112.76	100.52
Q [$\times 10^{-8} \text{m}^3/\text{s}$]	4.40	4.38	4.26
\dot{m} [$\times 10^{-5} \text{kg/s}$]	4.39	4.37	4.25
$R_{hyd(app)}$ [$\times 10^{12} \text{Pa s/m}^3$]	2.55	2.57	2.36
$\tau_{(hd)}$ [Pa]	27.78	27.88	26.15
$f_{(hd)}$ [-]	0.2876	0.2921	0.2755
dT_m/dz [K/m]	9.80	9.80	9.80
ΔT_m [K]	2.19	2.19	2.19
q_{conv} [mW]	401.40	399.62	388.51
$(T_s - T_m)_{(td)}$ [K]	0.25	0.24	0.23
$h(z)_{(td)}$ [$\text{kW/m}^2 \text{K}$]	8.16	8.19	8.70
$R_{ct}(z)_{(td)}$ [$\times 10^{-4} \text{m}^2 \text{K/W}$]	1.23	1.22	1.15

Table 4: Microchannels with $Re = 200$ and $q_s'' = 2 \text{ kW/m}^2$. Geometric, hydrodynamic and thermal quantities.

According to Table 4, the differences among the results obtained for the Microchannel 2 and the ones corresponding to the Microchannel 1 are minimal, as noted previously in Figure 4. As the cross-section area A_c of this tube is slightly smaller in relation to the one of Microchannel 1, there is a slight increase to the mean velocity of flow w_m , pressure gradient dp/dz , hydrodynamic power P_{hyd} , drop pressure Δp , hydrodynamic resistance R_{hyd} , shear stress τ and Darcy friction factor f , and a slight reduction to the mass flow rate \dot{m} and volumetric flow rate Q in this tube. Then, the Poiseuille number Po in the Microchannel 2 should be slightly higher in relation to that one in Microchannel 1. As the convection thermal resistance R_{ct} in the Microchannel 2 is slightly lower than in the Microchannel 1, there is a small improvement in the heat transfer conditions to the fluid, as noted by analysis of the local heat transfer coefficient h , the difference between the surface and mean temperatures $(T_s - T_m)$ and the total convection heat transfer rate q_{conv} for the same one, relatively to Microchannel 1. So, the local Nusselt number Nu in Microchannel 2 should be a little higher in relation to the one in Microchannel 1.

Regarding to the Microchannel 3, the differences observed in the geometric, thermal and hydrodynamic results are more significant, compared to the ones corresponding to the Micro-

channel 1. As the A_c of the Microchannel 3 is somewhat larger in relation to the Microchannel 1, w_m , dp/dz , P_{hyd} , Δp , R_{hyd} , τ and f are somewhat smaller in the same one, compared to the ones of Microchannel 1. Therefore, the same must occur to Po . Furthermore, Table 4 shows that \dot{m} and Q are lower in the Microchannel 3, although the A_c of the same one is larger than the one of Microchannel 1. In relation to heat transfer to the flow, the influence of the irregularity of the shape of the cross-section of the Microchannel 3, according to analysis of the temperature profiles in Figures 4(b-d), are quite noticeable too.

Table 4 indicates that h in the Microchannel 3 is higher in relation to the one of Microchannel 1. It is because the perimeter Per of the Microchannel 3 is smaller in comparison to the one of the Microchannels 1 and 2, as observed in Tables 1 and 4. Thereby, q_{conv} to the fluid is lower in Microchannel 3. Therefore, h is greater in Microchannel 3 in relation to that one in Microchannel 1. Consequently, the same should occur in relation to Nu .

The issue of heat transfer in Microchannel 3 is quite interesting. According to Table 5, the Microchannel 3, with $\eta > 0$, shows a higher h with lowest w_m , in relation to the Microchannels 1 and 2, although it shows the lowest q_{conv} of the channels considered. However, the A_c of the Microchannel 3 is larger compared to the one of Microchannel 1, which is not the case to Per and A_s of the same one. Then, the Microchannel 3 shows smaller q_{conv} even flowing a greater amount of fluid, compared to the other tubes. This is probably related to the irregular shape of the perimeter of the cross-section of this microchannel, which it is shown more influential in the process of heat transfer to the flow.

According to Table 4, it is noticed that dT_m/dz and ΔT_m are equal for all microchannels. By combining the Eqs. (6; 11; 13; 19), it is shown that the mean temperature gradient is defined by

$$\frac{dT_m}{dz} = \frac{\Delta T_m}{L} = \frac{4q_s''}{\mu Re c_p}, \quad (27)$$

which is constant for all microchannels, occurring the same to ΔT_m in these tubes.

6.2 Poiseuille Number

Figure 6 shows the results of Po according to Re for the tubes considered.

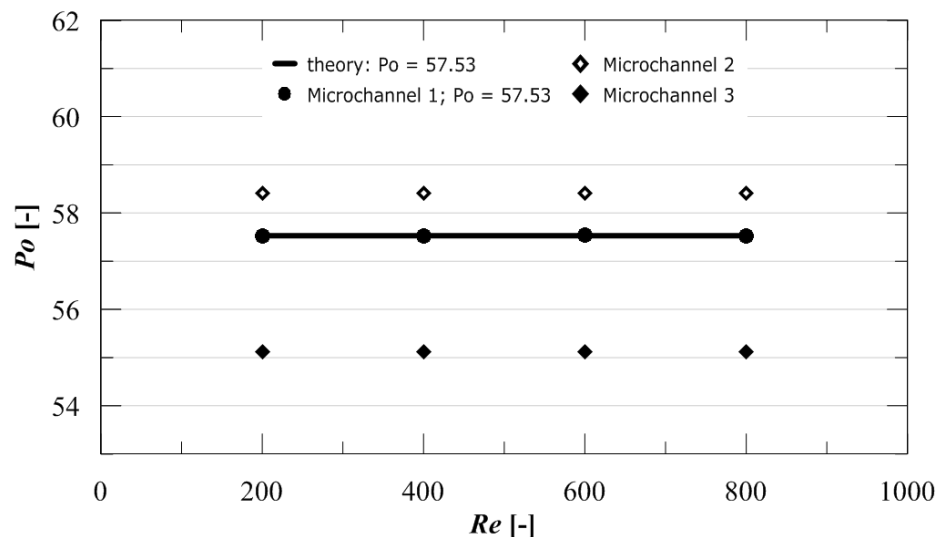


Figure 6: Poiseuille number vs. Reynolds number.

Figure 6 shows that Po in the Microchannel 2 exceeds slightly Po_t , whereas that it is considerably lower of Po_t in the Microchannel 3, as indicated previously, in the analysis of the Table 4.

Figure 7 shows the results of ε_{Po} according to Re for the tubes considered.

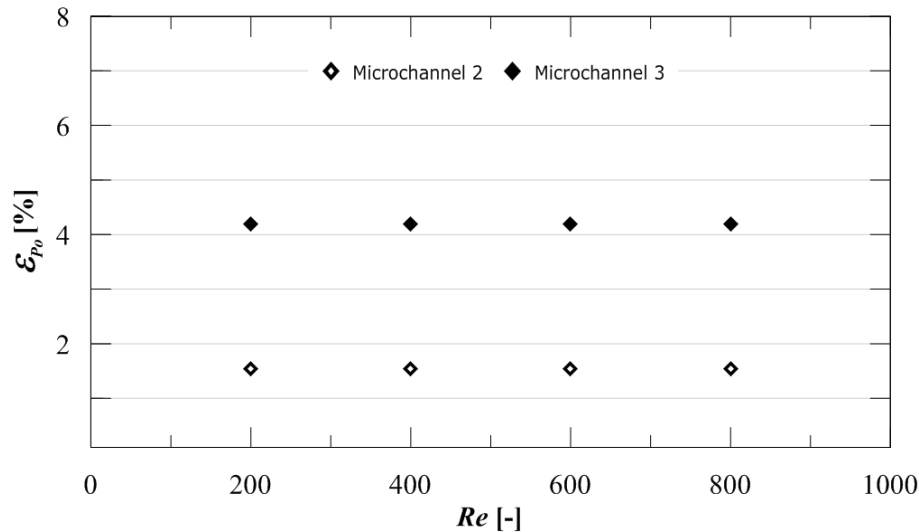


Figure 7: Deviation of Poiseuille number vs. Reynolds number.

Figure 7 shows that the results for ε_{Po} in the imperfect tubes were somewhat higher for the Microchannel 3, compared to the ones of the Microchannel 2, as expected.

The determination of f takes into account that the A_c of imperfect tubes is the same of the Microchannel 1. Considering the actual value of the A_c of the Microchannel 3 in Eq. (8), it is obtained ε_{Po} of about 1.25%. Taking into account also the real value of D_h of Microchannel 3 in Eq. (8), the ε_{Po} obtained for the same one increases to approximately 3.58%. However, if the Microchannel 3 is compared to a tube with perfect trapezoidal cross-section, such as that suggested by red lines in Figure 2, the results for Po can be in better agreement in this case, because for the hydrodynamically developed laminar flow in a tube with perfect trapezoidal cross-section, $Po_t = 58$ [49]. In this case, the result obtained for ε_{Po} in the Microchannel 3, considering its real A_c and D_h , comes to be approximately 2.75%, in relation to Po_t of the tube with perfect trapezoidal cross-section. As pointed out by Steinke and Kandlikar [21], this strengthens the fact that knowledge about the actual geometric shape of the cross-section of the tubes, as its width, height, Per and A_c , is very important for the correct determination of the hydrodynamic parameters of flow, as f and Po , at experimental level.

6.3 Nusselt Number

Figure 8 shows the results of Nu according to Re for the tubes considered.

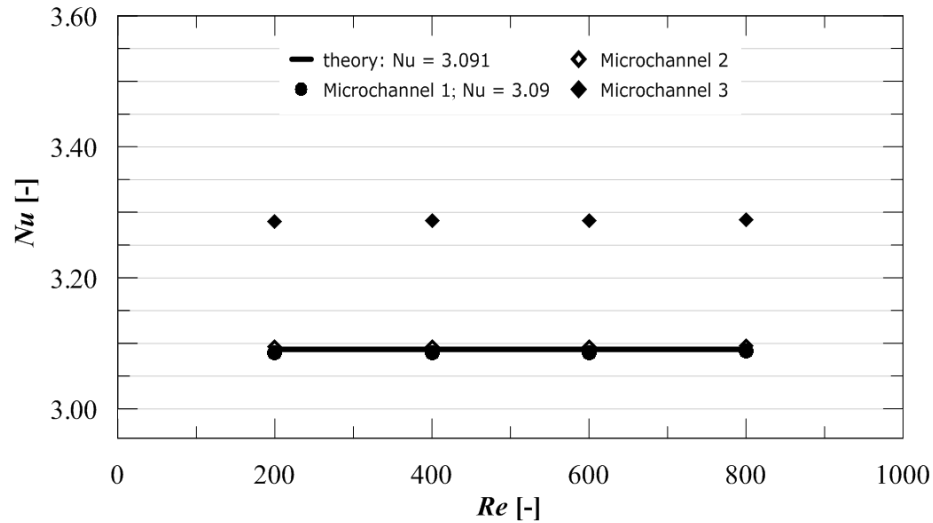


Figure 8: local Nusselt number vs. Reynolds number.

Figure 8 shows that Nu in the Microchannel 3 exceeds Nu_i , whereas that the same one is shown in perfect agreement to the Microchannel 2, as indicated previously, in the analysis of Table 4. The case of the Microchannel 3 indicates that Nu is more sensitive to the geometric shape of the cross-section of the microchannels, according to the reports of Croce and D'Agaro [45].

As the cross-section of the Microchannel 2 is the same nature (rectangular) as the cross-section of the Microchannel 1, and taking into account that their dimensions differed little from those of the Microchannel 1, Nu for the Microchannel 2 was in good agreement with the theoretical and numerical values corresponding to the Microchannel 1. However, the same didn't occur for Microchannel 3, since the cross-section of it is of trapezoidal nature. Thus, $Nu = 3.29$ for Microchannel 3 was in considerable disagreement with the theoretical and numerical values corresponding to the Microchannel 1, according to Figure 4. Even if the Microchannel 3 had been compared with a tube of perfect trapezoidal cross-section, as the ideal trapezoid indicated by red lines in Figure 2, the results for Nu may still not be in better agreement between themselves.

For thermally developed laminar flow in perfect trapezoid, indicated by red lines in Figure 2, assuming a length of 0.223 m for it and considering the thermal condition of constant heat flux applied on its surface, as in the tubes of this study, it is obtained that $Nu_i = 3.05$ [49], which is lower than the $Nu_i = 3.091$ of the Microchannel 1 with rectangular cross-section. Thus, $Nu = 3.29$ to the Microchannel 3 is still more discordant compared to $Nu_i = 3.05$ of the perfect trapezoid. However, this can be expected, since the perfect trapezoid has the highest Per and the highest A_s of the four tubes considered and, thus, the lowest Nu among these tubes. Therefore, the geometric shape of the cross-section is shown most influential in the process of heat transfer to the flow, as pointed out by Croce and D'Agaro [45].

Figure 9 shows the results of ε_{Nu} according to Re for the tubes considered.

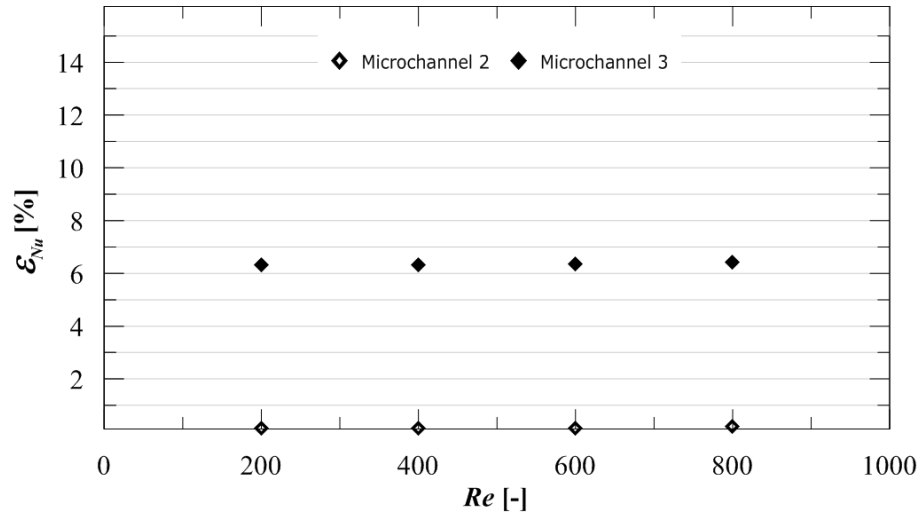


Figure 9: Deviation of local Nusselt number vs. Reynolds number.

As shown in Figure 9, the results for ϵ_{Nu} in Microchannel 2 are basically zero, whereas for the Microchannel 3 they are quite higher, as indicated in the analysis of Table 4.

7 CONCLUSIONS

The aim of this numerical study was to analyze how the hydrodynamic and heat transfer characteristics for the single-phase laminar flow in microscale, of a fluid with constant thermophysical properties, can be influenced by imperfections at the geometry of the microchannels, especially with respect to the cross-section of the same ones. For this purpose, all other scaling effects, such as surface roughness and viscous dissipation, for example, were omitted in the numerical model. It seeks to isolate and highlight the effects related only to the imperfections at the cross-section of microchannels on the hydrodynamic and thermal parameters of flow, as it is the case for Poiseuille and local Nusselt numbers, respectively. Although the simplifications considered in numerical model may overestimate the results founded, this study provided some general indications about the relative impacts to the imperfections at the cross-section on Poiseuille and Nusselt numbers in microchannels:

- The error at Poiseuille number can be reduced considering the real value of cross-section area of the microchannels, as pointed out in some experimental studies [21].
- The results of this study indicated that Nusselt number is more sensitive to shape of the cross-section of the microchannels, as pointed out in others numerical studies [45].

However, direct comparisons among experimental results and numerical results obtained in this study are not adequate. This is due to the experimental uncertainty present in the experimental data and the natural superposition of several different physical effects (of scaling), which were omitted in numerical model considered for this study, as well as other simplifications adopted for the same one.

Thus, more systematic numerical studies may be developed. Therefore, other models of imperfections at the cross-section of the microchannels should be considered.

8 ACKNOWLEDGMENTS

The authors acknowledge the Conselho Nacional de Desenvolvimento Científico e Tecnológico (CNPq) and Universidade do Vale do Rio dos Sinos (UNISINOS) for financial support for this work.

REFERENCES

- [1] G.P. Celata, M. Cumo, G. Zummo, Thermal-hydraulic characteristics of single-phase flow in capillary pipes. *Experimental Thermal and Fluid Science*, **28**, 87–95, 2004.
- [2] G.P. Celata, M. Cumo, V. Marconi, S.J. McPhail, G. Zummo, Microtube liquid single-phase heat transfer in laminar flow. *International Journal of Heat and Mass Transfer*, **49**, 3538–3546, 2006.
- [3] P. Tabeling, Introduction to Microfluidics. *New York: Oxford University Press*, 2005.
- [4] P. Rosa, T.G. Karayiannis, M.W. Collins, Single-phase heat transfer in microchannels: The importance of scaling effects. *Applied Thermal Engineering*, **29**, 3447–3468, 2009.
- [5] H.C. Chiu, J.H. Jang, H.W. Yeh, M.S. Wu, The heat transfer characteristics of liquid cooling heatsink containing microchannels. *International Journal of Heat and Mass Transfer*, **54**, 34–42, 2011.
- [6] P.Y. Wu, W.A. Little, Measurement of heat transfer characteristics of gas flow in fine channel heat exchangers used for microminiature refrigerators. *Cryogenics*, **24**, 415–420, 1984.
- [7] J. Pfahler, J. Harley, H. Bau, J. Zemel, Liquid Transport in Micron and Submicron Channels. *Sensors and Actuators A: Physical*, **22**, 431–434, 1990.
- [8] J. Pfahler, J. Harley, H. Bau, J. Zemel, Gas and Liquid Flow in Small Channels. *Micro-mechanical Sensors, Actuators, and Systems*, *ASME*, **32**, 49–60, 1991.
- [9] S.B. Choi, R.F. Barron, R.O. Warrington, Fluid Flow and Heat Transfer in Microtubes. *Micromechanical Sensors, Actuators, and Systems*, *ASME*, **32**, 123–134, 1991.
- [10] D. Yu, R. Warrington, R. Barron, T. Ameer, An experimental and theoretical investigation of fluid flow and heat transfer in microtubes. *In: Proceedings of ASME/JSME Thermal Engineering Conference*, **1**, 523–530, 1995.
- [11] D. Pfund, D. Rector, A. Shekarriz, A. Popescu, J.R. Welty, Pressure Drop Measurements in a Microchannel. *AIChE Journal*, **46**, 1496–1507, 2000.
- [12] G.M. Mala, D. Li, Flow characteristics of water in microtubes. *International Journal of Heat and Fluid Flow*, **20**, 142–148, 1999.
- [13] B. Xu, K.T. Ooi, N.T. Wong, W.K. Choi, Experimental investigation of flow friction for liquid flow in microchannels. *International Communications in Heat and Mass Transfer*, **27**, 1165–1176, 2000.
- [14] Z.X. Li, D.X. Du, Z.Y. Guo, Experimental study on flow characteristics of liquid in circular microtubes. *In: Proceedings of the International Conference on Heat Transfer and Transport Phenomena in Microscale*, Banff, Canada, October 15-20, 2000.

- [15] G. Tunc, Y. Bayazitoglu, Heat transfer in microtubes with viscous dissipation. *International Journal of Heat and Mass Transfer*, **44**, 2395–2403, 2001.
- [16] J. Judy, D. Maynes, B.W. Webb, Characterization of frictional pressure drop for liquid flows through Microchannels. *International Journal of Heat and Mass Transfer*, **45**, 3477–3489, 2002.
- [17] H.Y. Wu, P. Cheng, An Experimental Study of Convective Heat Transfer in Silicon Microchannels with Different Surface Conditions. *International Journal of Heat and Mass Transfer*, **46**, 2547–2556, 2003.
- [18] G.P. Celata, M. Cumo, M. Guglielmi, G. Zummo, Experimental Investigation of Hydraulic and Single-Phase Heat Transfer in 0.130 mm Capillary Tube. *Microscale Thermophysical Engineering*, **6**, 85–97, 2002.
- [19] G.P. Celata, M. Cumo, S.J. McPhail, G. Zummo, Characterization of fluid dynamic behaviour and channel wall effects in microtube. *International Journal of Heat and Fluid Flow*, **27**, 135–143, 2006.
- [20] G.P. Celata, G.L. Morini, V. Marconi, S.J. McPhail, G. Zummo, Using viscous heating to determine the friction factor in microchannels – An experimental validation. *Experimental Thermal and Fluid Science*, **30**, 725–731, 2006.
- [21] M.E. Steinke, S.G. Kandlikar, Single-phase liquid friction factors in microchannels. *International Journal of Thermal Sciences*, **45**, 1073–1083, 2006.
- [22] G.M. Mala, D. Li, J.D. Dale, Heat transfer and fluid flow in microchannels. *International Journal of Heat and Mass Transfer*, **40**, 3079–3088, 1997.
- [23] C. Yang, D. Li, J.H. Masliyah, Modeling forced liquid convection in rectangular microchannels with electrokinetic effects. *International Journal of Heat and Mass Transfer*, **41**, 4229–4249, 1998.
- [24] C.P. Tso, S.P. Mahulikar, The use of the Brinkman number for single phase forced convective heat transfer in microchannels. *International Journal of Heat and Mass Transfer*, **41**, 1759–1769, 1998.
- [25] K.C. Toh, X.Y. Chen, J.C. Chai, Numerical computation of fluid flow and heat transfer in microchannels. *International Journal of Heat and Mass Transfer*, **45**, 5133–5141, 2002.
- [26] J. Koo, C. Kleinstreuer, Viscous dissipation effects in microtubes and Microchannels. *International Journal of Heat and Mass Transfer*, **47**, 3159–3169, 2004.
- [27] J. Koo, C. Kleinstreuer, Analysis of surface roughness effects on heat transfer in microconduits. *International Journal of Heat and Mass Transfer*, **48**, 2625–2634, 2005.
- [28] G. Gamrat, M. Favre-Marinet, D. Asendrych, Conduction and entrance effects on laminar liquid flow and heat transfer in rectangular Microchannels. *International Journal of Heat and Mass Transfer*, **48**, 2943–2954, 2005.
- [29] P.S. Lee, S.V. Garimella, D. Liu, Investigation of heat transfer in rectangular microchannels. *International Journal of Heat and Mass Transfer*, **48**, 1688–1704, 2005.
- [30] T.Y. Lin, C.Y. Yang, Measurement of micro-tube surface temperature by the method of liquid crystal thermograph. In: *6th World Conference on Experimental Heat Transfer, Fluid Mechanics, and Thermodynamics*, Matsushima, Japan, April 17-21, 2005.

- [31] C.Y. Yang, T.Y. Lin, Heat transfer characteristics of water flow in microtubes. *Experimental Thermal and Fluid Science*, **32**, 432–439, 2007.
- [32] T.Y. Lin, C.Y. Yang, S.G. Kandlikar, Measurement of heat transfer in the entrance region of small diameter tubes. In: *Proceedings of the ASME 2009, 7th International Conference on Nanochannels, Microchannels and Minichannels*, Pohang, South Korea, June 22-24, 2009.
- [33] C.Y. Yang, C.W. Chen, T.Y. Lin, S.G. Kandlikar, Heat transfer and friction characteristics of air flow in microtubes. *Experimental Thermal and Fluid Science*, **37**, 12–18, 2012.
- [34] X.F. Peng, B.X. Wang, Forced convection and flow boiling heat transfer for liquid flowing through microchannels. *International Journal of Heat and Mass Transfer*, **36**, 3421–3427, 1993.
- [35] B.X. Wang, X.F. Peng, Experimental investigation on liquid forced-convection heat transfer through microchannels. *International Journal of Heat and Mass Transfer*, **37**, 73–82, 1994.
- [36] X.F. Peng, B.X. Wang, G.P. Peterson, H.B. Ma, Experimental investigation of heat transfer in flat plates with rectangular microchannels. *International Journal of Heat and Mass Transfer*, **38**, 127–137, 1995.
- [37] G. Maranzana, I. Perry, D. Maillet, Mini- and micro-channels: influence of axial conduction in the walls. *International Journal of Heat and Mass Transfer*, **47**, 3993–4004, 2004.
- [38] I. Tiselj, G. Hetsroni, B. Mavko, A. Mosyak, E. Pogrebnyak, Z. Segal, Effects of axial conduction on the heat transfer in micro-channels. *International Journal of Heat and Mass Transfer*, **47**, 2551–2565, 2004.
- [39] G.P. Celata, M. Cumo, S.J. McPhail, G. Zummo, Single-phase laminar and turbulent heat transfer in smooth and rough microtubes. *Microfluid Nanofluid*, **3**, 697–707, 2007.
- [40] D. Lelea, A.E. Cioabla, The viscous dissipation effect on heat transfer and fluid flow in micro-tubes. *International Communications in Heat and Mass Transfer*, **37**, 1208–1214, 2010.
- [41] G.L. Morini, Viscous heating in liquid flows in micro-channels. *International Journal of Heat and Mass Transfer*, **48**, 3637–3647, 2005.
- [42] P.L. Young, S.G. Kandlikar, Surface roughness effects on heat transfer in microscale single phase. In: *Proceedings of the Sixth International ASME Conference on Nanochannels, Microchannels and Minichannels*, Darmstadt, Germany, June 23-25, 2008.
- [43] C.H. Chen, Forced convection heat transfer in microchannel heat sinks. *International Journal of Heat and Mass Transfer*, **50**, 2182–2189, 2007.
- [44] G. Hetsroni, A. Mosyak, E. Pogrebnyak, L.P. Yarin, Heat transfer in microchannels: Comparison of experiments with theory and numerical results. *International Journal of Heat and Mass Transfer*, **48**, 5580–5601, 2005.
- [45] G. Croce, P. D'agaro, Numerical analysis of roughness effect on microtube heat transfer. *Superlattices and Microstructures*, **35**, 601–616, 2004.

- [46] G. Croce, P. D'agaro, C. Nonino, Three-dimensional roughness effect on microchannel heat transfer and pressure drop. *International Journal of Heat and Mass Transfer*, **50**, 5249–5259, 2007.
- [47] P.S. Lee, S.V. Garimella, Thermally developing flow and heat transfer in rectangular microchannels of different aspect ratios. *International Journal of Heat and Mass Transfer*, **49**, 3060–3067, 2006.
- [48] M.E. Steinke, S.G. Kandlikar, J.H. Magerlein, E.G. Colgan, A.D. Raisanen, Development of an Experimental Facility for Investigating Single-Phase Liquid Flow in Microchannels. *Heat Transfer Engineering*, **27**, 41–52, 2006.
- [49] R.K. Shah, A.L. London, Laminar flow forced convection in ducts: a source book for compact heat exchanger analytical data. *New York: Academic Press*, 1978.

NONLINEAR FRACTURE ANALYSIS OF CARBON NANOTUBES WITH STONE-WALES DEFECTS

Cengiz Baykasoglu¹, Esra Icer¹, Alper T. Celebi¹ and Ata Mugan¹

¹: Istanbul Technical University, Faculty of Mechanical Engineering, 34437, Istanbul, Turkey
e-mails: baykasoglu@itu.edu.tr, * icere@itu.edu.tr, celebial@itu.edu.tr, e-mail: mugan@itu.edu.tr

Keywords: Carbon Nanotubes, Stone–Wales defect, Fracture, Molecular Mechanics, Finite Element Method.

Abstract. *In this paper, a molecular mechanic based finite element model is employed to investigate the effects of Stone-Wales defects on mechanical properties of armchair and zigzag carbon nanotubes by considering large deformation and nonlinear geometric effects. Non-linear characteristic of the covalent bonds are obtained by using the modified Morse potential and effects of the large deformation and geometric nonlinearities are considered by updating the atomistic coordinates of the original nanotube structure at each load step. The results show that the fractures of all types of carbon nanotubes are brittle, but armchair nanotubes are stiffer than zigzag nanotubes and these defects significantly affect the mechanical performance of nanotubes. Fracture initiation and crack propagation direction issues are also studied. It is shown that the direction of crack propagation in armchair nanotube is in the maximum shear directions having an angle of $\pm 45^\circ$ along its circumference. Comparisons are made with the failure stress and strain results reported in literature that show good agreement with our results.*

1 INTRODUCTION

Carbon nanotubes (CNTs) have been extensively studied since their discovery in 1991 by Iijima due to their extraordinary mechanical, electronic and thermal properties [1,2]. The mass production of perfect CNTs is very challenging and experimental observations show that some defects such as Stone-Wales (SW or 5-7-7-5) and vacancy defects commonly exist in CNTs. These defects may be induced due to mechanical strain or may emerge during the growth and purification processing [3] and directly affects the mechanical behavior of CNTs [4]. Hence, prediction of mechanical behavior of CNTs having defects is very important and useful in the design of materials having nanotube structures.

Experimental measurements and computational simulations are commonly used to investigate the failure behavior of CNTs. Yu et al. [5] experimentally measured the tensile strength and failure strain of multi-walled carbon nanotubes (MWCNTs) and found 11–63 GPa for the failure strengths and 10–13% for the failure strains. These strain and stress values are significantly smaller than the computational simulation results in literature and these differences can be explained by the presence of defects and some slippage in the attachments which may occur at high-strain cases [6]. Quantum mechanics (QM), molecular dynamics (MD) and molecular mechanic (MM) simulations are widely used to determine the effects of SW defects on the mechanical properties of CNTs in literature [7-13]. Troya et al. [7] used QM methods and observed that SW defects cause a reduction in failure stress such as the reduction of (5,5) tube containing an aggregation of five SW defects range from 6.3% to 53.5%. Chandra et al. [8] studied the local elastic properties of CNTs in the presence of SW defects and observed the stiffness due to defects is reduced by about 30-50 % depending on chirality, tube diameters and loading conditions. Mielke et al. [9] used QM and MD methods and predicted that the presence of SW defects obviously reduce the fracture stress and strain values of CNTs. Belytschko et al. [10] investigated the fracture behavior of defected and non-defected CNTs and reported that the fracture is almost independent from the dissociation energy and depends primarily on the inflection point of the interatomic potential. The brittle fracture is observed and crack grow direction is found in the direction of maximum shear for a SW defected (40,40) armchair nanotube in [10]. Tserpes et al. [11] proposed an atomistic-based progressive fracture model and investigated the SW defects on fracture of SWCNTs by using commercial FE software. The reduction in failure stress and strain predicted ranging from 18 to 25 % and 30 to 41 %, respectively in [11]. Xiao et al. [12] developed an atomistic based finite bond element model for the prediction of fracture behavior SWCNTs and the reduction in failure stress is predicted ranging from 12 to 32 % in the presence of SW defects. Xiao et al. [13] also studied the tensile behaviors of carbon nanotubes with multiple Stone-Wales defects. We investigated nonlinear fracture behavior of vacancy and SW defected single layer graphene sheets (SLGSs) in [14] and developed coupled molecular/continuum mechanical model for SLGSs to enable solving large scale static and fracture problems of SLGSs [15].

In this paper, a molecular mechanic based finite element models are developed to investigate the effects of SW defects in mechanical properties of armchair and zigzag carbon nanotubes. Although progressive fractures of SLCNTs are studied earlier, they are obtained without consideration of geometric nonlinear effects. However, the fracture occurs at relatively large strain values; hence, large deformation effects and geometric nonlinearities have to be considered. The effects of large deformation and geometric nonlinearities are considered by using the modified Morse potential and updating the atomistic coordinates of the original nanotube structure at each load step. The results show that the fractures of all types of carbon nanotubes are brittle and SW defects negatively affect the mechanical performance of the

nanotubes. Comparisons are made with the failure stress and strain results reported in literature which show parallelism with our results.

2 NONLINEAR PROGRESSIVE FRACTURE MODEL OF SWCNTs

2.1 FE formulation of the covalent bonds

When CNTs are subjected to external forces, positions of the atomic nuclei are controlled by the covalent bonds between the C-C atoms. Hence, the deformation pattern of CNTs is very similar to the deformation of frame structures. To this end, C-C bond behavior is simulated by using the Euler-Bernoulli (EB) beam element formulation [16]. The EB beam element parameters are obtained by using harmonic expressions for potential energy terms [17, 18]. The non-linear characteristics of EB beam elements are obtained by using the modified Morse potential. We coded our own SWCNT FE models by using Matlab[®] and large deformation and nonlinear geometric effects are taken into account. At each load step, initial displacement is applied incrementally on SWCNTs and atomistic coordinates of the original SWCNT structures are updated. According to the modified Morse potential, the potential energy can be expressed as

$$U_{total} = \Sigma U_r + \Sigma U_\theta \quad (1)$$

$$U_r = D_e \left\{ \left[1 - e^{-\beta(r-r_0)} \right]^2 - 1 \right\} \quad (2)$$

$$U_\theta = \frac{1}{2} k_\theta (\theta - \theta_0)^2 + [1 + k_{sextic} (\theta - \theta_0)^4] \quad (3)$$

where U_r is the bond energy due to bond stretching, U_θ is the bond energy due to angle bending, and r and θ are respectively the current bond length and current angle between the adjacent bonds. Values of the parameters in the modified Morse potential functions are taken the same as those in [10]. The stretch force and angle-variation moment can be obtained by differentiation of Equations (2) - (3) as follows

$$F = 2\beta D_e (1 - e^{-\beta(r-r_0)}) e^{-\beta(r-r_0)} \quad (4)$$

$$M = k_\theta (\theta - \theta_0) + [1 + 3k_{sextic} (\theta - \theta_0)^4] \quad (5)$$

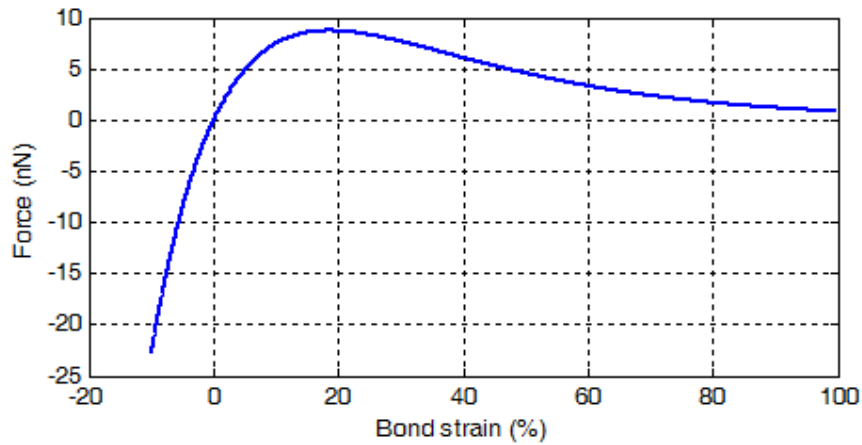


Figure 1: Force-strain curve of the modified Morse potential.

Belytschko et al. [10] reported that the bond angle-bending potential (U_θ) does not contribute to the stretching energy (U_r) and it has little effect on fracture behavior of CNTs. Hence, extra moment effect originating from Equation (5) is neglected. The cut-off distance value of 0.169 nm that corresponds to the inflection point at approximate strain value of 19 % in the modified Morse potential is employed (Figure 1). After the inflection point, the shape of the potential function is not important since material damage occurs [10].

2.2 FE models of SWCNTs

Geometries of different types of defect-free armchair and zigzag nanotube models are constructed by using a Matlab code. Two different types of SWCNTs are considered in the simulations such as (12, 12) armchair and (20, 0) zigzag nanotubes. Sufficiently long SWCNTs are used in simulations to prevent the end effects originating from boundary conditions and SW defects are located in the center of the SWCNTs. When CNTs are subjected to tension loadings, CNTs release its excess tension via formation of topological defects at critical tension value. The SW defect is a topological defect and involves the 90° rotation of a carbon bond about its center and is originally presented as the “SW transformation” [19]. Finally, four hexagons transform into two pentagons and two heptagons. Figure 2 shows schematically the SW formation in the undeformed hexagonal lattice.

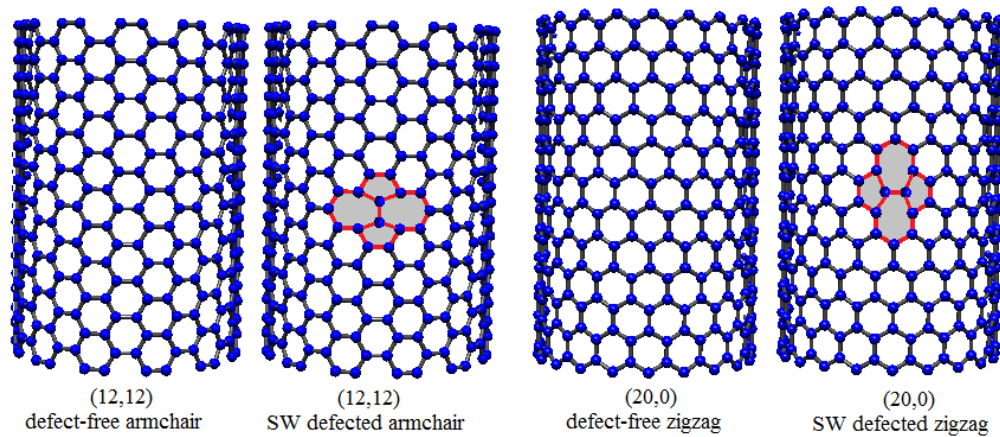


Figure 2: SW defects generated by rationing the C-C bond.

Nardelli et al. [20, 21] showed that defect nucleation in armchair CNTs under transverse tension occurs via SW transformation at critical tensile strain of 5% in CNTs. In addition, Zhang et al. [22] found that this transformation occurs at critical tensile strain of 6% for armchair CNTs and 12% for zigzag CNTs. In this study, strain barrier of 6 % for the armchair and 12 % for the zigzag SWCNTs are considered for the formation of the SW defects. Tserpes et al. [11] used a combination of the stress-strain curve of defect-free and SW-defected CNTs to simulate fracture behavior of SWCNTs. It is assumed in [11] that SWCNT dimensions remain unchanged after the formation of SW defects. Hence, deformation around the defect nucleation region is neglected in [11]. However, after the SW transformation, new configurations of the bonds affect the locations of neighboring atoms which change their locations into new lesser potential energy configurations. On the other hand, Xiao et al. [12, 13] proposed an interaction based mechanics approach to simulate the deformations caused by the formation of SW defects. In our study, to simulate the SW transformation, we started the simulations with defect-free SWCNTs similar to the [11]; then, SW transformation occurs and the configurations of bonds are changed at the defect formation strain; finally, initial pre-strain is applied to

obtain minimized energy configurations of atoms and the simulation is continued until catastrophic failure of the SWCNTs takes place.

3 COMPUTATIONAL RESULTS

All fracture computations of the MM model are completed by using a computer code developed in MATLAB environment. Described by the modified Morse potential, the non-linear behavior of bonds is represented by EB beam elements and an incremental procedure is followed similar to [11] to apply the loading. Initial secant modulus of beam elements (i.e., 6.93 TPa) is obtained through the stress-strain curve of the C-C bond according to the modified Morse potential [14, 15]. In the simulations, all the nodes at one end of SWCNTs are constrained, while the nodes at the other end are subjected to an incremental displacement. The secant modulus and nodal coordinates of each element of the original SWCNT structure is updated at each load step. The secant modulus of each element in the tube structure is set to $F/(A\varepsilon)$ at each load step, where A is the cross sectional area of the element, ε axial strain of the each element, and the interatomic force F is calculated by Equation (4). When the axial strain of a bond reaches to 19 % strain, its stiffness matrix is multiplied by a very small number to simulate the bond break. The strain of SWCNTs is calculated by $\varepsilon_L = (L_s - L_{s0})/L_{s0}$ where L_{s0} is the initial (equilibrium) length and L_s is the current length of the tube. The stress is calculated by $\sigma = F_g / (\pi dt)$ where F_g is the corresponding applied tensile force computed by the summation of the longitudinal reaction forces of the constrained nodes, d is the diameter of tube and t is the thickness of tube. In all calculations, 0.34 nm thickness in [10] is used for SWCNTs.

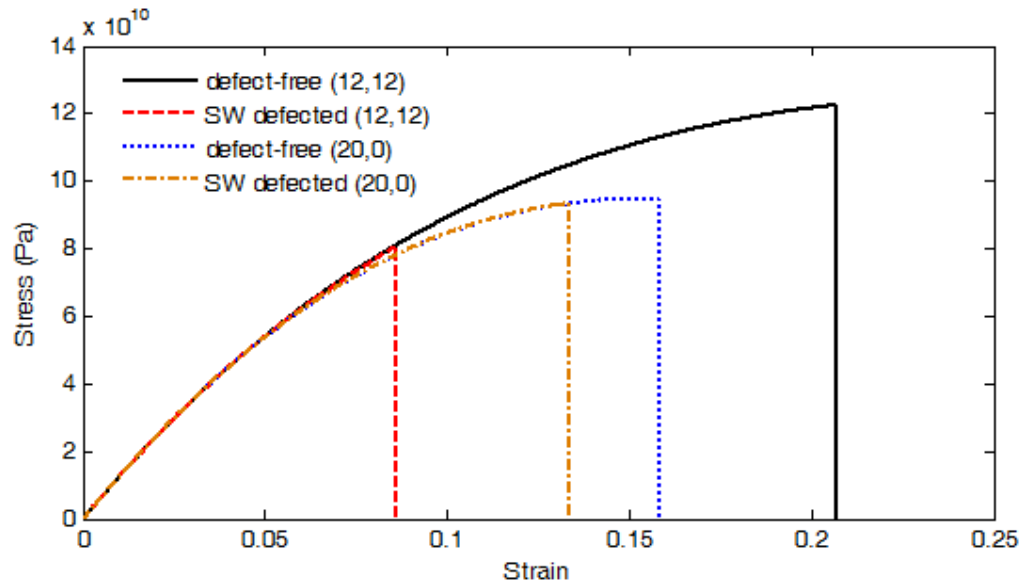


Figure 3: Stress-strain curves of defect-free and SW defected (12,12) and (20,0) SWCNTs under uniaxial load.

Figure 3 shows the calculated stress-strain relationships for defect-free and SW defected armchair (12,12) and zigzag (20,0) SWCNTs without nonlinear geometric effects. As can be seen from Figure 2, the predicted fracture stress and strain values reduce by the presence of SW defects in the structure as expected. As can be seen in Figure 3, the stress-strain curve

exhibits a sudden drop when the stress reaches to the fracture stress, so the fracture is considered to be brittle which are also reported in several studies in literature [5, 10, 12].

Study	Chirality	Defect	ϵ (%)	σ (GPa)
Present work	12,12	defect-free	21.1	122.8
Present work	12,12	SW	8.58	80.4
Present work	20,0	defect-free	15.9	94.7
Present work	20,0	SW	13.34	93.3
Tserpes et al. [11]	12,12	defect-free	19.61	121.86
Tserpes et al. [11]	12,12	SW	11.96	100
Tserpes et al. [11]	20,0	defect-free	15.75	97.68
Tserpes et al. [11]	20,0	SW	15.75	97.68
Xiao et al. [12]	12,12	defect-free	23.1	126.2
Xiao et al. [12]	12,12	SW	9.8	85.9
Xiao et al. [12]	20,0	defect-free	15.6	94.5
Xiao et al. [12]	20,0	SW	11.0	83.3

Table 1: Predicted failure strain (ϵ_f) and stress (σ_f) values of SWCNTs.

Table 1 shows the predicted failure strain and stress values of the SWCNTs along with results in literature. It is observed in Table 1 that calculated strain and stress values lie in the same range with the results reported in literature. The predicted fracture stress and strain values of armchair nanotube reduced about 34.5% and 59.3% by the presence of SW defect, respectively. On the other hand, the predicted fracture stress and strain values of zigzag nanotube reduced about 1.5% and 16.1% by the presence of SW defect, respectively. The SW defects resulted in much more reduction in fracture stress and strain values of the armchair SWCNTs than zigzag ones as bond rearrangement causes stress concentration in vertical bonds and early bond fracture occurs.

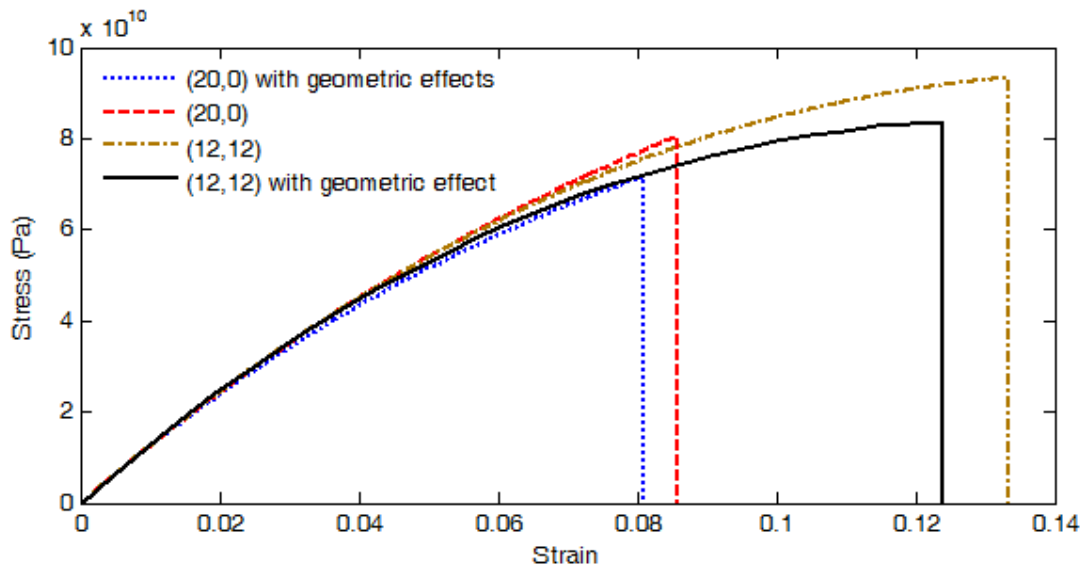


Figure 4: Stress-strain curves of SW defected nanotubes with non-linear geometric effect.

As can be seen in Table 1, Tserpes et al. [11] predicted that fracture stress and strain values of (12,12) armchair SWCNT reduced about 18% and 39%, respectively by the presence of

SW defect, and fracture stress and strain values of defected (20,0) zigzag SWCNT is the same as the zigzag ones. Xiao et al. [12] calculated reduction of fracture stress and strain values of (12,12) armchair SWCNT by the presence of SW defect and found about 32% and 58% for armchair SWCNT and about 12% and 29% for zigzag SWCNT, respectively. In addition, it should be noted that these strain and stress values are significantly smaller than the experimental results in [5] (i.e., range of 11–63 GPa for the failure strengths and 10–13% for the failure strains); these differences can be explained by the presence of defects and some slippage at the attachments which may occur at high-strain cases [6]. The fracture in SWCNTs occurs at relatively large strain values; therefore, we also investigated the effects of geometric nonlinearities on fracture behavior of SW defected SWCNTs. Figure 4 shows the stress-strain curves of SW defected SWCNTs with non-linear geometric effect. The predicted fracture stress and strain values of SW defected armchair SWCNTs reduced about 10.9% and 5.7% considering non-linear geometric effect, respectively. On the other hand, the predicted fracture stress and strain values of SW defected zigzag SWCNTs reduced about 10.3% and 3.5% considering non-linear geometric effects, respectively.

Our proposed approach is able to give the correct prediction of fracture initiation and post failure behavior of SWCNTs. However, modified Morse potential function is not capable of describing the behavior of SWCNTs after the covalent bonds are broken where the reconfiguration of bonds and structural transformations may occur. Figure 5 shows the crack evolution of the SW-defected armchair and zigzag SWCNTs via elimination of broken C-C bonds based on the cut-of distance failure criterion. As can be seen in Figure 5a, the fracture initiated from the vertical bond which connects the two pentagons and continued diagonal crack paths. Then, the crack propagates around the SWCNT in the $\pm 45^\circ$ direction along its circumference. Similar fracture patterns are also observed in literature [10, 11, 12]. As can be seen in Figure 5b, the fracture initiated from the vertical bonds of the upper heptagon which is shown in dark colour in Figure 5b and propagated circumferentially in the same row. The same crack propagation characteristic has also been observed in literature [11].

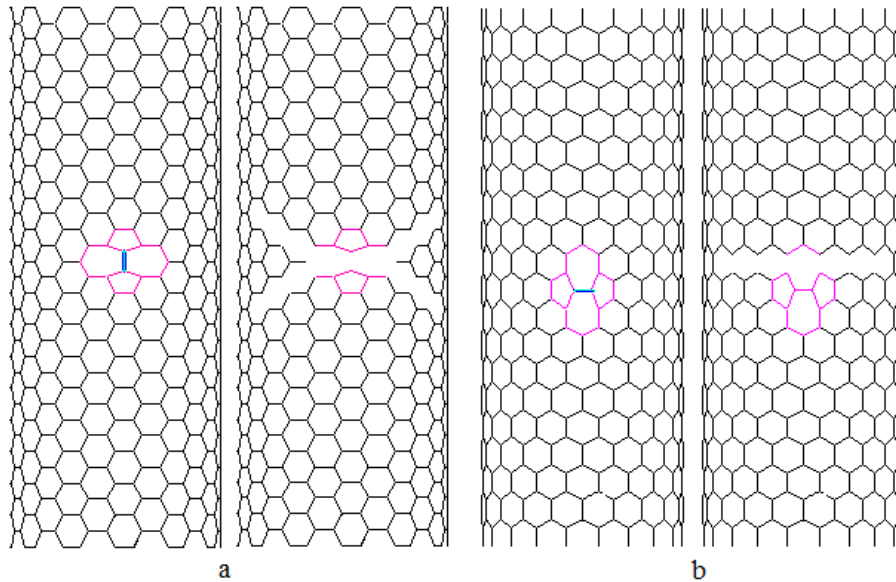


Figure 5: Fracture initiation and propagation directions of the SW-defected SWCNTs; (a) armchair, (b) zigzag SWCNTs.

4 CONCLUSIONS

In this paper, a MM based FE model is developed to predict the effects of Stone-Wales defects on mechanical properties of SWCNTs. The proposed approach includes large deformation and nonlinear geometric effects. Euler-Bernoulli beam elements are used to represent C-C bonds and non-linear characteristic of the beam elements are obtained by using the modified Morse potential. The results show that the fractures of all types of carbon nanotubes are brittle and the SW defects resulted in much more reduction in fracture stress and strain values of the armchair SWCNTs than zigzag ones. Fracture initiation and crack propagation direction issues are also studied. It is shown that crack propagation direction of armchair SWCNT is in maximum shear directions having an angle of $\pm 45^\circ$ along its circumference, and the fracture initiated from the vertical bonds of the upper heptagon and propagated circumferentially in the same row in case of zigzag SWCNTs. Comparisons are made with the failure stress and strain results reported in literature that show well agreement with our results.

REFERENCES

- [1] V.N. Popov, Carbon nanotubes: properties and application. *Materials Science and Engineering: R: Reports*, **43**(3), 61-102, 2004.
- [2] S. Iijima, Helical microtubules of graphitic carbon. *Nature*, **354**, 56-58, 1991.
- [3] J.C. Charlier, Defects in Carbon Nanotubes. *Accounts of Chemical Research*, **35**, 1063-1069, 2002.
- [4] R.W. Haskins, R.S. Maier, R.M. Ebeling, C.P. Marsh, D.L. Majure, A.J. Bednar et al., Tight-binding molecular dynamics study of the role of defects on carbon nanotube moduli and failure. *Journal of Chemical Physics*, **127**(7), 74708–74718, 2007.
- [5] M.F. Yu, O. Lourie, M.J. Dyer, K. Moloni, T.F. Kelly, R.S. Ruoff, Strength and breaking mechanism of multiwalled carbon nanotubes under tensile load. *Science*, **287**, 637–40, 2000.
- [6] S. Zhang, S.L. Mielke, R. Khare, D. Troya, R.S. Ruoff, G.C. Schatz et al., Mechanics of defects in carbon nanotubes: Atomistic and multiscale simulations. *Physical Review B*, **71**, 115403, 2005.
- [7] D. Troya, S.L. Mielke, G.C. Schatz, Carbon nanotube fracture – differences between quantum mechanical mechanisms and those of empirical potentials. *Chemical Physics Letters*, **382**, 133-141, 2003.
- [8] N. Chandra, S. Nimilae and C. Shet, Local elastic properties of carbon nanotubes in the presence of Stone-Wales defects. *Physical Review B*, **69**, 94101-1, 2004.
- [9] S.L. Mielke, D. Troya, S. Zhang, J-L. Li, S. Xiao, R. Car et al., The role of vacancy defects and holes in the fracture of carbon nanotubes. *Chemical Physics Letters*, **390**, 413-420, 2004.
- [10] T. Belytschko, S.P. Xiao, G.C. Schatz, R.S. Ruoff, Atomistic simulations of nanotube fracture. *Physical Review B*, **65**, 235430, 2002.
- [11] K.I. Tserpes, P. Papanikos, The effect of Stone-Wales defect on the tensile behavior and fracture of single-walled carbon nanotubes. *Composite Structures*, **79**, 581-589, 2007.

- [12] J.R. Xiao, J. Staniszewski, J.W. Gillespie, Fracture and progressive failure of defective graphene sheets and carbon nanotubes. *Composite Structures*, **88**, 602-609, 2009.
- [13] J.R. Xiao, J. Staniszewski, J.W. Gillespie, Tensile behaviors of graphene sheets and carbon nanotubes with multiple Stone-Wales defects. *Materials Science and Engineering: A*, **527**, 715-723, 2010
- [14] C. Baykasoglu, A. Mugan, Nonlinear fracture analysis of single-layer graphene sheets. *Engineering Fracture Mechanics*, **96**, 241-250, 2012
- [15] C. Baykasoglu, A. Mugan, Coupled molecular/continuum mechanical modeling of graphene sheets. *Physica E*, **45**, 151-161, 2012
- [16] G.R. Liu and S.S. Quek, *The finite element method A practical course*, Butterworth-Heinemann, Oxford, 2003.
- [17] C. Li, T.W. Chou, A structural mechanics approach for the analysis of carbon nanotubes. *International Journal Solids Structures*, **40**, 2487–2499, 2003.
- [18] K.I. Tserpes, P. Papanikos, Finite element modeling of single-walled carbon nanotubes. *Composites Part B*, **36**, 468–477, 2005.
- [19] A.J. Stone and D.J. Wales, Theoretical studies of icosahedral C₆₀ and some related species. *Chemical Physics Letters*. **128(5–6)**, 501–3, 1986.
- [20] M.B. Nardelli, B.I. Yakobson and J. Bernholc, Mechanism of strain release in carbon nanotubes. *Physical Review B*, **57**, R4277-R4280, 1998.
- [21] M.B. Nardelli, B.I. Yakobson and J. Bernholc, Brittle and Ductile Behavior in Carbon Nanotubes. *Physical Review Letters*, **81**, 4656-4659, 1998.
- [22] P. Zhang P, P.E. Lammert and V.H. Crespi, Plastic deformations of carbon nanotubes *Physical Review B*, **81**, 5346–5349, 1998.

FAST DETECTION OF CHAOTIC OR REGULAR BEHAVIOR OF DOUBLE PENDULUM SYSTEM: APPLICATION OF THE FAST NORM VECTOR INDICATOR METHOD

Dumitru N. Deleanu

Maritime University of Constanta
104, Mircea cel Batran street, Constanta, Romania
dumitru.deleanu@yahoo.com

Keywords: Double Pendulum Dynamics, Indicators of Regularity and Chaos.

Abstract. *It is well known that for non-linear Hamiltonian systems there exist ordered regions with quasi-periodic orbits and regions with chaotic orbits. Usually, these regions are distributed in the phase space in very complicated ways, which often makes it very difficult to distinguish between them, especially when we are dealing with many degrees of freedom. Recently, a new, very fast and easy to compute indicator of the chaotic or ordered nature of orbits has been introduced by Zotos (2012), the so-called "Fast Norm Vector Indicator (FNVI)". Using the double pendulum system, in the paper we present a detailed numerical study comparing the advantages and the drawbacks of the FNVI to those of the Smaller Alignment Index (SALI), a reliable indicator of chaos and order in Hamiltonian systems. Our effort was focused both on the traditional behavior of the FNVI for regular and fully developed chaos but on the "sticky" orbits and on the quantitative criterion proposed by Zotos, too.*

1 INTRODUCTION

Chaos theory is a scientific discipline that focuses on the study of non-linear dynamical systems that are highly sensitive to initial conditions. Today, chaos theory is applied in many other scientific disciplines: mathematics, biology, computer science, economics, engineering, finance, politics, population dynamics and so on.

Appearance of chaos has been identified through various methods/ indicators in the past. We mention here only the well-known tools: the time series method, phase-space method, Lyapunov exponents, bifurcation diagram, Kolmogorov entropy and the Poincare section of surface [1-4]. Some recent tools seem to be more efficient for distinguishing between chaotic or regular orbits, especially in higher order dynamical systems. First Lyapunov Indicator (FLI) was introduced by Froeschle et al. [5] and applied to the structure of a steroidal belt. Saha et al. applied the FLI to study certain discrete maps like Tinkerbell map, Ikeda map and Duffing map [6]. Other maps (Gaussian map, Delayed logistic map) were studied by Deleanu [7]. Fouchard et al. introduced a variant of FLI, the Orthogonal Fast Lyapunov Indicator [8]. Smaller Alignment Index (SALI) was proposed by Skokos [9] and has been successfully applied to some symplectic maps or Hamiltonian flows. A generalized version, the Generalized Alignment Index (GALI) was tested in 2007 [10]. A qualitative tool, the Dynamic Lyapunov Indicator (DLI) was introduced by Saha et al. and applied to various maps [11, 12]. The record could continue to include Spectral Distance (SD), the Dynamical Spectras of Stretching Numbers [13], the Relative Lyapunov Indicator [14], the 0-1 test [15], the Asymmetry Coefficients [16] or Dynamical Spectras of Helicity or Twist Angles [17].

Very recently, a simple, fast and efficient method called Fast Norm Vector Indicator (FNVI) was introduced by Zotos in order to distinguish rapidly and with certainty between ordered and chaotic motions in Hamiltonian systems. The method was applied in the case of a 2-Dof and a 3-Dof Hamiltonians [18].

We have thought that other numerical studies are necessary for a better understanding of the behavior of this indicator, especially in the transition zones between ordered regions and chaotic seas. In the same time, we have considered that some corrections must be made on the indicator proposed by the author. To this purpose, we present in the paper a detailed numerical study on the FNVI method using as a guide the double pendulum system.

The organization of the rest of the paper is as follows. Section 2 contains the details of the FNVI and SALI methods. In Section 3 we derive the Hamiltonian's equations of motion for the double pendulum system. All the calculations and numerical results are presented in Section 4. Finally, some concluding remarks are given in Section 5.

2 INDICATORS OF CHAOS AND ORDER: SALI AND FNVI

Let us consider an autonomous Hamiltonian system of N degrees of freedom (N dof), described by the Hamiltonian $H(q_1, q_2, \dots, q_N, p_1, p_2, \dots, p_N)$, where q_i and $p_i, i = 1, 2, \dots, N$ are the generalized coordinates and conjugate moments respectively.

An orbit in the $2N$ – dimensional phase space of this system is defined by the vector $\mathbf{x}(t) = (q_1(t), q_2(t), \dots, q_N(t), p_1(t), p_2(t), \dots, p_N(t))$, with $x_i = q_i, x_{i+N} = p_i, i = 1, 2, \dots, N$. The time evolution of this orbit is governed by Hamilton's equations of motion

$$\frac{dq_i}{dt} = \frac{\partial H}{\partial p_i}, \quad \frac{dp_i}{dt} = -\frac{\partial H}{\partial q_i}, i = 1, 2, \dots, N \quad (1)$$

while the time evolution of the deviation vector $\xi(0) = (dx_1(0), dx_2(0), \dots, dx_{2N}(0))$ from the

$\mathbf{x}(t)$ solution of Eqs. (1) is given by the variational equations

$$J \cdot \dot{\xi}' = DH \cdot \xi' \quad (2)$$

where (\cdot) denotes the transpose matrix and matrices J and DH are defined by

$$J = \begin{pmatrix} O_N & -I_N \\ I_N & O_N \end{pmatrix}, \quad DH_{i,j} = \frac{\partial^2 H}{\partial x_i \partial x_j}, i, j = 1, 2, \dots, 2N \quad (3)$$

2.1 Smaller Alignment Index (SALI)

To define the *SALI* for an orbit with initial conditions $\mathbf{x}(0) = (x_1(0), x_2(0), \dots, x_{2N}(0))$ we must follow the evolution in time of two initial deviation vectors $\xi_1(0)$ and $\xi_2(0)$. At every time step we normalize each vector to 1 and define the parallel alignment index

$$d_-(t) = \frac{\left\| \frac{\xi_1(t)}{\|\xi_1(t)\|} - \frac{\xi_2(t)}{\|\xi_2(t)\|} \right\|}{\left\| \frac{\xi_1(t)}{\|\xi_1(t)\|} + \frac{\xi_2(t)}{\|\xi_2(t)\|} \right\|} \quad \text{and the anti-parallel alignment index } d_+(t) = \frac{\left\| \frac{\xi_1(t)}{\|\xi_1(t)\|} + \frac{\xi_2(t)}{\|\xi_2(t)\|} \right\|}{\left\| \frac{\xi_1(t)}{\|\xi_1(t)\|} - \frac{\xi_2(t)}{\|\xi_2(t)\|} \right\|}.$$

Here, $\|\cdot\|$ denotes the Euclidean norm of a vector.

The *SALI* is defined as the minimum value of the above alignment indices at any point in time

$$SALI(t) = \min(d_-(t), d_+(t)) \quad (4)$$

Skokos proves that the two deviation vectors tends to coincide or become opposite for chaotic orbits, i.e. the *SALI* tends to zero. For ordered orbits, which lie on a torus, the two deviation vectors eventually become tangent to the torus but in general converge to different directions, so the *SALI* does not tend to zero. Its values fluctuate around a positive value [9].

2.2 The Fast Norm Vector Indicator (FNVI)

Let t^* be the predefined time step of the numerical integration of the system (1) and $[0, T]$ the interval of integration. The *FNVI* at the time moment $t = k t^*$ is defined as

$$FNVI(t) = \frac{1}{t} \left| \frac{\|\mathbf{x}(k t^*)\| - \|\mathbf{x}(0)\|}{\|\mathbf{x}(0)\|} \right| \quad (5)$$

Using a 2-Dof and a 3-Dof Hamiltonians Zotos showed that, after a very short transition period of fluctuation, the *FNVI* displays a nearly constant value for regular orbits, while it continues to fluctuate significantly for chaotic orbits [18]. It results a qualitative indicator regarding the nature of an orbit. Zotos proceeded one step further by introducing a quantitative criterion. He calculated for every orbit the maximum and minimum value of *FNVI* when $t \in [200s, 1000s]$ and defined

$$dFNVI = FNVI_{\max} - FNVI_{\min} \quad (6)$$

He proposed as a threshold value between regularity and chaoticity the value 0.05 so when $dFNVI > 0.05$ the orbit is chaotic, while when $dFNVI \leq 0.05$ the orbit is ordered.

3 HAMILTON'S EQUATIONS OF MOTION FOR THE DOUBLE PENDULUM

The double pendulum is one of the simplest examples of a time-independent Hamiltonian system that exhibits chaotic behavior. It is one simple pendulum fixed to the end of another simple pendulum as shown in Figure 1. The top and center pivots are assumed frictionless, and the coupled objects are free to rotate about them in the vertical plane under the action of gravity. The upper pendulum is modeled as a massless rod of length l_1 with a bob of mass m_1 on the end. The lower pendulum is attached to the mass of the upper pendulum and is similarly a massless rod of length l_2 and a bob of mass m_2 .

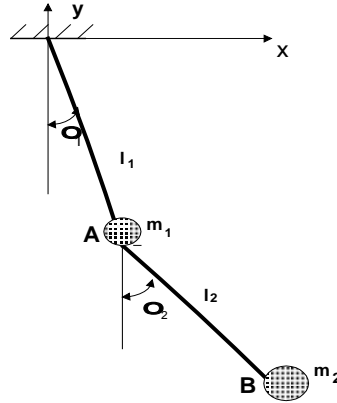


Figure 1: Double pendulum system

The double pendulum exhibits a rich behavior and provides a convenient demonstration of nonlinear dynamics and chaos [19, 20]. Its equations of motion may be derived using Hamiltonian dynamics. To do this, let consider the positions (x_1, y_1) and (x_2, y_2) of the bobs at a given instant of time

$$\begin{aligned} x_1 &= l_1 \sin \theta_1 & y_1 &= -l_1 \cos \theta_1 \\ x_2 &= l_1 \sin \theta_1 + l_2 \sin \theta_2 & y_2 &= -l_1 \cos \theta_1 - l_2 \cos \theta_2 \end{aligned} \quad (7)$$

Therefore, there are only two independent generalized coordinates, which can be taken to be the angles θ_1 and θ_2 that the two rods make with downward vertical direction. The kinetic (T) and potential (V) energies of the system are given by

$$T = \frac{1}{2} m_1 \left(\dot{x}_1^2 + \dot{y}_1^2 \right) + \frac{1}{2} m_2 \left(\dot{x}_2^2 + \dot{y}_2^2 \right) , \quad V = m_1 g y_1 + m_2 g y_2 \quad (8)$$

where g is the constant gravitational acceleration and dots denote the derivatives with respect to time. The Lagrangean relates the kinetic and potential energies of the system. It is described as

$$\begin{aligned} L \left(\theta_1, \theta_2, \dot{\theta}_1, \dot{\theta}_2 \right) &= T - V = \frac{1}{2} (m_1 + m_2) l_1^2 \dot{\theta}_1^2 + \frac{1}{2} m_2 l_2^2 \dot{\theta}_2^2 + m_2 l_1 l_2 \dot{\theta}_1 \dot{\theta}_2 \cos(\theta_1 - \theta_2) + \\ &+ (m_1 + m_2) g l_1 \cos \theta_1 + m_2 g l_2 \cos \theta_2 \end{aligned} \quad (9)$$

The generalized moments p_1 and p_2 can be found from the Lagrangean as follows

$$\begin{aligned}
 p_1 &= \frac{\partial L}{\partial \dot{\theta}_1} = (m_1 + m_2) l_1^2 \dot{\theta}_1 + m_2 l_1 l_2 \dot{\theta}_2 \cos(\theta_1 - \theta_2) \\
 p_2 &= \frac{\partial L}{\partial \dot{\theta}_2} = m_2 l_2^2 \dot{\theta}_2 + m_1 l_1 l_2 \dot{\theta}_1 \cos(\theta_1 - \theta_2)
 \end{aligned} \tag{10}$$

From (4), the angular velocities $\dot{\theta}_1$ and $\dot{\theta}_2$ can be expressed as functions of the coordinates and moments

$$\dot{\theta}_1 = \frac{l_2 p_1 - l_1 p_2 \cos(\theta_1 - \theta_2)}{l_1^2 l_2 [m_1 + m_2 \sin^2(\theta_1 - \theta_2)]}, \quad \dot{\theta}_2 = \frac{l_1 (m_1 + m_2) p_2 - l_2 m_2 p_1 \cos(\theta_1 - \theta_2)}{l_2^2 l_1 m_2 [m_1 + m_2 \sin^2(\theta_1 - \theta_2)]} \tag{11}$$

The Hamiltonian H is the Legendre transform of the Lagrangean L

$$\begin{aligned}
 H(\theta_1, \theta_2, \dot{\theta}_1, \dot{\theta}_2) &= \dot{\theta}_1 p_1 + \dot{\theta}_2 p_2 - L = -(m_1 + m_2) g l_1 \cos \theta_1 - m_2 g l_2 \cos \theta_2 + \\
 &+ \frac{m_2 l_2^2 p_1^2 + (m_1 + m_2) l_1^2 p_2^2 - 2 m_2 l_1 l_2 p_1 p_2 \cos(\theta_1 - \theta_2)}{2 l_1^2 l_2^2 m_2 [m_1 + m_2 \sin^2(\theta_1 - \theta_2)]}
 \end{aligned} \tag{12}$$

Hamilton's equations for the time rate of change of the generalized moments are

$$\begin{aligned}
 \dot{p}_1 &= -\frac{\partial H}{\partial \theta_1} = C_2 - C_1 - (m_1 + m_2) g l_1 \sin \theta_1 \\
 \dot{p}_2 &= -\frac{\partial H}{\partial \theta_2} = C_1 - C_2 - m_2 g l_2 \sin \theta_2
 \end{aligned} \tag{13}$$

where

$$\begin{aligned}
 K &= \frac{m_2 l_2^2 p_1^2 + (m_1 + m_2) l_1^2 p_2^2 - 2 m_2 l_1 l_2 p_1 p_2 \cos(\theta_1 - \theta_2)}{2 l_1^2 l_2^2 m_2 [m_1 + m_2 \sin^2(\theta_1 - \theta_2)]} \\
 C_1 &= \frac{p_1 p_2 \sin(\theta_1 - \theta_2)}{l_1 l_2 [m_1 + m_2 \sin^2(\theta_1 - \theta_2)]}, \quad C_2 = \frac{m_2 K \sin 2(\theta_1 - \theta_2)}{m_1 + m_2 \sin^2(\theta_1 - \theta_2)}
 \end{aligned} \tag{14}$$

The set of the four equations (5) and (13) describe the time evolution of any orbit in the four-dimensional phase - space $(\theta_1, \theta_2, p_1, p_2)$. Because the Hamiltonian is conserved in time, the orbits actually lie on a three-dimensional hyper-surface determined by the equation

$$E = H + g [(m_1 + m_2) l_1 + m_2 l_2] = \text{constant} \tag{15}$$

The constant $(m_1 + m_2) l_1 + m_2 l_2$ has been added to H so $E = 0$ at the stable equilibrium point $\theta_1 = \theta_2 = p_1 = p_2 = 0$ [21, 22].

4 NUMERICAL RESULTS AND DISCUSSION

To investigate the detailed dynamics of the double pendulum the equations of motion are solved numerically by using the Mat Lab's solver ODE 45. For the simulation assume that the two masses are equal to unity, $m_1 = m_2 = 1 \text{ kg}$, and that the two lengths are also equal to unity, $l_1 = l_2 = 1 \text{ m}$. The equation (15) reduce to

$$E = \frac{p_1^2 + 2p_2^2 - 2p_1p_2 \cos(\theta_1 - \theta_2)}{1 + \sin^2(\theta_1 - \theta_2)} + g(3 - 2\cos\theta_1 - \cos\theta_2) = \text{constant} \quad (16)$$

The accuracy of the integration may be checked by evaluating the energy of the pendulum at each integration step. Figure 2 shows the results for the four values of energy we will consider in the next simulations, namely $E_1=5J$, $E_2=10J$, $E_3=15J$ and $E_4=20J$. An obvious conservation of energy is easy to observe.

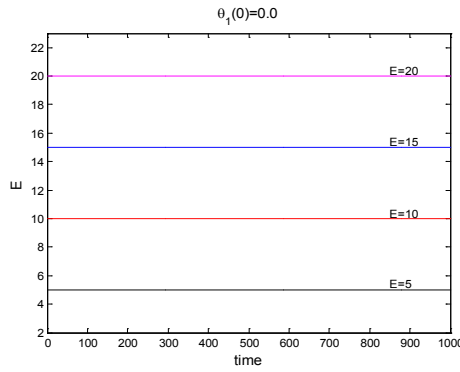


Figure 2: Conservation of the total energy E during the integration process

In order to illustrate the behavior of the FNVI in the case of the double pendulum system we consider two representative orbits. The first is an ordered orbit with initial condition $(\theta_1, \theta_2, p_1, p_2) = (1.1, 0.0, 0.0, 2.7746)$ and the second is a chaotic orbit with initial conditions $(\theta_1, \theta_2, p_1, p_2) = (0.0, 0.0, 0.0, 3.873)$. For both orbits, the value of energy is $E_3=15J$. The motion of the outer bob is depicted in Figure 3.

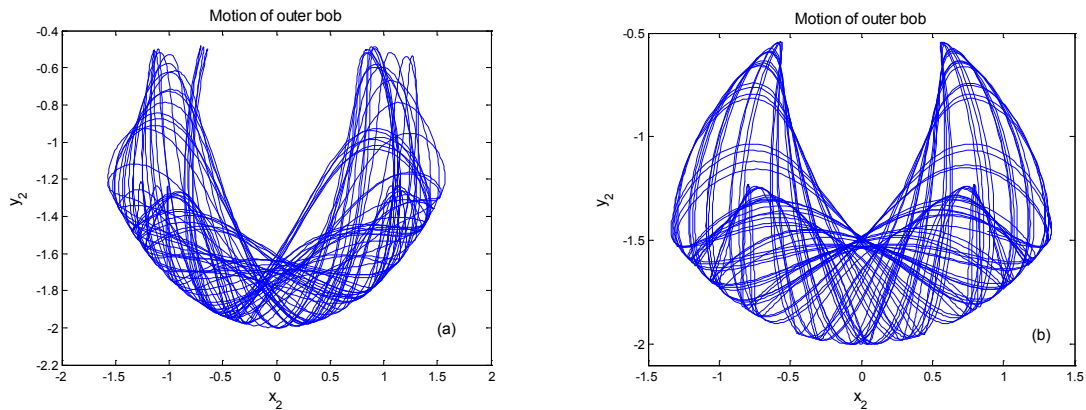


Figure 3: The motion of the outer bob: a) chaotic orbit; b) ordered orbit

When other two orbits are launched at a distance of 0.001 from these initial conditions, the orbits corresponding to the ordered case move practically together (indicating that there is no divergence of the two close orbits) while the orbits corresponding to the chaotic case move away from each other after a short time period, as shown in Figure 4.

Figure 5a presents the Poincare section of surface (PSS) of the two orbits defined by $\theta_2=0, p_2 \geq 0$. The points of the ordered orbit (red points) form a set of smooth closed curves while the points of the chaotic orbit (black points) appear randomly scattered. Finally, in Figure 5b we plot the evolution in time of $\log(SALI)$ for the two orbits. The $SALI$ of the ordered

orbit (grey points) fluctuates around $SALI = 0.38$, indicating the regular character of the orbit, while the $SALI$ of the chaotic orbit (black points) falls abruptly reaching the limit of the accuracy of the computer precision after about 500 time units. All the logarithms in the paper are taken in base 10.

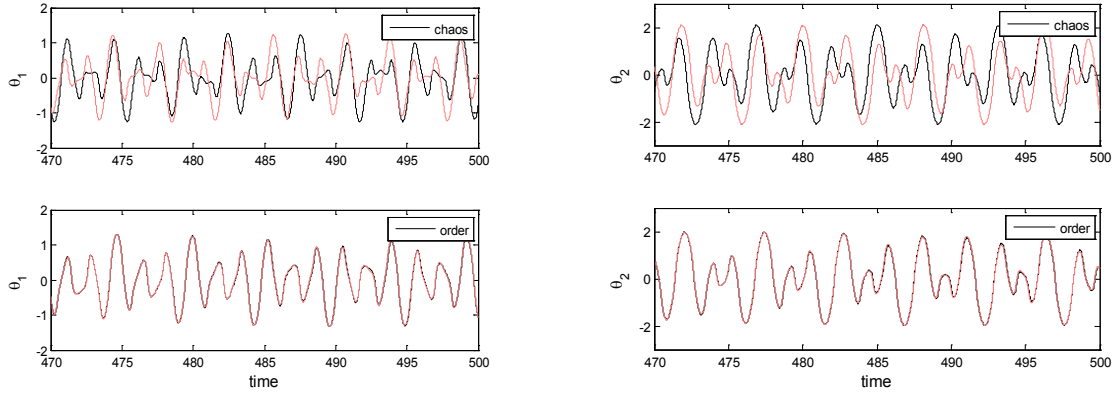


Figure 4: The time evolution of $\theta_1(t)$ and $\theta_2(t)$ for two very closed initial conditions in chaotic case (upper panels) and ordered case (lower panels)

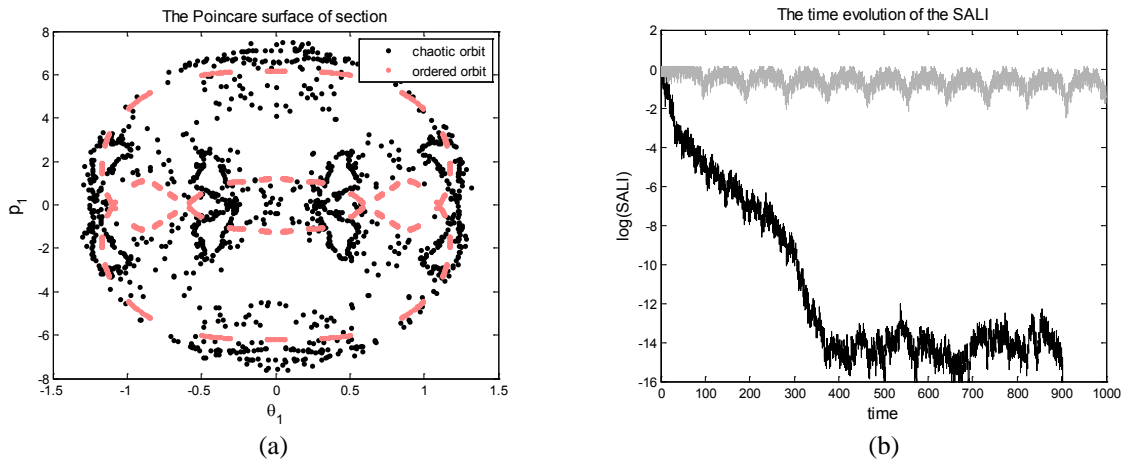


Figure 5: a) The PSS of the ordered orbit (red points) and chaotic orbit (black points); b) The time evolution of the $\log(SALI)$ for ordered orbit (grey points) and chaotic orbit (black points)

A short inspection of definition (5) shows a double dependence with t^* of $FNVI$. The same is valid for $dFNVI$. It is obvious that if the values of t^* increases the value of $dFNVI$ decreases. In fact, a dependence of the form $dFNVI \propto 1/t^*$ may be considered. We think that a better choice for the $FNVI$ could be

$$FNVI(t) = \frac{1}{k} \sum_{i=1}^k \frac{\left| \|\mathbf{x}(i t^*)\| - \|\mathbf{x}(0)\| \right|}{\|\mathbf{x}(0)\|} \quad (17)$$

In this way, $FNVI$ presents only a weak relationship with t^* , as shown in Table 1. No matter which value of t^* was considered, an evident distinction between the $FNVI$ plots for

the two orbits may be observed. *FNVI* displays large and random variations for the chaotic orbit while it remains almost constant for the regular one (see Figure 6a). We fixed $t^* = 0.05$ in the remainder of this paper. To see if these patterns remain unchanged if the total time of numerical integration increases, we computed the *FNVI* for the same orbits but for a time period of 5,000 time units (t.u). The obtained results are displayed in Figure 6b.

t^*		0.01	0.02	0.05	0.075	0.1	0.5
$dFNVI$ obtained with (17)	Ordered orbit	0.002814	0.002815	0.002823	0.002826	0.003021	0.005507
	Chaotic orbit	0.043784	0.043783	0.043778	0.043831	0.043854	0.043292

Table 1: The dependence of $dFNVI$ with t^* for the orbits discussed in Figure 5

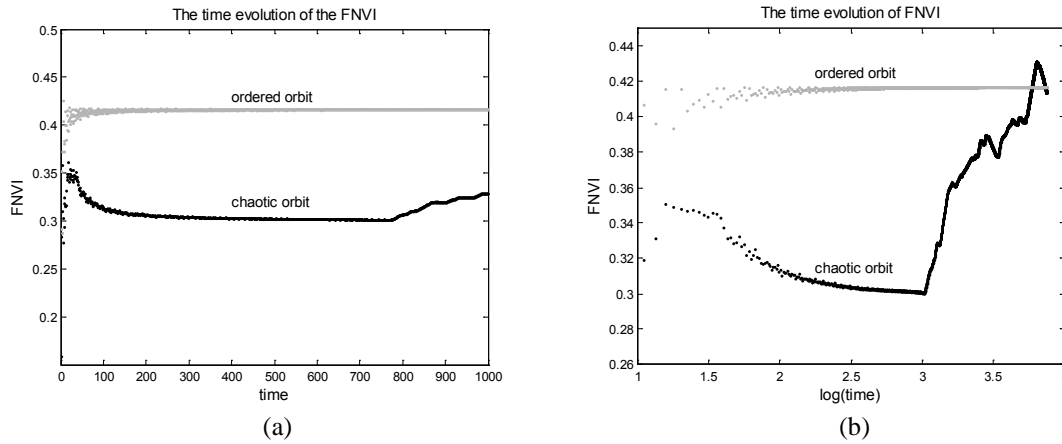
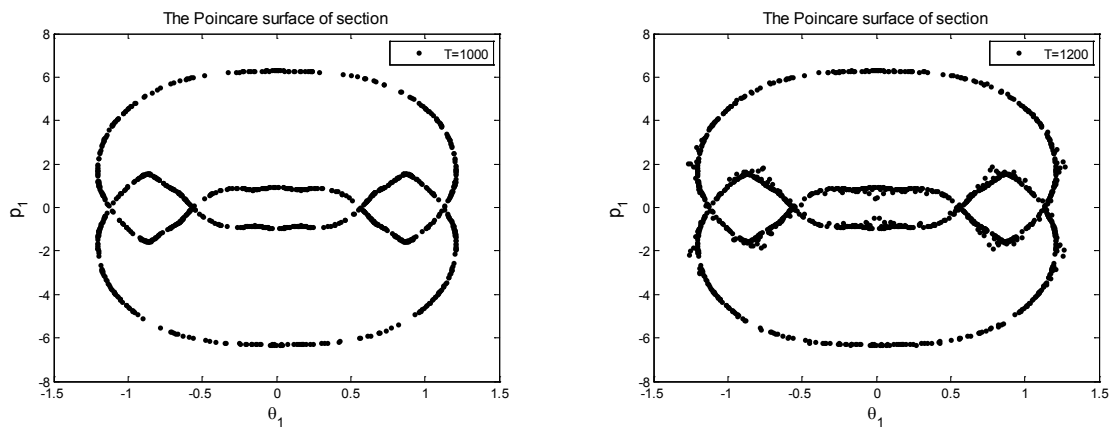


Figure 6: The time evolution of the FNVI for ordered orbit (grey points) and chaotic orbit (black points): a) $T=1,000$; b) $T= 5,000$

It is interesting to mention that the *CPU* time needed to obtain the results plotted in Figure 5b it was fifty times greater than for results seen in Figure 6a. This might be a problem in the case of "sticky" orbits, which remain at the borders of an island of stability for a long time before enters the chaotic sea. The *PSS* technique and the *SALI* method, which require considerable *CPU* time, might give erroneous results if the running time is short enough.



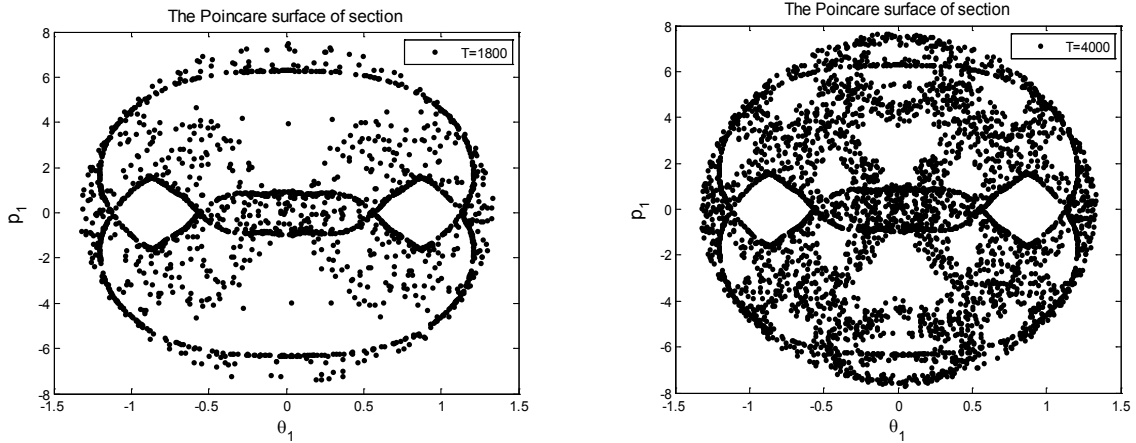


Figure 7: The PSS of the sticky orbit: a) T=1000; b) T=1200; c) T=1800; d) T=4000

To verify this, let consider the sticky orbit with initial conditions $(\theta_1, \theta_2, p_1, p_2) = (0.56525, 0.0, 0.0, 3.2174)$. Figure 7 shows the time evolution of the sticky orbit in the $PSS (\theta_1, p_1)$ for the integration times equal with T=1000 t.u., T=1200 t.u., T=1800 t.u. and T=4000 t.u. respectively. In the PSS corresponding to T=1000 t.u. the orbit seems to be regular. The first visible deviations from the smooth curve appear for T=1200 t.u. When T=4000 t.u. the orbit has left the borders of the island of stability and entered in the chaotic regime. Figure 8 presents the time evolution of the $FNVI$ and the $SALI$ for the same sticky orbit. The both figures indicate that after 1200 t.u. the orbit gradually alters its nature, from ordered to chaotic. The limit $SALI = 10^{-16}$ was obtained after T=2000 t.u. Although the conclusion is the same, the difference consists again in the CPU time.

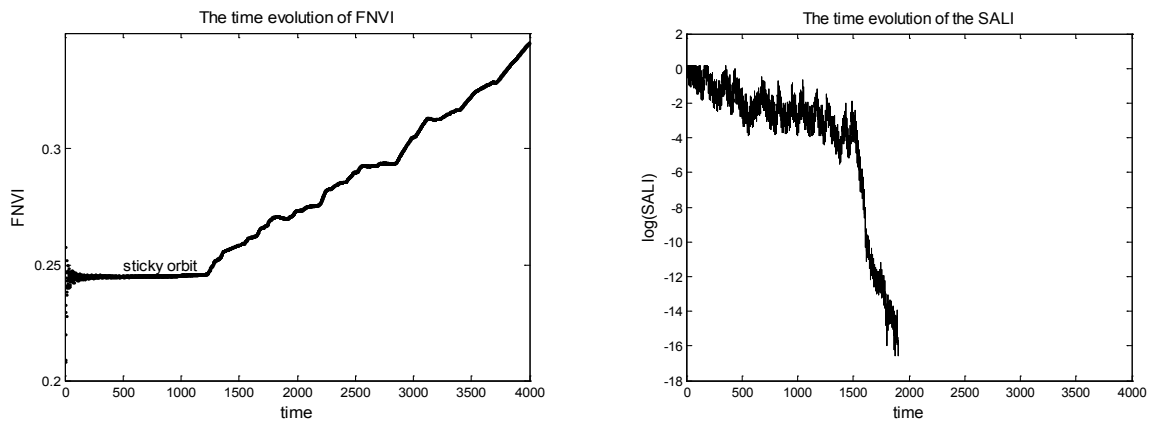


Figure 8: The time evolution of the $FNVI$ (left panel) and of the $SALI$ (right panel) for the sticky orbit discussed in Figure 7

In order to present the effectiveness of the $dFNVI$ indicator in detecting regions of order and chaos we compute the $dFNVI$ for a large grid of equally distributed initial conditions on the axis of the $PSS (\theta_1, p_1)$ of the double pendulum Hamiltonian. Firstly, in Figure 9 we present the $PSSs$ of the system for $E_1=5J$, $E_2=10J$, $E_3=15J$ and $E_4=20J$. Each section was constructed by numerically solving Eqs. (5) and (13) for 40×40 initial conditions, chosen to provide a good coverage of the energetically accessible region in the plane. The appearance and growth of chaos with energy is well-demonstrated.

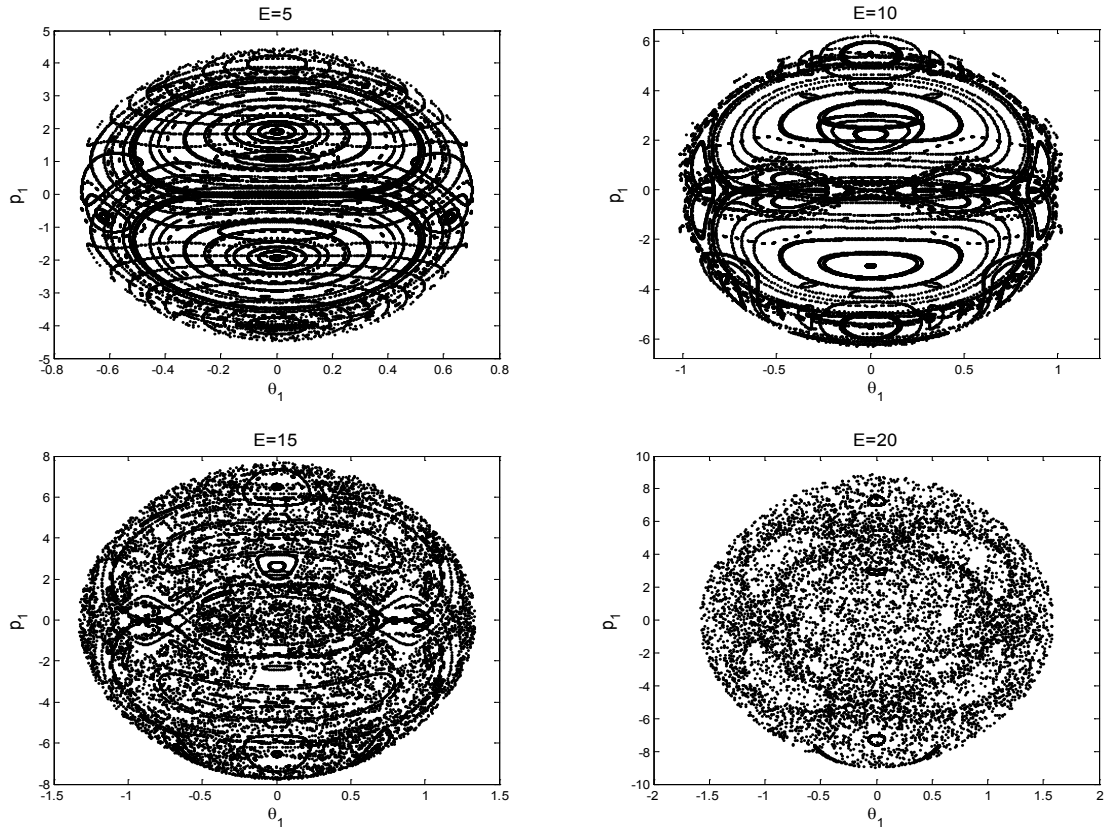


Figure 9: The PSSs of the double pendulum for increasing values of total energy E

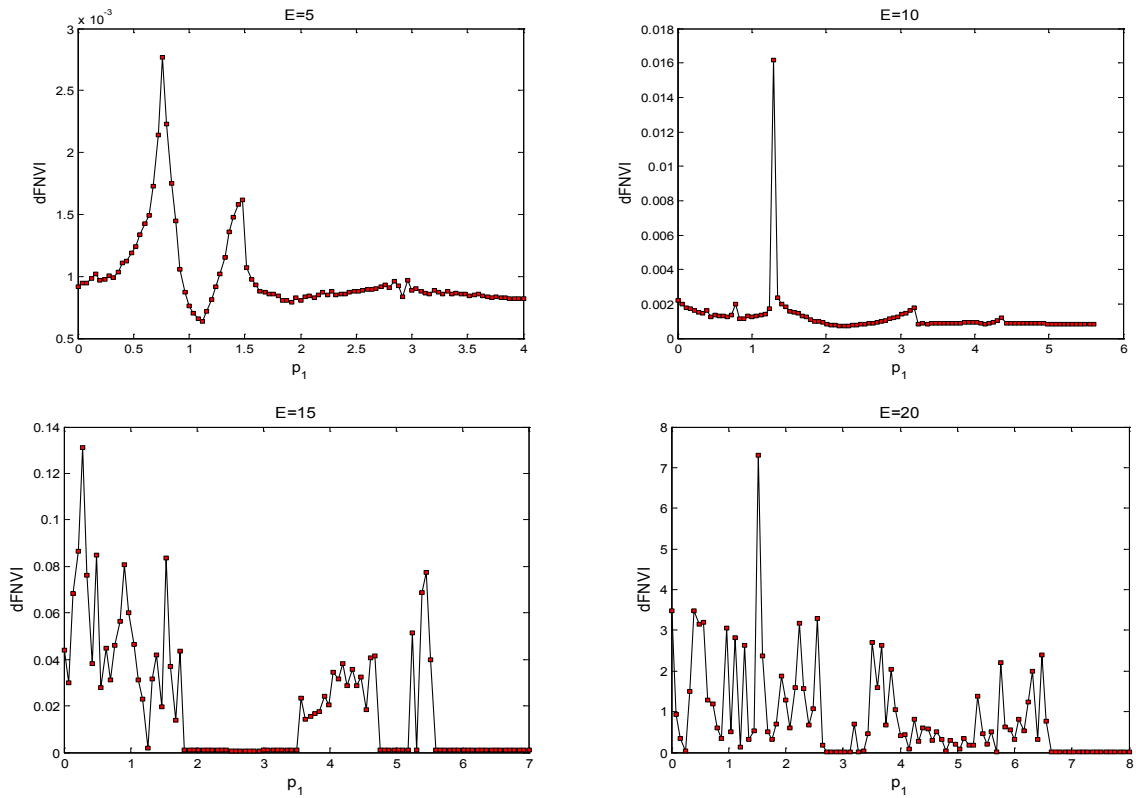


Figure 10: The variation of the $dFNVl$ values for initial conditions chosen on the semi-line $\theta_1=0, p_1 \geq 0$ of the corresponding PSS of the double pendulum system

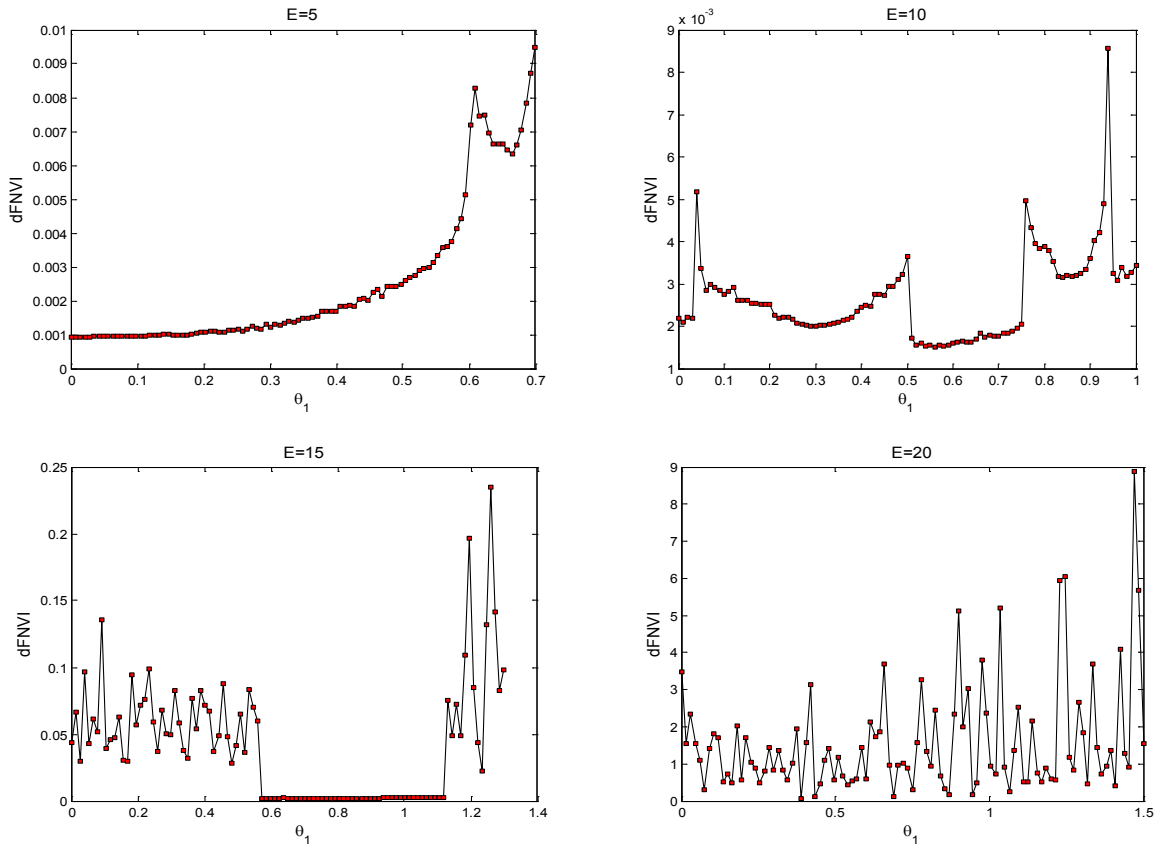


Figure 11: The variation of the $dFNVl$ values for initial conditions chosen on the semi-line $p_1=0, \theta_1 \geq 0$ of the corresponding PSS of the double pendulum system

Secondly, in an attempt to define a threshold value between chaoticity and regularity we chose two sets of 100 equally distributed initial conditions on the semi-lines $\theta_1=0, p_1 \geq 0$ and $p_1=0, \theta_1 \geq 0$ of the PSS s depicted in Figure 9 and calculated their $dFNVl$ values according with (6) and (17). The results are plotted in Figures 10 and 11. It is evident that as the value of the energy E increases, the values of the $dFNVl$ increase too, especially for the chaotic orbits.

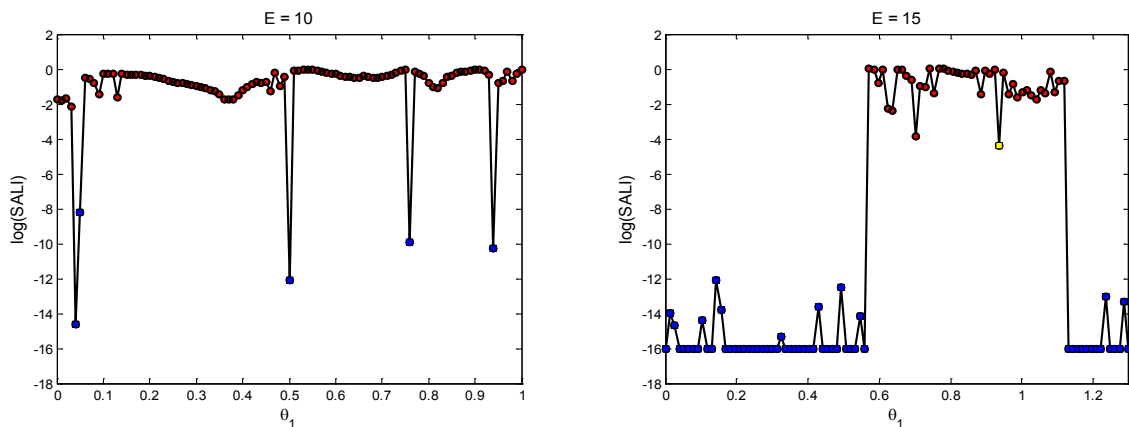


Figure 12: The variation of the $SALI$ values for initial conditions chosen on the semi-line $p_1=0, \theta_1 \geq 0$ of the corresponding PSS of the double pendulum system

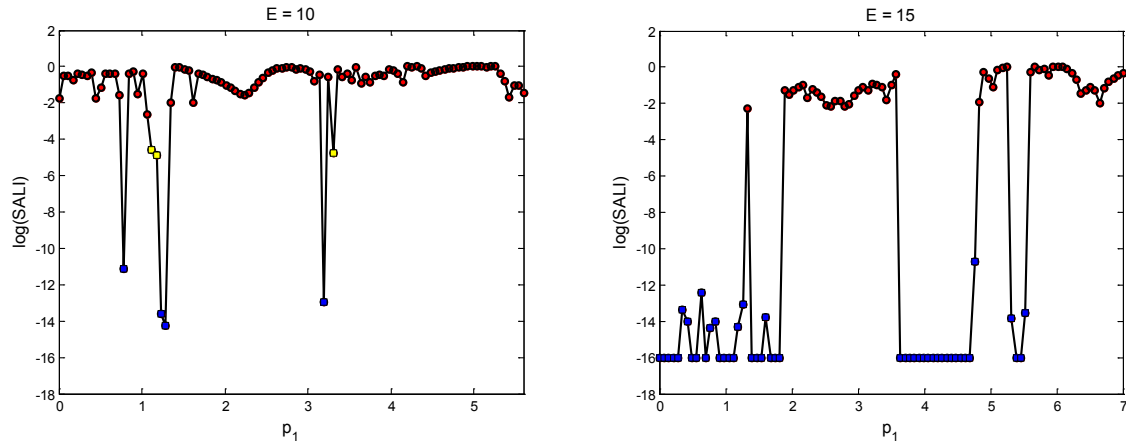


Figure 13: The variation of the *SALI* values for initial conditions chosen on the semi-line $\theta_1=0, p_1 \geq 0$ of the corresponding *PSS* of the double pendulum system

The same sets of initial conditions were used to compute the corresponding *SALI* values. The results are presented in Figures 12 and 13 only for $E_2=10J$ and $E_3=15J$. We assigned a coloured circle to every individual initial condition according to the *SALI*'s value: if it is smaller than 10^{-8} the circle is coloured bleu (the orbit is chaotic beyond any doubt). If $SALI \in [10^{-8}, 10^{-4})$ the circle is coloured yellow and finally, if $SALI \in [10^{-4}, 2)$ it is coloured red. Comparing Figures 10 and 13 and Figures 11 and 12 an obvious similitude between them is easy to observe. In fact, every orbit with $dFNVI \geq 0.01$ has $SALI \leq 10^{-8}$ therefore it is chaotic and almost all orbits having $dFNVI < 0.005$ are characterized by $SALI > 10^{-2}$ therefore they are ordered or "sticky" (with only three exceptions). None orbit has $dFNVI \in [0.005, 0.01]$.

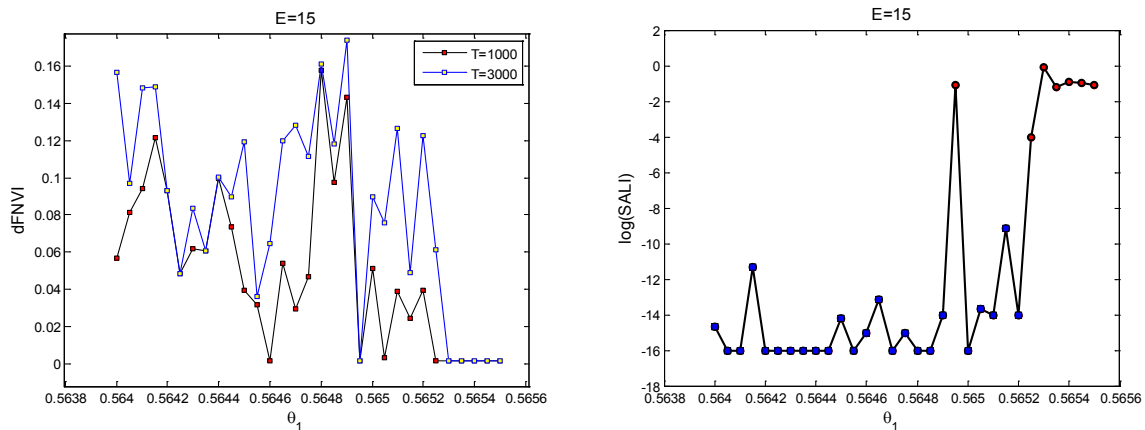


Figure 14: The variation of the *dFNVI* values (left panel) and *SALI* values (right panel) for initial conditions chosen on the interval $\theta_1 \in [0.564, 0.5655]$

Based on these numerical simulations, we propose as a threshold value between regularity and chaos the value 0.01. Thus when $dFNVI \geq 0.01$ the orbit is chaotic while when $dFNVI < 0.01$ it is ordered.

In order to clear up the exceptions mentioned above, we carried out a carefully analysis of the interval $\theta_1 \in [0.564, 0.5655]$, corresponding to the total energy $E_3=15J$ in Figure 12. This

zone hallmarks the passage from a region where the motion is chaotic to a huge island of stability and it is expecting that a significant number of sticky orbits could be detected in here. Figure 14 present our findings. In the left panel were displayed the $dFNVI$ values calculated for $T=1000$ t.u. and $T=3000$ t.u. while in the right panel were depicted the associated $SALI$ values, obtained with $T=1000$ t.u. Two remarks are in order. Firstly, a lot of $dFNVI$ values increase when the definition (6) is extended to the interval [200s, 3000s]. In this category must be included three orbits which resemble ordered on the time interval [200s, 1000s], but which are in fact sticky orbits. Secondly, the $SALI$ values always give the right verdict regarding the nature of the orbit. However, even if $T=3000$ t.u., the CPU time needed to obtain a $dFNVI$ value remains smaller than for a $SALI$ value.

5 CONCLUSIONS

In this paper we have illustrated the capacity of the Fast Norm Vector Indicator ($FNVI$) method in distinguishing between order and chaos in double pendulum system. For the sake of comparison, an accepted tool, the Smaller Alignment Index ($SALI$) was chosen. The main conclusions of the study can be summarized as follows:

- The $FNVI$ seems to be a fast and accurate qualitative tool in order to determine if an orbit is ordered or chaotic. The distinction between these two types of orbits is based on the different behavior of the $FNVI$. It was found to fluctuate significantly for chaotic orbits, while displays a nearly constant value for ordered orbits.
- An important advantage of the $FNVI$ method over the $SALI$ method is the short CPU time needed to provide a conclusive result regarding the character of the orbit. This is because the $FNVI$ method requires only the computation of the set of equations of motion while the $SALI$ method needs the computation of the variational equations too. The CPU time on a Intel (R) Core (TM) 2 Duo CPU T 5450 2.33 GHz, needed to obtain a conclusion, for an integration time of 1000 units of time, was about 12 sec/orbit with $FNVI$ method and about 200 sec/orbit with $SALI$ method. The CPU time could be a crucial criterion when we need to study a large number of orbits or when we follow the time evolution of a sticky orbit.
- The quantified version of the $FNVI$, the $dFNVI$, depends on the predefined time step t^* of the numerical integration. The proposed threshold value of 0.05 between order and chaos is valid, in our opinion, only for a particular t^* . An independent value of 0.01 could be considered instead, if the modified definition (17) of the $FNVI$ is utilized.
- Exploiting the advantages of the $dFNVI$ indicator, we have constructed detailed grid-plots where the chaotic and ordered regions are clearly distinguished. These grid-plots were plotted for increasing values of the total energy and were compared with the results supplied by the $SALI$ method.
- Because the $dFNVI$ was defined for the time interval [200s, 1000s] it is unable to distinguish between ordered and sticky orbits. For both types of orbits we found $dFNVI < 0.005$. This is because the sticky orbit, which is chaotic, need more time to escape from the outer region of an island of stability to the surrounding chaotic region. The $FNVI$ plots, extended on a larger time interval, make the correct distinction between the two types of orbit.

REFERENCES

- [1] G.L. Baker, J.P. Gollub, *Chaotic Dynamics: An Introduction*, Cambridge University Press, New York, 1990.
- [2] G. Benettin, C. Froeschle, J.P. Scheidecker, Kolmogorov entropy of a dynamical system with an increasing number of degrees of freedom, *Phys. Rev. A* **19**, 2454-2460, 1979.
- [3] R.L. Delaney, *An introduction to chaotic dynamical systems*, Addison-Wesley Publishing Company, New York, 1989.
- [4] A. Wolfe, B. Swift, H.L. Swenney, J.A. Vastano, Determining Lyapunov exponents from a time series, *Physica D* **16**, 285-317, 1985.
- [5] C. Froeschle, E. Lega, R. Gonczy, Fast Lyapunov Indicator. Application to asteroidal motion, *Celest. Mech. Dyn. Astron.*, **67**, 41-62, 1997.
- [6] L.M. Saha, R. Tehri, Application of recent indicators of regularity and chaos to discrete maps, *Int. J. of Appl. Math. and Mech.*, **6**, 86-93, 2010.
- [7] D. Deleanu, New applications of Fast Lyapunov Indicator for discrete-time dynamical systems, *Constanta Maritime University Annals*, **13**, 113-120, 2011.
- [8] M. Fouchard, E. Lega, Ch. Froeschle, C.I. Froeschle, On the relationship between Fast Lyapunov Indicator and periodic orbits for continuous flows, *Celest. Mech. Dyn. Astron.*, **83**, 205-222, 2002.
- [9] Ch. Skokos, Alignment indices: a new, simple method for determining the ordered or chaotic nature of orbits, *J. Phys. A: Math. Gen.*, **34**, 10029-10043, 2001.
- [10] Ch. Skokos, T. Bountis, Ch. Antonopoulos, Geometrical properties of local dynamics in Hamiltonian systems: the Generalized Alignment Index method, *Physica D.*, **231**, 30-54, 2008.
- [11] L.M. Saha, M. Budhraj, The largest eigenvalue: An indicator of chaos?, *Int. J. of Appl. Math. and Mech.*, **3(1)**, 61-71, 2007.
- [12] D. Deleanu, Dynamic Lyapunov Indicator: a practical tool for distinguishing between ordered and chaotic orbits in discrete dynamical systems, *Proceedings of the 10th WSEAS International Conference on Non-Linear Analysis, Non-Linear Systems and Chaos (NOLASC' 11)*, Iasi, Romania, July 1-3, 2011.
- [13] N. Voglis, G. Contopoulos, C. Efthymiopoulos, Detecting of ordered and chaotic motion using the dynamical spectra, *Celest. Mech. Dyn. Astron.*, **73**, 211-220, 1999.
- [14] Z. Sandor, B. Erdi, A. Szell, B. Funk, The Relative Lyapunov Indicator: an efficient method of chaos detection, *Celest. Mech. Dyn. Astron.*, **90**, 127-138, 2004.
- [15] G.A. Gottwald, I.A. Melbourne, A new test for chaos in deterministic systems, *Proc. Roy. Soc. London*, **460**, 603-611, 2004.
- [16] P. Waz, D.D. Waz, Assymetry coefficients as indicators of chaos, *Acta Physica Polonica*, **116**, 987-991, 2009.
- [17] G. Contopoulos, N. Voglis, Spectra of stretching numbers and helicity angles in dynamical systems, *Celest. Mech. Dyn. Astron.*, **14**, 1-20, 1996.

- [18] E.E. Zotos, The Fast Norm Vector Indicator method: a new dynamical parameter for detecting order and chaos in Hamiltonian systems, *Nonlinear Dyn.*, DOI 10.1007/s1107-012-0504-1.
- [19] T. Shinbrot, C. Grebogi, J. Wisdom, J.A. Yorke, Chaos in a double pendulum, *Am. J. Phys.*, **60**, 491-499, 1992.
- [20] R.B. Levien, S.M. Tan, Double pendulum: an experiment in chaos, *Am. J. Phys.*, **61**, 1038-1044, 1993.
- [21] T. Stachowiak, T. Okad, A numerical analysis of chaos in the double pendulum, *Chaos, Solitons and Fractals*, **29**, 417-422, 2006.
- [22] Z. Zhou, C. Whiteman, Motions of double pendulum, *Nonlinear Analysis, Theory, Method and Applications*, **26**, 1177-1191, 1996.

WARPING TRANSMISSION IN 3-D BEAM ELEMENT INCLUDING SECONDARY TORSIONAL MOMENT DEFORMATION EFFECT

Evangelos J. Sapountzakis¹, Vasileios J. Tsipiras¹ and Pavlos G. Gkesos²

¹ School of Civil Engineering, National Technical University
Zografou Campus, GR-157 80 Athens, Greece
e-mail: cvsapoun@central.ntua.gr, tsipiras@gmail.com

² Army Corps of Engineers, Hellenic Army General Staff, Ministry of Defence, Greece
Mesogeion Street 227-231, Holargos, PO BOX 15451
e-mail: gessos.paul@gmail.com

Keywords: Warping transmission, warping transfer, shear deformation effect, secondary torsional moment deformation effect, exact stiffness matrix, 3-D beam element.

Abstract. *In this paper a 3-D beam element including shear and secondary torsional moment deformation effects is formulated with general warping and bimoment transmission capabilities. The beam's cross section is an arbitrarily shaped doubly symmetric constant one, while its shape is assumed to remain undistorted. Shear deformation (due to shear forces) is taken into account employing shear correction factors determined through an energy approach. Secondary torsional moment deformation effects are modelled by introducing the primary angle of twist per unit length as an additional degree of freedom at each end node of the element and employing a torsional shear correction factor. An exact 14x14 stiffness matrix and the corresponding nodal load vector are formulated based on the solution of the global equilibrium differential equations of the beam. At joints connecting space members, all kinds of warping and bimoment transmission (not involving cross sectional distortion) are modelled, including free warping, full or partial warping restraint, full warping and bimoment continuity, complete direct and inverse warping transmission and general warping and bimoment transmission between intersecting members. A computer program is developed in a mathematical package permitting symbolic algebraic manipulations. Numerical results of great practical interest are worked out to illustrate the efficiency, the accuracy and the range of applications of the developed method.*

1 INTRODUCTION

In engineering practice we often come across the analysis of beam assemblages subjected to general loading conditions. Space frames and grid systems are most common examples along with structures such as curved beams and stiffened plates which are sometimes modelled as an assembly of straight members. Such structures often necessitate a rigorous analysis which is not always easy to be achieved due to several reasons.

Firstly, some commercial software packages neglect shear deformation effects (due to shear forces) in the global analysis of the structure. These effects influence notably the behaviour of short beams; often however they could also be significant in long beams of multimaterial cross section exhibiting weak shear connection between different material regions. This could also be the case in beams made of composite materials which are weak in shear. Secondly, in the beam element formulation of most commercial software packages a 12x12 stiffness matrix is considered where 2 degrees of freedom (DOFs) are related to torsion. In such a formulation the effects of nonuniform warping are neglected, thus only the primary (St. Venant) torsional mechanism resisting torsional actions is taken into account. It is well known that nonuniform warping affects significantly the global behaviour of open shaped thin walled cross section bars. Thus, several researchers have employed a 14x14 stiffness matrix with additional DOFs related to warping achieving the inclusion of such effects in the analysis. However, most of the relevant formulations consider the angle of twist per unit length at the element's nodes as additional DOF, thus the secondary torsional moment deformation effect (STMDE) [1] is not taken into account. The aforementioned types of structures influenced by shear deformation are affected similarly by secondary torsional moment deformation as well. Moreover, STMDE should be considered in the analysis of closed shaped thin walled cross section beams [1-3]. Regarding the formulation of the stiffness matrix and the corresponding nodal load vector, several researchers employ numerical methods such as the Finite Element Method (FEM) exploiting simple shape functions and taking proper care in order to avoid shear locking phenomena [4]. In the problem under examination, this procedure results in an approximate formulation, thus more than one element is usually required to model accurately a single straight span. However, the exploitation of the global equilibrium equations of the beam results in an exact stiffness matrix [5] and an inherently locking free formulation where no more than one element is required for each single straight span. It is also pointed out that in most cases the geometric constants (along with the shear correction factors required to accurately model shear and STMD effects) included in the beam element formulation are computed through Thin Tube Theory (TTT) (see for example [5]). The accuracy of this theory depends on the thickness of the shell elements comprising the thin walled beam and sometimes leads to inaccuracies [2].

Thirdly, in most modelling efforts regarding beam assemblages taking into account nonuniform warping effects, the warping and bimoment transmission between nonaligned intersecting members is treated in a simplified manner. Often, the warping DOFs of the elements' nodes at the joint are considered as fully free or fully restrained. Another frequently employed consideration is the assumption of full warping and bimoment continuity at the joint. This assumption is reliable for example in the modelling of straight members with intermediate torsional supports. The actual transmission conditions depend on the geometry of the joint of intersecting members [6]. However, in many geometric configurations encountered in engineering practice [6-9] the aforementioned treatments are not realistic. Shell or 3-D finite element idealizations permit very accurate modelling of every possible geometric design, however their use is costly and complex as compared to beam element

models. Thus the beam elements to be used should be enhanced with general warping and bimoment transmission capabilities.

Several researchers have investigated in the past the problem of warping transmission at joints of intersecting members. Baigent and Hancock [10] investigated among others the case of members of channel shaped cross section attached by the web to a stiffened joint plate. Fully free warping for both members at the joint region is a reliable modelling consideration in this case. Krenk and Damkilde [11] investigated among others the case of members of I-shaped cross section intersecting at a joint with three stiffeners. This configuration is modelled accurately by employing fully restrained warping conditions at the joint region for both members. Yang and McGuire [12] proposed a procedure based on warping springs for analyzing space frames with partial warping restraint. Basaglia et al. [6] analyzed among others several geometric configurations which are accurately modelled with complete direct or inverse warping transmission considerations. Tong et al. [13] investigated the joint of intersecting I-shaped cross section beams having a diagonal stiffener. By taking into account the bending and torsional stiffness of the stiffener, they formulated general relations linking the bimoments and warping DOFs of the intersecting members. Vacharajittiphan and Trahair [14] investigated the coupling of warping and distortion in nonaligned intersecting members. To the authors' knowledge, all studies related to the investigation of warping transmission in which beam elements are employed, neglect shear and STMD effects, while TTT is most commonly employed to determine the torsional geometric constants.

In this paper a 3-D beam element including shear and secondary torsional moment deformation effects is formulated with general warping and bimoment transmission capabilities. The beam's cross section is an arbitrarily shaped doubly symmetric constant one, while its shape is assumed to remain undistorted. Shear deformation (due to shear forces) is taken into account employing shear correction factors determined through an energy approach. Secondary torsional moment deformation effects are modelled by introducing the primary angle of twist per unit length as an additional degree of freedom at each end node of the element and employing a torsional shear correction factor. An exact 14×14 stiffness matrix and the corresponding nodal load vector are formulated based on the solution of the global equilibrium differential equations of the beam. At joints connecting space members, all kinds of warping and bimoment transmission (not involving cross sectional distortion) are modelled, including free warping, full or partial warping restraint, full warping and bimoment continuity, complete direct and inverse warping transmission and general warping and bimoment transmission between intersecting members. A computer program is developed in a mathematical package permitting symbolic algebraic manipulations. Numerical results of great practical interest are worked out to illustrate the efficiency, the accuracy and the range of applications of the developed method.

2 STATEMENT AND SOLUTION OF THE PROBLEM

2.1 Local stiffness matrix and nodal load vector formulation

Consider a 3-D beam element of length l (Fig.1) with an arbitrarily shaped doubly symmetric constant cross section, occupying the two dimensional multiply connected region Ω of the y, z plane bounded by the Γ_j ($j = 1, 2, \dots, K$) boundary curves, which are piecewise smooth, i.e. they may have a finite number of corners. The material of the bar is homogeneous isotropic and linearly elastic with modulus of elasticity E and shear modulus G , while the effects of cross sectional distortion and geometrical nonlinearity are ignored. In Fig.1a Syz is the coordinate system through the cross section's shear center. The bar is subjected to the

combined action of arbitrarily distributed or concentrated transverse loads $p_y = p_y(x)$, $p_z = p_z(x)$ and bending moments $m_y = m_y(x)$, $m_z = m_z(x)$ acting in the y and z directions, respectively, axial load $p_x = p_x(x)$, twisting $m_x = m_x(x)$ and warping $m_w = m_w(x)$ moments acting in the x direction (Fig.1b).

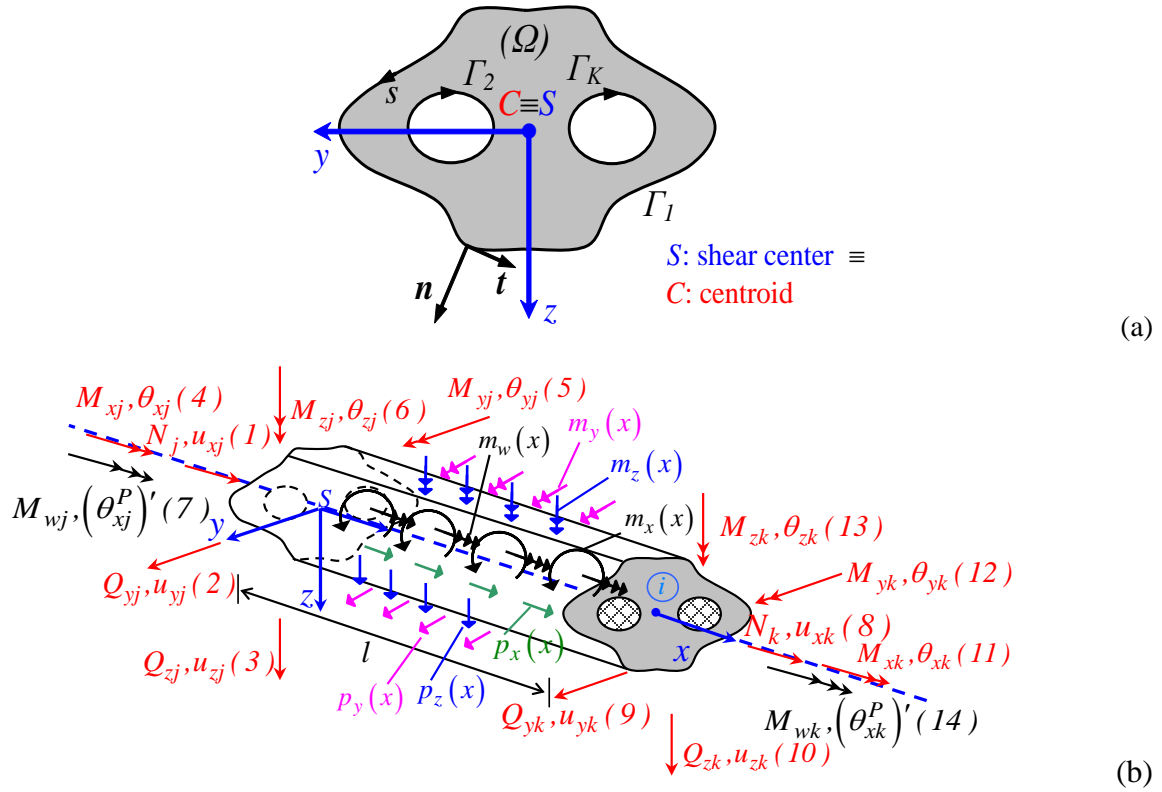


Figure 1: 3-D prismatic beam element with arbitrarily shaped doubly symmetric cross section occupying region Ω (a) subjected to general loading (b).

In order to take into account shear deformation effects in the study of the aforementioned element, the Timoshenko beam theory is employed along with the bending rotations θ_y , θ_z which are used as DOF at each end node (Fig.1b). θ_y , θ_z substitute the transverse displacement components per unit length u'_y , u'_z which are employed in the classic 3-D beam element based on the Euler - Bernoulli beam theory. Moreover, in order to take into account nonuniform (torsional) warping effects, an additional warping DOF is included at each end node of the element. In classic (Vlasov) nonuniform torsion theory, this DOF is the angle of twist per unit length θ'_x . In this paper, the primary angle of twist per unit length $(\theta_x^P)'$ is employed as additional DOF [1-2], permitting the inclusion of STMDE in the study of the element. This quantity is a 1-D measure of the intensity of warping of the cross section and its use is advantageous in the application of torsional boundary conditions, while in general $(\theta_x^P)' \neq \theta'_x$ with $(\theta_x^P)' - \theta'_x$ being a 1-D measure of the intensity of warping shear stresses.

From the above considerations, the local nodal displacement vector is expressed as (Fig.1b)

$$\{D^i\}^T = \left\{ u_{xj} \quad u_{yj} \quad u_{zj} \quad \theta_{xj} \quad \theta_{yj} \quad \theta_{zj} \quad (\theta_{xj}^P)' \quad u_{xk} \quad u_{yk} \quad u_{zk} \quad \theta_{xk} \quad \theta_{yk} \quad \theta_{zk} \quad (\theta_{xk}^P)' \right\} \quad (1)$$

along with the corresponding nodal load vector

$$\{F^i\}^T = \left\{ N_j \quad Q_{yj} \quad Q_{zj} \quad M_{xj} \quad M_{yj} \quad M_{zj} \quad M_{wj} \quad N_k \quad Q_{yk} \quad Q_{zk} \quad M_{xk} \quad M_{yk} \quad M_{zk} \quad M_{wk} \right\} \quad (2)$$

These vectors are linked with the 14x14 local exact stiffness matrix $[K^i]$ of the 3-D beam element [2]. This stiffness matrix is readily determined through a mathematical package [15] by solving analytically one global differential equation of equilibrium of axial forces and three systems of global differential equations of equilibrium of bending moments, transverse shear forces acting in the y and z directions, torsional and warping moments (see for example [1, 5]). This procedure results in a locking free element formulation [4]. The coefficients of these equations depend on the geometric constants of the element along with its shear correction factors which are employed to model shear and STMD effects [1-2]. These factors are determined through an energy approach [1-2]. The primary torsion constant, the warping constant and the shear correction factors depend on the primary and secondary warping functions and two stress functions which are determined from the numerical solution of four boundary value problems through BEM [2]. The adopted procedure is free from the assumptions of TTT. The aforementioned three systems of equations may be studied independently due to the assumption of geometrically linear conditions and the doubly symmetric shape of the cross section [16]. It is also worth noting that the nodal load vector is also readily computed analytically for frequently encountered distributions of externally applied actions along the length of the element. Finally, the local exact stiffness matrices and the corresponding nodal load vectors of the classic theories of nonuniform torsion (Vlasov) and flexure (Euler- Bernoulli) have also been formulated for comparison purposes.

After the solution of the problem and the determination of $\{D^i\}$, the stress resultants of the element may be readily computed through $[K^i]$. The primary and secondary twisting moments M_{xj}^P , M_{xj}^S are determined employing M_{xj} , $(\theta_{xj}^P)'$ as

$$M_{xj}^P = I_t^P \left(M_{xj} + G I_t^S (\theta_{xj}^P)' \right) / (I_t^P + I_t^S) \quad M_{xj}^S = M_{xj} - M_{xj}^P \quad (3a,b)$$

where I_t^P and I_t^S are the primary and secondary torsion constants [17], respectively, while it is noted that M_{xk}^P , M_{xk}^S may be computed through similar relations.

2.2 Global stiffness matrix formulation

The global stiffness matrix $[\bar{K}^i]$ linking the nodal displacement and load vectors at the global coordinate system is determined as

$$[\bar{K}^i] = [A_{SSFw}]^T [K^i] [A_{SSFw}] \quad (4)$$

where k_{w11} , k_{w21} , k_{w22} are stiffness parameters determined from the geometry of the joint.

v. Complete direct or indirect warping transmission (see for example [6]). In these cases the warping DOFs of the elements' nodes at a joint of intersecting space members have the same or the opposite value, respectively [6]. Here, the warping DOFs are initially treated as being independent to each other and the usual assembly procedure of the Direct Stiffness Method is followed. Then, the aforementioned relations are added as constraints to the global system of equations by means of the Lagrange multiplier technique [4, 6].

After taking into account the global stiffness matrices of the elements and the warping transmission conditions at joints of the structure under investigation, the usual assembly procedure of the Direct Stiffness Method is followed leading to the formulation of a global system of equations. This system is then solved and the unknown global nodal displacement vector of the structure is computed either symbolically or numerically. Afterwards, the usual post-processing procedure is followed in order to determine the remaining quantities of interest.

3 NUMERICAL EXAMPLES

Example 1

In the first example, a straight member of a thin walled hollow rectangular cross section previously studied by Murín and Kutis [3] has been analyzed in order to verify the accuracy of the results. The member is supported by two end and two intermediate simple torsional supports and is loaded by two concentrated torsional moments along its length [3]. The member has been modelled with 5 beam elements as in [3], while full warping and bimoment continuity is considered at the nodes of the member. The geometric constants reported by Murín and Kutis [3] and computed through TTT have been employed in order to verify the accuracy of the proposed method ($I_t^P = 8.9824 \times 10^{-2} m^4$, $I_t^S = 1.107 \times 10^{-3} m^4$, $C_S = 1.930 \times 10^{-4} m^6$).

In Table 1, the angle of twist and the primary angle of twist per unit length at the nodes are presented as obtained from the proposed method and from Murín and Kutis [3]. It is observed that the agreement between the two methods is excellent. In Table 2, the stress resultants at the beam elements' nodes are reported as obtained from the aforementioned methods, noting the good agreement of the results. In the same table, the corresponding results of the proposed method obtained by employing the geometric constants as they have been computed through BEM ($I_t^P = 9.133 \times 10^{-2} m^4$, $I_t^S = 1.347 \times 10^{-3} m^4$, $C_S = 2.273 \times 10^{-4} m^6$) are also presented. Significant discrepancies between the corresponding nonuniform torsional stress resultants obtained from the two methods are observed. Moreover, it is concluded that torsional loading is undertaken mainly through the primary torsional mechanism. However, the warping normal and shear stresses reach significant values locally [3], thus the secondary torsional mechanism and STMDE should not be neglected in stress analysis of bars of closed shaped thin walled cross sections.

Example 2

In the second example, a two member right angle frame previously studied by Tong et al. [13] has been analyzed in order to verify the accuracy of the results and demonstrate the range of applications of the developed method. The cross sections of both the beam and the column are thin walled I-shaped ones with total height $h = 0.300m$, total width $b = 0.150m$, flange width $t_f = 0.008m$ and web width $t_w = 0.006m$ ($A = 4.104 \times 10^{-3} m^2$, $A_y = 2.003 \times 10^{-3} m^2$,

$A_z = 1.687 \times 10^{-3} m^2$, $I_{yy} = 6.262 \times 10^{-5} m^2$, $I_{zz} = 4.505 \times 10^{-6} m^2$, $I_t^P = 7.094 \times 10^{-8} m^4$, $I_t^S = 4.303 \times 10^{-5} m^4$, $C_S = 9.592 \times 10^{-8} m^6$), while the joint of the intersecting members has a diagonal stiffener of width $t = 0.008m$ [13]. The right free end of the beam is loaded with a concentrated bimoment load, while the column bottom node is fully clamped. The beam and column have the same length of $l_b = l_c = 2.0m$ and are each modelled with one element, while general warping and bimoment continuity is considered at the joint.

Node	$\theta_x (\times 10^{-3} rad)$		$(\theta_x^P)' (\times 10^{-3} m^{-1})$	
	Murín and Kutis [3]	Present - geometric constants with TTT	Murín and Kutis [3]	Present - geometric constants with TTT
1	0	0	0.00185	0.001851
2	0.00412	0.00412	-4.801×10^{-6}	-4.801×10^{-6}
3	0	0	-0.00195	-0.001947
4	-0.00721	-0.00721	-4.20×10^{-6}	-4.200×10^{-6}
5	0	0	0.00102	0.001021
6	0	0	3.470×10^{-6}	3.471×10^{-6}

Table 1: Angle of twist and primary angle of twist per unit length of the member of example 1.

Elem. side	$M_w (kNm^2)$			$M_x^P (kNm)$			$M_x^S (kNm)$		
	Murín and Kutis [3]	Present - geom. const. with TTT	Present - geom. const. with BEM	Murín and Kutis [3]	Present - geom. const. with TTT	Present - geom. const. with BEM	Murín and Kutis [3]	Present - geom. const. with TTT	Present - geom. const. with BEM
1-2	0.0	0.0	0.0	14.9824	14.9808	14.9780	0.01907	0.02062	0.02363
2-1	0.12335	0.12333	0.14506	14.8183	14.8184	14.7831	0.18309	0.18305	0.21845
2-3	0.12335	0.12333	0.14506	-14.8164	-14.8164	-14.7809	-0.1822	-0.18217	-0.21750
3-2	0.00571	0.00571	0.00644	-14.9880	-14.9864	-14.9844	-0.01059	-0.01223	-0.01402
3-4	0.00571	0.00571	0.00644	-14.9816	-14.9800	-14.9767	-0.01051	-0.01215	-0.01391
4-3	-0.12335	-0.12331	-0.14504	-14.8099	-14.8100	-14.7731	-0.18218	-0.18215	-0.21746
4-5	-0.12335	-0.12331	-0.14504	14.8248	14.8248	14.7907	0.18311	0.18307	0.21849
5-4	0.06125	0.06124	0.07210	14.9154	14.9146	14.8980	0.0925	0.09335	0.11136
5-6	0.06125	0.06124	0.07210	0.07511	0.07424	0.08899	-0.09042	-0.08955	-0.10701
6-5	0.0	0.0	0.0	-0.01482	-0.01482	-0.01749	-0.00049	-0.00049	-0.00054

Table 2: Warping, primary and secondary twisting moments of the member of example 1.

At first, following the methodology of Tong et al. [13] the stiffness parameters of the link element modelling the joint are computed as $k_{w11} = k_{w22} = 50.780 knm^3$, $k_{w21} = -47.857 knm^3$. Subsequently, the structure is analyzed with beam elements taking into account or ignoring both shear and STMD effects. In Figs. 2 and 3, the angle of twist along the beam and the column, respectively, are presented as obtained from the proposed method, from the method of Tong et al. [13] where shear and STMD effects are ignored and from a FEM solution with shell elements reported in [13]. It is observed that the agreement between

the corresponding results of the two methods based on beam elements is excellent, verifying the accuracy of the proposed method. Moreover, it is noted that the results of the present method taking into account or ignoring shear and STMD effects practically coincide, demonstrating that these effects are negligible in this example. As expected, it is also deduced that the present formulation is free from locking effects. The agreement of these results with the ones of the FEM solution with shell elements is noteworthy, concluding the reliability of the proposed method. Finally, a solution with symbolic algebraic manipulations has also been established in the examined problem yielding the same results.

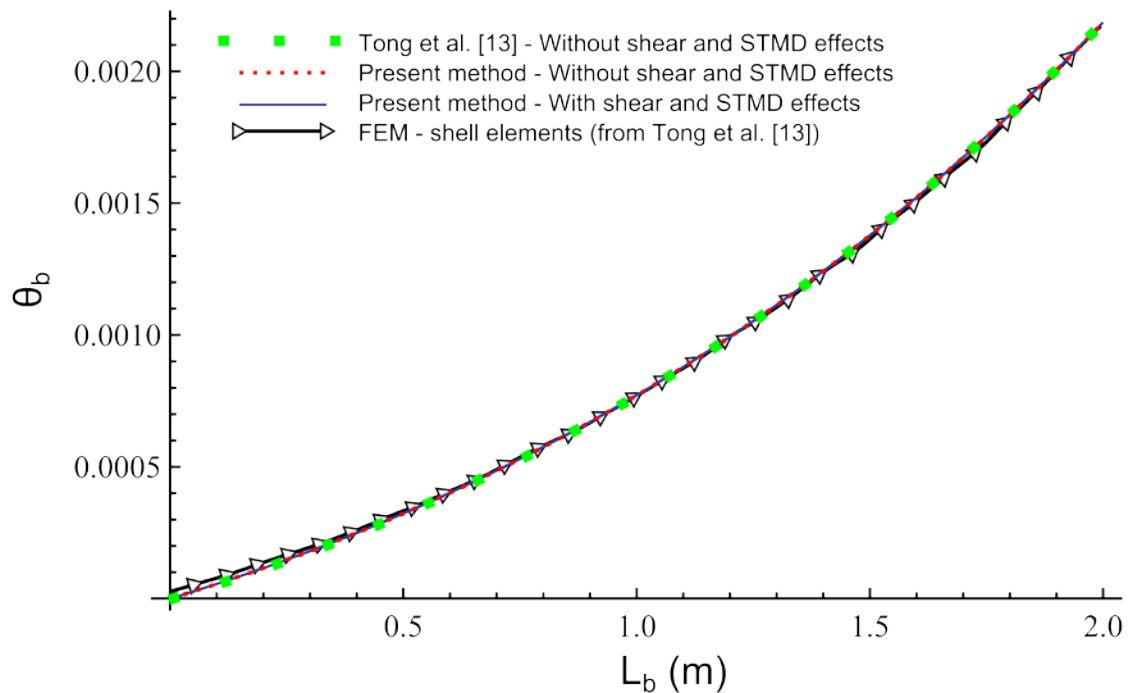


Figure 2: Angle of twist (rad) along the beam of the frame of example 2.

4 CONCLUSIONS

The main conclusions that can be drawn from this investigation are

- The proposed method may effectively analyze space beam assemblages and beams of arbitrarily shaped doubly symmetric cross section taking into account general warping and bimoment transmission conditions, shear and secondary torsional moment deformation effects.
- The employed local stiffness matrix is determined analytically through the solution of global differential equations of equilibrium resulting in a locking free element formulation.
- The developed computer program permits the solution of the problem through symbolic algebraic manipulations.
- The agreement of the developed procedure with previously reported results is noteworthy.
- The discrepancy between the torsional geometric constants computed through BEM and TTT affects notably the nonuniform torsional stress resultants of closed shaped thin walled cross section beams.

- The secondary torsional mechanism and secondary torsional moment deformation effects should not be neglected in stress analysis of beams of closed shaped thin walled cross sections.

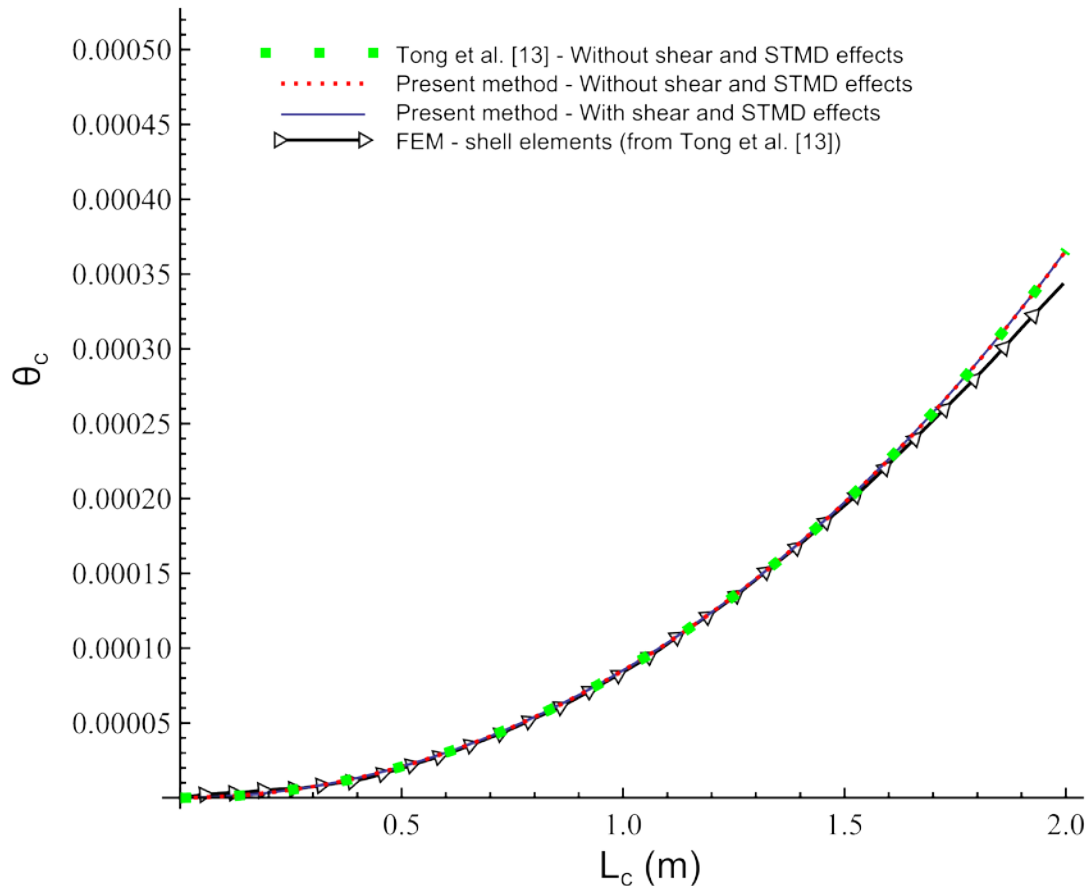


Figure 3: Angle of twist (rad) along the column of the frame of example 2.

ACKNOWLEDGEMENTS

This research has been co-financed by the European Union (European Social Fund - ESF) and Greek national funds through the Operational Program “Education and Lifelong Learning” of the National Strategic Reference Framework (NSRF) - Research Funding Program: THALES: Reinforcement of the interdisciplinary and/or inter-institutional research and innovation.

REFERENCES

- [1] V.G. Mokos and E.J. Sapountzakis, Secondary torsional moment deformation effect by BEM. *International Journal of Mechanical Sciences*, **53**, 897-909, 2011.
- [2] V.G. Mokos and E.J. Sapountzakis, A three-dimensional beam including torsional warping and shear deformation effects arising from shear forces and secondary torsional moments, *Proceedings of the 13th International Conference on Civil, Structural and Environmental Engineering Computing*, Chania, Crete, Greece, September 6-9, 2011.

- [3] J. Murín and V. Kutis, An Effective Finite Element for Torsion of Constant Cross-Sections Including Warping With Secondary Torsion Moment Deformation Effect, *Engineering Structures*, **30**, 2716-2723, 2008.
- [4] K.-J. Bathe, *Finite element procedures*, Prentice Hall, 1996.
- [5] N. Kim and M. Kim, Exact dynamic/static stiffness matrices of non-symmetric thin-walled beams considering coupled shear deformation effects, *Thin-Walled Structures*, **43**, 701-734, 2005.
- [6] C. Basaglia, D. Camotim and N. Silvestre, Torsion warping transmission at thin-walled frame joints: Kinematics, modelling and structural response, *Journal of Constructional Steel Research*, **69**, 39-53, 2012.
- [7] P.J.B. Morrell, J.R. Riddington, F.A. Ali and H.A. Hamid, Influence of joint detail on the flexural/torsional interaction of thin-walled structures, *Thin-Walled Structures*, **24**, 97-111, 1996.
- [8] S. Choi, G.-W. Jang and Y.Y. Kim, Exact matching condition at a joint of thin-walled box beams under out-of-plane bending and torsion, *Journal of Applied Mechanics, Transactions ASME*, **79**, art. no. 51018, 2012.
- [9] I.J. MacPhedran, Frame stability considering member interaction and compatibility of warping deformations, PhD thesis, University of Alberta, Edmonton, Canada, 2009.
- [10] A.H. Baigent and G.J. Hancock, Structural analysis of assemblages of thin-walled members, *Engineering Structures*, **4**, 207-216, 1982.
- [11] S. Krenk and L. Damkilde, Warping of joints in I-beam assemblages, *Journal of Engineering Mechanics*, **117**, 2457-2474, 1991.
- [12] Y.-B. Yang and W. McGuire, Procedure for analysing frames with partial warping restraint, *International Journal for Numerical Methods in Engineering*, **20**, 1377-1398, 1984.
- [13] G.S. Tong, X.X. Yan and L. Zhang, Warping and bimoment transmission through diagonally stiffened beam-to-column joints, *Journal of Constructional Steel Research*, **61**, 749-763, 2005.
- [14] P. Vacharajittiphan and N.S. Trahair, Warping and distortion at I-section joints, *ASCE J Struct Div*, **100** (ST3), 547-564, 1974.
- [15] Mathematica 8, Wolfram, 2011
- [16] F. Minghini, N. Tullini and F. Laudiero, Locking-free finite elements for shear deformable orthotropic thin-walled beams, *International Journal for Numerical Methods in Engineering*, **72**, 808-834, 2007.
- [17] V.J. Tsipiras and E.J. Sapountzakis, Secondary Torsional Moment Deformation Effect in Inelastic Nonuniform Torsion of Bars of Doubly Symmetric Cross Section by BEM, *International Journal of Non-Linear Mechanics*, **47**, 68-84, 2012.
- [18] S. Rao, *The finite element method in engineering, 4th edition*, Elsevier Science & Technology books, 2004.

A HYBRID DISPLACEMENT BOUNDARY ELEMENT FORMULATION FOR REISSNER PLATE WITH QUADRATIC ELEMENTS

Taha H. A. Naga¹, Youssef F. Rashed^{2*}

¹Department of engineering mathematics and physics, Faculty of engineering –Shoubra, Benha University, Egypt.

E-mail: thnaga@ymail.com, Tel.: 00 20 109 8747059

² Department of structural engineering, Cairo University, Giza, Egypt.

* Corresponding Author , E-mail: youssef@eng.cu.edu.eg, Tel.: 00 20 100 5112949

Keywords: Boundary element method, Variational formulation, Shear-deformable plates, Stiffness matrix.

Abstract. This paper presents the derivation of a new boundary element formulation for plate bending problems. The Reissner's plate bending theory is employed. Unlike the conventional direct or indirect formulations, the proposed integral equation is based on minimizing the relevant energy functional. In doing so, variational methods are used. A collocation based series, similar to the one used in the indirect discrete boundary element method, is used to remove domain integrals. Hence, a fully boundary integral equation is formulated. The main advantage of the proposed formulation is production of a symmetric stiffness matrix similar to that obtained in the finite element method. Numerical examples are presented to demonstrate the accuracy and the validity of the proposed formulation.

1. INTRODUCTION

Concerning the application of the BEM for thick plate bending problems, the direct boundary element formulation originally developed by Vander Weeën [1]. Hence, several applications were considered based on this theory; for example: Barcellos and Silva [2] extended the formulation to Mindlin plates. El-Zafrany et al. [3] divided the formulation into kernels for thin and others for thick plates. Ribeiro and Venturini [4] discussed the application of elasto-plastic analysis to the direct formulation. Westphal et al. [5] studied the fundamental solution used in plates. Marczak and Creus [6] considered the evaluation of singular integrals in the direct integral equation formulation. Fernandes and Konda [7] coupled the formulation with beams. To the author's best knowledge, none of these formulations considered a variational boundary integral formulation for the thick Reissner's plate bending.

This paper presents the derivation and verifications of new boundary element formulation for plate bending problems. Unlike the conventional formulations, the proposed formulation is based on generalized variational principle. The Reissner's plate bending model is employed. It is considered a boundary element model because the final integral equation involves some boundary integrals that require a boundary discretization evaluation in order to be evaluated. Furthermore, all the unknowns are boundary variables. The model is completely new. It differs from the classical boundary element formulation in the way it is generated and consequently in the final equations. A generalized variational principle is used as a basis for its derivation, whereas the conventional boundary element formulation is based on Green's formula.

2. THE PROPOSED BEM HYBRID DISPLACEMENT FORMULATION

The energy functional for the Reissner's plate bending problems could be obtained as follows (Dym and Shamed [8]):

$$\begin{aligned}
 \Pi_3(u_i(\mathbf{y}), \tilde{u}_i(\mathbf{x}), \tilde{p}_i(\mathbf{x})) &= \int_{\Omega(\mathbf{y})} \frac{1}{2} (M_{\alpha\beta}(\mathbf{y}) \chi_{\alpha\beta}(\mathbf{y}) + Q_{3\alpha}(\mathbf{y}) \psi_{3\alpha}(\mathbf{y})) d\Omega(\mathbf{y}) \\
 &- \int_{\Omega(\mathbf{y})} b_i(\mathbf{y}) u_i(\mathbf{y}) d\Omega(\mathbf{y}) - \int_{\Gamma_p(\mathbf{x})} \bar{p}_i(\mathbf{x}) \tilde{u}_i(\mathbf{x}) d\Gamma(\mathbf{x}) \\
 &+ \int_{\Gamma(\mathbf{x})} \tilde{p}_i(\mathbf{x}) (\tilde{u}_i(\mathbf{x}) - u_i(\mathbf{x})) d\Gamma(\mathbf{x})
 \end{aligned} \tag{1}$$

After integrating by parts the first two domain integral on the right hand side of equation (1) could be converted into boundary integrals (Rashed and Brebbia [9]) and taking into consideration the symmetry of the moment stress-resultant tensor and regrouping, equation (1) can be written as:

$$\begin{aligned}
 \Pi_3(u_i(\mathbf{y}), \tilde{u}_i(\mathbf{x}), \tilde{p}_i(\mathbf{x})) &= \int_{\Gamma(\mathbf{y})} \frac{1}{2} u_i(\mathbf{y}) p_i(\mathbf{y}) d\Gamma(\mathbf{y}) - \int_{\Omega(\mathbf{y})} \frac{1}{2} M_{\alpha\beta,\beta}(\mathbf{y}) u_\alpha(\mathbf{y}) d\Omega(\mathbf{y}) \\
 &- \int_{\Omega(\mathbf{y})} \frac{1}{2} Q_{3\alpha,\alpha}(\mathbf{y}) u_3(\mathbf{y}) d\Omega(\mathbf{y}) - \int_{\Omega(\mathbf{y})} b_i(\mathbf{y}) u_i(\mathbf{y}) d\Omega(\mathbf{y}) \\
 &- \int_{\Gamma_P(\mathbf{x})} \tilde{u}_i(\mathbf{x}) \tilde{p}_i(\mathbf{x}) d\Gamma(\mathbf{x}) + \int_{\Gamma(\mathbf{x})} \tilde{p}_i(\mathbf{x}) \tilde{u}_i(\mathbf{x}) d\Gamma(\mathbf{x}) \\
 &- \int_{\Gamma(\mathbf{x},\mathbf{y})} \tilde{p}_i(\mathbf{x}) u_i(\mathbf{y}) d\Gamma(\mathbf{x},\mathbf{y})
 \end{aligned} \tag{2}$$

The first four integrals in equation (2) involve the domain variables $u_i(\mathbf{x}), p_i(\mathbf{x})$. The following two integrals, involve the boundary variables $\tilde{p}_i(\mathbf{x}), \tilde{u}_i(\mathbf{x})$ and the last integral involves both the domain and boundary variables.

A new variational boundary element formulation for the Ressiner plate bending model is obtained by representing the three independent field variables $u_i, \tilde{p}_i, \tilde{u}_i$ via approximate schemes. Hence variational principles are used to minimize the functional Π_3 . The stationary condition (that corresponds to the equilibrium condition) for such a functional represents an approximate integral equation of the problems to approximate the domain terms ($u_i(\mathbf{y}), p_i(\mathbf{y})$ in which $\mathbf{y} \in \Omega(\mathbf{y})$) in the first four integrals in equation (25). As in the indirect boundary element or the super-position formulation for Ressiner's plate bending problems (Mohareb and Rashed[10]), the rotation and the displacement components vector at any point (\mathbf{y}) inside the domain Ω could be approximated via a collection series. This series contains the product of fundamental solution ($U_{ki}^*(\mathbf{y}, \xi_n)$) and an unknown set of fictitious concentrated tractions ($\gamma_k(\xi_n)$) located at a set of arbitrary source points (ξ_n), as follows:

$$u_i(\mathbf{y}) = U_{ki}^*(\mathbf{y}, \xi_n) \gamma_k(\xi_n) \tag{3}$$

Where the subscript (n) denotes arbitrary set of source points (its number could be taken later as the number of boundary nodes N) in which the fictitious tractions are applied along the direction (x_k).

In a similar way, the traction components at any point (\mathbf{y}) inside the domain Ω could be approximated via a collection series containing the products of fundamental solution ($P_{ki}^*(\mathbf{y}, \xi_n)$) and the same unknown fictitious concentrated tractions ($\gamma_k(\xi_n)$) which are located at the same set of points (ξ_n), as follows:

$$p_i(\mathbf{y}) = P_{ki}^*(\mathbf{y}, \xi_n) \gamma_k(\xi_n) \tag{4}$$

Using the representation given in equations (3) and (4), the first integral on the right hand side of equation (2) could be re-written as follows:

$$\begin{aligned}
 \int_{\Gamma(\mathbf{y})} \frac{1}{2} u_i(\mathbf{y}) p_i(\mathbf{y}) d\Gamma(\mathbf{y}) \\
 &= \frac{1}{2} \gamma_k(\xi_n) \left[\int_{\Gamma(\mathbf{y})} U_{ki}^*(\mathbf{y}, \xi_n) P_{mi}^*(\mathbf{y}, \xi_n) d\Gamma(\mathbf{y}) \right] \gamma_m(\xi_n) \\
 &= \frac{1}{2} \{\mathbf{Y}\}_{1 \times 3N}^T [\mathbf{F}]_{3N \times 3N} \{\mathbf{Y}\}_{3N \times 1}
 \end{aligned} \tag{5}$$

where,

$$[\mathbf{F}]_{3N \times 3N} = \int_{\Gamma(\mathbf{y})} U_{ki}^*(\mathbf{y}, \xi_n) P_{mi}^*(\mathbf{y}, \xi_n) d\Gamma(\mathbf{y}) \tag{6}$$

In which (N) is the number of boundary points.

The second and third domain integrals on the right hand side of the equation (2) are set to zeros. This is done by making use of considered approximations in equations (3, 4) and placing the source points (ξ_n) outside the plate boundary therefore:

$$\int_{\Omega(\mathbf{y})} \frac{1}{2} M_{\alpha\beta,\beta}(\mathbf{y}) u_\alpha(\mathbf{y}) d\Omega(\mathbf{y}) = 0 \tag{7}$$

and

$$\int_{\Omega(\mathbf{y})} \frac{1}{2} Q_{3\alpha,\alpha}(\mathbf{y}) u_3(\mathbf{y}) d\Omega(\mathbf{y}) = 0 \tag{8}$$

The last domain integral in equation (2) could be represented as follows:

$$\begin{aligned}
 \int_{\Omega(\mathbf{x})} b_i(\mathbf{y}) u_i(\mathbf{y}) d\Omega(\mathbf{y}) &= \gamma_k(\xi_n) \left[\int_{\Omega(\mathbf{y})} U_{ki}^*(\mathbf{y}, \xi_n) b_i(\mathbf{y}) d\Omega(\mathbf{y}) \right] \\
 &= \{\mathbf{Y}\}_{1 \times 3N}^T \{\mathbf{B}\}_{3N \times 1}
 \end{aligned} \tag{9}$$

where

$$\{\mathbf{B}\}_{3N \times 1} = \int_{\Omega(\mathbf{y})} U_{ki}^*(\mathbf{y}, \xi_n) b_i(\mathbf{y}) d\Omega(\mathbf{y}) \tag{10}$$

It has to be noted that the vector $\{\mathbf{B}\}$ in equation (10) is similar to the one that appears in the classical direct boundary element method (Brebbia *et al.* [12]) and could be transformed to the boundary using similar ways as those given by Rashed and Brebbia [9].

The boundary displacement and traction vectors denoted by (\tilde{u}_i) and (\tilde{p}_i) are approximated using quadratic boundary elements therefore:

$$\tilde{u}_i(\boldsymbol{\eta}) = \sum_{j=1}^{j=3} \phi^j(\boldsymbol{\eta}) u_i^j(\mathbf{x}_e) \quad \forall \mathbf{x} \text{ in } \Gamma_e \tag{11}$$

$$\tilde{p}_i(\boldsymbol{\eta}) = \sum_{j=1}^{j=3} \phi^j(\boldsymbol{\eta}) p_i^j(\mathbf{x}_e) \quad \forall \mathbf{x} \text{ in } \Gamma_e \tag{12}$$

Where, $u_i^j(x_e)$ and $p_i^j(x_e)$ are vectors whose components are nodal(x_e) values for boundary displacements and boundary tractions.

Using the representation given in equations (11) and (12), the fifth integral of equation (2) could be re-written as follows:

$$\int_{\Gamma_P(\mathbf{x})} \tilde{u}_i(\mathbf{x}) \bar{p}_i(\mathbf{x}) d\Gamma(\mathbf{x}) = \sum_{\text{elements } (\Gamma_e)} \{u_i^j(\mathbf{x}_e)\}^T \int_{\Gamma_e(\mathbf{x}_e)} \phi^j(\boldsymbol{\eta}) \bar{p}_i(\mathbf{x}_e) d\Gamma(\mathbf{x}_e) \quad (13)$$

$$= \{\mathbf{u}\}_{1 \times 3N}^T \{\bar{\mathbf{P}}\}_{3N \times 1} \quad (14)$$

where

$$\{\bar{\mathbf{P}}\}_{3N \times 1} = \int_{\Gamma_e(\mathbf{x}_e)} \phi^j(\boldsymbol{\eta}) \bar{p}_i(\mathbf{x}_e) d\Gamma(\mathbf{x}_e) \quad (15)$$

In which (N) is the number of the used boundary elements nodes. The sixth integral of equation (2) could be re-written as follows:

$$\int_{\Gamma_P(\mathbf{x})} \tilde{p}_i(\mathbf{x}) \tilde{u}_i(\mathbf{x}) d\Gamma(\mathbf{x}) = \sum_{\text{elements } (\Gamma_e)} \{p_i^j(\mathbf{x}_e)\}^T \left[\int_{\Gamma_e(\mathbf{x}_e)} [\psi^j(\boldsymbol{\eta})][\phi^j(\boldsymbol{\eta})]^T d\Gamma(\mathbf{x}_e) \right] u_i(\mathbf{x}_e) \quad (16)$$

$$= \{\mathbf{p}\}_{1 \times 3N}^T [\mathbf{L}]_{3N \times 3N} \{\mathbf{u}\}_{3N \times 1} \quad (17)$$

Where

$$[\mathbf{L}]_{3N \times 3N} = \int_{\Gamma_e(\mathbf{x}_e)} [\psi^j(\boldsymbol{\eta})][\phi^j(\boldsymbol{\eta})]^T d\Gamma(\mathbf{x}_e) \quad (18)$$

The last integral of equation (2) could be approximated as follows:

$$= \sum_{\text{elements } (\Gamma_e)} \{p_i^j(\mathbf{x}_e)\}^T \left[\int_{\Gamma_e(\mathbf{x}_e)} \psi^j(\boldsymbol{\eta}) U_{ki}^*(\mathbf{x}_e, \boldsymbol{\xi}_n) d\Gamma(\mathbf{x}_e) \right] \gamma_k(\boldsymbol{\xi}_n) \quad (19)$$

$$= \{\mathbf{p}\}_{1 \times 3N}^T [\mathbf{G}]_{3N \times 3N}^T \{\boldsymbol{\gamma}\}_{3N \times 1} \quad (20)$$

Where

$$[\mathbf{G}]_{3N \times 3N}^T = \int_{\Gamma_e(\mathbf{x}_e)} \psi^j(\boldsymbol{\eta}) U_{ki}^*(\mathbf{x}_e, \boldsymbol{\xi}_n) d\Gamma(\mathbf{x}_e) \quad (21)$$

It has to be noted that the matrix $[\mathbf{G}]$ in equation (21) is similar to the one that appears in the classical direct boundary element method (Karam and Telles [12]).

Using the approximations in equations (5, 7, 8, 9, 14, 17 and 20), equation (2) could be re-written as follows:

$$\Pi_3 = \frac{1}{2} \{\boldsymbol{\gamma}\}^T [\mathbf{F}] \{\boldsymbol{\gamma}\} - \{\mathbf{u}\}^T \{\bar{\mathbf{P}}\} + \{\mathbf{p}\}^T [\mathbf{L}] \{\mathbf{u}\} - \{\mathbf{p}\}^T [\mathbf{G}]^T \{\boldsymbol{\gamma}\} - \{\boldsymbol{\gamma}\}^T \{\mathbf{B}\} \quad (22)$$

The final system of algebraic equations could be obtained by computing the stationary conditions associate with Π_3 in equation (22). This can be obtained by taking the first variation of equation (22) as follows:

$$\delta\Pi_3 = \{\delta\boldsymbol{\gamma}\}^T([\mathbf{F}]\{\boldsymbol{\gamma}\} - [\mathbf{G}]\{\mathbf{p}\} - \{\mathbf{B}\}) + \{\delta\mathbf{u}\}^T([\mathbf{L}]^T\{\mathbf{p}\} - \{\bar{\mathbf{P}}\}) + \{\delta\mathbf{p}\}^T([\mathbf{L}]\{\mathbf{u}\} - [\mathbf{G}]^T\{\boldsymbol{\gamma}\}) \quad (23)$$

The functional Π_3 is stationary when its first variation $\delta\Pi_3$ vanishes for any arbitrary values of $(\delta\boldsymbol{\gamma}(\boldsymbol{\xi}_n), \delta\mathbf{u}(\mathbf{x})$ and $\delta\mathbf{p}(\mathbf{x}))$. Therefore the corresponding generalized Euler's equations are

$$[\mathbf{F}]\{\boldsymbol{\gamma}\} - [\mathbf{G}]\{\mathbf{p}\} - \{\mathbf{B}\} = 0 \quad (24)$$

$$[\mathbf{L}]^T\{\mathbf{p}\} - \{\bar{\mathbf{P}}\} = 0 \quad (25)$$

$$[\mathbf{L}]\{\mathbf{u}\} - [\mathbf{G}]^T\{\boldsymbol{\gamma}\} = 0 \quad (26)$$

The unknown vectors $\{\boldsymbol{\gamma}\}$ and $\{\mathbf{p}\}$ are expressed in terms of the vector $\{\mathbf{p}\}$ to obtain a final system of equations involving only the boundary unknown vector $\{\mathbf{p}\}$. Provided that the matrix $[\mathbf{G}]$ is not singular (Karam and Telles [12]), equation (26) could be re-written as follows:

$$\{\boldsymbol{\gamma}\} = [[\mathbf{G}]^T]^{-1}[\mathbf{L}]\{\mathbf{u}\} \quad (27)$$

Substituting equation (27) into equation (24) gives:

$$\{\mathbf{p}\} = [\mathbf{G}]^{-1}[\mathbf{F}][[\mathbf{G}]^T]^{-1}[\mathbf{L}]\{\mathbf{u}\} - [\mathbf{G}]^{-1}\{\mathbf{B}\} \quad (28)$$

Substituting equation (28) into equation (25) gives:

$$[\mathbf{L}]^T[\mathbf{G}]^{-1}[\mathbf{F}][[\mathbf{G}]^T]^{-1}[\mathbf{L}]\{\mathbf{u}\} - [\mathbf{L}]^T[\mathbf{G}]^{-1}\{\mathbf{B}\} - \{\bar{\mathbf{P}}\} = 0 \quad (29)$$

Introducing the following definitions:

$$[\mathbf{R}] = [[\mathbf{G}]^T]^{-1}[\mathbf{L}] \quad (30)$$

Hence equation (29) could be re-written as follows:

$$[\mathbf{R}]^T[\mathbf{F}][\mathbf{R}]\{\mathbf{u}\} - [\mathbf{R}]^T\{\mathbf{B}\} - \{\bar{\mathbf{P}}\} = 0 \quad (31)$$

Defining:

$$[\mathbf{K}] = [\mathbf{R}]^T[\mathbf{F}][\mathbf{R}] \quad (32)$$

and

$$\{\mathbf{Q}\} = [\mathbf{R}]^T\{\mathbf{B}\} + \{\bar{\mathbf{P}}\} \quad (33)$$

Hence, equation (29) could be re-written as follows:

$$[\mathbf{K}]_{3N \times 3N} \{\mathbf{u}\}_{3N \times 1} = \{\mathbf{Q}\}_{3N \times 1} \quad (34)$$

It has been noted that the obtained $[\mathbf{K}]$ or the stiffness matrix is symmetric, positive definite and similar to the one obtained from the finite element method (Zienkiewicz [13]). The vectors $\{\mathbf{u}\}$ and $\{\mathbf{Q}\}$ are the corresponding vectors of boundary displacements and forces.

3. SOLUTION AT INTERNAL POINTS

After solving equation (34), the vector $\{\boldsymbol{\gamma}\}$ is computed from equation (27). Hence the internal displacement vector at any point (\mathbf{y}) inside the domain (Ω) is computed using equation (3) as follows:

$$u_{\alpha}(\mathbf{y}) = U_{k\alpha}^*(\mathbf{y}, \xi_n)\gamma_k(\xi_n) \quad (35)$$

$$u_3(\mathbf{y}) = U_{k3}^*(\mathbf{y}, \xi_n)\gamma_k(\xi_n) \quad (36)$$

Stress resultants at any point (\mathbf{y}) inside the domain (Ω) are computed after carrying out relevant derivatives as follows:

$$u_{\alpha,\gamma}(\mathbf{y}) = U_{k\alpha,\gamma}^*(\mathbf{y}, \xi_n)\gamma_k(\xi_n) \quad (37)$$

and

$$u_{3,\gamma}(\mathbf{y}) = U_{k3,\gamma}^*(\mathbf{y}, \xi_n)\gamma_k(\xi_n) \quad (38)$$

Expanding the index (k) to (β) and (3) gives:

$$u_{\alpha,\gamma}(\mathbf{y}) = U_{\beta\alpha,\gamma}^*(\mathbf{y}, \xi_n)\gamma_{\beta}(\xi_n) + U_{3\alpha,\gamma}^*(\mathbf{y}, \xi_n)\gamma_3(\xi_n) \quad (39)$$

and

$$u_{3,\gamma}(\mathbf{y}) = U_{\beta 3,\gamma}^*(\mathbf{y}, \xi_n)\gamma_{\beta}(\xi_n) + U_{33,\gamma}^*(\mathbf{y}, \xi_n)\gamma_3(\xi_n) \quad (40)$$

The new derivatives $U_{\alpha\beta,\gamma}^*$, $U_{3\alpha,\gamma}^*$, $U_{\beta 3,\gamma}^*$, $U_{33,\gamma}^*$ are given in the appendix. It has to be noted that unlike the direct boundary element method (Vander Weeën [1]), all relevant derivatives herein are carried out with respect to the coordinate of the field point ($x_{\gamma}(\mathbf{y})$).

4. NUMERICAL EXAMPLES

4.1 Clamped circular plate subject to domain load

A thin, circular plate (radius a , thickness t , Young's modulus E) is clamped along its outer boundary as shown in Figure 1 and is subject to a uniformly distributed load with intensity $P=P_0$. The results for the generalized displacements at points (A and B) are evaluated by using different meshes and presented in table (1) together with analytical values and results obtained from the convention direct boundary elements using quadratic elements is given by Rashed [14].

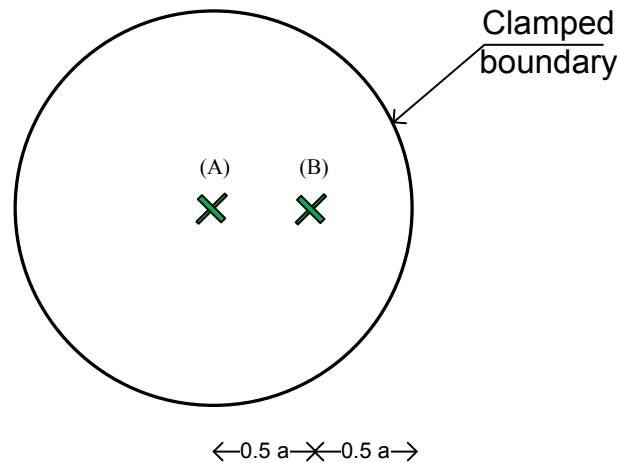


Figure 1: Clamped circular plate subjected to domain load

	$u_3(A) \times \frac{128D}{qa^4}$	$u_3(B) \times \frac{128D}{qa^3}$
Analytical solution	2	1.125
Presented BEM	2.0358	1.1356
Conv. direct. BEM [Rashed (2000)]	2.0307	1.1539
Finite element method	2.0375	1.1356

Table 1: Results for the generalized displacements at point (A, B)

It can be seen from Tables (1) that results for the present variational formulation and conventional boundary element method is accurate with respect to the analytical values.

4.2 Square plate with a square central opening

A square plate with a square central opening is subjected to a uniform surface load p . The external edges of the plate are simply supported and the internal edges are free, as shown in Figure 2-a) the deflection at the points A, B, and C are calculated. The results are evaluated by using mesh indicated in Figure 2-b) and presented in Table (2) together with results obtained from the conventional direct boundary element method, finite element method and the Finite difference method which given by Tottenham [15], Assume Poisson's ratio ν equal to 1/6.

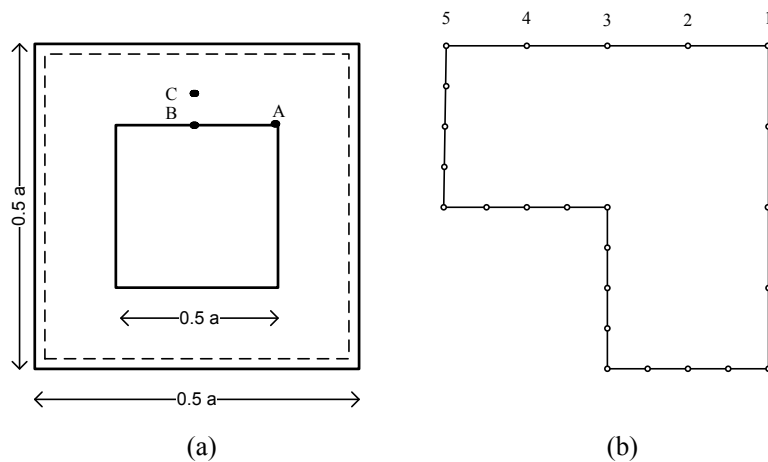


Figure 2 Square plate with central opening subjected to domain load

Displacement (x pa/100D)					
Boundary element method					
Point	Presented BEM	Indirect	Direct	Finite element method	Finite difference method
A	0.21802	0.2188	0.2191	0.2185	0.2174
B	0.2807	0.3107	0.2818	0.3156	0.3006
C	0.1535	0.1558	0.1559	-	0.1541

Table 2: Results for the generalized displacements at point (A, B, C)

It can be seen from Tables (2) that results for for the present variational formulation, conventional boundary element method, finite element method and finite difference method are in good agreement.

4.3 Curved Plate Bridge

The 0.3 m curved Plate Bridge shown Figure is subjected to a uniform surface load of intensity -2.0 t/m^2 . The Young's modulus for the plate material is $E=2.5 \times 10^7 \text{ t/m}^2$ and Poisson's ratio ν equal to 0.25. Figures (4, 5) demonstrate the Deflection and Moment M_{xx} at center line of plate are plotted from CBEM and present BEM.

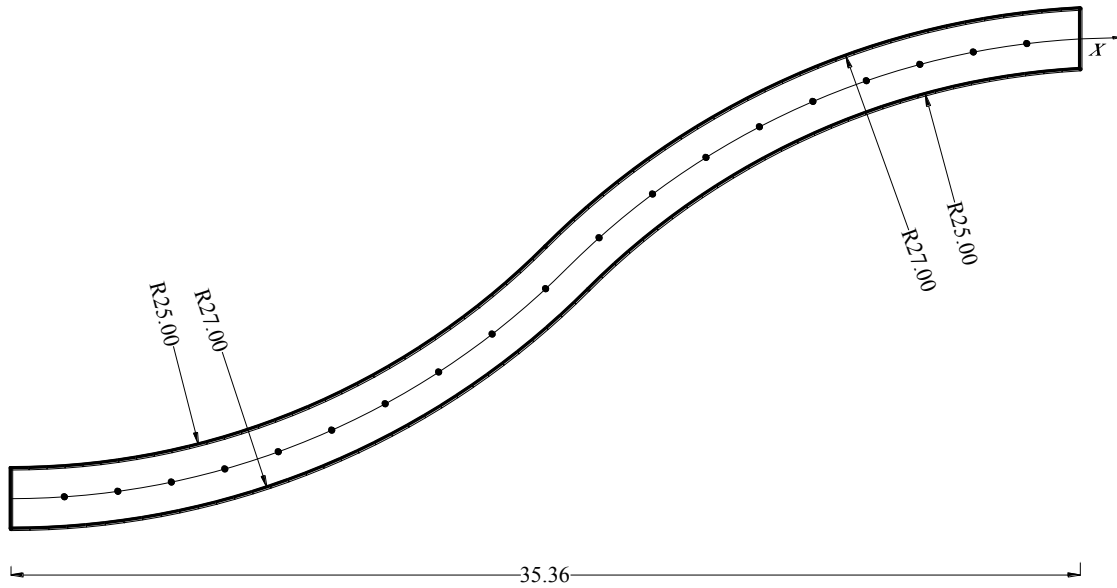


Figure 3 Curved Plate Bridge subjected to domain load

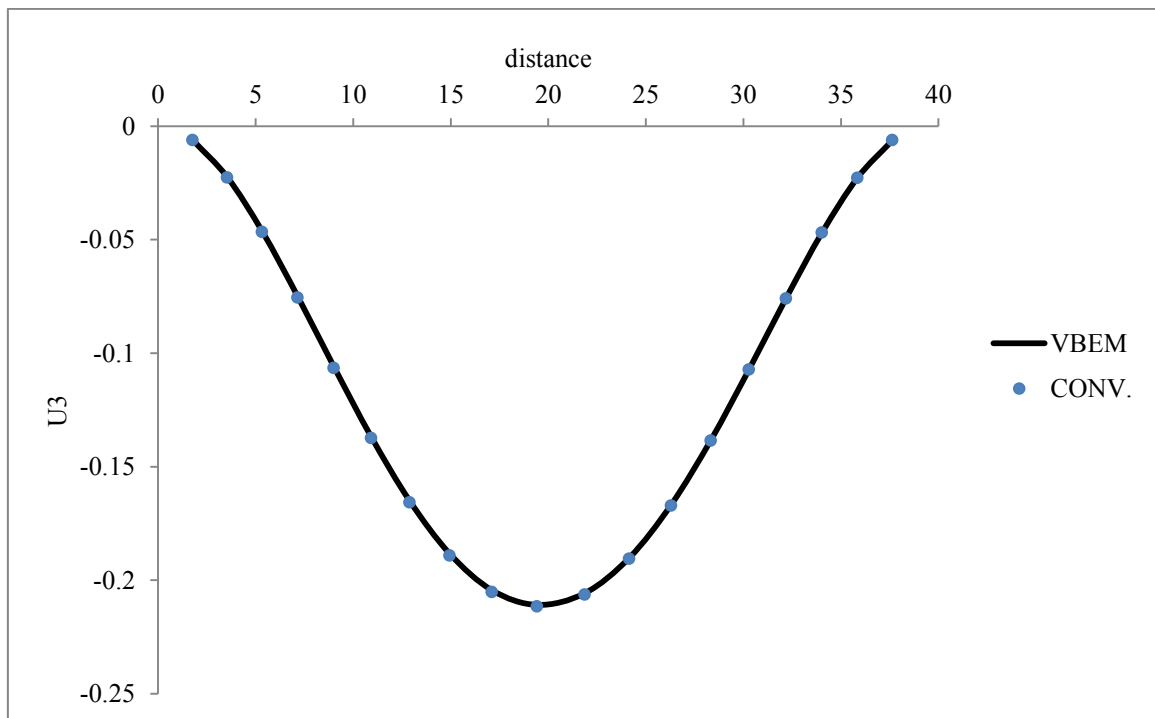


Figure 4: Deflection along center line

Figure 5: Moment M_{xx} along center line

5. CONCLUSIONS

In this paper, a variational boundary element formulation of Reissner's plate bending problems was derived. The formulation was based on minimizing the relevant energy functional. A collocation based series is used to remove domain integrals. Hence a fully boundary integral equation is formulated. The formulation was transformed into matrix equations using quadratic boundary elements, and was implemented into a computer code. Several examples with different boundary conditions were tested. It was demonstrated that the present formulation results were more accurate compared to results obtained from the conventional direct boundary elements, even with fewer number of elements. In addition, the present formulation produces symmetric stiffness matrix similar to that obtained from the finite element method. Therefore such formulation is very suitable to be coupled with boundary and finite elements or to produce a new family of super finite elements; which will be considered in future research.

ACKNOWLEDGMENT

The research reported here was supported by the European Union Project PIRSES-GA-2010-269222: Analysis and Design of Earthquake Resistant Structures (ADERS) of the FP7-PEOPLE-2010-IRSES, Marie Curie Actions. This support is gratefully acknowledged by the authors.

REFERENCES

- [1] Vander Weeën, F., Application of the boundary integral equation method to Reissner's plate model. *Int. J. Num. Methods Eng.*, **18**, 1-10, 1982
- [2] Barcellos C.S.; Silva, L.H.M., A boundary element formulation for Mindlin's plate model. In: BREBBIA, C.A. ;Venturini, W.S. eds. *Betech87. Computation Mechanics pub.*, 1987
- [3] El-zafrany, A.; Fadhil, S. ;Debbih, M. , An efficient approach for boundary element bending analysis of thin and thick plates. *Computers & Structures*, **56**, 565-576, 1995
- [4] Ribeiro, G. O.; Venturini, W. S., Elastoplastic analysis of Reissner's plates using the boundary element method. In: ALIABADI, M.H., ed. *Boundary element method for plate bending analysis*. 101-125, Southampton, CMP., 1998
- [5] Westphal JR.,T. ,Andrä, H. ; Schmack, E. Some fundamental solutions for Kirchhoff, Reissner and Mindlin plate and a unified BEM formulation. *Engineering Analysis with Boundary Elements*, **25**, 129-139, 2001
- [6] Marczak, R.J., Creus, G.J., Direct evaluation of singular integrals in boundary element analysis of thick plates. *Engineering Analysis with Boundary Element*, **26**, 653-665, 2002
- [7] G. R. Fernandes, D. H. Konda, A BEM formulation based on Reissner's theory to perform simple bending analysis of plates reinforced by rectangular beams, *Computation Mechanics pub.*, **42**, 671–683, 2008
- [8] Dym, C.L., I.H. Shamed, *Solid mechanics, a variational approach*, McGraw Hill Pub., 1973.
- [9] Rashed, Y.F., Brebbia, C.A., Eds., *Transformation of domain effects to the boundary*, WIT Press., 2003.
- [10] Mohareb, S.W., Rashed, Y.F., A dipole method of fundamental solutions applied to Reissner's plate bending theory, *Mech. Res. Comm.*, **36**, 939-948, 2009
- [11] Brebbia, C.A., Telles, J.C.F., Wrobel, L.C., *Boundary element techniques: Theory and Applications in Engineering*. Springer-Verlag, Berlin-Heidelberg, 1984.
- [12] Karam, V.J., Telles, J.C.F., On boundary elements for Reissner's plate theory. *Engineering Analysis*, **5**, 21-27, 1988.
- [13] Zienkiewicz, O.C., *The finite element method*, McGraw, 1977
- [14] Rashed, Y.F., *Boundary Element Formulations for Thick Plates*, Topics in engineering, Vol. 35. WIT press, Southampton and Boston, 2000.
- [15] Tottenham, H., *The boundary element method for plates and shells*. In: *Developments in Boundary Element Methods – I* (eds PK Banerjee and R Butterfield), Applied Science Publishers, London, pp. 173–207 ,1979

NUMERICAL INVESTIGATION OF A FULL-SCALE RC BRIDGE THROUGH 3D DETAILED NONLINEAR LIMIT-STATE SIMULATIONS

George Markou

Department of Civil Engineering, Alhosn University, Abu Dhabi, UAE
P.O.Box 38772, Abu Dhabi
g.markou@alhosnu.ae

Keywords: Bridge Modeling, Large-Scale Simulations, Nonlinear Analysis.

Abstract. *In this paper, a numerical investigation of the computational performance of ReConAn FEA will be performed through the full-scale 3D detailed modeling of a 100m span reinforced concrete bridge. The efficiency of the automatic procedure for generating embedded steel reinforcement elements inside the hexahedral finite elements will be presented and the numerical performance of the solver will be discussed. Furthermore, the numerical results that derived from the nonlinear numerical assessment of the bridge will be analyzed where a simplified finite element model developed in SAP2000 was used to compare the derived results from the 3D detailed simulation. In the 3D detailed modeling formulation adopted in this work, concrete is modeled through the use of 8-noded hexahedral elements that treat the cracking phenomenon through the smear crack approach and the reinforcement is modeled through the use of embedded 2-noded rod elements that incorporate the Menegotto-Pinto steel material model. The rebars are assumed to have perfect bonding thus the bond-slip between the rebars and concrete depends on failure of the concrete material. The piers with the pile cap and the bridge's trapezoidal shaped continuous deck are modeled through the use of the adopted concrete hexahedral element, while the 3D geometry of the reinforcement grid, inside the concrete domain, is modeled in detail according to the technical drawings. Finally, the elastomeric bearings are also modeled by using 8-noded hexahedral elements that discretize the exact geometry of the isolation system.*

1 INTRODUCTION

Modeling and analysis of reinforced concrete (RC) bridges has been a scientific topic that challenged and still challenges researchers and finite element (FE) software developers that deal with the assessment of the mechanical behavior of RC bridges in terms of ductility and maximum capacity. Allocating potential weaknesses in the design that derives from the complexity of the bridges' geometry is a difficult procedure given that implementing detailed modeling for this type of structures is usually a prohibitive numerical task due to the large-scale numerical models that derive during the analysis procedure. Nevertheless, it is indisputable that 3D detailed FE models derive the most accurate numerical results in terms of objectivity.

In order to assess the mechanical behavior of RC bridges under earthquake loads according to Eurocode [1] or AASHTO [2] provisions, several methods have been proposed the last three decades, which mainly involve three procedures: modal pushover analysis, linear dynamic analysis and linear static analysis [3]. Most researchers [4-18] study the mechanical behavior of bridge structures through the use of beam-column and 2D FEs (i.e. the shell FE), which gives them the ability, through simplification assumptions related to both material and geometrical features, to investigate the overall dynamic and nonlinear behavior of the under study RC structures for different types of load magnitudes. The simplified models provide the required numerical tools to study the overall behavior at the full-scale structural level but lack in providing the researchers with the ability to account localized nonlinear phenomena like cracking, reinforcement geometry, yielding of rebars, 3D mechanical behavior of elastomeric bearings and their interaction with the deck, piers and abutments, etc., thus having non-negligible effects on the numerical results and the overall mechanical behavior of the bridges that derive from this type of analysis models.

As it was stated in [14], the last two decades the scientists and practitioners shifted towards the performance based assessment and design concept, where the inelastic deformation demands derive directly from the numerical nonlinearities that are incorporated and used during the nonlinear analysis. This emphasizes the need of accurate nonlinear models that will be able to account for 3D nonlinearities and phenomena that result from both material and geometrical features of the under study structures. For this reason, several researchers began to lean towards the 2D [19, 20] and eventually 3D detailed modeling of independent structural members of the bridge [21-29]. Furthermore, scientists managed to model the complete structural geometry of bridges [30-36], in an attempt to address the above issue.

Mwafy et al. [35], propose an idealization methodology that foresees the modeling through SAP2000 [37] and Zeus NL [38] of the super-structure of the bridge A-1700 at Caruthersville, with beam-column elements and the sub-structure with cubic elasto-plastic elements, including the soil domain in their numerical model. The focus on describing a realistic idealization procedure in this research work [35] stresses the significance of having the ability to simulate large-scale structures through the use of 3D detailed models that account material nonlinearities, while the computational constraints that result when this type of modeling is adopted relates with the inability of standard computer systems to undertake such a numerical task.

Richard et al. [19] used ATENA software [39] to analyze a 50 years old concrete trough bridge through the use of a 2D finite element model that treats cracking through the use of the smeared crack approach and models the reinforcement with embedded truss elements. Their idealization assumption was also restraint by the computational demands that would have resulted if a full-scale 3D finite element model was constructed.

Tang and Hao [34], used 3D detailed modeling in specific structural parts of a cable-stayed bridge in order to simulate the mechanical behavior of RC in blast loads and then assess the

overall mechanical response of the bridge due to the loss of the carrying capacity of these structural members, through the use of less computational demanding FE models (beam and shell elements). The simulations that were performed in LS-DYNA [40], showed that the computational demand was excessive, even for the case of the numerical analysis of a single pier. It is important to note here that in this study the bond-slip between the steel reinforcement and concrete is accounted as a property of concrete failure. The same assumption was also made in [25, 27, 33, 41] and it is the approach that the current research work will adopt during the numerical analysis.

Bi and Hao [33] used LS-DYNA to construct a full-scale 3D model of a two-span RC bridge with a straight deck (total span of 60m) in order to study the pounding damage under spatial varying ground motions. The idealization procedure adopted in this study foreseen the use of solid concrete elements with embedded rebars near the pounding areas, while smeared models (reinforcement is assumed to be equally distributed over concrete elements), away from the pounding regions, were used in order to minimize the computational demand. The RC bridge consisted of eight unreinforced elastomeric bearing pads, which were modeled with 16 solid finite elements each.

Other commercial software can be also found in the international literature that were used to assess the mechanical behavior of RC bridge structures. Deng and Morcoux [29], Chacon and Mirambell [28], Frissen et al. [21], Zhou et al. [13], Johnson et al. [8], Kaviani et al. [12] and Ho et al. (GT STRUDL Technical Papers) [42], used ANSYS [43], ABAQUS [44], TNO DIANA [45], Strand7 [46], Drain 3DX [47], Opensees [48], ADINA [49] and GT STRUDL [42], respectively, so as to numerically assess RC bridges through the use of different FE models. Commercial software that are referenced in [42-49] have the ability of using 3D FE models that incorporate damage material models. Given the fact that modeling RC structures through the use of 3D detailed FE models that incorporate cracking propagation through the smeared approach and model the reinforcement with embedded rebar elements [50-58], is computationally challenging even for relatively small models, none of the referenced commercial and research software were used to model a full-scale RC bridge and perform a seismic assessment through push over analysis.

In this paper the full-scale modeling of a 100m span RC bridge with an arc-shaped deck will be performed by using ReConAn FEA research software [59]. The preliminary design is assessed by performing pushover analysis, while the numerical results are compared with the results that derive from a simplified model developed in SAP2000, which is also used to perform modal analysis. In the 3D detailed modeling formulation adopted in this work, concrete is discretized through the use of the 8-noded hexahedral element that accounts the cracking phenomenon through the smear crack approach. The reinforcement is modeled through the use of embedded 2-noded rod elements, which are assumed to have perfect bonding with concrete elements. The piers with the pile cap and the bridge's trapezoidal shaped continuous deck are modeled through the use of the adopted concrete hexahedral element, while the 3D geometry of the reinforcement grid, inside the concrete domain, is modeled in detail according to the preliminary technical drawings. The elastomeric bearings are also modeled in detail by using 8-noded hexahedral elements that discretize the exact geometry of the isolation system. So as to investigate the numerical response of the adopted model for simulating the mechanical behavior of the isolation system, a parametric investigation is performed. Finally, explicit modeling of the posttensioning system is developed and numerically investigated. After the construction of the complete detailed model, the seismic assessment of the RC bridge is presented.

2 GEOMETRY OF THE BRIDGE

As it is described in [60] the bridge has an effective span of 99.1 m, of which 51.55 m is the left span's length and 47.55 m is the right span's length. The total height of the two pylons is 5.1 m and the spacing between them is 5. The preliminary technical drawings that were used in this study assume a the total width of the trapezoidal deck of 10.4 m and a height of 2.3 m. For the reinforcing details and additional information related to the RC bridge's geometry refer to [60].

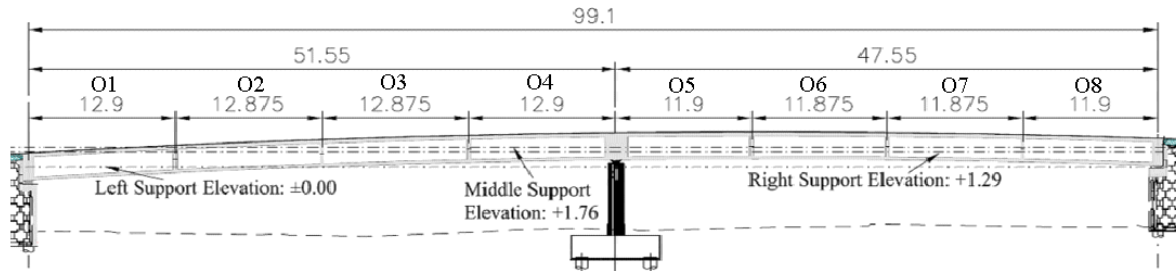


Figure 1. View of elevations.

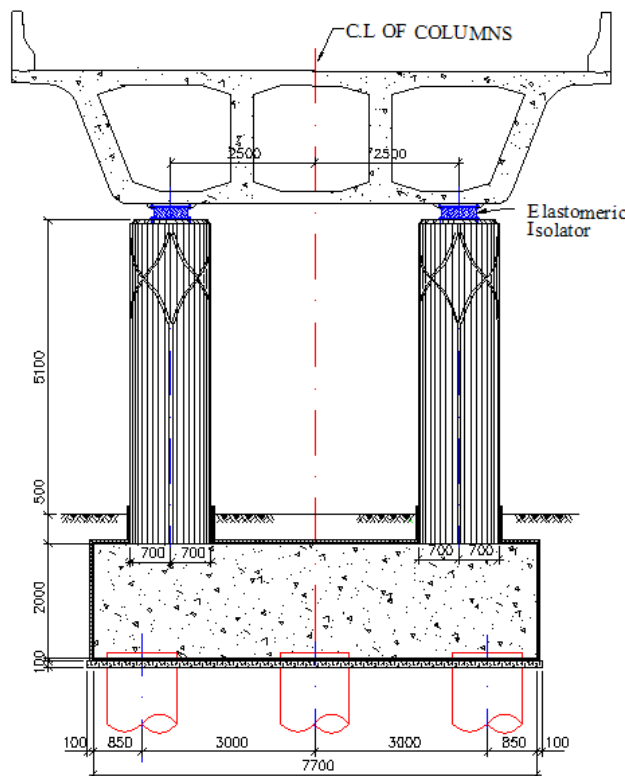


Figure 2. Geometry of the Pylons (dimensions in mm).

3 NUMERICAL IMPLEMENTATION

3.1 Finite Element Mesh, Material and Load Assumptions

The under study RC bridge was discretized through the use of hexahedral elements as it can be seen in Fig. 3. In order to reassure a stable thus accurate finite element mesh, a convergence analysis was performed for different structural parts of the bridge, while the average

hexahedral element mesh size used in the construction of the FE mesh was 20 cm. The selected hexahedral element size was found to be optimum when using the Kotsovos and Pavlovic [51] material model, which is adopted in this work. For the case of the steel embedded rebars (Fig. 4) the Menegotto-Pinto material model was used. The total number of concrete hexahedral elements used in the FE mesh shown in Fig. 3 was 102,622 and the total number of embedded rebar macro-elements was 47,839 (Fig. 4). In Fig. 5 the detailed FE mesh is illustrated where the model of the 3D geometry of the connection between the deck and the two piers can be also seen. As it was presented in [60], after the completion of the mesh generation method, the total number of embedded rebar elements was 520,624 and the required computational time was approximately 43 minutes. The embedded rebar mesh generation procedure that was used to allocate and generate the embedded rebar elements was proposed by Markou [61], which was an extension of the Markou and Papadrakakis [62] work.

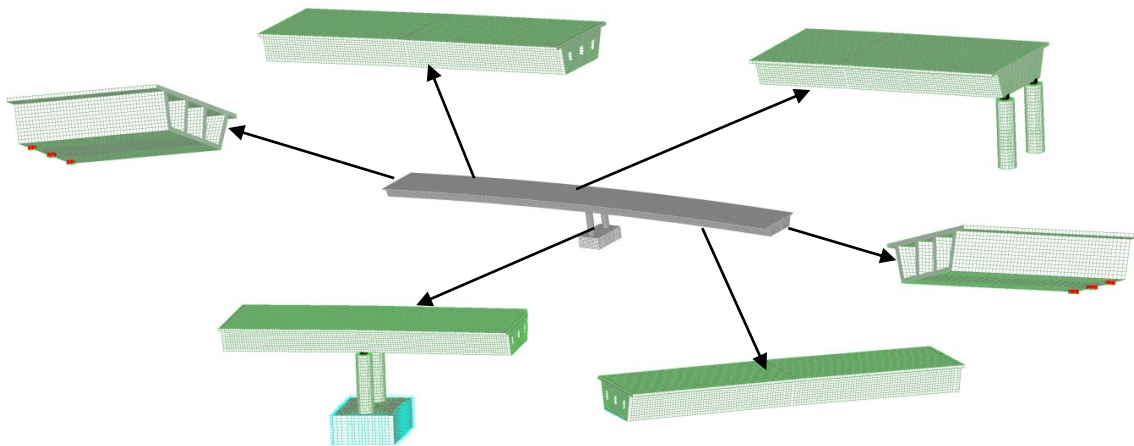


Figure 3. Models used for the mesh convergence analysis procedure.

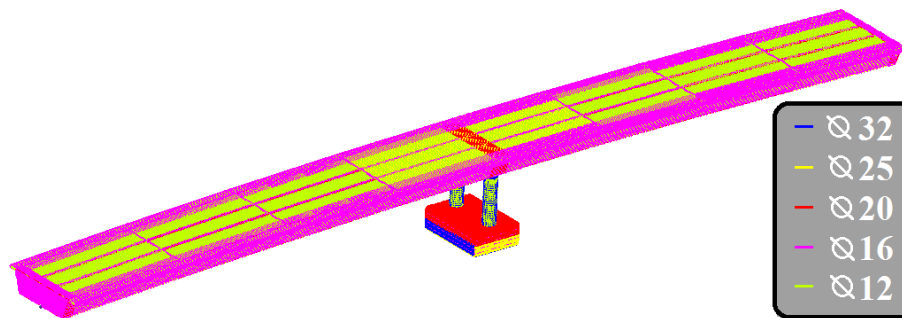


Figure 4. Macro-element rebar mesh.

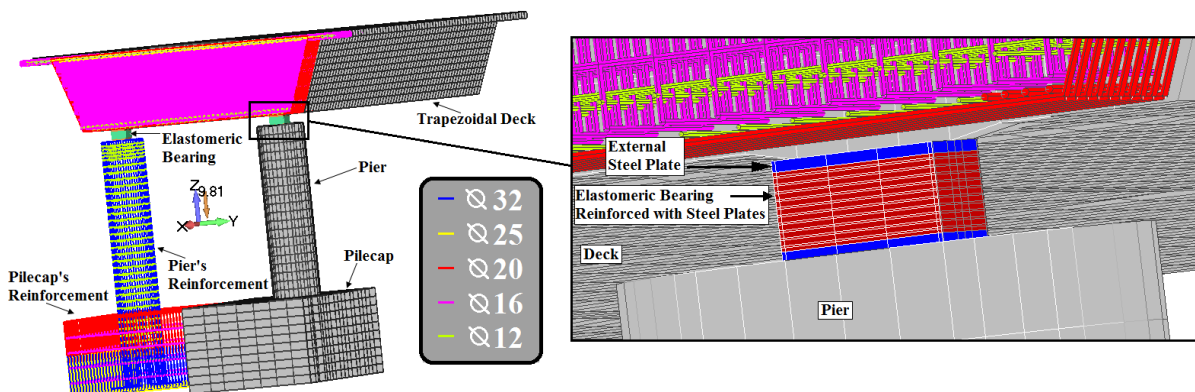


Figure 5. Detailed FE mesh of the bridge.

Table 1 shows the details related to the mesh used to discretize the RC bridge and the resulted embedded rebar elements. It is important to note here that the numerical data and results in Table 1 refer to the updated FE mesh that is used in this research work, which assumes a detailed modeling of the bearings through the use of 5,520 hexahedral elements (Fig. 6) instead of 312 that are used in [60]. The total number of bearings assumed is 8; three at the right and three at the left abutments, and two at the piers. Previous research work on 3D detailed modeling of standard reinforced elastomeric bearings can be found in [64].

a/a	Description	Value
1	Number of Hexahedral Concrete Elements	102,622
2	Number of Hexahedral Elements (Bearings)	5,520
2	Number of Nodes (hexa8 only)	175,784
3	Number of Macro-Elements	47,839
4	Total Number of Embedded Rebar FEs Generated	520,624
5	Total Number of Short Embedded Rebar FEs that were Discarded by the Filter Algorithm	1,439
6	Required Embedded Mesh Generation Time	42 m 22 s

Table 1. RC Bridge. General numerical details that derived after the solution of the complete FE model.

Due to the lack of data related to the materials of concrete and steel reinforcement, it is assumed that concrete is a C90 material and steel reinforcement an S500 material. Given that the bridge will be constructed in the UAE, the assumption of using a high strength concrete is common practice. The material properties that were adopted in the numerical models used are given in Table 2.

a/a	Material	Nominal Weight γ (kN/m ³)	Young Modulus E (GPa)	Hardening Ratio E_T (GPa)	Yielding Stress f_y (MPa)	Ultimate Stress f_u (MPa)	Ultimate Strain ϵ_u	Poisson Ratio ν
1	Concrete	24	44	-	-	90	-	0.2
2	Reinforcement Steel	78	200	2	500	695	0.10	0.3
3	Steel Plates	78	200	2	400	595	0.10	0.3
4	Elastomer	-	$3,5 \times 10^{-3}$	-	-	30	-	0.49

Table 2. Material properties.

Fig. 7 shows the simplified FE mesh that was constructed in SAP2000, which discretizes the deck with 11,792 shell elements and the piers through the use of beam-column FEs. The reinforced elastomeric bearings are modeled through the use of two joint links. The compressive, shear and rotational stiffness coefficients (K_C , K_S , $K_{\theta X}$, $K_{\theta Y}$, $K_{\theta Z}$, see Eqs. 1-7) of each standard reinforced elastomeric bearing were computed according to [66] by using the material properties depicted in Table 2 that were found in [65] and the geometrical characteristics given in Fig. 6.

$$K_C = \frac{EA}{t_{rl}} \quad (1)$$

$$K_S = \frac{GA}{t_{rl}} \quad (2)$$

$$K_{\theta i} = \frac{EI_i}{t_{rl}}, i = X, Y \text{ and } Z \text{ axis} \quad (3)$$

$$E = E_b + \left[\frac{C_1 GS^2}{1 + \frac{C_1 GS^2}{0.75 B}} \right] \quad (4)$$

$$E_b = 4G \left[1 - \left(\frac{q}{1 + q^2} \right)^2 \right] \quad (5)$$

$$q = L/W, L \text{ and } W: \text{length and width of the bearing } (W \leq L) \quad (6)$$

$$C_1 = 4 + q(6 - 3.3q) \quad (7)$$

where E is the effective Young modulus, A the gross area of the elastomer, t_{rl} the total thickness of the elastomeric material, G the shear modulus (1 MPa within the range proposed in [2]), I_i second moment of inertia about axis i , q the ratio, C_1 the constant related to the shape of the bearing and B the bulk modulus (2 GPa [66]). The numerical results that derived after implementing the above equations for the case of the middle elastomeric bearing (connects the pier with the deck) can be seen in Fig. 7 (the formulas were programmed in Matlab).

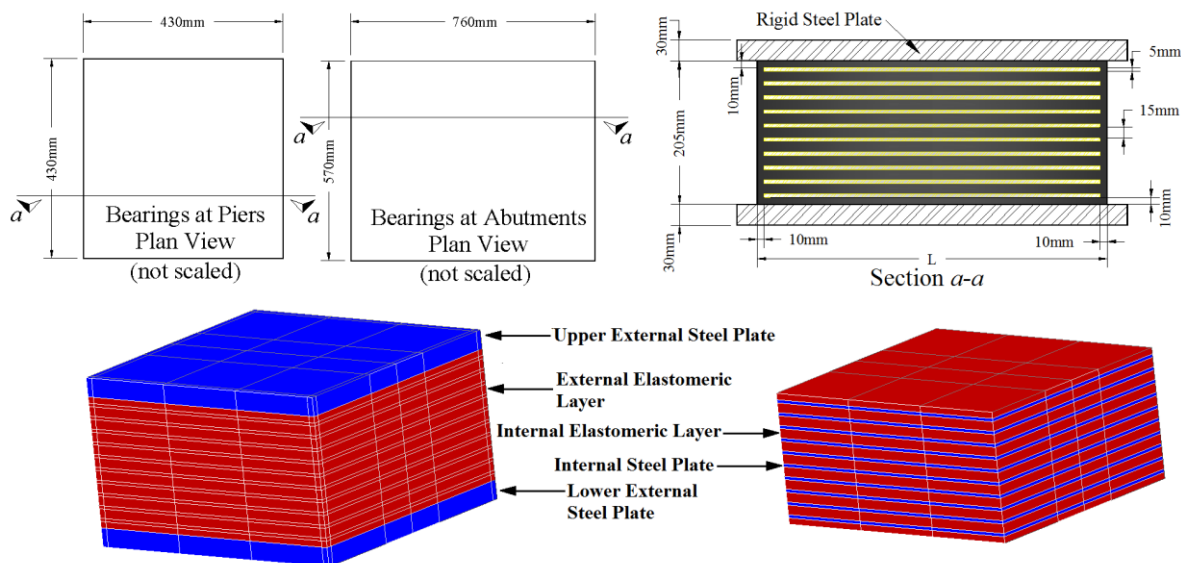


Figure 6. (Up) Geometrical features of the internal layers of the 8 elastomeric bearings and their plan views. (Down) Detailed FE mesh of the elastomeric bearings located at the heads of the two RC piers.

Shape Factor S	: 7.1667 unitless
Homogenous modulus E_b	: 3 MPa
Effective modulus E	: 282.9055 MPa
Compressive Stiffness K_c	: 337.4789 MN/m
Shear Stiffness K_s	: 1.1929 MN/m
Rotational Stiffness $K_{\theta x}$: 5.2 MNm/m
Rotational Stiffness $K_{\theta y}$: 5.2 MNm/m
Rotational Stiffness $K_{\theta z}$: 10.4 MNm/m

Figure 7. Numerical data related to the middle bearings as they resulted from Eqs 1-7 [66].

In order to assess the mechanical behavior of the RC bridge preliminary design the following procedure was implemented: a. The elastomeric bearings were modeled separately through the use of 3D detailed numerical model and were assessed so as to determine their maximum carrying capacity (Fig. 6) b. The complete FE mesh of the bridge was solved through the use of both ReConAn and SAP2000 so as to derive the mechanical response of the bridge by assuming an elastic behavior for all material models and by applying only the self-weight of the structure. c. The complete 3D detailed model with embedded rebar elements was solved for the self-weight of the structure so as to determine the numerical response thus assess the mechanical behavior of the preliminary design of the structure. d. The 3D detailed model is used to perform nonlinear limit state analysis to determine the seismic

carrying capacity of the RC bridge after redesigning. The numerical findings of the above steps will be presented below.

3.2 Steel Reinforced Elastomeric Bearings

All elastomeric bearings were discretized by using both 8-noded (Hexa8) and 20-noded (Hexa20) hexahedral elements (see mesh for middle bearing in Fig. 8). The scope of performing this numerical investigation was to determine the carrying capacity of the bearings' initial design while parametrically investigate the mechanical behavior of the composite material of the reinforced elastomeric bearings under compression and shear loading. Newhouse et al. [63] performed 3D detailed analysis by using a hyper-elastic material model for the elastomer, so as to determine the deformation that occurs when bearings are positioned with a superelevation through the use of ANSYS [43]. As it was mentioned in their work, the numerical results were in a good comparison with the experimental data while they concluded that analysis through the use of solid FEs can be an effective research tool.

For the case of the two middle bearings that connect the piers with the deck of the at hand RC bridge, when assuming a 30 MPa ultimate stress their ultimate carrying load is 555 tons. This ultimate value is larger than the 300 tons proposed by the producer VSL [67], which is the ultimate load of a similar elastomeric bearing (400x500mm). According to the VSL specifications, by applying a load of 300 tons the bearing develops a 150 kg/cm^2 . Accounting for the fact that the ultimate stress is 300 kg/cm^2 (30 MPa) then the required vertical load so as for the elastomer to reach the ultimate stress will be approximately double (600 tons). Therefore, numerically the model will fail when the rubber material reaches its maximum stress thus mechanically the elastomer will not be able to carry additional loads.

In this work, in order to simplify the analysis in terms of material complexity and computational demand, a typical von Mises material model is used to simulate the mechanical behavior of the elastomer and the steel plates. For this reason a numerical investigation was performed to determine the appropriate Young modulus of elasticity of the elastomer so as to derive realistic deformations according to the applied load. In addition to that, it is well known that for static loads the strain field within the bearing volume is mainly compressive in nature [63], with exceptions of tensile areas near the external elastomeric layers of the bearing (assuming that only a vertical load is implemented), thus the above assumption will not result significant differences. After performing the parametric investigation, which foresees the comparison between link elements (springs with stiffnesses equal to those given in Fig. 7) and the 3D detailed proposed model, it was found that when the elastomer is assigned a Young modulus of elasticity equal to 12 MPa, the two models derive similar results.

After the completion of the above parametric investigation, several analyses were performed in order to further study the numerical behavior of the model (for the middle bearings), which were mainly divided into two main categories. The first assumes that the load applied on the top steel plate of the bearing is a vertical load of 600 tons (so as to derive the ultimate carrying load V_u) and the second assumes four combinations of 18.5% (100 tons), 29.6% (160 tons), 37% (200 tons) and 50% (270 tons) of the derived ultimate vertical load V_u and a $H_u = 20$ tons horizontal nonlinear load. All analyses were performed by using both hexa8 and hexa20 FEs.

Fig. 8 shows the deformed shape of the Hexa20 FE mesh where the resulted vertical deformation for a vertical load of 540 tons (30 MPa ultimate stress was developed in the elastomeric material) was found to be equal to 30.4 mm which is 22.3% larger than the 24.8 mm that derived when using the Hexa8 FE. This is attributed to the more flexible numerical formulation of the Hexa20. It is evident that the elastomer expands vertically due to the excessive compression that is implemented at the external steel plate, where the laminated steel

plates constrain this lateral expansion. As Fig. 8 shows, the elastomer material at the external layer expands laterally due to the compression thus a folding type of deformation develops due to the steel plate reinforcement. A similar type of folding is noted in Fig. 9 in a real bearing specimen tested by Newhouse et al. [63] where the loading type was a combination of compression and horizontal load that derived from the pad's superelevation.

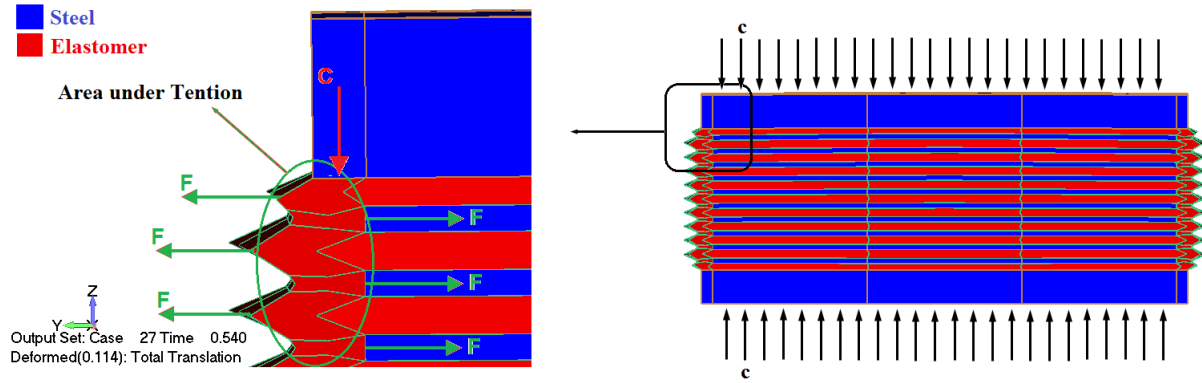


Figure 8. Hexa20 model. Deformed shape for $V = 540$ tons or 5.4MN.

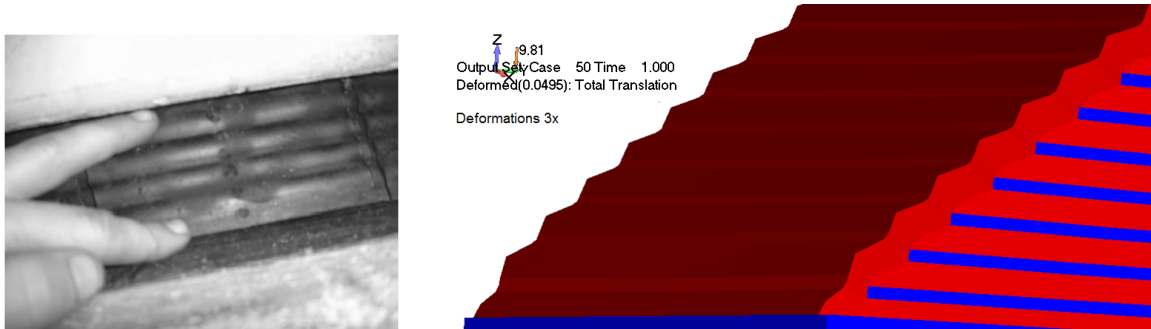


Figure 9. (Left) Deformed shape after tension debonding of reinforced elastomeric bearing with steel plates [63] and (Right) Deformed shape of bearing as it resulted from the Hexa20 model ($50\% V_u + 100\% H_u$).

Load Combination	Linear Vertical Dead Load V (tons / $a\%V_u$)	Max. Vertical Displ. at the 1 st load step (mm)		H Load for which zz -tension occurs at the elastomeric layer at the base (tons)		Maximum Horizontal Displ. for (mm)		Max. vertical expansion of the elastomeric layer at the base (mm)	
		Hexa8	Hexa20	Hexa8	Hexa20	Hexa8	Hexa20	Hexa8	Hexa20
1	100 / 18.5	4.87	5.71	28	44	45.6	46.8	0.15	0.22
2	160 / 29.6	7.76	9.11	44	68	46.1	47.6	0.1	0.16
3	200 / 37.0	9.70	11.4	56	84	46.6	48.2	0.07	0.13
4	270 / 50.0	13.1	15.3	72	112	47.5	49.5	0.04	0.08

Table 3. Numerical results as they derived from the analysis, when applying different load combinations.

After the completion of the first set of analyses (only vertical loads), the next set of numerical results derived by assuming different levels of vertical loads (which are assumed to be dead linear loads that are implemented at the first loading increment) and a horizontal load of 20 tons that was applied incrementally at the top external steel plate. The derived numerical results are summarized in Table 3. From the resulted numerical output, it can be concluded that the bearing's deformation is controlled mainly by the horizontal load given that its compressive stiffness is much larger than the corresponding shear. Fig. 10 shows the deformed shape and z -displacement contour of the Hexa20 model for the load combination 1. As it results, tension develops at the external elastomeric layer and the lower area of the bearing (1st elastomeric layer at the base and the bottom steel plate), which eventually tends to lift up.

Therefore, the larger the vertical load applied the smaller is the vertical lift up due to the horizontal loading.

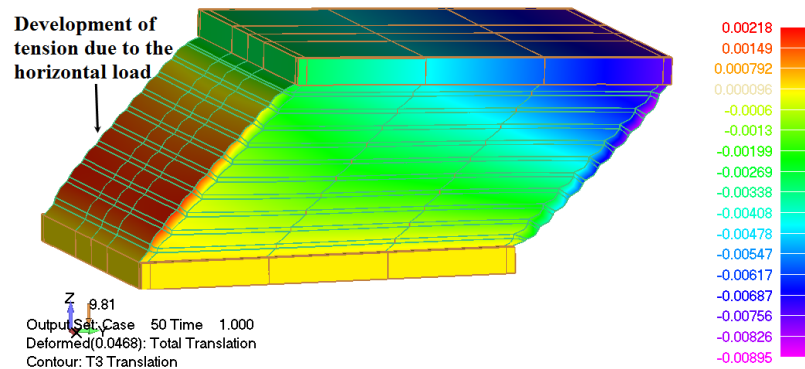


Figure 10. Deformed shape and translation contour along the z-axis of the elastomeric bearing due to the load combination 1 (Hexa20 FE model – Load Combination 1).

3.3 Linear Elastic Solution without Embedded Rebars

The next stage of assessing the numerical model and the overall mechanical behavior of the under study bridge was to linearly analyze the complete hexahedral model (Hexa8) by assuming only the self-weight of the structure. The results of this analysis were compared with the results that derived from the simplified SAP2000 FE model (Fig. 11) for which a mesh sensitivity analysis was performed in order to determine an optimum FE mesh size which will provide an acceptable accuracy and computational efficiency. Three FE sizes were tested (130 cm, 70 cm, 30 cm) and it was found that when discretizing the bridge by using rectangular FE shells with an edge size of 70 cm the numerical response of the mesh satisfied the above demands. Fig. 12 shows the z-axis translation contour as it derived from the Hexa8 FE mesh, where it results that the maximum deflection of the bridge is located at the left span of the deck and it is equal to 53.7 mm. The corresponding maximum deflection that resulted from the simplified model was 47 mm (Fig. 11) which is smaller. It was also found that the compressive deformation due to the bearings at the piers was 21 mm and 26.5 mm for the simplified and the detailed model, respectively. Therefore the difference in the maximum deflection results from the deformation of the elastomeric bearings. One of the reasons that the bearing's displacement for the case of the Hexa8 model is larger than the corresponding simplified model is the fact that ReConAn increases the nominal weight of concrete by 1.03 so as to account for the reinforcement self-weight. By representing the axial force that develops due to the self-weight of the structure at the top surface of each pier, according to SAP2000, the resulted compressive force equals to 5.83 MN. This level of compression exceeds the ultimate carrying capacity of the bearings (5.55 MN) that connect the piers to the deck thus redesigning will be required (increase of the bearings area). Fig. 13 shows the deformed shapes of the bearings at the middle and the abutments as they resulted from the Hexa8 model. It was found that the longitudinal x-translation of the left abutment was equal to 6.9 mm, while the simplified model derived a corresponding 3.1 mm. This finding confirms that the selected material properties for the case of the elastomer result a more flexible numerical behavior in comparison to the link element used in the simplified model.

It must be noted that the deflection differences, regarding the deck mechanical response, would have been larger if the shell FE mesh was enriched with kinematic constraints at the middle vertical diaphragm which has a total thickness of 2 m. This structural member induces additional stiffness in the deck's mechanical behavior thus when discretizing with shell FEs the actual stiffness contribution in the middle of the bridge cannot be captured realistically.

The same phenomenon applies for the 1 m thick vertical diaphragms located at the two ends of the bridge's trapezoidal deck.

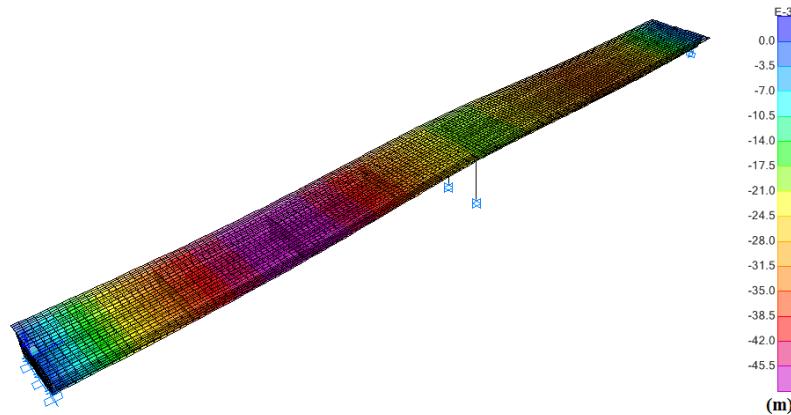


Figure 11. SAP2000 (Shell FEs). Deformed shape and translation contour along the z-axis of the RC bridge due to the self-weight.

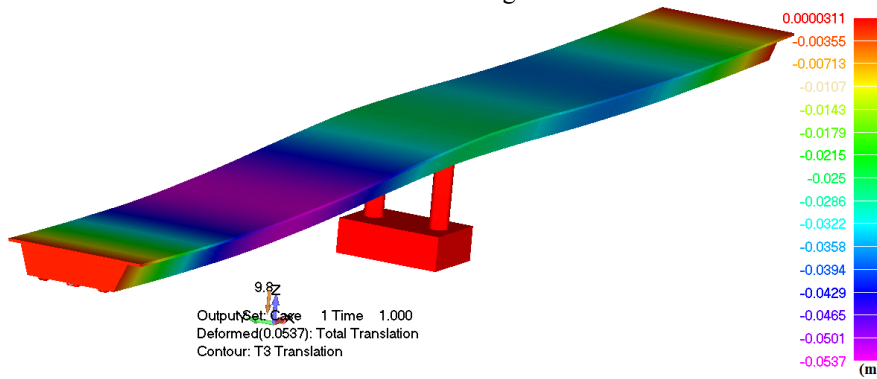


Figure 12. ReConAn (Hexa8 FEs). Deformed shape and translation contour along the z-axis of the RC bridge due to the self-weight.

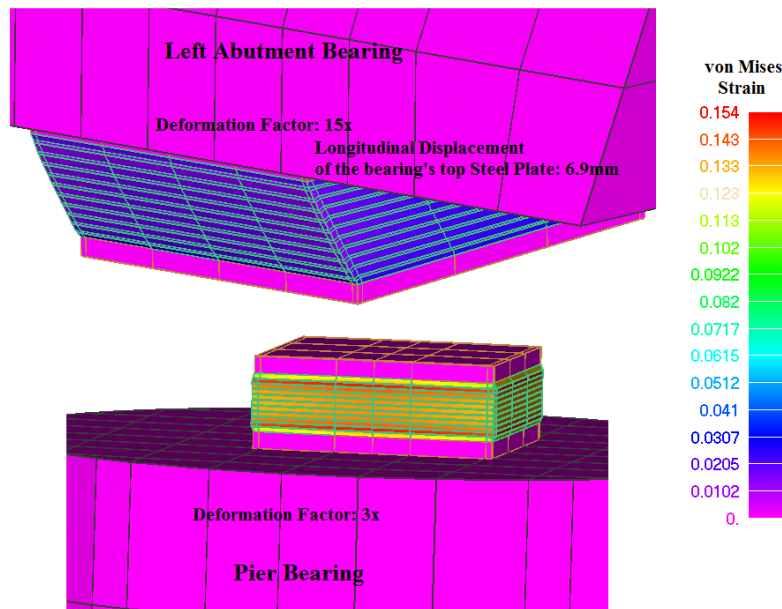


Figure 13. von Mises strain contour of the middle and left abutment elastomeric bearings.

An additional finding that resulted from this linear analysis is that the areas where the elastomeric bearings are connected with the deck develop stress concentrations, which are higher in the case of the simplified model due to the assumption that the bearings are modeled

through the use of link elements. The link elements are connected to the deck at a single node which contributes to this numerical phenomenon. Fig. 14 shows the solid von Mises stress contours for both models as they derived from the analysis. As it can be seen, the simplified model derives an 18.1 MPa von Mises stress at the connection areas of the bearing with the deck, while the 3D model results a 14.7 MPa von Mises stress. The deformed shape of the bearings can be seen in Fig. 13, where the solid von Mises strain contour is visualized.

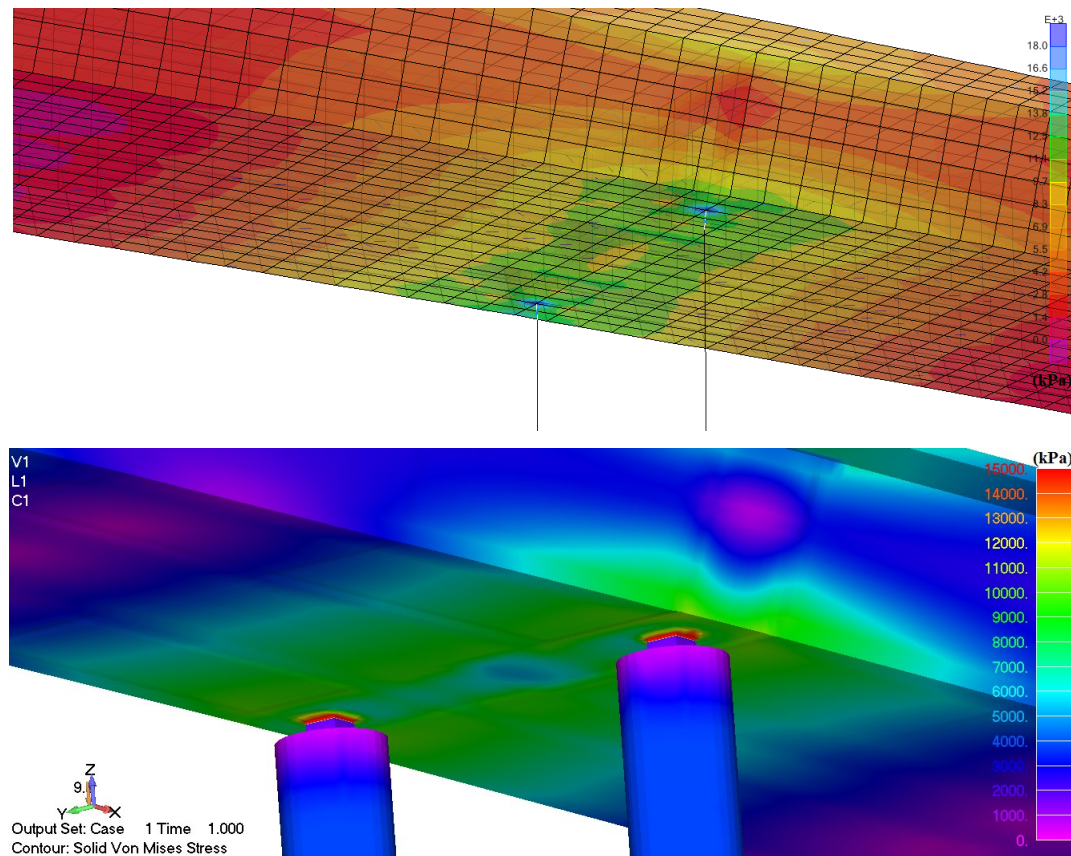


Figure 14. von Mises stress contours. (Up) Sap2000 and (Down) ReConAn.

The next assessment stage is to determine whether the RC bridge develops any cracks due to its self-weight thus the use of a pretension system will be required. The resulted maximum deflection from the linear analysis for the self-weight of the structure revealed that the behavior of the deck is relatively flexible given that pretension was not assumed.

3.4 Nonlinear Solution of the Complete 3D Detailed Model

In this section the numerical results that derived from the nonlinear solution of the complete 3D detailed model with embedded rebars will be presented. The FE mesh of Fig. 5 is used so as to simulate and investigate the mechanical behavior of the RC bridge under its self-weight. The aim of this numerical analysis is to investigate any stress concentrations and potential cracking development that eventually will reveal the weak areas of the bridge according to its preliminary design. The current model does not foresee any posttensioning thus cracks may develop.

After performing the analysis, the numerical results revealed that the RC bridge is not capable of carrying its self-weight without the development of cracks, therefore if we had assumed the service loads, the deck would have developed larger cracks. As it can be seen in Fig. 15, due to the relatively long spans of the bridge the lower area of the deck located at the

right span of the bridge develops horizontal cracks which are attributed to the stress field derived from bending and shear forces that are developed at the connection area between the vertical walls and the lower slab of the RC deck (Fig. 15c). At the left span of the bridge cracking was developed at the vertical diaphragm and at the middle area of the vertical walls (Figs. 15a and 15b, respectively).

Fig. 16 shows the von Mises stress contour that derived from the numerical analysis for the self-weight of the bridge at the pier's head, where the transfer of the compressive loads of the deck can be visualized. So as to represent the stress distribution that derives from the above procedure in a more revealing way, Fig. 16 shows the section cut of the model at the pier's bearing. The two bearings at the piers were found to be under designed (elastomeric material exceeded significantly the 50% of its ultimate stress) thus an increase of their plan view area was required.

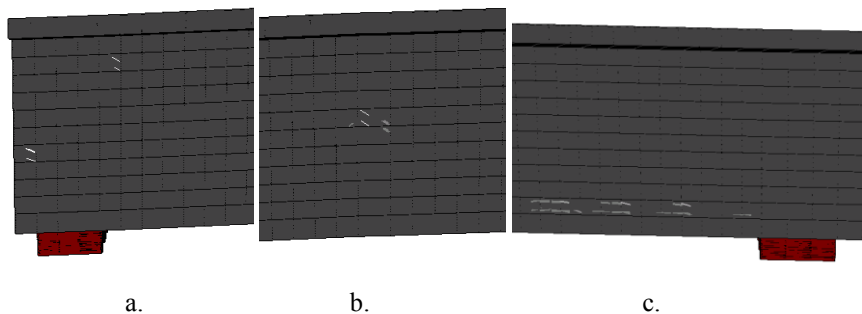


Figure 15. Crack patterns of the deck due to the self-weight load at the a. left support, b. middle of the left span and c. near the right support.

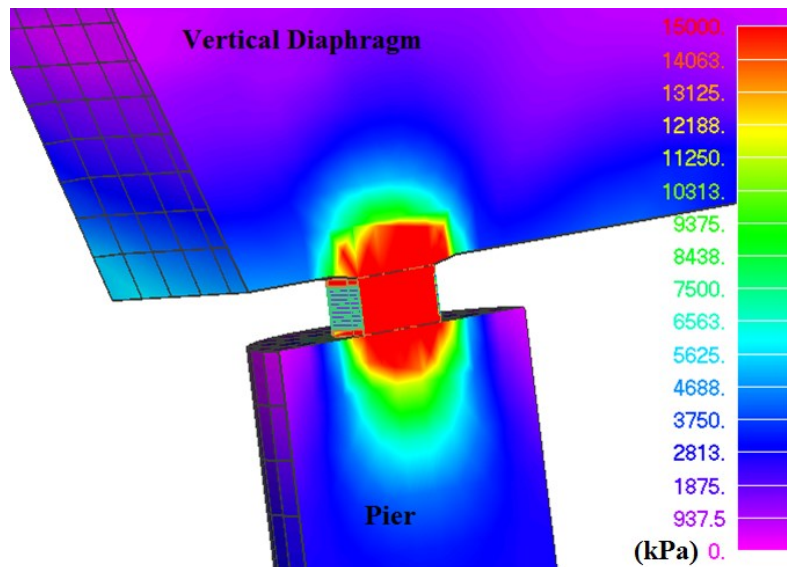


Figure 16. von Mises stress contour at the connection between the pier and the deck (section).

The maximum displacement of the bridge was found to be equal to 30.4 mm (middle nodes of the left span of the bridge). The stiffer behavior in comparison to the previous two models is attributed to the reinforcement that is modeled through the use of embedded rebar elements. It is evident that for this case, the reinforcement increases the stiffness of the deck in terms of the material behavior and the resulted maximum deflection was found to be decreased and smaller than both models that were presented in the previous section.

3.5 Redesign of the RC Bridge and Nonlinear Push Over Analysis

In this section the numerical results that were computed by using the modified FE mesh will be presented. As it was presented above, it was found that the bridge's mechanical response was not satisfactory for two main reasons: a. it develops relatively large deflections and b. cracks when the self-weight of the structure is applied. The relatively large deflections develop due to the soft behavior of the bearings located at the piers and the design of the deck's section. So as to alleviate these design issues, the elastomeric bearings at the piers were redesigned and their new dimensions are increased to 70x70cm, while the deck was reinforced with a posttensioning system which can be depicted in Fig. 17. The vertical walls are reinforced with three posttension cables that are modeled as embedded reinforcement with prestressing properties.

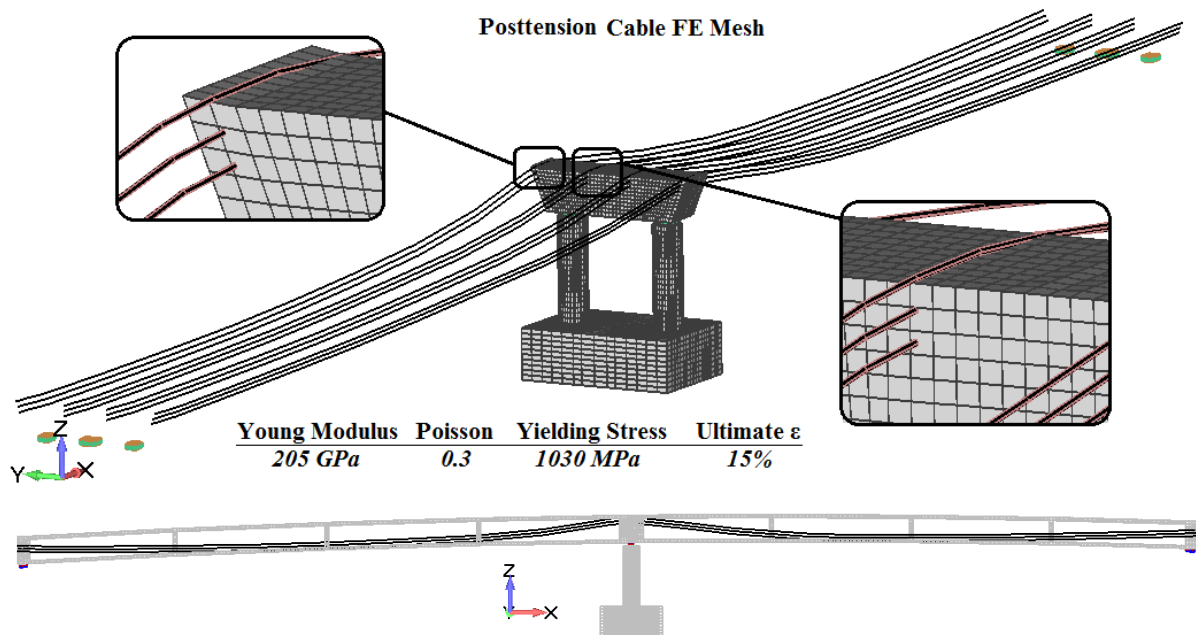


Figure 17. Material properties and FE Mesh of the posttensioned cables.

BEAM Property 11 - PrestressFI90_5MN	
Reinforcement property	
Property	Value
Slip Flag (0:NoSlip)	0
Type of Element for Reinf. 1:Rod 2:NBCFB(rect.) 3:NBCFB(circ.)	1
Number of Fibers (if NBCFB)	0
Number of Integ Points (if NBCFB)	0
Material Flag (1:Billinear 2:Menegotto Pinto)	1
Flag (always 1.0)	1
Steel Young Modulus	205000000
Steel Poisson	0.3
Steel Hardening	2050000
Steel Fy	1030000
Steel Failure (ef = 0.12)	0.15
Prestressed (0:No 1:Yes)	1
Prestressed Force (kN)	5000

Figure 18. Define posttensioning force for an embedded rebar property.

It is generally accepted that pre- and post- tensioning can be modeled by applying temperature change or a set of axial and distributed loads [42] on the RC structural member which is under compression (due to the pre- or post- tensioning). For the needs of this research work, ReConAn was integrated with the numerical ability of accounting pre- and post- tensioning forces applied directly at the cables that are modeled as embedded rebar elements. Fig. 18 shows the SMAD Custom Properties software developed by Stavroulakis [68], through which the pre- or post- tension force is defined as a custom property.

The algorithm that was developed so as to account the compression induced to concrete hexahedral elements at the material level, foresees the calculation of the initial stress σ_{i0} and ε_{i0} strain developed internally in the embedded posttensioned cable by using Eq. 8, while the internal force of the embedded cable $\mathbf{F}_{R,Int.}$ is transformed through the use of the kinematic expression given in Eq. 9, into a hexahedral internal force matrix $\mathbf{F}_{H,Int.}$ that is defined as the initial force condition of the hexahedral element. Then the internal force matrix of the hexahedral element that incorporates the corresponding embedded cable element is converted into an external load matrix $\mathbf{F}_{H,Ext.}$ through the use of Eq. 10, and applied to the corresponding hexahedral nodes. The numerical implementation of the posttensioning effect takes place in the first load increment where the computation of the initial stress state of the numerical model takes place. After the completion of the first load increment the nonlinear load is applied incrementally until complete failure, while the new stresses and strains are computed according to Eq. 11.

$$\sigma_{i0} = \frac{F_P}{A_i} \quad \varepsilon_{i0} = \frac{\sigma_{i0}}{E_S} \quad (8)$$

$$\mathbf{F}_{H,Int.} = \mathbf{T} \cdot \mathbf{L} \cdot \mathbf{F}_{R,Int.} \quad (9)$$

(24×1) (24×6) (6×2) (2×1)

$$\mathbf{F}_{H,Ext.} = -\mathbf{F}_{H,Int.} \quad (10)$$

(24×1) (24×1)

$$\sigma_{i+1} = \sigma_{i0} + \Delta \sigma_{i+1} \quad \varepsilon_{i+1} = \varepsilon_{i0} + \Delta \varepsilon_{i+1} \quad (11)$$

A parametric investigation was performed in order to verify the numerical performance of the proposed algorithm which explicitly models the posttensioning system. Fig. 19 shows two of the FE models that were developed in order to investigate the developed algorithm. The two RC beams foresee two different cable geometries through which the posttensioning force will be applied to the RC beams. Both models have 2 cables of 28 mm in diameter, while the first model assumes a straight cable placed at a 63 mm distance from the lower cord of the beam and the second model uses a curved cable geometry. The total applied posttensioning force was 100 kN per cable which was set so as to avoid any cracking in the concrete given that the beams are assumed to be weightless in an attempt to investigate the mechanical behavior induced from the posttensioning cable. The cable's yielding stress was equal to 555 MPa thus the 100 kN force represents only a 30% of the yielding force of the cable. The concrete's uniaxial compressive strength was set to 22.5 MPa.

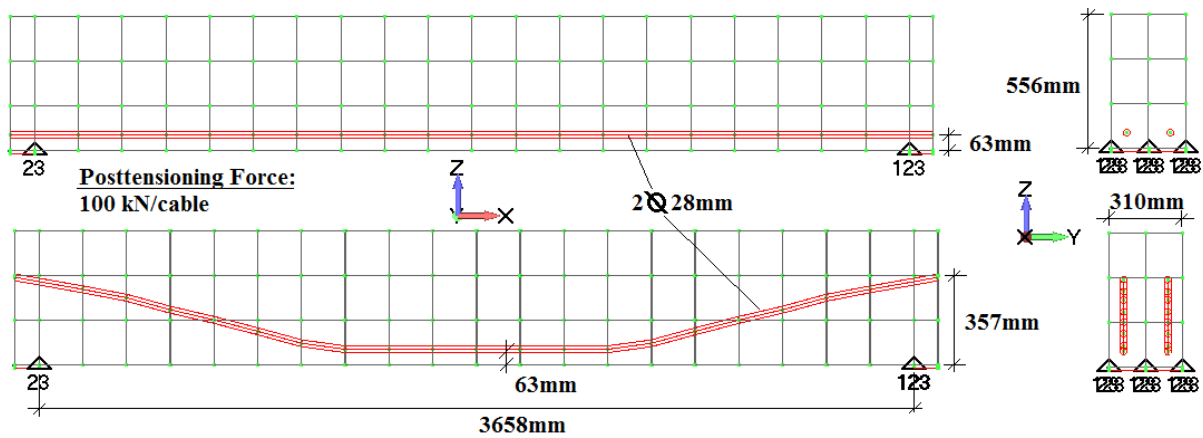


Figure 19. RC beam models with straight and curved posttensioning cables.

After analyzing the two models the derived uplifting maximum displacements were equal to 0.483 mm and 0.45 mm, for the first and second model, respectively. Fig. 20 illustrates the

deformed shapes of the two models and the XX stress contours as they resulted from the analysis. As it can be seen the contour levels that are used in both models are the same so as to compare the resulted stress fields in terms of compression and tension that results along the longitudinal axis of the beam. It is obvious that the posttensioned cable generates a compressive stress field at the lower level of the beam in both cases, while a tension is developed at the top cord of the two beams. In addition to that, the second model has a part of the top cord under tension (approximately 60% of the top cord is under tension) while the rest of the upper cord is under compression along the longitudinal axis of the beam. This is attributed to the curved geometry of the cable, which foresees the two ends of the cable to be located above the centroid of the two end sections located at the supports (see Fig. 19). Fig. 21 shows the deformed shape of the second model when the self-weight of the beam is accounted for.

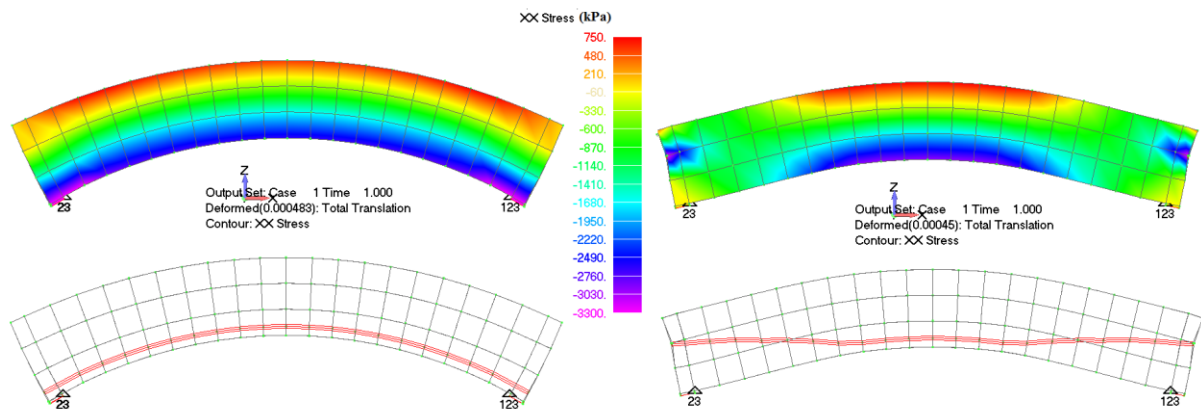


Figure 20. XX stress contour and deformed shape of the two RC beam models due to the posttensioning force (self-weight of the beam is neglected in both FE models).

An ultimate limit state analysis was performed for the case of the second model by applying a uniform distributed load on the top cord of the beam's section. Fig. 22 shows the resulted $P-\delta$ curve as it derived from the numerical analysis. As it can be seen, the beam has a negative displacement (uplift due to posttension) until the total vertical applied load reaches the 80 kN of magnitude. The $P-\delta$ curve shows that the first cracking occurs for a total load of 213.2 kN and that the beam fails for a total load of 754.5 kN and a 15.2 mm maximum deflection. The same RC beam was analyzed but without assuming any posttensioning (see $P-\delta$ curve in Fig. 22), so as to compare the mechanical behaviors of the same beam geometries and reinforcement, where one beam was prestressed and the other was not. The beam without posttension, cracks from the first load increment, while it fails for a smaller load. Fig. 23 shows the deformed shapes and the crack patterns for characteristic load levels as they resulted from the analysis of the beam with posttension.

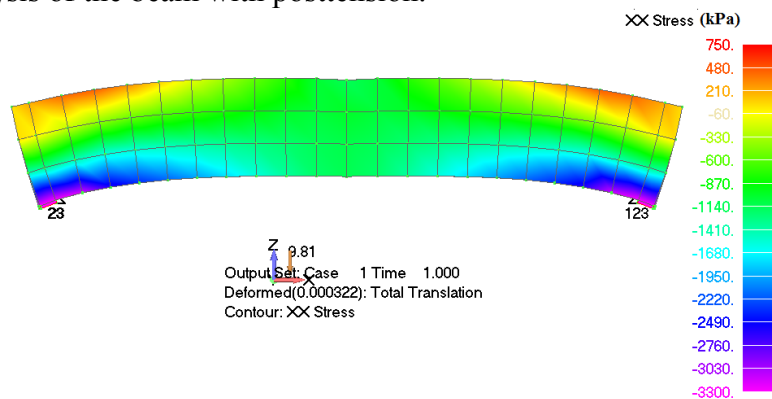


Figure 21. XX stress contour and deformed shape of the RC beam model with the curved cable (self-weight of the beam is accounted for).

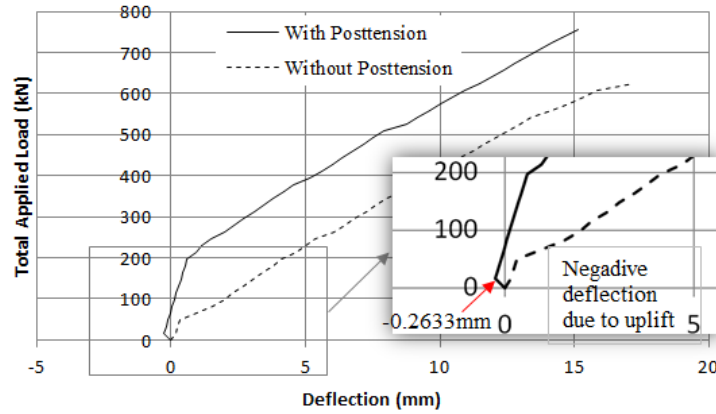


Figure 22. P- δ curve for the case of the second model (curved cable with posttension).

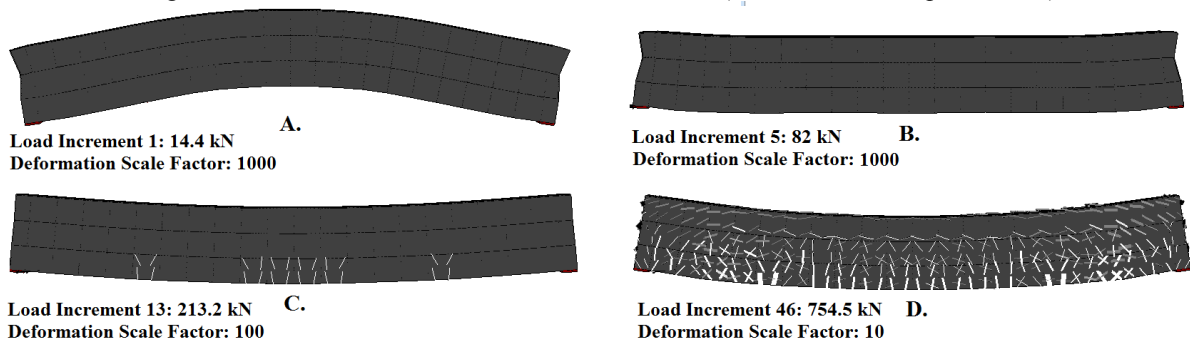


Figure 23. Deformed shapes and crack patterns for the case of the second model (curved cable with posttension).

After the parametric investigation of the posttensioning algorithm the numerical model of the RC bridge was solved by neglecting the self-weight and any other gravitational loads so as to investigate the overall behavior of the bridge due to the posttension. It is important to note that each cable element is assumed to have a circular section of 90 mm in diameter, while for this first full-scale posttensioning analysis it was assumed that the applied prestress force was equal to 250 kN (5% of the final applied prestress force).

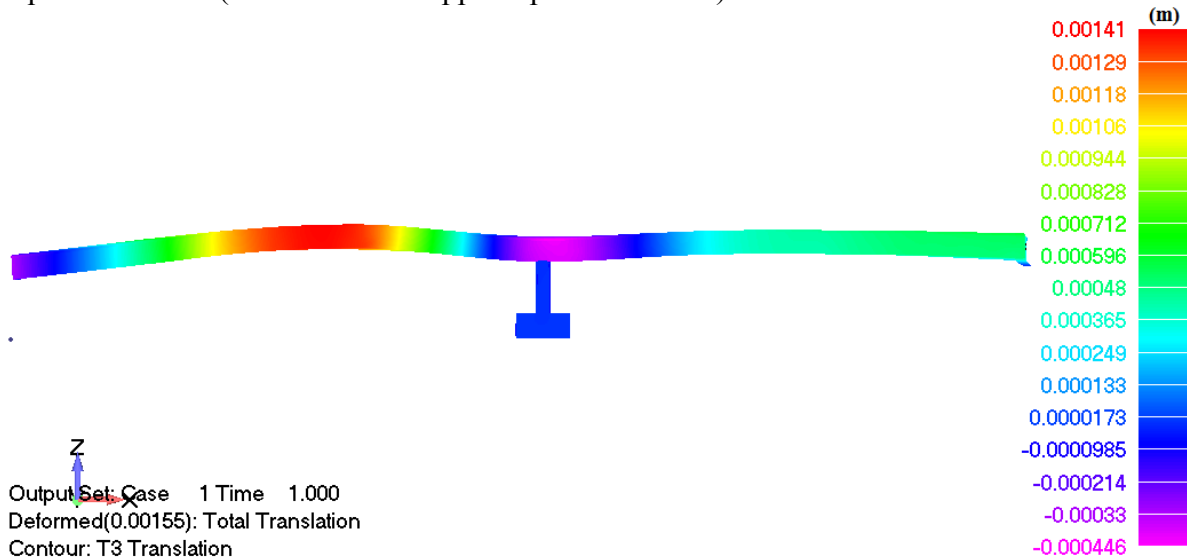


Figure 24. Deformed shape of the RC bridge due to posttensioning (self-weight is not accounted).

Fig. 24 shows the resulted deformed shape due to the prestress force applied in the 12 post-tensioned cables embedded in the four vertical walls of the RC deck. As it can be seen the two spans uplift while the middle elastomeric bearing is under compression due to the negative

moment developed at the area where the deck connects with the piers (posttensioned cables have a negative eccentricity, see Fig. 17). This numerical finding points out that the posttensioning system results an additional vertical load that is transferred to the bearings connecting the piers with the deck. The same observation was made by applying the prestress in the simplified model in SAP2000 by assigning negative strain at the shell elements of the deck that incorporate the prestress cables.

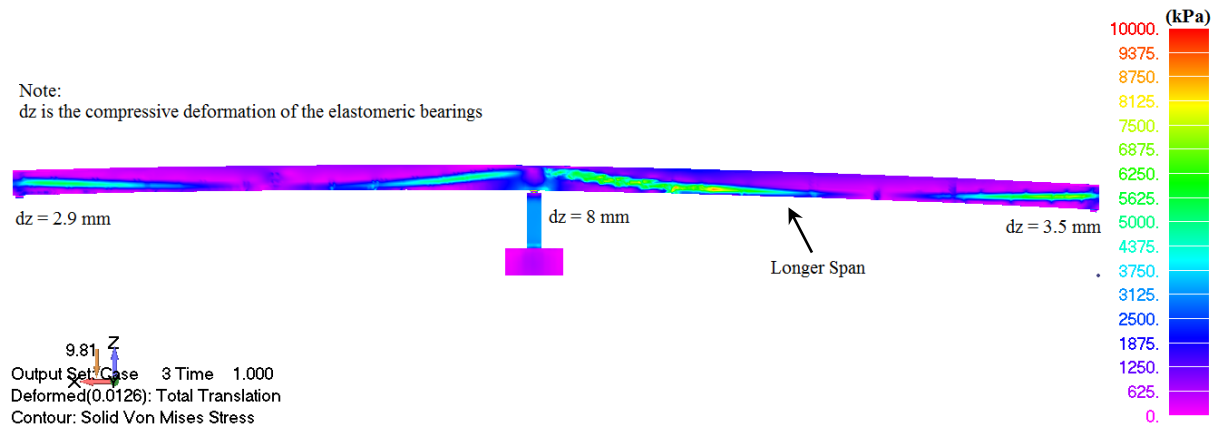


Figure 25. Deformed shape and von Mises stress distribution for service loads.

Given that the purpose of this work is to assess the seismic capacity of the bridge, presenting the posttensioning system's assessment will not take place below. It is important to note that the final model used to perform the push over analysis assumes a prestress force of $P_p = 5000$ kN per cable. Fig. 25 shows the von Mises stress distribution of the bridge as it resulted from the analysis by assuming the service loads (self-weight of the bridge, self-weight of the asphalt layer and the live load). According to the analysis the maximum deflection (including body translation) of the longest span of the deck, was equal to 12.6 mm, its maximum deflection relative to the supports, was equal to 5.8 mm, while the corresponding compressive deformation of the elastomeric bearings at the piers was 8 mm (Fig. 25).

a/a	Parameter	Value
1	Ground Type	B
2	Soil Factor S	1.2
3	Importance Factor γ	1.3
4	Acceleration a_g	0.2g
5	Behavior Factor q	1.0
6	Limit of the constant spectral acceleration branch T_C	0.5 seconds
7	Mode along the Y-axis T	1.36 seconds
8	Design Spectrum Acceleration $S_d(T) = a_g S[2.5/q][T_C/T]$	0.191g
9	Total Base Shear V_S	7.66 MN

Table 4. Seismic parameters assumed for the computation of the total base shear according to EC8.

The final step before performing the push over analysis was to calculate the total quasi-static seismic load and apply it on the model. As it is described in [3], one of the most commonly used methods to perform nonlinear analysis for the derived seismic loads is the Modal Push over Analysis (MPA), which is the method adopted in this work. The total seismic load was calculated according to EC8 [1] by using the type I response spectrum. The assumptions made for the calculation of the design spectrum acceleration and total base shear are given in Table 4.

After performing the modal analysis through the use of SAP2000, it was found that the under study bridge has its two first modes being translational oscillations along the X and Y axes, respectively. Given that the Y axis is the lateral axis of the model, the push over analysis was performed by applying the horizontal seismic load on the deck's vertical wall along the Y global axis (2nd dominant mode, see Fig. 26).

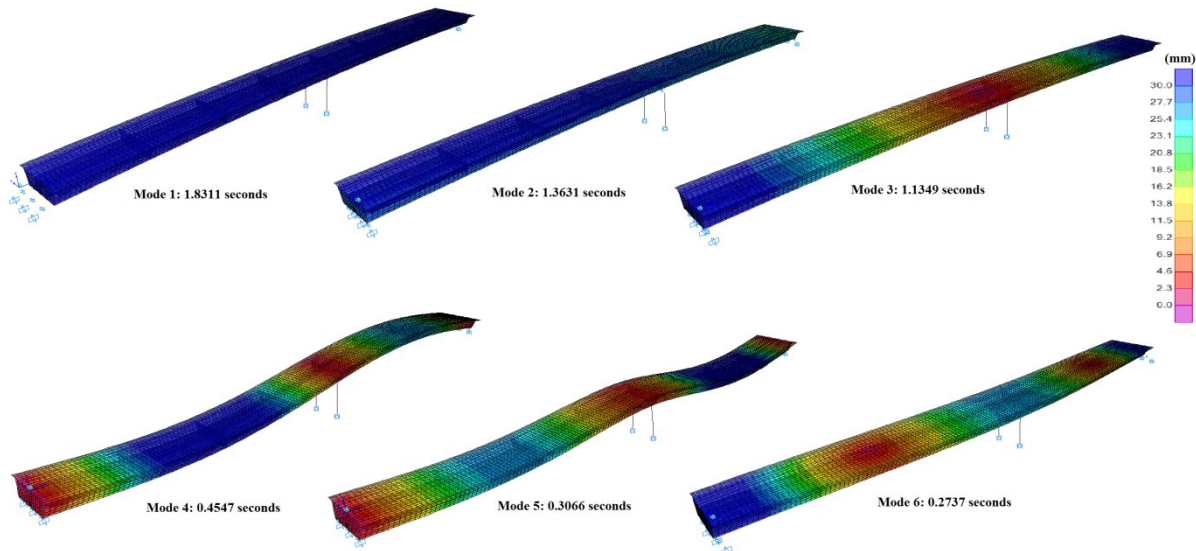


Figure 26. Mode shapes as they derived from SAP2000 (simplified model).

A total of 15MN were applied on the vertical wall of the deck through the use of 10 load increments. The work convergence criterion was set equal to 10^{-4} while it is relaxed to a 10^{-3} in the case that the required internal iterations were more than 10, in an attempt to decrease the computational time and retain an acceptable numerical accuracy. It is important to note here that when solving a hexahedral mesh with more than 100,000 elements the numerical errors that are generated due to the accuracy of the calculations used in the algorithm alone, are significant given the large number of elements, thus using a numerically unstable material model that releases significant unbalanced forces during each iteration especially when cracking occurs, achieving convergence becomes a numerically cumbersome task. The corresponding derived errors for the under study model are shown in Fig. 27.

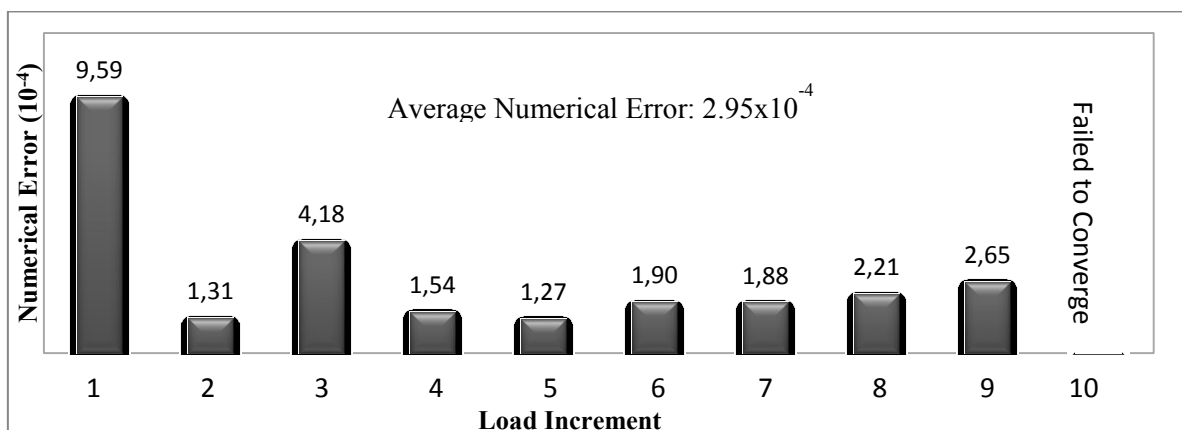


Figure 27. Numerical errors per load increment as they resulted from the nonlinear analysis.

The numerical results from the nonlinear analysis showed that the deformed shape of the under study bridge due to the horizontal load was similar to the 2nd modal shape while the elastomeric bearings were the structural members that developed significant deformations. As

it can be seen in Fig. 28, point β which is located at a distance of 39 m from point α , exhibits the maximum horizontal displacement, while the deck behaves as a beam under bending. In addition to that, the left span (which is the longest one) transfers a larger load to its left support (point α) and this is the reason why the horizontal displacement of the deck at the left support is larger than that of the right support (point δ). Fig. 29 shows the resulted P- δ curves for the four monitored points (α , β , γ & δ) shown in Fig. 28 and the corresponding curves of the top nodes of the two piers. As it can be observed from Fig. 29, the two piers do not exhibit the same horizontal displacement given the rotation of the deck about the Z global axis (Fig. 30), thus the overall deformation of the bridge was asymmetric.

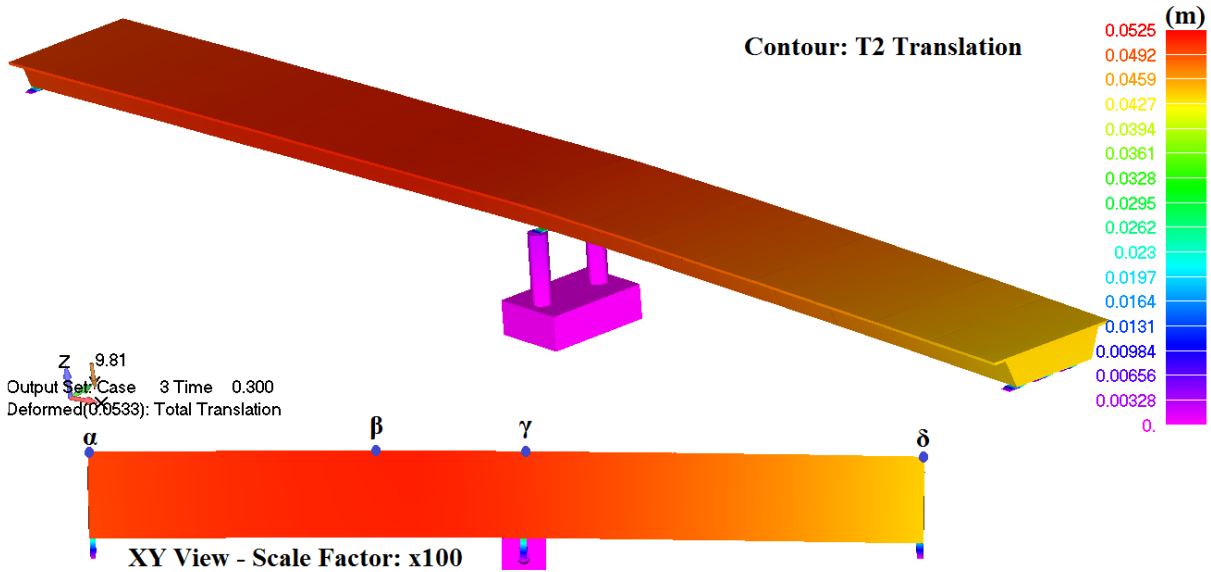


Figure 28. Deformed shape at load increment 3 (Total applied horizontal load 4.5 MN).

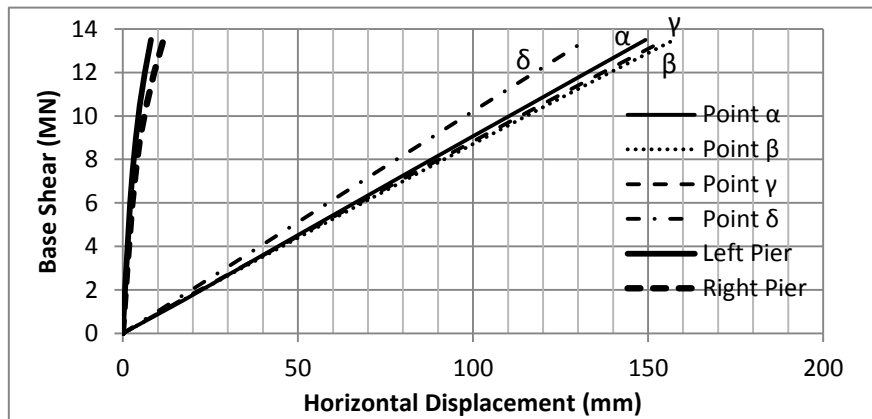


Figure 29. P- δ curves.

It is evident that the failure mechanism is controlled by the elastomeric bearing while the deck of the bridge does not develop any significant cracks prior to complete failure ($V_{max} = 13.5$ MN). The final model of the RC bridge is capable of carrying the code's design base shear demand (7.66 MN) and the piers manage to resist to the developed bending moments at their base. The maximum horizontal displacement prior to failure was found to be equal to 157.4 mm which is attributed to the use of elastomeric bearings that decouple the mechanical behavior of the deck and the piers thus modify significantly the stiffness of the bridge. It is evident that the piers and the deck does not deform significantly so as to develop rebar failures or even in this case rebar yielding.

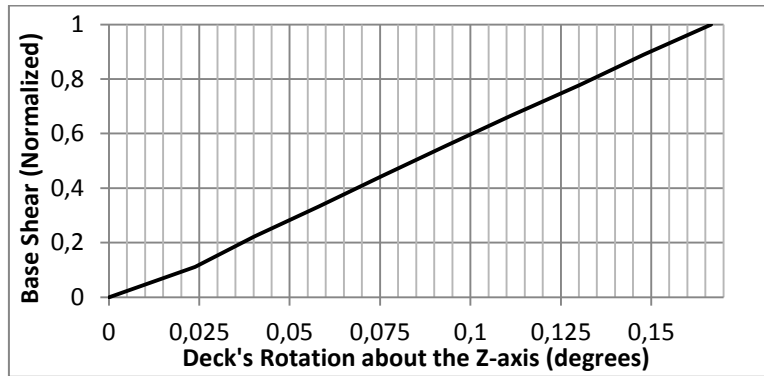
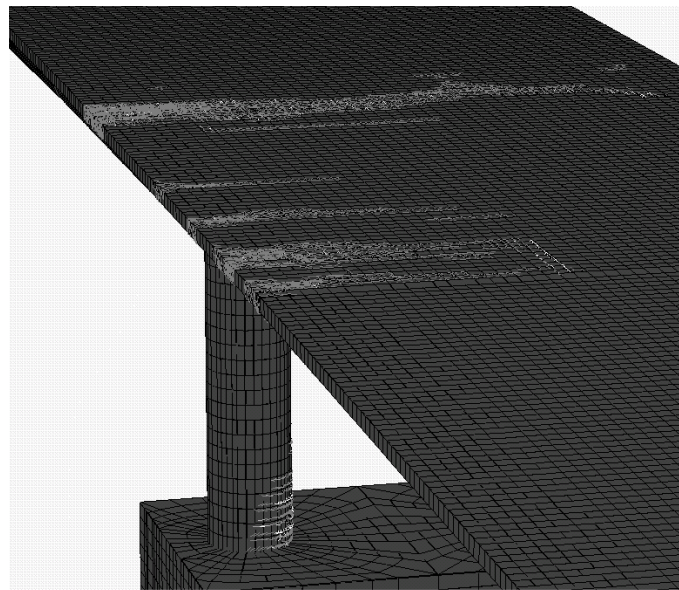
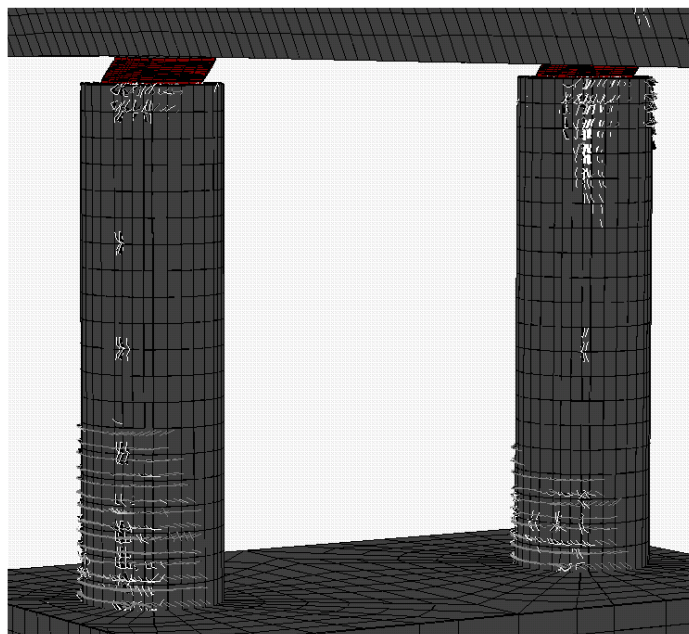


Figure 30. Deck's rotation due to the horizontal loading.



(A)



(B)

Figure 31. Crack patterns developed prior to failure. (A) Deck and (B) Piers of the bridge.

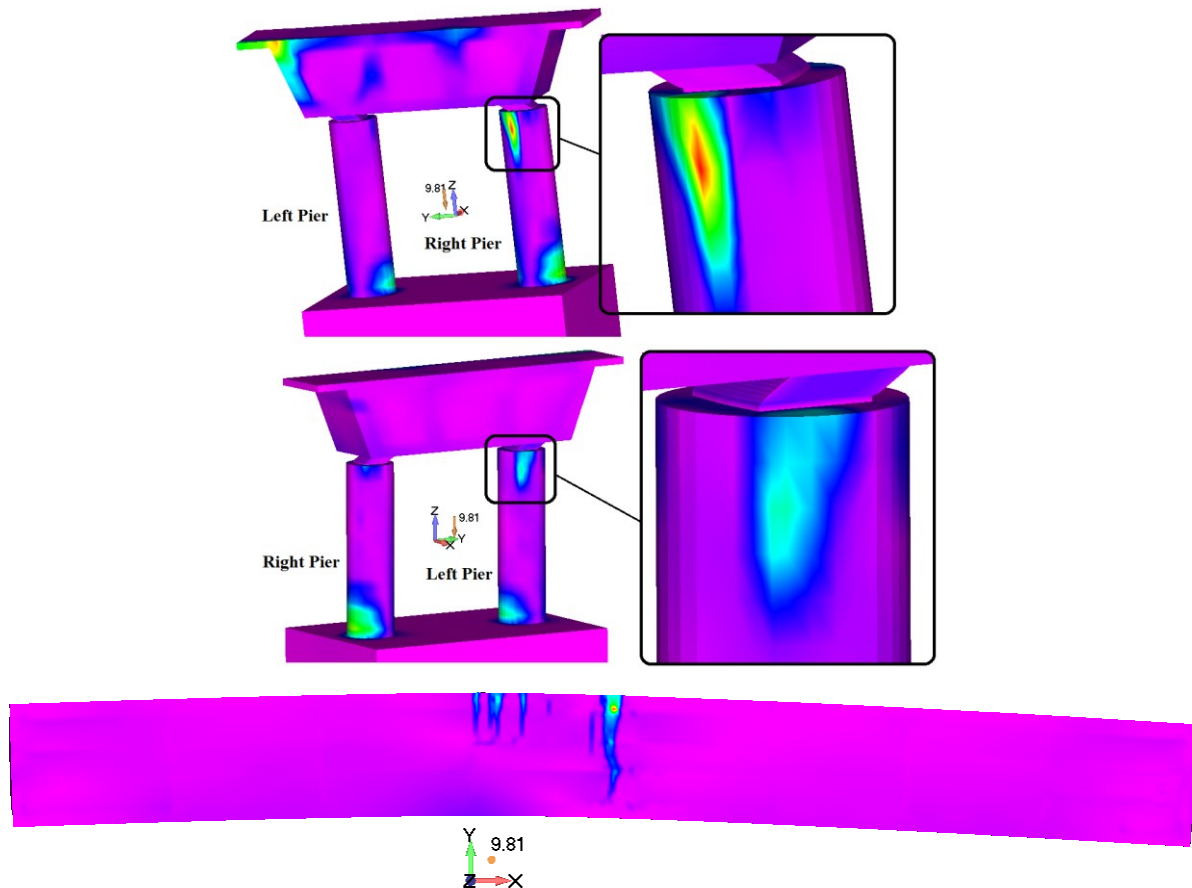


Figure 32. von Mises strain contours of the (Up) piers and middle vertical diaphragm and (Down) upper slab of the deck (seismic load direction: Y-axis).

As it can be seen in Fig. 31 the cracks that developed prior to failure are mainly located at the base and head of the piers, and the upper slab of the deck that is under tension due to the out-of-plane bending of the deck. Tensile cracks were also developed at the lower slab of the deck in a similar pattern as that shown in Fig. 31a & 32. The cracks that developed at the base of the piers are attributed to the bending moments that are generated due to the horizontal loads transferred from the bearings to the piers, while the diagonal cracks at the head of the two piers are attributed to shear and torsional deformations. This numerical finding illustrates the importance of using sufficient shear reinforcement so as to avoid any future vulnerability of these structural members (Fig. 32) during an earthquake excitation. For this reason many designers increase the diameter of the head of the piers so as to increase the shear resistance and avoid any local cracking. In this case, an increase of the piers heads is also proposed.

From the computational point of view, the total required computational time required to complete all numerical procedure was 46 hours and 30 minutes. 2.3% of the total computational time was attributed to the mesh generation procedure, while 26.5% was attributed to the output data writing process. As it can be depicted from Table 5, the nonlinear solution procedure requires almost 71% of the total computational time thus it is evident that it is the numerical procedure that derives the highest computation demands (mainly due to the stiffness inversion procedure – total number of stored stiffness matrix elements 798,697,535). It is also important to note here that the 33 hours required for the nonlinear solution procedure correspond to the numerical solution of a total of 100 internal iterations thus for the solution of each internal iteration it was required 19 minutes and 48 seconds.

a/a	Description	Value
1	Number of Hexahedral Elements	109,338
2	Number of Nodes (hexa8 only)	177,149
3	Number of Macro-Elements	49,172
4	Total Number of Embedded Rebar FEs Generated	529,332
5	Total Number of Short Embedded Rebar FEs that were Discarded by the Filter Algorithm	887
6	Required Embedded Mesh Generation Time	65 m 5 s
7	Required RAM for the Stiffness Matrix	5.95 Gb
8	Max Required RAM Allocated by the Software	20.65 Gb
9	Computational Time for Solving 10 Load Increment	33 hrs
10	Computational Time for Writing the Output Data	12 hrs 20m
11	Total Computational Time	46 hrs 30m

Table 5. General numerical details that derived after the nonlinear analysis of the complete FE model.

4 CONCLUSIONS

- The numerical investigation of the mechanical behavior of a full-scale RC bridge was performed through the use of 3D detailed analysis.
- The detailed mesh of the bridge was constructed through the use of 8-noded hexahedral elements that treat the cracking phenomenon through the smeared crack approach. The reinforcement grid is modeled through the use of embedded rod elements inside the hexahedral mesh.
- After performing the embedded mesh generation method [60] the derived results underline the importance of having a computationally efficient embedded rebar mesh generation techniques that will allocate large numbers of embedded rebars inside hexahedral meshes.
- A parametric investigation and a numerical calibration of the elastomeric bearings were performed so as to derive the optimum material parameters in modeling the exact geometry of the isolation system of the under study bridge.
- A simplified model was also constructed in SAP2000 so as to perform linear analysis and compare the numerical results that derived from the detailed model. As it was shown the deflection that resulted from the two models were close.
- Prestress was included in the 3D detailed model by incorporating an algorithm that provides the ability of assigning the posttension force at the tendons (which are also modeled as embedded rebar elements) as an initial force condition. The requirement in prestress resulted after performing a static nonlinear analysis for the dead loads of the 3D detailed model. Further investigation is required so as to verify the numerical performance of the prestress algorithm (comparison with experimental results of prestress beams, which will be the subject of future research work).
- The preliminary analysis revealed that the elastomeric bearings at the piers were under-designed thus an increase of the initial area was proposed.
- The RC bridge was seismically assessed according to EC8, were it was found that the code's demand was satisfied. In addition to that, it was found that the bearings at the two

piers controlled the failure mechanism of the bridge given that they are the structural members that fail first.

- Regarding the derived deformed shape and crack pattern of the bridge, it was found that the deck behaves in a similar manner to a beam that is under bending while rotation of the deck about the gravity axis (Z-axis) occurs due to the uneven spans. This rotation affects the deformed shape of the piers, which crack at the base due to bending but develop shear deformations at the heads due to both shear forces and torsion that results from the deck's rotation. Avoiding the development of shear cracks at the heads of the piers during an earthquake excitation, an increase of the piers head's diameter is proposed.
- From the computational point of view, it was found that the nonlinear solution is the most computationally demanding procedure (71%), while the I/O for writing the output data required 26.5% of the total operational time. This illustrates the computational efficiency of the embedded mesh generation method (2.3%) thus underlines the requirement of using parallel processing for the computationally demanding stages of the at hand numerical problem. Nevertheless, the overall computational response of the software, illustrates the potential of solving this type of numerical problems in a very short period of time given the future advances in both hardware and compiling technology.
- The numerical limitations of using 3D detailed FE models, for analyzing the mechanical behavior of RC bridges, have been investigated. The numerical findings underline the importance of optimum algorithmic design and the use of accurate but efficient numerical models that will alleviate the significant problem of the computational demand when dealing with large-scale FE meshes. This type of modeling approach is ideal for assessing the design of any type of RC structures and the seismic or carrying capacity of existing RC structures. Given that the FEs used above can model any type of 3D geometry, the interaction with soil can also be accounted for.
- Future research work foresees the incorporation of a parallel solution algorithm for the nonlinear procedure, which was found to be the most time consuming numerical process.

REFERENCES

- [1] CEN, prEN1998-2, EC8-2: Design provisions for earthquake resistance of structures. Part 2: Bridges, 2003.
- [2] AASHTO LRFD, *AASHTO LRFD Bridge Design Specifications*, American Association of State Highway and Transportation Officials, Washington, D.C, 2007.
- [3] R. Goel, A. Chopra, Nonlinear Analysis of Ordinary Bridges Crossing Fault-Rupture Zones, *Journal of Bridge Engineering*, **14**(3), 216–224, 2009.
- [4] A.S. Elnashai, D.C. McClure, Effect of Modeling Assumptions and Input Motion Characteristics on Seismic Design Parameters of RC Bridge Piers, *Earthquake Engineering & Structural Dynamics*, **25**(5), 435–463, 1996.
- [5] T.S. Paraskeva, A.J. Kappos, A.G. Sextos, Extension of modal pushover analysis to seismic assessment of bridges, *Earthquake Engineering & Structural Dynamics*, **35**(10), 1269–1293, 2006.
- [6] T. Potisuk, C. Higgins, Field Testing and Analysis of CRC Deck Girder Bridge, *Journal of Bridge Engineering*, **12**(1), 53–63, 2007.

-
- [7] H. Li, J. Wekezer, L. Kwasniewski, Dynamic Response of a Highway Bridge Subjected to Moving Vehicles, *Journal of Bridge Engineering*, **13**(5), 439–448, 2008.
- [8] N. Johnson, M. Saiidi, D. Sanders, Nonlinear Earthquake Response Modeling of a Large-Scale Two-Span Concrete Bridge, *Journal of Bridge Engineering*, **14**(6), 460–471, 2009.
- [9] W. Lee, S. Billington, Modeling Residual Displacements of Concrete Bridge Columns under Earthquake Loads Using Fiber Elements, *Journal of Bridge Engineering*, **15**(3), 240–249, 2010.
- [10] A. Aviram, K.R. Mackie, B. Stojadinovic, Nonlinear Modeling of Bridge Structures in California, *ACI*, **271**, 1-26, 2010.
- [11] Z.-C. Wang, W.-X. Ren, Dynamic Analysis of Prestressed Concrete Box-Girder Bridges by using the Beam Segment Finite Element Method, *International Journal of Structural Stability and Dynamics*, **11**(2), 379-399, 2011.
- [12] P. Kaviani, F. Zareian, E. Taciroglu, Seismic behavior of reinforced concrete bridges with skew-angled seat-type abutments, *Engineering Structures*, **45**, 137–150, 2012.
- [13] Y. Zhou, J. Prader, J. Weidner, N. Dubbs, F. Moon, A. Aktan, Structural Identification of a Deteriorated Reinforced Concrete Bridge *Journal of Bridge Engineering*, **17**(5), 774–787, 2012.
- [14] A.J. Kappos, M.S. Saiidi, M.N. Aydinoglou, T. Isaković, *Seismic design and assessment of Bridges. Inelastic methods and case studies*, Springer, Geotechnical, Geological and Earthquake Engineering, 2012.
- [15] P. Théoret, B. Massicotte, D. Conciatori, Analysis and Design of Straight and Skewed Slab Bridges, *Journal of Bridge Engineering*, **17**(2), 289–301, 2012.
- [16] E.T. Filipov, L.A. Fahnestock, J.S. Steelman, J.F. Hajjar, J.M. LaFave, D.A. Foutch, Evaluation of quasi-isolated seismic bridge behavior using nonlinear bearing models, *Engineering Structures*, **49**, 168-181, 2013.
- [17] I.F. Moschonas, A.J. Kappos, Assessment of concrete bridges subjected to ground motion with an arbitrary angle of incidence: static and dynamic approach, *Bulletin of Earthquake Engineering*, **11**(2), 581-605, 2013.
- [18] A.Abdel-Mohti, G. Pekcan, Assessment of seismic performance of skew reinforced concrete box girder bridges, *International Journal of Advanced Structural Engineering*, **5**, 1-18, 2013.
- [19] B. Richard, S. Epailard, Ch. Cremona, L. Elfgren, L. Adelaide, Nonlinear finite element analysis of a 50 years old concrete trough bridge, *Engineering Structures*, **32**, 3899-3910, 2010.
- [20] Ch.Ch. Chou, H.-J. Chang, J.T. Hewes, Two-plastic-hinge and two dimensional finite element models for post-tensioned precast concrete segmental bridge columns, *Engineering Structures*, **46**, 205–217, 2013.
- [21] C.M. Frissen, M.A.N. Hendriks, N. Kaptijn, 3D Finite element analysis of Multi-beam Box girder Bridges – assessment of cross-sectional forces in joints, M.A.N. Hendriks, J.G. Rots, eds, *Third DIANA World Conference*, Tokyo, Japan 9-11 October, 2002.
- [22] W. Kwan, S. Billington, Unbonded Posttensioned Concrete Bridge Piers. II: Seismic Analyses, *Journal of Bridge Engineering*, **8**(2), 102–111, 2003.

- [23] J. Cervenka, W. Cervenka, Z. Janda, *Safety assessment of railway bridges by non-linear analysis*, In: Bien, Elfgrén, Olofsson eds, Sustainable bridges, Wroclaw, DWE, 2007.
- [24] Z. Sun, B. Si, D. Wang, X. Guo, Experimental research and finite element analysis of bridge piers failed in flexure-shear modes, *Earthquake Engineering and Engineering Vibration*, **7**(4), 403-414, 2008.
- [25] V.K. Papanikolaou, A.J. Kappos, Numerical study of confinement effectiveness in solid and hollow reinforced concrete bridge piers: Part 1: Methodology and Part 2: Analysis results and discussion. *Engineering Structures*; **87**, 1427–1439, 1440-1450, 2009.
- [26] T.L.T. Nguyen, P.F. Silva, M.T. Manzari, A. Belarbi, System Modeling for Seismic Performance Assessment and Evaluation of Reinforced Concrete Bridge Columns, *ACI*, **271**, 125-146, 2010.
- [27] Y. Sha, H. Hao, Nonlinear finite element analysis of barge collision with a single bridge pier, *Engineering Structures*, **41**, 63-76, 2012.
- [28] R. Chacon, E. Mirambell, E. Real, Strength and ductility of concrete-filled tubular piers of integral bridges, *Engineering Structures*, **46**, 234–246, 2013.
- [29] Y. Deng, G. Morcouc, Efficient Prestressed Concrete-Steel Composite Girder for Medium-Span Bridges: II - Finite Element Analysis and Experimental Investigation, *Journal of Bridge Engineering*, In Press, 2013.
- [30] P. Zhu, M. Abe, Y. Fujino, Modelling three-dimensional non-linear seismic performance of elevated bridges with emphasis on pounding of girders, *Earthquake Engineering & Structural Dynamics*; **31**, 1891–1913, 2002.
- [31] Z. Ma, S. Chaudhury, J. Millam, J. Hulsey, Field Test and 3D FE Modeling of Decked Bulb-Tee Bridges, *Journal of Bridge Engineering*, **12**(3), 306–314, 2007.
- [32] X.H. He, X.W. Sheng, A. Scanlon, D.G. Linzell, X.D. Yu, Skewed concrete box girder bridge static and dynamic testing and analysis, *Engineering Structures*, **39**, 38–49, 2012.
- [33] K. Bi, H. Hao, Numerical simulation of pounding damage to bridge structures under spatially varying ground motions, *Engineering Structures*, **46**, 62-76, 2013.
- [34] E.K.C. Tang, H. Hao, Numerical simulation of a cable-stayed bridge response to blast loads, Part I: Model development and response calculations, Part II: Damage prediction and FRP strengthening, *Engineering Structures*, **32**, 3180-3192, 3193-3205, 2010.
- [35] A. Mwafy, O.-S. Kwon, A. Elnashai, Seismic assessment of an existing non-seismically designed major bridge-abutment-foundation system, *Engineering Structures*, **32**, 2192-2209, 2010.
- [36] CSI, SAP2000 structural analysis program. Berkeley (California): Computers and Structures Inc; 2006. www.csiberkeley.com
- [37] SC Solutions, Inc., California, Seismic Evaluation of the Cooper River Bridge, ADINA Tech Briefs, 2006. www.adina.com/newsgD4.shtml
- [38] Elnashai AS, Papanikolaou V, Lee D. ZEUS-NL a system for inelastic analysis of structures. Urbana (IL): Mid-America Earthquake Center, University of Illinois at Urbana-Champaign; 2008.
- [39] V. Cervenka, L. Jendele, J. Cervenka, *ATENA Program Documentation, Part 1: Theory*, Prague; 2008. www.cervenka.cz

- [40] LS-DYNA. LS-DYNA user manual. Livermore Software Technology Corporation, 2007. www.ls-dyna.com
- [41] S. Lan, J.E. Crawford, K.B. Morrill, Design of reinforced concrete columns to resist the effects of suitcase bombs. *In: Proceedings of the 6th Asia-Pacific Conference on Shock & Impact Loads on Structures*, pp. 325-332, 2005.
- [42] GT STRUDL, Structural Design & Analysis Software. www.gtstrudl.gatech.edu
- [43] ANSYS, *Release 11.0 Documentation for ANSYS*, ANSYS help, 2009. www.ansys.com
- [44] Abaqus FEA, Simulia - Dassault Systèmes, 2010. www.3ds.com
- [45] TNO Diana BV, *User's Manual*, 2011. <http://tnodiana.com/>
- [46] Strand7, Using Strand7 Manual, Strand7 Pty Ltd, 2010. www.strand7.com
- [47] DRAIN-3DX, Static and Dynamic Analysis of Inelastic 3D Structures, 2011.
- [48] McKenna F, Fenves GL, Scott MH. Open system for earthquake engineering simulation. California: University of California Berkeley; 2000. <http://opensees.berkeley.edu>
- [49] ADINA for structural analysis, User's Manual, ADINA R&D, Inc. www.adina.com
- [50] H. Hartl, Development of a Continuum-Mechanics-Based Tool for 3D Finite Element Analysis of Reinforced Concrete Structures and Application to Problems of Soil-Structure Interaction, *Ph.D. Thesis, Graz University of Technology, Institute of Structural Concrete*; 2002.
- [51] M.D. Kotsovos, M.N. Pavlovic, *Structural concrete – finite-element analysis for limit-state design*, Thomas Telford Publications; 1995.
- [52] C. Girard, J. Bastien, Finite Element bond slip model for concrete columns under cyclic loads, *Journal of Structural Engineering, ASCE*, **128**(12), 1502–1510, 2002.
- [53] Mirzabozorg H, Ghaemian M. Nonlinear behavior of mass concrete in 3d problems using a smeared crack approach, *Earthquake Engineering & Structural Dynamics*, **34**, 247–269, 2005.
- [54] G.C. Lykidis, K.V. Spiliopoulos, 3D Solid Finite-Element Analysis of Cyclically Loaded RC Structures Allowing Embedded Reinforcement Slippage, *Journal of Structural Engineering*, **134**(4), 629-638, 2008.
- [55] L. Jendele, J. Cervenka, V. Saouma, R. Pukl, On the choice between discrete or smeared approach in practical structural FE analyses of concrete structures, CERVENKA CONSULTING, Predvoje 22, 16200 Prague 6, Czech Republic and CEAE Dep., University of Colorado at Boulder, USA.
- [56] G. Markou, *Modeling of Reinforced Concrete Structures*, LAP Lambert Academic Publishing, 2011.
- [57] G. Markou, M. Papadrakakis, An efficient generation method of embedded reinforcement in hexahedral elements for reinforced concrete simulations, *Advances in Engineering Software ADES*, **45**(1), 175-187, 2012.
- [58] G. Markou and M. Papadrakakis, Modeling of Reinforced Concrete Structures with 3d detailed finite element models, *AHU Journal of Engineering and Applied Sciences*, **4**(2), 47-63, 2012.

- [59] ReConAn FEA Analysis software, 2011.
http://alhosnu.ae/Markou/index_files/ReConAn.htm
- [60] G. Markou, Generating Embedded Rebar Elements for Large-Scale RC Models, M. Papadrakakis, M. Kojic, I. Tuncer eds., SEECOM III, 3rd South-East European Conference on Computational Mechanics, an ECCOMAS and IACM Special Interest Conference Kos Island, Greece, 12–14 June, 2013.
- [61] G. Markou, Embedded reinforcement mesh generation method for large-scale RC simulations: Case study, *AHU Journal of Engineering & Applied Sciences*, **5**(1), 23-42, 2012.
- [62] G. Markou and M. Papadrakakis, An efficient generation method of embedded reinforcement in hexahedral elements for reinforced concrete simulations, *Advances in Engineering Software ADES*, **45**(1), 175-187, 2012.
- [63] Ch.D. Newhouse, S.A. Bole, W.R. Burkett, P.T. Nash, M. El-Shami, Study of Elastomeric Bearings for Superelevated U-Beam Bridges, *Research Report, Texas University*, October, 2009.
- [64] R.A. Cook, D.T. Allen, M.H. Ansley, Stiffness Evaluation of Neoprene Bearing Pads under Long-Term Loads, *Research Report, University of Florida*, March, 2009.
- [65] J. Wekezer, E. Taft, L. Kwasniewski, S. Earle, Investigation of impact factors for FODT bridges. FDOT Structures research laboratory final report, *Research Report, University of Florida*, December, 2010.
- [66] Australian Standards, AS 5100.4 SUPP 1-2006 bridge design - bearings and deck joints, Standards Australia, 2006.
- [67] VSL, CTT Elastomeric Bearings. www.vsl.com/document.php?getfile=2719
- [68] G. Stavroulakis, M. Papadrakakis, Advances on the domain decomposition solution of large scale porous media problems, *Computer Methods in Applied Mechanics and Engineering*, **196**, 1935-1945, 2009.

DESIGN OF RC SECTIONS IN THE ULTIMATE LIMIT STATE UNDER BENDING AND AXIAL FORCE ACCORDING TO EC2

Vagelis Plevris, George Papazafeiropoulos and Manolis Papadrakakis

National Technical University of Athens
Institute of Structural Analysis and Antiseismic Research
Zografou Campus, Athens 15780, Greece

e-mail: yplevris@central.ntua.gr, gpapazafeiropoulos@yahoo.gr, mpapadra@central.ntua.gr

Keywords: Reinforced Concrete, RC, Section, Design, Eurocode, Reinforcement.

Abstract. *In the imminent future the design of concrete structures in Europe will be governed by the application of Eurocode 2 (EC2). In particular, EC2 – Part 1-1 [1] deals with the general rules and rules for concrete buildings. An important aspect of the design is specifying the necessary tensile (and compressive, if needed) steel reinforcement required for a Reinforced Concrete (RC) section, in order to ensure that the RC member will be able to resist the design loads.*

According to EC2-Part 1-1 three different simplified diagrams for the stress-strain behavior of concrete for RC sections design can be assumed: (a) the equivalent rectangular stress block, (b) the parabolic-rectangular stress-strain relation and (c) the bi-linear stress-strain relation as a simplification of the parabolic-rectangular case. In this study the three approaches suggested by EC2-Part 1-1 are investigated for the design of rectangular RC cross-sections with tensile steel reinforcement to resist loading due to bending moment and axial force. The tensile strength of concrete is neglected and concrete is supposed to work only in compression. For each case analytical relations are extracted in detail with a step-by-step detailed procedure, the relevant assumptions are highlighted and results for four beam design examples are finally presented.

1 LITERATURE REVIEW

Rosca and Petru [2] study the design of a reinforced concrete section subjected to bending using the two stress–strain relationships mentioned in EC2, namely the parabola-rectangle stress distribution and the rectangular distribution, and the differences are underlined. Two dimensionless quantities are used to convert the parabola-rectangle stress distribution to an equivalent concentrated force for the concrete in compression. Also analytical relations which determine the limit between single reinforcement (only tensile) and double reinforcement (tensile and compressive) are provided. The results drawn from the use of these two stress distributions, namely, parabola–rectangle and rectangle, showed that the differences between the amounts of reinforcement are less than 1% for singly reinforced sections and less than 2% for doubly reinforced sections.

Dulinskas and Zabulionis in [3] and [4] propose a method for the substitution of the non-linear stress diagram with descending branch with an equivalent rectangular stress block when the non-linear stress-strain relationship for concrete in compression is described according to EC2. Analytical relationships in explicit form for area, the first moment of area, the coordinate of centroid of the nonlinear stress diagram with descending branch, the ratio between the depth of the rectangular stress block and that of the equivalent nonlinear stress diagram with descending branch in respect to the concrete strength are given. Coefficients suitable for the substitution of parabola stress diagram with descending branch given in EC2 with an equivalent rectangular stress block are presented. These coefficients have to ensure that the substitution is equivalent, i.e. the carrying capacity of the compression zone calculated using either of the two stress diagrams should be the same.

Židonis in [5] tries to replace the nonlinear stress-strain diagram of concrete adopted by EC2 for structural analysis by another more general curvilinear diagram which relates stress and strain of concrete. The new stress-strain diagram permits direct integration without the need to discretize the stress-strain curve. Thus it makes the integration easier and can be applied to the concrete classes from C8/10 up to C90/105. Analytical stress-strain relations are presented for concrete which can fit the stress-strain curves specified in EC2 within an error of 1.5%. Finally, examples of application of the proposed stress-strain diagram are illustrated.

In [6] a method is presented and formulas are provided for application of non-linear concrete stress diagram for cross-section strength calculation in accordance with the limit state (partial factors) method. Commonly reinforced concrete flexural members with rectangular compression zone and the neutral axis within the cross-section are considered (beam-type members); the effect of the descendant part of stress-strain diagram on strength of cross-sections of beam type members is investigated and the limit between commonly and abundantly reinforced concrete beams is determined. Finally the results of the new method are compared with those of EC2, where rectangular compression zone stress diagram for concrete is assumed. A table is extracted in which all necessary information needed to perform design for bending of a reinforced concrete section for all concrete strength classes are shown.

Although the above studies deal with the application of the most suitable stress-strain diagram for concrete for the “optimal” design of cross sections using different approaches, to the authors’ knowledge, there is no study in which explicit formulas and/or graphs are provided to achieve the design of RC concrete sections according to EC2-Part 1-1 for all the three stress-strain relations provided. In the present study, the three suggested stress-strain diagrams of EC2 are investigated and analytical formulas are given for the step-by-step design of RC sections according to any one of the three design approaches.

2 DESIGN ASSUMPTIONS

The following design assumptions are made:

- Design is based on characteristic concrete cylinder strengths, not cube strengths.
- Plane sections remain plane.
- Strain in the bonded reinforcement, whether in tension or compression, is the same as that in the surrounding concrete.
- Tensile strength of the concrete is ignored.
- Concrete stress distribution is considered according to the three cases of Eurocode 2, as will be shown in detail in the next paragraphs.
- Stress in steel reinforcement is considered according to the stress-strain relation of Eurocode 2 for steel, as will be shown in detail in the next paragraphs.

3 CONCRETE PROPERTIES

According to EC2-1-1 the compressive strength of concrete is denoted by concrete strength classes which relate to the characteristic (5%) cylinder strength f_{ck} , or cube strength $f_{ck,cube}$, in accordance with EN 206-1. Higher strengths of concrete are covered by Eurocode 2, up to class C90/105. The strength classes for concrete are presented in the table below.

f_{ck} (MPa)	12	16	20	25	30	35	40	45	50	55	60	70	80	90
$f_{ck,cube}$ (MPa)	15	20	25	30	37	45	50	55	60	67	75	85	95	105

Table 1. Strength classes for concrete.

where f_{ck} is the characteristic compressive cylinder strength of concrete at 28 days and $f_{ck,cube}$ is the corresponding cube strength. The value of the design compressive strength is defined as

$$f_{cd} = a_{cc} \frac{f_{ck}}{\gamma_c} \quad (1)$$

where:

- γ_c is the partial safety factor for concrete at the Ultimate Limit State, which is given in Table 2.1N of EC2-1-1. For persistent and transient design situations, $\gamma_c=1.5$
- a_{cc} is the coefficient taking account of long term effects on the compressive strength and of unfavourable effects resulting from the way the load is applied. The value of a_{cc} for use in a country should lie between 0.8 and 1.0 and may be found in its National Annex. The recommended value is 1.

It should be noted that higher concrete strength shows more brittle behavior, reflected by shorter horizontal branch, as will be shown in the stress-strain relations, later.

4 CONCRETE STRESS-STRAIN RELATIONS FOR THE DESIGN OF CROSS-SECTIONS

Eurocode 2 Part 1-1 suggests the use of three approaches for the stress-strain relations of concrete for the design of cross sections:

- Parabola-rectangle diagram (more detailed)
- Bi-linear stress-strain relation (less detailed)
- Rectangular stress distribution (simplest)

The three above approaches will be described in detail in the following sections.

4.1 Parabola-rectangle diagram for concrete under compression

According to EC2-1-1 (Paragraph 3.1.7), for the design of cross-sections, the following stress-strain relationship may be used:

$$\sigma_c = \begin{cases} f_{cd} \left[1 - \left(1 - \frac{\varepsilon_c}{\varepsilon_{c2}} \right)^n \right] & \text{for } 0 \leq \varepsilon_c < \varepsilon_{c2} \\ f_{cd} & \text{for } \varepsilon_{c2} \leq \varepsilon_c \leq \varepsilon_{cu2} \end{cases} \quad (2)$$

where:

- n is the exponent given by

$$n = \begin{cases} 2.0 & \text{for } f_{ck} \leq 50 \text{ MPa} \\ 1.4 + 23.4 \left(\frac{90 - f_{ck}}{100} \right)^4 & \text{for } 50 < f_{ck} \leq 90 \text{ MPa} \end{cases} \quad (3)$$

- ε_{c2} is the strain at reaching the maximum strength given by

$$\varepsilon_{c2} (\%) = \begin{cases} 2.0 & \text{for } f_{ck} \leq 50 \text{ MPa} \\ 2.0 + 0.085 (f_{ck} - 50)^{0.53} & \text{for } 50 < f_{ck} \leq 90 \text{ MPa} \end{cases} \quad (4)$$

- ε_{cu2} is the ultimate strain given by

$$\varepsilon_{cu2} (\%) = \begin{cases} 3.5 & \text{for } f_{ck} \leq 50 \text{ MPa} \\ 2.6 + 35 \left(\frac{90 - f_{ck}}{100} \right)^4 & \text{for } 50 < f_{ck} \leq 90 \text{ MPa} \end{cases} \quad (5)$$

The above equation is depicted in the following figure, where compressive stresses (and strains) are shown as positive.

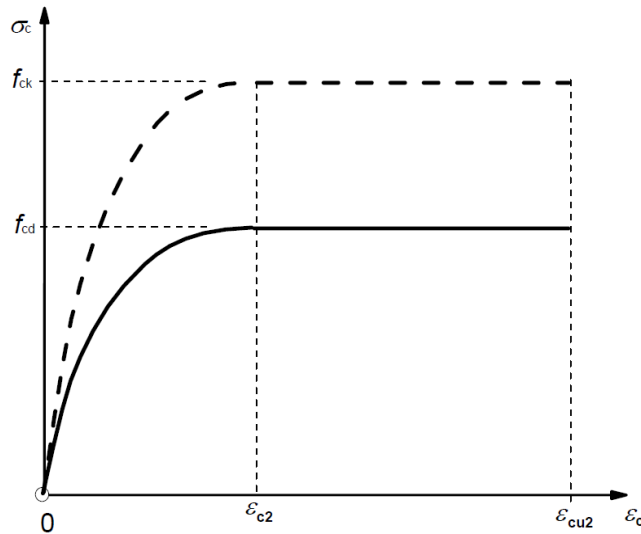


Figure 1: Parabola-rectangle diagram for concrete under compression.

4.2 Bi-linear stress-strain relation

According to Paragraph 3.1.7(2) of EC2-1-1, other simplified stress-strain relationships may be used if equivalent or more conservative than the one defined in Eq. (2), for instance bi-linear according to the following figure, where again compressive stress and shortening strain are shown as absolute values.

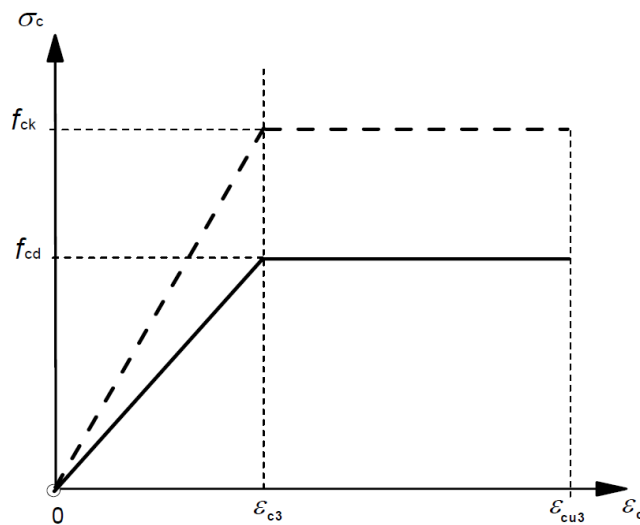


Figure 2: Bi-linear stress-strain relation.

where the values of ε_{c3} and ε_{cu3} are given by

$$\varepsilon_{c3}(\%) = \begin{cases} 1.75 & \text{for } f_{ck} \leq 50 \text{ MPa} \\ 1.75 + 0.55 \cdot \frac{f_{ck} - 50}{40} & \text{for } 50 < f_{ck} \leq 90 \text{ MPa} \end{cases} \quad (6)$$

$$\varepsilon_{cu3}(\text{‰}) = \begin{cases} 3.5 & \text{for } f_{ck} \leq 50 \text{MPa} \\ 2.6 + 35 \left(\frac{90 - f_{ck}}{100} \right)^4 & \text{for } 50 < f_{ck} \leq 90 \text{MPa} \end{cases} \quad (7)$$

4.3 Rectangular stress distribution

According to Paragraph 3.1.7(3) of EC2-1-1, a rectangular stress distribution may be assumed for concrete, as shown in the following figure.

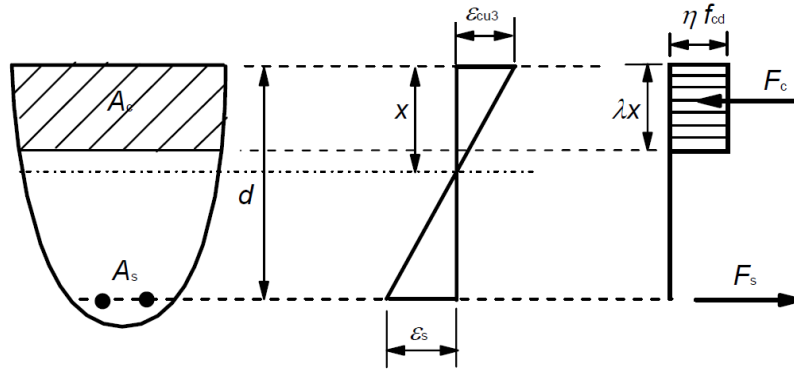


Figure 3: Rectangular stress distribution.

where:

- d is the effective depth of a cross-section
- x is the neutral axis depth
- A_s is the cross sectional area of the tensile steel reinforcement
- F_c is the concrete force (compressive, positive, as in the figure)
- F_s is the steel reinforcement force (tensile, positive, as in the figure)
- The factor λ defining the effective height of the compression zone and the factor η defining the effective strength, are calculated from:

$$\lambda = \begin{cases} 0.8 & \text{for } f_{ck} \leq 50 \text{MPa} \\ 0.8 - \frac{f_{ck} - 50}{400} & \text{for } 50 < f_{ck} \leq 90 \text{MPa} \end{cases} \quad (8)$$

$$\eta = \begin{cases} 1.0 & \text{for } f_{ck} \leq 50 \text{MPa} \\ 1.0 - \frac{f_{ck} - 50}{200} & \text{for } 50 < f_{ck} \leq 90 \text{MPa} \end{cases} \quad (9)$$

Note: If the width of the compression zone decreases in the direction of the extreme compression fibre, the value ηf_{cd} should be reduced by 10%.

5 STEEL PROPERTIES

The design strength for steel is given by

$$f_{yd} = \frac{f_{yk}}{\gamma_s} \quad (10)$$

where:

- γ_s is the partial safety factor for steel at the Ultimate Limit State, which is given in Table 2.1N of EC2-1-1. For persistent and transient design situations, $\gamma_s=1.15$

- f_{yk} is the characteristic yield strength of steel reinforcement.

Table C.1 of Annex C of EC2-1-1 gives the properties of reinforcement suitable for use with the Eurocode. The properties are valid for temperatures between -40°C and 100°C for the reinforcement in the finished structure. Any bending and welding of reinforcement carried out on site should be further restricted to the temperature range as permitted by EN 13670.

Product form	Bars and de-coiled rods			Wire Fabrics			Requirement or quantile value (%)
Class	A	B	C	A	B	C	-
Characteristic yield strength f_{yk} or $f_{0,2k}$ (MPa)	400 to 600						5,0
Minimum value of $k = (f_t/f_y)_k$	$\geq 1,05$	$\geq 1,08$	$\geq 1,15$ $< 1,35$	$\geq 1,05$	$\geq 1,08$	$\geq 1,15$ $< 1,35$	10,0
Characteristic strain at maximum force, ε_{uk} (%)	$\geq 2,5$	$\geq 5,0$	$\geq 7,5$	$\geq 2,5$	$\geq 5,0$	$\geq 7,5$	10,0
Bendability	Bend/Rebend test			-			
Shear strength	-			0,3 A f_{yk} (A is area of wire)			Minimum
Maximum deviation from nominal mass (individual bar or wire) (%)	Nominal bar size (mm) ≤ 8 > 8			$\pm 6,0$ $\pm 4,5$			5,0

Table 2. Properties of steel reinforcement (Table C.1 of Annex C of EC2-1-1).

The application rules for design and detailing in Eurocode 2 are valid for a specified yield strength range, f_{yk} from 400 to 600 MPa. The yield strength f_{yk} is defined as the characteristic value of the yield load divided by the nominal cross sectional area. The reinforcement shall have adequate ductility as defined by the ratio of tensile strength to the yield stress, $(f_t/f_y)_k$ and the elongation at maximum force, ε_{uk} .

5.1 Steel stress-strain relations for the design of cross-sections

For normal design, either of the following assumptions may be made for the stress-strain relation for steel (see figure below):

1. An inclined top branch with a strain limit of ε_{ud} and a maximum stress of $k \cdot f_{yk} / \gamma_s$ at ε_{uk} , where $k = (f_t/f_y)_k$ (see the above Table 2).
2. A horizontal top branch without the need to check the strain limit.

The value of ε_{ud} for use in a country may be found in its National Annex. The recommended value is $0.9\varepsilon_{uk}$. The design value of the steel modulus of elasticity E_s may be assumed to be 200 GPa.

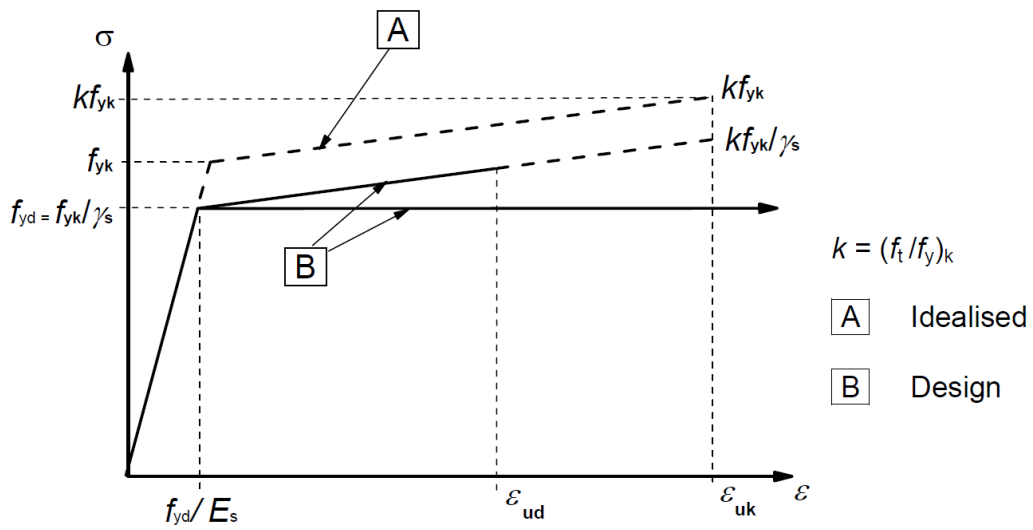


Figure 4: Idealised and design stress-strain diagrams for reinforcing steel (for tension and compression)

In the present study we will use the second approach, assuming a horizontal top branch for the steel stress-strain relation, but also limiting the maximum strain to ϵ_{ud} , as shown in the following figure.

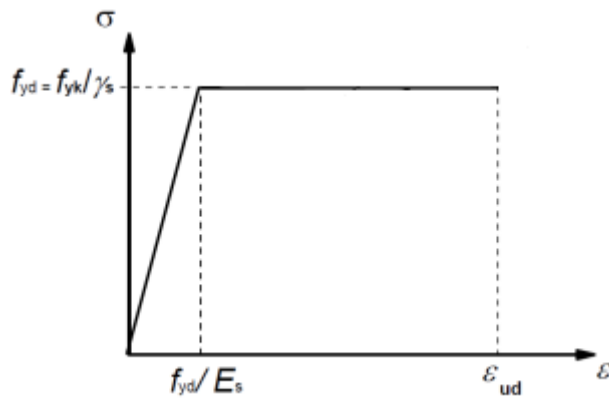


Figure 5: Design stress-strain diagram for reinforcing steel (for tension and compression) used in the present study.

6 INVESTIGATION OF THE SIMPLIFIED RECTANGULAR STRESS DISTRIBUTION CASE

The figure below shows a typical rectangular cross section and the distribution of strains and stresses (forces).

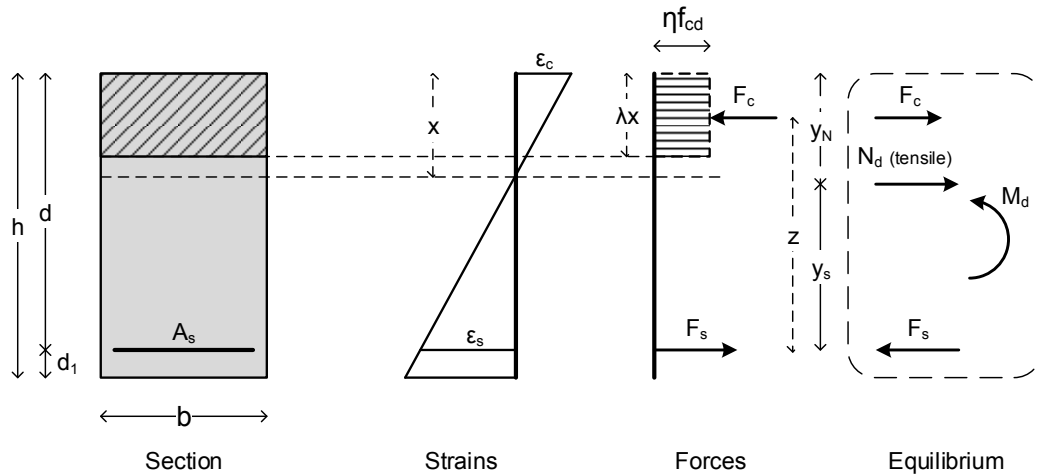
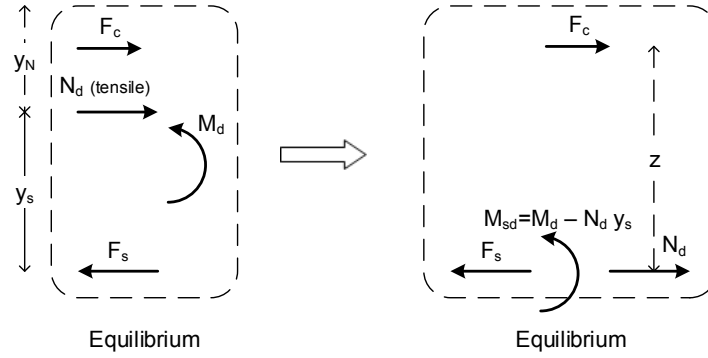


Figure 6: Cross section, strain and forces distribution and section equilibrium.

In the above figure:

- h is the height of the rectangular section
- d_1 is the distance from the lower edge of the section to the center of the reinforcement
- ε_s is the tensile strain in the steel reinforcement
- ε_c is the compressive strain in the concrete upper edge
- λ is a factor defining the effective height of the compression zone
- η is a factor defining the effective strength of the compression zone
- M_d is the applied external bending moment (puts the lower edge of the section in tension if positive)
- N_d is the applied external axial force (tensile for the section if positive), applied at a position y_N measured from the top of the section towards the lower edge of it. Note: If we have central tension, then $y_n = h/2$
- y_s is the distance from the steel reinforcement to the position of the external applied axial force
- z is the distance of the concrete force F_c from the steel reinforcement.

The goal of the design is to calculate the needed cross sectional area of steel reinforcement A_s . In order to calculate A_s , we need first to calculate the unknown quantities x and z . We move the external force N_d to the position of the steel reinforcement and we have the figure below.


 Figure 7: Equilibrium after moving the external force N_d to the position of the steel reinforcement.

From the equilibrium of the section in the x-direction, we have:

$$\Sigma F_x = 0 \Rightarrow F_c + N_d - F_s = 0 \Rightarrow F_s = F_c + N_d \quad (11)$$

We have also:

$$y_s + y_n = d \Rightarrow y_s = d - y_n \quad (12)$$

The effective bending moment is:

$$M_{sd} = M_d - N_d \cdot y_s \quad (13)$$

From the geometry of the section, we have:

$$z + \frac{\lambda x}{2} = d \Rightarrow z = d - \frac{\lambda x}{2} \quad (14)$$

The concrete force is given by:

$$F_c = \lambda x \cdot n f_{cd} \cdot b \quad (15)$$

From the equilibrium of moments at the position of the steel reinforcement (Figure 7) we have (clockwise moment taken as positive):

$$\Sigma M_{steel} = 0 \Rightarrow F_c \cdot z - M_{sd} = 0 \Rightarrow M_{sd} = F_c \cdot z \quad (16)$$

By substituting Eq. (15) in Eq. (16), we have:

$$M_{sd} = \lambda x \cdot n f_{cd} \cdot b \cdot z \quad (17)$$

By substituting Eq. (14) in Eq.(17), we have:

$$M_{sd} = \lambda x \cdot n f_{cd} \cdot b \cdot \left(d - \frac{\lambda x}{2} \right) = x \cdot (\lambda \cdot n f_{cd} \cdot b \cdot d) - x^2 \cdot \left(n f_{cd} \cdot b \cdot \frac{\lambda^2}{2} \right) \Rightarrow \quad (18)$$

$$\left(\frac{n f_{cd} \cdot b \cdot \lambda^2}{2} \right) \cdot x^2 - (\lambda \cdot n f_{cd} \cdot b \cdot d) \cdot x + M_{sd} = 0 \quad (19)$$

The above equation can be written as:

$$Ax^2 + Bx + C = 0 \quad (20)$$

where

$$A = \frac{nf_{cd} \cdot b \cdot \lambda^2}{2}, \quad B = -(\lambda \cdot nf_{cd} \cdot b \cdot d), \quad C = M_{sd} \quad (21)$$

The above quantities A, B and C are all known, so by solving the quadratic Eq. (20) we can determine the quantity x . The discriminant of the quadratic equation is:

$$\Delta = B^2 - 4A \cdot C = (\lambda \cdot nf_{cd} \cdot b \cdot d)^2 - 2nf_{cd} \cdot b \cdot \lambda^2 \cdot M_{sd} \quad (22)$$

The solution of the quadratic equation is:

$$x_{1,2} = \frac{-B \pm \sqrt{\Delta}}{2A} = \frac{d}{\lambda} \pm \frac{\sqrt{\Delta}}{2A} \Rightarrow \begin{cases} x_1 = \frac{d}{\lambda} - \frac{\sqrt{\Delta}}{2A} \\ x_2 = \frac{d}{\lambda} + \frac{\sqrt{\Delta}}{2A} \end{cases} \quad (23)$$

Given the requirement that $0 \leq x \leq d$ and the fact that $\lambda = 0.80$ for $f_{ck} \leq 50$ MPa and $\lambda < 0.80$ for $50 < f_{ck} \leq 90$ MPa, it is obvious that $d/\lambda > d$, and as a result $x_2 > d$ which is not acceptable. So the only acceptable solution is $x = x_1$ and thus:

$$x = \frac{d}{\lambda} - \frac{\sqrt{\Delta}}{2A} \quad (24)$$

After calculating x , it is easy to calculate also z with Eq. (14), F_c with Eq. (15) and F_s with Eq. (11). We have also:

$$F_s = A_s \cdot \sigma_s \Rightarrow A_s = \frac{F_s}{\sigma_s} \quad (25)$$

In the above equations, σ_s is the steel stress at the Ultimate Limit State (ULS) of the section. The yield strain ε_{ys} for steel is:

$$\varepsilon_{ys} = \frac{f_{yd}}{E_s} \quad (26)$$

where

$$f_{yd} = \frac{f_{yk}}{\gamma_s} \quad (27)$$

if $\varepsilon_s \geq \varepsilon_{ys}$ then the steel works in full stress and $\sigma_s = f_{yd}$. Otherwise, if $\varepsilon_s < \varepsilon_{ys}$ then the steel does not work in full stress and $\sigma_s < f_{yd}$. In general, the steel stress σ_s is given by:

$$\sigma_s = \begin{cases} f_{yd} \cdot \frac{\varepsilon_s}{\varepsilon_{ys}} = E_s \cdot \varepsilon_s & \text{if } 0 < \varepsilon_s < \varepsilon_{ys} \\ f_{yd} & \text{if } \varepsilon_s \geq \varepsilon_{ys} \end{cases} \quad (28)$$

In order to determine the area of steel reinforcement A_s , we need to determine the steel stress σ_s and thus we should determine the steel strain ε_s . In order to determine ε_s given the

value of x , we first need to know if the steel reinforcement or the concrete is critical (at the ultimate strain) at the Ultimate Limit State of the section.

In the present study, the steel reinforcement is limited to ε_{ud} . If the steel reinforcement is critical, then $\varepsilon_s = \varepsilon_{ud}$ and $\varepsilon_c < \varepsilon_{cu3}$. Otherwise, if the concrete is critical, then $\varepsilon_c = \varepsilon_{cu3}$ and $\varepsilon_s < \varepsilon_{ud}$. In the special case where both materials are critical, then $\varepsilon_s = \varepsilon_{ud}$ and $\varepsilon_c = \varepsilon_{cu3}$. These three possible states are presented in detail in the figure below.

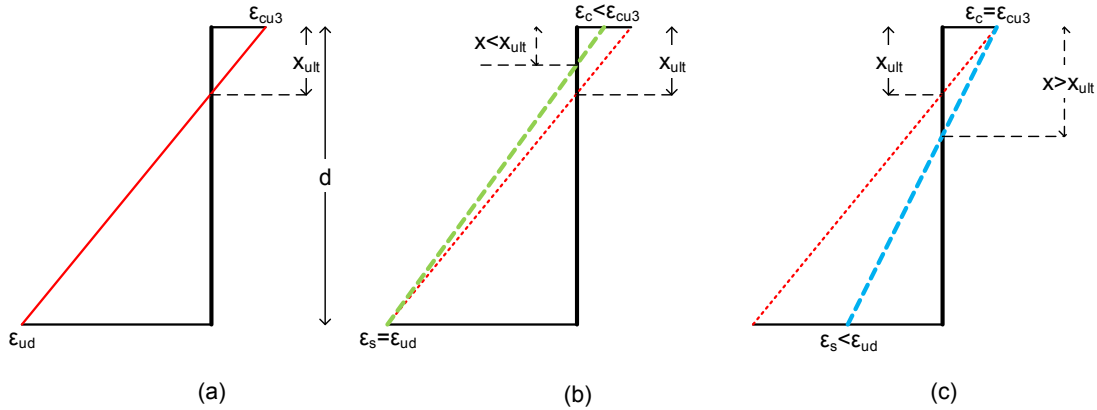


Figure 8: Three possible states of the strains of the cross section.

(a) Both materials are at the ultimate strain, (b) Steel at the ultimate strain, (c) Concrete at the ultimate strain.

In order to find out if the concrete or the steel is critical, we first calculate x_{ult} which is the neutral axis depth for the special case of both materials being critical, as in the figure above – Case (a). It should be noted that this is only a theoretical case and it does not correspond to equilibrium of the cross section. Using similar triangles, we have:

$$\frac{\varepsilon_{cu3}}{x_{ult}} = \frac{\varepsilon_{cu3} + \varepsilon_{ud}}{d} \Rightarrow x_{ult} = \frac{\varepsilon_{cu3}}{\varepsilon_{cu3} + \varepsilon_{ud}} \cdot d \quad (29)$$

Then we have 2 cases:

Case 1: $x < x_{ult}$, as shown in Figure 8 (b)

The steel reinforcement is at the critical strain, $\varepsilon_s = \varepsilon_{ud}$, while $\varepsilon_c < \varepsilon_{cu3}$. In this case, it is ensured that the steel works in full stress, and thus

$$\sigma_s = f_{yd} \quad (30)$$

And the steel area is given by:

$$A_s = \frac{F_s}{\sigma_s} = \frac{F_s}{f_{yd}} \quad (31)$$

The concrete strain ε_c in this case can be calculated by:

$$\frac{\varepsilon_c}{x} = \frac{\varepsilon_c + \varepsilon_{ud}}{d} \Rightarrow \varepsilon_c = \frac{x}{d} (\varepsilon_c + \varepsilon_{ud}) \quad (32)$$

Case 2: $x > x_{ult}$, as in shown in Figure 8 (c)

The concrete zone is at the critical strain, $\varepsilon_c = \varepsilon_{cu3}$ while $\varepsilon_s < \varepsilon_{ud}$. The steel strain ε_s can be calculated by:

$$\frac{\varepsilon_s}{d-x} = \frac{\varepsilon_{cu3} + \varepsilon_s}{d} \Rightarrow \varepsilon_s = \left(1 - \frac{x}{d}\right) (\varepsilon_{cu3} + \varepsilon_s) \quad (33)$$

In this case, it is not sure whether the steel works in full stress or not. The steel strain ε_s has to be checked if it is above or below the steel yield strain ε_{ys} as follows:

- **Case 2a: The steel works in full stress, $\varepsilon_s \geq \varepsilon_{ys}$**

The steel reinforcement works in full stress, above the yield strain and as a result the steel area can be calculated by Eq. (31).

- **Case 2b: The steel does not work in full stress, $\varepsilon_s < \varepsilon_{ys}$**

The steel reinforcement does not work in full stress, as it works below the yield strain. The steel stress σ_s can be calculated by Eq. (28) and the steel area can be calculated by Eq. (25). In this case, although the reinforcement area can be calculated, the design with only tensile reinforcement is not economic. Either compressive reinforcement should be considered, or an increase in the effective depth of the cross-section d .

6.1 Comment on the above cases

Eurocode 2 allows the designer to not limit the ultimate strain for steel when a horizontal top branch is assumed for the stress-strain diagram for steel. In this case, the concrete zone is assumed to be at the ultimate strain at all times at the ULS of the section under any design loads and the steel strain can take any value, without any limitation. If this is the case, then in the above investigation we have to set $x_{ult}=0$ and we have always the case of Figure 8(c) where the concrete zone is at the ultimate strain for all design cases.

This assumption can make things simpler and the calculations much easier. For reasons of completeness, in the present study we will continue to assume that the ultimate strain for steel is limited to ε_{ud} . This is done in order for the proposed methodology to be able to be extended also in the case where not a horizontal, but an inclined top branch is assumed for the steel stress-strain relation, with a maximum stress of $k \cdot f_{yk} / \gamma_s$ at ε_{uk} , where $k = (f_t / f_y)_k$. In this case Eurocode 2-Part 1-1 enforces the use of the strain limit of ε_{ud} for steel.

If the designer uses the proposed methodology and sets $\varepsilon_{ud} = \infty$, then we have the case of forcing the concrete zone to the ultimate strain and letting the steel take any strain value, as suggested by the Eurocode for the case of horizontal top branch stress-strain diagram. This will be illustrated also in the numerical examples section.

7 INVESTIGATION OF THE BI-LINEAR STRESS-STRAIN RELATION CASE

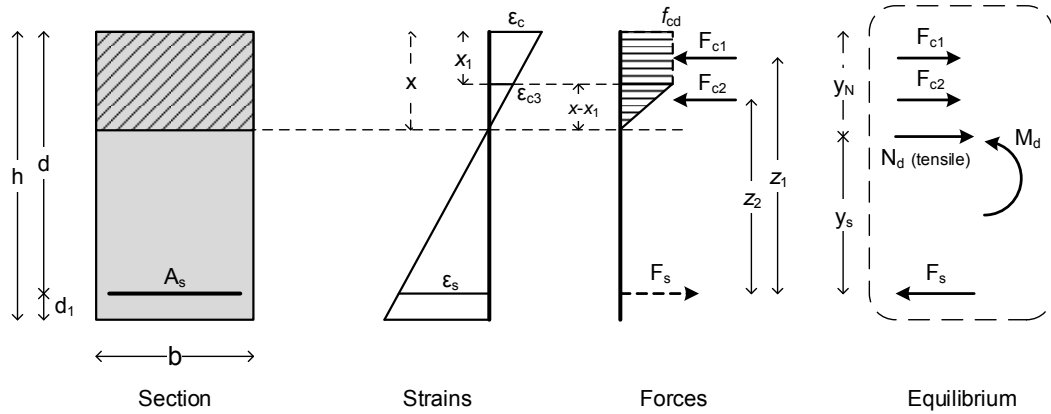


Figure 9: Cross section, strain and forces distribution and section equilibrium for the bi-linear stress-strain relation case, assuming $\varepsilon_c > \varepsilon_{c3}$.

The goal of the design is again to calculate the needed cross sectional area of steel reinforcement A_s . In order to calculate A_s , we need first to calculate the unknown quantities x , z_1 and z_2 . We move again the external force N_d to the position of the steel reinforcement and we have the figure below.

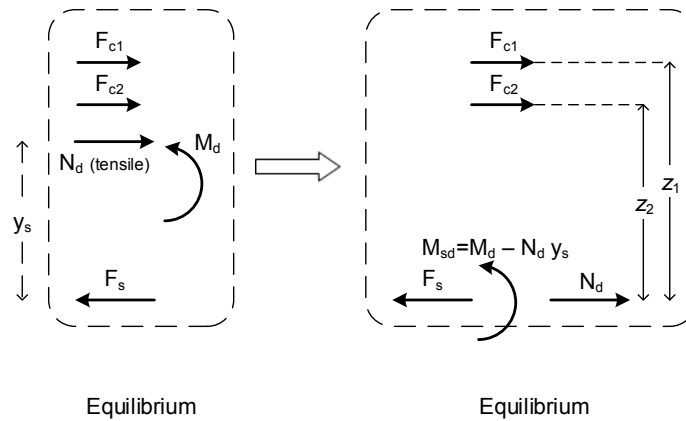


Figure 10: Equilibrium after moving the external force N_d to the position of the steel reinforcement.

We need to determine if at the ULS the concrete zone or the steel is at the critical strain. Again, first we put both materials at the ultimate strain, so we have:

$$\varepsilon_c = \varepsilon_{cu3} \quad (34)$$

$$\varepsilon_s = \varepsilon_{ud} \quad (35)$$

$$\frac{\varepsilon_{cu3}}{x} = \frac{\varepsilon_{ud} + \varepsilon_{cu3}}{d} = \frac{\varepsilon_{cu3} - \varepsilon_{c3}}{x_1} \Rightarrow \begin{cases} x = \frac{\varepsilon_{cu3}}{\varepsilon_{ud} + \varepsilon_{cu3}} \cdot d \\ x_1 = \frac{\varepsilon_{cu3} - \varepsilon_{c3}}{\varepsilon_{ud} + \varepsilon_{cu3}} \cdot d \end{cases} \quad (36)$$

$$F_{c1} = x_1 \cdot f_{cd} \cdot b \quad (37)$$

$$z_1 = d - \frac{x_1}{2} \quad (38)$$

$$F_{c2} = \frac{1}{2}(x - x_1) \cdot f_{cd} \cdot b \quad (39)$$

$$z_2 = d - x_1 - \frac{x - x_1}{3} = d - \frac{x + 2x_1}{3} \quad (40)$$

$$F_c = F_{c1} + F_{c2} \quad (41)$$

We will calculate the sum of moments at the steel reinforcement position. The sign of the sum of moments will show us whether the concrete zone or the steel is at the ultimate strain at the ULS. The sum of moments is (clockwise positive):

$$\Sigma M_{steel} = F_{c1} \cdot z_1 + F_{c2} \cdot z_2 - M_{sd} \quad (42)$$

We have then two cases:

Case 1. $\Sigma M \geq 0$

The concrete force has to be decreased for the equilibrium of the cross section. The steel stays at the ultimate strain ($\varepsilon_s = \varepsilon_{ud}$), while for concrete $\varepsilon_c \leq \varepsilon_{cu3}$, as shown in the figure below.

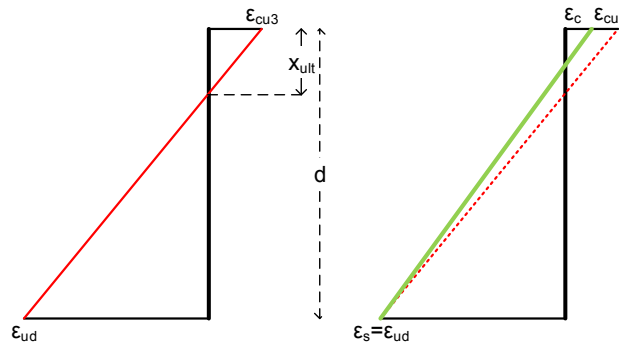


Figure 11: (b) Case 1: $\Sigma M \geq 0$, Steel at the ultimate strain.

Case 2. $\Sigma M < 0$

The concrete force has to be increased for the equilibrium of the cross section. Concrete stays at the ultimate strain ($\varepsilon_c = \varepsilon_{cu3}$), while for steel $\varepsilon_s < \varepsilon_{ud}$, as shown in the figure below.

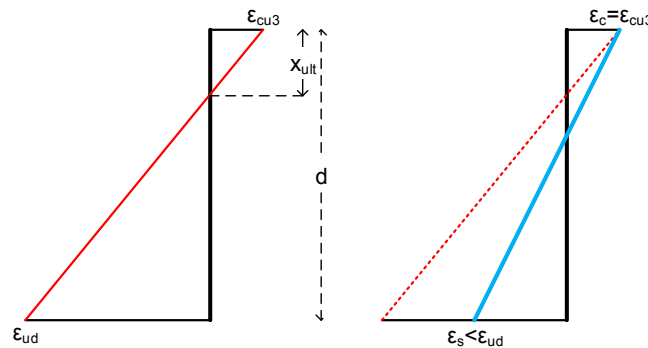


Figure 12: Case 2: $\Sigma M < 0$, concrete zone at the ultimate strain.

For both cases, we need to determine the value of x that satisfies the equilibrium of the cross section. After having determined x , we can then proceed with the other calculations and

finally end up with the needed reinforcement area A_s . The value of x can be determined by using trial and error iterations, or by using some kind of optimization in order to achieve section equilibrium. Good tools for this are MS Excel (Goal Seek or Solver functions) and also Matlab with its built-in root-finding and optimization tools. In the present study, we have used three equivalent approaches, (a) Solver function of MS Excel, (b) Matlab and (c) a home-made code which finds x by performing iterations, dividing the allowable height of the section by two at each iteration until convergence (equilibrium). All three approaches provide the same results at the end, as expected.

In the next sections, we will assume a value for x and we will end up with the equilibrium equation, i.e. the sum of moments at the steel reinforcement position which has to be zero at the equilibrium.

Case 1. $\Sigma M \geq 0$, Steel at the ultimate strain

We assume an initial value for x and we use the following equations:

$$\varepsilon_s = \varepsilon_{ud} \quad (43)$$

$$\frac{\varepsilon_c}{x} = \frac{\varepsilon_{ud}}{d-x} \Rightarrow \varepsilon_c = \frac{x}{d-x} \cdot \varepsilon_{ud} \quad (44)$$

- **Case 1a: If $\varepsilon_c > \varepsilon_{c3}$**

In this case we have the triangular diagram plus a rectangular diagram for the concrete zone and the upmost fiber of the concrete section works at the ultimate stress f_{cd} . From the similar triangles we have:

$$\frac{x_1}{\varepsilon_c - \varepsilon_{c3}} = \frac{d}{\varepsilon_c + \varepsilon_s} \Rightarrow x_1 = \frac{\varepsilon_c - \varepsilon_{c3}}{\varepsilon_c + \varepsilon_s} \cdot d \quad (45)$$

$$F_{c1} = x_1 \cdot f_{cd} \cdot b \quad (46)$$

$$z_1 = d - \frac{x_1}{2} \quad (47)$$

$$F_{c2} = \frac{1}{2}(x - x_1) \cdot f_{cd} \cdot b \quad (48)$$

$$z_2 = d - x_1 - \frac{x - x_1}{3} = d - \frac{2x_1 + x}{3} \quad (49)$$

$$F_c = F_{c1} + F_{c2} \quad (50)$$

$$\Sigma M_{steel} = F_{c1} \cdot z_1 + F_{c2} \cdot z_2 - M_{sd} \quad (51)$$

After we reach the equilibrium ($\Sigma M_{steel} = 0$), and given that the steel reinforcement works in full stress, above the yield strain, the steel area can be easily calculated by Eq. (31).

- **Case 1b: If $\varepsilon_c \leq \varepsilon_{c3}$**

In this case we have only the triangular diagram for the concrete zone, there is no rectangular part for the stresses and the upmost fiber of concrete works at stress $\sigma_c \leq f_{cd}$, as follows:

$$\sigma_c = \frac{\varepsilon_c}{\varepsilon_{c3}} \cdot f_{cd} \leq f_{cd} \quad (52)$$

$$F_{c2} = \frac{1}{2} x \cdot \sigma_c \cdot b \quad (53)$$

$$z_2 = d - \frac{x}{3} \quad (54)$$

$$F_c = F_{c2} \quad (55)$$

$$\Sigma M_{steel} = F_{c2} \cdot z_2 - M_{sd} \quad (56)$$

Again, after we reach the equilibrium ($\Sigma M_{steel}=0$), and given that the steel reinforcement works in full stress, above the yield strain, the steel area can be calculated by Eq. (31).

Case 2. $\Sigma M < 0$, concrete zone at the ultimate strain

We assume an initial value for x and we use the following equations:

$$\varepsilon_c = \varepsilon_{cu3} \quad (57)$$

$$\frac{\varepsilon_{cu3}}{x} = \frac{\varepsilon_s}{d-x} = \frac{\varepsilon_{cu3} - \varepsilon_{c3}}{x_1} \Rightarrow \begin{cases} \varepsilon_s = \frac{d-x}{x} \cdot \varepsilon_{cu3} \\ x_1 = \frac{\varepsilon_{cu3} - \varepsilon_{c3}}{\varepsilon_{cu3} + \varepsilon_s} \cdot d \end{cases} \quad (58)$$

$$F_{c1} = x_1 \cdot f_{cd} \cdot b \quad (59)$$

$$z_1 = d - \frac{x_1}{2} \quad (60)$$

$$F_{c2} = \frac{1}{2} (x - x_1) \cdot f_{cd} \cdot b \quad (61)$$

$$z_2 = d - x_1 - \frac{x - x_1}{3} = d - \frac{2x_1 + x}{3} \quad (62)$$

$$F_c = F_{c1} + F_{c2} \quad (63)$$

$$\Sigma M_{steel} = F_{c1} \cdot z_1 + F_{c2} \cdot z_2 - M_{sd} \quad (64)$$

- **Case 2a:** $\varepsilon_s \geq \varepsilon_{ys}$

The steel reinforcement works in full stress, above the yield strain and as a result the steel area can be calculated by Eq. (31).

- **Case 2b:** $\varepsilon_s < \varepsilon_{ys}$

The steel reinforcement does not work in full stress, as it works below the yield strain. The steel stress σ_s can be calculated by Eq. (28) and the steel area can be calculated by Eq. (25).

8 INVESTIGATION OF THE PARABOLIC-RECTANGULAR STRESS-STRAIN RELATION CASE

For the parabolic-rectangle stress-strain relation case, we use the same methodology as in the case of the bilinear stress-strain relation. The only difference is the shape of the concrete stress distribution where the triangular section becomes now parabolic, and also the ultimate

strain and the strain corresponding to the start of the rectangular section which become ε_{cu2} (instead of ε_{cu3}) and ε_{c2} (instead of ε_{c3}), respectively, as shown in the figure below.

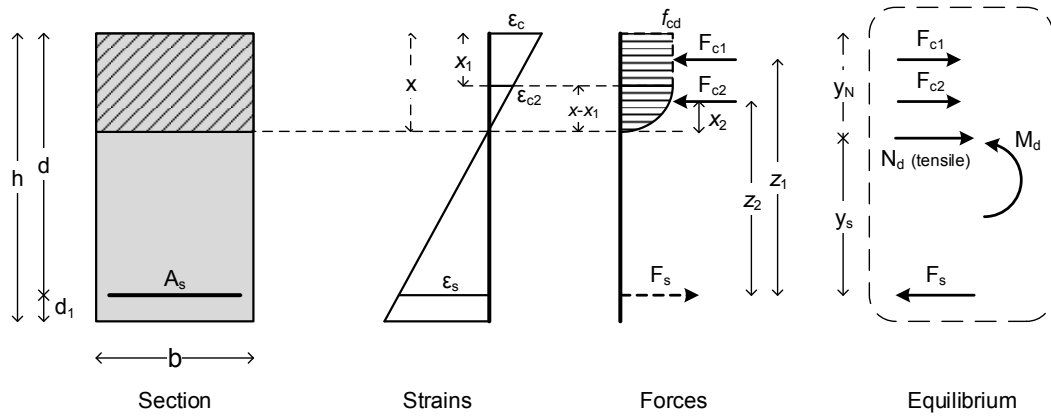


Figure 13: Cross section, strain and forces distribution and section equilibrium for the parabolic-rectangular stress-strain relation case, assuming $\varepsilon_c > \varepsilon_{c2}$.

In the above figure, x_2 is the distance from the neutral axis to the centroid of the parabolic section. The parabolic section is “full” in the figure, as $\varepsilon_c > \varepsilon_{c2}$. In the bi-linear case, the calculation of the area and centroid of the non-rectangular part was obvious, because of the triangular shape, but for the parabolic case, integration has to be used, as will be described in detail later.

Again, we need to determine if at the ULS the concrete zone or the steel is at the critical strain. First, we put both materials at the ultimate strain, so we have:

$$\varepsilon_c = \varepsilon_{cu2} \quad (65)$$

$$\varepsilon_s = \varepsilon_{ud} \quad (66)$$

$$\frac{\varepsilon_{cu2}}{x} = \frac{\varepsilon_{ud} + \varepsilon_{cu2}}{d} = \frac{\varepsilon_{cu2} - \varepsilon_{c2}}{x_1} \Rightarrow \begin{cases} x = \frac{\varepsilon_{cu2}}{\varepsilon_{ud} + \varepsilon_{cu2}} \cdot d \\ x_1 = \frac{\varepsilon_{cu2} - \varepsilon_{c2}}{\varepsilon_{ud} + \varepsilon_{cu2}} \cdot d \end{cases} \quad (67)$$

$$F_{c1} = x_1 \cdot f_{cd} \cdot b \quad (68)$$

$$z_1 = d - \frac{x_1}{2} \quad (69)$$

The above equations are almost the same as the ones used in the bi-linear case, but of course in the parabolic-rectangle case we use ε_{c2} and ε_{cu2} instead of ε_{c3} and ε_{cu3} . Yet, this time in order to calculate F_{c2} we need to integrate Eq. (2) to calculate the area of the parabolic part. For the parabolic part of the stress, i.e. for strains ε_c in the region $[0, \varepsilon_{c2}]$, we have the indefinite integral:

$$\int \sigma_c d\varepsilon_c = \int f_{cd} \left[1 - \left(1 - \frac{\varepsilon_c}{\varepsilon_{c2}} \right)^n \right] d\varepsilon_c = \varepsilon_c f_{cd} + \frac{\varepsilon_{c2} f_{cd} \left(1 - \frac{\varepsilon_c}{\varepsilon_{c2}} \right)^{n+1}}{n+1} \quad (70)$$

Thus the area E_1 of the full parabolic part $[0, \varepsilon_{c2}]$ is given by the definite integral:

$$E_1 = \int_0^{\varepsilon_{c2}} \sigma_c d\varepsilon_c = \frac{n}{n+1} \varepsilon_{c2} f_{cd} \quad (71)$$

The area E_1 of the full parabolic part is shown in the figure below in black color.

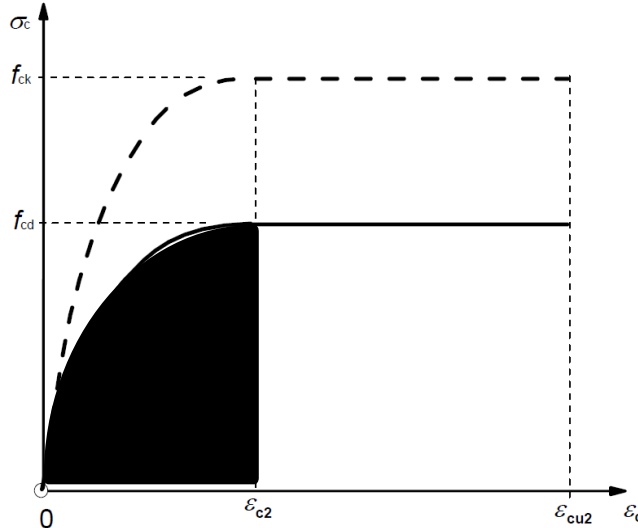


Figure 14: Area E_1 of the full parabolic part (for strains up to ε_{c2}) in black color.

If the integration is done on the cross section height, for the strain ε_{c2} the corresponding height of the section is $(x-x_1)$ and as a result the corresponding area of the full parabolic part A_1 is given by:

$$A_1 = \frac{n}{n+1} (x-x_1) f_{cd} \quad (72)$$

The area A_1 of the full parabolic part is shown in the figure below in black color.

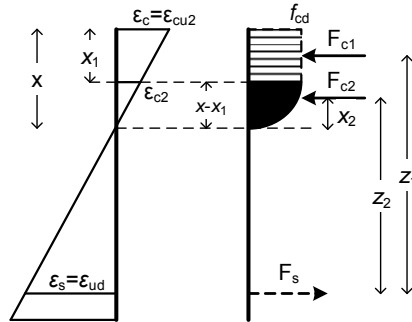


Figure 15: Strain and forces distribution.

The area A_1 of the full parabolic part is shown in black color.

The concrete force F_{c2} is given by:

$$F_{c2} = A_1 \cdot b = \frac{n}{n+1} (x-x_1) f_{cd} \cdot b \quad (73)$$

In order to calculate z_2 we need to calculate the distance x_2 defining the centroid of the A_1 area. In terms of strains, the centroid $\varepsilon_{\text{centroid}}$ of the E_1 area is given by the definite integral:

$$\varepsilon_{centroid1} = \frac{1}{E_1} \int_0^{\varepsilon_{c2}} \varepsilon_c \sigma_c d\varepsilon_c \quad (74)$$

The indefinite integral in this case is given by:

$$\int \varepsilon_c \sigma_c d\varepsilon_c = \int \varepsilon_c f_{cd} \left[1 - \left(1 - \frac{\varepsilon_c}{\varepsilon_{c2}} \right)^n \right] d\varepsilon_c = \frac{\varepsilon_c^2 f_{cd}}{2} + \frac{f_{cd} (\varepsilon_{c2} - \varepsilon_c)^{n+1} (\varepsilon_{c2} + \varepsilon_c (n+1))}{\varepsilon_{c2}^n (n+2)(n+1)} \quad (75)$$

Thus the centroid of the full parabolic part is given by:

$$\varepsilon_{centroid1} = \frac{1}{E_1} \int_0^{\varepsilon_{c2}} \varepsilon_c \sigma_c d\varepsilon_c = \frac{n+3}{2(n+2)} \cdot \varepsilon_{c2} \quad (76)$$

If the integration is done on the section height, for the strain ε_{c2} the corresponding height of the cross section is $(x-x_1)$ and as a result the corresponding centroid of the full parabolic part x_2 is given by:

$$x_2 = \frac{\varepsilon_{centroid1}}{\varepsilon_{c2}} \cdot (x-x_1) = \frac{n+3}{2(n+2)} \cdot (x-x_1) \quad (77)$$

Then we have

$$z_2 = d - x + x_2 \quad (78)$$

$$F_c = F_{c1} + F_{c2} \quad (79)$$

Again, we will calculate the sum of moments at the steel reinforcement position. The sign of the sum of moments will show us whether the concrete zone or the steel is at the ultimate strain at the ULS. The sum of moments is (clockwise positive):

$$\Sigma M_{steel} = F_{c1} \cdot z_1 + F_{c2} \cdot z_2 - M_{sd} \quad (80)$$

We then have again two cases:

Case 1. $\Sigma M \geq 0$

The concrete force has to be decreased for the equilibrium of the cross section. The steel stays at the ultimate strain ($\varepsilon_s = \varepsilon_{ud}$), while $\varepsilon_c \leq \varepsilon_{cu2}$.

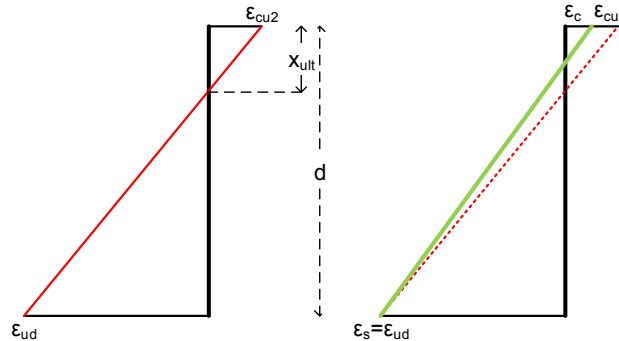


Figure 16: (b) Case 1: $\Sigma M \geq 0$, Steel at the ultimate strain.

Case 2. $\Sigma M < 0$

The concrete force has to be increased for the equilibrium of the cross section. The concrete stays at the ultimate strain ($\varepsilon_c = \varepsilon_{cu2}$), while $\varepsilon_s < \varepsilon_{ud}$.

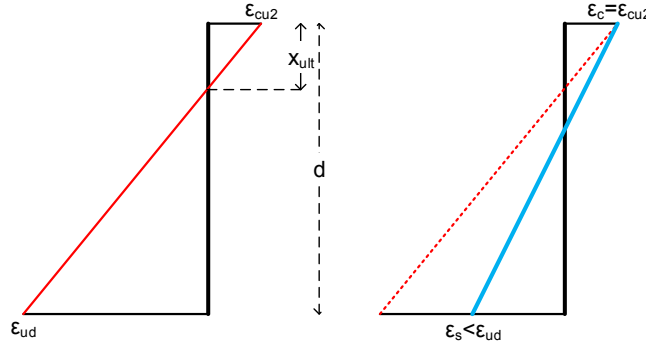


Figure 17: Case 2: $\Sigma M < 0$, concrete zone at the ultimate strain.

The methodology is exactly the same as the one of the bi-linear case. To start, we assume a value for x and we should change it until we reach the final equilibrium. The equations below end up with the calculation of the sum of moments which has to be zero at the equilibrium.

Case 1. $\Sigma M \geq 0$, Steel at the ultimate strain

We assume an initial value for x and we use the following equations:

$$\varepsilon_s = \varepsilon_{ud} \quad (81)$$

$$\frac{\varepsilon_c}{x} = \frac{\varepsilon_{ud}}{d-x} \Rightarrow \varepsilon_c = \frac{x}{d-x} \cdot \varepsilon_{ud} \quad (82)$$

- **Case 1a: If $\varepsilon_c > \varepsilon_{c2}$**

In this case we have the parabolic diagram plus a rectangular diagram and the upmost fiber of concrete works at the ultimate stress f_{cd} . From the similar triangles we have:

$$\frac{x_1}{\varepsilon_c - \varepsilon_{c3}} = \frac{d}{\varepsilon_c + \varepsilon_s} \Rightarrow x_1 = \frac{\varepsilon_c - \varepsilon_{c3}}{\varepsilon_c + \varepsilon_s} \cdot d \quad (83)$$

$$F_{c1} = x_1 \cdot f_{cd} \cdot b \quad (84)$$

$$z_1 = d - \frac{x_1}{2} \quad (85)$$

In a similar way as previously (integrations), and since we have again a full parabolic part, we have:

$$F_{c2} = \frac{n}{n+1} (x - x_1) f_{cd} \cdot b \quad (86)$$

$$x_2 = \frac{n+3}{2(n+2)} \cdot (x - x_1) \quad (87)$$

$$z_2 = d - x + x_2 \quad (88)$$

$$F_c = F_{c1} + F_{c2} \quad (89)$$

$$\Sigma M = F_{c1} \cdot z_1 + F_{c2} \cdot z_2 - M_{sd} \quad (90)$$

After we reach the equilibrium ($\Sigma M=0$), and given that the steel reinforcement works in full stress, above the yield strain, the steel area can be easily calculated by Eq. (31).

- **Case 1b: If $\varepsilon_c \leq \varepsilon_{c2}$**

In this case we have only part of the parabolic diagram, there is no rectangular diagram and the upmost fiber of concrete works at stress $\sigma_c \leq f_{cd}$.

$$\sigma_c = \frac{\varepsilon_c}{\varepsilon_{c2}} \cdot f_{cd} \leq f_{cd} \quad (91)$$

This time in order to calculate F_{c2} we need to integrate Eq. (2) to calculate the area of the parabolic part, not for the full parabola (up to ε_{c2}), but for the region $[0, \varepsilon_c]$ where $\varepsilon_c \leq \varepsilon_{c2}$. Using the indefinite integral of Eq. (70) we can calculate the corresponding area E_2 of the parabolic part for the region $[0, \varepsilon_c]$ where $\varepsilon_c \leq \varepsilon_{c2}$ as a definite integral as follows:

$$E_2 = \int_0^{\varepsilon_c} \sigma_c d\varepsilon_c = f_{cd} \varepsilon_c + \frac{\varepsilon_{c2} f_{cd} \left(\left(1 - \frac{\varepsilon_c}{\varepsilon_{c2}} \right)^{n+1} - 1 \right)}{n+1} = f_{cd} \left(\varepsilon_c - \frac{\varepsilon_{c2} \left(1 - \left(1 - \frac{\varepsilon_c}{\varepsilon_{c2}} \right)^{n+1} \right)}{n+1} \right) \quad (92)$$

The area E_2 of the parabolic part for the region $[0, \varepsilon_c]$ is shown in the figure below in black color.

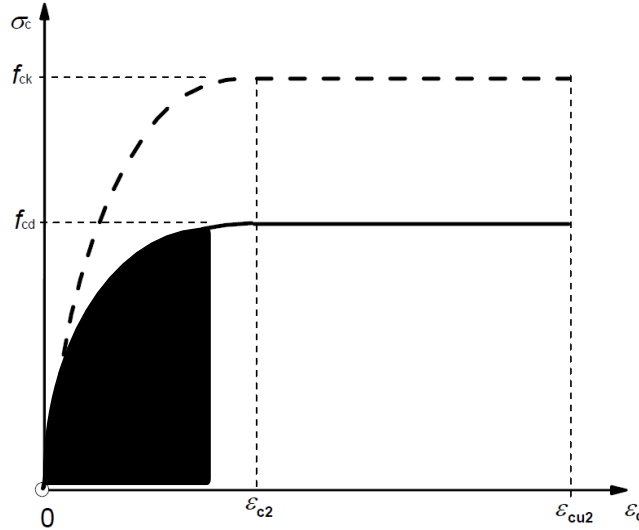


Figure 18: Area E_2 of the parabolic part for the region $[0, \varepsilon_c]$ where $\varepsilon_c < \varepsilon_{c2}$, in black color.

If the integration is done on the section height, for a strain $\varepsilon_c < \varepsilon_{c2}$ the corresponding height of the cross section is x while for the theoretical strain ε_{c2} the corresponding height of the cross section would be $x \cdot \varepsilon_{c2} / \varepsilon_c$ and as a result the corresponding area of the parabolic part A_2 is given by:

$$A_2 = f_{cd} \left(x - \frac{\frac{\varepsilon_{c2}}{\varepsilon_c} x \left(1 - \left(1 - \frac{\varepsilon_c}{\varepsilon_{c2}} \right)^{n+1} \right)}{n+1} \right) = f_{cd} \cdot x \left(1 - \frac{\frac{\varepsilon_{c2}}{\varepsilon_c} \left(1 - \left(1 - \frac{\varepsilon_c}{\varepsilon_{c2}} \right)^{n+1} \right)}{n+1} \right) \quad (93)$$

The area A_2 of the parabolic part in this case is shown in the figure below in black color.

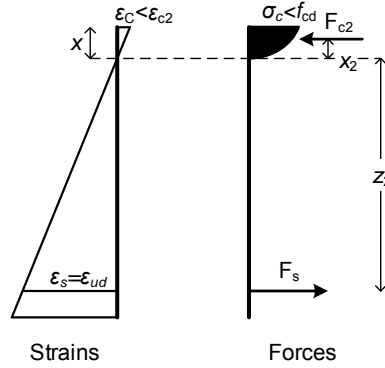


Figure 19: Strains and forces distribution.

The area A_2 of the parabolic part (for strains up to $\varepsilon_c < \varepsilon_{c2}$) is shown in black color.

The concrete force F_{c2} is given by:

$$F_{c2} = A_2 \cdot b = f_{cd} \cdot x \cdot b \left(1 - \frac{\frac{\varepsilon_{c2}}{\varepsilon_c} \left(1 - \left(1 - \frac{\varepsilon_c}{\varepsilon_{c2}} \right)^{n+1} \right)}{n+1} \right) \quad (94)$$

The calculation of z_2 for this case is the most difficult part. In order to calculate z_2 we need to calculate the distance x_2 defining the centroid of the A_2 area, as shown in Figure 19. In terms of strains, the centroid $\varepsilon_{centroid2}$ of the E_2 area is given by the following formula:

$$\varepsilon_{centroid2} = \frac{1}{E_2} \int_0^{\varepsilon_c} \varepsilon_c \sigma_c d\varepsilon_c \quad (95)$$

The definite integral $\int_0^{\varepsilon_c} \varepsilon_c \sigma_c d\varepsilon_c$ can be calculated from the indefinite integral of Eq. (75) as follows:

$$\int_0^{\varepsilon_c} \varepsilon_c \sigma_c d\varepsilon_c = \frac{\varepsilon_c^2 f_{cd}}{2} + \frac{f_{cd} (\varepsilon_{c2} - \varepsilon_c)^{n+1} (\varepsilon_{c2} + \varepsilon_c (n+1)) - f_{cd} \varepsilon_{c2}^{n+2}}{\varepsilon_{c2}^n (n+2)(n+1)} \quad (96)$$

If the integration is done on the section height, for the strain ε_c the corresponding height of the cross section is x and as a result the corresponding centroid of the full parabolic part x_2 is given by:

$$x_2 = \frac{\varepsilon_{centroid2}}{\varepsilon_c} \cdot x \quad (97)$$

Then we have

$$z_2 = d - x + x_2 \quad (98)$$

$$F_c = F_{c2} \quad (99)$$

Again, we will calculate the sum of moments at the steel reinforcement position. The sign of the sum of moments will show us whether the concrete zone or the steel is at the ultimate strain at the ULS. The sum of moments is (clockwise positive):

$$\Sigma M_{steel} = F_{c2} \cdot z_2 - M_{sd} \quad (100)$$

Case 2. $\Sigma M < 0$, concrete zone at the ultimate strain

We assume an initial value for x and we use the following equations:

$$\varepsilon_c = \varepsilon_{cu2} \quad (101)$$

$$\frac{\varepsilon_{cu2}}{x} = \frac{\varepsilon_s}{d-x} = \frac{\varepsilon_{cu2} + \varepsilon_s}{d} = \frac{\varepsilon_{cu2} - \varepsilon_{c2}}{x_1} \Rightarrow \begin{cases} \varepsilon_s = \frac{d-x}{x} \cdot \varepsilon_{cu2} \\ x_1 = \frac{\varepsilon_{cu2} - \varepsilon_{c2}}{\varepsilon_{cu2} + \varepsilon_s} \cdot d \end{cases} \quad (102)$$

$$F_{c1} = x_1 \cdot f_{cd} \cdot b \quad (103)$$

$$z_1 = d - \frac{x_1}{2} \quad (104)$$

$$F_{c2} = \frac{n}{n+1} (x - x_1) f_{cd} \cdot b \quad (105)$$

$$x_2 = \frac{n+3}{2(n+2)} \cdot (x - x_1) \quad (106)$$

$$z_2 = d - x + x_2 \quad (107)$$

$$F_c = F_{c1} + F_{c2} \quad (108)$$

$$\Sigma M = F_{c1} \cdot z_1 + F_{c2} \cdot z_2 - M_{sd} \quad (109)$$

- **Case 2a:** $\varepsilon_s \geq \varepsilon_{ys}$

The steel reinforcement works in full stress, above the yield strain and as a result the steel area can be calculated by Eq. (31).

- **Case 2b:** $\varepsilon_s < \varepsilon_{ys}$

The steel reinforcement does not work in full stress, as it works below the yield strain. The steel stress σ_s can be calculated by Eq. (28) and the steel area can be calculated by Eq. (25).

9 NUMERICAL RESULTS

Four concrete sections will be examined in total. All three approaches for the stress-strain relations of concrete for the design of cross sections will be examined:

- Rectangular stress distribution
- Bi-linear stress-strain relation
- Parabola-rectangle diagram

Below are the common properties for all numerical examples:

- Steel class B500C ($f_{yk}=500$ MPa)
- $E_s=200$ GPa
- $\gamma_c=1.50$, $\gamma_s=1.15$
- $\varepsilon_{uk}=75$ ‰
- $\varepsilon_{ud}=0.9 \cdot \varepsilon_{uk}$
- $a_{cc}=1$

9.1 Numerical example 1

The section of the first numerical example has the following properties:

- Concrete class C20/25
- Height $h=50$ cm
- Width $b=25$ cm
- $d_1=5$ cm
- $M_d=60$ kNm
- $N_d=0$

Below are the results of the design, for each of the three approaches for the stress-strain relations of concrete.

	Rectangular	Bilinear	Parabola-rectangle
A_s (cm ²)	3.22	3.22	3.22
ε_c (‰)	3.5	3.5	3.5
ε_s (‰)	26.5	24.6	26.8
x (m)	0.052	0.056	0.052
Critical material	Concrete	Concrete	Concrete

Table 3. Design results for the 1st numerical example.

It is clear that all three approaches give the same final result for the needed steel reinforcement area. Only minor differences can be found in the strains and the concrete zone height x .

9.2 Numerical example 2

The section of the second numerical example has the following properties:

- Concrete class C30/37
- Height $h=60$ cm
- Width $b=30$ cm
- $d_1=5$ cm
- $M_d=100$ kNm
- $N_d=50$ kN
- $y_N=h/2$

Below are the results of the design, for each of the three approaches for the stress-strain relations of concrete.

	Rectangular	Bilinear	Parabola-rectangle
A_s (cm ²)	4.90	4.91	4.90
ε_c (‰)	3.5	3.5	3.5
ε_s (‰)	53.1	49.6	53.8
x (m)	0.034	0.036	0.034
Critical material	Concrete	Concrete	Concrete

Table 4. Design results for the 2nd numerical example.

The three approaches give again almost the same final result for the needed steel reinforcement area. Again minor differences can be found in the strains and the concrete zone height x .

9.3 Numerical example 3

The section of the third numerical example has the following properties:

- Concrete class C70/85
- Height $h=70$ cm
- Width $b=30$ cm
- $d_1=5$ cm
- $M_d=150$ kNm
- $N_d=100$ kN
- $y_N=h/2$

Below are the results of the design, for each of the three approaches for the stress-strain relations of concrete.

	Rectangular	Bilinear	Parabola-rectangle
A_s (cm ²)	6.60	6.60	6.60
ε_c (‰)	2.1	2.4	2.3
ε_s (‰)	67.5	67.5	67.5
x (m)	0.020	0.023	0.023
Critical material	Steel	Steel	Steel

Table 5. Design results for the 3rd numerical example.

Again, the results are the same for all three cases. This time the steel is the critical material (at the ultimate strain) at the section equilibrium. The results above are calculated assuming a horizontal top branch for the steel stress-strain relation, but also limiting the maximum strain to ε_{ud} . Eurocode 2 allows the designer to not limit the ultimate strain for steel when a horizontal top branch is assumed for the stress-strain diagram for steel. In this case, the concrete zone is assumed to be at the ultimate strain at all times at the ULS and the steel strain can take any value, without any limitation. If we set $\varepsilon_{ud}=\infty$ (a very big number), then we have the results of the following table.

	Rectangular	Bilinear	Parabola-rectangle
A_s (cm ²)	6.60	6.60	6.60
ε_c (‰)	2.7	2.7	2.7
ε_s (‰)	84.7	77.4	78.4
x (m)	0.020	0.022	0.021
Critical material	Concrete	Concrete	Concrete

Table 6. Design results for the 3rd numerical example – No limitation for the steel strain.

We see that there is no difference in the required area of reinforcement A_s for the two cases, the results are exactly the same and only the reported material strains change. Of course, this time the critical material is the concrete zone, not the steel reinforcement.

9.4 Numerical example 4

The section of the fourth numerical example has the following properties:

- Concrete class C30/37
- Height $h=50$ cm
- Width $b=25$ cm
- $d_1=5$ cm
- $M_d=378$ kNm
- $N_d=0$

Below are the results of the design, for each of the three approaches for the stress-strain relations of concrete.

	Rectangular	Bilinear	Parabola-rectangle
A_s (cm ²)	26.14	33.78	26.67
ε_c (‰)	3.5	3.5	3.5
ε_s (‰)	2.14	1.69	2.13
x (m)	0.279	0.304	0.280
Critical material	Concrete	Concrete	Concrete
$\varepsilon_s/\varepsilon_{ys}$	0.98	0.78	0.98

Table 7. Design results for the 4th numerical example.

This time the results are different and in the bilinear case the difference is big. Taking a careful look at the results we can see that in this example, for all cases, $\varepsilon_s < \varepsilon_{ys}$ which means that the steel reinforcement works below the yield strain and as a result the steel cannot work in its full potential (f_{yd} stress). These are cases where the design is poor and not economic and the designer should either increase the height of the section or add compressive reinforcement, also.

In such cases with $\varepsilon_s < \varepsilon_{ys}$, the exact value of the steel strain ε_s is significant in the calculation of the final required reinforcement area as it affects directly the steel stress. In the bilinear case, ε_s is calculated as 1.69 ‰, lower than in the other two cases, and that affects the required reinforcement which is 33.78 cm², much more than in the other two cases.

The difference is big, but these cases are theoretical since in practical cases we would never design a section in such a way that the steel reinforcement would work below the yield strain.

10 CONCLUSIONS

- Eurocode 2-Part 1-1 gives us new tools in order to design concrete cross sections. Three approaches may be used for the stress-strain relation of concrete and another two approaches for the stress-strain relation of steel reinforcement. The simplest approach for concrete is the use of the Rectangular stress distribution. The other two approaches use the Bi-linear stress-strain relation and the Parabola-rectangle diagram, respectively.
- This paper presents a detailed methodology for the design of rectangular cross sections with tensile reinforcement, for all the three cases and for all concrete classes, covering all concrete classes, from C12/15 to C90/105. The methodology is general and all other Eu-

rocode parameters, such as γ_c , γ_s , a_{cc} , and others can be adjusted according to the preferences of the designer, without any limitation.

- The three approaches for concrete give almost the same results with each other for all “normal” cases examined. The differences are very slight and not significant from an engineering point of view. Big differences may occur in some “abnormal” cases where the effective moment is big for the section and as a result the steel reinforcement works below the yield strain ε_{ys} . In any case, these cases have to do with bad section design and they should be avoided. The best solution for these cases is to add height to the concrete section, and/or add compressive reinforcement also.
- Eurocode 2 allows the designer to not limit the ultimate strain for steel when a horizontal top branch is assumed for the stress-strain diagram for steel. In this case, the concrete zone is assumed to be at the ultimate strain at all times at the ULS and the steel strain can take any value, without any limitation. In the proposed methodology this can be achieved by setting $\varepsilon_{ud}=\infty$ (a very big number) for the allowed steel strain. This was investigated in a numerical example where the steel was the critical material and the result showed that it made no difference in the final steel reinforcement area.
- A more detailed investigation has to be made regarding the three stress-strain approaches for concrete in order to check if there are cases where the three approaches can lead to different results. The next research step should be to use the proposed methodology in order to generate dimensionless charts showing the required reinforcement for any loading and any section. In this way, a general direct comparison of the three cases can be performed.

REFERENCES

- [1] EN 1992-1-1. Eurocode 2: Design of concrete structures. Part 1-1: General rules and rules for buildings. Brussels, 2004.
- [2] B. Rosca, M. Petru, Reinforced Concrete Section Design to Bending according to EN 1992-1-1/2004 – Eurocode 2. *Buletinul Institutului Politehnic din Iasi*, 53-66, 2009.
- [3] E. Dulinskas, D. Zabulionis, Analysis of equivalent substitution of rectangular stress block for nonlinear stress diagram. *ISSN 1392 – 1207, Mechanika*, **6 (68)**, 53-66, 2007.
- [4] D. Zabulionis, E. Dulinskas, Analysis of compression zone parameters of cross-section in flexural reinforced concrete members according to EC2 and STR 2.05.05. *ISSN 1392 – 1207, Mechanika*, **3 (71)**, 12-19, 2008.
- [5] I. Židonis, Strength calculation method for cross-section of reinforced concrete flexural member using curvilinear concrete stress diagram of EN-2. *11th International Conference on Modern Building Materials, Structures and Techniques (MBMST 2013)*, Vilnius, Lithuania, May 16 – 17, 2013.
- [6] I. Židonis, A simple-to-integrate formula of stress as a function of strain in concrete and its description procedure. *ISSN 1392 – 1207, Mechanika*, **4(66)**, 23-30, 2007.

COMPUTATIONAL SIMULATION OF CROSS ROLL STRAIGHTENING

Jindrich Petruska¹ and Tomas Navrat²

¹ Brno University of Technology, Faculty of Mechanical Engineering
Technicka 2896/2, 616 69 Brno, Czech Republic
e-mail: petruska@fme.vutbr.cz

² Brno University of Technology, Faculty of Mechanical Engineering
Technicka 2896/2, 616 69 Brno, Czech Republic
navrat@fme.vutbr.cz

Keywords: Cross roll straightening, FEM, plastic bending.

Abstract. *The paper deals with numerical analysis of the process of cross roll straightening of circular bars in a seven-roll straightening machine. In this machine, initially curved bar rotates along its axis as it progresses through laterally staggered rolls, being loaded by a fluctuating bending moment beyond its elastic limit. To simulate the process efficiently, special program was developed, based on a beam-type finite element, Euler scheme of material flow along the straightened bar and nonlinear iterative solution of the elasto plastic material behavior. Based on the input data, process characteristics like roller loading, product deflection, curvature and plasticization can be quickly obtained. With reliable solution of the direct problem, optimal intermeshing of rollers for given input data can be found in an iterative process. The paper describes main features of the algorithm and examples of its application.*

1 INTRODUCTION

In the process of cross roll straightening, initially curved circular bar rotates along its axis as it progresses through laterally staggered rolls, being loaded by a fluctuating bending moment beyond its elastic limit (Fig. 1). Resulting redistribution of residual stress is aimed at minimization of both curvature and residual stress. The principal problem is to choose optimal roll intermeshing strategy to minimize residual stress and curvature for given input parameters - initial bar curvature, its diameter, yield stress and material hardening.

In previous years such strategies were based mainly on empirical experience combined with elementary analytical approaches [1]. With the advent of the Finite Element Method, more complex computational models can be created and many phenomena of the cross roll straightening are being solved. Nevertheless, there are still limitations to apply the FEM for straightening process in the industrial practice due to its capacity and time demands [2]. This is the reason to use simpler and quick computational models. Generally they are based on the integration of the curvature of the leveled product [3]-[5].

In this paper we suggest a reversed procedure, starting from the suggested roll staggering. Fast algorithm is then used to evaluate curvatures along the leveled product, bending moments, roll loadings, together with full stress/strain history in each material point, residual stress distribution and final curvature. The program in MATLAB is based on FEM using a simple beam element with Euler description of material flow through the leveling machine. With fast and reliable solution of the problem, optimal setting of the leveling rolls can be found in an iterative process. In the paper we shall present suggested algorithm and our experience with its stability and general effectiveness.

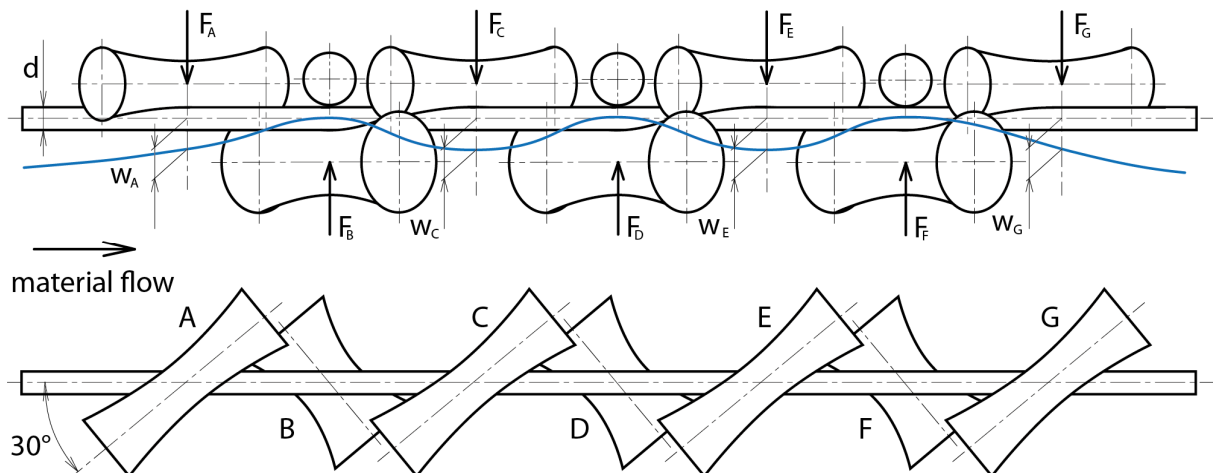


Figure 1: Schematic representation of the leveling process.

2 GENERAL ASSUMPTIONS OF THE PROCESS SIMULATION

In Fig. 1 we show schematic representation of the 7-roller cross roll leveling machine. Material of the bar is moving through the machine from the left side, rotating along its longitudinal axis on rollers which are skewed by 30 degrees. The three bottom supporting rollers are the driving rollers, vertically fixed, whereas the four top rollers are adjustable to obtain optimal bending to straighten the product.

The algorithm is based on several basic assumptions:

1. The bar deflection, slope and curvature can be described by bending theory of beams with one dimensional state of stress.
2. Simple point contacts with fixed pitch exist between the rollers and the bar.

3. Stationary situation with constant value of input curvature of the bar is supposed.
4. Material model is characterized by bilinear σ – ϵ curve with linear elastic and linear plastic hardening part, and kinematic hardening rule.

Input parameters are represented by the bar diameter, modulus of elasticity E , yield stress σ_y , hardening E_T , input curvature and by vertical intermeshing of the adjustable rollers. Output parameters are the deflection, slope and curvature along the bar, distribution of bending moments, shear forces and roller reactions and distribution of axial stress, elastic, plastic and total strain in any cross section along the beam, including residual stress and curvature at the end (Figs. 4, 5).

3 BASIC EQUATIONS AND SOLUTION ALGORITHM

The algorithm is based on iterative solution of a linearized equation

$$\mathbf{K}_{T,i-1} \cdot \Delta \mathbf{U}_i = \mathbf{R}_{i-1}, \quad (1)$$

$$\mathbf{U}_i = \Delta \mathbf{U}_i + \mathbf{U}_{i-1}, \quad (2)$$

where \mathbf{K}_T is global tangential stiffness matrix composed of 120 two-node FE beam elements (see Fig. 2, ref. [6]) with two degrees of freedom, displacement and slope, in each node. \mathbf{R} is a matrix of residual nodal shear forces and bending moments, \mathbf{U} global matrix of nodal displacements and slopes. The beam element according to Fig. 2 has four degrees of freedom in the matrix δ

$$\delta = \begin{bmatrix} w_1 \\ w_1' \\ w_2 \\ w_2' \end{bmatrix} \text{ and the element stiffness matrix } \mathbf{k} = \frac{E \cdot J}{L^3} \cdot \begin{bmatrix} 12 & 6 \cdot L & -12 & 6 \cdot L \\ 6 \cdot L & 4 \cdot L^2 & -6 \cdot L & 2 \cdot L^2 \\ -12 & -6 \cdot L & 12 & -6 \cdot L \\ 6 \cdot L & 2 \cdot L^2 & -6 \cdot L & 4 \cdot L^2 \end{bmatrix} \quad (3)$$

where E is the elastic modulus, J the area moment of inertia and L the element length.

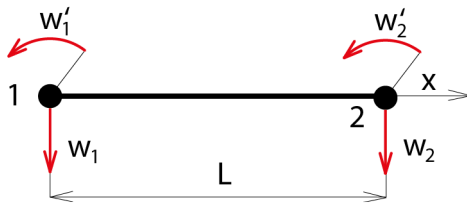


Figure 2: Beam element.

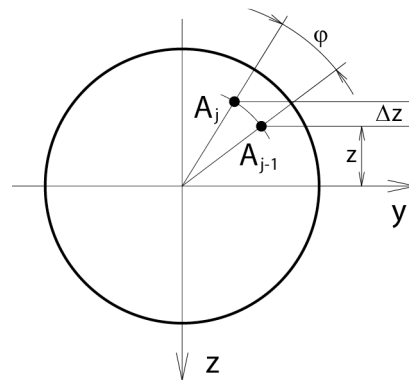


Figure 3: Cross section of the bar.

During every iteration, correction for nonlinear material behavior is realized. It is based on the computation of curvature in each element,

$$w'' = \mathbf{B} \cdot \delta \quad (4)$$

where δ is obtained for each element from actual displacements U_i , and \mathbf{B} is the curvature approximation matrix [6]

$$\mathbf{B} = \left[-\frac{6}{L^2} + \frac{12 \cdot x}{L^3}, \quad -\frac{4}{L} + \frac{6 \cdot x}{L^2}, \quad \frac{6}{L^2} - \frac{12 \cdot x}{L^3}, \quad -\frac{2}{L} + \frac{6 \cdot x}{L^2} \right]. \quad (6)$$

To simulate the movement of the bar through the leveling machine, Euler-type scheme is adopted. The material then moves through the beam elements, which have fixed positions in space. Development of the plastic deformation linked with the history of stress distribution over the bar cross section is always tracked from the first node on the left side of the beam in the loop over j -index from $j = 2$ to 121, until the last node is reached. First, the curvature increment between two subsequent nodes is evaluated

$$\Delta w_j'' = w_j'' - w_{j-1}''. \quad (6)$$

Next, the strain increment in any point A of the cross section, caused by axial displacement is obtained from

$$\Delta \varepsilon_{as} = \Delta w_j'' \cdot z, \quad (7)$$

and the strain increment caused by rotation

$$\Delta \varepsilon_r = w_j'' \cdot \Delta z. \quad (8)$$

In eqs. (7) and (8), z is the distance of each point of the cross section from the neutral axis of bending and Δz the change of this distance caused by rotation between the points $j-1$ and j , as can be seen in Fig. 3.

Total strain increment is

$$\Delta \varepsilon = \Delta \varepsilon_{as} + \Delta \varepsilon_r \quad (9)$$

and testing stress

$$\sigma_j = \sigma_{j-1} + E \cdot \Delta \varepsilon \quad (10)$$

where σ_{j-1} is the stress distribution over the cross section in the previous nodal point. For the first node, the initial stress distribution connected with the initial curvature of the bar is taken into account. Similarly, the state in the last node for converged solution then corresponds to residual stress and curvature of the beam leaving the leveling machine.

Correction of the testing stress according to plastic behavior of material together with correct distribution of elastic and plastic component of total strain is realized by algorithm published elsewhere [6], [7]. Typical distribution of stress over the cross section can be seen in Fig. 4.

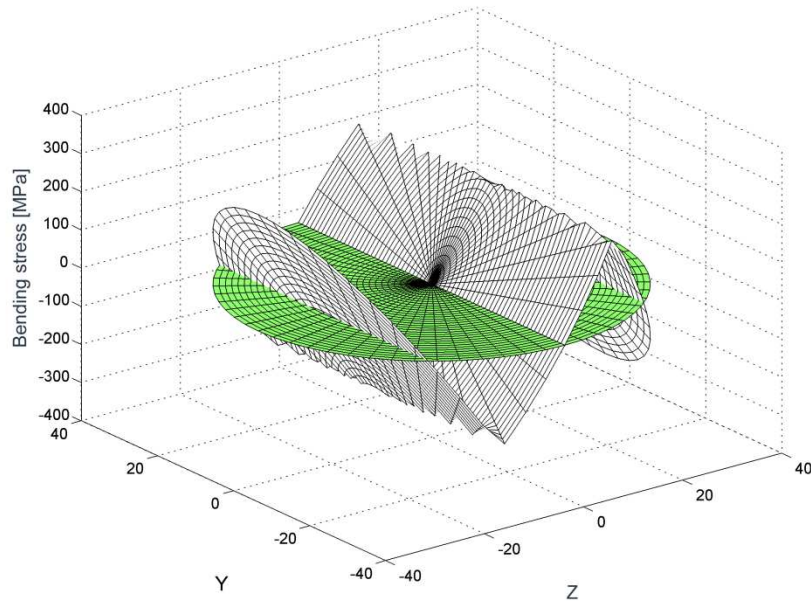
Nonlinear distribution of stress according to Fig. 4 results in correction of bending moment, which is modified according to

$$M_m = \iint \sigma(z) \cdot z \, dS, \quad (11)$$

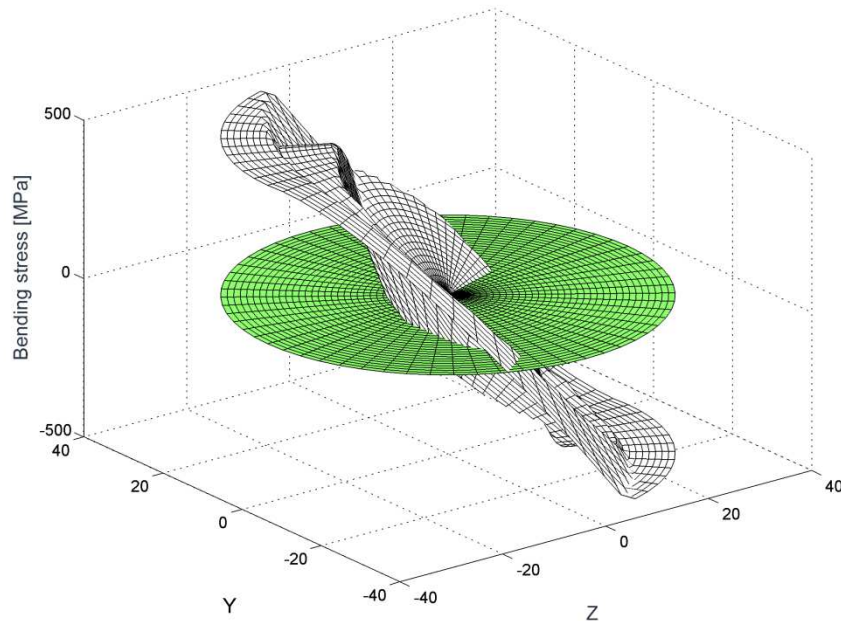
where z is the vertical coordinate and S the cross section area. From the modified moment, equivalent nodal loading matrix \mathbf{f} is easily computed for each element

$$\mathbf{f} = \int_0^L \mathbf{B}(x) \cdot M_m(x) \cdot dx, \quad (12)$$

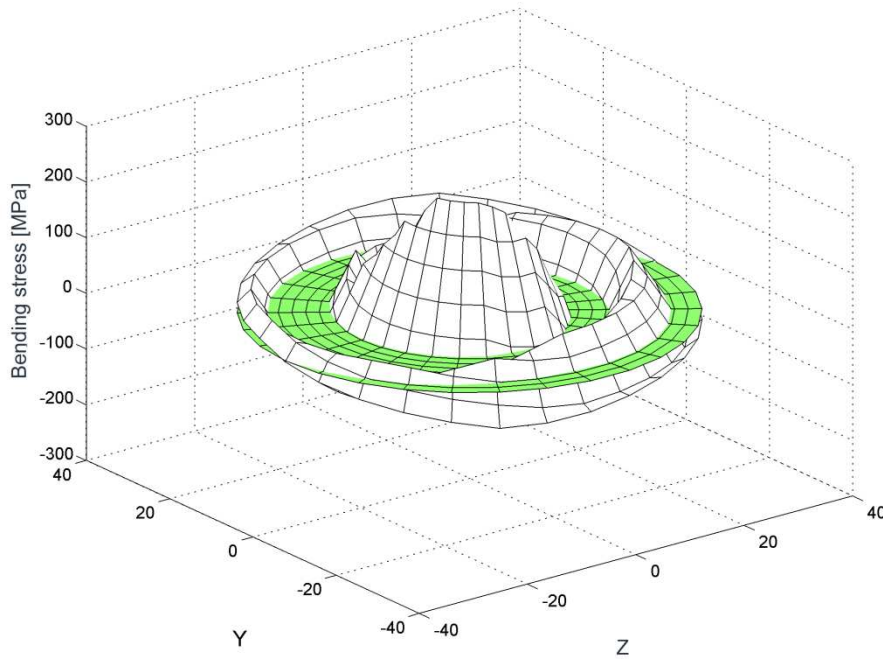
where $\mathbf{B}(x)$ is the curvature approximation matrix according to Eq.(5), L is the element length and $M_m(x)$ is a linear approximation of the modified bending moment along the finite element, obtained from the values in nodal points. Global matrix of equivalent nodal loads \mathbf{F}_i is then obtained by contributions from all finite elements and matrix of residual loads for the next iteration is $\mathbf{R}_i = -\mathbf{F}_i$.



a) initial state



b) intermediate state at roll D



c) residual stress after leveling

Figure 4: Distribution of elastic plastic bending stress σ .

In case of growing plastic strain, i.e. for active plastic loading, also the stiffness matrix must be modified. It is realized by changing the beam flexural rigidity according to

$$(EJ)_m = \iint E_m(z) \cdot z^2 dS, \text{ where} \quad (13)$$

$$E_m = E \cdot \left(1 - \frac{E}{E + H}\right) \text{ and } H = \frac{E \cdot E_T}{E - E_T}. \quad (14)$$

E , E_T is the modulus of elasticity and tangential hardening modulus, respectively – see [7]. Modified flexural rigidity according to Eq. (13) enters the stiffness matrix (3) of each plasticized element. It results in a new tangential stiffness matrix \mathbf{K}_{Ti} prepared for the next iteration.

Finally, the convergence criteria are checked and the procedure is either stopped or returned back to Eq.1 with iteration number i increased by one.

4 PROGRAM VERIFICATION

The algorithm presented above was programmed in MATLAB and verified by specific tests. Its performance was compared with full time-consuming FE analysis and with simple analytical models of our industrial partner with acceptable results. It can be illustrated by the following testing example: Circular cross section bar with diameter of 70 mm is moved through the leveling machine with subsequent intermeshing of adjustable rollers: 0, 12, 10 and 0 mm. Material is characterized by yield stress of 500 MPa and no hardening. In Fig. 5 we show the deflection, slope, curvature, bending moment, shear force and maximal bending stress along the length of the leveled bar. Fig. 4c) shows the distribution of residual stress over the cross section of the bar after leaving the machine. Maximal value of residual stress

after straightening is 240 MPa. Initial radius of curvature 10 m was straightened to final value of 182 m. Loading of leveling rollers A-G (Fig. 1) is 16.5 kN, 60.9 kN, 101.1 kN, 111.6 kN, 95.5 kN, 55.0 kN and 14.4kN.

The results correspond to detailed FEM analysis realized by ANSYS, the solution procedure is stable and very fast in comparison to multipurpose FEM package. Presented example was solved in 60 iterations with total running time 8 min on a standard PC. This performance, together with user friendly interface makes our program an ideal tool for optimization of the leveling process.

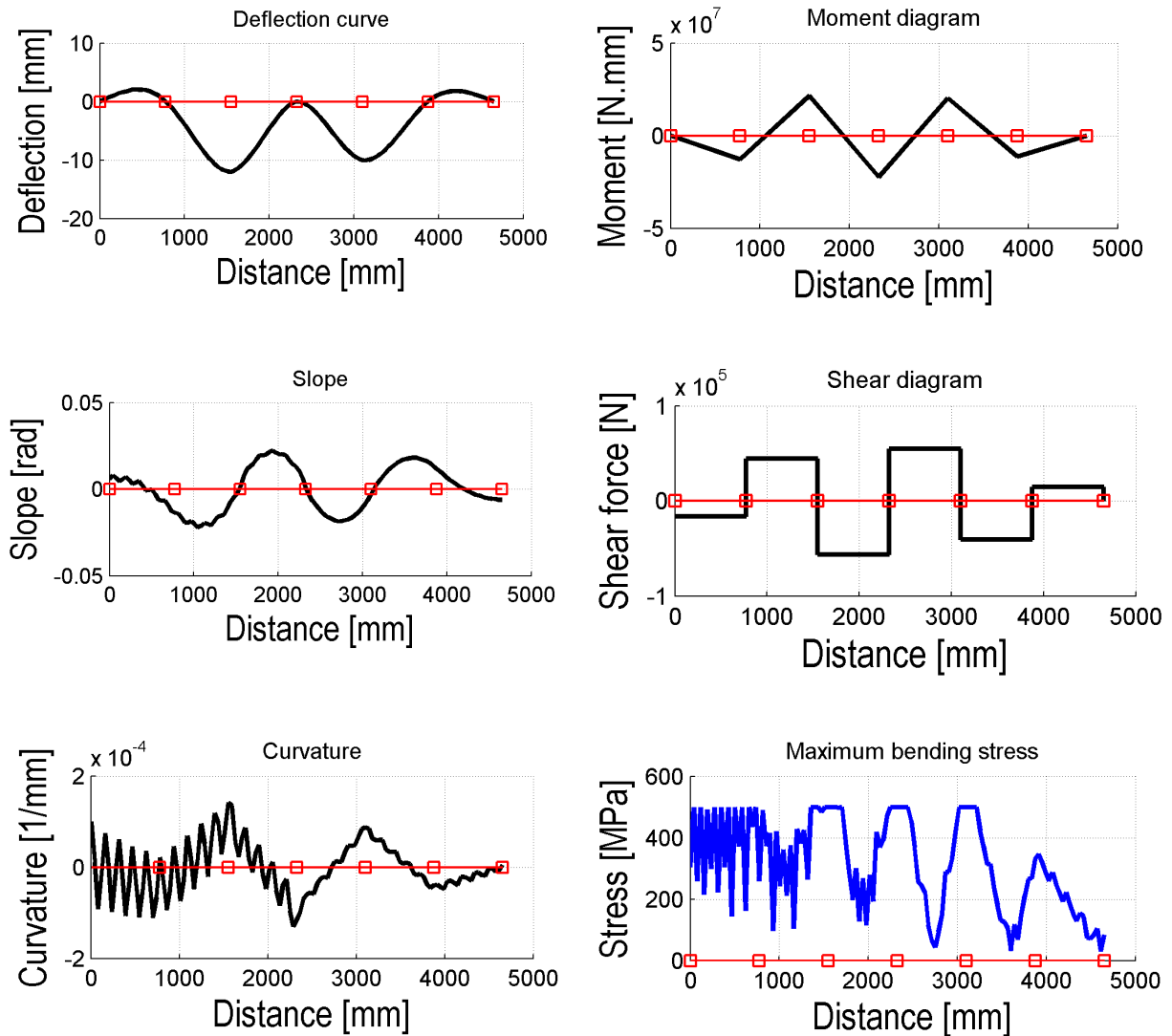


Figure 5: Results of the testing example: deflection, slope, curvature, bending moment, shear force and maximal bending stress along the leveled bar.

5 CONCLUSIONS

User friendly and fast program for direct solution of cross roll leveling process of circular bars was developed and tested. The algorithm is based on simple FE beam element with Euler

scheme material flow and nonlinear iterative solution of the final equations using Newton-Raphson scheme. It was created with the aim to gain a user friendly and fast tool for analysis of practical industrial problems, applicable for engineering optimization of leveling schemes. Modular structure of the program is prepared to enhance its applicability to other similar processes like plate leveling, tensile leveling of thin sheets, cross roll straightening of tubes, etc. Some improvements are being prepared also in precise evaluation of position of the contact point between the rollers and product. Other improvements should include the influence of shear force to product deflection or better modelling of material. Especially the cyclic hardening/softening of material can have a substantial influence on the results. This will be the main direction of further development with strong accent to practical industrial applicability of the results.

ACKNOWLEDGEMENT

Financial help of the grant projects GA101/09/1630 and European Regional Development Fund project CZ.1.05/2.1.00/01.0002 is gratefully acknowledged.

REFERENCES

- [1] H. Tokunaga: On the Roller Straightener, *Bul. JSME* **15** (1961) 605-611.
- [2] H. Huh, J. H. Heo, H. W. Lee: Optimization of a roller leveling process for Al7001T9 pipes with FEA and Taguchi method, *Int. J. Mach. Tool. Manuf.* **43** (2003) 345–350.
- [3] M. Nastran, K. Kuzman: Stabilisation of mechanical properties of the wire by roller straightening, *J. Mat. Proc. Tech.* **125-126** (2002) 711-719.
- [4] E. Doege, R. Menz, S. Huinink: Analysis of the leveling process based upon an analytic forming model, *Manuf. Technol.* **51**(2002) 191-194.
- [5] Z. Liu, Y. Wang, X. Yan: A new model for plate leveling process based on curvature integration method, *Int. J. Mech. Sci.* **54** (2012) 213–224.
- [6] R. D. Cook: *Concepts and Applications of Finite Element Analysis*, J.Wiley, 1981
- [7] D. R. J. Owen, E. Hinton: *Finite Elements in Plasticity*, Pineridge Press, Swansea, 1980

GENERATING EMBEDDED REBAR ELEMENTS FOR LARGE-SCALE RC MODELS

George Markou¹ and Manolis Papadrakakis²

¹Department of Civil Engineering, Alhosn University, Abu Dhabi, UAE
P.O.Box 38772, Abu Dhabi
g.markou@alhosnu.ae

²Department of Civil Engineering, National Technical University of Athens
GR-15780 Athens, Greece
mpapadra@cental.ntua.gr

Keywords: Embedded Reinforcement, Mesh Generation, Large-Scale Models.

Abstract. *Modeling of reinforced concrete structures through the use of 3D detailed models derives significant numerical issues especially when dealing with large-scale meshes that incorporate large numbers of reinforcement bars embedded in the hexahedral mesh. In 3D detailed reinforced concrete simulations, mapping the reinforcement grid inside the concrete hexahedral finite elements is performed by using the end-point coordinates of the rebar macro-elements. This procedure is computationally demanding when dealing with large-scale models, where the required computational time for the reinforcement mesh generation can be excessive. This research work investigates the numerical robustness and computational efficiency of the embedded rebar mesh generation method proposed by Markou [14] that was an extension of the Markou and Papadrakakis [8] research work. The under study embedded rebar mesh generation method foresees the automatic allocation and generation of embedded steel reinforcement inside hexahedral finite elements for 32-bit and 64-bit windows based applications. In order to investigate the numerical and computational performance of the embedded rebar mesh generation method, a full-scale model of the RC frame of the Alhosn University Campus in Abu Dhabi and a RC bridge are constructed and used so as to allocate and generate the embedded rebar finite elements. The numerical results that derived from the ReConAn FEA solver for the at hand numerical implementations are briefly presented.*

1 INTRODUCTION

Modeling of reinforced concrete (RC) structures with the use of 3D detailed models is usually performed by research teams [1-5] or by large consultancy companies [6-7] that foresee the thorough investigation of the mechanical behavior of geometrically complicated RC structures. Researchers have been using this modeling type so as to verify experimental results or develop new constitutive models in an attempt to derive a numerically objective modeling method that will eventually provide the ability of performing assessment analysis for any type of RC structure geometry and design.

As it was described in [8], when modeling 3D RC structures with the finite element (FE) method, three main approaches are available for the simulation of reinforcement: smeared, discrete, and embedded [9-11]. The smeared and discrete formulations have been found to be unsuitable for complicated reinforcement grid geometries thus undergo several restrictions when implemented. On the other hand, the embedded reinforcement formulation provides the ability of representing the grid's geometry in an exact manner without the need of modifying the actual arrangement of rebars to conform with the concrete FE mesh [12-13].

In order to optimize the performance of the Barzegar and Maddipudi [9] embedded mesh generation method, which is an extension of the work of Elwi and Hruday [10], Markou and Papadrakakis [8] proposed the introduction of a geometrical constraint in order to decrease the computational effort for generating the input data of the embedded rebar elements, particularly when dealing with relatively large-scale numerical models. Their proposed method (Fig. 1) was incorporated in ReConAn FEA [5] which was developed and built to run in a 32-bit operating systems.

The purpose of this research work is to present the numerical performance of the embedded mesh generation method proposed by Markou [14] in the case of large-scale RC numerical simulations.

2 GENERATING REINFORCEMENT INSIDE HEXAHEDRAL ELEMENTS

The under study embedded mesh generation method considers arbitrary positioning of the rebars inside the concrete elements [8], as shown in Fig. 2, while avoiding a nonlinear search procedure for the calculation of the natural coordinates of the embedded reinforcement nodes in the corresponding prismatic hexahedral elements. By separating the mesh generation algorithm into two main parts (Fig. 1), the geometry of each hexahedral element is categorized (prismatic or non-prismatic) and accordingly treated in order to compute the natural coordinates of its containing embedded rebar elements. For the detailed description of this method, refer to the relative reference [8].

The embedded reinforcement mesh generation method proposed in [8], was integrated and built in for a 64-bit operating system so as to overcome the problem that rises related to the physical memory allocation issue, which in the case of the 32-bit architecture is limited to 2 Gb. In addition to that the method was integrated with a filtering algorithm [14] that provides the ability to allocate relatively short embedded rebar finite elements, during the mesh allocation procedure. This filtering procedure provides the ability to control the mesh quality of the embedded rebar elements thus avoiding the numerical phenomenon of the local stiffness concentration due to the relatively short embedded rebar finite element length (Fig. 3). The flowchart diagram of the integrated embedded reinforcement mesh generation algorithm can be seen in Fig. 4.

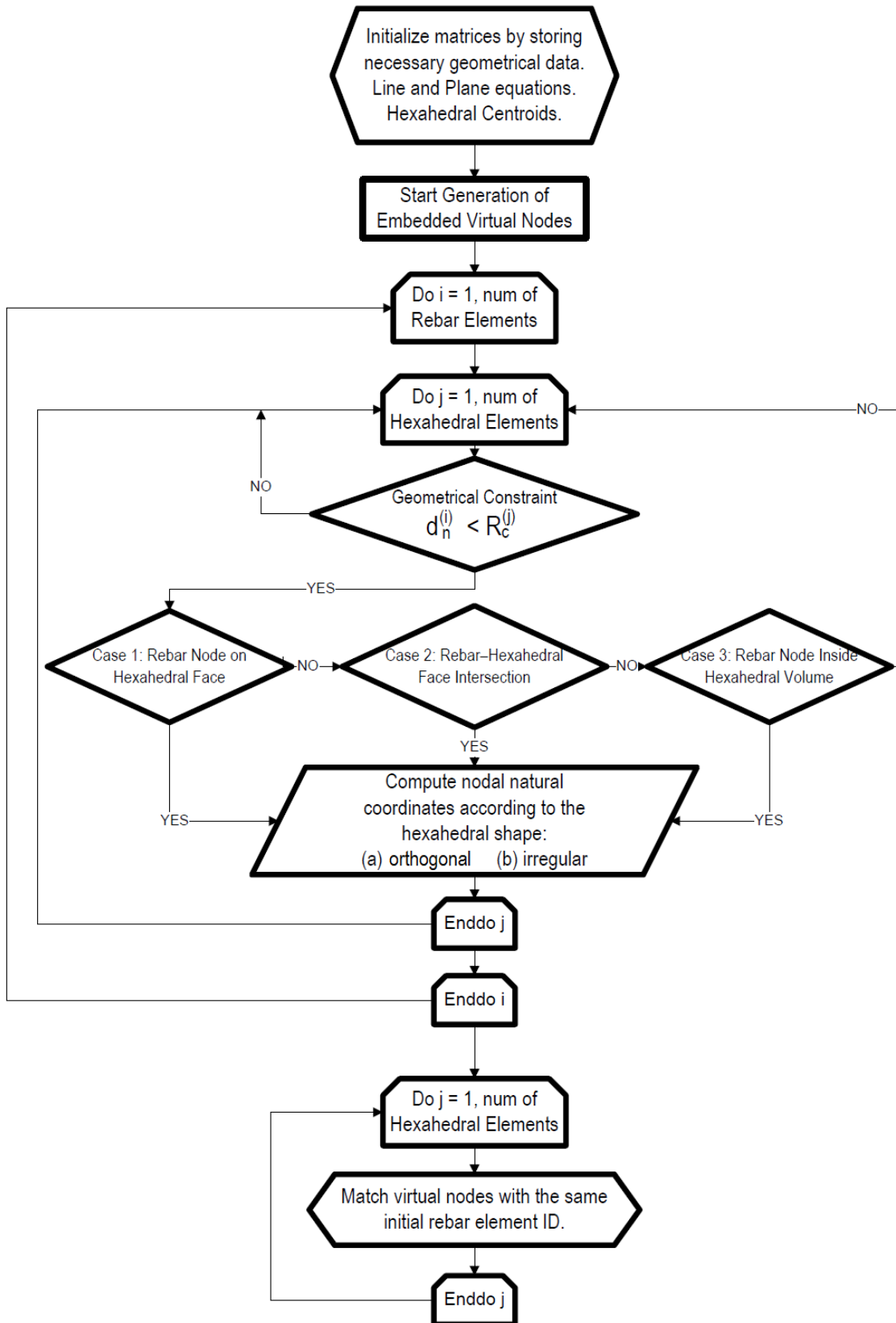


Figure 1. Flow chart of the embedded rebar mesh generation method [14].

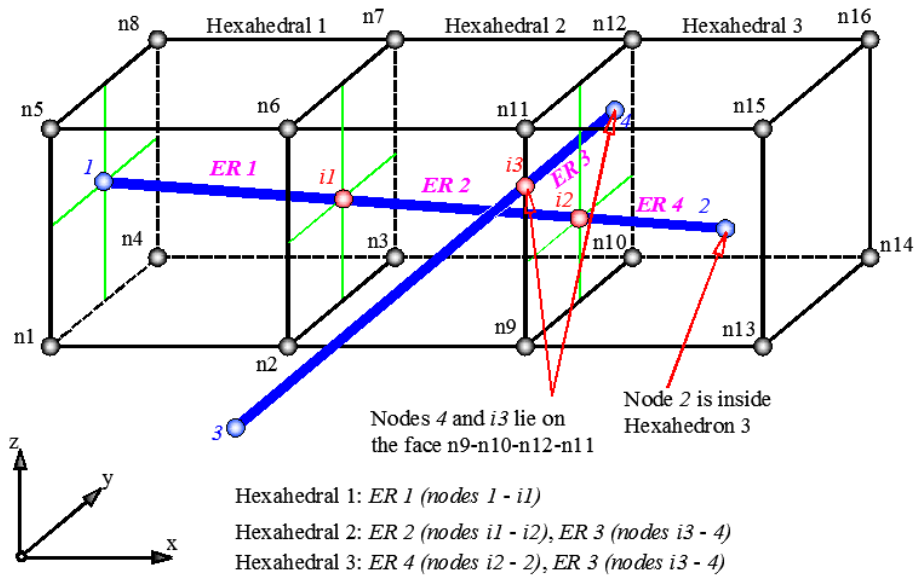


Figure 2. Embedded reinforcement rebars inside hexahedral elements [8].

As it can be seen in Fig. 4, the updated algorithm foresees the scanning of the rebar mesh so as to allocate short embedded elements that might result due to the irregular hexahedral mesh during the embedded rebar allocation procedure. In this case the embedded rebar mesh generation algorithm has the ability to filter the embedded rebar elements that have a very short length (see Fig. 3), while it controls the quality of the derived embedded mesh.

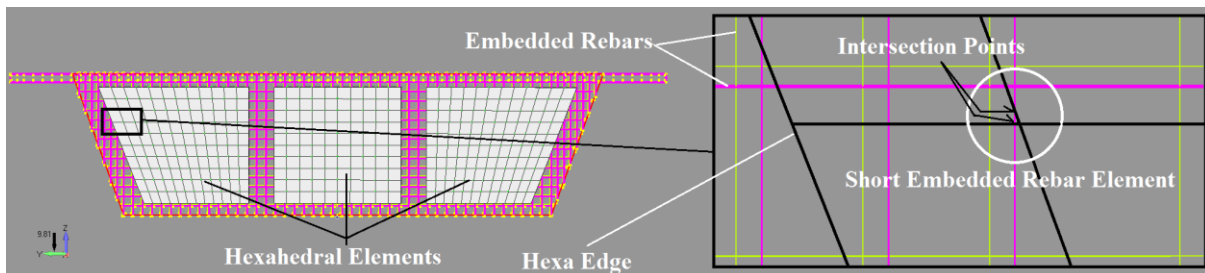


Figure 3. Hexahedral and embedded rebar elements of a RC bridge’s vertical diaphragm. Short embedded rebar element case.

3 NUMERICAL IMPLEMENTATION

In order to assess the embedded mesh generation method, the Alhosn University’s Male Campus and a RC bridge are used for constructing two 3D detailed meshes. The results from the embedded mesh generation procedures are discussed and the numerical results that derived from the solutions of the two models will be shortly presented. It must be noted that all numerical tests were performed on a 64-bit windows operating system (3.3GHz CPU).

3.1 RC Building

The RC building (Alhosn University Male Campus) that was used so as to construct the 3D mesh is shown in Fig. 5, while the geometry of its RC frame is given in Fig. 6. As it can be seen, the building has a total width of 20.45m and a 25.6m length. The total height of the building is 13.2m (Ground floor, 1st-3rd floor), while the basement of the structure is also accounted for in the under study model (Fig. 7).

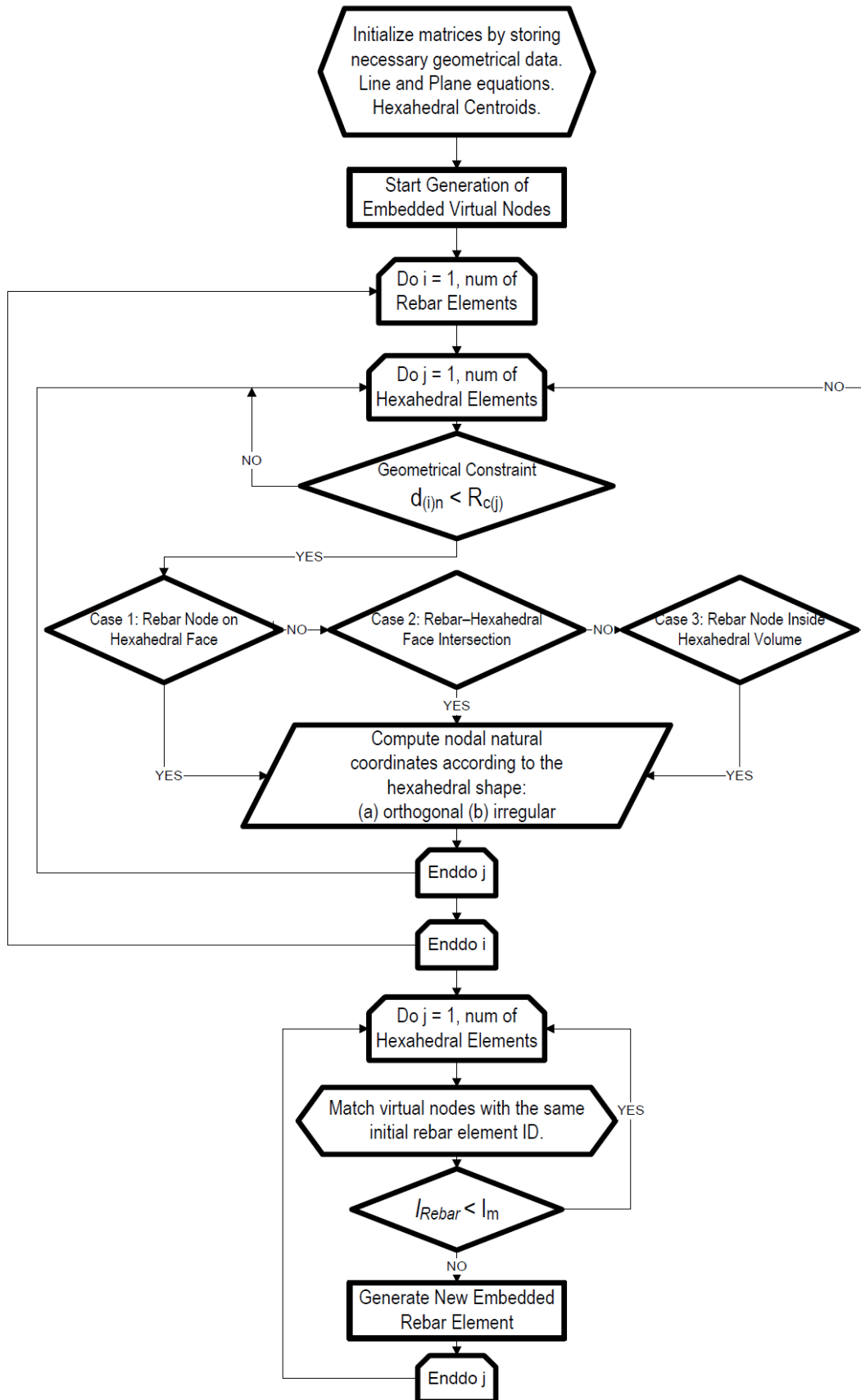


Figure 4. Flow chart of the updated embedded rebar element mesh generation method [14].



Figure 5. Alhosn University's Male Campus in Abu Dhabi, UAE.

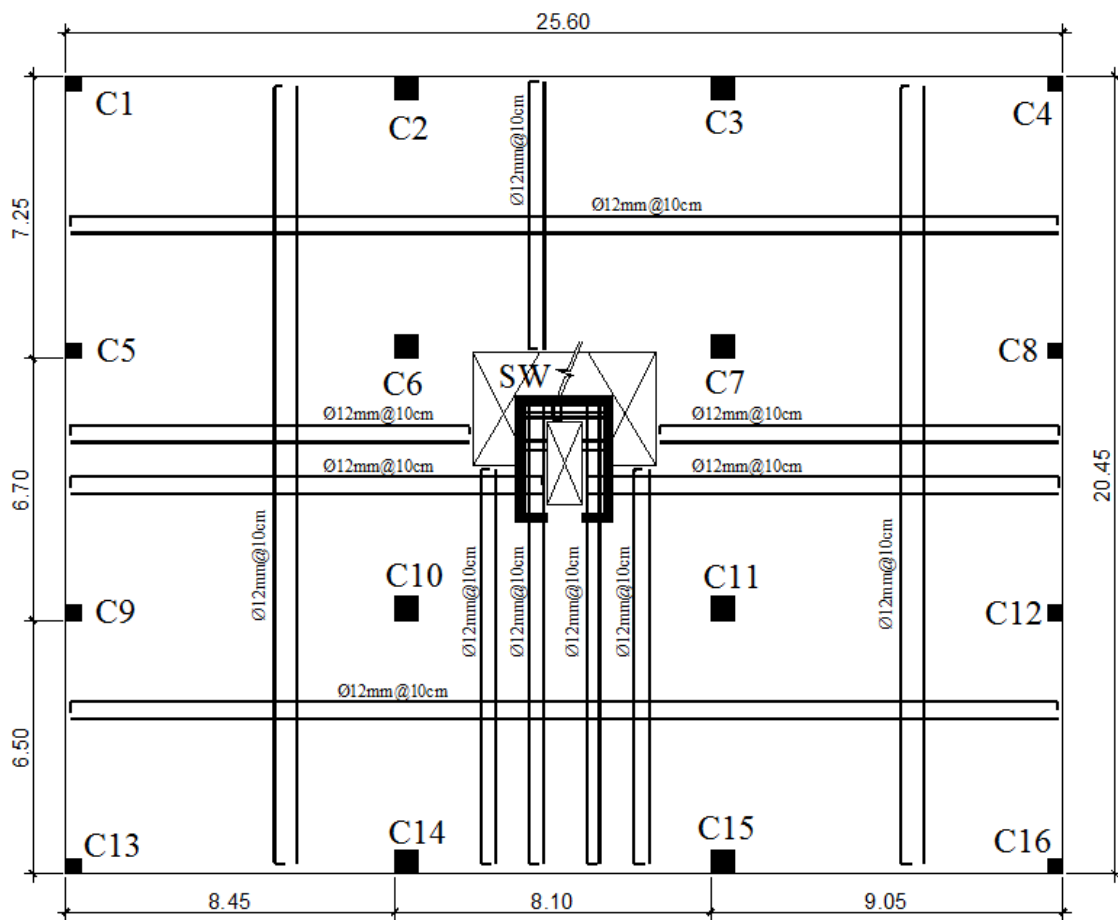


Figure 6. Reinforcement details of the slab (Ground – 3rd Floor).

In the UAE, the most common framing system used is that of the flat slabs, which is also the framing system adopted in this research work. As it can be depicted in Fig. 6, the shear wall of the elevator is located in the center of the structure, while a total of 16 columns are placed symmetrically about the structure's core. The geometry of the columns' sections are 40x40cm and 60x60cm. The thickness of the slab is assumed to be equal to 30cm while the reinforcement details are shown in Figs. 6 & 8. The 40x40cm columns are reinforced with 8Ø20mm longitudinal rebars and two hoops Ø8mm@10cm as stirrups, while the 60x60cm columns are reinforced with 12Ø22mm longitudinal rebars and three hoops Ø10mm@10cm

as stirrups. For the case of the shear wall, $72\text{Ø}18\text{mm}$ longitudinal rebars are used and $\text{Ø}8\text{mm}@10\text{cm}$ as stirrups (Fig. 8).

Regarding the foundation type, it is assumed that the building is based on a general foundation slab which is 80cm thick. The foundation slab is reinforced with 14mm rebars every 10cm along the X and Y directions, while the foundation soil is also discretized with hexahedral elements in an attempt to make the numerical model more realistic. A retaining wall (Fig. 7) is foreseen at the perimeter of the basement which has a thickness of 20cm, which is reinforced with 12mm rebars at every 15cm as the principal reinforcement and 8mm rebars at every 15cm as the secondary reinforcement.

3.1.1. Construction and Management of the Hexahedral Mesh

ReConAn FEA uses Femap [15] through which the initial mesh is constructed, while the input file is exported into a text file (.neu \rightarrow neutral file) that is used to generate the FE numerical model during the analysis of the numerical problem. For controlling the mesh quality the “Analysis by Parts” approach is used, which foresees the division of the mesh during the construction procedure into parts, while for each part an independent solution is performed to check for any mesh inconsistencies. Following the completion of this procedure all parts are combined and connected into the final mesh that is used to simulate the complete geometry of the structure. Fig. 9 shows the final mesh of the 75,080 8-noded hexahedral elements as it resulted from the mesh construction phase. The details related to the mesh are given in Table 1 and as it can be seen, the total number of concrete elements is 43,250, while the total number of nodes (excluding the embedded rebar macro-elements’ nodes) is 119,232. The hexahedral edge size that was used to construct the concrete FE mesh of the RC frame was between 20-40 cm.

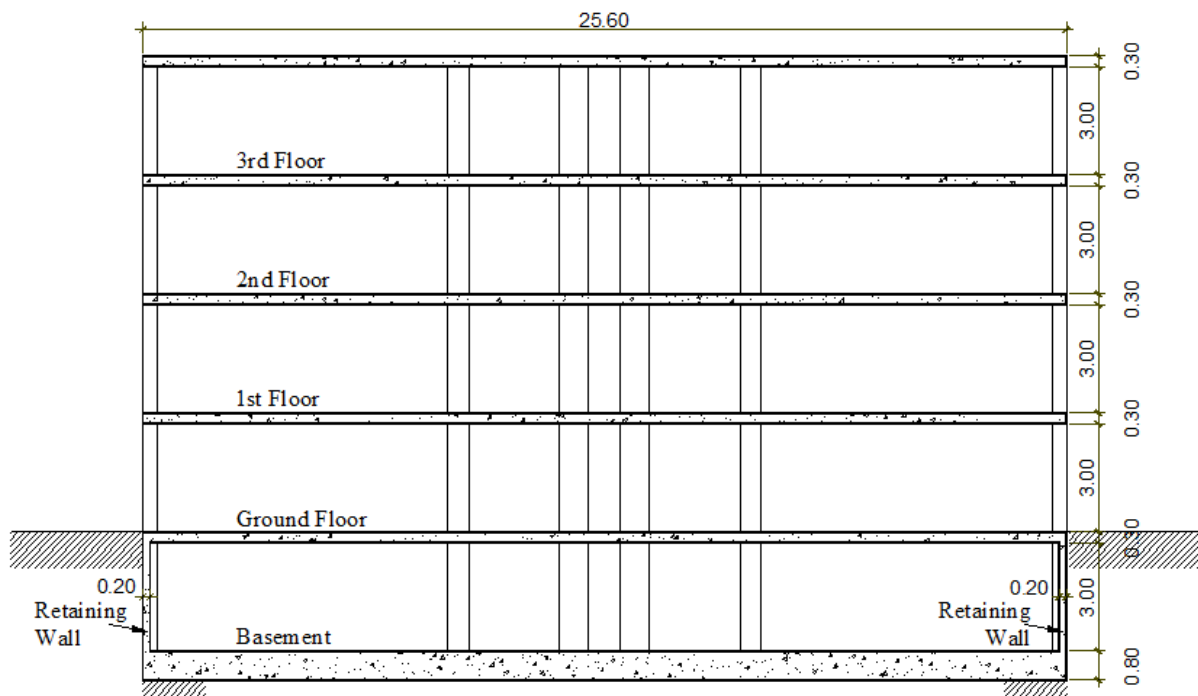
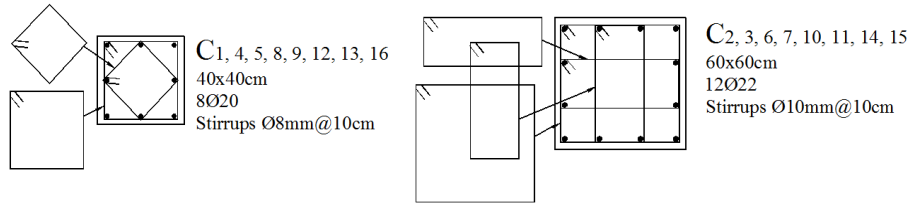


Figure 7. Section a-a of the building.



Note: Concrete cover 35 mm.

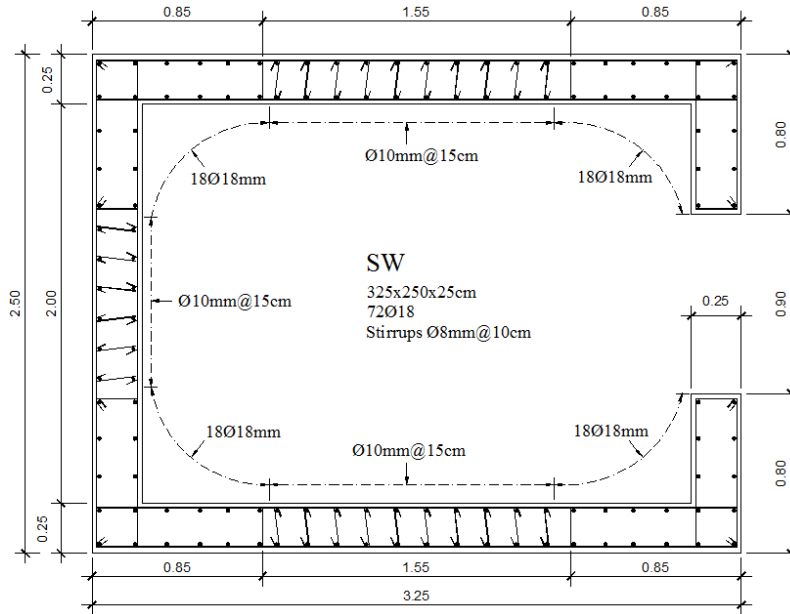


Figure 8. Reinforcement details of the columns and shear wall.

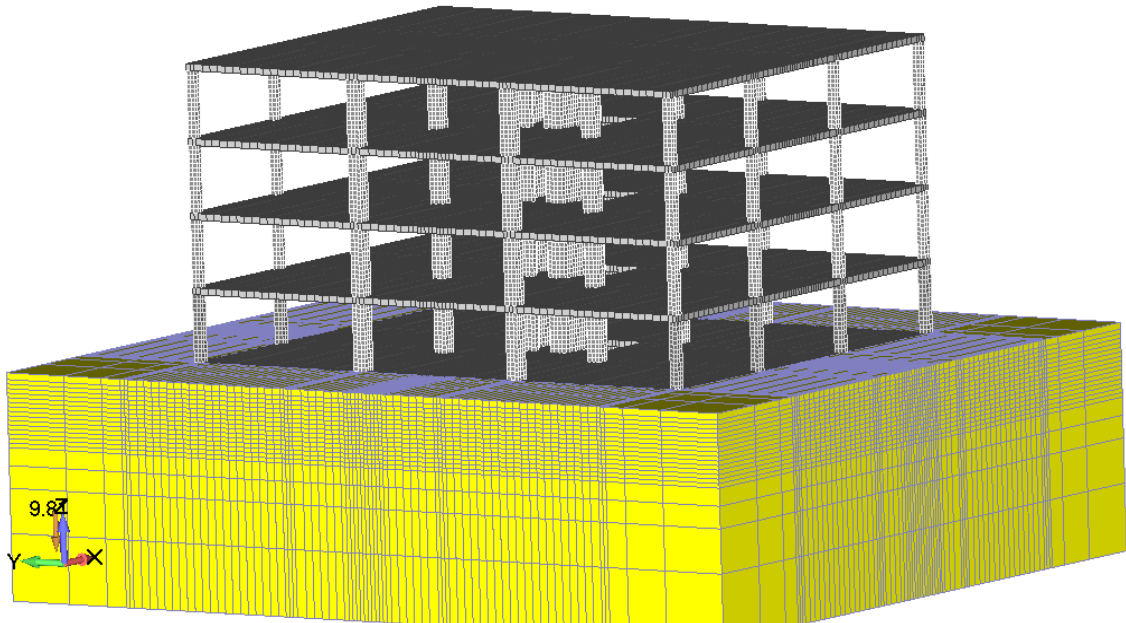


Figure 9. FE mesh of the 8-noded hexahedral elements.

The hexahedral mesh of the building was divided into 6 groups where each group was assigned with the corresponding Layers (a total of 25 layers). Fig. 10 shows the groups of Lay-

ers used during the hexahedral mesh construction procedure so as to manage graphically each part of the model. After the completion of the hexahedral mesh construction, the model was analyzed for the self-weight loads so as to ensure that the resulted numerical model was ready to be processed to the next stage which was the embedded rebar macro-element mesh construction. Fig. 11 shows the deformed shape and the von Mises stress distribution as it resulted from the Convergence Analysis stage (linear elastic analysis for the self-weight of the structure).

a/a	Description	Value
1	Hexa8 total number of Soil elements	31,830
2	Hexa8 Concrete elements	
	2.1 Foundation Slab	4,810
	2.2 Retaining Wall	3,630
	2.3 Slabs	23,410
	2.4 Columns 40x40	2,400
	2.5 Columns 60x60	5,400
	2.6 Shear Wall	3,600
	Total	43,250
3	Total number of Hexa8 elements	75,080
4	Total number of Hexa8 nodes	119,232

Table 1. FE mesh data related to the 8-noded hexahedral mesh.

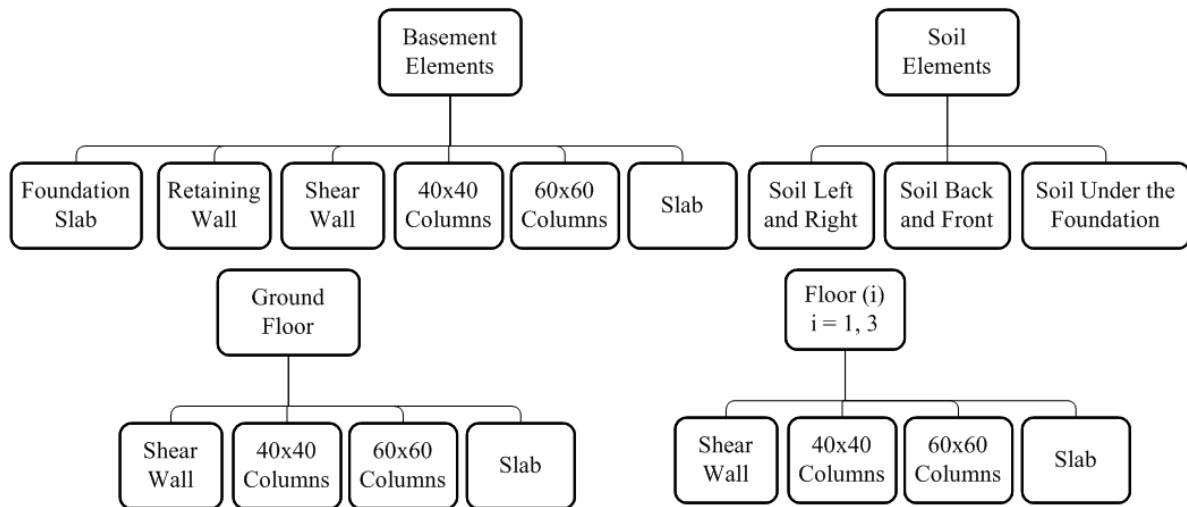


Figure 10. Layer organization chart of the hexahedral mesh.

3.1.2. Constructing, Managing and Verifying the Embedded Reinforcement FE Mesh

As it is shown in Fig. 12, the embedded rebar mesh was divided into 22 Layers according to the RC frame's geometrical features. Furthermore, after the completion of the construction of the embedded rebar macro-element mesh for each structural member of the basement's frame, a convergence analysis was performed (foundation slab, basement columns/shear wall/retaining wall/slab, see Figs. 13-14) so as to assess the derived FE mesh. After the successful completion of the convergence analysis, the embedded rebar macro-elements of the basement's frame were replicated to the rest of the floors deriving the final embedded rebar

macro-element mesh (see Table 2). Fig. 15 shows the final embedded reinforcement macro-elements as they resulted from the mesh construction procedure.

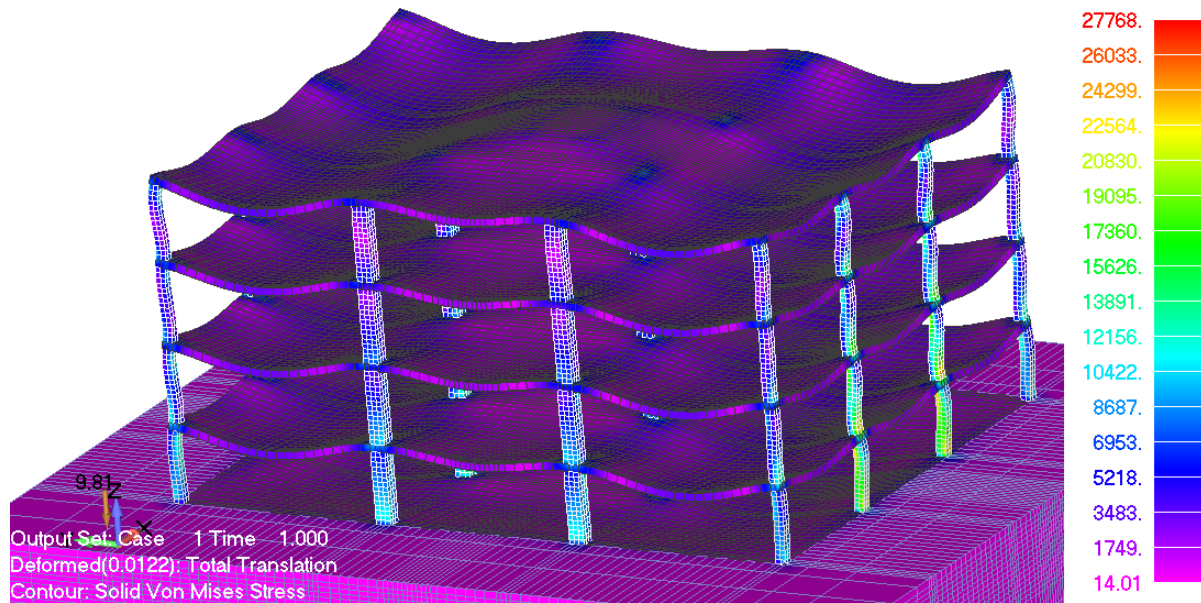


Figure 11. Deformed shape and von Mises stress distribution of the hexahedral mesh as it resulted from the Convergence Analysis stage.

a/a	Structural Member	c	Macro-Elements
1	Foundation Slab	20	9,712
2	Retaining Wall	3	14,304
3	Columns 40x40	3	13,824
4	Columns 60x60	3	20,736
5	Shear Wall	3	18,180
6	Slabs	20	53,503
Total:			130,259
i	Basement with Foundation Slab	-	46,750
ii	Ground Floor		20,990
ii	1 st Floor		20,990
iii	2 nd Floor		20,990
iv	3 rd Floor		20,539

Table 2. Embedded rebar macro-elements that derived from the mesh construction procedure.

3.1.3. Solution of the Complete Model

At this stage the complete model (Fig. 15) is going to be analyzed in order to allocate and generate the final embedded rebar mesh through the use of the under study embedded rebar mesh generation method. It must be noted at this point that the geometric constraint c [8] for the embedded rebar mesh generation procedure inside the vertical and horizontal structural members was set equal to 3 and 20, respectively, as it can be seen in Table 2. For the columns and shear walls the geometric constraint parameter c was set to 3 and for the rest of the frame equal to 20. Table 3 shows the details of the resulted FE mesh, the total required time for generating the embedded rebar elements and the numerical details related to the solution of the FE model.

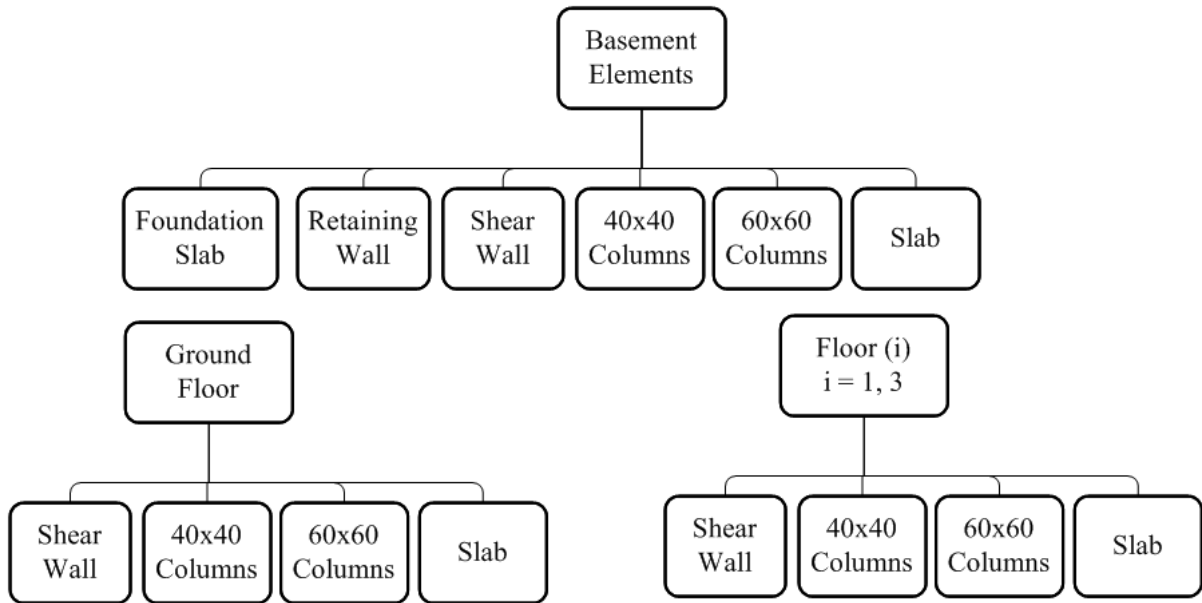


Figure 12. Layer organization chart of the embedded rebar macro-element mesh.

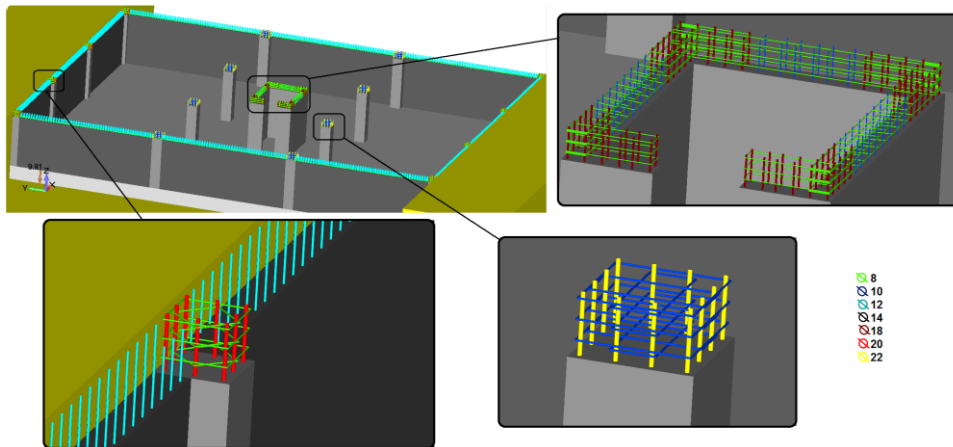


Figure 13. Macro-element rebar mesh construction phase. Hexahedral and macro-elements (Basement and Foundation Slab).

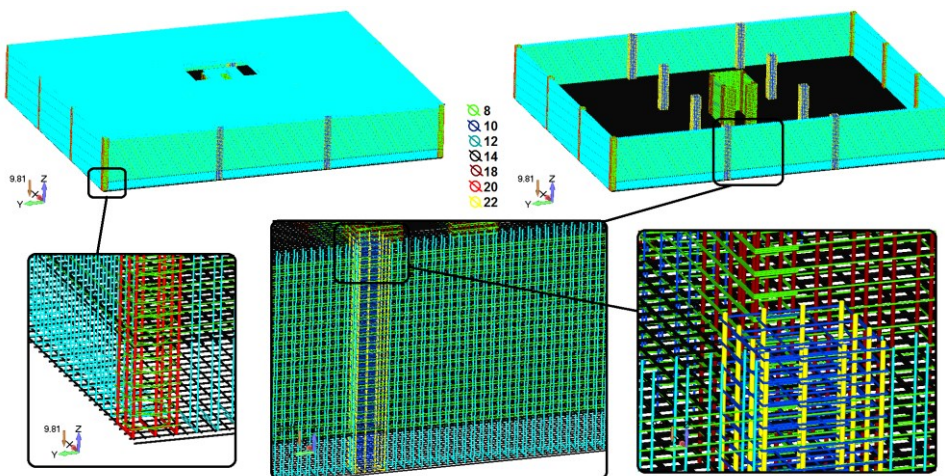


Figure 14. Macro-element rebar mesh of the Basement and the Foundation Slab (46,750 macro-elements).

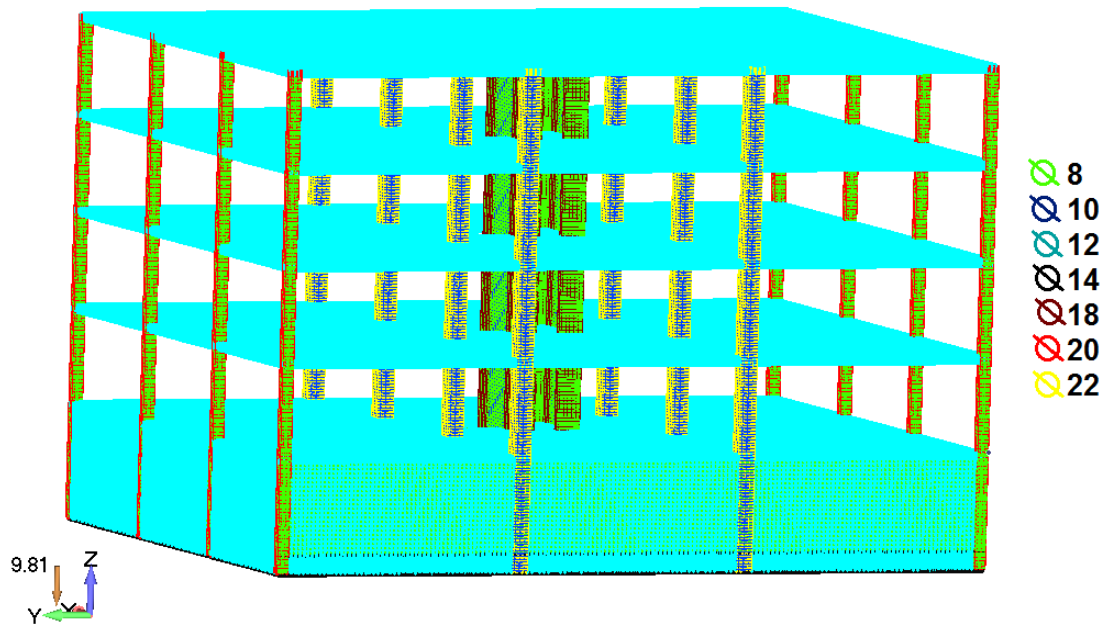


Figure 15. Macro-element rebar mesh of the RC frame of the building (130,259 macro-elements).

a/a	Description	Value
1	Number of Hexahedral Elements	75,080
2	Number of Nodes (hexa8 only)	119,232
3	Number of Macro-Elements	130,259
4	Total Number of Embedded Rebar FEs Generated	532,311
5	Total Number of Short Embedded Rebar FEs that were Discarded by the Filter Algorithm	5,408
6	Required Embedded Mesh Generation Time	75 min
7	Required RAM for the Stiffness Matrix	10.73 Gb
8	Number of Stiffness Matrix Elements	1,440,509,266
9	Total Required RAM for the Solution Procedure	22.73 Gb
10	Computational Time for Solving 1 Load Increment	52 min
11	Computational Time for Writing the Output Data	172 min
12	Total Computational Time: i. Read/Initialize Problem ii. Generate Embedded Mesh iii. Solve the System of Equations for 1 Load Increment / 1 Internal Iteration iv. Write Output Data (out.txt file size: 645 Mb) v. Other	324 min

Table 3. Numerical and computational results that derived after the solution of the complete FE model.

As it can be seen from Table 3, the total required time for the embedded mesh generation procedure was 75 minutes. The total number of generated embedded rebar FEs was 532,311 while the total number of short embedded rebar FEs that were discarded due to their small length was 5,408 (short length rebar criterion $l_{\min} = 5$ mm). The deformed shape of the embedded rebar mesh resulted by applying only the self-weight of the structure (Figs. 16-17).

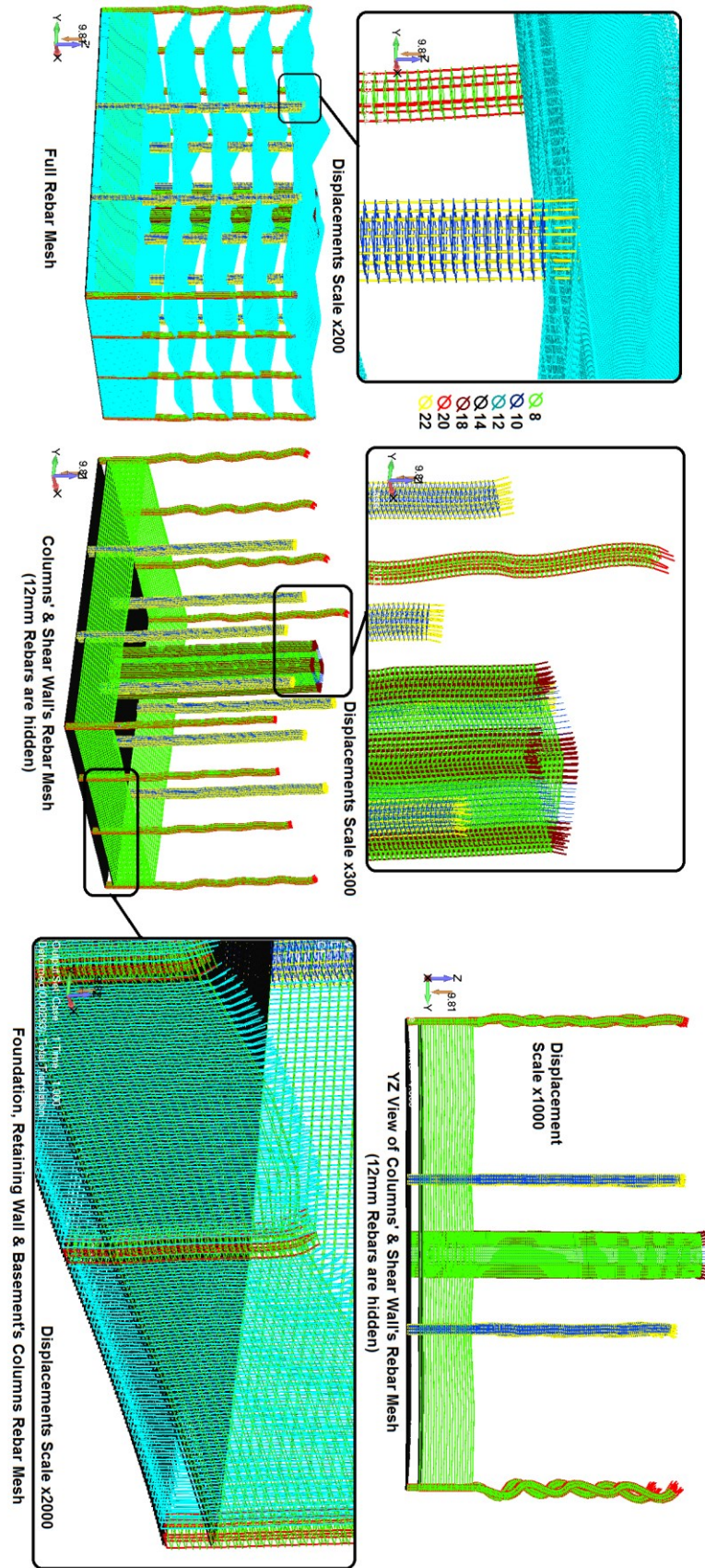


Figure 16. Deformed shape of the embedded rebar FE mesh.

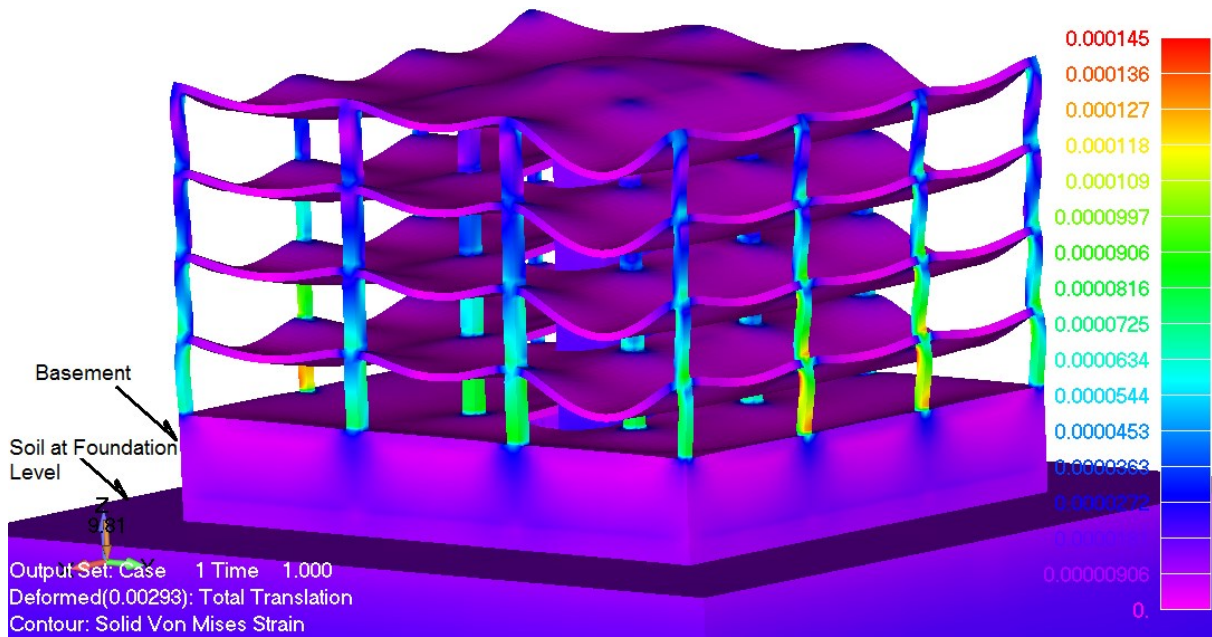


Figure 17. Deformed shape and von Mises strain distribution of the concrete elements.

In order to solve the numerical model for a single load increment, ReConAn required 52 minutes, while the total computational time was 324 minutes. The required embedded rebar mesh generation time represents 23.15% of the total computational time. The resulted computational ratio is relatively small given that the at hand numerical problem was solved for a single load increment, thus for the case of a nonlinear solution procedure with several load increments and internal iterations, the computational time of the actual nonlinear solution procedure would have been significantly larger. This is also verified through the next numerical implementation presented in this section. The requirements in RAM according to Table 3, shows that the allocation of the stiffness matrix requires the largest amount of physical memory than any other matrix used during the solution procedure. As it resulted the total required RAM for allocating the stiffness matrix for the at hand model was 10.73 Gb and to solve this numerical implementation a total of 22.73 Gb of RAM were required.

Fig. 16 shows the deformed shape of the embedded rebar mesh as it resulted from the analysis. The displacements are scaled so as to graphically represent the deformed shape of the frame (scale factors used in Fig. 16: x200-x2000). The deformed shape of the embedded rebar elements illustrate the robustness of the proposed embedded mesh generation method that manages to successfully allocate and generate more than half a million embedded rebar elements that are used to simulate the complete reinforcement grid of the under study RC structure. The deformed shape of the embedded rebar elements shows that their displacements, which are controlled by the hexahedral nodes' displacements, follow the concrete element mesh (Fig. 17) deformed shape. Fig. 17 shows the deformed shape and the von Mises strain distribution for the hexahedral elements as they resulted from the analysis procedure that was executed for the complete FE model. As it was expected, the superstructure undergoes a larger deformation in relation to the basement and the foundation soil that did not develop significant deformations (Fig. 17). Strain concentrations were mainly observed at the column-slab joints of the flat-slab framing system of the RC structure.

3.2 RC Arc-Shaped Bridge

This numerical test was chosen in order to illustrate the actual limitations of the embedded mesh generation method when dealing with large-scale implementations. The different stages until the solution of the full-scale model are described below.

3.2.1. Geometrical Features and Reinforcement Details of the RC Bridge

The geometry of the under study RC bridge is shown in Fig. 18. As it can be seen, the bridge has an effective span of 99.1 m, of which 51.55 m is the left span's length and 47.55 m is the right span's length. The total height of the two pylons is 5.1 m and the spacing between them is 5 m. A typical section of the bridge is given in Fig. 19, where the geometrical features can be depicted. The technical drawings show that the total width of the deck is 10.4 m and it has a height of 2.3 m. The different thicknesses of each structural component of the bridge's deck are given in Table. 4.

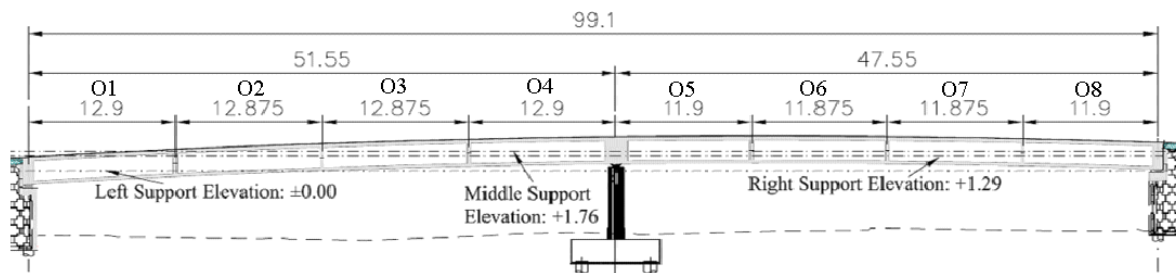


Figure 18. RC Bridge. View of elevations.

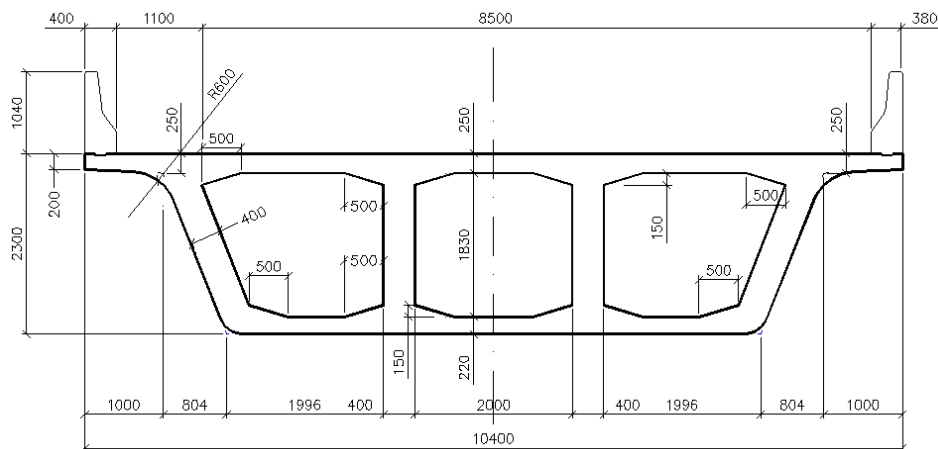


Figure 19. RC Bridge. Geometry of the section of the deck (dimensions in mm).

The reinforcement details of the Pylons are shown in Fig. 20, where it can be seen that 26 rebars of $\text{Ø}32$ mm are used and the stirrups have a diameter of $\text{Ø}12$ mm. Fig. 21 shows the reinforcement details of the pile cap. It is important to note that the model will assume fixed supports at the base of the pile cap, thus the 6 piles and the soil will not be included in the FE mesh.

Fig. 22 shows a typical deck section reinforcement detailing which foresees the use of 12, 16 and 20 mm rebars, while the geometry of the reinforcement arrangement of the support diaphragms can be depicted in Figs. 23 & 24.

a/a	Structural component	Thickness in cm
1	Upper Deck	25
2	Lower Deck	22
3	Overhangs	20
4	Vertical Walls	40
5	Vertical Diaphragms	30
6	Vertical Diaphragms at Supports	100
7	Vertical Diaphragm above Pylons	200

Table 4. RC Bridge. Thicknesses of different structural components of the deck.

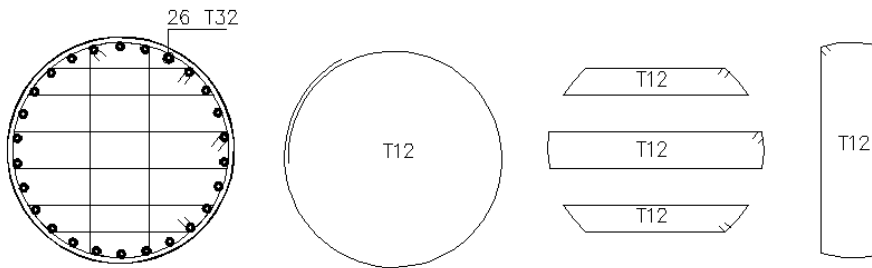


Figure 20. RC Bridge. Reinforcement details of the Pylon's section.

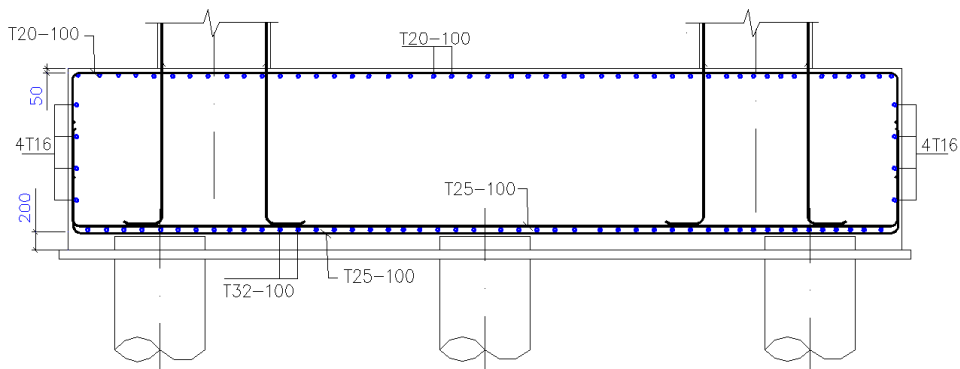


Figure 21. RC Bridge. Reinforcement details of the pile cap.

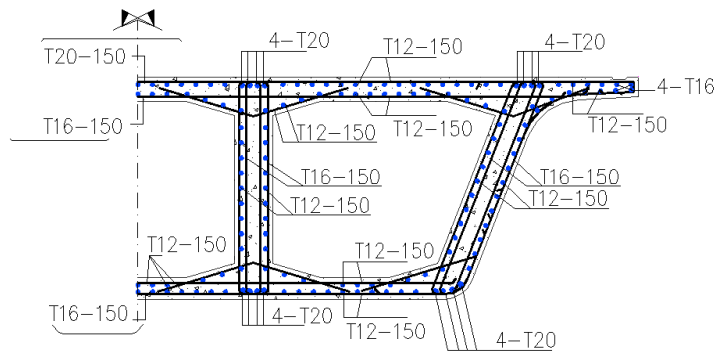


Figure 22. RC Bridge. Reinforcement details of a typical deck section.

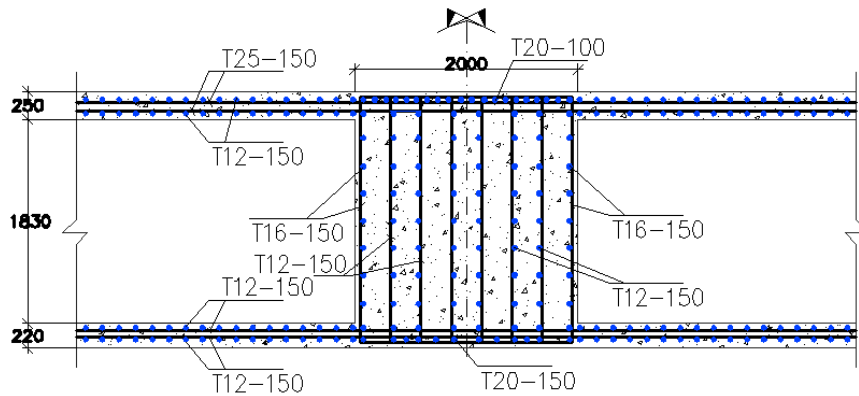


Figure 23. RC Bridge. Reinforcement details of the middle diaphragm.

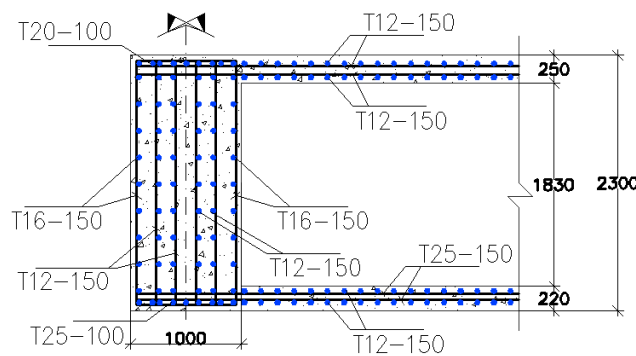


Figure 24. RC Bridge. Reinforcement details of the diaphragms at the left and right supports.

3.2.2. Constructing, Managing and Verifying the Hexahedral FE Mesh

Fig. 25 shows the final mesh of the 102,934 hexahedral elements (8-noded). The details related to the mesh are given in Table 5 and as it can be seen, the total number of concrete elements is 102,622, while the total number of nodes (excluding the embedded rebar macro-elements) is 168,400. The average hexahedral edge size used to derive the FE mesh of the RC bridge was 20 cm.

a/a	Structural Member	Hexa8
1	Opening O1 Deck + Left Support Diaphragm	13,824
2	Opening O2 Deck	11,254
3	Opening O3 Deck	11,254
4	Opening O4 Deck + Half of the Middle Diaphragm	12,662
5	Opening O5 Deck + Half of the Middle Diaphragm	12,432
6	Opening O6 Deck	10,558
7	Opening O7 Deck	10,558
8	Opening O8 Deck + Right Support Diaphragm	11,800
9	Two Pylons	3,080
10	Pile Cap	5,200
11	Elastomeric Bearings + Steel Plates	312
Total		102,934

Table 5. RC Bridge. Hexahedral element distribution.

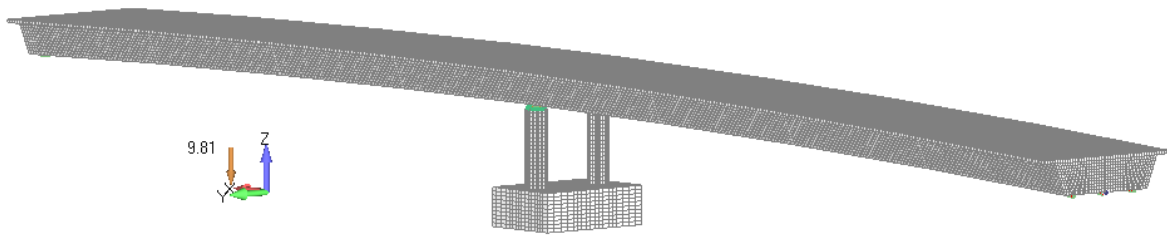


Figure 25. RC Bridge. FE mesh of 8-noded hexahedral elements.

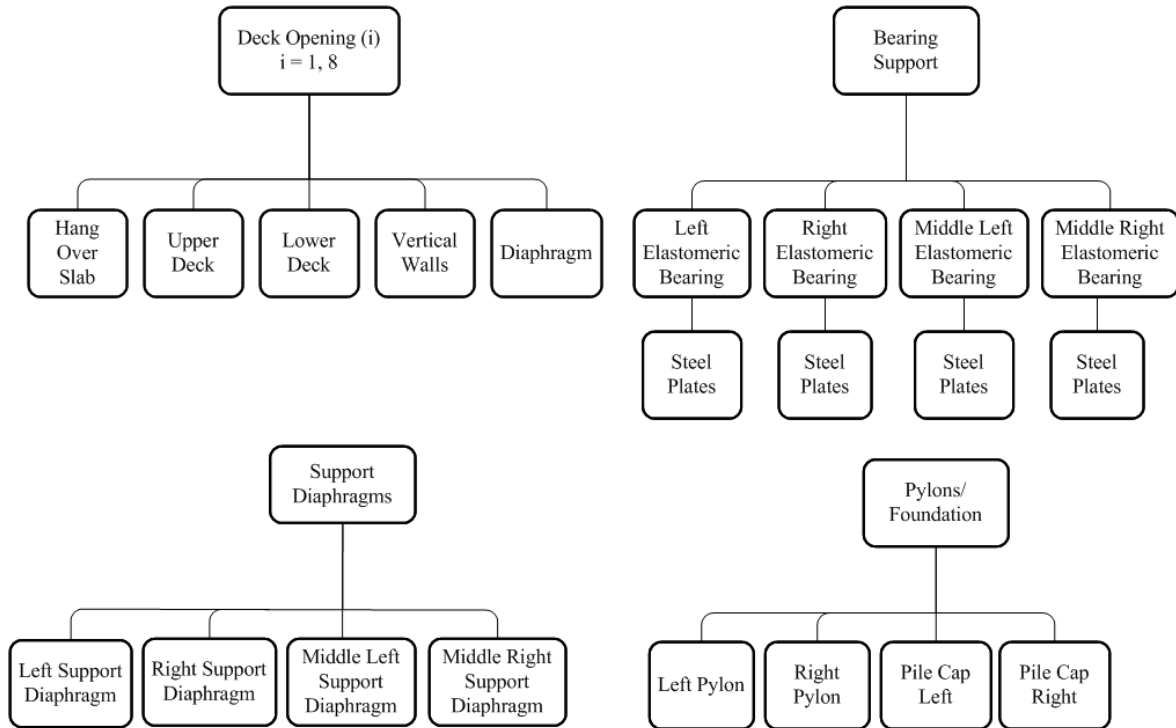


Figure 26. RC Bridge. Hexahedral mesh Layer organization chart.

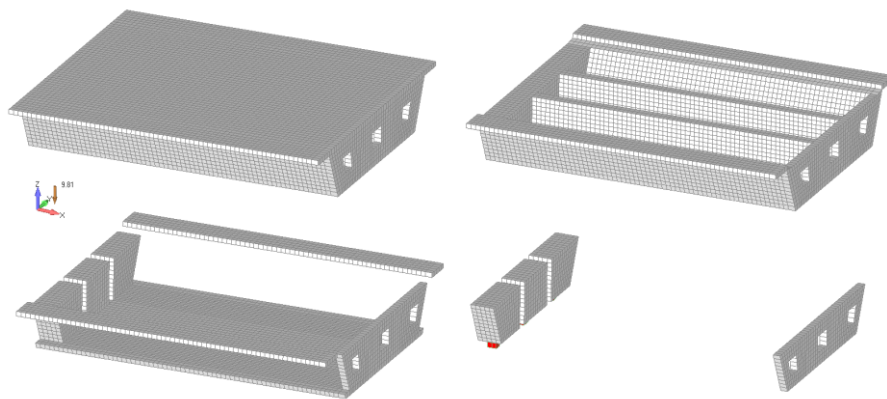


Figure 27. RC Bridge. Hexahedral mesh of the 1st Deck Opening O1. Graphical activation and deactivation of Layers.

The proposed logic behind the topological sorting of the Layers (Fig. 26) is based on the assumption that the hexahedral mesh of the bridge will be divided into four main groups of Layers (a. Deck Span, b. Bearing Supports, c. Support Diaphragms and d. Pylons/foundation), while in each main group of Layers the mesh of all structural members (Upper Deck, Vertical

Walls, etc.), which belong to a specific opening of the bridge, will be assigned into the designated Layer. The graphical illustration of the 56 Layers used in order to manage the hexahedral elements' mesh is shown in Fig. 26 and the use of Layers is demonstrated in Fig. 27 for the case of the deck opening O1.

The distribution of the hexahedral elements, according to the assumed Layers for the management of the hexahedral elements' mesh, are given in Table 5. It is evident that the largest number of hexahedral elements is located at the deck of the RC bridge. After the completion of the mesh convergence investigation, the resulted FE mesh consisted of 102,934 from which 102,622 are concrete hexahedral elements. The "Analysis by Parts" method was also implemented in order to verify that each part of the under construction hexahedral FE mesh (Fig. 28) was consistent, thus avoiding inducing numerical instabilities during the embedded mesh generation procedure and the analysis procedure of the complete model.

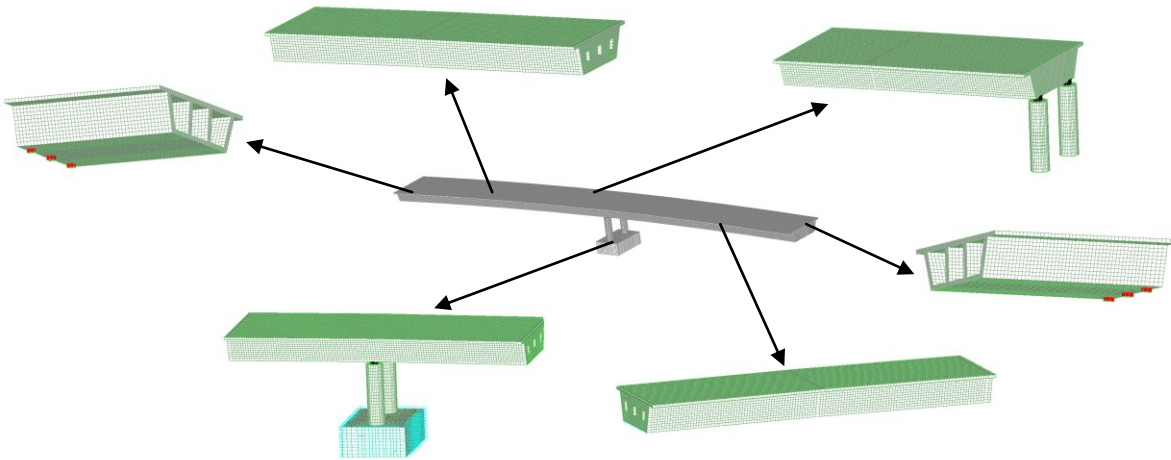


Figure 28. RC Bridge. Models used for the mesh convergence analysis procedure ("Convergence Analysis by Parts").

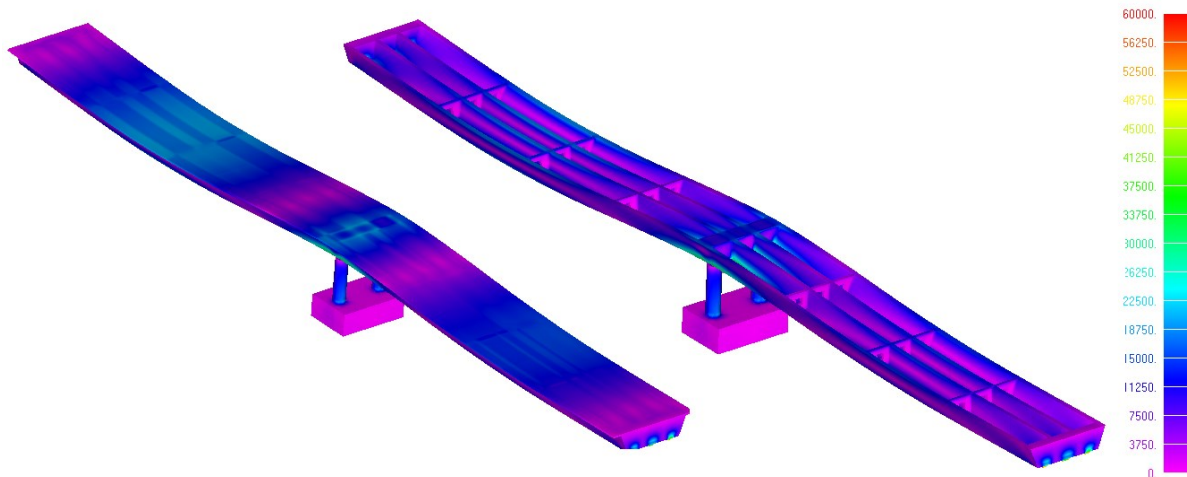


Figure 29. RC Bridge. Deformed shape and von Mises Stress contour. (Left) View of the full model and (Right) Internal view of the vertical and diaphragmatic walls.

The hexahedral mesh construction was finalized by performing the analysis of the complete hexa8 FE mesh by applying the self-weight of the structure. The deformed shape and the von Mises Stress distribution as they derived from the analysis are shown in Fig. 29. It must be noted here that the total number of unknowns for the case of the final hexahedral FE mesh was 502,478, the total number of the stiffness matrix elements was 657,655,263 and the re-

quired physical memory for solving the numerical model without the embedded reinforcement was 7.6 Gb.

3.2.3. Constructing, Managing and Verifying the Embedded Reinforcement FE Mesh

Given the fact that the required computational time for the analysis of this model will be significant, any mesh irregularities will induce numerical instabilities forcing the nonlinear analysis to terminate, while the size of the mesh will make it time-consuming if any mesh modification issues arise. For this reason the same mesh managing approach illustrated in the previous section was adopted in order to control the resulted embedded rebar mesh in a step-by-step logic (Layers and Analysis by Parts).

As it is shown in Fig. 30, the embedded rebar mesh was divided into 48 Layers according to the RC bridge's geometry. The 48 Layers were divided into 3 main groups so as to optimize the viewing procedure and the allocation of each reinforcement arrangement according to its positioning inside the structure. Furthermore, after the completion of the construction of the embedded rebar macro-element mesh for each structural member (see Table 6) of the bridge, a convergence analysis was performed so as to assess the derived FE model for each structural part of the bridge's model.

The embedded rebar mesh construction began by constructing and testing the Pylon/Pile Cap mesh (Fig. 31). The geometry of the hexahedral mesh of these structural members is irregular and mainly non-prismatic due to the circular sections of the pylons, while the embedded rebar mesh construction of the embedded rebar macro-elements was performed by using long macro-elements that intersect more than 15 hexahedral elements. In some areas of the Pile Cap mesh, rebar macro-elements penetrate up to 20 hexahedral elements.

a/a	Structural Member	c		Macro-Elements	Embedded Rebar FEs
1	Span O1 Deck + Left Support Diaphragm (Fig. 41)	15		6,721	70,614
2	Span O2 Deck (Fig. 42)	15		5,092	61,476
3	Span O3 Deck (Fig. 43)	15		5,100	62,954
4	Span O4 Deck (Fig. 44)	15		4,046	50,401
5	Middle Diaphragm (Fig. 45)	30		1,656	25,172
6	Span O5 Deck (Fig. 46)	15		4,601	52,673
7	Span O6 Deck (Fig. 47)	15		4,805	56,416
8	Span O7 Deck (Fig. 48)	15		4,818	55,693
9	Span O8 Deck + Right Support Diaphragm (Fig. 49)	15		5,546	63,504
10	Two Pylons and Pile Cap (Figs. 38 & 39)	5	15	5,454	21,721
Total				47,839	520,624

Table 6. RC Bridge. Embedded rebar macro-elements and resulted embedded rebar FEs that derived from the procedure of the convergence analysis by parts.

After the completion of the embedded rebar macro-element mesh of the Pylons and the Pile Cap, the model was analyzed in order to assess the resulted FE mesh. During the embedded mesh generation procedure, for the case of the Pile Cap, the incremental parameter c was set equal to 15 and for the case of the Pylons, equal to 5. The total number of the embedded rebar elements that were generated was 21,721.

Fig. 32 shows the deformed shape of the embedded rebar mesh as it derived from the analysis of the model. As it can be seen, the mesh generation procedure managed to allocate the embedded rebar elements without any numerical instabilities, while the irregular geometry of

the hexahedral elements did not result any numerical issues during the mesh generation procedure. The deformed shape and stress contour shown in Fig. 32 resulted by applying the self-weight of the structure and a distributed load of 1 kN/node at the tip of each Pylon.

Table 6 shows the distribution of the total number of the embedded rebar macro-elements used to construct the reinforcement grid of the RC bridge. As it can be depicted, the total number of embedded rebar macro-elements used was 47,839 and the total number of embedded rebars that were generated through the Analysis by Parts procedure was 520,624. It must be noted here that the parameter c was set between 5-30 (Table 6) given that the macro-elements were constructed so as to penetrate between 1-30 hexahedral elements.

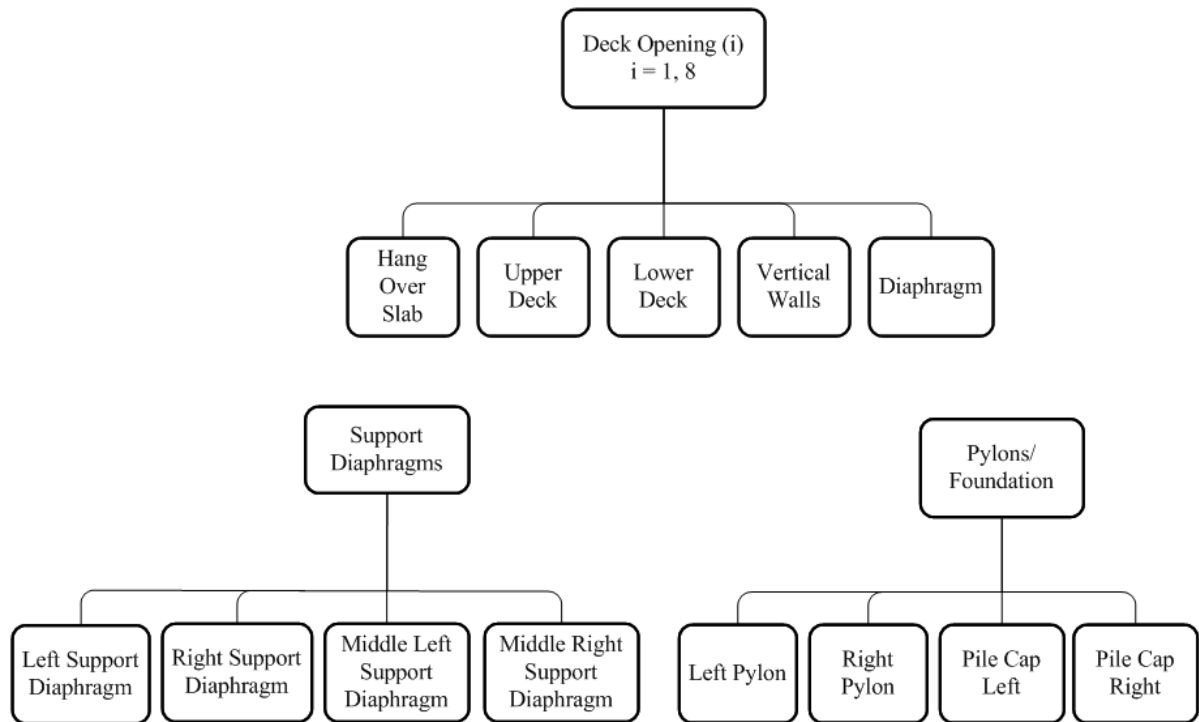


Figure 30. RC Bridge. Embedded rebar mesh Layer organization chart.

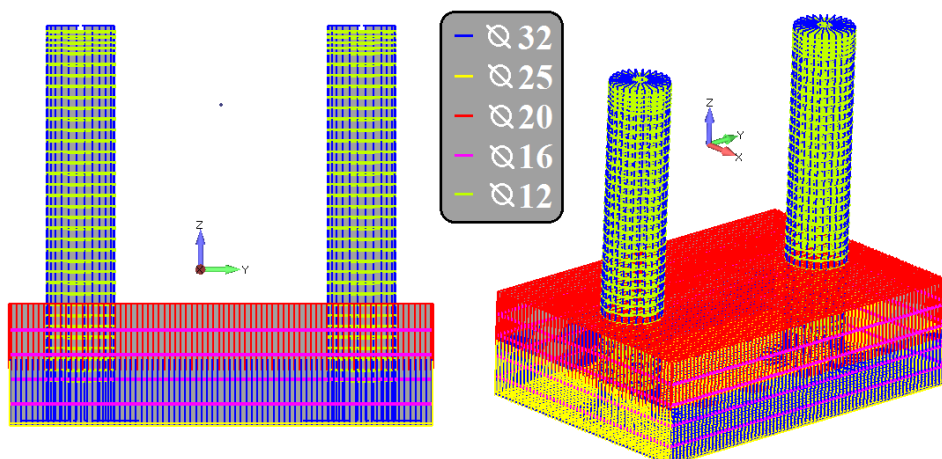


Figure 31. RC Bridge. Embedded rebar mesh of the Pylons and Pile Cap (5,454 embedded rebar macro-elements).

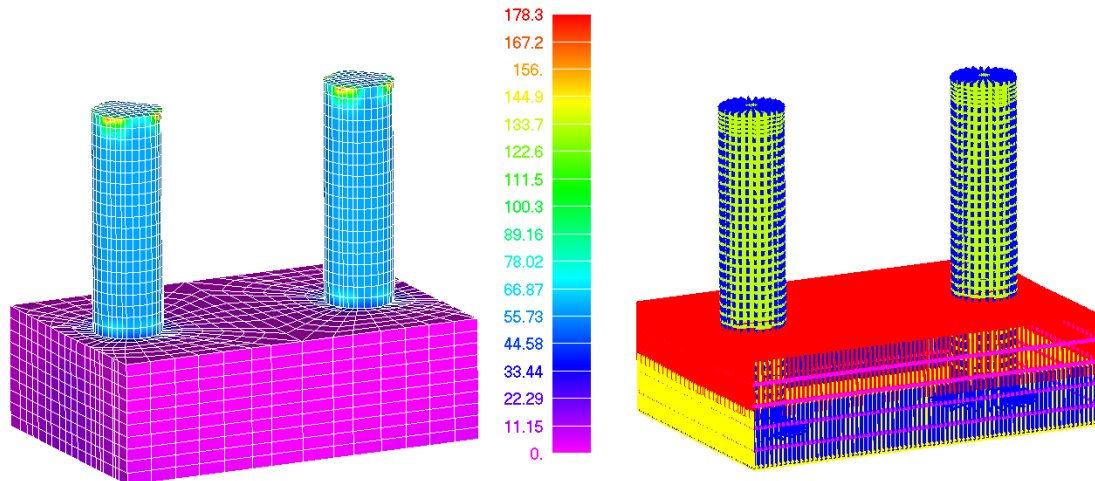


Figure 32. RC Bridge. (Left) von Mises Stress contour and (Right) Deformed shape of the embedded rebar elements of the two Pylons and the Pile Cap (21,721 embedded rebar elements generated).

3.2.4. Solution of the Complete Model

At this stage the complete model (Fig. 33) can be used so as to allocate and generate the final embedded rebar mesh through the use of the integrated embedded mesh generation method. Table 7 shows the details of the resulted FE mesh, the total required time for generating the embedded rebar elements and numerical details related to the solution of the FE model.

a/a	Description	Value
1	Number of Hexahedral Elements	102,934
2	Number of Nodes (hexa8 only)	168,400
3	Number of Macro-Elements	47,839
4	Total Number of Embedded Rebar FEs Generated	520,624
5	Total Number of Short Embedded Rebar FEs that were Discarded by the Filter Algorithm	1,439
6	Required Embedded Mesh Generation Time	42 m 22 s
7	Required RAM for the Embedded Mesh Generation	2 Gb
8	Required RAM for the Stiffness Matrix	5.225 Gb
9	Max Required RAM Allocated by the Software	11.5 Gb
10	Computational Time for Solving 1 Load Increment	18 m
11	Computational Time for Writing the Output Data	53 m
12	Total Computational Time: i. Read/Initialize Problem ii. Generate Embedded Mesh iii. Solve the System of Equations for 1 Load Increment / 1 Internal Iteration iv. Write Output Data (out.txt file size: 475 Mb)	118 m

Table 7. RC Bridge. General numerical details that derived after the solution of the complete FE model.

As it can be seen from Table 7, the total required time for the embedded mesh generation procedure was 42 minutes 22 seconds and the corresponding required RAM allocated for this task was 2 Gb. The total number of generated embedded rebar FEs was 520,624 while the total number of short embedded rebar FEs that were discarded due to their small length was 1,439. The deformed shape of the embedded rebar mesh (Fig. 34), resulted by applying only

the self-weight of the structure. The solution of the complete model required a total of 11.5 Gb of RAM from which the 5.225 Gb was required for the stiffness matrix allocation. So as to solve the model for a single load increment, ReConAn required 18 minutes, while the total computational time for reading, initializing, generating the embedded mesh, solving the system of equations (for 1 load step and 1 internal iteration) and writing the output data, was 118 minutes. The required embedded mesh generation time represents 36% of the total operation time. This ratio is relatively small given that the numerical problem foresees the solution of 1 load increment and 1 internal iteration. In addition to that, the numerical results illustrate the significance of having a computationally robust and efficient embedded mesh generation procedure.

As it can be seen in Fig. 34, the deformed shape of the embedded rebar mesh was graphically illustrated by increasing the derived displacements 500 times. The deformed shape shows that the embedded rebar mesh follows the sinusoidal deformed shape of the bridge's deck as it resulted from the numerical solution procedure.

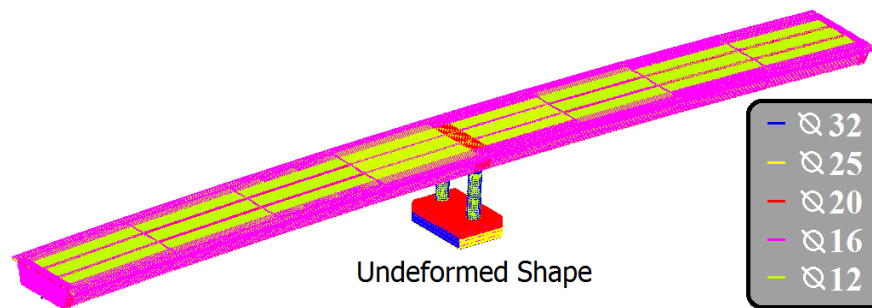


Figure 33. RC Bridge. Macro-element rebar mesh.

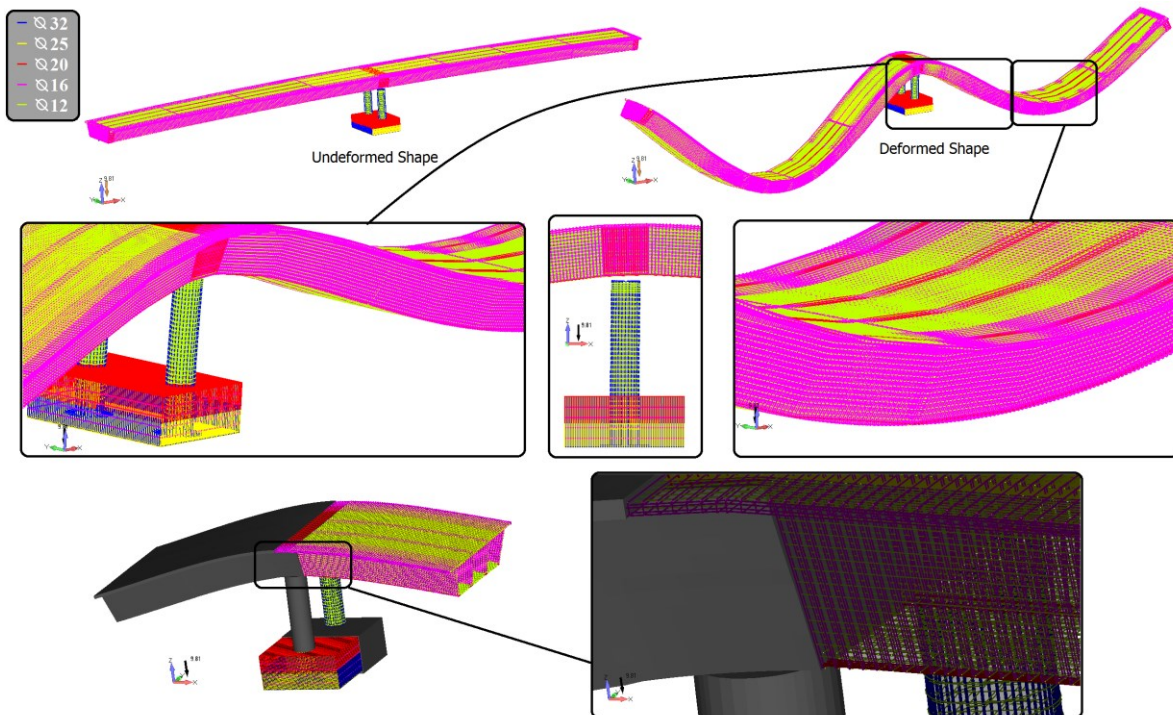


Figure 34. RC Bridge. Deformed shape of the embedded rebar FE mesh.

After applying a vertical nonlinear load of 135,125MN, which was distributed uniformly along the area of the deck, the numerical problem was solved and the resulted crack pattern

for 60% of the total applied load is shown in Fig. 35. The solution procedure failed to converge when 90% of the total nonlinear load was applied. For solving the 8 load increments the solver required 24 hours and to write the output data 8 hours. This means that the required embedded rebar mesh generation procedure requires less than 3% of the total computational time illustrating the numerical efficiency of the embedded rebar mesh generation method.

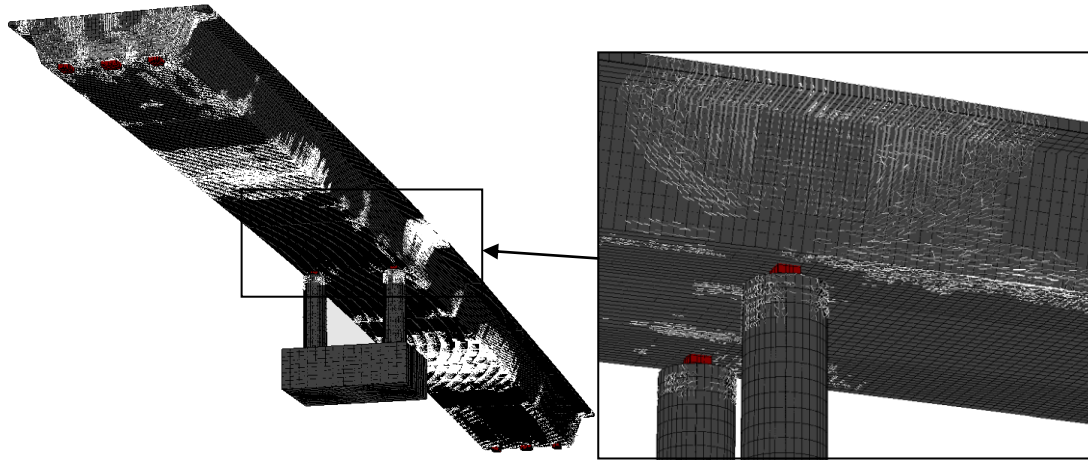


Figure 35. RC Bridge. Crack pattern for 60% of the total applied load.

3.2.5. Double Deck Model

In an attempt to increase the previous FE mesh so as to further investigate the numerical performance of the under study mesh generation method, the numerical model that was presented in Fig. 33 is increased by replicating the bridge one time. Fig. 36 shows the new mesh, while in Table 8 the numerical details related to the mesh can be depicted.

Table 8 shows the numerical details that derived after the solution of the increased mesh, where it can be seen that the total number of embedded rebar elements that were generated was 1,052,892. If the number of generated embedded rebar elements is compared with the one that resulted from the previous section, then it will result that an additional 11,644 embedded rebar elements were generated. This is attributed to the connection beam that connects the two pile caps as shown in Fig. 36. The embedded mesh generation procedure managed to complete the embedded rebar allocation/generation procedure in 304 minutes and 5 seconds.

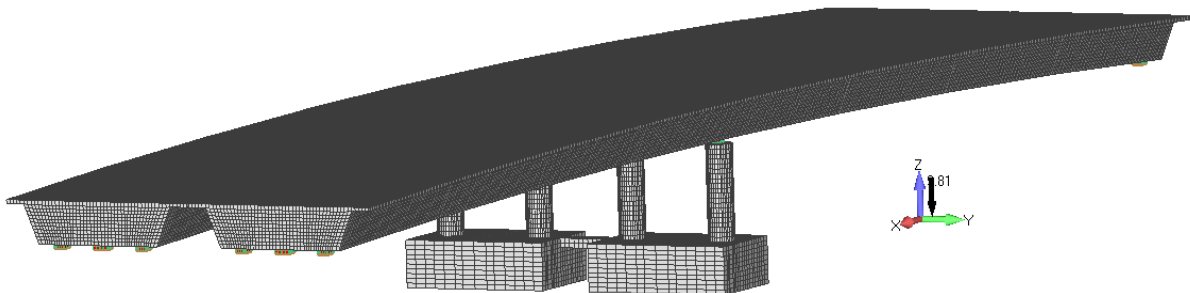


Figure 36. Double Deck RC Bridge. FE mesh of 8-noded hexahedral elements.

The required computational time for the embedded rebar mesh generation procedure represents the 10.48% of the total computational time. An important observation that derives by comparing the new ratio with that resulted in the previous section (36%), is that the computational performance of the under study method maintained its efficiency in relation to the solution algorithm that required an excessive time so as to solve a single load increment. This also

underlines the need of using a parallel solver that will significantly reduce the computational time for solving the system of equations.

Fig. 37 shows the deformed shape of the model as it resulted from the numerical analysis. As it can be seen, the embedded rebar elements have the same deformed shape thus follow the deformation of the concrete domain.

a/a	Description	Value
1	Number of Hexahedral Elements	205,928
2	Number of Nodes (hexa8 only)	336,908
3	Number of Macro-Elements	95,082
4	Total Number of Embedded Rebar FEs Generated	1,052,892
5	Total Number of Short Embedded Rebar FEs that were Discarded by the Filter Algorithm	2,878
6	Required Embedded Mesh Generation Time	304 m 5 s
7	Required RAM for the Stiffness Matrix	19.52 Gb
8	Max Required RAM Allocated by the Software	30.0 Gb
9	Computational Time for Solving 1 Load Increment	27 hr
10	Computational Time for Writing the Output Data	10 hr 32 min
11	Total Computational Time: i. Read/Initialize Problem ii. Generate Embedded Mesh iii. Solve the System of Equations for 1 Load Increment / 1 Internal Iteration iv. Write Output Data (out.txt file size: 970 Mb)	48 hr 29 min

Table 8. Double Deck RC Bridge. General numerical details that derived after the solution of the complete FE model.

4 CONCLUSIONS

The integrated embedded mesh generation method, which is an extension of the Markou and Papadrakakis method [8], was used to generate the embedded rebar mesh of a RC building and a RC bridge. The parametric investigation performed for the required computational time in generating the embedded rebar elements, in a 64-bit operating system, verifies the computational robustness and efficiency of the method in generating embedded rebar finite elements inside regular and irregular hexahedral meshes.

For the case of the RC building, the FE mesh that was used consisted of 75,080 hexahedral elements and 130,259 embedded rebar macro-elements. After performing the analysis for this numerical implementation it derived that the embedded rebar mesh generation method managed to allocate 537,719 embedded rebar elements from which 5,804 had a length shorter than 5 mm and were excluded from the analysis procedure. The mesh generation procedure required 75 minutes.

In order to further investigate the performance of the integrated embedded rebar mesh generation method, a full-scale model of a RC bridge was constructed and analyzed. The construction of the model eventually derived a total number of 102,934 hexahedral elements and 47,839 embedded rebar macro-elements. After mesh generation procedure, the derived RC bridge numerical model consisted of 623,576 finite elements from which 102,622 are hexahedral concrete FEs that treat the cracking phenomenon with the smeared crack approach. Solving a FE model that incorporated a numerically unstable material formulation with numerical

discontinuities is by default a cumbersome procedure even for benchmark problems that assume a limited number of hexahedral elements (100-1000 hexahedral elements). Dealing with a large-scale numerical simulation, controlling the resulted FE mesh from the embedded rebar mesh generation level is of significant importance given that it controls the numerical outcome of the embedded mesh generation and solution procedures. The mesh generation procedure required 42 minutes 22 seconds, which illustrates the computational efficiency of the method, while the limitations of the embedded mesh generation algorithm were not practically reached.

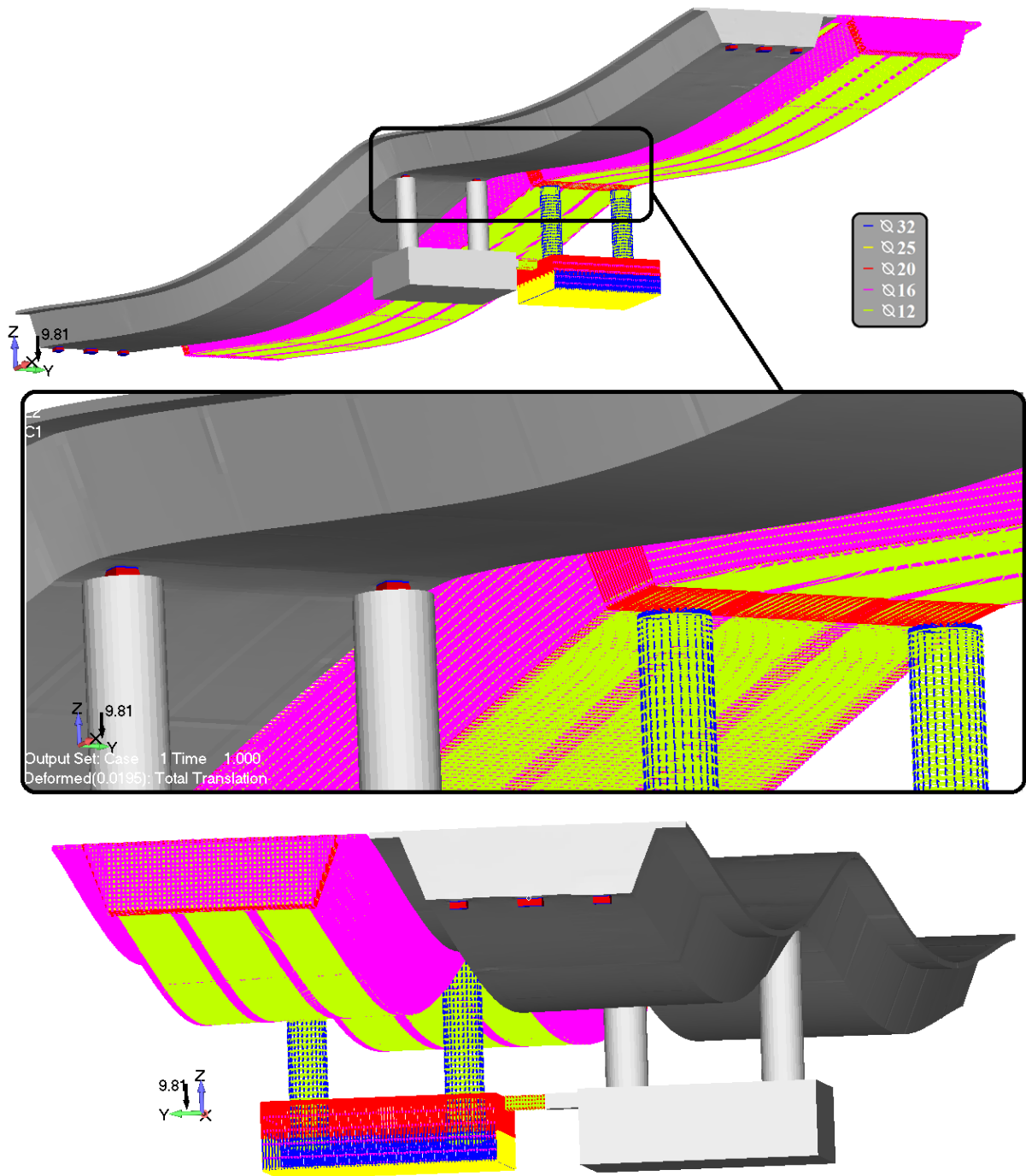


Figure 37. Double Deck RC Bridge. Deformed shape of the hexahedral and embedded rebar FE meshes.

In order to further investigate the computational performance of the under study method, the mesh of the RC Bridge was increased by 2. After the numerical analysis of the increased FE model, which consisted of 205,928 hexahedral concrete FEs and 95,082 embedded rebar macro-elements, the algorithm managed to generate 1,055,770 embedded rebar elements from which 2,878 had a length shorter than 5 mm and were excluded from the analysis procedure. The required computational time for the generation of the embedded rebar elements was 304 minutes and 5 seconds. The numerical investigation demonstrates the numerical efficiency of the under study numerical method.

Finally, it is important to state that modeling RC structures through the use of 3D detailed modeling that discretize the reinforcement grid with embedded rebar elements, has a drawback that relates to the construction of the embedded rebar macro-element mesh, especially in cases where the geometry of the structure has an irregular geometry. This procedure requires a significant effort which makes it prohibitive to be used for commercial purposes. So as to address this issue, an automatic mesh generation algorithm is required to be developed for generating the embedded rebar macro-element mesh inside the hexahedral elements in order to optimize (in terms of time) the embedded rebar macro-element mesh construction procedure.

5 ACKNOWLEDGEMENTS

The author would like to acknowledge the financial support from the Alhosn University of Abu Dhabi and the Vice Chancellor Prof. Abdul Rahim Sabouni for his support throughout this research work.

REFERENCES

- [1] L. Jendele and J. Cervenka, On the solution of multi-point constraints – Application to FE analysis of reinforced concrete structures, *Computers and Structures*, **87**, 970–980, 2009.
- [2] M.D. Kotsovos and M.N. Pavlovic, *Structural concrete. Finite Element Analysis for Limit State Design*, Thomas Telford: London, 1995.
- [3] K.V. Spiliopoulos and G. Lykidis, An efficient three-dimensional solid finite element dynamic analysis of reinforced concrete structures, *Earthquake Engng Struct. Dyn.*, **35**, 137–157, 2006.
- [4] H. Hartl, Development of a continuum mechanics based tool for 3d FEA of RC Structures and application to problems of soil-structure interaction, Ph.D. Thesis, Faculty of Civil Engineering, Graz Univ. of Technology, 2000.
- [5] G. Markou, Detailed Three-Dimensional Nonlinear Hybrid Simulation for the Analysis of Full-Scale Reinforced Concrete Structures, Ph.D. Thesis, Institute of Structural Analysis and Seismic Research, National Technical University of Athens, 2011.
- [6] V. Cervenka, *Large Deflections*, Cervenka Consulting, 2010.
- [7] V.T. Hristovski and H. Noguchi, Finite Element Modeling of RC Members Subjected to Shear, *Third DIANA World Conference, Tokyo, Japan 9-11 October 2002*.
- [8] G. Markou and M. Papadrakakis, An efficient generation method of embedded reinforcement in hexahedral elements for reinforced concrete simulations, *Advances in Engineering Software ADES*, **45**(1), 175-187, 2012.

- [9] F. Barzegar and S. Maddipudi, Generating reinforcement in FE modeling of concrete structures, *Journal of Structural Engineering*, **120**, 1656 –1662, 1994.
- [10] A.E. Elwi and T.M. Hrudey, Finite element model for curved embedded reinforcement, *Journal of Engineering Mechanics*, **115**, 740 –754, 1989.
- [11] ASCE Task Committee on Concrete and Masonry Structures, *Finite element analysis of reinforced concrete*, ASCE, 1982.
- [12] M.A.H. Abdel-Halim and T.M. Abu-Lebdeh, Analytical study of concrete confinement in tied columns, *Journal of Structural Engineering*, *ASCE*, **115**(11), 2810-2828, 1989.
- [13] F. Gonzalez Vidoso, M.D. Kotsovos and M.N. Pavlovic, Three-dimensional finite element analysis of structural concrete, *Proc., Second Int. Conf. on Computer Aided Anal. and Des. of Concrete Struct.*, N. Bicanic, and H. Mang, eds., Vol. II, Pineridge Press, Swansea, Wales, 1029-1040, 1990.
- [14] G. Markou, Embedded reinforcement mesh generation method for large-scale RC simulations: Case study, *AHU Journal of Engineering & Applied Sciences*, **5**(1), 23-42, 2012.
- [15] Siemens P.L.M. Software, *World-class finite element analysis (FEA) solution for the Windows desktop*, Siemens Product Lifecycle Management Software Inc, 2009.

NEURAL NETWORK APPROXIMATION OF THE MASONRY FAILURE UNDER BIAxIAL COMPRESSIVE STRESS

Panagiotis G. Asteris¹, Vagelis Plevris²

¹Department of Civil & Construction Engineering Educators
School of Pedagogical & Technological Education
Heraklion, GR 141 21, Athens, Greece

²Department of Civil & Structural Engineering Educators
School of Pedagogical & Technological Education
Heraklion, GR 141 21, Athens, Greece

e-mail: asteris@aspete.gr, vplevris@gmail.com

Keywords: Masonry, anisotropy, failure criterion, failure surface, biaxial stress, Neural Network, NN, approximation.

Abstract. *Masonry is a material that exhibits distinct directional properties because the mortar joints act as planes of weakness. To define failure under biaxial stress, a three-dimensional surface in terms of the two normal stresses and shear stress, or the two principal stresses and their orientation to the bed joints, is required.*

Researchers have long been aware of the significance of the bed joint angle to the applied load and many experimental tests have been carried out on brick masonry discs to produce indirect tensile stresses on joints inclined at various angles to the vertical compressive load. The highest strength of the masonry has been observed for the cases when the compressive load was perpendicular to the bed joints or when the principal tensile stress at the center of the disc was parallel to the bed joints. In this case failure occurred through bricks and perpendicular joints. The lowest strength has been observed when the compressive load was parallel to the bed joints or when the principal tensile stress at the center of the disc was perpendicular to the bed joints. In this case failure occurred along the interface of brick and mortar joint.

In the present study, the preliminary results of an ongoing research on the failure of brittle anisotropic materials are presented. In particular, Neural Networks (NNs) are used in order to approximate the experimental failure curves of a brittle anisotropic material such as masonry, that has been investigated in depth by Page [1]. For each angle θ (0° , 22.5° , 45°), a Neural Network is trained with the experimental data of Page as inputs. Then the NN is asked to produce the whole failure curve for each angle as its output, filling also the gaps between the experimental points with appropriate approximations. The results show the great potential of using NN for the approximation of the masonry failure under biaxial compressive stress.

1 INTRODUCTION

Despite the fact that masonry is one of the oldest structural materials and, actually, the main element in monumental structures such as churches, castles, mosques etc., our knowledge regarding its mechanical behavior is not as thorough as it should be and many aspects of its behavior remain to be investigated. One reason for this lack of extensive studies is the highly anisotropic brittle nature of masonry, which makes complicated, difficult and expensive, the realization of reliable experimental tests under conditions of biaxial stress, and, even more, under conditions of biaxial tension or heterosemous stress. Taking into account the numerous uncertainties of the problem, a computational model, describing the masonry failure surface in a simple manner should be an efficient tool for the investigation of the behavior of masonry structures. Many analytical criteria for masonry structures have been already proposed [2-7]. Experimental investigations can also be considered as an important support to the aforementioned efforts [1, 8, 9, 10].

In the present study, we use the experimental data reported by Page [1], referring to a total of 102 panels, that have been already used by many other researchers [2, 3, 11]. Ratios of vertical compressive stress σ_1 to horizontal compressive stress σ_2 of ∞ (uniaxial σ_1), 10, 4, 2 and 1 have been used in conjunction with a bed joint angle θ with respect to the σ_1 , in directions of 0° , 22.5° , 45° , 67.5° and 90° . A minimum of four tests were performed for each combination of σ_1, σ_2 and θ . The aim of the present paper is to introduce an anisotropic (orthotropic) Neural Network – generated failure surface under biaxial stress for masonry.

2 LITERATURE REVIEW

Masonry exhibits distinct directional properties due to the influence of the mortar joints. Depending upon the orientation of the joints to the stress directions, failure can occur in the joints alone or simultaneously in the joints and the blocks. The failure of masonry under uniaxial and biaxial stress state has been studied experimentally in the past by many researchers but to the authors' knowledge there has not been any attempt to apply a Neural Network for such a prediction.

Only a few studies incorporate the use of Neural Networks (NNs) for the approximation of masonry behavior in general. Zhang et al. in [12] apply artificial intelligent techniques for directly predicting the cracking patterns of masonry wallets, subjected to vertical loading. The von Neumann neighborhood model and the Moore neighborhood model of cellular automata (CA) are used to establish the CA numerical model for masonry wallets. Techniques for the analysis of wallets whose bed courses have different angles with the horizontal bottom edges are also introduced. Two criteria are used to match zone similarity between a “base wallet” and any new “unseen” wallets. This zone similarity information is used to predict the cracks in unseen wallets. A back-propagation neural network is also used for predicting the cracking pattern of a wallet based on the CA model of the wallet and some data of recorded cracking at zones.

El-Shafie et al. [13] propose a model based on radial basis function neural networks (RBFNN) for predicting creep in concrete and masonry structures and is compared to a multi-layer perceptron neural network (MLPNN). Accurate prediction of creep is achieved due to the simple architecture and fast training procedure of RBFNN model especially when compared to MLPNN model. The RBFNN model shows good agreement with experimental creep data from brickwork assemblages.

Zhou et al. [14] propose an artificial intelligent technique for predicting the failure/cracking loads of laterally loaded masonry wall panels based on their corresponding failure/cracking patterns derived from the laboratory experiments. The numerical modes of

failure/cracking patterns of experimental wall panels and the corresponding normalized failure/cracking loads are used as the input and output for the NN training. Three types of NN models for predicting the failure/cracking load of the unseen wall panel are achieved by repeatedly training and adjusting to optimize its parameters.

Mathew et al. [15] propose the use of NN for solving complex nonlinear problems for the analysis of masonry panels under biaxial bending. A Neural Network, trained with the use of a set of data, which is representative of the problem domain, is shown to be successful in solving new problems with reasonable accuracy. The experimental results obtained from the testing of panels are analyzed, and the method that gives good correlation between the theoretical prediction and the experimental result is recommended for other panels of similar properties and boundary conditions. An artificial intelligence based technology, the case-based reasoning (CBR), has been used to solve new problems by adapting solutions to similar problems solved in the past, which are stored in the case library. A hybrid system is described that utilizes the capabilities of both ANNs and CBR.

3 EXPERIMENTAL DATA

The experimental data of Page [1] have been used as inputs for the NN model in the present study. The figures below show the original data together with the mean curves for each bed joint angle that attempt to fit these data.

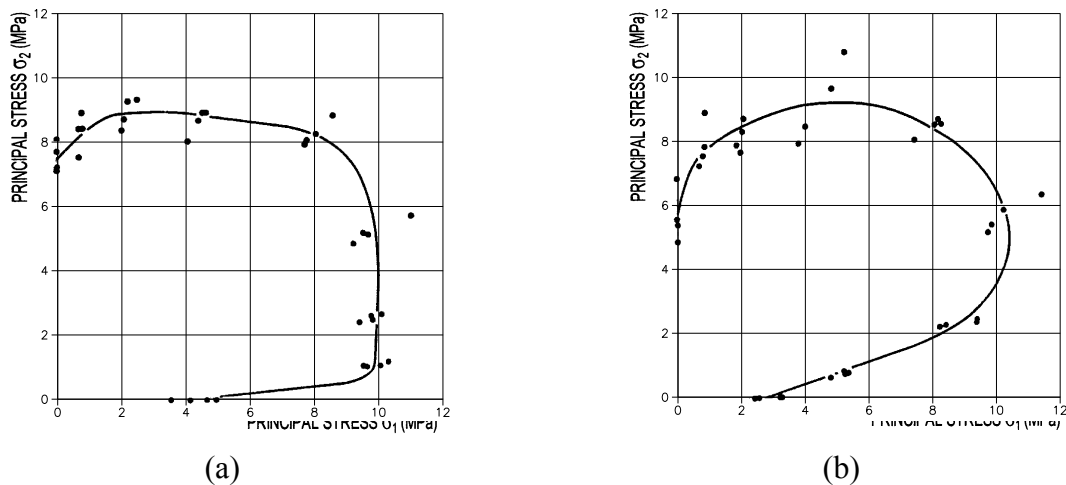


Figure 1: Failure of Brickwork under Biaxial Compression, (a) $\theta=0^\circ$, (b) $\theta=22.5^\circ$ [1].

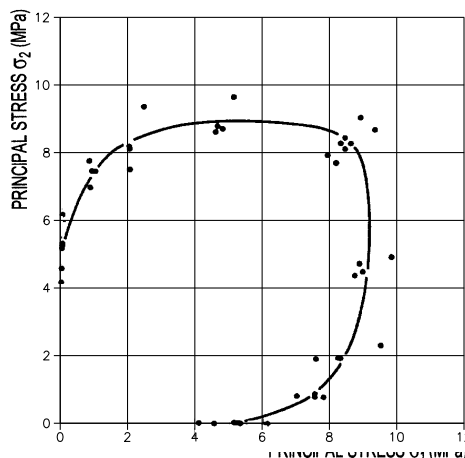


Figure 2: Failure of Brickwork under Biaxial Compression, $\theta=45^\circ$ [1].

It should be noted that the data for $\theta=45^\circ$ are symmetric to the 45° line ($\sigma_1=\sigma_2$), due to the nature of the loading, while the cases $\theta=67.5^\circ$ and $\theta=90^\circ$ are equivalent to the cases $\theta=22.5^\circ$ and $\theta=0^\circ$, respectively and will not be examined separately. The table below shows the analytical data for the $\theta=0^\circ$ case.

σ_I (MPa)	σ_{II} (MPa)	σ_I/f_{wc}	σ_{II}/f_{wc}	Average σ_I/f_{wc}	Average σ_{II}/f_{wc}	Angle $\varphi = \text{Atan}(\sigma_{II}/\sigma_I)$	Radius r
3.53	0.00	0.47	0.00				
4.14	0.00	0.55	0.00				
4.66	0.00	0.62	0.00				
4.96	0.00	0.66	0.00	0.57	0.00	0.0000	0.5717
9.59	0.85	1.27	0.11				
9.70	0.87	1.28	0.12				
10.11	0.90	1.34	0.12				
10.37	1.01	1.37	0.13	1.32	0.12	0.0909	1.3210
9.46	2.26	1.25	0.30				
9.85	2.43	1.30	0.32				
9.92	2.30	1.31	0.30				
10.15	2.45	1.34	0.32	1.30	0.31	0.2353	1.3398
9.33	4.67	1.23	0.62				
9.62	5.01	1.27	0.66				
9.74	4.95	1.29	0.65				
11.15	5.48	1.48	0.72	1.32	0.66	0.4672	1.4761
7.84	7.76	1.04	1.03				
7.89	7.91	1.04	1.05				
8.20	8.10	1.09	1.07				
8.72	8.67	1.15	1.15	1.08	1.07	0.7820	1.5222
4.16	7.95	0.55	1.05				
4.55	8.57	0.60	1.13				
4.66	8.84	0.62	1.17				
4.74	8.81	0.63	1.17	0.60	1.13	1.0836	1.2792
2.12	8.34	0.28	1.10				
2.21	8.67	0.29	1.15				
2.32	9.21	0.31	1.22				
2.63	9.32	0.35	1.23	0.31	1.18	1.3156	1.2148
0.76	7.55	0.10	1.00				
0.76	8.42	0.10	1.11				
0.87	8.42	0.11	1.11				
0.87	8.93	0.11	1.18	0.11	1.10	1.4737	1.1074
0.00	7.15	0.00	0.95				
0.00	7.27	0.00	0.96				
0.00	7.69	0.00	1.02				
0.00	8.12	0.00	1.07	0.00	1.00	1.5708	1.0000

Table 1. Failure of Brickwork under Biaxial Compression, $\theta=0^\circ$ [1] and relevant calculations.

The first two columns of the table contain the original experimental data, namely the failure principal stresses σ_I and σ_{II} in MPa. For every loading case, four tests have been conducted. The next two columns contain the same data in a dimensionless form where the stresses have been divided with the stress f_{wc} which is the masonry strength for the case $\sigma_I=0$ (last four rows of the table). The value of f_{wc} has been calculated as the average of the four values (high-

lighted in bold in the above table) as 7.56 MPa. The next two columns are the averages of the four tests for each loading case.

For the data to be suitable for the Neural Network training, a conversion to polar coordinates (r, φ) has been taken place, where the radius r is given by

$$r = \sqrt{\sigma_{I,aver}^2 + \sigma_{II,aver}^2} \quad (1)$$

where $\sigma_{I,aver}$ and $\sigma_{II,aver}$ are the average stresses for each loading case (columns 5, 6). The polar angle φ (column 7) is given by

$$\varphi = \text{Arc tan} \left(\frac{\sigma_{II}}{\sigma_I} \right) \quad (2)$$

The polar radius r is given in the last column (column 8) of the above table. For each angle θ case ($\theta=0^\circ, 22.5^\circ, 45^\circ$), a Neural Network is trained with the angle φ as its input and the radius r as its output. The figure below shows the data of the above table, where also the average values (used for the NN training) have been highlighted with red rectangles.

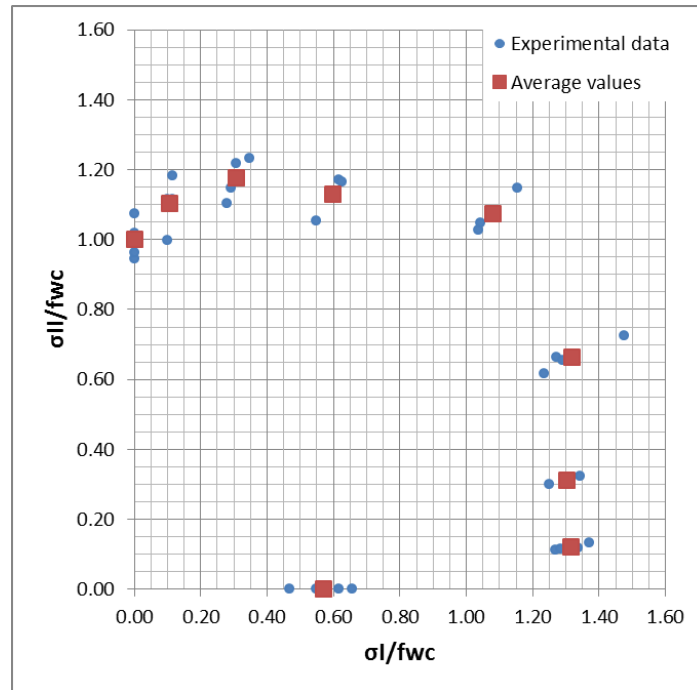


Figure 3: Normalized experimental data and average values for the $\theta=0^\circ$ case.

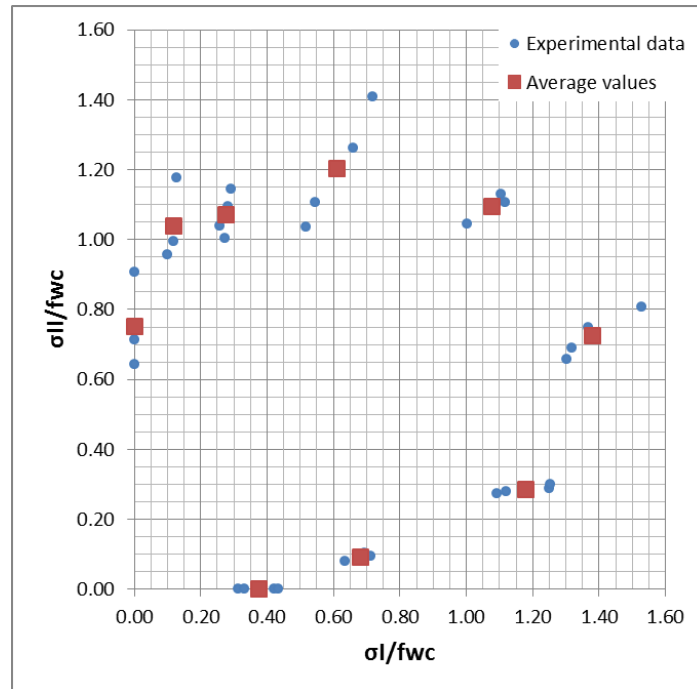
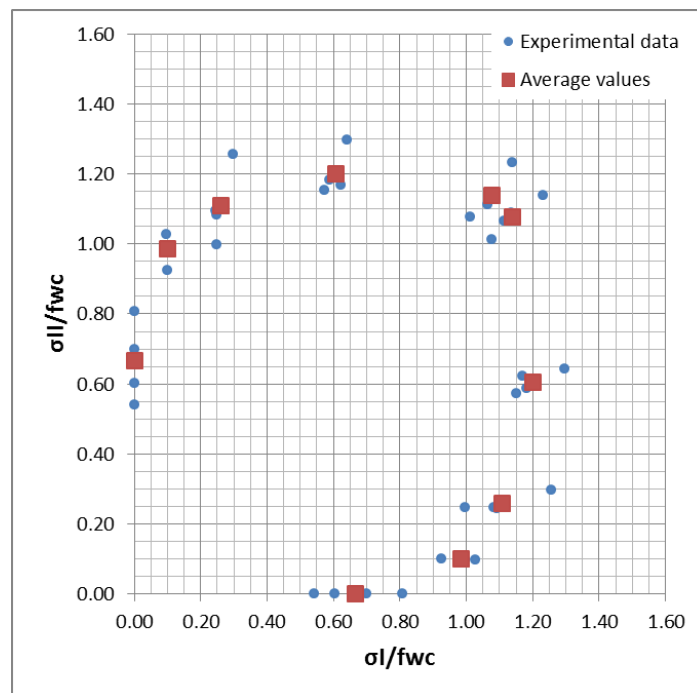
The tables and figures below show the corresponding data for the other two cases ($\theta=22.5^\circ$ and $\theta=45^\circ$).

σ_I (MPa)	σ_{II} (MPa)	σ_I/f_{wc}	σ_{II}/f_{wc}	Average σ_I/f_{wc}	Average σ_{II}/f_{wc}	Angle $\varphi = \text{Atan}(\sigma_{II}/\sigma_I)$	Radius r
2.37	0.00	0.31	0.00				
2.50	0.00	0.33	0.00				
3.19	0.00	0.42	0.00				
3.28	0.00	0.43	0.00	0.38	0.00	0.0000	0.3752
4.79	0.60	0.63	0.08				
5.24	0.78	0.69	0.10				
5.22	0.71	0.69	0.09				
5.38	0.71	0.71	0.09	0.68	0.09	0.1352	0.6890
8.26	2.08	1.09	0.27				
8.47	2.12	1.12	0.28				
9.44	2.18	1.25	0.29				
9.47	2.27	1.25	0.30	1.18	0.29	0.2382	1.2132
9.84	4.96	1.30	0.66				
9.95	5.22	1.32	0.69				
10.33	5.65	1.37	0.75				
11.56	6.10	1.53	0.81	1.38	0.73	0.4843	1.5581
7.57	7.89	1.00	1.04				
8.22	8.31	1.09	1.10				
8.35	8.53	1.10	1.13				
8.46	8.35	1.12	1.10	1.08	1.09	0.7927	1.5359
3.91	7.83	0.52	1.04				
4.12	8.37	0.54	1.11				
4.98	9.54	0.66	1.26				
5.43	10.65	0.72	1.41	0.61	1.20	1.1018	1.3493
2.06	7.59	0.27	1.00				
1.95	7.84	0.26	1.04				
2.15	8.27	0.28	1.09				
2.20	8.65	0.29	1.14	0.28	1.07	1.3178	1.1053
0.76	7.23	0.10	0.96				
0.89	7.53	0.12	1.00				
0.93	7.80	0.12	1.03				
0.98	8.89	0.13	1.18	0.12	1.04	1.4580	1.0467
0.00	4.87	0.00	0.64				
0.00	5.39	0.00	0.71				
0.00	5.59	0.00	0.74				
0.00	6.85	0.00	0.91	0.00	0.75	1.5708	0.7508

Table 2. Failure of Brickwork under Biaxial Compression, $\theta=22.5^\circ$ [1] and relevant calculations.

σ_I (MPa)	σ_{II} (MPa)	σ_I/f_{wc}	σ_{II}/f_{wc}	Average σ_I/f_{wc}	Average σ_{II}/f_{wc}	Angle $\varphi =$ $\text{Atan}(\sigma_{II}/\sigma_I)$	Radius r
4.09	0.00	0.54	0.00				
4.56	0.00	0.60	0.00				
5.14	0.00	0.68	0.00				
5.29	0.00	0.70	0.00				
6.11	0.00	0.81	0.00	0.67	0.00	0.0000	0.6666
6.99	0.77	0.93	0.10				
7.52	0.72	0.99	0.10				
7.52	0.80	0.99	0.11				
7.76	0.74	1.03	0.10	0.99	0.10	0.1012	0.9905
7.54	1.88	1.00	0.25				
8.19	1.88	1.08	0.25				
8.27	1.85	1.09	0.24				
9.50	2.24	1.26	0.30	1.11	0.26	0.2301	1.1379
8.71	4.32	1.15	0.57				
8.83	4.70	1.17	0.62				
8.94	4.45	1.18	0.59				
9.80	4.86	1.30	0.64	1.20	0.61	0.4677	1.3446
8.14	7.64	1.08	1.01				
8.41	8.05	1.11	1.07				
8.59	8.22	1.14	1.09				
9.32	8.61	1.23	1.14	1.14	1.08	0.7565	1.5675
7.64	8.14	1.01	1.08				
8.05	8.41	1.07	1.11				
8.22	8.59	1.09	1.14				
8.61	9.32	1.14	1.23	1.08	1.14	0.8143	1.5675
4.32	8.71	0.57	1.15				
4.70	8.83	0.62	1.17				
4.45	8.94	0.59	1.18				
4.86	9.80	0.64	1.30	0.61	1.20	1.1031	1.3446
1.88	7.54	0.25	1.00				
1.88	8.19	0.25	1.08				
1.85	8.27	0.24	1.09				
2.24	9.50	0.30	1.26	0.26	1.11	1.3407	1.1379
0.77	6.99	0.10	0.93				
0.72	7.52	0.10	0.99				
0.80	7.52	0.11	0.99				
0.74	7.76	0.10	1.03	0.10	0.99	1.4696	0.9905
0.00	4.09	0.00	0.54				
0.00	4.56	0.00	0.60				
0.00	5.14	0.00	0.68				
0.00	5.29	0.00	0.70				
0.00	6.11	0.00	0.81	0.00	0.67	1.5708	0.6666

Table 3. Failure of Brickwork under Biaxial Compression, $\theta=45^\circ$ [1] and relevant calculations.

Figure 4: Normalized experimental data and average values for the $\theta=22.5^\circ$ case.Figure 5: Normalized experimental data and average values for the $\theta=45^\circ$ case.

4 ARTIFICIAL NEURAL NETWORKS

The development of artificial neural networks was initially inspired and motivated by insights into how biological brains – and in particular mammalian brains – function. It was found that mammalian brains learn as connections between neurons are strengthened – the result of electrochemical processes triggered by external or internal stimuli (experiences). As

in biological systems, learning involves adjustments to the synaptic connections that exist between the neurons. NNs, like human beings, learn by example.

Although parallels with biological systems are often described, there is still so little known (even at the lowest cell level) about biological systems, that the models that are being used for artificial neural systems seem to introduce an oversimplification of the 'biological' models. The real, biological nervous system is highly complex and includes some features that may seem superfluous based on an understanding of artificial networks.

In the first work on the processing of neural networks [16], it was shown theoretically that networks of artificial neurons could implement logical, arithmetic, and symbolic functions. Simplified models of biological neurons were set up, now usually called perceptrons or artificial neurons. These simple models accounted for neural summation, i.e. potentials at the post-synaptic membrane would sum in the cell body. Later models also provided for excitatory and inhibitory synaptic transmission.

Artificial Neural Networks are made up of fully or partially interconnecting artificial neurons (programming constructs that mimic the properties of biological neurons). Artificial neural networks may either be used to gain an understanding of biological neural networks, or for solving artificial intelligence problems without necessarily creating a model of a real biological system. *Artificial Intelligence* (AI) and *cognitive modeling* try to simulate some properties of neural networks. While similar in their techniques, AI has the aim of solving particular tasks, while cognitive modeling aims to build mathematical models of biological neural systems. In the AI field, artificial neural networks have been trained to perform complex functions in various scientific fields and have been applied successfully to identification, classification, simulation, inverse simulation, speech recognition, pattern recognition, image analysis and adaptive control, and also in order to construct software agents (in computer games) or autonomous robots.

5 NEURAL NETWORKS ARCHITECTURE

In the present study, we use a *Back-Propagation Neural Network* (BPNN). Here, the output values are compared with the correct answer to compute the value of a predefined error-function. By various techniques, the error is then fed back through the network. Using this information, the algorithm adjusts the weights of each connection in order to reduce the value of the error function by some small amount. After repeating this process for a sufficiently large number of training cycles, the network will usually converge to some state where the error of the calculations is small. In this case, one would say that the network has *learned* a certain target function. As the algorithm's name implies, the errors propagate backwards from the output nodes to the inner nodes. So technically speaking, back-propagation is used to calculate the gradient of the error of the network with respect to the network's modifiable weights. To adjust weights properly, one applies a general method for non-linear optimization that is called gradient descent. In order to minimize the error, the derivative of the error function with respect to the network weights is calculated, and the weights are then changed such that the error decreases (thus going downhill on the surface of the error function). For this reason, back-propagation can only be applied on networks with differentiable activation functions. Back-propagation usually allows quick convergence on satisfactory local minima for error in the kind of networks to which it is suited.

A BPNN is a feed-forward, multilayer network of standard structure, i.e. neurons are not connected in the layer but they join the layer neuron with all the neurons of previous and subsequent layers, respectively. A BPNN has a standard structure that can be written in short as

$$N - H_1 - H_2 - \dots - H_{NL-1} - M \quad (3)$$

where N is the number of inputs, H_l is the number of neurons in the l -th hidden layer, NL is the number of layers (including the output layer) and M is the number of output neurons. Figure 6 depicts an example of a BPNN composed of an input layer with 4 neurons, two hidden layers with 3 neurons each and an output layer with 2 neurons, i.e. a 4-3-3-2 BPNN.

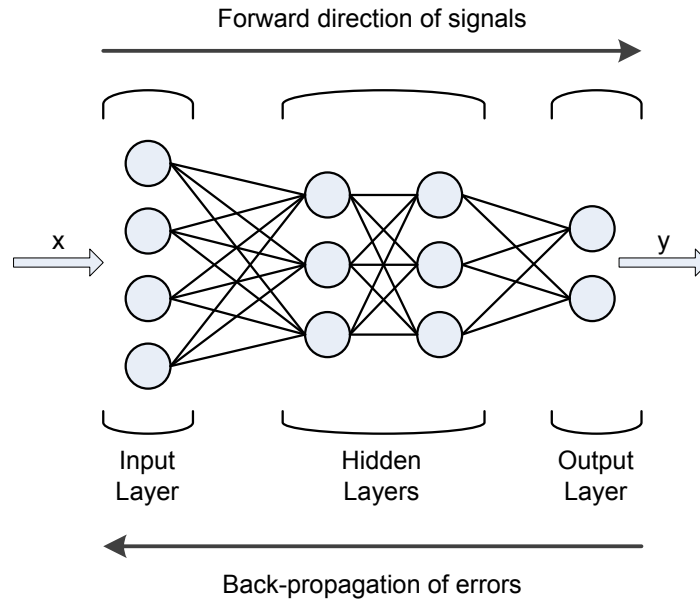


Figure 6: A three-layer 4-3-3-2 BPNN (input not counted as a layer).

In the present study, we use a Back-Propagation Neural Network with two hidden layers, one input layer and one output layer. The input layer has one node (neuron) which corresponds to the angle φ , while the output layer has also one node which corresponds to the radius r . The two hidden layers have 8 nodes each, ending in a 1-8-8-1 BPNN architecture, for the first two cases ($\theta=0^\circ$ and $\theta=22.5^\circ$). For the third case ($\theta=45^\circ$) the two hidden layers have 12 nodes each, ending in a 1-12-12-1 BPNN architecture. The input and output values are normalized before the NN training and the inverse normalization is done in order to take the NN results for other data afterwards.

A single node (neuron) of a hidden layer, with a single R -element input vector is shown below.

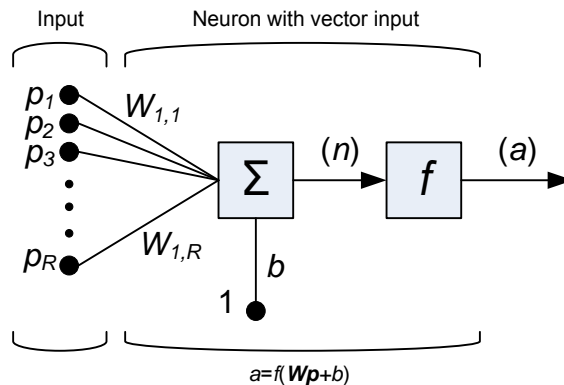


Figure 7: A neuron with a single R -element input vector.

For each node, the individual element inputs p_1, \dots, p_R are multiplied by weights $w_{1,1}, \dots, w_{1,R}$ and the weighted values are fed to the summing junction. The sum is $\mathbf{W} \cdot \mathbf{p}$, the dot product of the (single row) matrix $\mathbf{W}=[w_{1,1}, \dots, w_{1,R}]$ and the vector $\mathbf{p}=[p_1, \dots, p_R]^T$. The neuron has a bias b , which is summed with the weighted inputs to form the net input n which is the argument of the transfer function f :

$$n = w_{1,1}p_1 + w_{1,2}p_2 + \dots + w_{1,R}p_R + b = \mathbf{W} \cdot \mathbf{p} + b \quad (4)$$

In the above case, \mathbf{p} is a column vector ($R \times 1$), \mathbf{W} is a row vector ($1 \times R$) and b is a scalar.

5.1 Transfer function

The transfer function used is the hyperbolic tangent function, the same for all the hidden and the input layer, while the transfer function for the output layer is a linear function. The output of the hyperbolic tangent function and its derivative are given by

$$a = f(n) = \frac{e^{2n} - 1}{e^{2n} + 1} = \lambda \cdot \tan(\lambda x) \quad (5)$$

$$f'(n) = 4 \frac{e^{2n}}{(e^{2n} + 1)^2} = 1 - a^2 \quad (6)$$

This function yields output values in the interval $[-1, 1]$, while its derivative yields output values in the interval $[0, 1]$. The graphical representations of the hyperbolic tangent function and its derivative are shown in the figure below.

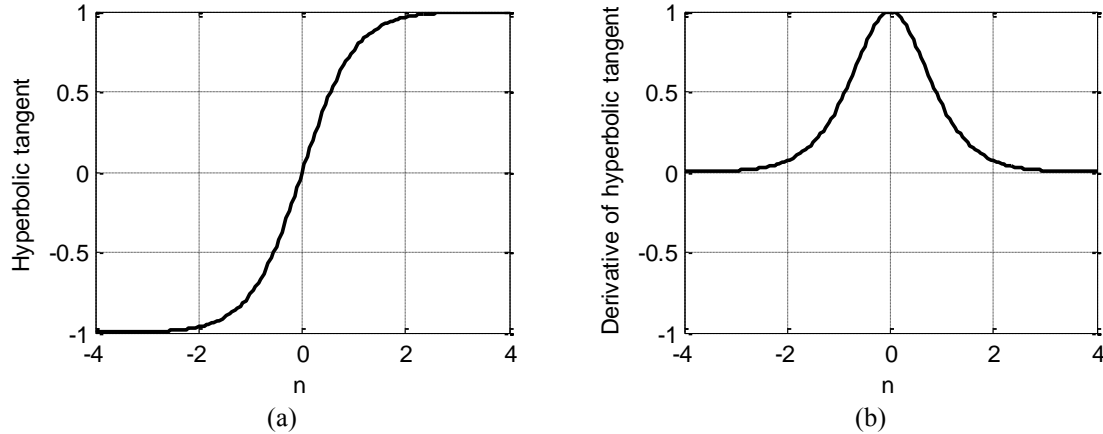


Figure 8: (a) Hyperbolic tangent function, (b) Its derivative.

6 NEURAL NETWORK APPROXIMATION RESULTS

We train the three NNs with the input and output data of Tables 1, 2, 3 (last two columns) and then each NN is asked to produce the full curves for each bed joint angle, for a set of 64 points. The results are shown in the figures below.

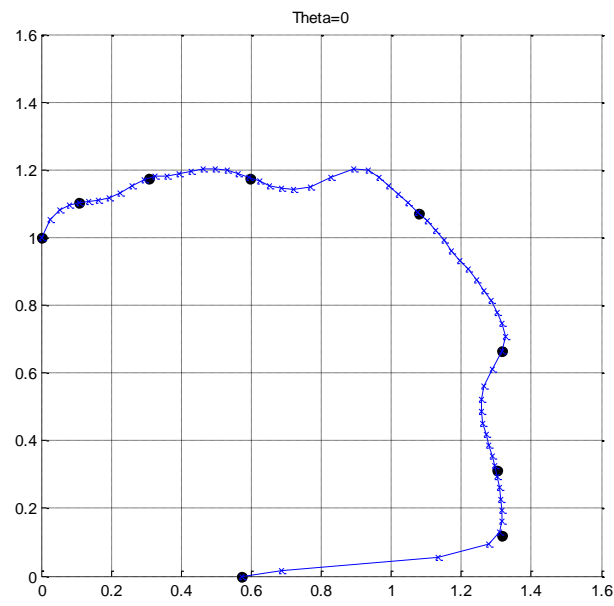


Figure 9: NN approximation result for the case $\theta=0^\circ$.

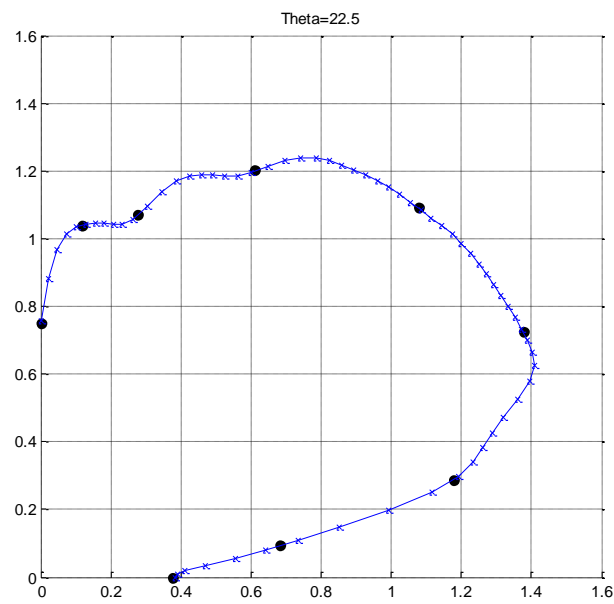


Figure 10: NN approximation result for the case $\theta=22.5^\circ$.

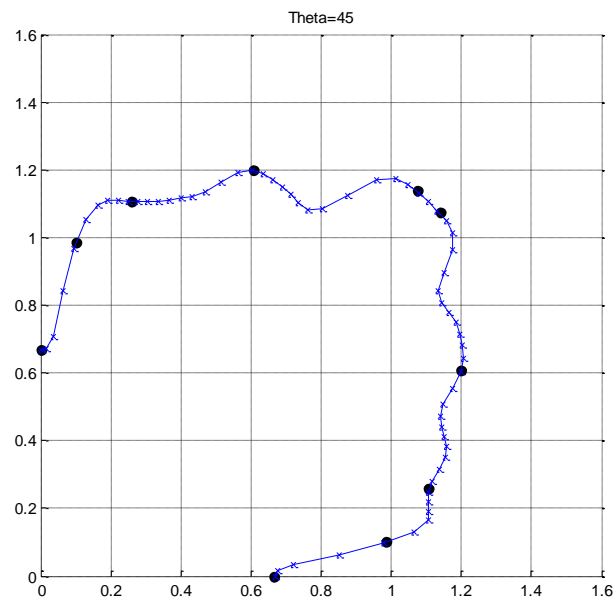


Figure 11: NN approximation result for the case $\theta=45^\circ$.

In the above figures, the black dots denote the input data, i.e. the data corresponding to the last two columns of Tables 1, 2, 3. The blue curve denotes the NN prediction of the fitting curve.

We can see that the NN manages to fit all the training data with excellent accuracy, while the approximation between the training data points appears to be adequate. An important characteristic is that for the third case ($\theta=45^\circ$) the NN manages to produce results that are symmetric (with good accuracy) to the line of 45° ($\sigma_I=\sigma_{II}$), an expected outcome due to the symmetry that masonry exhibits with respect to the 45° degrees axis.

7 CONCLUSIONS

In the present study, preliminary results of an ongoing research project, on the failure of anisotropic brittle material such as masonry are presented. In particular, Neural Networks are used in order to approximate the experimental results for masonry failure [1]. For each angle θ a NN is trained with the experimental data as inputs and then each NN is asked to produce the whole failure curve for each angle as its output, filling also the gaps between the experimental points.

The NNs showed great performance in fitting the experimental input data, while they manages to fit all the training data with very good accuracy, also producing results that are symmetric (with good accuracy) to the line of 45° ($\sigma_I=\sigma_{II}$) for the third case ($\theta=45^\circ$). This is in very good agreement to the characteristic symmetry of the masonry. The results show the great potential of using NN for the approximation of the masonry failure under biaxial compressive stress.

A more detailed investigation has to be made regarding the use of NN for the generation of the failure surface for any angle θ . The next research step would be to try to combine the results of the three separate NNs into a single NN that would also take the angle θ as its input. The trained NN should be then able to produce the whole 3D failure surface for any angle θ .

REFERENCES

- [1] Page, A. W., "The biaxial compressive strength of brick masonry", Proc. Instn Civ. Engrs, Part 2, Vol. 71, Sept., 893-906, 1981.
- [2] Dhanasekar, M., Page, A. W., and Kleeman P. W., "The failure of brick masonry under biaxial stresses." Proceedings, *The Institution of Civil Engineers, Part 2*, 79, 295-313, 1985.
- [3] Naraine, K., and Sinha, S., "Cyclic Behavior of Brick Masonry under Biaxial Compression." Journal of Structural Engineering, ASCE, Vol. 117, No. 5, 1336-1355, 1991.
- [4] Scarpas, A., "Non-local Plasticity Softening Model for Brittle Materials / Experimental Evidence / Analytical Modelling / Preliminary Results." Research Report, Laboratory of Reinforced Concrete, National Technical University of Athens, 1991.
- [5] Syrmakezis, C. A., Chronopoulos, M. P., Sophocleous, A. A., and Asteris, P. G., "Structural analysis methodology for historical buildings." Proceedings of the Fourth International Conference on Structural Studies of Historical Buildings, STREMA 95, Vol. 1, 373-382, 1995
- [6] Syrmakezis, C. A., Asteris, P. G., and Sophocleous, A. A., "Earthquake resistant design of masonry tower structures." Proceedings, Fifth International Conference on Structural Studies of Historical Buildings, STREMA 97, 25-27 June, San Sebastian, Spain, 377-386, 1997
- [7] Asteris, P. G., "Unified Yield Surface for the Nonlinear Analysis of Brittle Anisotropic Materials", Nonlinear Sci. Lett. A, Vol.4, No.2, 46-56, 2013.
- [8] Samarasinghe, W., "The in-plane failure of brickwork," PhD thesis, University of Edinburgh, 1980.
- [9] Page, A. W., "A biaxial failure criterion for brick masonry in the tension-tension range." The International journal of Masonry Construction, Vol. 1, No. 1, 1980.
- [10] Tassios, Th. P., and Vachliotis, Ch. (1989). "Failure of masonry under heterosemous biaxial stresses." Proc. Int. Conf. Conservation of Stone, Masonry-Diagnosis, Repair and Strengthening, Athens.
- [11] Syrmakezis, C. A., Asteris, P. G., "Masonry Failure Criterion Under Biaxial Stress State", Journal of Materials in Civil Engineering, Vol. 13, No. 1, 2001.
- [12] Zhang, Y., Zhou, G., Xiong, Y., and Rafiq, M. "Techniques for Predicting Cracking Pattern of Masonry Wall Using Artificial Neural Networks and Cellular Automata." J. Comput. Civ. Eng., 24(2), 161-172, 2010.
- [13] Ahmed El-Shafie, T. Abdelazim, Aboelmagd Noureldin. "Neural network modeling of time-dependent creep deformations in masonry structures", Neural Computing and Applications, 19(4), 583-594, 2010.
- [14] Zhou, G., Pan, D., Xu, X., and Rafiq, Y., "Innovative ANN Technique for Predicting Failure/Cracking Load of Masonry Wall Panel under Lateral Load." J. Comput. Civ. Eng., 24(4), 377-387, 2010.
- [15] A. Mathew, B. Kumar, B. P. Sinha, R. F. Pedreschi, Analysis of Masonry Panel under Biaxial Bending Using ANNs and CBR, Journal of Computing in Civil Engineering, 13(3), 170-177, 1999.

- [16] Lettvin, J. Y., Maturana, H. R., McCulloch, W. S., and Pitts, W. H. "What the Frog's Eye Tells the Frog's Brain." *Proceedings of the Institute of Radic Engineers*, 47(11), 1940-1951, 1959

IMPROVING THE ACCURACY OF A FINITE-VOLUME METHOD FOR COMPUTING RADIATIVE HEAT TRANSFER IN THREE- DIMENSIONAL UNSTRUCTURED MESHES

Georgios N. Lygidakis¹ and Ioannis K. Nikolos²

^{1,2} Department of Production Engineering and Management, Technical University of Crete
Chania, GR-73100, Greece

¹e-mail: glygidakis@isc.tuc.gr

²e-mail: jnikolo@dpem.tuc.gr

Keywords: Radiative heat transfer, node-centered finite-volume method, 2nd order accurate spatial/temporal scheme, h-refinement.

Abstract. *In recent years, the Finite-Volume Method (FVM), being one of the most widely applied techniques in Computational Fluid Dynamics (CFD), has gained some popularity in solving radiative heat transfer problems. In order to avoid excessive amounts of false scattering and improve the accuracy of this method, two techniques, well established in CFD scientific field, were developed for a parallelized algorithm using FVM for the prediction of radiative heat transfer for absorbing, emitting and scattering gray media in hybrid unstructured grids. The first one considers a second order accurate spatial/temporal scheme for the calculation of radiative heat fluxes, while the second one uses a grid adaptation technique during the progress of the solution. The second order spatial scheme is based on the Monotonic Upstream Scheme for Conservation Laws (MUSCL) reconstruction of the radiative intensities, using additionally a slope limiter to control the total variation of the reconstructed field. A second order in time Runge-Kutta method is utilized for the solution of the time dependent Radiative Transfer Equation (RTE), avoiding the oscillations derived from the coupling of the higher order spatial scheme and the standard iterative solution of the non time-dependent RTE. The second technique is the h-refinement, which enhances the algorithm with the capability of local grid adaptation, based on the splitting of the existing elements into new ones. Special treatment is needed for hybrid grids, due to the variety of element types (tetrahedral, prismatic and pyramidal) and their division alternatives. The algorithm is validated against benchmark test cases, proving its potential for improving the accuracy with the implementation of the afore-mentioned techniques.*

1 INTRODUCTION

As radiative heat transfer is a major mode of heat transfer in many engineering and industrial applications, many researchers have been devoted in the development of computational methods for the prediction of heat transfer due to radiation. Among the developed ones, the Finite-Volume Method (FVM), initially proposed by Raithby and Chui [1], has gained some popularity solving radiative heat transfer problems, because of its simplicity and its ability to be implemented in complex geometries. Considering these characteristics, this method has been widely employed in the prediction of radiative heat transfer in various shapes of enclosures, described by structured or unstructured tetrahedral (triangular for 2D), hybrid or polygonal grids and cartesian or cylindrical coordinates [2-12]. Additionally, it possesses another attractive feature, the treatment of radiation in a similar to flow way, as the formulation and the solution of the discrete equations is a common procedure for fluid flow and radiation [2, 11, 12, 13]. Therefore, it proves to be especially familiar for Computational Fluid Dynamics (CFD) scientists, compared for example with Monte-Carlo method, which is based on view factors, requiring as such additional knowledge and experience [12, 13]. Nevertheless, two shortcomings of the FVM have been mainly identified, reducing the accuracy of its results, namely, the ray effect and false scattering [14-16]. The first is associated with the angular discretization, while its effects can be mitigated by the utilization of more finite control angles [14]. The second one, studied in this work, is associated with the spatial discretization and corresponds to the false or numerical diffusion in CFD [15], while its effects can be subdued in general by using finer grids or more accurate spatial schemes [16].

Considerable efforts have been exerted for the development of algorithms, encountering effectively the false scattering by employing higher order accurate spatial schemes [15, 16]. Although such a practice is common in the computation of the convective fluxes of the Navier-Stokes equations in CFD, it is rarely implemented for the evaluation of the radiative heat fluxes [16]. For a first order scheme, the evaluation of the numerical fluxes in each face of a control volume, which corresponds to an edge connecting adjacent nodes in the node-centered scheme, is based on the values at these end-points. On the contrary, a second order scheme takes into account the values of more mesh nodes, by reconstructing the values of the two end-nodes with the Taylor series expansions, such as in the MUSCL (Monotonic Upstream Scheme for Conservation Laws) technique [17]. In addition, a slope limiter, such as Van Albeda-Van Leer [17, 18] and Min-mod [17, 19], should accompany the higher order scheme in order to control the total variation of the reconstructed field and assure the monotonicity between the two states of the interface of the control volumes. Moreover, a second order scheme can sometimes derive negative unphysical values of radiative intensity, which are usually mitigated by a fix-up procedure [16]. However, such a remedy along with the common practice solving the Radiative Transfer Equation (RTE) with simple iterative approximations [11, 12] can lead to oscillations or even to the failure of the solution. In order to face this deficiency, the time-dependent RTE [20-22] can be employed for a pseudo-transient simulation in conjunction with a more accurate temporal scheme, such as the Runge-Kutta method [23], considering that a higher order spatial scheme shall be accompanied by an also higher order temporal method.

As stated already, the mitigation of false scattering can be succeeded with the utilization of finer grids, requiring increased computational effort. Considering that for many practical problems some phenomena are sufficiently localized, grid adaptation can be employed to increase the spatial resolution and consequently the accuracy of the results in a specific region, without increasing significantly the memory and computational requirements [24-27]. In general, grid adaptation methods can be divided in two categories, namely redistribution and re-

finement [27]. In the first category of methods, the nodes are repositioned in order a finer discretization to be succeeded in selected regions. Despite the conservation of the total node number, these methods encounter difficulties in cases including complex geometries. The methods of the second category are based on the addition of degrees of freedom following predefined rules, as the h-refinement, implemented in this study. The mesh is enriched by dividing the existing elements into new ones; the procedure begins with the selection of the area for enrichment, using appropriate criteria, and continues with the division of the corresponding edges, faces and elements of this area. Special treatment is needed for hybrid meshes, due to the variety of the element types (hexahedral, tetrahedral, prismatic and pyramidal) and their division alternatives. Except for the previous categorization, mesh adaptation methods can be divided according to the type of the grid (hybrid or tetrahedral) [24, 27] or the type of the computational system (serial or parallel) [26].

In this study, a second order accurate spatial/temporal scheme along with the h-refinement technique is developed to enhance a parallelized node-centered finite-volume algorithm for the prediction of radiative heat transfer in three-dimensional unstructured hybrid grids, including absorbing-emitting and scattering mediums [11, 12]. Our main aim is to improve the accuracy of the algorithm in relatively coarse meshes, in which a first order accurate spatial scheme imports non-negligible false scattering amounts. As such, a second order spatial scheme, based on the MUSCL reconstruction of the radiative intensity values, along with the Van Albada-Van Leer and the Min-mod slope limiters, is incorporated. In order to avoid oscillations, derived by the second order spatial scheme in conjunction with the fix-up procedure and the standard iterative solution of the non time-dependent RTE, a second order accurate in time Runge-Kutta method is employed for the solution of the corresponding time-dependent equation. In addition, the h-refinement technique is included to increase the spatial resolution locally in selected areas of unstructured hybrid grids, including tetrahedral, prismatic, and pyramidal elements (the latter utilized only in the transition region of the grid from the prismatic to the tetrahedral elements). The relatively increased requirements for memory and computational effort, derived from the previous methods, are subdued by the utilization of an edge-based data structure along with a parallelized implementation, based on the domain decomposition approach and MPI (Message Passing Interface) [11, 12]. Finally, the proposed numerical approach is validated against benchmark test cases, confirming its capability to mitigate false scattering and consequently improve the accuracy of the solution in coarse computational grids. This feature makes relatively negligible the increase of the computational requirements, derived by the incorporation of the second order accurate spatial/temporal scheme and the h-refinement method.

2 MATHEMATICAL ANALYSIS

2.1 Governing equation and discretization

The radiative intensity for an absorbing, emitting and scattering gray medium at any node P in position \vec{r} along a path \hat{s} can be calculated either for steady-state or transient simulations by the time-dependent RTE [20] as:

$$\frac{1}{c} \frac{dI_p(\vec{r}, \hat{s})}{dt} + \frac{dI_p(\vec{r}, \hat{s})}{ds} = -\beta I_p(\vec{r}, \hat{s}) + k_\alpha I_b(\vec{r}) + \frac{\sigma_s}{4\pi} \int_{4\pi} I_p'(\vec{r}, \hat{s}_i') \Phi(\hat{s}, \hat{s}_i') d\omega \quad (1)$$

where I_p is the radiative intensity of node P , c is the propagation speed of radiation in the medium, β ($\beta=k_\alpha+\sigma_s$) is the extinction coefficient, k_α is the absorption coefficient, σ_s is the scattering coefficient and I_b is the black body intensity, based on the temperature of the medium

in the position \vec{r} . As such, the left hand side terms of the RTE express the rate of change of the intensity in time t and in position/direction \vec{r}, \hat{s} , the latter defined in this study by the polar and azimuthal angles θ and φ , respectively. The first right hand side term expresses the attenuation by absorption and scattering to other directions, while the second one the black body emission. Finally, the third term, which is described by the Scattering Phase Function (SPF) $\Phi(\hat{s}, \hat{s}_i')$, represents the radiation obtained by scattering from the other directions [11, 12, 13].

As far as the discretization is concerned, the RTE has to be solved for a discrete number of finite solid angles (angular discretization) and a discrete number of finite control volumes (spatial discretization). The finite solid angles, in which the directional domain is divided for the angular discretization, are defined usually by lines of constant longitude and constant latitude on the surface of a sphere (Figure 1) [11, 13]. For the spatial discretization, a node-centered scheme is utilized in this study, in accordance with which the median control volume of a node is constructed by connecting lines defined by edge midpoints, barycenters of faces and barycenters of elements, sharing this node [11, 28]; the contributions to the control volume of a node P from different types of elements (prismatic, pyramidal and tetrahedral) adjacent to this node are illustrated in Figure 2.

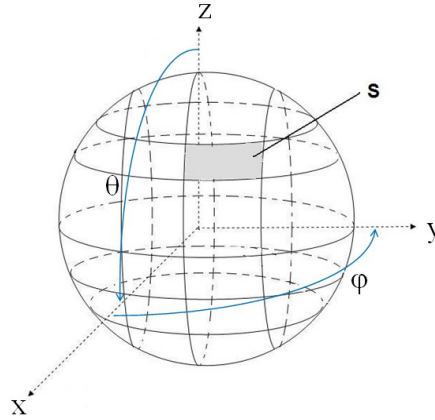


Figure 1: Angular discretization.

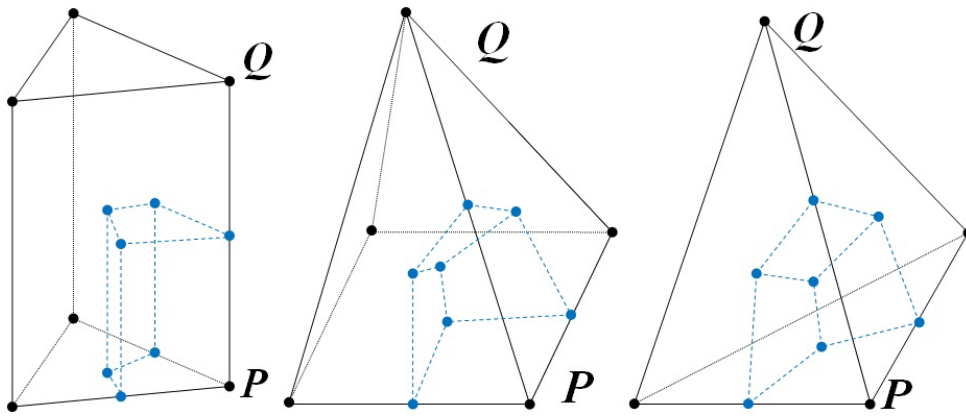


Figure 2: Contributions of three different types of elements (prismatic, pyramidal and tetrahedral) to the control volume of a node P .

2.2 Formulation of discrete equations

Considering the discretization schemes (spatial and angular) of the previous paragraph, the RTE is integrated for a node P over its spatial finite control volume V_P and over a finite solid

angle Ω^{mn} , while subsequently (with the implementation of the divergence theorem) it is formulated as:

$$\Delta I_P^{mn} \frac{V_P \Delta \Omega^{mn}}{c \Delta t} + \sum_i I_i^{mn} D_{ci}^{mn} \Delta A_i = [-\beta I_P^{mn} + S_R^{mn}] V_P \Delta \Omega^{mn} \quad (2)$$

where D_{ci}^{mn} is the directional weight of the solid angle mn and the surface i of the control volume, while S_R^{mn} is the sum of the emissive and in-scattering terms, which are defined as [6, 11]:

$$D_{ci}^{mn} = \int_{\theta^{m-}}^{\theta^{m+}} \int_{\varphi^{n-}}^{\varphi^{n+}} (\hat{s} \cdot \hat{n}_i) \sin \theta d\theta d\varphi \quad (3)$$

$$\hat{s} = \sin \theta \cos \varphi \hat{e}_x + \sin \theta \sin \varphi \hat{e}_y + \cos \theta \hat{e}_z \quad (4)$$

$$\hat{n}_i = n_x \hat{e}_x + n_y \hat{e}_y + n_z \hat{e}_z \quad (5)$$

$$\Delta \Omega^{mn} = \int_{\theta^{m-}}^{\theta^{m+}} \int_{\varphi^{n-}}^{\varphi^{n+}} \sin \theta d\theta d\varphi \quad (6)$$

$$S_R^{mn} = k_\alpha I_b + \frac{\sigma_s}{4\pi} \int_{4\pi} I_P^{m'n'} \Phi(m'n', mn) d\omega = k_\alpha \frac{\sigma T^4}{\pi} + \frac{\sigma_s}{4\pi} \sum_{m'_i=1}^{N_\theta} \sum_{n'_i=1}^{N_\varphi} I_P^{m'_i n'_i} \bar{\Phi}(m'_i n'_i, mn) \Delta \Omega^{m'_i n'_i} \quad (7)$$

Quantity $\bar{\Phi}(m'_i n'_i, mn)$ is the average scattering phase function, expressing the scattering contribution of the control angle $m'_i n'_i$ (incident angle) to the control angle mn (in-scattering angle) [11]; for isotropic scattering it is assumed equal to unity, while for anisotropic one its value depends on the utilized model (i.e. Legendre polynomials) [11, 29, 30, 31]. Though the angles θ^m and φ^n can be defined arbitrarily, they are obtained from the equal division of the 4π steradians into $N_\theta \times N_\varphi$ directions, such that $\Delta \theta^m = \theta^{m+} - \theta^{m-} = \pi/N_\theta$ and $\Delta \varphi^n = \varphi^{n+} - \varphi^{n-} = 2\pi/N_\varphi$ [6, 11]. Considering this angular discretization, the directional weight D_{ci}^{mn} and the discrete control angle $\Delta \Omega^{mn}$ can be evaluated as:

$$D_{ci}^{mn} = D_{ci,x}^{mn} + D_{ci,y}^{mn} + D_{ci,z}^{mn} = \int_{\theta^{m-}}^{\theta^{m+}} \int_{\varphi^{n-}}^{\varphi^{n+}} (\hat{s} n_x \hat{e}_x + \hat{s} n_y \hat{e}_y + \hat{s} n_z \hat{e}_z) \sin \theta d\theta d\varphi$$

$$D_{ci,x}^{mn} = \frac{n_x}{2} (\sin \varphi^{n+} - \sin \varphi^{n-}) [(\theta^{m+} - \theta^{m-}) - (\cos \theta^{m+} \sin \theta^{m+} - \cos \theta^{m-} \sin \theta^{m-})] \quad (8)$$

$$D_{ci,y}^{mn} = \frac{n_y}{2} (\cos \varphi^{n-} - \cos \varphi^{n+}) [(\theta^{m+} - \theta^{m-}) - (\cos \theta^{m+} \sin \theta^{m+} - \cos \theta^{m-} \sin \theta^{m-})]$$

$$D_{ci,z}^{mn} = \frac{n_z}{2} (\varphi^{n+} - \varphi^{n-}) (\sin^2 \theta^{m+} - \sin^2 \theta^{m-})$$

$$\Delta \Omega^{mn} = \int_{\theta^{m-}}^{\theta^{m+}} \int_{\varphi^{n-}}^{\varphi^{n+}} \sin \theta d\theta d\varphi = (\varphi^{n+} - \varphi^{n-}) (\cos \theta^{m-} - \cos \theta^{m+}) \quad (9)$$

By applying the step scheme, which resembles a simple upwind scheme in CFD, the value of the radiative intensity of a downstream face is set equal to that of the upstream node [6, 11, 12], resulting in the following expression for the second left hand side term of equation (2):

$$I_i^{mn} D_{ci}^{mn} = I_P^{mn} D_{ci,out}^{mn} + I_Q^{mn} D_{ci,in}^{mn} \quad (10)$$

In structured meshes the application of the previous equation is straightforward, as the angular discretization is selected to match exactly with the control volumes' faces. On the contrary, in unstructured grids the control angles are inevitably overlapped [6, 11, 12], requiring appropriate manipulation for a more accurate solution, such as the bold approximation and the pixelation method. According to the first approximation, an overhang solid angle is considered wholly either outgoing or incoming, depending on the sign of its directional weight [11] (Figure 3a-b). Considering this remedy for the overhang problem, the directional weights of equation (10) are defined as:

$$\begin{aligned} D_{ci,out,bold}^{mn} &= \alpha_{ci,bold}^{mn} \left| D_{ci}^{mn} \right| \\ D_{ci,in,bold}^{mn} &= -(1 - \alpha_{ci,bold}^{mn}) \left| D_{ci}^{mn} \right| \\ \alpha_{ci,bold}^{mn} &= \begin{cases} 1 & \text{if } D_{ci}^{mn} \geq 0 \\ 0 & \text{if } D_{ci}^{mn} < 0 \end{cases} \end{aligned} \quad (11)$$

where $\alpha_{ci,bold}^{mn}$ is the approach coefficient for the directional weight D_{ci}^{mn} . Respectively, in the pixelation approach each control angle is divided in smaller ones, for which the bold approximation is employed [6] (Figure 3c), resulting in the following expressions for the directional weights:

$$\begin{aligned} D_{ci,out,pix}^{mn} &= \alpha_{ci,pix}^{mn} \sum_{m_i=1}^{N_m} \sum_{n_i=1}^{N_n} \left| D_{ci}^{m_i n_i} \right| \\ D_{ci,in,pix}^{mn} &= -(1 - \alpha_{ci,pix}^{mn}) \sum_{m_i=1}^{N_m} \sum_{n_i=1}^{N_n} \left| D_{ci}^{m_i n_i} \right| \\ \alpha_{ci,pix}^{mn} &= \frac{\sum_{m_i=1}^{N_m} \sum_{n_i=1}^{N_n} \max(D_{ci}^{m_i n_i}, 0)}{\sum_{m_i=1}^{N_m} \sum_{n_i=1}^{N_n} \left| D_{ci}^{m_i n_i} \right|} \end{aligned} \quad (12)$$

where $\alpha_{ci,pix}^{mn}$ is the corresponding approach coefficient, calculated by the sum of the positive subangles' directional weights, divided by the sum of the absolute values of them. Although this approximation is usually applied only in the overhang control angles of the nodes [2, 6], in this study it is implemented to all the nodes and control angles in a pre-computation stage. As the values of those coefficients and directional weights do not vary during the iterative solution of the RTE, they are evaluated before the beginning of the procedure, assuring a reduced computation time per iteration. As such, the RTE is reformulated independently of the employed approximation as:

$$\Delta I_P^{mn} \frac{V_P \Delta \Omega^{mn}}{c \Delta t} = \left[-\beta I_P^{mn} + S_R^{mn} \right] V_P \Delta \Omega^{mn} - \sum_i I_P^{mn} D_{ci,out}^{mn} \Delta A_i - \sum_i I_Q^{mn} D_{ci,in}^{mn} \Delta A_i \quad (13)$$

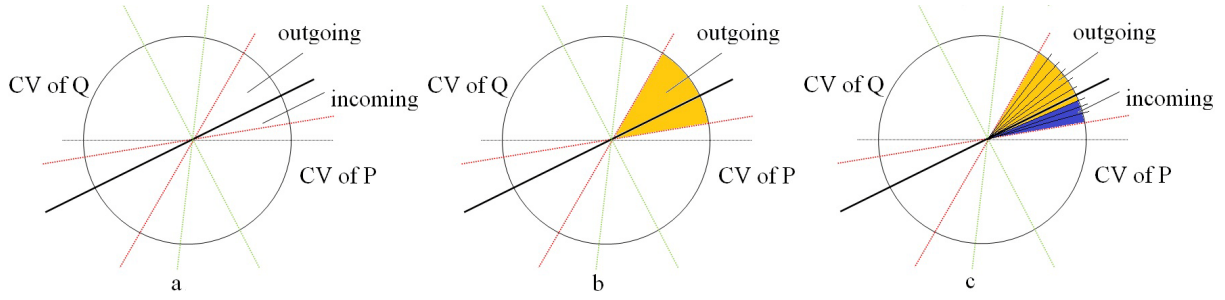


Figure 3: a) Schematic of the control angle overhang problem. b) Implementation of the bold approximation. c) Implementation of the pixelation method.

Boundaries' contributions have also to be considered in the corresponding nodes' flux balances, in order their equation sets to be admissible for solution. The boundary conditions in radiative heat transfer concern walls, inlets, outlets and symmetric planes; the first three types are managed in the same way, as opaque and diffuse surfaces, while for the last one a slightly different manipulation is required. As such, the wall boundary conditions are usually implemented in an explicit way (Dirichlet), assigning to the boundary nodes intensity values, computed as the sum of their blackbody intensity, due to their temperature, and the reflection of the incoming intensities [2, 6, 11, 12]. Despite the common practice, these boundary conditions are applied implicitly in this study, implementing the step scheme between the boundary node and a “ghost” node outside the grid. Considering this manipulation, equation (13) for a boundary node P is defined as:

$$\Delta I_P^{mn} \frac{V_P \Delta \Omega^{mn}}{c \Delta t} = [-\beta I_P^{mn} + S_R^{mn}] V_P \Delta \Omega^{mn} - \sum_i I_P^{mn} (D_{ci,out}^{mn} \Delta A_i + D_{ci,out,w}^{mn} \Delta A_w) - \sum_i (I_Q^{mn} D_{ci,in}^{mn} \Delta A_i + I_w^{mn} D_{ci,in,w}^{mn} \Delta A_w) = R_P^{mn} \quad (14)$$

where $D_{ci,out,w}^{mn}$ is the directional weight going outward of the control volume of node P and $D_{ci,in,w}^{mn}$ is the corresponding directional weight coming inwards to the same control volume. Depending on the employed bold or pixelation scheme, such directional weights are calculated using either equation (11) or (12). For the computation of the radiative intensity of the “ghost” node, I_w^{mn} , which appears in the previous equation, the following equation is utilized:

$$I_w^{mn} = \varepsilon_w I_{b,P} + \frac{1 - \varepsilon_w}{\pi} \sum_{m_i=1}^{N_\theta} \sum_{n_i=1}^{N_\varphi} I_P^{m_i n_i} D_{ci,out,w}^{m_i n_i} \quad (15)$$

As far as the symmetry boundary conditions are concerned, the same implicit scheme is applied, evaluating radiative intensity of the “ghost” node, I_w^{mn} , such as the net heat flux become zero at the symmetry plane, resembling in that way a specularly reflecting wall [32]. Therefore, the intensities of such a boundary node, going out of its control volume to the symmetry plane, are placed as incoming in its control volume in the mirroring direction. Employing mirroring boundary conditions, which is commonly met in CFD, results in reduced memory and computational requirements, due to the smaller utilized mesh. Nevertheless, for its implementation, the angular discretization should be appropriately performed, in order the mirroring plane to coincide with a discrete solid angle limit; otherwise an interpolation scheme should be employed [32].

2.3 Time integration

An explicit scheme, using a four stage Runge-Kutta (RK(4)) method, is implemented for the time integration of the RTE and its iterative solution as follows [17, 23]:

$$\begin{aligned}
 \Delta I_P^{mn} \frac{V_P \Delta \Omega^{mn}}{c \Delta t_P} &= R_P^{mn} \\
 (I_P^{mn})^{l+1,0} &= (I_P^{mn})^l \\
 (I_P^{mn})^{l+1,k} &= (I_P^{mn})^l + \alpha_k \frac{c \Delta t_P}{V_P \Delta \Omega^{mn}} R_P^{mn} \left((I_P^{mn})^{l+1,k-1} \right), \quad k = 1, \dots, 4 \\
 (I_P^{mn})^{l+1} &= (I_P^{mn})^{l+1,4}
 \end{aligned} \tag{16}$$

where α_1 , α_2 , α_3 and α_4 are the constants of the method with values 0.11, 0.26, 0.5 and 1.0 respectively, attributing the procedure with a second order accuracy in time [17, 23]. The term l is the current external iteration number, k is the current Runge-Kutta iteration number and Δt_P is the local pseudo-time step [17, 33], based on the length $\alpha_{edge,P}$ of the shortest edge of the grid connected to the node P , which is defined for a steady-state simulation as [17, 20]:

$$c \Delta t_P \leq \frac{1}{2} \min(\alpha_{edge,P}) \tag{17}$$

Employing the local pseudo-time stepping scheme, a common practice in steady-state CFD simulations, accelerates the convergence of the iterative solution, as for each node the maximum permissible time step is utilized [17]. Nevertheless, for transient-unsteady simulations a global time step should be applied instead, computed as the smaller of the local ones. In case the iterative procedure derives a negative unphysical value of intensity (usually in the initial iterations along with a higher order spatial scheme), a fix-up procedure is implemented, setting this value equal to zero [16]. Once the new intensity values are calculated, they should be exchanged between the adjacent subdomains for a parallelized implementation of the algorithm [11, 12].

3 HIGH ORDER SPATIAL SCHEME

For a first order accurate spatial scheme the left and right states of a face of a control volume of a node P , which coincides with an edge PQ in the node-centered scheme, are approximated by the values at the end-points of the edge. However, for a higher order scheme, these states are defined by the reconstructed values of the same nodes implementing the Taylor series expansions; the MUSCL scheme is employed in this study, accompanied with a slope limiter to control the total variation of the reconstructed field [17, 18, 19, 34]. Considering this approximation, the left and right values at the midpoint of an edge PQ are defined as [17, 34]:

$$\begin{aligned}
 (I_{PQ}^{mn})^L &= I_P^{mn} + \frac{1}{2} (\nabla I^{mn})_P \vec{r}_{PQ} \\
 (I_{PQ}^{mn})^R &= I_Q^{mn} - \frac{1}{2} (\nabla I^{mn})_Q \vec{r}_{PQ}
 \end{aligned} \tag{18}$$

where \vec{r}_{PQ} is the vector connecting the end-nodes P and Q . For the calculation of the extrapolation gradients $(\nabla I^{mn})_P$ and $(\nabla I^{mn})_Q$ at these end-points, the Green-Gauss linear representation method is employed, described as [17, 34]:

$$\left(\nabla I^{mn}\right)_P = \frac{1}{V_P} \left(\sum_{i, \text{edge } PQ} \frac{1}{2} \left(I_P^{mn} + I_Q^{mn} \right) \hat{n}_i \Delta A_i + \sum_{i, P\text{-wall}} I_P^{mn} \cdot \hat{n}_{i,w} \Delta A_w \right) \quad (19)$$

where the last term of the equation is activated only in case the node P is a boundary one. Once these gradients are computed, they should be exchanged between the adjacent subdomains for a parallelized implementation of the algorithm [11, 12, 35, 36, 37]. Considering equation (18), equation (10), describing the step scheme, is reformulated as:

$$I_i^{mn} D_{ci}^{mn} = \left(I_{PQ}^{mn} \right)^L D_{ci, \text{out}}^{mn} + \left(I_{PQ}^{mn} \right)^R D_{ci, \text{in}}^{mn} \quad (20)$$

As stated before, a slope limiter is required, in order the total variation in the reconstructed field to be minimized; the Van Albada-Van Leer (VLVA) [17, 18] and the Min-mod [17, 19] are included in the present study. They are both based on the centered $\left(\nabla I_{PQ}^{mn}\right)^c$ and the upwind $\left(\nabla I_P^{mn}\right)^u, \left(\nabla I_Q^{mn}\right)^u$ gradients, defined as [18, 19]:

$$\begin{aligned} \left(\nabla I_{PQ}^{mn}\right)^c \cdot \vec{r}_{PQ} &= I_Q^{mn} - I_P^{mn} \\ \left(\nabla I_P^{mn}\right)^u &= 2\left(\nabla I_P^{mn}\right) - \left(\nabla I_{PQ}^{mn}\right)^c \\ \left(\nabla I_Q^{mn}\right)^u &= 2\left(\nabla I_Q^{mn}\right) - \left(\nabla I_{PQ}^{mn}\right)^c \end{aligned} \quad (21)$$

while their utilization transforms equation (18), which derives the reconstructed values of the left and right states of the examined edge PQ , as follows:

$$\begin{aligned} \left(I_{PQ}^{mn} \right)^L &= I_P^{mn} + \frac{1}{2} \cdot X \left(\left(\nabla I_P^{mn}\right)^u \cdot \vec{r}_{PQ}, \left(\nabla I_{PQ}^{mn}\right)^c \cdot \vec{r}_{PQ} \right) \\ \left(I_{PQ}^{mn} \right)^R &= I_Q^{mn} - \frac{1}{2} \cdot X \left(\left(\nabla I_Q^{mn}\right)^u \cdot \vec{r}_{PQ}, \left(\nabla I_{PQ}^{mn}\right)^c \cdot \vec{r}_{PQ} \right) \end{aligned} \quad (22)$$

where X is the limiter function, defined for the Van Albada-Van Leer limiter as [18]:

$$X(a, b) = \begin{cases} \frac{(a^2 + e)b + (b^2 + e)a}{a^2 + b^2 + 2e} & ab > 0 \\ 0 & ab \leq 0 \end{cases} \quad (23)$$

and for the Min-mod limiter as [19]:

$$X(a, b) = \begin{cases} a & \text{if } |a| < |b| \text{ and } ab > 0 \\ b & \text{if } |b| < |a| \text{ and } ab > 0 \\ 0 & \text{if } ab \leq 0 \end{cases} \quad (24)$$

where e is a very small number with a typical value of 10^{-16} to prevent division by zero. If the second order scheme derives a negative unphysical intensity (usually in the initial iterations), the first order scheme is employed instead. By utilizing a higher order spatial scheme, the R/H side term of equation (14) is defined as:

$$R_p^{mn} = \left[-\beta I_p^{mn} + S_R^{mn} \right] V_p \Delta \Omega^{mn} - \sum_i \left(I_{PQ}^{mn} \right)^L \left(D_{ci,out}^{mn} \Delta A_i + D_{ci,out,w}^{mn} \Delta A_w \right) - \sum_i \left(\left(I_{PQ}^{mn} \right)^R D_{ci,in}^{mn} \Delta A_i + I_w^{mn} D_{ci,in,w}^{mn} \Delta A_w \right) \quad (25)$$

4 GRID ADAPTATION

Except for the second order accurate schemes, false scattering can be reduced by utilizing finer grids, which however call for increased memory requirements and computational effort. Local grid refinement techniques can be applied during the solution procedure to increase the accuracy in preselected regions along with significant computational savings, as they avoid the generation of new meshes from scratch. Such methods are widely employed in CFD simulations, especially in cases including sufficiently localized phenomena as shocks or in cases encountered for the first time in which no previous knowledge exists about the necessary spatial accuracy. Considering the above states the serial h-refinement method is incorporated in the present algorithm, which concerns the enrichment of the grid with new nodes as midpoints of the edges positioned in the targeted area, along with the division of those edges and the corresponding faces and elements.

The h-refinement technique can be divided basically in three main steps: a) The detection of the desired areas for adaptation and the marking of the corresponding edges for division, which is succeeded by defining appropriate criterions, targeting usually regions of the field with high gradients of a specific variable or regions with a specific characteristic. b) The spread of marking information to the neighboring edges, as the marking derived by the first step cannot lead to an admissible refinement pattern for the construction of the new mesh; the neighboring edges to the marked ones have to be examined by looping several times over the elements of the mesh [27]. This edge-based structure makes h-refinement particularly attractive for implementation in hybrid grids, including various types of elements. c) The embedding of new nodes as midpoints of the marked edges and the division of these edges; the corresponding faces and elements are divided then accordingly [27]. The whole procedure is based on some predefined rules, which are described as follows:

1. Every new, embedded as midpoint of an edge, node of the grid is a common point of all the neighbouring faces and elements.

2. Every new edge is a common edge of all the neighbouring elements.

3. There are five permitted ways for the division of a tetrahedron (Figure 4), resulting in [24, 25, 26, 27]: a) two new tetrahedrons, b) four new tetrahedrons, c) eight new tetrahedrons, d) two new tetrahedrons, one new pyramid and one new prism and e) one new tetrahedron and one new pyramid. The last two ways (*d* and *e*) are required only in the transitional region of the grid, from the prismatic to the tetrahedral elements [11, 12], while the third division type *c* can be implemented in three possible ways, depending on the selection of the internal diagonal edge; the shortest one should always be chosen in order not to produce distorted tetrahedrons [27].

4. There are two permitted ways for the division of a prism (Figure 5), resulting in two and four new prisms respectively [24, 25, 26].

5. There are three permitted ways for the division of a pyramid (Figure 6), producing [24, 25, 26]: a) two new pyramids, b) three new prisms and a new pyramid and c) a new prism and a new pyramid.

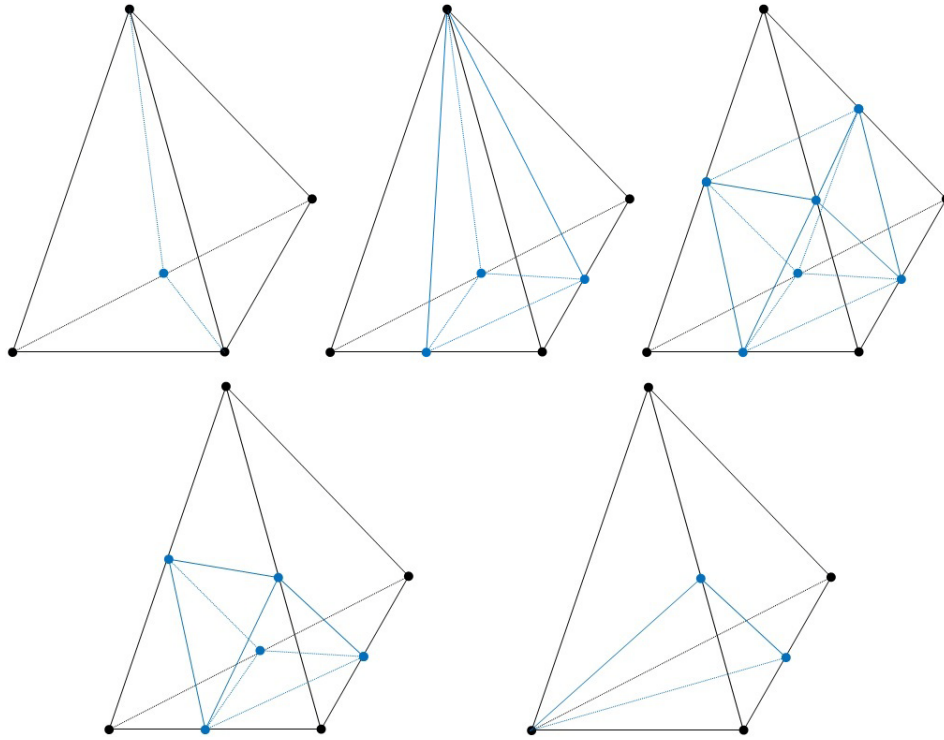


Figure 4: Permitted ways for the division of tetrahedrons.

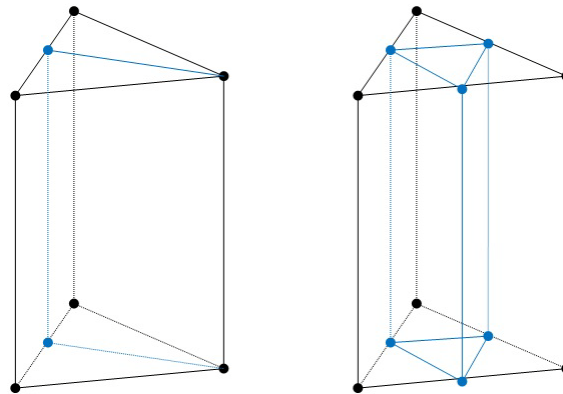


Figure 5: Permitted ways for the division of prisms.

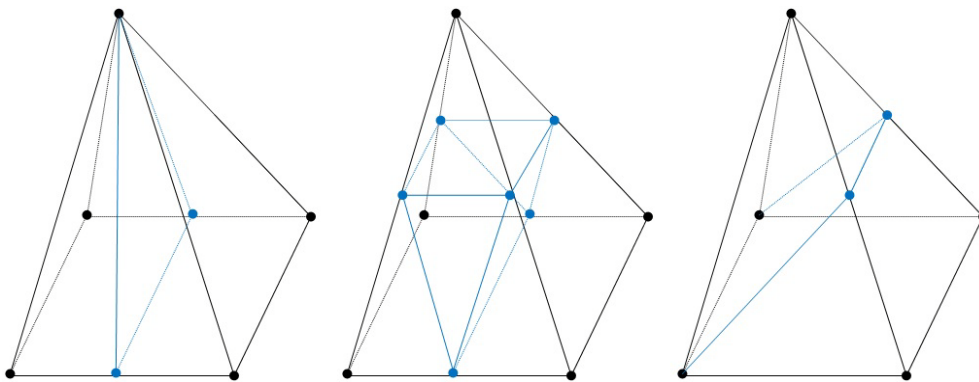


Figure 6: Permitted ways for the division of pyramids.

6. A triangular face can be divided in two or four new triangular faces, while a rectangular one can be divided only in two new rectangular faces [27].

7. The coordinates and the variables associated with a new node are defined as the arithmetic averages of the respective values at the two end-points of the edge.

5 EVALUATION

The present algorithm has been validated against benchmark test cases, comparing its results with the corresponding ones of reference solvers. The comparison is succeeded via the distributions of dimensionless incident radiative heat flux $Q^*(\vec{r})$ of the present and the reference solvers, defined as [38]:

$$Q^*(\vec{r}) = \frac{Q(\vec{r})}{E} = \frac{\int I(\vec{r}, \hat{s}) \cdot (\hat{s} \cdot \hat{n}_i) d\omega}{\sigma T^4} \quad (26)$$

where $Q(\vec{r})$ is the incident radiative heat flux in position \vec{r} , while E is the initial radiative energy, responsible for the heat transfer [11, 12]. The numerical results were obtained after the radiative intensity residual is decreased at least four orders of magnitude, computed as:

$$res = \frac{\sum_{p=1}^{N_p} \sum_{m=1}^{N_\theta} \sum_{n=1}^{N_\varphi} |I_p^{mn,l+1} - I_p^{mn,l}|}{N_p} \quad (27)$$

where N_p is the number of nodes of the whole mesh. In the next paragraphs evaluation cases including radiative heat transfer via an isothermal gray medium in a hexahedral, a J-shaped and a baffled cubic enclosure are presented.

5.1 A hexahedral enclosure with trapezoidal bases

The first quasi-3D benchmark test case considers radiative heat transfer in a hexahedral enclosure with trapezoidal bases, as illustrated in Figure 7. Two subproblems were encountered for this enclosure on a DELL^(R) T7400 workstation with 2 Intel^(R) Xeon^(R) E5410 4-core processors at 2.33GHz.

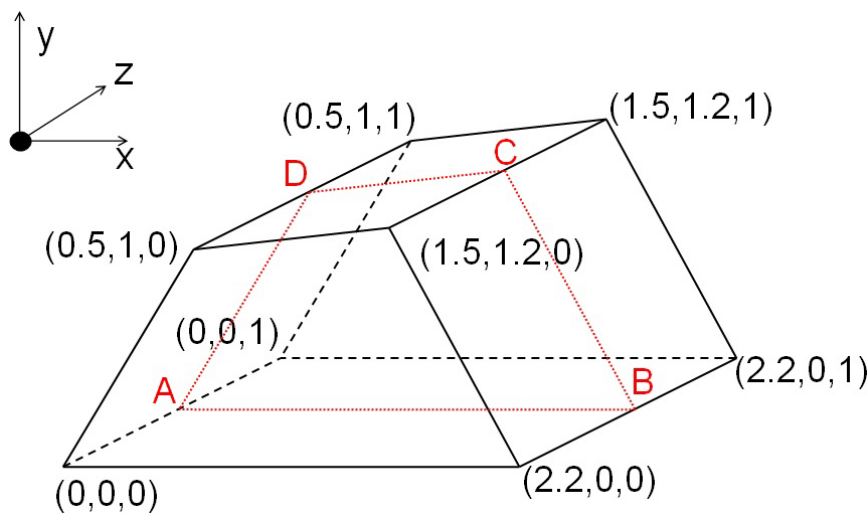


Figure 7: Dimensions of the hexahedral enclosure with trapezoidal bases.

For the first subcase, the enclosure is assumed to be composed by radiatively black ($\varepsilon=1$) and cold walls ($T_w=0$ K), except for the two trapezoidal bases ($z=0$ and $z=1$), in which symme-

try boundary conditions are imposed. The included medium is considered absorbing and emitting, but no scattering ($\sigma=0 \text{ m}^{-1}$), maintained at constant temperature ($T_m=100 \text{ K}$) with an absorbing coefficient equal to unity ($k_a=1 \text{ m}^{-1}$). The utilized initial mesh includes 8,507 nodes, 12,608 tetrahedrons 10,754 prisms and 28 pyramids, while for parallelization it is decomposed in two subdomains (Figure 8). For angular discretization, the “sphere” is divided in 16 azimuthal - 4 polar angles, along with the pixelation method. In Figure 9 the distributions of dimensionless incident radiative heat flux along the A-B (left) and the B-C (right) lines of the mesh for all the available spatial schemes are illustrated, compared with the exact ones of Murthy and Mathur [39], while in Figure 10 the distributions along the C-D (left) and the D-A (right) lines are shown. The above mentioned solutions are obtained after the radiative intensity residual is decreased at least four orders of magnitude, requiring approximately two seconds per iteration for the first order spatial scheme and five seconds per iteration for the second order ones. As far as the effectiveness of the spatial schemes is concerned, the second order ones extract more accurate results comparing with the first order one; as expected the schemes jointed with limiters derive better distributions as the simple second order scheme seems to overpredict the intensity flux near the cold wall boundaries.

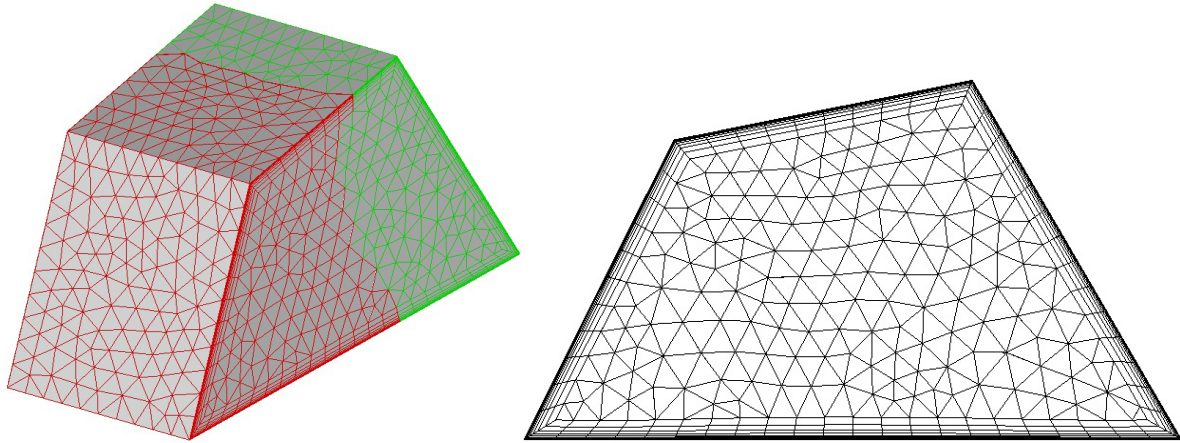


Figure 8: Utilized mesh (left) and mesh density on the face with $z=0$ (right) for the hexahedral enclosure.

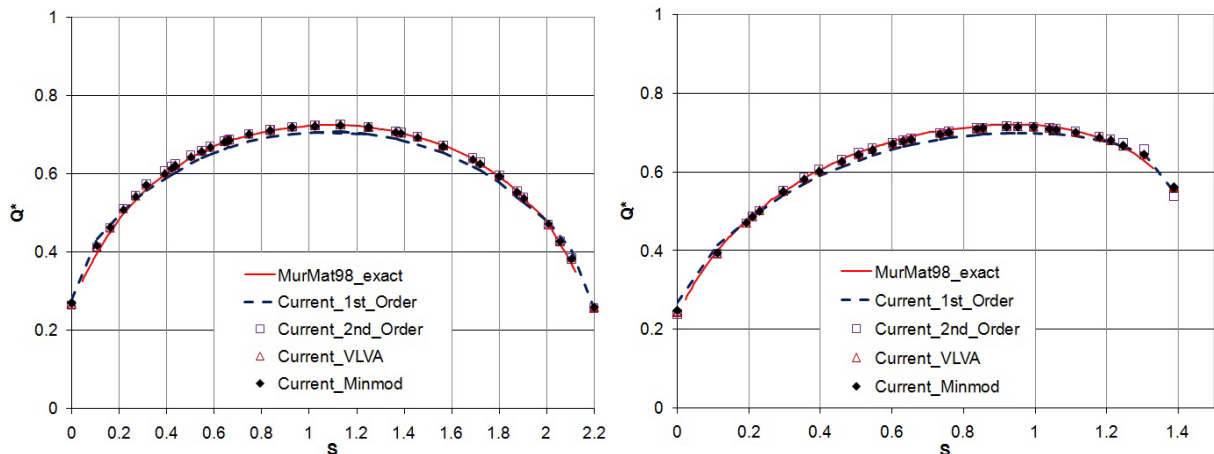


Figure 9: Distributions of dimensionless incident radiative heat flux along the A-B (left) and the B-C line (right).

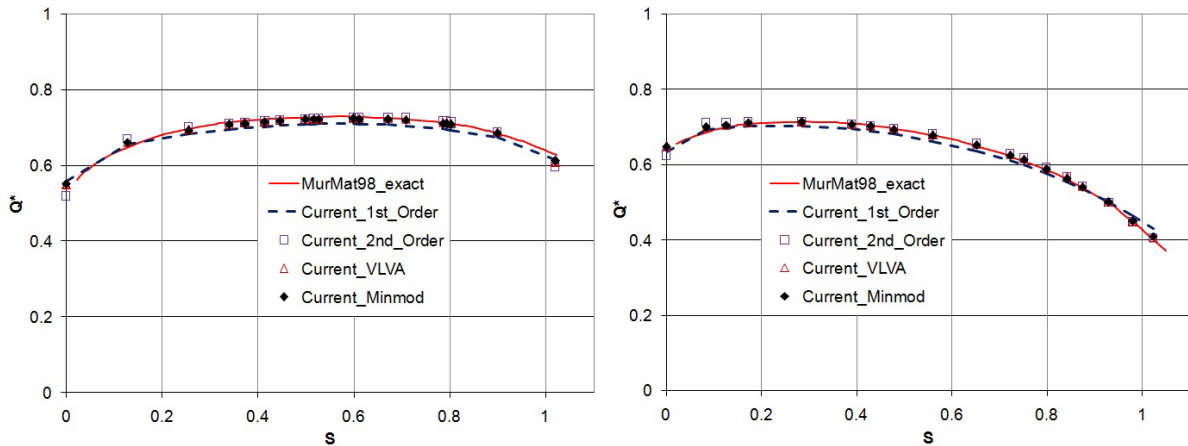


Figure 10: Distributions of dimensionless incident radiative heat flux along the C-D (left) and the D-A line (right).

In the second subcase the same conditions are imposed for the medium and the walls, except for the absorption coefficient, which takes three different values ($k_a=0.1 \text{ m}^{-1}$, $k_a=1 \text{ m}^{-1}$, $k_a=10 \text{ m}^{-1}$). The utilized mesh consists of 22,788 nodes, 53,692 tetrahedrons and 23,184 prisms, while for parallelization it is decomposed in two partitions, as illustrated in Figure 11. For angular discretization 20 azimuthal and 8 polar angles are employed along with the pixelation method. The attention in this subcase is towards the evaluation of the improvement, derived by the grid adaptation. As such the current mesh is refined, utilizing a criterion which targets the region up to 0.1 m away from the cold boundaries, resulting in a new grid, consisted of 83,305 nodes, 184,522 tetrahedrons and 92,736 prisms (Figure 12). Due to that the solution, derived by the refined mesh for the case with absorption coefficient equal to 10, didn't reach the respective reference one at the regions near the cold boundaries, a second grid adaptation was performed targeting the region of these solid angles, resulting in a new mesh, composed of 190,771 nodes, 428,159 tetrahedrons and 217,812 prisms (Figure 12). All the solutions were obtained after the radiative intensity residual is decreased at least five orders of magnitude, requiring approximately twelve seconds per iteration for the initial mesh, thirty seconds for the one after the first refinement and sixty seconds for the final grid. In Figure 13 the distributions of dimensionless incident radiative heat flux along the A-B line of the initial and the refined meshes for the three absorption coefficients, are presented, compared with the corresponding exact ones of Murthy and Mathur [39].

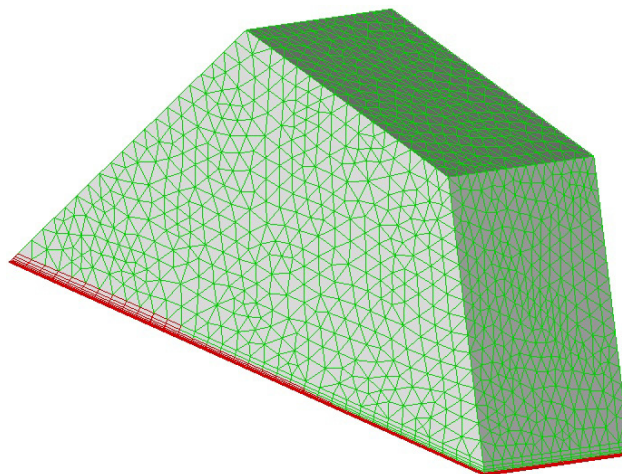


Figure 11: Utilized mesh for the hexahedral enclosure.

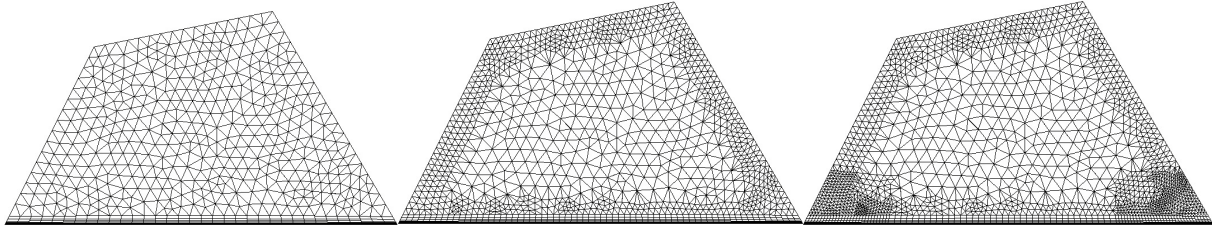


Figure 12: Mesh density on the face with $z=0$ before refinement, after the first refinement and after the second one.

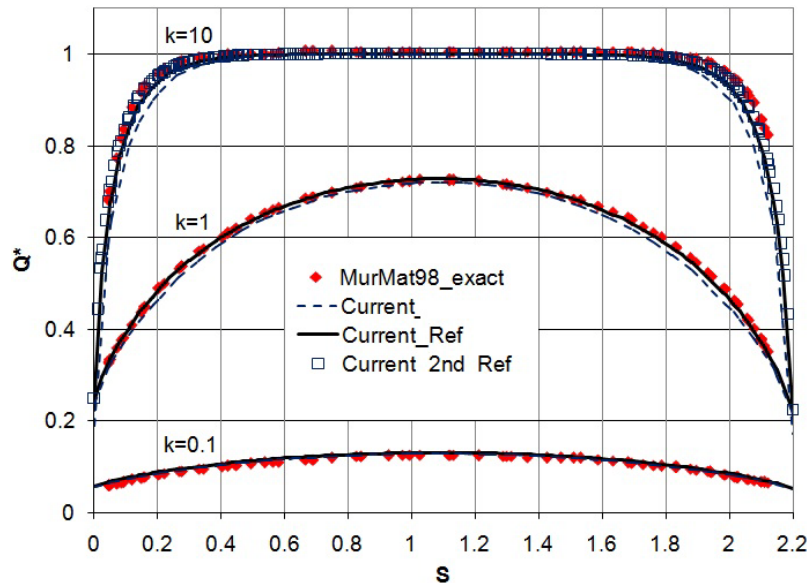


Figure 13: Distributions of dimensionless incident radiative heat flux along the A-B line for three different values of absorption coefficient, utilizing the initial and the refined meshes.

For the simulation with absorption coefficient equal to 0.1 there isn't any obvious improvement. On the contrary for the other subcases, the difference between the initial and the refined grids is evident, revealing the ability of h-refinement to derive more accurate solutions, without the need to start from the beginning the generation of a new finer grid. Although the improvement, provided by grid adaptation, isn't so important, compared to the one derived by the second order accurate schemes, it can be proved helpful, depending on the examined problem.

5.2 A J-shaped enclosure

The second test case concerns radiative heat transfer in a J-shaped enclosure, as illustrated in Figure 14. It includes an absorbing and emitting cold medium ($T_m=0$ K), while all the walls are considered black ($\varepsilon=1$) and cold ($T_w=0$ K), except for the upper one at $y=2.4$ maintained at constant temperature equal to 100K and the two bases ($z=0$ and $z=1$), in which symmetry boundary conditions are imposed. The utilized mesh is composed of 4,040 nodes, 11,132 tetrahedrons, and 2,800 prisms, while for its parallelized simulation it is divided in two partitions (Figure 15). A quite dense angular discretization of 30 azimuthal and 4 polar angles was utilized along with the pixelation approach, due to the significant ray effect, which was encountered. A value of 0.01 m^{-1} is assigned to the absorption coefficient, while the scattering coefficient remains equal to zero ($\sigma_s=0$). In Figure 16 the dimensionless incident radiative heat flux distributions along the ABCD line for all the available spatial schemes are illustrated, compared with the computed ones of Man Young Kim et al. [9]. The results were obtained

after radiative intensity residual was decreased at least four orders of magnitude, while the simulation for the first order scheme lasted about 5 minutes and for the second order ones about 14 minutes on the same to the previous case workstation. A deviation between the results of the first order scheme and the second order ones is clearly distinguished in the areas near the points A, B and C, proving the potential of the latter schemes for more accurate predictions even in relatively coarse grids. In addition, the simple second order scheme seems to mispredict slightly the radiative intensity fluxes in specific regions (i.e. point B), comparing its results with these of the schemes enhanced with limiters.

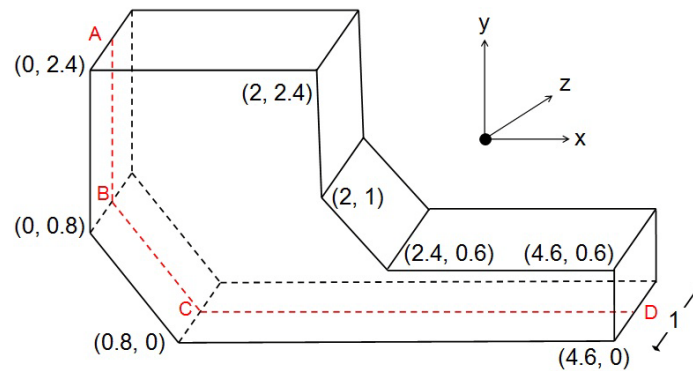


Figure 14: Dimensions of the J-shaped enclosure.

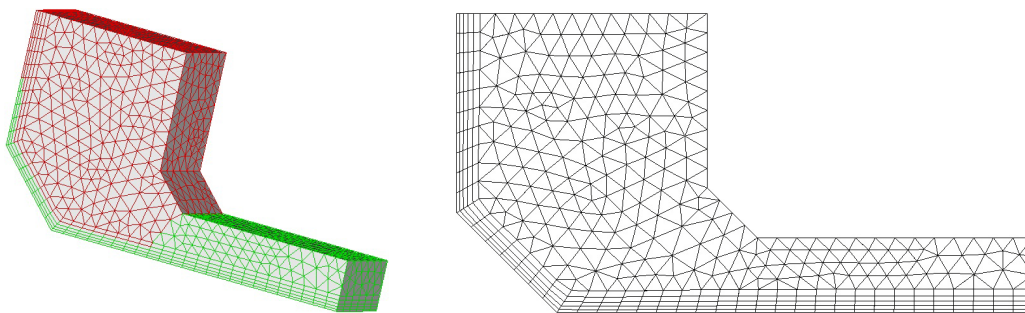


Figure 15: Utilized mesh (left) and mesh density on the face with $z=0$ (right).

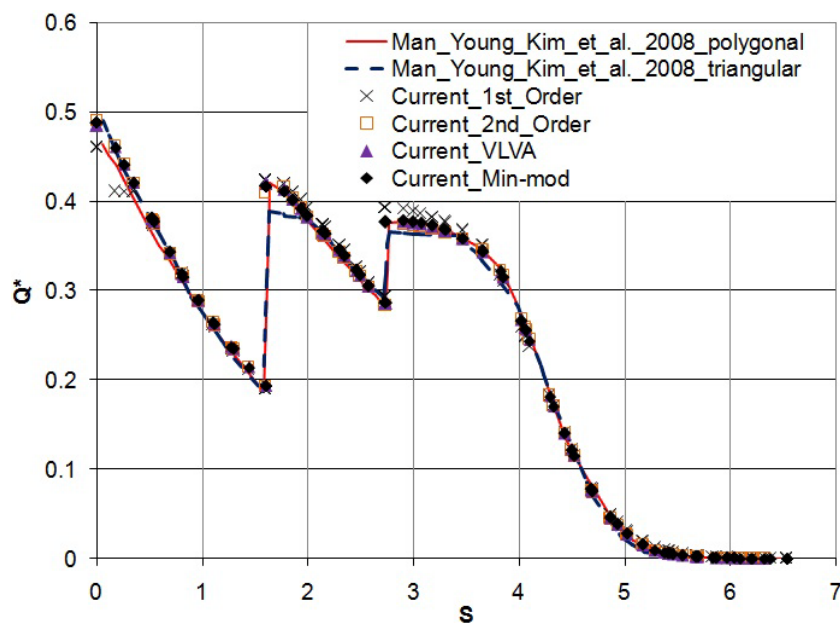


Figure 16: Distributions of dimensionless incident radiative heat flux along the ABCD line.

5.3 A cubic enclosure with three baffles

A cubic enclosure with three baffles (Figure 17), including an absorbing and emitting medium, maintaining a constant heating power $E_m=10\text{W/m}^2$ is examined in this case. All the walls, including the three baffles, are considered black ($\varepsilon=1$) with a constant emissive power $E_w=1\text{W/m}^2$, except for the two bases ($z=0$ and $z=1$), in which symmetry boundary conditions are imposed. The utilized mesh includes 21,228 nodes, 28,212 tetrahedrons and 29,016 prisms, while for parallelization it is divided in two subdomains (Figure 18). For angular discretization 24 azimuthal and 4 polar angles are employed along with the pixelation method. The results were extracted after radiative intensity residual was decreased at least six orders of magnitude, requiring (on a PC with an AMD FX(tm)-8120 Eight-Core Processor at 3.10 GHz) approximately five seconds per iteration for the first order scheme and fourteen seconds per iteration for the second order ones. In Figure 19 the distributions of incident radiative heat flux (Q in kW/m^2) along the ABCD line for the four available spatial schemes are illustrated, compared to the corresponding computed with Z-M (Zone-Method) ones of Coelho et al. [40]. As expected, a significant improvement to the accuracy of the computed fluxes implementing the second order schemes is identified; a slight overestimation by the simple second order scheme is observed again, unlike the schemes coupled with the limiters, due to the unbounded reconstructed values of radiative intensity.

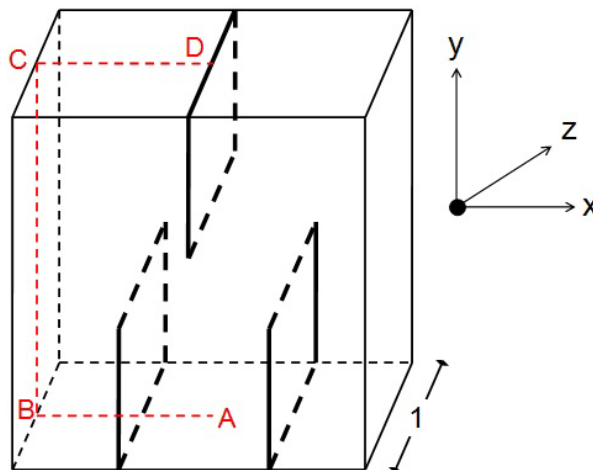


Figure 17: Dimensions of the cubic enclosure with the three baffles.

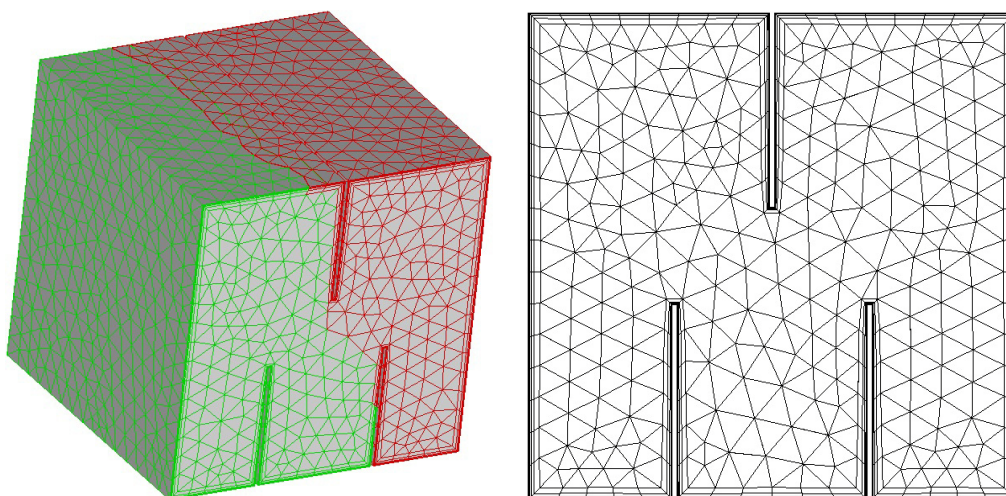


Figure 18: Utilized mesh (left) and mesh density on the face with $z=0$ (right).

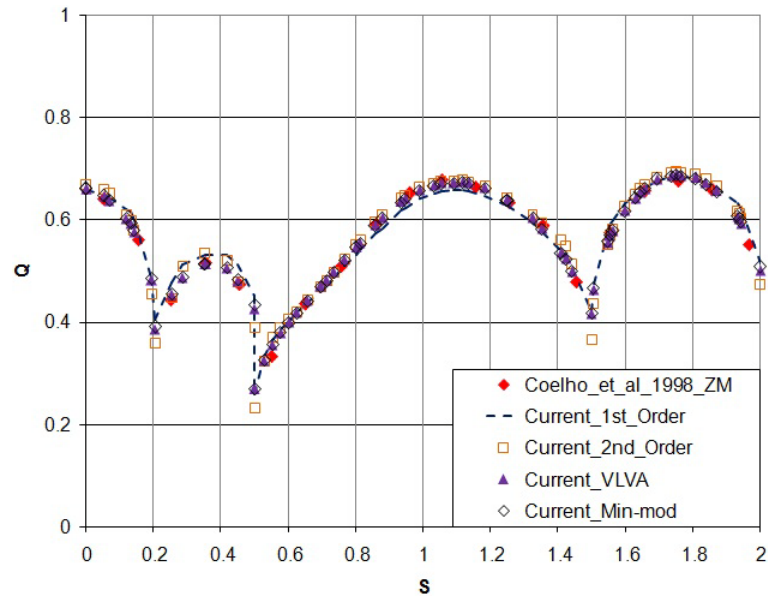


Figure 19: Distributions of incident radiative heat flux along the ABCD line for the initial mesh with black enclosures.

In order to assure that the differentiation between the first and the second order spatial schemes originates indeed from the upgrading of the spatial resolution, a twice dense mesh was utilized, including 46,198 nodes, 58,624 tetrahedrons and 66,024 prisms, in which all the available schemes were implemented again. A slight improvement is noticed for the first and the simple second order scheme in the region between 0.2m and 0.4m, while for the schemes enhanced with limiters no difference can be identified (Figure 20).

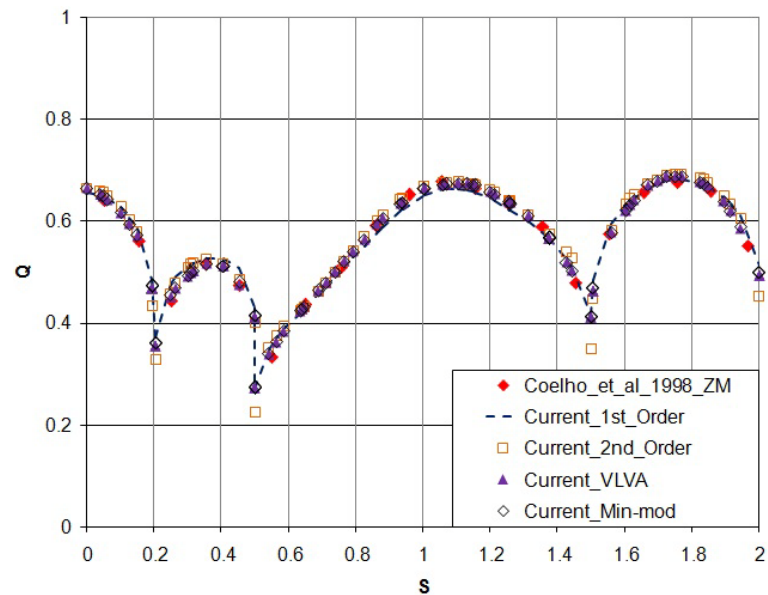


Figure 20: Distributions of incident radiative heat flux along the ABCD line for the twice dense mesh with black enclosures.

An additional case was encountered with grey walls instead, considering an emissivity value equal to 0.8 for the walls and 0.6 for the baffles. In Figure 21 the corresponding distributions of incident radiative heat flux are presented, all closely compared to the ones computed with Z-M (Zone-Method) of Coelho et al. [40].

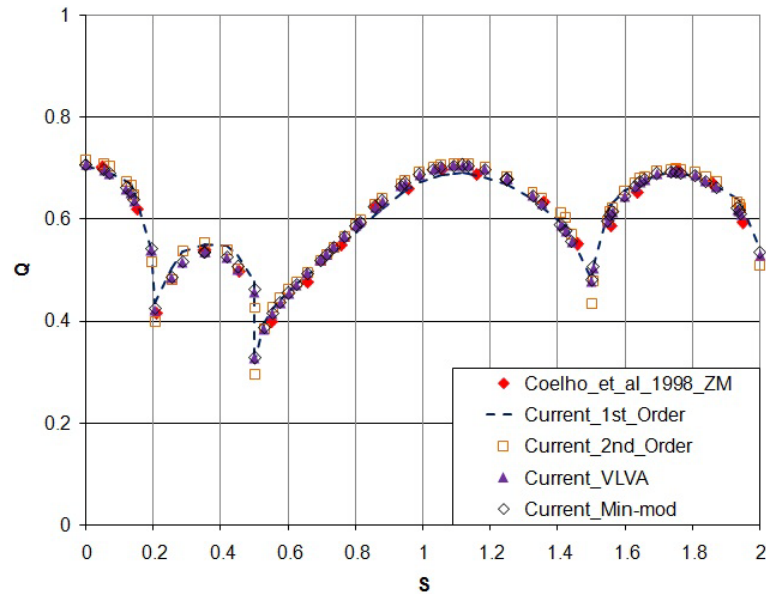


Figure 21: Distributions of incident radiative heat flux along the ABCD line for the initial mesh, with gray enclosures.

6 CONCLUSIONS

In this study an algorithm using a second order scheme in space and time, along with the h-refinement technique and a precomputational pixelation method is developed to improve the accuracy of radiative heat transfer predictions in three-dimensional unstructured hybrid grids. Though the previous methods are well established methodologies in CFD, they are rarely implemented in the prediction of radiative heat transfer. As the numerical results reveal, the higher order spatial schemes, especially these jointed with slope limiters, mitigate sufficiently the false scattering, derived by the finite spatial discretization. Their employment along with a second order in time method for the iterative solution of the time dependent RTE prevents the development of oscillations during the simulation, which is usually met when the second order spatial scheme is coupled to the standard iterative solution of the RTE [11, 12]. In addition, h-refinement technique revealed its potential to improve the accuracy of the algorithm during the progress of the solution, when the utilized mesh isn't fine enough, avoiding the generation of a finer mesh from the beginning. Although their employment increases the computational and memory requirements, they can be assumed relatively negligible, considering the accuracy improvement succeeded in coarse grids.

ACKNOWLEDGEMENTS

Part of this work was funded by ELXIS Engineering Consultants S.A. and the EUROSTARS Project (E!5292) "Structural and aerodynamic design of TUNNELS under Fire Emergency Conditions".

REFERENCES

- [1] G.D. Raithby and E.H. Chui, A finite-volume method for predicting a radiant heat transfer in enclosures with participating media, *J. Heat Transfer*, **112**, 415-423, 1990.

-
- [2] G. Kim, S. Kim and Y. Kim, Parallelized unstructured-grid finite volume method for modeling radiative heat transfer, *J. Mech. Sci.Tech.*, **19**, 1006-1017, 2005.
- [3] E.H. Chui, G.D. Raithby and P.M.J. Hughes, Prediction of radiative transfer in cylindrical enclosures with the finite volume method, *J. Thermophys. Heat Transfer*, **6**, 605-611, 1992.
- [4] J.Y. Murthy and S.R. Mathur, Radiative heat transfer in axisymmetric geometries using an unstructured finite-volume method, *Num. Heat Transfer B*, **33**, 397-416, 1998.
- [5] S.W. Baek and M.Y. Kim, Modification of the discrete ordinates method in an axisymmetric cylindrical geometry, *Num. Heat Transfer B*, **31**, 313-326, 1998.
- [6] M.Y. Kim, S.W. Baek and J.H. Park, Unstructured finite-volume method for radiative heat transfer in a complex two-dimensional geometry with obstacles, *Num. Heat Transfer B*, **39**, 617-635, 2001.
- [7] M.B. Salah, F. Askri, K. Slimi and S.B. Nasrallah, Numerical resolution of the radiative transfer equation in a cylindrical enclosure with the finite volume method, *Int. J. Heat Mass Transfer*, **47**, 2501-2509, 2004.
- [8] P. Talukdar, M. Steven, F.V. Issendorff and D. Trimis, Finite volume method in 3-D curvilinear coordinates with multiblocking procedure for radiative transport problems, *Int. J. Heat Mass Transfer*, **48**, 4657-4666, 2005.
- [9] M.Y. Kim, S.W. Baek and S.I. Park, Evaluation of the finite-volume solutions of radiative heat transfer in a complex two-dimensional enclosure with unstructured polygonal meshes, *Num. Heat Transfer B*, **54**, 116-137, 2008.
- [10] C. Kim, M.Y. Kim, M.Y. Yu and S.C. Mishra, Unstructured polygonal finite-volume solutions of radiative heat transfer in a complex axisymmetric enclosure, *Num. Heat Transfer B*, **57**, 227-239, 2010.
- [11] G.N. Lygidakis and I.K. Nikolos, Using the finite-volume method and hybrid unstructured meshes to compute radiative heat transfer in 3-D geometries, *Num. Heat Transfer B*, **62**, 289-314, 2012.
- [12] G.N. Lygidakis and I.K. Nikolos, A parallelized node-centered finite volume method for computing radiative heat transfer on 3D unstructured hybrid grids, *11th Bien. Conf. Engin. Sys. Des. Anal. (ASME-ESDA 2012)*, Nantes, France, 2 - 4 July, 2012.
- [13] G.D. Raithby, Discussion of the finite volume method for radiation, and its application using 3D unstructured meshes, *Num. Heat Transfer B*, **35**, 389-405, 1999.
- [14] J.C. Chai, H.S. Lee and S.H. Patankar, Ray effect and false scattering in the discrete ordinates method, *Num. Heat Transfer B*, **24**, 373-389, 1993.
- [15] P.J. Coelho, Bounded skew high-order resolution schemes for the discrete ordinates method, *J. Computational Physics*, **175**, 412-437, 2002.
- [16] R. Capdevila, C.D. Perez-Segarra and A. Oliva, Development and comparison of different spatial numerical schemes for the radiative transfer equation resolution using three-dimensional unstructured meshes, *J. Quant. Spectrosc. Radiat. Transfer*, **111**, 264-273, 2010.
- [17] J.Blazek, *Computational fluid dynamics: principles and applications*, Kidlington, Elsevier Science, 2001.

- [18] G.D. Van Albada, B. Van Leer and W.W. Roberts, A comparative study of computational methods in cosmic gas dynamics, *J. Astrophys. Astron.*, **108**, 46-84, 1982.
- [19] P.K. Sweby, High resolution schemes using flux limiters for hyperbolic conservation laws, *SIAM J. for Numer. Anal.*, **21**, 995-1011, 1984.
- [20] B. Hunter and Z. Guo, Comparison of the discrete-ordinates method and the finite-volume method for steady-state and ultrafast radiative transfer analysis in cylindrical coordinates, *Num. Heat Transfer B*, **59**, 339-359, 2011.
- [21] Z.M. Tan and P.F. Hsu, Transient radiative heat transfer in three-dimensional homogenous and non homogenous participating media, *J. Quant. Spectrosc. Radiat. Transfer*, **73**, 181-194, 2002.
- [22] J.C. Chai, One-dimensional transient radiation heat transfer modeling using a finite-volume method, *Num. Heat Transfer B*, **44**, 187-208, 2003.
- [23] M.H. Lallemand, Etude de schemas Runge-Kutta a 4 pas pour la resolution multigrille des equations d' Euler 2D, *Raport de Recherche, INRIA*, 1988.
- [24] Y. Kallinderis, A 3-D finite volume method for the Navier Stokes equations with adaptive hybrid grids, *Applied Numerical Mathematics*, **20**, 387-406, 1996.
- [25] A. Khawaja, T. Minyard and Y. Kallinderis, Adaptive hybrid grid methods, *Computer Methods in Applied Mechanics and Engineering*, **180**, 1231-1245, 2000.
- [26] C. Kavouklis and Y. Kallinderis, Parallel adaptation of general three-dimensional hybrid meshes, *J. Computational Physics*, **229**, 3454-3473, 2010.
- [27] R. Lohner, Finite element methods in CFD: grid generation, adaptivity and parallelization, AGARD-R-787, *Proc. of the AGARD-FDP-VKI special course at VKI*, Rhode-Saint-Genese, 2-6 March, 1992.
- [28] G.N. Lygidakis and I.K. Nikolos, An unstructured node-centered finite volume method for computing 3D viscous compressible flows on hybrid grids, *7th Int. Cong. on Comp. Mech. (7th GRACM)*, Athens, Greece, 30 June - 2 July, 2011.
- [29] H. Jimbo, R. Liming and T. Heping, Effect of anisotropic scattering on radiative heat transfer in two-dimensional rectangular media, *J. Quant. Spectrosc. Radiat. Transfer*, **78**, 151-161, 2003.
- [30] G.C. Clark, C.M. Chu and S.W. Churchill, Angular distribution coefficients for radiation scattered by a spherical particle, *J. Opt. Soc. of Am.*, **47**, 81-84, 1957.
- [31] J.E. Hunt, The Generation of angular distribution coefficients for radiation scattered by a spherical particle, *J. Quant. Spectrosc. Radiat. Transfer*, **10**, 857-864, 1970.
- [32] J. Liu, H.M. Shang and Y.S. Chen, Development of an unstructured radiation model applicable for two-dimensional planar, axisymmetric, and three-dimensional geometries, *J. Quant. Spectrosc. Radiat. Transfer*, **66**, 17-33, 2000.
- [33] A. Fiterman, R. Ben-Zvi and A. Kribus, DOTS: Pseudo-time-stepping solution of the discrete ordinate equations, *Num. Heat Transfer B*, **35**, 163-183, 1999.
- [34] T.J. Barth, Aspects of unstructured grids and finite-volume solvers for the Euler and Navier-Stokes equations, AGARD-R-787, *Proc. of the AGARD-FDP-VKI special course at VKI*, Rhode-Saint-Genese, 2-6 March, 1992.

- [35] B. Smith, P. Bjorstad and W. Gropp, *Domain Decomposition. Parallel multilevel methods for elliptic partial differential equations*, Cambridge University Press, Cambridge, 1996.
- [36] METIS: <http://glaros.dtc.umn.edu/gkhome/views/metis>.
- [37] S. Lanteri, Parallel solutions of compressible flows using overlapping and nonoverlapping mesh partitioning strategies, *Parallel Comput.*, **22**, 943–968, 1996.
- [38] T.K. Kim and H. Lee, Effect of anisotropic scattering on radiative heat transfer in two-dimensional rectangular enclosures, *Int. J. Heat Mass Transfer*, **31**, 1711-1721, 1988.
- [39] J.Y. Murthy and S.R. Mathur, A finite volume method for radiative heat transfer using unstructured meshes, *36th Aerospace Sciences Meeting & Exhibit (AIAA98-0860)*, Reno, NV, 12 - 15 January, 1998.
- [40] P.J. Coelho, J.M. Goncalves and M.G. M.G. Carvalho, Modelling of radiative heat transfer in enclosures with obstacles, *Int. J. Heat Mass Transfer*, **41**, 745-756, 1998.

THE INFLUENCE OF PUMPING PARAMETERS IN FLUID-DRIVEN FRACTURES

E. Sarris and P. Papanastasiou

Department of Civil and Environmental Engineering
University of Cyprus
P.O. BOX 20537, 1678 Nicosia, Cyprus
E-mail: esarris@ucy.ac.cy, panospap@ucy.ac.cy

Keywords: Hydraulic fracturing, Cohesive zone, Poroelastoplasticity, Fracture mechanics.

Abstract. *In the present work we investigate the main pumping parameters that influence a fluid driven fracture in both cohesive poroelastic and poroelastoplastic weak formations. These parameters include the fluid viscosity and the injection rate.*

The fracture is driven in weak permeable porous formation by injecting an incompressible viscous fluid at the fracture inlet assuming plane strain conditions. Fluid flow in the fracture is modeled by lubrication theory. Pore fluid movement in the porous formation is based on the Darcy law. The coupling follows the Biot theory while the irreversible rock deformation is modeled with the Mohr-Coulomb yield criterion with associative flow rule. Fracture propagation criterion is based on the cohesive zone approach. Leak-off is also considered. The investigation is performed numerically with the finite element method to obtain the fracture length, opening and propagation pressure vs time.

We demonstrate that the pumping parameters are influencing the fracture geometry in weak formations through the diffusion which creates back stresses and large plastic zones. It is shown that the back stresses act as a barrier and larger net pressures are needed to propagate the fracture. This effect in the poroelastoplastic formation is responsible for the creation of larger plastic zones. These influences for large viscosity or high injection rates result in larger fracture profiles and propagation pressures. These findings may explain partially the discrepancies in net-pressures between field measurements and conventional model predictions.

1 INTRODUCTION

The hydraulic fracturing process has been employed widely and successfully by the industry to enhance the production of oil and gas from underground reservoirs for many years. Lately the need for new environmental friendly fuels has oriented the research in exploiting unconventional gas reservoirs utilizing novel hydraulic fracturing techniques. Furthermore, based on the applicability of the technique it not surprising that it's one of the most attractive subjects for research by many disciplines. Among the most successful applications of the hydraulic fracturing technique is the preconditioning of ore rock to promote caving, the determination of the insitu stress in rock, the formation of barriers to block contamination, stimulate geothermal reservoirs for heat production and recently the underground storage of carbon dioxide. Hydraulic fracturing is not only a man-made technique, there are also physical processes that present similarities like the magma-driven fractures and the turbulent water flow driving basal fracture in glacier beds [1, 2]. Recently, some research works have showed that industrial numerical models rely on the ability to simulate fracture propagation under realistic non-uniform insitu conditions so as to predict accurately the complicated fracture geometry with the even more complicated fracture fluid rheology. There is no existing methodology to accurately measure fracture geometry during and after the process thus numerical modelling is of great importance [3,4].

A large number of studies in hydraulic fracturing have been devoted to the theoretical understanding the near tip effects [4-6]. These contributions have helped in the establishment of scaling framework by formulating mathematically the fluid driven problem to obtain analytical and semi analytical solutions. The focus of their work was based on the injection of incompressible Newtonian or non-Newtonian fluids in elastic impermeable and permeable formations for simple fracturing geometries like the plane strain KGD or the PKN and the axisymmetric penny shape models. The asymptotic solutions obtained for these idealized models serve as a benchmark for numerical simulations. These research works have identified two competing energy dissipation mechanisms and two competing storage mechanisms. In the first case, energy is dissipated in creating and extending the fracture in the porous formation and by viscous flow inside the fracture. In the second case, the storage mechanisms are the fluid leak-off stored in the porous formation and the fluid stored in the fracture. Asymptotic solutions of such processes generally correspond to a fracture driven under limiting conditions or when one of the energy dissipation mechanisms associated with the viscous fluid flow, the toughness of the material, the fluid storage in the formation or the fluid storage in the fracture can be neglected when another dominates. These asymptotic regimes are as follows [4]: (i) storage toughness, (ii) storage viscosity, (iii) leak-off toughness (iv) leak-off viscosity. Nonetheless, due to the significant limitations of the analytical models listed above, numerical models are utilized to overcome the rigorous mathematical difficulties that are associated with the existence of the singularity at the fracture tip and the fluid lag region of the fracture by using the cohesive zone approach. The cohesive fracture growth has been extensively used to model fracture growth in porous and non-porous materials.

The usual parameter that is available and can be measured in the field is the wellbore pressure and it is not surprising that many contributors have devoted effort in its accurate prediction during a treatment. Standard fracture simulators usually underestimate this parameter as they do not account for irreversible effects (poroelastoplastic). A research on net pressures (difference between fracturing fluid pressure and the far-field confining stress) indicated that the net pressures encountered in the field can be 50-70% higher than the predicted ones [7]. This dictates the importance of the poroelastoplastic behavior of weak rocks in hydraulic fracturing. Recently, a research work based on numerical studies has showed that accounting for

poroelastoplasticity in the simulations, the fracture width is 22.25% wider than the elastic fracture and 15.2% wider than the poroelastic. Accordingly, the pressure needed to propagate a poroelastoplastic fracture, at wellbore, is 20.9% higher from a poroelastic and 31.8% higher from the elastic fracture [8]. All these studies had ignored the influence of the pumping parameters and its effects on the porous rock deformations.

In this research work we extend the recent work of [8] in order to evaluate the influence of the pumping parameters of the diffusion process in fluid driven fractures for both poroelastic and poroelastoplastic conditions. The yielding mechanism used in the present work is associated with frictional sliding, either along particles or micro-cracks. The rock is modeled by the Mohr-Coulomb flow theory, the fracture propagation criterion used is the cohesive zone law, the fluid flow inside the fracture is described by lubrication theory and the pore fluid movement inside the porous domain is successfully modeled with the Darcy law. With the solution of the numerical model described above we have found that the pumping parameters affect the diffusion process in the cases examined, poroelastic and poroelastoplastic. The diffusion process which is a major mechanism in hydraulic fracture operations influences further the obtained results on the fluid pressures, fracture dimensions and plastic yielding. Furthermore results are also influenced by the transition from the fracture toughness dominated regime to the viscosity dominated regime. This is another important feature of our numerical model for predicting fractures in both fracture toughness and viscosity dominated regimes. The results obtained are important for improving numerical simulators of modeling hydraulic fracturing in particular. We focused on short fractures in weak formations as such fractures can be used for sand control applications. Furthermore, these results can be used in the prediction of vertical fractures and containment in shale-natural gas stimulations where there are serious environmental concerns on the risk of ground-water contamination.

This paper is organized as follows: in the second part, we describe the governing equations that are involved in the physical processes: the fluid flow, the rock deformation, the fracture propagation, the methodology that was adopted in the numerical model and the scaling of the plastic zones. In the third part, we present and critically evaluate the numerical results and highlight the conclusions on the important parameters.

2 MODELING METHODOLOGY

In a typical hydraulic fracturing treatment, the fracturing fluid is blended with proppant material and injected into the wellbore that is appropriately cased and perforated so as to fracture the porous reservoir in preferential paths. When the injection of the fracture blend is performed at high rates, the pressure that is build up splits and drives the fracture hydraulically in the direction where the energy needed to create newly surface is minimized and usually this direction is perpendicular to the minimum insitu stress [1,8]. The construction of numerical models that will describe accurately the aforementioned process calls for understanding the involved four important coupled processes [9,3,4]. These coupled phenomena include: (i) fluid flow inside the fracture pressurizes the fracture faces and the porous formation deforms; (ii) viscous fluid flow inside the fracture; (iii) fracture and porous formation exchange fluids; and (iv) fracture propagation is a moving boundary problem. Therefore, simulating the above processes requires the solution of a system of non-linear partial differential equations that are associated with the above coupled processes.

The objective of this research work is to investigate the main parameters influencing the diffusion process when the fracture dominated regime goes from toughness to viscosity dominance and furthermore how the diffusion process caused from this situation affects the development of the plastic zones. The leak-off is treated as unidirectional (1D-isotropic) and the scope is to investigate any effects associated with the coupled processes such as changes in

the deformation due to diffusion of fracture and pore fluid and how the flow and pressure is influenced by mechanical deformation. Additionally, the fluid losses that surround the fracture tip area and the bulk of the fracture are capable to generate back stresses. This effect cannot be ignored in hydraulic fracture operations as these non-linear mechanisms are capable to generate excessive pore pressures or alter the fluid characteristics of the fracturing fluids. Furthermore, they may explain the differences observed in net-pressures between field measurements and model predictions.

2.1 Cohesive zone model

There are few studies utilizing the cohesive zone model in fluid driven fractures. Some important studies in this area include the important work of [10] in which they used the cohesive zone approach to model the fracture process in impermeable and permeable rocks. Other important contributions are those of Papanastasiou [11,12] in which he has successfully modeled coupled fluid-solid driven fractures and linked the net pressures with plastic yielding associated with the fracture process. Hydraulic conductivity from the fracture towards the formation was analyzed by [13] which they proposed the influence of the transversal conductivity with the aim of applying these elements in hydro-mechanical diffusion problems. Recently, [14,15] have performed numerical simulations based on a variable stiffness bilinear traction separation model to investigate the influence of the cohesive zone in hydraulic fracturing in both, porous and non porous weak formations. In another study, [16] used the cohesive zone model to analyze viscosity dominated plane strain and penny shape hydraulic fractures. An enhanced three noded cohesive element was developed by [17] to model hydraulic fractures in permeable formations. They further analyzed the influence of permeability, fracture fluid viscosity and leak-off on a poroelastic fracture and validated their model with asymptotic solutions.

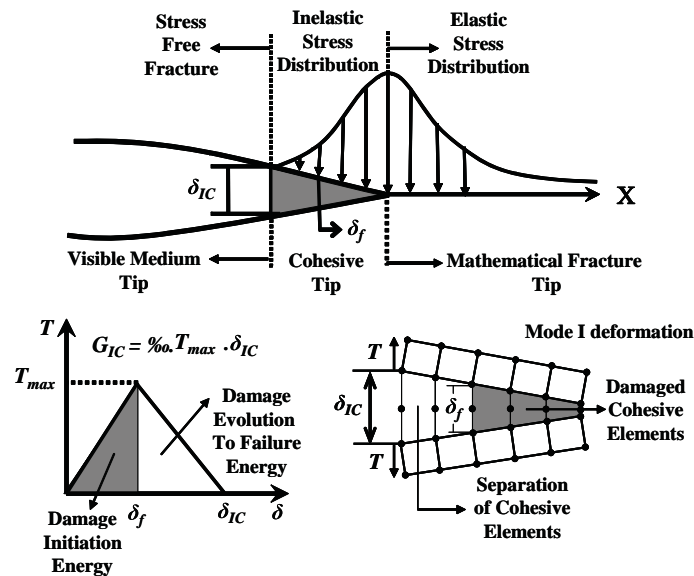


Figure 1: Representation of the cohesive fracture process

As stated in the abundant literature, the concept of the cohesive zone is laid on the fact that the tractions can be transferred through the fictitious fracture faces in the cohesive zone, also called process zone (Figure 1). If analyzed in the micro-mechanical scale, this process zone is the local zone ahead of the fracture tip where micro voids and micro cracks initiate and grown until coalesce with the main body of the fracture.

The transferred normal traction is a function of the separation and falls to zero at a critical opening and then the fracture propagates. The evolution of the fracture is governed by energy balance between the work of the external loads and the sum of the bulk energy of the unfractured part and the energy dissipated in the fracture process (figure 1). The constitutive behavior of the cohesive zone is defined by the traction-separation relation derived from laboratory tests. The traction-separation constitutive relation for the surface is such that with increasing separation, the traction across this cohesive surface reaches a peak value and then decreases and eventually vanishes, permitting for a complete separation.

Simple cohesive zone models can be described by two independent parameters which are usually, for mode-I plane strain, the normal work of separation or the fracture energy G_{IC} and either the tensile strength σ_t or the complete separation length δ_{IC} . An additional parameter in these models is the slope of the initial loading which may define a range from rigid-softening to elastic-softening response under tensile stress-state. The area under the traction-separation curve equals with fracture energy G_{IC} which is the work needed to create a unit area of fully developed fracture. Rice has showed that the critical value J-integral can be equivalent with the critical value of the fracture energy $J_{IC} = G_{IC}$, when the size of the cohesive zone is small compared to the fracture length. For elastic solids this energy is related to the rock fracture toughness K_{IC} through [18]:

$$K_{IC} = \sqrt{G_{IC} \cdot E^*} \quad (1)$$

where E^* is the plain strain modulus $E/(1-\nu^2)$. The rock fracture toughness can be calculated from laboratory tests. For the case of the rigid-softening behavior the traction-separation relation is uniquely determined by:

$$\sigma = \sigma_t(1 - \delta/\delta_{IC}) \quad (2)$$

where σ_t is the uniaxial tensile strength of the rock and δ_{IC} is the critical opening displacement at which σ falls to zero. The value of δ_{IC} is given by:

$$\delta_{IC} = \frac{2K_{IC}^2(1-\nu^2)}{E\sigma_t} \quad (3)$$

For the case of the elastic loading the cohesive constitutive relations were augmented and modified to take into account the initial part of the curve as follows [8]:

$$\sigma = \sigma_t(\delta/\delta_{el}) \quad (4)$$

With the limit of elastic deformation is given by:

$$\delta_{el} = \sigma_t/k_n \quad (5)$$

where k_n is the stiffness of the traction-separation relation in the loading regime with units of [MPa/m]. In the post-peak softening regime the cohesive constitutive relation is given by:

$$\sigma = \sigma_t \left[1 - \frac{(\delta - \delta_{el})}{(\delta_{IC} - \delta_{el})} \right] \quad (6)$$

The assumption that the cohesive zone localizes, due to its softening behavior, into a narrow band ahead of the visible fracture is very convenient for finite element analysis where the softening behavior can be modeled by cohesive zone elements [8, 14, 15].

2.2 Governing equations of fluid flow

The mechanical response of porous formations is usually complicated by irreversible deformation coupled with diffusion of pore fluid. However, minimizing the effect of the pore fluid diffusion to investigate the influence of the irreversible deformations represents only a small part of the problem. Furthermore, the fluid driven problem in an inelastic saturated porous media further complicates the analysis as the diffusion of the fracturing fluid in the rock formation introduces some rate-dependency in the overall solution and behavior of the numerical model. Thus it is necessary to develop an appropriate numerical model to further investigate the coupling of pore pressure diffusion with non-linear rock deformation and damage criteria.

The type of flow constitutive response comprises as longitudinal and transversal flow along the fracture walls [13, 19]. The numerical model for the fluid flow is constructed for the complete length of the predetermined fracture path. There is one to one correspondence between the plane strain “flow” and “domain” elements at the corner nodes along the fracture path, ensuring that the fluid mass is conserved across their surface. The lubrication theory assumes laminar flow (uniformly viscous incompressible Newtonian) and it accounts for the time dependent rate of the fracture opening. The continuity equation which imposes the conservation of mass in one dimensional flow in the longitudinal direction is as follows:

$$\frac{\partial w}{\partial t} + \frac{\partial \mathbf{q}}{\partial x} + q_i = Q \quad (7)$$

where \mathbf{q} is the mass flow rate along fracture length x , q_i is the fluid transverse loss in the rock mass, w is the fracture opening and Q is the injection rate (B.C).

For a fluid flow between parallel plates the lubrication equation relates the pressure gradient to the fracture width for a Newtonian fluid of viscosity μ , yields from the conservation of momentum balance:

$$\mathbf{q} = v.w = -\frac{w^3}{12\mu} \frac{\partial p}{\partial x} \quad (8)$$

where p denotes the fluid pressure and v the average velocity of the fluid on a cross-section in the fracture. At this point the effective channel viscosity μ^* can be defined related to the fluid viscosity through the relation $\mu^* = 12 \mu$. Equation (8) determines the pressure profile along the fracture from the local width and local flow rate.

The transverse flow which describes the leak-off from the fracture to the surrounding formation is evaluated as a localized potential drop by using a six node cohesive element (figure 1). In these elements, the boundary nodes are shared with the nodes of the adjacent continuum formation so that the nodes of the continuum elements represent the potentials in the pore system on each side of the cohesive interface. The central nodes of the cohesive elements represent the average potential of the fluid in the fracture considered as a channel. According to this distribution of hydraulic head within the cohesive elements, two different potential drops exist as [13]:

$$q_i^u = k_i^u (h^u - h^i) \quad q_i^d = k_i^d (h^d - h^i) \quad (9)$$

where q_i is the transversal fluid loss, k_t is the transversal transmissivity, h^i is the hydraulic head inside the fracture. The superscript u and d stand for up and down element faces respectively. Combining equations (7-9) we obtain the Reynolds lubrication equation as [20]:

$$\frac{\partial w}{\partial t} + k_t^u (h^u - h^i) + k_t^d (h^d - h^i) = \frac{1}{12\mu} \left(\frac{w^3 \partial p}{\partial x} \right) + Q \quad (10)$$

The terms h^i , h^u and h^d are uniquely related to the fluid pressure gradients that are actually the tractions acting on the open surfaces of the cohesive elements. According to equation (10) as the cohesive elements undergo complete failure, the cohesive tractions vanish and there is no contribution from the cohesive elements on the open part of the fracture. The fluid pressure which opens the fracture is balanced by the far field stress acting across the cohesive zone and by the cohesive tractions still acting on that zone thus effectively avoiding the singularity at the fracture tip. The only constrain in equation (10) is that the tractions acting on the entire fracture and cohesive zone must be in equilibrium [16].

For the numerical solution we define a nominal small initial width and a small initial length as initial conditions. Generally, the pressure along the fracture is not known a priori and it is a part of the solution. The position of the fluid-front is defined by the mass conservation in the fracture. The behavior of the fluid movement through the saturated porous formation with respect to the solid, is assumed that obeys the Darcy law. This classical transport law for isotropic porous media relates q to the gradient of the fluid pressure p according to:

$$q = -(k/\mu)(\nabla p - f) \quad (11)$$

where q is the fluid flux, k is the intrinsic permeability (assumed to be constant), ∇ is the gradient operator and f are the fluid volume forces. Note that we assume that the fluid in the fracture is identical rheologically to the pore fluid.

2.3 Rock deformation

The inelastic rock behavior is a function of the material parameters and loading conditions. Examining the near tip area of the fracture, due to the high stress concentration, solutions from LFM cannot accurately analyze the fracture process. In conventional rock mechanics, failure of rock formations is analyzed for dry domains (i.e. no pore pressure acting in the system). However, the usual assumption when analyzing failure of rocks in poromechanical systems is that the rock is fluid saturated. Since the formations in petroleum related rock mechanics are generally saturated, this assumption is quite valid and it is important to investigate how saturation influences the failure process. The total stresses σ_{ij} are related to the effective stresses σ'_{ij} through:

$$\sigma_{ij} = \sigma'_{ij} - \alpha p \quad (12)$$

where p is the fluid pressure, α is the poroelastic constant $\alpha = 1 - (K_f/K_s)$, K_f is the fluid bulk modulus the K_s is the solid grain bulk modulus. The effective stresses govern the deformation and failure of the rock. In this case the failure criterion is modified to account the fluid pressure constrain by introducing the effective stress into the dry form of the failure criterion. The modified Mohr-Coulomb criterion describing failure in porous conditions is [15]:

$$\sigma_1 - p_f = 2c \frac{\cos \varphi}{1 - \sin \varphi} + (\sigma_3 - p_f) \frac{1 + \sin \varphi}{1 - \sin \varphi} \quad (13)$$

where σ_1 is the maximum insitu stress, σ_3 is the maximum insitu stress, p_f is the pore pressure acting in the system, c is the material cohesion and φ is the material friction angle. The sign convention adopted here is according to classical mechanics i.e compression is negative.

The only extra parameters that are needed to model the inelastic behavior of the porous continuum as described above are the material cohesion c , the material friction angle φ and the dilation angle ψ , that controls the volumetric change due to yielding and dilation of the material. However, in order to keep the parameters to a minimum, we have assumed associative plasticity theory which justifies the equivalence of the material friction angle with the dilation angle. Furthermore, in the hydraulic fracturing problem, the initial in-situ mean pressure in the near area of the fracture tip decreases during propagation and under such conditions it is reasonable to assume an associative behaviour. Summarizing, the rock mass remote from the fracture is initially elastic, then deforms plastically and then unloads elastically after the fracture has advanced.

2.4 Propagation regimes and plastic zone scaling

The fluid driven problem with leak-off in a poroelastoplastic formation is characterized by the four controlling parameters. (i) the volumetric injection rate Q , (ii) the fluid viscosity μ , (iii) the leak off coefficient C and (iv) the plane strain modulus E . Furthermore, the leak off coefficient is influenced by the minimum insitu stress σ_0 through [17]:

$$C_L \approx \frac{k}{\mu} \frac{\sigma_0}{\sqrt{\pi c}} \quad (19)$$

Where k is the intrinsic permeability, μ is the fluid viscosity, σ_0 is the minimum insitu stress and c is the poroelastic intrinsic diffusion coefficient which is a function of the Biot modulus M , shear modulus G , drained K and undrained K_u bulk modulus. Equation (19) implies that large insitu stress and permeabilities will result in high fluid losses in the formation. In a similar way small values of fluid viscosity will also result in high fluid losses. According to [6] the fracture propagation is governed by two energy dissipation mechanisms (rock splitting and viscous fluid flow) and two storage mechanisms (inside the fracture and in the porous formation). The relative magnitude of the dissipation processes is characterized by the dimensionless toughness K_d and reflects the ratio of energy rate expended in fracturing the rock to viscous dissipation. The dimensionless toughness is linked to the dimensionless viscosity M_d and reflects the energy expended in the viscous fluid flow [6, 4].

$$K_d = \frac{8}{\sqrt{2\pi}} k_{ic} \left(\frac{1}{12\mu Q_o (E/1-\nu^2)^3} \right)^{1/4}, \quad M_d = (K_d)^{-4} \quad (20)$$

From the above relations we can determine whether the fracture is driven in the toughness $K_d > 1$ or viscosity $M_d > 1$ dominated regime.

The characteristic length of a fracture driven in an elastoplastic formation that relates the material properties and the fluid rheology parameters with the size of the plastic zones is given by [21]:

$$\ell_p \sim \frac{E'^2 (\mu v)}{\sigma_T^3} \quad (21)$$

where E' is the plane strain modulus, μ is the fluid viscosity, v is the propagation velocity and σ_T is the tensile yield strength. According to this characteristic length, high values of elastic

modulus, viscosity, propagation velocity and low values of rock strength will lead to higher stress concentrations near the tip and higher plastic zones are expected to develop. The dominant term in the viscous fluid flow is (μv) and is the aim of our investigation with regarding the influence of the pumping parameters on the resulting plastic zone development.

3 NUMERICAL ANALYSIS

The system of equations describing the fluid driven problem was solved with the finite element method. A sufficient fine mesh around the predefined fracture path was used to ensure numerical accuracy from the sharp changes that are created in the geometry of the propagating tip. The theoretical bounds for the cohesive element size was originally discussed by [18] and improved by [22]. According to their work, two main factors influence the element size. First is the cohesive zone size d_z and has to be small enough to accurately resolve the stress distributions in the cohesive process zone around the fracture tip. The cohesive zone is an inherent length scale determined by material parameters and it is a very small length scale in most cases. The second factor is the macroscopic stiffness reduction due to the cohesive separation along element boundaries if the initial stiffness of the cohesive surfaces is finite. The cohesive element size must be chosen to ensure element size independency from the aforementioned factors in fracture propagation simulations. The allowable range of element size d_z in plane strain conditions is given by:

$$d_z \ll \frac{9\pi G_{IC} E'}{32 T_{max}^2} \quad (22)$$

where G_{IC} is the fracture energy for mode-I separation, E' is the plane strain modulus, T_{max} is the maximum traction.

Calculations were carried out in Abaqus (2010), a nonlinear finite element code suit of programs. The usual 4-node, plane strain, isoparametric elements were used to model the domain and 6-node cohesive elements to model the fluid flow in the fracture and the fracturing process. Both types of elements, additionally from their u, v translation degree of freedom (D.O.F), are equipped with a pore pressure D.O.F to account for the fluid diffusion in the porous domain. The two additional nodes in the cohesive elements, positioned in their center, are used to simulate the longitudinal and transversal fluid flow during propagation. The discretized domain was considered to be 30x30 m and the predefined path of the fracture was defined to be 11 m only (cohesive elements) in order to save computational time. The wellbore location is at the left-lower corner and the fracture is assumed to grow in both directions along the axis-x. For a long fracture the size of the wellbore is negligible and is usually ignored in the modeling. This remark, along with the condition that the wellbore is cased, cemented and fully bonded with the rock formation, justifies the use of symmetry conditions within a reasonable accuracy. Symmetry conditions were imposed at the bottom ($dy=0$, fixed displacements) and at the left ($dx=0$, fixed displacements) side of the models. The in-situ stresses were generated as initial stresses and by applying the equilibrium load at the far end edges. At the top edge the value of σ_3 (MPa) was considered as the minimum in situ stress and at the right side of the models the value of σ_1 (MPa) was considered as the maximum in situ stress. An initial condition is also required for defining an initial fracture length for the flow. This length was considered 0.1 m which is approximately equal with the perforation length.

3.1 Model validation

The first part of this investigation is devoted to the presentation of the results from the analysis of the fluid driven problem propagating in a poroelastic formation with fluid losses to demonstrate the fully coupled solution. We have performed comparisons with the asymptotic solution of [9] and the numerical computations of [17] when the fracture is driven in a fracture toughness dominant regime. We have also compared with the asymptotic solution of [6] and the numerical computations of [17] when the fracture is driven in a viscosity dominant regime. The parameters of the numerical computations to be consistent with the numerical results of [17] are as follows: Young modulus, 17 GPa; Poisson ratio, 0.2; Fracture energy for mode-I separation, 120 Pa.m; Critical separation traction, 1.25 MPa; Injection rate, 0.001 m²/sec; Permeability, 10⁻¹⁵ m²; fluid viscosity, 0.0001 Pa.sec; compressive far field stress, 3.7 MPa; Porosity, 0.2; Leak-off coefficient, 6.28x10⁻⁵ m.sec^{-1/2}. The difference between our numerical model and the numerical model of [17] is that we introduce an initial stiffness to the cohesive surfaces that is characterized by an independent parameter. Therefore, the cohesive zone model adopted by [17] here can be regarded as a special case with initially rigid-linear softening bilinear law.

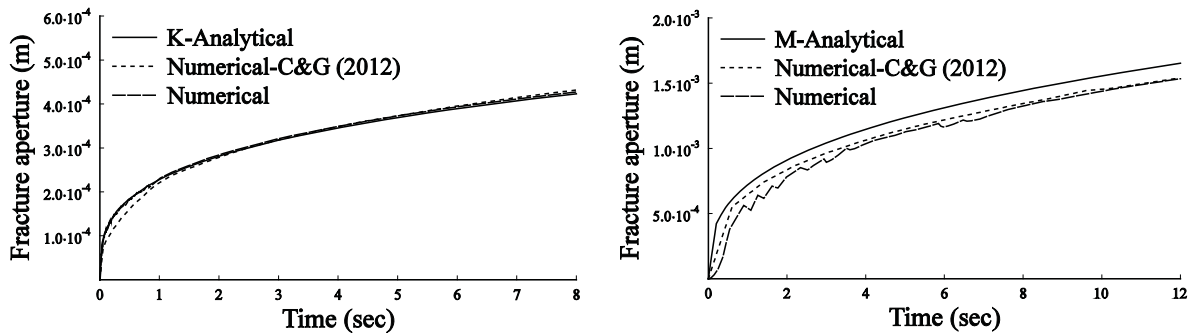


Figure 2: Validation of toughness K-dominated and viscosity M-dominated fractures

Figure (2a) presents the numerical solution of the fracture aperture at wellbore versus time in comparison with the near-K analytical solution of [9] and the numerical solution of [17]. The fracture was left to propagate for 8 seconds (approximately 5m long). From the comparison that is performed, it is seen that the agreement between the near-K analytical and the numerical results is very good. Figure (2b) shows the numerical solution of the fracture aperture at wellbore versus time in comparison with the analytical solution of [6] and the numerical solution of [17]. The fracture was left to propagate for 12 seconds (approximately 5m long). The fluid viscosity was raised to 0.1 Pa.sec. The results from this simulation are in good agreement between the numerical results of [17] but not so good with the M-analytical solution. The reason for this disagreement is that the analytical solution is based on the assumption of LEFM fracture propagation and leak-off is governed by Carter's law. In the numerical solution, fracture propagation based on the cohesive zone assumption and fluid losses are based on the diffusion equation (equation 10) which is more accurate to the author's opinion. The losses demonstrate the action of back-stresses which induce a negative stress on the fracture walls causing the fracture to close. This effect is in agreement with the numerical numerical solution presented by [17]. A small discrepancy is also observed for early times (0-3 sec) within acceptable limits due to the fracture loading (pumping schedule considered as boundary condition), and the high value of fluid viscosity. The apparent discontinuities that are ob-

served on the numerical solution are attributed to the mesh resolution. However, no refinement it needed as seen from the convergence with the other solutions presented.

From the above analysis we have showed that our model is capable of simulating fluid driven fractures in both, the fracture toughness and viscosity dominated regimes under poroelastic conditions. We will extend the applicability of the numerical model to account for the poroplastic zone development according to the scaling presented in equation (21).

3.2 Computational results

This section presents the computations that were performed to analyze the fluid driven fracture propagating in poroelastic and poroelastoplastic weak formations. The purpose of this investigation is the link of the pumping parameters (fluid viscosity and injection rate) with the plastic zone development while the fracture is driven in both K-dominated and M-dominated regimes. The input parameters which the numerical computations were performed are given in Table 1. These parameters include the rock properties, the pumping parameters, and cohesive zone properties. For the poroelastic case it is assumed that any compressibility effects will not affect the fracture geometry or the fluid pressure (i.e incompressible formations). In both cases we consider an initial pore pressure exist in the formation and is assumed to have a uniform value of 1.85 MPa. For the poroelastoplastic case, the only extra parameters that are needed to consider porous deformation and propagation the material cohesion c , and friction angle φ . The cohesive zone is assumed to have a unit normal and anti-plane thickness. The effective insitu stress field was considered as σ_1 , 14 MPa; σ_2 , 9 MPa; σ_3 , 3.7 MPa. As initial conditions, we have used a void ratio equal to 0.333 and an initial gap (perforation length) equal to 0.1m.

Variable	Value
Elastic Rock Properties	
Young modulus, E (MPa)	16200
Poisson ratio, ν	0.3
Domain hydraulic conductivity, k (m/sec)	2.421E-10
Inelastic Rock Properties	
Cohesion, c (MPa)	1.515
Friction and dilation angle, $\varphi^0 = \psi^0$	28
Cohesive zone properties	
Maximum Traction, σ_t (MPa)	0.5
Cohesive stiffness, K_n (MPa)	162E+3
Cohesive energy, $J_{IC} = G_{IC}$ (kPa.m)	0.112
Transverse conductivity k_t^u, k_t^d (m/sec)	2.421E-10
Pumping Parameters	
Viscosity, μ (Poise)	1 / 5 / 10 / 50 / 100
Injection rate, Q (E-03 m ² /sec)	0.5 / 5.0 / 10.0 / 15.0 / 20.0

Table 1: Input parameters and material properties

The fluid pressure responsible for splitting the formation and driving hydraulically the fracture are generated from the injection rate and is expressed as the fluid loading inside the fracture. For convergence reasons, the injection rate was set to climb its final flow rate value at the first 0.05 seconds of the injection time. This introduces an initial slope in the pumping schedule used; however its effect is considered negligible. The computational results presented next correspond are divided into two categories: influence of injection flow rate and influence of fluid viscosity under poroelastic and poroelastoplastic conditions.

3.3 Influence of the injection flow rate

As explained before, when driving hydraulically a fracture in a porous formation there are four asymptotic regimes. In order to suppress the significant influence of the leak-off toughness and leak-off viscosity and to study the fracturing process in the toughness and viscosity dominated regimes, we have performed all simulations with a very small value of transversal conductivity and for early times to ensure that the scaling will remain in the near storage regimes (equation 20). At the first part of this investigation, we have kept a constant value of viscosity (1 Poise) and perform simulations for different injection rates ranging from $0.5E-03$ to $20.0E-03$ that correspond to different propagation velocities ranging from slow to fast fracture propagation respectively. According to the scaling of equations (20), this ensures that the fracture will propagate under the toughness dominated regime. This investigation raises the possibility to investigate the parameters affecting the diffusion process in hydraulic operations. All comparisons are made after the fractures were left to reach 1.5m long.

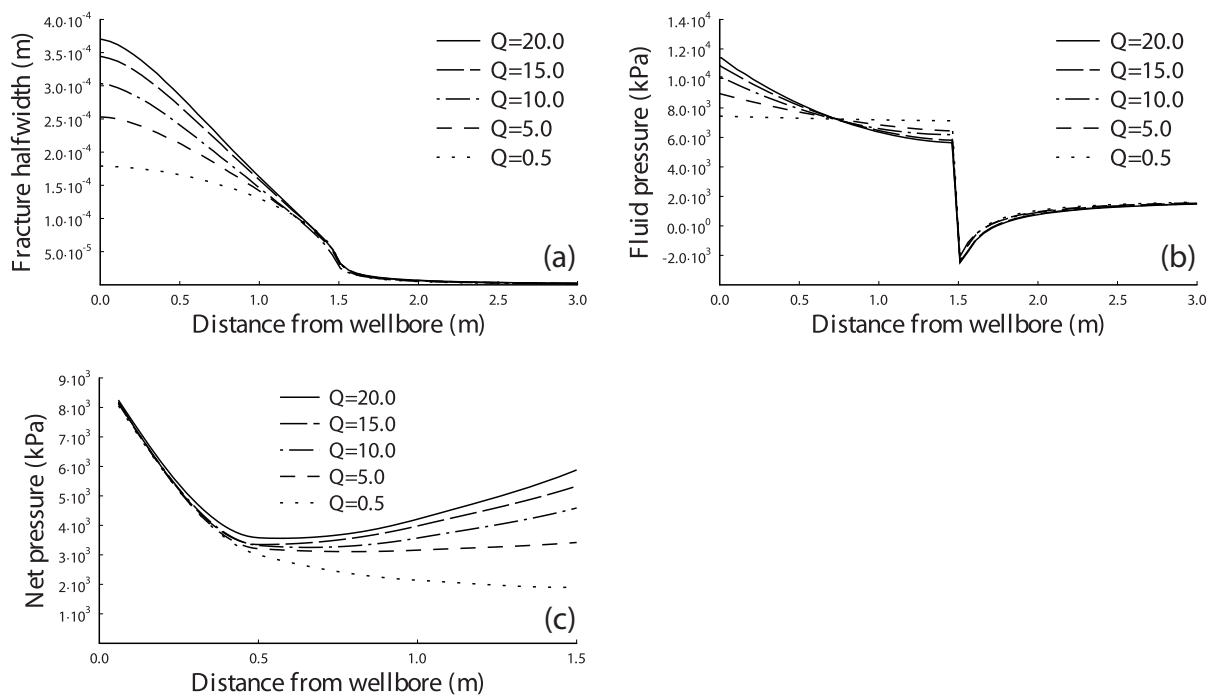


Figure 3: Influence of flow rate under poroelastic conditions

Figure (3a-c) presents the parametric analysis performed for the investigation of the influence of the flow rate under poroelastic conditions. Figure (3a) presents the fracture profiles for the different values of injection rates. It is seen that the fracture is significantly wider when is driven with fast propagation velocity while the aperture is significantly narrow (3 times) when the propagation velocity is slow. This is explained from the small fluid leak-off that is permitted in the models. For the fast propagation case (figure 3b) it is seen that the fluid pressures turn highly non-uniform and rise inside the fracture as a result of the small diffusion predicted by the model. Accordingly, large loading is observed at the fracture inlet and smaller loading at the fracture tip. This is responsible for the wider profiles. For the slow propagation case, the fluid pressure inside the fracture is practically uniform allowing for larger fluid leak-off and the created back stresses become significant thus producing narrower fracture profiles. Figure (3c) presents the fluid net-pressures. It is showed that the net pressure with the slow propagation velocity after the formation breakdown decreases to a constant val-

ue as expected. As the fracture is driven with higher flow rates, leak-off is minimized causing the net-pressure to increase. We conclude that the obtained results are a direct result of the time scale difference between the diffusion process and the pumping schedule imposed with the different flow rates.

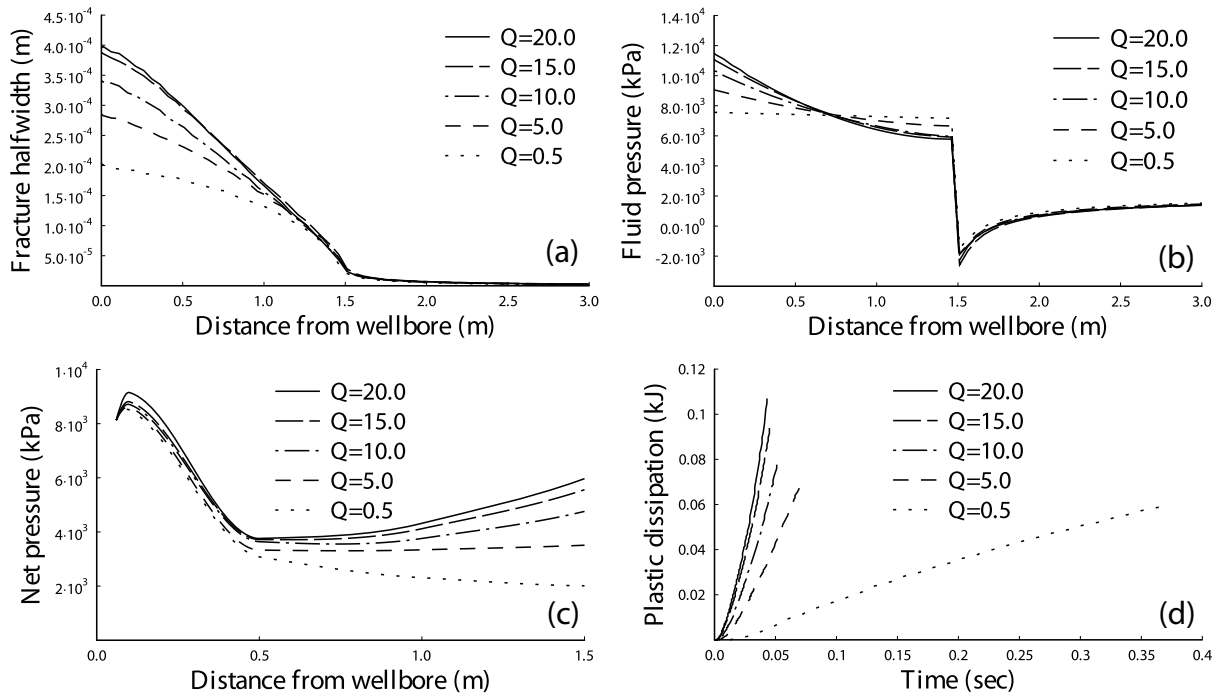


Figure 4: Influence of flow rate under poroelastoplastic conditions

Figure (4a-d) presents the parametric analysis performed for the investigation of the influence of the flow rate under poroelastoplastic conditions. Figure (4a) presents the fracture profiles for the different values of injection rates. It is seen that the fracture is significantly wider when the injection rate is large corresponding to fast propagation velocity. The fracture aperture is significantly narrow when the propagation velocity is slow. This behaviour, as in the poroelastic case, is explained from the small fluid leak-off that is permitted in the models. When the poroelastoplastic fracture is compared with the poroelastic for each injection flow rate it is seen the poroelastoplastic fracture is always wider. This is explained by the action of plastic yielding that the fracture is experiencing. Figure (4b) presents the fluid pressure inside the propagating fracture. For the fast propagation case it is seen that the fluid pressure as showed in the poroelastic fracture is highly non-uniform. The value is significantly higher and is observed at the fracture inlet while is smaller at the fracture tip. This action explains the wider profiles. For the slow propagation case, the fluid pressure inside the fracture is practically uniform allowing for larger fluid leak-off and the created back stresses become significant thus producing narrower fracture profiles. When the fluid pressures are compared between the poroelastoplastic and the poroelastic formations, it is seen that in the poroelastoplastic case are always larger as expected due to the influence of plasticity. Figure (4c) presents the fluid net-pressures for the fracture profiles of figure (4a). It is seen that just after the injection starts, pressure starts to build up. This is pressure built up is associated with the plastic zone development. After the plastic zones have fully developed, the pressure starts to decay. This behavior is similar for all cases of injection rates examined. The predicted net pressure with the slow propagation velocity after the formation breakdown decreases to a constant value as expected. As the fracture is driven with higher flow rates, leak-off is minimized

causing the net-pressure to increase. This is once again a result of the limited diffusion causing the fluid pressure to become non-uniform resulting in wider fracture profiles. As explained earlier, this is a result of the time scale difference between the diffusion process and the pumping schedule. From the elevated net pressures predicted from the numerical model the energy that is dissipated due to plastic yielding versus time for all the cases examined is showed in figure (4d). It is showed that with high injection rates significantly larger plastic dissipation is created in the numerical models. For small injection rates, more time is needed to reach the desired length (1.5m) however smaller plastic yielding is created. This result suggest that it is better to propagate a fluid driven fracture with small injection rate in expense of the propagation time because the created hydraulic pressure is uniform and any unnecessary plastic yielding associated with high injection rate to create non-uniform loading inside the fracture is avoided.

3.4 Influence of the fracture fluid viscosity

The second part of this investigation is concerned with the influence of the fluid viscosity in the diffusion process and how the plastic zone development is affected when the fracture is driven in the viscosity dominated regime (equation 20). In order to analyze the results we have kept a constant value of injection rate ($0.5E-03$) and perform simulations for different values of fluid viscosity ranging from 1 to 100 Poise. These values of fluid viscosity correspond from small to highly viscous fluid flow. Such values of fluid viscosity (100 Poise) actually confirm a fracture driven in the viscosity dominated regime. We have used the value of the smallest injection rate to minimize any interaction effects between the fluid viscosity and the injection rate scaling term ($\mu.v$) for the investigation of the plastic zone length as showed in the scaling of equation (21). As in the previous investigation (section 3.3) all comparisons are made after the fractures where left to reach 1.5m long.

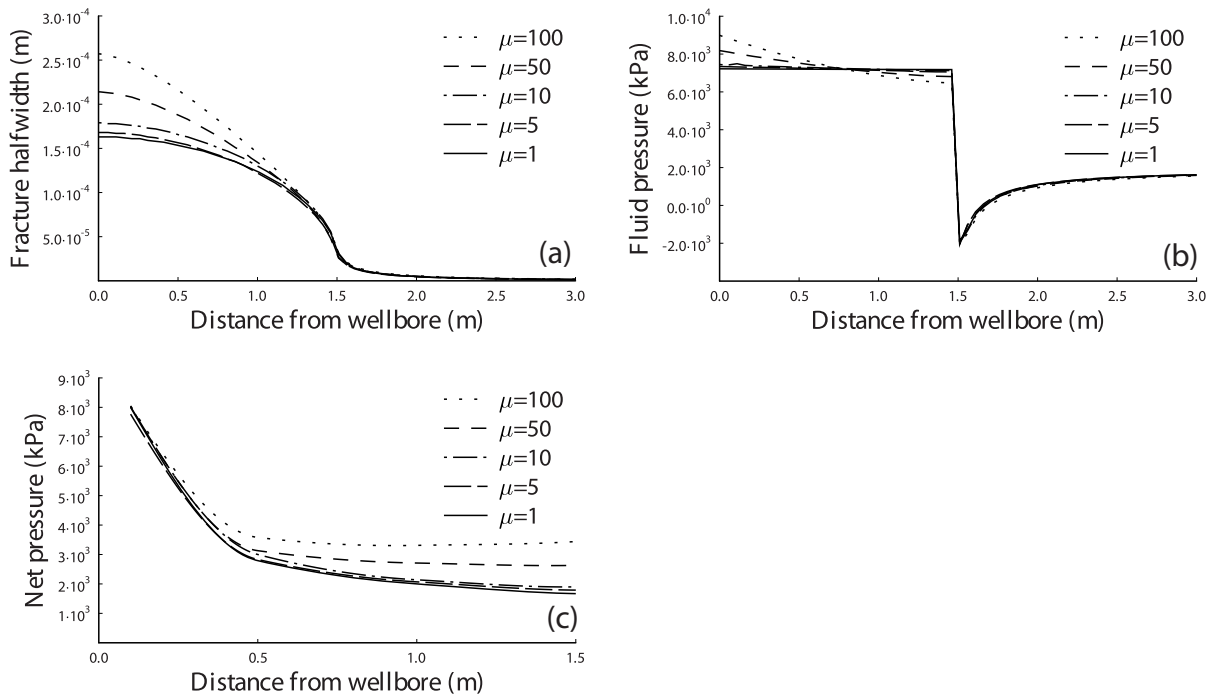


Figure 5: Influence of viscosity under poroelastic conditions

Figure (5a-c) presents the numerical solution for a viscosity dominated fracture which is driven under poroelastic conditions. The investigated variable is the fluid viscosity. Figure (5a) shows the fracture profiles for the different values of fluid viscosities. From figure (5a) it is seen that for small values of fluid viscosity (1-10 Poise) the action of the viscous fluid flow does not present any significant effects on the fracture profiles. In fact the fractures present similar profile. However, the fracture is significantly wider when is driven with highly viscous fluid while the aperture is narrower (2 times) when fracturing is performed with a low viscosity fluid. This is explained from the small fluid leak-off that is permitted in the models through the transverse hydraulic conductivity (filter cake) and the action of the viscous fluid flow. For the case where the fracture is driven with a highly viscous fluid (figure 5b) it is seen that the fluid pressures turn highly non-uniform with the larger loading values observed at the fracture inlet and smaller loading at the fracture tip. This is responsible for the wider profiles. For the other case, where the fracture is driven with a less viscous fluid, the fluid pressure inside the fracture is practically uniform therefore allowing for larger fluid leak-off and as a result the created back stresses become significant resulting in narrow fracture profiles. Figure (5c) presents the fluid net-pressures obtained for the fracture profiles of figure (5a). From this figure (5c) it is showed that the net pressure predicted with the less viscous fluids after the formation breakdown decreases to a constant value as expected. When the fracture is driven with highly viscous fluid, leak-off is minimized causing the net-pressure to increase. We conclude that the obtained results are a direct result of the action of the viscous fluid flow. This means that higher net and fluid pressures are created and the resulting fracture profiles are wider when the fracture is driven in the viscosity dominated regime. Furthermore, this phenomenon is amplified with the time scale difference between the diffusion process and the pumping schedule imposed with the different flow rates.

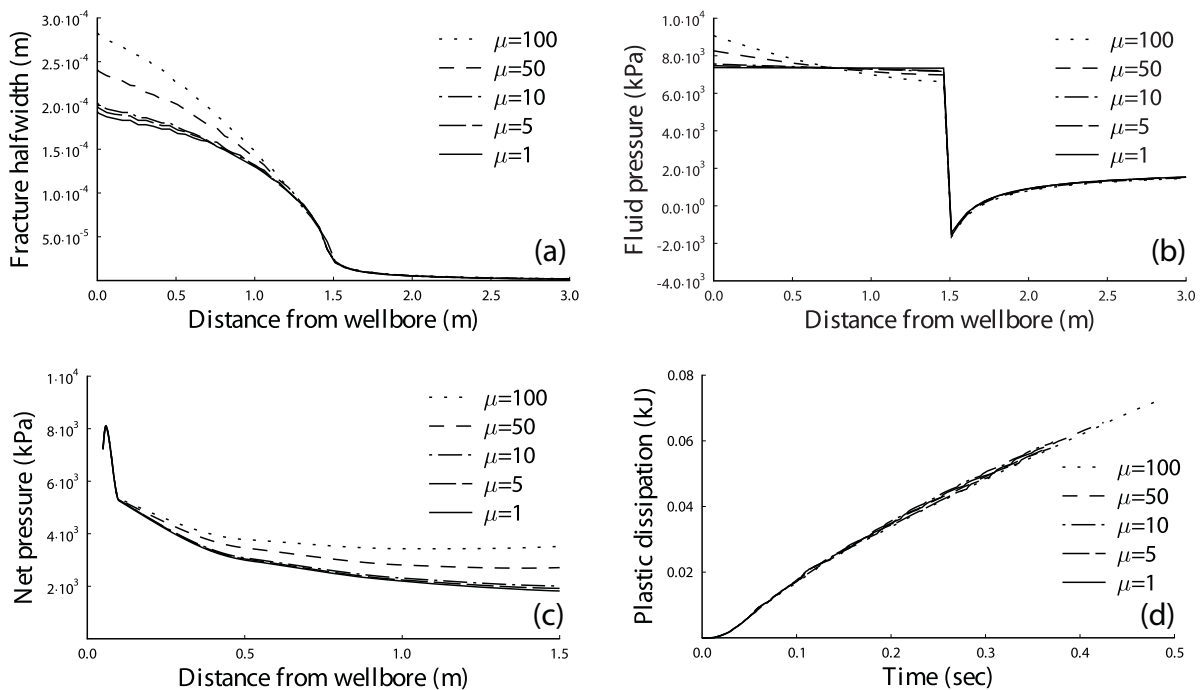


Figure 6: Influence of viscosity under poroelastoplastic conditions

Figure (6a-d) presents the computational results for a viscosity dominated fracture which is driven under poroelastoplastic conditions. Figure (6a) shows the fracture profiles for the different values of fluid viscosities. From figure (6a) it is seen that for small values of fluid vis-

cosity (1-10 Poise) the action of the viscous fluid flow does not present any significant effect on the fracture profiles. These observations are the same as the poroelastic case. This can be attributed to the set of parameters chosen for these simulations. The fracture is significantly wider when is driven with highly viscous fluid while the aperture is narrower when fracturing is performed with a low viscosity fluid. This behaviour is explained once again, due to the small fluid leak-off that is permitted in the models through the transverse hydraulic conductivity (filter cake) and the action of the viscous fluid flow. When the fractures are compared for all the viscosity cases between the poroelastic and poroelastoplastic fractures, the fractures are always significantly wider in the poroelastoplastic cases. This demonstrates that when irreversible effects are considered, the fracture profile is enlarged by both the action of the viscosity dominated regime and plastic yielding.

This result is supported by figure (6b) that presents the fluid pressures inside the fracture. Higher fluid pressures are observed, presenting highly non-uniform profile with the larger loading values being at the fracture inlet and smaller loading at the fracture tip. This type of fluid loading has a direct effect on the elliptic shape of the fracture. This behaviour is responsible for wider profiles.

When examining the net pressures of figure (6c), a small increase is created just after the injection starts suggesting pressure build up. This pressure is associated with the plastic zone development. After the plastic zones have developed, the pressure starts to decay. This behavior is similar for all cases examined with different values of fluid viscosity. Immediately after formation breakdown, the net pressures evaluated from the highly viscous cases tend to elevate. For small viscosities, the fluid diffuses freely in the formation and the pressure tends to a constant value. For high viscosities the diffusion process is affected and the pressure increases. This behaviour is explained by the fact that the fracture is driven in the viscosity dominated regime and furthermore from the plasticity considered in the models.

Figure (6d) shows the energy that is dissipated from plasticity versus time for all the cases examined. It is showed that more time is needed to propagate the fracture to a certain extend (1.5m in length) when is driven with highly viscous fluids. The plastic dissipation curves follow the same path. From this plot we show that when the fracture is driven with highly viscous fluids, larger plastic zones are obtained as a result of the viscosity dominated fracture. For small fluid viscosity the plastic dissipation is almost the same and reaches the same fracture length at the same time.

We conclude that the obtained results are a direct result of the action of the viscous fluid flow which in turn affects the plastic zone development resulting in wider fracture profiles and larger fluid pressures compared to the poroelastic case. Furthermore, this phenomenon is amplified with the time scale difference between the diffusion process and the pumping schedule imposed with the highly viscous fluids used.

4 CONCLUSIONS

- A set of fully coupled poroelastic and poroplastic models have been presented.
- From the comparison with asymptotic solutions and other numerical studies we have demonstrated that our models are capable for predicting fluid driven fractures in toughness dominated and viscosity dominated regimes with excellent accuracy.
- When the fractures are driven with high flow rates under poroelastic conditions the fluid pressures turn non-uniform inside the fracture because the time scale of the fracture fluid diffusion is significantly different from the time scale of the fluid injection. As a result of

the small diffusion that is allowed from the fracture towards the formation the obtained fracture profiles are wider and the net pressures after breakdown increase.

- When the fractures are driven with high flow rates under poroelastoplastic conditions the fluid pressures preserve their non-uniform profile inside the fracture for the same reason as the poroelastic case. As a result larger plastic yielding is created when the fracture is driven with high flow rates suppressing even more the diffusion process. The fracture profiles obtained under poroelastoplastic conditions are wider from the poroelastic case. Furthermore, the fluid pressures needed to extend the fracture are larger and the net pressures after break down increase as a result of the diffusion process.
- Hydraulic fracturing in the viscosity dominated regime under poroelastic conditions present similar behavior. When the fractures are driven with highly viscous fluids under poroelastic conditions the fluid pressures turn non-uniform inside the fracture. This is done because of the action of the viscous fluid flow. This type of flow affects the diffusion and the fluid is not allowed to diffuse properly in the formation thus increasing the pressure at the fracture inlet and decreasing the pressure near the tip area. This has a direct result over the elliptic shape of the fracture. As a result of the small diffusion that is allowed from the fracture towards the formation the obtained fracture profiles are wider and the net pressures after breakdown increase.
- Hydraulic fracturing in the viscosity dominated regime under poroelastoplastic conditions influence even further the results. When the fractures are driven with highly viscous fluids under poroelastoplastic conditions the fluid pressures turn non-uniform inside the fracture as a result of the action of the viscous fluid flow. This type of flow affects the diffusion and the fluid is not allowed to diffuse properly in the formation thus increasing the pressure at the fracture inlet and decreasing the pressure near the tip area. This non-uniform pressure creates larger plastic zones which in turn affects the elliptic shape of the fracture. The resulting fracture profiles are wider, the fluid and net pressures are larger from the poroelastic case. Furthermore, the net pressures increase after breakdown as a result of the action of the highly viscous fluid flow.

ACKNOWLEDGEMENTS

This work was co-funded by the European Regional Development Fund and the Republic of Cyprus through the Research Promotion Foundation (Project: DIDAKTOR/0311/58).

REFERENCES

- [1] P. Valko, M.J. Economides, Hydraulic fracture mechanics. John Wiley and Sons, New York, 1995.
- [2] V.C. Tsai, J.R. Rice, A model for turbulent hydraulic fracture and application to crack propagation at glacier beds. *Journal of Geophysical Research*, 115, 1-18, 2010.
- [3] J. Adachi, E. Siebrits, A. Peirce, J. Desroches, Computer simulation of hydraulic fractures. *International Journal of Rock Mechanics and Mining. Sciences*, 44, 739-757, 2007.
- [4] J. Hu, D.I. Garagash, Plane strain propagation of a fluid-driven crack in a permeable rock with fracture toughness. *ASCE Journal of Engineering Mechanics*, 136, 1152-1166, 2010.
- [5] B. Lecampion, E. Detournay, An implicit algorithm for the propagation of hydraulic fracture with a fluid lag. *Computer Methods in Applied Mechanics and Engineering*, 196, 4863-4880, 2007.

-
- [6] J. Adachi, E. Detournay, Plain strain propagation of a hydraulic fracture in permeable rock. *Engineering Fracture Mechanics*, 75, 4666-4694, 2008.
- [7] D.B. Van Dam, P. Papanastasiou, C.J. De Pater, Impact of rock plasticity on hydraulic fracture propagation and closure. *Journal SPE Productions & Facilities*, 17, 149-159, 2002.
- [8] E. Sarris, P. Papanastasiou, Modeling of hydraulic fracturing in a poroelastic cohesive formation. *International Journal of Geomechanics*, 12, 160-167, 2012a.
- [9] A.P. Bungler, E. Detournay, D.I. Garagash, Toughness-dominated hydraulic fracture with leak-off. *International Journal of Fracture*, 134, 175-190, 2005.
- [10] J.T. Boone, A.R. Ingraffea, A numerical procedure for simulation of hydraulically driven fracture propagation in poroelastic media. *International Journal for Numerical and Analytical Methods in Geomechanics*, 14, 27-47, 1990.
- [11] P. Papanastasiou, The influence of plasticity in hydraulic fracturing. *International Journal of Fracture*, 84, 61-79, 1997.
- [12] P. Papanastasiou, An efficient algorithm for propagating fluid driven fractures. *Computational Mechanics*, 24, 258-267, 1999a.
- [13] J.M. Segura, I. Carol, On zero-thickness interface elements for diffusion problems. *International Journal for Numerical and Analytical Methods in Geomechanics*, 28, 947-962, 2004.
- [14] E. Sarris, P. Papanastasiou, The influence of cohesive process zone in hydraulic fracturing modelling. *International Journal of Fracture*, 167, 33-46, 2011.
- [15] E. Sarris, P. Papanastasiou, Numerical modeling of fluid-driven fractures in cohesive poroelastoplastic continuum. *International Journal for Numerical and Analytical Methods in Geomechanics*, DOI: 10.1002/nag.2111, 2012b.
- [16] Z. Chen, Finite element modeling of viscosity-dominated hydraulic fractures. *Journal of Petroleum Science and Engineering*, Doi: 10.1016/j.petrol.2011.12.021, 2012.
- [17] B. Carrier, G. Sylvie, Numerical modeling of hydraulic fracture problem in permeable medium using cohesive zone model. *Engineering Fracture Mechanics*, 79, 312-328, 2012.
- [18] J.R. Rice, A path independent integral and the approximate analysis of strain concentration by notches and cracks. *Journal of Applied Mechanics*, 35, 379-386, 1968.
- [19] Abaqus, Version 6.10 Theory Manual, Providence, RI, 2010.
- [20] A. Peirce, E. Detournay, An implicit level set method for modeling hydraulically driven fractures. *Computer Methods in Applied Mechanics and Engineering*, 197, 2858-2885, 2008.
- [21] P. Papanastasiou, M. Thiercelin, Influence of inelastic rock behavior in hydraulic fracturing. *International Journal of Rock Mechanics, Mining Sciences and Geomechanical Abstracts*, 30, 1241-1247, 1993.
- [22] V. Tomar, J. Zhai, M. Zhou, Bounds for element size in a variable stiffness cohesive finite element model. *International Journal for Numerical Methods in Engineering*, 61, 1894-1920, 2004.

STRUCTURAL AND MULTI-FUNCTIONAL OPTIMIZATION USING MULTIPLE PHASES AND A LEVEL-SET METHOD

G. Allaire¹, F. Jouve², and G. Michailidis^{1,3}

¹CMAP, Ecole Polytechnique
91128 Palaiseau, France
e-mail: gregoire.allaire@polytechnique.fr

² LJLL, University Paris Diderot
(UMR 7598), Paris, France
e-mail: jouve@math.jussieu.fr

³ Renault DREAM-DELT'A
Guyancourt, France
e-mail: michailidis@cmap.polytechnique.fr

Keywords: Shape and topology optimization, multi-functional optimization, multi-materials, signed distance function.

Abstract. *In this work we address the problem of structural and multi-functional shape and topology optimization using several elastic materials in a fixed working domain. The description and the evolution of the interfaces between the different phases is done using the level-set method. We use a smooth Hooke's tensor, instead of a discontinuous one. The continuous case can be seen as an approximation of the sharp interface case, and in this context, the signed distance function corresponding to each interface is used for modeling the smooth Hooke's tensor. A directional shape derivative is calculated for the objective function to minimize. We show 2d results for compliance minimization, as well as an example of multi-functional optimization, coupling structural and thermal problems.*

1 INTRODUCTION

Shape and topology optimization methods have become quite known among engineers and researchers during the last decades. They reduce significantly the amount of time needed for the design of a new mechanical part, help to optimize existing designs, or even provide solutions to problems where intuition is very limited. Such a case is the optimal distribution of several materials, possibly having much different mechanical properties, in order to treat a multi-functionality criterion (e.g. stiffness and thermal isolation).

The modeling of a multi-material structure is usually done via a discontinuous Hooke's tensor. However, this choice can introduce severe complications in the numerical calculation of a shape derivative [2, 3, 8] and thus a smooth interpolation scheme is often preferable [3]. Moreover, a regularized Hooke's tensor seems to be more appropriate for some applications [14].

Many articles have been published on this topic in the framework of the SIMP (Solid Isotropic Material with Penalization) method (see [10, 11, 16] and the references therein). Several interpolation schemes have been proposed for the construction of the smooth Hooke's tensor and the penalization of intermediate densities. In the framework of the phase-field method for topology optimization, Zhou et al. [15] used a generalized Cahn-Hilliard model of multiphase transition to perform multimaterial structural optimization.

In the framework of the level set method for shape and topology optimization [1, 12], Mei et al. [5] and Wang et al. [13] were the first to present a regularized model for the Hooke's tensor using a multi-phase level-set method. In [3], Allaire et al. have used the same level-set representation and the signed-distance function to construct a smooth interpolation scheme for the Hooke's tensor. A directional shape derivative has been calculated and it has been shown that the problem converges to the one of sharp interface when the interpolation width tends to zero.

In this work, we address the problem of structural and multi-functional shape and topology optimization. The same level-set representation and shape derivation as in [3] has been used. The method is first applied on a structural problem, where a single phase is substituted by two and three phases. Finally, a multi-functional problem is presented considering a structural and a thermal problem and two materials with much different mechanical properties.

2 SETTING OF THE PROBLEM

Without loss of generality, we limit ourselves with the description of the problem of compliance minimization using two materials. The extension to more phases is described in section 5.

We search to optimize the position of the interface Γ of two materials, 0 and 1, occupying two domains Ω^0 and Ω^1 . Instead of assuming a sharp interface between the two materials, we work with a continuous and differentiable Hooke's tensor A . We assume that the material properties are smoothly interpolated in a region of width 2ϵ around the initial sharp interface, represented by the zero level set of a function ψ .

We introduce a working domain D (a bounded domain of \mathbb{R}^d , ($d = 2$ or 3)) which contains all admissible shapes, i.e. $\Omega^0 \cup \Omega^1 \subseteq D$. The volume and surface loads are given as two vector-valued functions defined on D , $f \in L^2(D)^d$ and $g \in H^1(D)^d$. The displacement field u is the

unique solution in $H^1(D)^d$ to the linearized elasticity system

$$\begin{cases} -\operatorname{div}(A(d_{\Omega^1}(x)) e(u)) = f & \text{in } D \\ u = 0 & \text{on } \Gamma_D \\ (A(d_{\Omega^1}(x)) e(u))n = g & \text{on } \Gamma_N, \end{cases} \quad (1)$$

where $e(u)$ is the strain tensor, equal to the symmetrized gradient of u , $\Gamma_D \cup \Gamma_N \subset \partial D$ and $d_{\Omega^1}(x)$ is the signed-distance function to Ω^1 .

We remind that if $\Omega \subset \mathbb{R}^d$ is a bounded domain, then the **signed distance function** to Ω is the function $\mathbb{R}^d \ni x \mapsto d_{\Omega}(x)$ defined by :

$$d_{\Omega}(x) = \begin{cases} -d(x, \partial\Omega) & \text{if } x \in \Omega \\ 0 & \text{if } x \in \partial\Omega \\ d(x, \partial\Omega) & \text{if } x \in \overline{\Omega}^c \end{cases}, \quad (2)$$

where $d(\cdot, \partial\Omega)$ is the usual Euclidean distance.

The Hooke's tensor A is of the general form

$$A(d_{\Omega}(x)) = \begin{cases} A_1 & , \text{if } d_{\Omega}(x) < -\epsilon, \\ f(d_{\Omega}(x)) & , \text{if } -\epsilon \leq d_{\Omega}(x) \leq +\epsilon, \\ A_0 & , \text{if } d_{\Omega}(x) > +\epsilon, \end{cases} \quad (3)$$

where $f(d_{\Omega}(x))$ is a smooth interpolation function. For example, a simple choice is to consider

$$A(d_{\Omega}(x)) = \begin{cases} A_1 & , \text{if } d_{\Omega}(x) < -\epsilon, \\ \frac{A_1+A_0}{2} - \frac{(A_1-A_0)d_{\Omega}(x)}{2\epsilon} & , \text{if } -\epsilon \leq d_{\Omega}(x) \leq +\epsilon, \\ -\frac{A_1-A_0}{2\pi} \sin\left(\frac{\pi d_{\Omega}(x)}{\epsilon}\right) & , \text{if } -\epsilon \leq d_{\Omega}(x) \leq +\epsilon, \\ A_0 & , \text{if } d_{\Omega}(x) > +\epsilon. \end{cases} \quad (4)$$

Remark 2.1 *In 4 we have made a simple choice for the interpolation of the material properties between the two materials. Of course, one can choose any type of smooth interpolation. Moreover, the interpolation function can contain parameters that are also subject to optimization (f.e. the interpolation width ϵ) and a geometric and parametric optimization can be combined using a method of alternating directions.*

A classical choice for the objective function $J(\Omega)$ to be minimized is the compliance (the work done by the loads)

$$J(\Omega^1) = \int_D f \cdot u dx + \int_{\Gamma_N} g \cdot u ds = \int_D A(d_{\Omega^1}(x)) e(u) : e(u) dx. \quad (5)$$

3 SHAPE DERIVATIVE

In order to find a descent direction for advecting the shape, we compute a shape derivative for the objective function (5). The notion of the shape derivative dates back, at least, to Hadamard and there has been more contributions to its development. In this work, we follow the approach of Murat and Simon for shape derivation [6]. Starting from a smooth reference open set Ω , we consider domains of the type

$$\Omega_{\theta} = (Id + \theta)(\Omega),$$

with $\theta \in W^{1,\infty}(\mathbb{R}^d, \mathbb{R}^d)$. It is well known that, for sufficiently small θ , $(Id + \theta)$ is a diffeomorphism in \mathbb{R}^d .

Definition 3.1 *The shape derivative of $J(\Omega)$ at Ω is defined as the Fréchet derivative in $W^{1,\infty}(\mathbb{R}^d, \mathbb{R}^d)$ at 0 of the application $\theta \rightarrow J((Id + \theta)(\Omega))$, i.e.*

$$J((Id + \theta)(\Omega)) = J(\Omega) + J'(\Omega)(\theta) + o(\theta) \quad \text{with} \quad \lim_{\theta \rightarrow 0} \frac{|o(\theta)|}{\|\theta\|} = 0, \quad (6)$$

where $J'(\Omega)$ is a continuous linear form on $W^{1,\infty}(\mathbb{R}^d, \mathbb{R}^d)$.

Hadamard’s structure theorem assures that the shape derivative of a functional can be written in the form

$$J'(\Omega)(\theta) = \int_{\partial\Omega} V(s)\theta(s) \cdot n(s)ds, \quad (7)$$

where V is the integrand of the shape derivative that depends on the specific objective function. Then, a descent direction can be found by advecting the shape in the direction $\theta(s) = -tV(s)n(s)$ for a small enough descent step $t > 0$. For the new shape $\Omega_t = (Id + t\theta)\Omega$, we can formally write

$$J(\Omega_t) = J(\Omega) - t \int_{\partial\Omega} V^2 ds + \mathcal{O}(t^2), \quad (8)$$

which guarantees a descent direction.

Remark 3.1 *A weaker notion of differentiability is that of the **directional derivative** of a functional $J(\Omega)$ at Ω in the direction $\theta \in V$, V being a banach space, which is defined as the limit in \mathbb{R} (if it exists)*

$$J'(\Omega)(\theta) = \lim_{\delta \rightarrow 0} \frac{J((Id + \delta\theta)(\Omega)) - J(\Omega)}{\delta}. \quad (9)$$

Moreover, if the directional derivative at Ω exists for all $\theta \in \Omega$ and if $\theta \rightarrow J'(\Omega)(\theta)$ is a continuous linear application from V in \mathbb{R} , then we say that J is differentiable in the sense of Gâteaux at Ω .

The shape derivative of (5) has been calculated in [3] and we refer to this article for all technical details. The main difference with [5, 13] is that we calculate a shape derivative of the signed-distance function d_{Ω^1} , which should not be confused with the level-set function ψ used to describe and advect the shape, instead of performing variations of ψ .

Denoting $ray_{\Gamma}(x) \subset \mathbb{R}^d$ the set of points y such that d_{Ω^1} is differentiable at y , and whose projection on Γ is x ($p_{\Gamma}(y) = x$), κ_i ($i = 1, \dots, d - 1$) the principal curvatures of Γ at point $p_{\Gamma}(x)$, the shape derivative reads

$$J'(\Gamma)(\theta) = - \int_{\Gamma} \theta(x) \cdot n^1(x) [f_1(x) + f_0(x)] dx, \quad (10)$$

where

$$f_1(x) = \int_{ray_{\Gamma}(x) \cap \Omega^1} \frac{\partial A}{\partial d_{\Omega^1}} e(u) : e(u) \prod_{i=1}^{d-1} (1 + d_{\Omega^1}(s)\kappa_i(x)) ds \quad (11)$$

and

$$f_0(x) = \int_{ray_{\Gamma}(x) \cap \Omega^0} \frac{\partial A}{\partial d_{\Omega^1}} e(u) : e(u) \prod_{i=1}^{d-1} (1 + d_{\Omega^1}(s)\kappa_i(x)) ds. \quad (12)$$

A descent direction (a notion of a shape gradient) is then revealed as

$$\theta(x) = n^1(x) [f_1(x) + f_0(x)] \quad \forall x \in \Gamma.$$

4 LEVEL-SET REPRESENTATION

We favor an Eulerian approach and use the level-set method [7] to capture the subdomains Ω^0 and Ω^1 on a fixed mesh. Then, the boundary of Ω^0 and Ω^1 is defined by means of a level set function ψ such that (see Fig.(1))

$$\begin{cases} \psi(x) = 0 & \Leftrightarrow x \in \partial\Omega^0 \cap \partial\Omega^1 \cap D, \\ \psi(x) < 0 & \Leftrightarrow x \in \Omega^1, \\ \psi(x) > 0 & \Leftrightarrow x \in \Omega^0. \end{cases} \quad (13)$$

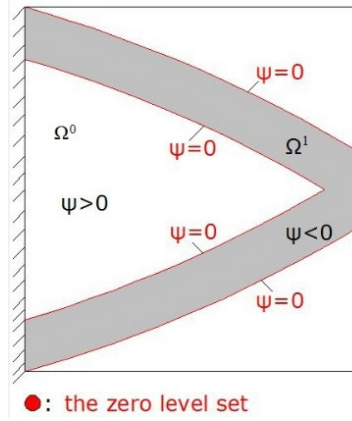


Figure 1: Level-set representation of the domains Ω^0 and Ω^1 .

During the optimization process the shape is being advected with a velocity $V(x)$ derived from shape differentiation, as we will see in the sequel. The advection is described in the level-set framework by introducing a pseudo-time $t \in \mathbb{R}^+$ and solving the Hamilton-Jacobi equation

$$\frac{\partial\psi}{\partial t} + V|\nabla\psi| = 0, \quad (14)$$

using an explicit upwind scheme [9].

5 EXTENSION TO MORE THAN 2 MATERIALS

The method presented above can be easily extended to multi-materials (see also [13]). In fact, in order to represent m materials, we need $n = \log_2 m$ level-set functions. To simplify the exposition we discuss the case of $m = 4$ phases which can be represented by two level set functions ψ_1 and ψ_0 corresponding to two "super-domains" O_1 and O_0 (see Fig.(2)).

More precisely, we define $\Omega^1 = O_1 \cap O_0^c$, $\Omega^2 = O_1^c \cap O_0$, $\Omega^3 = O_1 \cap O_0$, $\Omega^4 = O_1^c \cap O_0^c$, where O_i^c denotes the complementary of O_i . There are many ways of regularizing the Hooke's tensor A for this new problem. For example, one can use a regularized version of the Heaviside functions H_1 and H_0 of the super-domains O_1 and O_0 , defined for $i = 0, 1$ as

$$H_i(d_i) = \begin{cases} 0 & \text{if } d_i < -\epsilon, \\ \frac{1}{2} + \frac{d_i}{2\epsilon} + \frac{1}{2\pi} \sin\left(\frac{\pi d_i}{\epsilon}\right) & \text{if } -\epsilon \leq d_i \leq +\epsilon, \\ 1 & \text{if } d_i > +\epsilon, \end{cases}$$

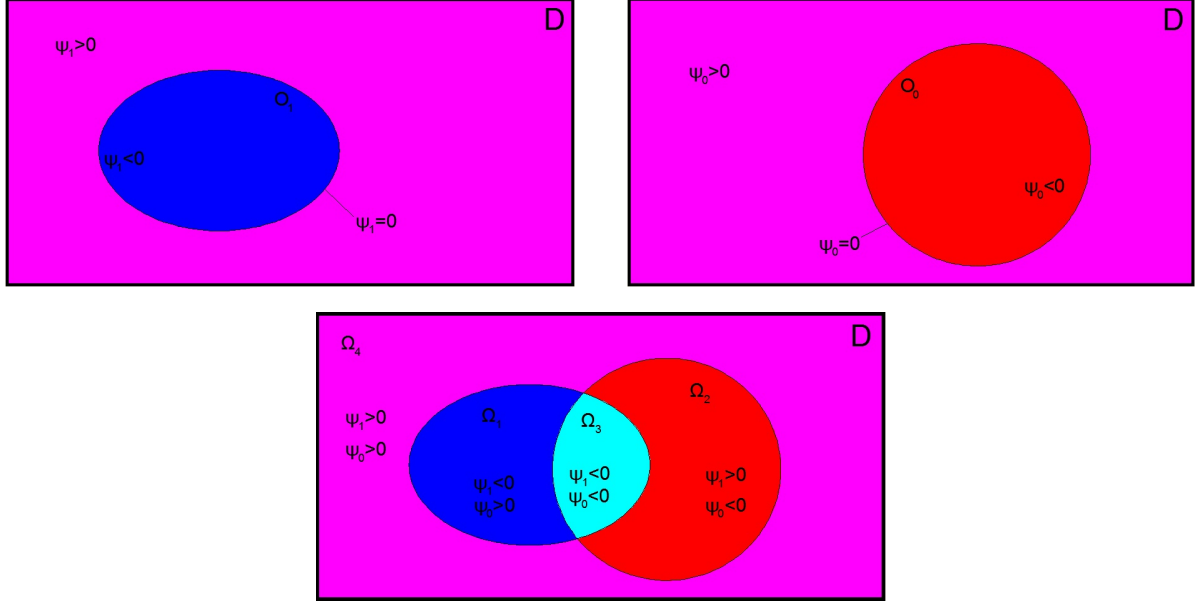


Figure 2: Two level-set functions defined on the same domain (top) and the four domains derived from combinations of their values (down).

where d_i is the signed-distance function to the super-domain O_i and then define the Hooke's tensor A as

$$A(d_1, d_0) = +A_1(1 - H_1(d_1))H_0(d_0) + A_2(1 - H_0(d_0))H_1(d_1) \\ + A_3(1 - H_1(d_1))(1 - H_0(d_0)) + A_4H_0(d_0)H_1(d_1).$$

Moreover, as the regularizing parameter $\epsilon \rightarrow 0$, the problem will converge to a problem of multi-materials with a sharp interface.

In this last case, the total compliance takes the form:

$$J(d_1, d_0) = \int_D A(d_1, d_0)e(u) : e(u). \quad (15)$$

We can consider two separate vector fields θ_1 and θ_0 for the advection of the domains O_1 and O_0 . Then, we calculate the shape derivative of the objective function (15) for each vector field separately and advect each of the domains O_1 and O_0 using their corresponding advection velocity (see [3]).

6 NUMERICAL RESULTS

6.1 Structural example

The first example is a 2×1 structure, clamped at the right and left part of its boundary and with a unit force applied at the middle of its lower part (see Fig.(3)). First, we minimize the compliance of the structure using one material with normalized Young modulus $E^1 = 1$, under the constraint $\int_{\Omega} dx = |D|/2$, where $|D|$ is the total volume of the domain D . The second material has $E^2 = eps \ll 1$ and simulates void. A simple augmented lagrangian algorithm is applied to enforce the volume constraint. The initialization and the optimized shape are shown in Fig.(4).

Suppose now that we want to replace half of this material with a weaker (but probably cheaper) material. In this case, we need to use three different phases, i.e. we need two

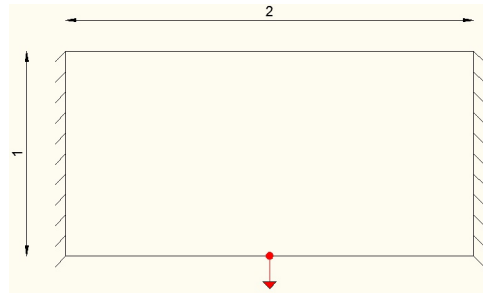


Figure 3: Boundary conditions.

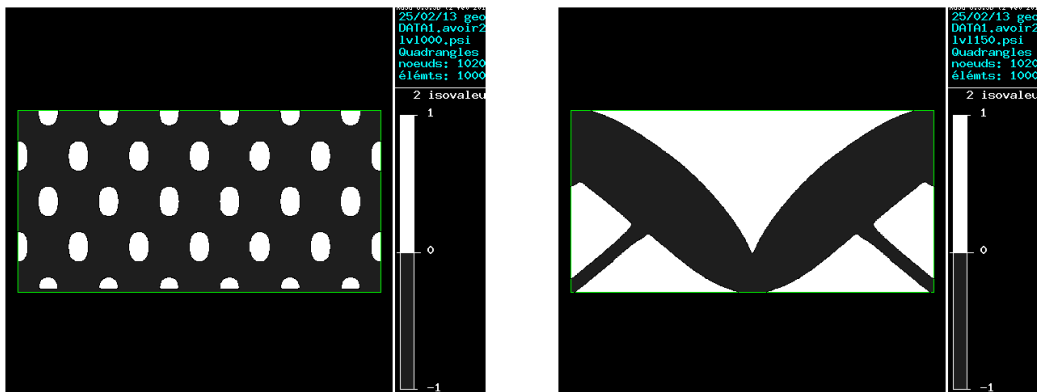


Figure 4: Initialization (left) and optimized shape (right) using one material.

level-set functions. Using two level-set functions we define four phases with Young modulus $E^1 = 1$, $E^2 = eps$, $E^3 = 0.5$ and $E^4 = eps$, i.e. materials 2, 4 represent void. The volume constraints read now $\int_{\Omega^1} dx = |D|/4$ and $\int_{\Omega^3} dx = |D|/4$. The initialization and the optimized shape are shown in Fig.(5).

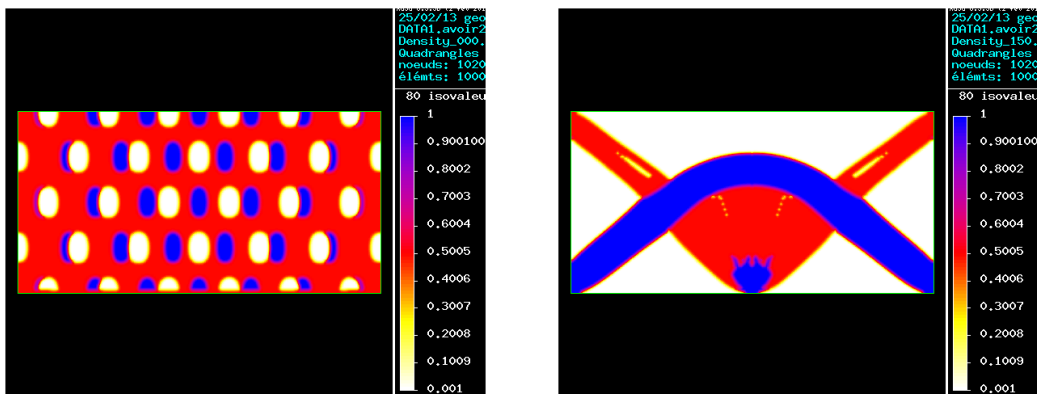


Figure 5: Initialization (left) and optimized shape (right) using two materials.

Using always two level-set functions we can optimize structures with up to three distinct phases and void. Choosing $E^1 = 1$, $E^2 = eps$, $E^3 = 0.7$ and $E^4 = 0.5$ and imposing $\int_{\Omega^1} dx = |D|/8$, $\int_{\Omega^3} dx = |D|/4$ and $\int_{\Omega^4} dx = |D|/8$, a local minimum is shown in Fig.(6).

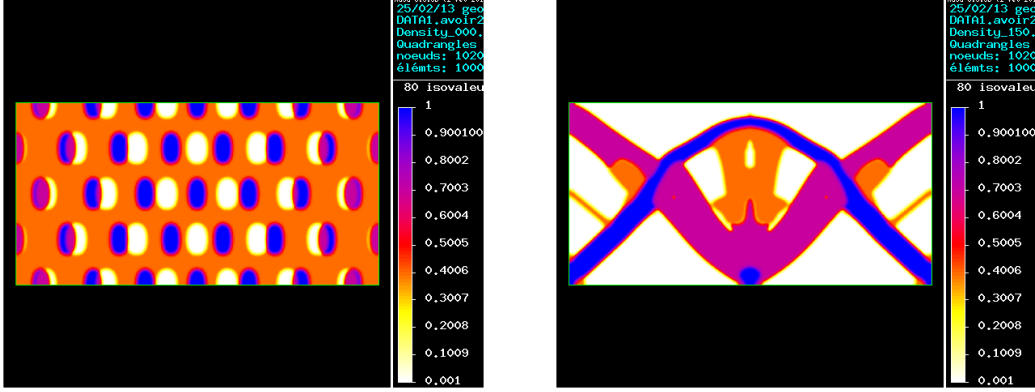


Figure 6: Initialization (left) and optimized shape (right) using three materials.

6.2 Multi-functional example

The second example couples a structural and a thermal problem. A 6×1 structure is considered (see Fig.(7)), having two non-optimizable areas (in blue) at the upper and lower part, occupied by material 1. The structure is subjected to two uncoupled mechanical problems. For the structural load case, the shape is considered clamped at its right and left boundary and a load is applied at the middle of the lower part. For the thermal load case, homogeneous Dirichlet conditions are considered for the lower part and the structure is subjected to a thermal flux either "in-plane" (Φ_2) or "out-of-plane" (Φ_1). The PDE describing the thermal problem reads

$$\left\{ \begin{array}{ll} -\operatorname{div}(k(d_{\Omega^1}(x)) \nabla T) = 0 & \text{in } D, \\ T = 0 & \text{on } \Gamma_D, \\ k(d_{\Omega^1}(x)) \frac{\partial T}{\partial n} = \Phi_i & \text{on } \Gamma_N, \\ \frac{\partial T}{\partial n} = 0 & \text{on } \Gamma_0, \end{array} \right. \quad (16)$$

where $i = 1$ or 2 . Our goal is to distribute in an optimal way two materials with different properties, so as to create a structure that is stiff and thermally isolating at the same time. Material 1 has normalized Young modulus and thermal conductivity $E^1 = k^1 = 1$, while material 2 has $E^2 = k^2 = 0.1$, i.e. material 1 is stiffer but thermally more conductive than material 2.

As objective function to minimize, we will adopt the following choice presented in [4]

$$J(\Omega^1) = \frac{(\int_D A(d_{\Omega^1}(x)) e(u) e(u) dx)^{1-a}}{(\int_D k(d_{\Omega^1}(x)) \nabla T \cdot \nabla T dx)^a}, \quad a \in [0, 1]. \quad (17)$$

The term in the nominator is the mechanical compliance, while the term in the denominator is the thermal compliance. The parameter "a" is chosen so as to highlight the importance of one or the other load case. For $a = 0$ the problems turns to the minimization of the mechanical compliance and thus all the optimisable area will be covered with the stiff material 1, while for $a = 1$ the problem is to minimize the thermal compliance, i.e. maximize the thermal isolation, and therefore the material 2 will be chosen. For intermediate values of "a", the algorithm will search for an optimal mixture of the two materials.

We consider both the case of "out-of-plane" and "in-plane" flux. The initialization for both cases is shown in Fig.(8). The optimized shape and the convergence diagram for "out-of-plane" flux and $a = 0.3$ is depicted in Fig.(9). In this figure we can see clearly that material 1 (in blue)

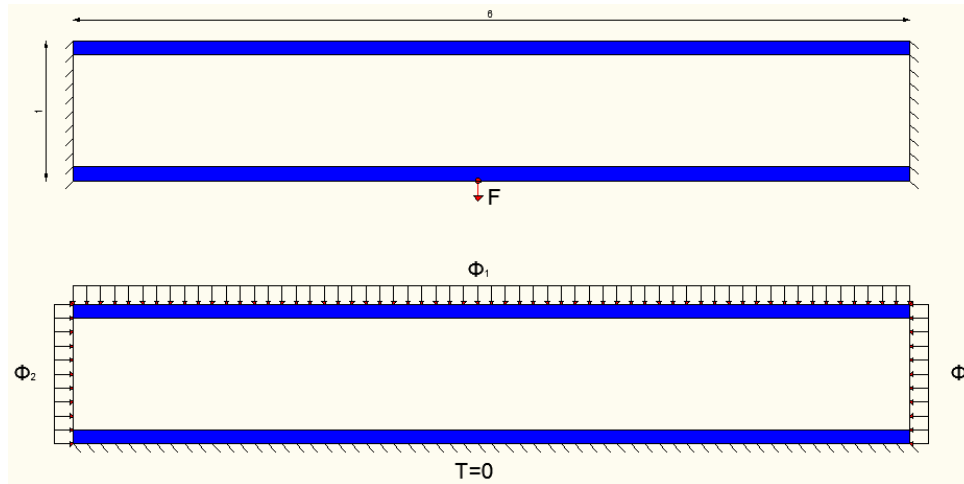


Figure 7: Boundary conditions. "Out-of-plane" flux corresponds to $\Phi_1 \neq 0$, $\Phi_2 = 0$, while "in-plane" flux corresponds to $\Phi_2 \neq 0$, $\Phi_1 = 0$.

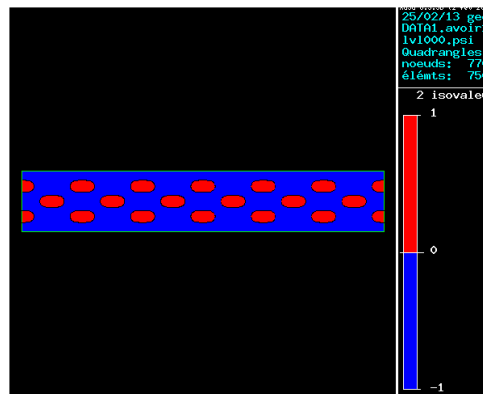


Figure 8: Initialization.

is placed so as to bear the structural load, whereas material 2 (in red) tries to prevent the thermal flux.

The case of "in-plane" flux is shown in Fig.(10) for $a = 0.5$. In this case, material 2 tries to isolate thermally the structure by being concentrated around the place that the flux is applied.

REFERENCES

- [1] G. Allaire, F. Jouve and A.M. Toader, *Structural optimization using shape sensitivity analysis and a level-set method*, J. Comput. Phys., 194 (2004) pp. 363–393.
- [2] G. Allaire, F. Jouve, N. Van Goethem, *Damage and fracture evolution in brittle materials by shape optimization methods*, J. Comp. Phys. 230, pp.5010-5044 (2011).
- [3] G. Allaire, C. Dapogny, G. Delgado and G. Michailidis, *Multi-phase structural optimization via a level set method*, In preparation.
- [4] L. Laszczyk, R. Dendievel, O. Bouaziz and Y. Bréchet, *Optimisation des propriétés équivalentes de motifs périodiques: Cas d'un panneau architecturé en flexion*, 10e colloque national en calcul des structures, 2011.

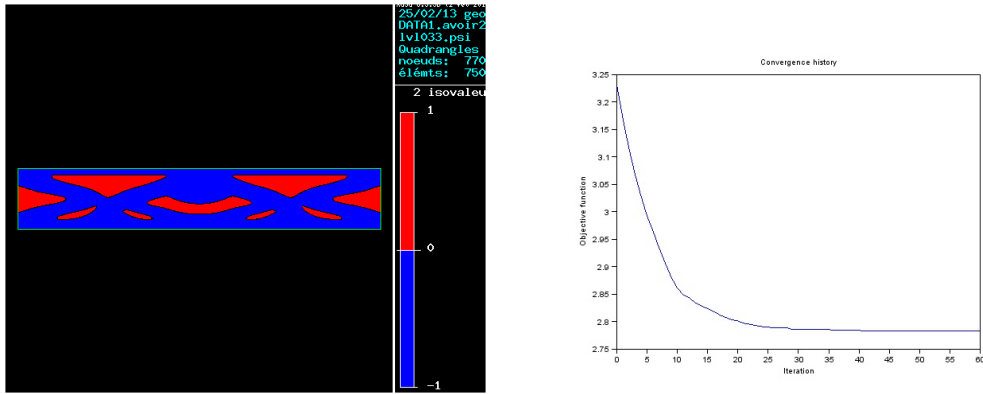


Figure 9: Optimized shape and convergence diagram for "out-of-plane" flux and $a = 0.3$.

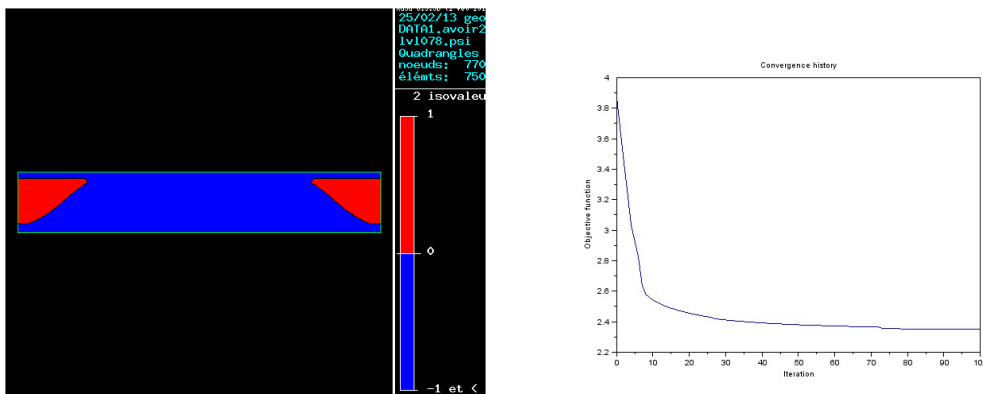


Figure 10: Optimized shape and convergence diagram for "in-plane" flux and $a = 0.5$.

- [5] Y. Mei and X. Wang, *A level set method for structural topology optimization with multi-constraints and multi-materials*, ACTA MECHANICA SINICA, Vol.20, No.5, (2004).
- [6] F. Murat and J. Simon, *Sur le contrôle par un domaine géométrique*, Technical Report RR-76015, Laboratoire d'Analyse Numérique (1976).
- [7] S. Osher and J.A. Sethian, Front propagating with curvature dependent speed: algorithms based on Hamilton-Jacobi formulations. *J. Comp. Phys.* **78**, 12-49 (1988).
- [8] O. Pantz, *Sensibilité de l'équation de la chaleur aux sauts de conductivité* C. R. Acad. Sci. Paris, Ser. I 341 (2005).
- [9] J.A. Sethian, *Level-Set Methods and fast marching methods: evolving interfaces in computational geometry, fluid mechanics, computer vision and materials science*, Cambridge University Press (1999).
- [10] O. Sigmund and S. Torquato, *Design of materials with extreme thermal expansion using a three-phase topology optimization method*, Journal of the Mechanics and Physics of Solids, 45(6):1037-1067 (1997).
- [11] O. Sigmund, *Design of multiphysics actuators using topology optimization-part ii: Two-material structures*, Computer methods in applied mechanics and engineering, 190(49):6605-6627 (2001).

- [12] M.Y. Wang, X. Wang and D. Guo, *A level-set method for structural topology optimization*, *Comput. Methods Appl. Mech. Engrg.*, **192**, 227-246 (2003).
- [13] M. Wang and X. Wang, *Color level sets: a multi-phase method for structural topology optimization with multiple materials*, *Comput. Methods Appl. Mech. Engrg.* 193 (2004).
- [14] N. Vermaak, G. Michailidis, Y. Brechet, G. Allaire, G. Parry and R. Estevez, *Material Interface Effects on the Topology Optimization of Multi-Phase Thermoelastic Structures Using A Level Set Method*, In preparation.
- [15] S. Zhou and Q. Li, *Computational design of multi-phase microstructural materials for extremal conductivity*, *Computational Materials Science*, 43:549-564 (2008).
- [16] S. Zhou and M.Y. Wang, *Multimaterial structural optimization with a generalized Cahn-Hilliard model of multiphase transition*, *Struct Multidisc Optim*, 33:89-111 (2007).

DISCRETE OPTIMIZATION APPROACH FOR STEEL FRAMES AND TRUSSES, BASED ON GENETIC ALGORITHM

Ioana D. Balea¹, Radu Hulea¹, and Georgios E. Stavroulakis²

¹ Technical University of Cluj-Napoca
400020 Cluj-Napoca, Romania
e-mail: ioana.balea@mecon.utcluj.ro

² Technical University of Crete
Kounoupidiana, Akrotiri, Greece
gestavr@dpem.tuc.gr

Keywords: optimization, steel, eurocode, genetic algorithms

Abstract. *This paper presents an implementation of Eurocode load cases for discrete global optimization algorithm for planar and space structures based on the principles of finite element methods and genetic algorithms. The final optimal design is obtained using IPE sections chosen as feasible by the algorithm, from the available steel sections from industry, used for ease of comparison with benchmarks. The algorithm is tested on several planar steel frames and a truss from the literature, with good results.*

1 INTRODUCTION

In all engineering fields, designers attempt to find solutions that combine performance and satisfaction of critical requirements. But these techniques and requirements are subject to constant change. The oldest surviving books on engineering are two thousand year old - Ten Books on Architecture by Vitruvius. These demonstrate that the way engineers thought about design in ancient times appears to have been fundamentally the same as how we think today, and the problems faced at the time and in that technological context, just as complex as those we face today. So, for the past two thousand years, engineers have been tackling design problems defined by competing goals and bounded by technical, aesthetic and economic constraints. Architects and engineers have always had to be masters of a wide variety of knowledge and skill, to be broadly interdisciplinary people. The design of structures in ancient times was based on geometry, and, to whichever form was used for buildings, ancient engineers found limits of use defined by failure. And, just as the ancient Greeks and Romans learned by the method of trial and error and deduced rules of thumb, accumulating knowledge and engineering advances today guides us in extending the state of the art towards new limits. Though engineers may not be building now ancient monuments, our contemporary masterpieces of engineering design and technology have their origins in the same type of conceptu-

alization processes. A design with loose constraints might float off into irrelevance. Constraint offers an opportunity for growth and innovation. Designers can obtain the optimum within the imposed conditions by using optimization techniques. In the field of structural engineering, structures designed in this way are safer, more reliable and less expensive than the traditional designed ones, where the success of the design is based solely on the experience of the engineer. Optimization techniques require some expertise, but with the implementation of these algorithms in computer aided design software it can become a very powerful tool in the hands of engineers. In general, the optimization techniques used in structural design can be categorized into classical and heuristic search methods.

Classical optimization methods such as linear programming, nonlinear programming and optimality criteria often require substantial gradient information. In these methods the final results depend on the initially selected points and the number of computational operations increases as the size of the structure increases. The solution in these methods does not necessarily correspond to the global optimum. Many engineering design problems are too complex to be handled with mathematical programming methods. In comparison, heuristic search methods do not require the data as in the conventional mathematical programming and have better global search abilities than the classical optimization algorithms [1]. For the past 60 years a new branch of optimization techniques was continuously developed, which mimics the design methods existing in nature. Genetic algorithms, simulated annealing and evolutionary strategies are among such algorithms that are used in the design optimization of structures. Among these, genetic algorithms, are a search method that is based on the principal of the survival of the fittest and adaptation. They operate on a population of design variables sets. Each population consists of individuals that are potential solutions to the design problem. A fitness value is calculated for each individual using the objective function and constraints as a measure of performance of the design variables. If the individual is fit, it is selected as candidate to take part in the construction of the next population, if not then it is discarded. The solution to a general optimization process can be associated with this system behavior. The genetic algorithm (GA) is one of the best-known heuristic methods; it has been used to solve structural optimization problems by some researches such as Rajeev and Krishnamoorthy [2], Saka and Kameshki [3], Camp et al. [4], Pezeshk et al. [5], Erbatur et al. [6], Shook et al. [7], among many others.

2 PLANAR FRAME AND TRUSS OPTIMIZATION PROBLEMS

The structural optimization problem could be formulated as follows, for a structure that consists of M nodes and N bars with cross-sectional areas: A_i , $i=1,2,\dots,N$. All cross-sectional areas A_i compose the vector \mathbf{x} of the optimization parameters:

$$\mathbf{x}=[A_1 \ A_2 \ \dots \ A_N]^T \quad (1)$$

The problem to be solved refers to the computation of the vector \mathbf{x} achieving the minimum weight W of the frame or truss

$$W = \sum_{i=1}^N \rho A_i L_i \quad (2)$$

for given stress- and deflection-constraints (dis-placement-constrained trusses):

$$\begin{aligned} \sigma_i &\leq \sigma_{0i} & 1 \leq i \leq N \\ u_i &\leq u_{0i} & 1 \leq i \leq M \end{aligned} \quad (3)$$

In equation (3), s_{0i} and u_{0i} denote the allowable stress and displacement upper limits, respectively.

3 EUROCODE PROVISIONS

Constraints regarding material strength and stability are taken from “EN 1993: Design of steel structures” [8] and implemented in the algorithm. Resistance must be checked by verification by the partial factor method. The design resistance for cross-sections is:

$$N_{c,Rd} = \frac{Af_y}{\gamma_{M0}}$$

The design should satisfy the requirements under the most unfavorable loading cases considered. Elastic analysis is routinely used to obtain member forces for subsequent use in the member checks based on the ultimate strength considerations. This is well accepted, can be shown to lead to safe solutions, and has the great advantage that superposition of results may be used when considering different load cases. In the Eurocodes, partial factors γ_{Mi} are applied to different components in various situations to reduce their resistances from characteristic values to design values (or, in practice, to ensure that the required level of safety is achieved). The uncertainties (material, geometry, modeling, etc.) associated with the prediction of resistance for a given case, as well as the chosen resistance model, dictate the value of γ_M that is to be applied. The choice for the different loading scenarios was made considering all the predictable conditions and situations that can appear during the construction phase and the utilization phase of the building.

$$E_d = E \cdot (\gamma_{G,j} \cdot G_{k,j}; \gamma_{Q,1} \cdot Q_{k,1}; \gamma_{Q,i} \cdot \psi_{0,i} \cdot Q_{k,i}) \quad (2)$$

Where:

E_d – design load

γ – Partial coefficient

G – Permanent action

Q – Variable action

ψ – Coefficient variable action

4 THE OPTIMIZATION ALGORITHM

Evolutionary Computation (EC) is an enormous field of research concerned with the application of Evolutionary Algorithms (EA) to complex real-world optimization problems (for a literature review see Kicinger [9]). These methods are stochastic search algorithms modeling the natural phenomenon of evolution, a combination of the Darwinian concept of survival of the fittest and the inheritance of genetic material within a species. Because of their heuristic nature they generally cannot guarantee to find a global optimum solution, however, they can be applied to highly complex models for which standard optimization methods (e.g. gradient based algorithms) are not applicable, and in practice they often yield promising results. The terminology of EC is inspired by the resemblance to biological processes and lots of terms are borrowed from genetics and cellular biology. A candidate design solution is called an individual and a set of such solutions is called population. The representation (parameterization, encoding) of an individual is called a genome consisting of a series of genes. For some algorithms the search space (genotype space) is explicitly separated from the solution space (phenotype space) and a link between the two is made by a mapping procedure that codes (phenotype to genotype space) and decodes (genotype to phenotype space) the candidate solutions. Producing new solutions by modifying individual solutions is referred to as mating or

breeding and the resulting solutions are called offspring. A fitness value is assigned to each individual indicating its quality in the context of the given problem in order to compare different candidate solutions. Selection is then used in order to determine which of the parents and the offspring survive and are transferred to the new population, which is typically called a new generation. Although many different implementations of EAs exist, the basic concept of the so-called canonical EA forms the basis of all of them. The canonical EA can be understood as a search process in which a population experiences gradual changes and consists of the following steps:

Canonical EA
 1: $t=0$
 2: Initialize the population
 3: Evaluate the entire population
 4: while (not termination condition) do
 5: $t=t+1$
 6: Mating selection
 7: Apply variation operators
 8: Evaluate offspring
 9: Select individuals for survival
 10: end while

The mating selection process favors individuals with higher fitness values over candidate solutions with below-average fitness values, or for minimization problems a lower fitness value indicates better quality of the candidate solution. New individuals are created by copying them and applying genetic variation operators. The most used operators are mutation and recombination (crossover). The steps 5 to 9 of the algorithm are repeated until a given termination condition, e.g. a maximum number of generations or evaluations or a target fitness value is met.

<i>Population size</i>	300
Crossover parameter	0.7
Mutation parameter	0.1
Maximum number of iterations	100

Table 1: The specifications of the used GA method

The optimization problems addressed within this paper have a single objective, but they are also subjected to an arbitrary number of constraints. The number of optimization parameters defines the size of the genotype and accordingly the size of the search space. A fitness function mapping the evaluated stiffness, strength and mass measures from the FE analysis to a unique fitness value was defined.

5 NUMERICAL IMPLEMENTATION

The first example refers to nine variables (nine-bar truss), the second to eight design variables (eight-element frame), and finally the third to 105 variables (105-bar truss).

In total, 20 program runs were performed, of which 5 are presented. The profiles used in the optimization procedures are presented below

5.1 The first optimization problem : frame 8 bars 8 nodes

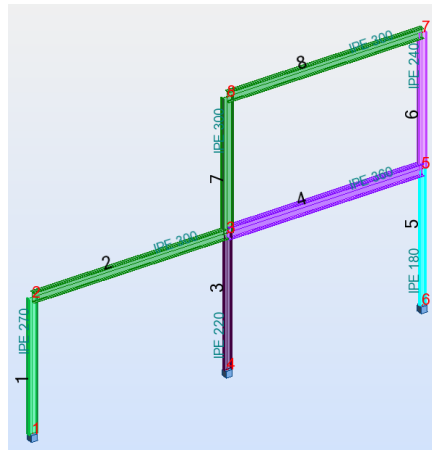


Figure 1: Structure no. 1 – 8 bars

The problem has 8 variables represented by cross sections of the elements.

Bar	Uniformly distributed load							
	Permanent loads		Live Loads		S now Loads		Wind Loads	
	X	Z	X	Z	X	Z	X	Z
1	0	0	0	0	0	0	-2.5	0
2	0	-10	0	-15	0	-6	0	0
3	0	0	0	0	0	0	0	0
4	0	-10	0	-15	0	0	0	0
5	0	0	0	0	0	0	-5	0
6	0	0	0	0	0	0	-5	0
7	0	0	0	0	0	0	-2.5	0
8	0	-10	0	-15	0	-6	0	0

Table 2: Loads used for problem 1.

Bar	Profiles				
	Run 1	Run 2	Run 3	Run 4	Run 5
1	IPE 120	IPE 140	IPE 120	IPE 140	IPE 120
2	IPE 180	IPE 200	IPE 180	IPE 200	IPE 160
3	IPE 330	IPE 270	IPE 330	IPE 300	IPE 360
4	IPE 140	IPE 180	IPE 180	IPE 140	IPE 140
5	IPE 330	IPE 330	IPE 330	IPE 330	IPE 330
6	IPE 140	IPE 140	IPE 140	IPE 120	IPE 120
7	IPE 200	IPE 200	IPE 200	IPE 180	IPE 160
8	IPE 330	IPE 330	IPE 330	IPE 330	IPE 390
Total weight	1193.9	1200.4	1217.5	1152.5	1240.7

Table 3: Profiles chosen by algorithm

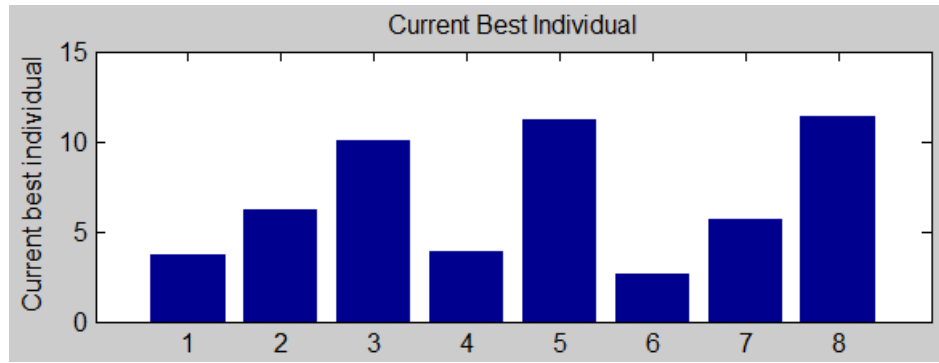


Figure 2: Best individual

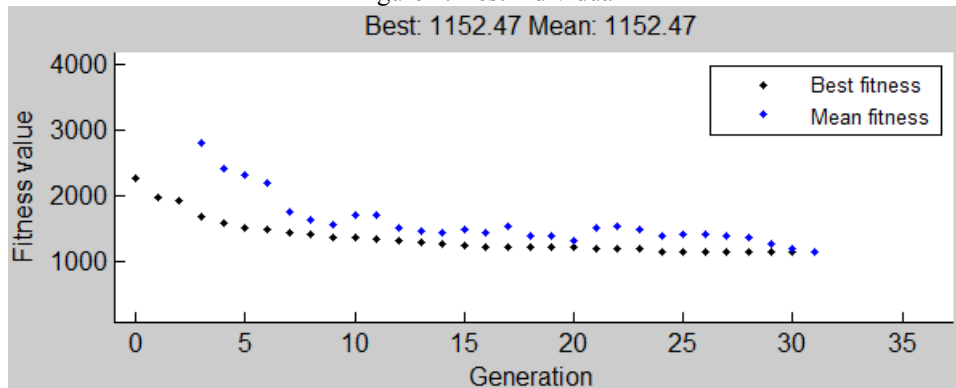


Figure 3: Convergence of algorithm

The structure was also optimized using Autodesk Robot Structural Analysis. By employing this software a total weight of 1466 Kg by comparison with the 1152Kg solution obtained when using the Matlab code.

5.2 The second optimization problem: truss 9 bars 6 nodes

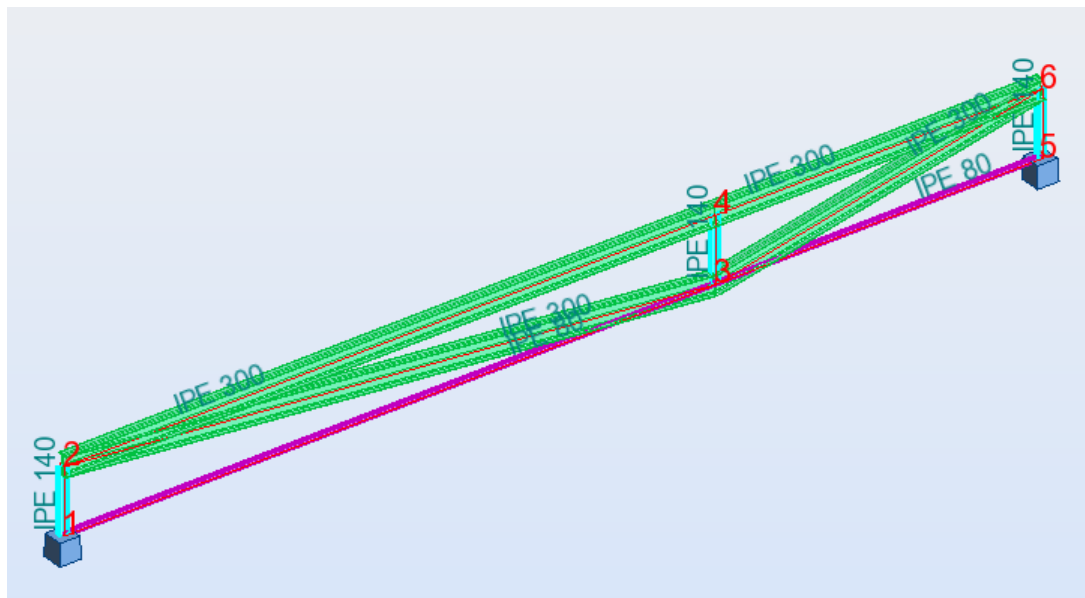


Figure 4: Structure no. 2 – 9 bars

The problem has 9 variables represented by cross sections of the elements.

Nodes			
	Permanent Loads	Live loads	Snow loads
	Z	Z	Z
1	0	0	0
2	-50	-75	-30
3	0	0	0
4	-75	-112.50	-45
5	0	0	0
6	-25	-37.5	-15

Table 4: Loads on structure

Bar	Profiles				
	Run 1	Run 2	Run 3	Run 4	Run 5
1	IPE 80	IPE 80	IPE 80	IPE 80	IPE 80
2	IPE 80	IPE 80	IPE 80	IPE 80	IPE 80
3	IPE 300	IPE 300	IPE 300	IPE 300	IPE 300
4	IPE 300	IPE 330	IPE 300	IPE 300	IPE 330
5	IPE 180	IPE 180	IPE 140	IPE 140	IPE 140
6	IPE 300	IPE 300	IPE 300	IPE 300	IPE 300
7	IPE 180	IPE 140	IPE 140	IPE 200	IPE 140
8	IPE 300	IPE 300	IPE 300	IPE 300	IPE 300
9	IPE 180	IPE 220	IPE 140	IPE 160	IPE 140
Total weight	1402.25	1456.0	1402.25	1414.6	1436.8

Table 5: Profiles chosen by algorithm

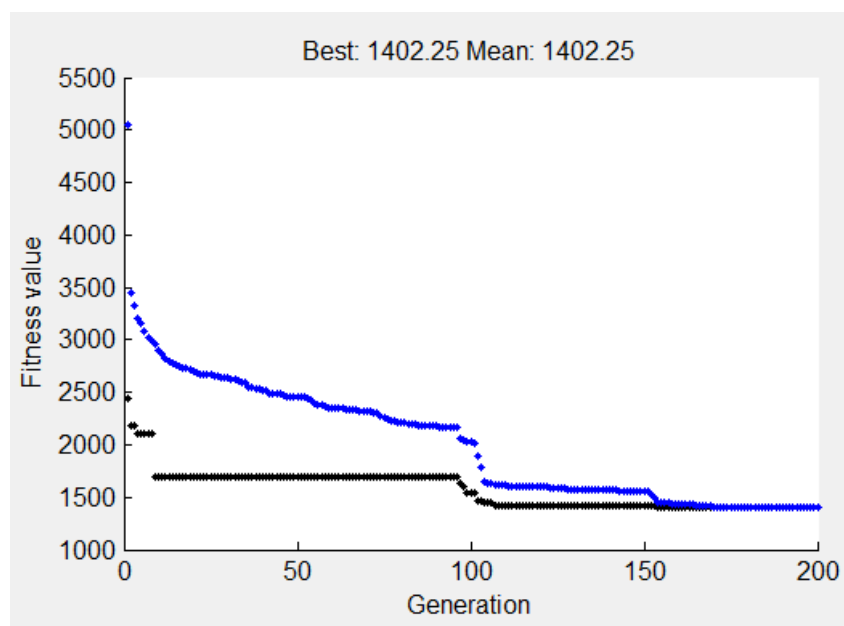


Figure 5: Convergence of algorithm

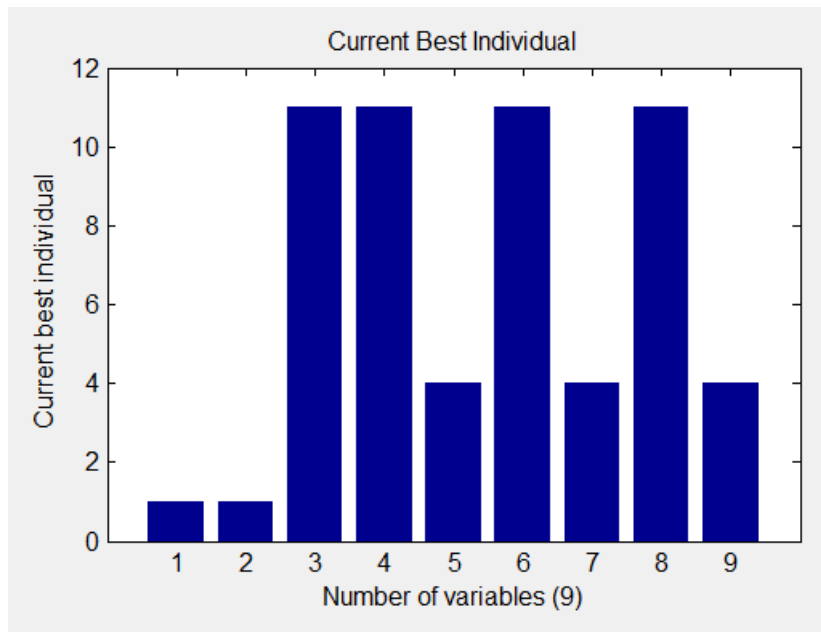


Figure 6: Best individual

The structure was also optimized using Autodesk Robot Structural Analysis. By employing this software a total weight of 1403 kg was obtained, close to the 1402 Kg solution obtained when using the algorithm developed in Matlab.

5.3 The third optimization problem: truss 120 bars 49 nodes

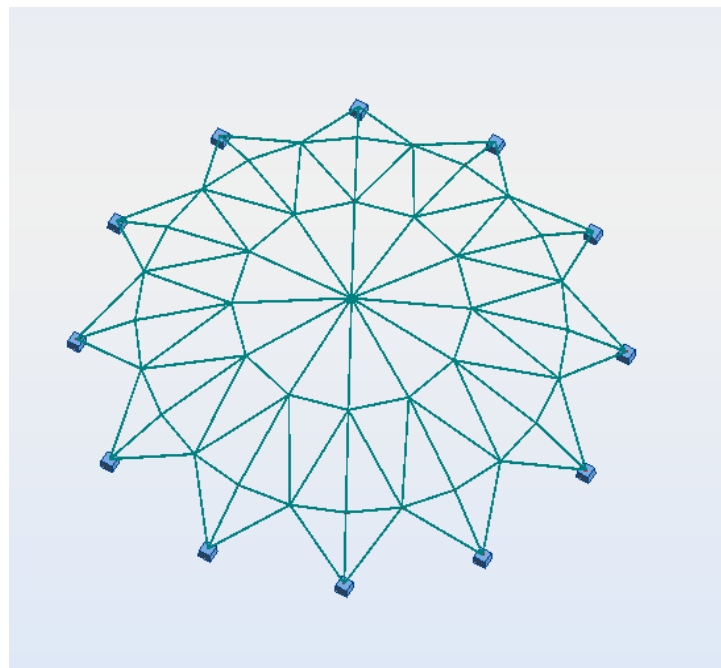


Figure 7: Structure no. 3 – 120 bars

The problem has 120 variables represented by cross sections of the elements.

Bar	Profiles				
	Run 1	Run 2	Run 3	Run 4	Run 5
Total weight	14008.1	15080.4	14941.6	14466.9	14953.9

Table 7: Profiles chosen by algorithm

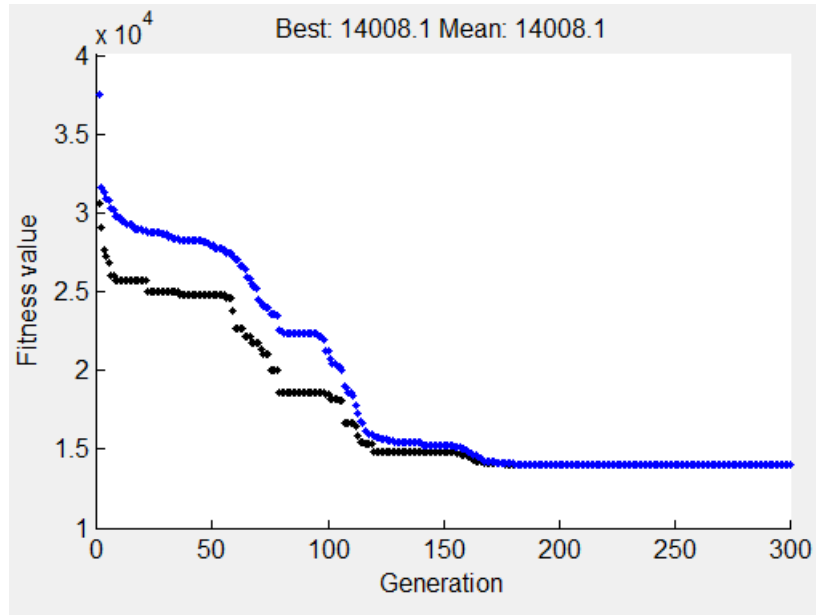


Figure 8: Convergence of the algorithm

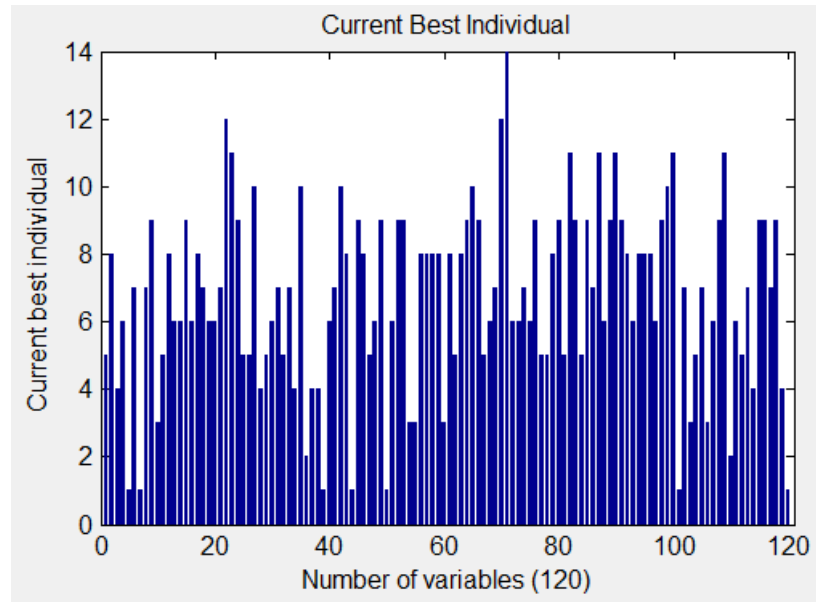


Figure 9: Best individual

6 CONCLUSIONS

Structural Optimization, while very interesting, is a tricky class of optimization problems, usually being characterized by a large number of variables that represent the shape of the design and the stiffness of the available materials. In any practical problem, the researcher deals with a unique combination of mentioned factors and has to decide what numerical tools to use

or modify to reach the final goal. Therefore, the optimization of a structure always relies on both creativity and intuition, it is said that optimization combines both science and art.

Acknowledgements

This paper was supported by the project "Improvement of the doctoral studies quality in engineering science for development of the knowledge based society-QDOC" contract no. POSDRU/107/1.5/S/78534, project co-funded by the European Social Fund through the Sectorial Operational Program Human Resources 2007-2013. A special thanks goes to the Technical University of Crete for hospitality and support.

REFERENCES

- [1] A. Belegundu, "A Study of Mathematical Programming Methods for Structural Optimization. PhD thesis," University of Iowa, Dept. of Civil and Environmental Engineering, 1982.
- [2] S. Rajeev and C. Krishnamoorthy, "Discrete Optimization of Structures Using Genetic Algorithms," *Journal of Structural Engineering*, vol. 118, no. 5, pp. 1233-1250, 1992.
- [3] S. M.P. and K. E., "Optimum Design of Multi-Storey Sway Steel Frames to BS 5950 using a Genetic Algorithm," in *Advances in Engineering Computational Technology*, Edinburgh, UK, Civil-Comp Press, 1998, pp. 135-141.
- [4] C. V. Camp and S. .: G. Pezeshk, "Optimized Design of Two-Dimensional Structures Using A Genetic Algorithm," *Journal of Structural Engineering, ASCE*, vol. 124, no. 5, pp. 551-559, 1998.
- [5] S. Pezeshk and C. C. V., "State of the Art on the Use of Genetic Algorithms in Design of Steel Structures," in *Recent Advances in Optimal Structural Design*, S. Burns (Editor), American Society of Civil Engineers, 2002.
- [6] F. Erbaturo and M. M. Al-Hussainy, "Optimum design of frames," *Comp. and Struct.*, vol. 5/6, no. 45, pp. 887-891, 1992.
- [7] D. A. Shook and e. al., "GA-optimized fuzzy logic control of a large scale building for seismic loads," *Engineering Structures*, vol. 30, pp. 436-449, 2008.
- [8] *Eurocode 3: EN 1993-1-1 Design of steel structures – Part 1-1: general rules and rules for buildings*.
- [9] K. R., A. T. and D. J. K., "Evolutionary computation and structural design: A survey of the state-of-the-art," *Comp. and Struct.*, vol. 83, no. 23-24, pp. 1943-1978, 2005.

MULTI-OBJECTIVE SHAPE DESIGN OPTIMIZATION INTO AN XFEM FRAMEWORK

Manolis Georgioudakis, Nikos D. Lagaros*, Manolis Papadrakakis

Institute of Structural Analysis & Seismic Research,
National Technical University Athens
Zografou Campus, Athens 15780, Greece
{geoem, nlagaros, mpapadra}@central.ntua.gr

Keywords: extended finite element method, fracture mechanics, crack propagation, multi-objective shape optimization, metaheuristics.

Abstract. *Almost every real world problem involves simultaneous optimization of several incommensurable and often competing objectives which constitutes a multi-objective optimization problem. In multi-objective optimization problems the optimal solution is not unique as in single-objective optimization problems. In this paper, a multi-objective shape design optimization is implemented within the context of Extended Finite Element Method (XFEM). Two objective functions dealing with maximum service life (represented by maximizing the number of fatigue cycles), and minimum weight subjected to specified minimum service life and an upper limit on volume are considered. Structural performance entities are selected as constraints and geometrical data are employed as shape design variables. Nature inspired optimization techniques have been proven to be quantitatively appealing, since they have been proved to be robust and efficient even for the most complex problems examined. These methods, also known as metaheuristics, are used for combinatorial optimization problems. Special techniques with parallel processing for solving nested XFEM propagation problem are considered, in order to reduce the total computational cost.*

1 INTRODUCTION

Gradient-based optimizers capture very fast the right path to the nearest optimum, irrespective if it is a local or a global optimum but it cannot assure that the global optimum can be found. On the other hand metaheuristics, due to their random search, are being considered more robust in terms of global convergence; they may suffer, however, from a slow rate of convergence towards the global optimum. When metaheuristics are adopted to perform the optimization, the solution of the finite element equations is of paramount importance since more than 95% of the total computing time is spent for the solution of the finite element equilibrium equations [1]. A second characteristic is that in place of a single design point metaheuristics work simultaneously with a population of design points in the space of design variables. This allows for a natural implementation of the evolution procedure in parallel computer environments.

In single-objective optimization problems the optimal solution is usually clearly defined since it is the minimum or maximum value of the objective function. This does not hold in real world problems where multiple and conflicting objectives frequently exist. Instead of a single optimal solution, there is usually a set of alternative solutions, generally denoted as the set of Pareto optimal solutions. These solutions are optimal in the wider sense since no other solution in the search space is superior to them when all objectives are considered. In the absence of preference information, none of the corresponding trade-offs can be said to be better than the others. On the other hand, the search space can be too large and too complex, which is the usual case of real world problems, hence the implementation of gradient based optimizers for this type of problems becomes even more cumbersome. Thus, efficient optimization strategies are required able to deal with the presence of multiple objectives and the complexity of the search space. Metaheuristics and in particular EA have several characteristics that are desirable for this kind of problems and most frequently outperform the deterministic optimizers such as gradient based optimization algorithms. In sizing optimization the aim is to minimize the objective function which is usually the weight or the cost of the structure under certain restrictions imposed by the design codes when the characteristics of the cross-sections of the members are under investigation.

The aim of this paper is to couple a multi-objective shape design optimization within context of Extended Finite Element Method (XFEM) [2]. To this purpose, two objective functions dealing with (a) maximum service life (by maximizing the number of fatigue cycles), and (b) minimum weight subjected to specified minimum service life and an upper limit on volume. Metaheuristic optimization methods and in particular algorithms based on evolution strategies are implemented for the solution of the problem at hand. After a brief review of XFEM procedure, the problem formulation and the optimization algorithm used is described.

2 X-FEM CONCEPTS IN BRIEF

Since its first introduced by Moës *et al.* [2], eXtended Finite Element Method (XFEM) has gained a significant interest of researchers and became a powerful tool to simulate crack propagation phenomena [3]. Based on the concept of *partition of unity*, X-FEM allows special local enrichment functions to be incorporated into a standard finite element approximation, while preserving the classical displacement variational settings and meshing concepts. Hence, mesh does not need to conform to the problem geometry due to discontinuous enrichment functions and remeshing techniques are not required during crack propagation.

2.1 Basic Formulation

For solid mechanics problems, the equation to be solved is usually on the displacement \mathbf{u} of the body. The discretization of displacement field in order to model crack surfaces and crack tips, then reads:

$$\mathbf{u}^h(\mathbf{x}) = \mathbf{u}(\mathbf{x}) + \mathbf{u}^H(\mathbf{x}) + \mathbf{u}^{\text{tip}}(\mathbf{x}) \quad (1)$$

where the approximate displacement function \mathbf{u}^h can be expressed in terms of the standard \mathbf{u} , crack-split \mathbf{u}^H and crack-tip \mathbf{u}^{tip} , or more explicitly:

$$\mathbf{u}^h = \underbrace{\sum_{i \in I} \mathbf{u}_i N_i}_{\text{standard part}} + \underbrace{\sum_{j \in J} \mathbf{b}_j N_j H(f(\mathbf{x})) + \sum_{k \in K} N_k \left(\sum_{l=1}^4 \mathbf{c}_k^l F_l(\mathbf{x}) \right)}_{\text{enriched part}} \quad (2)$$

In (2) the last two terms on the right part, are the terms associated to enrichment functions. The function H (Heaviside function) is the jump function and is used to introduce discontinuity in crack faces. It has the following formulation:

$$H(\xi) = \text{sign}(\xi) = \begin{cases} -1 & \forall \xi > 0 \\ 1 & \forall \xi < 0 \end{cases} \quad (3)$$

Also, $f(\mathbf{x})$ showing the side of the crack where \mathbf{x} is located and can be the signed distance function to the crack, N are the standard shape functions and \mathbf{b}_j , \mathbf{c}_k are the vectors of additional degrees of nodal freedom for modeling crack faces and crack tips respectively. I is the set of all nodes in the mesh, J is the set of nodes in the mesh whose shape function support is completely cut by the crack and K is the set of nodes enriched by the crack tip enrichment functions which are inside a specific zone around crack tip. F_l are tip enrichment functions (branch functions) used to increase the accuracy of the numerical solution around crack tip and their formulation is dependent on the nature of the problem to be solved. In this study, crack propagation problem was solved within the linear elastic fracture mechanics framework (LEFM), in which the size of the plastic zone around the crack tip is very small compared to the structure size. So, these functions are chosen based on the asymptotic behavior of the displacement field at the crack tip:

$$F_l(r, \theta) = \left\{ \sqrt{r} \sin \frac{\theta}{2}, \sqrt{r} \cos \frac{\theta}{2}, \sqrt{r} \sin \theta \sin \frac{\theta}{2}, \sqrt{r} \sin \theta \cos \frac{\theta}{2}, \right\} \quad (4)$$

where (r, θ) is a polar co-ordinate system with its origin at the crack tip and $\theta=0$ tangent to the crack at its tip.

2.2 Fracture parameters calculation

The introduction of the discrete approximation (2) into the principle of virtual work leads to a system of linear equations. The stress intensity factors (SIFs) K_I and K_{II} for modes I and II, respectively, are computed using the domain form of the J-integral as described in [4]. Once SIFs are obtained, fracture parameters such as ΔN and θ_c can be easily computed from (5, 7):

$$\Delta N = \frac{\Delta \alpha}{C(\Delta K_{\text{eq}})^m} \quad (5)$$

where ΔN is the total cycles for crack to grows by length Δa . Usually the crack growth Δa is very small and in this study is predetermined equal to $a/10$, where a is the initial crack length. C and m are material constants. For general mixed mode loading, ΔK_{eq} is given by:

$$\Delta K_{eq} = \sqrt{\Delta K_I^2 + \Delta K_{II}^2} \quad (6)$$

where $\Delta K = K_{max} - K_{min}$ is the SIF range. The direction in which the crack will propagate from its current tip, θ_c , is obtained using the maximum hoop stress criteria [2]. The angle θ_c depends on the stress intensity factors, K_I and K_{II} , and is given by:

$$\theta_c = 2 \arctan \frac{1}{4} \left(\frac{K_I}{K_{II}} \pm \sqrt{\left(\frac{K_I}{K_{II}} \right)^2 + 8} \right), \quad -\pi < \theta_c < \pi \quad (7)$$

2.3 Level Set Method for modeling crack

Level Set Method (LSM) offers an elegant way of modeling discontinuities. Is a numerical technique for tracking the motion of interfaces and has been successfully applied for modeling cracks. The key point in modeling of crack and any discontinuity using level set method is to represent the discontinuity as a zero level set function. For the modeling of crack we define the level set function as a signed distance function. As the crack is a discontinuity which does not divide the domain into two distinct parts completely, rather a portion of the domain is divided, hence to fully characterize a crack we define two level set functions (i) a normal level set function ϕ and a tangential level set function ψ (see Figure 1). Both the two level set functions are defined as a signed distance functions. According to Figure 1, ϕ is the distance of points from the tangent line to the crack face (l_{sn}) and ψ is the distance from the line perpendicular to the crack at the crack tip (l_{st}). The crack is then defined as the set of the points for which $l_{sn} = 0$ and $l_{st} \leq 0$ and the crack tip is defined the point for which $l_{sn} = l_{st} = 0$. Such representation of crack is suitable for coupling LSM with XFEM, where enrichment functions are used, since it makes it also easy to obtain polar coordinates of points with respect to crack tip according to:

$$r = \sqrt{l_{st}^2 + l_{sn}^2} \quad \theta = \arctan \left(\frac{l_{st}}{l_{sn}} \right) \quad (8)$$

Also, level sets are used for selection of enriched nodes. To determine whether a node lies above or below the crack, one simply needs to retrieve sign of ψ at that point. So, if the crack cuts through an element, then $\phi \leq 0$ and $\psi_{min}\psi_{max} \leq 0$, where ψ_{min} and ψ_{max} are the minimum and maximum values of ψ at the nodes of this element. Through the XFEM process the new crack tip is computed and the a new crack segment is added to the current crack path taking into account only the level set function update. Thus, no need for re-meshing is required.

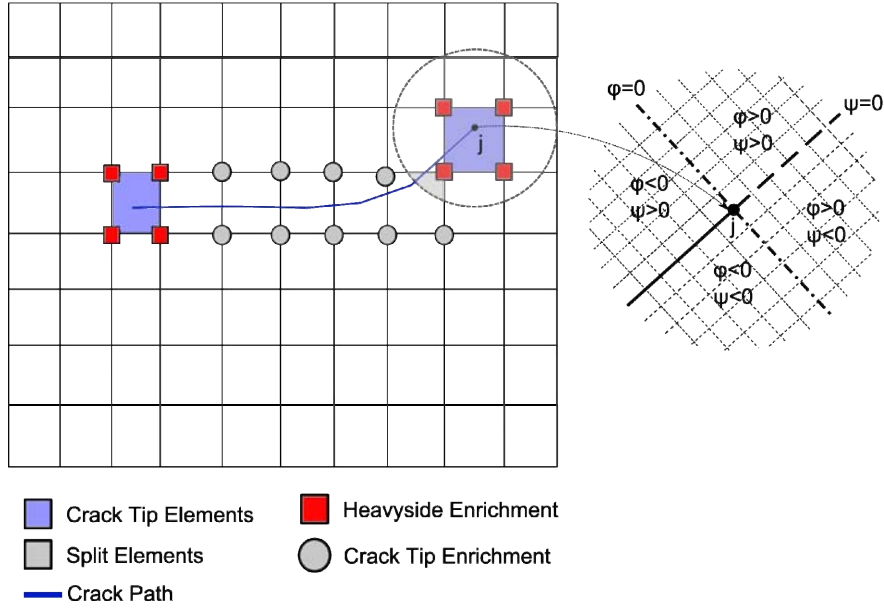


Figure 1: Nodal enrichment and level set functions in crack tip for the node j .

3 THE STRUCTURAL OPTIMIZATION PROBLEM

Structural optimization problems are characterized by various objective and constraint functions that are generally non-linear functions of the design variables. These functions are usually implicit, discontinuous and non-convex. The mathematical formulation of structural optimization problems with respect to the design variables, the objective and constraint functions depend on the type of the application. However, all optimization problems can be expressed in standard mathematical terms as a non-linear programming problem (NLP), which in general form can be stated as follows:

$$\begin{aligned} \min \quad & F(\mathbf{s}) \\ \text{subject to} \quad & g_j(\mathbf{s}) \leq 0 \quad j=1, \dots, k \\ & s_i^{\text{low}} \leq s_i \leq s_i^{\text{up}}, \quad i=1, \dots, n \end{aligned} \quad (9)$$

where \mathbf{s} is the vector of design variables, $F(\mathbf{s})$ is the objective function to be minimized, $g_j(\mathbf{s})$ are the behavioural constraints, s_i^{low} and s_i^{up} are the lower and the upper bounds of the i^{th} design variable.

There are mainly three classes of structural optimization problems: sizing, shape and topology or layout. Initially structural optimization was focused on sizing optimization, such as optimizing cross sectional areas of truss and frame structures, or the thickness of plates and shells. The next step was to consider finding optimum boundaries of a structure, and therefore to optimize its shape. In the former case the structural domain is fixed, while in the latter case it is not fixed but it has a predefined topology. In both cases a non-optimal starting topology can lead to sub-optimal results. To overcome this deficiency structural topology optimization needs to be employed, which allows the designer to optimize the layout or the topology of a structure by detecting and removing the low-stressed material in the structure which is not used effectively.

In structural shape optimization problems the aim is to improve the performance of the structure by modifying its boundaries. This can be numerically achieved by minimizing an

objective function subjected to certain constraints [5]. All functions are related to the design variables, which are some of the coordinates of the key points in the boundary of the structure. The shape optimization methodology proceeds with the following steps: (i) At the outset of the optimization, the geometry of the structure under investigation has to be defined. The boundaries of the structure are modelled using cubic B-splines that, in turn, are defined by a set of key points. Some of the coordinates of these key points will be the design variables which may or may not be independent to each other. (ii) An automatic mesh generator is used to create a valid and complete finite element model. A finite element analysis is then carried out and the displacements and stresses are evaluated. In order to increase the accuracy of the analysis an h-type adaptivity analysis may be incorporated in this stage. (iii) If a gradient-based optimizer is used then the sensitivities of the constraints and the objective function to small changes of the design variables are computed either with the finite difference, or with the semi-analytical method. (iv) The optimization problem is solved; the design variables are being optimized and the new shape of the structure is defined. If the convergence criteria for the optimization algorithm are satisfied, then the optimum solution has been found and the process is terminated, else a new geometry is defined and the whole process is repeated from step (ii).

4 MULTI-OBJECTIVE STRUCTURAL OPTIMIZATION

In practical applications of structural optimization the material weight or the structural cost rarely gives a representative measure of the performance of the structure. In fact, several conflicting and incommensurable criteria usually exist in real-life design problems that have to be dealt with simultaneously. This situation forces the designer to look for a good compromise design between the conflicting requirements. This kind of problems is called optimization problems with many objectives. The consideration of multi-objective optimization in its present sense originated towards the end of the 19th century when Pareto presented the optimality concept in economic problems with several competing criteria (Pareto, 1897). Since then, although many techniques have been developed in order to deal with multi-objective optimization problems the corresponding applications were confined strictly to mathematical functions. The first applications in the field of structural optimization with multiple objectives appeared at the end of the seventies.

4.1 Criteria and conflict

The designer looking for the optimum design of a structure is faced with the question of selecting the most suitable criteria for measuring the economy, the strength, the serviceability or any other factor that affects the performance of a structure. Any quantity that has a direct influence on the performance of the structure can be considered as a criterion. On the other hand, those quantities that must satisfy some imposed only requirements are not criteria but they can be treated as constraints. Most of the structural optimization problems are treated with one single-objective usually the weight of the structure, subjected to some strength constraints. These constraints are set as equality or inequality constraints using some upper and lower limits. When there is a difficulty in selecting these limits, then these parameters are better treated as criteria.

One important basic property in the multi-criterion formulation is the conflict that may or may not exist between the criteria. Only those quantities that are competing should be treated as independent criteria whereas the others can be combined into a single criterion to represent the whole group. The local conflict between two criteria can be defined as follows: The functions f_i and f_j are called locally collinear with no conflict at point s if there is $c > 0$ such that

$\nabla f_i(\mathbf{s}) = c \nabla f_j(\mathbf{s})$. Otherwise, the functions are called locally conflicting at \mathbf{s} . According to this definition any two criteria are locally conflicting at a point of the design space if their maximum improvement is achieved in different directions. The global conflict between two criteria can be defined as follows: The functions f_i and f_j are called globally conflicting in the feasible region \mathcal{F} of the design space when the two optimization problems $\min_{\mathbf{s} \in \mathcal{F}} f_i(\mathbf{s})$ and $\min_{\mathbf{s} \in \mathcal{F}} f_j(\mathbf{s})$ have different optimal solutions.

4.2 Formulation of a multiple objective optimization problem

In formulating an optimization problem the choice of the design variables, criteria and constraints represents undoubtedly the most important decision made by the engineer. In general the mathematical formulation of a multi-objective problem includes a set of n design variables, a set of m objective functions and a set of k constraint functions and can be defined as follows:

$$\begin{aligned} \min_{\mathbf{s} \in \mathcal{F}} \quad & [f_1(\mathbf{s}), f_2(\mathbf{s}), \dots, f_m(\mathbf{s})]^T \\ \text{subject to} \quad & g_j(\mathbf{s}) \leq 0 \quad j=1, \dots, k \\ & s_i \in \mathbb{R}^d, \quad i=1, \dots, n \end{aligned} \tag{10}$$

where the vector $\mathbf{s} = [s_1 \ s_2 \ \dots \ s_n]^T$ represents a design variable vector and \mathcal{F} is the feasible set in design space \mathbb{R}^n . It is defined as the set of design variables that satisfy the constraint functions $g(\mathbf{s})$ in the form:

$$\mathcal{F} = \{ \mathbf{s} \in \mathbb{R}^n \mid g(\mathbf{s}) \leq 0 \} \tag{11}$$

Usually there exists no unique point which would give an optimum for all m criteria simultaneously. Thus the common optimality condition used in single-objective optimization must be replaced by a new concept the so called Pareto optimum: A design vector $\mathbf{s}^* \in \mathcal{F}$ is Pareto optimal for the problem of Eq. (10) if and only if there exists no other design vector $\mathbf{s} \in \mathcal{F}$ such that:

$$f_i(\mathbf{s}) \leq f_i(\mathbf{s}^*) \text{ for } i = 1, 2, \dots, m \tag{12}$$

with $f_j(\mathbf{s}) < f_j(\mathbf{s}^*)$ for at least one objective j . The solutions of optimization problems with multiple objectives constitute the set of the Pareto optimum solutions. The problem of Eq. (10) can be regarded, as being solved after the set of Pareto optimal solutions has been determined. In practical applications, however, the designer seeks for a unique final solution. Thus a compromise should be made among the available Pareto optimal solutions.

5 METAHEURISTICS

Nature has been solving various problems over millions or even billions of years. Only the best and robust solutions remain based on the principle of the survival of the fittest. Similarly, heuristic algorithms use the trial-and-error, learning and adaptation to solve problems. Modern metaheuristic algorithms are almost guaranteed to an efficient performance for a wide range of combinatorial optimization problems. The main aim of research in optimization and algorithm development is to design and/or choose the most suitable and efficient algorithms for a given optimization problem. In this section metaheuristics based on evolution strategies implemented for solving single-objective and multi-objective optimization problems are presented.

Several methods have been proposed in the past for treating structural multi-objective optimization problems [6, 7]. In this study two algorithms are used in order to handle the two-

objective optimization problem at hand. The first one is based on the nondomination sort genetic algorithm (NSGA) developed by Deb *et al.* [9] while the second one is based on the strength Pareto evolutionary algorithm (SPEA) developed by Zitzler *et al.* [9]. The evolution strategies method has been proved very efficient for solving single objective structural optimization problems [10, 11], therefore ES method is combined with the philosophies of the first two multi-objective optimization methods (NSGA and SPEA). The resulting multi-objective optimization algorithms are denoted as NSES($\mu+/\lambda$) and SPES($\mu+/\lambda$).

5.1 Nondominated Sorting Evolution Strategies (NSES)

The main part of the NSES algorithm is the Fast-Nondomination-Sort procedure according to which a population is sorted in non-dominated fronts and it is based on the work by Deb *et al.* [8]. This algorithm identifies nondominated individuals in the population, at each generation, to form Pareto fronts, based on the concept of nondominance. After this step, the basic operators of ES are implemented. In the ranking procedure, the nondominated individuals in the current population are first identified. Then, these individuals are assumed to constitute the first nondominated front assigning a large dummy fitness value to each one. All these solutions have an equal reproductive potential. In order to maintain population diversity, these nondominated solutions are then shared with their dummy fitness value. Afterward, the individuals of the first front are ignored temporarily, and the rest of the population is processed in the same way to identify individuals for the second nondominated front. They are also assigned a dummy fitness value, which is a little smaller than the worst shared fitness value observed in the solutions of the first nondominated front. This process continues until the whole population is classified into nondominated fronts. Since the nondominated fronts are defined, the population is then reproduced according to the dummy fitness value.

5.2 Strength Pareto Evolution Strategies (SPES)

The basic option of SPES($\mu+/\lambda$) algorithm was proposed in [9] as an approach that incorporates several of the desirable features of other well-known multiobjective evolutionary algorithms. SPES($\mu+/\lambda$) implements elitism through the maintenance of an external set of best solutions found during the whole iteration loop. Elitism, when applied by an evolutionary algorithm, guarantees that the solutions with higher fitness will not be eliminated during the execution of the optimization algorithm. The nondominated solutions in the external set are used to determine the fitness of the current population (set of solutions) and also take part in the selection process for reproduction. In SPES($\mu+/\lambda$), the fitness of a solution in the population depends on the best solutions in the external set but is independent of the number of solutions. This solution dominates, or is dominated, within the population. The most important aspects of this algorithm are the fitness assignments and the clustering procedure. In each iteration, a population of individuals $\mathbf{B}_p^{(g)}$ is obtained, and the nondominated solutions of this population are copied to $\mathbf{A}^{(g)}$ (external population). Next, the solutions of $\mathbf{A}^{(g)}$ that are dominated by other solutions are eliminated, obtaining the front of Pareto of $\mathbf{A}^{(g)}$. In SPES($\mu+/\lambda$), the number of externally stored nondominated solutions is limited to λ . If the number of solutions of the Pareto front is greater than λ , it is necessary to reduce the external population by some means of clustering.

6 NUMERICAL EXAMPLES

For numerical purposes in order to illustrate the efficiency of coupling the aforementioned methods and for testing the efficiency of the ES-based metaheuristics employed for solving

the multi-objective optimization problem, we used the example of Figure 2 that shows crack growth inside a fillet in a structural member. The detailed configuration of the problem can be found in [3]. Four design variables were selected, while Table 1 shows the upper, lower bounds as well as the increment in each step of optimization process. For the multi-objective problem the two objectives considered are: (a) maximum service life (by maximizing the number of fatigue cycles), and (b) minimum weight subjected to specified minimum service life and an upper limit on volume. Two types of constraints are considered: (i) stress and (ii) displacement constraints.

Design Variable	Upper Bound	Lower Bound	Step
b_1	100.0	50.0	1.0
b_2	100.0	50.0	1.0
r_3	30.0	10.0	1.0
t_4	7.0	3.0	0.5

Table 1: Design variables with upper, lower and step. All dimensions in mm.

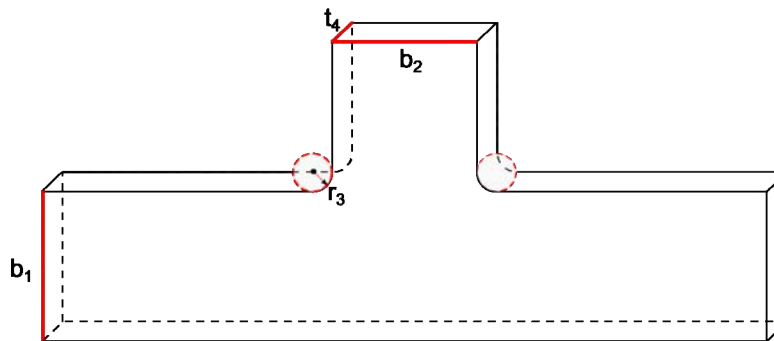
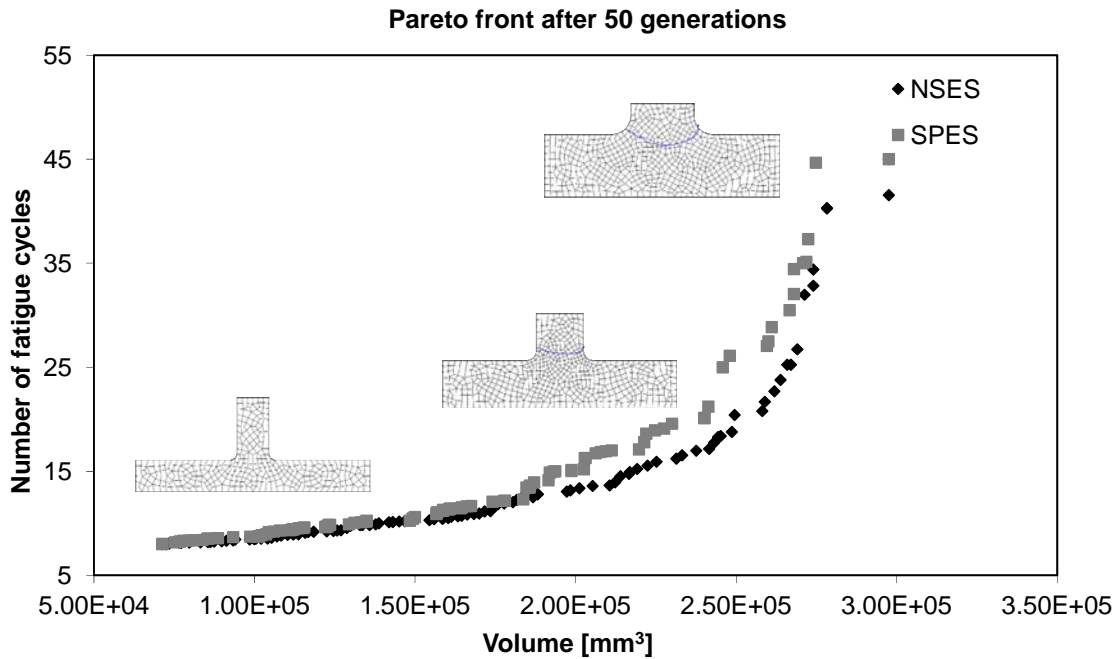
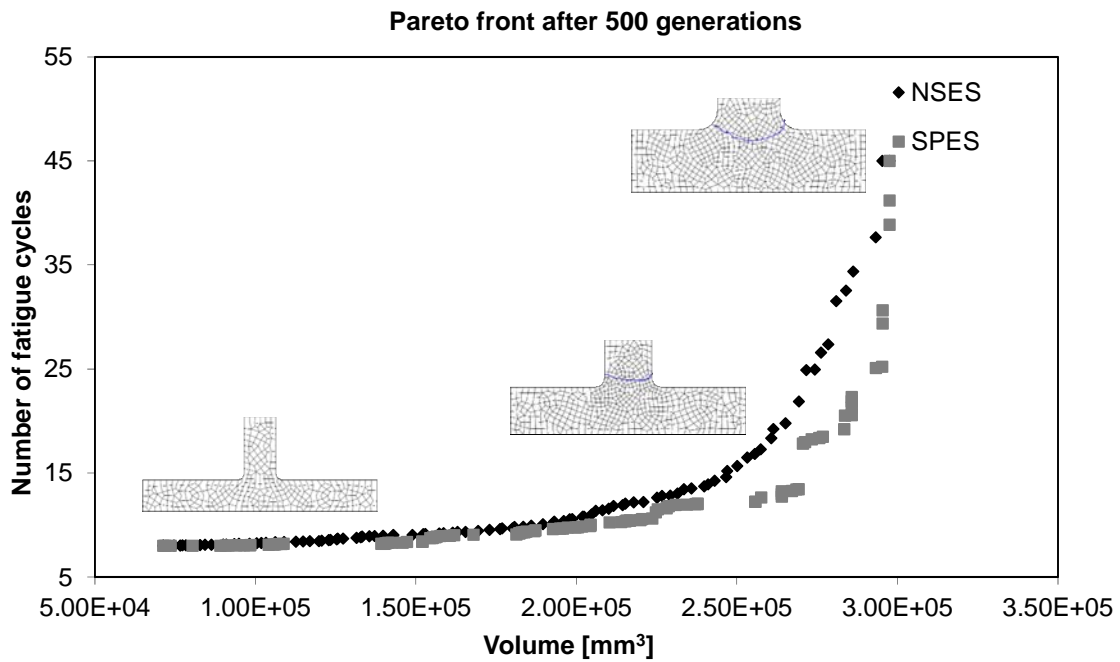


Figure 2: Selected design variables of specimen.

For the multi-objective optimization methods the simple yet effective, multiple linear segment penalty function is used in this study for handling the constraints. According to this technique if no violation is detected, then no penalty is imposed on the objective function. If any of the constraints is violated, a penalty, relative to the maximum degree of constraints' violation, is applied to the objective functions, while the optimization schemes used are NSES(10+10) and SPES(10+10). The resultant Pareto front curve is depicted in Figure 3, with the volume of the structure and the number of fatigue cycles on the horizontal and vertical axis, respectively. The Pareto front curve shows a strong conflict between the two objective functions in question. In order to assess the two methods the Pareto front curves obtained after 50 and 500 generations are compared (see Figures 3(a) and 3(b), respectively). As it can be seen a good quality Pareto front curve is obtained for all three methods. As can be seen, 50 generations are sufficient to obtain a good quality Pareto front curve for both methods adopted.



(a)



(b)

Figure 3: Pareto front curves after: (a) 50 and (b) 500 generations

7 CONCLUSIONS

In this study successful implementation of metaheuristics is presented for solving multi-objective structural shape optimization problem in an extended finite element method framework. Multi-objective evolution strategies based optimization methods in particular the non-

dominated sorting evolution strategies and the strength Pareto evolution strategies methods are used.

Comparing the two algorithms it can be said that evolution strategies based algorithms can be considered as efficient tools for multi-objective design optimization of structural problems such as shape optimization. In terms of computational efficiency it appears that all three methods considered require similar computational effort with approximately the same number of generation steps. In both problems, a large number of solutions need to be found and evaluated in search of the optimum one. The metaheuristics employed in this study have been found efficient in finding an optimized solution, overcoming excessive computational effort, local optima while they are capable dealing with discrete variables when needed.

REFERENCES

- [1] Papadrakakis, M., Tsompanakis, Y., Lagaros, N.D. (1999) Structural shape optimization using Evolution Strategies. *Engineering Optimization Journal*, **31**, 515-540.
- [2] Moës N., Dolbow J., Belytschko T, A finite element method for crack growth without remeshing, *International Journal of Numerical Methods in Engineering*, **46**:131–150, 1999.
- [3] Stolarska M., Chopp D.L., Moës N. and Belytschko T., Modelling crack growth by level sets in the extended finite element method. *International Journal of Numerical Methods in Engineering*, **51**:943–960, 2001.
- [4] Moran B, Shih CF. Crack tip and associated domain integrals from momentum and energy balance. *Engineering Fracture Mechanics*, **27**:615–641, 1987.
- [5] Ramm E., Bletzinger K.-U., Reitering R., Maute K., (1994). The challenge of structural optimization, In *Advances in Structural Optimization*, Topping B.H.V., Papadrakakis M. (Eds), CIVIL-COMP Press, Edinburgh, 27-52.
- [6] Coello Coello, C.A. (2000). An updated survey of GA-based multi-objective optimization techniques. *ACM Computing Surveys*; **32**(2): 109-143.
- [7] Marler, R.T., Arora, J.S. (2004). Survey of multi-objective optimization methods for engineering, *Structural and Multidisciplinary Optimization*; **26**(6): 369-395.
- [8] Deb, K., Pratap, A., Agarwal, S., Meyarivan, T. (2002). A fast and elitist multi-objective genetic algorithm: NSGA-II. *IEEE Transactions on Evolutionary Computation*; **6**(2): 182-197.
- [9] Zitzler E., Laumanns M., Thiele L. (2001). SPEA 2: improving the strength Pareto evolutionary algorithm. In: Giannakoglou K, Tsahalis D, Periaux J, Papailou P, Fogarty T. (Eds.), EUROGEN 2001, evolutionary methods for design, optimization and control with applications to industrial problems, Athens, Greece, 95-100.
- [10] Bäck, T., Schwefel, H-P. (1993). An overview of evolutionary algorithms for parameter optimization, *Journal of Evolutionary Computation*; **1**(1): 1-23.
- [11] Lagaros, N.D., Fragiadakis, M., Papadrakakis, M. (2004). Optimum design of shell structures with stiffening beams. *AIAA Journal*; **42**(1): 175-184.

EVALUATION OF WELDING RESIDUAL STRESS IN STAINLESS STEEL PIPES BY USING THE L_{CR} ULTRASONIC WAVES

Yashar Javadi¹, Vagelis Plevris²

¹Islamic Azad University-Semnan Branch
Semnan, Iran
yasharejavadi@yahoo.com

²Department of Civil & Structural Engineering Educators
School of Pedagogical & Technological Education
Heraklion, GR 141 21, Athens, Greece
vplevris@gmail.com

Keywords: Ultrasonic Stress Measurement; Acoustoelastic Effect; Welding Residual Stress; L_{CR} .

Abstract. *The ultrasonic residual stresses evaluation is based on the acoustoelastic effect that refers to the velocity change of the elastic waves when propagating in a stressed media. The experimental method using the longitudinal critically refracted (L_{CR}) waves requires an acoustoelastic calibration and an accurate measurement of the time-of-flight on both stressed and unstressed media. This paper evaluates welding residual stresses in welded pipe-pipe joint of austenitic stainless steel. The residual stresses in inner and outer surface of pipes were evaluated by L_{CR} ultrasonic waves by using 1 Mhz, 2 Mhz, 4 Mhz and 5 Mhz transducers. It has been shown that the difference in residual stresses between inner and outer surfaces of pipes and also between base metal and welded zone can be inspected by L_{CR} waves.*

1 INTRODUCTION

Residual stresses are present in materials without any external pressure, and normally result from deformation heterogeneities appearing in the material. They have very important role in the strength and service life of structures. Welding is an assembly process often used in different industries, especially in the pressure vessel industry. According to the process and temperatures reached during this operation, dangerous thermo-mechanical stresses may appear in the welded joint. To achieve a proper design of structure and control their mechanical strength in service, it is very important to determine the residual stress levels with a non-destructive method. The high industry request for the stress measurement techniques encouraged development of several methods like X-ray diffraction, incremental hole drilling, and the ultrasonic waves methods. Many studies showed that there is no universal or absolute method that gives complete satisfaction in the non-destructive stress monitoring of the mechanical components. Many parameters such as material, geometry, surface quality, cost, and accuracy of the measurement, etc., must be taken into account in choosing an adequate technique. The ultrasonic technique was selected for stress measurement because it is non-destructive, easy to use, and relatively inexpensive. However, it is slightly sensitive to the microstructure effects (grains size [1], [2], [3], carbon rate [4], [5], texture [6], [7], [8], [9], and structure [10], [11], [12]) and to the operating conditions (temperature [13], [14], coupling [15], [16], etc.). The ultrasonic estimation of the residual stresses requires separation between the microstructure and the acoustoelastic effects.

2 THEORETICAL BACKGROUND

Within the elastic limit, the ultrasonic stress evaluating technique relies on a linear relationship between the stress and the travel time change, i.e. the acoustoelastic effect [17], [18]. The L_{CR} technique uses a special longitudinal bulk wave mode, as shown in Figure 1, which travels parallel to the surface, particularly propagating beneath the surface at a certain depth. The L_{CR} waves are also called surface skimming longitudinal waves (SSLW) by some authors. Brekhovskii [19], Basatskaya and Ermolov [20], Junghans and Bray [21], Langenberg et al. [22] had some detailed discussions on the characteristics of the L_{CR} .

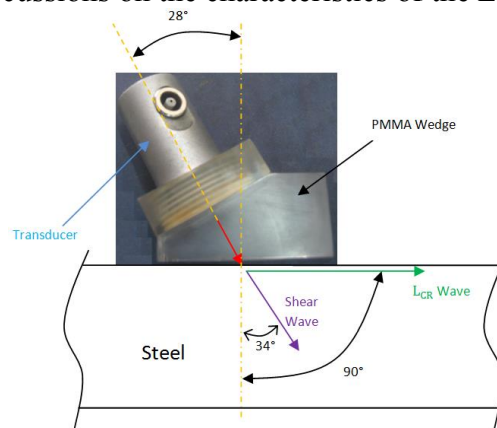


Figure 1: L_{CR} probe for PMMA (Plexiglas) wedge on steel.

Ultrasonic stress measurement techniques are based on the relationship of wave speed in different directions with stress. Figure 2 shows elements of a bar under tension where the ultrasonic wave propagates in three perpendicular directions.

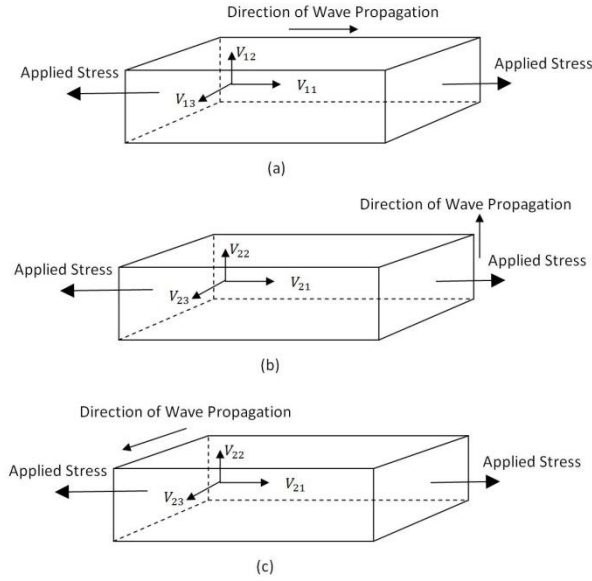


Figure 2: Velocity of plane wave and stress field in orthogonal directions [23].

The first index in the velocities represents the propagation direction for the ultrasonic wave and the second represents the direction of the movement of the particles. In Figure 2a the wave propagates parallel to the load and V_{11} represents the velocity of the particles in the same direction (longitudinal wave), meanwhile V_{12} and V_{13} represents the velocity in a perpendicular plane (shear waves).

In Figure 2b and Figure 2c the waves propagating in the other directions and the velocities are shown. The V_{22} velocity is for longitudinal waves propagating perpendicular to the stress direction. The sensitivity of these waves to the strain has been established by Egle and Bray [17] in tensile and compressive load tests for a bar of rail steel. The waves with particle motion in the direction of the stress fields showed the greatest sensitivity to stress, and those with particle motions perpendicular to the stress field showed the least. The most considerable variation in travel time with the strain was found for longitudinal waves, followed by the shear waves when the particles vibrate in the direction of the load. The other waves do not show significant sensitivity to the strain. The velocities of the longitudinal plane waves traveling parallel to load can be related to the strain (α) by the following expressions:

$$\rho_0 V_{11}^2 = \lambda + 2\mu + (2l + \lambda)\theta + (4m + 4\lambda + 10\mu)\alpha_1 \quad (1)$$

where ρ_0 is the initial density; V_{11} is the velocity of waves in the direction 1 with particle displacement in the direction 1; λ, μ the second order elastic constants (Lame's constants); l, m, n are the third order elastic constants; $\theta = \alpha_1 + \alpha_2 + \alpha_3$ which α_1, α_2 and α_3 are components of the homogeneous triaxial principal strains. For a state of uniaxial stress, $\alpha_1 = \varepsilon$, $\alpha_2 = \alpha_3 = -\nu \varepsilon$, where ε is the strain in the direction 1 and ν is the Poisson's ratio. Using these values, Eq. (1) becomes:

$$\rho_0 V_{11}^2 = \lambda + 2\mu + [4(\lambda + 2\mu) + 2(\mu + 2m) + \nu\mu(1 + \frac{2\lambda}{\mu})]\varepsilon \quad (2)$$

The relative sensitivity is the variation of the velocity with the strain and can be calculated by Eq. (3). In this equation, L_{11} is the dimensionless acoustoelastic constant for L_{CR} waves.

$$\frac{dV_{11}/V_{11}}{d\varepsilon} = 2 + \frac{(\mu + 2m) + \nu\mu(1 + 2l/\lambda)}{\lambda + 2\mu} = L_{11} \quad (3)$$

The values of acoustoelastic constants for the other directions can be obtained in the same way. The variation in the v_{11} velocity, controlled by the coefficient L_{11} , is much greater than the other ones, indicating that these waves are the best candidates to be used in the stress evaluation. Stress can be calculated by the one-dimensional application of the stress–strain relations in elastic solids. Eq. (3) can be rearranged to give the stress variation in terms time-of-flight (dt/t_0), as shown in the Eq. (4), where t_0 is the time for the wave to go through a stress free path in the material being investigated.

$$d\sigma = \frac{E(dV_{11}/V_{11})}{L_{11}} = \frac{E}{L_{11}t_0} dt \quad (4)$$

where $d\sigma$ is the stress variation (MPa) and E is the elasticity modulus (MPa). The same equation can be used for the other directions of the waves, provided the value of the acoustoelastic coefficient L is changed. For a fixed probe distance, the travel time of the longitudinal wave decreases in a compressive stress field and increases in a tensile field. The acoustoelastic constant (L) functionally links the stress and the velocity or travel time change.

3 EXPERIMENTAL PROCEDURES

3.1 Sample Description

The materials tested (TP304L) are commonly used for pressure vessel applications. Two passes butt-weld joint geometry without gap was performed. Two 12inch pipes with thickness of 11 mm and 34 cm length were welded in V-groove (90° included angle). Two rectangular tension test specimens were extracted from A240-TP304L plate with the same thickness and chemical composition of two pipes to determine the acoustoelastic constant.

3.2 Measurement Device

The measurement device, shown in Figure 3, includes an Ultrasonic box with integrated pulser and receiver, computer and three normal transducers assembled on a united wedge. A three-probe arrangement was used, with one sender and two receivers in order to eliminate environment temperature effect to the travel time. Twelve transducers in four different frequencies were used which their nominal frequencies were 1 Mhz, 2 Mhz, 4 Mhz and 5 Mhz. Using different frequencies helps to evaluate residual stresses through the thickness of the pipes. The diameter of all the piezoelectric elements were 6 mm. Transducers was assembled on a united PMMA wedge. The ultrasonic box is a 100 Mhz ultrasonic testing device which has a synchronization between the pulser signal and the internal clock, that controls the A/D converter. This allows very precise measurements of the time of flight – better than 1 ns.

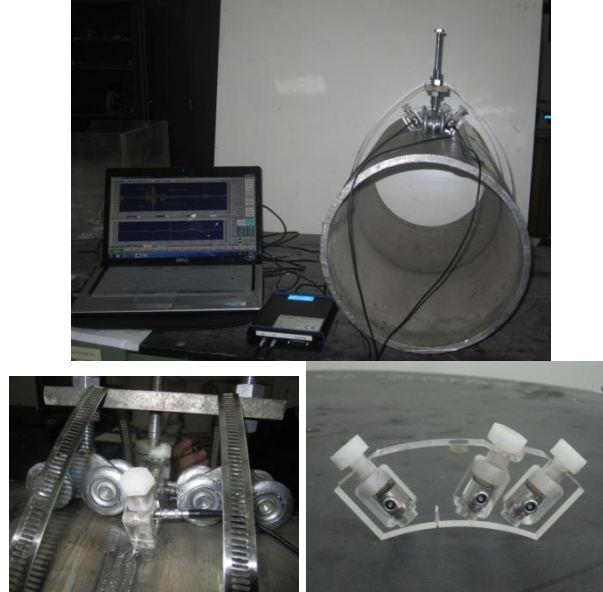


Figure 3: Measurement Devices.

3.3 Determination of L_{CR} Depth

When the L_{CR} technique is applied to an application with limited wall thickness, the depth of the L_{CR} wave penetration is expected to be somehow a function of frequency, with the low frequencies penetrating deeper than the high frequencies. Four different frequencies have been used in this work to evaluate the residual stress through the thickness of the pipes. Therefore depth of any frequencies should be exactly measured. The setup which is shown in Figure 4 is used here to measure the depth of the L_{CR} wave. Two transducers as sender and receiver with the same frequency are used to produce L_{CR} wave. A slot is performed between the transducers by milling tool to cut the L_{CR} wave. The depth of the slot is increased step by step and the amplitude of the L_{CR} wave is measured in each step. When the amplitude of the L_{CR} wave is equal to the noise, milling process is stopped and the depth of slot is announced as the depth of the L_{CR} waves for the tested frequency. The material used here is the same of the welded pipes. The results of this measurement are shown in Table 1. From this table it can be concluded that depth of L_{CR} wave is 5 mm, 2 mm, 1.5 mm and 1mm for transducer with nominal frequencies of 1 Mhz, 2 Mhz, 4 Mhz and 5 Mhz respectively.

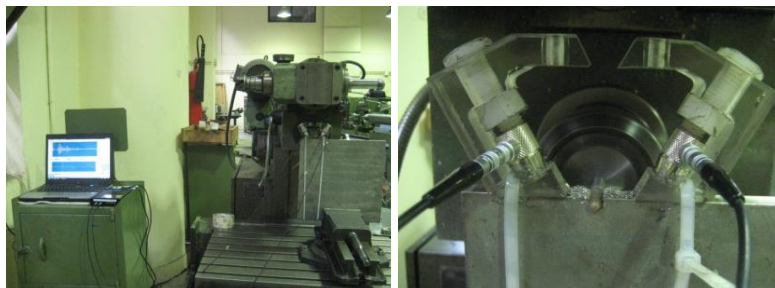
Figure 4: Experimental setup to measure depth of L_{CR} wave.

Table 1. The results of L_{CR} depth measurement

1 Mhz			2 Mhz			4 Mhz			5 Mhz		
D	A	T	D	A	T	D	A	T	D	A	T
0	0.75	13.09	0	0.55	10.91	1	0.35	10.58	1	0.28	10.6
0.5	0.66	13.1	0.5	0.5	10.93	1.5	0.3	10.6	1.5	noise	-
1	0.6	13.14	1	0.42	10.98	2	noise	-			
1.5	0.54	13.18	1.5	0.4	11.02						
2	0.49	13.21	2	0.34	11.06						
2.5	0.47	13.26	2.5	noise	-						
3	0.43	13.29									
3.5	0.42	13.33									
4	0.4	13.37									
4.5	0.33	13.37									
5	0.2	13.37									
5.5	noise	-									

*D: Depth of Machining (mm); A: Amplitude; T: Time of Flight (μ s)

3.4 Evaluation of the Calibration Constants

To evaluate the calibration constants (acoustoelastic constant, free stress time-of-flight), the calibration samples were taken from a stainless steel 304L plate with exactly the same thickness and chemical composition of the pipes. Two rectangular tension test specimens were extracted to determine acoustoelastic constant (L_{11}) with average of the results. To evaluate the residual stress from Eq.(4), the value t_0 is measured directly from the stress-free samples and the acoustoelastic constant is deduced experimentally from a uniaxial tensile test associated with an ultrasonic measurement (Figure 5). Acoustoelastic constant represents the slope of the relative variation curve of the time-of-flight and the applied stress, as shown in Figure 6.

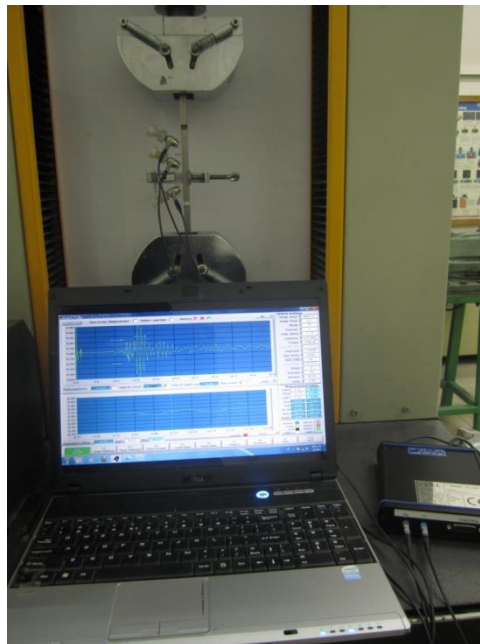


Figure 5: Tensile test to evaluate acoustoelastic constant (L_{11}).

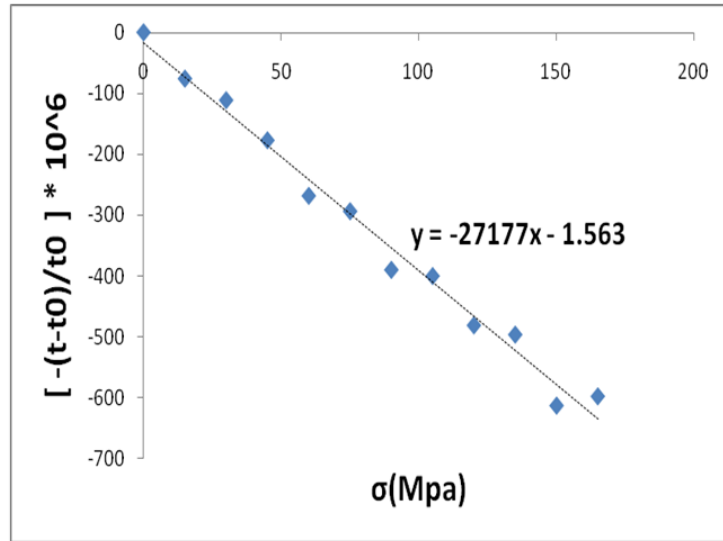


Figure 6: Result of Tensile test to evaluate acoustoelastic constant.

4 RESULTS AND DISCUSSION

In this study, the ultrasonic measurement concerns the residual stresses through the thickness of welded pipes. The measurements were parallel to the weld axis therefore the hoop residual stress of pipes is evaluated. The values of the residual stresses relating to each weld zone were calculated from the equations (1-4) and the results are shown in Figure 7 - Figure 10.

The characteristics of welding residual stress distribution in the stainless pipe are very complex especially for hoop stresses. Hoop residual stresses distribution which is shown in Figure 11-Figure 12 and has been extracted from D. Deng [24] is more popular in the references.

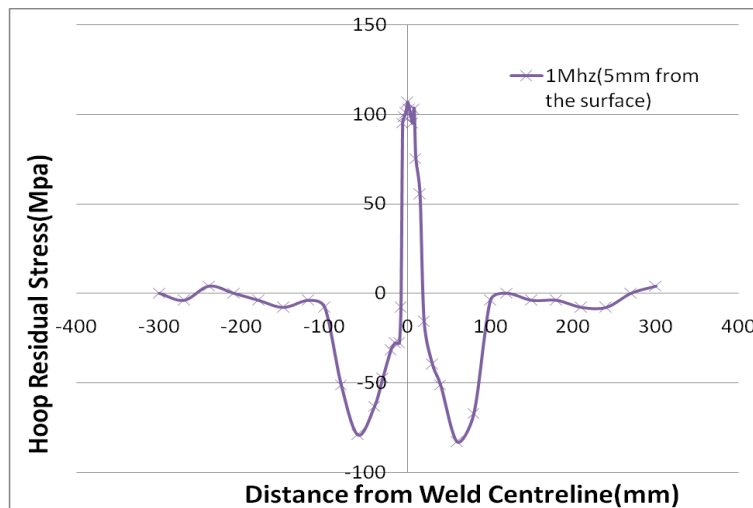


Figure 7: Ultrasonic stress measurement results by 1Mhz LCR wave.

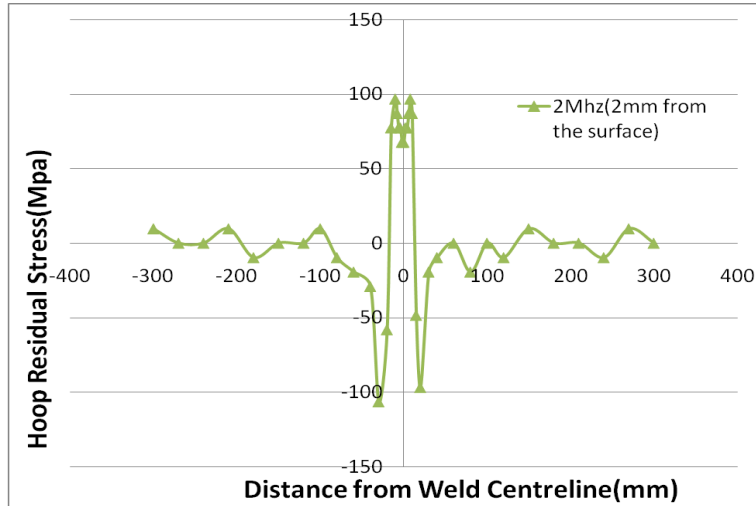


Figure 8: Ultrasonic stress measurement results by 2 Mhz L_{CR} wave.

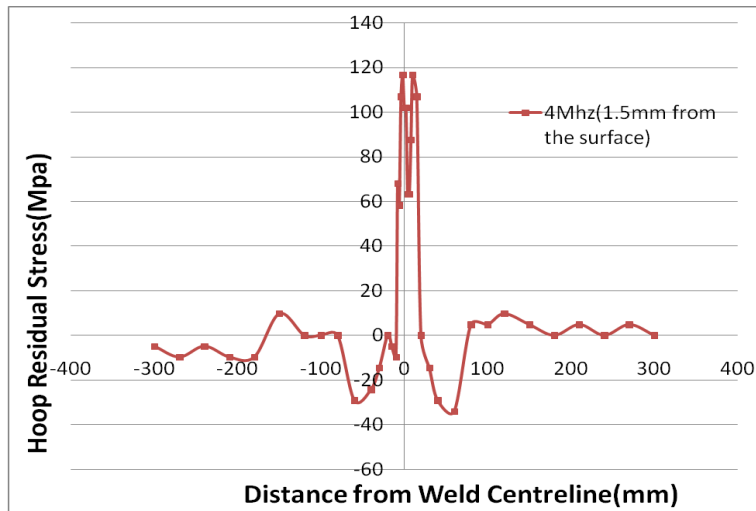


Figure 9: Ultrasonic stress measurement results by 4 Mhz L_{CR} wave.

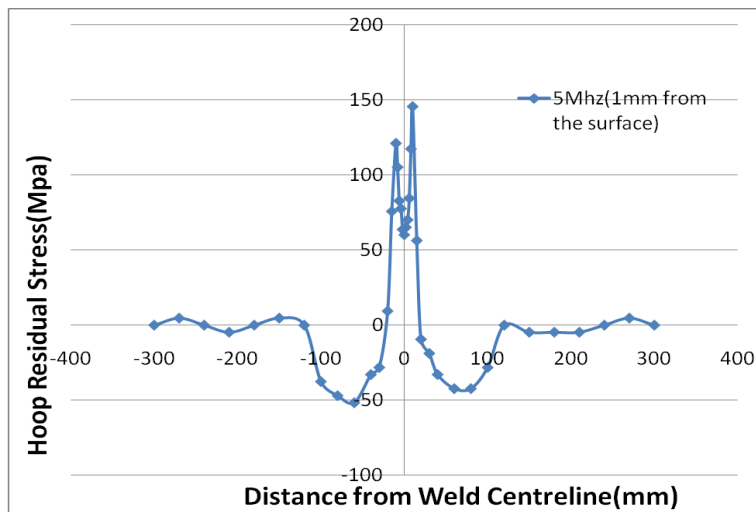


Figure 10: Ultrasonic stress measurement results by 5 Mhz L_{CR} wave.

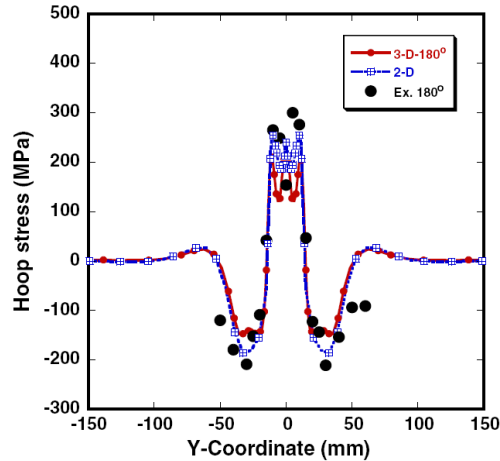


Figure 11: Hoop stress distribution on the inside surface of pipes (extracted from [24]).

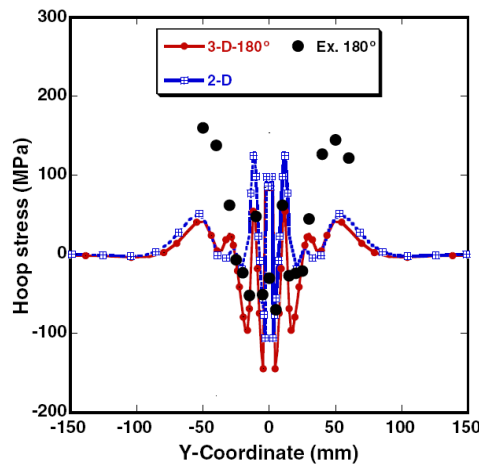


Figure 12: Hoop stress distribution on the outside surface of pipes (extracted from [24]).

Figure 11 shows that, on the inside surface, tensile hoop stresses are generated at the weld zone and its vicinity, and compressive stresses are produced away from the weld centerline [24]. But Figure 12 shows the distribution of the hoop stress on the outside surface is very complex. From the simulation and experiment results of D. Deng [24], it can be found that the shape is “like a wave and very sensitive to the distance from the weld centerline”.

Comparing Figure 11 and Figure 12 with residual stress results of this paper, shows reasonable agreement. It can be noticed that the results of 1 Mhz measurement (which is done in 5mm from the surface) is similar to the average of the inside and outside surfaces of the pipes. Because, the thickness of the pipes is 11 mm and 1 Mhz L_{CR} wave travels in the half of the thickness approximately. Also, it is obvious from Figure 8, Figure 9 and Figure 10 that with increasing the frequency (so decreasing the distance from the surface) residual stress distribution is became more similar to the hoop stress distribution on the outside surface of the pipes. In these frequencies, tensile stress exactly on the weld centerline is less than its vicinity and their difference considerably increase in high frequencies.

Therefore the ultrasonic residual stress measurement used in this paper, is capable of inspecting the welding residual stresses through the thickness of the stainless steel pipes.

5 CONCLUSIONS

This paper confirms the potential of the ultrasonic residual stress measurement in inspecting the welding residual stresses through the thickness of the stainless steel pipes. It has been shown that the hoop residual stress of the pipes is very complex and very sensitive to the distance from the weld centerline on the outside surface of the pipes. Near the surface of the pipes, tensile stress exactly on the weld centerline is less than its vicinity and their difference considerably increase in high frequencies. However, the L_{CR} waves can nondestructively measure the welding residual stresses of pipes.

REFERENCES

- [1] N. Grayli, J.C. Shyne, Effect of microstructure and prior austenite grain size on acoustic velocity and attenuation in steel, *Rev Prog NDE*, 4(B)(1985), pp. 927–936.
- [2] R. Herzer, E. Schneider, Instrument for the automated ultrasonic time-of-flight measurement a tool for materials characterization, Springer, 1989, pp. 673–680.
- [3] P. Palanchamy, A. Joseph, T. Jayakumar, Ultrasonic velocity measurements for estimation of grain size in austenitic stainless steel, *NDT E Int*, 28(1995), pp. 179–185.
- [4] EP. Papadakis, *Physical acoustics and microstructure of iron alloys*, *Int Mater Rev*, 29(1984), pp. 1–24.
- [5] C. Hakan Gür, B. Orkun Tuncer, Nondestructive investigation of the effect of quenching and tempering on medium-carbon low alloy steels, *Int J Microstruct Mater Prop*, 1(2005), pp. 51–60.
- [6] MA. Ploix, R. El Guerjouma, J. Moysan, G. Corneloup, B. Chassignole, *Acoustical characterization of austenitic stainless-steel welds for experimental and modeling*, *NDT. J Soc Adv Sci*, 17(2005), pp. 76–81.
- [7] M. Spies, E. Schneider, Non-destructive analysis of texture in rolled sheets by ultrasonic techniques, *Text Microstruct*, 12(1990), pp. 219–213.
- [8] GC. Johnson, Acoustoelastic response of a polycrystalline aggregate with orthotropic texture, *J Appl Mech*, 52(1985), pp. 659–663.
- [9] CM. Sayers, Ultrasonic velocities in anisotropic polycrystalline aggregates, *J Phys D Appl Phys*, 15(1982), pp. 2157–2167.
- [10] C. Hakan Gür, İ. Çam, Comparison of magnetic Barkhausen noise and ultrasonic velocity measurements for microstructure evaluation of SAE 1040 and SAE 4140 steels, *Materials Charact*, 58(2007), pp. 447–454C.
- [11] YH. Nam, YI. Kim, SH. Nahm, Evaluation of fracture appearance transition temperature to forged 3Cr-1Mo-0.25 V steel using ultrasonic characteristics, *Mater Lett.*, 60(2006), pp. 3577–3581.
- [12] JH. Cantrell, K. Salama, *Acoustoelastic characterization of materials*, *Int Mater Rev*, 36(1991), pp. 125–145.
- [13] K. Salama, Relationship between temperature dependence of ultrasonic velocity and stress, *Quantitative non-destructive evaluation*, 1985, pp. 1109–1119

- [14] H. Mohbacher, E. Schneider, K. Goebbels, *Temperature dependence of third-order elastic constants*, Proc 9th international conference on experimental mechanics, 3(1990), pp. 1189–1197.
- [15] D.I. Crecraft, The measurement of applied and residual stresses in metals using ultrasonic waves, *J Sound Vib.*, 5(1967), pp. 173–192.
- [16] A. Lhémery, P. Calmon, S. Chatillon, N. Gengembre, Modeling of ultrasonic fields radiated by contact transducer in a component of irregular surface, *Ultrasonics*, 40(2002), pp. 231–236.
- [17] D.M. Egle, D.E. Bray, Measurement of acoustoelastic and third order elastic constants for rail steel, *J. Acoust. Soc. Am.*, 60(1976), pp. 741–744.
- [18] D.E. Bray, R.K. Stanley, *Nondestructive Evaluation*, CRC Press, Boca Raton, FL revised edition, 1997.
- [19] L.M. Brekhovskii, *Waves in Layered Media*, Academic Press, 1(1960).
- [20] L.V. Basatskaya, I.N. Ermolov, Theoretical study of ultrasonic longitudinal subsurface waves in solid media, 1980.
- [21] P. Junghans, D.E. Bray, Beam characteristics of high angle longitudinal wave probes, In: R.N. Pangbom, 1991.
- [22] K.J. Langenberg, P. Fellenger, R. Marklein, On the nature of the so-called subsurface longitudinal wave and/or the surface longitudinal ‘creeping’ wave, *Res. Nondest. Eval.*, 2(1990), pp. 59–81.
- [23] D.E. Bray, W. Tang, Evaluation of Stress Gradients in Steel Plates and Bars with the L_{CR} Ultrasonic Wave, *Nuclear Engineering and Design*, 207(2001), pp. 231-240.
- [24] Dean Deng, Hidekazu Murakawa, Numerical simulation of temperature field and residual stress in multi-pass welds in stainlesssteel pipe and comparison with experimental measurements, *Computational Materials Science*, 2005.

ANALYSIS OF THE NONLINEAR STOCHASTIC DYNAMICS OF AN ELASTIC BAR WITH AN ATTACHED END MASS

Americo Cunha Jr^{1 2}, Rubens Sampaio¹

¹Department of Mechanical Engineering
Pontifícia Universidade Católica do Rio de Janeiro
Rua Marquês de São Vicente, 225, Gávea, Rio de Janeiro - RJ, Brasil - 22453-900
email: americo.cunhajr@gmail.com rsampaio@puc-rio.br

²Laboratory of Multi-Scale Modeling and Simulation
Université Paris-Est Marne-la-Vallée
5, Boulevard Descartes 77454, Marne-la-Vallée Cedex 2, France
email: americo@univ-paris-est.fr

Keywords: nonlinear dynamics, stochastic modeling, maximum entropy principle, uncertainty quantification, Monte Carlo method.

Abstract. *This work studies the nonlinear dynamics of a one-dimensional elastic bar, attached to discrete elements, with viscous damping, random elastic modulus, and subjected to a Gaussian white-noise distributed external force. The system analysis uses the maximum entropy principle to specify the elastic modulus (γ) probability distribution and uses Monte Carlo simulations to compute the propagation of uncertainty in this discrete–continuous system. After describing the deterministic and the stochastic modeling of the system, some configurations of the model are analyzed in order to characterize the effect of a lumped mass in the overall behavior of this dynamical system. The simulation results show that the system response presents multimodal probability distribution, irregular distribution of energy throughout the spectrum of frequencies, and a limit behavior, for large values of the lumped mass, similar to a mass-spring system.*

1 INTRODUCTION

The dynamics of a mechanical system depends on some parameters such as physical and geometrical properties, constraints, external and internal loading, initial and boundary conditions. Most of the theoretical models used to describe the behavior of a mechanical system assume nominal values for these parameters, such that the model gives one response for a given particular input. In this case the system is *deterministic* and its behavior is described by a single set of differential equations. However, in real systems they do not have a fixed value since they are subjected to uncertainties of measurement, imperfections in manufacturing processes, change of properties, etc. This variability in the set of system parameters leads to a large number of possible system responses for a given particular input. Now the system is *stochastic* and there is a family of differential equations sets (one for each realization of the random parameters) associated to it.

In order to quantify variability of the responses of mechanical systems which are of interest in engineering applications, several recent works have been applying techniques of stochastic modeling, to take into account the inaccuracies due to model and data uncertainty, and uncertainty quantification, to compute the propagation of incertitude of the random parameters through the system. For instance, the reader can see [14, 11, 10], in the context of drillstring dynamics, as well as the work of [19] in hydraulic fracturing. Other studies applying stochastic techniques to describe the random dynamics of flexible structures are [12, 13] and [3]. The analysis of the stochastic dynamics of a highly nonlinear system, with three degrees of freedom, can be seen in [6]. The readers interested in structures built by heterogeneous hyperelastic materials is encouraged to consult [2]. To see the latest theoretical advances of stochastic modeling in structural dynamics, the reader is encouraged to consult the work of [18].

This work aims to conduct a purely theoretical study of the propagation of uncertainty in the dynamics of a nonlinear continuous random system with discrete elements attached to it. This theoretical study aims to illustrate a consistent methodology to analyze the stochastic dynamics of nonlinear mechanical systems. In this sense, this work considers a one-dimensional elastic bar, with random elastic modulus, fixed on the left extreme and with a lumped mass and two springs (one linear and another nonlinear) on the right extreme (fixed-mass-spring bar), subjected to an external force which is proportional to a Gaussian white-noise.

This paper is an extension of work done in [3, 4], which includes additional results and a deeper analysis of the original results. It is organized as follows. Section 2 presents the deterministic modeling of the problem, the discretization procedure and the algorithm used to solve the equation of interest. The stochastic modeling of the problem is shown in section 3, as well as the construction of a probability distribution for the elastic modulus, using the maximum entropy principle, and a brief discussion on the Monte Carlo method. In section 4, some configurations of the model are analyzed in order to characterize the effect of lumped mass in the system dynamical behavior. Finally, in section 5, the main conclusions are emphasized.

2 DETERMINISTIC APPROACH

The system of interest in this study case is the elastic bar fixed at a rigid wall, on the left side, and attached to a lumped mass and two springs (one linear and one nonlinear), on the right side, such as illustrated in Figure 1. From now on, the fixed-mass-spring bar.

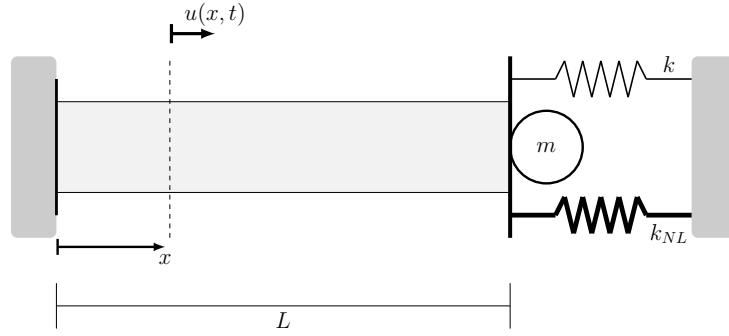


Figure 1: Sketch of a bar fixed at one and attached to two springs and a lumped mass on the other extreme.

2.1 Strong Formulation

The physical quantity of interest is the bar is its displacement field u , which depends on the position x and the time t , and evolves, for all $(x, t) \in (0, L) \times (0, T)$, according to the following partial differential equation

$$\rho A \frac{\partial^2 u}{\partial t^2} + c \frac{\partial u}{\partial t} - \frac{\partial}{\partial x} \left(EA \frac{\partial u}{\partial x} \right) + \left(ku + k_{NL}u^3 + m \frac{\partial^2 u}{\partial t^2} \right) \delta(x - L) = f(x, t), \quad (1)$$

where ρ is mass density, A is the cross section area, c is the damping coefficient, E is the elastic modulus, k is the stiffness of the linear spring, k_{NL} is the stiffness of the nonlinear spring, m is the lumped mass, and f is a distributed external force, which depends on x and t . The symbol $\delta(x - L)$ denotes the delta of Dirac distribution at $x = L$.

The boundary conditions for this problem are given by

$$u(0, t) = 0, \quad \text{and} \quad EA \frac{\partial u}{\partial x}(L, t) = 0. \quad (2)$$

The initial position and the initial velocity of the bar are respectively given by

$$u(x, 0) = u_0(x), \quad \text{and} \quad \frac{\partial u}{\partial t}(x, 0) = v_0(x), \quad (3)$$

where u_0 and v_0 are known functions of x , defined for $0 \leq x \leq L$.

Moreover, it is noteworthy that u is assumed to be as regular as needed for the initial-boundary value problem of Eqs.(1), (2), and (3) to be well posed.

2.2 Weak Formulation

Let \mathcal{U}_t be the class of (time dependent) basis functions and \mathcal{W} be the class of weight functions. These sets are chosen as the space of functions with square integrable spatial derivative, which satisfy the essential boundary condition defined by Eq.(2).

The weak formulation of the problem under study says that one wants to find $u \in \mathcal{U}_t$ that satisfy, for all $w \in \mathcal{W}$, the weak equation of motion given by

$$\mathcal{M}(\ddot{u}, w) + \mathcal{C}(\dot{u}, w) + \mathcal{K}(u, w) = \mathcal{F}(w) + \mathcal{F}_{NL}(u, w), \quad (4)$$

where \mathcal{M} is the mass operator, \mathcal{C} is the damping operator, \mathcal{K} is the stiffness operator, \mathcal{F} is the distributed external force operator, and \mathcal{F}_{NL} is the nonlinear force operator. These operators are, respectively, defined as

$$\mathcal{M}(\ddot{u}, w) = \int_0^L \rho A \ddot{u}(x, t) w(x) dx + m \ddot{u}(L, t) w(L), \quad (5)$$

$$\mathcal{C}(\dot{u}, w) = \int_0^L c \dot{u}(x, t) w(x) dx, \quad (6)$$

$$\mathcal{K}(u, w) = \int_0^L E A u'(x, t) w'(x) dx + k u(L, t) w(L), \quad (7)$$

$$\mathcal{F}(w) = \int_0^L f(x, t) w(x) dx, \quad (8)$$

$$\mathcal{F}_{NL}(u, w) = -k_{NL} (u(L, t))^3 w(L), \quad (9)$$

where $\dot{\cdot}$ is an abbreviation for temporal derivative and $'$ is an abbreviation for spatial derivative.

The weak formulations for the initial conditions of Eq.(3), which are valid for all $w \in \mathcal{W}$, are respectively given by

$$\widetilde{\mathcal{M}}(u(\cdot, 0), w) = \widetilde{\mathcal{M}}(u_0, w), \quad (10)$$

and

$$\widetilde{\mathcal{M}}(\dot{u}(\cdot, 0), w) = \widetilde{\mathcal{M}}(v_0, w), \quad (11)$$

where $\widetilde{\mathcal{M}}$ is the associated mass operator, defined as

$$\widetilde{\mathcal{M}}(u, w) = \int_0^L \rho A u(x, t) w(x) dx. \quad (12)$$

2.3 Galerkin Formulation

To approximate the solution of the variational problem given by Eqs.(4) to (11), the Galerkin method [5] is employed, which approximates the displacement field u by a linear combination of the form

$$u(x, t) \approx \sum_{n=1}^N u_n(t) \phi_n(x), \quad (13)$$

where the basis functions ϕ_n are the orthogonal modes of the conservative and non-forced dynamical system associated to the fixed-mass-spring bar, and the coefficients u_n are time-dependent functions. This results in the following system of ordinary differential equations

$$[M] \ddot{\mathbf{u}}(t) + [C] \dot{\mathbf{u}}(t) + [K] \mathbf{u}(t) = \mathbf{f}(t) + \mathbf{f}_{NL}(\dot{\mathbf{u}}(t)), \quad (14)$$

supplemented by the following pair of initial conditions

$$\mathbf{u}(0) = \mathbf{u}_0 \quad \text{and} \quad \dot{\mathbf{u}}(0) = \mathbf{v}_0, \quad (15)$$

where $\mathbf{u}(t)$ is the vector of \mathbb{R}^N in which the n -th component is the $u_n(t)$, $[M]$ is the mass matrix, $[C]$ is the damping matrix, $[K]$ is the stiffness matrix. Also, $\mathbf{f}(t)$, $\mathbf{f}_{NL}(\mathbf{u}(t))$, \mathbf{u}_0 , and \mathbf{v}_0 are vectors of \mathbb{R}^N , which respectively represent the external force, the nonlinear force, the initial position, and the initial velocity. The initial value problem of Eqs.(14) and (15) has its solution approximated by Newmark method [5].

3 STOCHASTIC APPROACH

3.1 Probabilistic Model

Consider a probability space $(\Theta, \mathbb{A}, \mathbb{P})$, where Θ is sample space, \mathbb{A} is a σ -field over Θ and \mathbb{P} is a probability measure. In this probabilistic space, the elastic modulus is assumed to be a random variable $E : \Theta \rightarrow \mathbb{R}$ that associates to each event $\theta \in \Theta$ a real number $E(\theta)$. Also, the distributed external force acting on the system is given by the random field $F : [0, L] \times [0, T] \times \Theta \rightarrow \mathbb{R}$ such that

$$F(x, t, \theta) = \sigma \phi_1(x) N(t, \theta), \quad (16)$$

where σ is the force amplitude, and $N(t, \theta)$ is a Gaussian white-noise with zero mean and unit variance. A white-noise is a random process which all instants of time are uncorrelated. In other words, the behavior of the process at any given instant of time has no influence on the other instants. A typical realization of the random external force, given by Eq.(16), for fixed position, is shown in Figure 2.

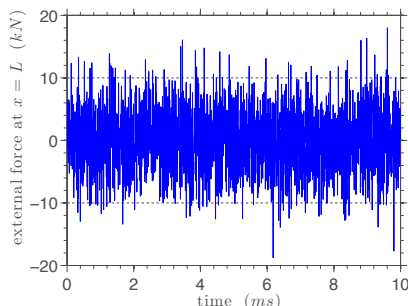


Figure 2: This figure illustrates a realization of the random external force.

3.2 Elastic Modulus Distribution

The elastic modulus cannot be negative, so it is reasonable to assume the support of random variable E as the interval $(0, \infty)$. Therefore, the probability density function (PDF) of E is a nonnegative function $p_E : (0, \infty) \rightarrow \mathbb{R}$, which respects the following normalization condition

$$\int_0^{\infty} p_E(\xi) d\xi = 1. \quad (17)$$

Also, the mean value of E is known real number μ_E , i.e.,

$$\mathbb{E}[E] = \mu_E, \quad (18)$$

where the expected value operator of E is defined as

$$\mathbb{E}[E] = \int_0^\infty E(\xi)p_E(\xi)d\xi \tag{19}$$

Finally, one also wants E to have a finite variance, i.e.,

$$\mathbb{E}[(E - \mu_E)^2] < \infty, \tag{20}$$

which is possible [17], for example, if

$$\mathbb{E}[\ln(E)] < \infty. \tag{21}$$

Following the suggestion of [17], the maximum entropy principle is employed in order to consistently specify p_E . This methodology chooses for E the PDF which maximizes the differential entropy function, defined by

$$\mathbb{S}[p_E] = - \int_0^\infty p_E(\xi) \ln(p_E(\xi)) d\xi, \tag{22}$$

subjected to (17), (18), and (21), the restrictions that effectively define the known information about E .

Respecting the constraints imposed by (17), (18), and (21), the PDF that maximizes Eq.(22) is given by

$$p_E(\xi) = \mathbb{1}_{(0,\infty)} \frac{1}{\mu_E} \left(\frac{1}{\delta_E^2}\right)^{\left(\frac{1}{\delta_E^2}\right)} \frac{1}{\Gamma(1/\delta_E^2)} \left(\frac{\xi}{\mu_E}\right)^{\left(\frac{1}{\delta_E^2} - 1\right)} \exp\left(-\frac{\xi}{\delta_E^2 \mu_E}\right), \tag{23}$$

where $\mathbb{1}_{(0,\infty)}$ denotes the indicator function of the interval $(0, \infty)$, δ_E is the dispersion factor of E , and Γ indicates the gamma function. This PDF characterizes a gamma distribution.

3.3 Stochastic Equation of Motion

As a consequence of the randomness of F and E , the displacement of the bar becomes a random field $U : [0, L] \times [0, T] \times \Theta \rightarrow \mathbb{R}$, which evolves according the following stochastic partial differential equation

$$\rho A \frac{\partial^2 U}{\partial t^2} + c \frac{\partial U}{\partial t} - \frac{\partial}{\partial x} \left(EA \frac{\partial U}{\partial x} \right) + \left(kU + k_{NL}U^3 + m \frac{\partial^2 U}{\partial t^2} \right) \delta(x - L) = F(x, t, \theta), \tag{24}$$

being the partial derivatives now defined in the mean square sense [9]. This problem has boundary and initial conditions similar to those defined in Eqs.(2) and (3), by changing u for U only.

3.4 Stochastic Solver: Monte Carlo Method

Uncertainty propagation in the stochastic dynamics of the discrete–continuous system under study is computed by Monte Carlo (MC) method [7, 16, 15]. This stochastic solver uses a Mersenne twister pseudorandom number generator [8], to obtain many realizations of E and F . Each one of these realizations defines a new Eq.(4), so that a new weak problem is obtained. After that, these new weak problems are solved deterministically, such as in section 2.3. All the MC simulations reported in this work use 4096 samples to access the random system.

4 NUMERICAL EXPERIMENTS

The numerical experiments presented in this section adopt the following deterministic parameters for the studied system: $\rho = 7900 \text{ kg/m}^3$, $c = 5 \text{ kNs/m}$, $A = 625\pi \text{ mm}^2$, $k = 650 \text{ N/m}$, $k_{NL} = 650 \times 10^{13} \text{ N/m}^3$, $L = 1 \text{ m}$, $\sigma = 5 \text{ kN}$ and $T = 10 \text{ ms}$. The random variable E , is characterized by $\mu_E = 203 \text{ GPa}$ and $\delta_E = 10\%$. The initial conditions for displacement and velocity are respectively given by

$$u_0(x) = \alpha_1 \phi_3(x) + \alpha_2 x, \quad \text{and} \quad v_0(x) = 0, \quad (25)$$

where $\alpha_1 = 0.1 \text{ mm}$ and $\alpha_2 = 0.5 \times 10^{-3}$. Note that u_0 reaches the maximum value at $x = L$. This function is used to “activate” the spring cubic nonlinearity, which depends on the displacement at $x = L$. A parametric study, with $m^* = 0.1, 1, 10, 50$, is performed to investigate the effect of the end mass on the bar dynamics, where the discrete–continuous mass ratio is defined as

$$m^* = \frac{m}{\rho AL}. \quad (26)$$

4.1 Displacement, Velocity, and Phase Space

The mean value of displacement $U(L, \cdot, \cdot)$ and an envelope of reliability, wherein a realization of the stochastic system has 98% of probability of being contained, are shown, for different values of m^* , in Figure 3. By observing this figure one can note that, as the value of lumped mass increases, the decay of the system displacement amplitude decreases significantly. This indicates that this system is not much influenced by damping for large values of m^* .

Furthermore, for all values of m^* , the amplitude of the confidence interval increases with time. This indicates that the uncertainty of the system is greater in the stationary regime. This greater uncertainty in the stationary response of the system is due to white-noise forcing. As the initial conditions do not affect the steady state, the response in this regime is subjected to greater variability. This statement can also be checked if the reader look at Figure 4, which shows information similar to the one presented in Figure 3, but now for velocity $\dot{U}(L, \cdot, \cdot)$.

The mean phase space of the fixed-mass-spring bar at $x = L$ is shown, for different values of m^* , in Figure 5. The observation made in the previous paragraphs can be confirmed by analyzing this figure, since the system mean orbit tends from a stable focus to an ellipse as m^* increases. In other words, the limiting behavior of the system when $m^* \rightarrow \infty$ is a mass-spring system.

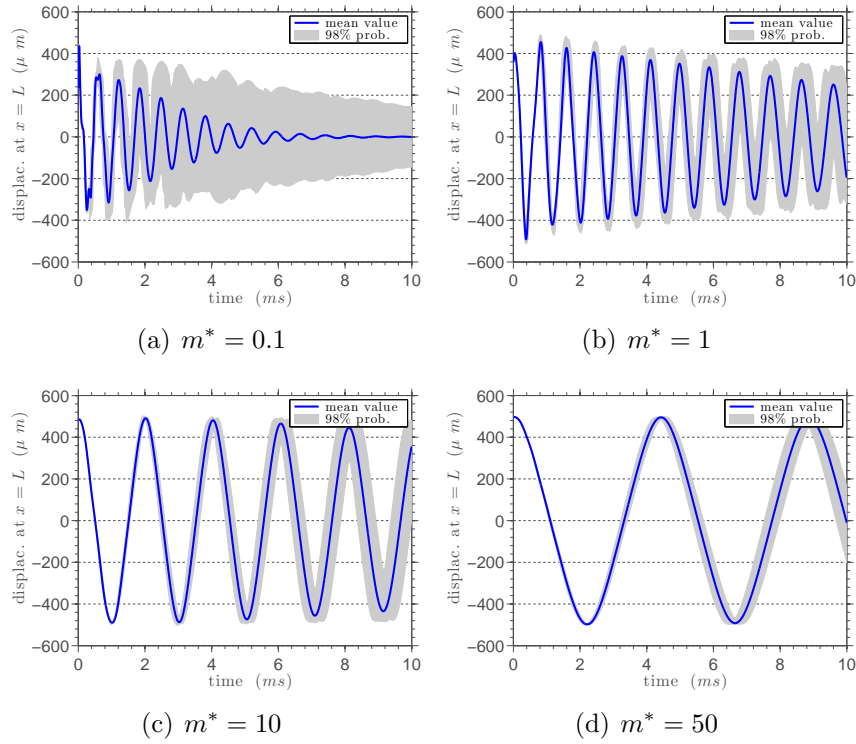


Figure 3: This figure illustrates the mean value (blue line) and a 98% of probability interval of confidence (grey shadow) for the random process $U(L, \cdot, \cdot)$, for several values of the discrete–continuous mass ratio.

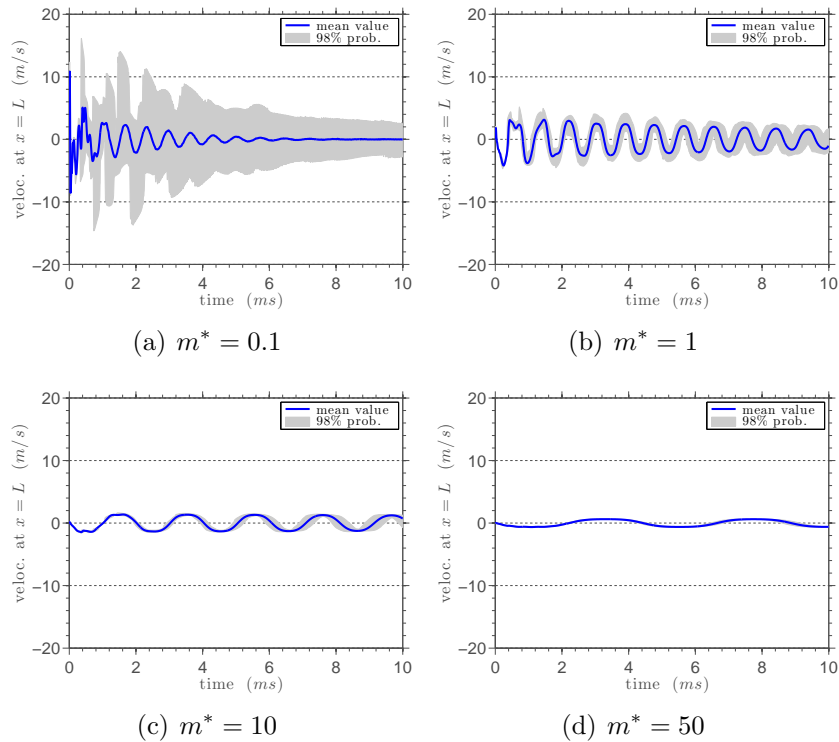


Figure 4: This figure illustrates the mean value (blue line) and a 98% of probability interval of confidence (grey shadow) for the random process $\dot{U}(L, \cdot, \cdot)$, for several values of the discrete–continuous mass ratio.

This limit behavior, which tends to a conservative system, occurs because, with the increasing of m^* , most of the mass of the system becomes concentrated at the right extreme of the bar. Thus, the bar behaves like a massless spring. Also, as the damping is distributed along the bar and the mass of it became negligible, the viscous dissipation becomes ineffective.

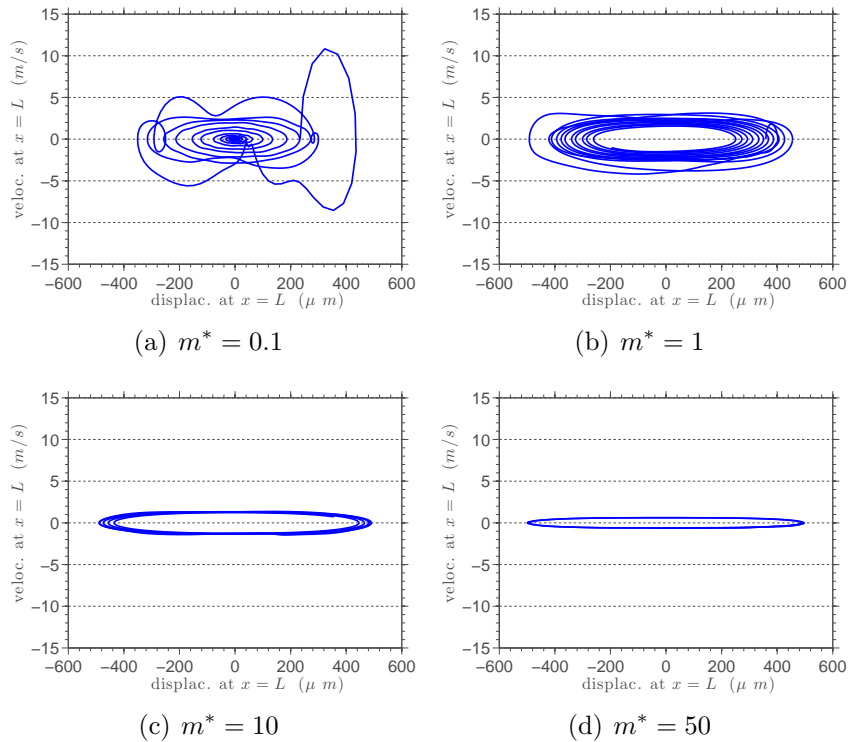


Figure 5: This figure illustrates the mean value of the fixed-mass-spring bar phase space at $x = L$, for several values of the discrete–continuous mass ratio.

4.2 Probability Density Function

The difference between the system dynamical behavior, for different values of m^* , is even clearer if one looks to the PDF estimations¹ of the normalized² random variable $U(L, T, \cdot)$, which are presented in Figure 6.

For $m^* = 0.1$, the distribution is approximately symmetric around the mean, with three modes. The central mode slightly displaced to the left of the mean. The other two modes are symmetrical around the first mode. This symmetry implies in a symmetrical behavior around the mean for the displacement at $(x, t) = (L, T)$, that can be observed in Figure 3.

On the other hand, when $m^* = 1$ or 10 the distribution still is multimodal, however asymmetrical around the mean. This asymmetry implies that the most frequent value of the realizations is not the mean value. Note in the Figure 3 that the displacements are not uniformly distributed around the mean.

¹ These estimates were obtained using a kernel smooth density technique [1].

² In this context normalized means a random variable with zero mean and unit standard deviation.

Furthermore, it can be noted that, when $m^* = 50$, the distribution is unimodal and approximately symmetrical around the mean. Thus, the greatest probability occurs around the mean value of $U(L, T, \cdot)$. Thus, the dispersion around the mean is very small, which can be verified in the confidence interval shown in Figure 3.

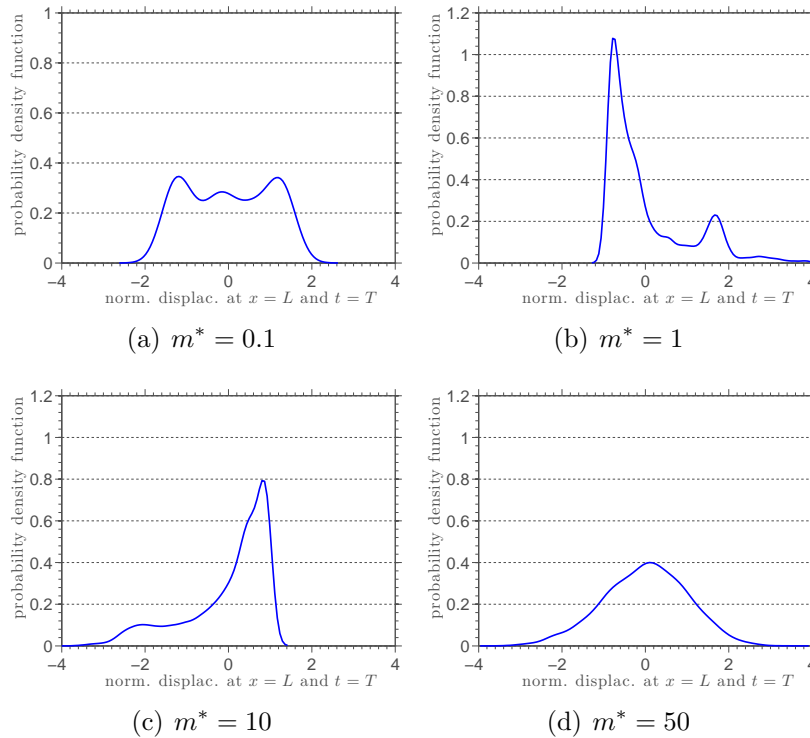


Figure 6: This figure illustrates estimations to the PDF of the (normalized) random variable $U(L, T, \cdot)$, for several values of the discrete–continuous mass ratio.

4.3 Power Spectral Density

The energy distribution of the bar through the frequency spectrum can be seen in Figure 7, which shows the power spectral density (PSD) function of the bar velocity at $x = L$.

It may be noted that, when the value of m^* is changed, the energy is irregularly redistributed along the spectrum of frequencies. This behavior can be explained by the presence of the spring cubic nonlinearity, and by the white-noise forcing, that excites the mechanical system at all frequencies of the spectrum.

Also, it can be noted that, large values of m^* have a greater number of peaks in higher frequencies. However, in all cases analyzed, the peaks with greater height, and thus, the more energy, appears at the lower frequencies of the spectrum.

5 CONCLUDING REMARKS

This work presents a model to describe the nonlinear dynamics of an elastic bar, attached to discrete elements, with viscous damping, random elastic modulus, and subjected to a Gaussian white-noise distributed external force. The elastic modulus is modeled as a random variable with gamma distribution, being the probability distribution of this parameter obtained by the use of the maximum entropy principle.

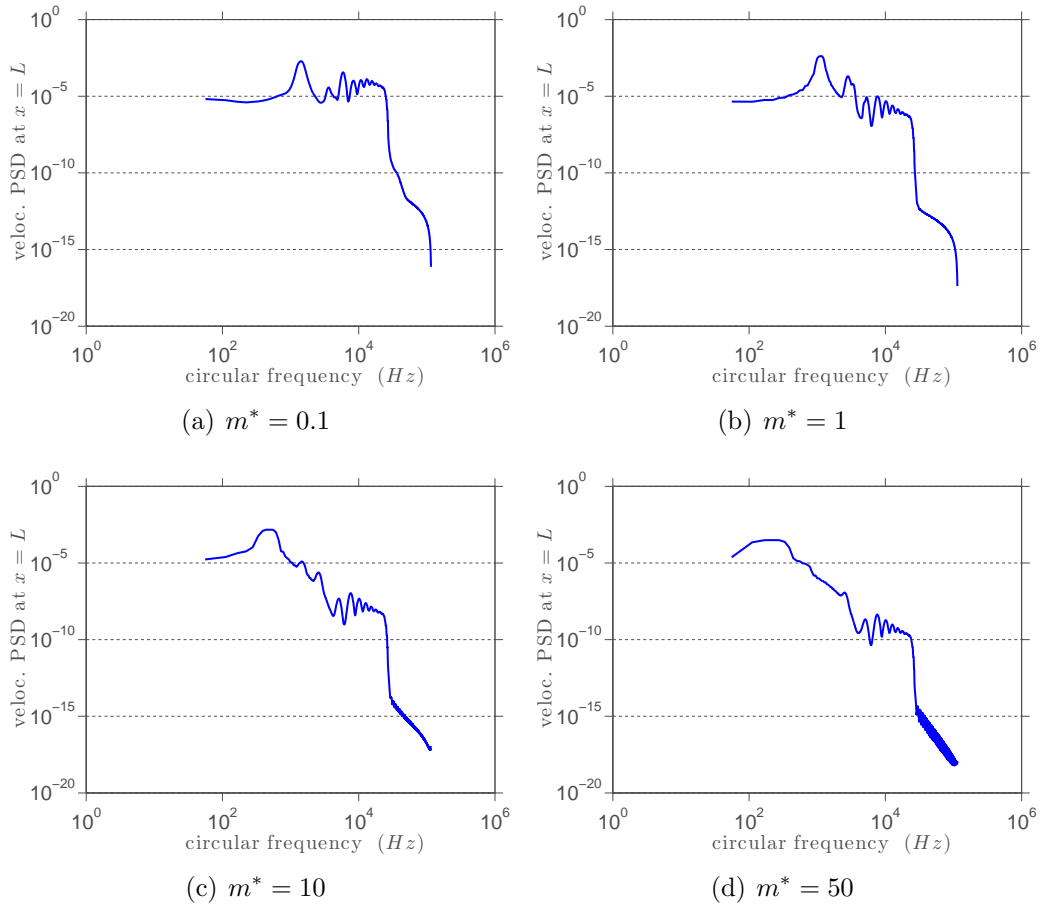


Figure 7: This figure illustrates estimations to the PSD of the random process $\dot{U}(L, \cdot, \cdot)$, for several values of the discrete–continuous mass ratio.

Several configurations of the model are analyzed in to order to characterize the effect of the lumped mass in the overall behavior of the random dynamical system. This analysis shows that the dynamics of the random system is significantly altered when the values of the lumped mass are varied. It is observed that this system behaves, in the limiting case where the lumped mass is very large, such as a spring mass system. Furthermore, it can be noticed probability distributions for the bar displacement with multimodal behavior, and an irregular redistribution of energy in the power spectrum of velocity.

ACKNOWLEDGMENTS

The authors are indebted to Brazilian Council for Scientific and Technological Development (CNPq), Coordination of Improvement of Higher Education Personnel (CAPES), and Foundation for Research Support in Rio de Janeiro State (FAPERJ) for the financial support given to this research.

REFERENCES

- [1] A. W. Bowman and A. Azzalini. *Applied Smoothing Techniques for Data Analysis*. Oxford University Press, New York, 1997.
- [2] A. Clément, C. Soize, and J. Yvonnet. Uncertainty quantification in computational

- stochastic multiscale analysis of nonlinear elastic materials. *Computer Methods in Applied Mechanics and Engineering*, 254:61–82, 2013.
- [3] A. Cunha Jr and R. Sampaio. Effect of an attached end mass in the dynamics of uncertainty nonlinear continuous random system. *Mecánica Computacional*, 31:2673–2683, 2012.
- [4] A. Cunha Jr and R. Sampaio. Uncertainty propagation in the dynamics of a nonlinear random bar. In *Proceedings of the XV International Symposium on Dynamic Problems of Mechanics*, 2013.
- [5] T. J. R. Hughes. *The Finite Element Method*. Dover Publications, New York, 2000.
- [6] R. Q. Lima and R. Sampaio. Stochastic analysis of an electromechanical coupled system with embarked mass. *Mecánica Computacional*, 31:2783–2800, 2012.
- [7] Jun S. Liu. *Monte Carlo Strategies in Scientific Computing*. Springer, New York, 2001.
- [8] M. Matsumoto and T. Nishimura. Mersenne twister: a 623-dimensionally equidistributed uniform pseudo-random number generator. *ACM Transactions on Modeling and Computer Simulation*, 8:3–30, 1998.
- [9] A. Papoulis and S. U. Pillai. *Probability, Random Variables and Stochastic Processes*. McGraw-Hill, New- York, 4th edition, 2002.
- [10] T. G. Ritto, M. R. Escalante, R. Sampaio, and M. B. Rosales. Drill-string horizontal dynamics with uncertainty on the frictional force. *Journal of Sound and Vibration*, 332:145–153, 2013.
- [11] T. G. Ritto and R. Sampaio. Stochastic drill-string dynamics with uncertainty on the imposed speed and on the bit-rock parameters. *International Journal for Uncertainty Quantification*, 2:111–124, 2012.
- [12] T. G. Ritto, R. Sampaio, and E. Cataldo. Timoshenko beam with uncertainty on the boundary conditions. *Journal of the Brazilian Society of Mechanical Sciences and Engineering*, 30:295–303, 2008.
- [13] T. G. Ritto, R. Sampaio, and F. Rochinha. Model uncertainties of flexible structures vibrations induced by internal flows. *Journal of the Brazilian Society of Mechanical Sciences and Engineering*, 33:373–380, 2011.
- [14] T. G. Ritto, C. Soize, and R. Sampaio. Non-linear dynamics of a drill-string with uncertain model of the bit rock interaction. *International Journal of Non-Linear Mechanics*, 44:865–876, 2009.
- [15] C. P. Robert and G. Casella. *Monte Carlo Statistical Methods*. Springer, New York, 2010.
- [16] R. W. Shonkwiler and F. Mendivil. *Explorations in Monte Carlo Methods*. Springer, New York, 2009.

- [17] C. Soize. A nonparametric model of random uncertainties for reduced matrix models in structural dynamics. *Probabilistic Engineering Mechanics*, 15:277 – 294, 2000.
- [18] C. Soize. Stochastic modeling of uncertainties in computational structural dynamics - recent theoretical advances. *Journal of Sound and Vibration*, 332:2379—2395, 2013.
- [19] S. Zio and F. Rochinha. A stochastic collocation approach for uncertainty quantification in hydraulic fracture numerical simulation. *International Journal for Uncertainty Quantification*, 2:145–160, 2012.

SEECM III
Proceedings of the
3rd South-East European Conference on Computational Mechanics

M. Papadrakakis, M. Kojic, I. Tuncer (Eds)

First Edition, February 2014

ISBN: **978-960-99994-4-1**



Institute of Structural Analysis and Antiseismic Research
National Technical University of Athens, Greece